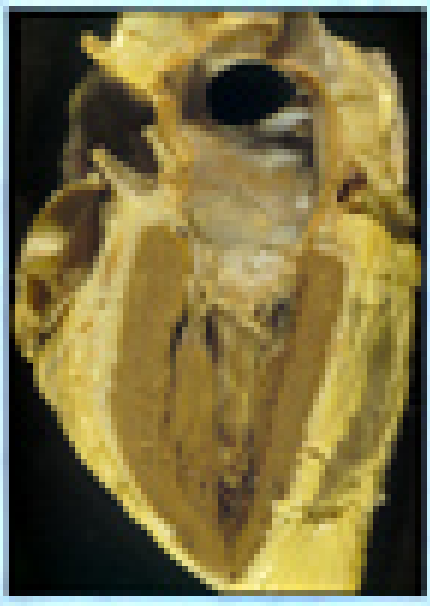

Atlas of Gross Pathology

with Histologic Correlation

ALAN G. ROSE

CAMBRIDGE Medicine

CAMBRIDGE www.cambridge.org/9780521868792

This page intentionally left blank

ATLAS OF GROSS PATHOLOGY

Detailed understanding of gross pathology is mandatory for successful pathologists, but this knowledge also provides a sound foundation for those intending to become surgeons, internists, and obstetrician/gynecologists. Some knowledge of gross pathology is important for members of the allied health professions and dental students. For pathologists, pathology residents, and pathology assistants, knowledge of gross pathology is essential for guidance in selecting the correct areas of pathologic lesions to sample for microscopy and frozen section examination. This atlas aims to provide a comprehensive illustration and description of a wide range and number of pathologic processes and diseases affecting all the major organs of the body. Emphasis is placed on how the anatomic structure of different organs may determine the pattern of involvement by disease processes and how such patterns may aid in the correct diagnosis of the gross pathology. In some cases, multiple illustrations of disease processes are given to show evolution of the disease. Histologic illustrations of selected gross lesions are also included where relevant. The atlas is illustrated with more than 1,200 color photographs.

Dr. Alan G. Rose, MD, FRCPath, FACC, is Professor of Pathology at the University of Minnesota Medical School. He is also the Director of Autopsy Service at the University of Minnesota Medical Center, Fairview; the Residency and Fellowship Training Program; and the Medical School Pathology Teaching Program at the University of Minnesota.

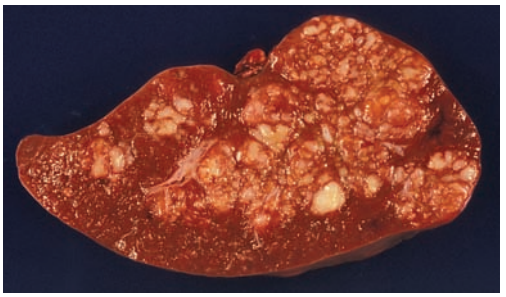

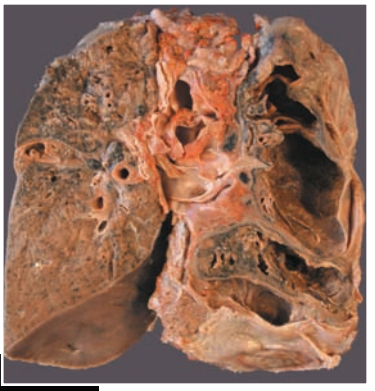

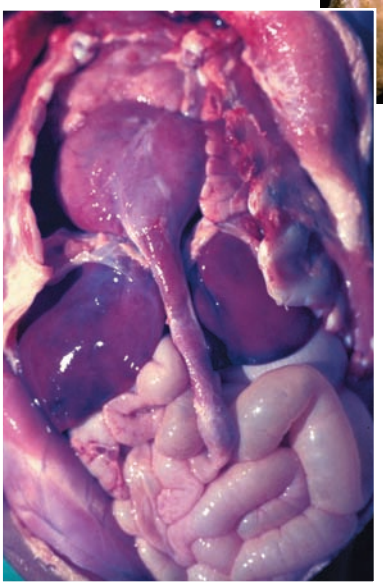

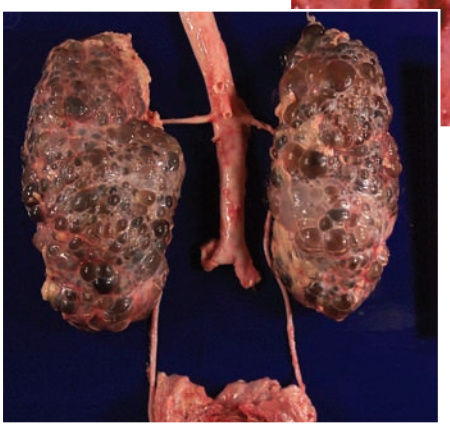

ATLAS OF GROSS PATHOLOGY

with Histologic Correlation

ALAN G. ROSE
University of Minnesota

CAMBRIDGE
UNIVERSITY PRESS

CAMBRIDGE UNIVERSITY PRESS
Cambridge, New York, Melbourne, Madrid, Cape Town, Singapore, São Paulo

Cambridge University Press
The Edinburgh Building, Cambridge CB2 8RU, UK
Published in the United States of America by Cambridge University Press, New York

www.cambridge.org
Information on this title: www.cambridge.org/9780521868792

First published in print format 2008

ISBN-13 978-0-511-43679-6 eBook (EBL)

ISBN-13 978-0-521-86879-2 hardback

CONTENTS

ATLAS OF GROSS PATHOLOGY

1 Cardiac Diseases

CONGENITAL DISEASES

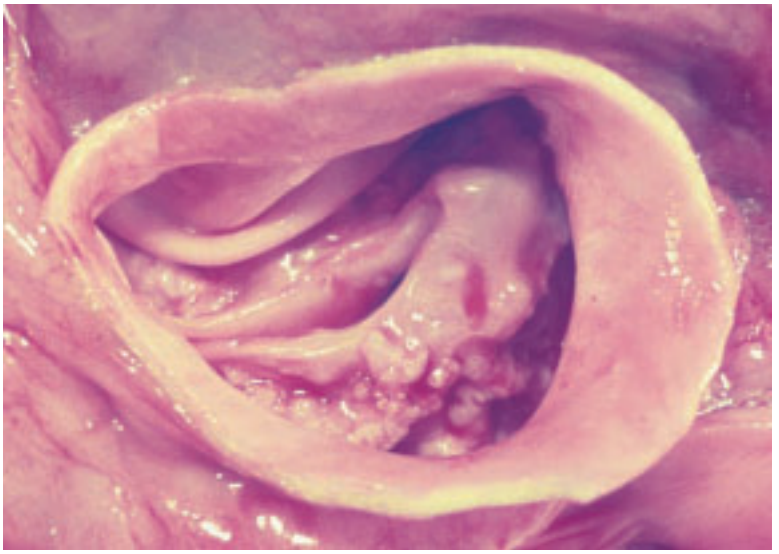

1-1. Unicuspid unicommissural aortic valve has become stenotic in middle age due to calcification of the abnormally stressed single cusp.

1-2. Congenital aortic stenosis due to a bicuspid aortic valve with thick, dysplastic cusps. Each cusp is approximately the same length as the other (i.e., stenosis occurs because no abnormally long conjoined cusp is present).

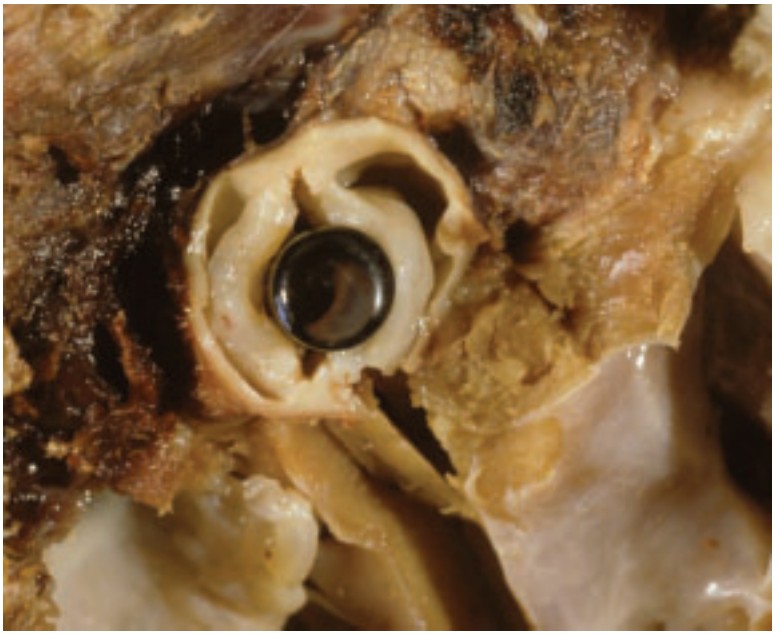

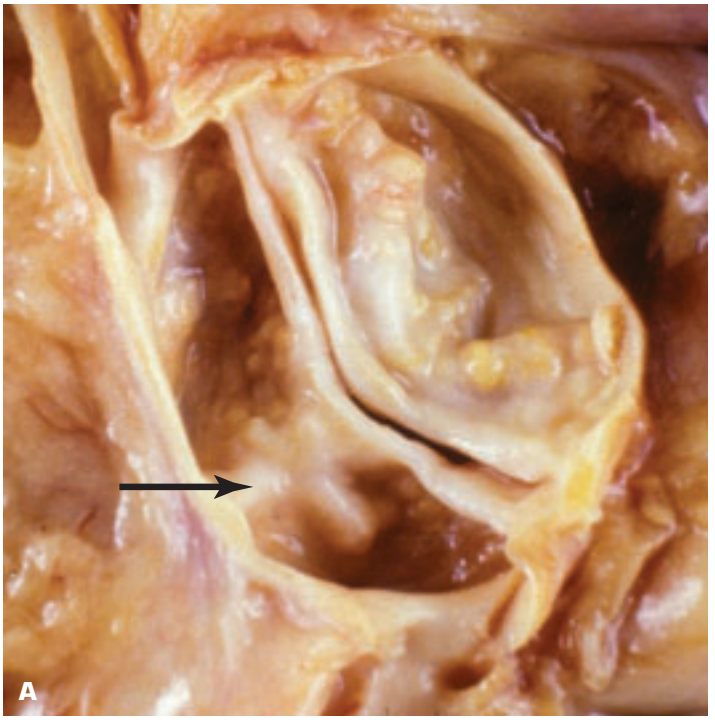

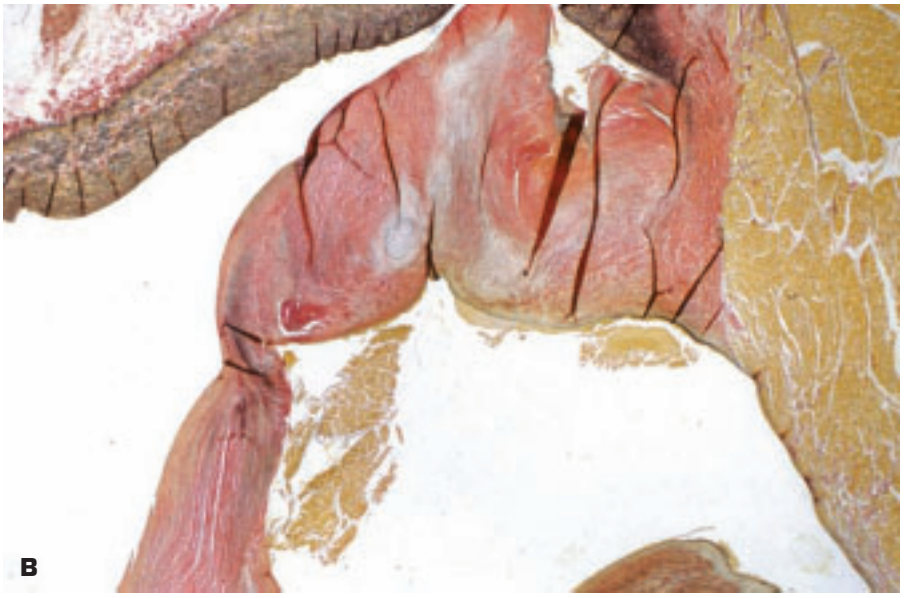

1-3. A. Aortic stenosis due to calcified congenital bicuspid aortic valve in a 50-year-old man. The longer conjoined cusp on the left is characterized by the presence of a raphe (*arrow*) that does not reach up to the free margin of the cusp. **B.** Microscopic section through the raphe shows fibrous tissue and no evidence of two preexisting separate aortic cusps (that may have fused).

1-4. Infective endocarditis affecting a bicuspid aortic valve in a patient who also has a small perimembranous ventricular septal defect situated immediately below the valve.

1-5. Congenital pulmonary stenosis: a small central hole is present at the top of a tent-like dome of fibrous tissue. The presence of four commissures gives an appearance suggesting four cusps are fused in forming this obstructing fibrous dome.

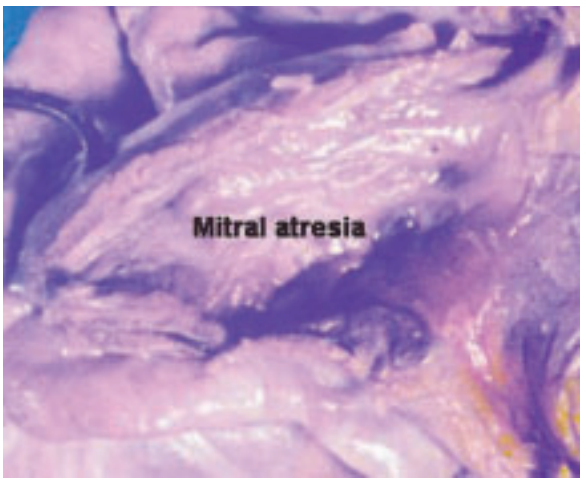

1-6. Congenital mitral atresia: no mitral valve is present, and there is only a central shallow dimple in the fibrous tissue occupying the space where the mitral valve should have been formed.

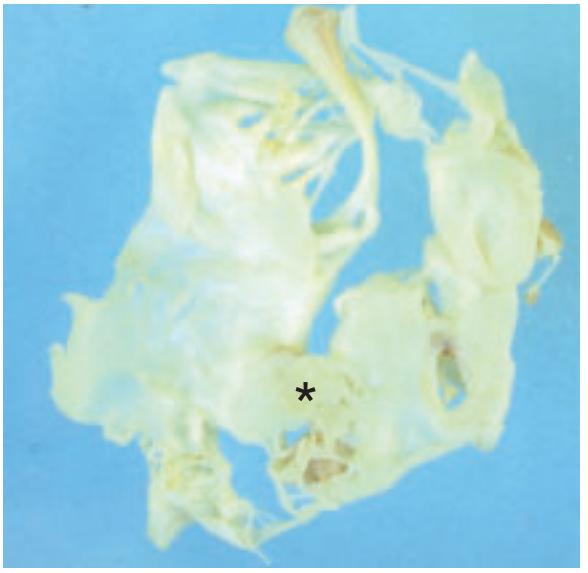

1-7. Appearance of a surgically excised mitral valve with double mitral orifice. The orifice of the valve is subdivided by a mass of abnormal valvular tissue (*) linking the two cusps.

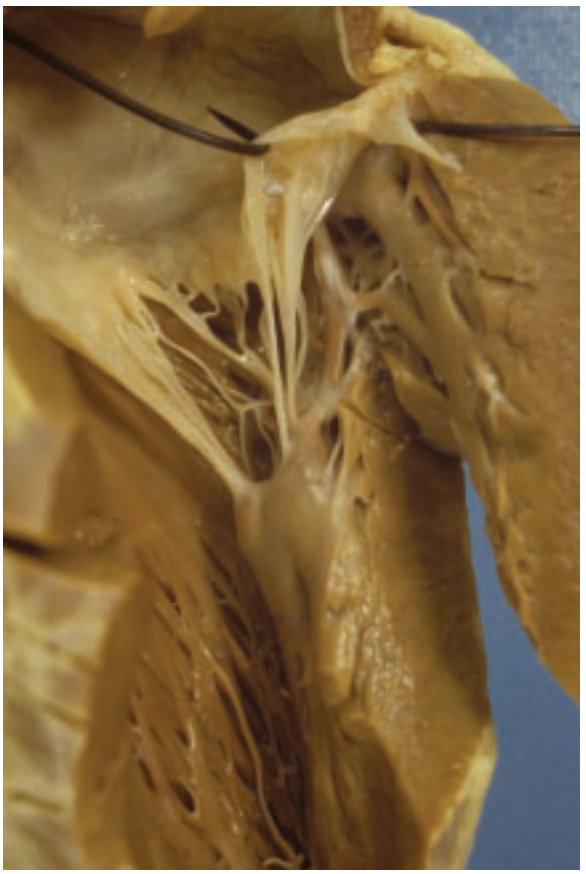

1-8. Parachute mitral valve, which may be functionally stenotic, is characterized by all of the chordae tendineae of the mitral valve being attached to a single papillary muscle. The diagnosis may easily be missed if the other missing papillary muscle is not noted.

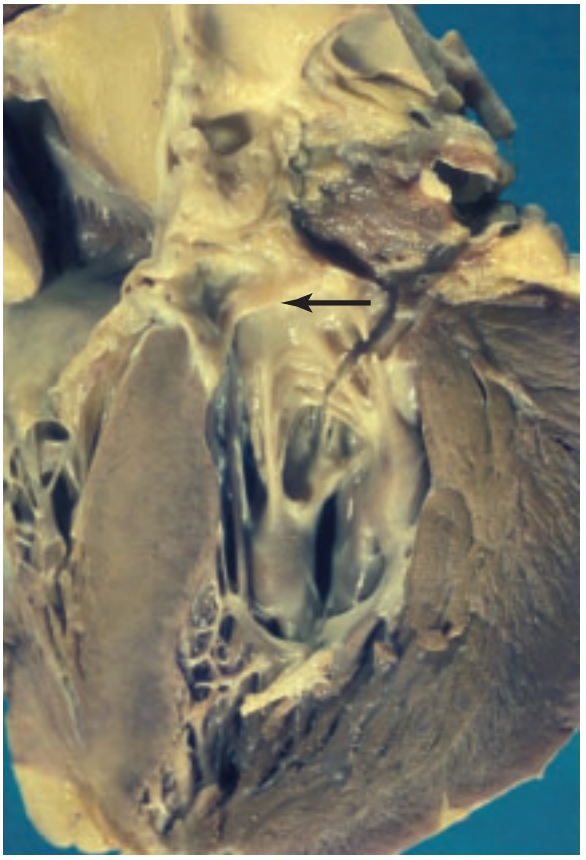

1-9. Recurrent subaortic membranous stenosis (*arrow*) after prior resection of an obstructing fibrous membrane running across the muscular ventricular septum and the anterior mitral leaflet. The membrane may re-form repeatedly after resection in some individuals. The aortic valve is thickened and deformed secondary to the effects of the subaortic obstruction-induced jet lesion.

1-10. Ebstein's anomaly of the tricuspid valve showing atrialization of the proximal portion of the right ventricle due to downward displacement of the tricuspid valve ring. The very large, dysplastic tricuspid valve is also plastered down against the underlying right ventricular endocardium in multiple areas, rendering the valve incompetent.

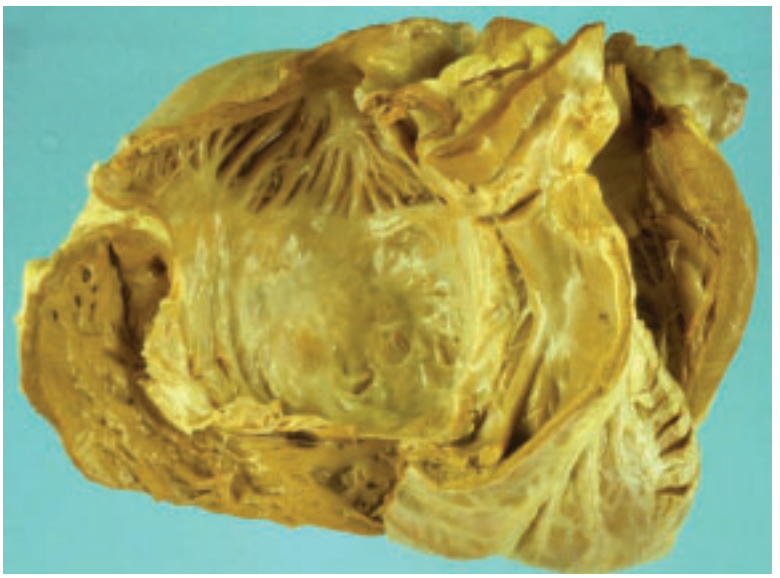

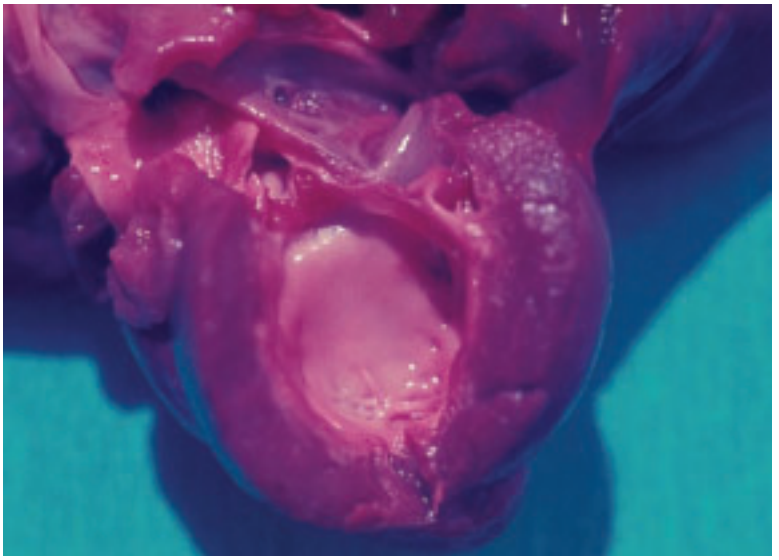

1-11. Endocardial fibroelastosis: the left ventricle is lined by a porcelain-like layer of fibrous tissue. Some patients give a history of maternal mumps infection during pregnancy.

1-12. Probe indicates a patent foramen ovale, and a small red thrombus is adherent to the nearby margin of the fossa ovalis (*right*). Transvenous atrial closure devices have been developed to seal such defects and thus prevent passage of thrombus via the patency to reach the left atrium.

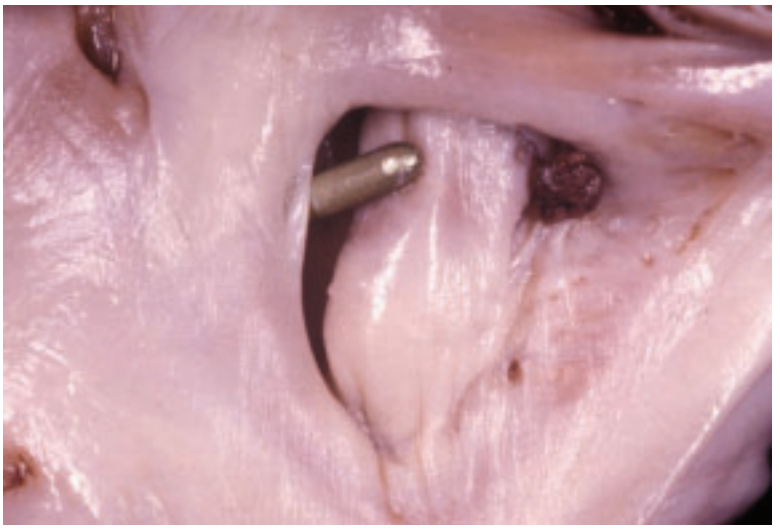

1-13. A paradoxical embolus occurs when a thrombus passes from the right atrium into the left atrium and then into the systemic circulation producing arterial occlusion. **A.** View from right atrium of a paradoxical embolus (*arrow*) passing across a patent foramen ovale. **B.** Left atrial view of the other end of the thromboembolus (*arrow*) that is passing across the patent foramen ovale.

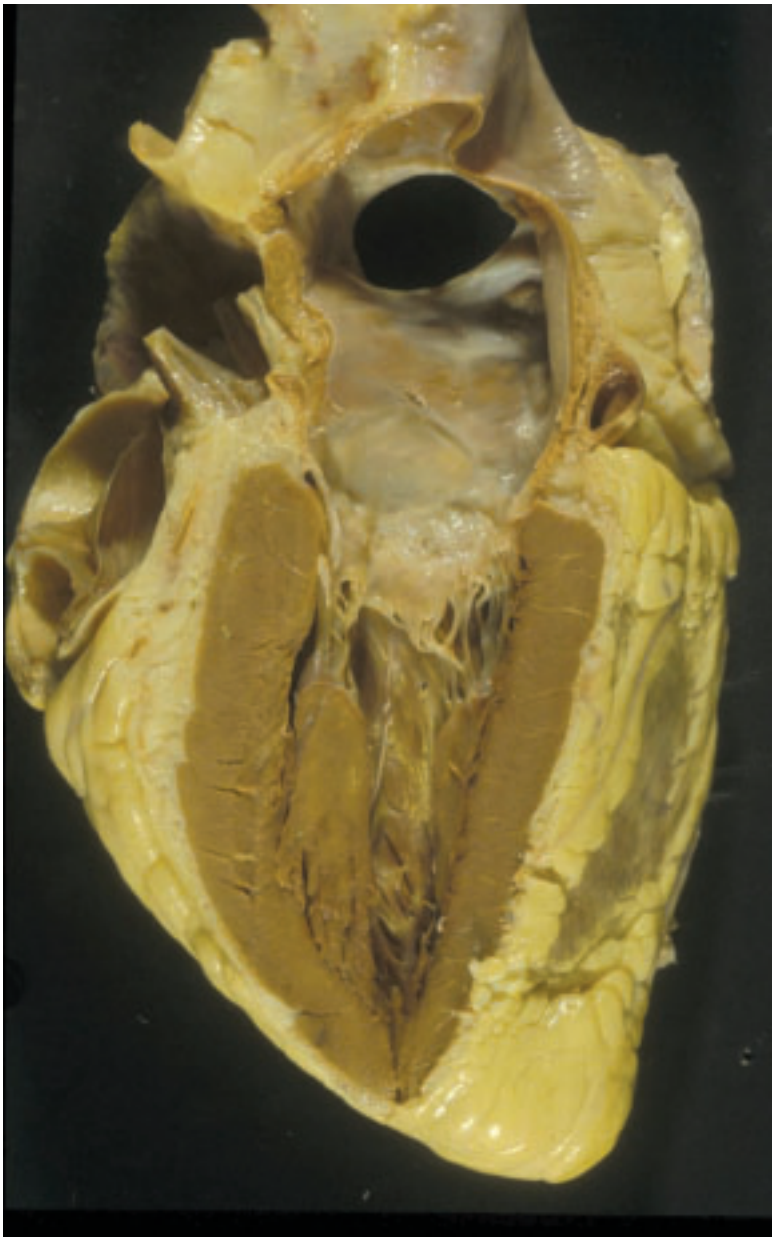

1-14. Secundum atrial septal defect at site usually occupied by the fossa ovalis in the interatrial septum.

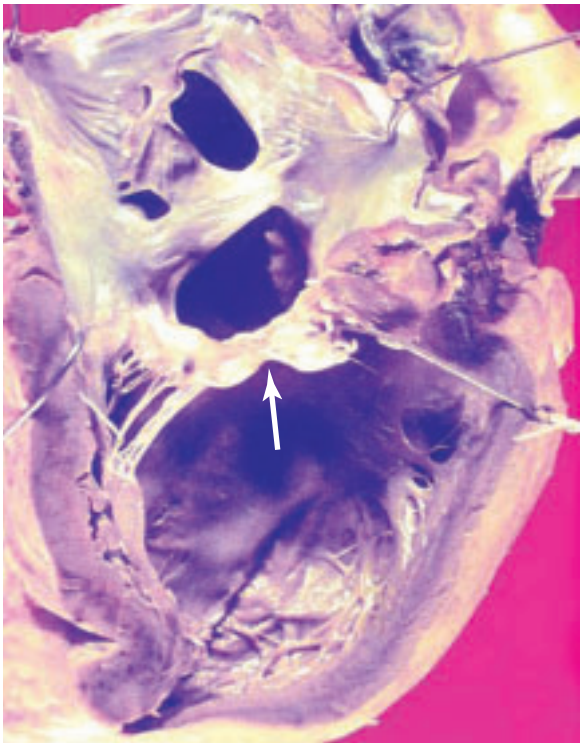

1-15. Ostium secundum (upper hole) and ostium primum (lower hole) defects seen on left side of the heart. The anterior cusp of the mitral valve has a cleft (*arrow*) in it as part of the ostium primum defect. This 48-year-old woman presented with pulmonary hypertension due to the long-standing left-to-right shunt at atrial level. She died while awaiting a heart-lung transplant.

1-16. Appearance of anterior leaflet of the mitral valve in ostium primum defect with two separate atrioventricular valves: multiple short tethering chordae limited the movement of the anterior mitral cusp during left ventricular systole. In addition to closing the defect with a patch, the surgeon needs to cut these abnormal chordae to allow normal mitral valve function.

1-17. Aneurysm of the fossa ovalis (flap valve) may be a primary abnormality per se or may be associated with valvular disease (e.g., mitral valve atresia). The aneurysm always points into the lower pressure zone. Such aneurysms may also be acquired in later life.

1-18. Perimembranous ventricular septal defect: the hole includes the area of the membranous septum plus some surrounding muscular tissue.

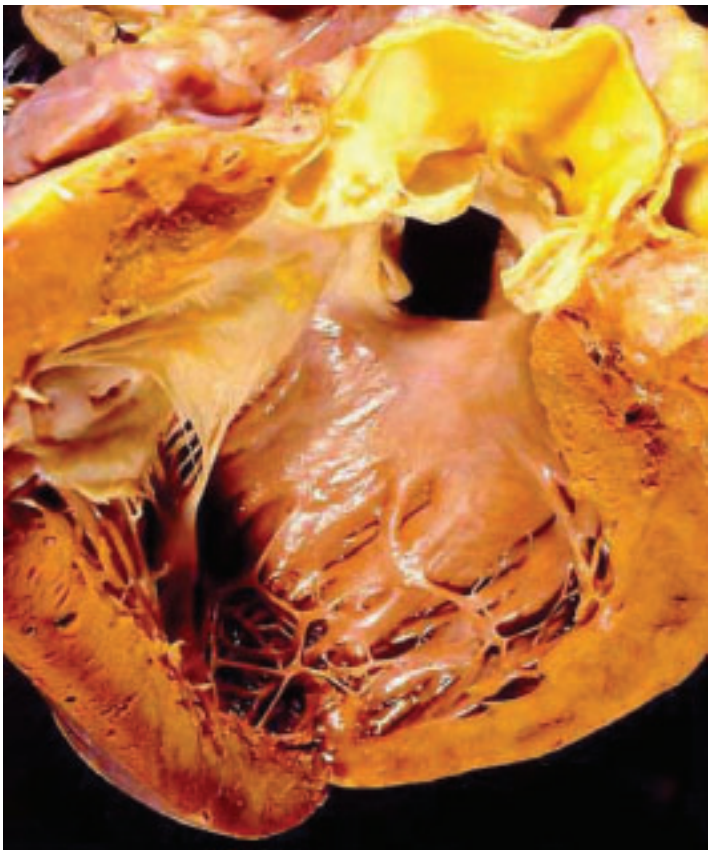

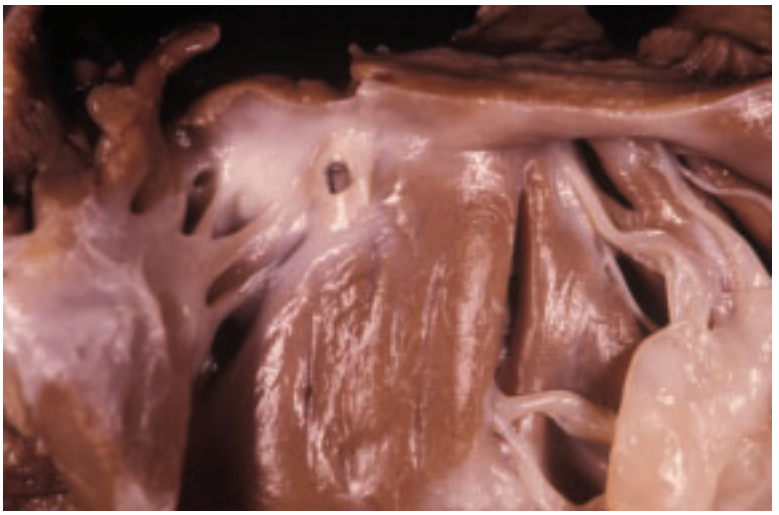

1-19. Right ventricular end of a small muscular ventricular septal defect shows surrounding endocardial fibrous thickening due to turbulent blood flow (jet lesion).

1-20. Top Dacron patch seals atrial septal defect and lower Dacron patch sealing ventricular septal defect (VSD) is the site of infection (infective endocarditis of VSD patch). The patch has been sampled for microbiology and histology.

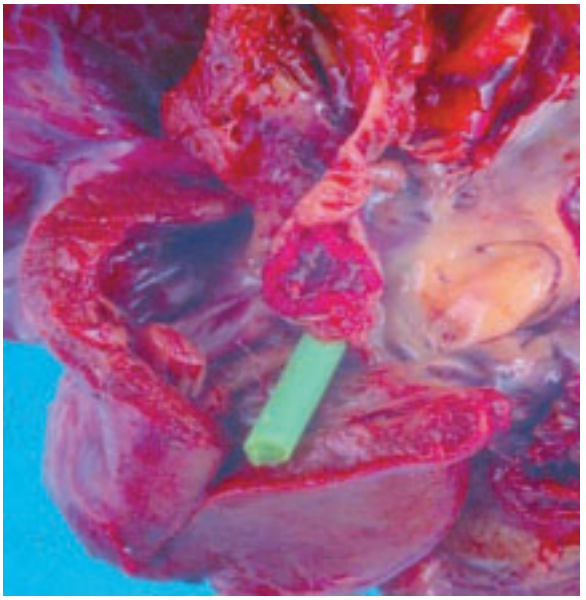

1-21. Postoperative tetralogy of Fallot showing dehiscence of Dacron patch sealing right side of an infracristal ventricular septal defect. A probe passes upward from the right ventricle behind the free margin of the patch to enter the left ventricle (not seen in this view).

1-22. Total anomalous pulmonary venous drainage: the confluence of the four pulmonary veins has no connection to the left atrium, but in this patient drained inferiorly below the diaphragm. Note that the apex of the heart has been displaced vertically to expose the major pulmonary veins.

1-23. Cor triatriatum results from failure of incorporation of the common pulmonary vein into the left atrium during the fifth week of embryological development. A fibromuscular diaphragm subdivides the left atrium into two chambers linked by a small hole. **A.** Upper chamber with small hole in its floor (probe). **B.** Lower chamber that leads directly into mitral valve orifice.

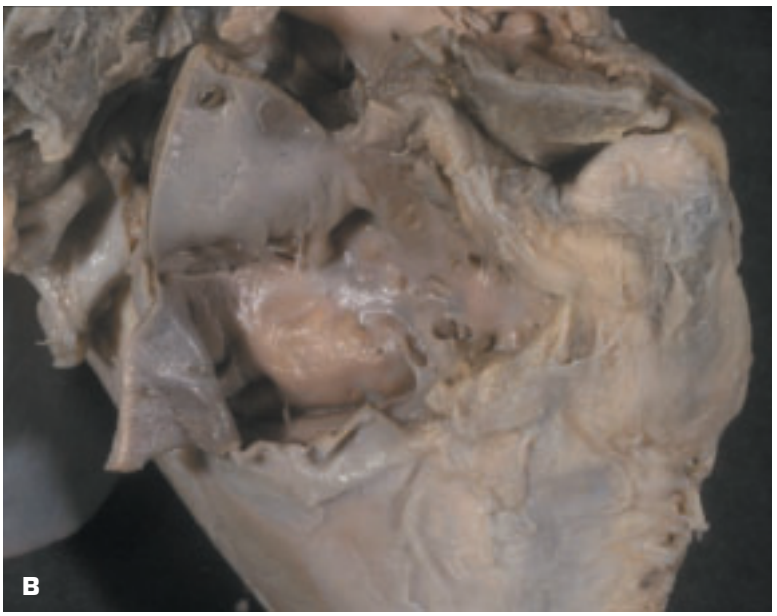

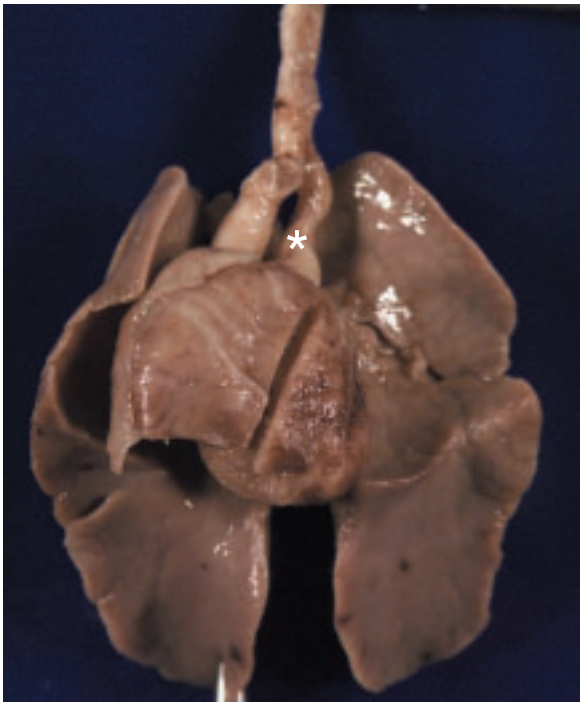

1-24. Patent ductus arteriosus (*) passes upward from pulmonary artery to join the aorta.

1-25. Surgically resected coarctation of the aorta has been bisected longitudinally to reveal a curtain-like fold of aortic tissue that affects the superior, anterior, and posterior portions of the aorta, but spares its inferior portion. One theory of causation attributes ectopic ductal tissue as the cause of the lesion.

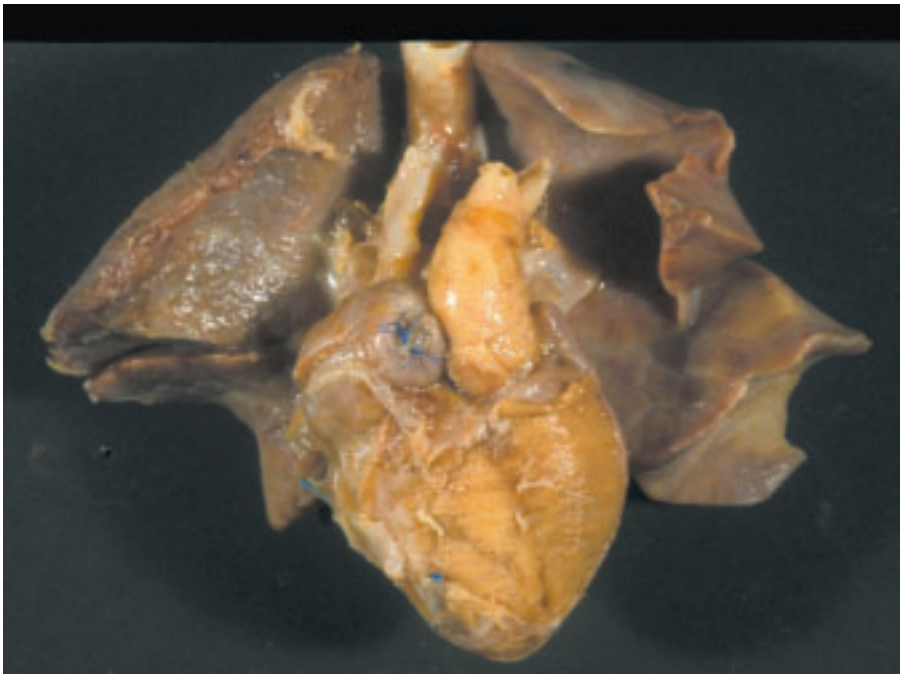

1-26. Transposition of the great arteries. The aorta (note the origins of the arch branches) is seen to be arising from the right ventricle at the expected origin of the pulmonary artery, and the latter (not visible in this view) arises from the left ventricle. The descending thoracic aorta had a left-sided descent.

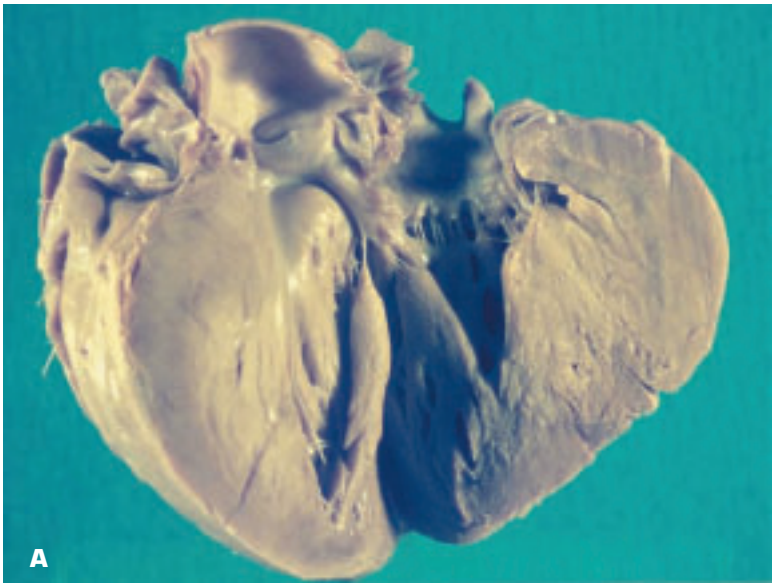

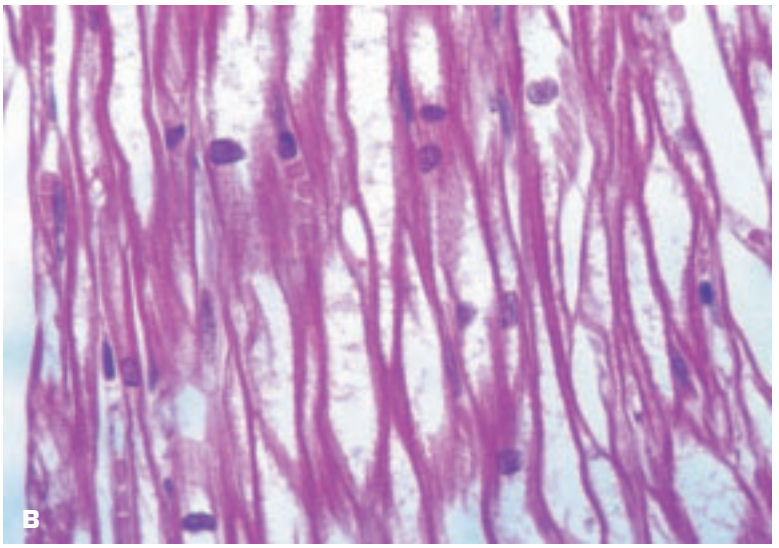

1-27. A. Glycogen storage disease has produced massive concentric hypertrophy of the cardiac chambers. **B.** Histology shows swollen, vacuolated myocytes due to massive accumulation of glycogen.

1-28. A. Bosselated appearance of left ventricular endocardium in histiocytoid cardiomyopathy. **B.** Histologic appearance of innermost portion of left ventricle showing vacuolated Purkinje fibers and myocytes expanding the subendocardium.

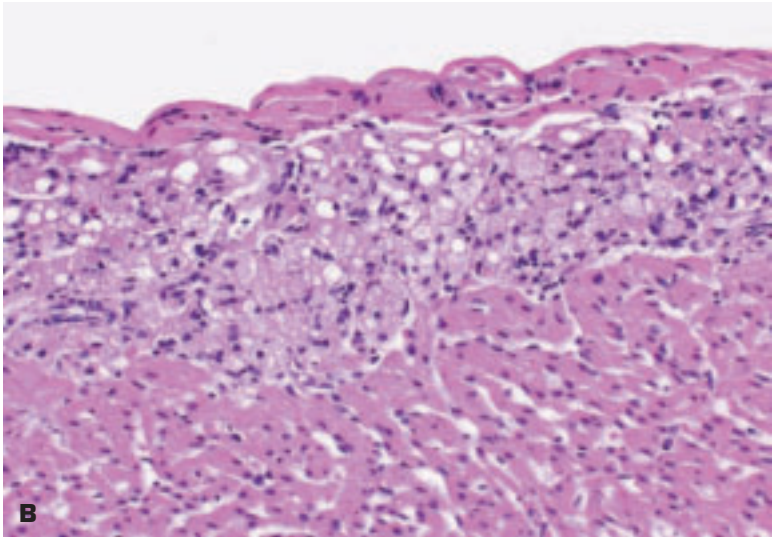

1-29. A. Biventricular coronary-cameral fistulae have led to marked ectasia and elongation of the major coronary arteries so that they resemble a "bag of worms" in appearance. The coronary arteries have had to carry much more blood than normal to compensate for blood lost into the cardiac chambers. **B.** Histologic appearance of left ventricle showing large arterial branches reaching to the endocardial zone.

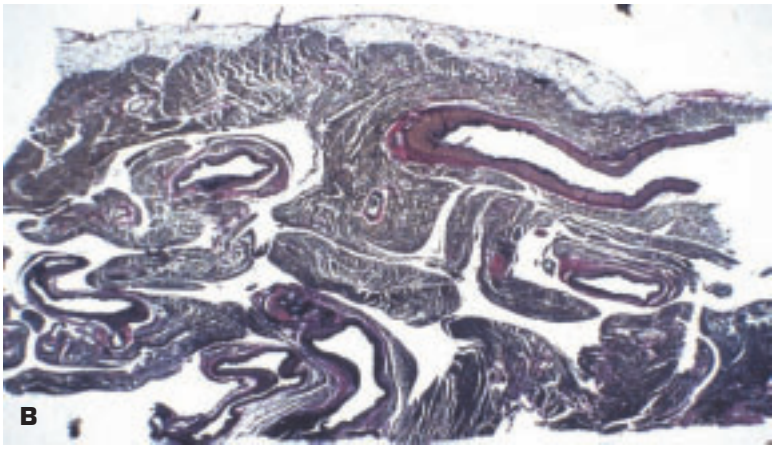

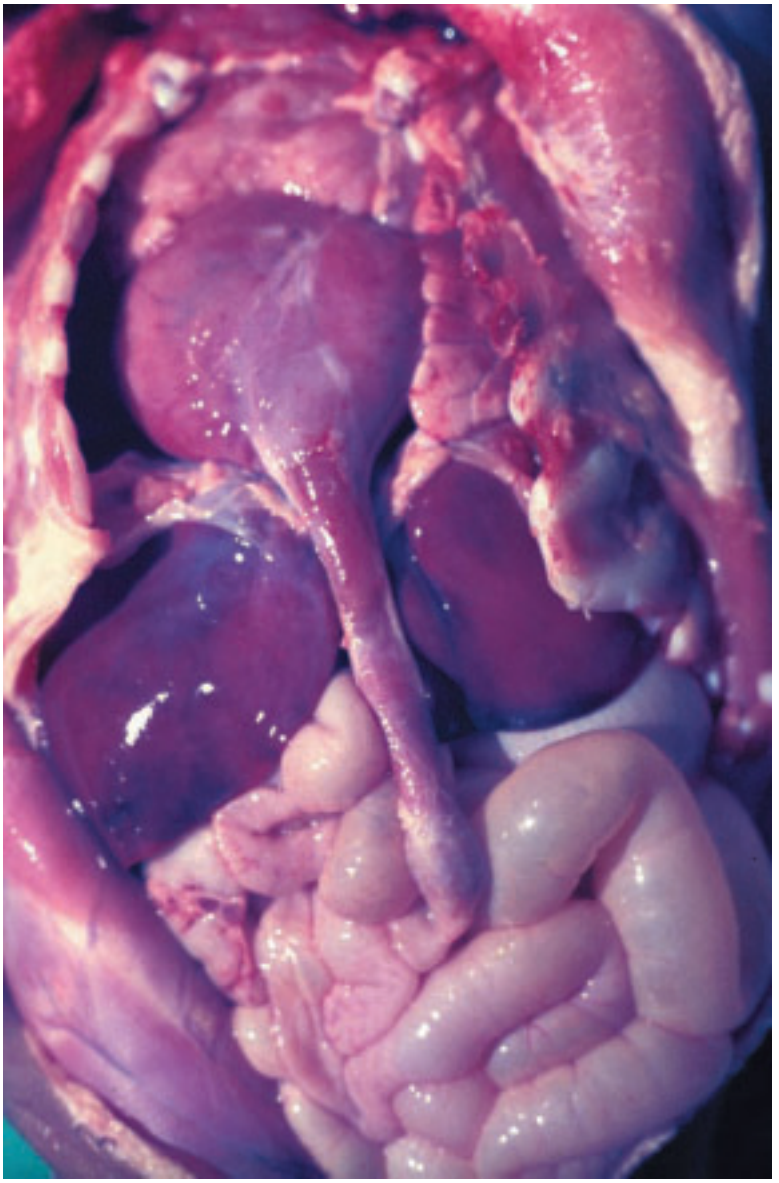

1-30. Congenital diverticulum arising from the apex of the left ventricle passed through the diaphragm anterior to the liver to terminate in the abdomen. Patient had pulsating umbilical swelling during life. Death was due to a hypoplastic left ventricle.

1-31. A. Senile calcific aortic stenosis due to calcium deposits in a tricuspid aortic valve that render the cusps relatively immobile. The deposits are mainly situated on the outflow aspect of all three cusps. **B.** Lipid deposits (central pale area) within the cusp that develop with age form the nidus for development of the calcification. **C.** Massive calcification expands the thickness of the cusp.

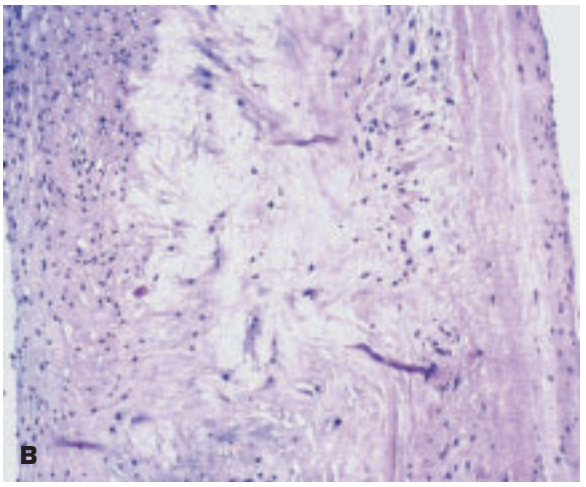

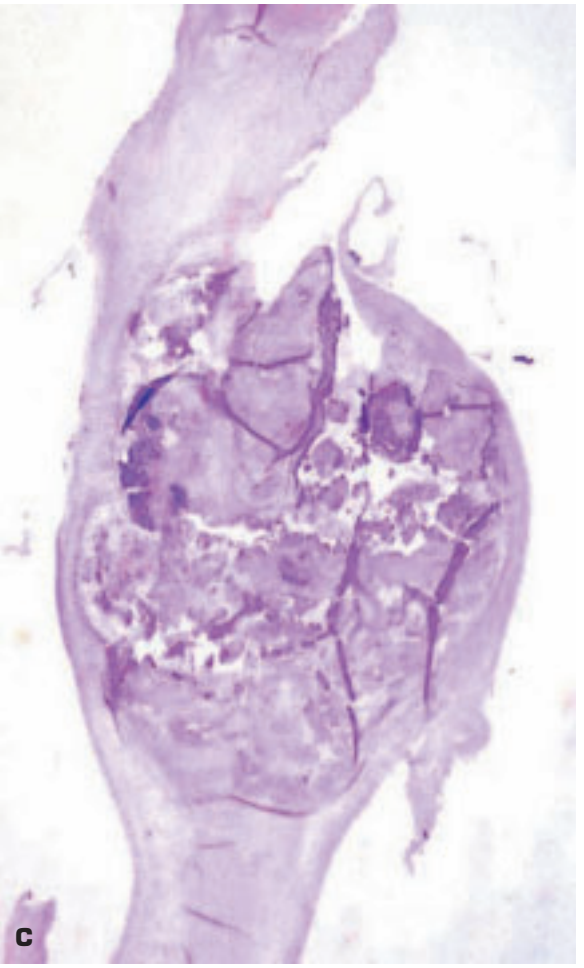

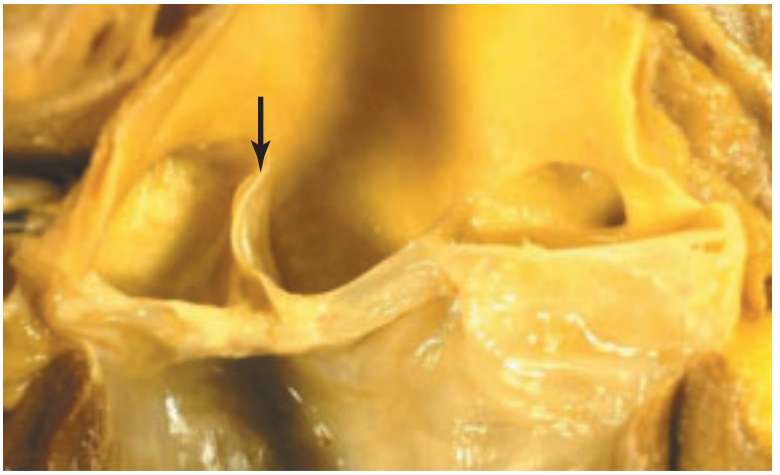

1-32. Acquired bicuspid aortic valve due to fusion (*arrow*) of one commissure. The fusion reaches right up to the free margin of the two united cusps and is unlike a raphe of a congenital bicuspid valve that would not reach up this high.

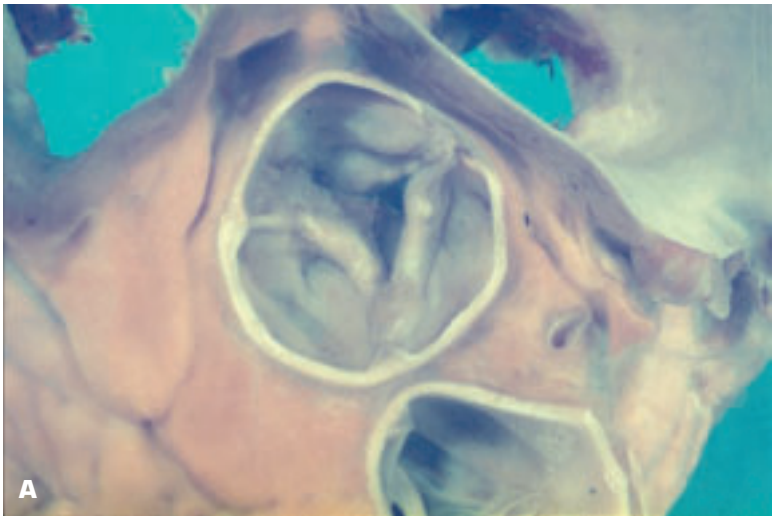

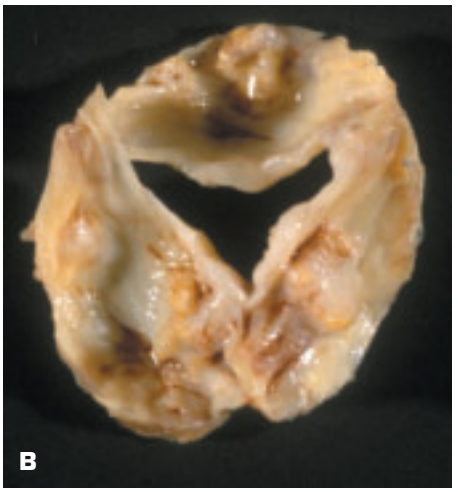

1-33. A. Acquired aortic stenosis due to rheumatic fever shows the typical triangular orifice due to partial fusion of all three commissures. Note also the thickness of the cusps. **B.** Surgically excised specimen of acquired aortic stenosis due to tricommissural fusion shows similar features.

1-34. Acquired aortic stenosis in patients with left ventricular assist devices. For the assist pump to work well, the aortic valve stays permanently closed, favoring thrombosis and organization leading to commissural fusion. Left lower picture shows organizing thrombus on the inflow aspect of the aortic valve. Right lower picture shows commissural fusion leading to aortic stenosis.

1-35. Marantic endocarditis: note the large vegetations (thrombotic deposits) on the aortic valve in a patient with prior coronary arterial bypass grafts. Note hemoglobin staining of the aortic intima by intravascular hemolysis due to septicemia. Vegetations showed no sign of infection microscopically.

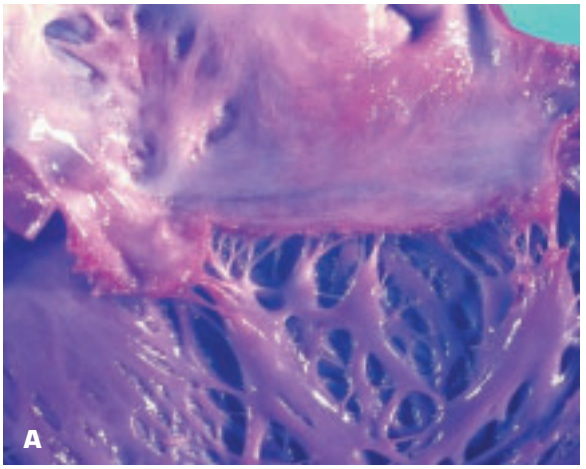

1-36. A. Small, firmly adherent, verrucous vegetations of acute rheumatic fever lie on contact area of the mitral valve cusps. Left atrium posterior wall has a MacCallum's patch (i.e., area of endocardial thickening due to the trauma of a regurgitant jet of blood from mitral incompetence). In acute rheumatic fever, increased numbers of Aschoff bodies may be found at this site of mechanical injury. **B.** Histology of rheumatic vegetation showing an Aschoff body with overlying fibrin deposition. **C.** Two Aschoff bodies in the proliferative phase lie on either side of a small intramyocardial coronary artery.

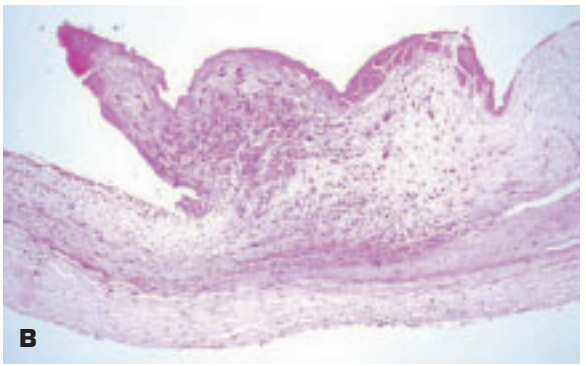

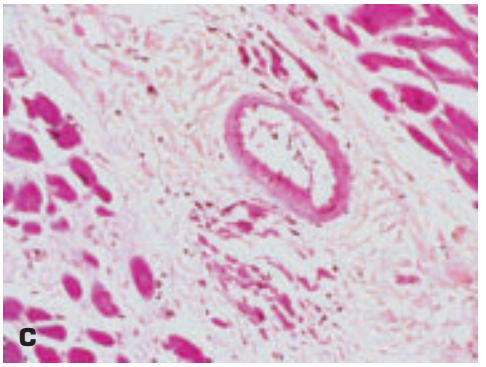

1-37. Tight mitral stenosis with a fish mouth orifice due to repeated attacks of acute rheumatic fever.

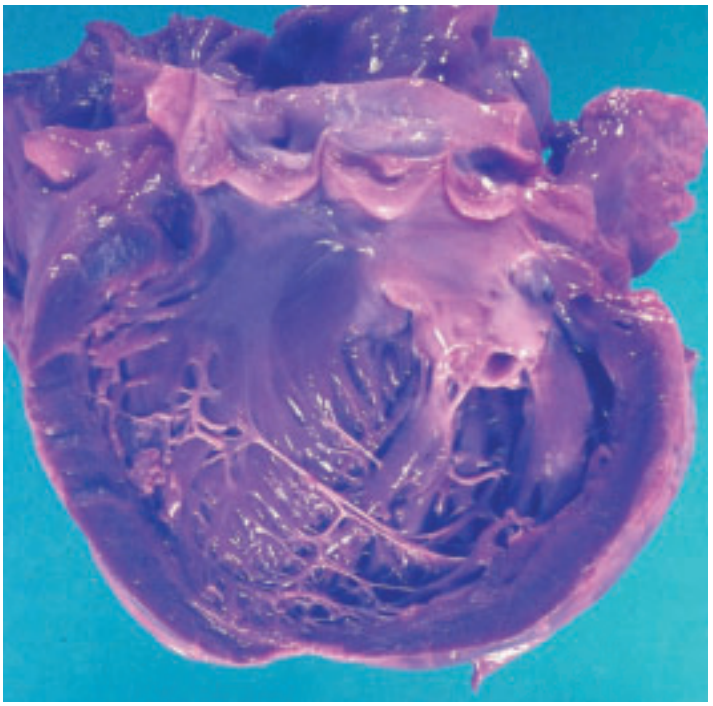

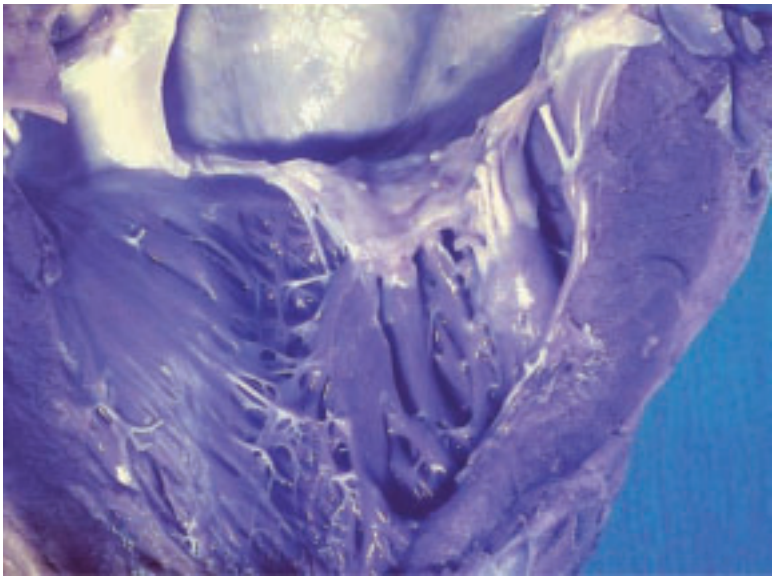

1-38. Severe postrheumatic mitral stenosis showing thickened, shortened cusps; fused commissures; and fused chordae tendineae.

1-39. Surgically excised mitral stenosis due to calcification at one commissure. The presence of the calcification (yellow-brown, ulcerated-looking area on the right) prevents the use of valvotomy to treat the stenosis. The calcification should not be mistaken for infective endocarditis. Infection rarely affects mitral stenosis and is more common in mitral regurgitation.

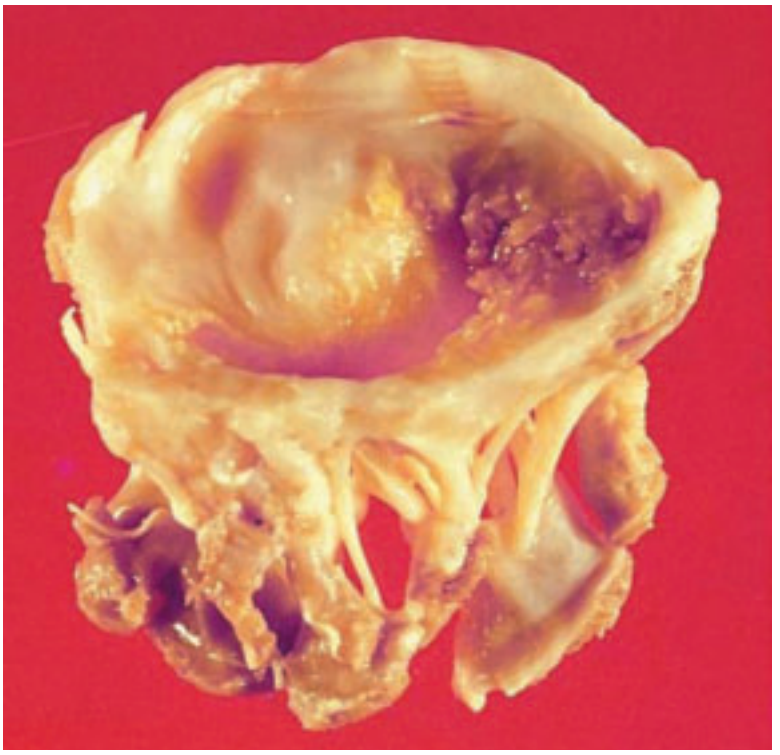

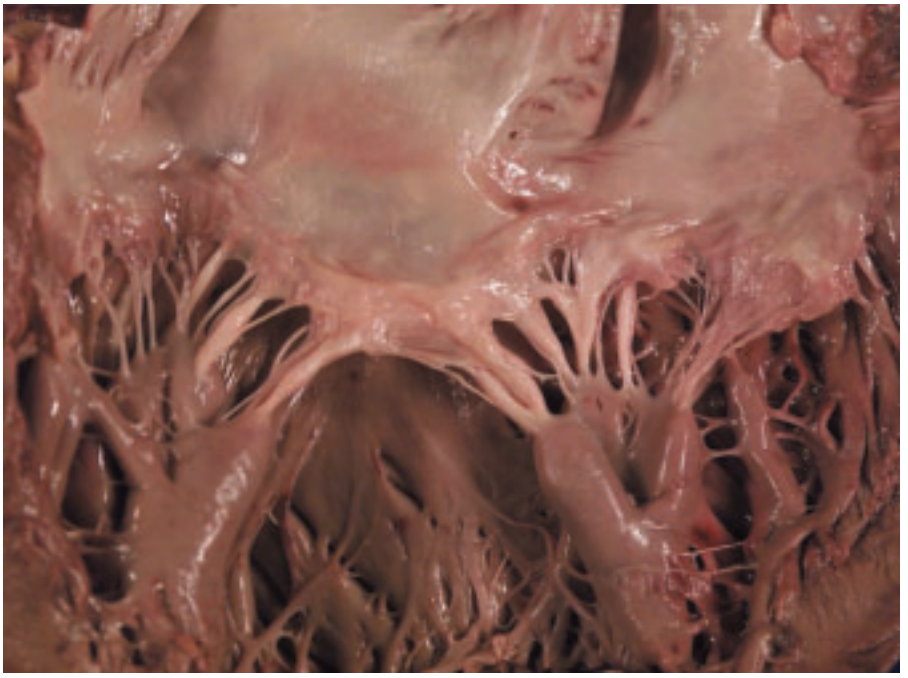

1-40. Several mitral valve chordae are thickened in this patient with micronodular cirrhosis. This association has been noted more often in patients with alcoholic cirrhosis, and the pathogenesis is believed to be related to failure to detoxify an unknown substance that elicits an endocardial overlay lesion in some chordae.

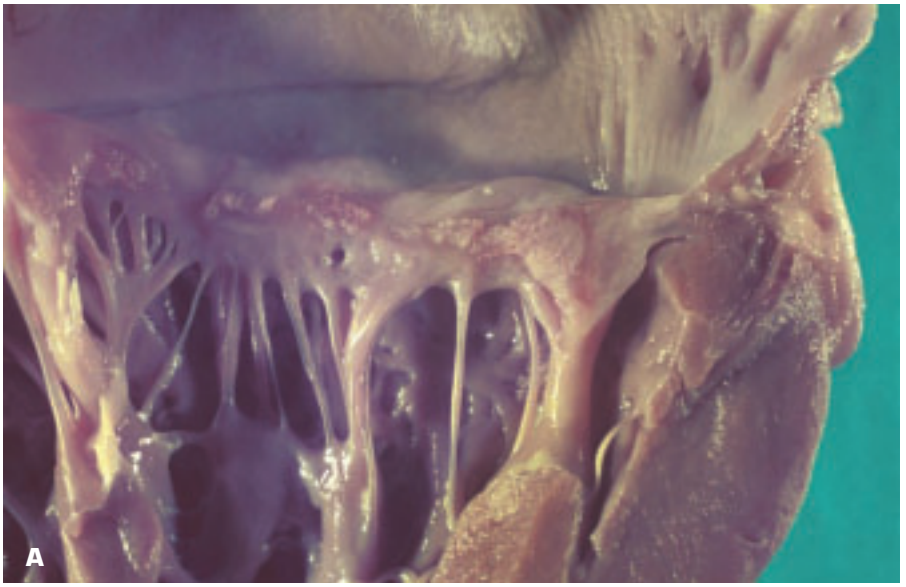

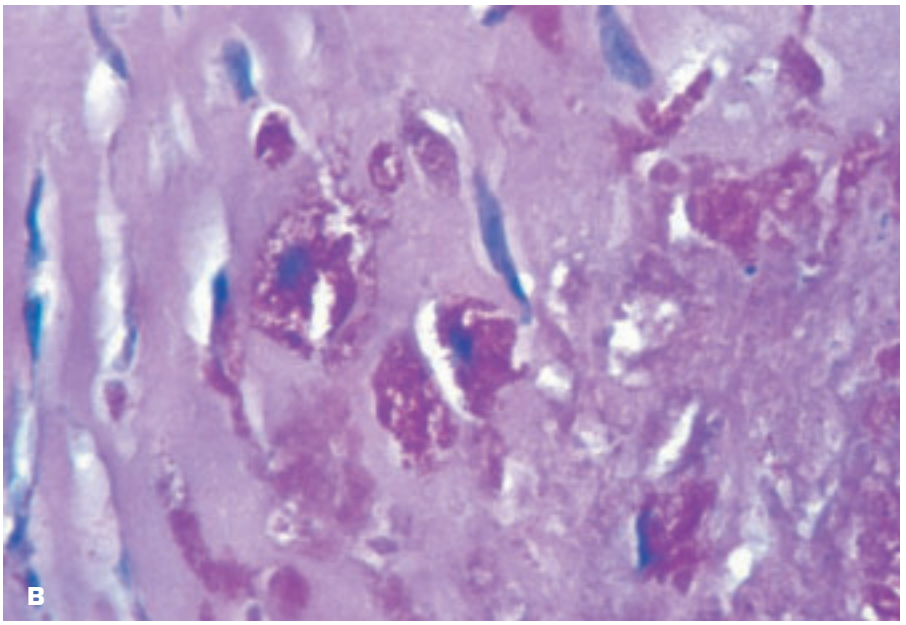

1-41. A. Mitral stenosis in Whipple disease: healing vegetations lie along the contact area of the cusps, which show fibrosis and chordal fusion. **B.** Histology shows histiocytes containing abundant periodic acid-Schiff–positive intracellular material with ghost outlines of bacteria in between.

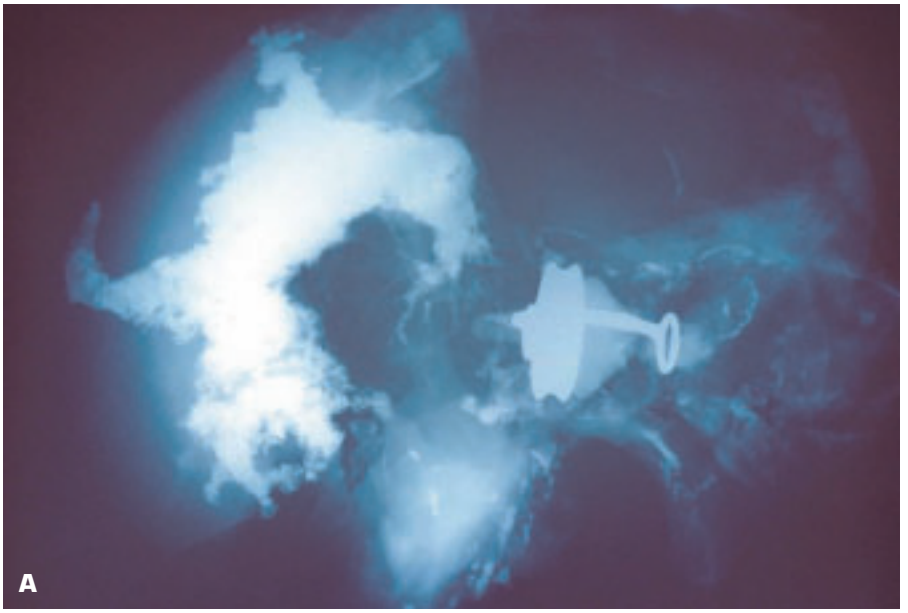

1-42. A. Radiograph of heart with an aortic prosthesis showing massive calcification of the mitral annulus, which is C shaped due to the anterior mitral leaflet making up part of the annulus. **B.** Mitral annular calcification (*arrow*) lies behind the mitral cusp in this sectioned heart. In patients who receive hemodialysis, the calcified material may become liquified and may mimic an abscess in appearance.

1-43. Floppy mitral valve. **A.** Left atrial view of intact mitral valve showing hemorrhoidal appearance due to multiple hooding of the valve. **B.** Opened mitral valve showing multiple redundant folds (hoods) on posterior leaflet prolapsing back into the left atrium. Intervening portions of the cusp appear normal. **C.** Hoods develop at sites of absent fibrosal collagen and expanded spongiosa (loose connective tissue rich in acid mucopolysaccharide). *(continued on next page)*

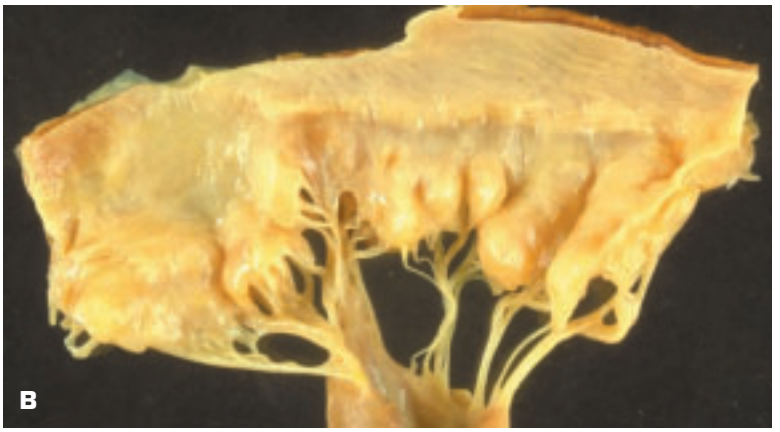

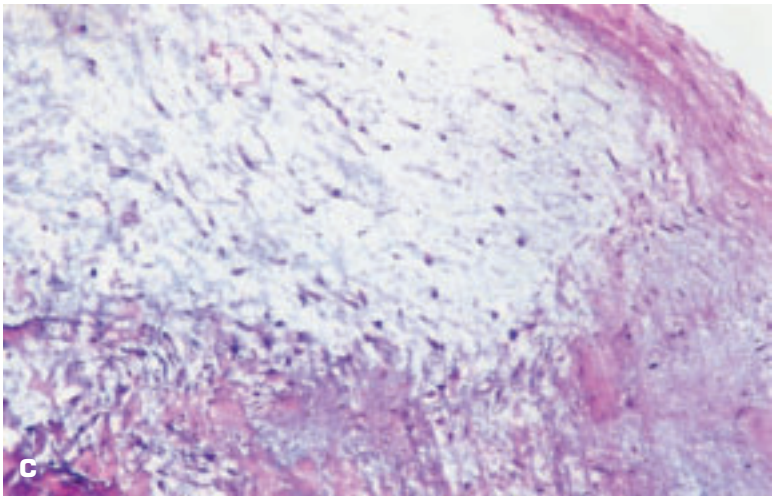

1-43. *(Continued)* **D.** Endocardial friction lesion of endocardium behind chordae. **E.** Histologic appearance of the friction lesion showing red staining collagen layer expanding the endocardium. Chordal rupture may result in some cases.

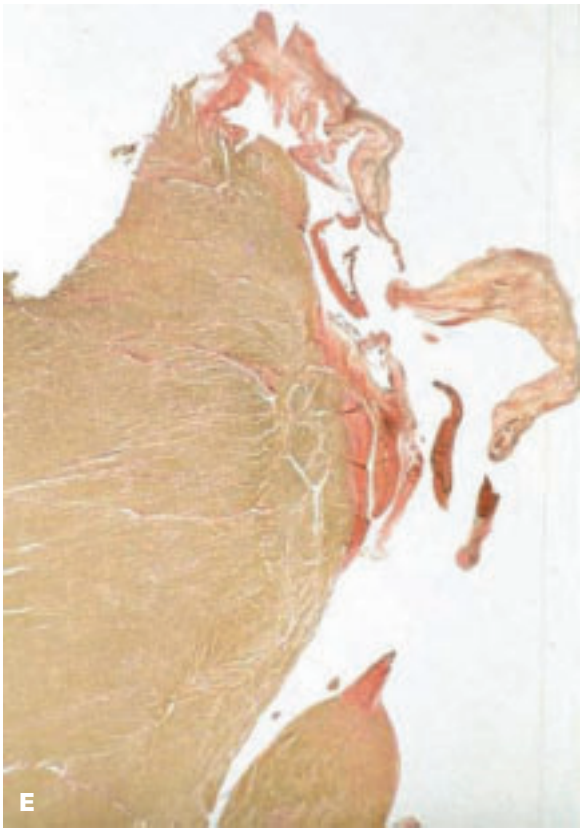

1-44. Floppy mitral valve of long duration shows diffuse cuspal fibrosis and chordal thickening that may mimic healed rheumatic fever.

1-45. Infective endocarditis complicating a floppy mitral valve.

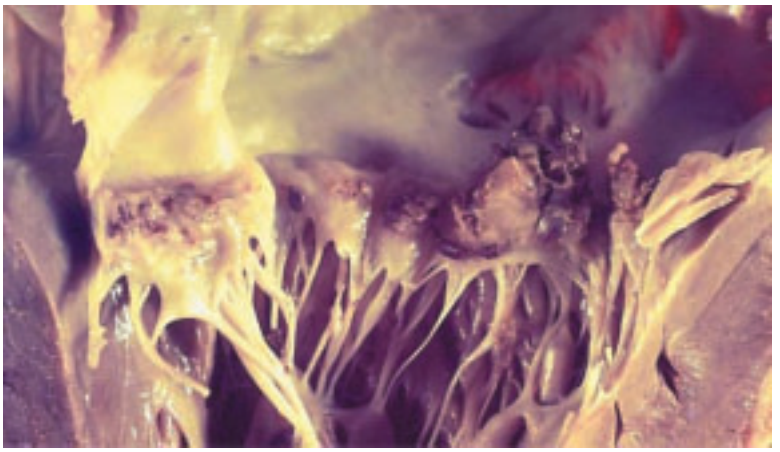

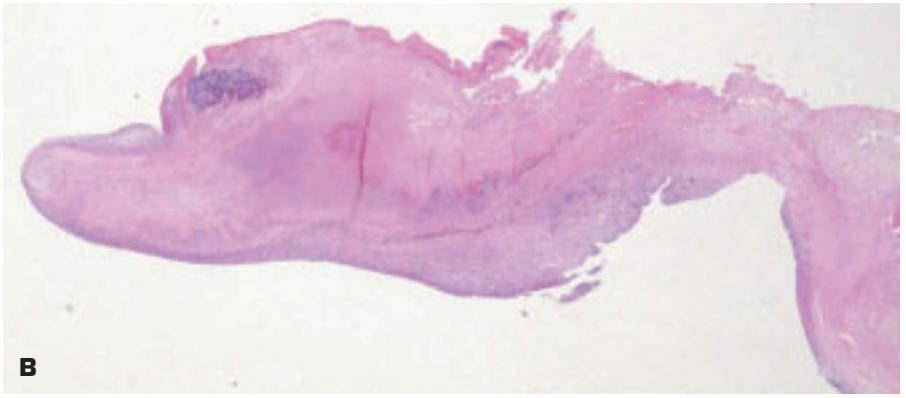

1-46. A. Infective endocarditis of a normal aortic valve with perforation of two valve cusps. **B.** Histologic appearance of aortic valve infective endocarditis with focal basophilia due to presence of pus cells within vegetation on the cusp.

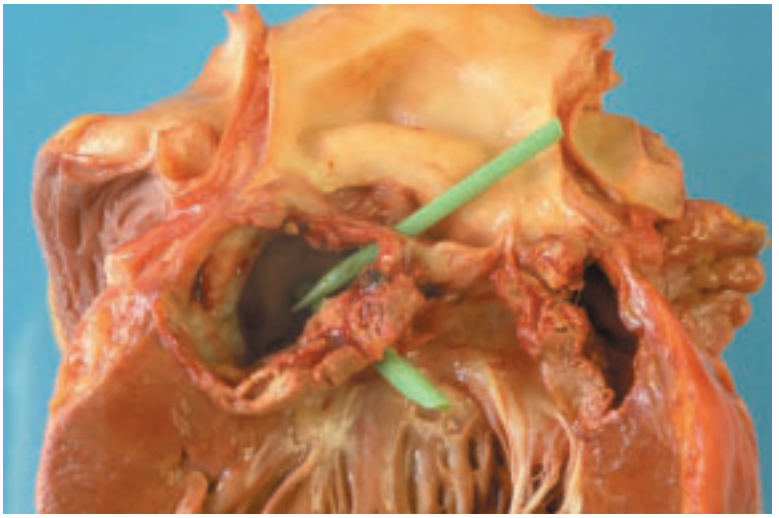

1-47. Massive ring abscess of aortic valve in a patient with Q fever endocarditis due to *Coxiella burnetii* infection. Surgical correction, including aortic root replacement, would be the only way to cure this patient. Alternatively, a valved tube graft from the cardiac apex to the aorta, combined with occlusion of the aortic root, may have been attempted.

1-48. Severe destruction of chordae and anterior cusp of mitral valve due to infective endocarditis caused by a virulent *Staphylococcus aureus* organism.

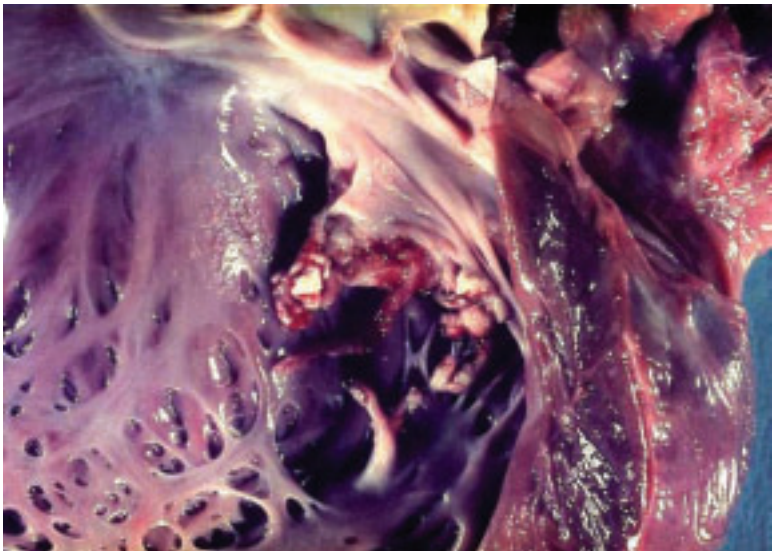

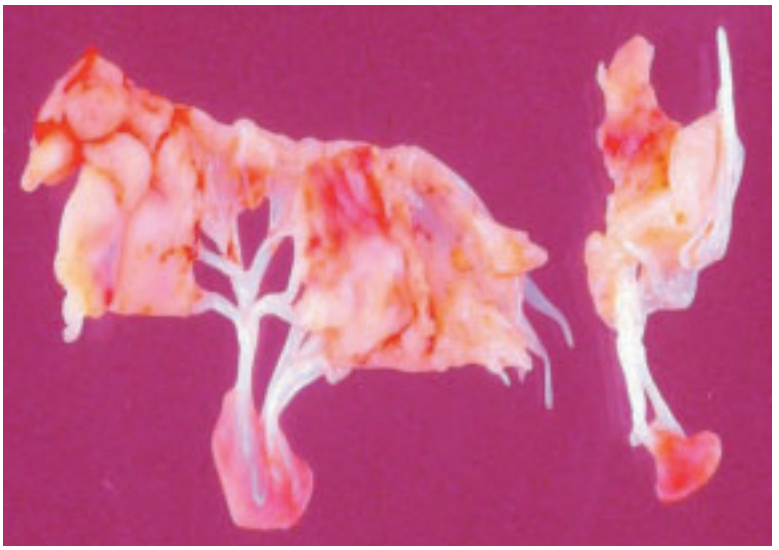

1-49. Surgically excised tricuspid valve for infective endocarditis.

1-50. Because of the low right-sided blood pressure and gentler circulation, vegetations on the right-sided heart valves may attain a much larger size than on the left side of the heart. These two vegetations filled much of the right ventricle and the right atrium.

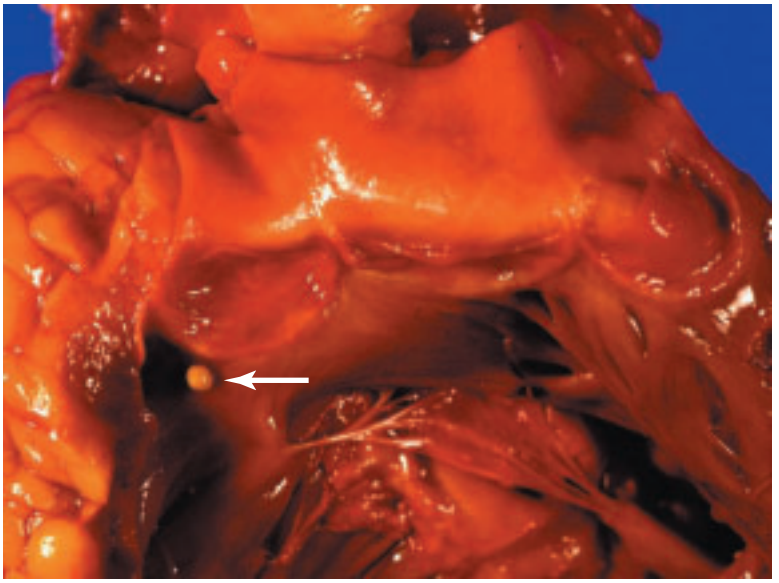

1-51. Endocardial vegetation (*arrow*) close to pulmonary valve due to infection by *Candida albicans.*

1-52. Ruptured mycotic aneurysm of anterior leaflet of mitral valve due to infective endocarditis. Note that the aneurysm faces into the lower-pressured left atrium.

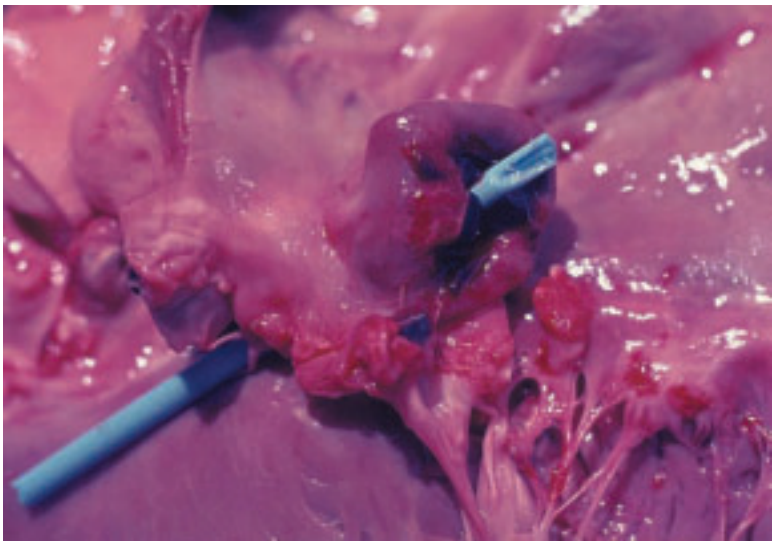

1-53. Prosthetic valve endocarditis occurs in the host tissue adjacent to the prosthesis and leads to prosthetic ring sutures pulling out of the infected host tissue, causing incompetence of the valve. Plastic probe indicates this area in the photograph.

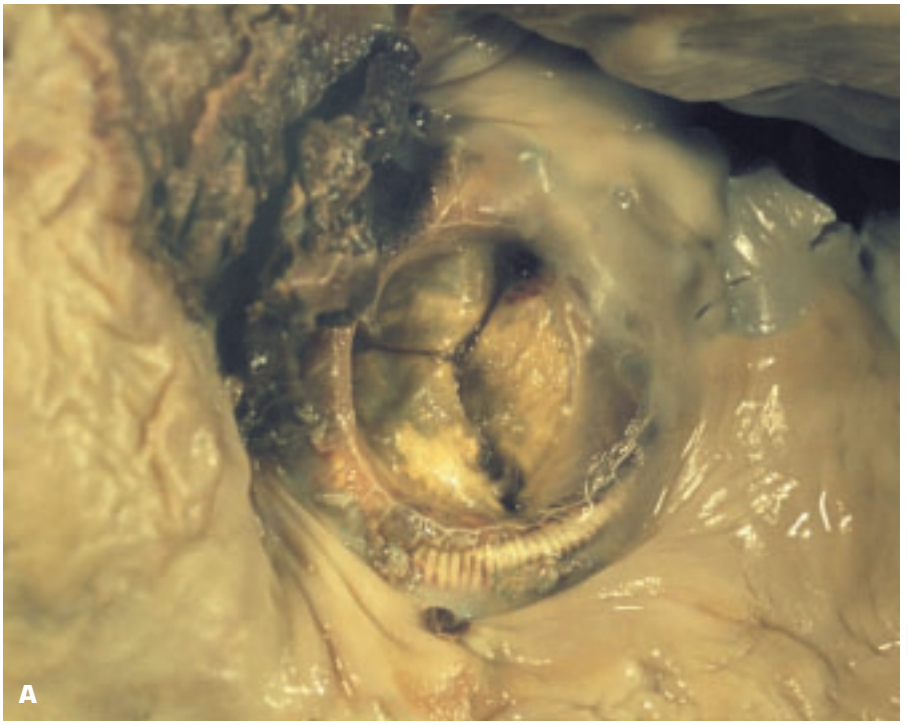

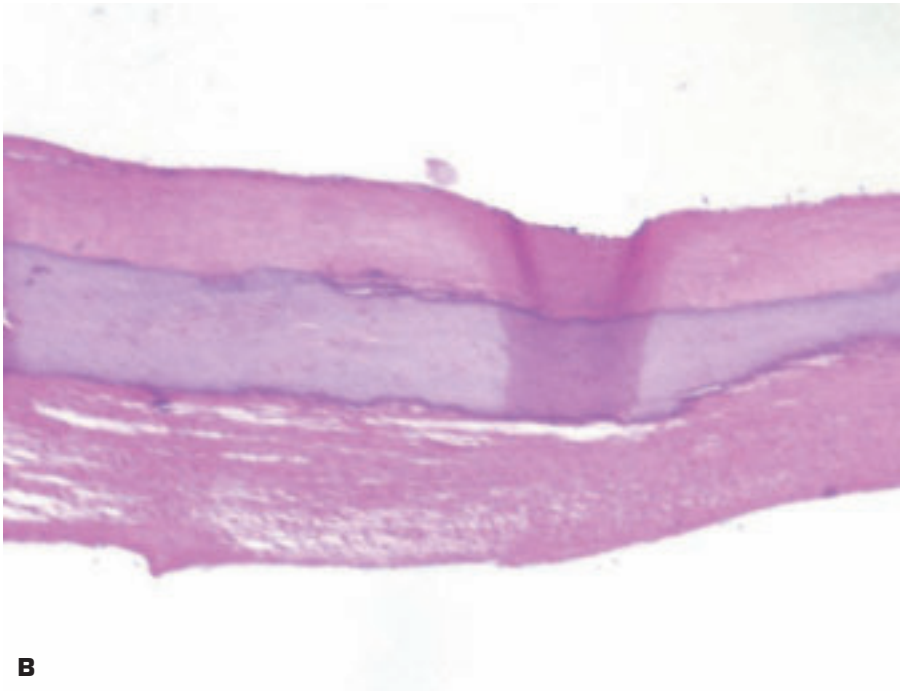

1-54. A. Calcification of a Hancock porcine aortic valve prosthesis has produced severe mitral stenosis in this young girl. Thrombus overlying the atriotomy wound site attests to the short duration that the prosthesis had been in situ. **B.** Histology of a cusp shows central calcification of the cuspal collagen in an area that would have become fixed last during glutaraldehyde fixation. Unlike formaldehyde, glutaraldehyde is a poorly penetrating fixative.

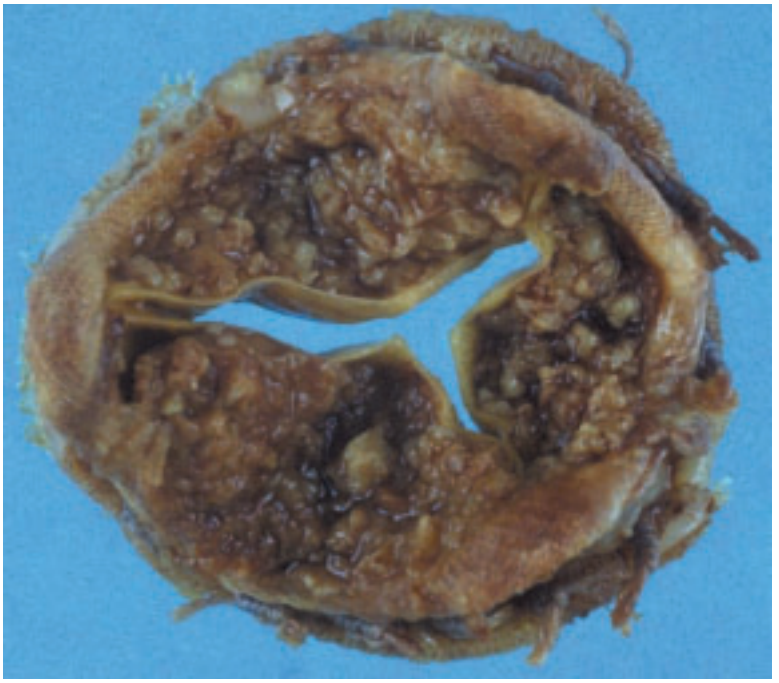

1-55. Massive thrombus fills the valve pockets on the outflow aspect of this porcine aortic valve prosthesis, leading to prosthetic valvular stenosis.

1-56. Surgical suture looped around one strut of this bovine pericardial heart valve prosthesis has tilted up the prosthesis so that it greatly obstructs the subaortic outflow tract of the left ventricle and led to death of the patient soon after surgery. The prosthesis was inserted from the left atrial aspect, and the strut and suture were invisible to the surgeon performing the operation.

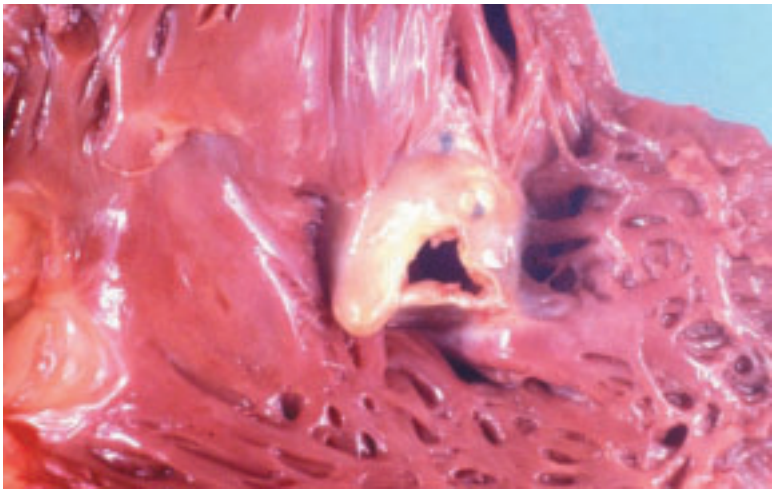

1-57. Pannus tissue overgrowth has produced stenosis of this Ionescu-Shiley bovine pericardial mitral valve prosthesis and obscured the original cusps. Some bland fibrin-platelet thrombus is present on the free margins of the cusps.

1-58. Severe prosthetic stenosis of this St. Jude Medical mechanical prosthesis has resulted from bilateral thrombus at the hinge mechanism area that has led both cusps to be fixed in the slightly open position.

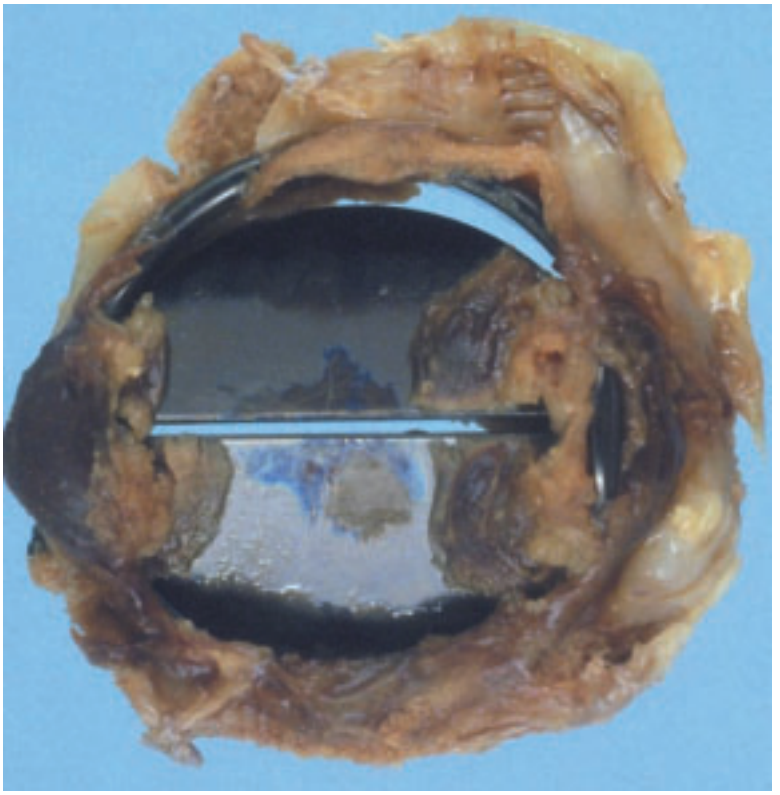

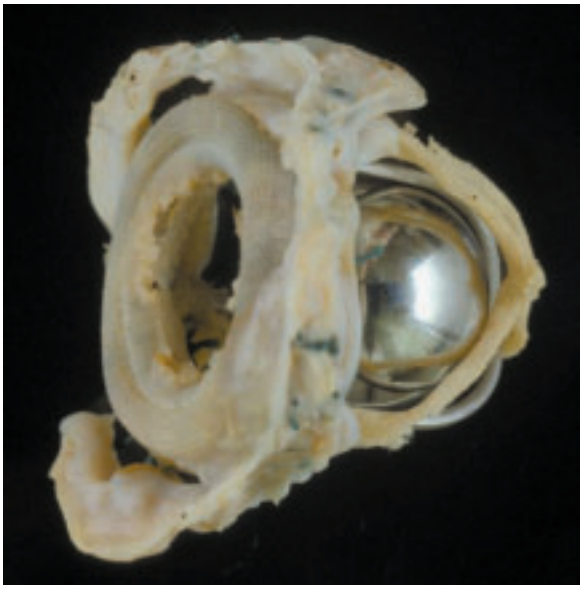

1-59. Cloth wear in this Starr-Edwards ball valve mitral prosthesis has led to partial detachment of the cloth from the cage struts. Abundant thrombus had become attached to the free cloth, and the cloth wear became apparent only after the thrombus had been cleared from the cloth surface.

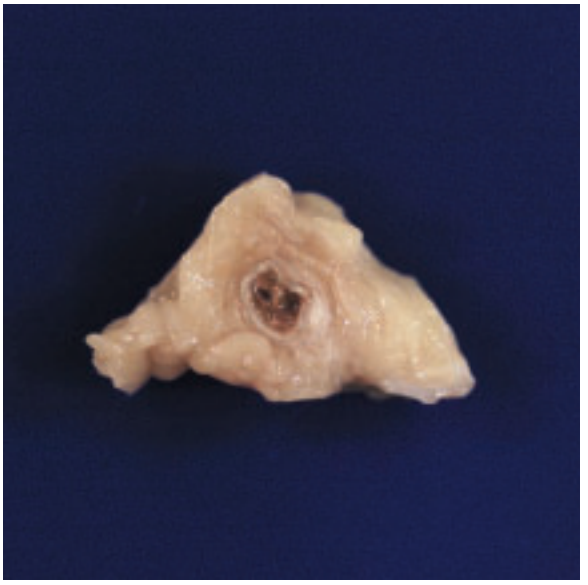

1-60. Totally occlusive thrombus fills the lumen of this atherosclerotic coronary artery.

1-61. Top panel shows a recent regional, anteroseptal, transmural myocardial infarct (*left*) as a pale area in the left ventricle. Propagated red thrombus is seen within sections of the left anterior coronary artery (*right*). Bottom panel (*left*) shows a ventricular slice with a healed posterior myocardial infarct, plus a more recent, reperfused infarct that appears hemorrhagic in appearance. The thrombosed causative coronary occlusion is seen in sections of the coronary artery (*right*).

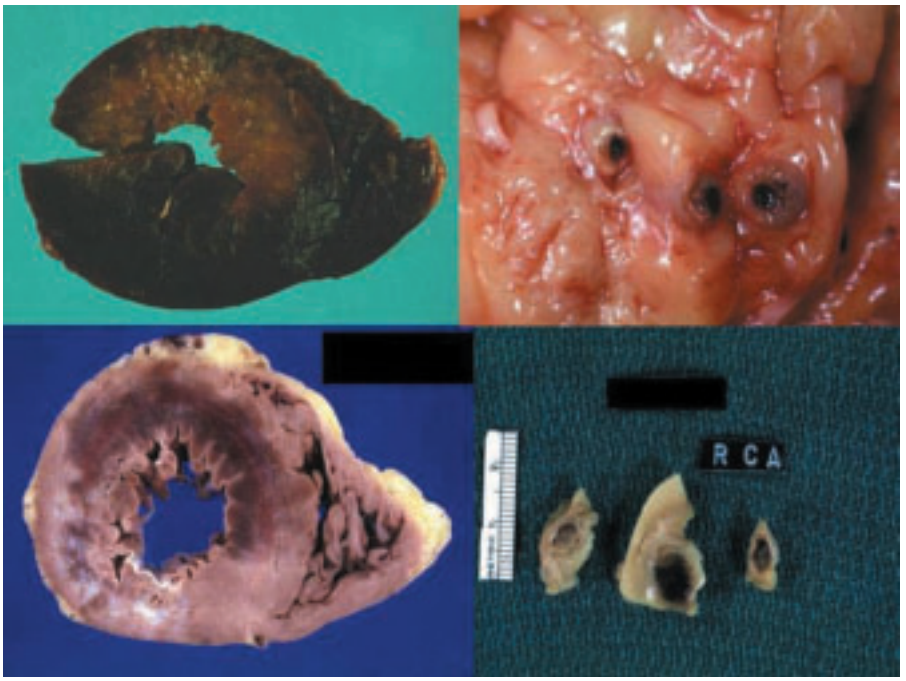

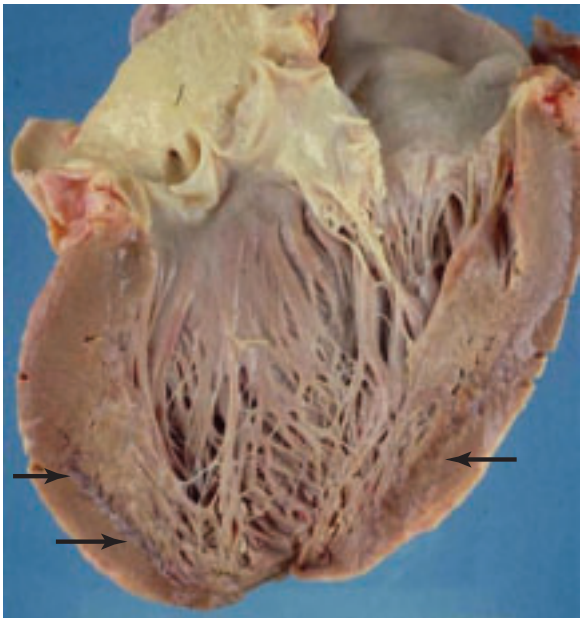

1-62. Global, subendocardial infarction (arrows) of the left ventricle has resulted from more than 80% stenosis of all three major epicardial coronary arteries. The subendocardial myocytes are replaced by fibrous tissue, and ongoing acute ischemic necrosis of small groups of myocytes was noted histologically.

1-63. Thrombus (*arrow*) lies within longitudinally opened atheromatous coronary artery (*top*), and segments (*middle*) of transversely sectioned coronary artery contain occlusive thrombus. Bottom picture shows close-up view of ruptured fibrous cap of an atheromatous plaque with thrombus (*right*) in direct contact with cholesterol crystals (*left*).

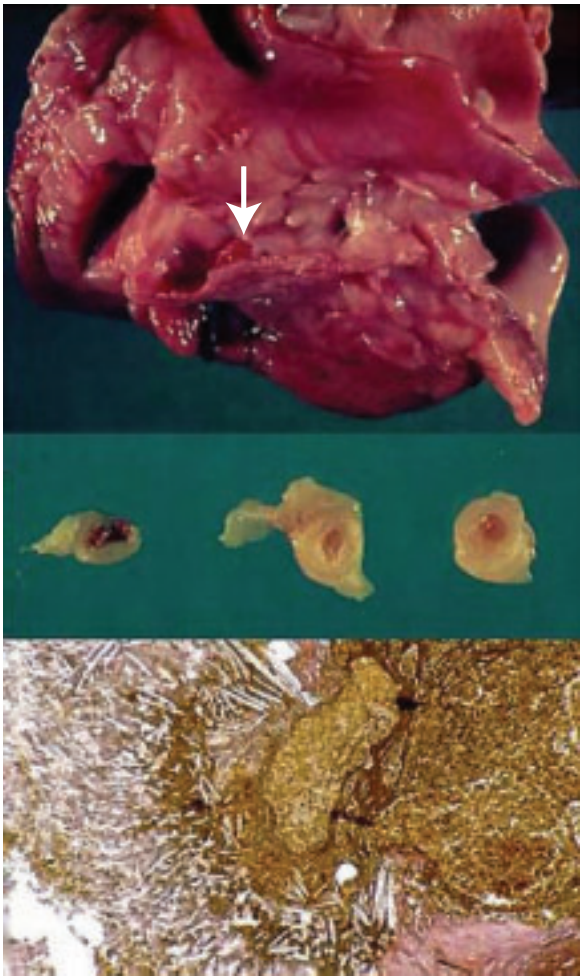

1-64. A. Thromboembolus (derived from left atrial aspect of mitral valve prosthesis) totally occludes ostium of left coronary artery in aortic root. **B.** Histologic appearance of the occluding thrombus.

1-65. Acute dissecting aneurysm (*arrow*) of proximal left anterior descending coronary artery.

1-66. Stent lies within a resected segment of coronary artery.

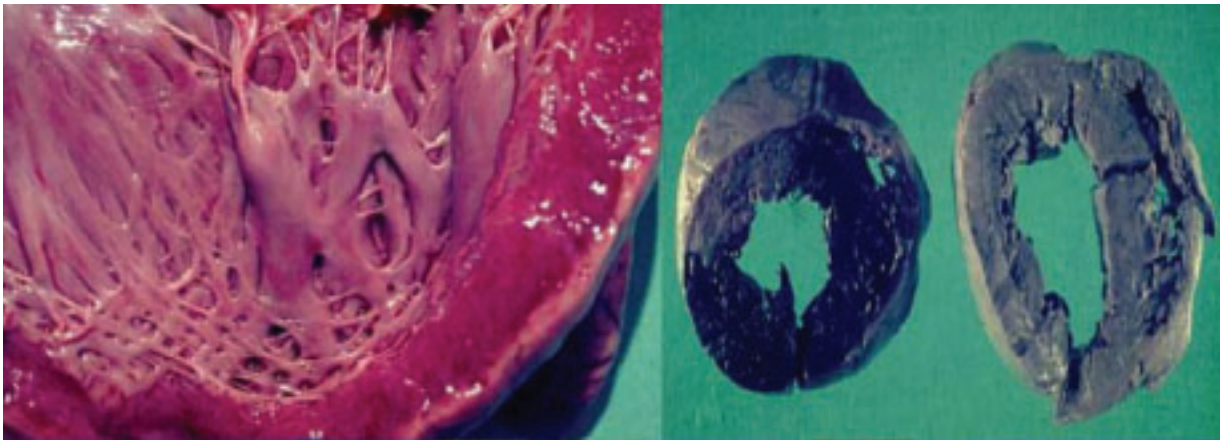

1-67. A very recent (about 4 hours by history) myocardial infarct of left ventricle (*left*) shows only edematous myocardium on its cut surface. Right shows two biventricular slices from the same heart with a 6-hour duration myocardial infarct; the infarct is well delineated as the nonstaining area in the blue-stained left slice that had been incubated with nitroblue tetrazolium.

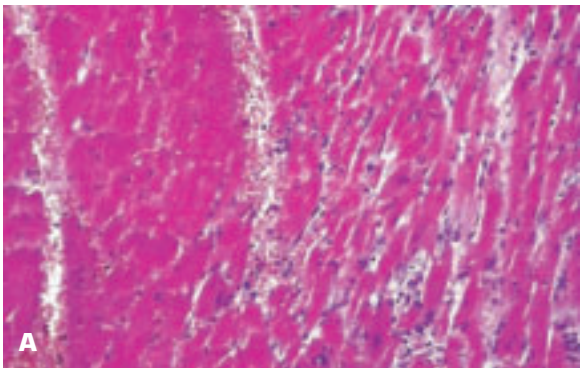

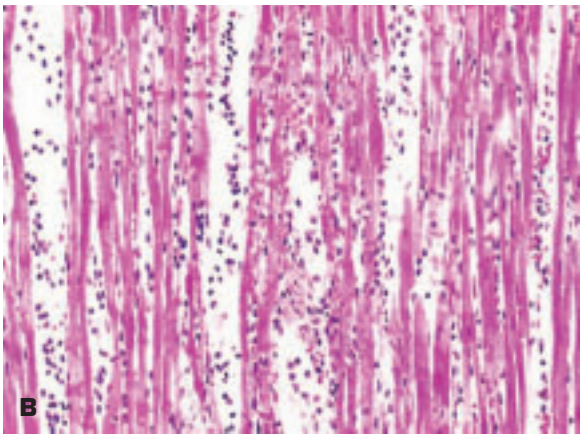

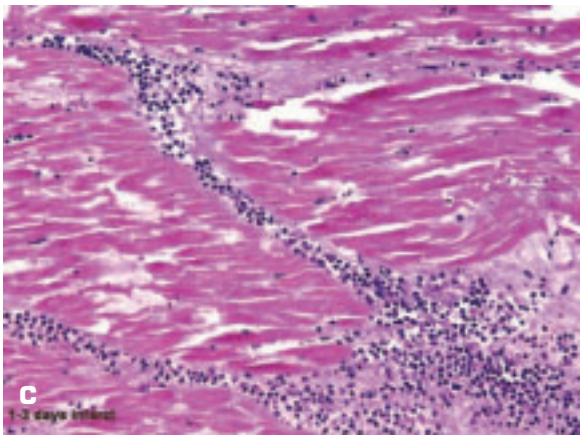

1-68. Histology of acute myocardial infarction. **A.** Edge of an infarct of about 6 hours duration showing coagulative necrosis (*left*) and damaged, viable myocytes (*right*). **B.** Edge of expanding infarct of about 12 hours duration showing contraction band necrosis of myocytes, interstitial edema, plus a prominent polymorphonuclear leukocytic infiltration. **C.** Central portion of a myocardial infarct of about 4 days duration showing neutrophils infiltrating between myocytes showing advanced coagulative necrosis.

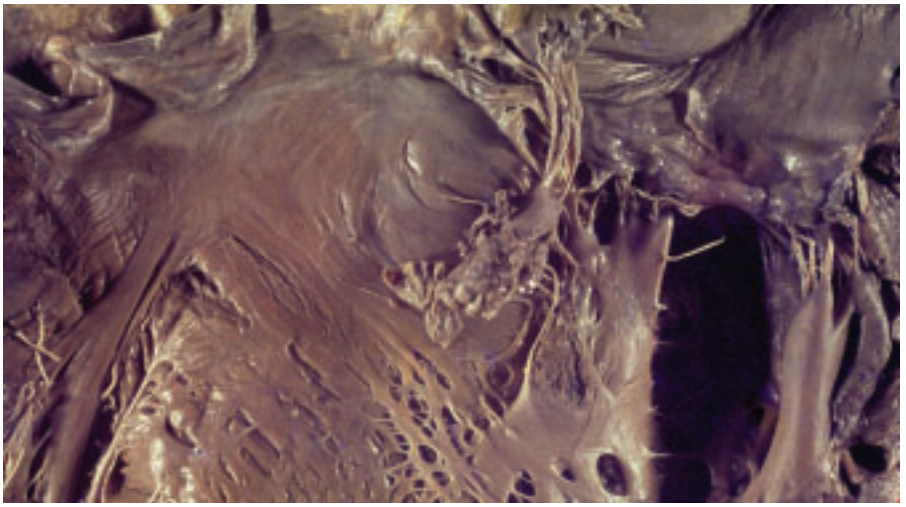

1-69. Ruptured papillary muscle head complicating acute myocardial infarction of left ventricle.

1-70. Acquired ventricular septal defect due to ruptured interventricular septum complicating acute myocardial infarction.

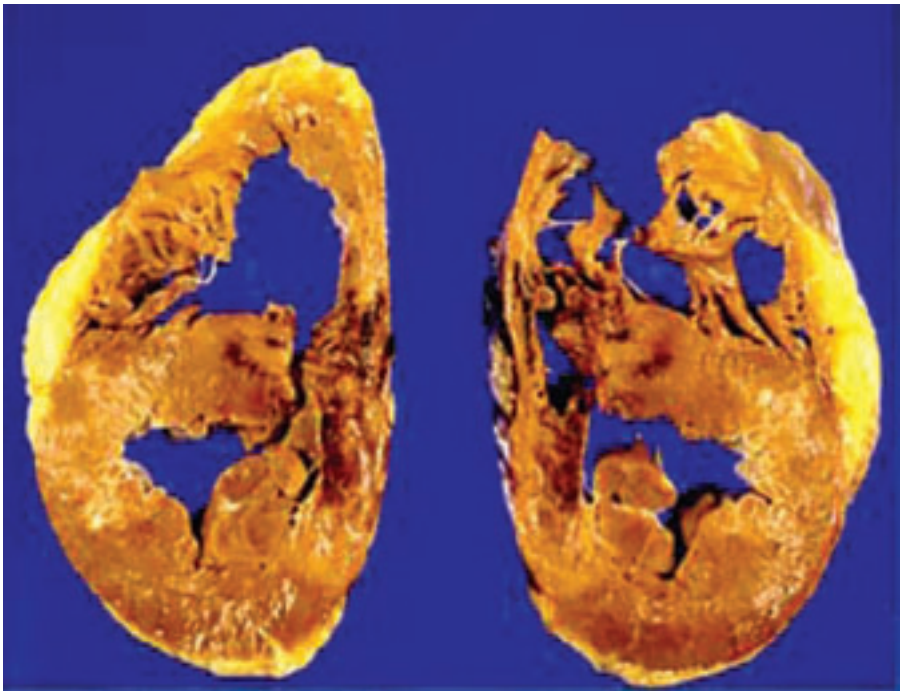

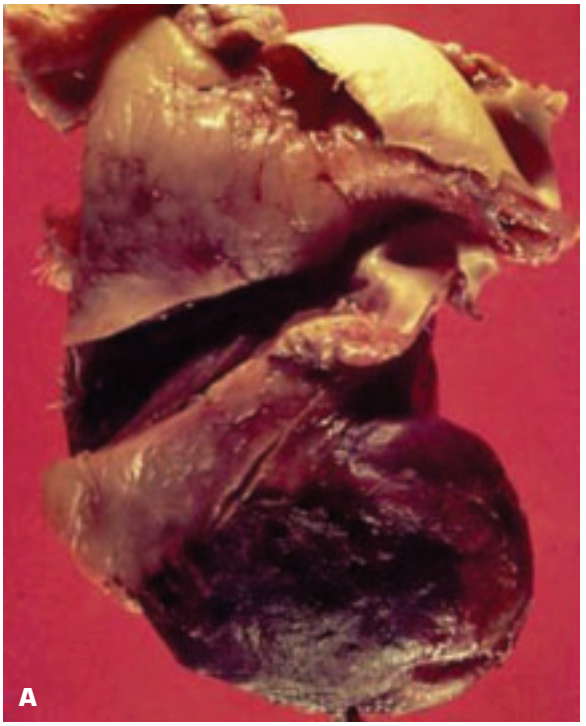

1-71. A. Cardiac aneurysm of left ventricular apex complicating myocardial infarction. **B.** Remnants of the original myocardial wall in the wall of the aneurysm signify the presence of a true cardiac aneurysm.

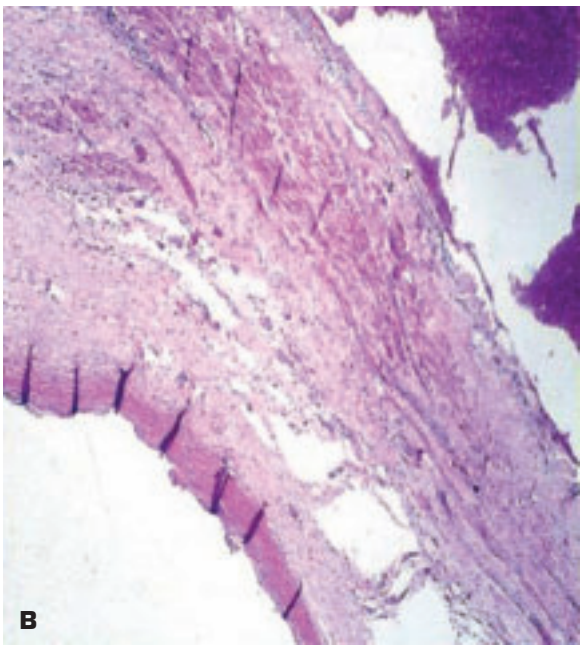

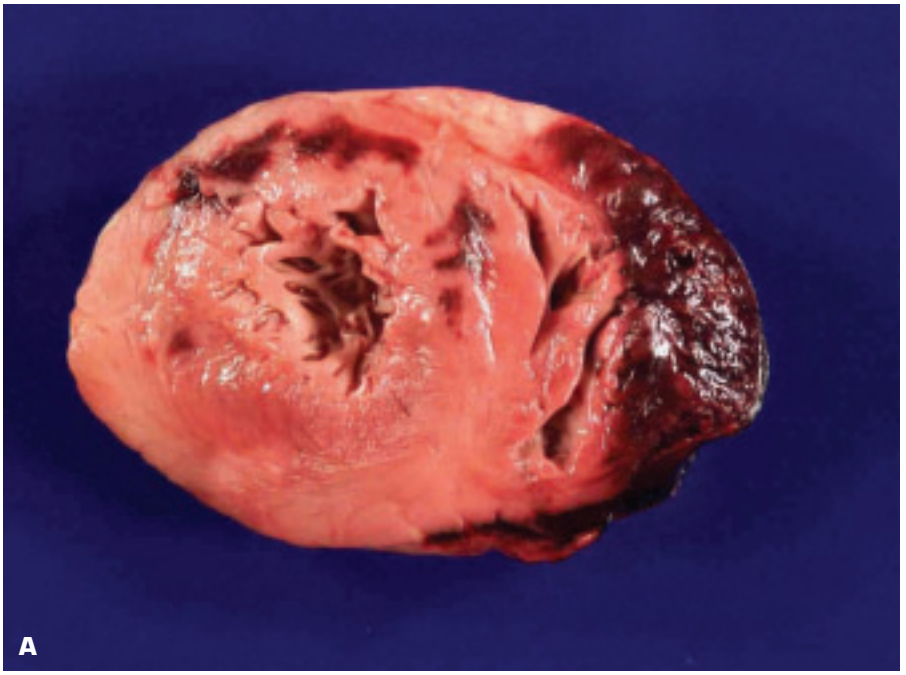

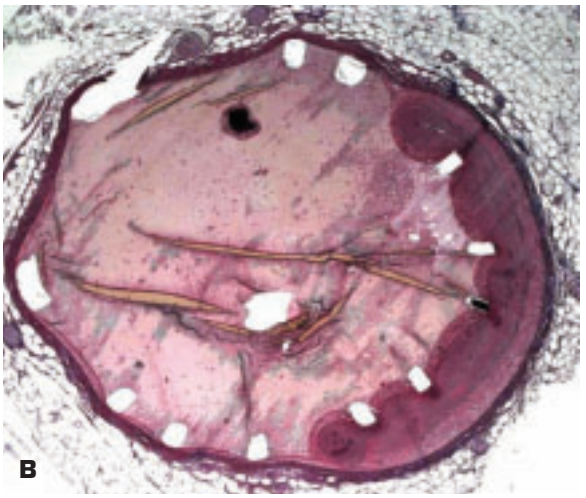

1-72. A. Transverse section of ventricles showing focal hemorrhage within the left ventricle due to a reperfused myocardial infarct. A large intraepicardial hematoma is present over the right ventricle, and death occurred due to massive hemopericardium (cardiac tamponade) that clinically mimicked cardiac rupture. **B.** Section of right coronary artery shows that a stent has been placed within the lumen of a dissection of the artery, and the original lumen is totally compressed. Hemopericardium resulted from intraepicardial bleeding from the dissection, and in turn, this ruptured into the pericardial sac. Bleeding was also favored by the potent antiplatelet agents given for the stent.

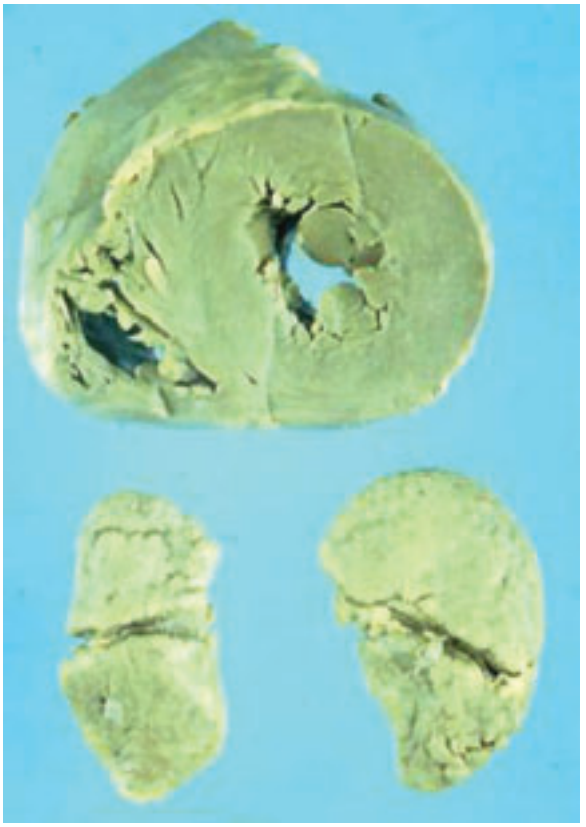

1-73. Transverse biventricular slice of heart showing concentric hypertrophy of left ventricle, incipient chamber dilatation, and the end-stage kidneys from this same patient who had renovascular hypertension.

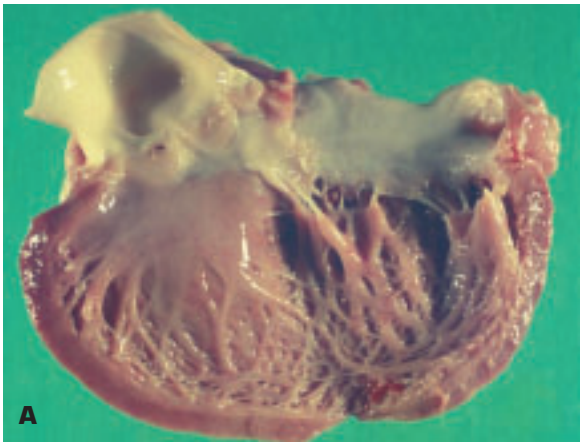

1-74. Acute viral myocarditis. **A.** Dilated, nonhypertrophied heart with slightly mottled myocardium. **B.** Severe interstitial lymphocytic infiltration of the ventricular myocardium with focal loss of myocytes.

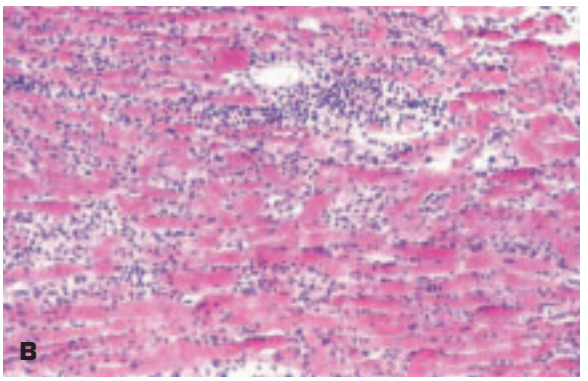

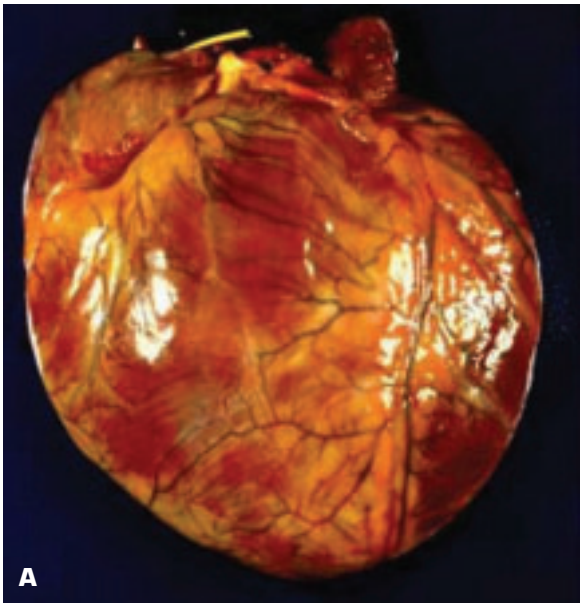

1-75. Idiopathic dilated cardiomyopathy. **A.** Enlarged, football-shaped, globular heart due to generalized chamber hypertrophy and dilatation. **B.** Transverse slice of heart showing diffuse hypertrophy and dilatation of both ventricles. **C.** Longitudinal section of heart showing abundant stasis thrombi at the apices of both ventricles. *(continued on next page)*

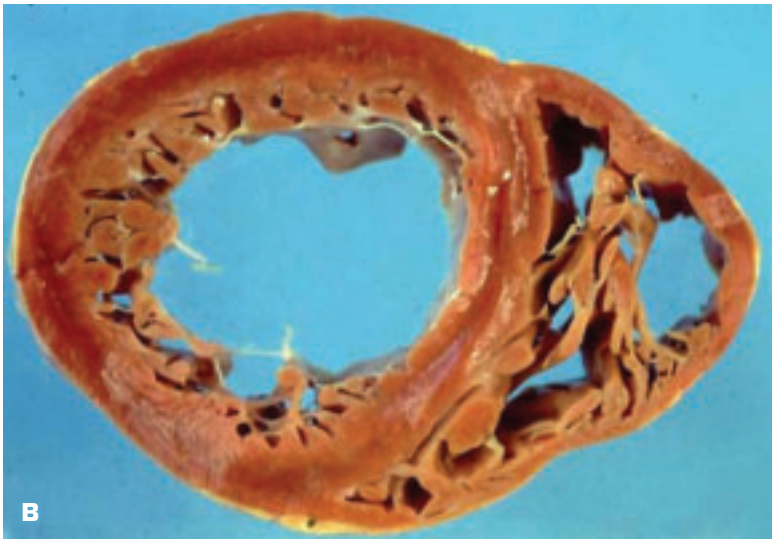

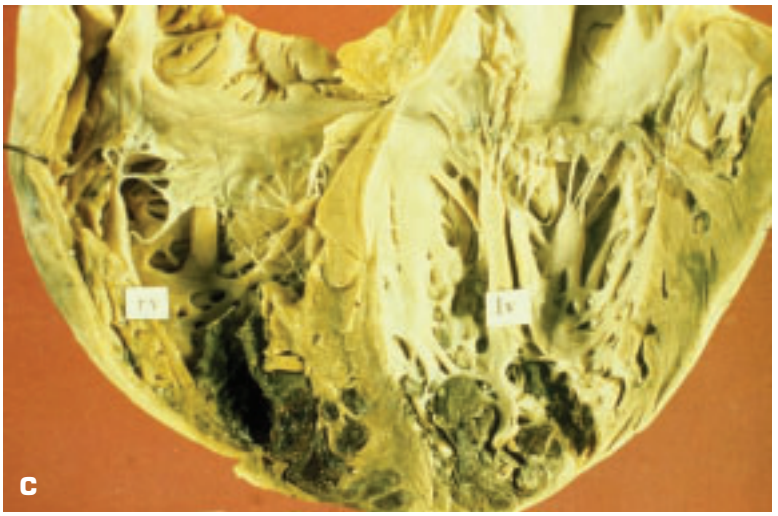

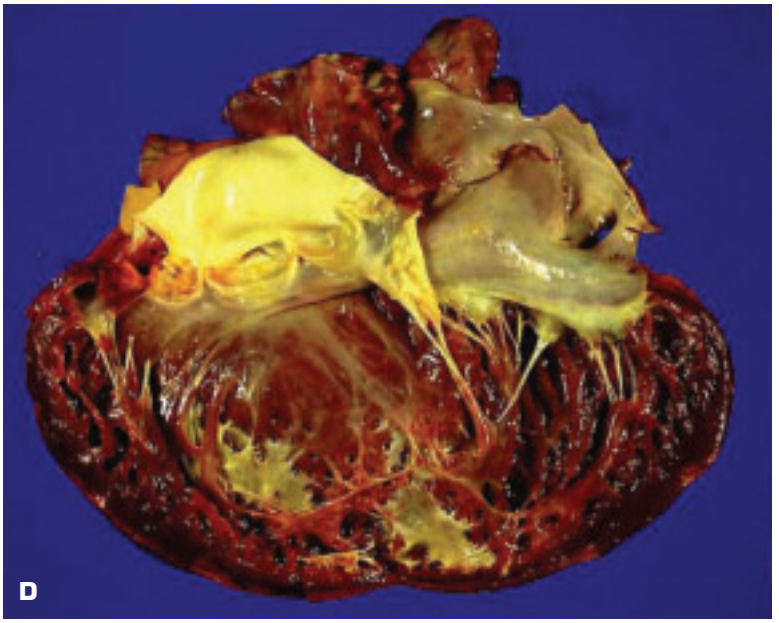

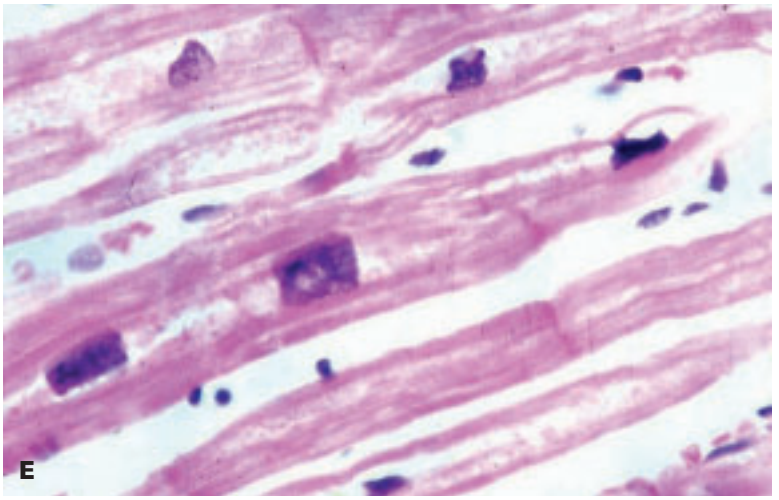

1-75. *(Continued)* **D.** Endocardial scarring near left ventricular apex due to organization of endocardial thrombi. **E.** Histologic evidence of myocyte hypertrophy, namely squared off (box car) nuclei.

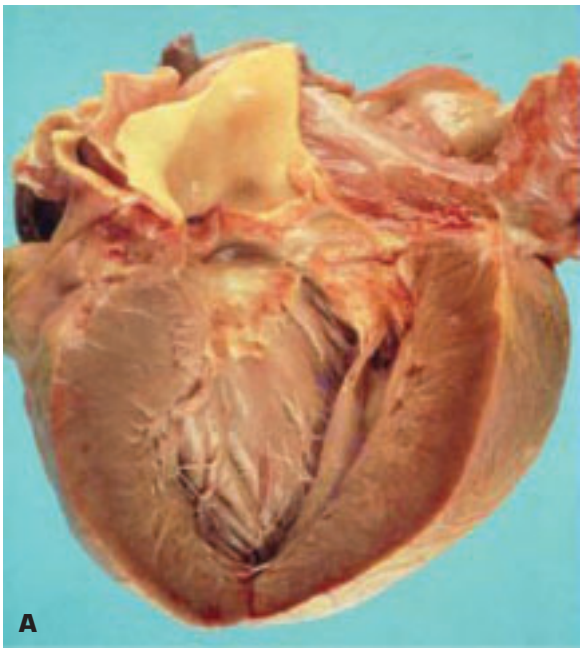

1-76. Hypertrophic cardiomyopathy. **A.** Noteworthy features include massive concentric hypertrophy of left ventricle, inward bulging interventricular septum with mirror image plaque of anterior mitral leaflet, and reactive thickening of anterior leaflet of mitral valve. Note that the mirror image plaque lies more inferiorly than the mitral valve because, during life, tension in its papillary muscles holds the valve at a lower level than after death. **B.** Transverse biventricular slice showing asymmetric septal hypertrophy (interventricular septum is thicker than free wall of left ventricle). **C.** Myocyte disarray in a section taken from midportion of the interventricular septum.

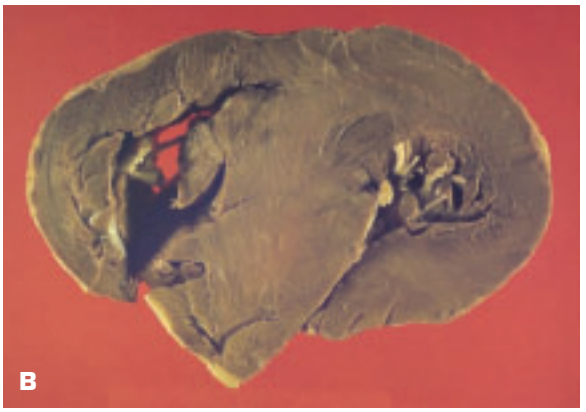

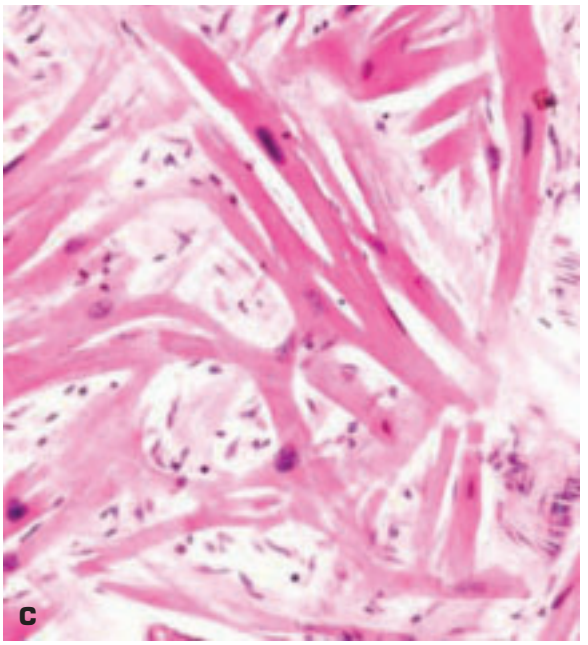

1-77. Sigmoid septum (*) associated with aging. The aorta comes off from the right side of the top of the interventricular septum rather than straight up from its summit. Clinically, a cardiologist may have difficulty distinguishing this entity from true hypertrophic cardiomyopathy.

1-78. Restrictive cardiomyopathy. **A.** Amyloidosis of the heart with the amyloid deposits being most visible as granular elevations on the right atrial endocardial surface. **B.** Amyloid nodular deposit in endocardium (Congo Red stain). **C.** Amyloid deposits in a small artery and its surrounding connective tissue (sulphated Alcian blue stain).

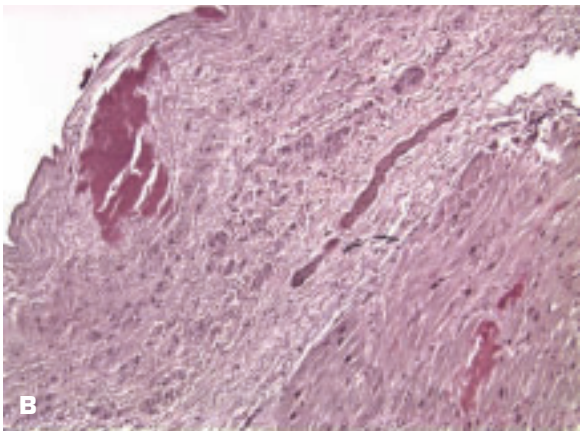

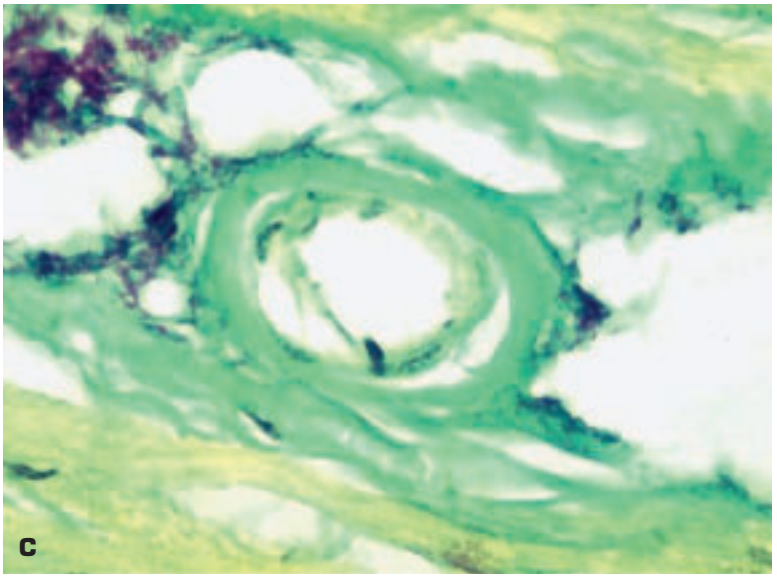

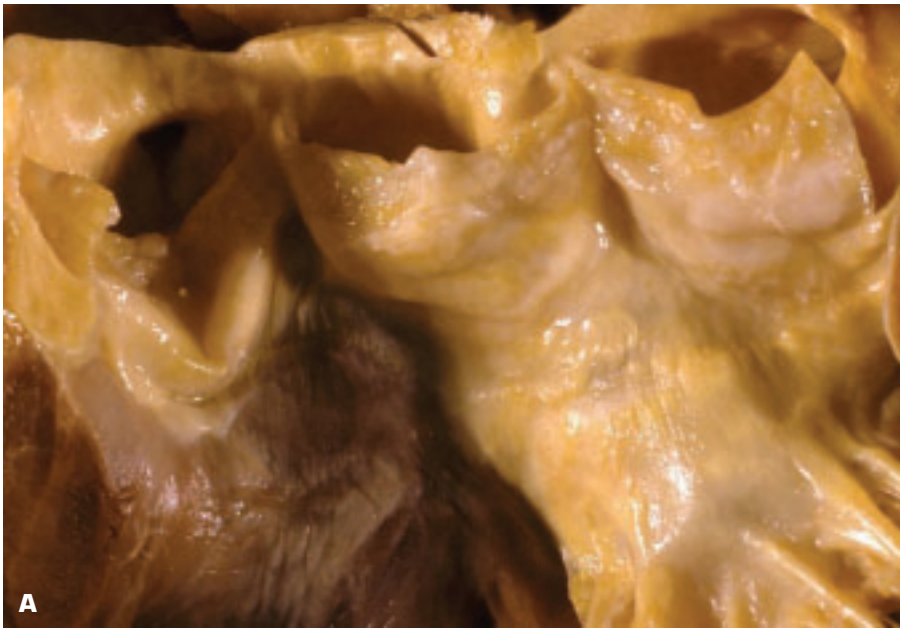

1-79. A. Cardiac amyloidosis with prominent involvement of the left-sided heart valves. **B.** Histology of aortic valve cusp showing massive amyloid deposits (methyl violet stain).

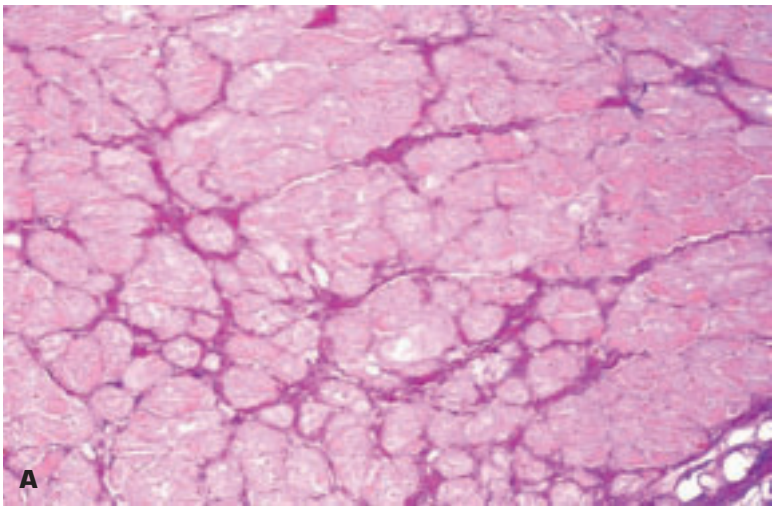

1-80. Other causes of a restrictive cardiomyopathy. **A.** Diffuse interstitial fibrosis of unknown cause led to a restrictive cardiomyopathy in this patient. **B.** Hemochromatosis: the iron-laden heart is a weak heart! Note the greater than normal brown color of the myocardium. **C.** Histology shows massive blue-staining iron deposits within cardiac myocytes (Perl's Prussian blue stain).

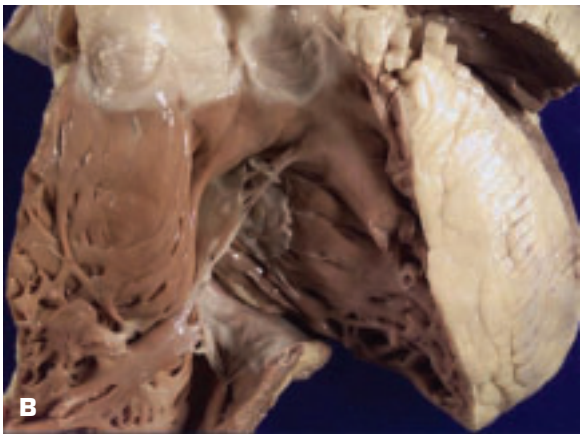

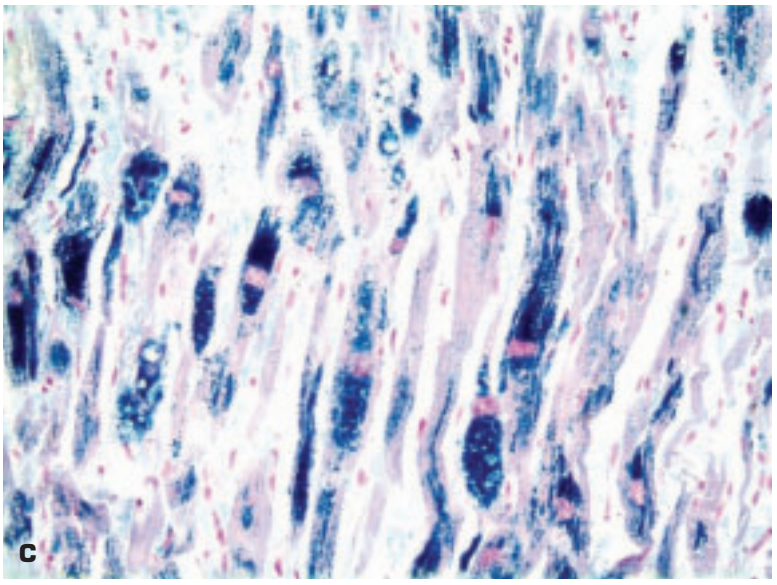

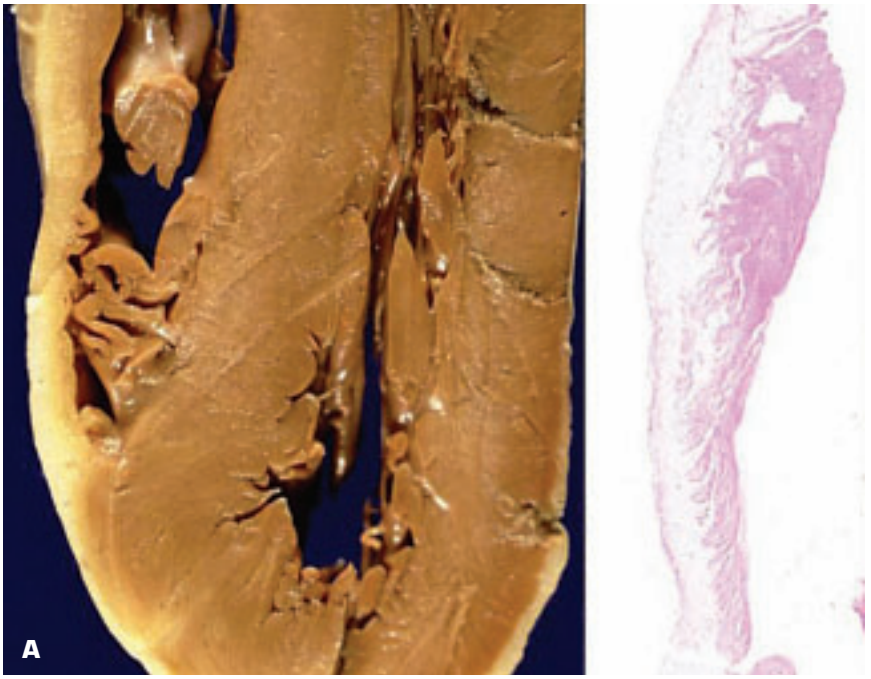

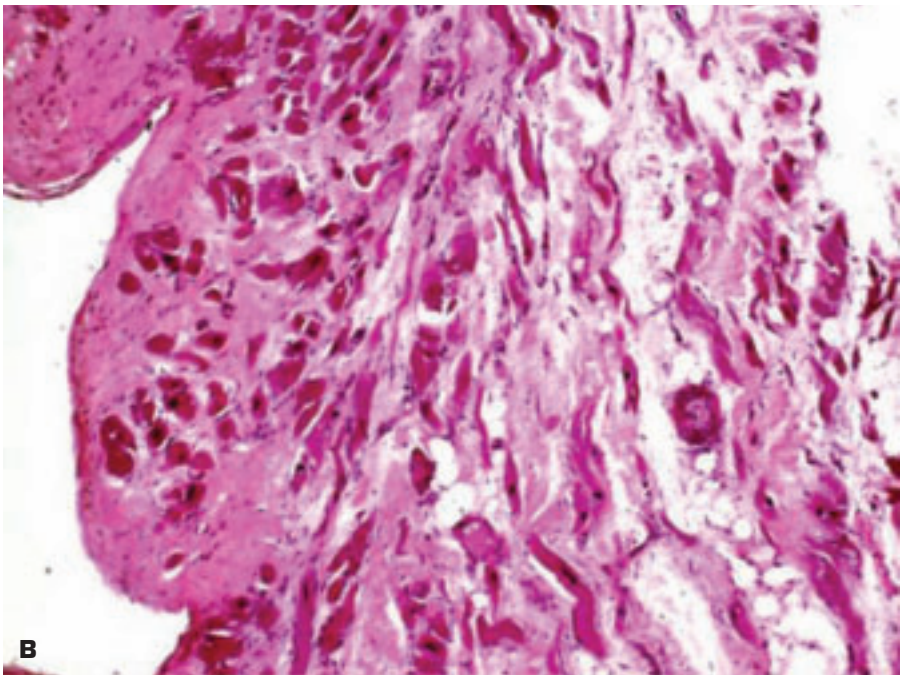

1-81. A. Arrhythmogenic right ventricular dysplasia/cardiomyopathy in a young boy who suffered sudden, unexpected death. Note the greatly thinned apical free wall of the right ventricle (RV). Low-power histology of the RV is shown in the right panel. **B.** Isolated myocytes lie within fibroadipose tissue and fibrous tissue. Some cases may show lymphocytic infiltrates.

1-82. A. Noncompaction of the left ventricle (NCLV) showing absence of the normal smoothness to the septal wall of the left ventricle; this heart was explanted at the time of cardiac transplantation from a 4-year-old girl with severe heart failure. NCLV will probably be included as a new form of idiopathic cardiomyopathy in future classifications of cardiomyopathy. **B.** Microscopic appearance of noncompacted left ventricle.

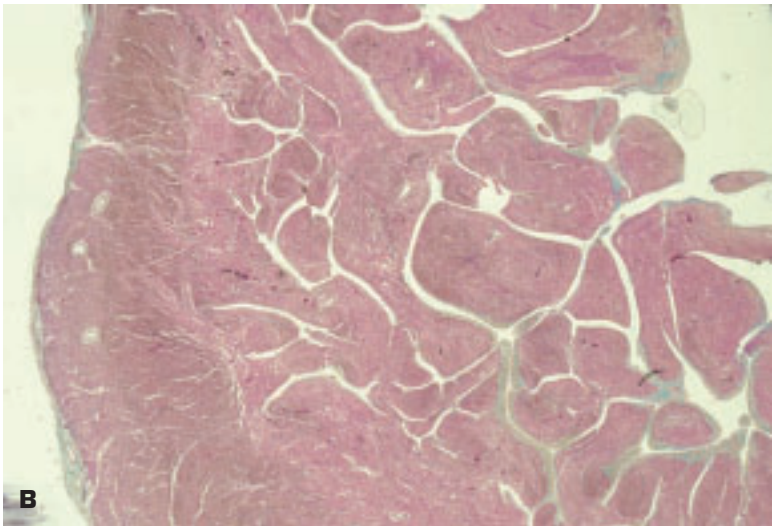

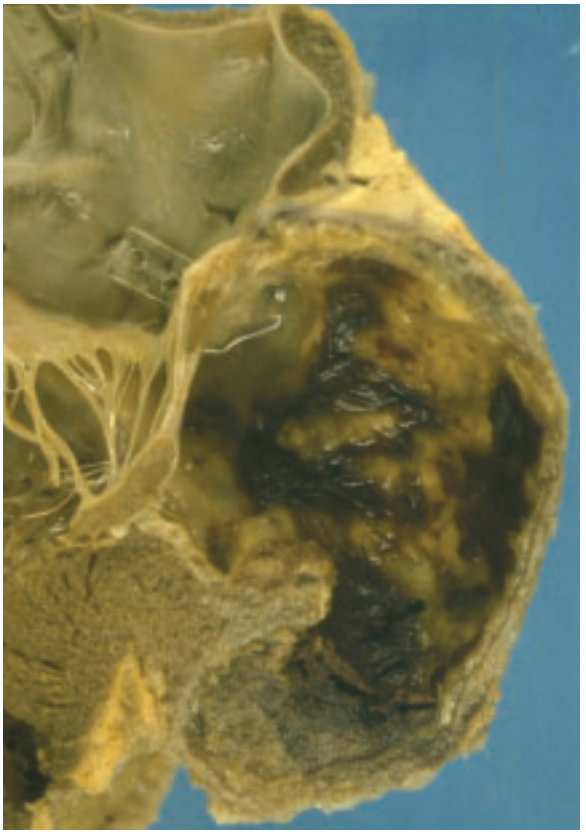

1-83. Idiopathic submitral aneurysm is believed to result from a developmental weakness of the attachment between the mitral annulus and the left ventricle. The condition is more common in certain tribes in southern Africa than in Caucasian populations.

1-84. Orthotopic cardiac transplantation. Note the marked difference in appearance between the normal donor left atrial component and the postrheumatic calcified organized thrombi in the recipient's left atrial component. This donor heart failed due to graft arteriopathy (chronic rejection). Graft arteriopathy is characterized by histologic evidence of myocardial fibrosis and luminal narrowing of both epicardial and intramyocardial coronary arteries (see Fig. 1-86C and D).

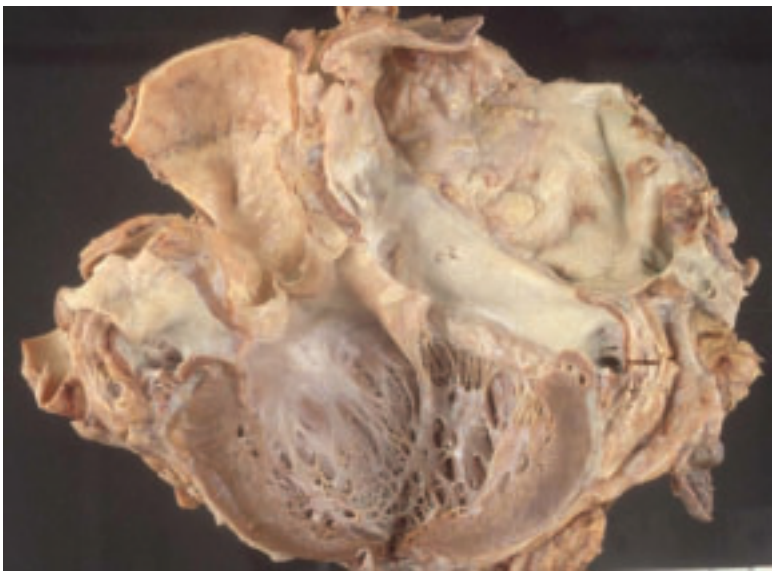

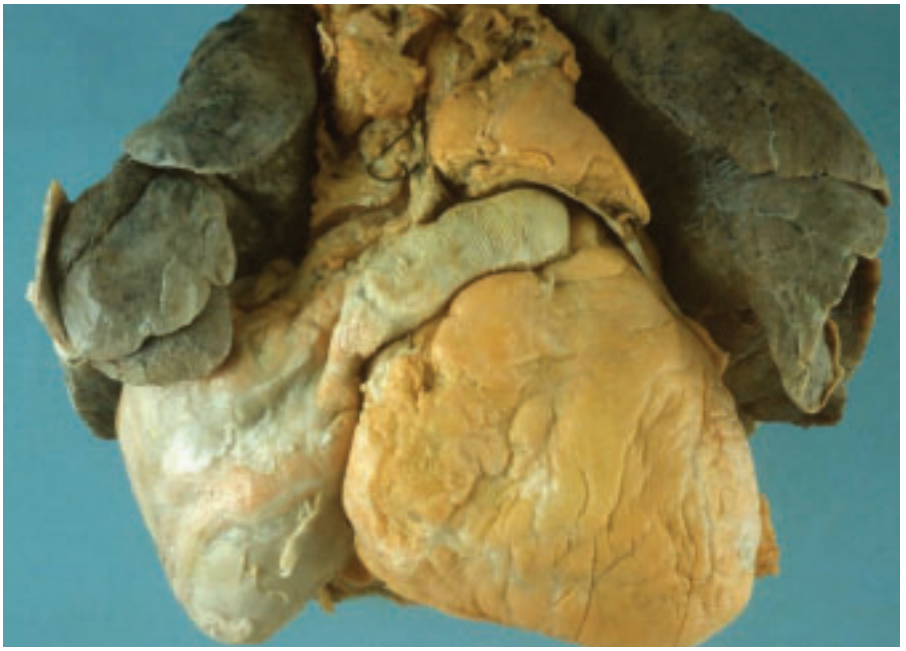

1-85. Heterotopic cardiac transplantation ("piggy-back heart"): the donor heart lies on the left side of the picture, and a Dacron tube graft links the two pulmonary arteries.

1-86. A. Severe acute rejection with arteritis leading to focal areas of ischemic infarction of the left ventricle in an explanted donor heart. Immunosuppression had been discontinued shortly before the heart was removed and replaced by another donor heart. **B.** Histology of severe acute rejection showing marked interstitial lymphocytic infiltration. *(continued on next page)*

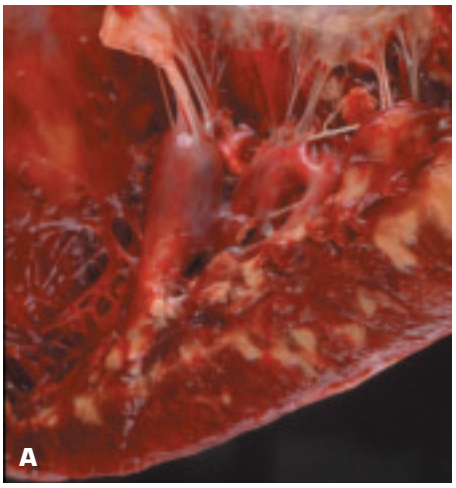

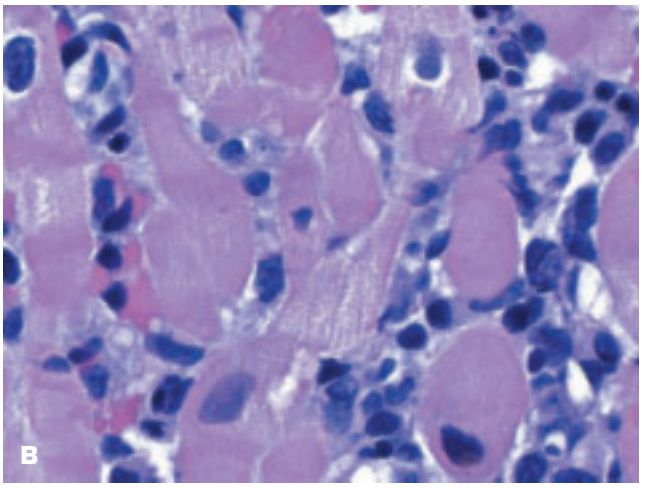

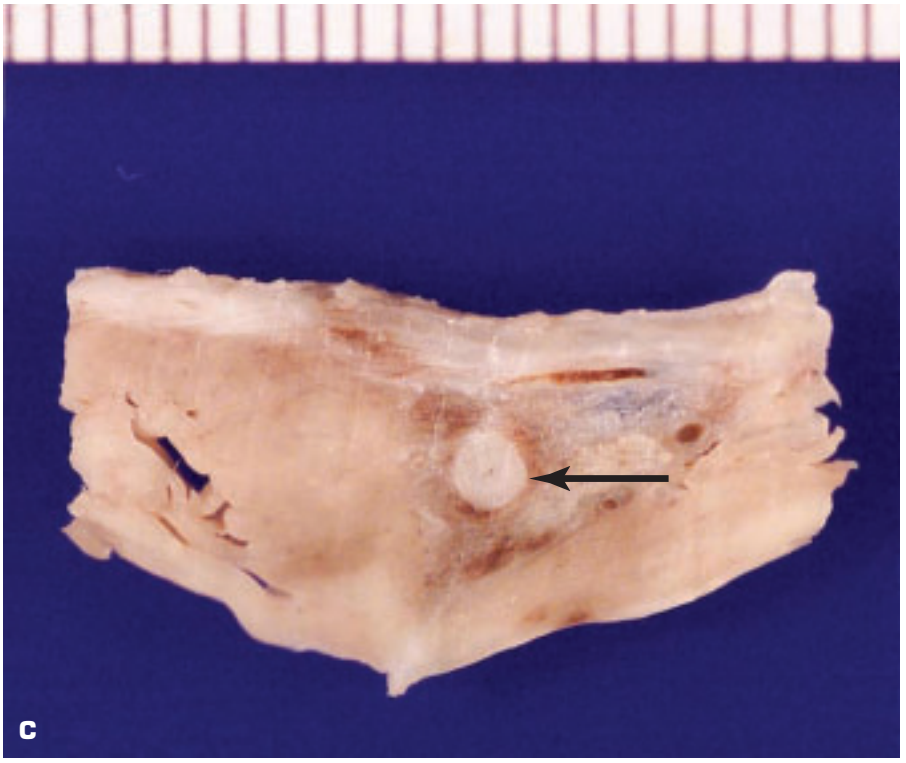

1-86. *(Continued)* **C.** Macroscopic appearance of greatly thickened donor heart coronary artery (arrow) with pinhole lumen due to graft arteriopathy (chronic rejection). **D.** Histology of the same artery showing marked intimal fibrous thickening, residual arteritis, and medial hyalinization.

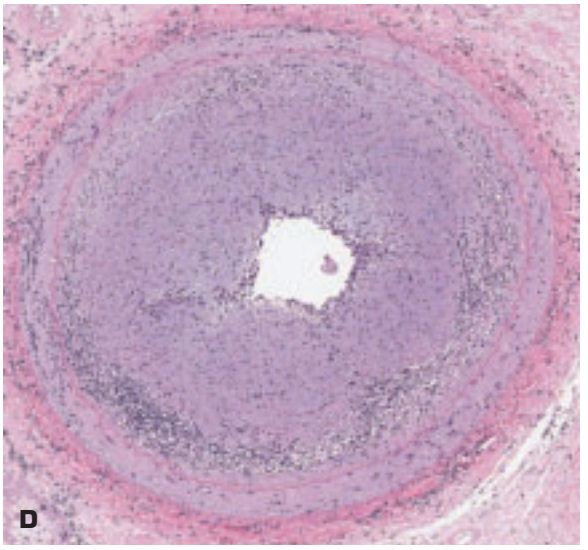

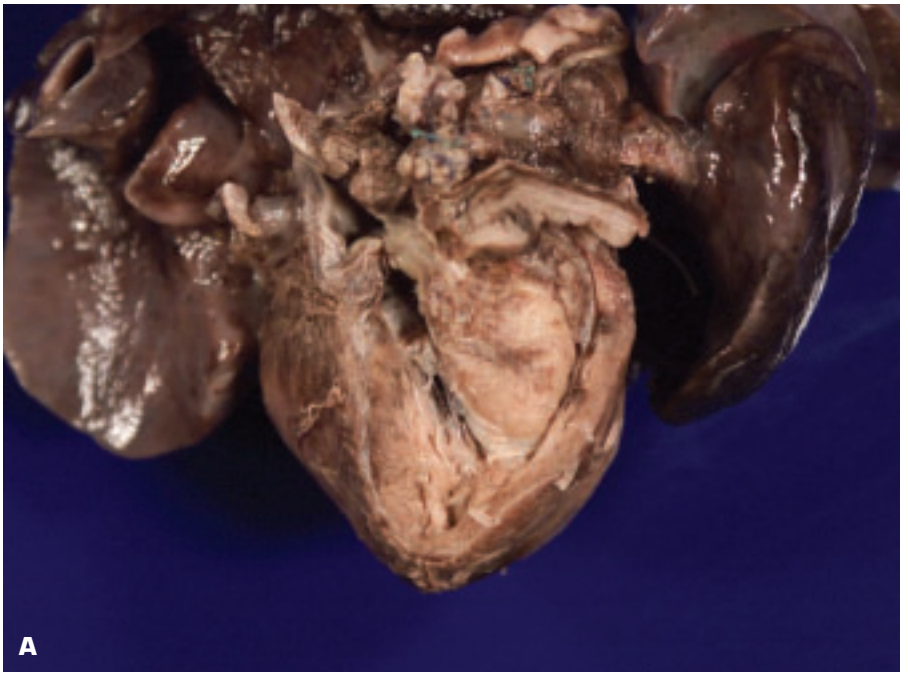

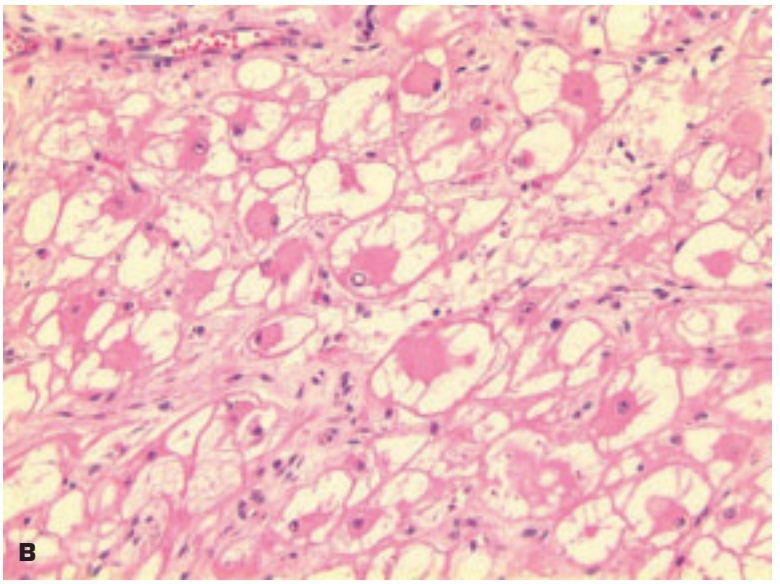

1-87. A. Right ventricular view of incompletely excised rhabdomyoma affecting interventricular septum in a young child. **B.** Histology shows the typical glycogen vacuolated "spider-like" rhabdomyoblasts.

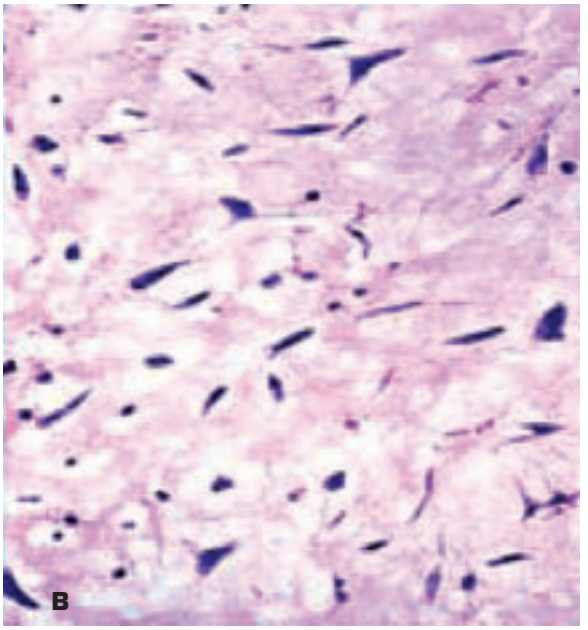

1-88. A. Myxoma of left atrium is attached by a short stalk to the area of the fossa ovalis. **B.** Typical histology of a myxoma showing spindle- and stellate-shaped cells lying in a loose, myxoid stroma rich in acid mucopolysaccharides. The tumor cells may be arranged in cords that later give rise to capillaries. **C.** Adenomatoid tumor (*pointer*) of atrioventricular node is elevating right atrial endocardium near coronary sinus ostium. **D.** Histology of adenomatoid tumor shows large, epithelioid cells lining a tubular space.

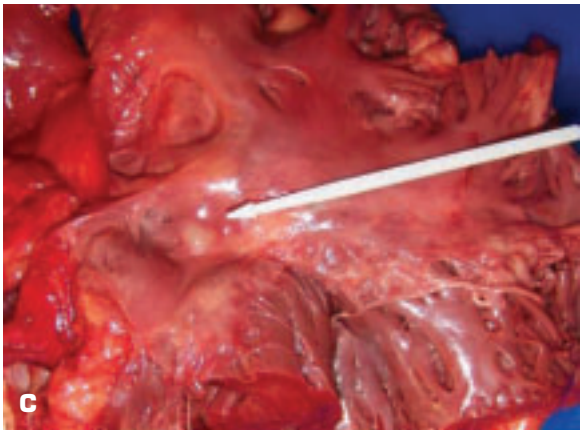

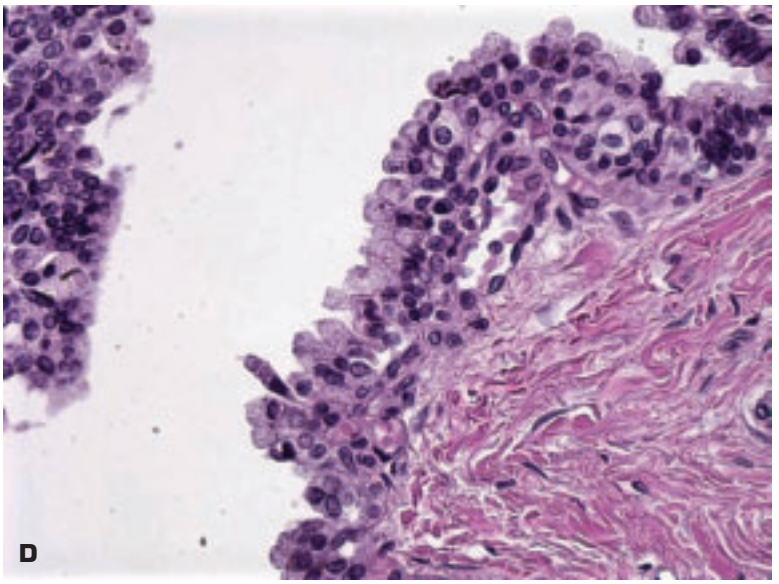

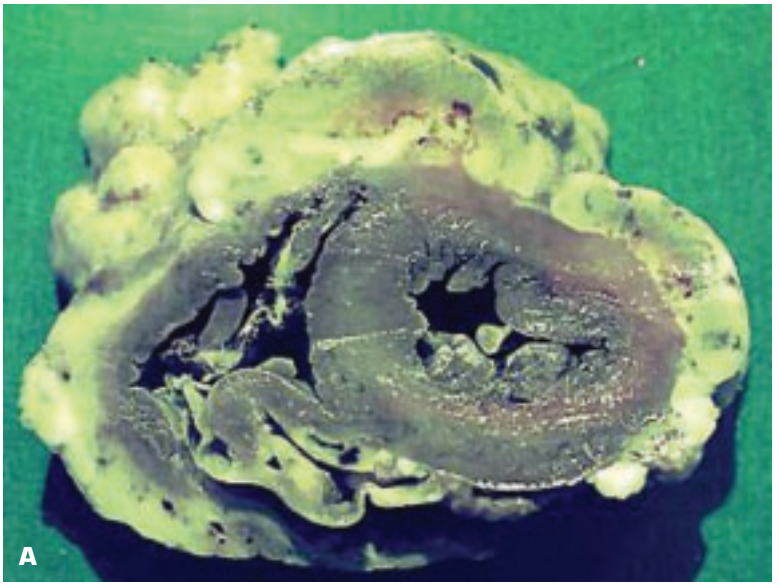

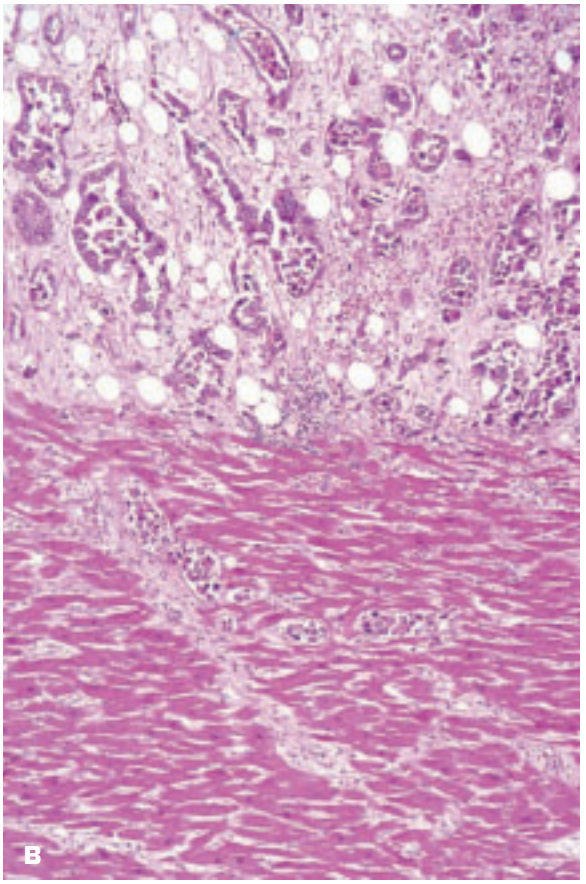

1-89. A. Metastatic lung cancer to the epicardium; secondary tumors are 20 times more common than primary cardiac tumors. **B.** Histology shows moderately differentiated adenocarcinoma occupying the epicardial layer. **C.** Polypoid endocardial metastatic deposit of a plasmacytoma.

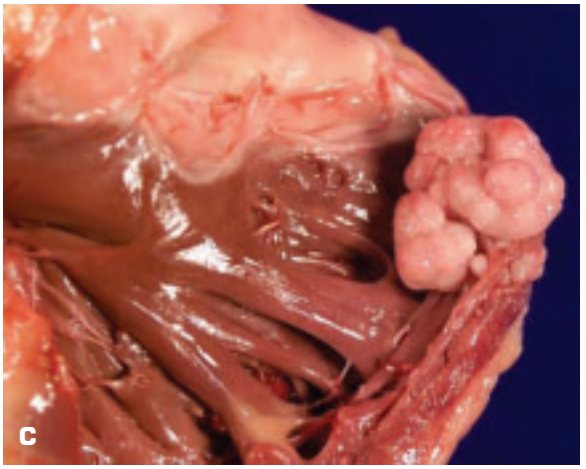

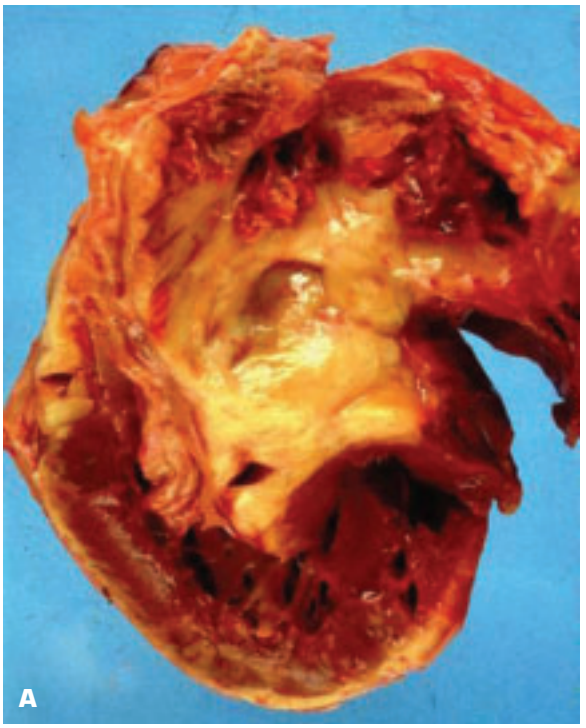

1-90. A. Metastatic lymphoma to the heart from mediastinal lymph nodes usually infiltrates via the interatrial fibroadipose tissue layer and, in this patient, extended into the upper portion of the interventricular septum (seen here from the right side) to produce complete heart block. Hematogenous spread may affect any portion of the myocardium. **B.** Histology shows diffuse infiltration by atypical lymphocytes separating the atrial myocytes.

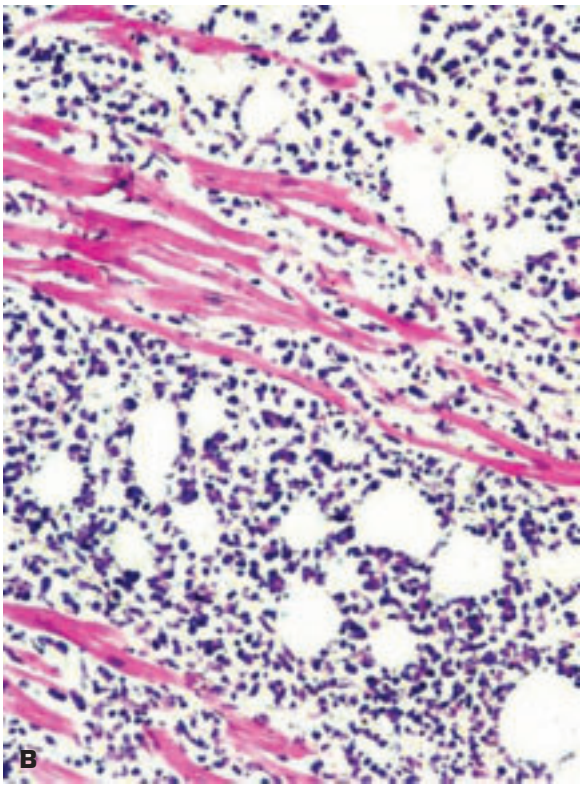

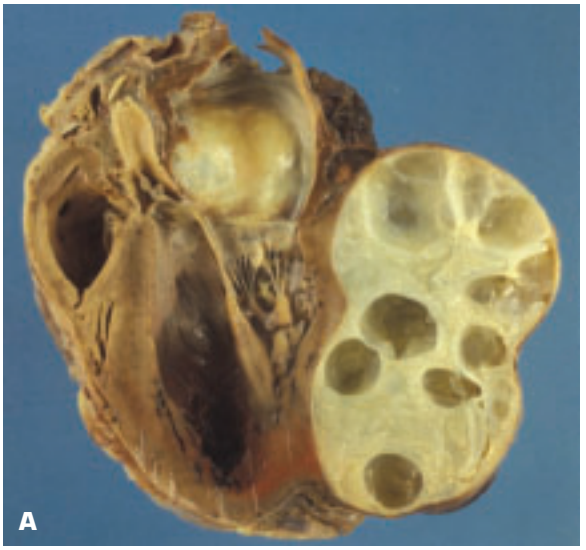

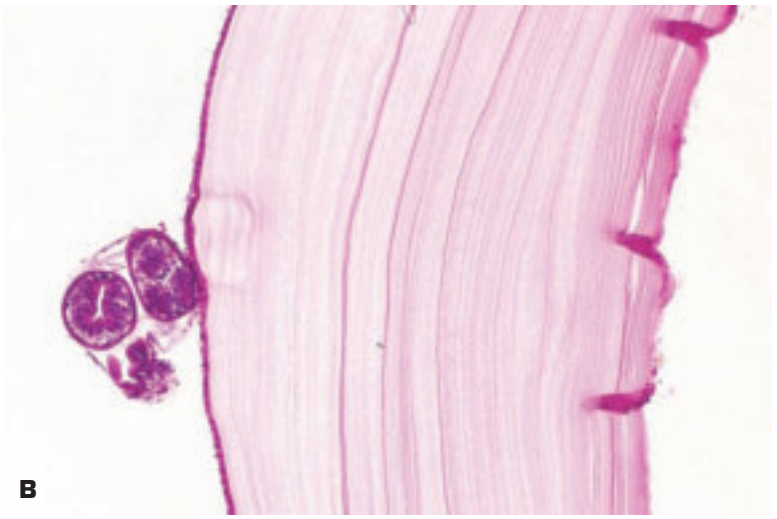

1-91. Hydatid disease (echinococcosis) of the heart. **A.** Hydatid cysts are present within the free wall of the left ventricle (*right*) and in the interatrial septum. **B.** Histology of the cyst wall (periodic acid-Schiff stain) shows scolices lying attached to the germinal epithelium (*left*).

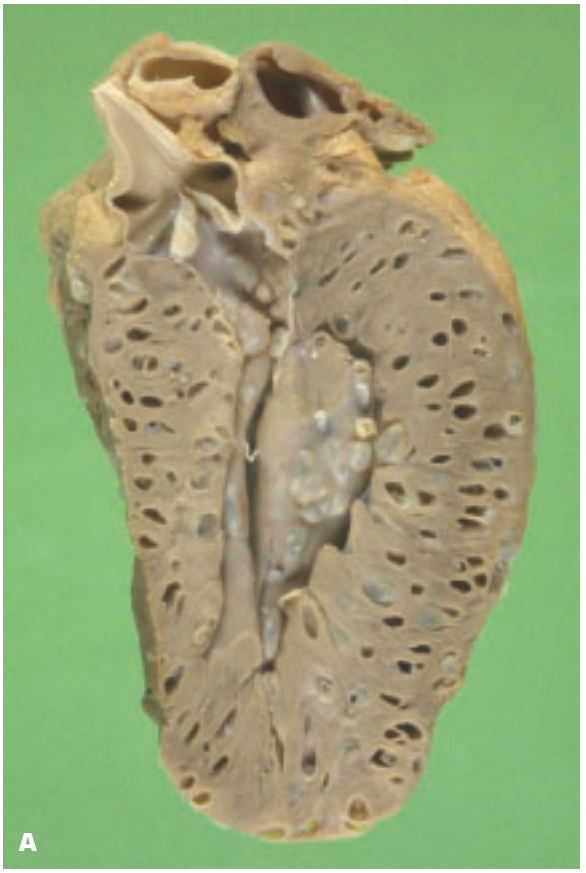

1-92. Cysticercosis of the heart due to *Taenia saginata* (pork tapeworm). **A.** Innumerable small cysts (each containing a single scolex) are scattered throughout all layers of the left ventricle. **B.** Histology of the cyst wall and portion of a scolex.

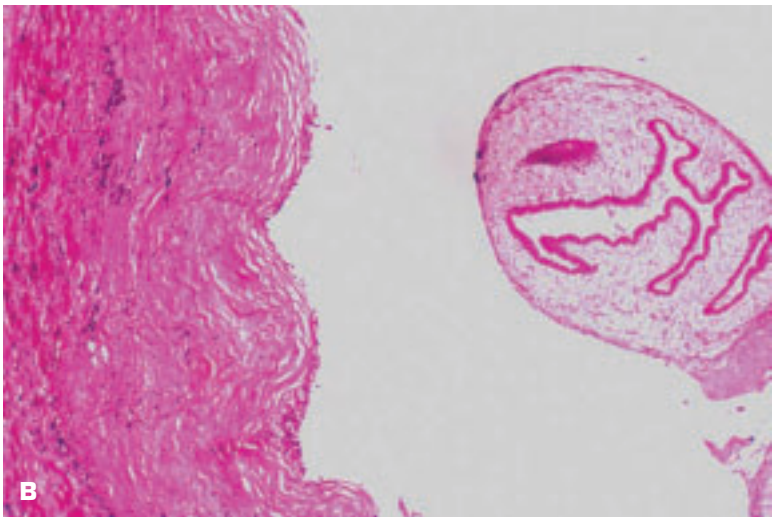

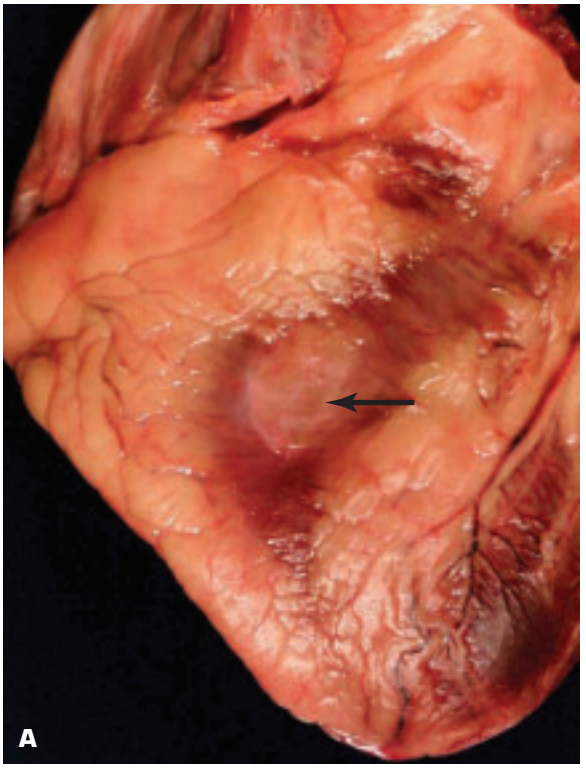

1-93. A. Macroscopic appearance of a milk spot (previously called "soldier's heart") (*arrow*). **B.** Histology shows the contrast between the normal, thin epicardium (*top left*) and the thickened, organized epicarditis that has produced the milk spot.

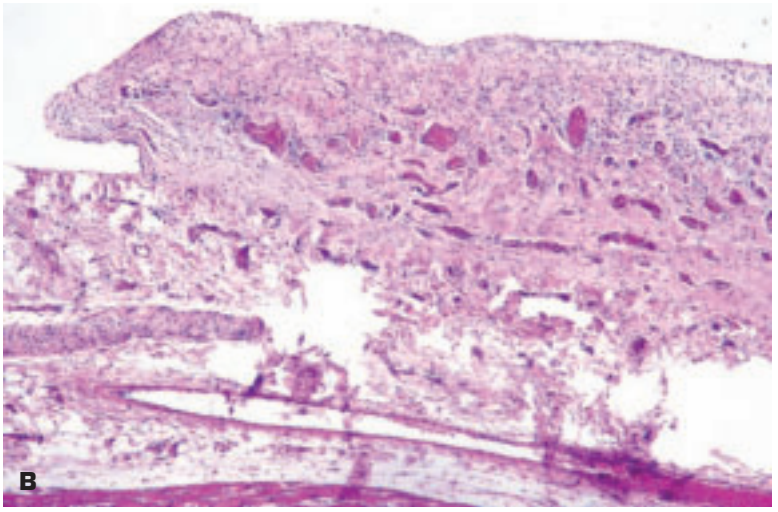

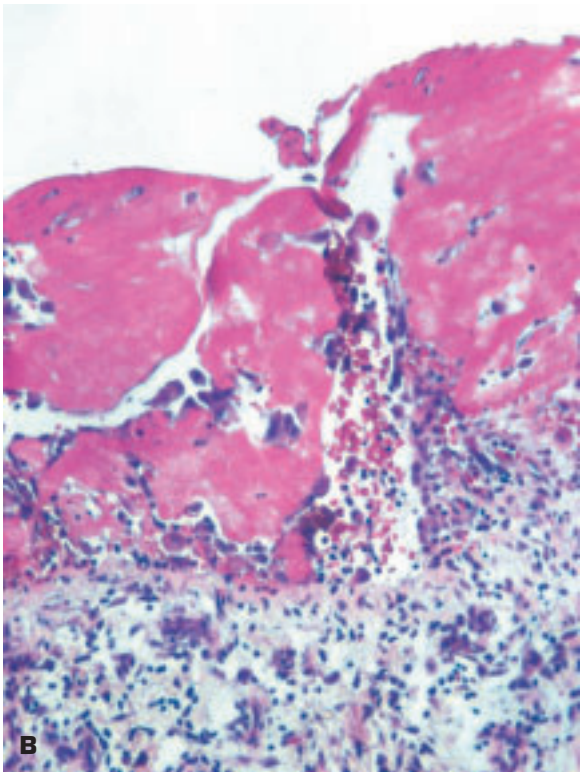

1-94. A. Fibrinous pericarditis (the beloved "bread-and-butter pericarditis" of pathologists, alluding to the strands of fibrin drawn up by the opposing visceral and parietal layers of the pericardium analogous to pulling apart two slices of buttered bread). **B.** Organizing fibrinous pericarditis showing histiocytes engulfing fibrin. **C.** Cardiac tamponade due to hemopericardium: removal of the parietal pericardium shows clotted blood filling the pericardial cavity in a patient with a ruptured myocardial infarct.

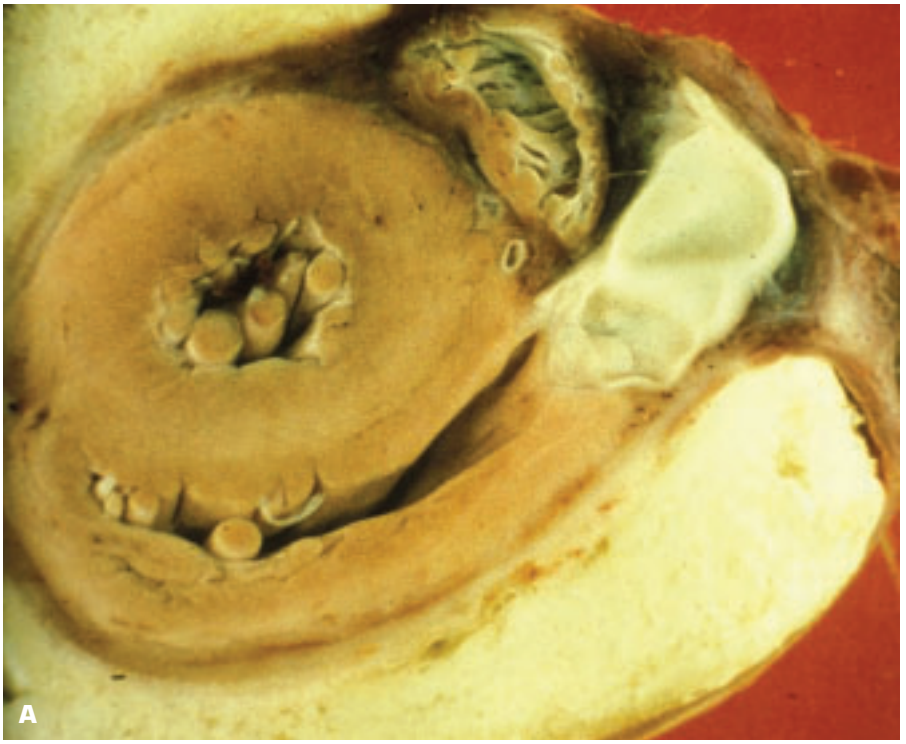

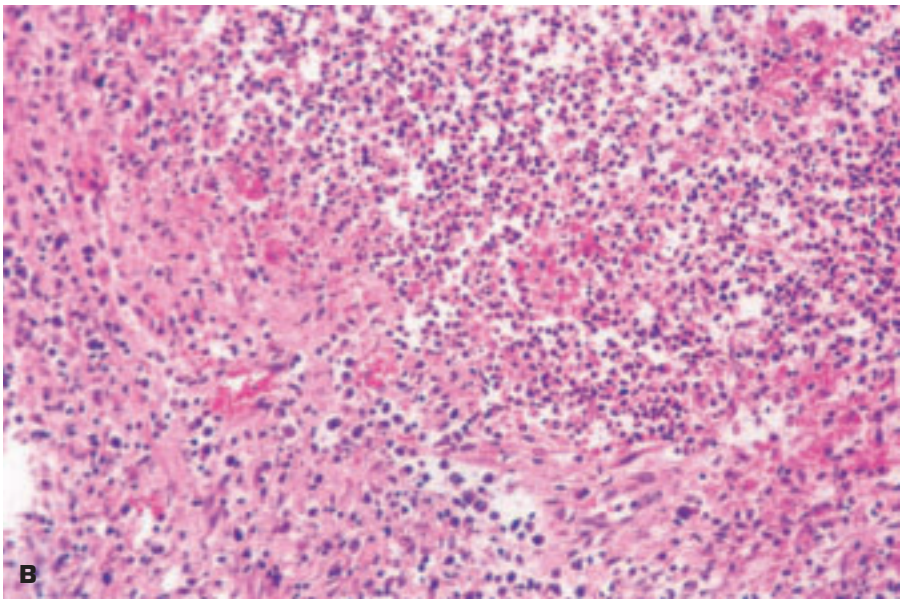

1-95. A. Fibrinopurulent pericarditis showing pus filling the pericardial cavity. **B.** Histology of the exudate shows numerous polymorphonuclear leukocytes as well as some histiocytes indicating a chronic purulent exudate.

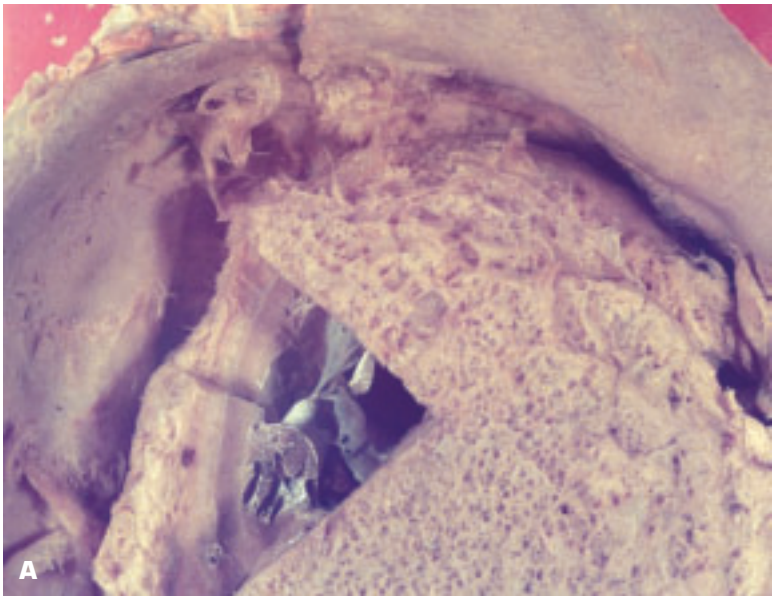
A

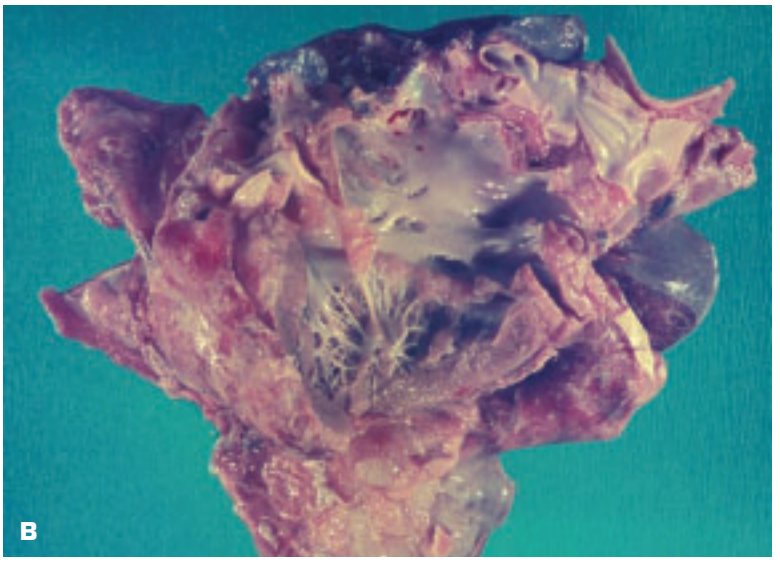
B

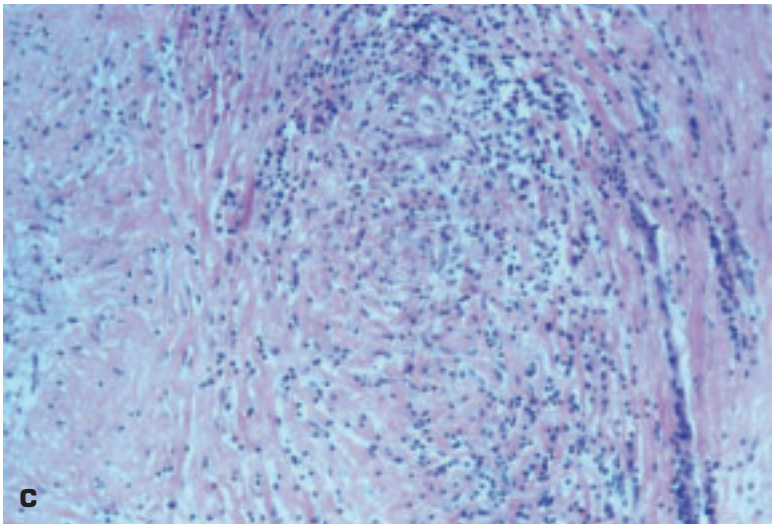
C

1-97. Constrictive pericarditis due to healed tuberculosis. **A.** Heart is encased in a greatly thickened, calcified parietal pericardium. **B.** Transverse section of another heart shows fused, fibrosed parietal and visceral layers of the pericardium with compression of the cardiac chambers that are unable to fill fully in diastole.

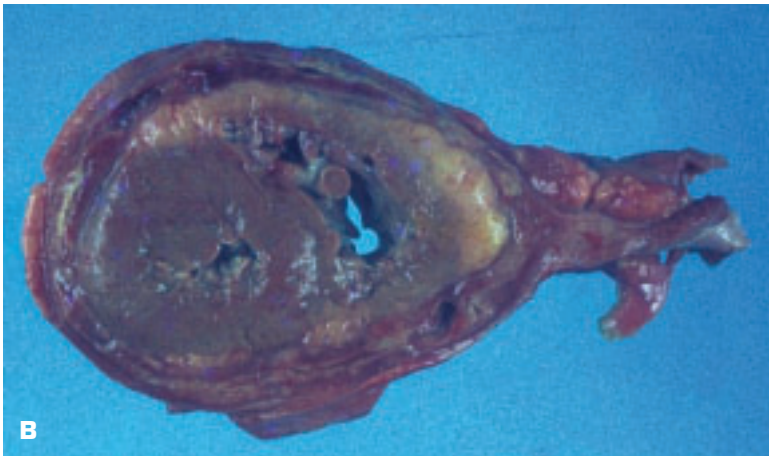

Facing page:

1-96. Active tuberculous pericarditis. **A.** Recent active tuberculous pericarditis with focal yellow tubercles visible on parietal pericardium. **B.** Healed tuberculous pericarditis. Inflamed, densely adherent parietal pericardium has become considerably thickened. Tuberculous infection had spread to the pericardium from adherent mediastinal lymph nodes. **C.** Active granulomatous inflammation with fibrosis due to tuberculosis.

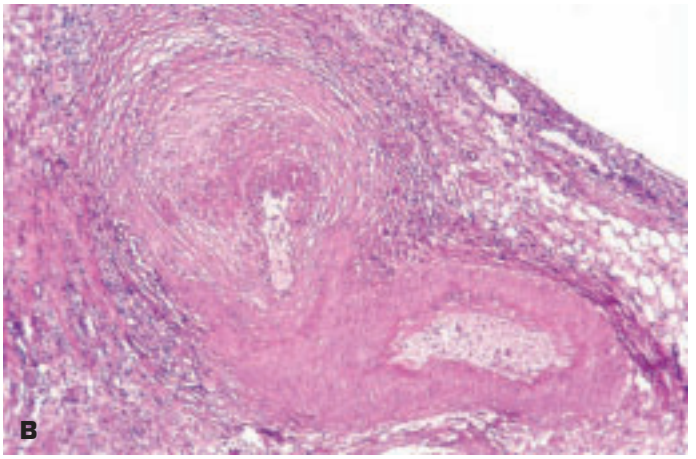

1-98. Polyarteritis nodosa affecting the heart. **A.** Multiple aneurysms of varying sizes lie along the course of the major epicardial coronary arteries and their branches. **B.** Small epicardial coronary artery shows arteritis with aneurysm formation and much of the lumen of the aneurysm is filled by organizing thrombus.

1-99. HeartMate left ventricular (LV) assist device showing pump housing lying within the abdomen and portion of liver and stomach prolapsing between the afferent (*right,* attached to LV apex) and efferent (*left,* terminates in aortic root) drive lines. Porcine bioprosthetic aortic valves within the drive lines assure unidirectional blood flow.

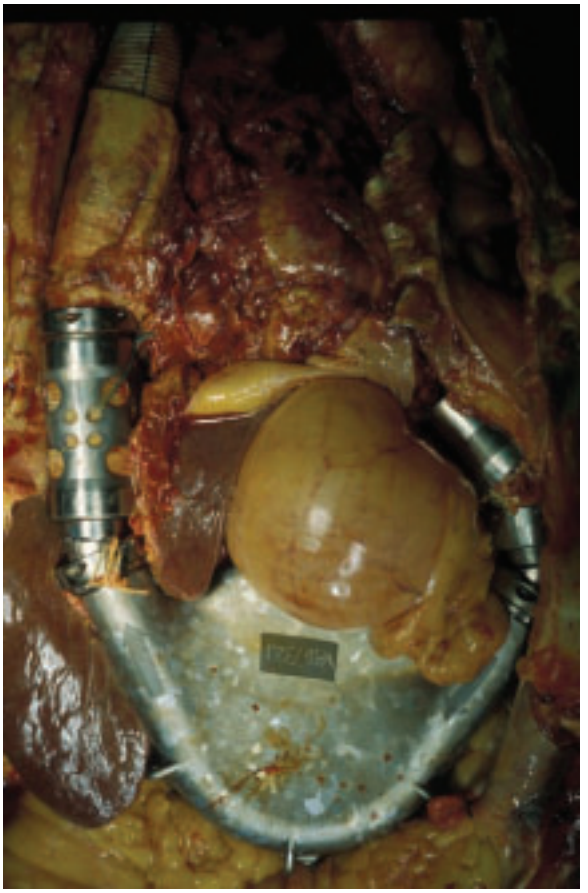

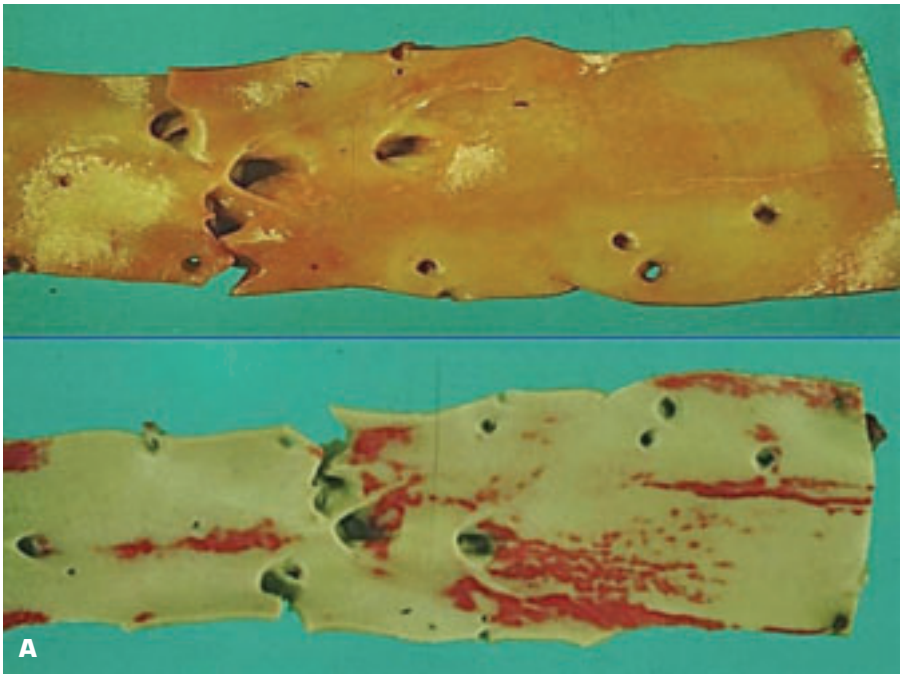

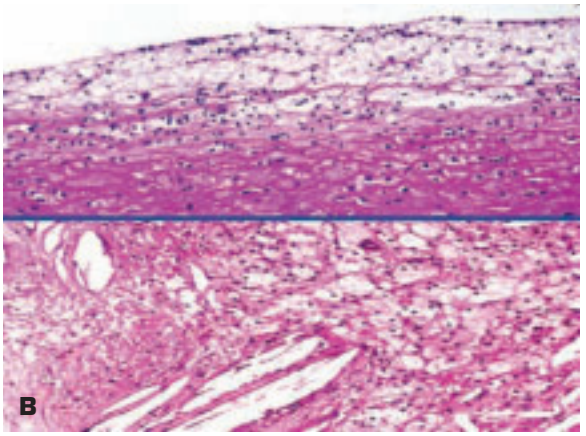

1-100. Fatty streaks and dots on the aortic intima may be precursor lesions of atherosclerosis. The lesions are reversible and are commonly present in young individuals, even babies. **A.** This figure shows two pictures of the same aorta of a young person. The top picture shows a fair number of fatty streaks and dots. In the lower figure, the same aorta has been stained with a fat stain (Oil Red O), and this shows far more dots and streaks than were observed in the natural aorta. **B.** The top histologic section shows that a fatty streak comprises lipid-laden histiocytes occupying the intima. The lower section shows a "progressing fatty streak" in which death of some of the histiocytes has led to release of free lipid into the intima and formation of cholesterol crystals. This event is an important stage in the conversion of a fatty streak to early atherosclerosis because the lipid evokes a further histiocytic and fibromatous response in the intima.

1-101. Dystrophic calcification of the aorta at the junction of the sinus and tubular portion of the aorta (i.e., at the top lip of the sinuses of Valsalva) should not be mistaken for atherosclerosis. The condition has also been termed Stevenson's bar. Elongated calcific protrusions may occasionally obstruct the coronary ostia.

1-102. Ascending arch and descending thoracic aorta. Note that the ascending aorta (*bottom left*) shows no significant atherosclerosis, unlike the remainder of the aorta in which prominent atherosclerosis has developed. This is a common, unexplained phenomenon that is fortunate because coronary arterial bypass grafting uses the ascending aorta.

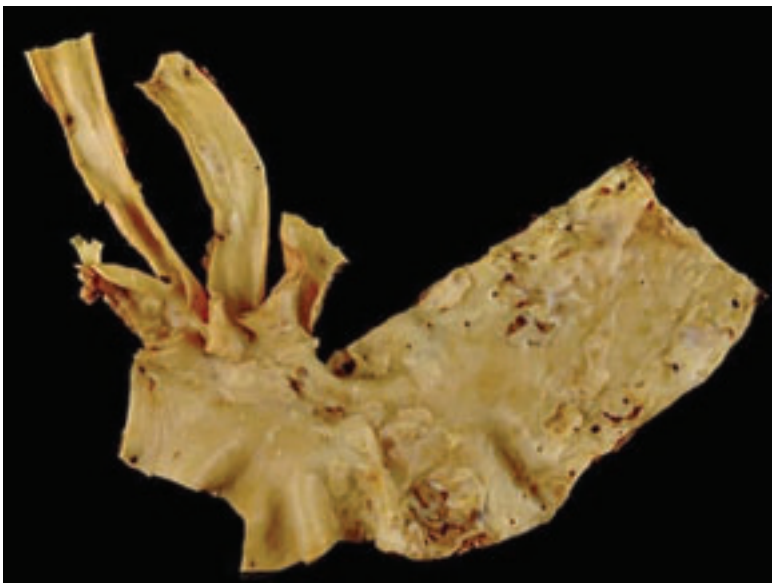

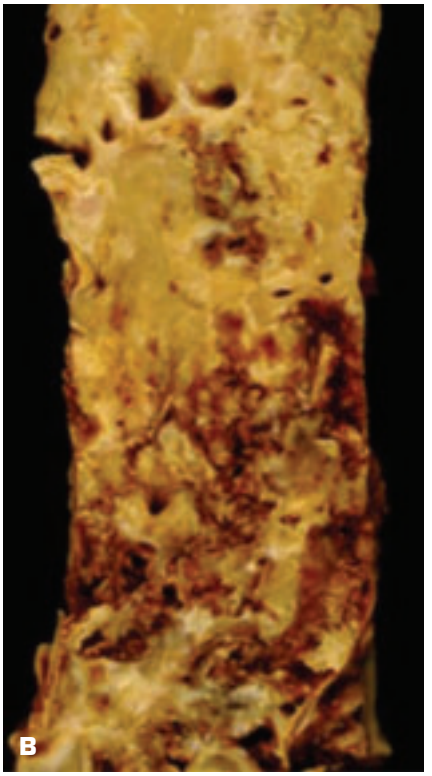

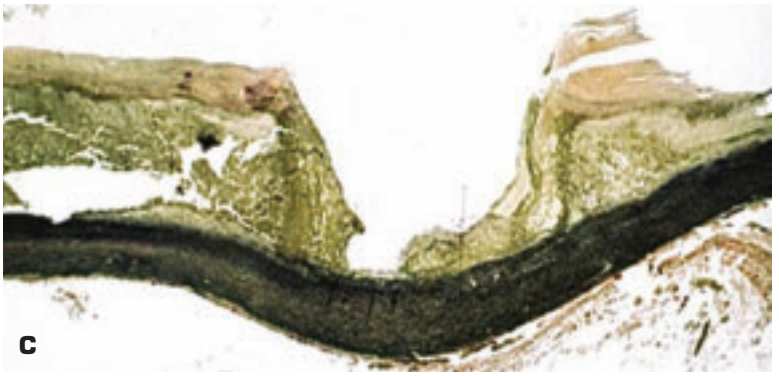

1-103. Due to the effects of gravity, atherosclerosis tends to be most severe in the abdominal aorta. **A.** Severe atherosclerosis with abundant superadded surface thrombi. An atheroembolus (*) occludes the ostium of the celiac artery. **B.** Severe atherosclerosis of the abdominal aorta below the renal arteries with surface ulcerations and extensive associated mural calcification. **C.** The defect in the center of this atherosclerotic plaque is the site of origin of an atheroembolus. **D.** Atheromatous embolism has occluded this artery within the pancreas.

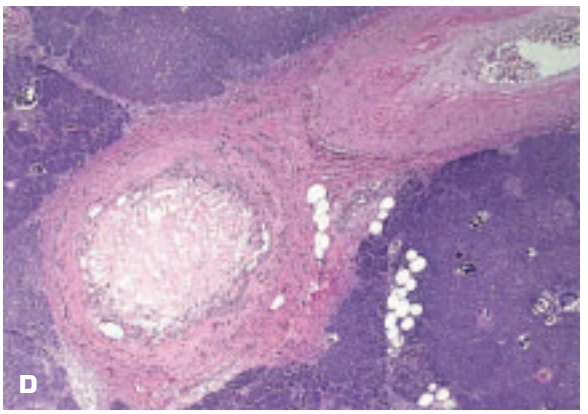

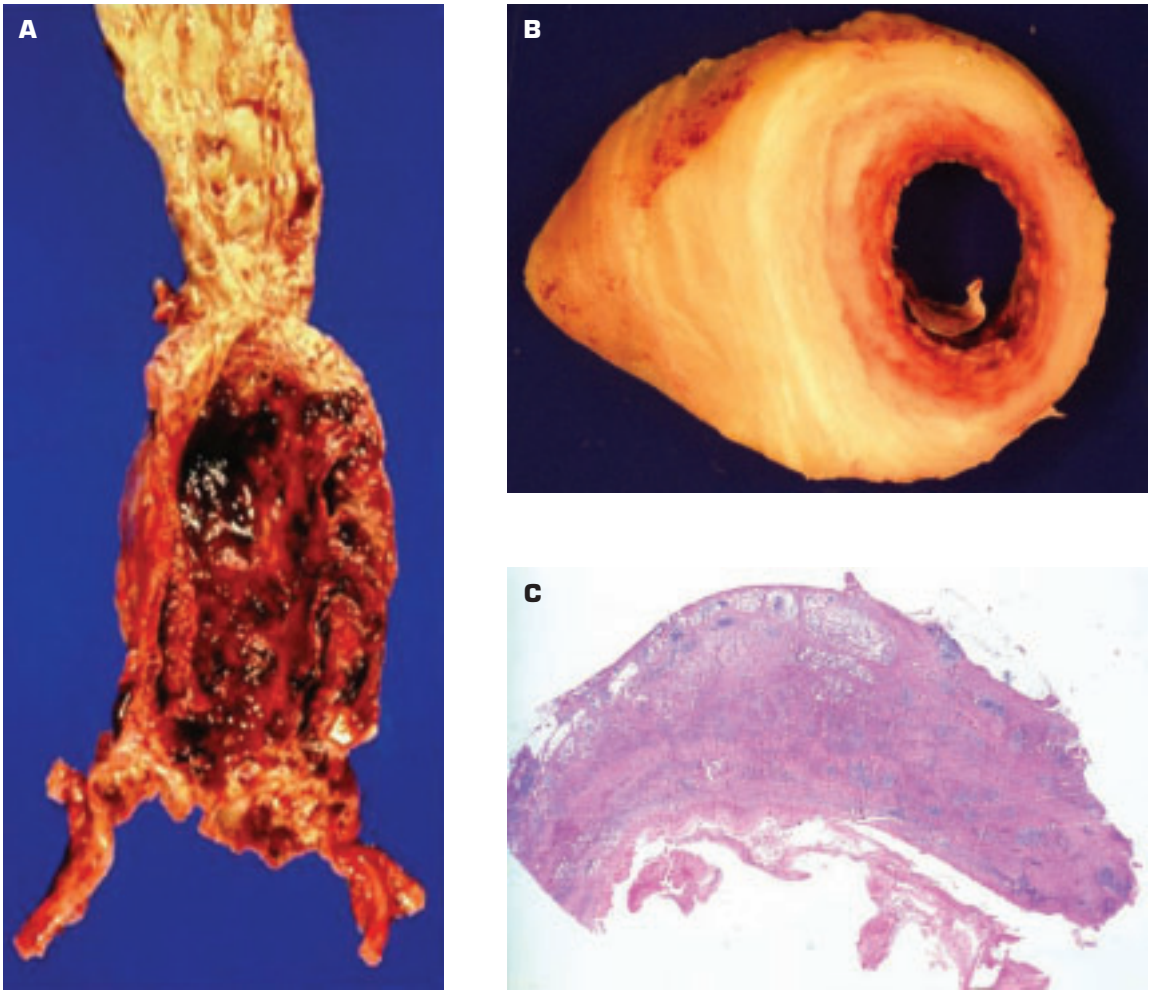

1-104. A. Atherosclerotic abdominal aortic (AAA) aneurysm has a fusiform shape due to circumferential weakening of the aortic wall over a long area below the origin of the renal arteries. **B.** Thrombus surgically removed from an AAA aneurysm; surgeons no longer resect the wall of the aneurysm in performing a repair. **C.** Histology of an "inflammatory variant" of AAA aneurysm shows a thicker than usual aneurysmal wall due to nonspecific chronic inflammation and fibrosis.

Facing page:

1-105. A. Severe atherosclerotic narrowing of the left anterior descending coronary artery and its diagonal branch. Atherosclerosis has more severe stenotic effects in smaller arteries such as the coronaries than in the aorta. **B.** Histology of coronary thrombosis (*top*) following rupture of the fibrous cap of an atheromatous plaque (*bottom*). **C.** Transmural rupture of artery with severe atherosclerosis following balloon angioplasty. Note the tear (arrow) at the bottom of the transversely sectioned coronary artery.

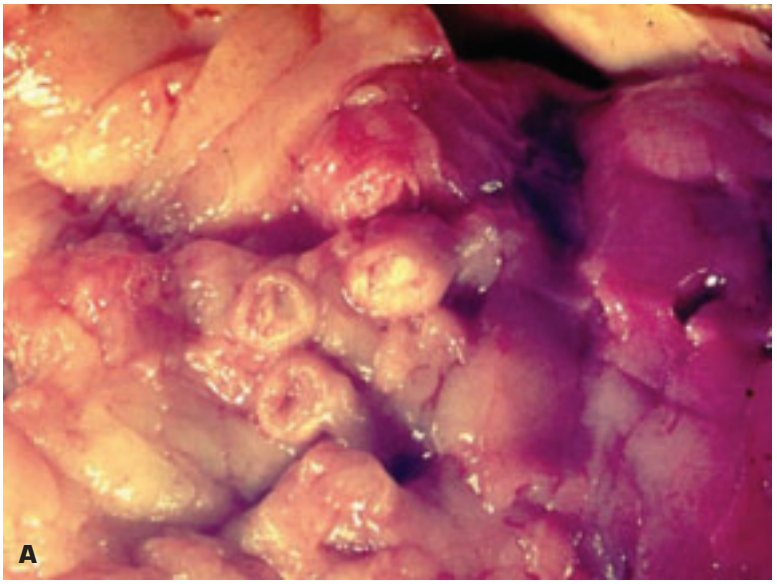
A

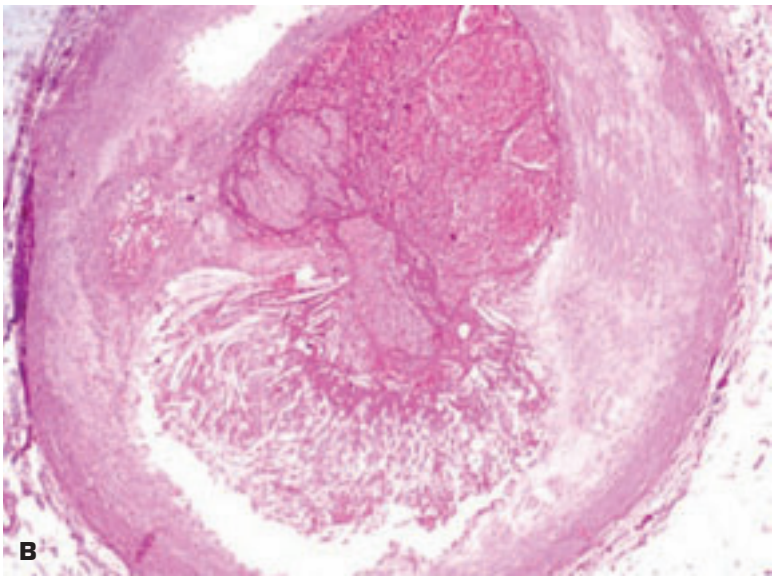
B

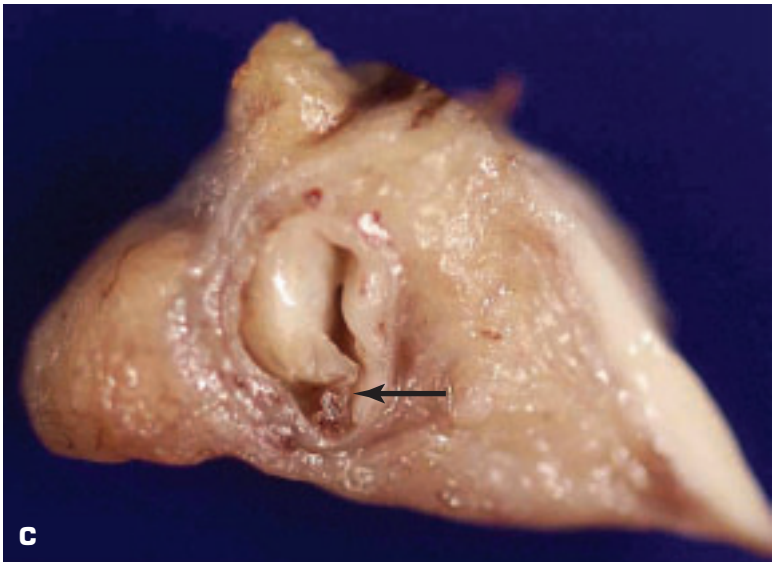
C

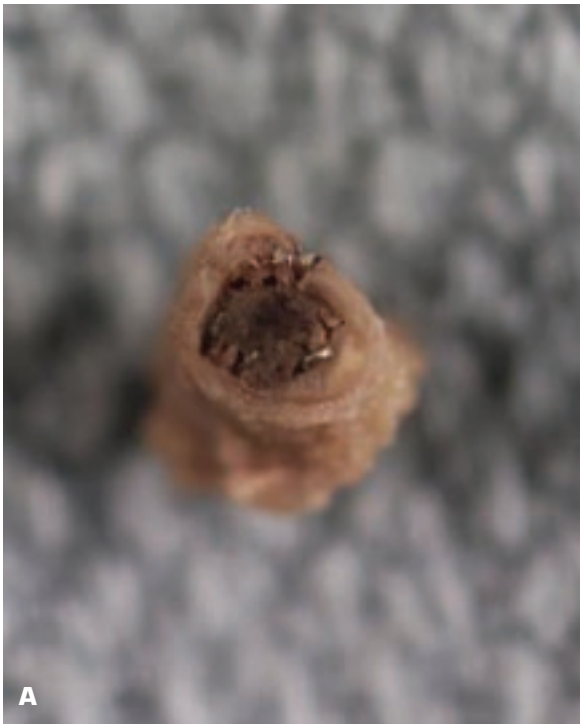

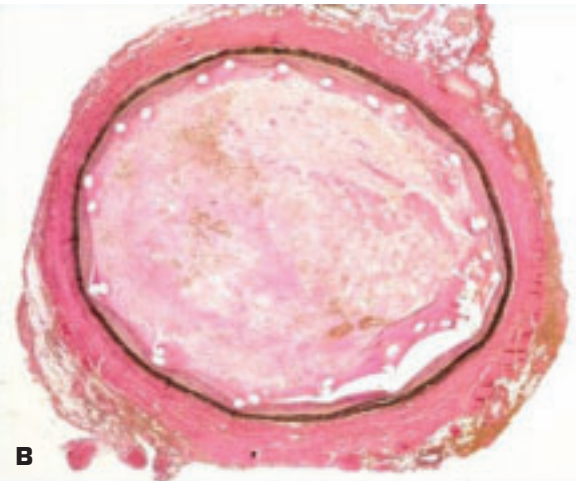

1-106. A. Transverse section of a stented coronary artery that became thrombosed due to poor anticoagulation. **B.** Histology of the same vessel shows occlusive luminal thrombus in direct contact with the bare metal posts that have no tissue overgrowth.

1-107. Thromboembolus (*center*) occludes a septal perforator branch of the left anterior descending coronary artery. The patient who had a mitral valve prosthesis was clinically believed to have died of an arrhythmia.

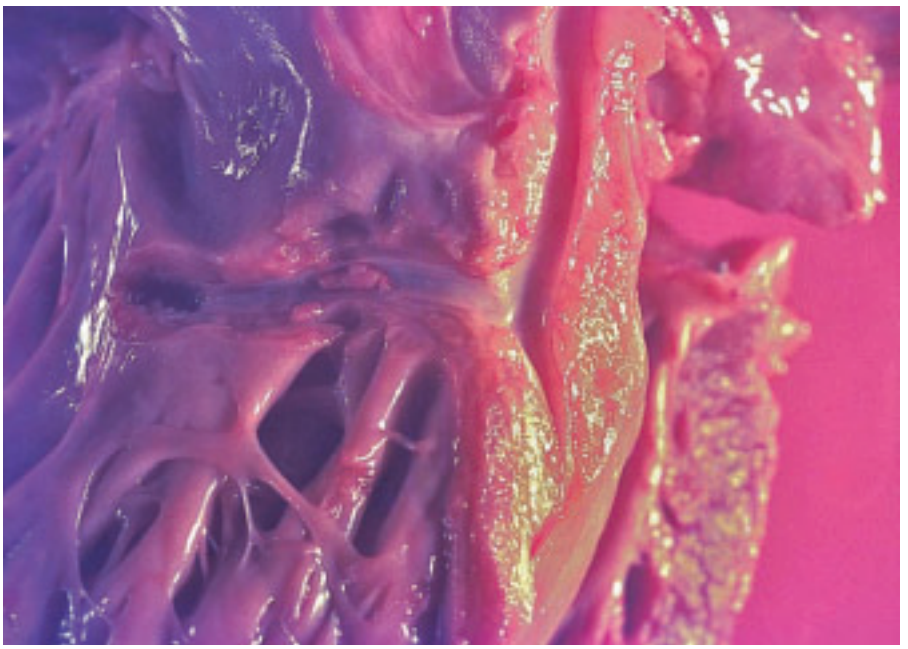

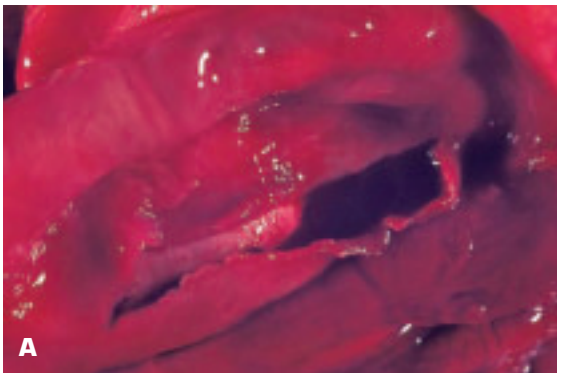

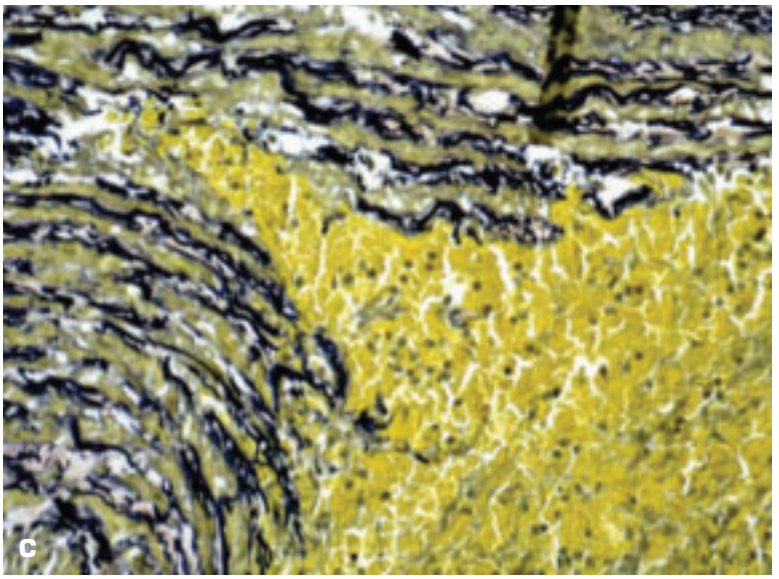

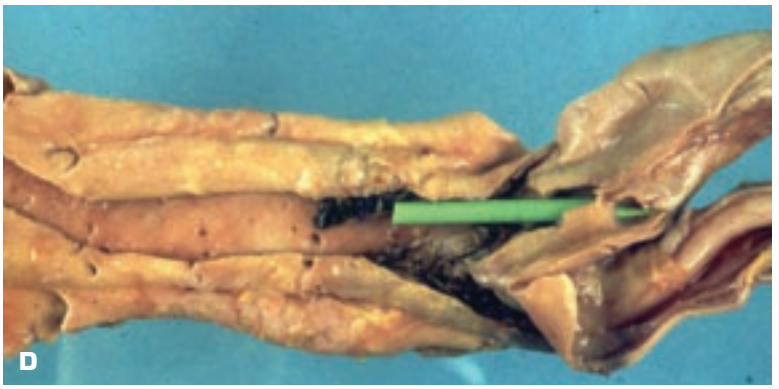

1-108. Dissecting aneurysm of the aorta may be due to systemic hypertension or to weakening of the media by medionecrosis associated with aging or Marfan syndrome. **A.** External rupture of the proximal aorta due to a dissecting aneurysm led to the death of this patient by cardiac tamponade. **B.** The false channel that has split the media is clearly seen. **C.** Distal end of the traveling intramural hematoma is histologically seen to be taking a line of least resistance by parting the longitudinally orientated elastic lamellae. **D.** Double-barreled aorta due to a chronic dissection in which the false channel containing the plastic probe supplied the circulation to the right common iliac artery via a reentry tear (tip of plastic probe).

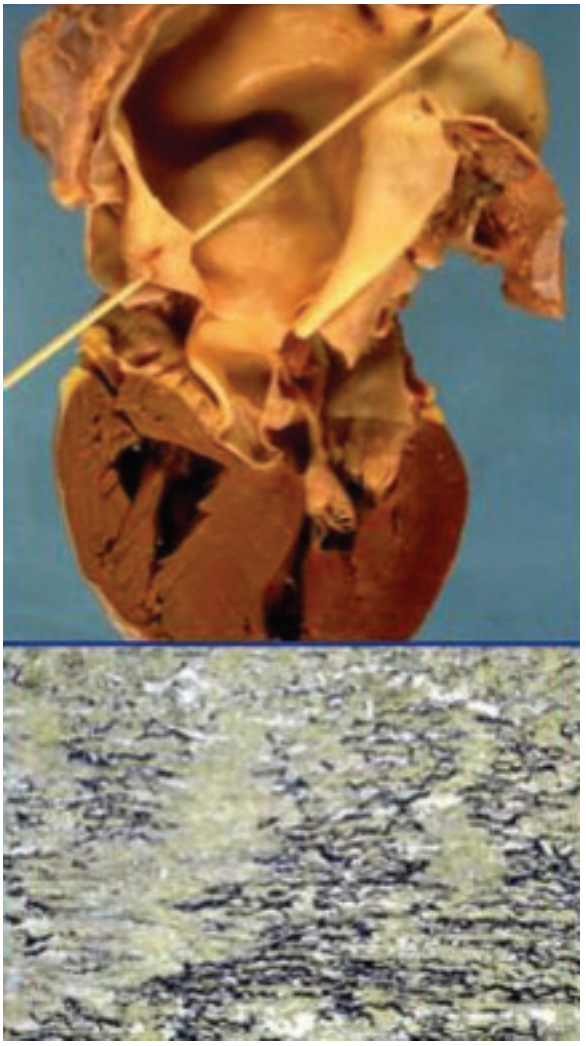

1-109. Cystic medionecrosis. Aneurysmal dilatation of the ascending aorta and the aortic arch (*top*) with dissecting aneurysm that has arisen at probe site. Bottom panel shows focal areas of loss of elastic lamellar units on this elastic-stained section; such areas are rich in acid mucopolysaccharides.

1-110. Chronic false aneurysm of the aorta that had been previously transected due to an automobile accident. The aortic adventitia and compressed surrounding mediastinal tissues had maintained continuity of blood flow between the severed ends of the aorta. The patient died due to rupture of the thin-walled false aneurysm.

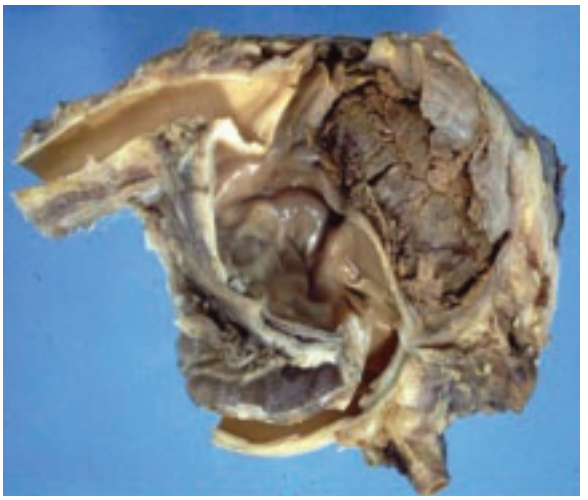

1-111. Idiopathic aortitis (Takayasu disease) of the aorta. **A.** The scarred aorta shows multiple saccular aneurysms due to focal weakening of its wall. **B.** Histology of Takayasu disease showing two false aneurysms that have arisen at sites of medial destruction.

1-112. A. Syphilitic aortitis with "tree bark" wrinkling of the intimal surface and multiple saccular aneurysms, one of which contains a massive thrombus. **B.** Histology shows healed mesaortitis (*top*); elastin stains black and collagen stains red. Bottom panel shows a transverse section through aortic route inclusive of one coronary arterial origin. Note that the aortitis has spilled over as intimal thickening of the proximal coronary artery with resultant stenosis.

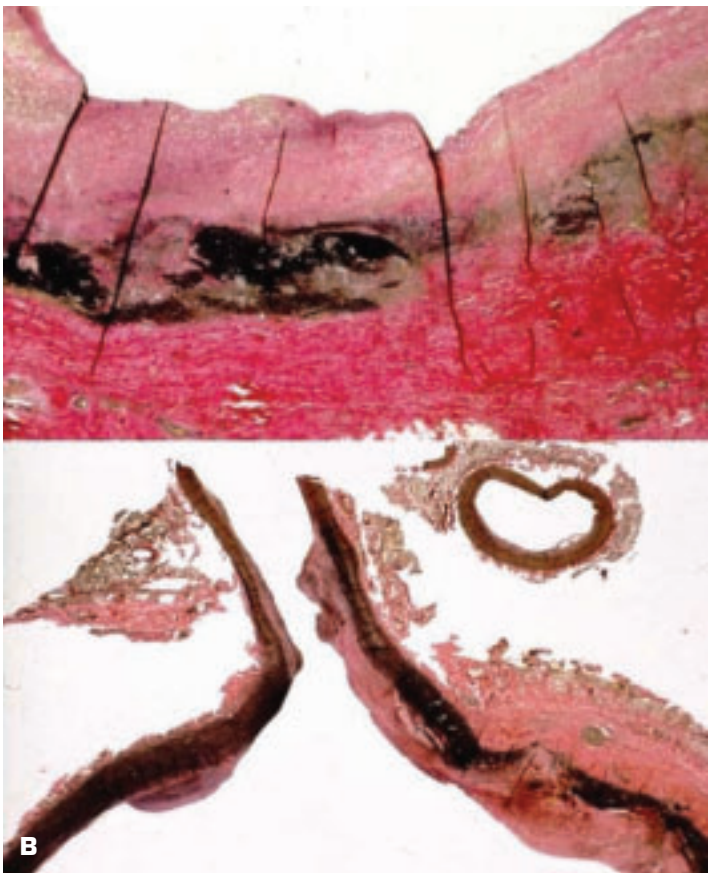

1-113. A. Scaphoid facies of a child with Hurler syndrome showing coarse features, prominent supraorbital ridges, and depressed nasal bridge. **B.** A montage of coronary arterial sections from a child with Hurler syndrome showing marked intimal thickening and severe luminal stenosis due to an accumulation of Hurler cells, increased fibrosis, and accumulation of interstitial mucopolysaccharide. Bone marrow transplantation may prevent the arterial complications.

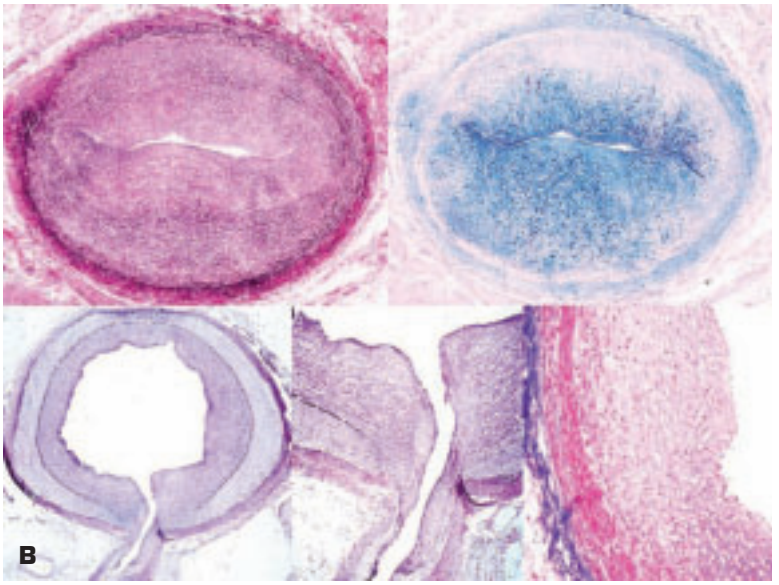

1-114. Kawasaki disease is the most common cause of acquired coronary arterial disease in children in North America. It is an acute multisystemic vasculitis of infancy and early childhood, which presents with fever, rash, conjunctivitis, mucosal inflammation, erythema of palms and soles, and cervical lymphadenopathy. In this patient, healed Kawasaki disease has produced a coronary arterial aneurysm (*left and top right*) that subsequently became totally thrombosed. Histology of the aneurysm wall (*bottom right*) shows no active arteritis at this time.

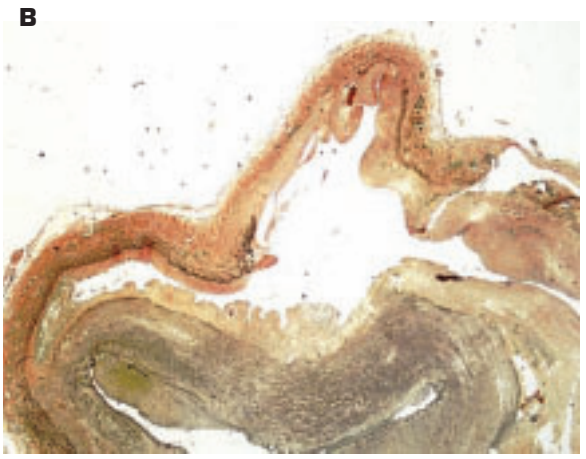

1-115. Cystic adventitial disease of a joint-related artery is an idiopathic, cystic accumulation of mucinous material in the adventitia of an artery possibly related to trauma, ectopic ganglion cyst, or "dysplasia." **A.** Macroscopic appearance of a resected segment of popliteal artery shows an adventitial cyst whose expansion is compressing the arterial lumen. Both levels show luminal thrombosis that was the indication for surgical resection and grafting, instead of the usual adventitial drainage therapy. Angioplasty is not used for this lesion. **B.** Histology of the adventitial cyst (*top*) and recent thrombus is seen within the compressed arterial lumen (*bottom*).

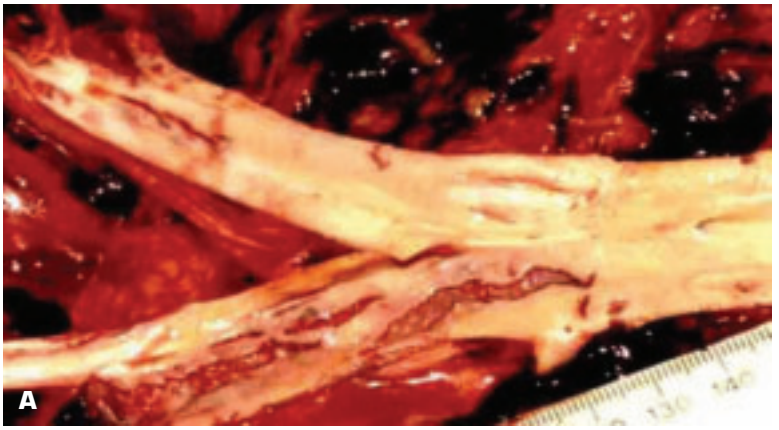

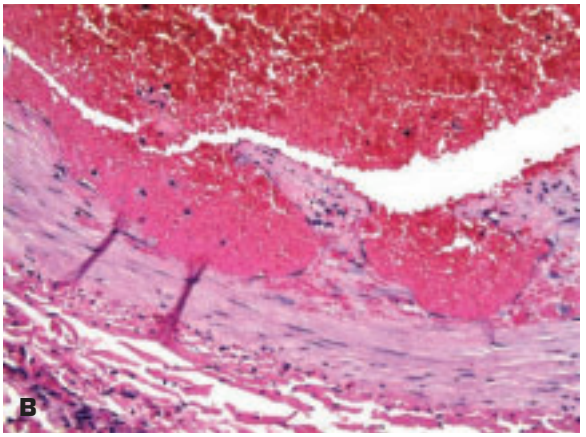

1-116. Segmental mediolytic arteriopathy (SMA) is defined as a peculiar, noninflammatory lesion of visceral and/or coronary arteries characterized by focal medial lytic changes that may lead to hemorrhage, dissection, or thrombosis. Theories of causation include vasospastic response to shock or fibromuscular dysplasia. This author believes that the condition results from overactivity of serum elastase. **A.** SMA is manifesting as multiple longitudinal tears in the terminal aorta and both common iliac arteries. **B.** Histology shows evolving tears at focal areas of mediolysis.

1-117. Fatal stab wound in the heart. **A.** Left panel shows transverse slice of both ventricles with hematoma enveloping left anterior descending (LAD) coronary artery. **B.** Right panel (histology) shows that the knife has cut open the LAD coronary artery.

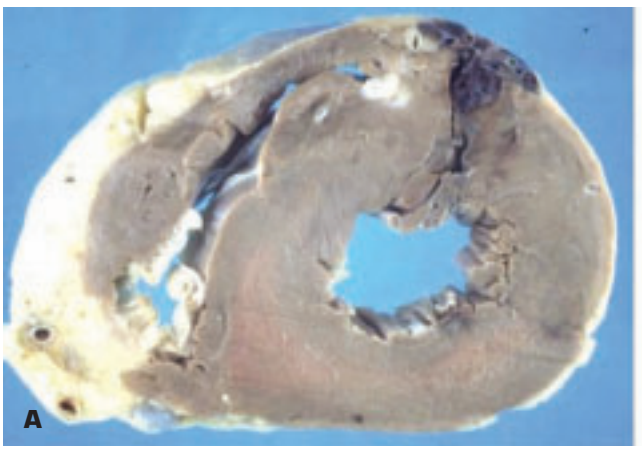

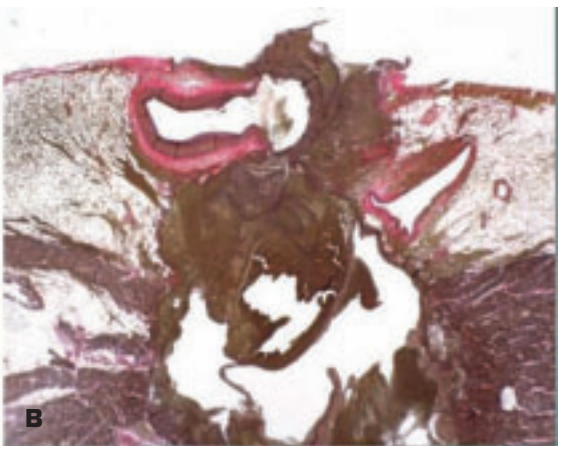

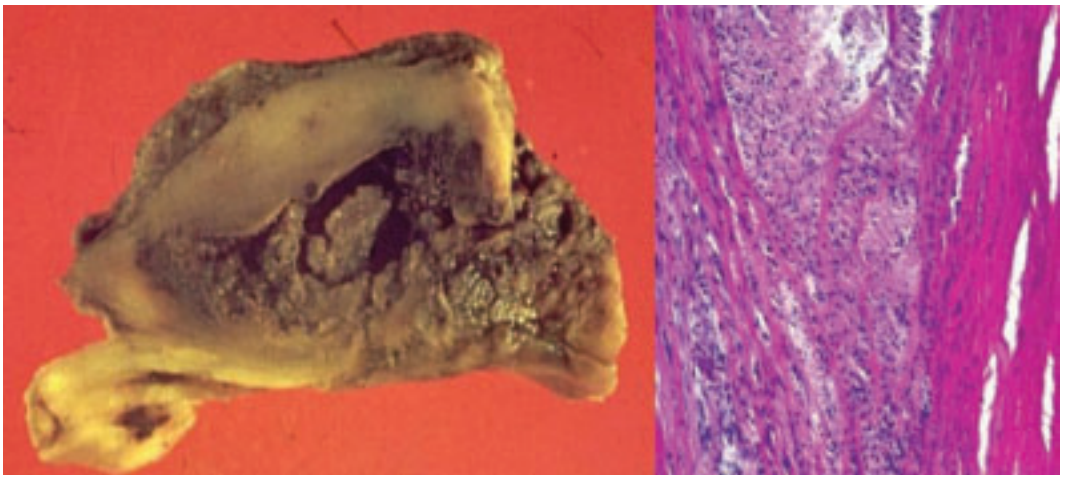

1-118. Mycotic aneurysm of the aorta (*left panel*) shows friable thrombus merging with outer more compact thrombus. The wall of this small aneurysm is difficult to discern, accounting for the propensity for early rupture of a mycotic aneurysm. Right panel shows the histologic feature of masses of neutrophils separating the aortic lamellae.

1-119. Fibromuscular dysplasia (FMD) of the renal artery. The two pictures on the left show a renal artery exhibiting the most common form of FMD, namely medial hyperplasia. Note the segmental, irregular string of beads or corkscrew pattern comprising the ridges that separate the outpouching of the lumen. The histologic section (*right*) shows a ridge that has been demonstrated by a longitudinal section of the artery. Contrary to most arterial conditions, longitudinal sectioning is the best way to demonstrate the histology of FMD.

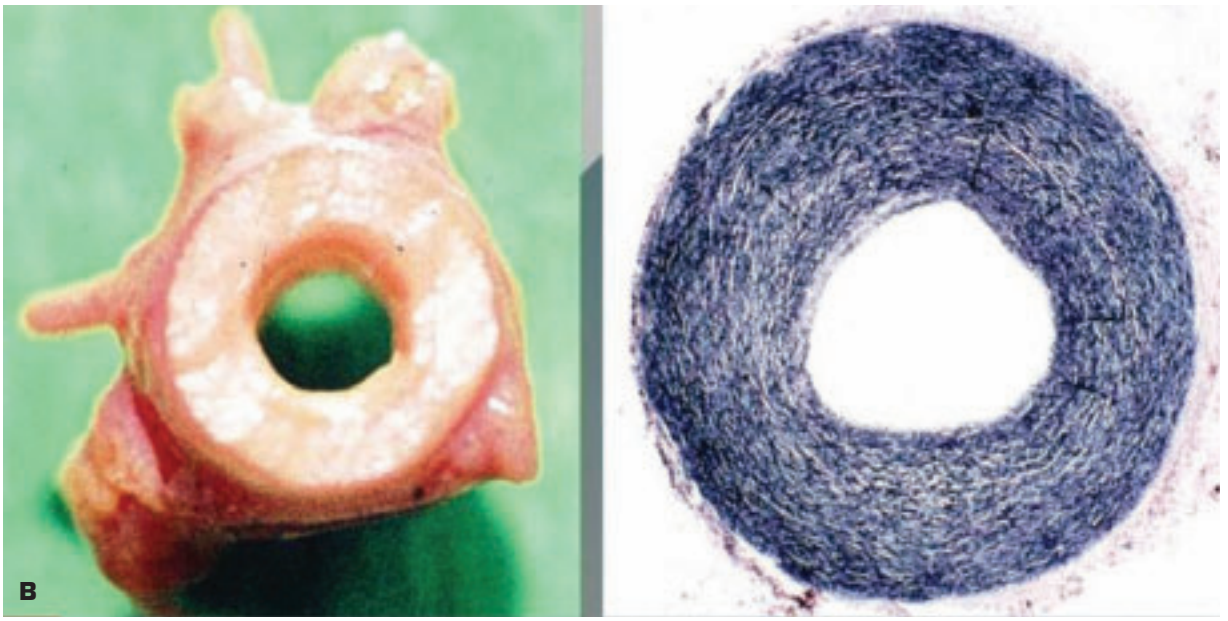

1-120. A. Congenital stenosing arteriopathy (CSA), so-called macaroni arteries, is a unique form of congenital arterial dysplasia affecting the aorta and its major branches. Branches of the aortic arch are seen (*center*) and the descending aorta is present (*top right*). **B.** Transverse section of carotid artery (*left*) and its elastic-stained histology (*right*) shows that arterial mural thickening results from a hyperplasia of medial lamellar units with an outer medial disarray pattern.

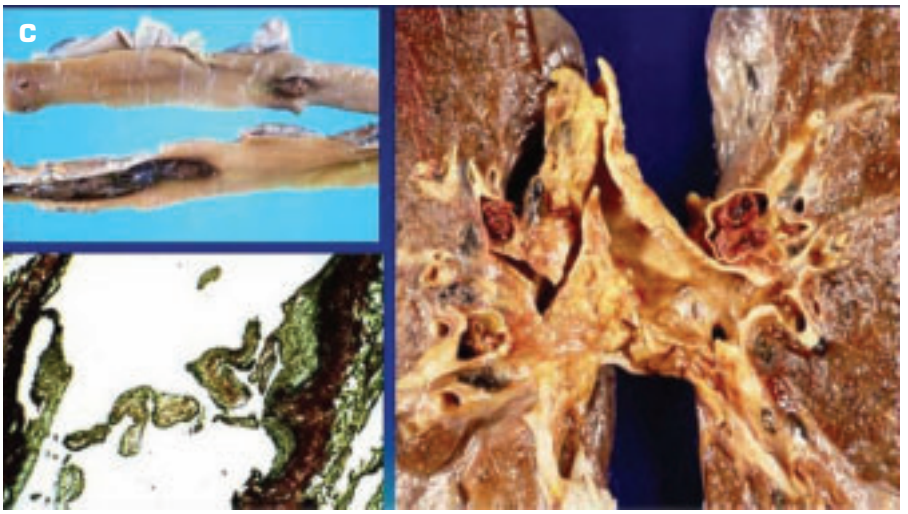

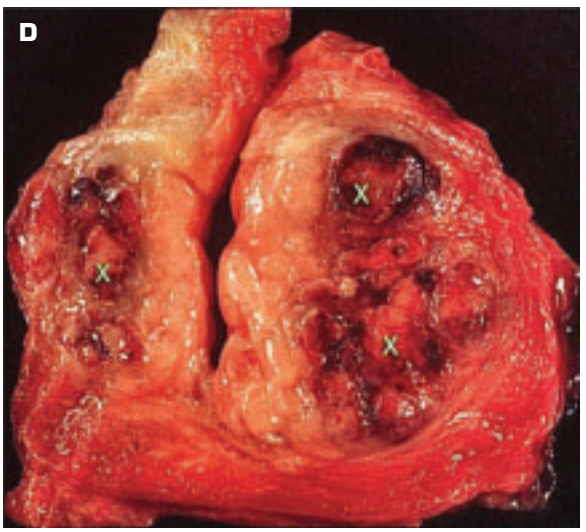

1-121. Venous thrombosis. **A.** Transverse section of a thrombosed large vein shows lines of Zahn (*arrow*) indicative of an antemortem thrombus derived from flowing blood. **B.** Histology confirms that the pale lines correspond to deposits of fibrin and platelets between the masses of coagulated erythrocytes. **C.** Clockwise from top left: bilateral iliofemoral venous thrombosis with embolization of the thrombus from the top vein (portion of thrombus is missing); major thromboemboli occlude the left and right pulmonary arteries; and histology of a web in a pulmonary artery – the web results from an old organized thromboembolus. **D.** In both males and females, the pelvic veins may be the source of cryptic thromboembolism. This picture shows massive thrombosis (X) of the periprostatic venous plexus.

1-122. Inferior venal caval umbrella has successfully detained multiple thrombi that were on their way to the lungs. Flat thrombi have also developed on the struts of the umbrella.

1-123. A. Thrombosis of the superior mesenteric (*bottom arrow*) and portal (*top arrow*) veins inferior to the liver (*top*). **B.** Resultant venous infarction of the small intestine has occurred.

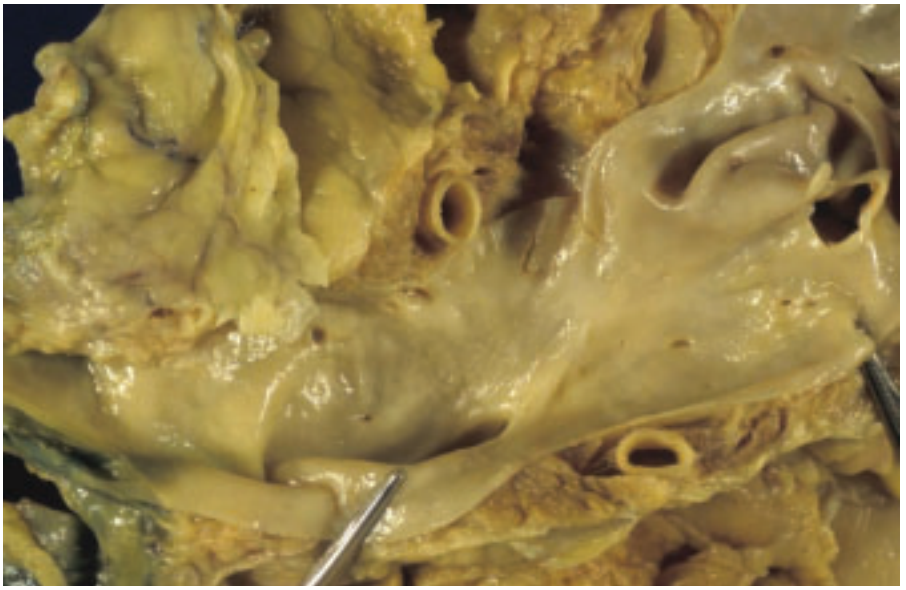

1-124. Greatly dilated splenic vein (*probe*) in cirrhosis-induced portal hypertension. Rupture of the splenic vein may rarely occur, and although the resultant retroperitoneal hemorrhage may be less dramatic than an arterial rupture, it may still kill the patient.

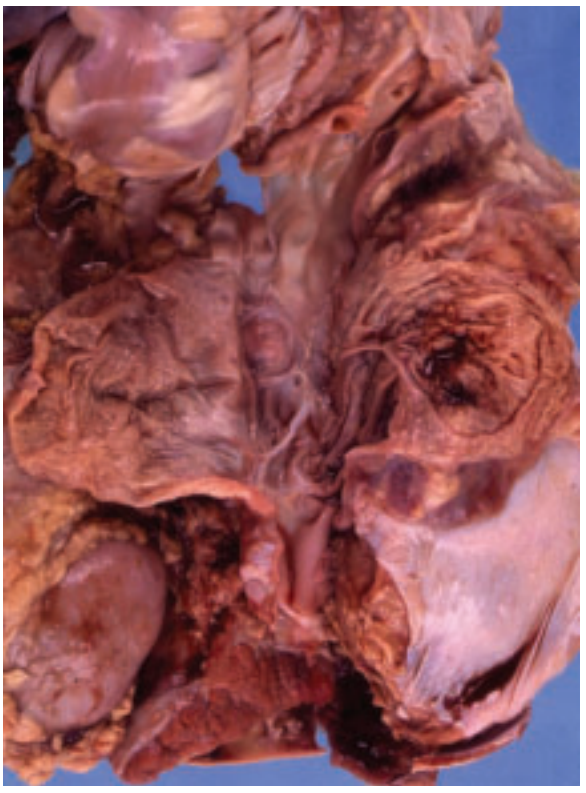

1-125. Idiopathic aneurysm of the inferior vena in a young girl who died of thromboembolism as a result of massive thrombus detaching from the aneurysm and traveling to her pulmonary arteries.

2 Pulmonary Pathology

2-1. Atelectasis (alveolar collapse due to absence of air) has produced a zone of lung tissue that is depressed below the surrounding aerated lung tissue and has a redder and more solid appearance.

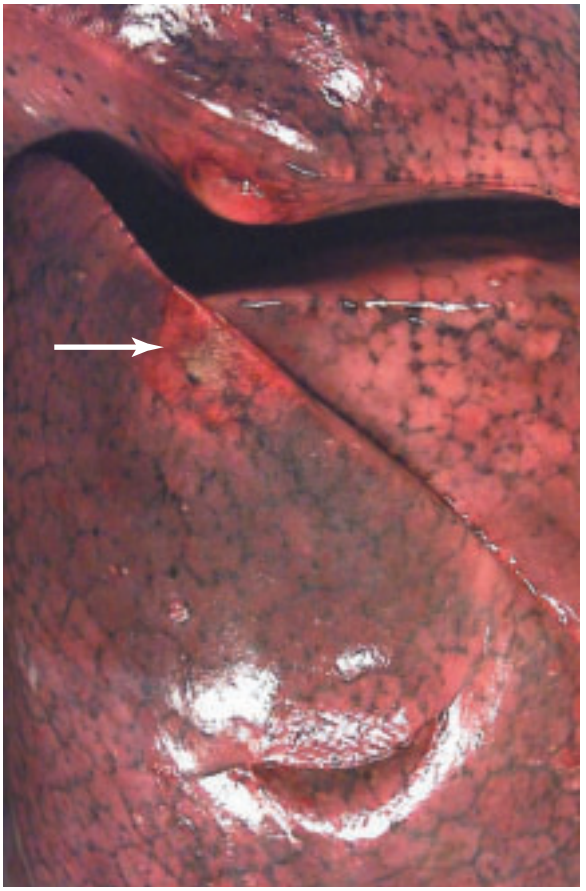

2-2. Localized fibrinous pleurisy (*arrow*) over parenchymal lesions due to *Aspergillosis*. The fibrin deposit produces a roughened appearance to the pleural surface.

2-3. Anthracosis of the lung: pleural lymphatics around lobules are outlined by carbon deposits. See also Figs. 2-26A and 2-43A, which each show marked anthracosis in addition to a malignancy.

2-4. Lobar pneumonia. **A.** Consolidation affects the entire left lower lobe of lung. This is typical of a pneumococcal (*Streptococcus pneumoniae*) infection in which hypersensitivity leads to an outpouring of fluid within the lung. The infection spreads to all alveoli via the pores of Kohn. *Klebsiella pneumoniae* may also cause a lobar pneumonia, but the cut surface of the affected lobe usually has a more mucoid appearance due to the organisms' thick, gelatinous capsule. **B.** Stage of red hepatization: low-power histology shows congestion, and alveoli are filled with neutrophils. **C.** Grey hepatization: intraalveolar exudate compresses the capillaries.

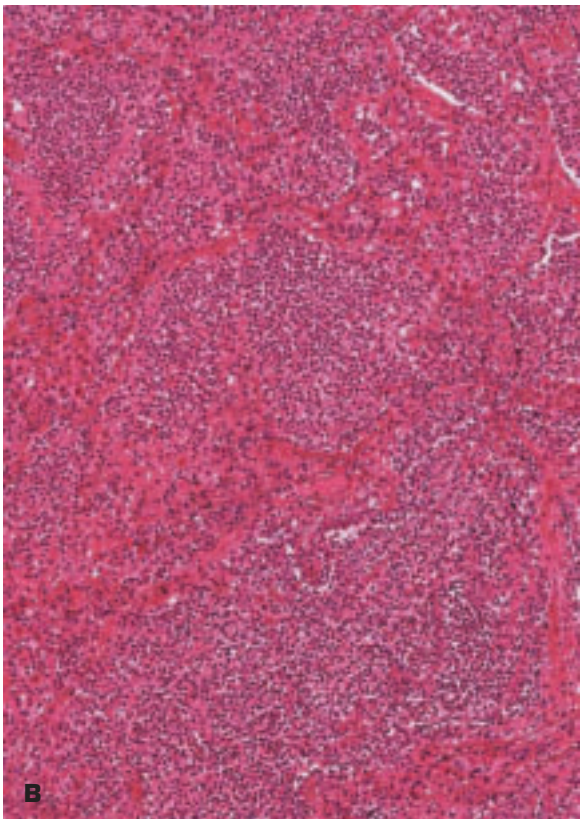

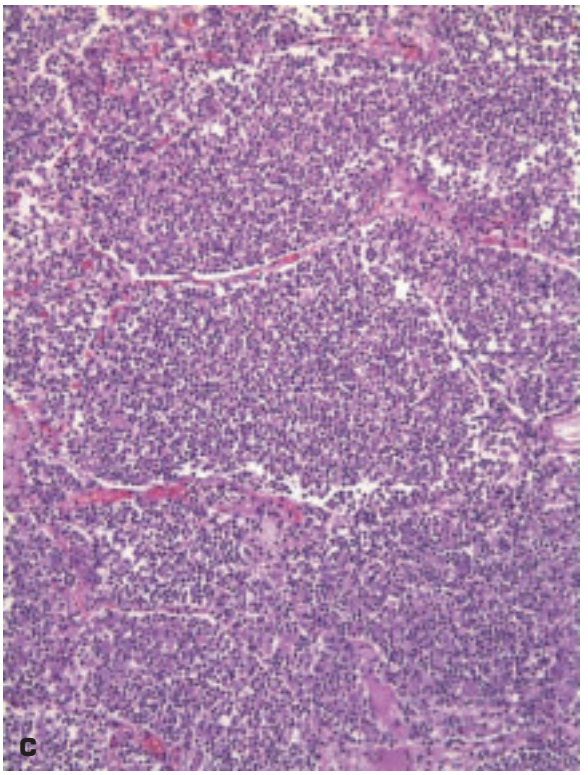

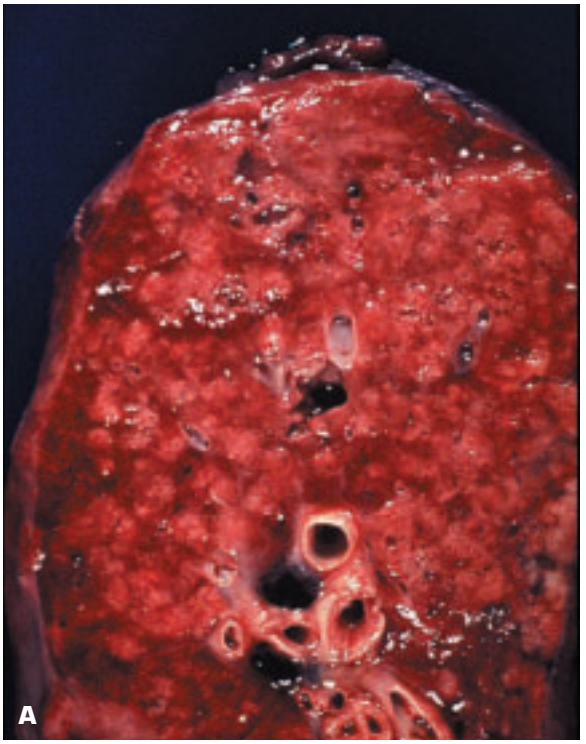

2-5. Bronchopneumonia. **A.** Extensive bronchopneumonia in upper lobe of lung is seen as areas of yellow-white consolidation centered on bronchi and bronchioles against a congested pulmonary parenchyma. Overall, bronchopneumonia occurs more commonly in the lower lobes of the lungs. **B.** Focal area of acute bronchopneumonia with surrounding edema. Air bubbles are present within the intraalveolar edema fluid. Bacterial colonies are seen on the left of the picture. **C.** High-power view of bronchopneumonia.

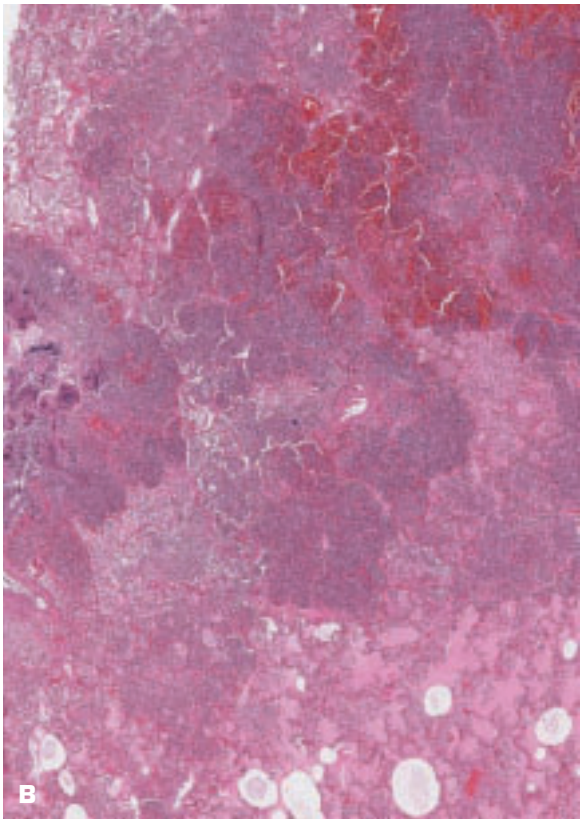

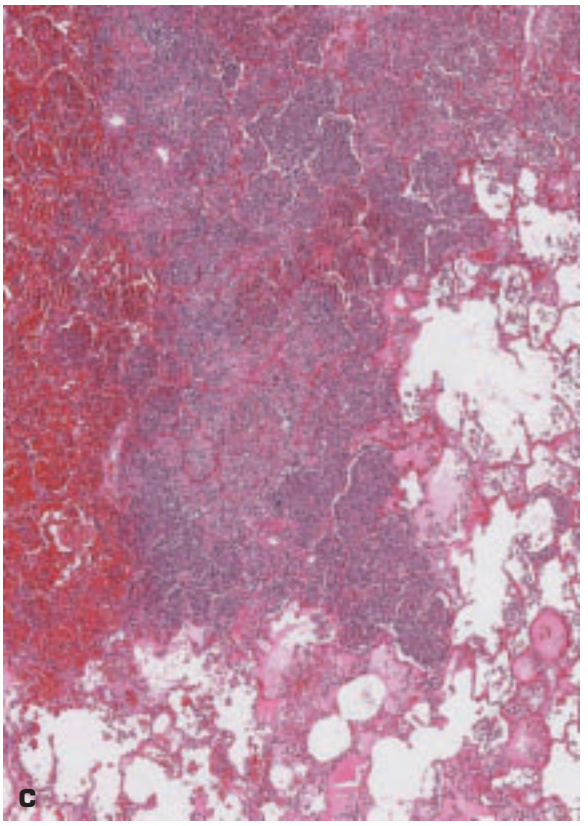

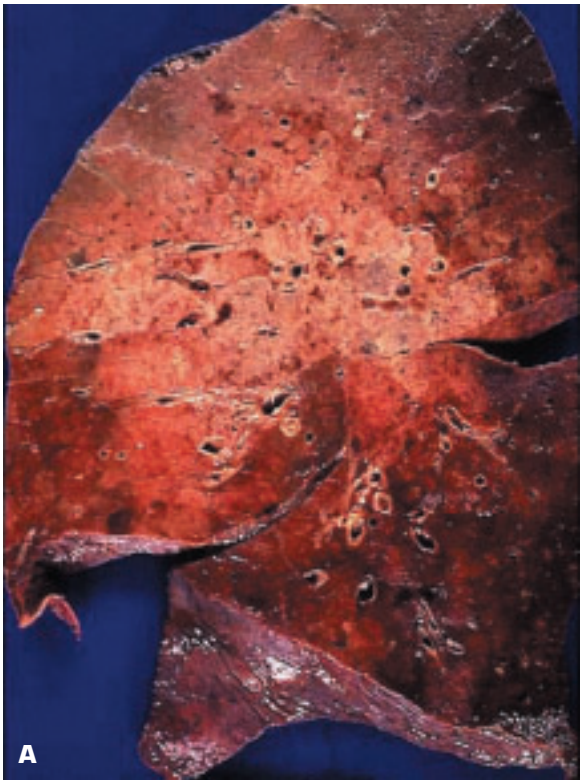

2-6. A. Nearly the entire upper lobe of the lung shows consolidation. Such a pattern of subtotal consolidation may be noted with lobar pneumonia that has been treated with antibiotics, or it may occur with a *Klebsiella* infection and has been termed "lobular pneumonia." Rarely, confluent bronchopneumonia may produce extensive consolidation mimicking lobar pneumonia. **B.** Histologic appearance of bronchiolitis obliterans organizing pneumonia (BOOP) in which the lumens of many bronchioles are obstructed by loose fibrous masses.

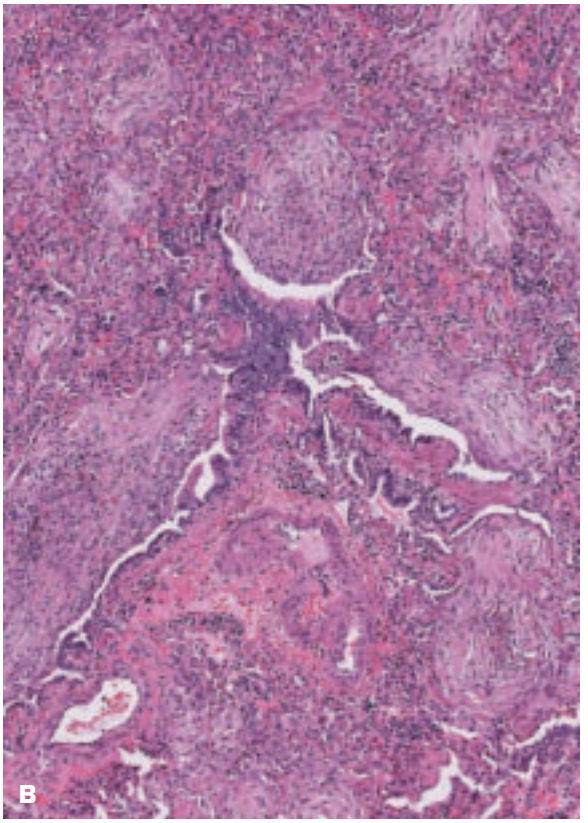

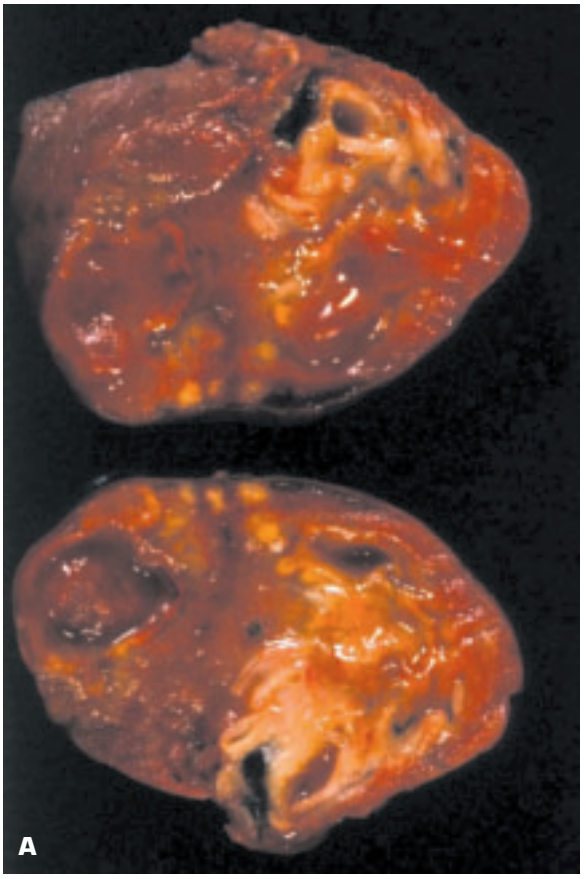

2-7. A. Surgical resection of portion of lung with lung abscesses caused by staphylococcal bronchopneumonia. **B.** Histologic appearance of a lung abscess fulfilling the criterion of a localized area of destruction of the lung parenchyma, with the space being occupied by polymorphonuclear leukocytes. *(continued on next page)*

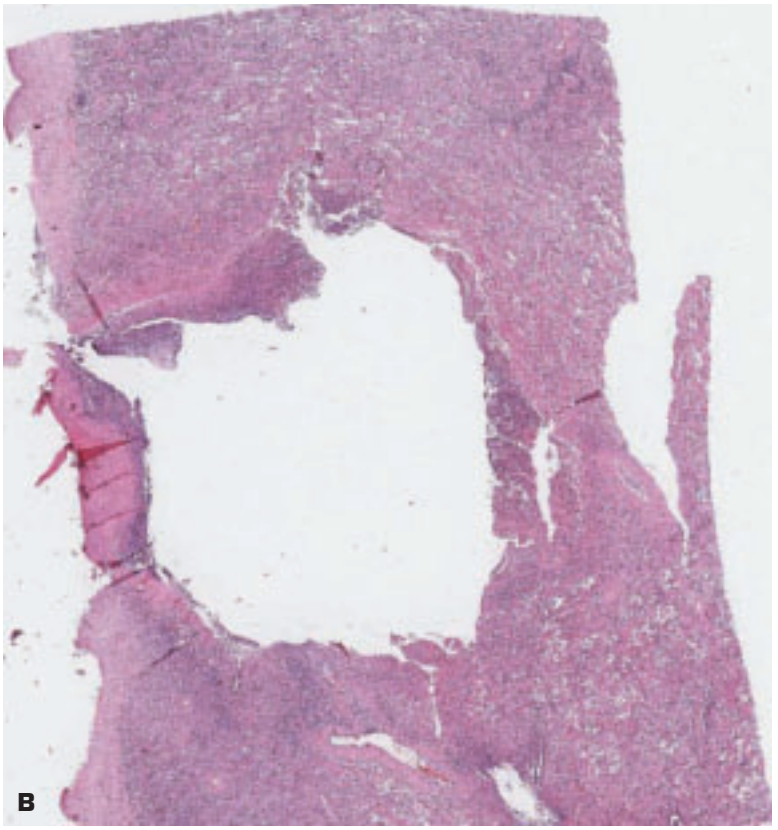

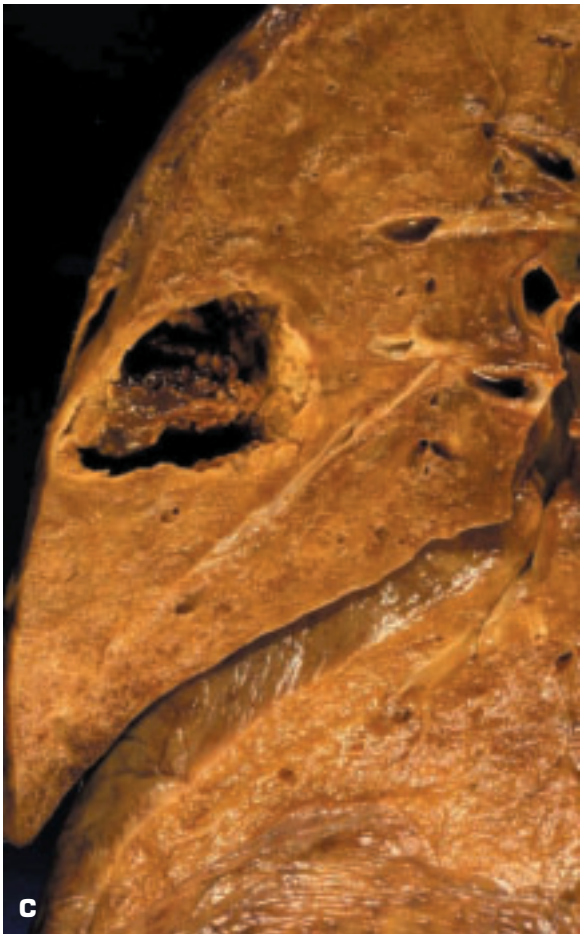

2-7. *(Continued)* **C.** Chronic lung abscess shows residual pus attached to pulmonary artery that spans the abscess cavity. The pulmonary arteries are much more resistant to destruction by an abscess than are the bronchioles, veins, and lung parenchyma. **D.** Inflamed granulation tissue lines a chronic abscess cavity.

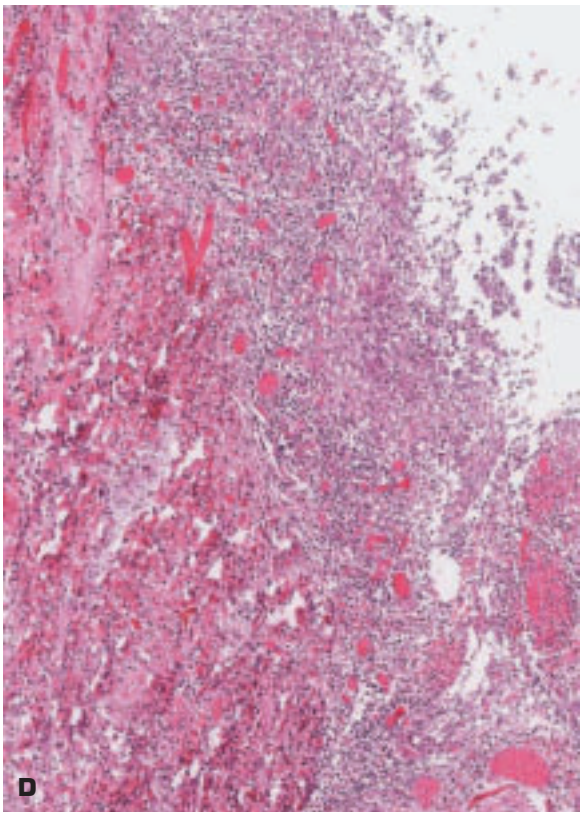

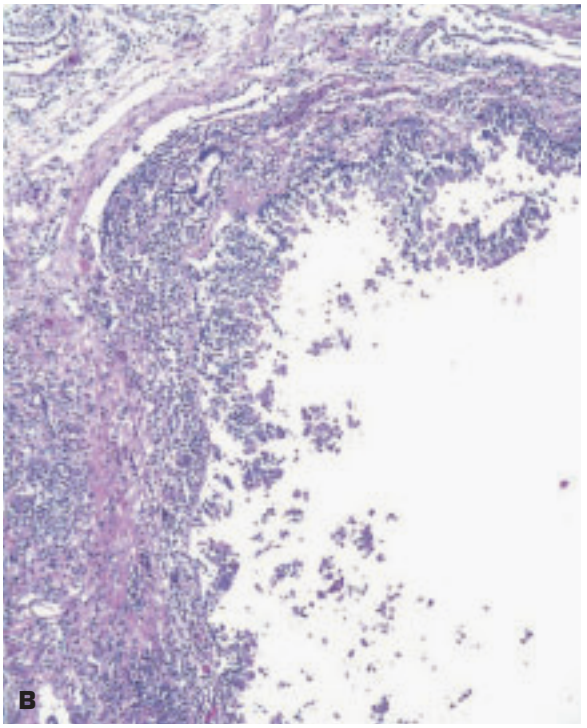

2-8. A. Early bronchiectasis with ectasia of a small bronchus (*arrows*) near the periphery of the lung. It is unusual to see a bronchial structure of this size in such a peripheral position. **B.** Histology of the small bronchus shows chronic inflammation with dilatation of its lumen and loss of both cartilage and much of the smooth muscle coat.

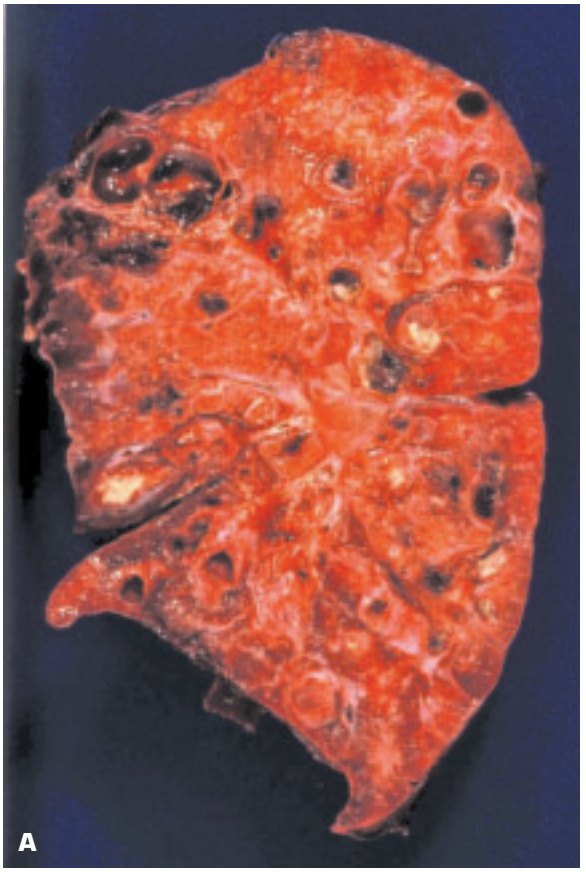

2-9. A. Active bronchiectasis in a patient with cystic fibrosis (CF). All stages of bronchiectasis are noted, and the multicentric peribronchial whitish-colored consolidation is due to lymphoid hyperplasia. **B.** Bronchial casts comprising dense, viscid sputum expectorated from a patient with CF.

2-10. End-stage bronchiectasis with almost no residual functioning lung parenchyma.

2-11. A. Bilateral, patchy, ill-defined areas of consolidation due to infection with *Pneumocystis jiroveci*. Such infections are more common in immunocompromised individuals, including persons with acquired immunodeficiency syndrome (AIDS). **B.** Microscopically, the alveoli are seen to contain a foamy exudate, and the thickened interstitium contains a mononuclear cellular infiltrate. **C.** Grocott methenamine silver stain shows an intraalveolar collection of helmet-shaped cysts of *Pneumocystis*.

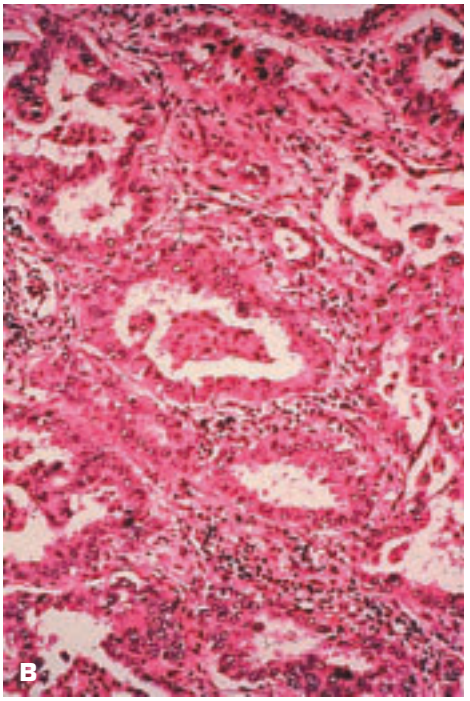

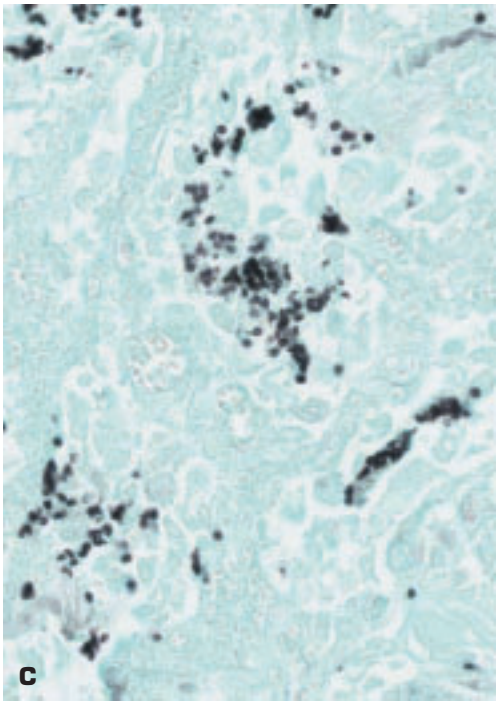

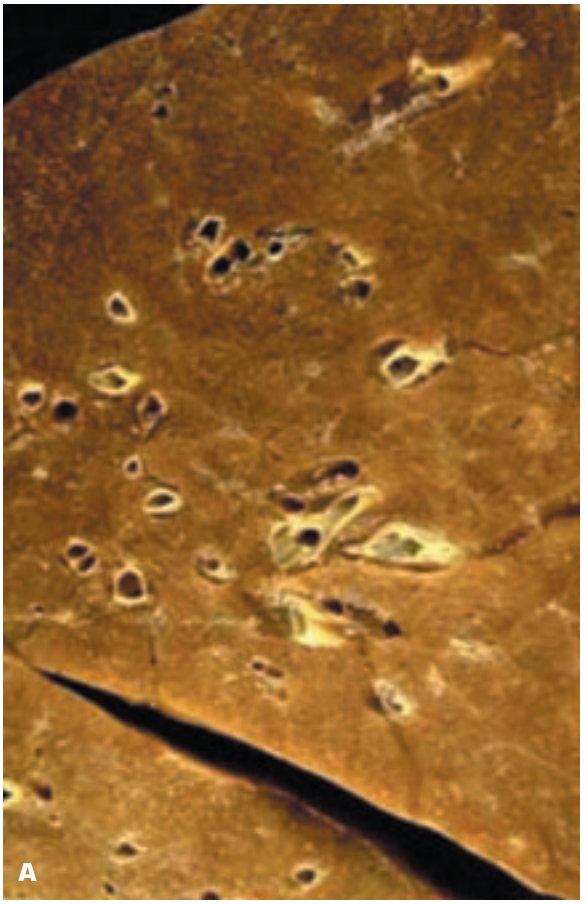

2-12. A. Ill-defined, diffuse pneumonic consolidation due to *Cryptococcus neoformans* (*Torula*) infection in a patient with systemic lupus erythematosus. **B.** Mucin-stained section shows abundant yeast-like organisms with a mucin-positive capsule consistent with *Torula*.

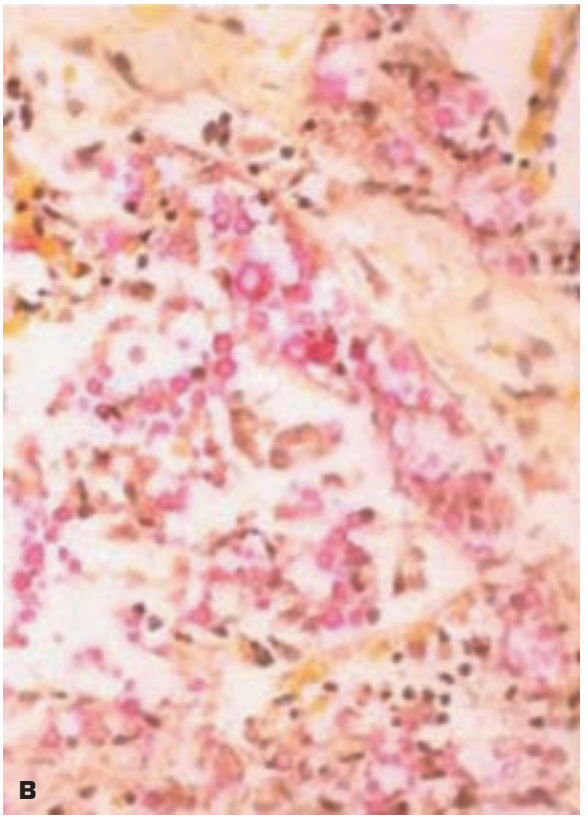

2-13. A. Pneumonitis with a bronchopneumonic pattern in areas due to cytomegalovirus (CMV) pneumonia. **B.** Typical CMV inclusions are seen within several greatly enlarged alveolar lining cells. **C.** Positive immunohistochemical staining of the viral inclusions by a specific antibody to CMV.

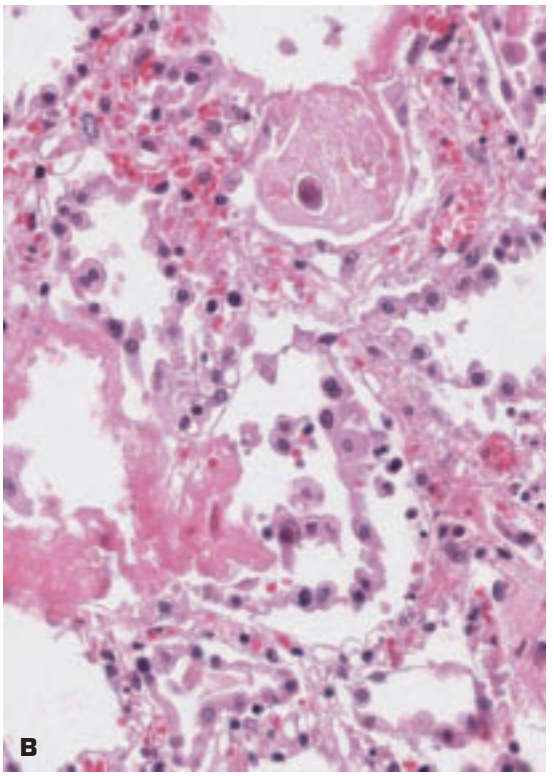

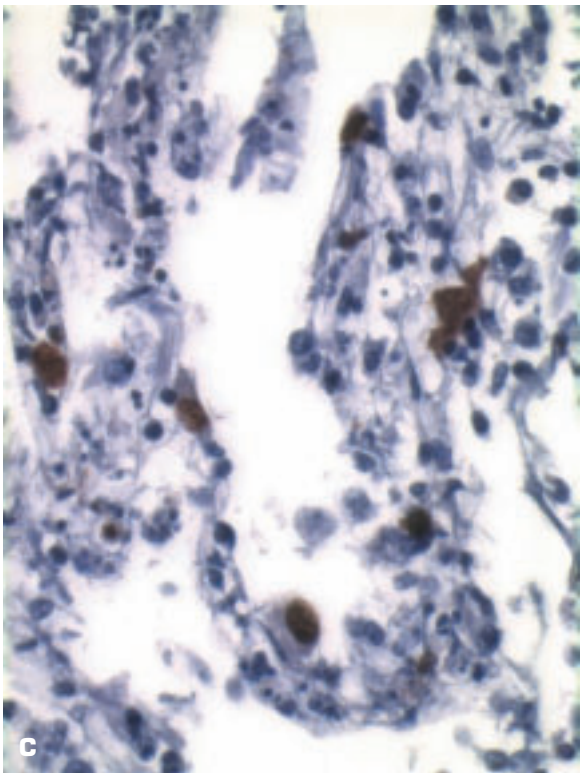

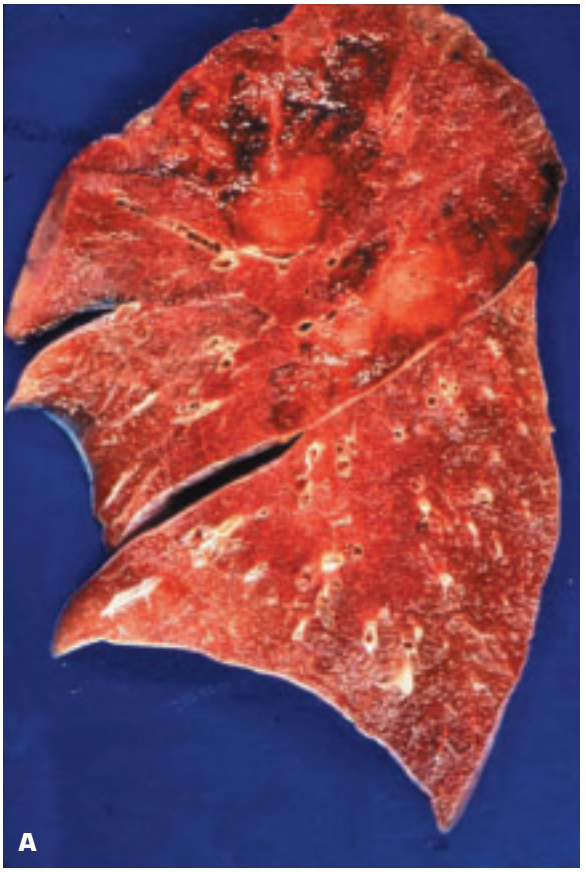

2-14. A. Upper and middle lobes of right lung contain multiple infarct-like lesions, some of which appear hemorrhagic due to *Aspergillus niger* infection of the lung. **B.** Early *Aspergillus* lesion (*bottom arrow*) in the lung shows fungal elements infiltrating through the wall (*top arrow*) of a small pulmonary vessel and into its lumen. The angioinvasive nature of the fungus with secondary thrombosis accounts for the ischemic nature of its resultant tissue lesions. *(continued on next page)*

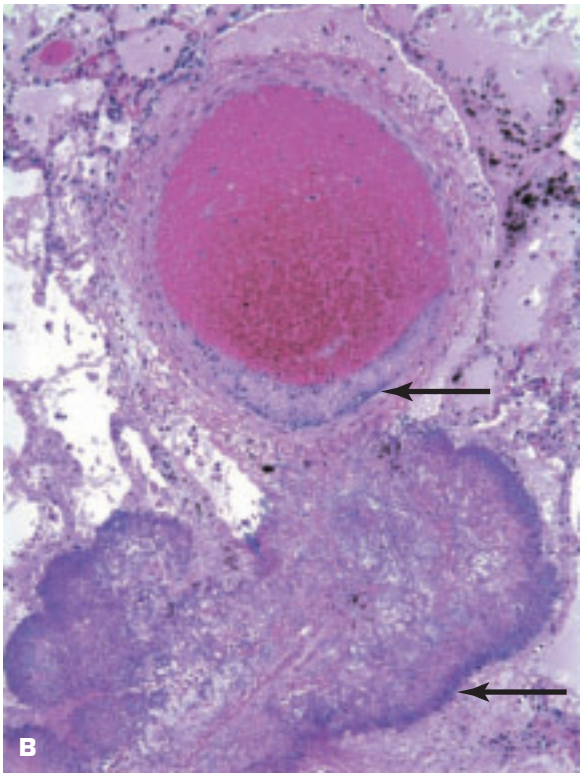

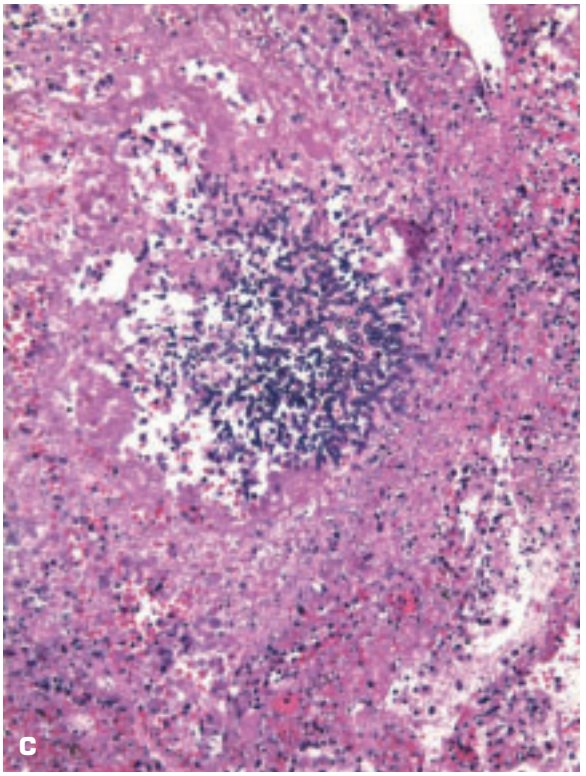

2-14. *(Continued)* **C.** *Aspergillus* hyphae growing within infarcted and inflamed lung tissue. **D.** Silver stain shows 45-degree branching of septate hyphae characteristic of *Aspergillus* fungus.

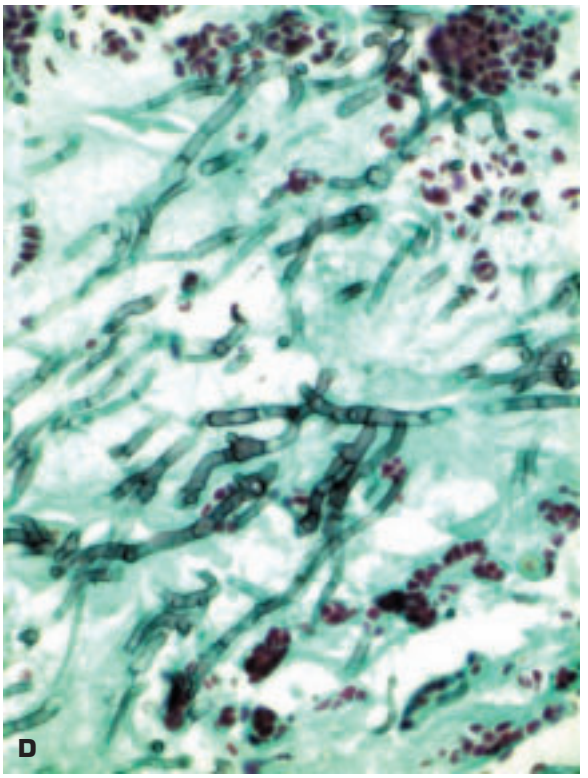

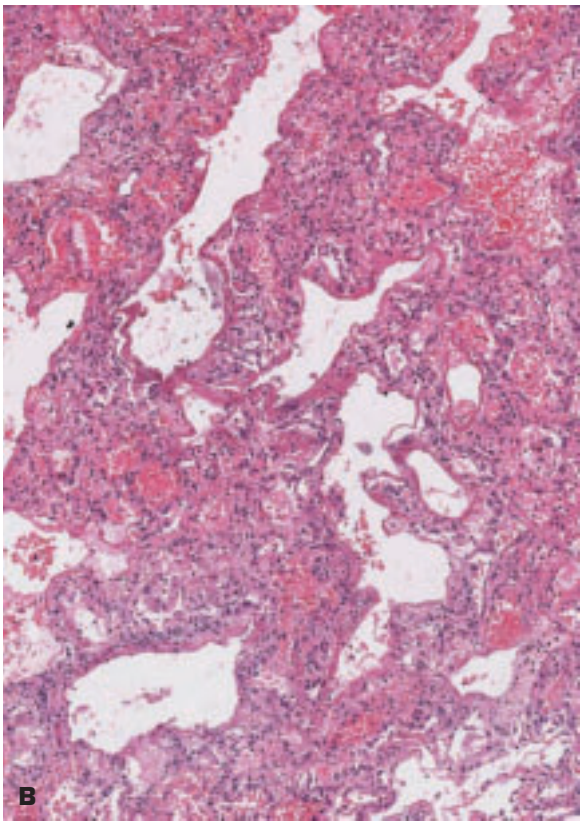

2-15. A. Diffuse consolidation of both lungs due to diffuse alveolar damage (DAD) (adult respiratory distress syndrome). **B.** Many alveoli are lined by deposits of fibrin lying on areas that have lost their alveolar lining cells. *(continued on next page)*

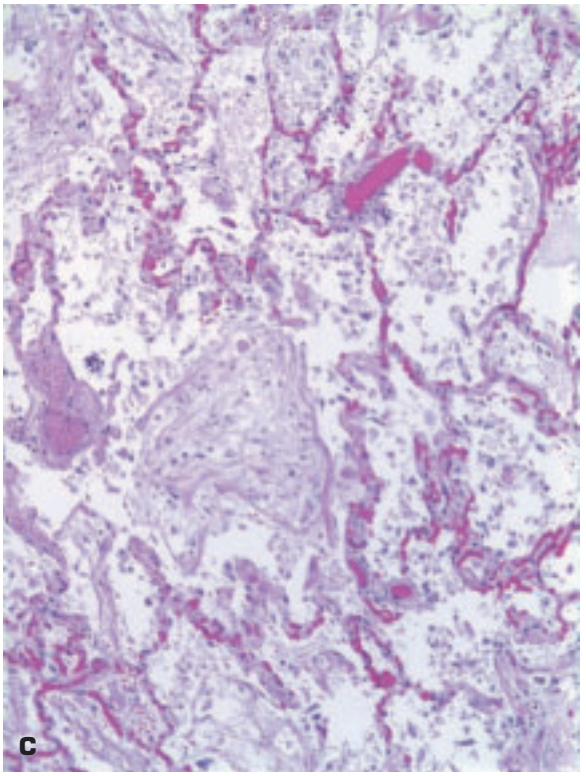

2-15. *(Continued)* **C.** Later stage of DAD with organization of intraalveolar fibrin. **D.** Late stage of nonfatal DAD with fibrosis and cystic change due to air trapping in the lung.

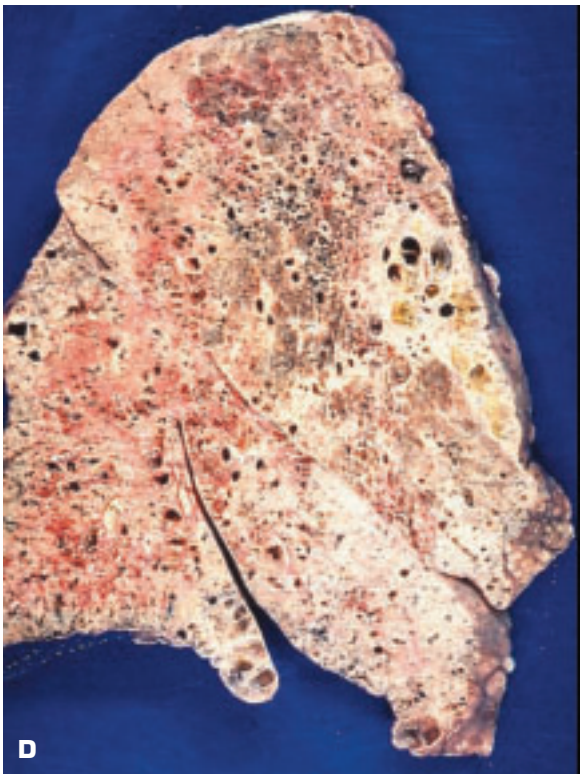

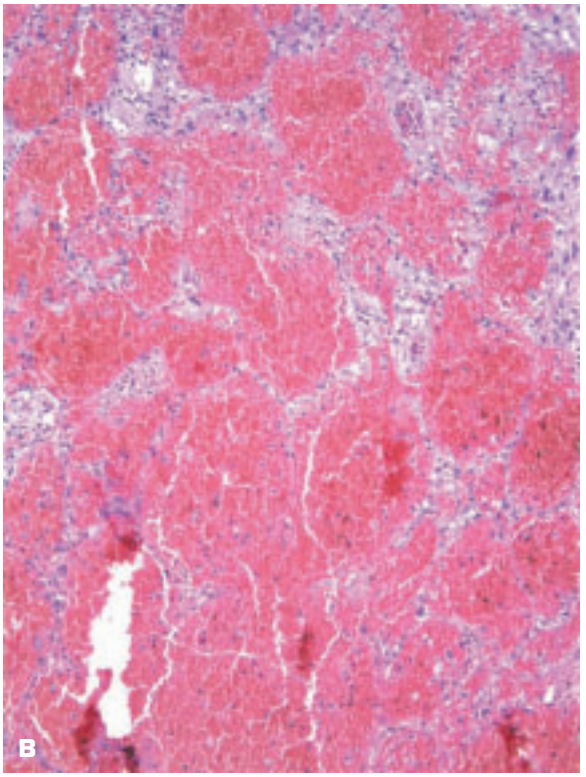

2-16. A. Hemorrhagic appearance of the posterior aspect (inferior aspect in a reclining patient) of both lungs due to inhalation of blood following a hematemesis due to a bleeding gastric ulcer. **B.** Alveoli are filled with blood, and reactive changes are noted in the alveolar septa.

2-17. Diffuse intrapulmonary hemorrhage in a patient with Goodpasture syndrome.

2-18. A. Yellow-colored areas of pneumonic consolidation due to histoplasmosis pneumonia. **B.** Histology shows a tuberculoid granulomatous inflammation due to histoplasmosis. *(continued on next page)*

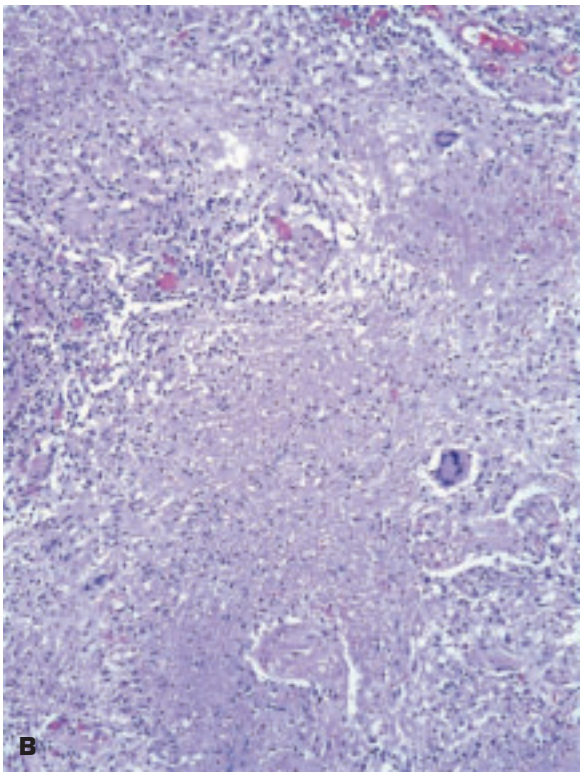

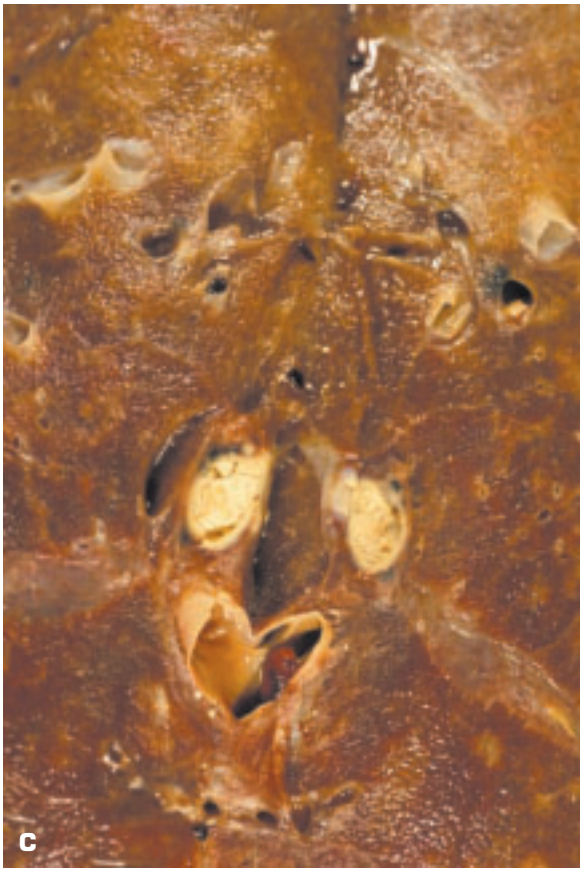

2-18. *(Continued)* **C.** Healed, caseous lesion of histoplasmosis with fibrous capsule in lung parenchyma is reminiscent of a tuberculous infection. The proximity to the lung hilum (note adjacent major pulmonary artery branch) means one cannot exclude the process occurring in an intrapulmonary lymph node. **D.** Histology shows coagulative necrosis (caseation). **E.** Methenamine silver stain shows yeast-like histoplasmosis organisms within the caseous material.

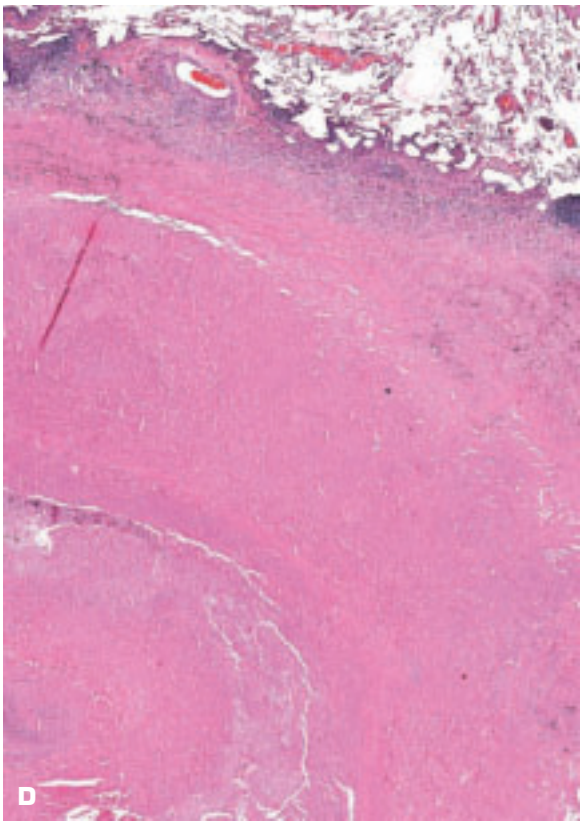

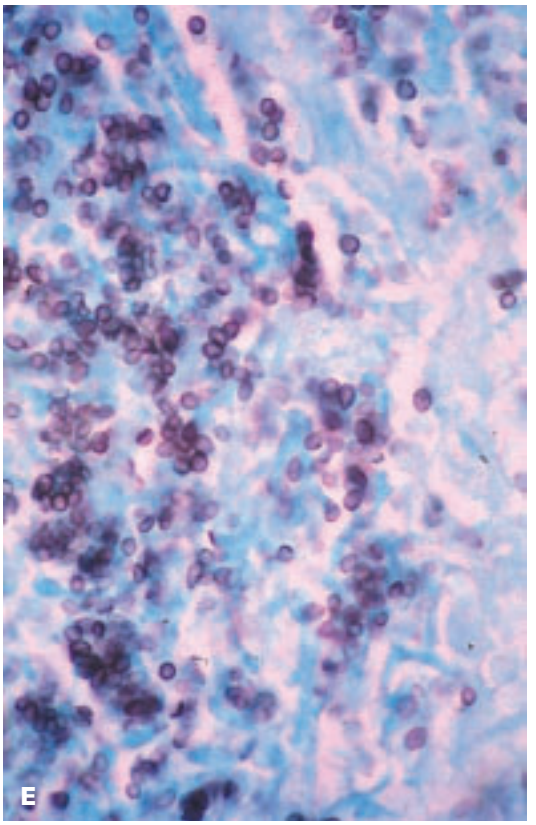

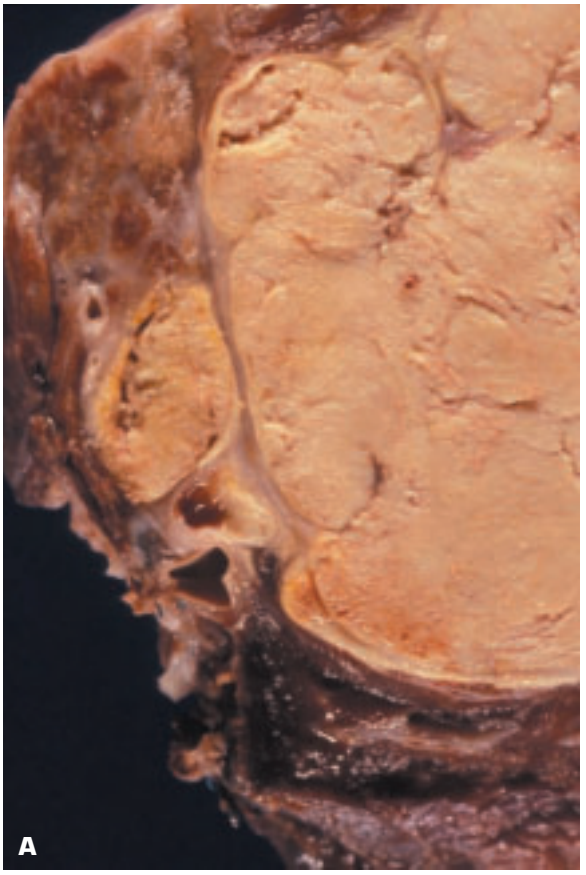

2-19. A. Coagulative necrosis and granulomatous inflammation of the lung in a case of infection with *Coccidioides immitis* (coccidioidomycosis). Unlike histoplasmosis, these granulomas seldom calcify. **B.** A spherule of *C. immitis* containing numerous endospores is seen in the lower half of the picture, and free-lying endospores are seen in the upper portion of the picture.

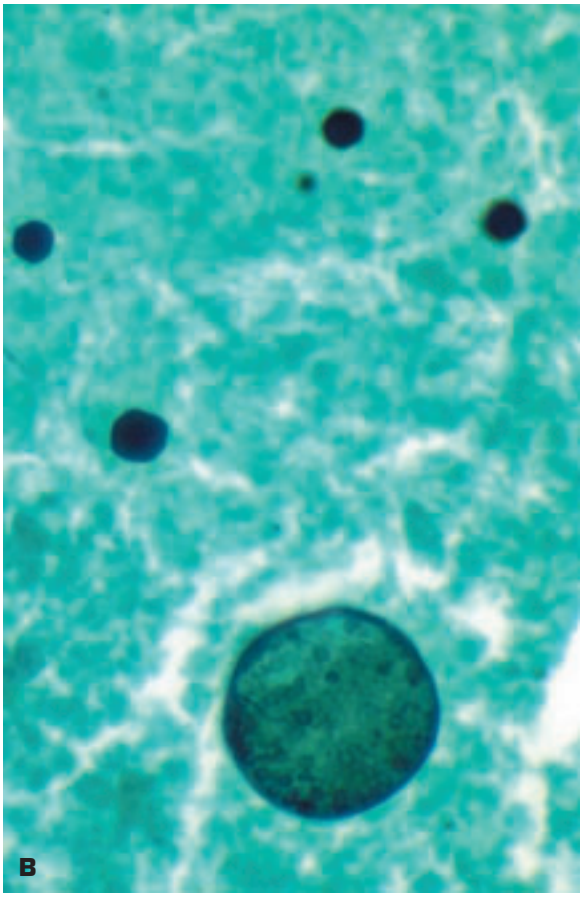

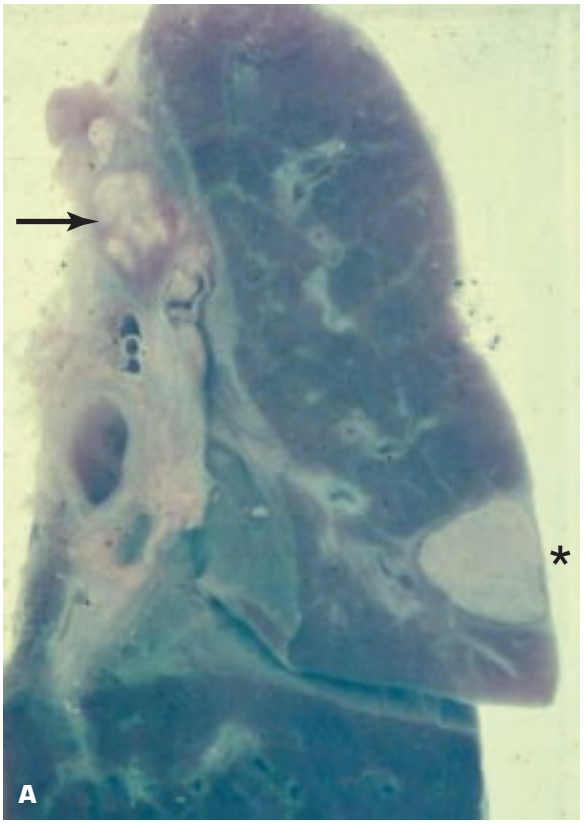

2-20. A. Primary tuberculosis (TB) with midlung parenchymal (Ghon complex) (*) and hilar nodal involvement (*arrow*) by TB combine to produce a Ranke complex. **B.** Progressive primary pulmonary TB in a young child showing massive caseation of hilar lymph nodes and widespread tuberculous bronchopneumonia secondary to bronchogenic spread of the disease. *(continued on next page)*

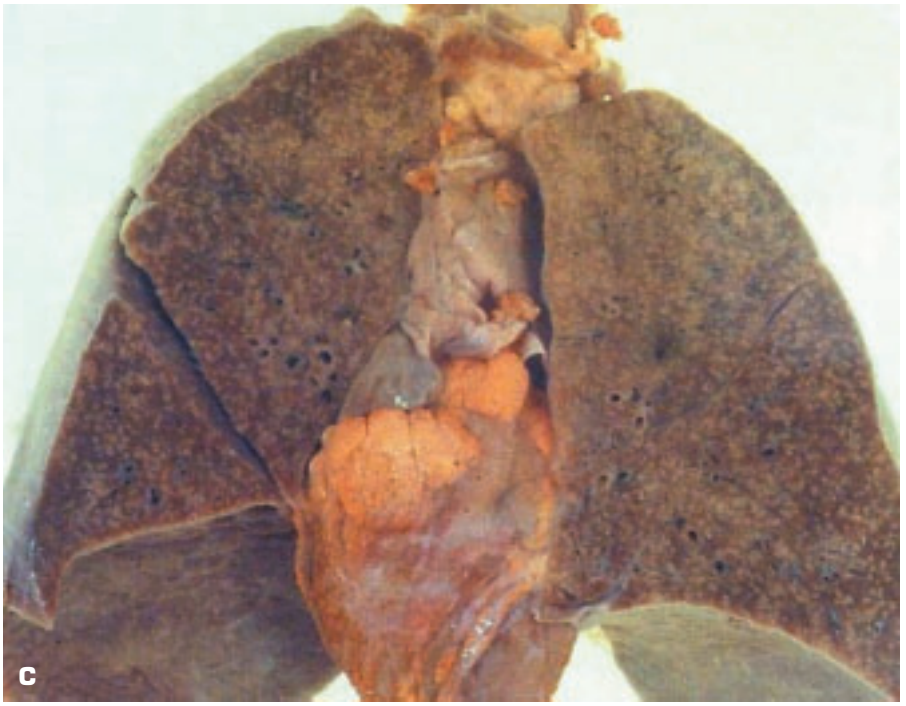

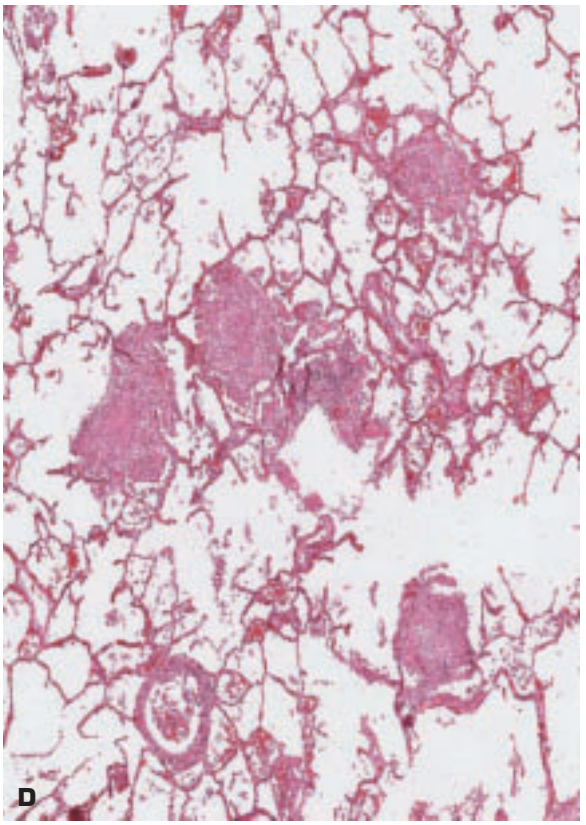

2-20. *(Continued)* **C.** Miliary TB of both lungs due to blood spread of tubercle bacilli via the thoracic duct or following erosion of a tuberculous node into a pulmonary vein or venule. (Photos courtesy of Dr. R.M. Bowen.) **D.** Histology of subacute military TB of the lung showing multiple, small discrete tuberculous granulomas, a few of which show early central necrosis.

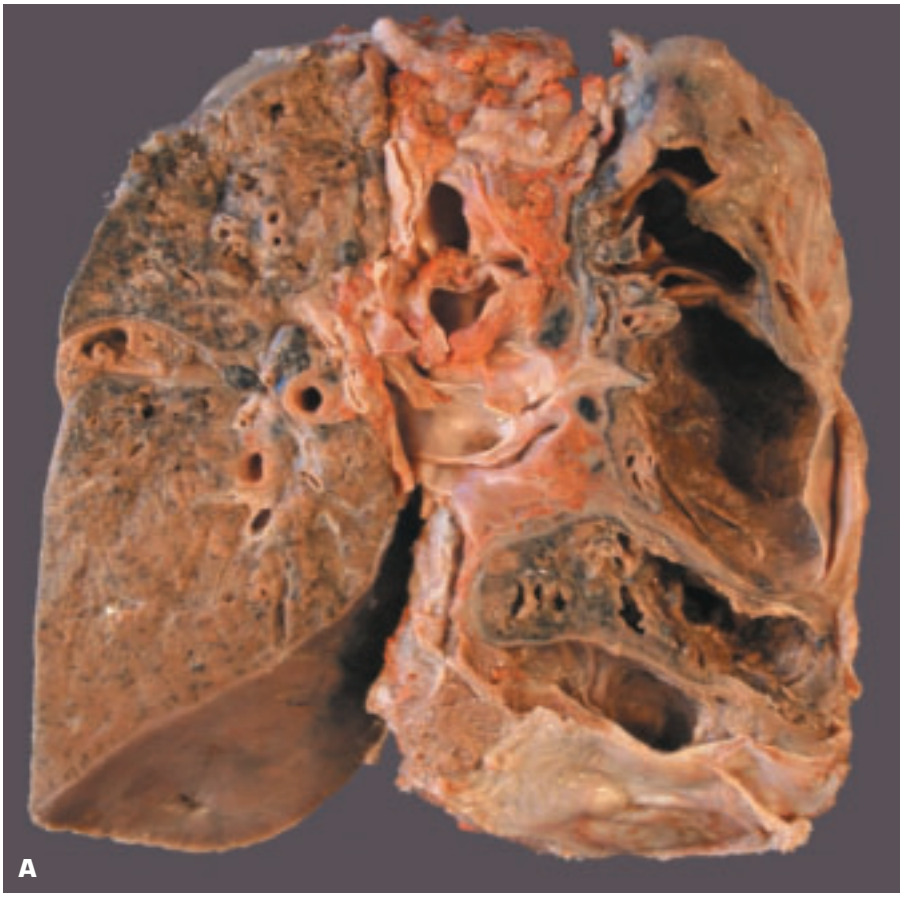

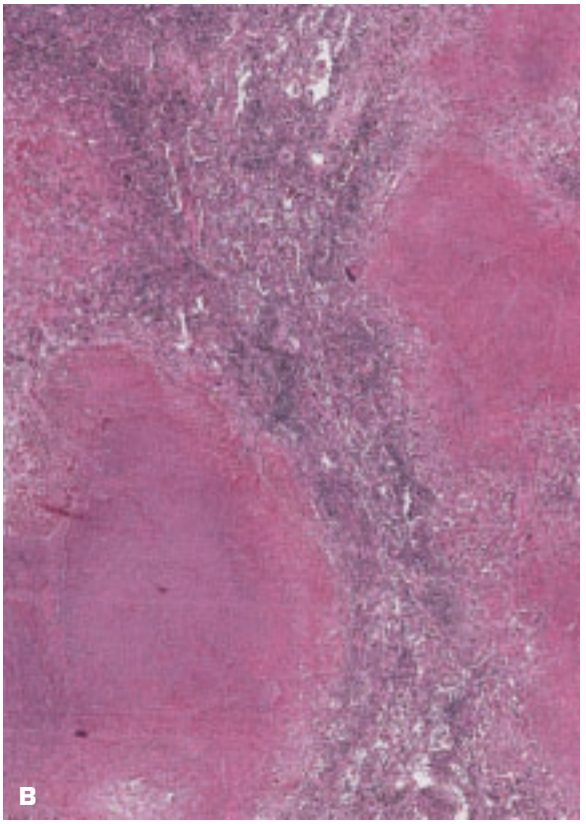

2-21. A. Adult, reinfective tuberculosis (TB) showing massive cavitation (pulmonary arteries span cavities) and marked pleural fibrosis and minimal lymph nodal involvement. The difference from primary TB is due to the greater rigidity of the adult bronchi, as well as the presence of immunity and hypersensitivity. Immunity limits spread of tubercle bacilli to the regional lymph nodes, and hypersensitivity favors necrosis and cavitation following expectoration of necrotic material from eroded bronchi. (Photo courtesy Dr. R.M. Bowen.) **B and C.** Coagulative necrosis with surrounding epithelioid histiocytes and Langhans giant cells plus lymphocytes comprising the inflammatory response to active TB infection. *(continued on next page)*

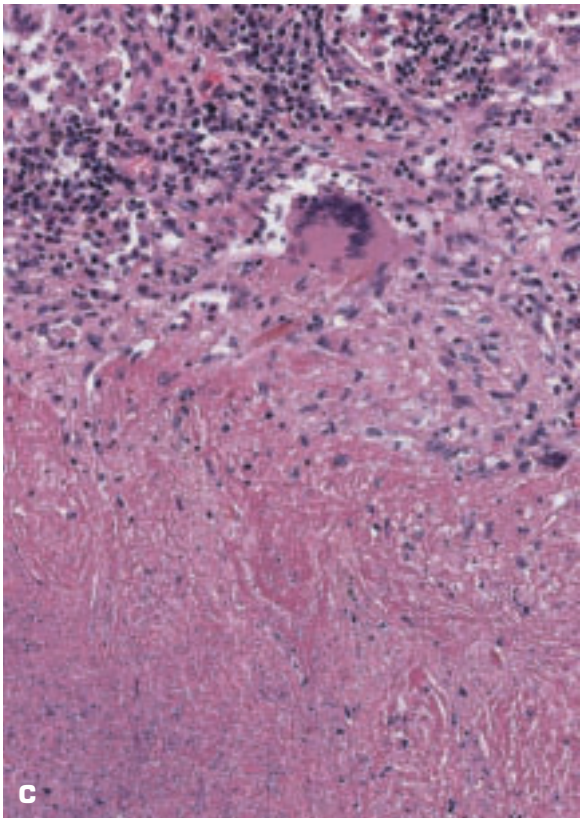

2-21. *(Continued)* **D.** Mycobacterium tuberculosis acid-fast bacilli are characterized by a beaded and slightly curved appearance.

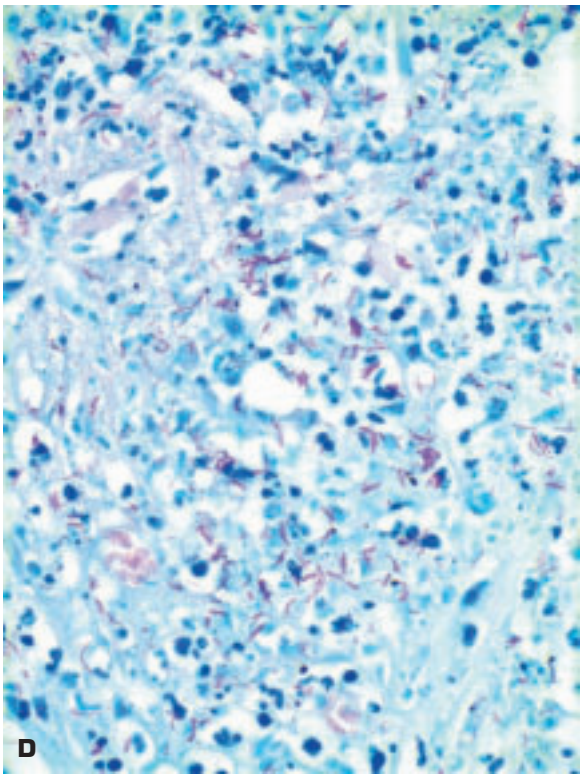

2-22. A. Pulmonary fibrosis in steroid-treated sarcoidosis. **B.** Noncaseating, tuberculoid granuloma of sarcoidosis in the lung. The granulomas are centered on venules in about 80% of cases and involve arteries to a much lesser degree. In parts of the world where tuberculosis (TB) is common, the pathologist is not in a position to make the differential diagnosis between TB and sarcoidosis on a biopsy without clinical input.

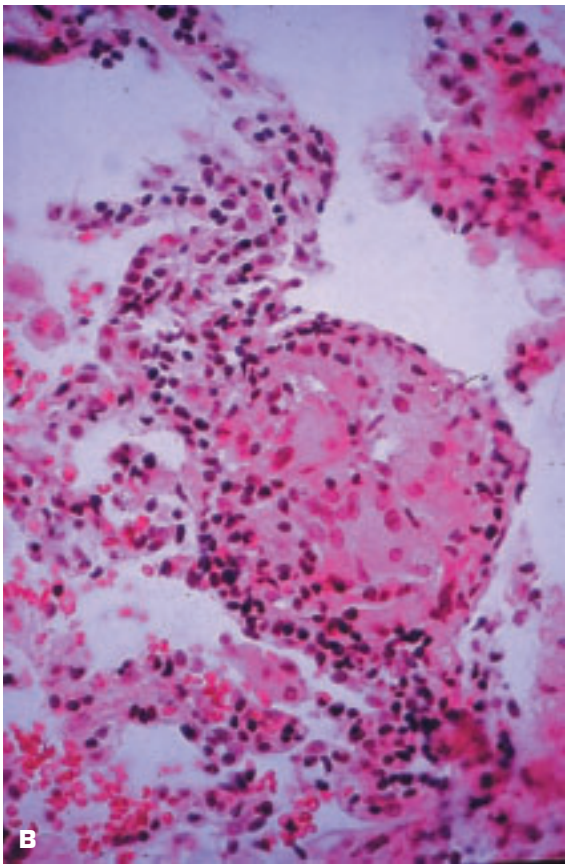

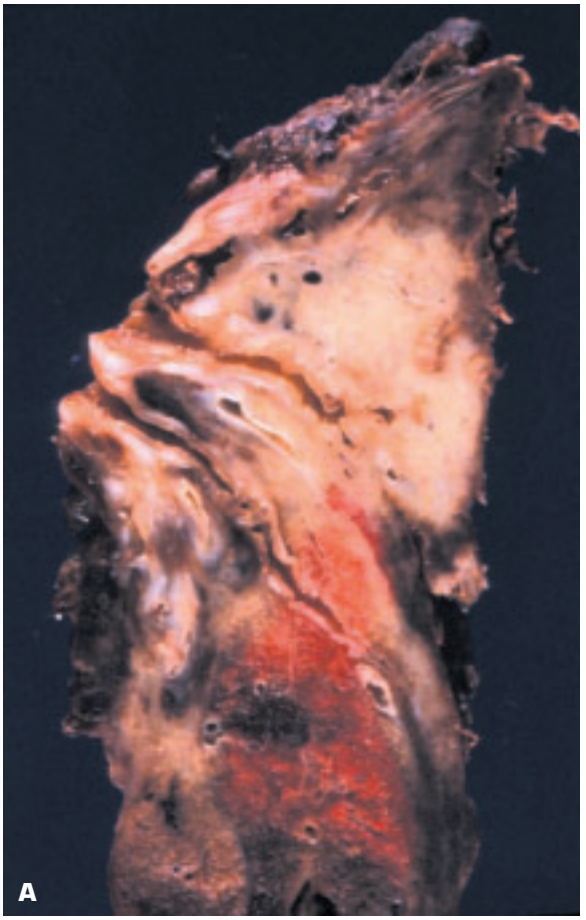

2-23. A. Wegener granulomatosis (WG): note the pale area in the upper lobe due to a combination of necrosis (*yellow areas*) and reparative fibrosis (*white areas*). **B.** Pulmonary cavitation in WG may mimic tuberculosis, and Langhans-type giant cells may be observed in both conditions. *(continued on next page)*

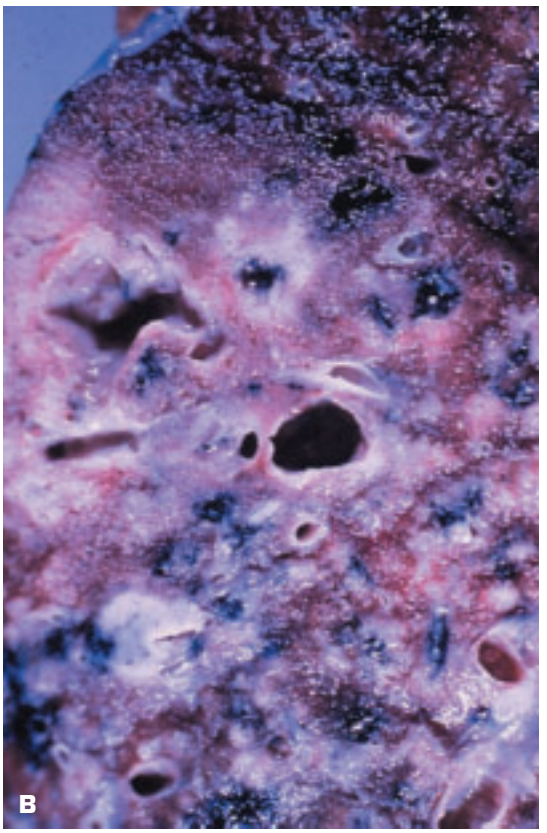

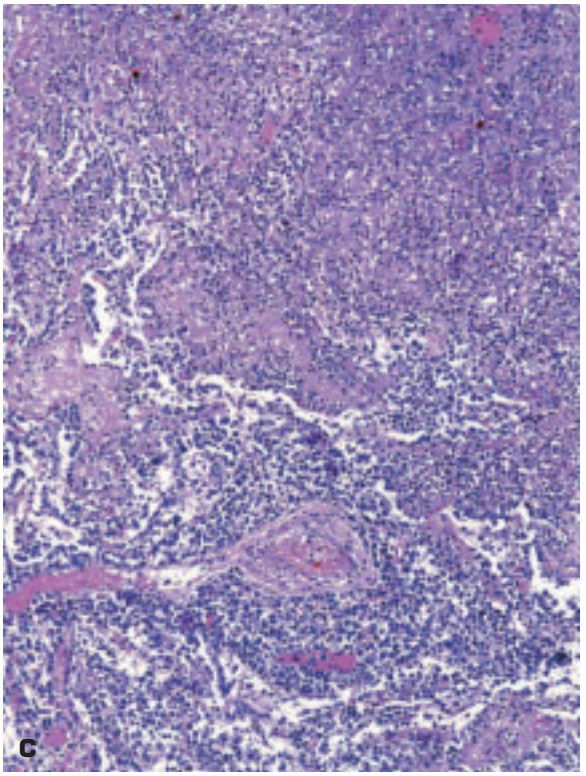

2-23. *(Continued)* **C.** Treated WG. The presence of a small vessel vasculitis, a mixed inflammatory infiltrate, and parenchymal serpiginous necrosis (not seen here) is characteristic of WG. **D.** Small pulmonary arterial vasculitis in WG.

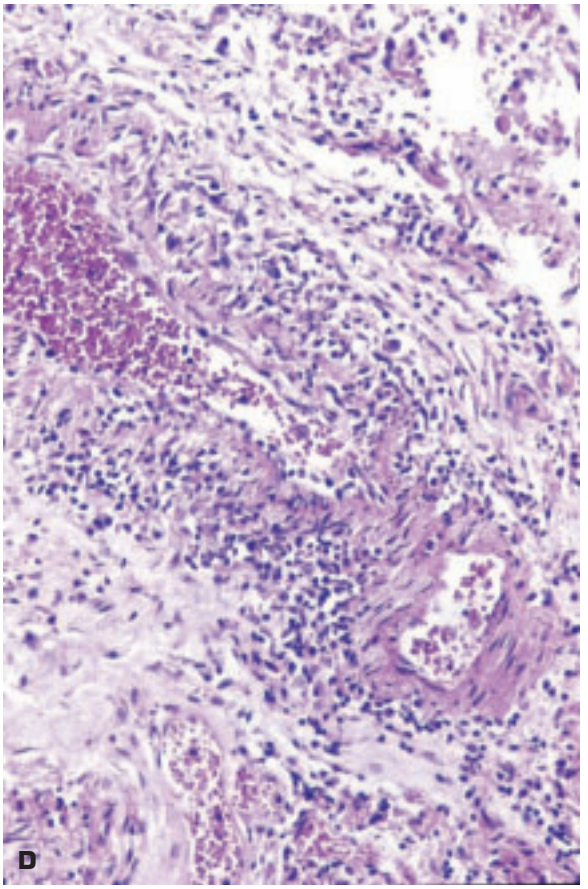

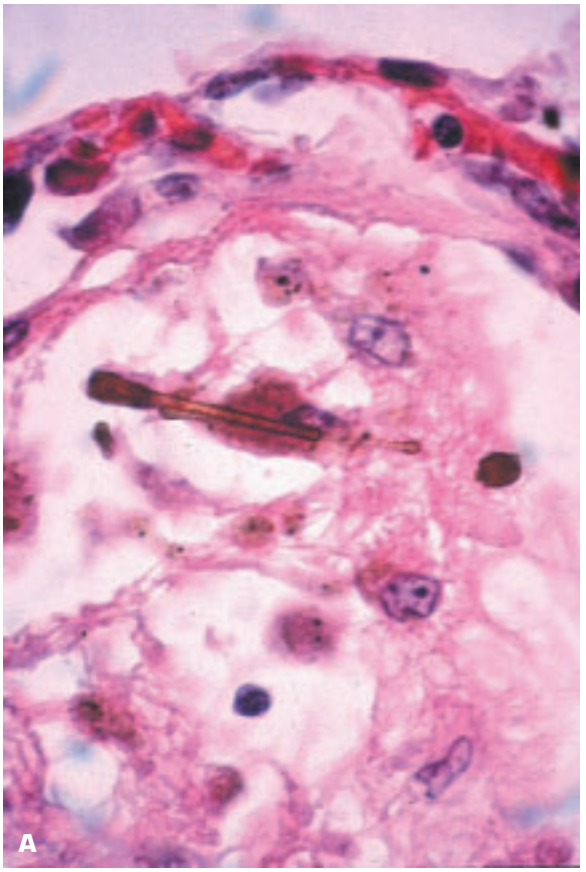

2-24. A. Asbestos (ferruginous) body (AB) in the lung comprises a thin, almost invisible, colorless, nonbirefringent, needle-like fiber of asbestos that is rendered visible by deposits of iron (hemosiderin) and protein on its surface in a beaded fashion. The ABs are most numerous toward the bases of the lungs due to the effect of gravity and may pass through the lungs. Dense structures such as bone (e.g., ribs) and very dense collagen (e.g., central tendon of the diaphragm) may arrest the asbestos fibers' passage in the body, and the outcome is local irritation and fibrogenesis, resulting in the following distribution for fibrous plaques due to asbestos fibers. **B.** Fibrous plaques (*) on the parietal pleura are distributed along the inner aspect of the ribs, while sparing the intercostal muscles that failed to arrest passage of the asbestos fibers. Fibrous plaques may occur with asbestos exposure in the absence of asbestosis. *(continued on next page)*

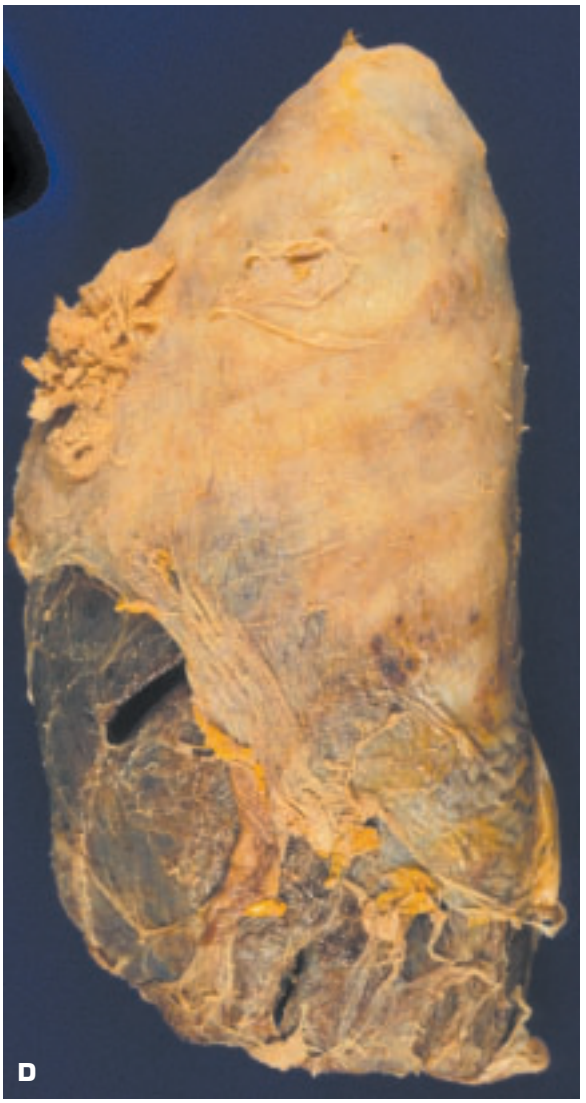

2-24. *(Continued)* **C.** Similarly, on the upper surface of the diaphragm, the plaques are confined to the pleura overlying the central tendon of the diaphragm and are rarer on its muscular portion. **D.** Asbestosis may lead to obliteration of the pleural space due to the parietal pleura becoming firmly attached to the visceral pleura. Note the rib markings on the exterior of the parietal pleura that is covering most of the lung.

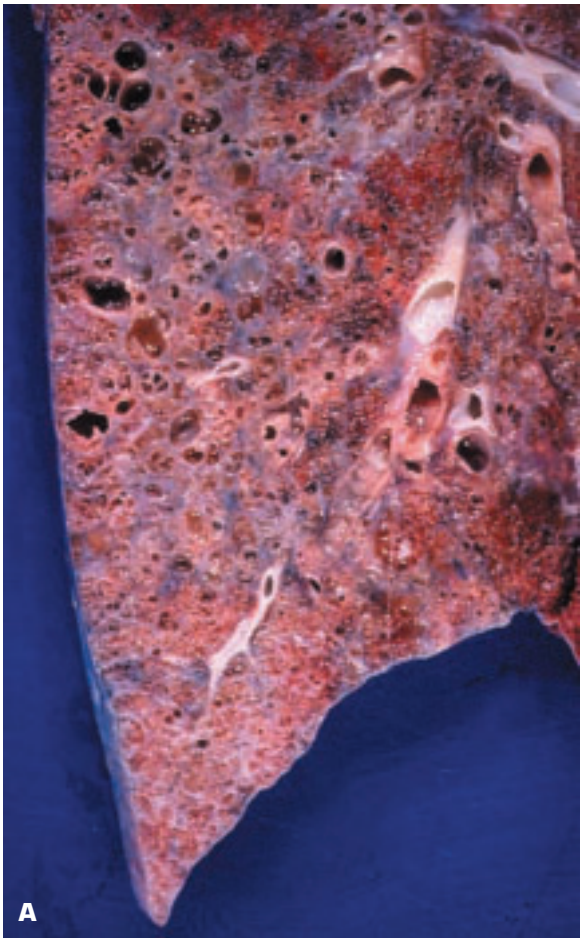

2-25. A. Asbestosis has produced widespread, patchy interstitial pulmonary fibrosis and cyst formation ("honeycomb" lung) due to air trapping in the lung. **B.** Histologic appearance of advanced asbestosis with widespread fibrosis and cystic dilatation of airspaces.

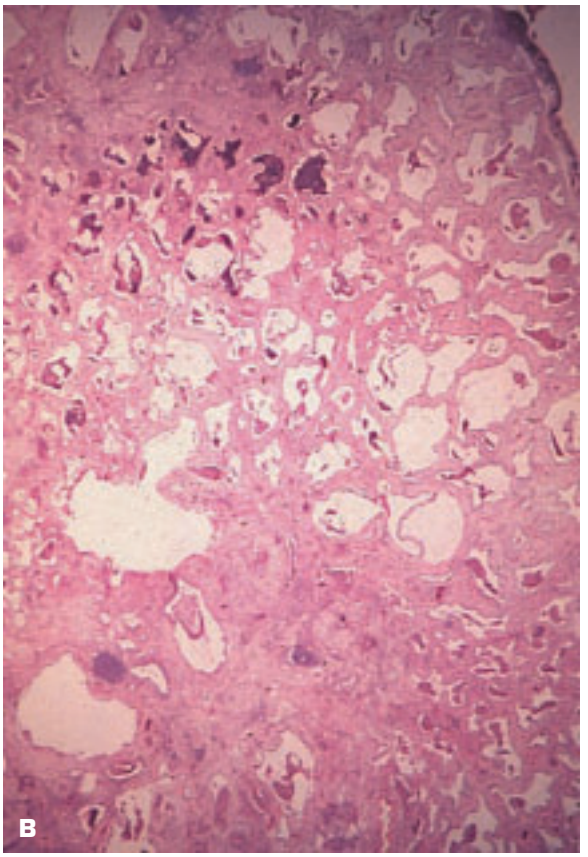

2-26. A. Malignant mesothelioma on the pleural surface and spreading into the interlobar fissures of an extremely anthracotic lung. **B.** Malignant mesothelioma entirely encases the left lung and is infiltrating into the lung from the exterior. **C.** Histology of a malignant mesothelioma exhibiting a spindle-cell pattern in a prominent fibrous stroma.

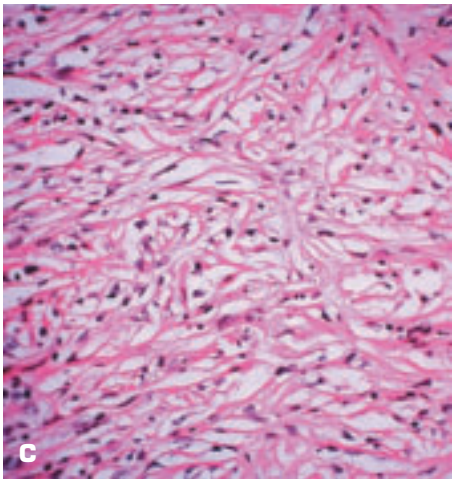

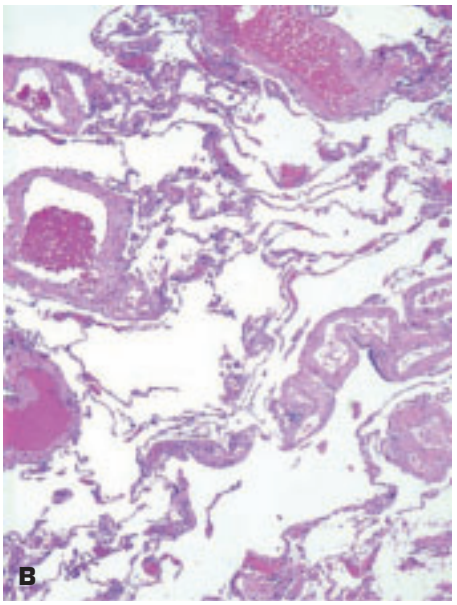

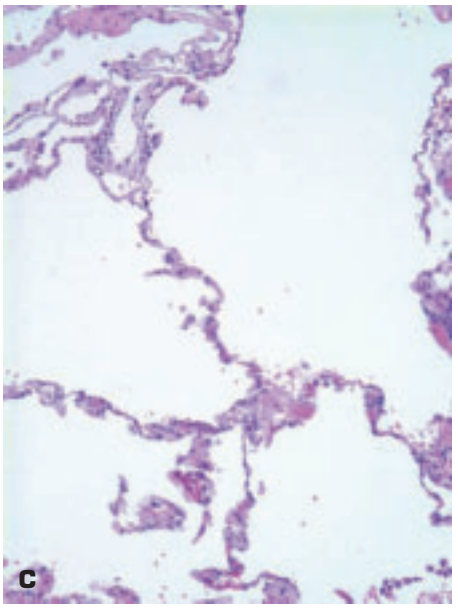

2-27. A. Whole lung section shows pan-acinar emphysema of lung in a patient with α-1-antitrypsin deficiency. **B and C.** Histology shows destruction of alveolar walls in a diffuse fashion.

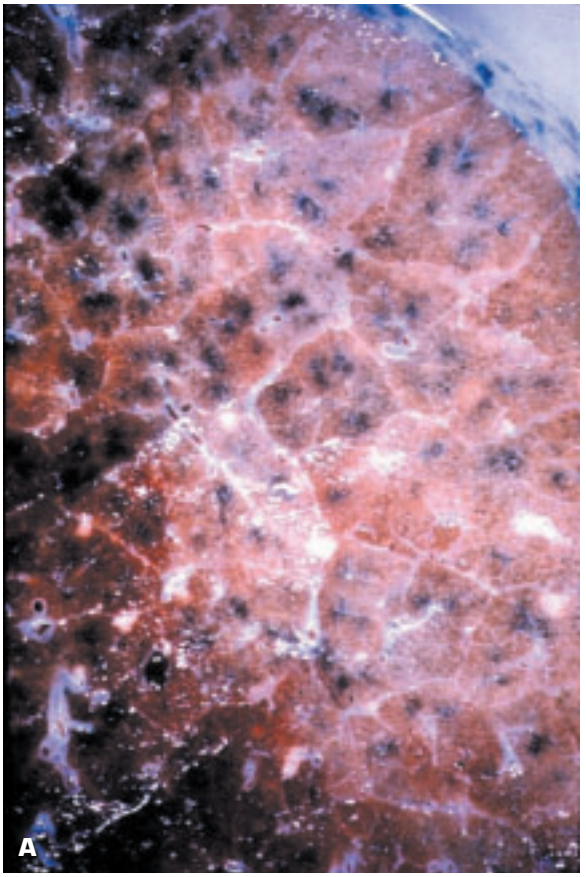

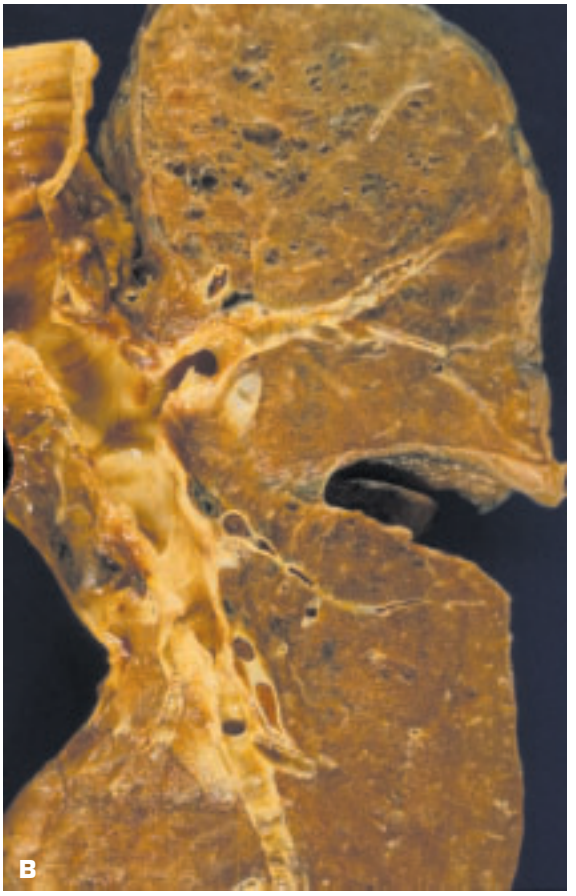

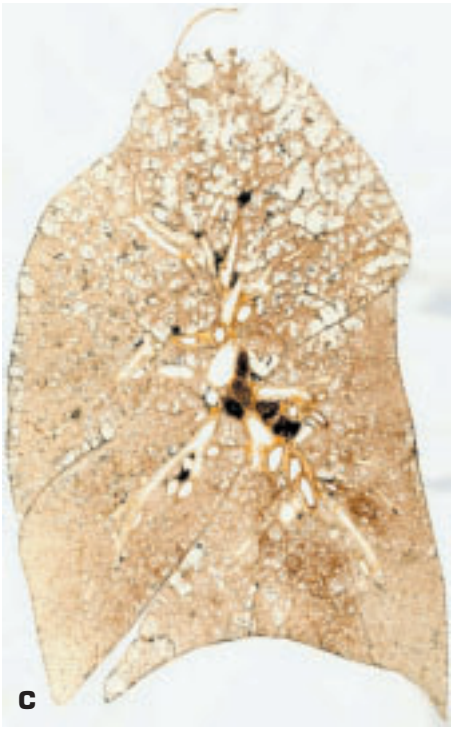

2-28. Centrilobular emphysema of the lungs, commonly related to cigarette smoking, is most severe in the upper portions of the lungs. **A.** Centrilobular carbon deposits in the lung. **B.** Early centrilobular emphysema in left upper lobe of lung. **C.** Whole lung section of moderate centrilobular emphysema. *(continued on next page)*

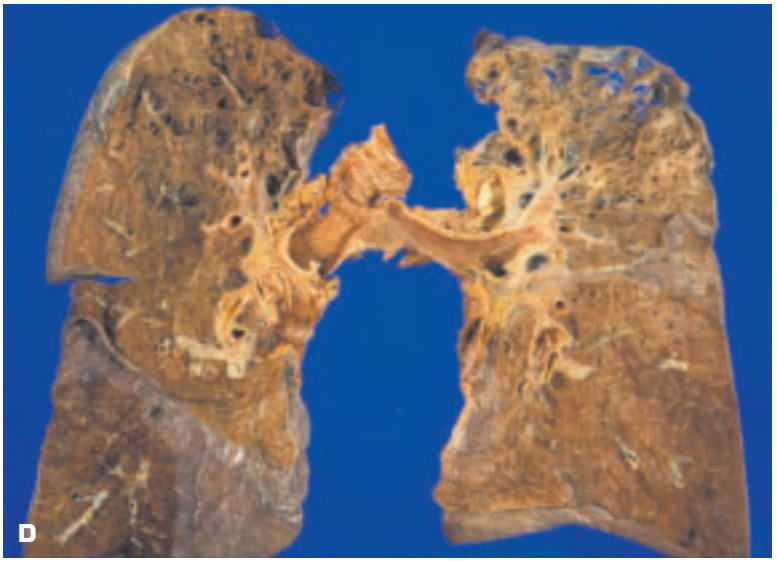

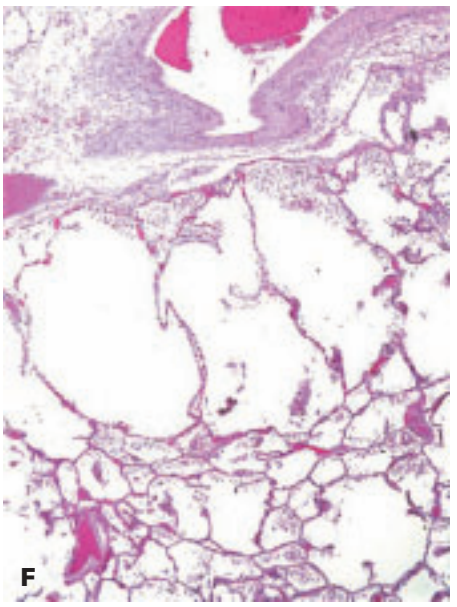

2-28. *(Continued)* **D.** More severe centrilobular emphysema is most noticeable in both upper lobes. **E.** Whole lung section of severe centrilobular emphysema. **F.** Centrilobular emphysema histology shows maximal alveolar destruction in the center of the lobule closest to the bronchiolar and lobular pulmonary arterial branches.

2-29. Bullous emphysema of the lung in a 6-year-old child with Marfan syndrome resulting from intrapulmonary deficiency of elastin.

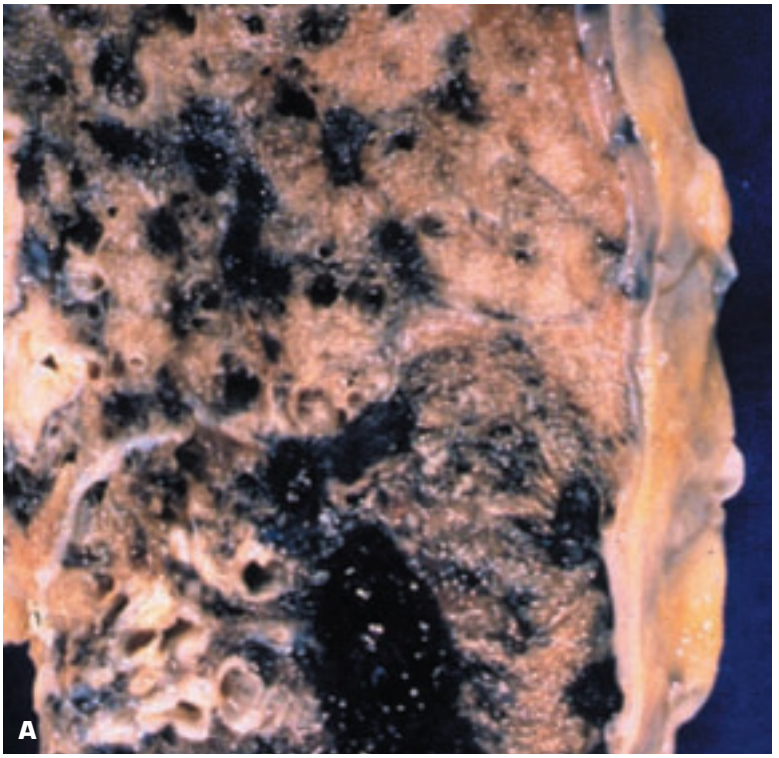

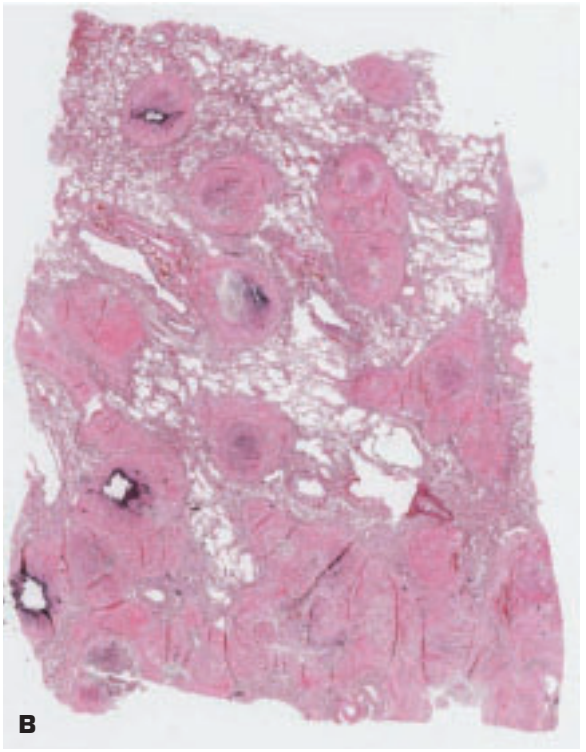

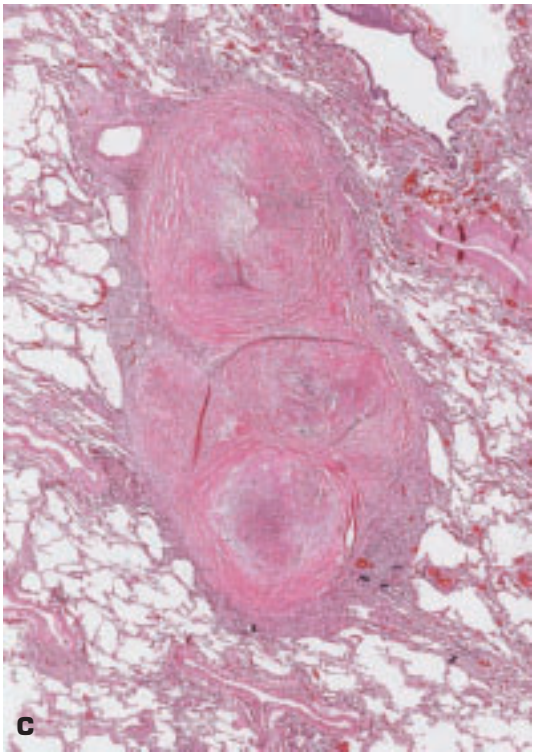

2-30. Silicosis is a form of pneumoconiosis due to inhalation of silicon dioxide (silica) (e.g., due to sand blasting). **A.** Note the pale, large, rounded silicotic nodules against a black background due to severe associated anthracosis. **B and C.** Histologic appearance of multiple, coalescing silicotic nodules composed of concentrically arranged collagen fibers with surrounding aggregates of lymphocytes and fibroblasts.

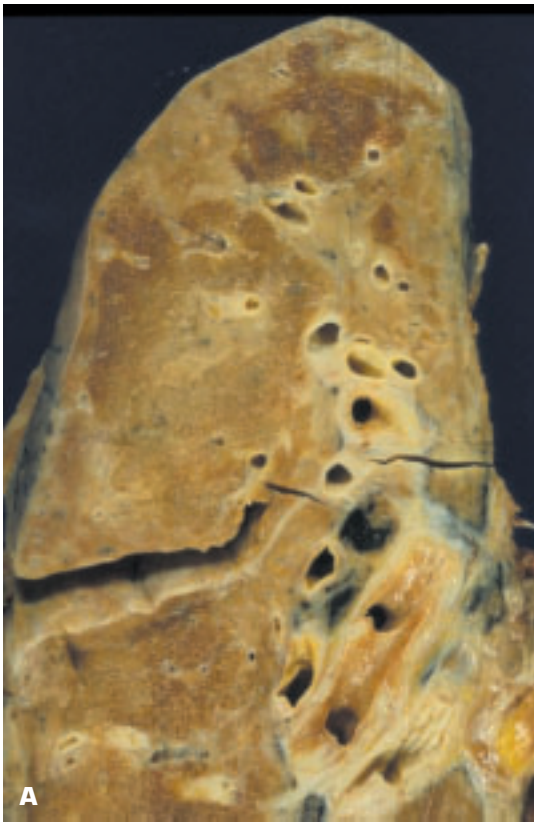
A

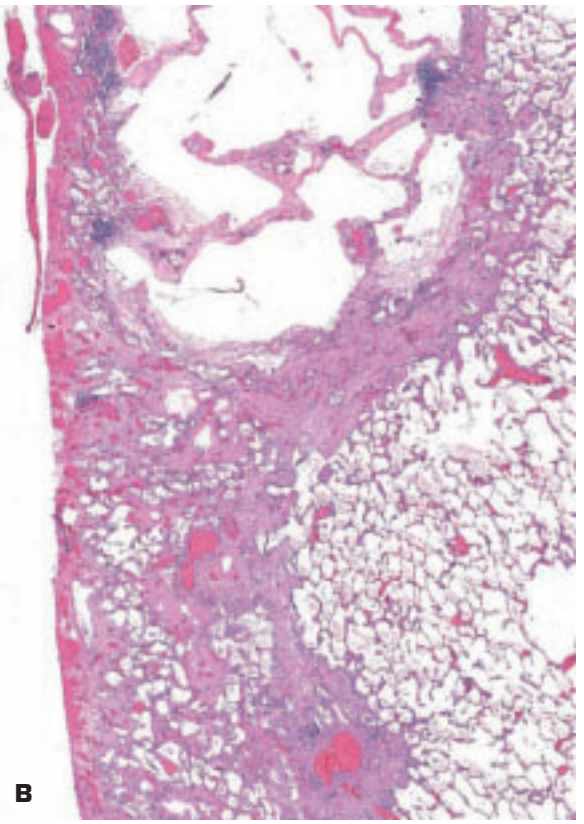
B

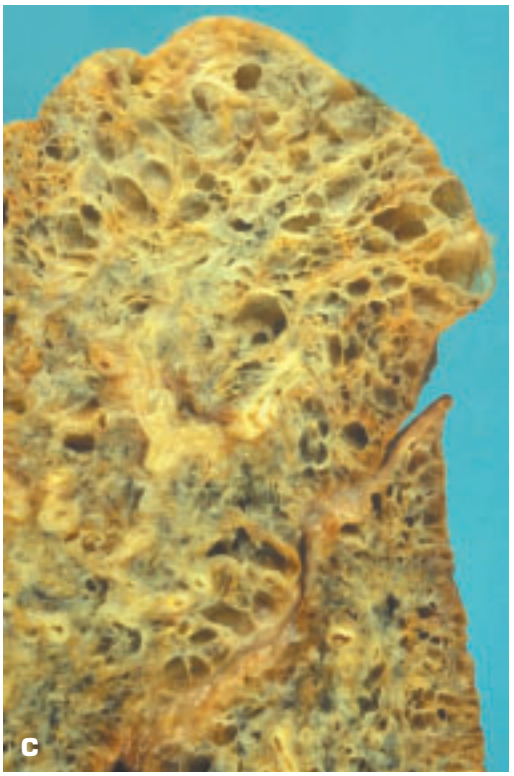
C


D

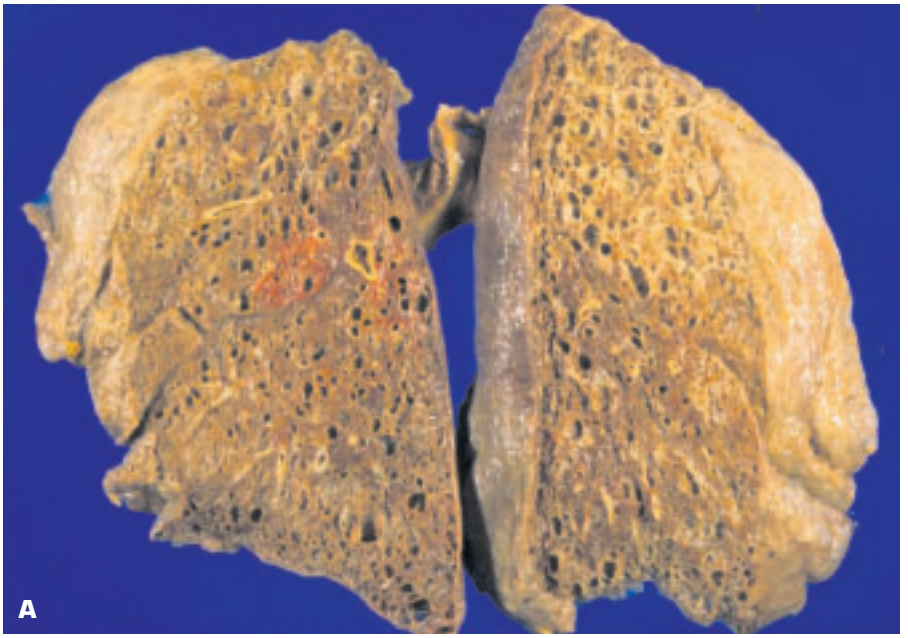

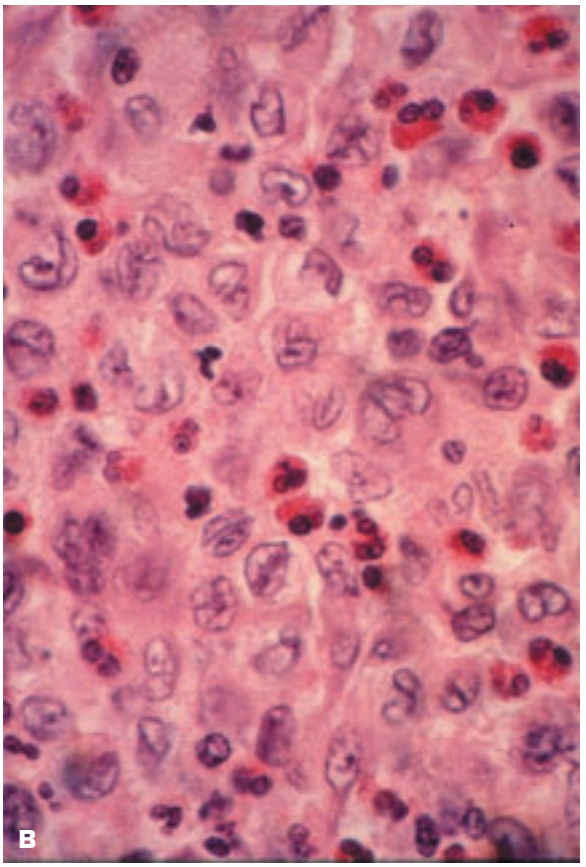

2-32. A. Bilateral patchy pulmonary consolidation and early honeycombing due to Langerhans cell histiocytosis (a proliferation of dendritic cells or macrophages also called "histiocytosis X" or "eosinophilic granuloma"). **B.** Numerous eosinophils lie scattered between aggregates of large phagocytes with foamy cytoplasm and grooved nuclei (Langerhans cells). Because not all tumor cells contain Birbeck granules on electron microscopy, staining for S-100 and CD1a may assist in the diagnosis.

Facing Page:

2-31. A. Macroscopic appearance of fibrosing alveolitis; note the tendency toward involvement of the more peripheral portions of the lung parenchyma. **B.** Subpleural fibrosis and early honeycombing in fibrosing alveolitis. **C.** End-stage honeycomb lung due to fibrosing alveolitis. **D.** External appearance of honeycomb lung shows a cobble stone-like pattern.

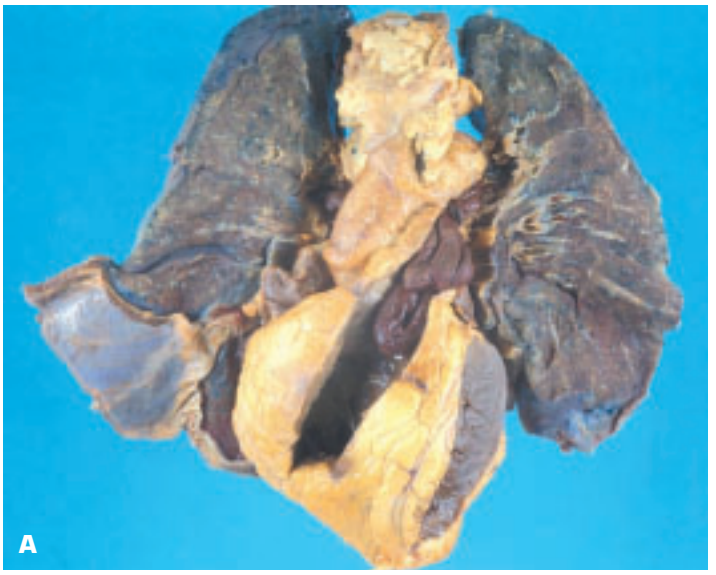
A

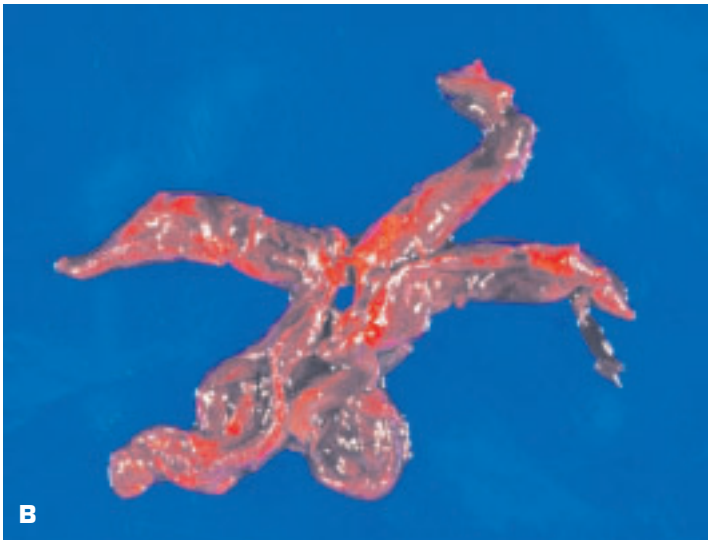
B

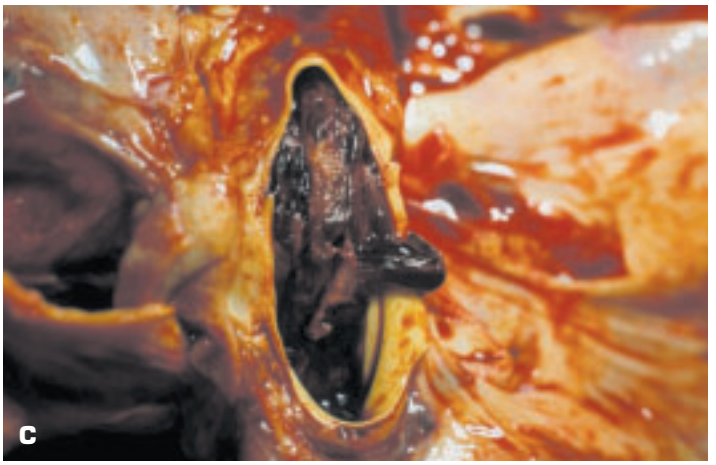
C

2-34. A. Wedge-shaped lung infarct with base on the pleural surface (arrow indicates thromboembolism). The lung has a dual blood supply, and pulmonary arterial occlusion may only produce infarction (as opposed to incomplete/subinfarction) if cardiac failure negates the protective effect of the bronchial circulation. **B.** Histologic edge of pulmonary infarct is seen in lower left. *(continued on next page)*

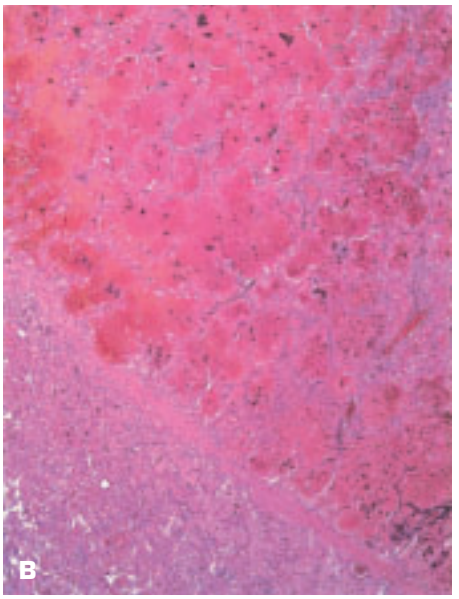

Facing Page:
2-33. A. Massive, fatal pulmonary thromboembolism (TE) of main pulmonary artery extending into its bifurcation due to TE from iliofemoral segment venous thrombosis. Note the coiled up thrombus filling the pulmonary artery. **B.** Unraveled thrombus from another patient's massive TE reveals a venous thrombus with thrombotic extensions from side branches of the venous system. **C.** Right main pulmonary artery is filled by a thromboembolus.

2-34. *(Continued)* **C.** The darker-colored infarct situated subpleurally on the right is surrounded by an extensive area of hemorrhagic-looking lung parenchyma exhibiting incomplete (sub)infarction in which the alveolar walls are viable and intraalveolar hemorrhage has occurred. **D.** Histology of incomplete (sub)infarct showing intraalveolar hemorrhage, but viability of the alveolar walls is maintained by the bronchial circulation.

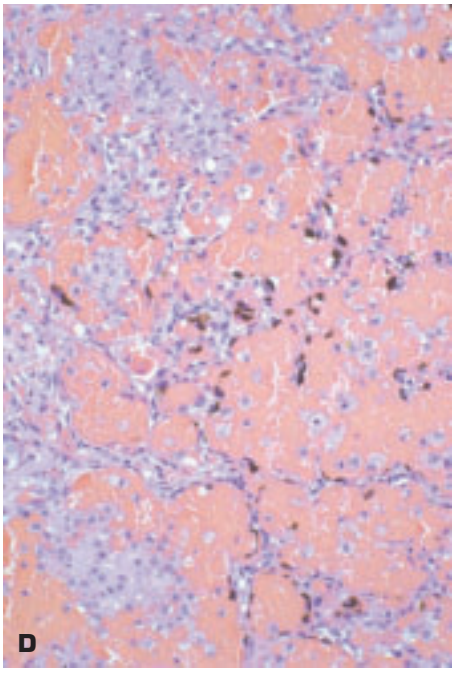

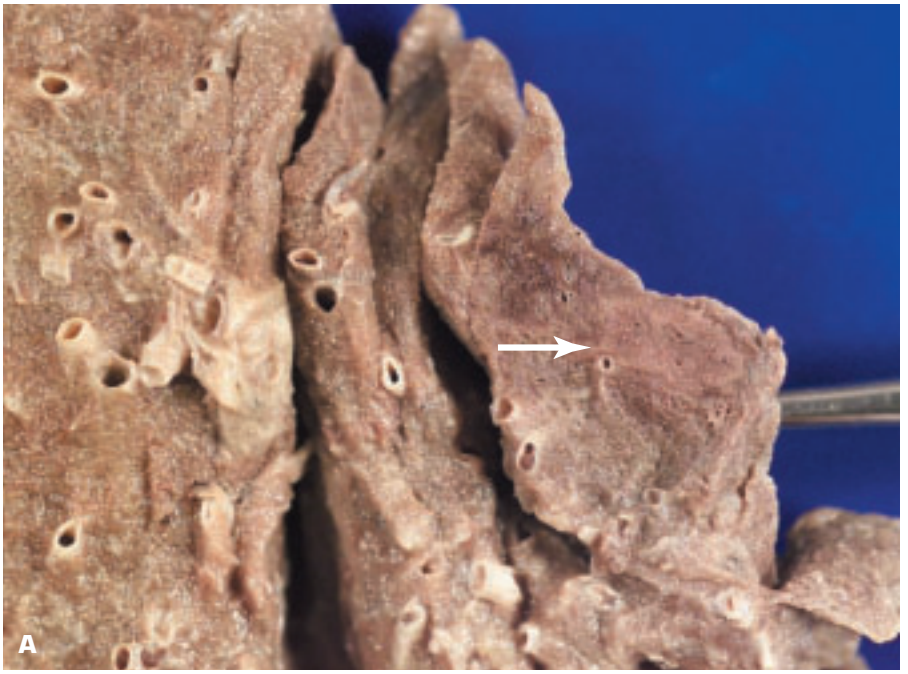

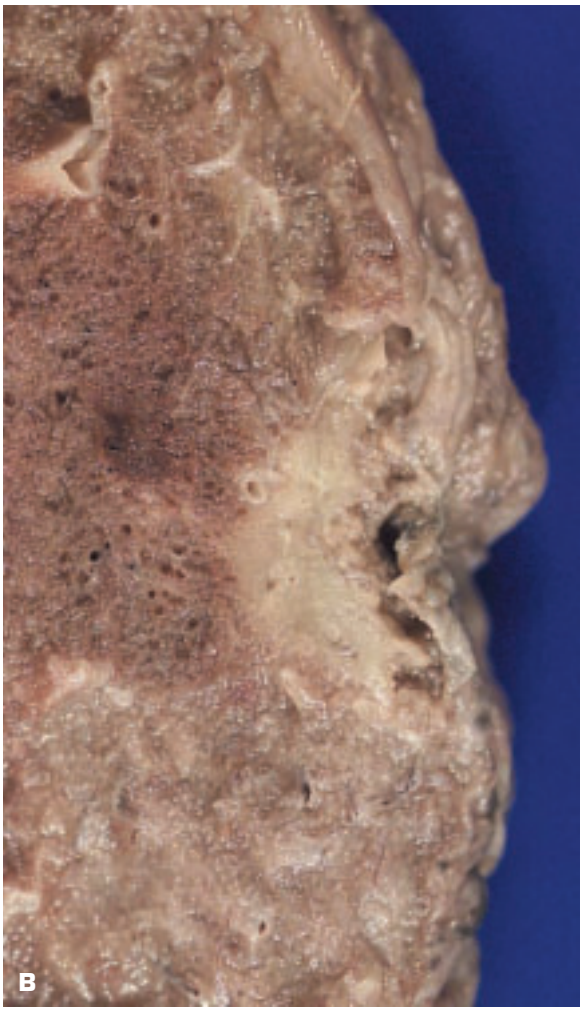

2-35. The lung has an excellent healing capacity, so healed infarcts of the lung are seldom observed; sometimes, only a wafer-thin scar remains as a testament to the previous infarct. **A.** Healing bland (noninfected) infarct of the lung is seen as a slightly hemorrhagic, shrunken, scarred area (*arrow*) beneath the pleural surface. **B.** Healing septic (infected) infarct of the lung showing cavitation of the infarct close to the pleural surface. Yellow color is due to the presence of neutrophils within the infarct.

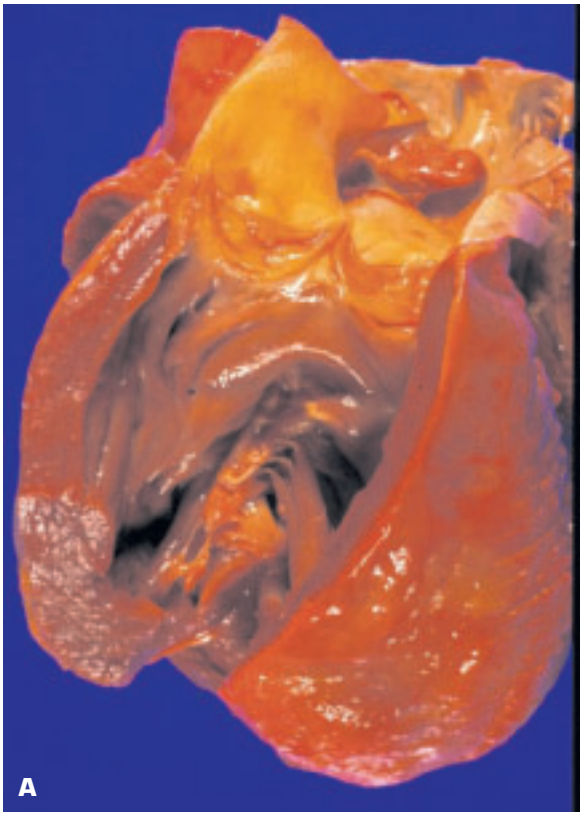

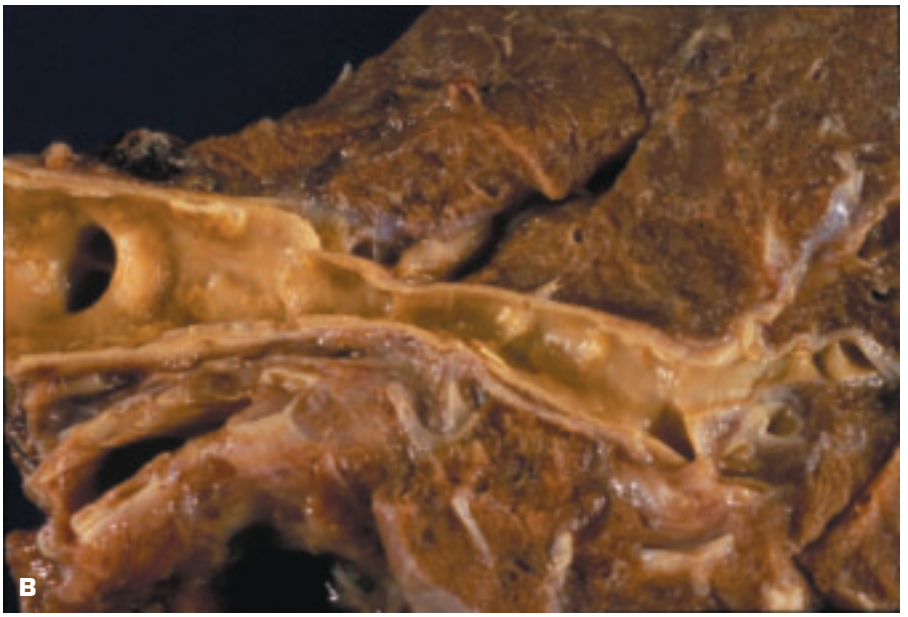

2-36. Gross morphology indicative of pulmonary hypertension may be observed in the right ventricle and main pulmonary arteries. **A.** Disproportionate right ventricular hypertrophy and dilatation. **B.** Atherosclerosis of the main pulmonary artery and its branches occurs predominantly with pulmonary hypertension, and the only other cause is extreme old age (e.g., older than 90 years). In pulmonary hypertension, the arteries appear thicker than normal and are more protuberant on the cut surface of the lung.

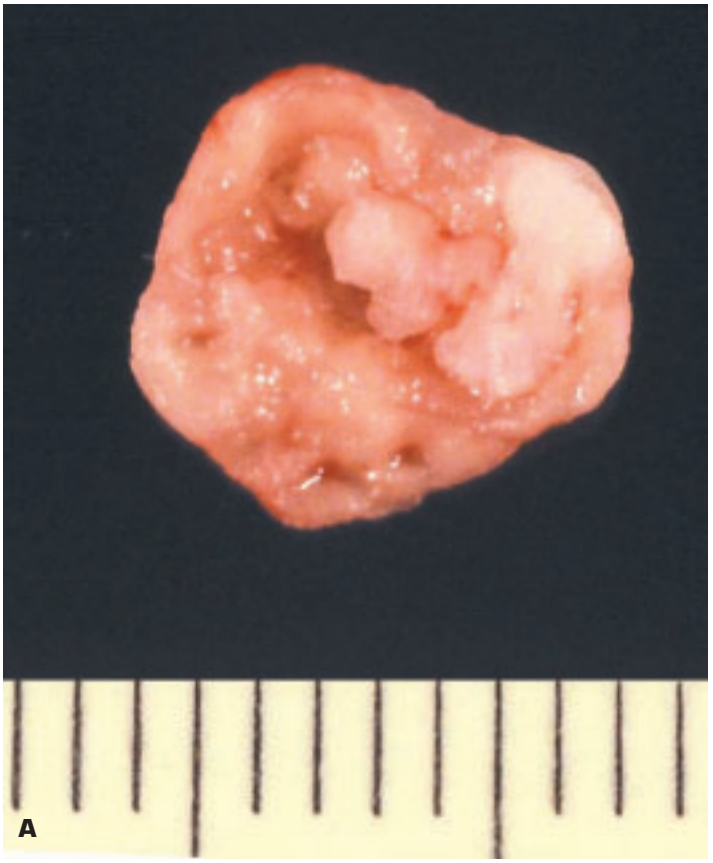

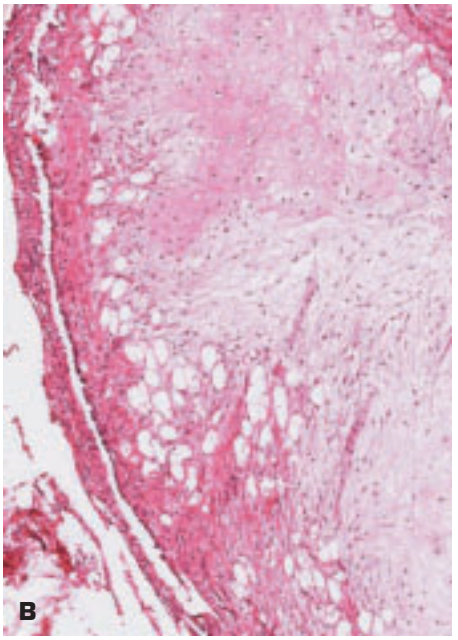

2-37. A. Surgically removed chondroid hamartoma of the lung. **B.** Histology of chondroid hamartoma shows compressed epithelial structures overlying a rounded mass of benign cartilaginous tissue.

2-38. Pulmonary blastoma showing focal areas of necrosis and hemorrhage on its cut surface.

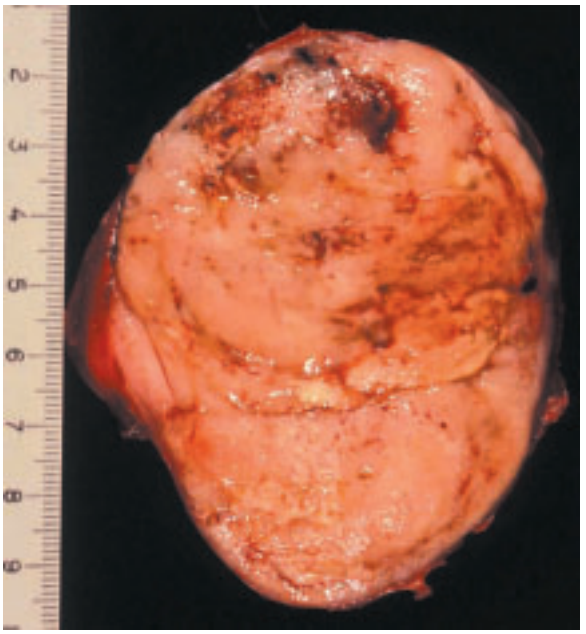

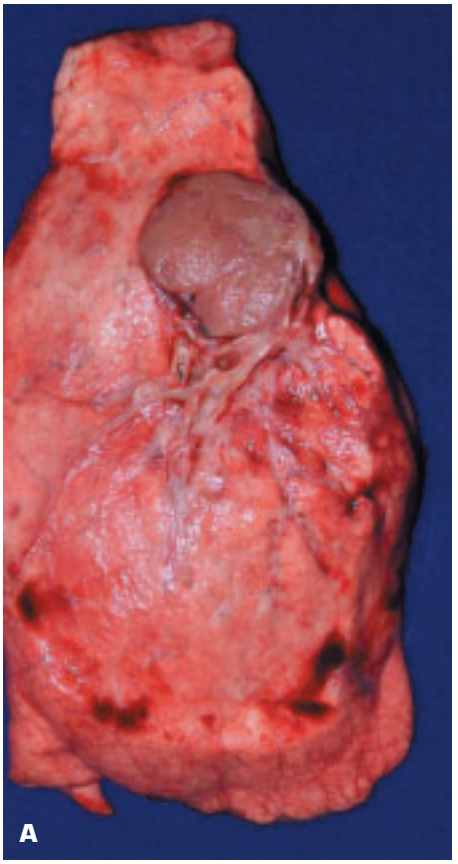

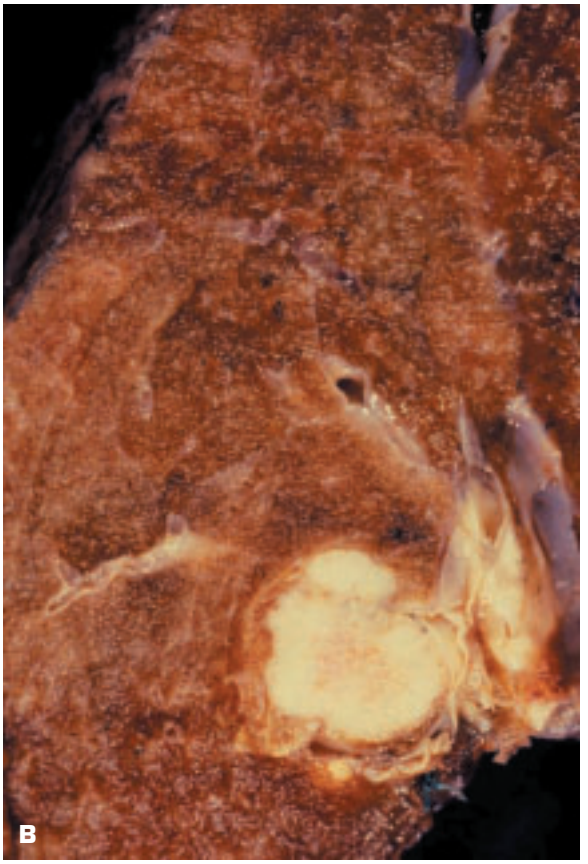

2-39. A. Carcinoid tumor of lung in a lobectomy specimen. **B.** Carcinoid tumor expanding and infiltrating the wall of a large bronchus and compressing the adjacent pulmonary artery. **C.** Typical histology of a carcinoid tumor comprising small nests of uniform-looking small, dark cells.

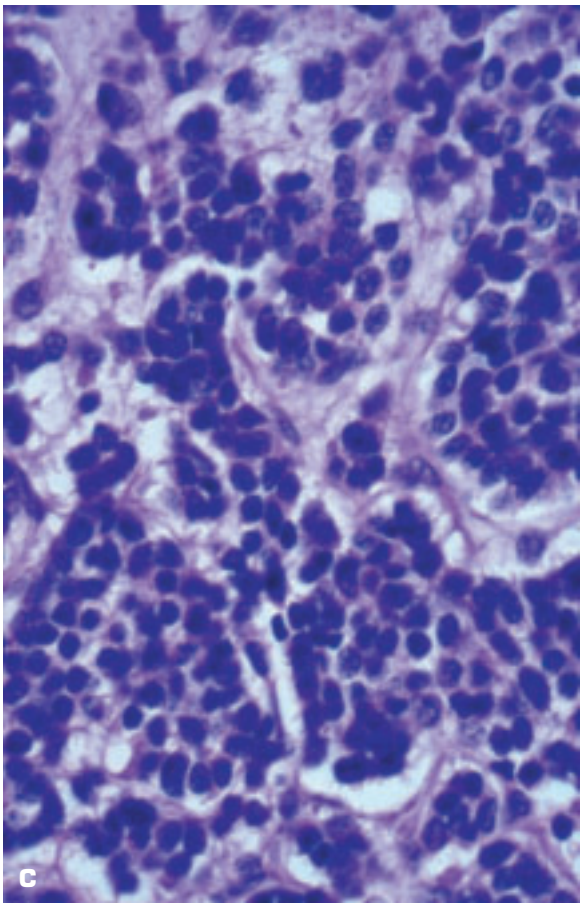

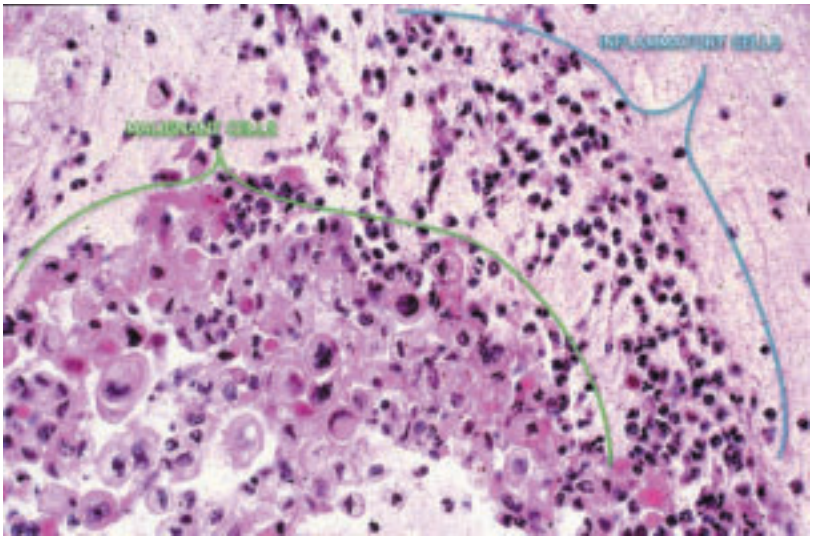

2-40. Sputum cytology from a patient with lung cancer shows highly atypical, anaplastic malignant epithelial cells encompassed by acute inflammatory cells (polymorphonuclear leukocytes).

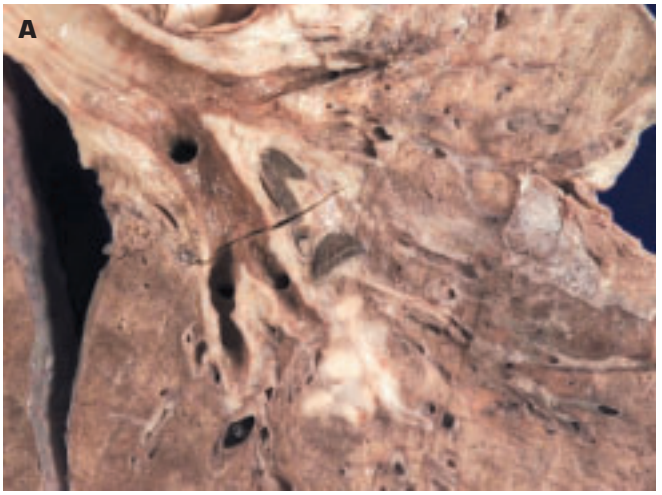

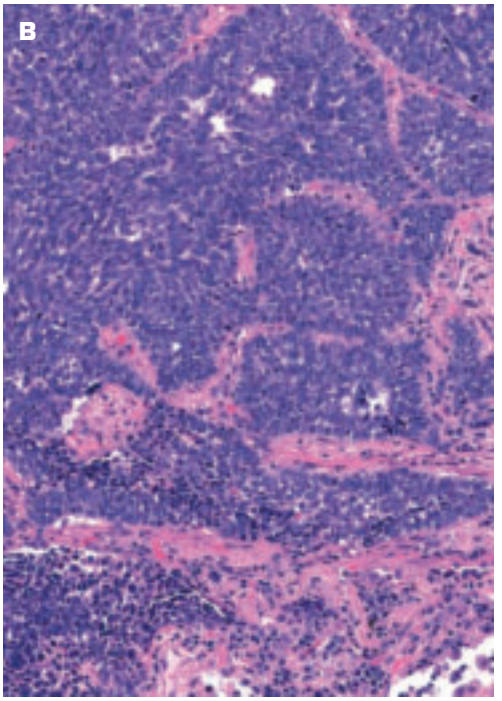

2-41. A. Early lung cancer arising from a left lower lobe bronchus. **B.** Histology shows a poorly differentiated neuroendocrine carcinoma.

2-42. A. Small cell carcinoma that has arisen in the right main bronchus (*left side of picture*) has also infiltrated into the left main bronchus and the left lung parenchyma. **B.** Histology shows a poorly preserved small cell carcinoma.

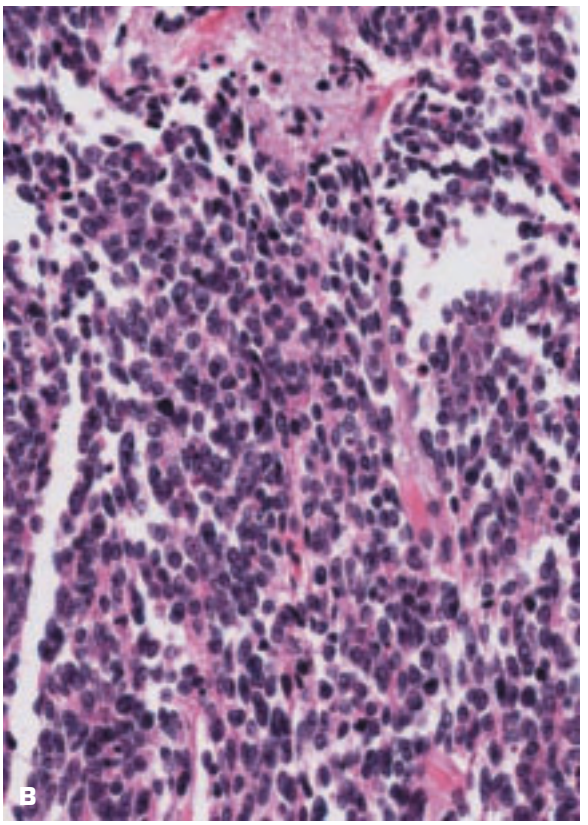

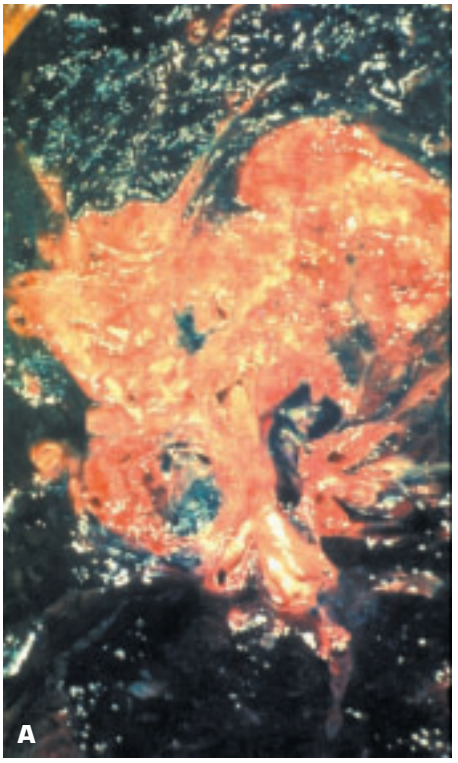

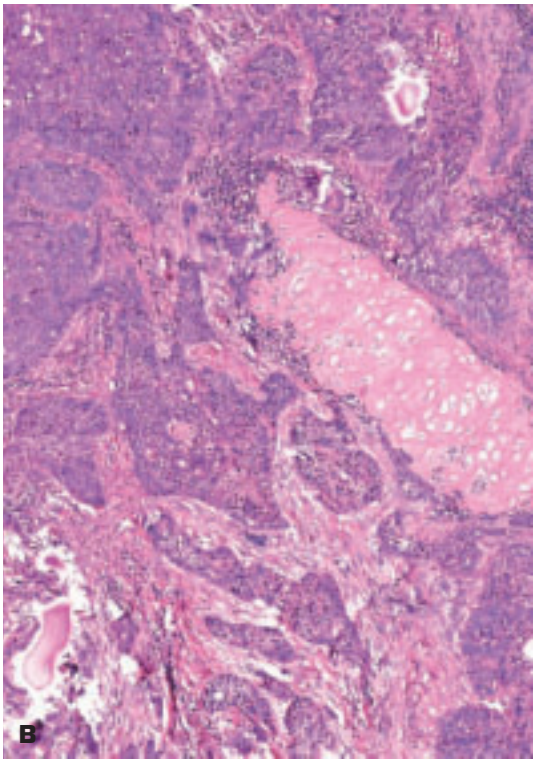

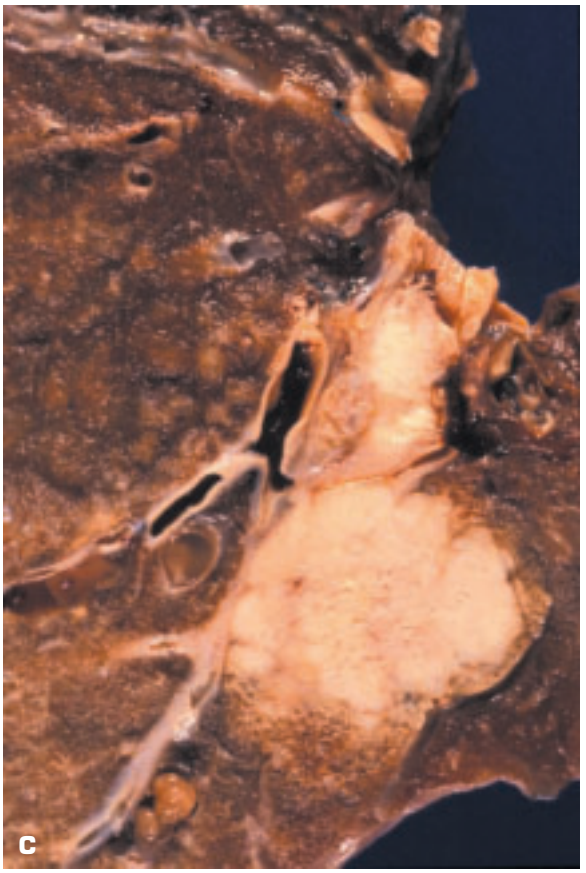

2-43. A. Squamous carcinoma has arisen in a severely anthracotic lung. **B.** Histology shows a moderately differentiated squamous carcinoma. **C.** Poorly differentiated adenosquamous carcinoma arising in the main bronchus of a lung. *(continued on next page)*

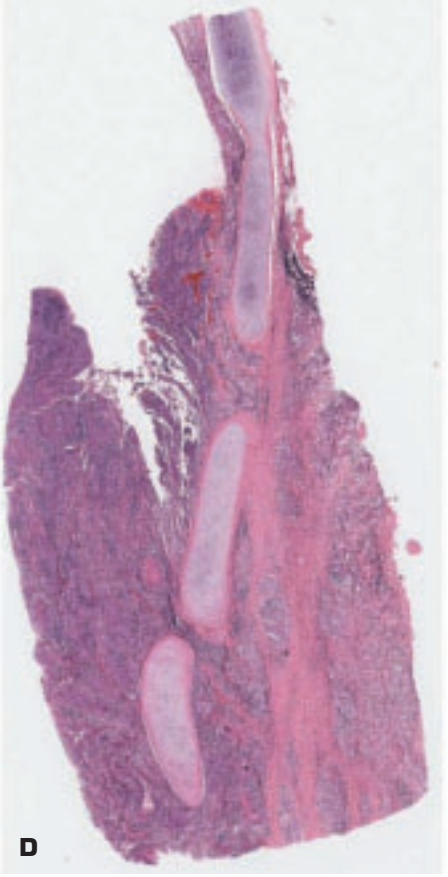

2-43. *(Continued)* **D.** Cartilage rings survive within a bronchogenic carcinoma. **E.** By obstructing the main bronchus, a large cell carcinoma has led to multiple lung abscesses and pneumonic consolidation. An illustration of the dictum that stasis favors infection.

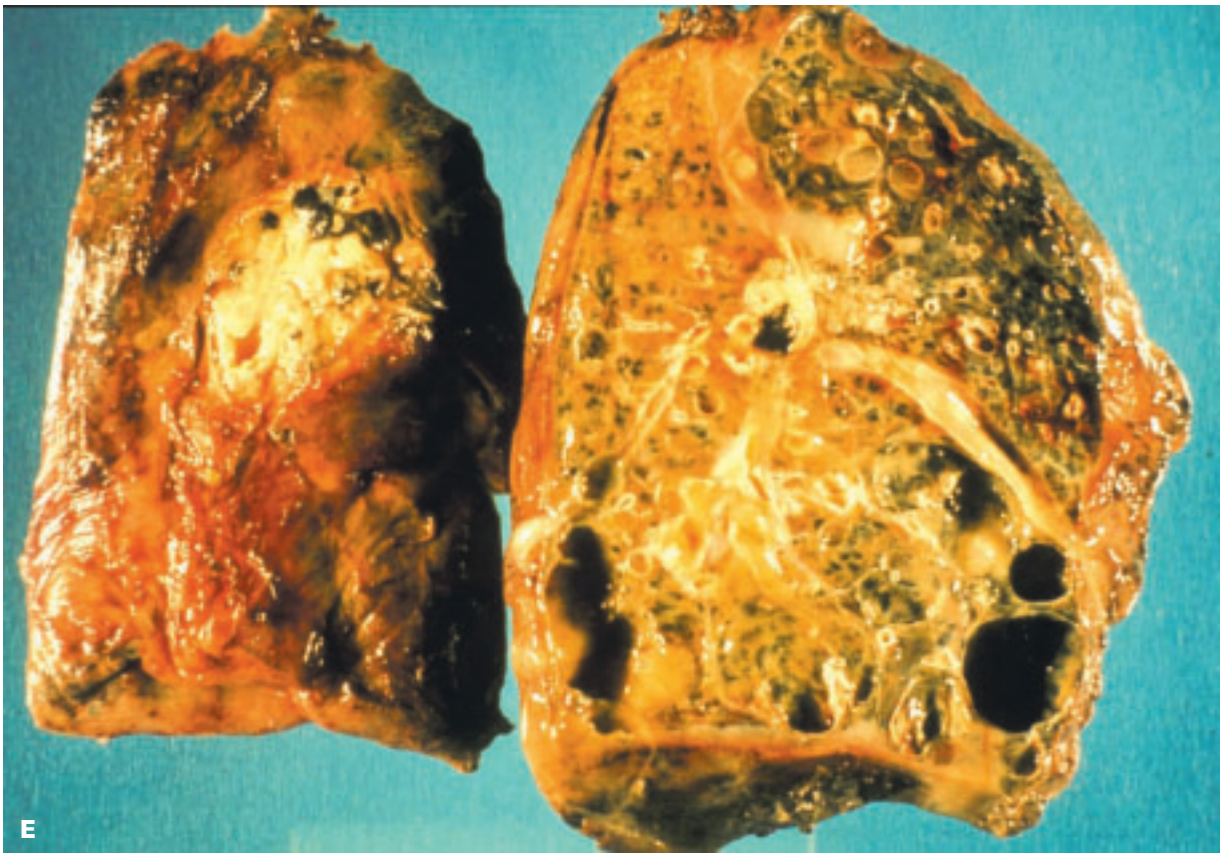

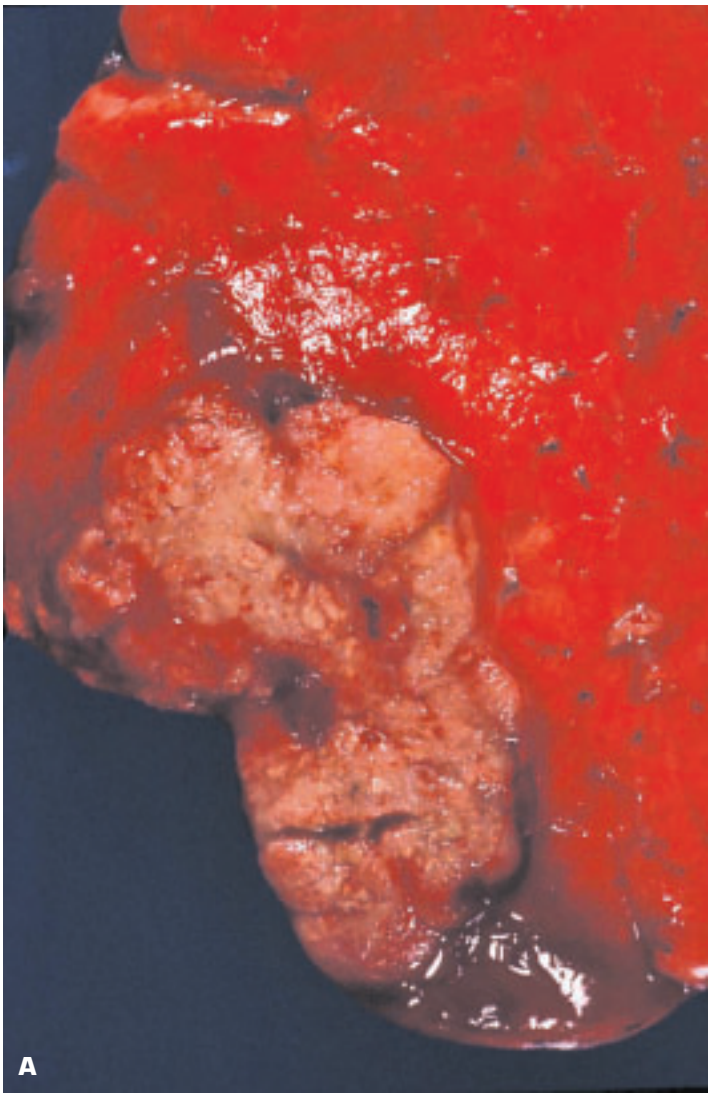

2-44. A. Peripherally situated adenocarcinoma of the lung. This tumor is less often associated with cigarette smoking than is squamous carcinoma of the lung. **B.** High-power view of a mucin-rich adenocarcinoma.

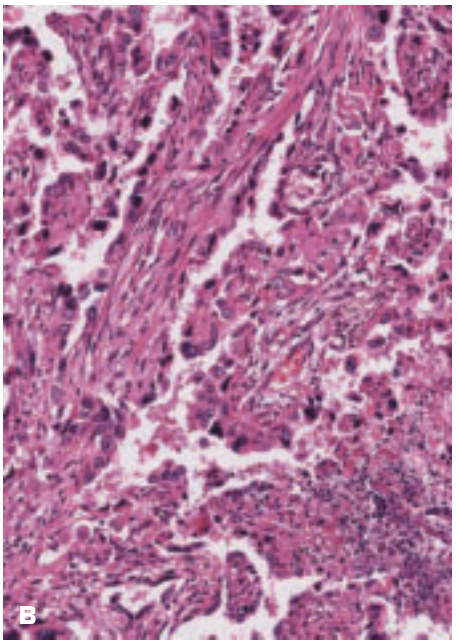

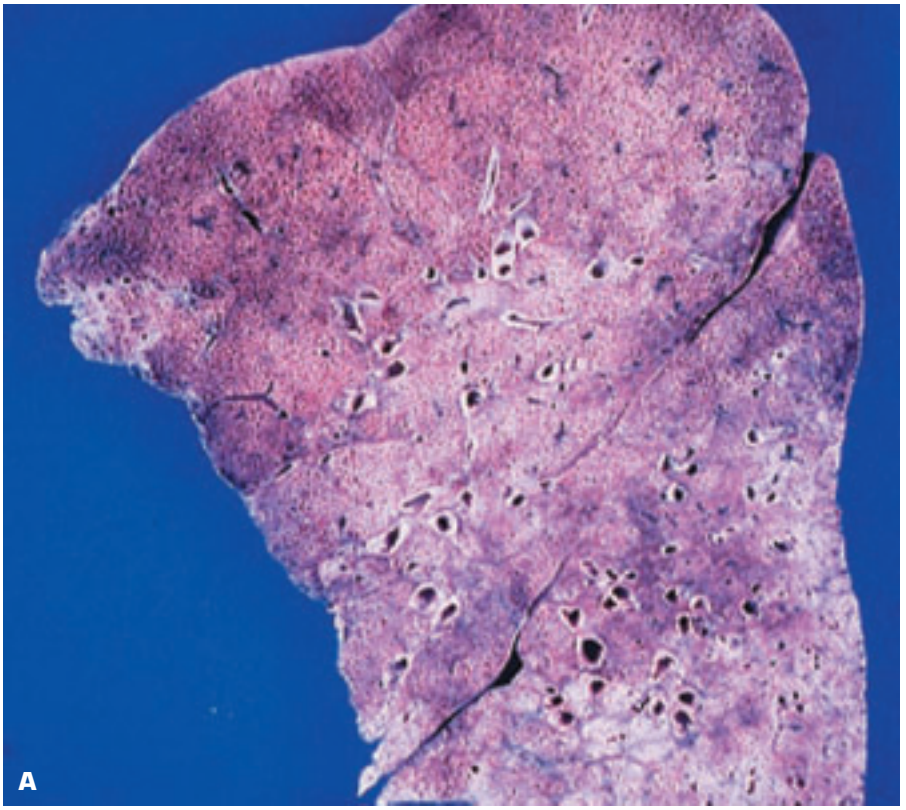

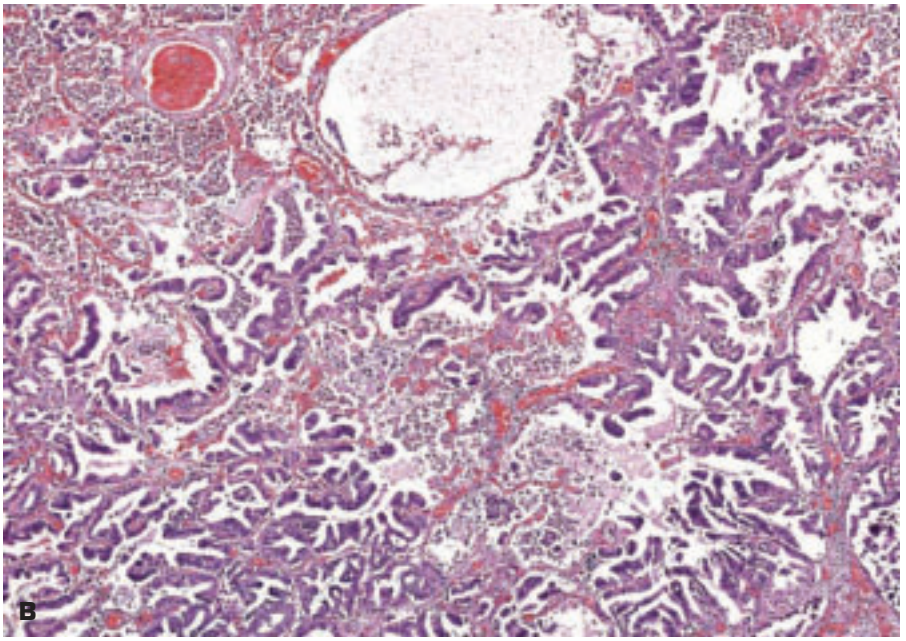

2-45. A. Bronchiolar-alveolar carcinoma of the lung macroscopically mimics a pneumonic process. **B.** Histology of bronchiolar-alveolar carcinoma shows alveoli lined by a well-differentiated adenocarcinoma that is respecting the mural structure of the alveoli.

2-46. Extensive necrotic lymphomatoid granulomatosis of the lung, now recognized as an extranodal, angiocentric B cell lymphoma with a benign, exuberant T cell response and having a predilection for the lungs. The malignant B cells often contain the Epstein-Barr virus.

2-47. A. Metastatic carcinoma of the urinary bladder in the lung lies in a subpleural position. **B.** Partially necrotic metastatic thymic carcinoma in the lung.

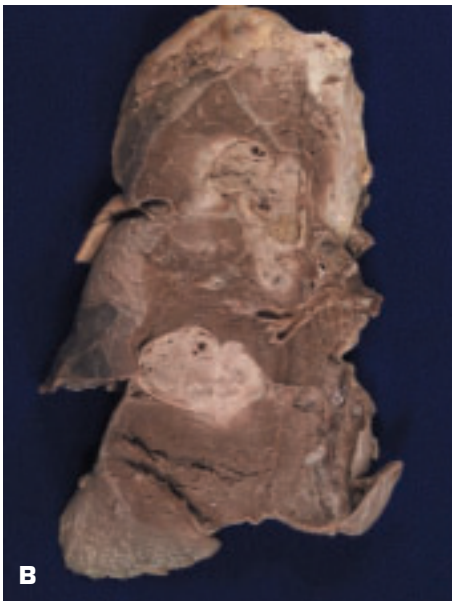

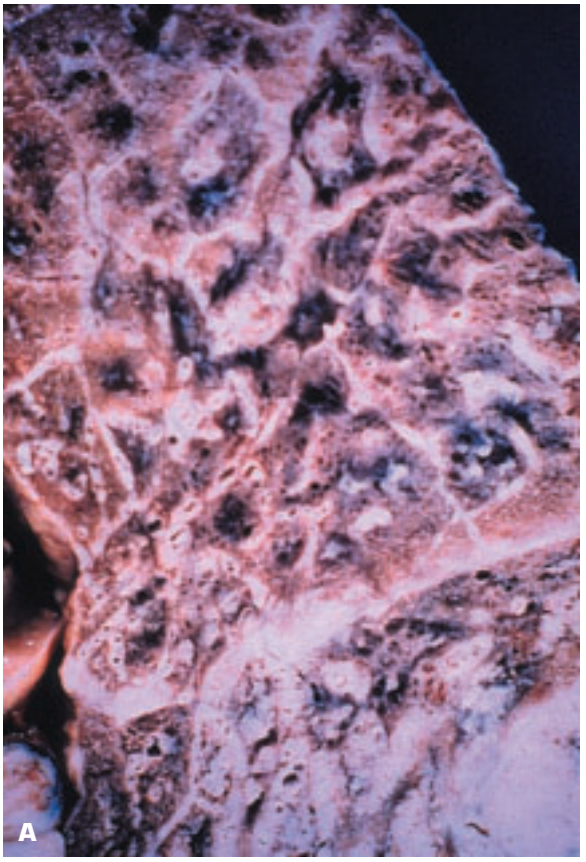

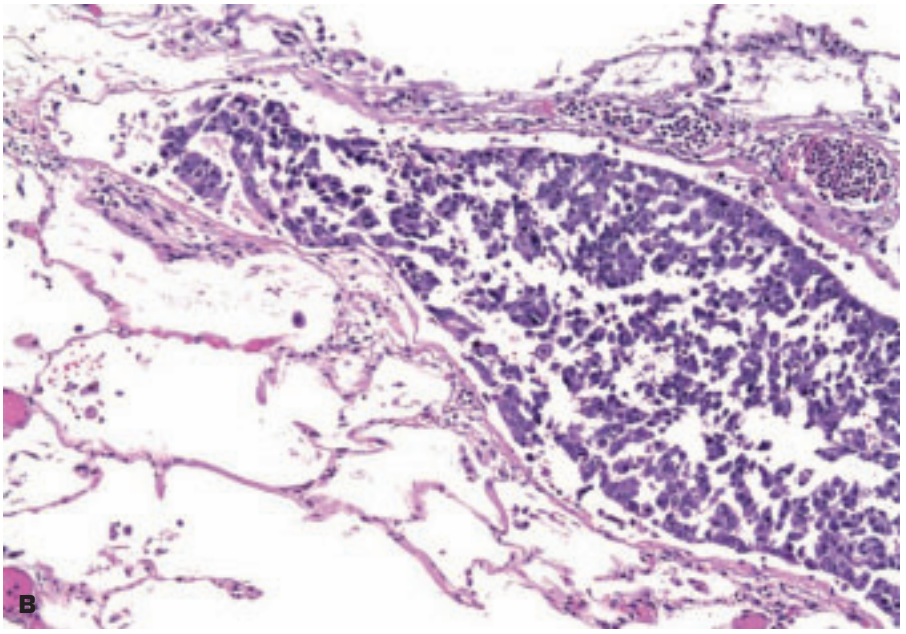

2-48. A. Diffuse lymphatic permeation of the lung by carcinoma. This may present as a 'crazy paving' pattern on chest x-ray. **B.** Interlobular septal lymphatic contains metastatic carcinoma.

2-49. A. Posttransplant lymphoproliferative disease. Note the solid white tissue in the upper lobe and scattered nodules in the lower lobe and on the pleural surface. **B.** Posttransplant B-cell lymphoma in the hilar lymph nodes.

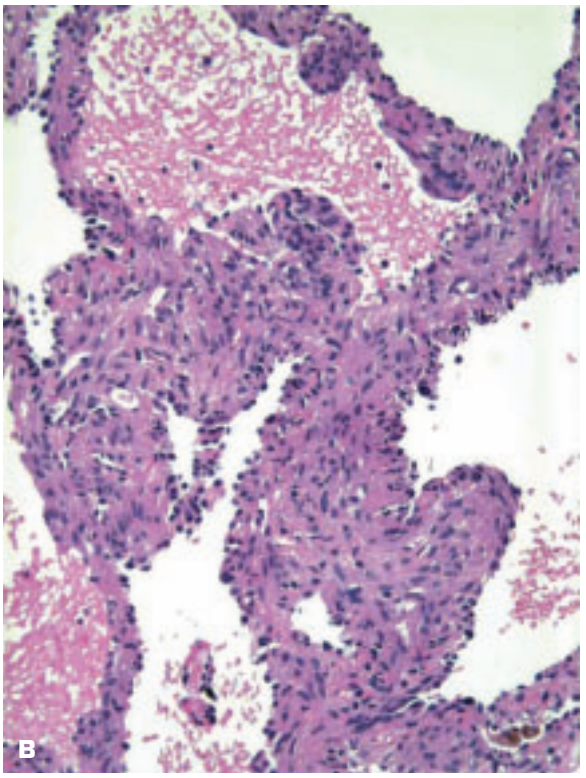

2-50. Lymphangioleiomyomatosis of the lungs. **A.** Cut surface of the lung has a reticulated, meaty appearance due to diffuse involvement by lymphangioleiomyomatosis. **B.** Histology of pulmonary lymphangioleiomyomatosis shows a marked diffuse, smooth muscle cell proliferation in the pulmonary interstitium.

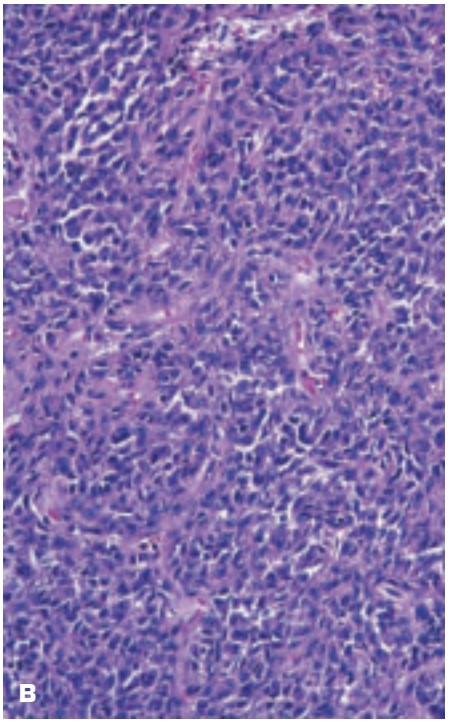

2-51. Malignant fibrous tumor of the pleura. In the past, this tumor was regarded as a form of mesothelioma, but it is now believed to arise from noncommitted mesenchymal cells situated deep to the mesothelial lining. **A.** Solid, fleshy tumor has arisen on visceral pleura and lies outside the lung, protruding into the pleural cavity. **B.** Histology shows anaplastic, spindle-shaped cells arranged in an interweaving pattern.

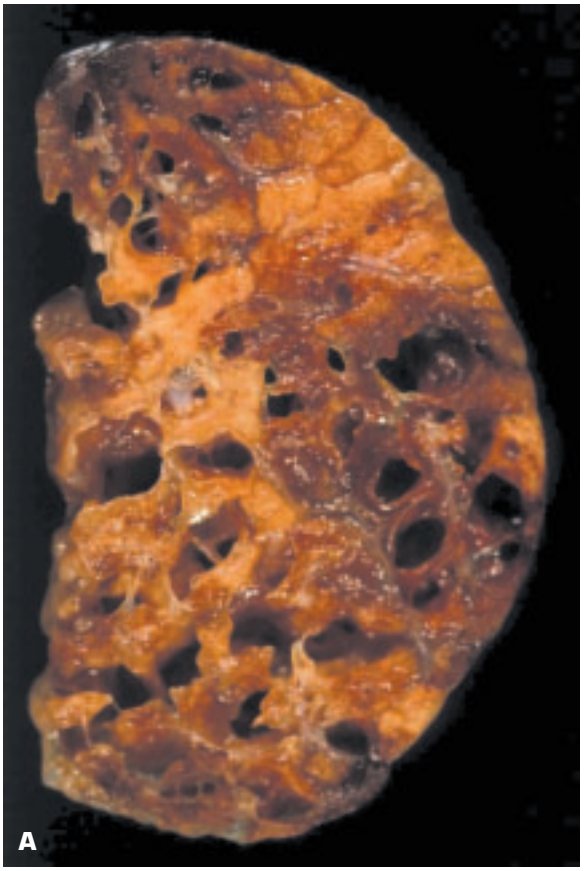

2-52. Interstitial (surgical) emphysema. **A.** Appearance of a lobe of lung affected by chronic interstitial air trapping (surgical emphysema of the lung) showing numerous rounded defects produced by air trapped within the lung interstitium. **B.** Mediastinal emphysema due to air leakage from the lung. **C.** Interstitial emphysema of the mesentery: note the numerous air bubbles present within the mesenteric tissue.

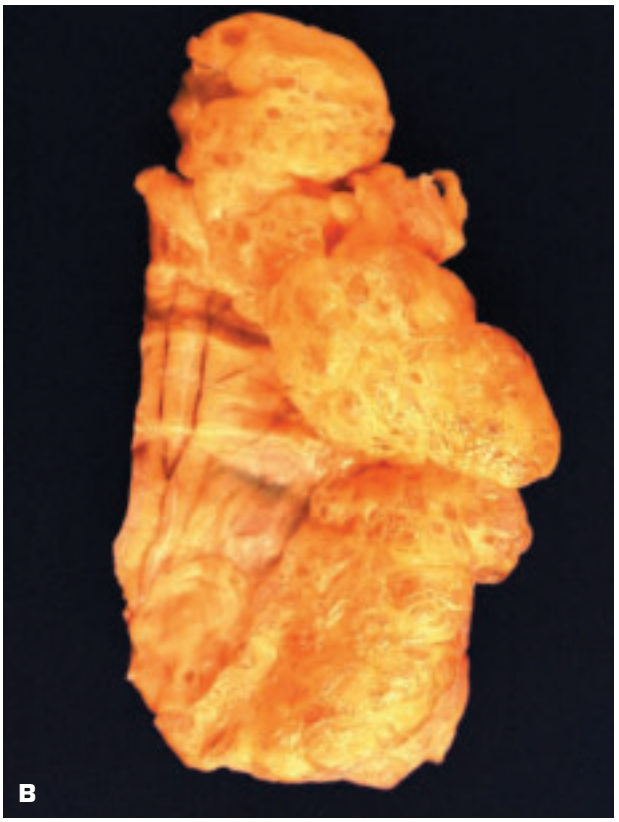

2-53. Lung transplantation. **A.** Severe acute rejection of a donor lung is characterized by a hemorrhagic, devitalized appearance to the lung tissue. **B.** Bronchial anastomosis lines in bilateral lung transplantation. *(continued on next page)*

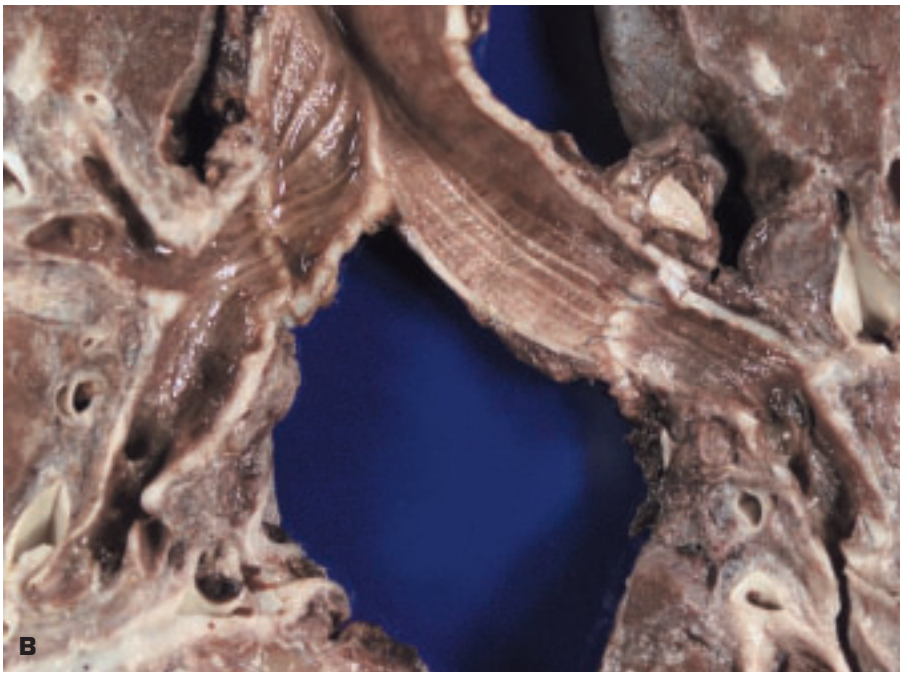

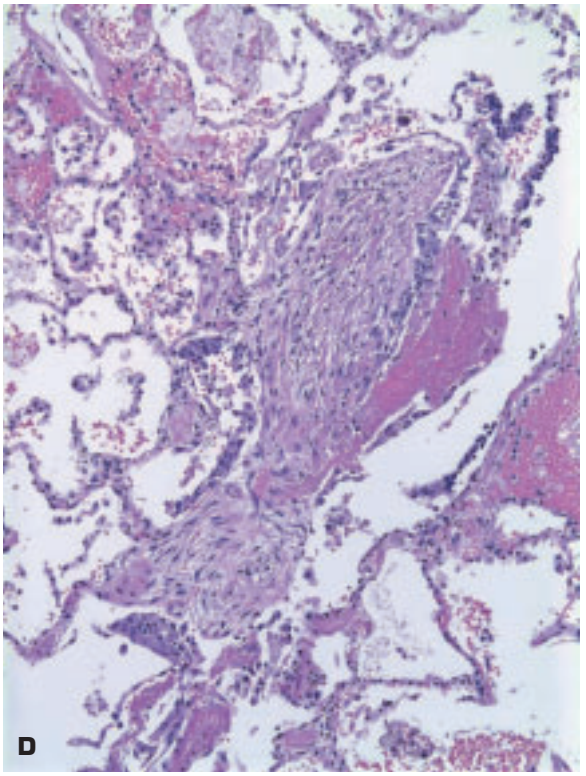

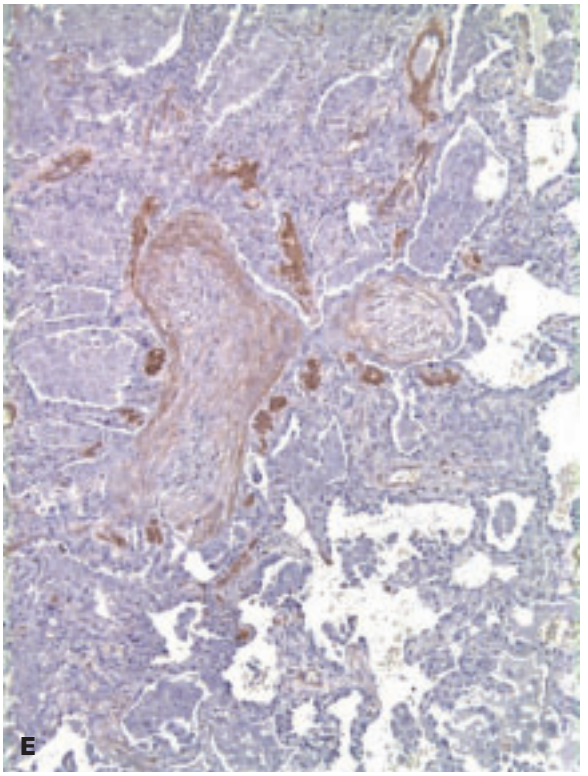

2-53. *(Continued)* **C.** Chronic rejection of a 5-year-old bilateral lung transplant. **D.** Bronchiolitis obliterans in a lung transplant. Loss of small airways may also occur in chronic rejection. **E.** Smooth muscle actin immunostaining serves to delineate small bronchioles filled by loose fibrous tissue in bronchiolitis obliterans.

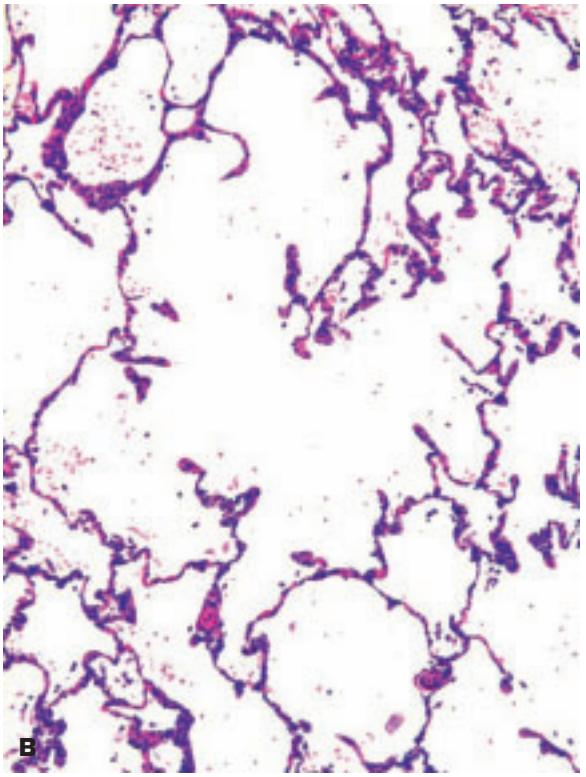

2-54. A. Macroscopic appearance of congenital lobar emphysema is characterized by overdistention of the affected lobe. The condition is a potentially reversible life-threatening cause of neonatal respiratory distress. Absent bronchial cartilage may lead to bronchial collapse during expiration, leading to air trapping. **B.** Overdistention of alveoli, as seen in this picture, may be associated with either hypoalveolar or polyalveolar counts.

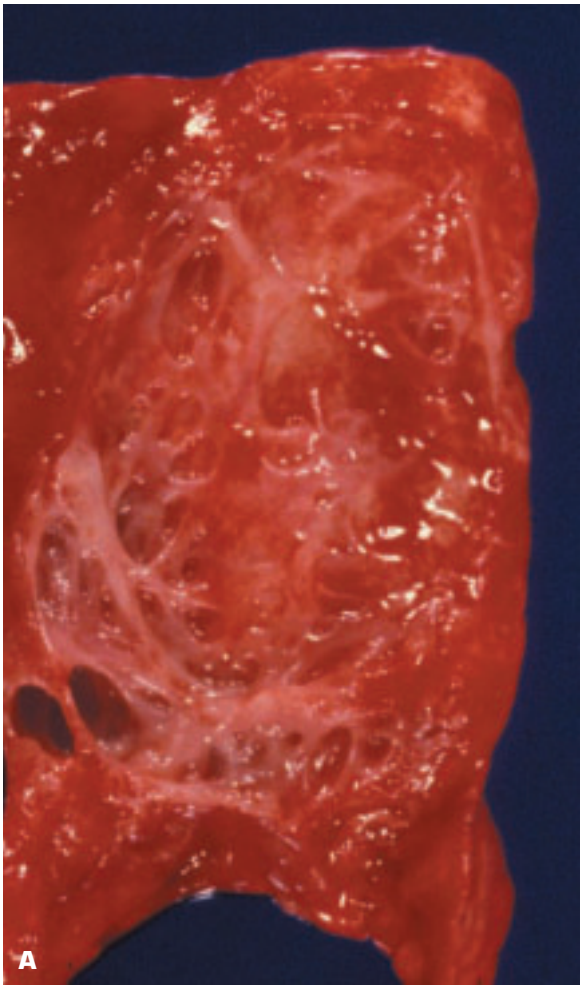

2-55. Congenital cystic adenomatoid malformation (CAM) is a hamartomatous malformation of the lung that comprises about 25% of all congenital lung lesions. CAM communicates with the tracheobronchial tree and the pulmonary arterial and venous circulations. **A.** Bisected CAM surgically resected from a young child shows multiloculated larger cysts and smaller cysts of varying size within the lesion. **B.** Histology shows an adenomatoid proliferation of structures and cysts resembling bronchioles.

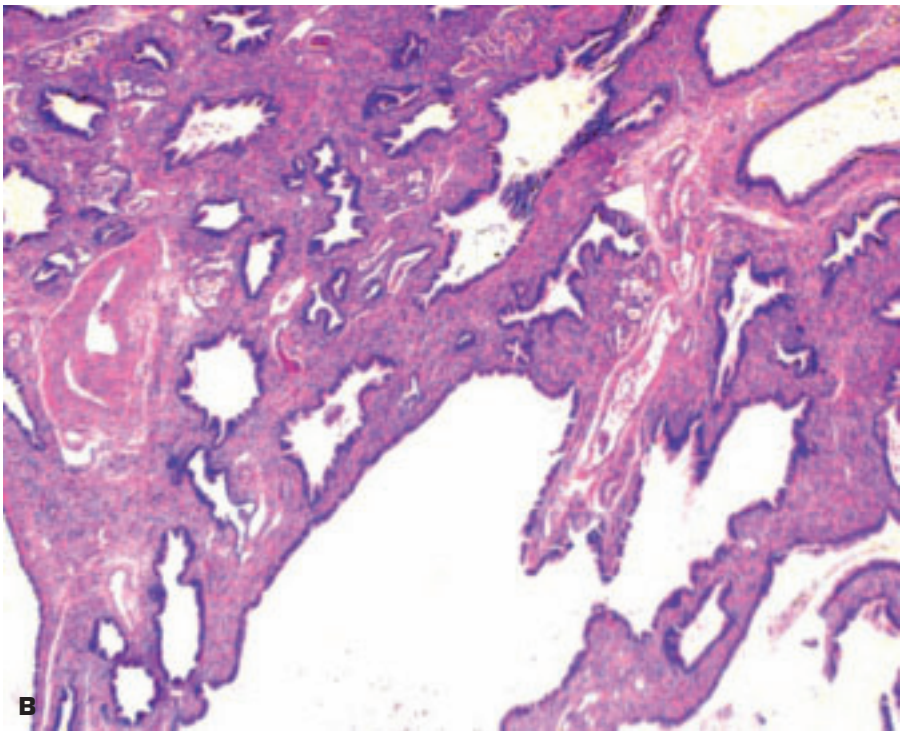

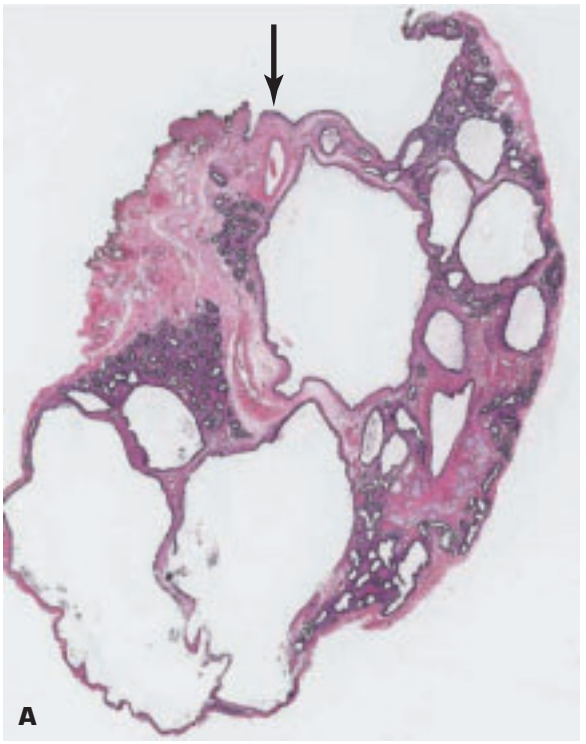

2-56. Pulmonary sequestration. **A.** Note the supplying systemic artery (*arrow*) in the center top of the section. **B.** Higher-power view showing cysts and dilating spaces lined by bronchial epithelium. Unlike cystic adenomatoid malformation, pulmonary sequestration has no bronchial communication and is supplied by anomalous systemic arteries.

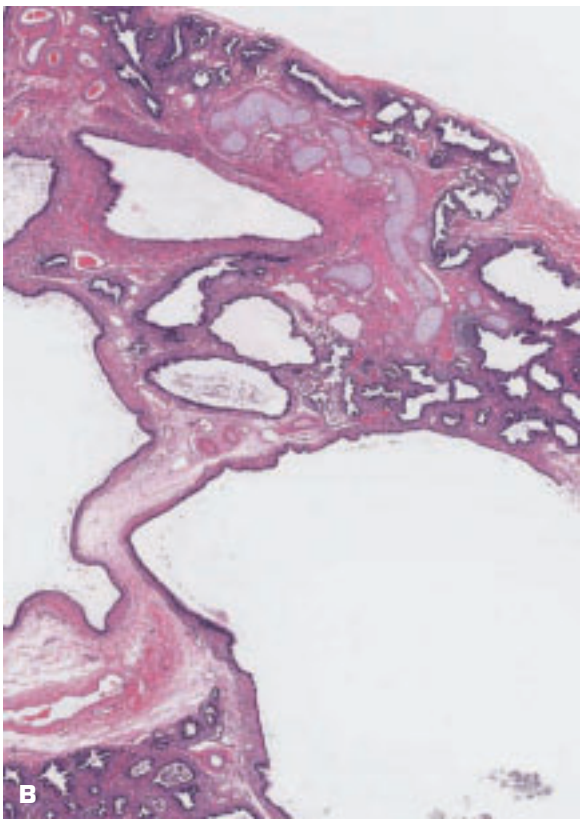

2-57. Solitary bronchogenic cyst was an incidental finding in this lung.

2-58. Bochdalek hernia (*arrow*) behind left hemidiaphragm allowed stomach, small gut, spleen, and portion of large gut to enter the left chest and to compress the left lung (*top right*), which is much smaller than the right lung.

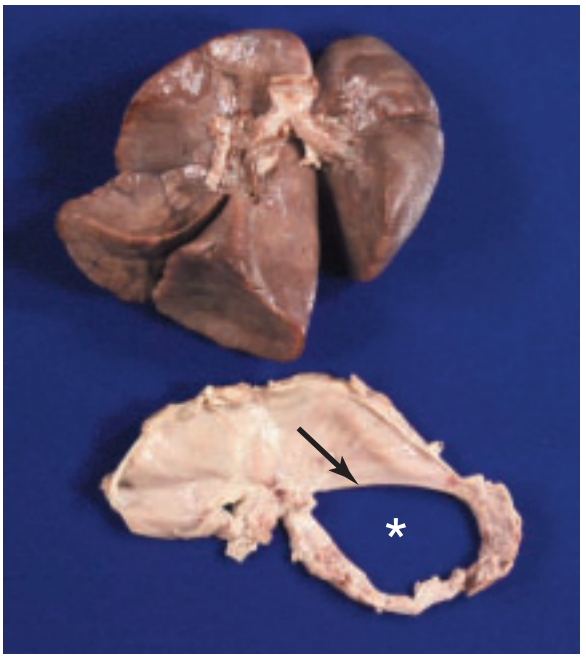

2-59. Bronchomalacia of right lung has led to atelectasis and focal areas of consolidation due to repeated lung infections.

3 Kidneys, Ureters, and Urinary Bladder

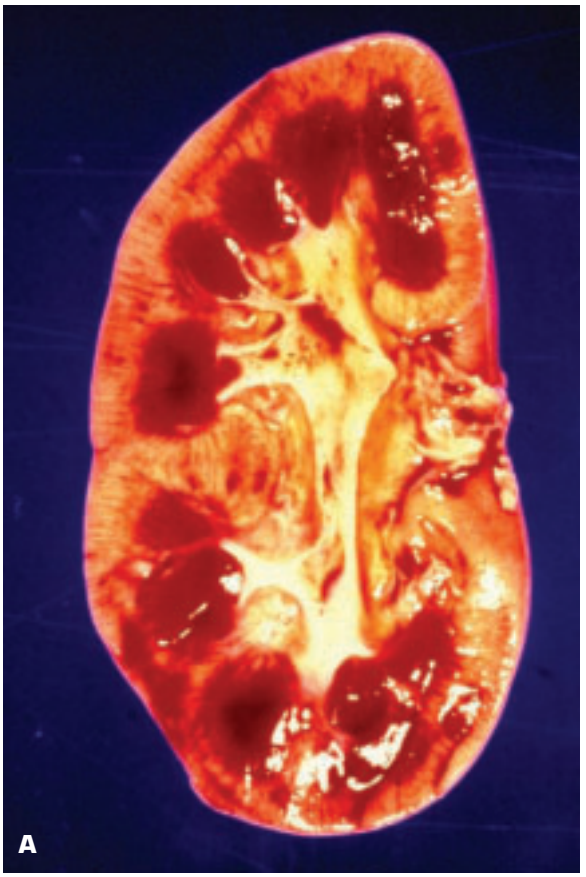

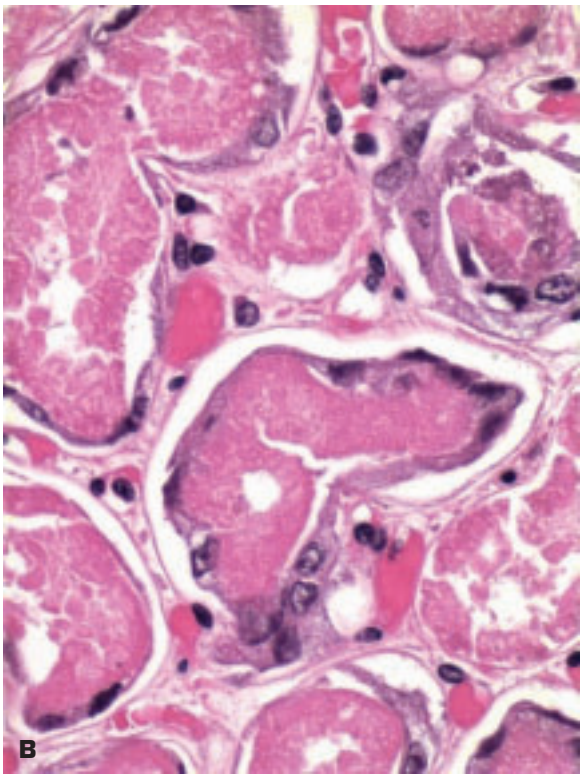

3-1. A. Kidney in acute tubular necrosis (ATN) showing pale, swollen cortex and congested medulla. **B.** Elongated, stretched out, regenerating proximal tubular lining cells encompass the necrotic epithelium. If no regeneration is seen, then appearances are difficult to distinguish from postmortem autolysis. ATN may result from ischemia, nephrotoxins, or circulating heme proteins.

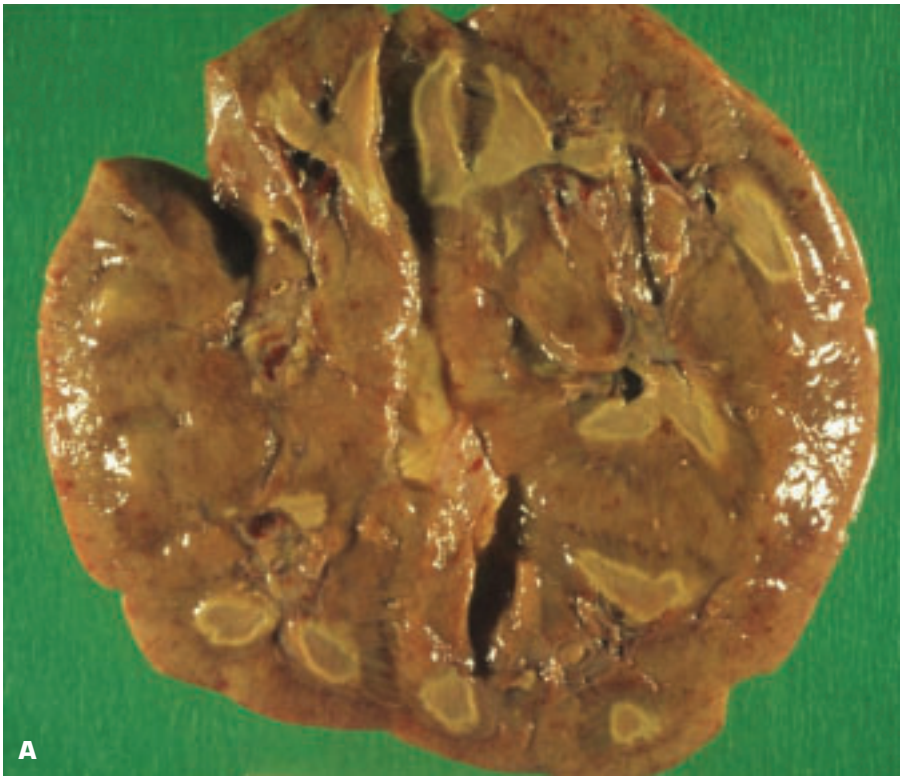

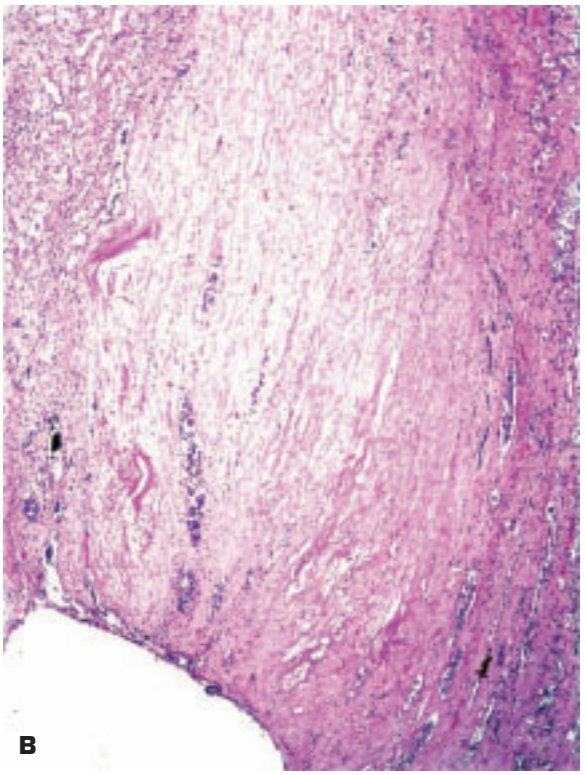

3-2. A. Papillary necrosis (PN) associated with diabetes mellitus (DM) is seen in this bisected kidney. The repetitive distribution of the necrosis limited to the renal papillae is the key diagnostic feature of PN. PN may occur with DM (often with pyelonephritis), drugs (aspirin and phenacetin), hydronephrosis, and sickle cell disease. In drug-induced PN, the papillae may show necrosis of varying ages, unlike PN associated with DM, in which the necrosis is all of the same duration. PN in sickle cell disease may not affect all papillae. **B.** Histology of PN. Note the pale-colored necrotic papilla that is already showing some blunting of its free surface. The necrotic area may ultimately slough off and be excreted in the urine.

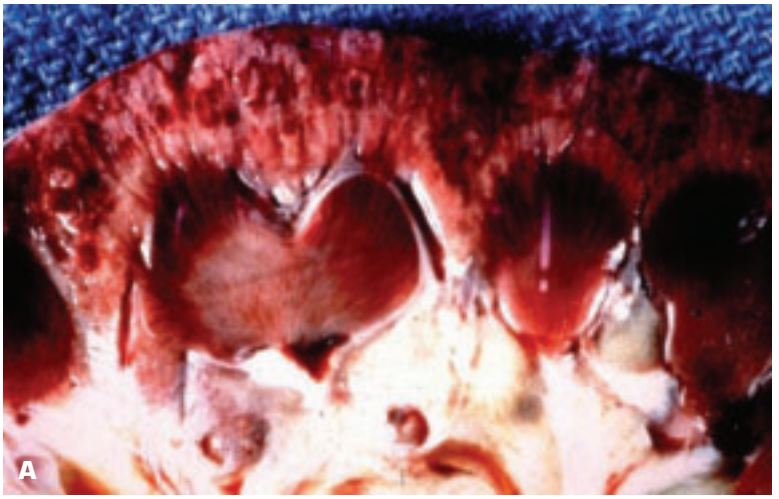

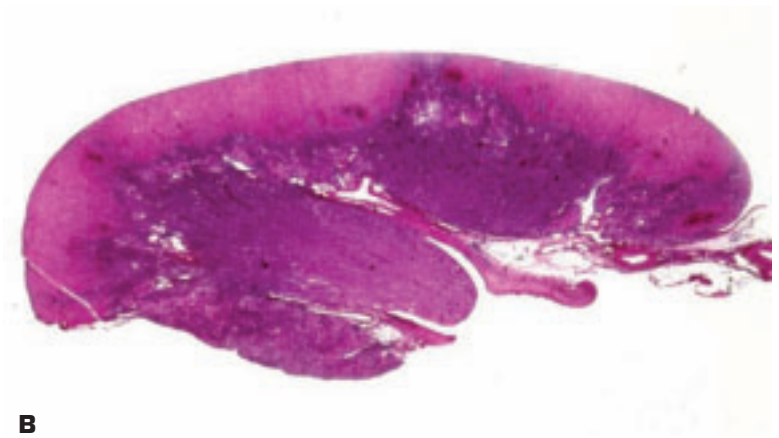

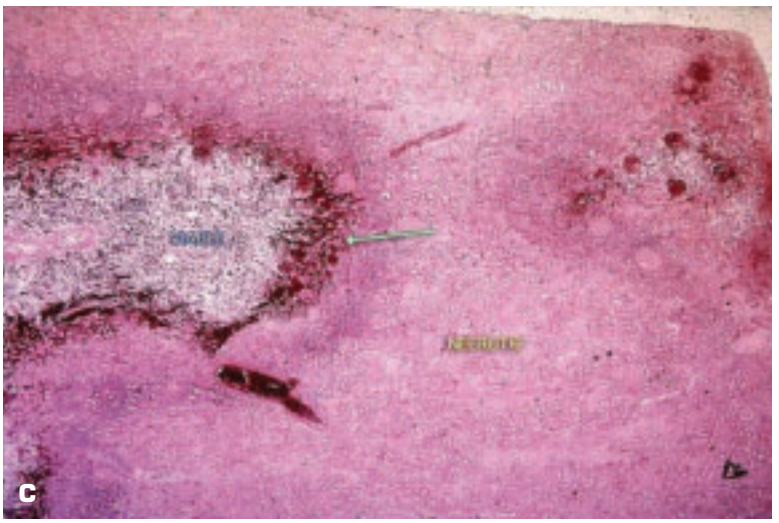

3-3. A. Diffuse cortical necrosis of the kidney resulting from profound hypotension. The hallmark feature is necrosis limited to the renal cortex. **B.** Histology shows poor staining of the necrotic cortical zone. **C.** Higher power shows a few tubules and glomeruli surviving in a perivascular distribution (*arrow*), while the rest of the cortex is diffusely necrotic.

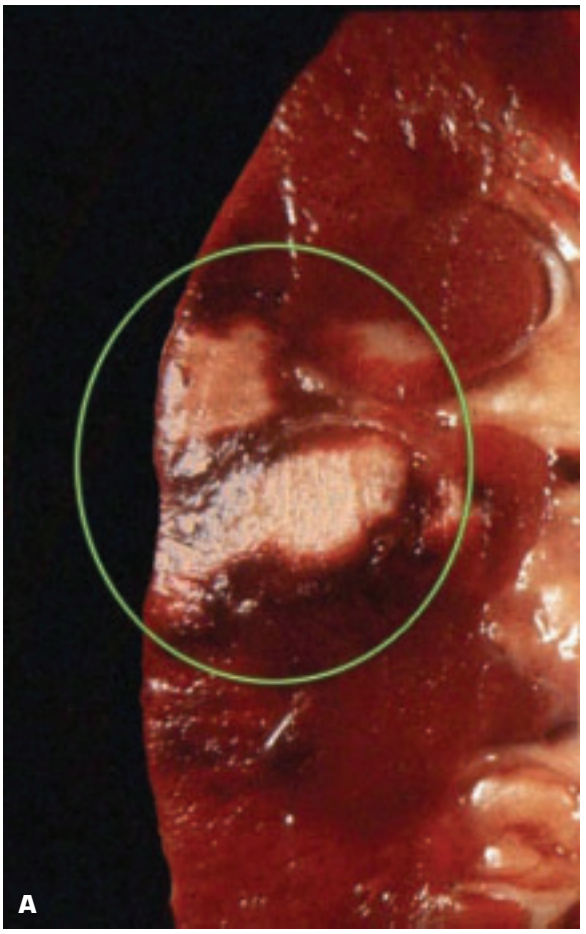

3-4. A. Pale, decolorized renal infarcts (*circled*) affecting cortex and medulla. Renal infarcts are pale because there is no open interstitium for blood to percolate into (unlike the lung). **B.** Histologic junction of infarct (*top*) and surviving renal tissue (*arrows*); note the subcapsular survival of scanty renal tissue on the surface of the kidney (*left*).

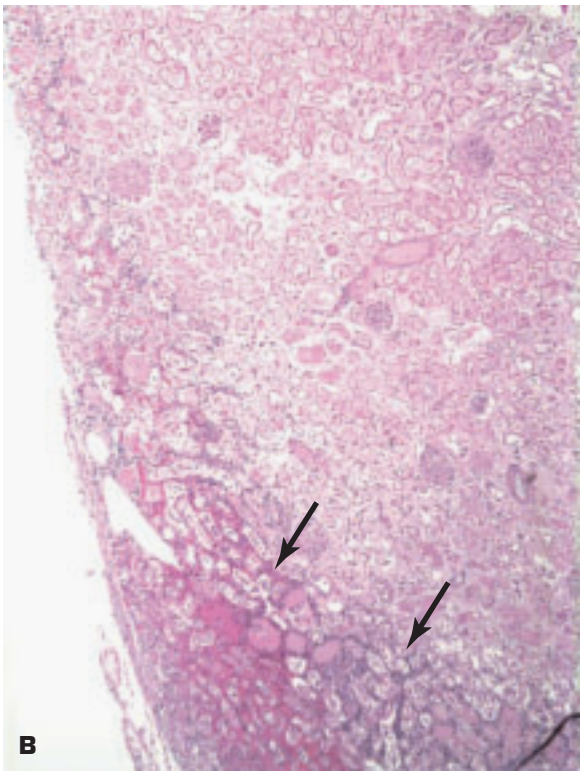

3-5. A. Healed renal infarct at upper pole of kidney (*circled*). **B.** Histologic appearance of a healed infarct. Note the V-shaped profile of the healed infarct compared to the U-shaped scar profile of healed pyelonephritis.

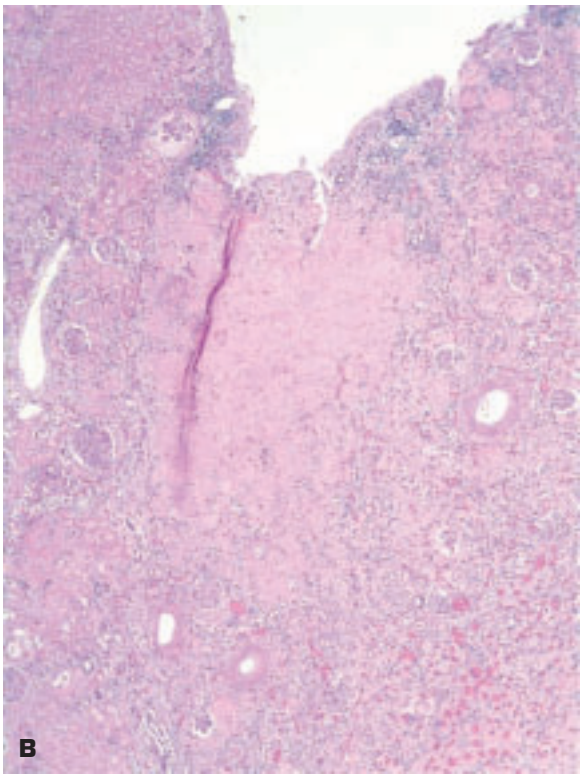

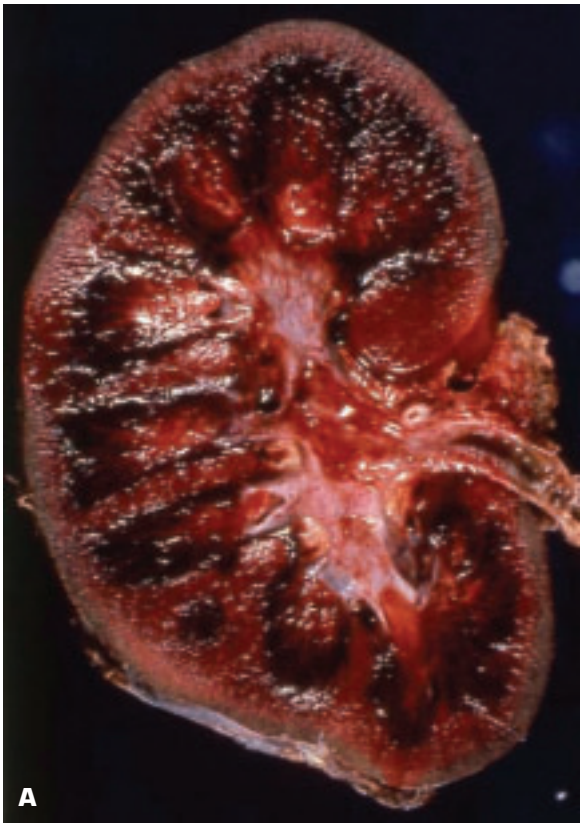

3-6. A. Renal vein thrombosis has produced hemorrhagic infarction of the entire kidney. **B.** Histology confirms renal infarction with massive interstitial hemorrhage consistent with circulatory arrest secondary to cessation of venous outflow from the kidney.

3-7. Triple renal arteries (a variation of normal anatomy) supply this kidney.

3-8. The kidney on the left has suffered from (atherosclerotic) renal artery stenosis ("Goldblatt kidney") and has undergone atrophy with symmetric reduction in size. This ischemic kidney caused systemic hypertension via increased production of renin, angiotensin II, and aldosterone, resulting in accelerated nephrosclerosis of the opposite kidney (on the right of the picture). The narrowed renal artery supplying the ischemic kidney protected it from hypertension; hence, the nonscarred renal surface observed in the atrophied kidney.

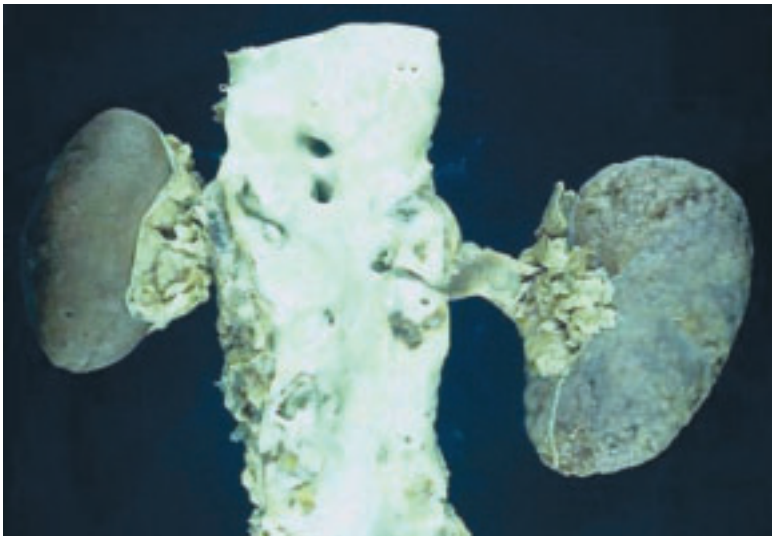

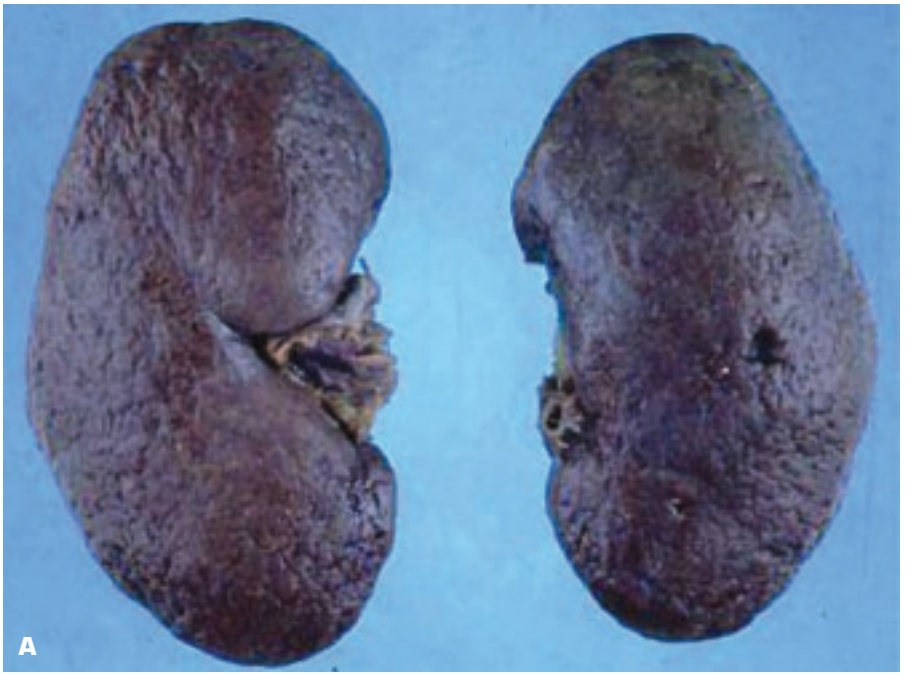

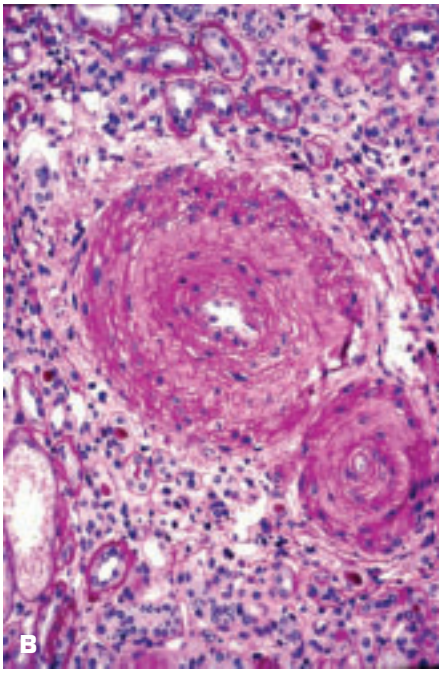

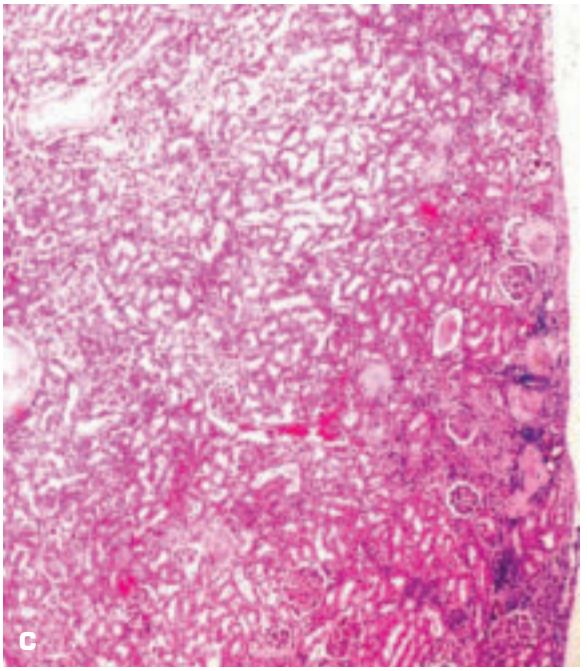

3-9. A. Fine surface granularity of benign nephrosclerosis due to aging or lower-level systemic hypertension tends to be more coarse than that seen in chronic glomerulonephritis. **B.** Small intrarenal arteries show intimal fibroplasia plus replication of the elastic laminae and hyalinization of the media. **C.** Wedge-shaped area of slowly developed ischemic atrophy due to the vascular narrowing.

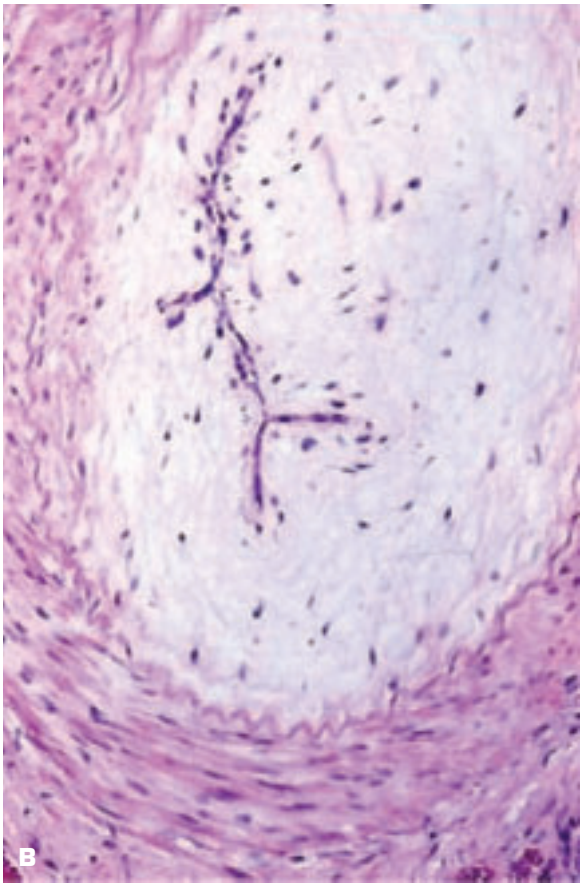

3-10. Malignant hypertension. **A.** Macroscopic appearance of the kidneys in new-onset malignant hypertension is characterized by normal-size kidneys showing focal small hemorrhages on the capsular surfaces. **B.** Myxoid edema of intima in small intrarenal artery is leading to further renal ischemia and aggravation of the hypertension. *(continued on next page)*

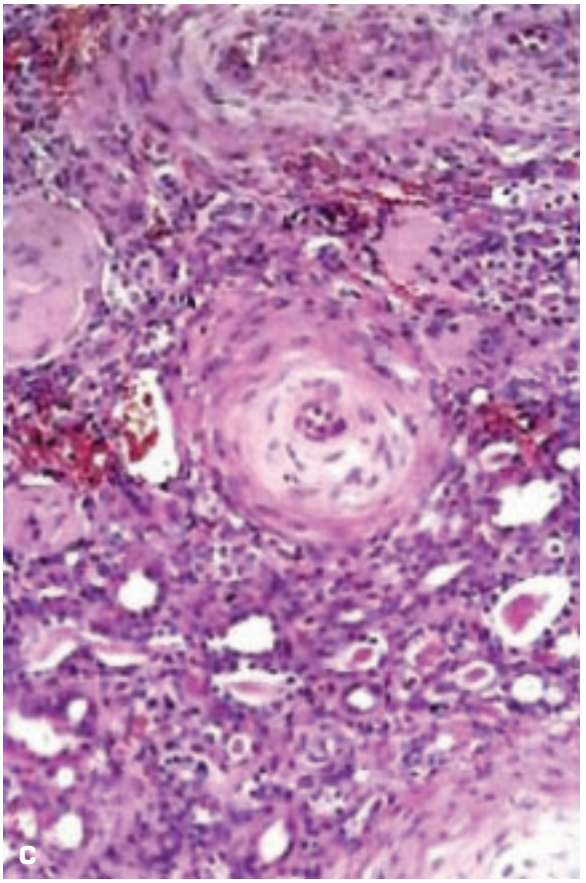

3-10. *(Continued)* **C.** Concentric intimal onion peel-like layering of intimal fibrosis in a small intrarenal artery. **D.** Fibrinoid necrosis of renal arterioles and hemorrhage within a glomerulus.

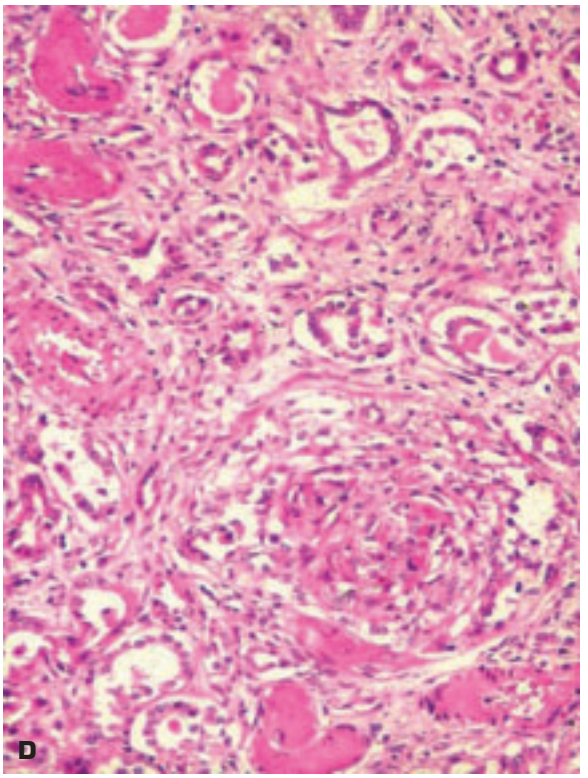

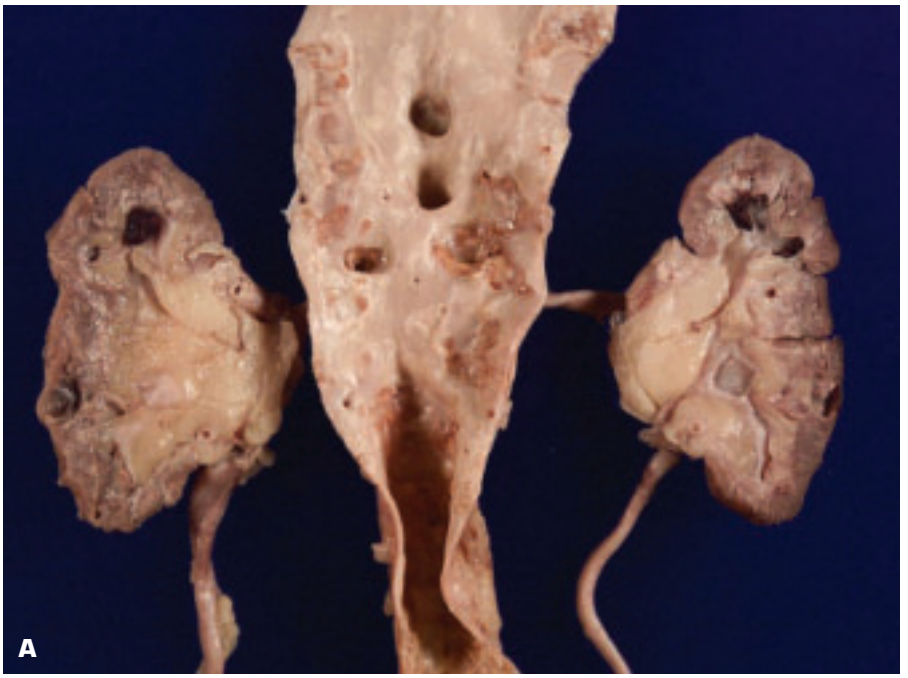

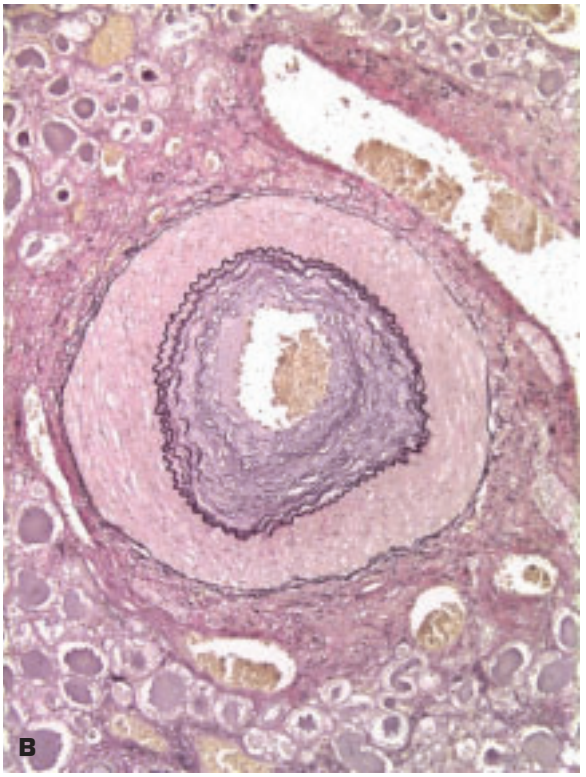

3-11. A. Nonsteroidal antiinflammatory drug nephropathy. Both kidneys show cortical atrophy and loss of several renal papillae due to prior papillary necrosis, while other papillae show residual evidence of necrosis. Expansion of the peripelvic fat compensates for the parenchymal atrophy. **B.** Loss of renal parenchyma is associated with endarteritic thickening of small renal arteries.

3-12. Tubulointerstitial nephritis. **A.** The fibrotic nature of the renal interstitium is easily discerned in this gross photo; fibrous tissue appears gray-white in the picture. **B.** Histologic section: trichrome stains collagen blue between atrophic tubules.

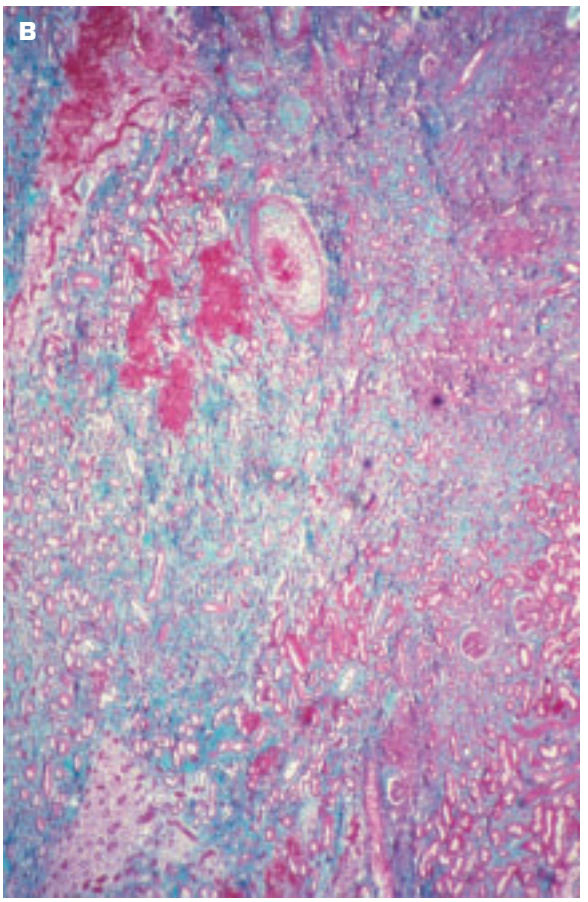

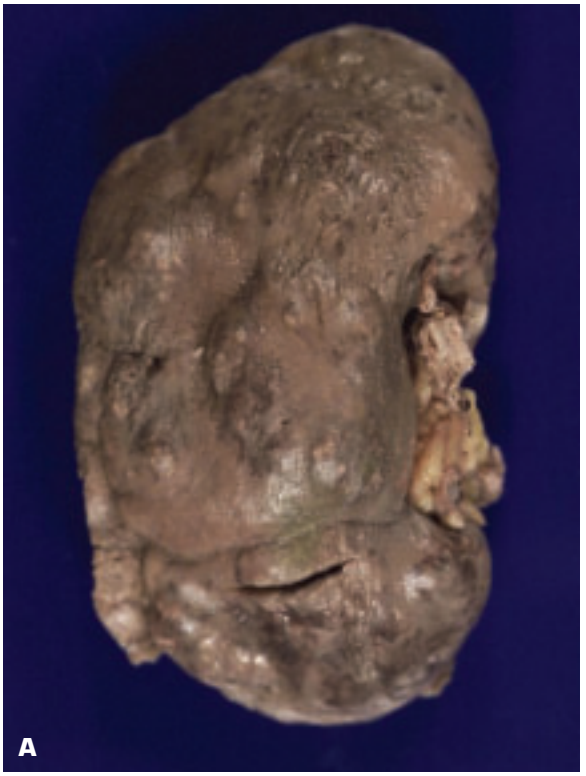

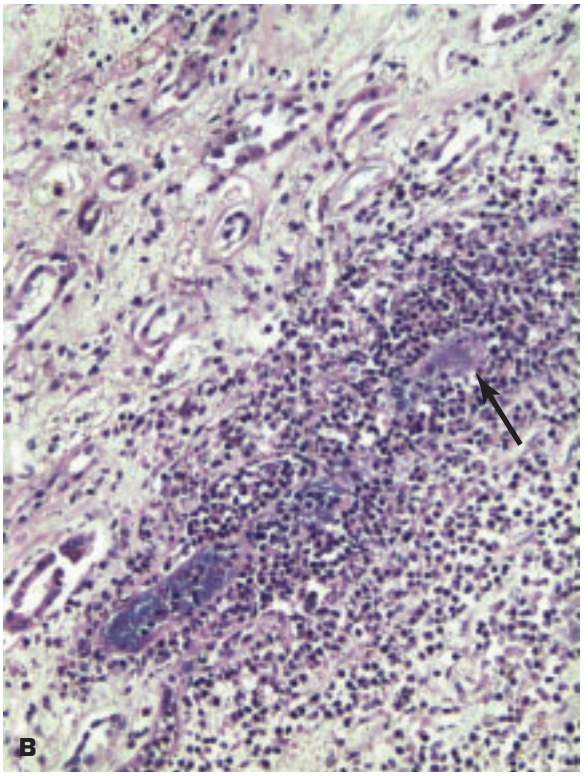

3-13. Acute pyelonephritis may occur via hematogenous spread of infection to the kidney or by ascending infection via cystitis with vesicoureteral reflux or due to hydronephrosis (e.g., due to a renal stone). **A.** Acute on chronic pyelonephritis with numerous septic foci present in an already scarred kidney. **B.** Acute pyelonephritis with coccal organisms (*arrow*) and neutrophils. **C.** Acute pyelonephritis is present (*top left*) with incipient subcapsular abscess formation. *(continued on next page)*

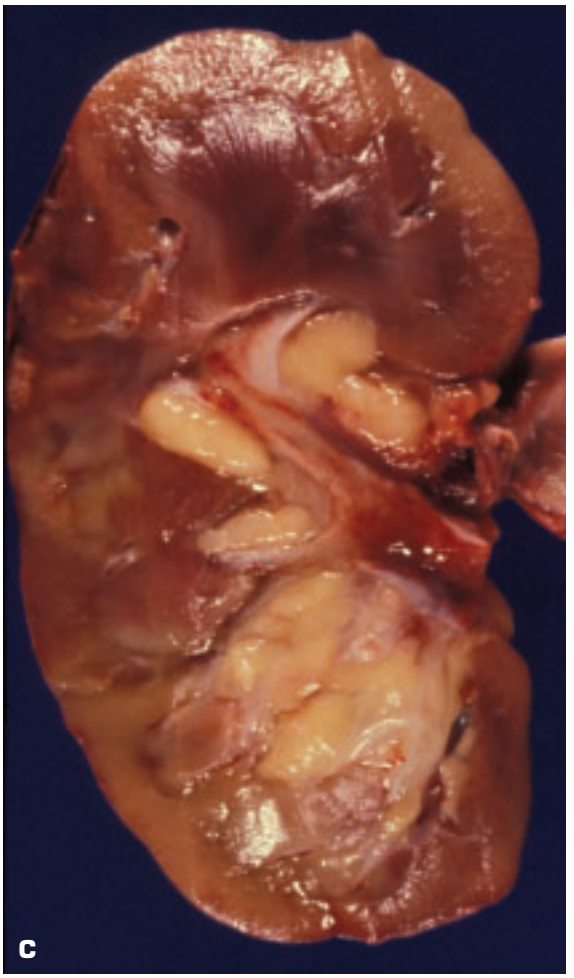

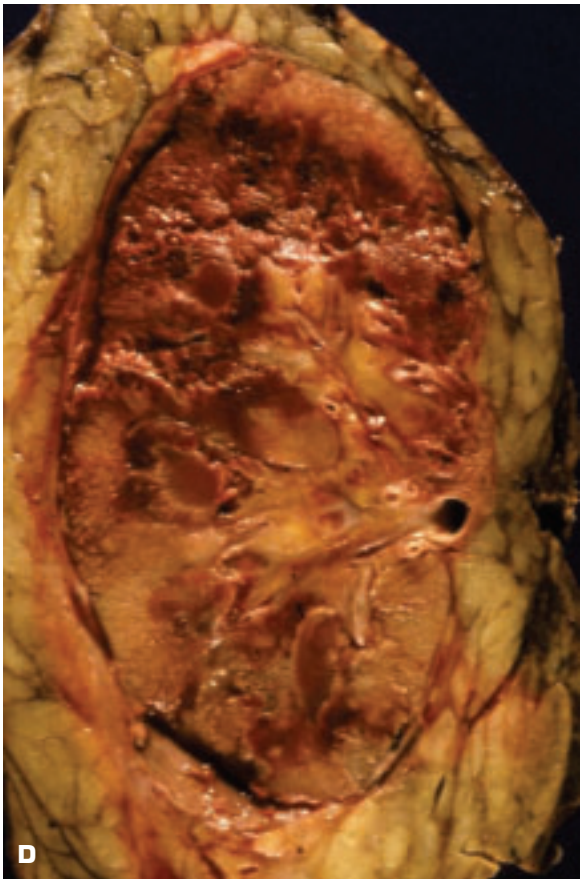

3-13. *(Continued)* **D.** Very severe acute ("emphysematous") pyelonephritis with spaces in the infected renal parenchyma due to the action of gas-producing microorganisms. Papillary necrosis is also noted. **E.** Xanthogranulomatous pyelonephritis: the yellowish areas contain foamy macrophages in addition to the usual inflammatory cells. The patient had moderate hydronephrosis that was complicated by a *Proteus* infection.

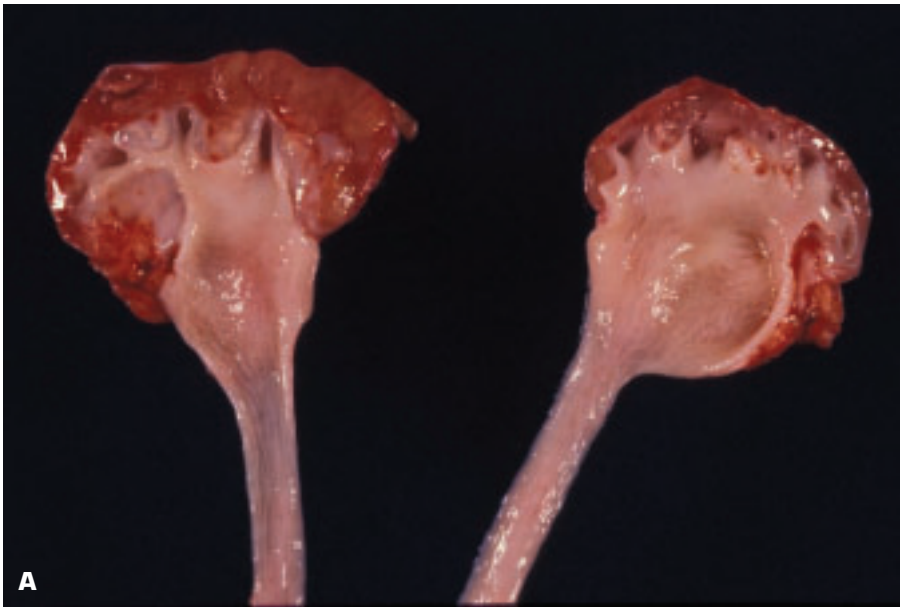

3-14. Obstructive uropathy results from structural or functional abnormalities of the urinary tract that impede urine flow, which may cause renal dysfunction (obstructive nephropathy) and dilatation of the collecting system (hydronephrosis). **A.** Bilateral hydronephrosis with acute on chronic pyelonephritis in a child due to urinary tract obstruction. Note the dilated ureters and renal pelves. **B.** Hydronephrosis with thinned renal parenchyma in an adult kidney.

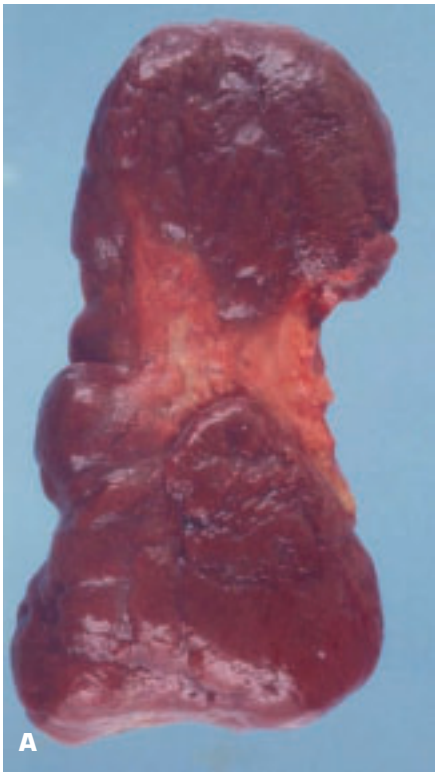

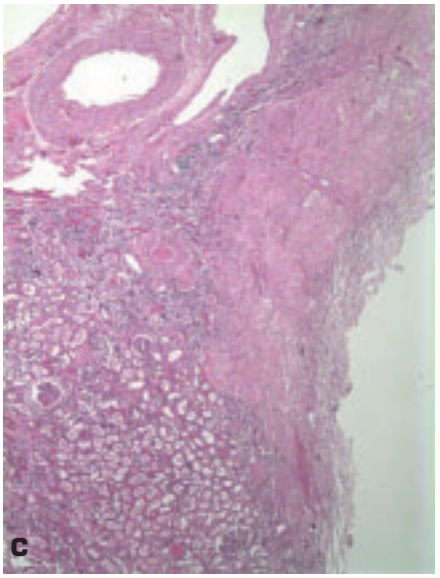

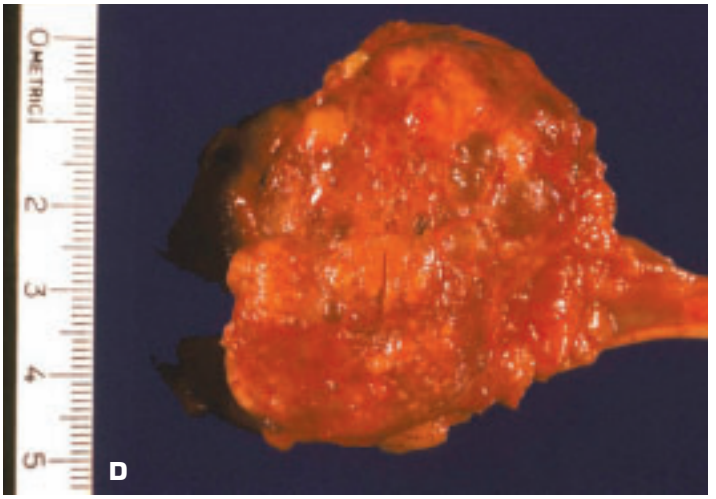

3-15. Healed pyelonephritis is characterized by parenchymal scarring plus distortion of the calyceal system. **A.** Broad U-shaped scar of healed pyelonephritis. **B.** Healed pyelonephritis associated with vesicoureteral reflux has produced scarring of both poles of the kidney with calyceal distortion due to infection of the peripheral compound papillae. (Obstruction produces infection of the papillae.) **C.** Histology of healed pyelonephritis scar shown in A shows the fibrosis extends from the capsule to the calyx. **D.** End-stage chronic pyelonephritis with shrunken scarred kidney exhibiting multiple, small acquired cysts.

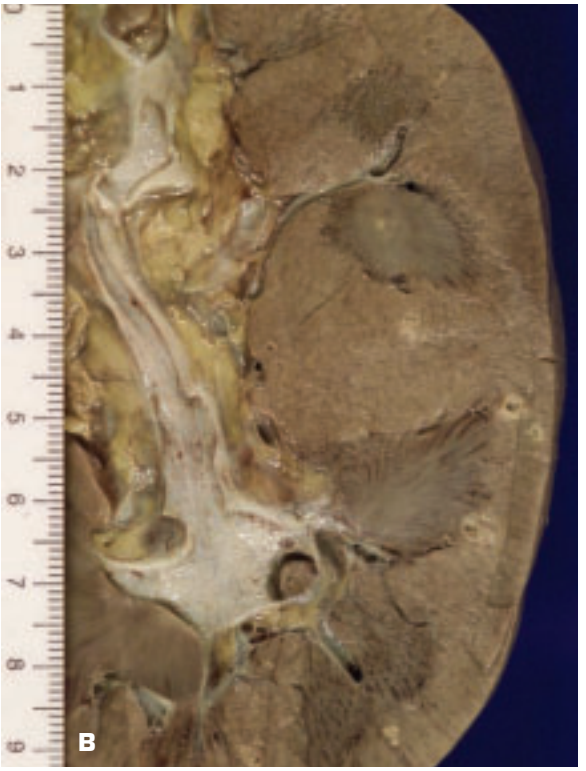

3-16. Hematogenous disseminated *Candida albicans* infection. **A.** Renal surface is studded with multiple small fungal abscesses. **B.** Cut surface shows cavitation of some of the lesions due to loss of the contents of the abscess. **C.** Histology shows *Candida* pseudohyphae (*top*) in an area of tissue destruction and inflammation.

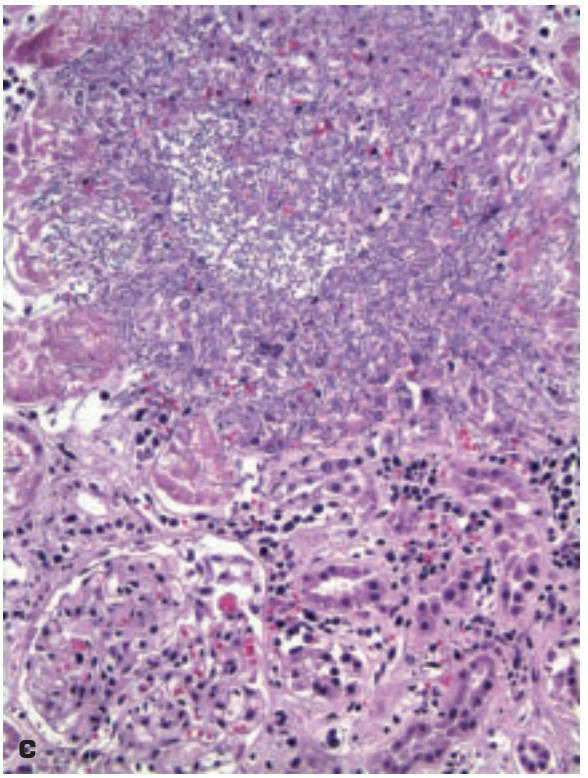

3-17. Renal tuberculosis secondary to hematogenous spread of tubercle bacilli. The renal pelvis, the calyces and the ureters are lined by shaggy, caseous-looking material. From the kidney, the infection may spread down the ureters and reach the bladder, the male sexual glands, and the epididymis.

3-18. Bilateral partial double ureters. No renal pathology is present.

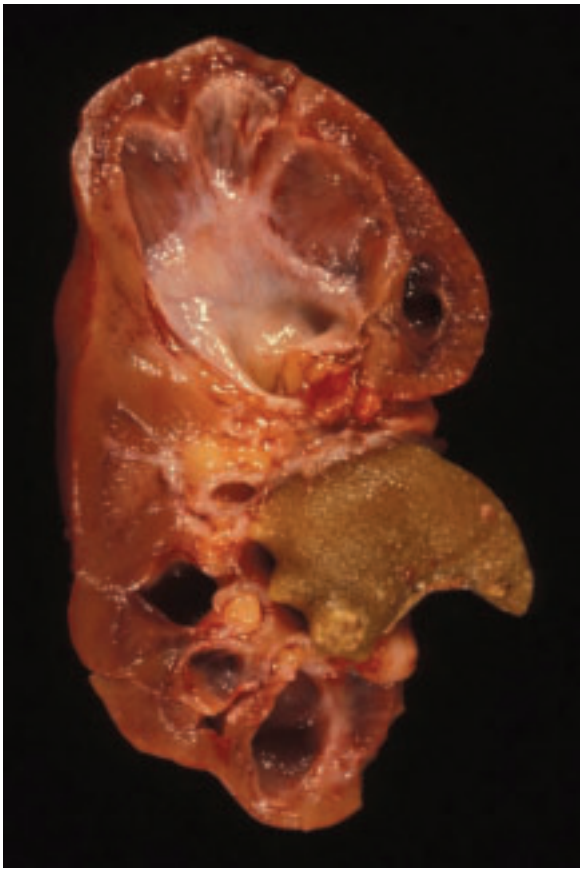

3-19. Staghorn calculus in pelviureteric junction. Kidney shows dilated, distorted calyces and areas of healed pyelonephritis.

3-20. Bilateral catheters ("stents") pass from bladder to both renal pelves to relieve bilateral ureteral stenosis.

3-21. Kidney of a young child with acute proliferative glomerulonephritis appears slightly mottled. The gross appearance cannot be used to make the diagnosis of glomerulonephritis; renal histology is used for this purpose.

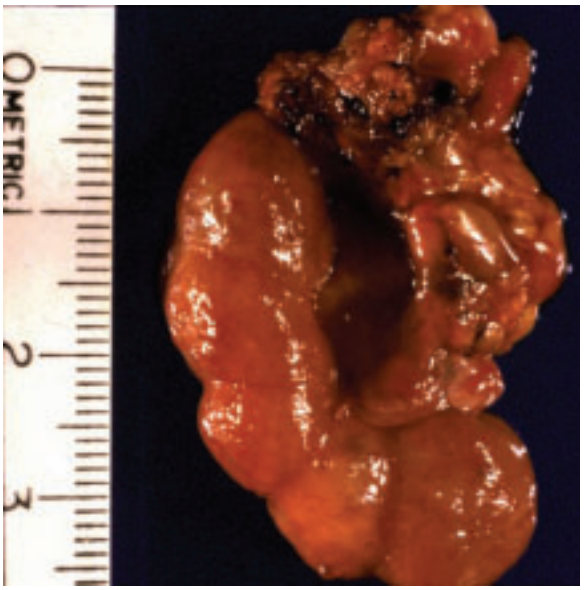

3-22. A. Hemorrhagic biopsy site in a kidney with membranoproliferative glomerulonephritis (GN). Patient died of shock from massive hemorrhage from the biopsy site. **B.** Poststreptococcal proliferative GN. **C.** Rapidly progressive GN with crescent formation within Bowman's capsule. *(continued on next page)*

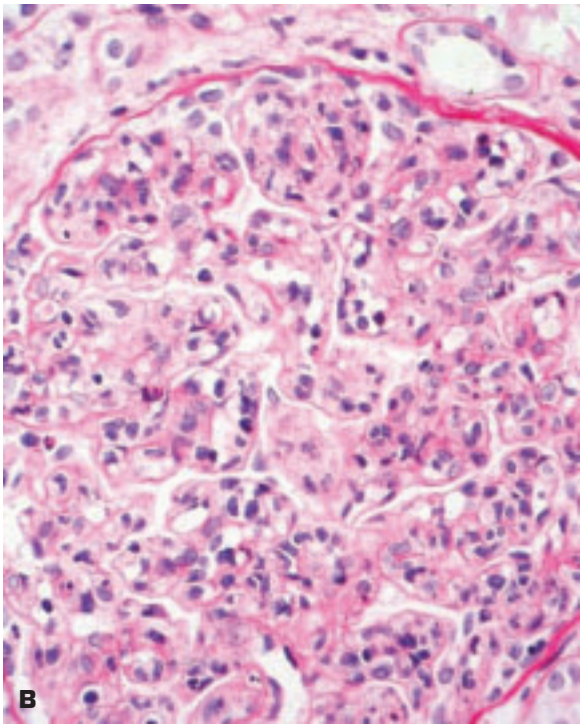

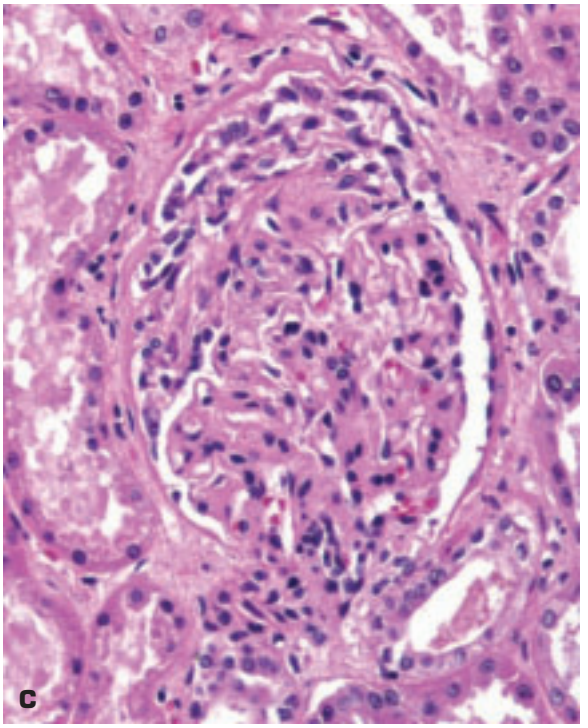

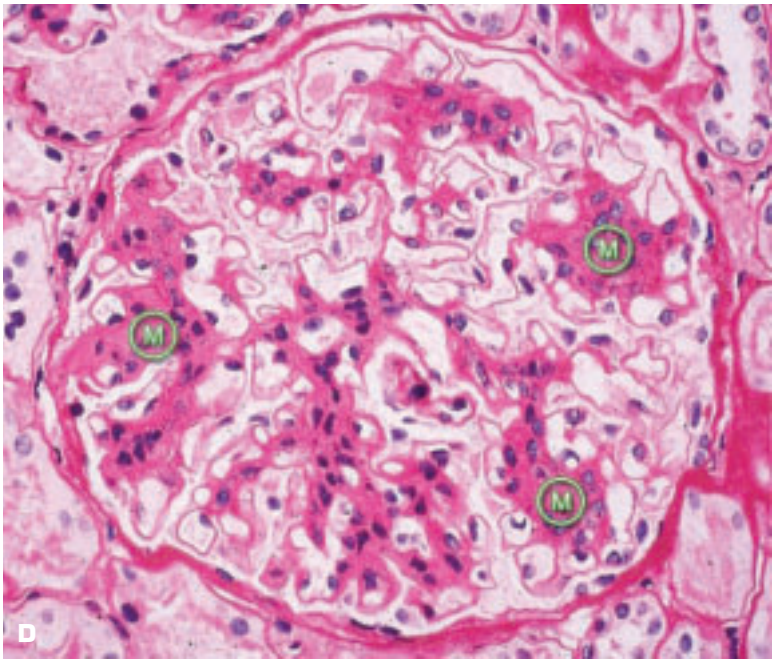

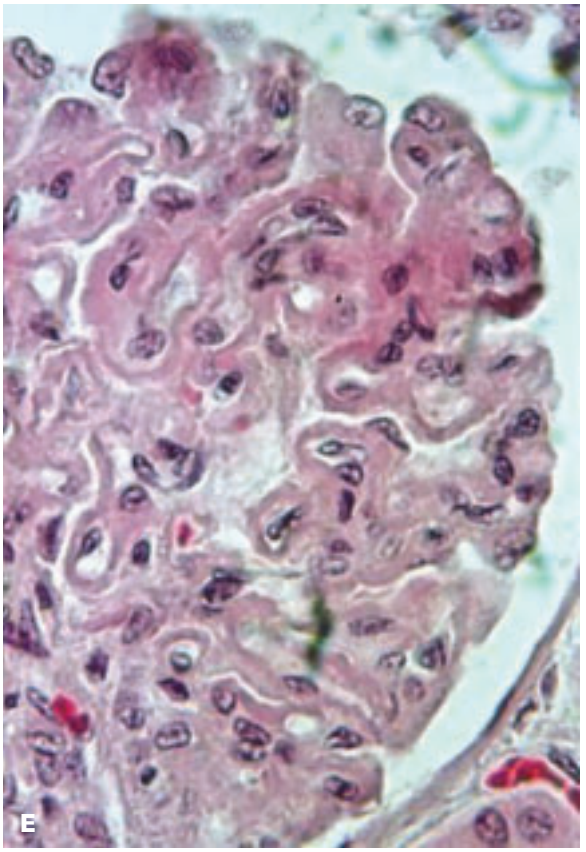

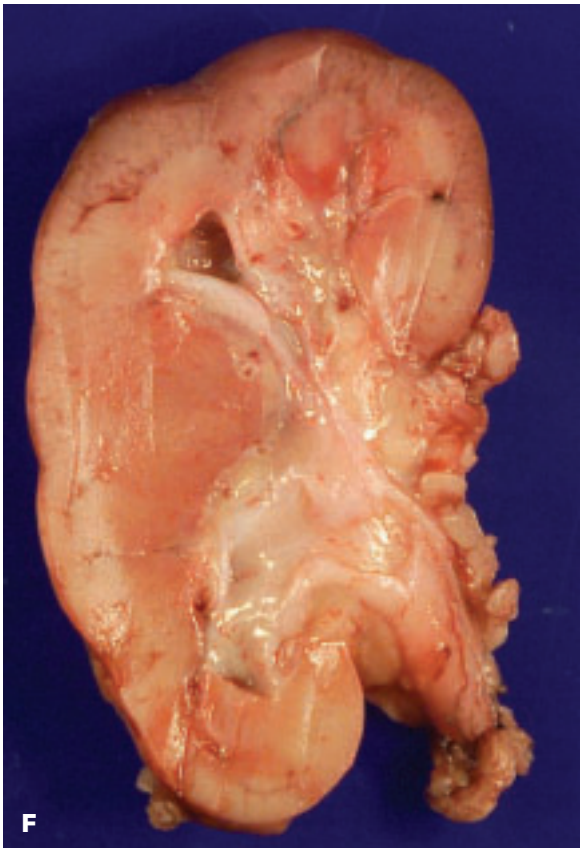

3-22. *(Continued)* **D.** IgA nephropathy with mesangial thickening (M). **E.** Membranous GN. Note the diffuse thickening of the basement membranes. **F.** Macroscopic appearance of chronic GN with blurring of the demarcation between the thinned pale cortex and the medulla.

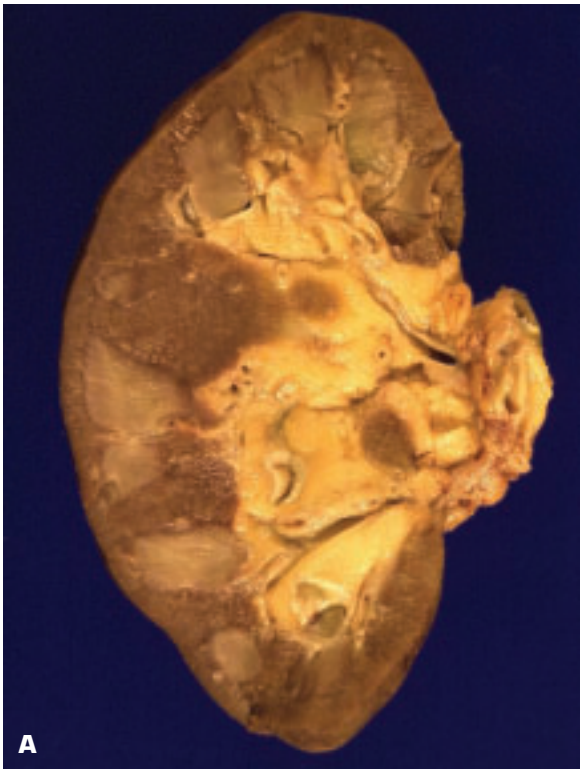

3-23. Diabetic nephropathy (glomerulosclerosis) accounts for about one-third of cases of chronic renal failure. **A.** Narrowed renal cortex due to diabetic nephropathy. **B.** Histology of advanced diabetic glomerulosclerosis with prominent Kimmelstiel-Wilson nodules (increased mesangial matrix) within sclerosing glomeruli. **C.** Finely granular surface of end-stage renal failure of undetermined cause – glomerulonephritis or diabetic glomerulosclerosis may lead to a similar end-stage kidney.

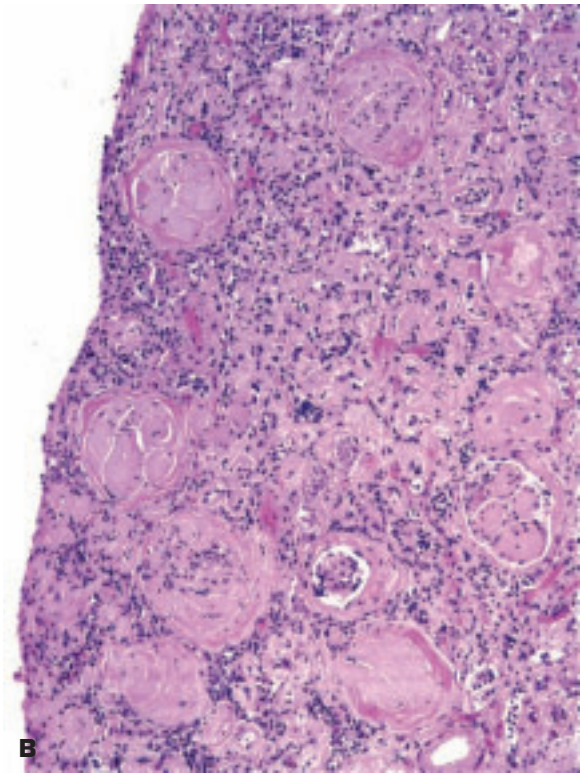

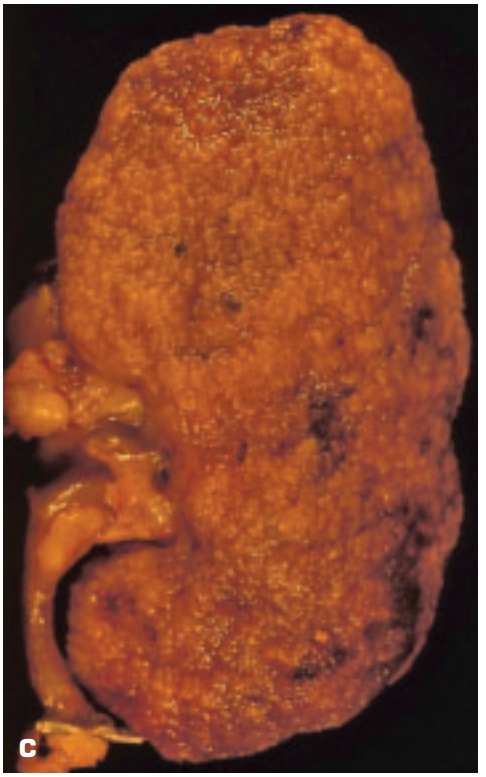

3-24. Congenital nephrotic syndrome (CNS). This kidney appears pale and slightly sclerotic macroscopically. CNS occurs in the first 3 months of life. Histology is needed to distinguish subtypes (e.g., Finnish CNS, diffuse mesangial sclerosis-type CNS).

3-25. Primary oxaluria due to deficiency of hepatic enzymes leading to decarboxylation of glyoxylate has led to oxalate nephropathy. The kidney is reduced in size and shows diffuse scarring, and oxalate stones are present within the calyceal system at both renal poles.

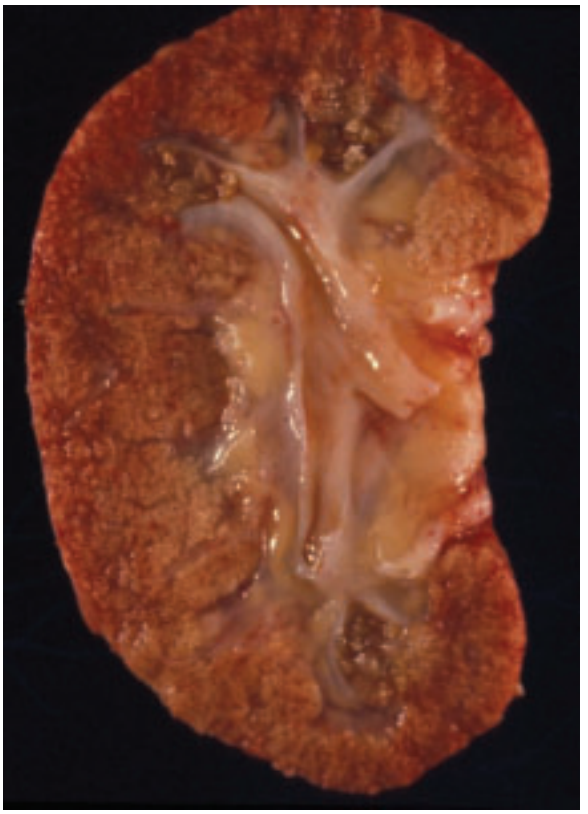

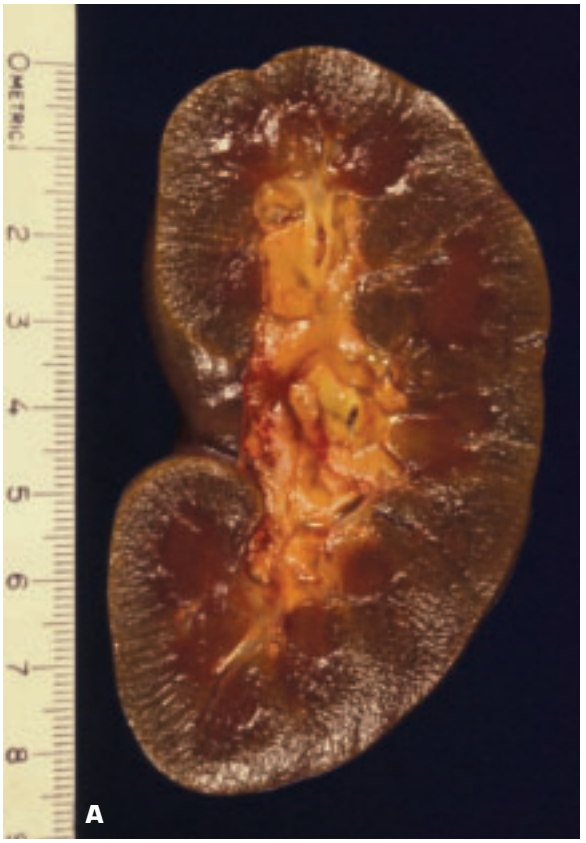

3-26. Bile nephrosis: acute renal failure of uncertain cause may occur in patients with jaundice. **A.** Bile-stained kidney in patient with cirrhotic liver failure. **B.** Bile plugs (*arrows*) are noted within the lumen of some renal tubules.

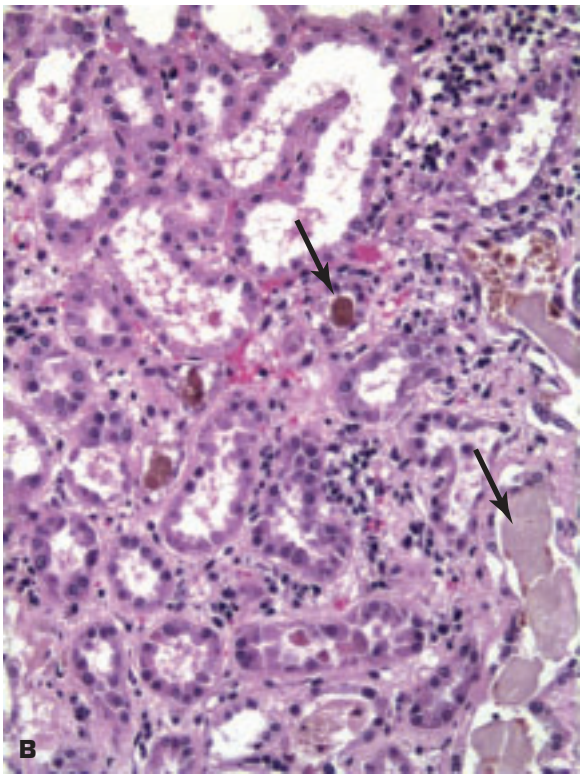

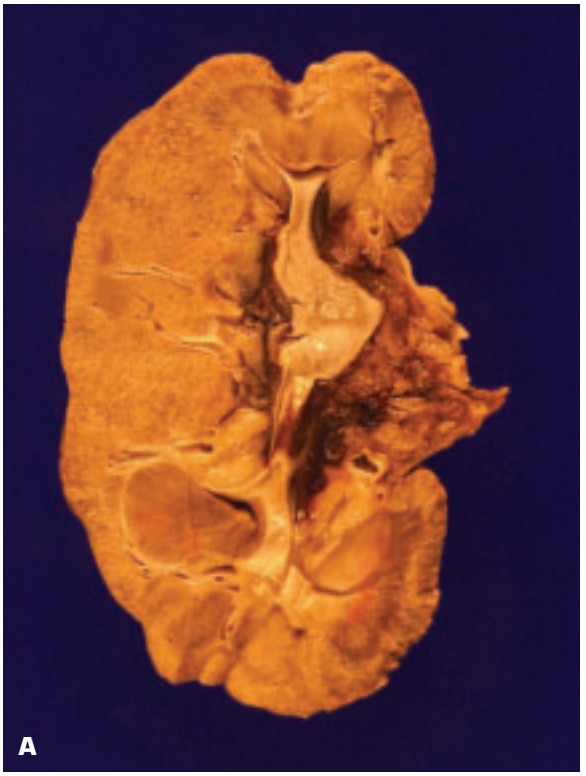

3-27. Pericalyceal hemorrhage is a useful indicator of a bleeding tendency and occurs around the mobile, contractile renal pelvis from disruption of small capillaries that normally seal off by platelet coagulation. **A.** Pericalyceal hemorrhage in a kidney bearing some old vascular scars. **B.** Histology confirms the pericalyceal situation of the hemorrhage.

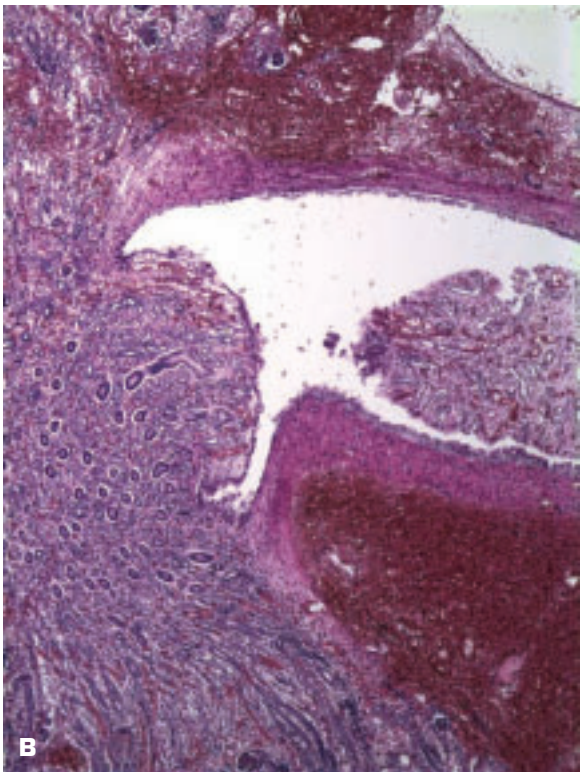

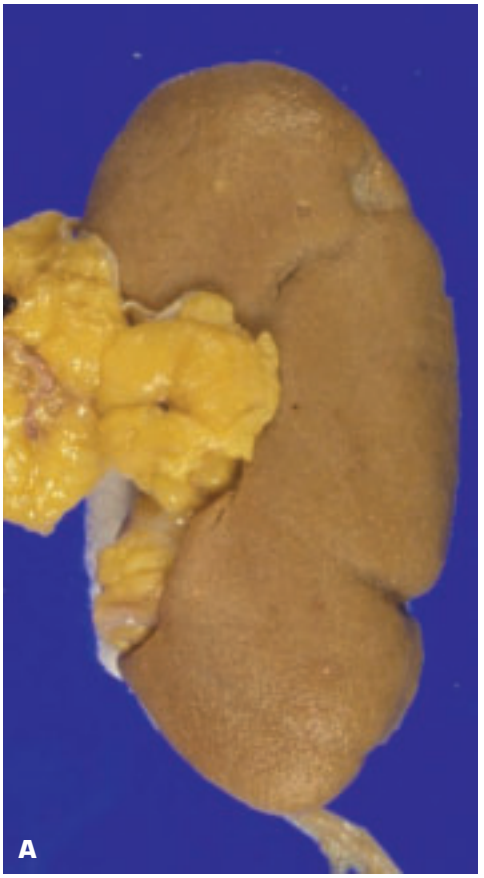

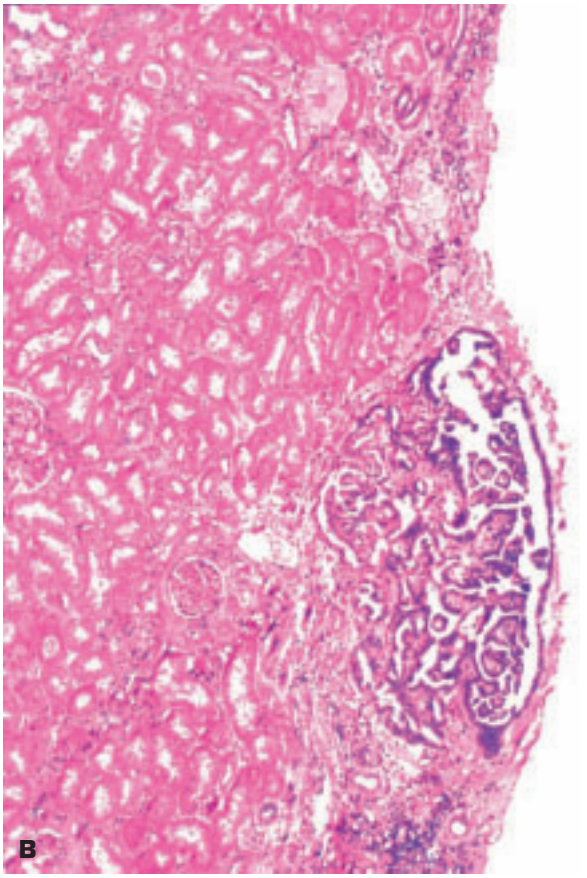

3-28. A. Kidney with ischemic atrophy also bears very small subcapsular adenomas near to each pole. **B.** Histology of a subcapsular papillary adenoma shows tubules arranged in a papillary fashion. All such "adenomas" are presently regarded as early cancers.

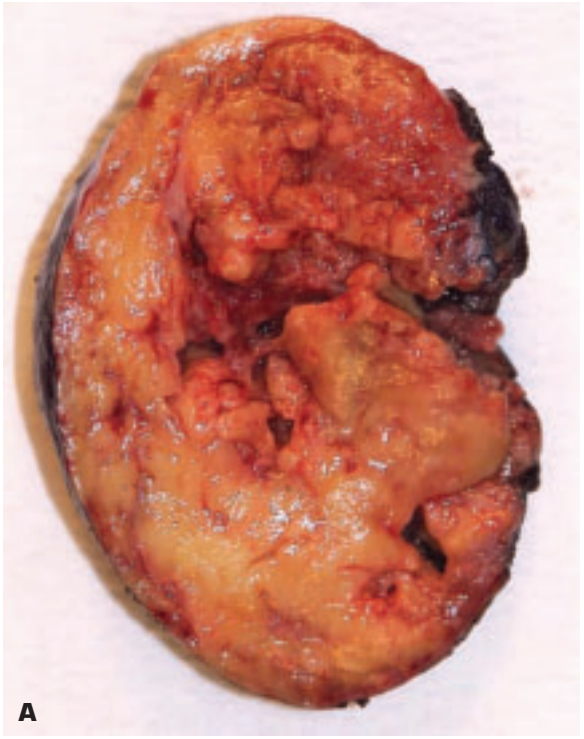

3-29. A. Surgically removed angiomyolipoma (AML) of the kidney shows a macroscopic predominance of adipose tissue. Histology may also show vessels and smooth muscle. AML has an incidence of 25% to 50% in patients with tuberous sclerosis. **B.** Histology of another AML in which smooth muscle proliferation predominates and some cellular atypism and mitotic activity is noted.

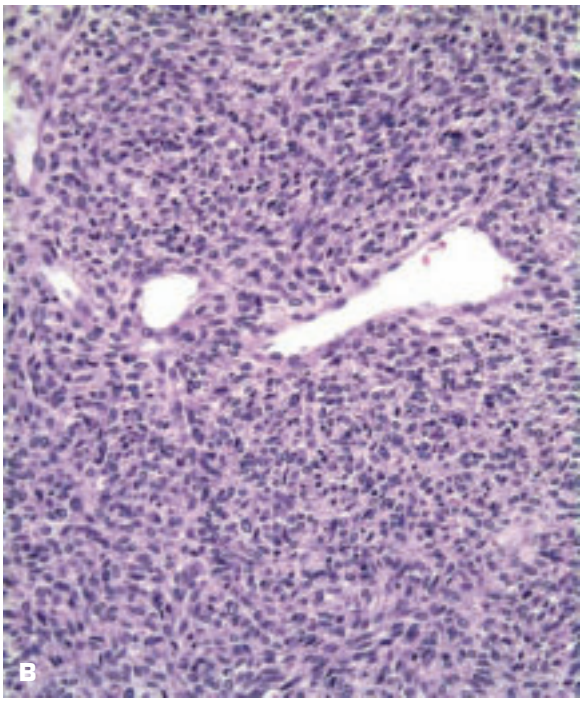

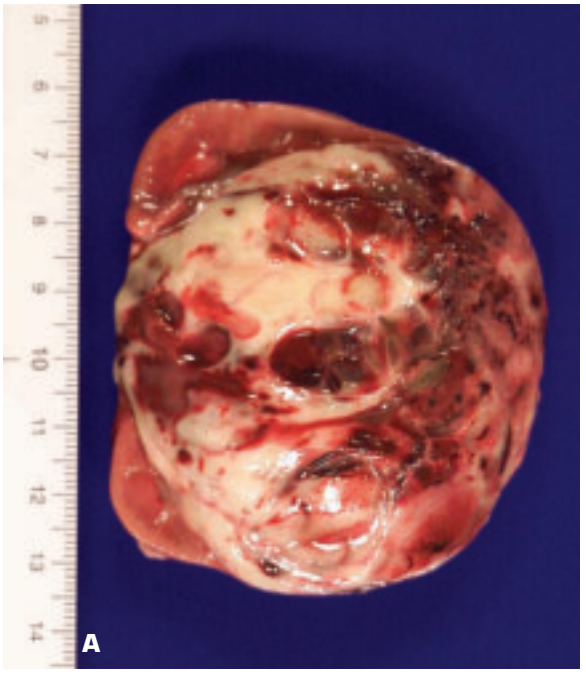

3-30. Mesoblastic nephroma of the kidney is a congenital benign neoplasm or hamartoma that is encountered in the first 3 months of life. **A.** Partially necrotic, fleshy-looking mesoblastic nephroma replacing most of the kidney has to be distinguished from a Wilms' tumor by histology. **B.** Histology of mesoblastic nephroma shows two surviving glomeruli within a proliferation of myofibroblastic spindle cells.

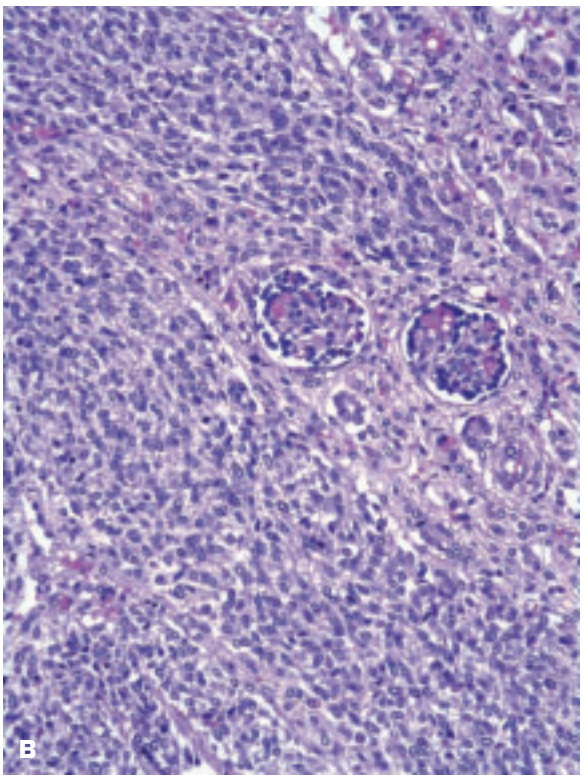

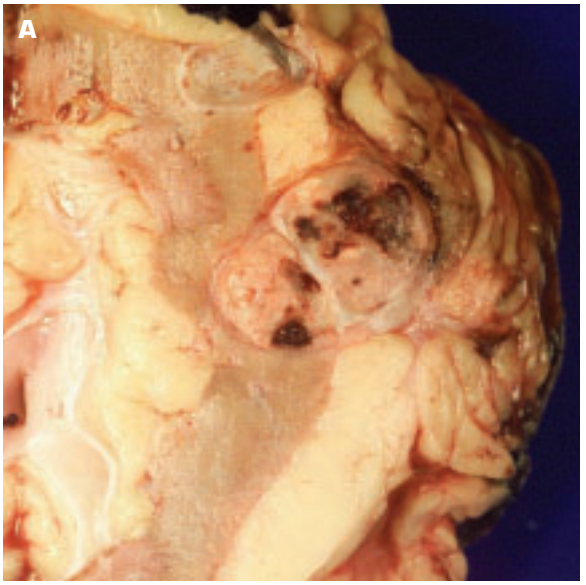

3-31. Renal cell carcinoma is the most common primary renal tumor in adults and may be occult. It is more common in males and affects the upper pole of the kidney more often than elsewhere. Etiology includes tobacco exposure and von Hippel-Lindau disease. **A.** Small clear cell renal cell carcinoma (hypernephroma, Grawitz tumor) is spreading into perirenal adipose tissue. Note the very abundant peripelvic and pericapsular fibroadipose tissue. **B.** Histology shows a clear cell-type renal carcinoma comprising rounded cells with a translucent cytoplasm. **C.** Typical lobulated, whorled, tan-colored cut surface of a renal cell carcinoma. *(continued on next page)*

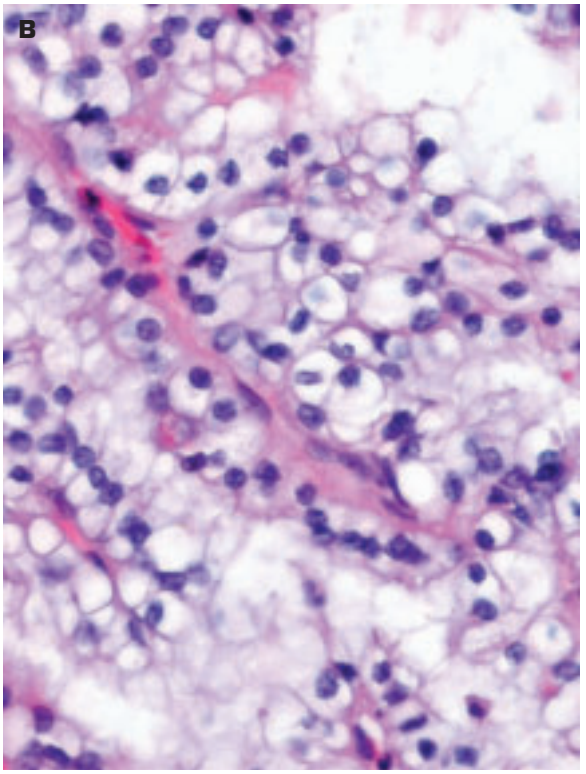

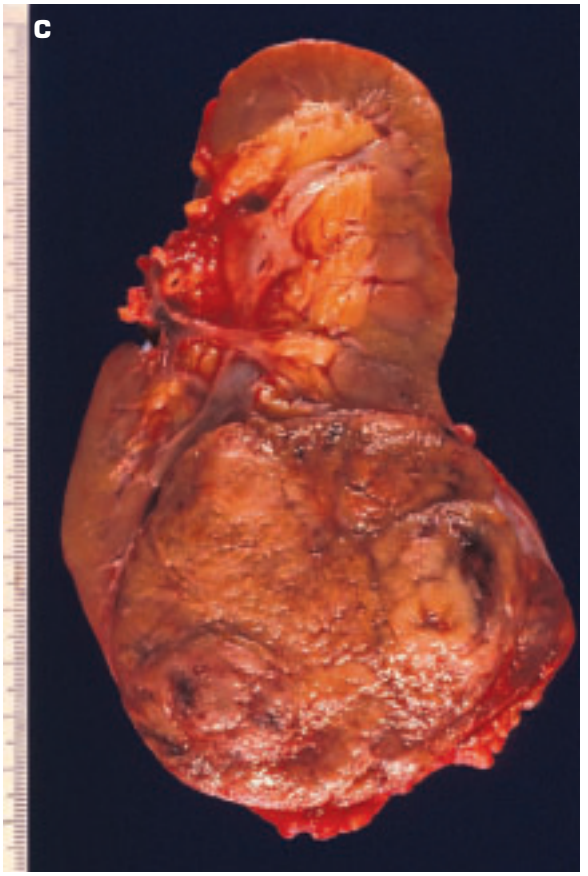

3-31. *(Continued)* **D.** Abundant lipid within the tumor cells as well as necrosis may give the tumor a yellow color, as in this case. **E.** Invasion of the renal vein (*) and inferior vena cava (*arrow*) by renal cell carcinoma.

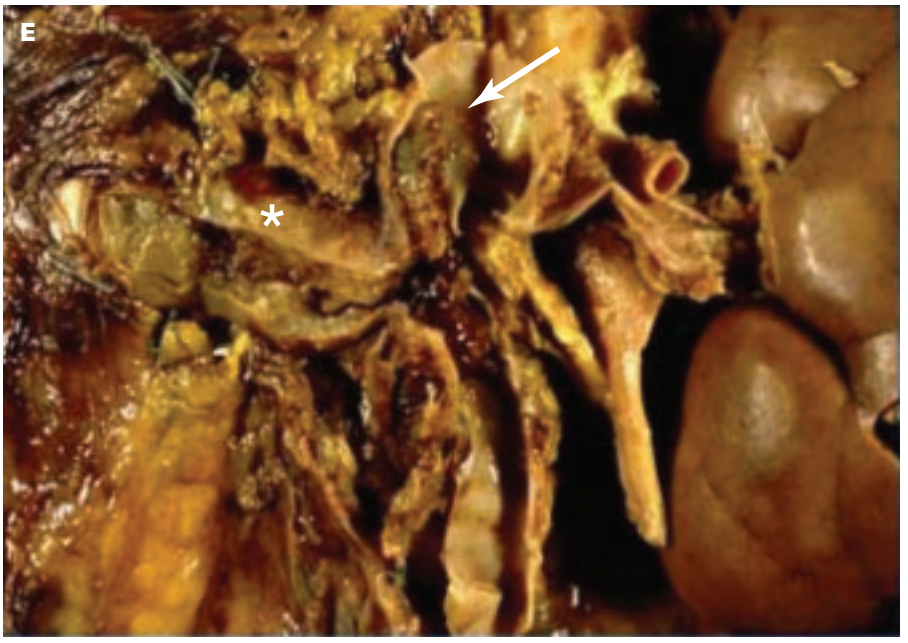

3-32. Papillary urothelial (transitional cell) carcinoma of renal pelvis. Note the exophytic, multifronded nature of the tumor. The resection lines have been marked with ink. Urothelial carcinomas comprise about 5% to 10% of primary renal tumors.

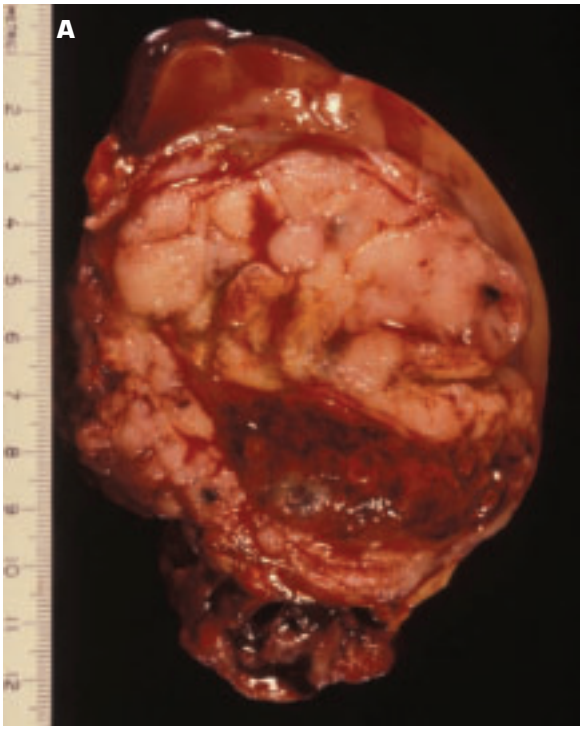

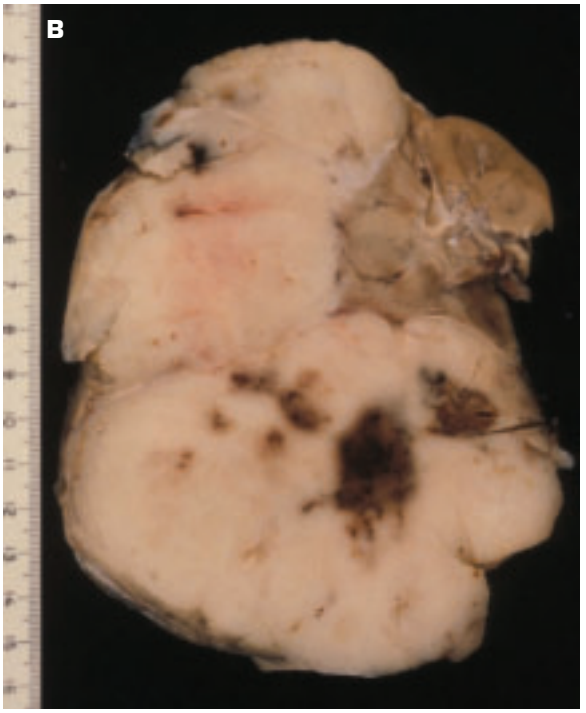

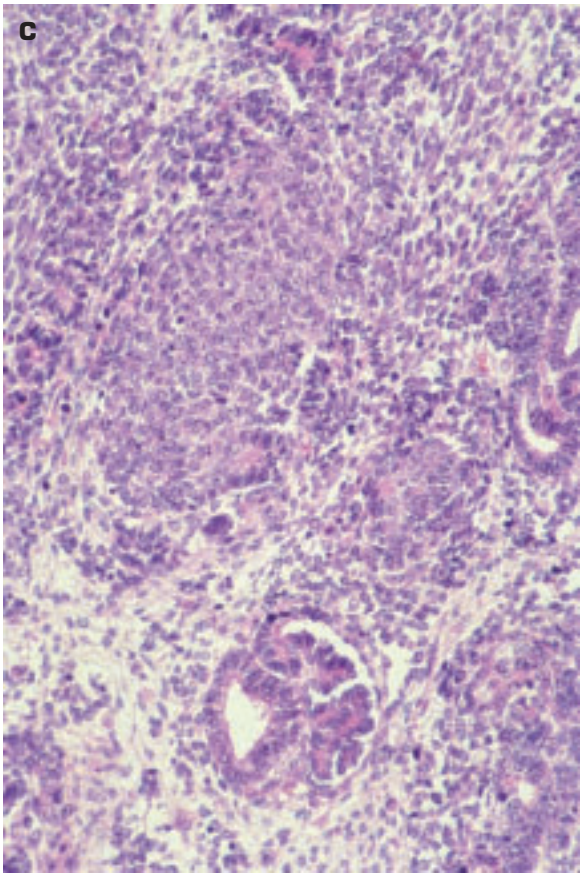

3-33. Wilms' tumor (nephroblastoma) of the kidney is the most common intraabdominal solid tumor in children younger than 10 years. It is a malignant tumor composed of embryonal nephrogenic elements, including blastemal, stromal, and epithelial tissues. Not all elements are present in all tumors. **A.** Solid, bulging, fleshy tan-white, partially necrotic tumor has replaced much of the kidney and is encompassed by a thin rim of renal tissue. **B.** This Wilms' tumor appears whiter due to formalin fixation and has extended beyond the confines of the kidney. Foci of necrosis and hemorrhage appear as darker zones within the tumor. **C.** Histology shows hypercellular areas comprising undifferentiated blastema, loose stroma with undifferentiated mesenchymal cells and immature tubules and a glomeruloid body (*bottom*).

3-34. Metastatic poorly differentiated adenocarcinoma at inferior pole of kidney.

3-35. Renal transplantation. **A.** Note the two end-stage native kidneys in normal position, the atrophic first donor kidney (*lower left*), and the larger second donor kidney (*lower right*). **B.** Subtotal renal infarction due to hyperacute (antibody-mediated) rejection. *(continued on next page)*

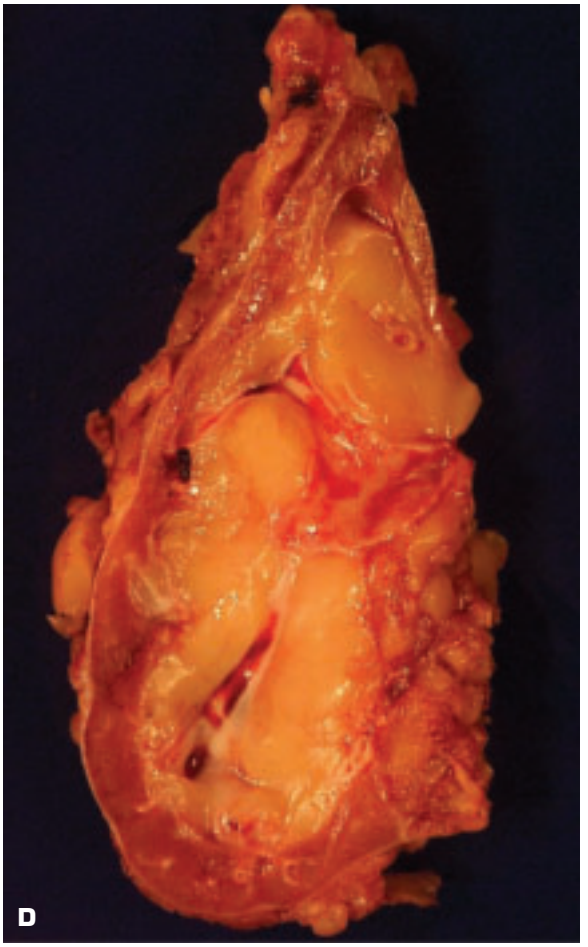

3-35. *(Continued)* **C.** Severe acute rejection of donor kidney. Focal infarcts are present. **D.** Severe chronic rejection (graft arteriopathy). Note the severe parenchymal atrophy and the thick-walled arteries.

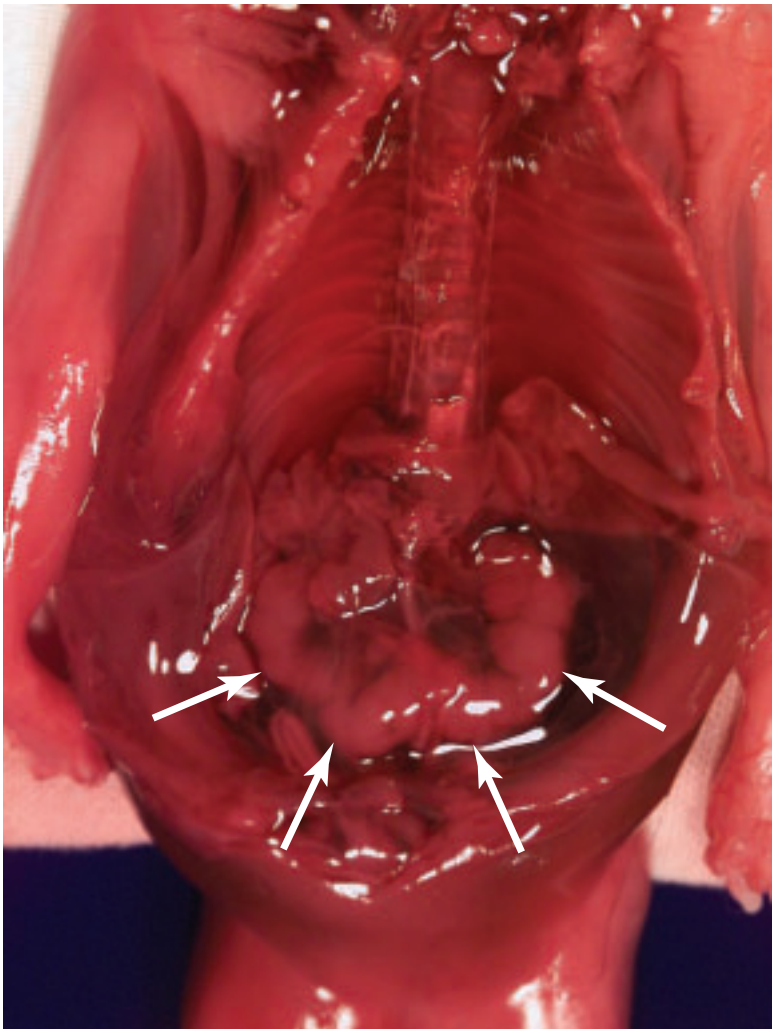

3-36. Opened fetal abdomen with bowel removed showing a horseshoe kidney (*arrows*) due to congenital fusion of both lower poles anterior to the great vessels.

3-37. Hypoplastic kidney. **A.** Note the small size of the kidney relative to the pelvis and ureter, plus the reduced number of renal lobes (renunculi). **B.** Bisected hypoplastic kidney showing scanty renal parenchymal tissue.

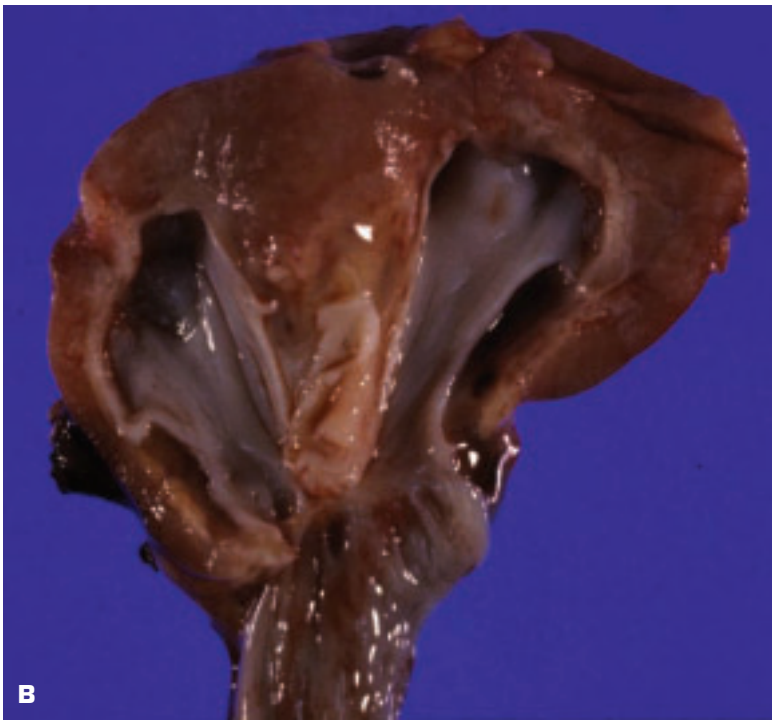

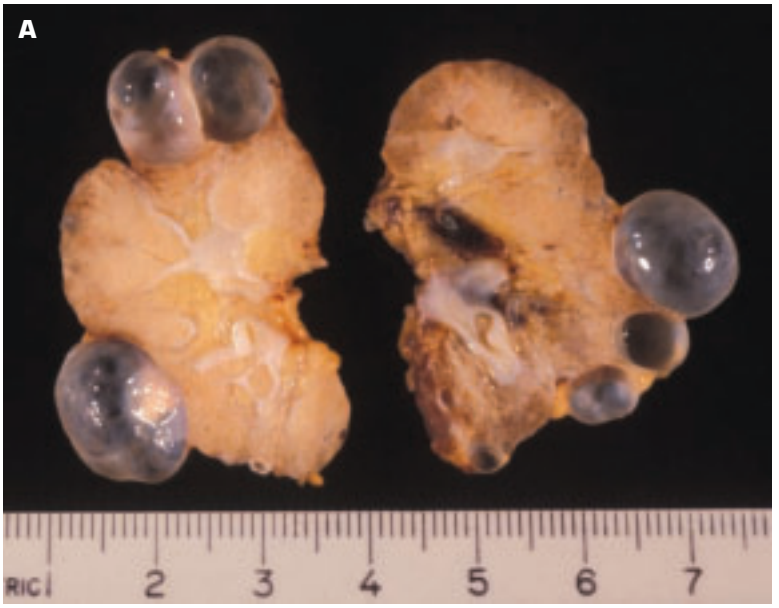

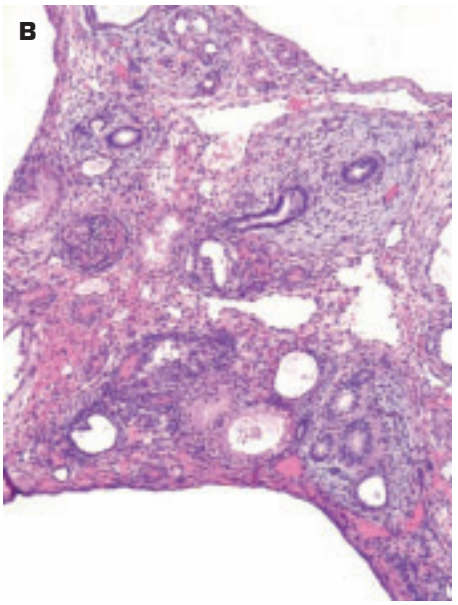

3-38. Cystic renal dysplasia (CRD) is an abnormality in metanephric differentiation that may be unilateral or bilateral and is usually cystic. Histology shows immature collecting ductules, undifferentiated mesenchyme, and even focal cartilage. **A.** Bisected kidney shows a less severe form of CRD with multiple cysts and focally a significant degree of disorganization of parenchymal architecture. **B.** Histology of bisected kidney shows portions of cysts, variably dilated epithelial-lined ducts, periductal myxoid stroma, and an immature glomerulus. **C.** Severe multicystic, unilateral CRD with markedly deficient renal parenchyma that presented as a flank mass.

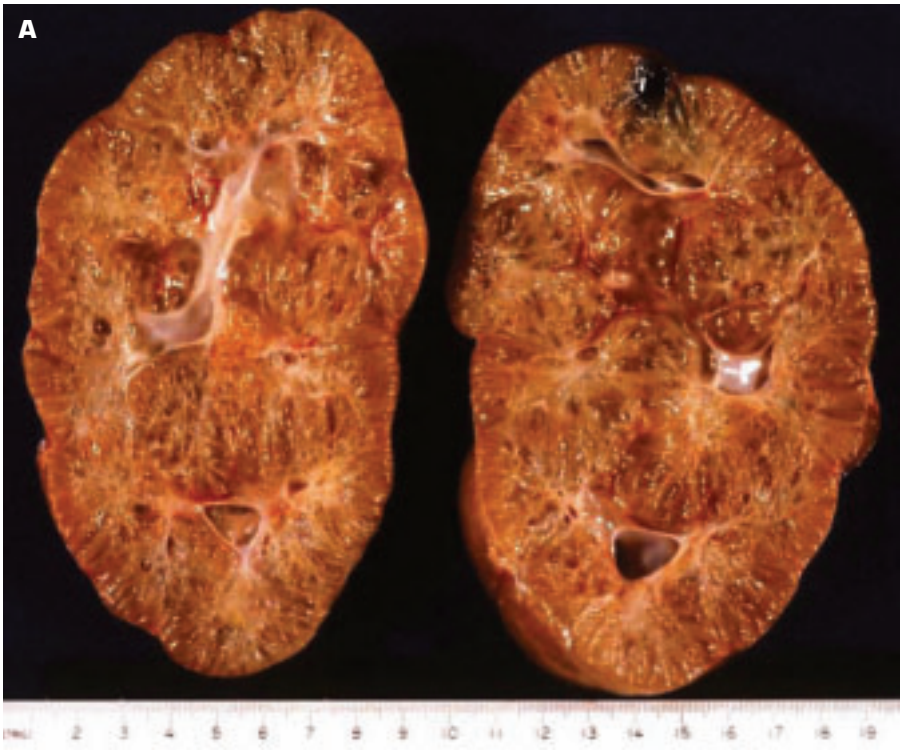

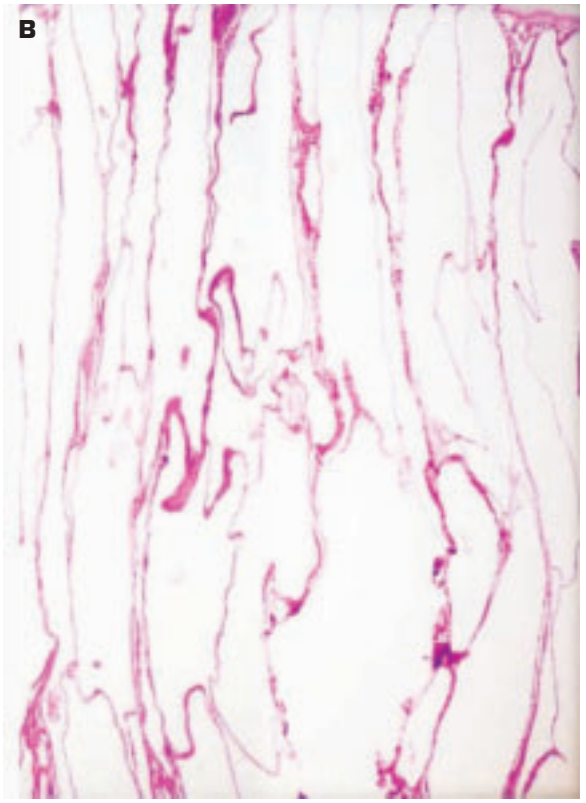

3-39. A. Autosomal recessive (infantile) polycystic disease (ARPKD). Elongated streaks represent dilated tubules. **B.** Histology of ARPKD shows dilated collecting tubules extending to the capsular surface (*top*).

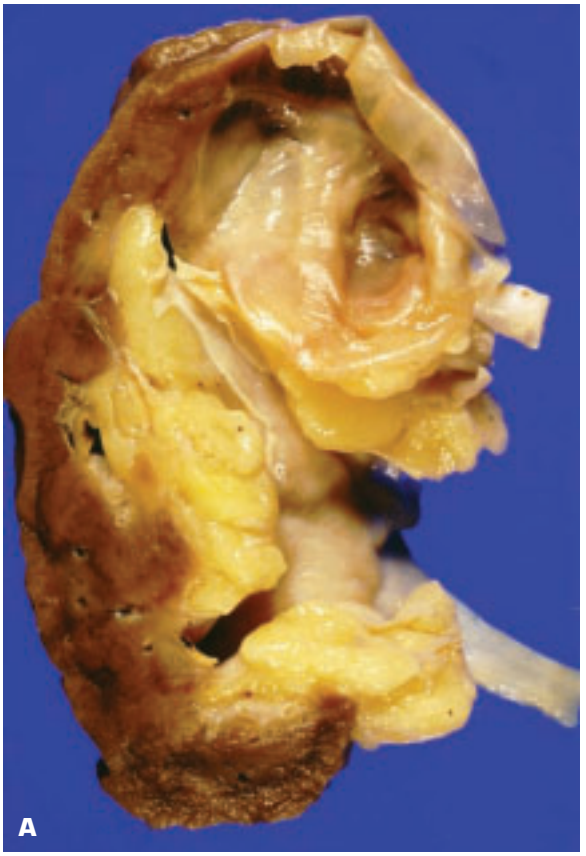

3-40. A. Simple cyst occupies upper pole of kidney. **B.** Dialysis-related multiple small cysts in a coarsely scarred kidney.

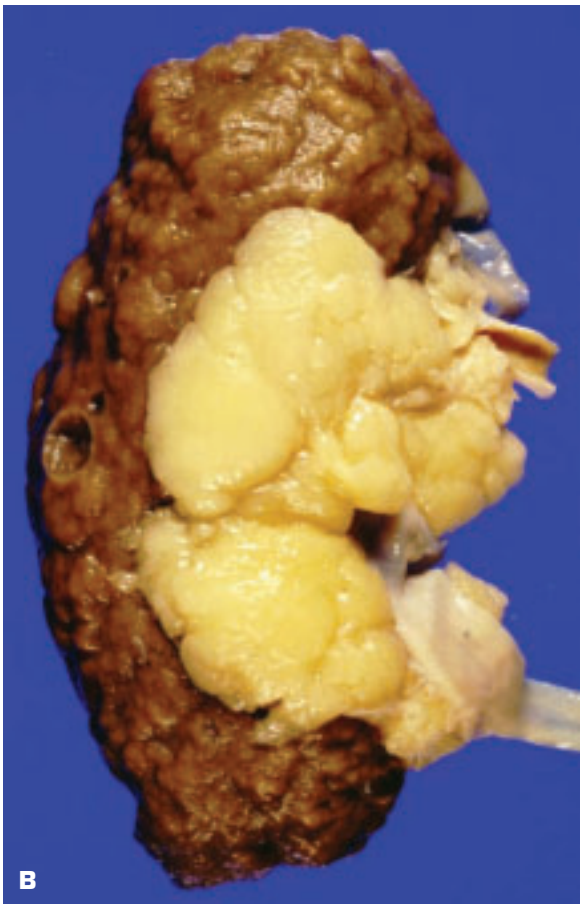

3-41. A. Early stage of autosomal dominant (adult) polycystic kidney disease (ADPKD). A significant amount of renal parenchyma is still present. **B.** Late stage of ADPKD showing greatly enlarged renal profiles due to innumerable cysts of varying size replacing the renal parenchyma. *(continued on next page)*

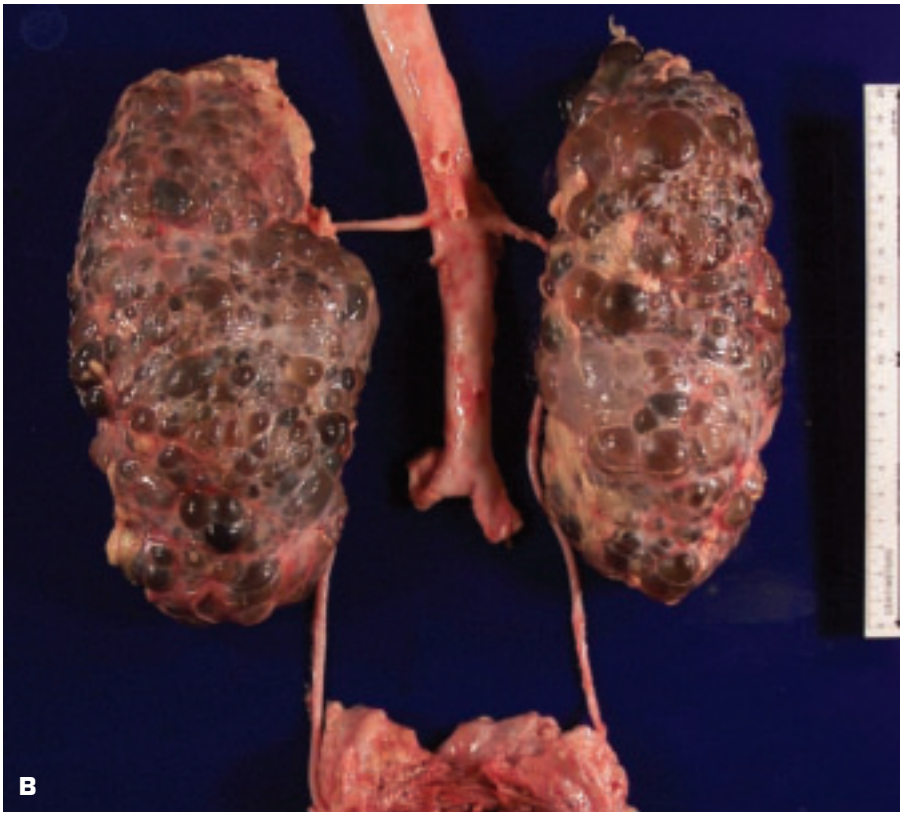

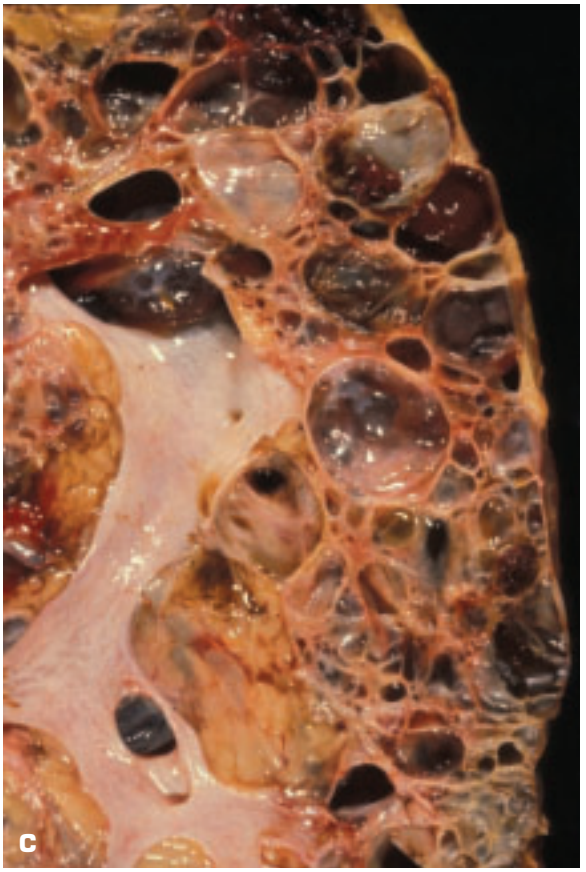

3-41. *(Continued)* **C.** Cut surface of ADPKD showing variable-size, irregular cysts with no recognizable intervening normal parenchyma. Most cysts contain clear fluid and the pelvis is distorted. **D.** Histology of ADPKD shows a single glomerulus alongside several cysts.

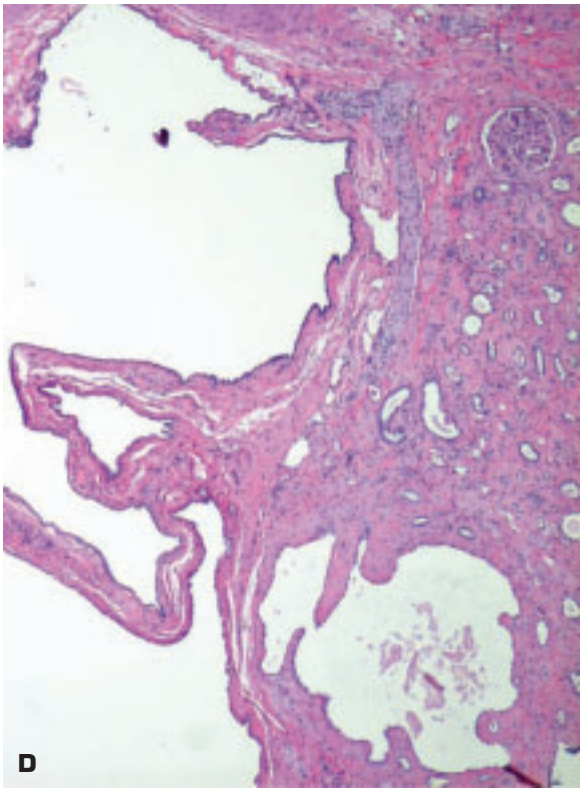

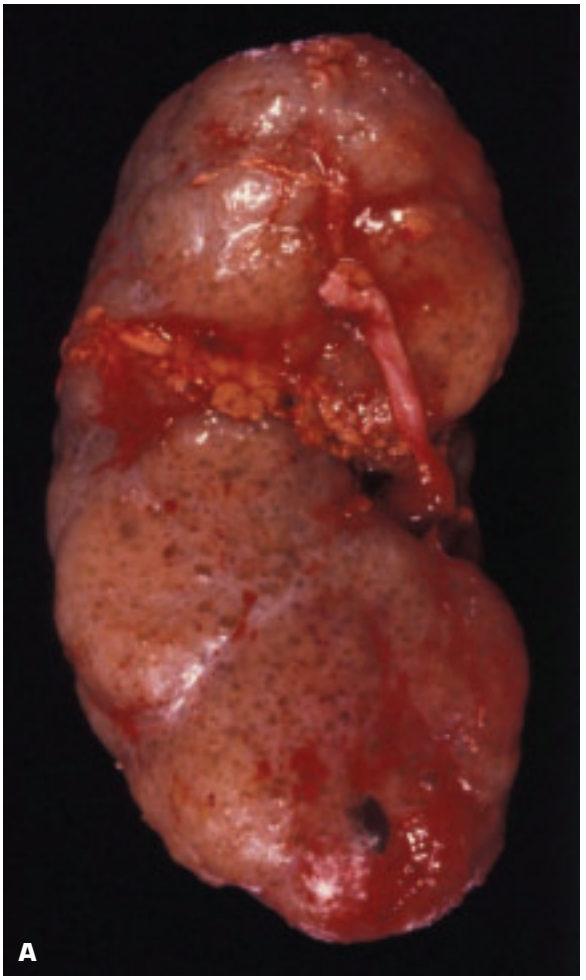

3-42. A. Kidney of a young child showing glomerulocystic kidney disease (GCKD) with numerous subcapsular cysts. In about 50% of cases, GCKD is an early manifestation of ADPKD. **B.** Histology of GCKD shows cysts arising due to dilatation of Bowman's space and the first part of the proximal convoluted tubule.

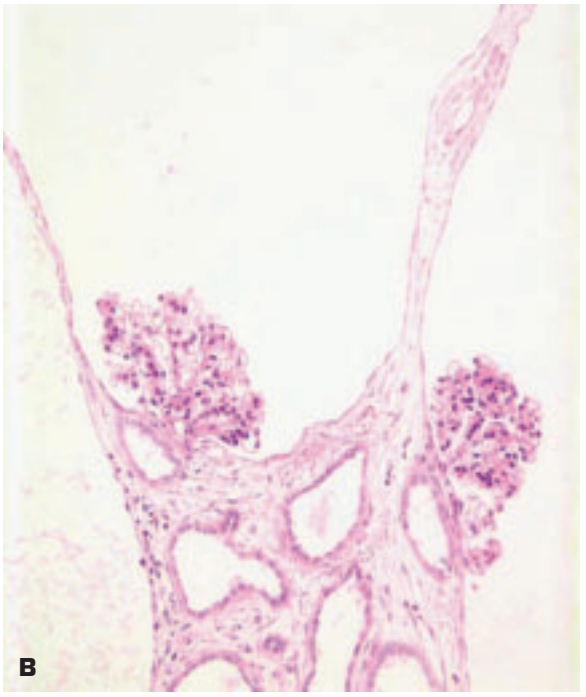

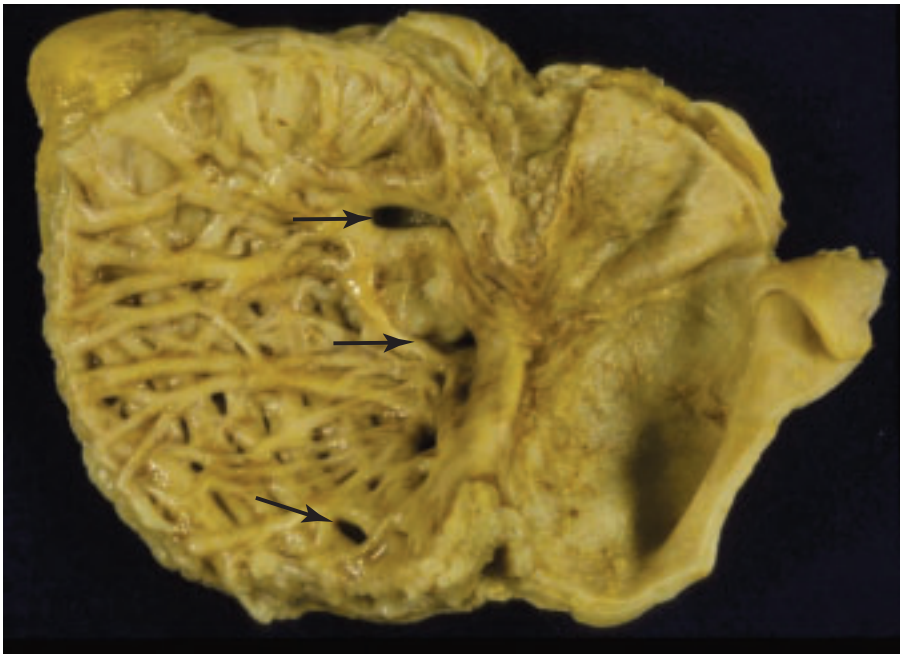

3-43. Multiple acquired diverticula (*arrows*) lie between hypertrophied muscular bundles in a hypertrophied bladder of a patient who had severe prostatic hyperplasia. Congenital diverticulum of the bladder tends to be a solitary lesion.

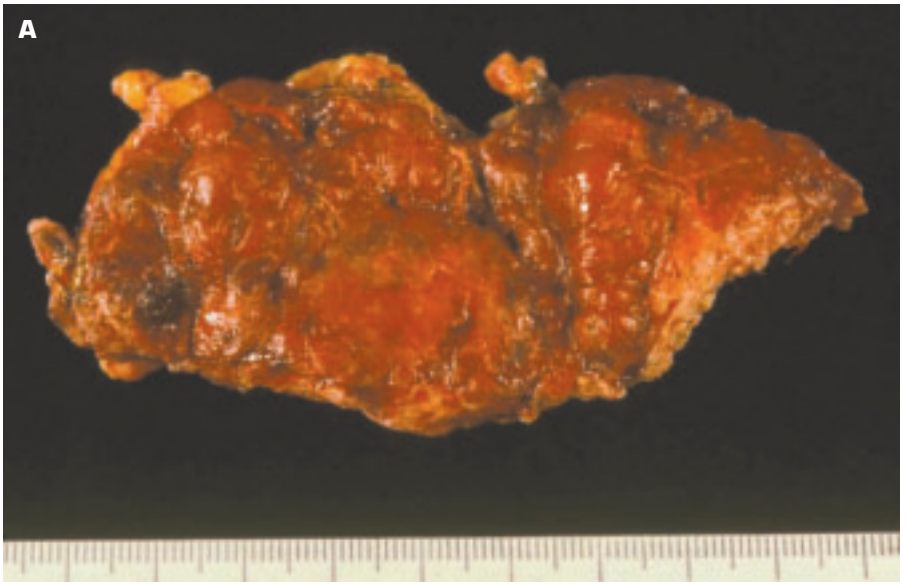

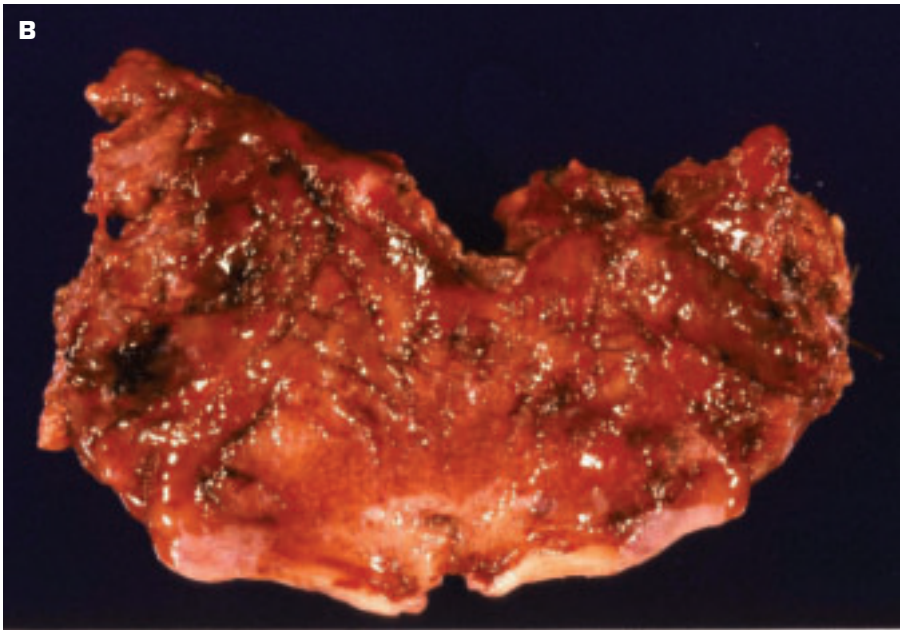

3-44. Acute inflammation of the urinary bladder. **A.** Acute hemorrhagic cystitis showing a greatly reddened, inflamed bladder mucosa with areas of hemorrhage breaching the mucosal surface. **B.** Follicular cystitis shows focal pale nodules elevating the inflamed mucosa from below due to the presence of lymphoid follicles as part of a more chronic inflammatory response.

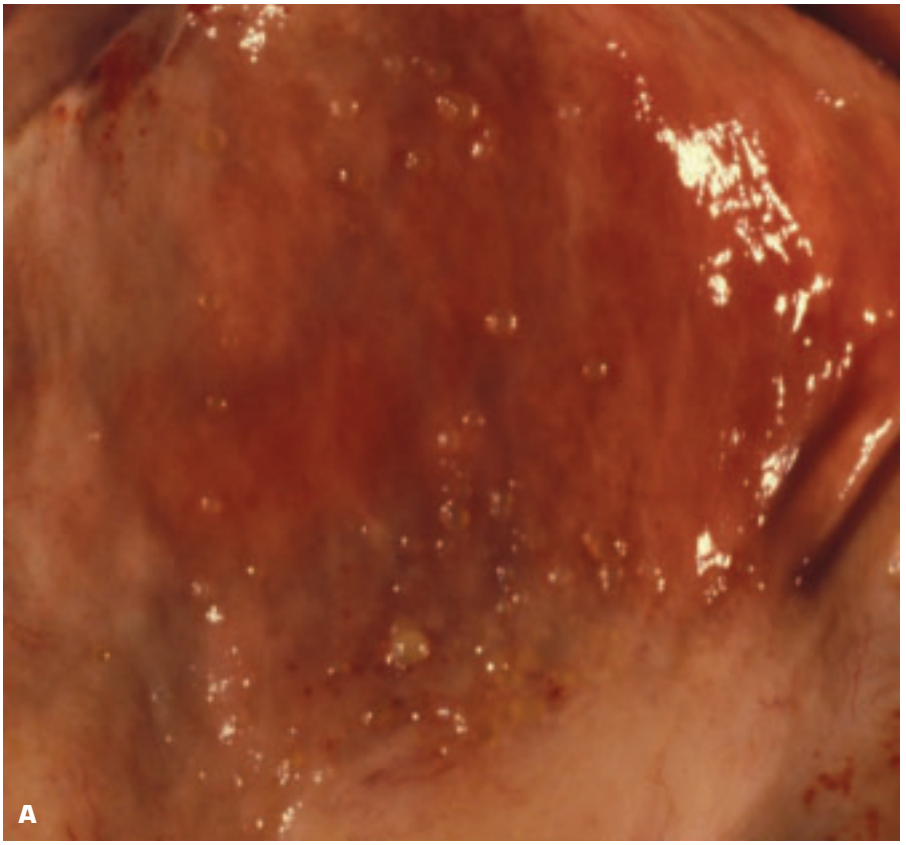

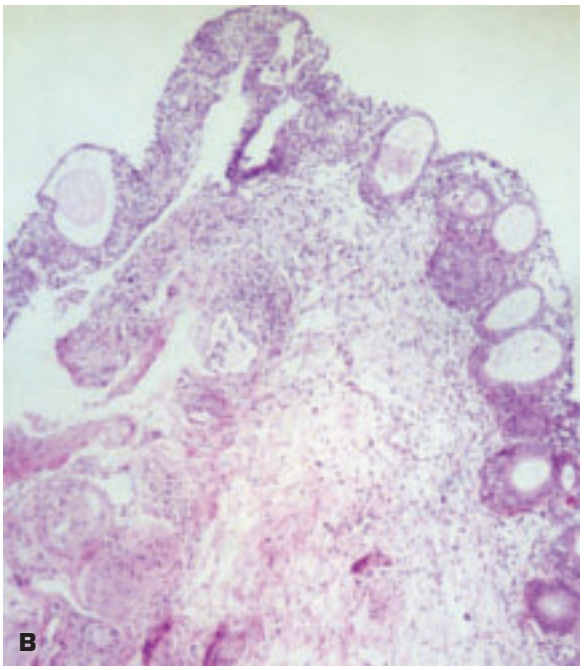

3-45. Cystitis cystica of the bladder results from (Brunn) nests of urothelial cells growing downward into the lamina propria and developing cystic spaces lined by urothelium. **A.** Numerous thin-walled cysts elevate the bladder mucosa. **B.** Histologic appearance of the cystic Brunn nests.

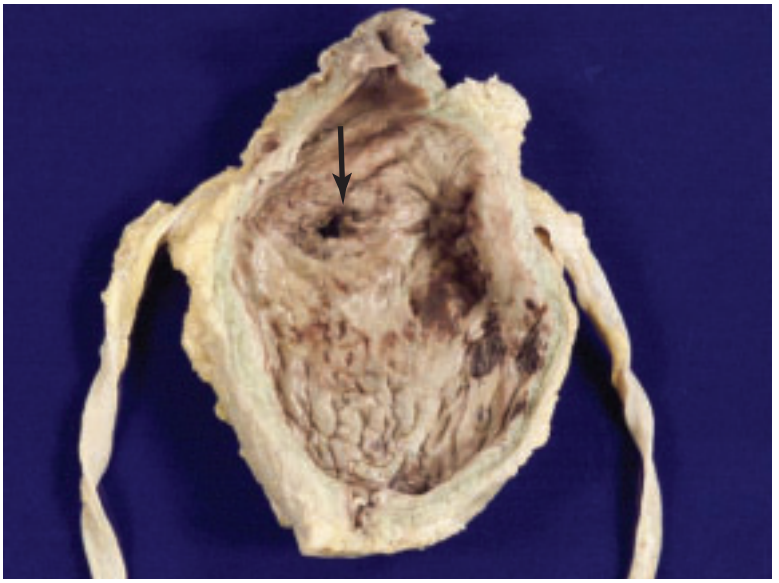

3-46. Bladder perforation (*arrow*) due to pressure of tip of a Foley catheter in a patient with graft-versus-host disease after bone marrow transplant.

3-47. A. Urothelial (transitional cell) carcinoma in situ of the urinary bladder. If untreated, up to 75% of cases go on to invasive cancer. **B.** Histology of carcinoma in situ (surface is to the right).

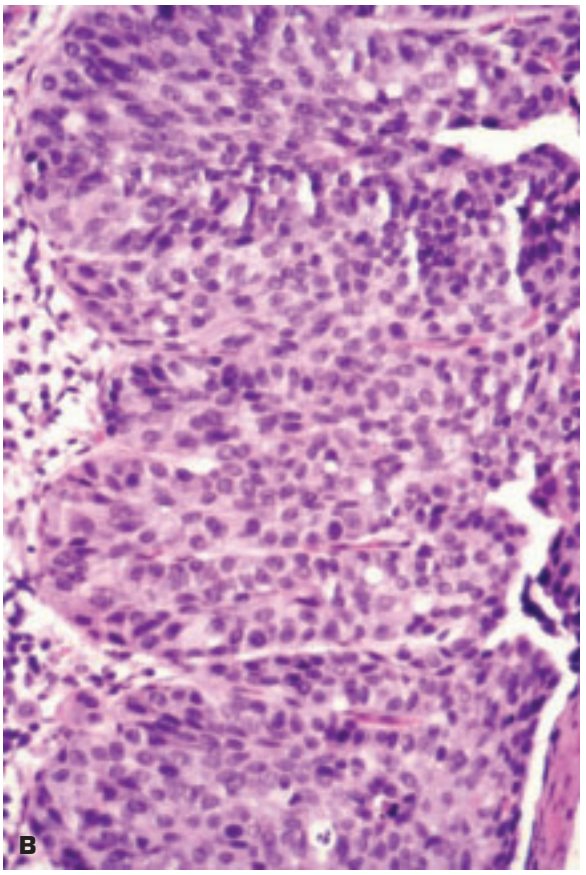

3-48. A. Invasive urothelial carcinoma (*) of the bladder is invading the muscle coat on the right side of the picture. **B.** Moderately differentiated urothelial carcinoma of bladder.

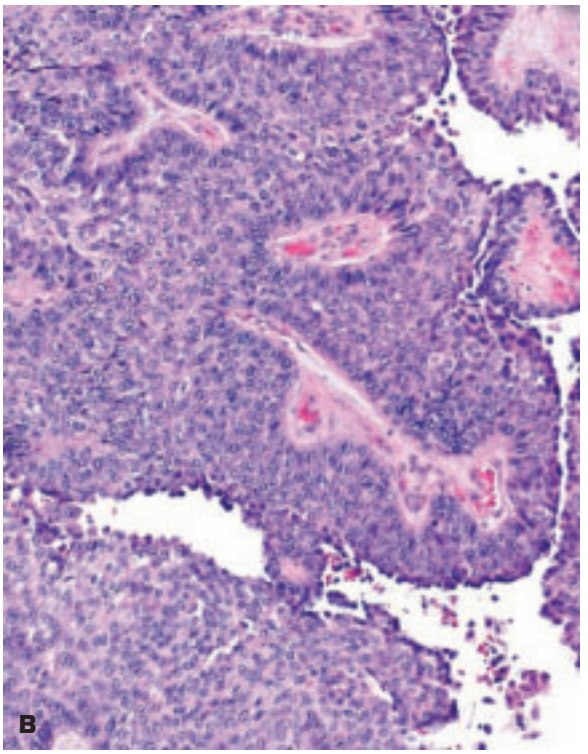

3-49. Bladder stones lie in a small recess alongside a fleshy-looking squamous carcinoma.

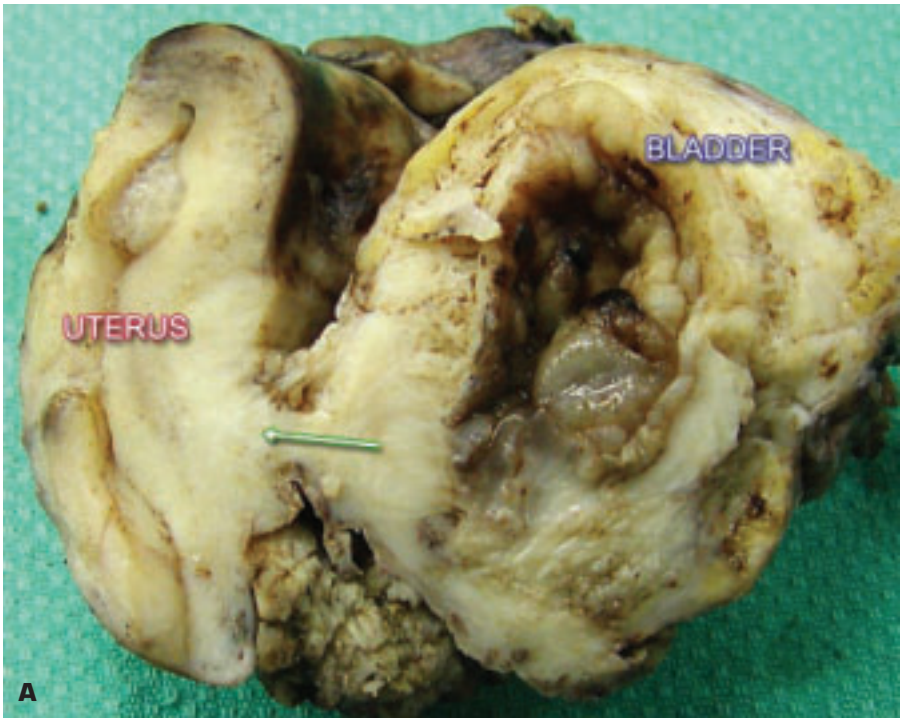

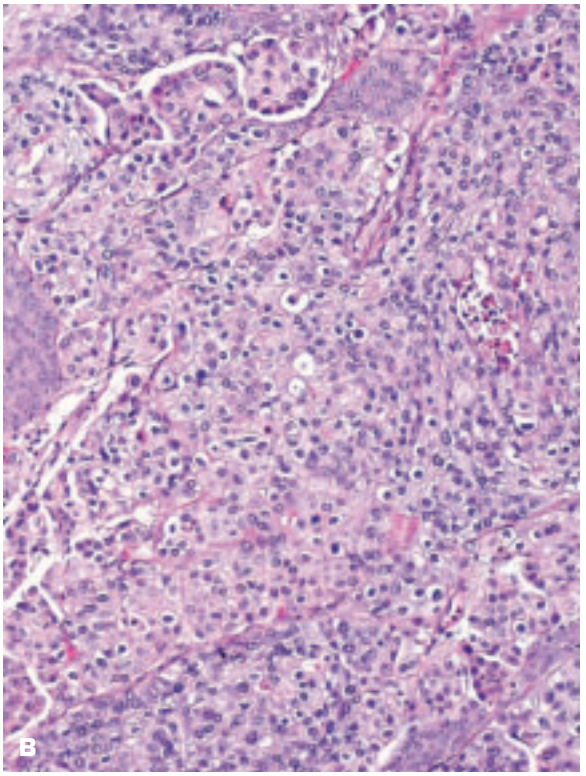

3-50. A. Advanced urothelial cancer of the bladder has spread posteriorly (*arrow*) to invade the uterus. **B.** Poorly differentiated urothelial carcinoma.

4 Liver, Biliary System, and Pancreas

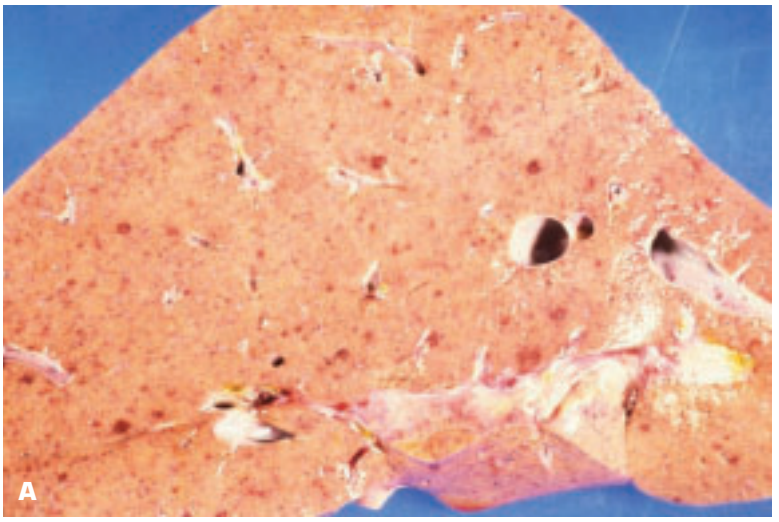

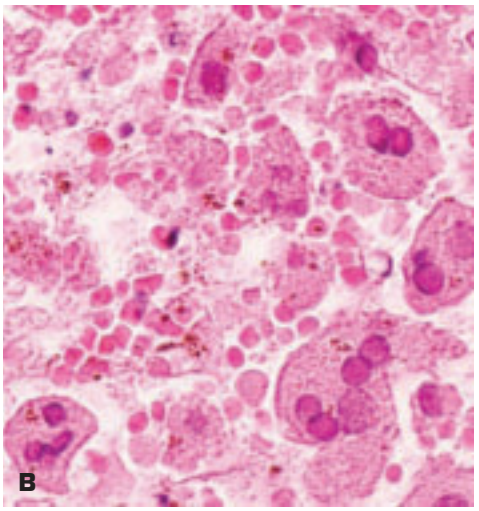

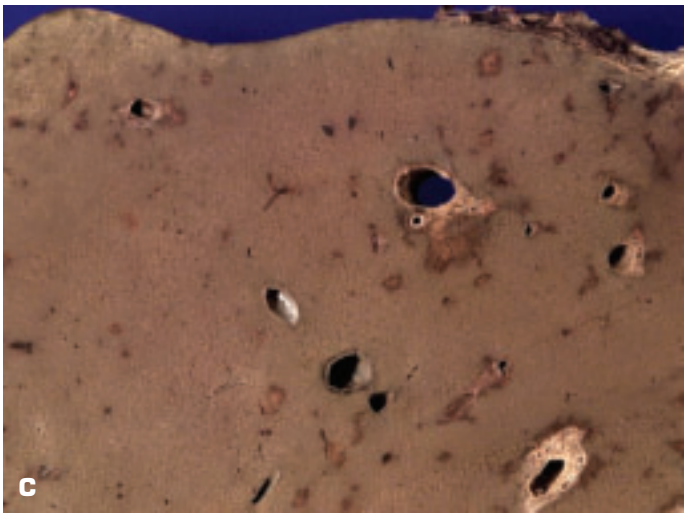

4-1. A. Fatty liver due to malnutrition in a child shows multifocal necroses, each surrounded by a hemorrhagic ring due to disseminated herpesvirus simplex infection. **B.** Cowdry type A intranuclear inclusions due to herpes simplex viral infection. Note the marginated chromatin at the edge of the affected nuclei. **C.** Close-up view of focal necroses in a formalin fixed liver due to herpesvirus infection in an immunocompromised adult. Note that each randomly distributed area of necrosis is surrounded by a localized zone of hemorrhage, giving a targetoid appearance to the lesions.

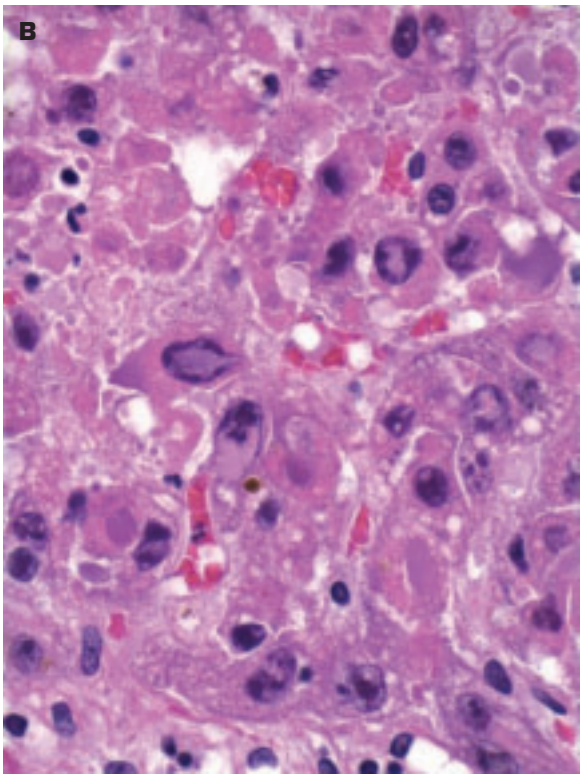

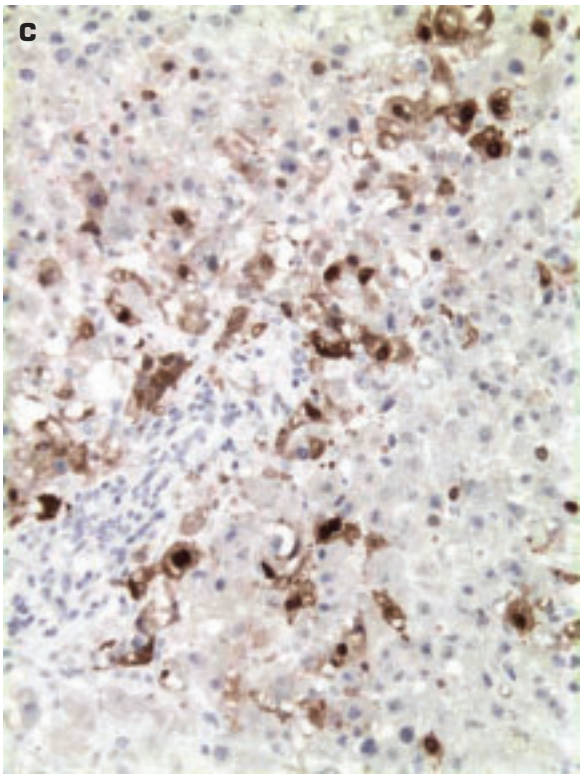

4-2. Adenovirus infection of the liver. **A.** Multiple areas of focal necrosis, some becoming confluent, are scattered throughout the liver. **B.** Histology shows intranuclear inclusions. **C.** Positive intranuclear immunoperoxidase staining using a specific antibody for adenovirus.

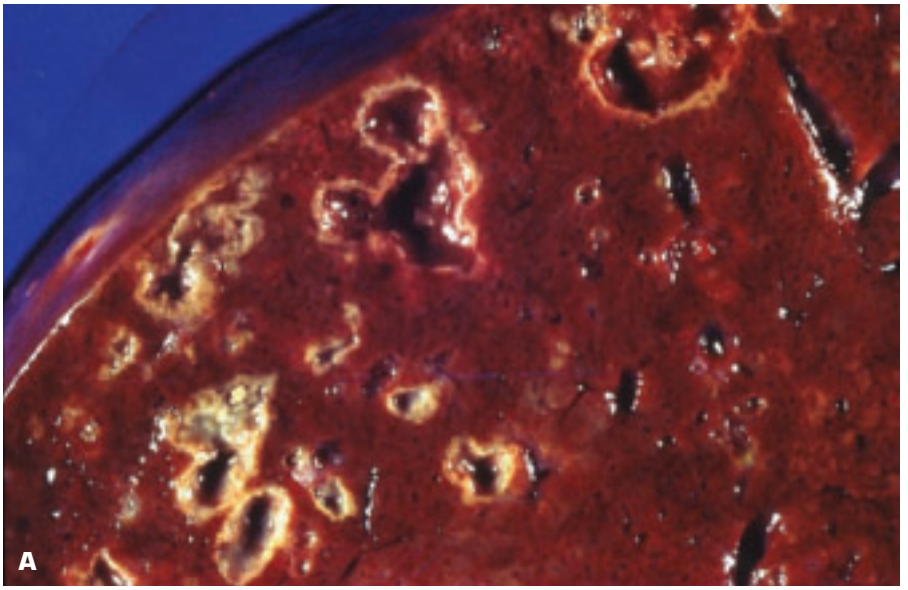

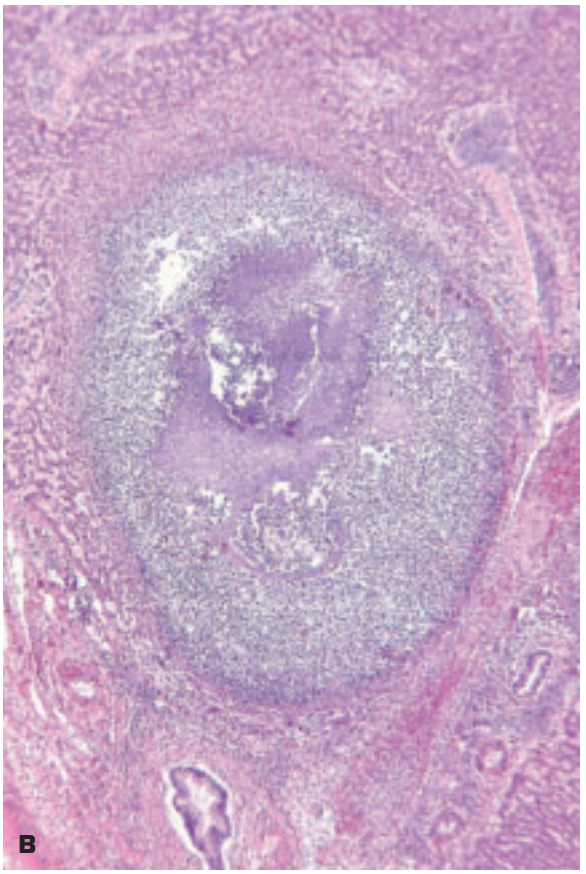

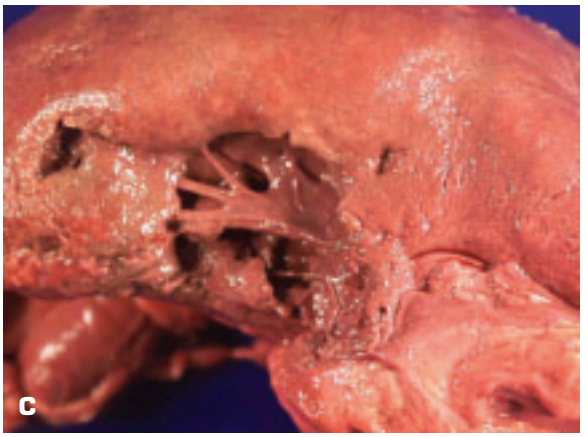

4-3. A. Multiple abscesses within the liver secondary to portal pyemia derived from a septic focus in the portal vein drainage territory. **B.** Histologically, the abscess comprises central remnants of necrotic liver tissue interspersed and surrounded by polymorphonuclear leucocytes. Outside this lies a zone of compressed liver parenchyma. **C.** The pus has been washed out of this large liver abscess to reveal blood vessels spanning the abscess cavity.

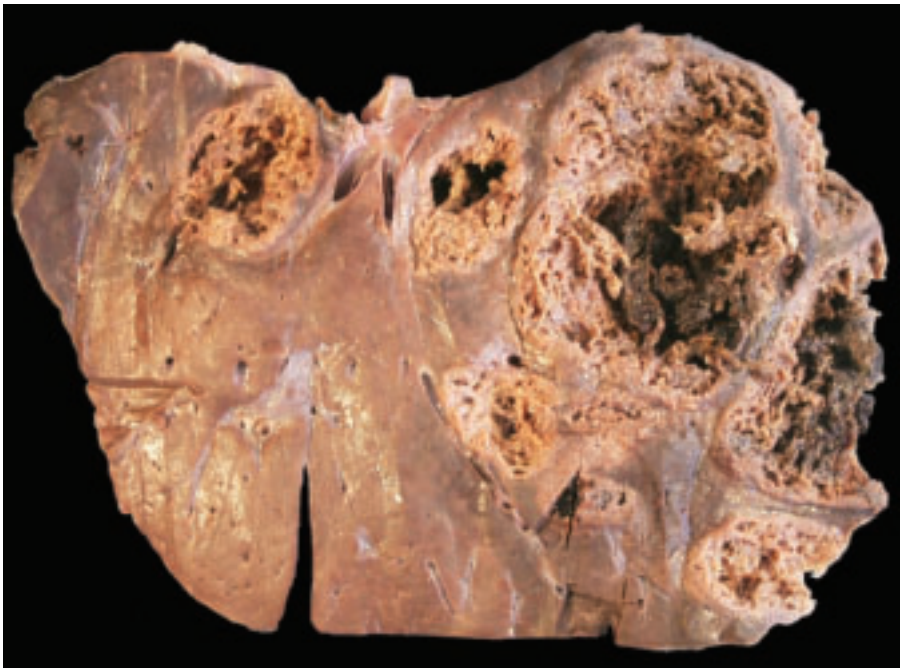

4-4. Multiple amebic abscesses of the liver show the characteristic roughened, necrotic inner lining to the abscesses. Note the absence of signs of acute inflammation around the lesions because the amebae produce substances to reduce the inflammatory response. Hemorrhage into an abscess may produce "anchovy sauce" pus. The abscesses may erode through the diaphragm to produce intrapulmonary lesions or pericardial tamponade. (Photo courtesy of Dr. R.M. Bowen.)

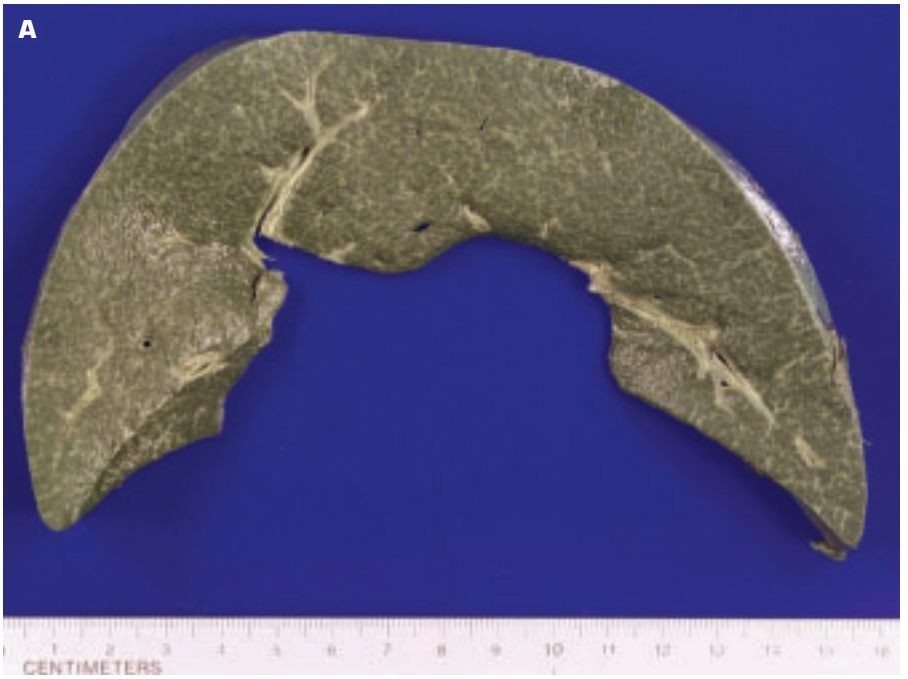

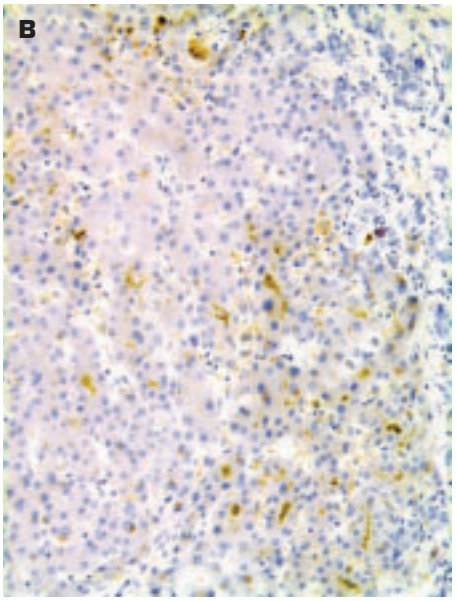

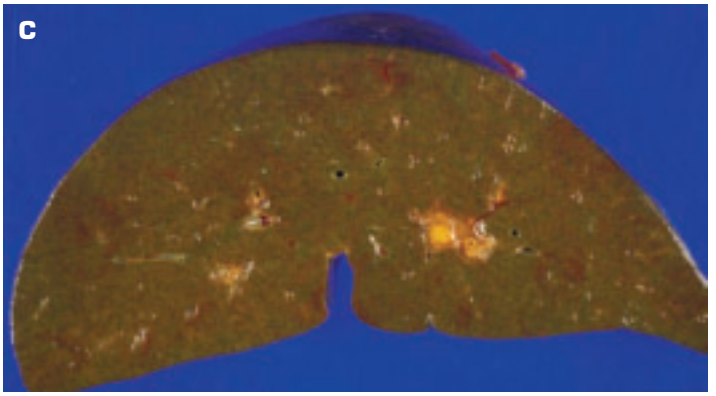

4-5. Intrahepatic cholestasis. The green color in both macroscopic pictures (A and C) is due to the reduction of bilirubin to biliverdin by the formaldehyde fixative. **A.** Total parenteral nutrition-induced hepatic cholestasis and hepatic fibrosis, which might have proceeded to cirrhosis had the patient survived longer. **B.** The bile stasis, as evidenced by bile filled canaliculi, is well demonstrated histologically in this hematoxylin-only stained section. **C.** Cholestasis due to systemic bacterial infection. Multiple focal yellow granulomata due to histoplasmosis are also present.

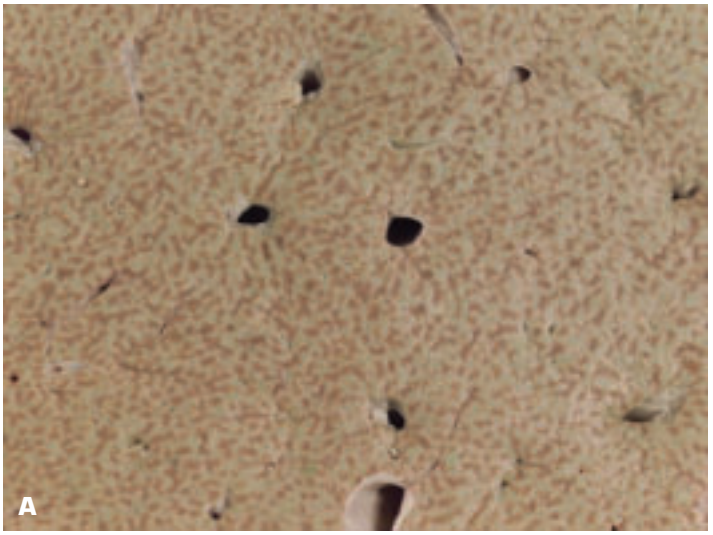

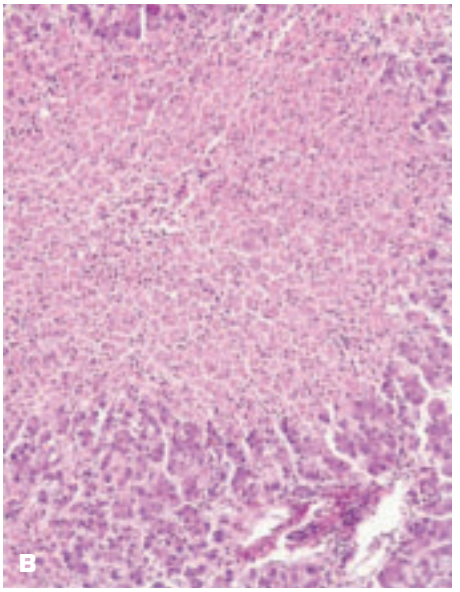

4-6. Acetaminophen toxicity. This young man took large doses of acetaminophen in combination with excessive ethanol – a lethal combination because chronic ethanol consumption increases the 3A4 isoform of cytochrome P450, which increases the metabolism of acetaminophen. **A.** Close-up view of liver shows centrilobular zonal necrosis (paler green areas), with sparing of the peripheral portions of the lobules (brown-colored areas). **B.** Histology shows that centrilobular zonal necrosis has expanded to affect much of this lobule.

4-7. Sclerosing cholangitis in a patient with ulcerative colitis. Note the marked hepatic fibrosis that has occurred secondary to fibrous obliteration of many of the intra- and extrahepatic bile ducts. Cholestasis is a prominent feature.

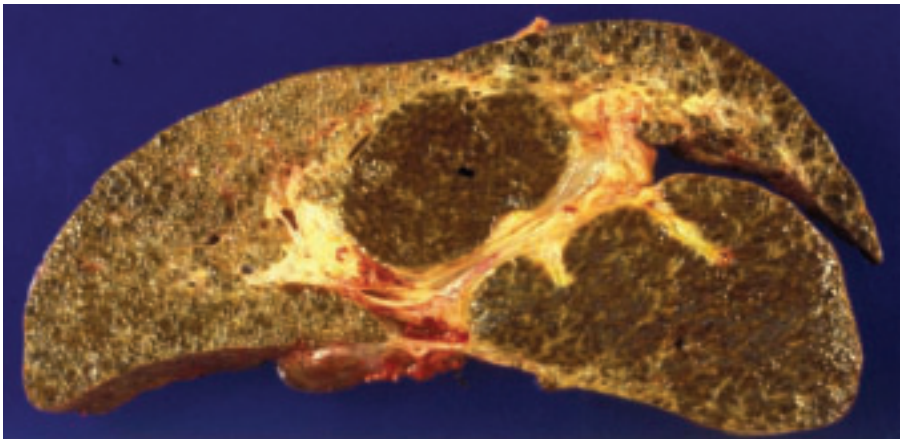

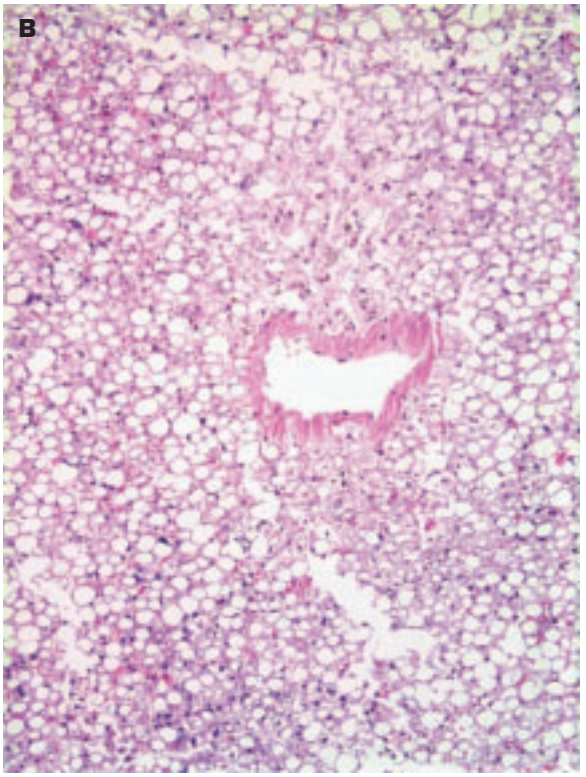

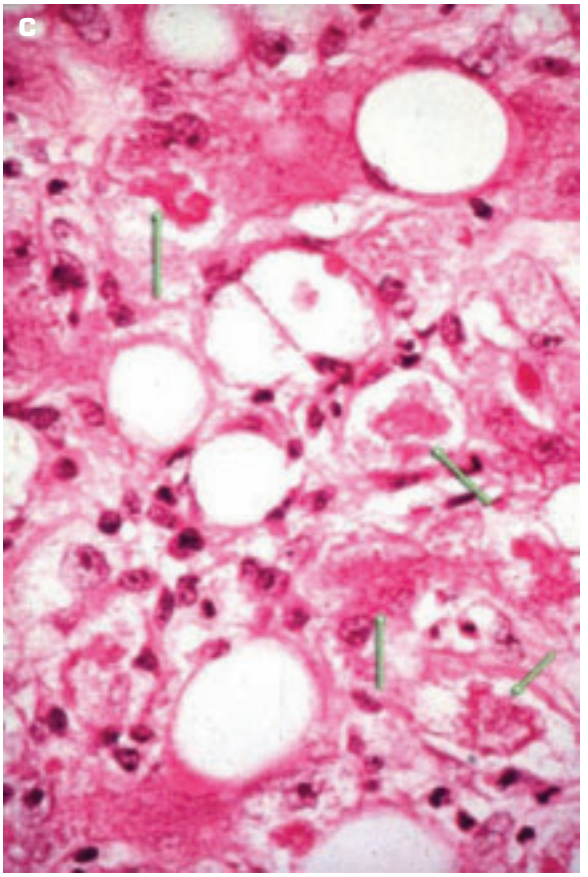

4-8. Precirrhotic alcoholic liver disease. **A.** Extremely fatty liver (steatosis) in a chronic alcoholic. **B.** Microscopically, the hepatocytes look more like adipocytes. **C.** Intracellular deposits of Mallory's alcoholic hyaline are indicated by arrows.

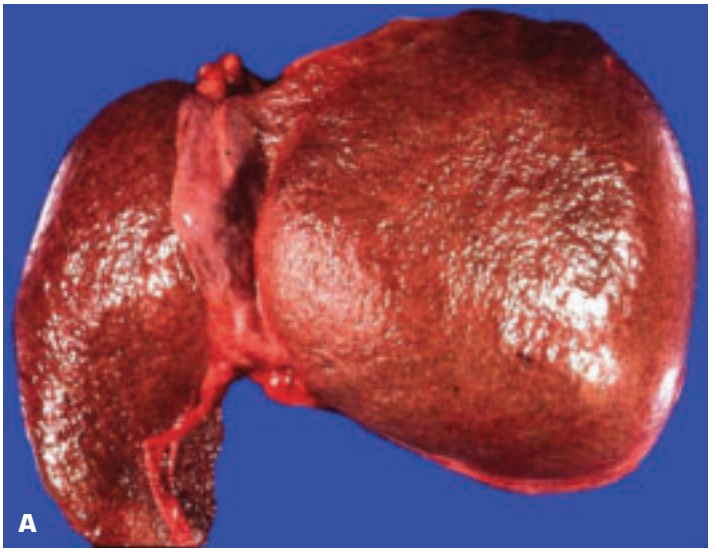

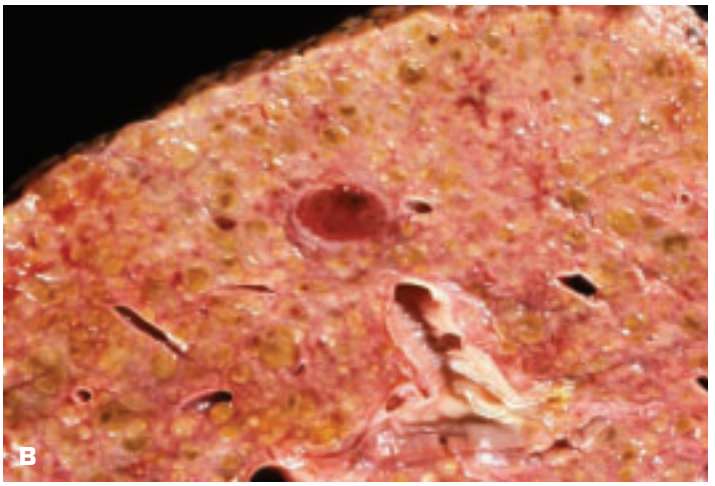

4-9. Micronodular cirrhosis of the liver. **A.** Note the uniformly fine, nodular upper surface of the liver. **B.** Cut surface of fixed liver shows regenerating nodules that are less than 3 mm in diameter. Some nodules are bile stained due to the nodules failing to attain an adequate connection to the biliary drainage system.

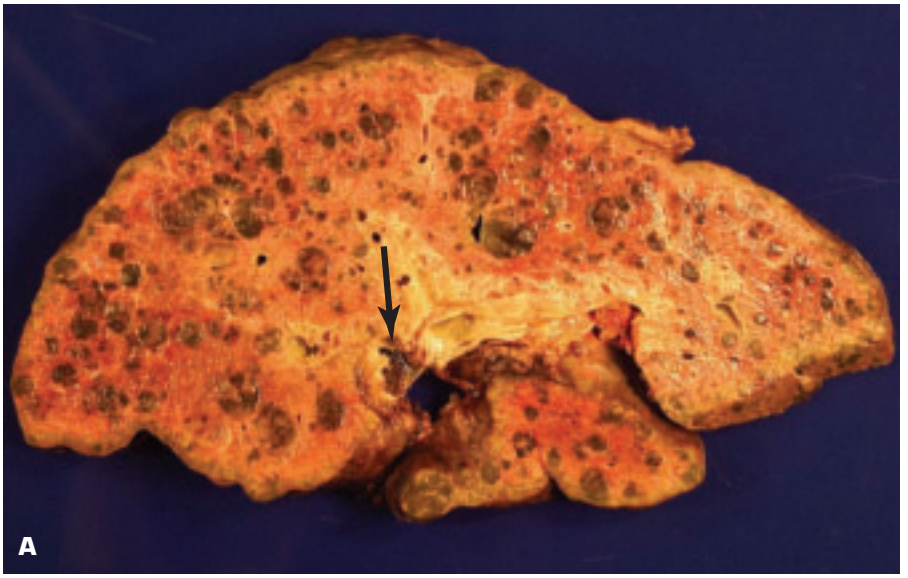

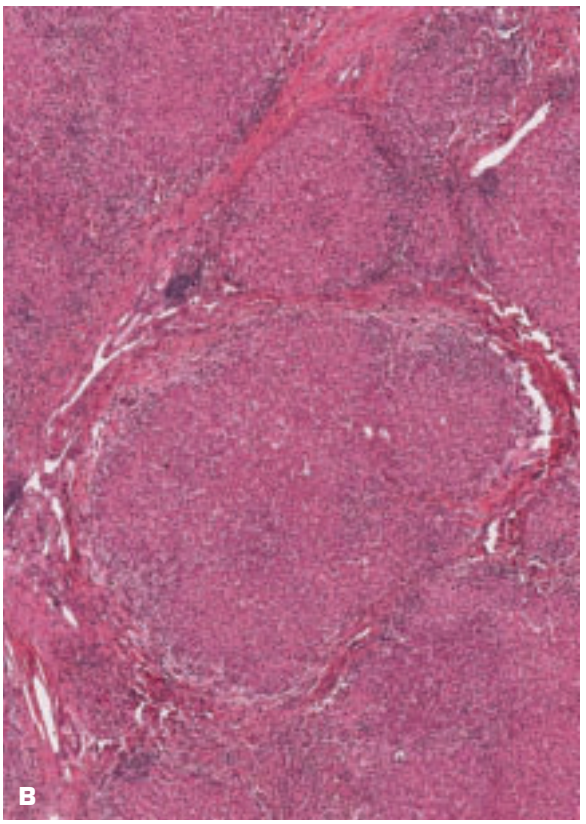

4-10. A. Mixed micro- and macronodular cirrhosis of the liver in a patient with hepatis virus C infection. A transvenous intrahepatic portosystemic shunt (*arrow*) is present in the transected portal vein at the porta hepatis. **B.** Histology shows cirrhosis with evidence of persistent chronic hepatitis (numerous lymphocytes are present in the portal tracts).

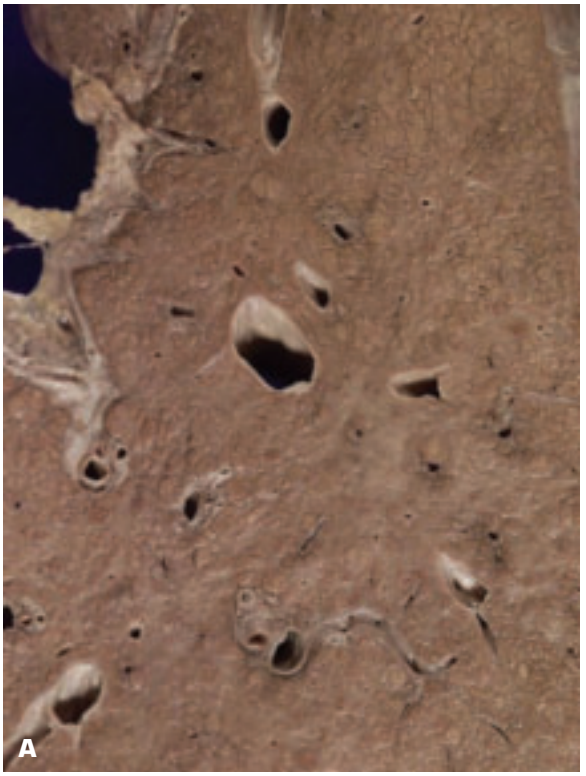

4-11. Patient with hemochromatosis (bronzed diabetes). **A.** Hemochromatosis-induced micronodular cirrhosis due to defective intestinal mucosal block for iron absorption. The liver has a distinctly brown color due to excessive deposition of hemosiderin within the hepatocytes. **B.** Perl's Prussian blue stain shows excessive intrahepatic iron deposits.

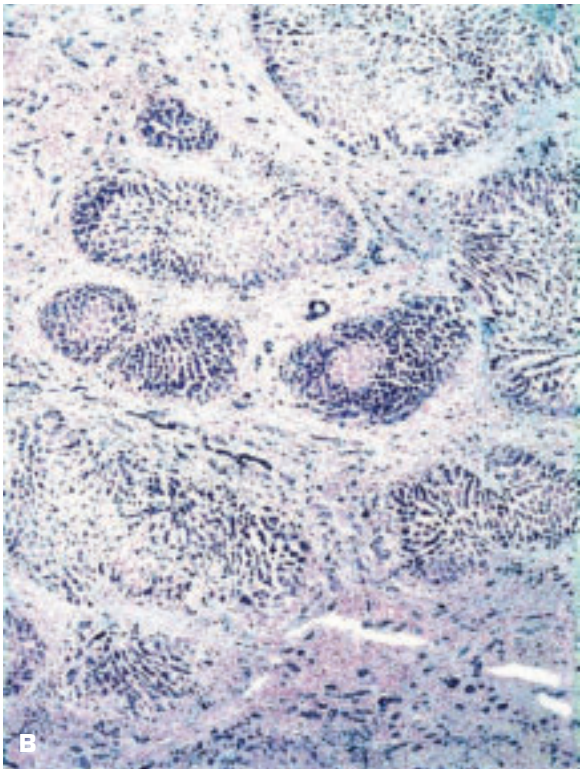

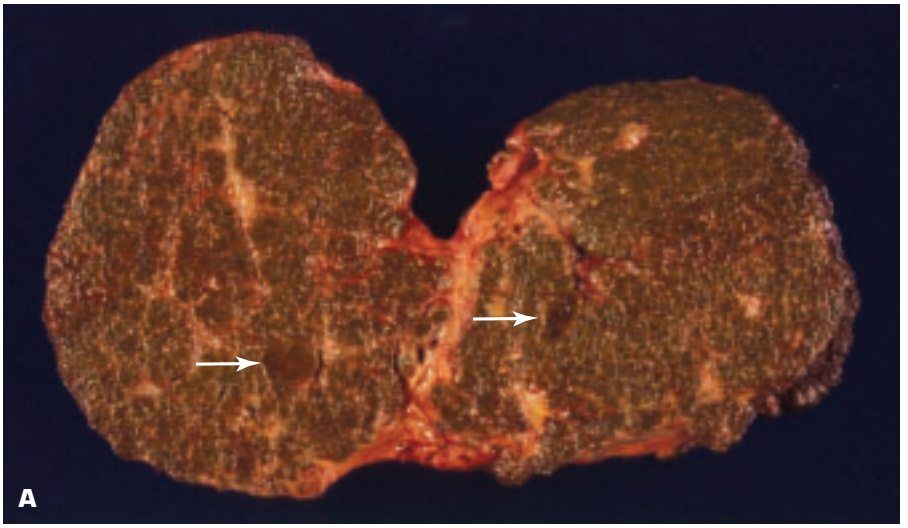

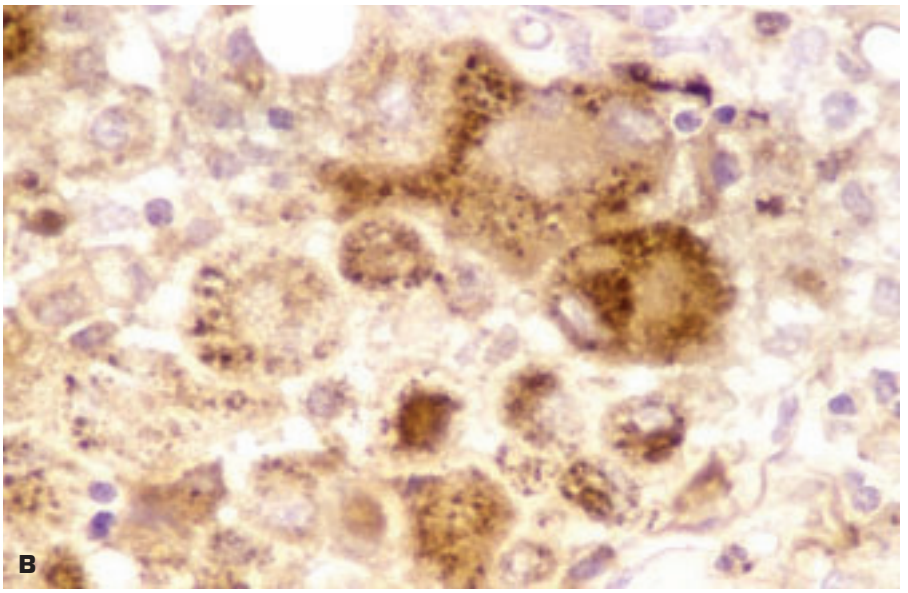

4-12. Patient with an alpha-1-antitrypsin deficiency. **A.** Micronodular cirrhosis of the liver with two larger nodules (*arrows*) of early, multicentric hepatocellular carcinoma. **B.** Immunoperoxidase staining reveals excessive accumulation of alpha-1-antitrypsin within hepatocytes due to difficulty with its exosecretion from these cells.

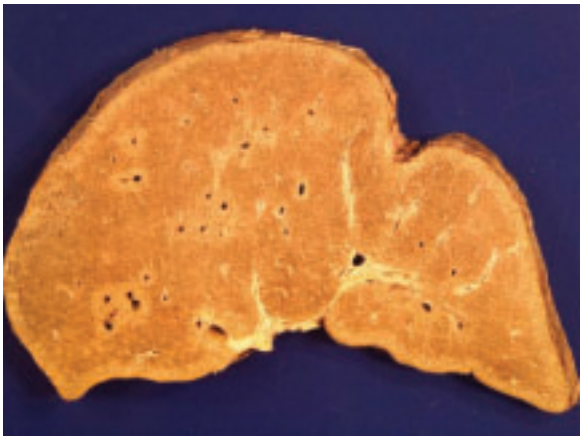

4-13. Micronodular cirrhosis in a patient with protoporphyria.

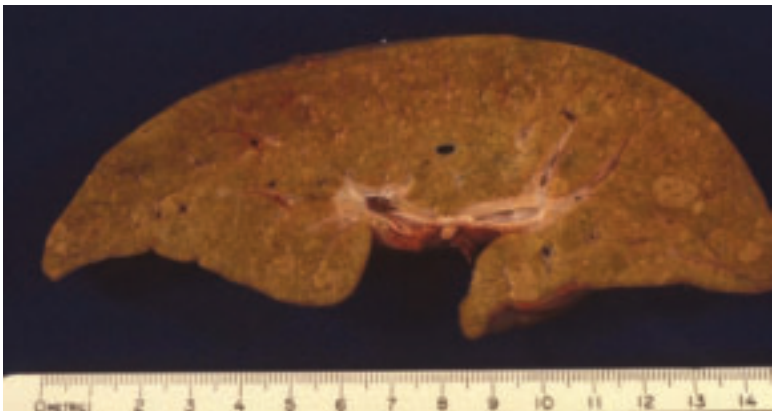

4-14. Mixed micro- and macronodular cirrhosis in a patient with tyrosinemia.

4-15. Close-up view of inferior hepatic surface showing mixed micro- and macronodular cirrhosis. Micronodular cirrhosis tends in time to become converted into a macronodular form. Macronodular cirrhosis may also follow submassive necrosis of the liver.

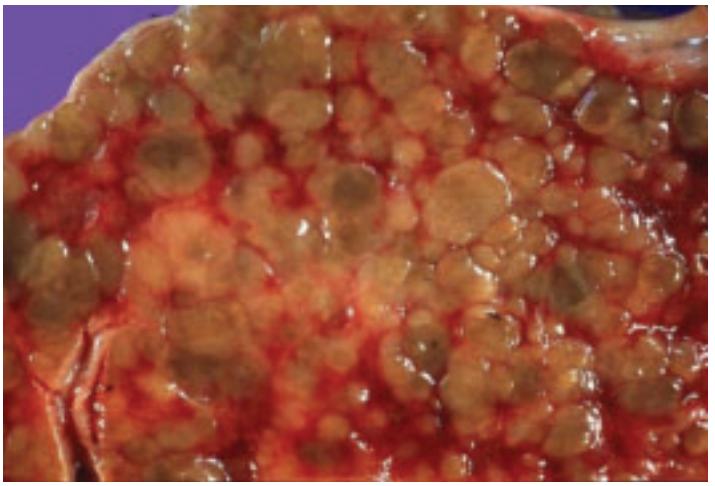

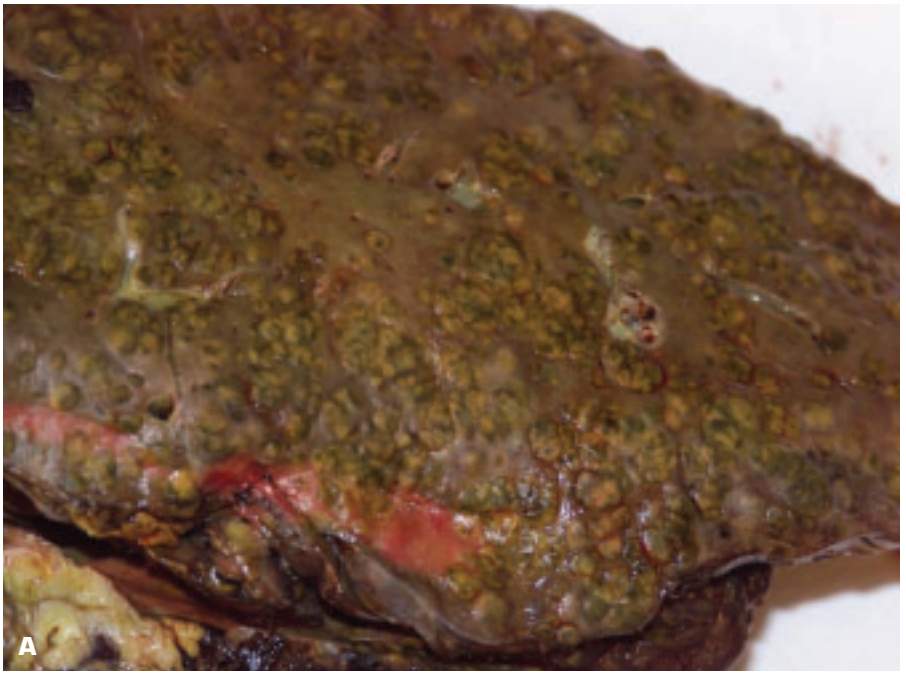

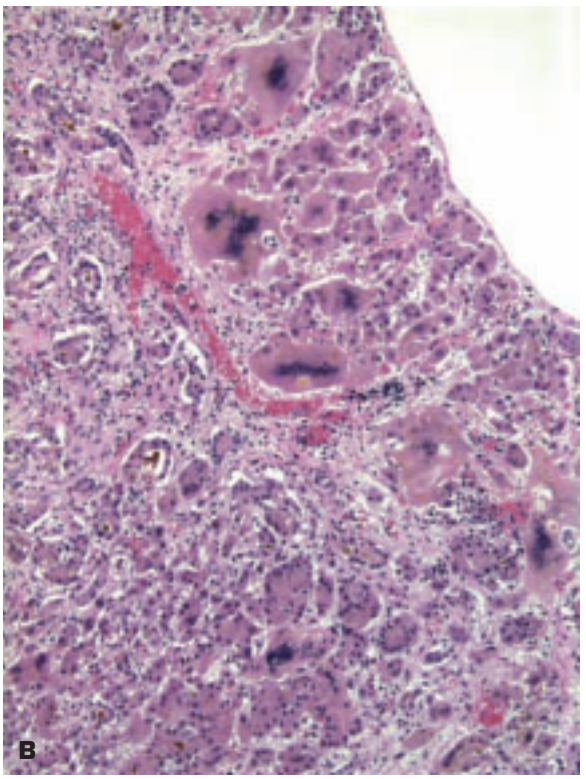

4-16. A. Submassive necrosis of the liver is evolving into macronodular cirrhosis. **B.** Histology of postnecrotic regeneration of the liver 16 days after submassive necrosis. Some of the regenerating hepatocytes appear enlarged and atypical.

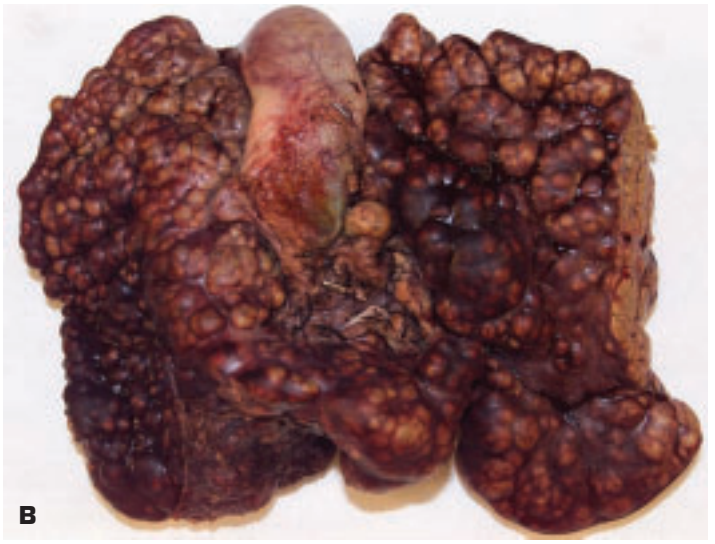

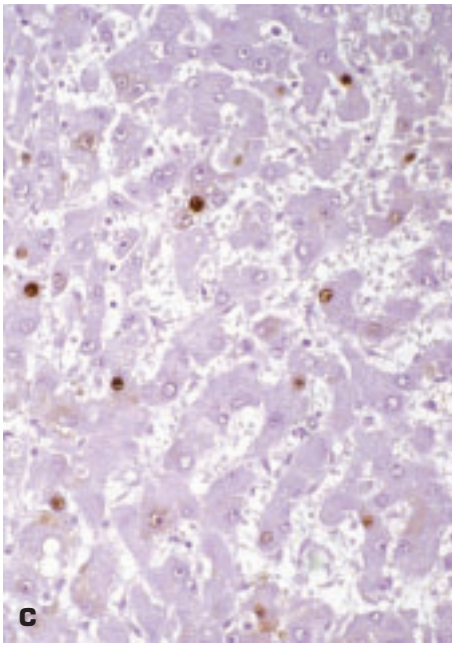

4-17. A and B. Macronodular cirrhosis of the liver in two patients with hepatitis B virus infection. **C.** Positive immunoperoxidase staining for hepatitis B core antigen in the liver.

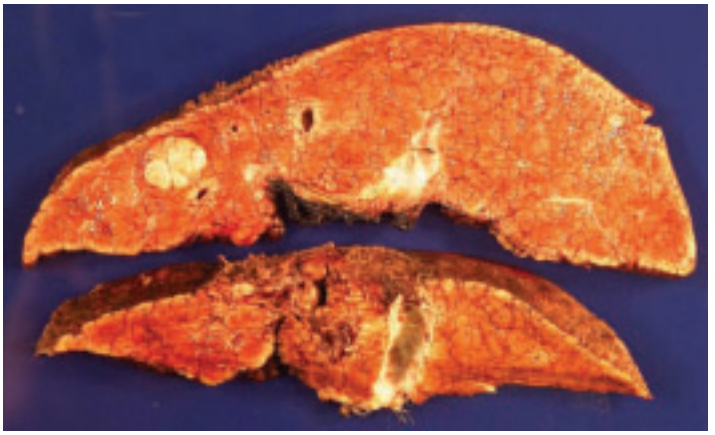

4-18. Macronodular cirrhosis complicated by a hepatocellular carcinoma in a patient with chronic hepatitis B infection. A bisected transvenous intravascular portosystemic shunt is observed in the lower liver slice.

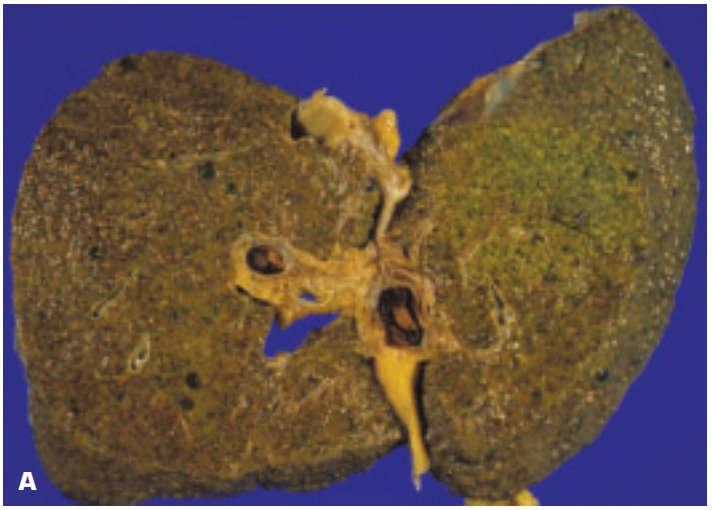

4-19. A. Portal vein thrombosis complicating micronodular cirrhosis. **B.** Histology shows an early organizing thrombus within the portal vein. A totally recanalized thrombus is referred to as cavernous transformation of the portal vein.

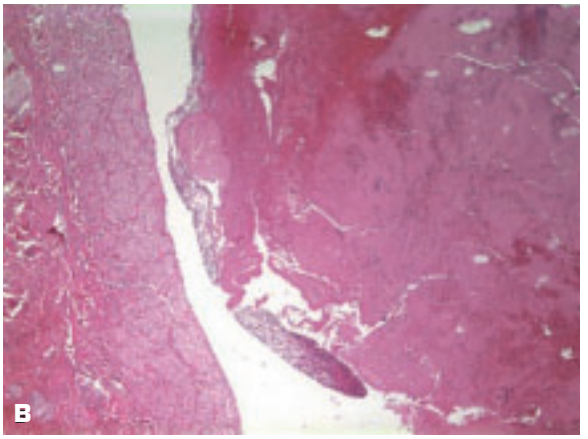

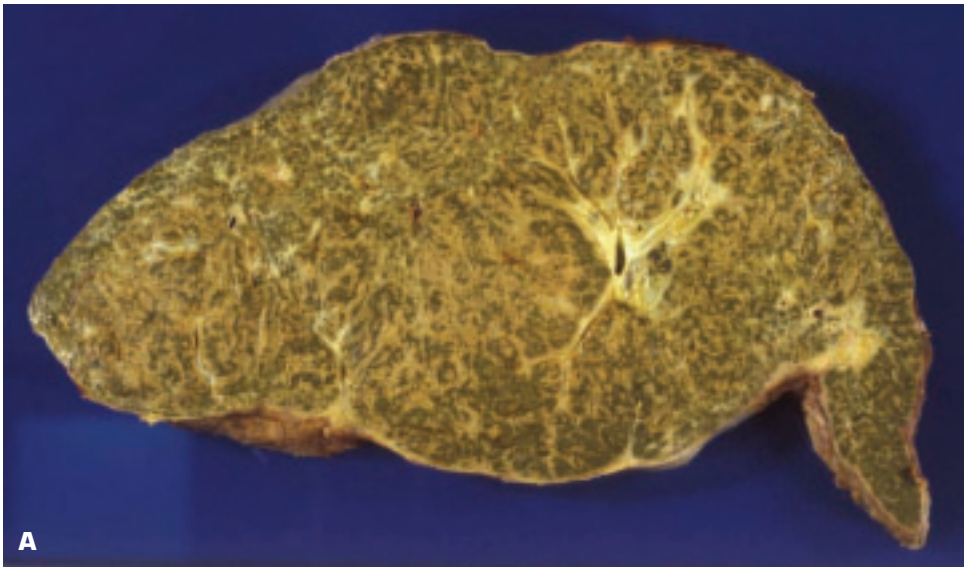

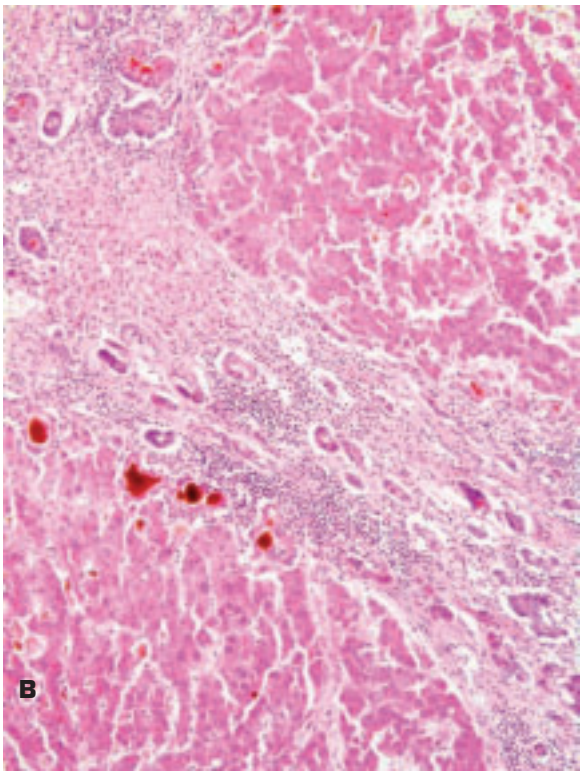

4-20. A. Biliary cirrhosis due to long-standing obstruction to biliary flow. **B.** Cirrhosis and marked obstruction to bile flow is noted histologically.

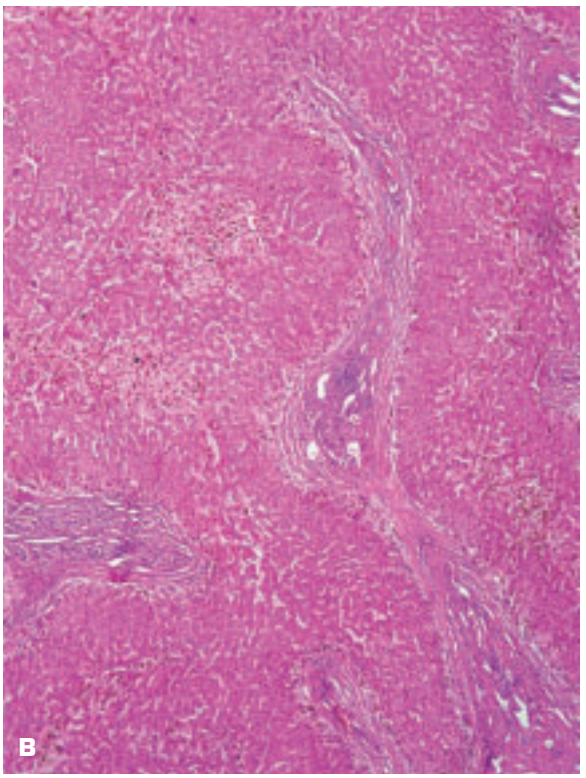

4-21. A. Congenital extrahepatic biliary atresia has led to incipient cirrhosis of the liver in an infant. **B.** Histology shows fibrosis linking portal tracts and marked centrilobular cholestasis.

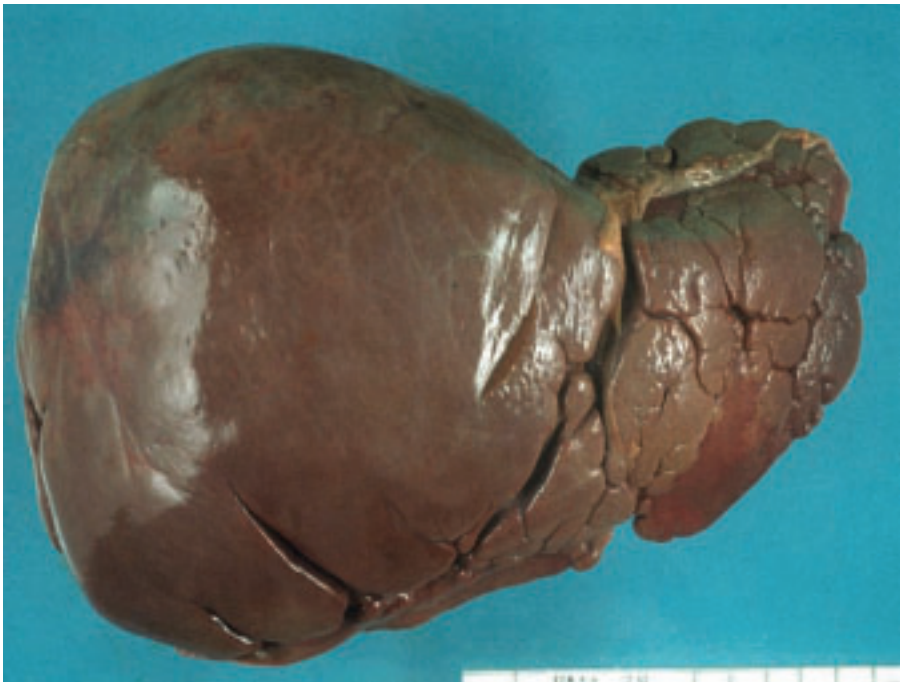

4-22. Hepar lobatum of the liver. Healing of multiple gummata of tertiary syphilis has produced pseudolobulation of the liver due to in-drawing of the capsule by the fibrous scars.

4-23. A. Nutmeg liver of chronic passive congestion. **B.** Histology shows that marked centrilobular congestion has led to centrilobular zonal necrosis.

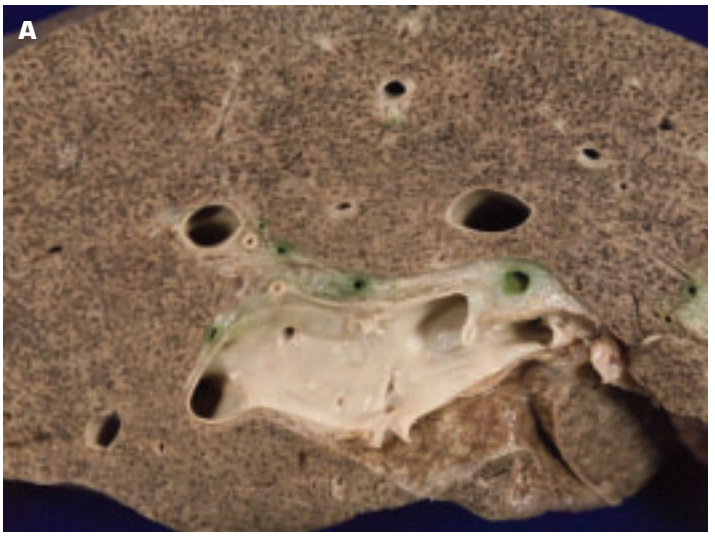

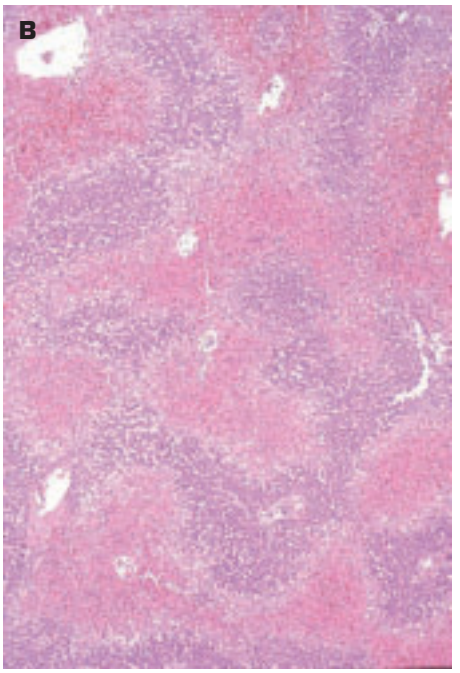

4-24. A. Cardiac "cirrhosis" of the liver comprises hepatic fibrosis and signs of regenerative activity secondary to long-standing, right-sided cardiac failure. **B.** Histology shows hepatic fibrosis without features of true cirrhosis.

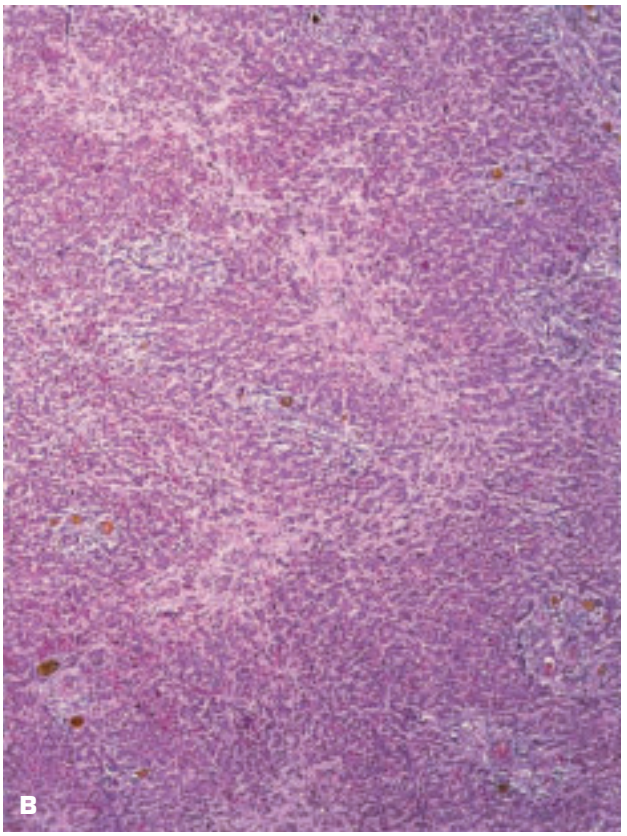

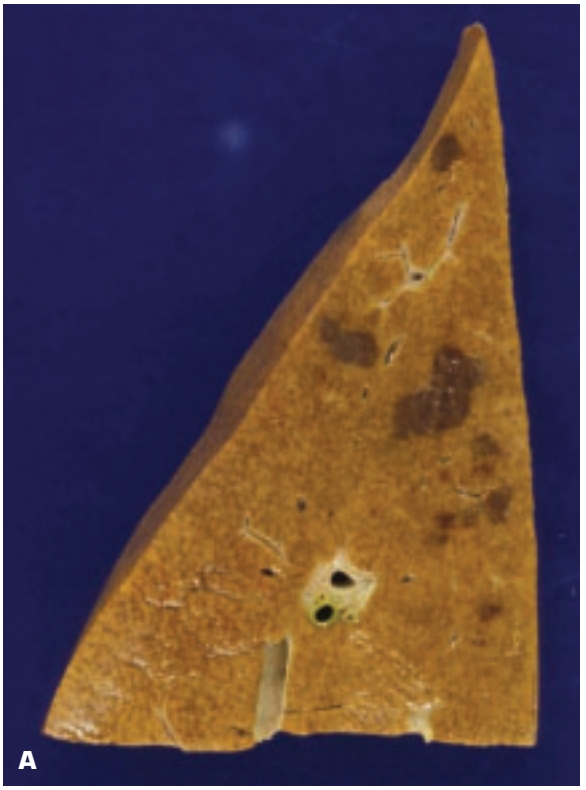

4-25. A. Focal areas of increased congestion of the liver, plus parenchymal atrophy due to localized venous obstruction, are termed *Zahn infarcts*. **B.** Histology shows intense congestion of the hepatic sinusoids, as well as tissue atrophy with some disruption of the hepatic plates in areas secondary to the venous obstruction.

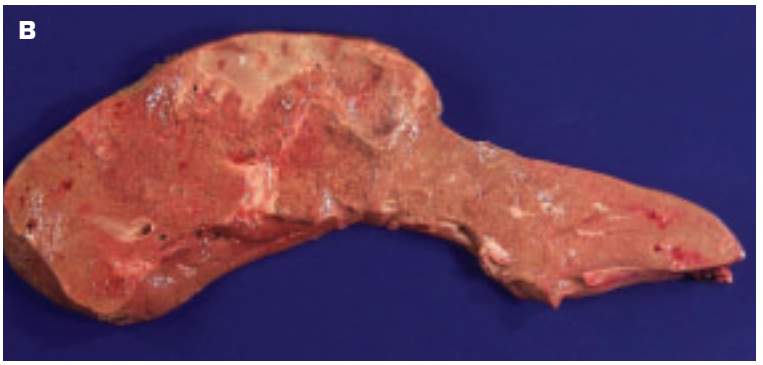

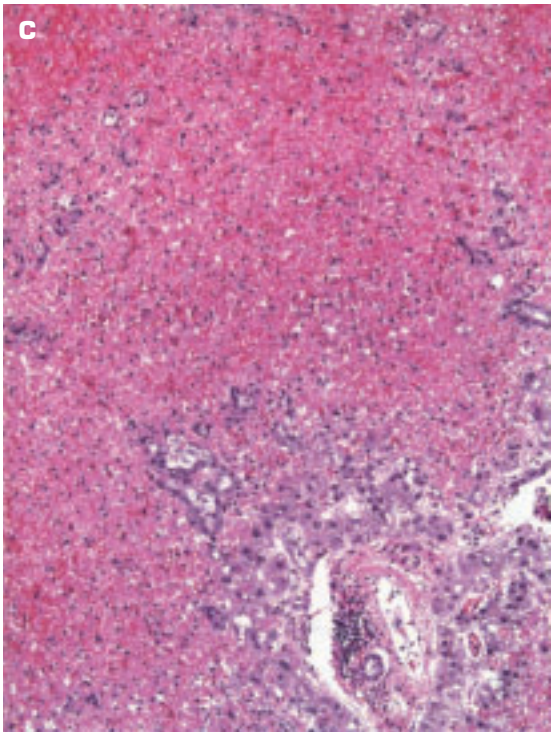

4-26. A. Recent massive ischemic infarction (*pale zones*) of large areas of the liver in a young child who suffered severe hypotension while undergoing cardiac surgery. **B.** Well-established, pale areas of infarction of the liver in an adult. **C.** Histology of recent ischemic necrosis of the liver showing minimal periportal survival of hepatic parenchyma. The dilated sinusoids give a spurious appearance of hemorrhage.

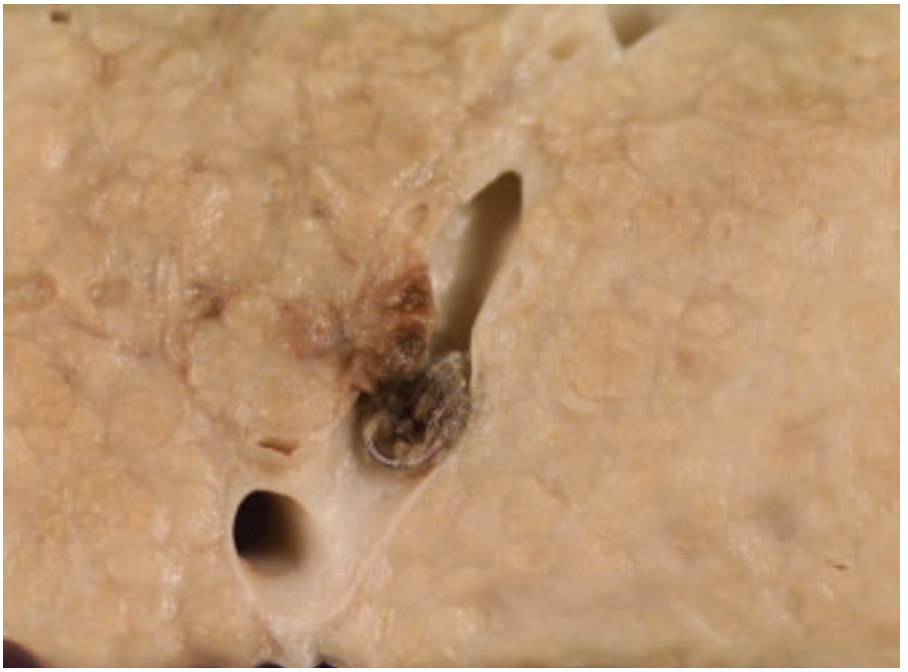

4-27. A cirrhotic patient with bleeding from an intrahepatic branch of the portal vein had this intravascular coil inserted by a radiologist to try and stop the bleeding. The thrombotic material attached to the coil is intentional and furthers the therapeutic occlusion of the vessel.

4-28. Nodular regenerative hyperplasia of the liver. Note the multiple indistinct, pale-colored nodules. Such patients may develop portal hypertension in the absence of cirrhosis.

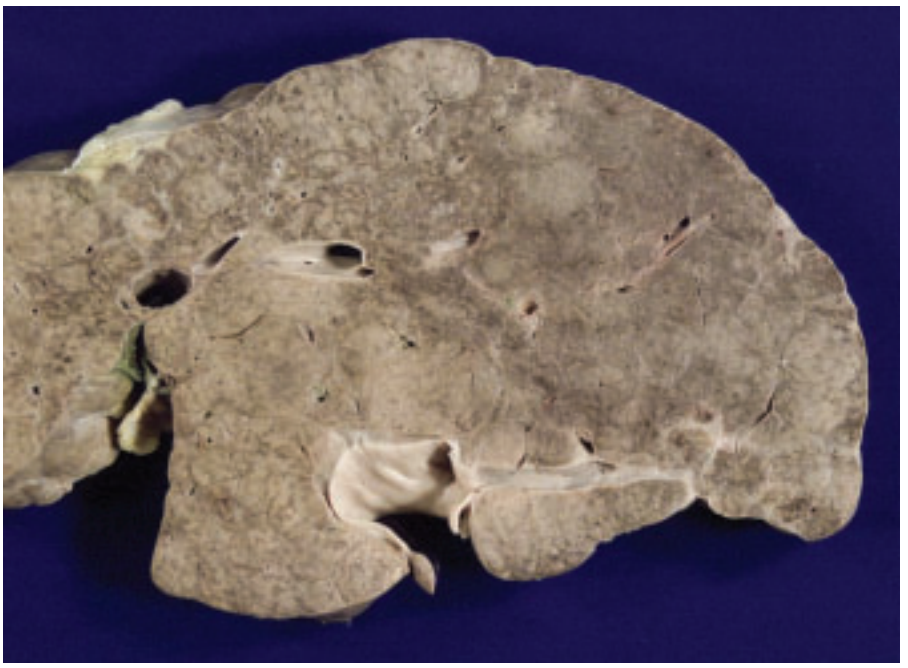

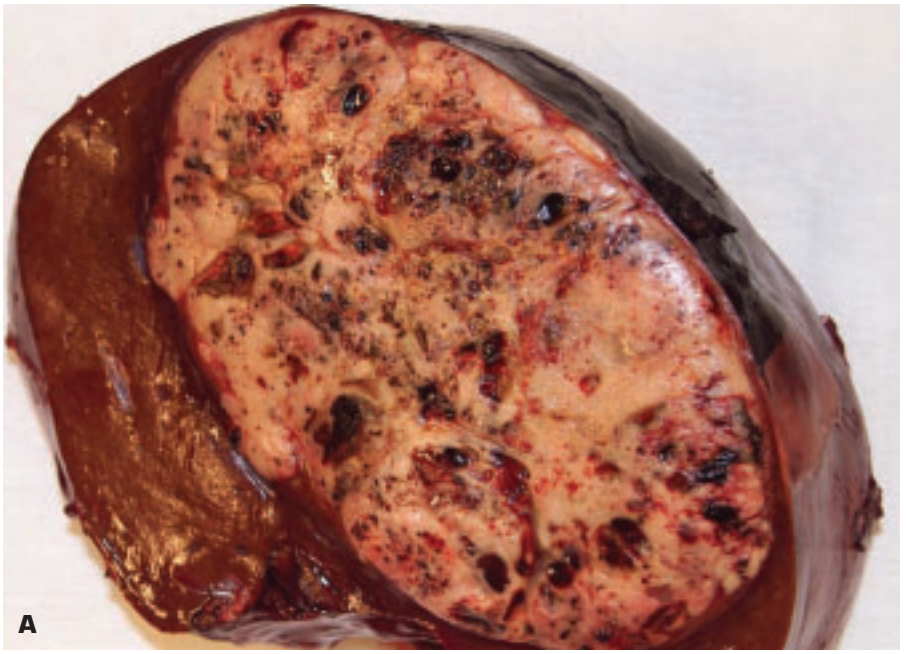

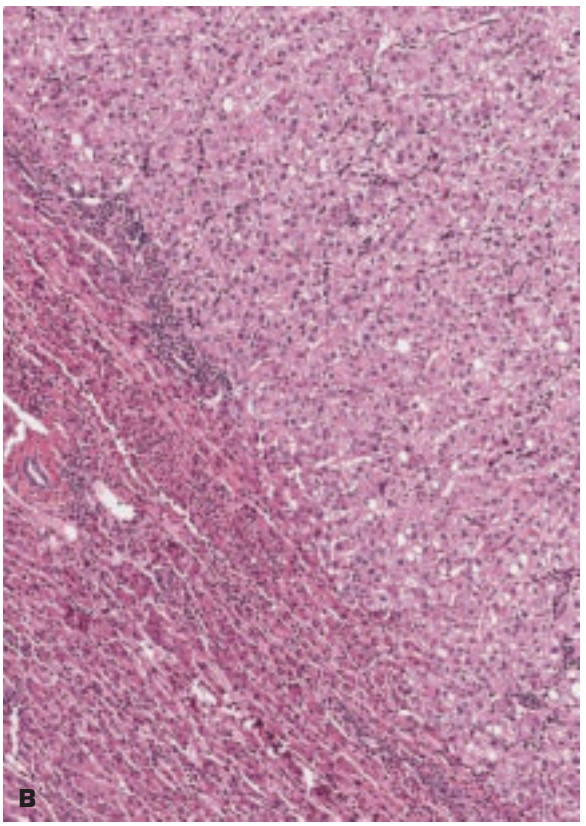

4-29. A. Large yellow-white hepatocellular carcinoma shows focal areas of hemorrhage and necrosis on its cut surface that bulges above the adjacent compressed liver tissue. Note the absence of cirrhosis in the latter. **B.** Histology of moderately differentiated hepatocellular carcinoma (*top right*) shows the malignant cells to resemble normal liver cells (*lower left*) in appearance, but they are larger in size and more atypical looking.

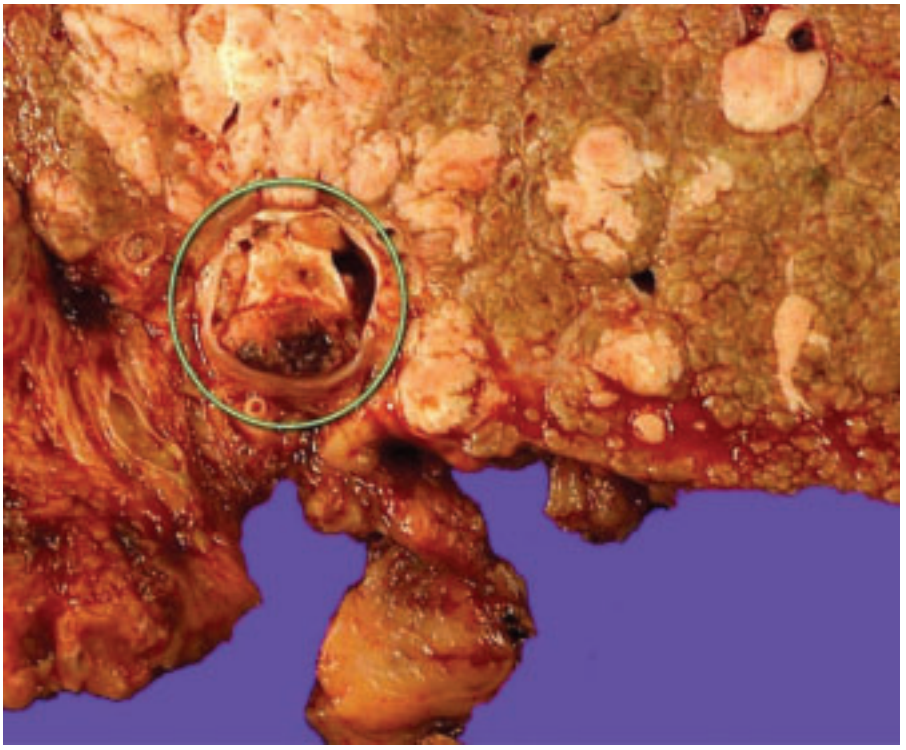

4-30. Hepatocellular carcinoma has invaded into and is growing within the portal vein (*circled*).

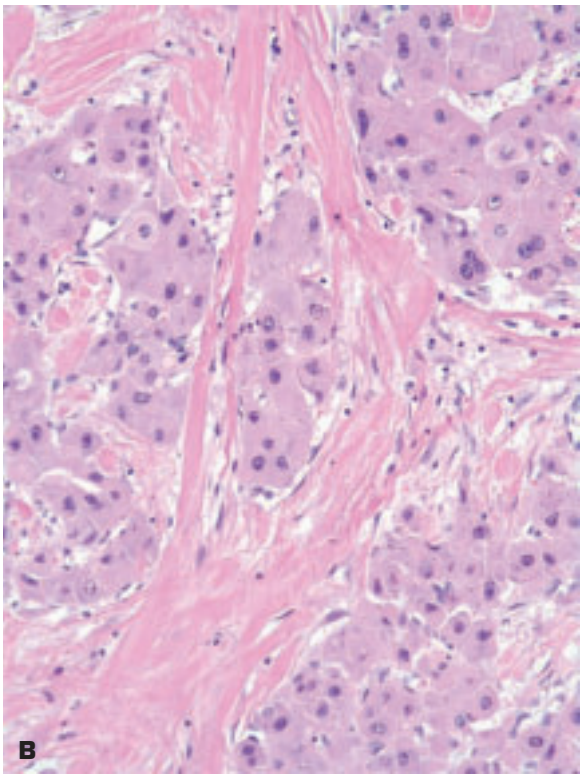

4-31. A. Bisected fibrolamellar carcinoma of the liver shows central degeneration and scarring. This tumor occurs in younger patients without cirrhosis and has a fairly good prognosis (50% cure rate). **B.** The histology of the fibrolameller carcinoma shows small groups of malignant oncocytic-looking hepatocytes surrounded by bands of fibrous tissue.

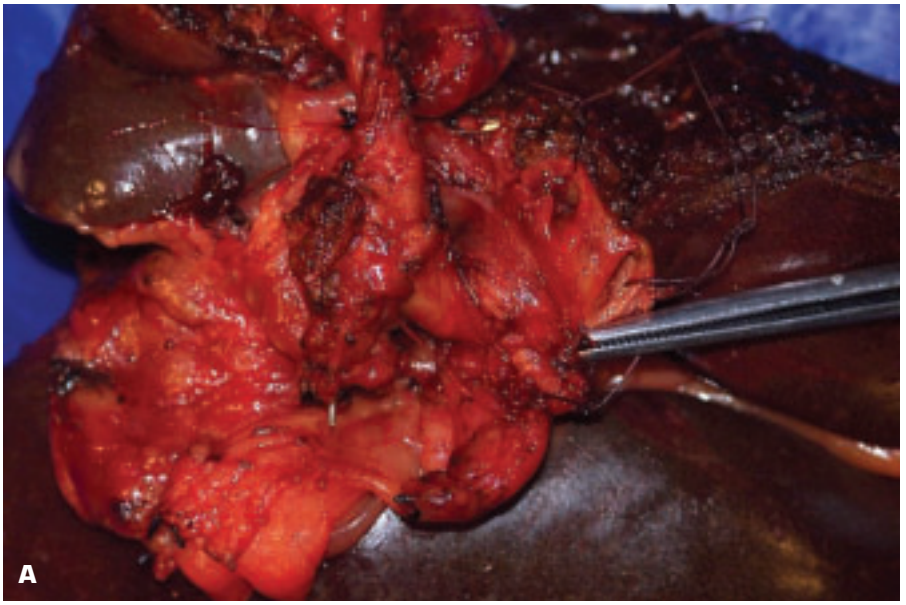

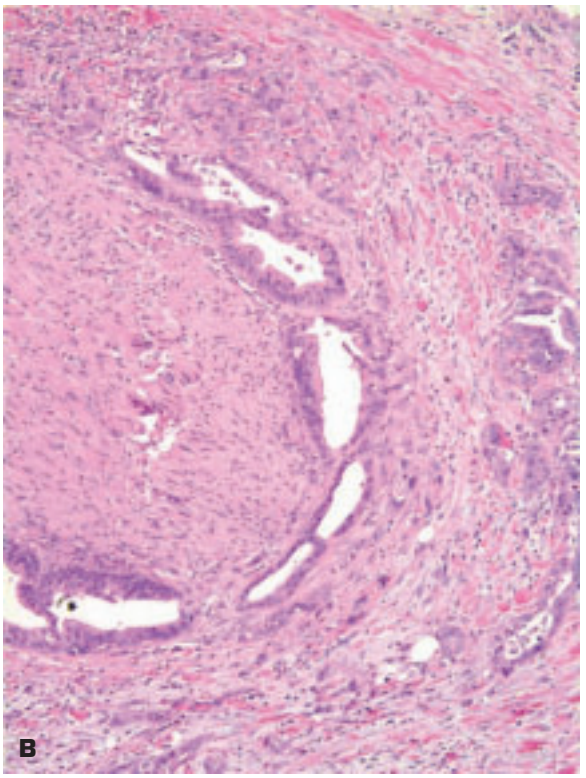

4-32. A. Cholangiocarcinoma (Klatskin tumor) is invading into the proximal portion of the hepatic duct in the porta hepatis. **B.** Histology shows a poorly differentiated adenocarcinoma within perineural lymphatics.

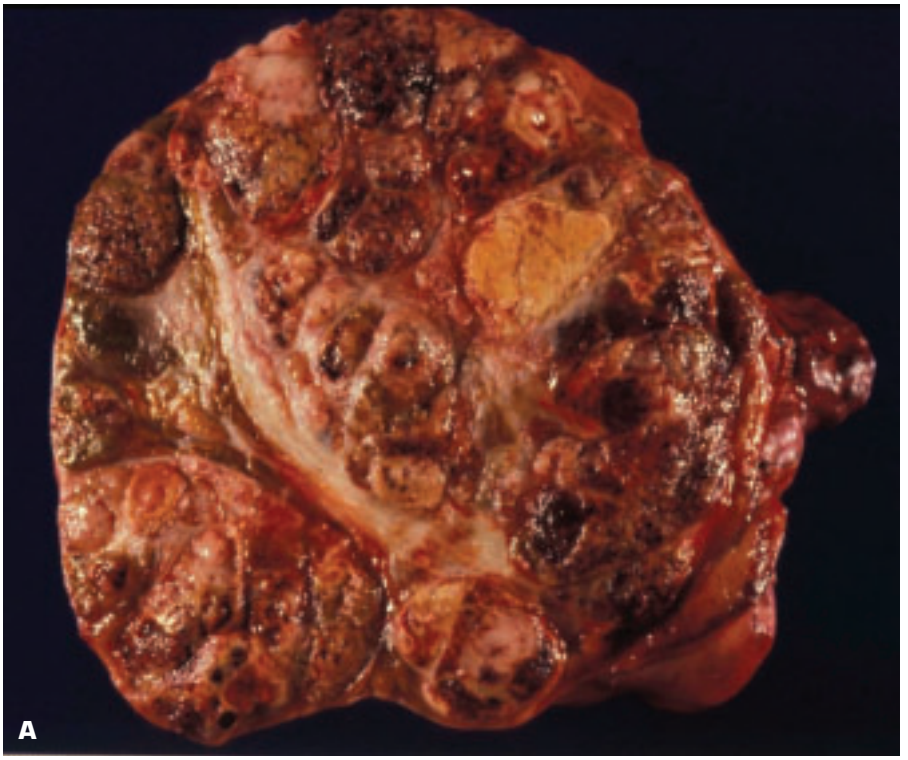

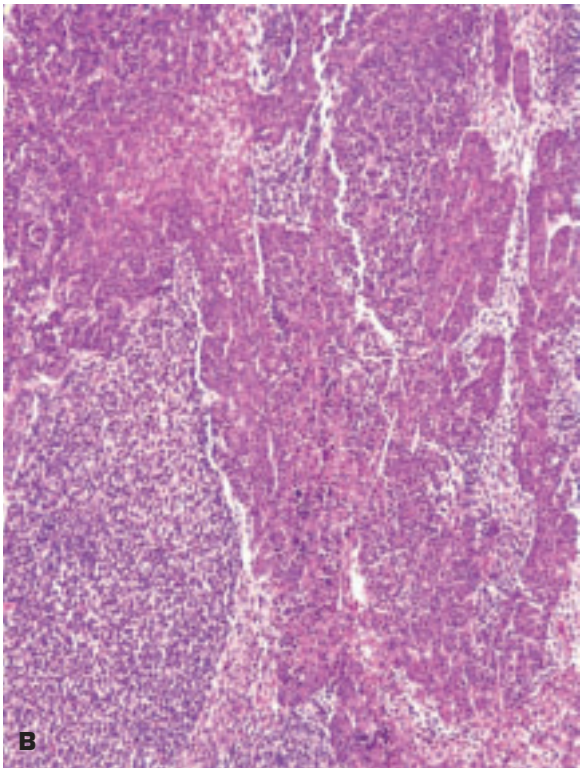

4-33. A. Hepatoblastoma of the liver presenting as a fleshy, focally hemorrhagic and necrotic solid tumor. **B.** Histologically, the tumor shows a biphasic pattern comprised of epithelial and mixed mesenchymal elements. Unlike a hepatocellular carcinoma, the epithelial cells of a hepatoblastoma are smaller than normal liver cells.

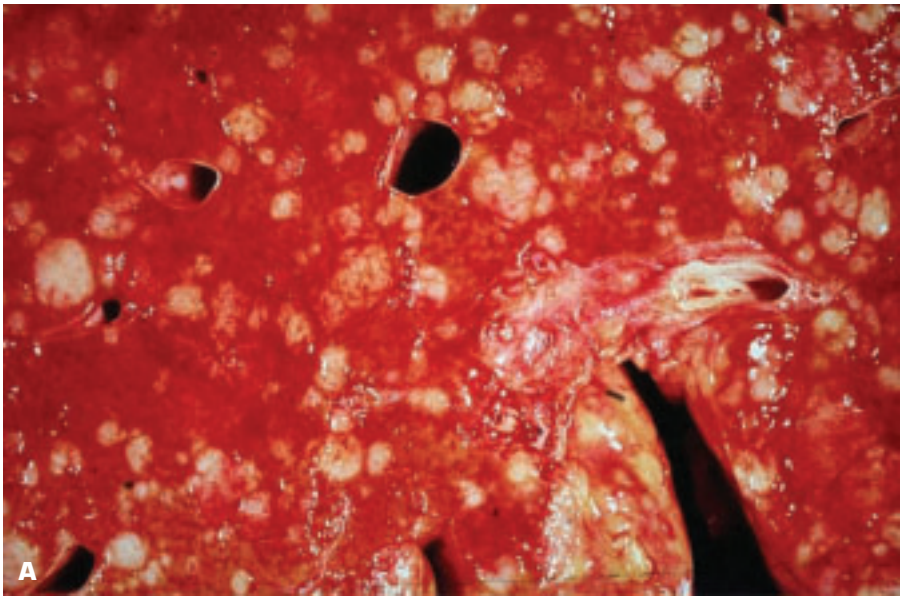

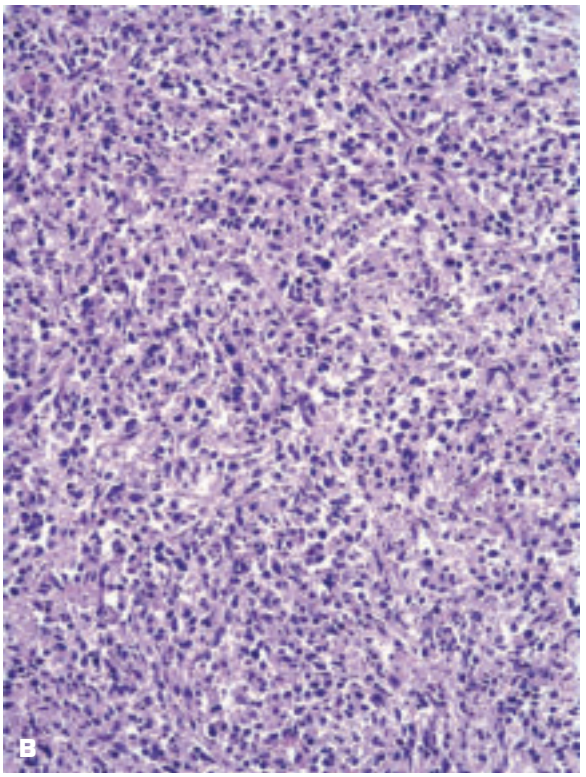

4-34. A. Metastatic lymphoma presenting as multiple variable-size white nodules in the liver. **B.** Histology shows a diffuse anaplastic large cell lymphoma.

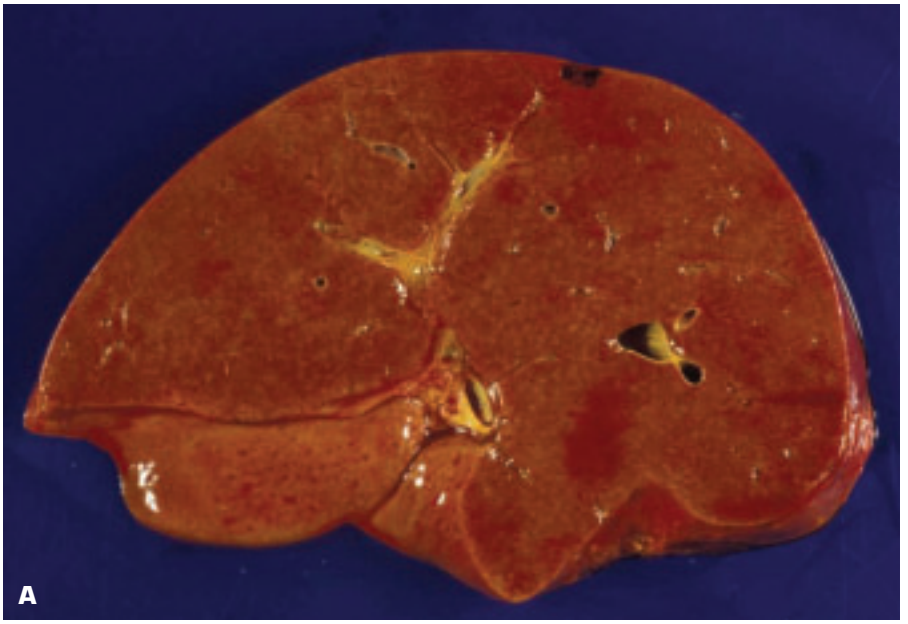

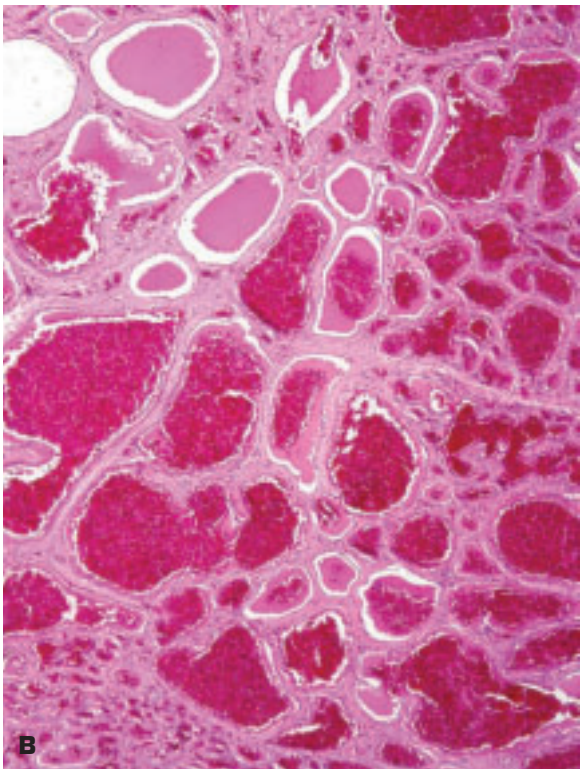

4-35. Hemangioma of the liver may show a range of appearances. **A.** Subcapsular (*top right*) cavernous hemangioma of liver. **B.** Cavernous hemangioma is characterized histologically by endothelial-lined vascular spaces that are much wider in diameter than capillaries. *(continued on next page)*

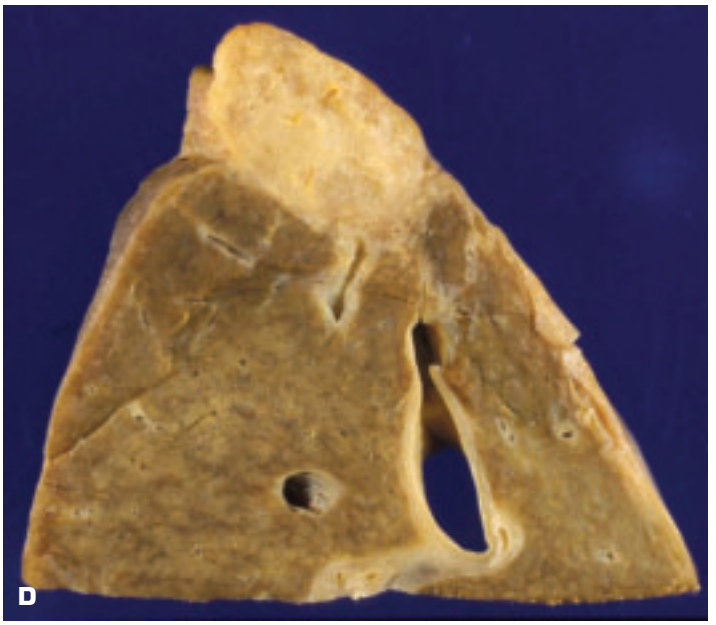

4-35. *(Continued)* **C.** Partially thrombosed cavernous hemangioma shows pale areas of organizing thrombus within the hemangioma. **D.** Old thrombosed, organized, and partially calcified cavernous hemangioma of the liver.

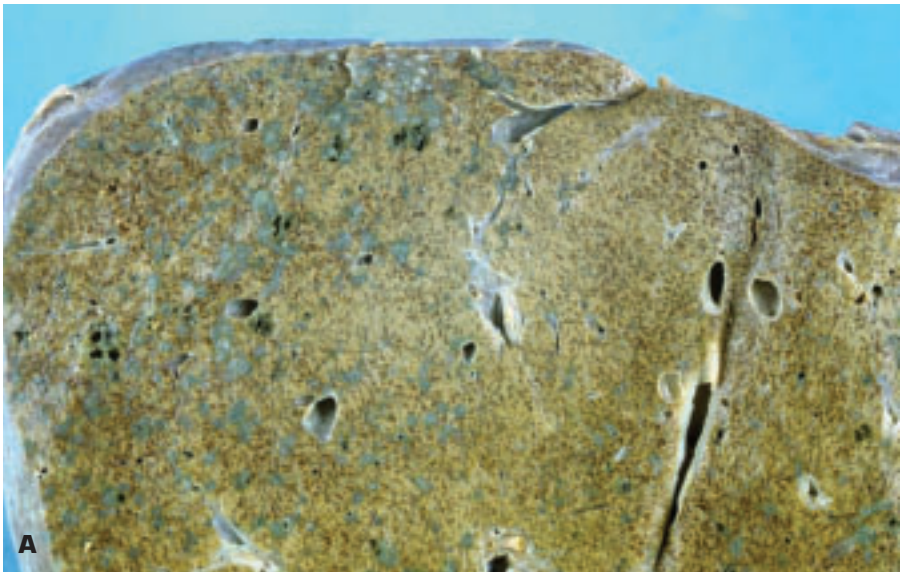

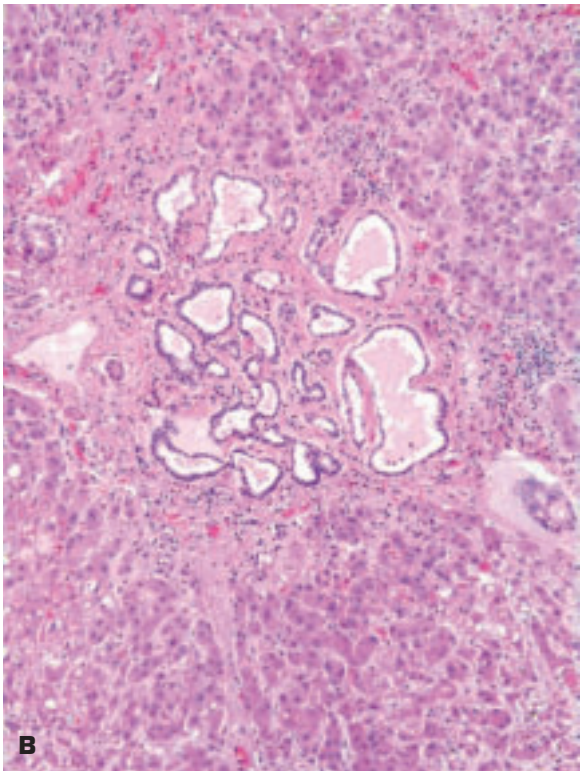

4-36. A. Multiple bile duct hamartomas (von Meyenburg complexes) presenting as numerous small, focal white nodules with some associated fibrous tissue. The liver also has an overall nutmeg pattern due to passive congestion. **B.** Histologically, the hamartoma comprises a localized collection of bile ductules in a loose connective tissue stroma. In a patient undergoing laparotomy for intraabdominal malignancy, the hamartomas may be biopsied for frozen section to exclude metastatic carcinoma. Polyarteritis nodosa may also lead to the formation of von Meyenburg complexes via liver ischemia, but the more usual effect on the liver is the production of multiple saccular aneurysms along the course of small arteries (see Fig. 4-70).

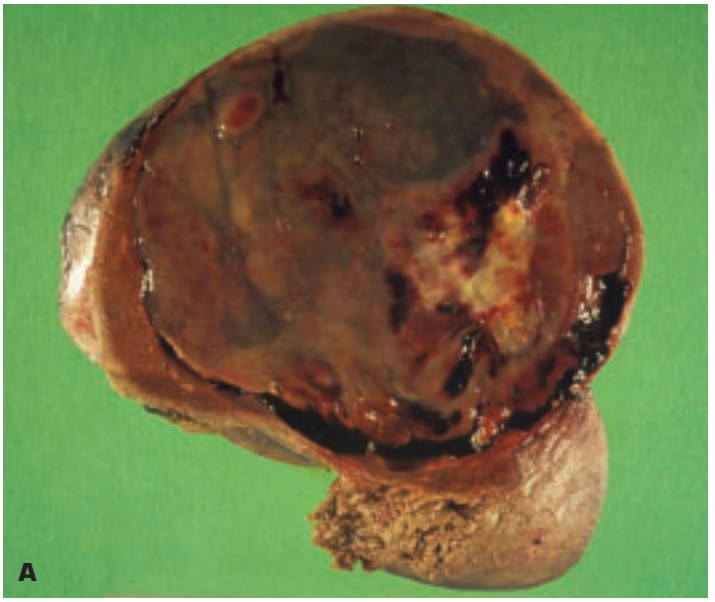

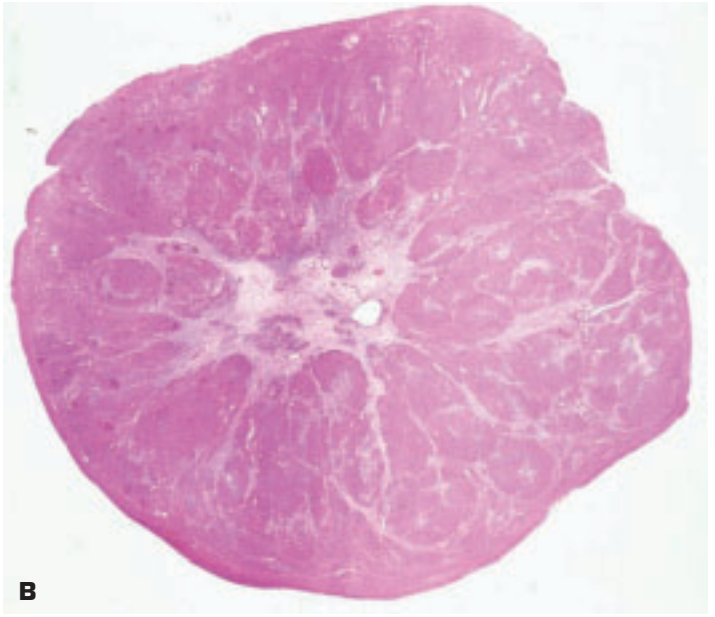

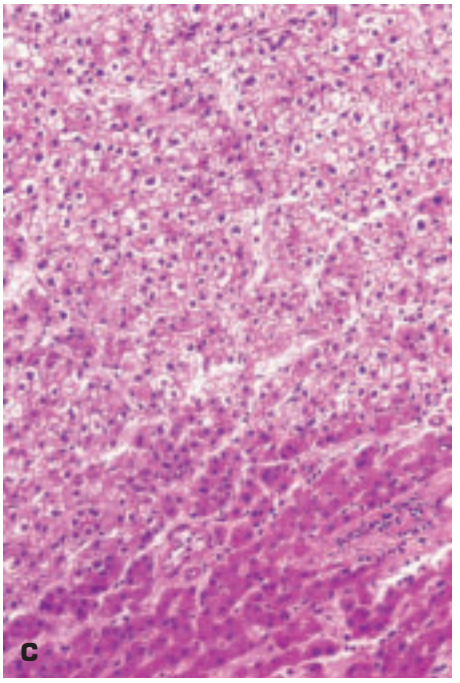

4-37. A. Focal nodular hyperplasia of the liver showing central degeneration and fibrosis. **B.** The central scarred zone is clearly evident on microscopy of the lesion. **C.** The hyperplastic liver cells (*top*) merge smoothly with the adjacent compressed normal liver cells.

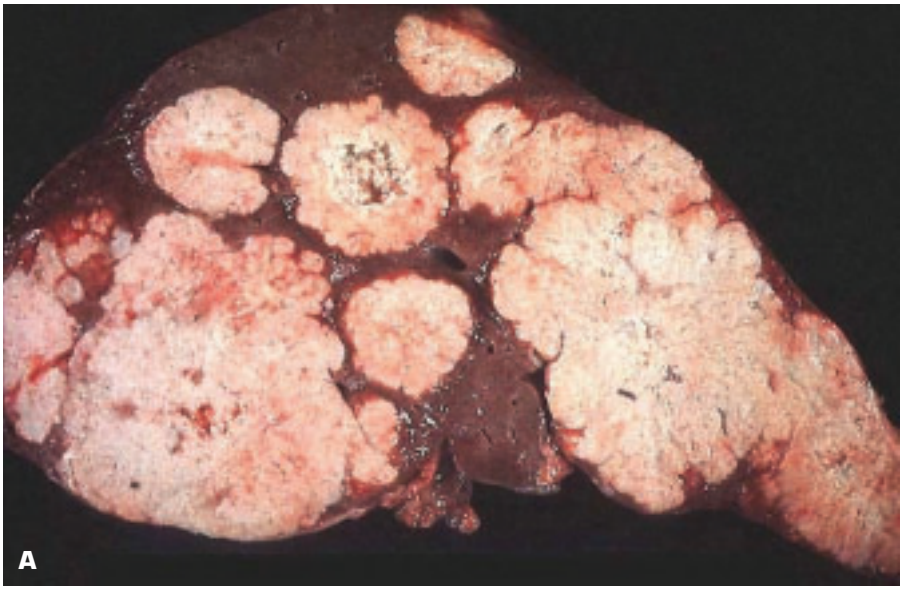

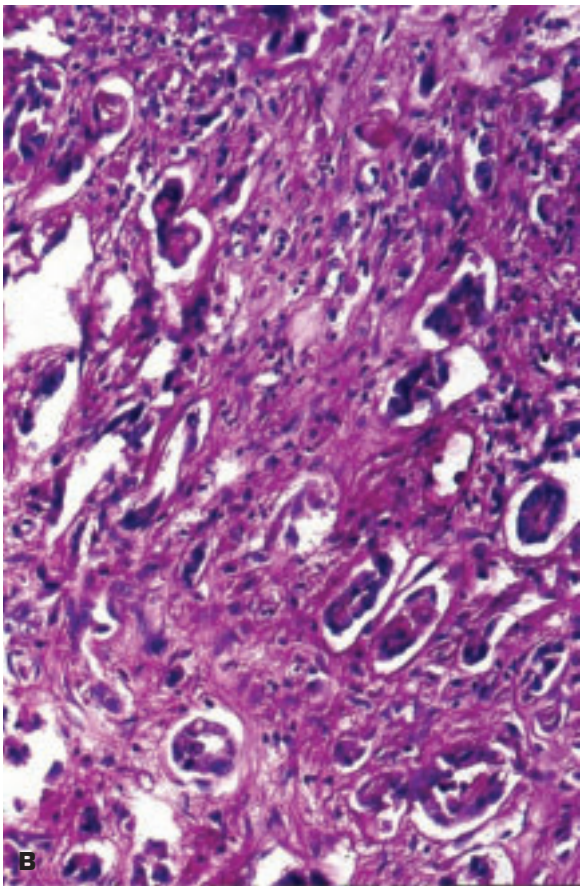

4-38. The liver is a common site for metastatic tumors. **A.** Multiple rounded nodules of metastatic adenocarcinoma occupy much of the liver. **B.** Histology shows moderately differentiated adenocarcinoma. *(continued on next page)*

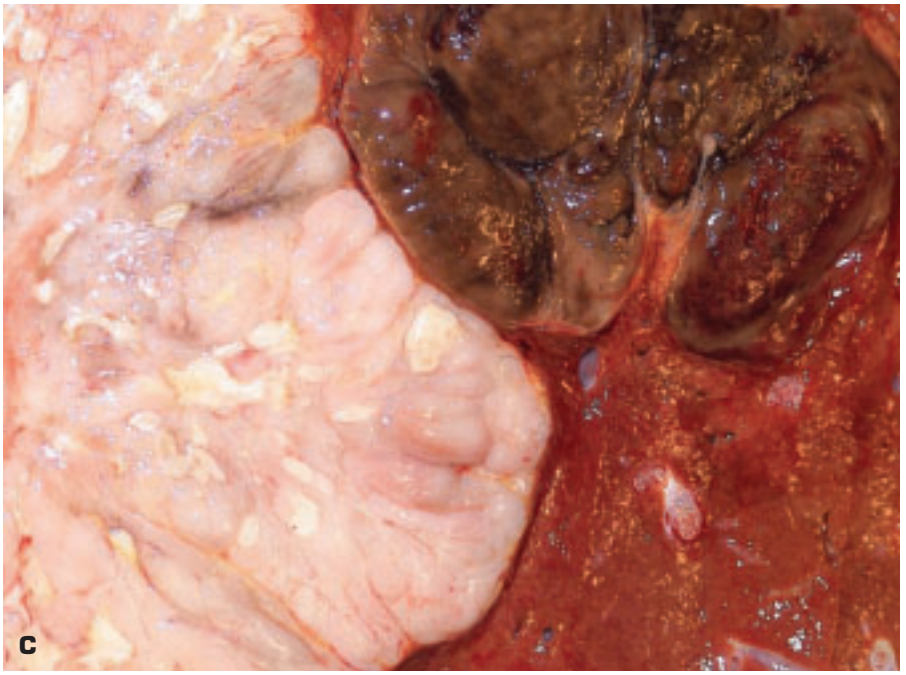

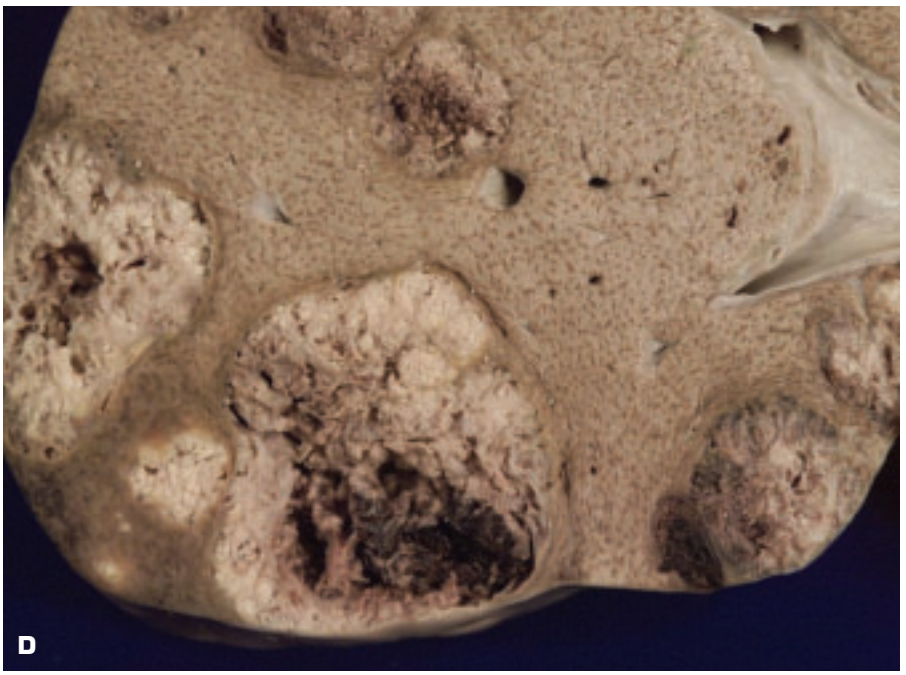

4-38. *(Continued)* **C.** Metastatic malignant melanoma showing prominent melanin production in only some of the nodules. **D.** Central umbilication due to central necrosis of the tumor nodules is a common feature in secondary cancers. *(continued on next page)*

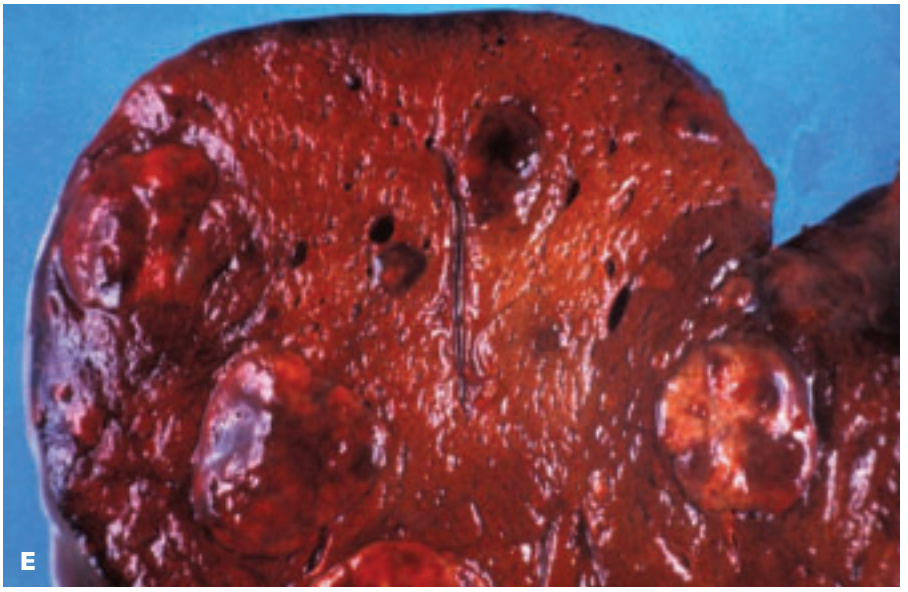

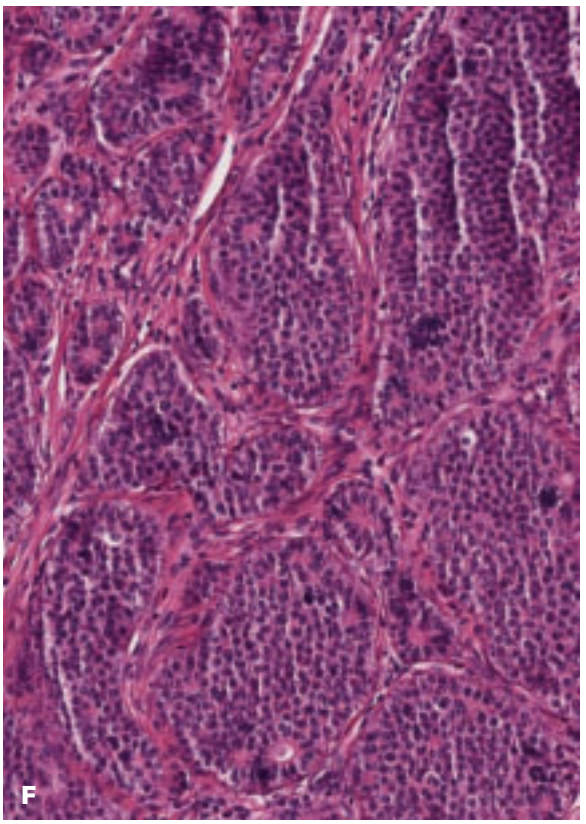

4-38. *(Continued)* **E.** Metastatic carcinoid tumor in the liver that had produced the carcinoid syndrome because the serotonin was able to bypass the liver's metabolism and gain entry into the systemic circulation. **F.** Histology of carcinoid tumor showing islands of uniform-looking cells devoid of anaplasia.

4-39. Isolated simple cyst of the liver.

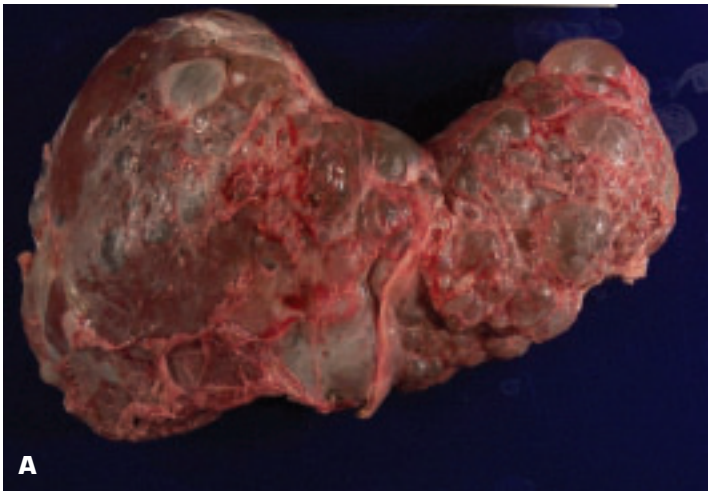

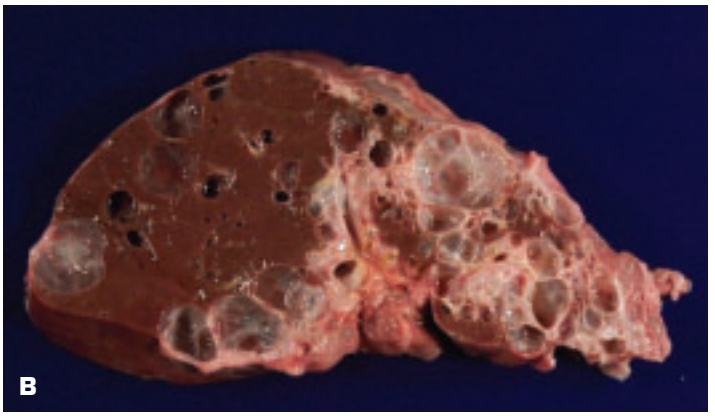

4-40. A. Polycystic liver disease in an adult with autosomal dominant (type III) polycystic kidney disease. **B.** Transversely sectioned liver shows multiple, interconnecting cysts of varying size, more abundant in the left lobe. **C.** Histologic appearance of portion of a small cyst.

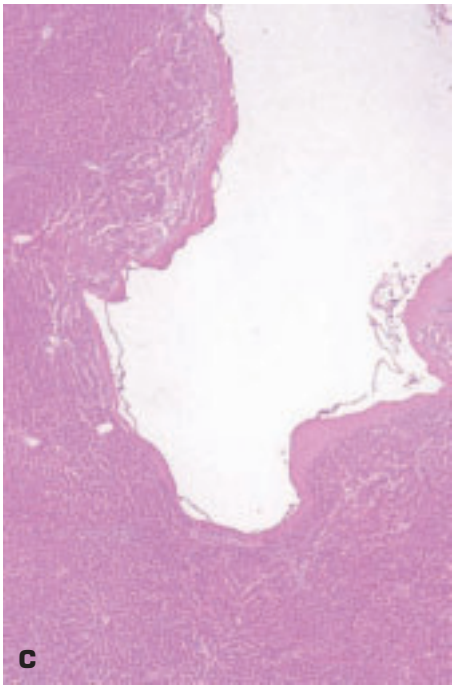

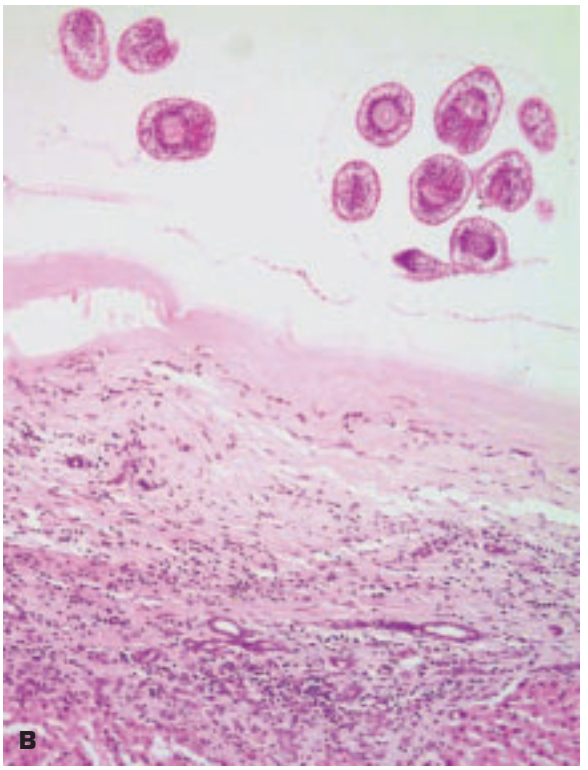

4-41. Miscellaneous cysts of the liver. **A.** Hydatid cyst of the liver whose contents have been evacuated. Note that during aspiration or excision the spillage of even a small amount of the cyst fluid may induce anaphylaxis due to hypersensitivity to the hydatid. **B.** Histology of the cyst wall showing the presence of multiple diagnostic scolices lying close to the detached germinal membrane. **C.** Mucinous cystadenoma of the ovary: the mucinous contents lie to the right of the cyst.

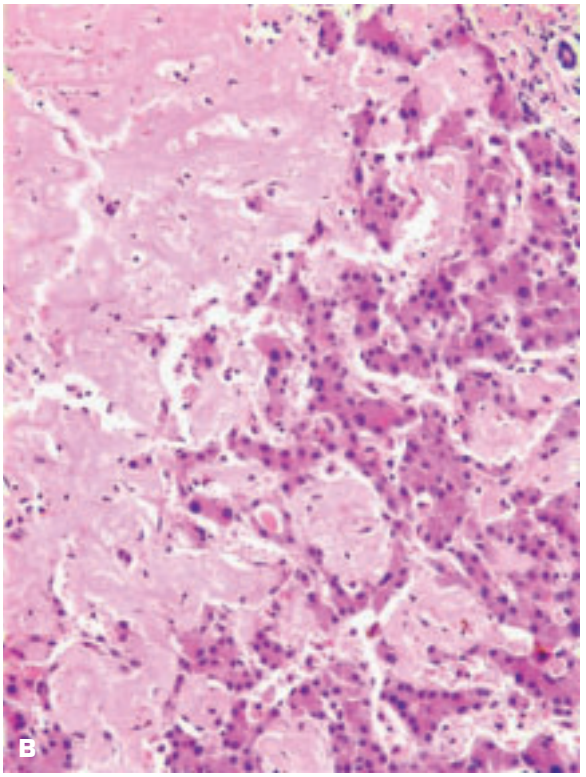

4-42. Amyloidosis of the liver. **A.** Macroscopically the liver has a waxy, firm, sharp-edged appearance, and its weight is greatly increased. **B.** Microscopic appearance of amyloid as eosinophilic, structureless, hyaline material replacing atrophic hepatic parenchyma.

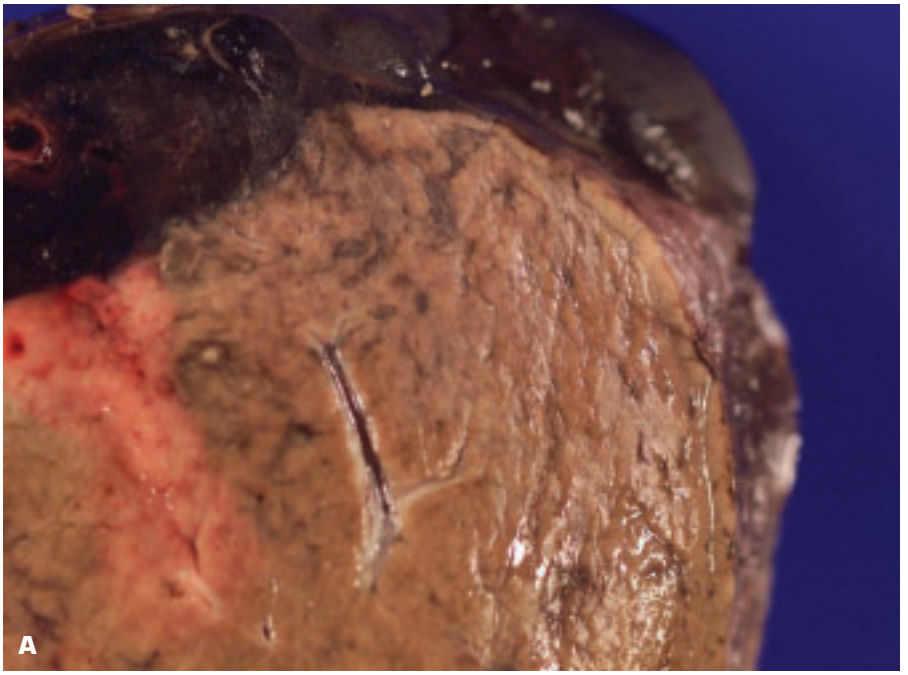

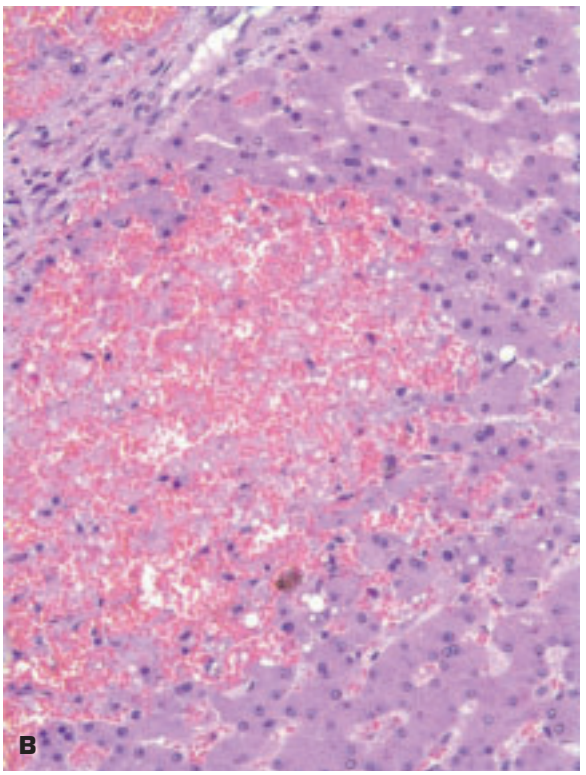

4-43. Peliosis hepatis. **A.** Bleeding derived from the blood-filled spaces (peliosis hepatis), seen as darker areas in the liver, has produced a large subcapsular hematoma (*top left*). **B.** The histologic hallmark of peliosis hepatis is disruption of the endothelial lining of the sinusoids with extravasation of blood out of the sinusoids into Disse's space and beyond to produce blood-filled spaces within the liver.

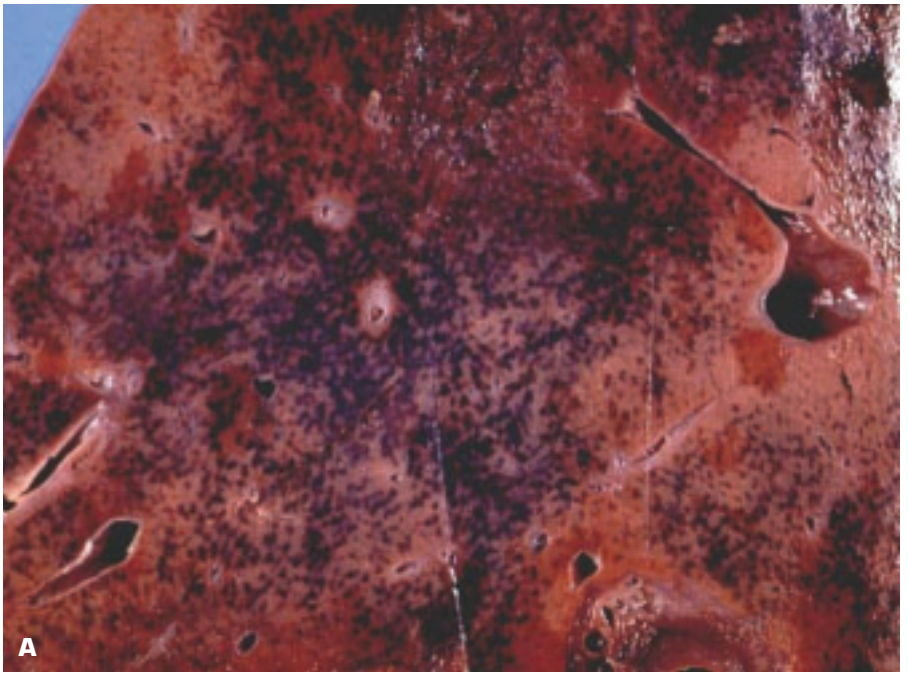

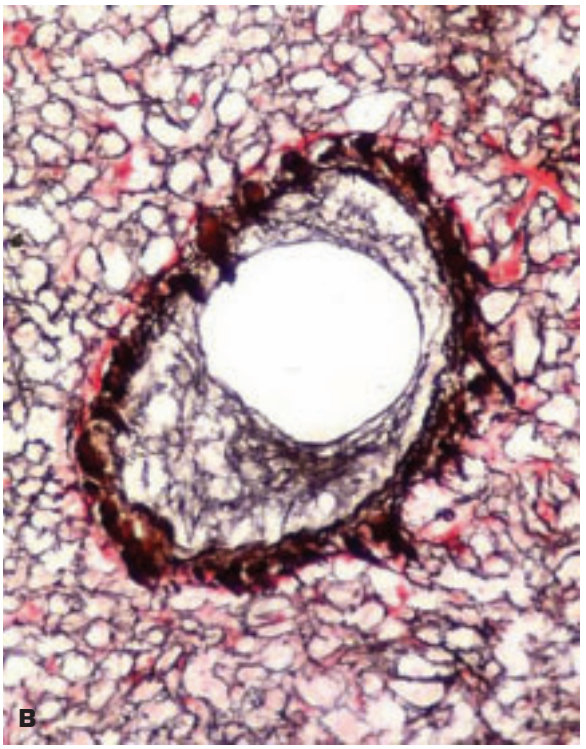

4-44. Hepatic venooclusive disease (HVOD). **A.** Intense passive congestion of the liver due to widespread severe obstruction to venous outflow has produced a "super-nutmeg" pattern in the liver. **B.** Elastic van Gieson stain shows significant narrowing of a small sublobular hepatic vein due to HVOD.

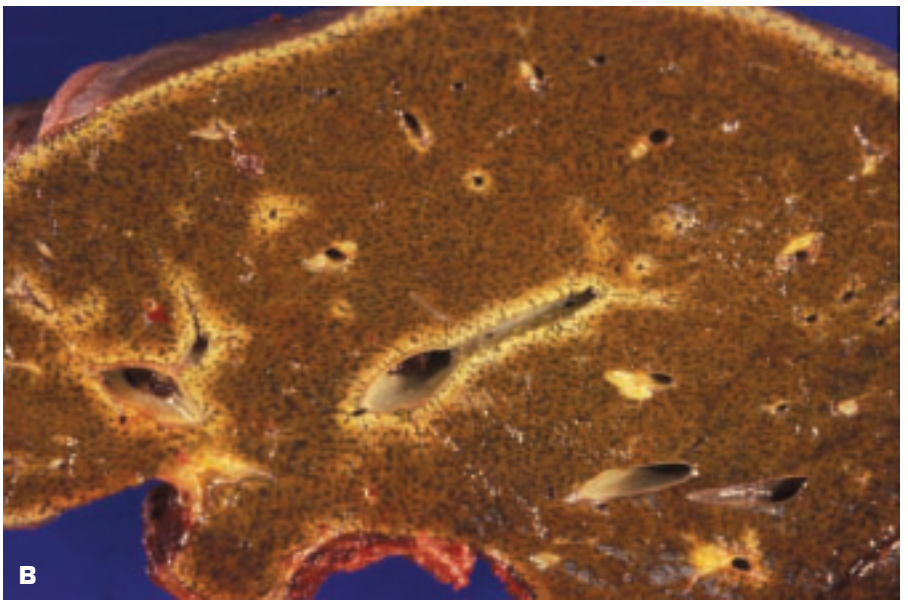

4-45. Liver transplantation. **A.** Severe acute rejection has produced extensive necrosis of this donor liver. **B.** Chronic rejection (graft arteriopathy) has produced thickening of blood vessel walls, as well as some atrophy and fibrosis of the graft. *(continued on next page)*

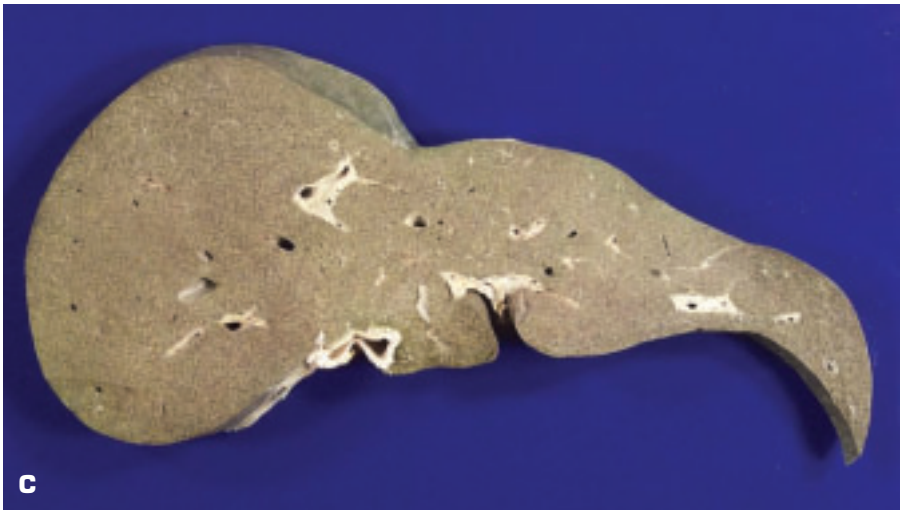

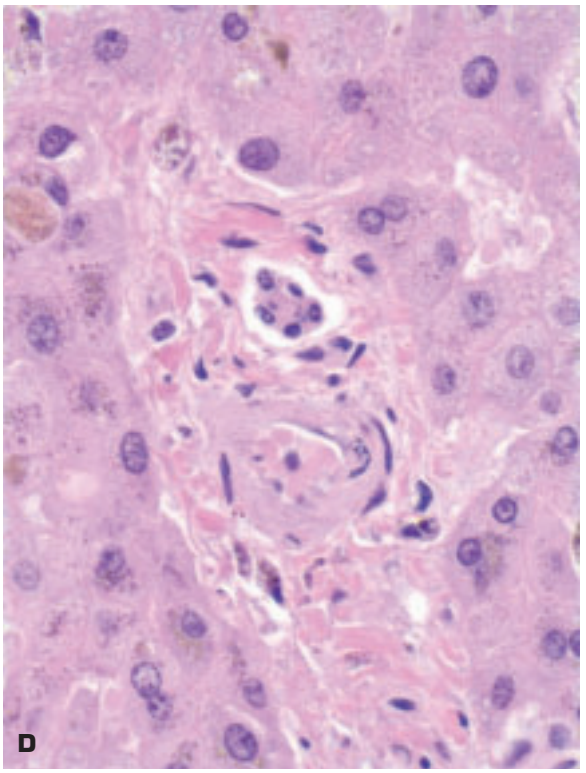

4-45. *(Continued)* **C.** Jaundiced liver due to graft-versus-host disease (GVHD) in a bone marrow transplant recipient. **D.** Apoptotic destruction of bile ductular epithelium due to GVHD.

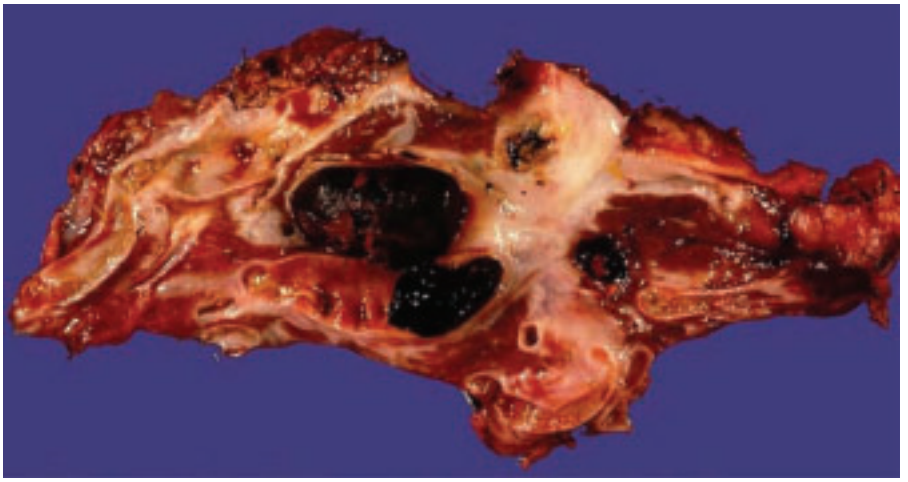

4-46. Intrahepatic pure pigment gallstones within the dilated biliary tree. Partial hepatectomy was performed after repeated attacks of cholangitis.

4-47. Gallstones lie within a dilated common bile duct.

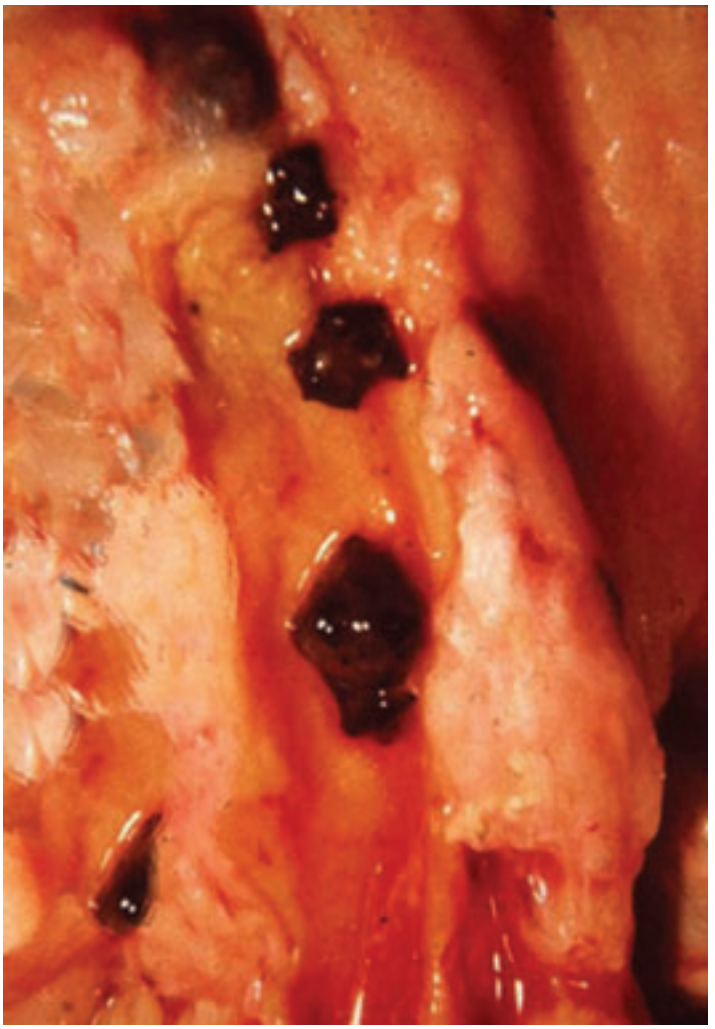

4-48. Congenital choledochal cyst of the common bile duct. Such cysts may occur inside or outside the liver and may predispose to cholangitis. The cysts are more common in Japan and affect girls more than boys.

4-49. Strawberry gallbladder: cholesterosis gives the mucosa a speckled appearance due to cholesterol-laden macrophages in the lamina propria of the gallbladder.

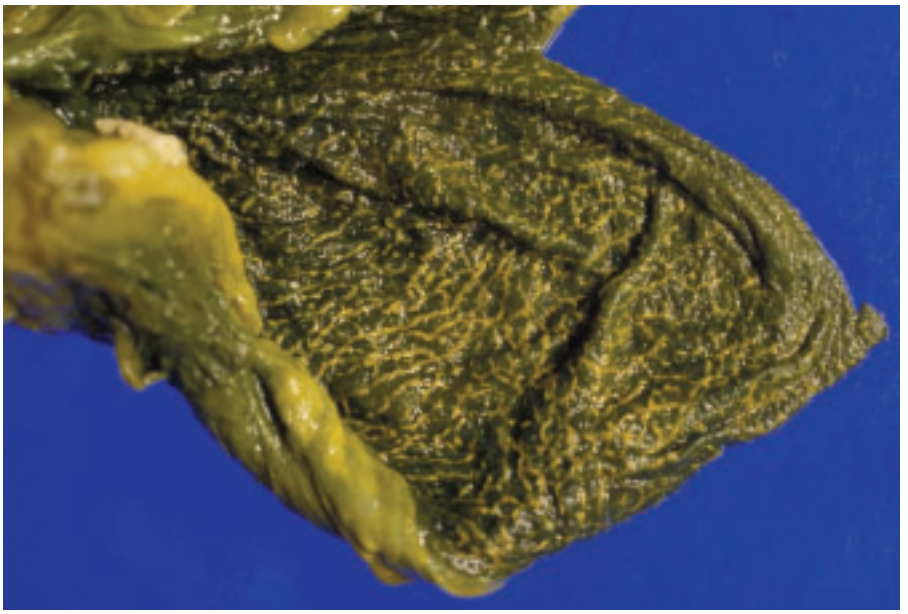

4-50. A. Cholesterol-rich gallstones within a very thickened, fibrosed gallbladder. **B.** Bisected cholesterol-rich gallstones within gallbladder show the typical radiating crystalline appearance of cholesterol crystals. *(continued on next page)*

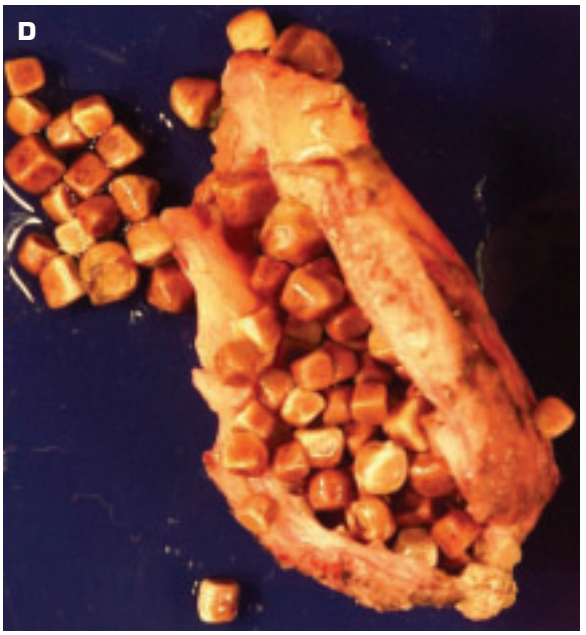

4-50. *(Continued)* **C.** Mixed cholesterol and bile pigment stones. **D.** Chronic cholecystitis. Fibrosed gallbladder contains numerous multifaceted mixed gallstones.

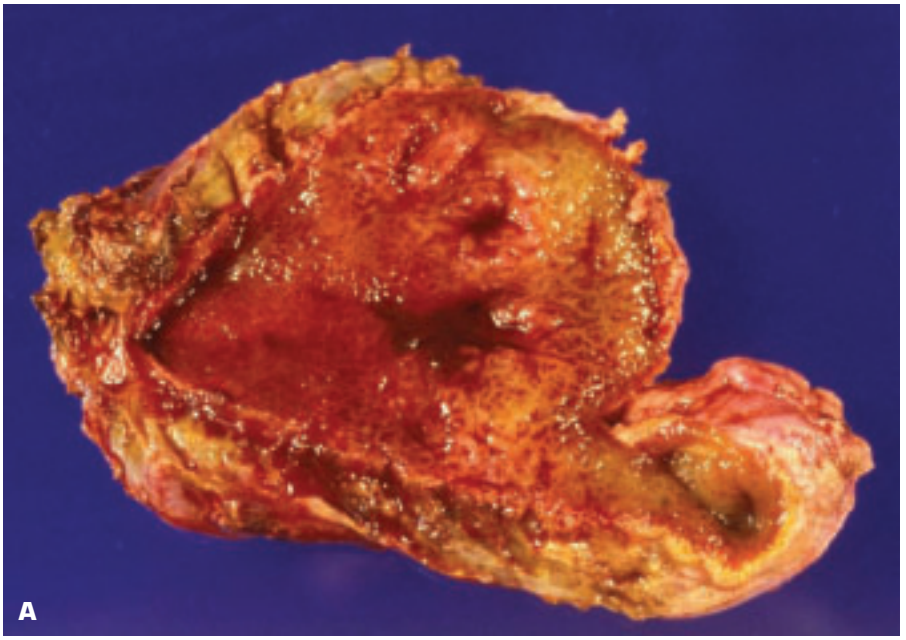

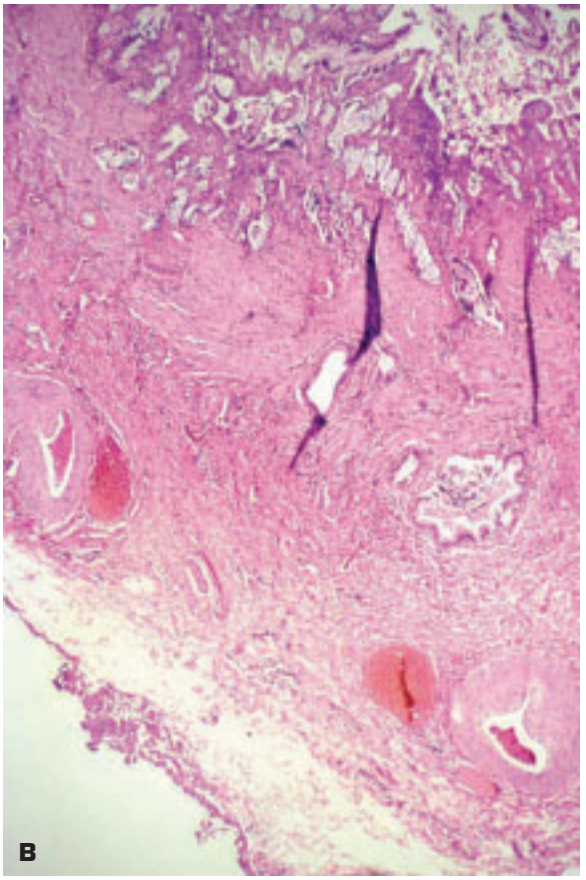

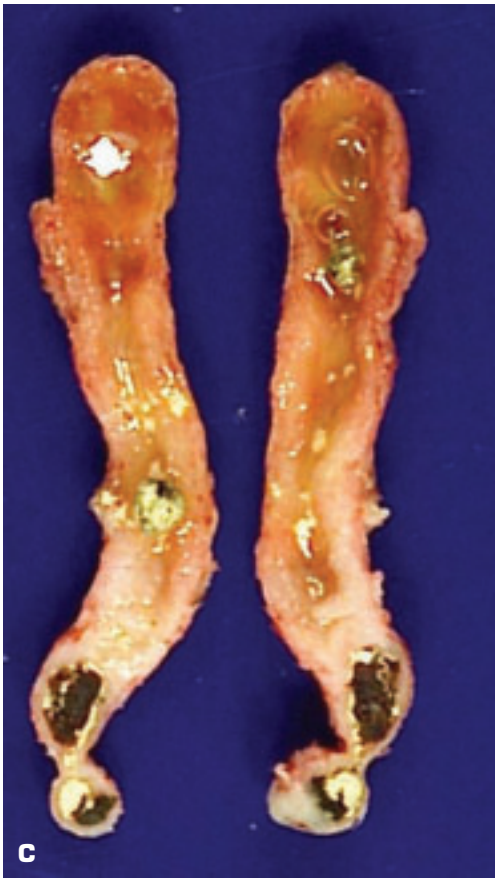

4-51. A. Chronic cholecystitis has produced significant mural thickening of the gallbladder. **B.** Rokitansky-Aschoff sinuses (adenomyosis) in chronic cholecystitis. **C.** Fibrous contracture of the gallbladder due to chronic cholecystitis related to calculi. *(continued on next page)*

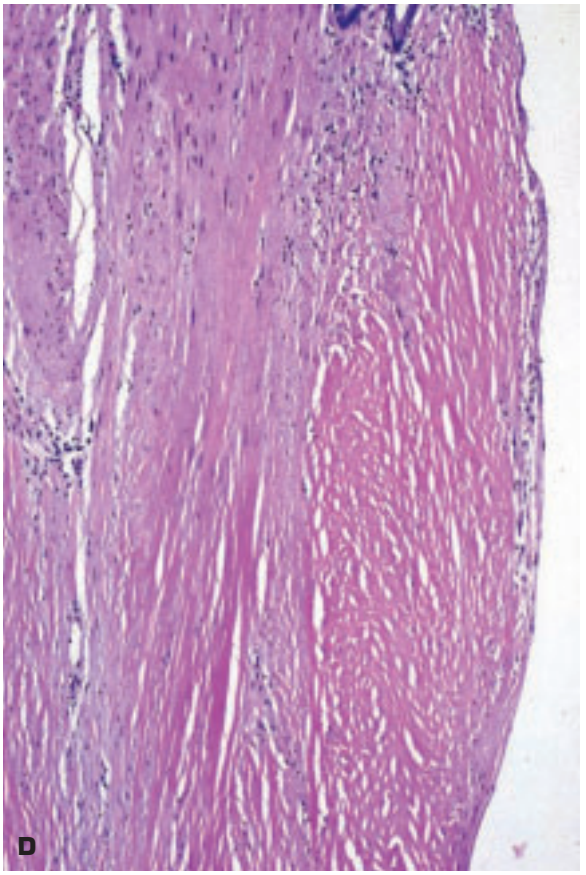

4-51. *(Continued)* **D.** Histology shows fibrous tissue has replaced mucosa and the muscle coat. **E.** Mucocele of the gallbladder due to sterile obstruction of the neck (see gallstone). The lack of inflammation allows the gallbladder to distend with mucus without rupturing. Such a gallbladder has to be carefully handled during surgical excision to avoid rupture and the implantation of mucus-secreting cells on the peritoneum that may produce pseudomyxoma peritonei.

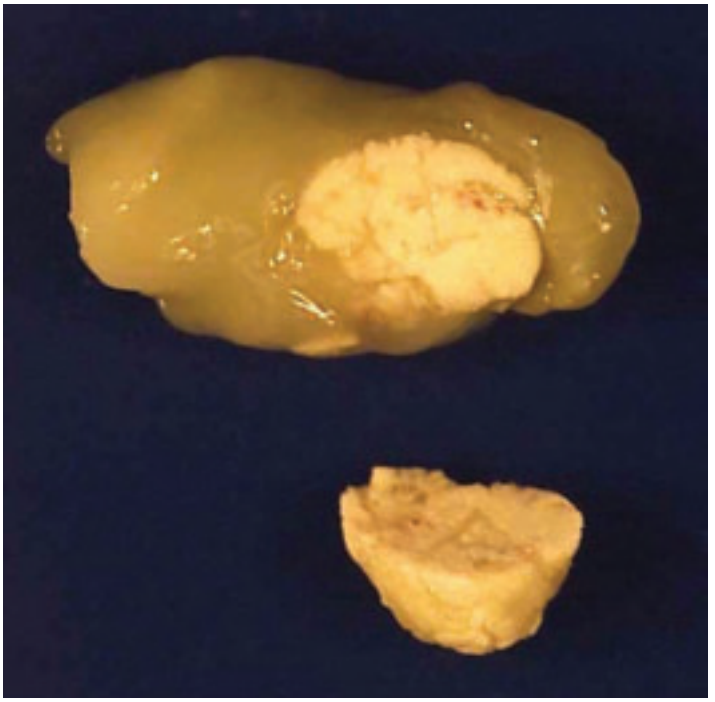

4-52. Granulomatous inflammation due to *Trichosporon beigelii* protruding externally from the wall of the gallbladder.

4-53. Carcinoma of the gallbladder. **A.** Adenocarcinoma (white tissue, *bottom right*) of a gallbladder that contains a large gallstone. **B.** Diffusely infiltrating adenocarcinoma in a gallbladder containing four gallstones.

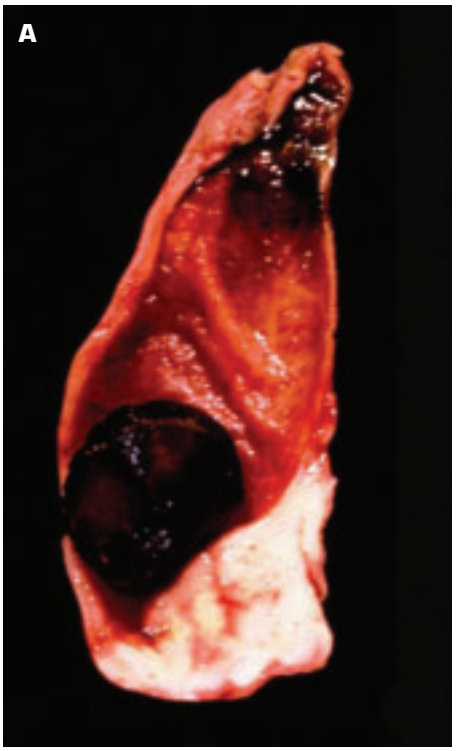

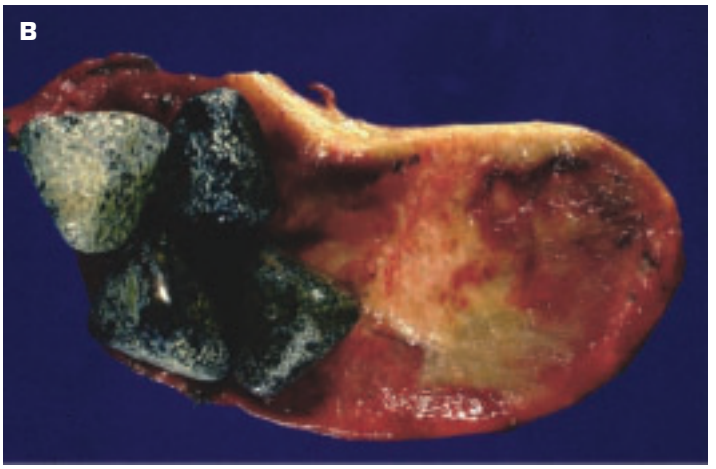

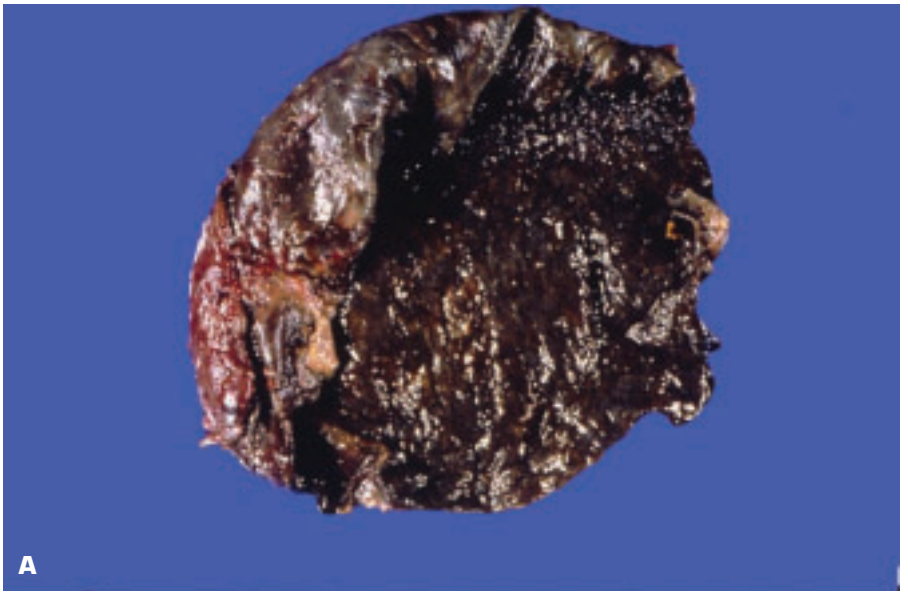

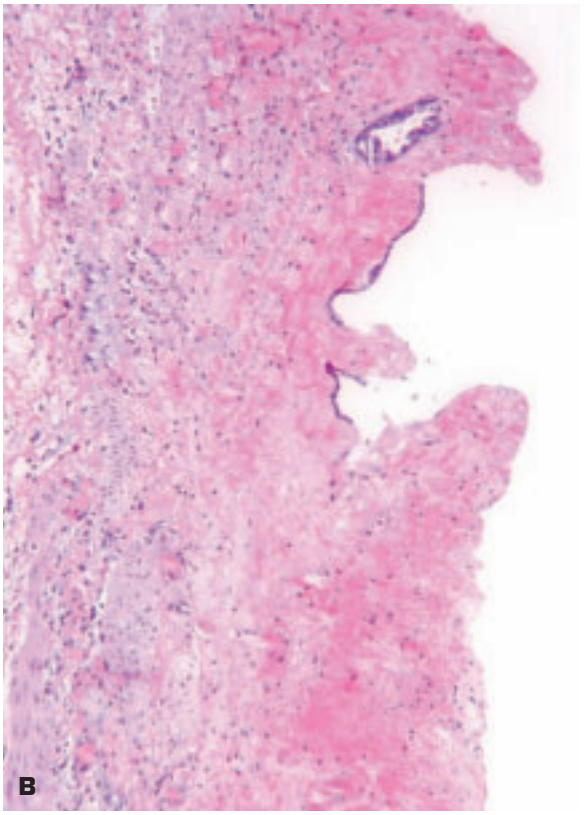

4-54. Necrosis of the gallbladder. **A.** Gangrene of the gallbladder complicating acute cholecystitis. **B.** Histologic appearance of ischemic cholecystopathy shows fresh hemorrhage within the necrotic mucosa.

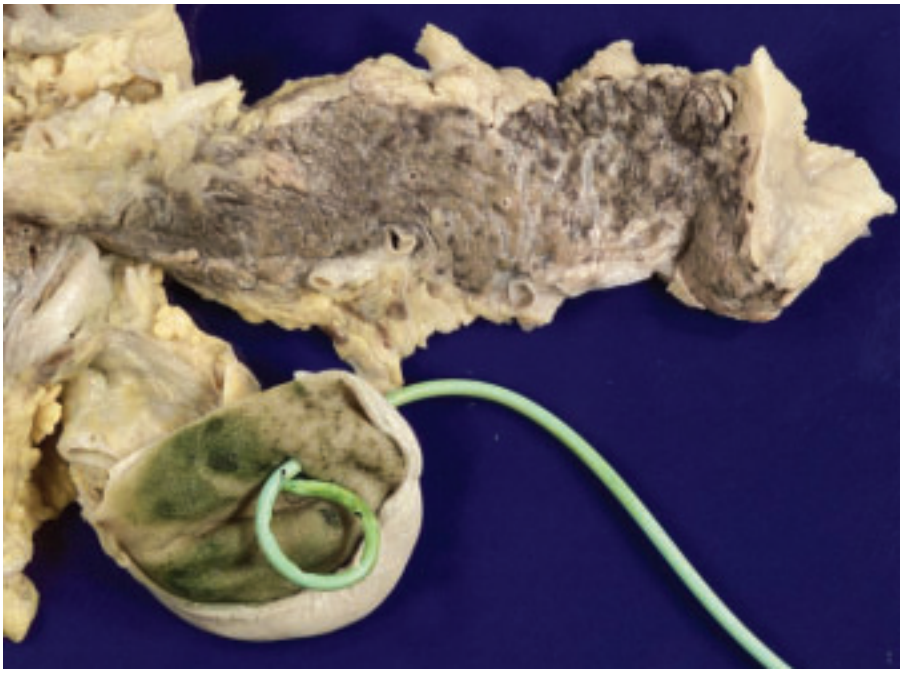

4-55. Surgical catheter drainage of the gallbladder (*bottom left*) to remove sludge that had led to acute hemorrhagic pancreatitis (*top right*) by obstructing the ampulla of Vater.

4-56. Adenocarcinoma (*arrow*) of the ampullary end of the common bile duct.

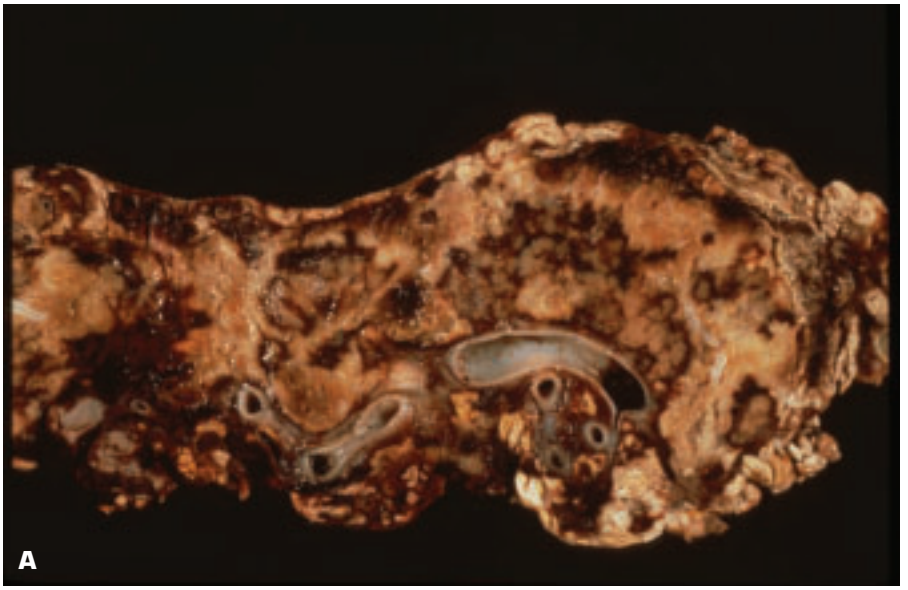

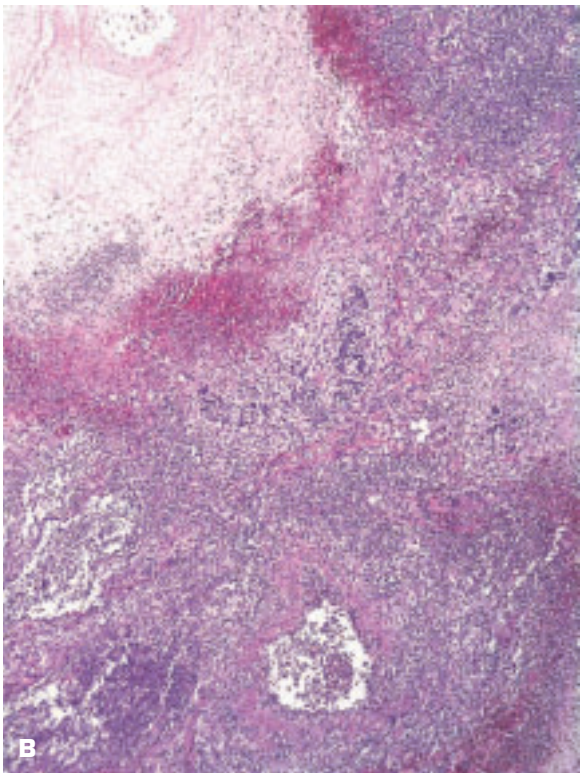

4-57. Acute pancreatitis. **A.** Close-up view of cut surface of hemorrhagic pancreatitis. **B.** Histology shows necrotic pancreatic tissue (*top left*) surrounded by hemorrhage and acute inflammation.

4-58. Pancreatic pseudocyst (*top left*) in a patient with recurrent acute hemorrhagic pancreatitis (*center*).

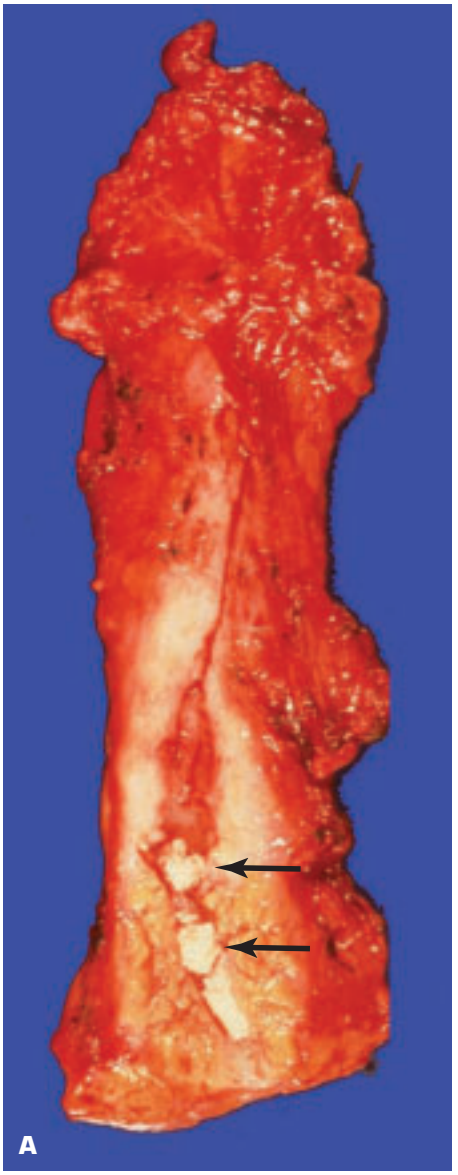

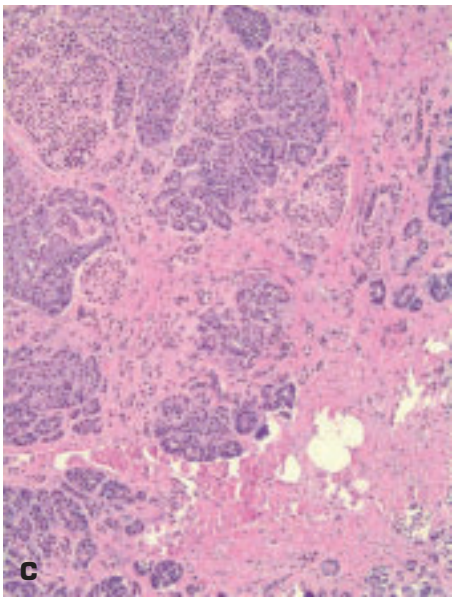

4-59. Chronic calcifying pancreatitis. **A.** Pancreas shows dense fibrosis and calculi (*arrows*) within the dilated pancreatic duct. **B.** More advanced chronic calcific pancreatitis with both parenchymal and intraductal calcific deposits. **C.** Histology shows atrophic acini embedded in dense fibrous tissue.

4-60. Bisected pancreas showing calculus (*arrows*) within pancreatic duct.

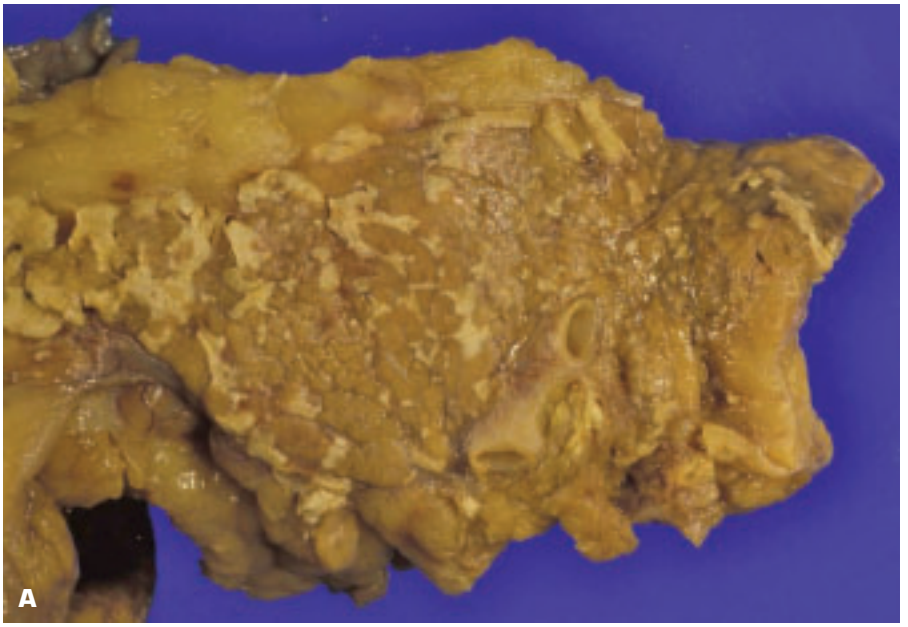

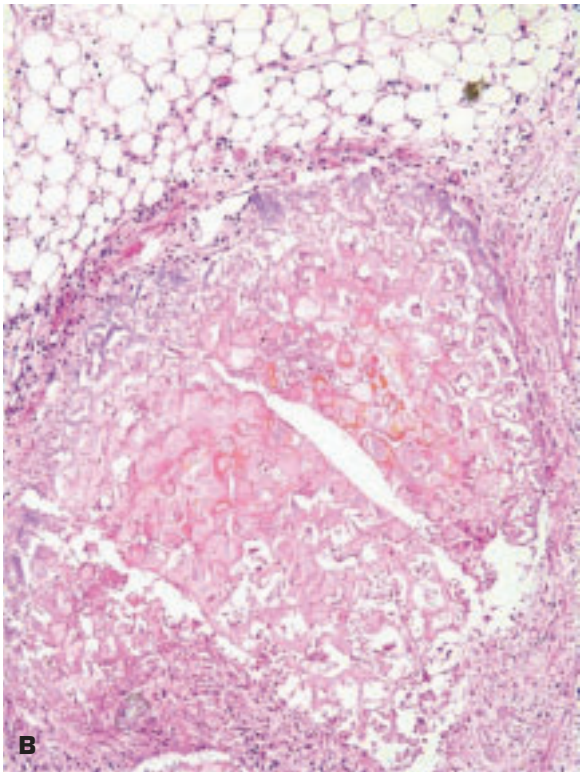

4-61. Fat necrosis of the pancreas. **A.** Necrotic interstitial fibroadipose tissue of the pancreas has a chalky yellow-white color due to the deposition of triglycerides/fatty acids as calcium soaps. **B.** Histology of fat necrosis showing central necrotic adipocytes covered by fatty acids precipitated as calcium soaps.

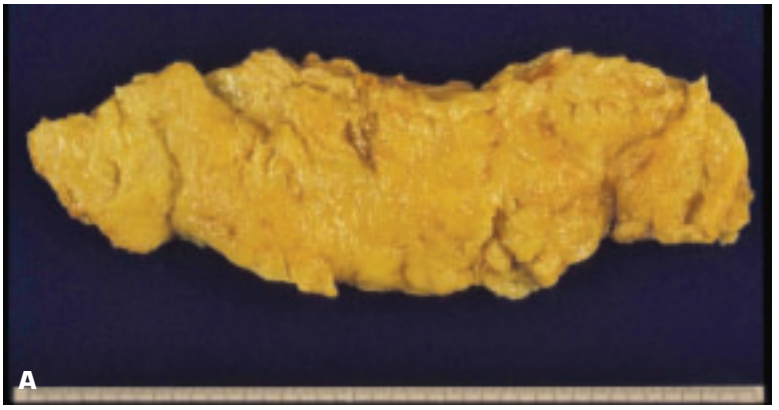

4-62. Pancreas in cystic fibrosis. **A.** Total adipose replacement of the pancreatic parenchyma is more commonly observed than the pancreatic cysts and fibrosis after which the condition was originally named. **B.** Histology shows naked islets of Langerhans (devoid of surrounding acinar tissue) lie within the fibroadipose tissue. **C.** Histology of another pancreas showing cystic dilatation of ducts and replacement fibrosis of the parenchyma (i.e., cystic fibrosis).

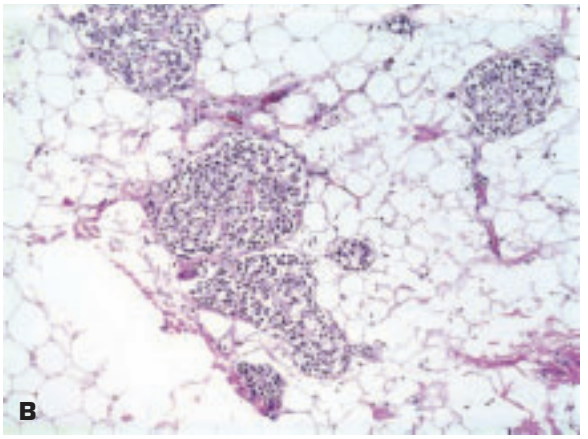

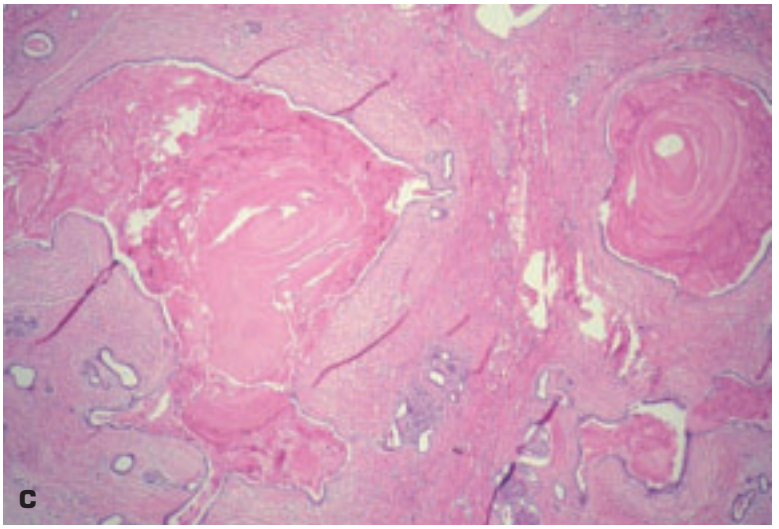

4-63. Hemorrhagic infarction of the pancreas following thrombotic obstruction of its venous drainage.

4-64. Pancreas in hemochromatosis (*lower*) shows atrophy and brown coloration due to excessive parenchymal iron deposits. Compare with a normal control pancreas (*upper*) from another patient.

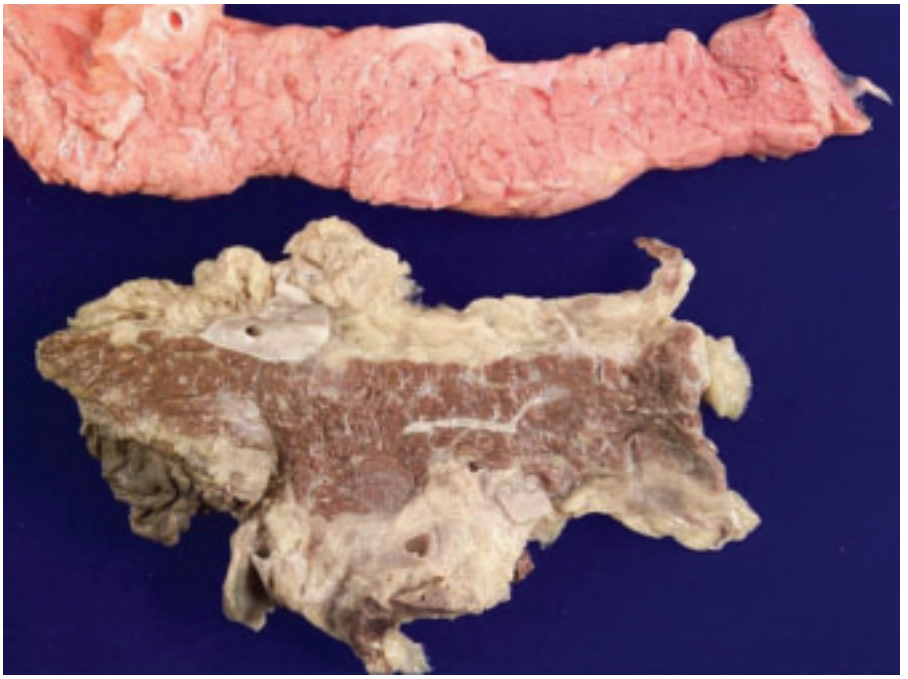

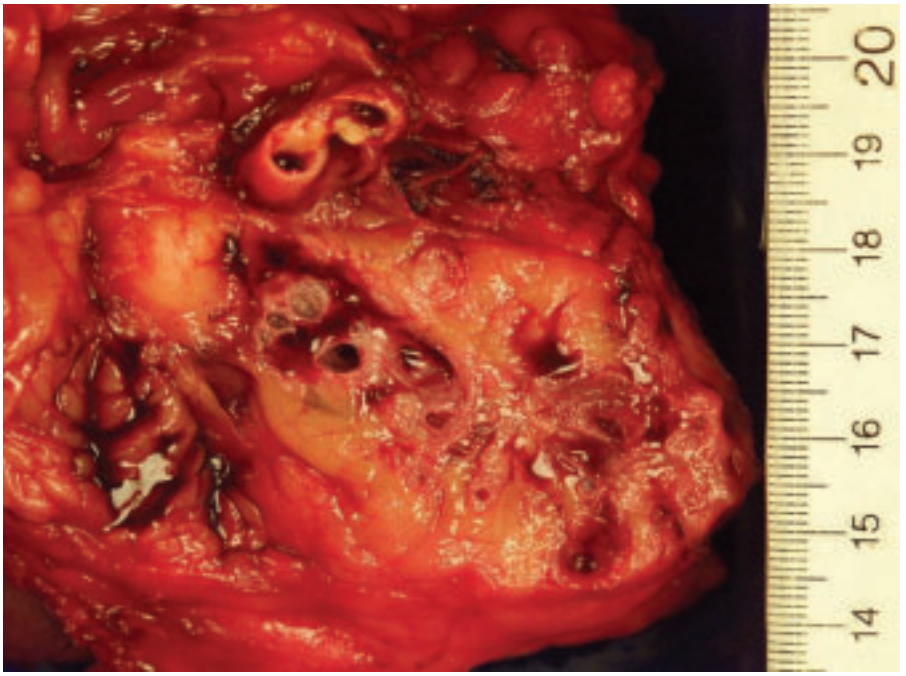

4-65. Intraductal papillary mucinous neoplasm (also termed *pancreatic intraepithelial neoplasia*) may present varied gross features. In this patient, multiple pancreatic ducts are dilated due to overproduction of mucus.

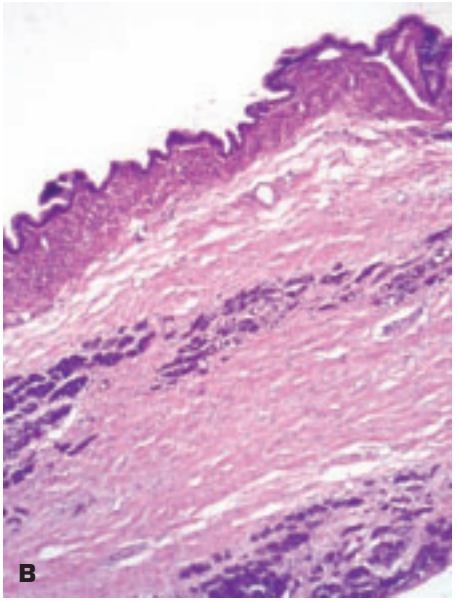

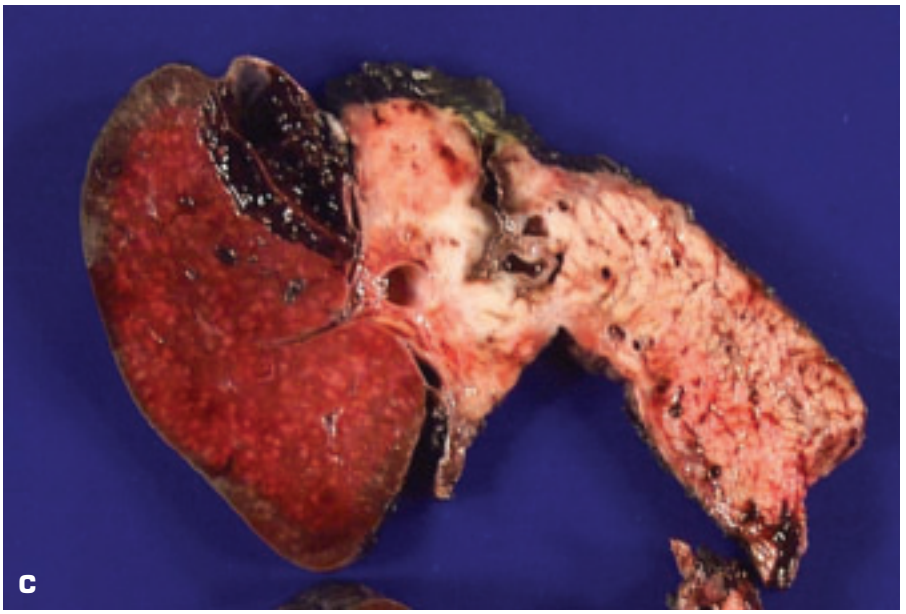

4-66. A. Mucinous cystadenoma of tail of pancreas. The unilocular cyst contains abundant inspissated mucin. **B.** The lining comprises a single layer of well-differentiated mucinous epithelium. Fibrosis is noted in the adjacent compressed pancreatic tissue. **C.** Mucinous cystadenocarcinoma of the tail of the pancreas abuts on the spleen (*left*).

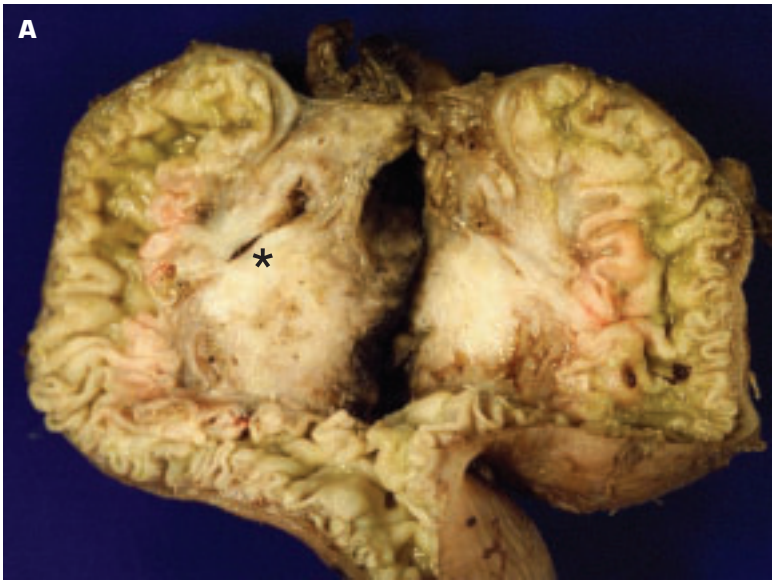

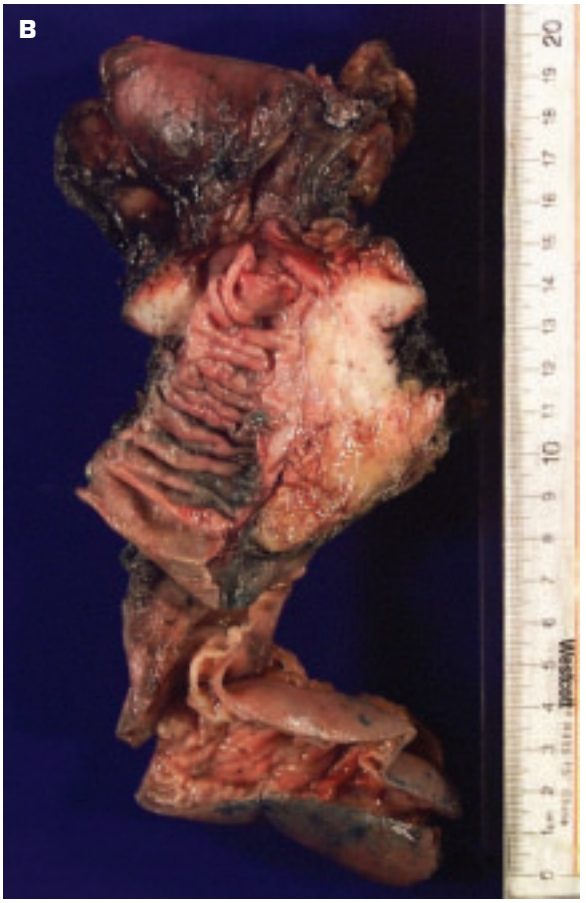

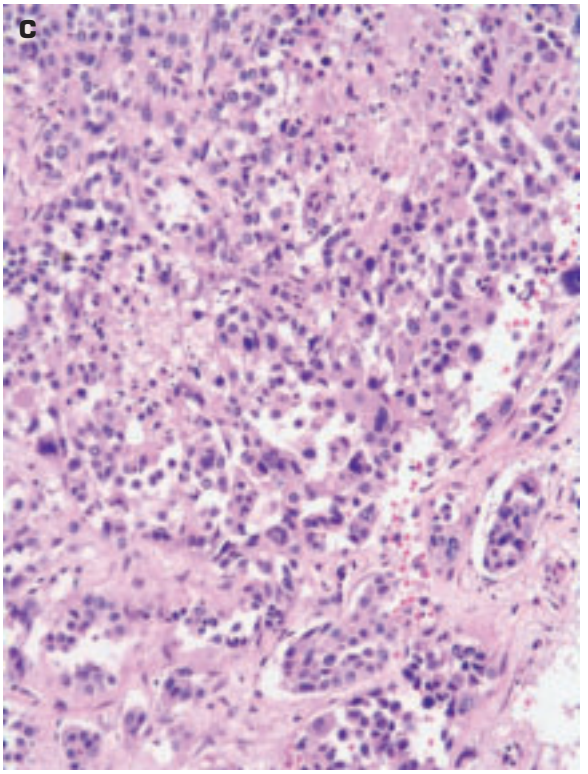

4-67. Adenocarcinoma of the head of the pancreas. **A.** Bisected carcinoma surrounds the common bile (*) duct as it reaches the ampulla of Vater in the second part of the duodenum. **B.** Cancer of the pancreas is beginning to invade into duodenum (*left*) and extends to reach the inked resection line (*right*) in this Whipple resection. **C.** Histology of a poorly differentiated adenocarcinoma of the pancreas.

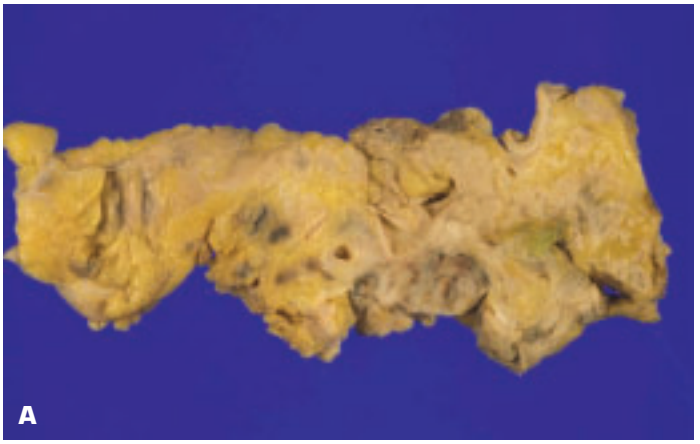

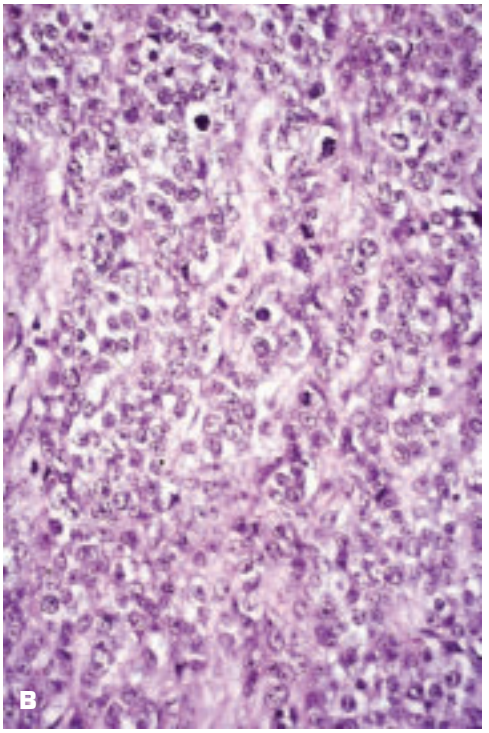

4-68. A. Malignant lymphoma within the intra- and peripancreatic lymph nodes is spreading into the pancreatic parenchyma in areas. **B.** Histology shows a diffuse, large cell lymphoma.

4-69. Ruptured mycotic aneurysm (*arrow*) of the splenic artery in the head of pancreas.

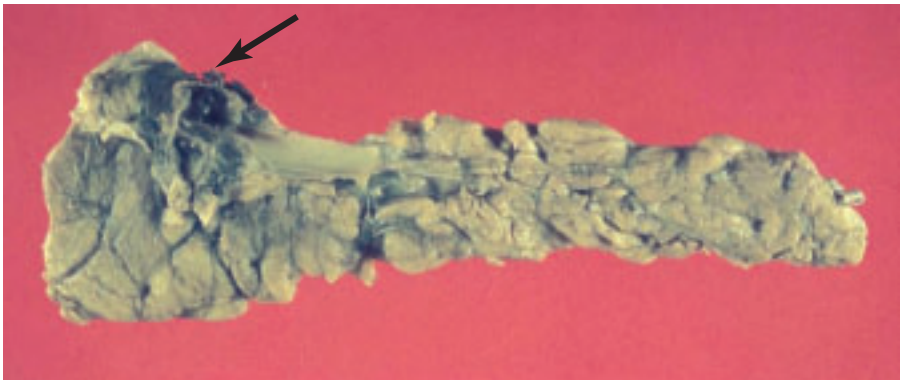

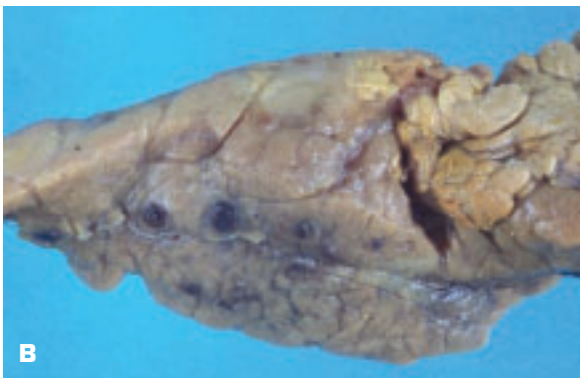

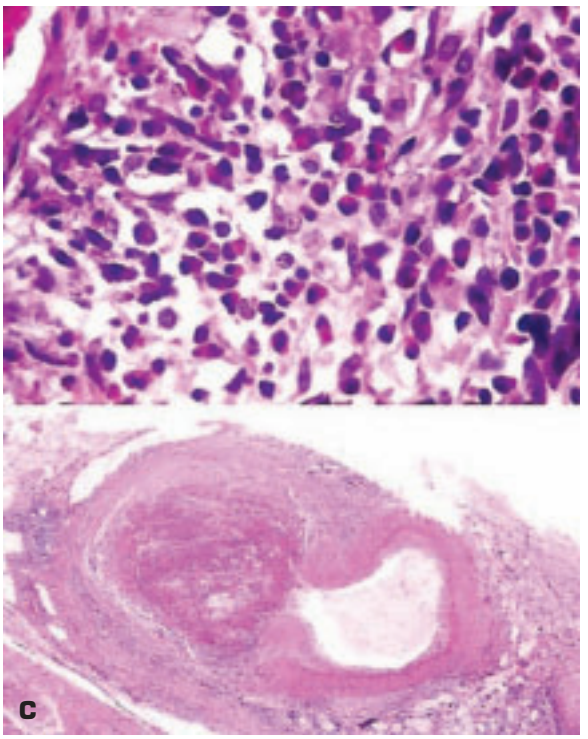

4-70. Polyarteritis nodosa of pancreas. **A.** Multiple large thrombus-filled aneurysms within head of pancreas. **B.** Multiple small aneurysms along the course of a small intrapancreatic artery. **C.** Histology shows a polymorphous inflammatory response (including many eosinophils) in the wall of an artery (*top*) and thrombus filling a false aneurysm that communicates with a small artery (*bottom*).

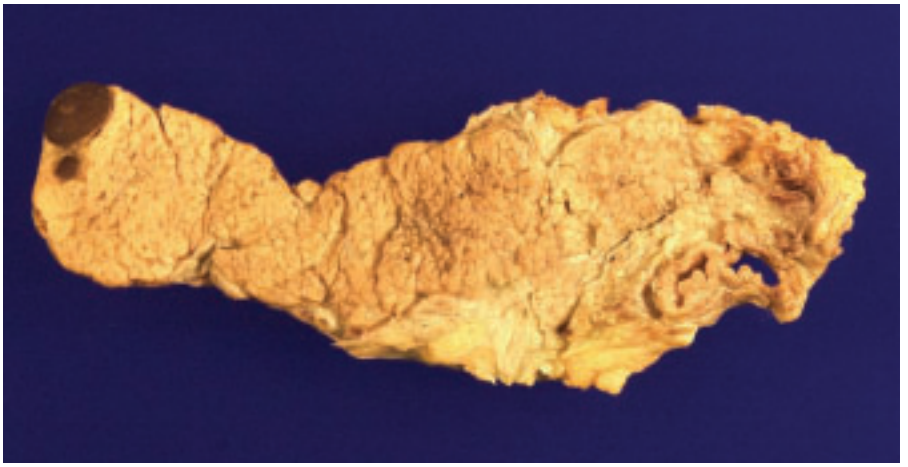

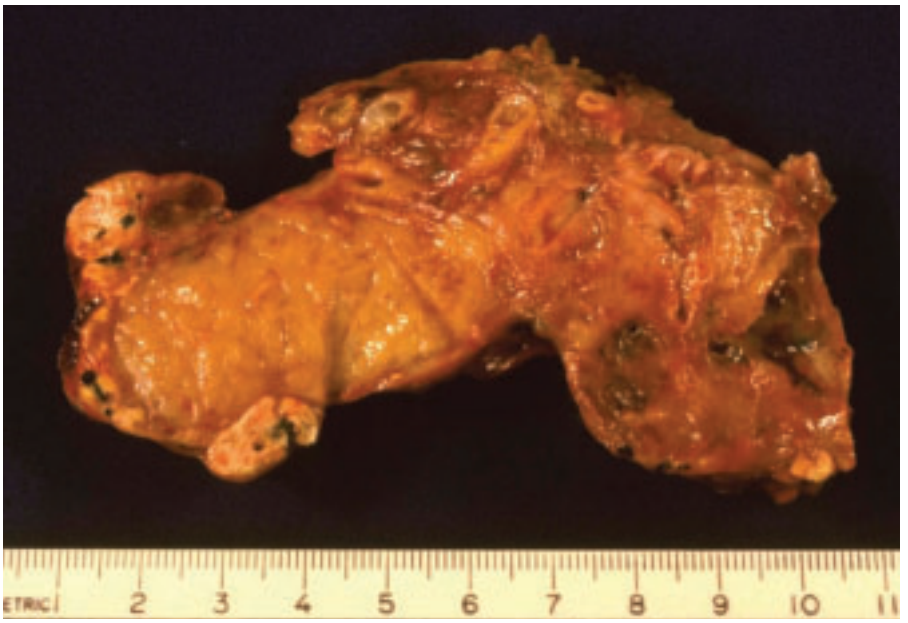

4-71. Transplantation of the pancreas. **A.** Autopsy revealed the donor pancreas to contain two small accessory spleens (splenunculi) in its tail (*top left*). The patient died of severe graft-versus-host disease that may have been facilitated by the donor lymphoid containing splenic tissue present in the donor pancreas. **B.** Chronic rejection of the pancreas (graft arteriopathy) manifesting as thickened, narrowed blood vessels and atrophic, fibrosed parenchyma.

5 Salivary Glands and GIT

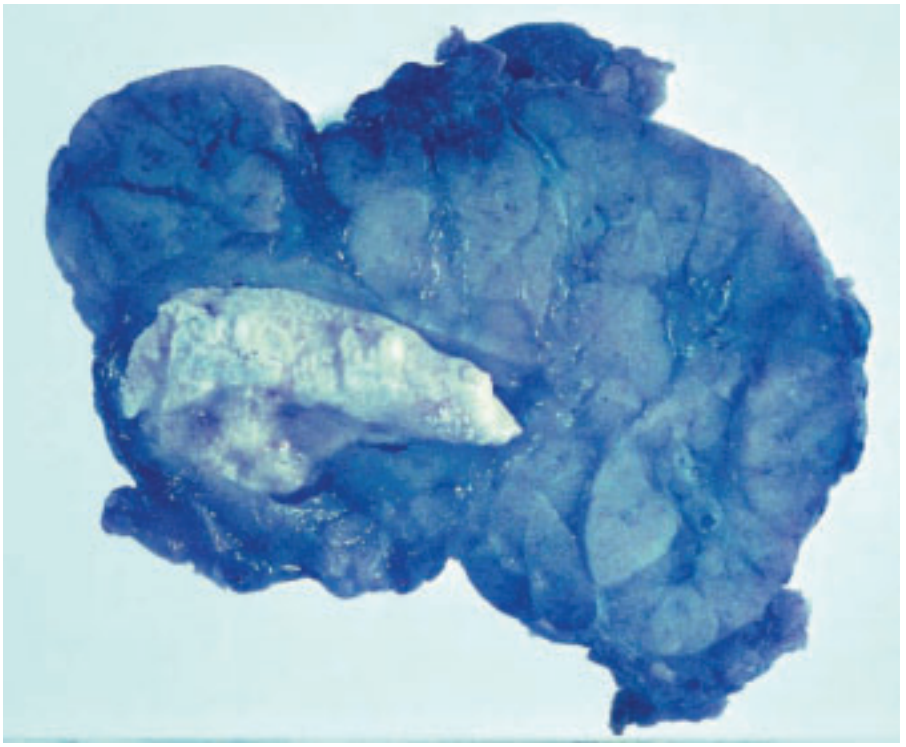

5-1. Calcific calculus obstructs main duct of submandibular gland close to one end of the gland. The parenchyma shows mild atrophy and fibrosis.

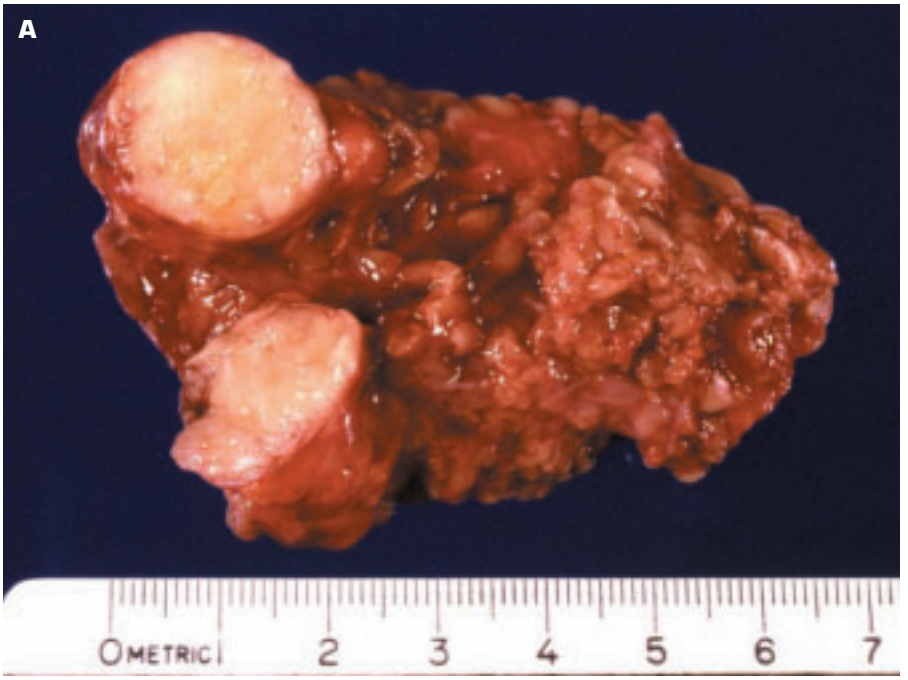

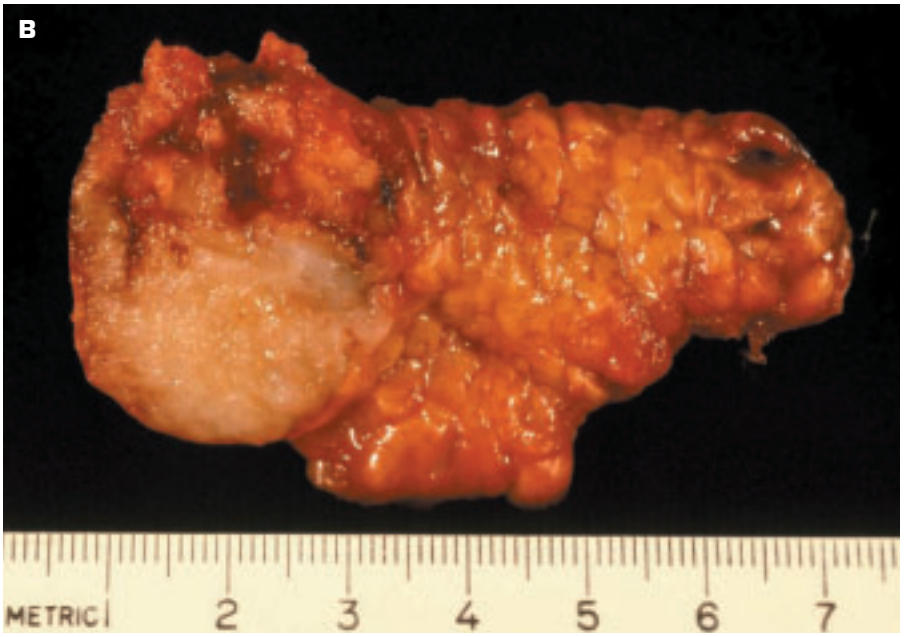

5-2. A. Small circumscribed pleomorphic adenoma of the parotid gland has a multilobulated variegated cut surface. **B.** This pleomorphic adenoma has a less well-defined edge with isolated nodules of tumor extending into the surrounding parenchyma (*top left*). Incomplete excision of the tumor may leave such nodules behind, leading to recurrence of the tumor. Chondroid areas macroscopically appear more mucoid. *(continued on next page)*

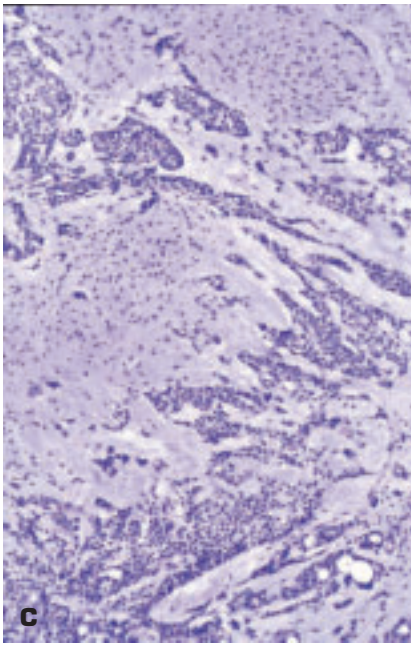

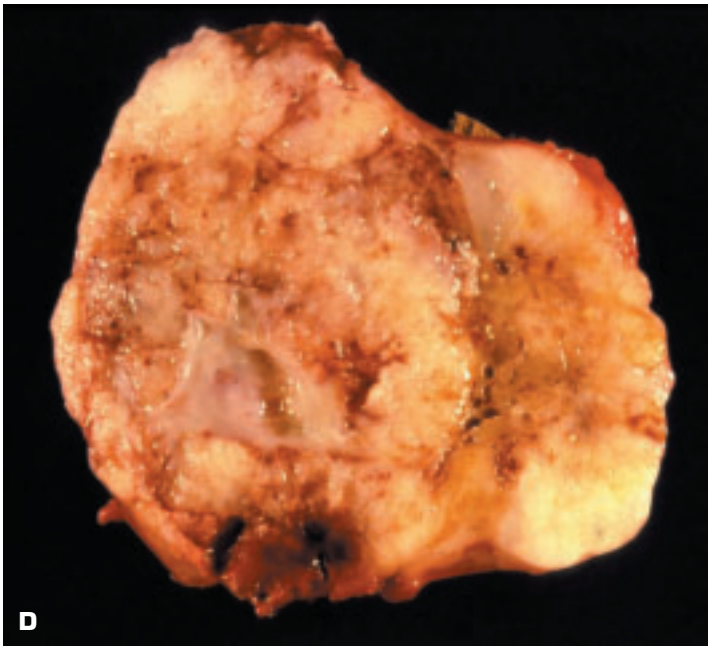

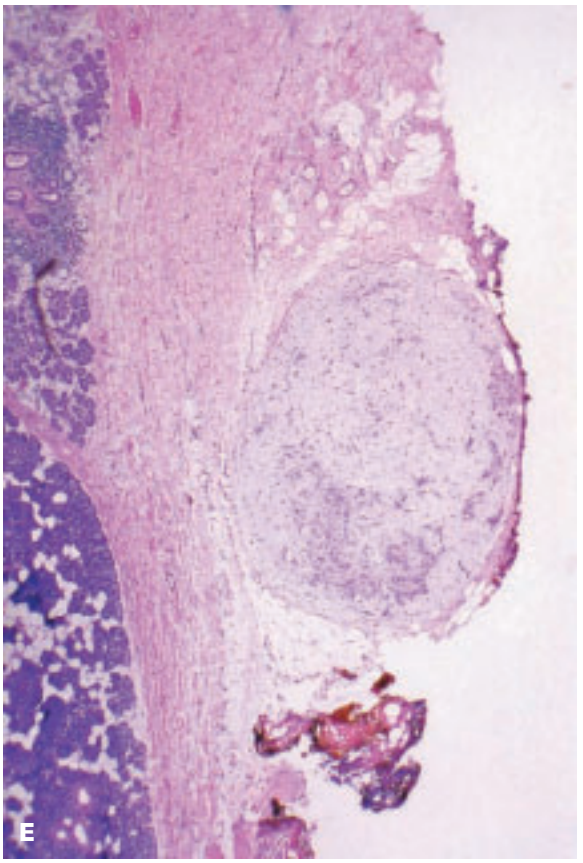

5-2. *(Continued)* **C.** Histology of pleomorphic adenoma (mixed parotid tumor), showing a mixture of proliferating ductal and myoepithelial cells and areas of myxoid and chondroid differentiation. **D.** Cross-section of a pleomorphic adenoma that was excised with minimal surrounding tissue. The areas of myxoid/chondroid differentiation are easily apparent. **E.** Further excision revealed histologic evidence of a residual nodule of tumor tissue that abuts on the inked resection margin.

5-3. Malignant change in a pleomorphic adenoma has converted the tumor into an adenocarcinoma that has ill-defined margins due to infiltration of the adjacent salivary glandular tissue by the malignancy.

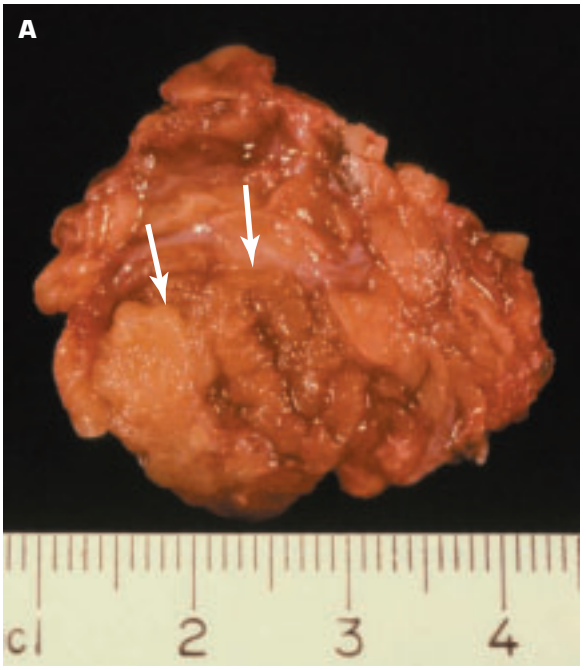

5-4. Monomorphic adenomas of the salivary glands may occur (e.g., the most common are the Warthin tumor [papillary cystadenoma lymphomatosum], basal cell adenoma, oxyphilic adenoma [oncocytoma], canalicular adenoma, myoepithelioma, and clear cell adenoma). Warthin tumors are more common in men and may be bilateral or multifocal in the same gland. **A.** Early Warthin tumor (*arrows*) has a lighter tan color than the normal glandular tissue. **B.** This more advanced Warthin tumor shows the more typical multicystic areas on its cut surface. **C.** Histology: oncocytes line the ducts, some of which have become expanded into cystic spaces. Follicular lymphoid tissue is also present.

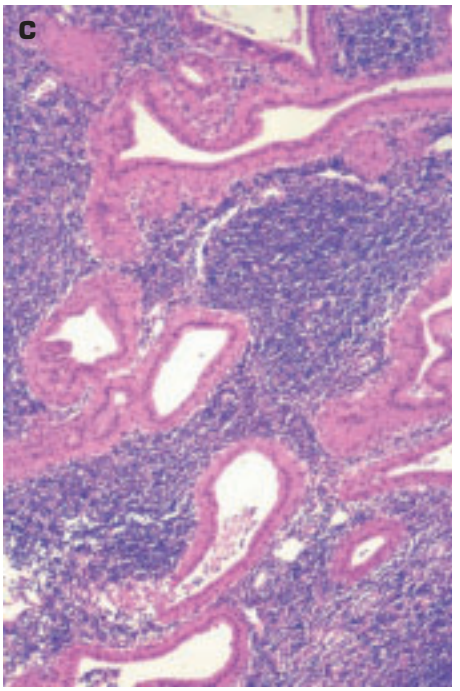

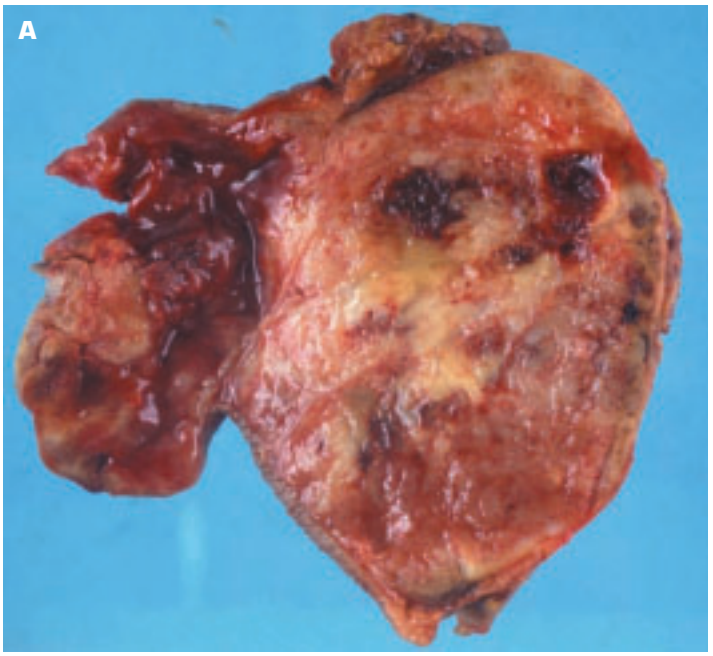

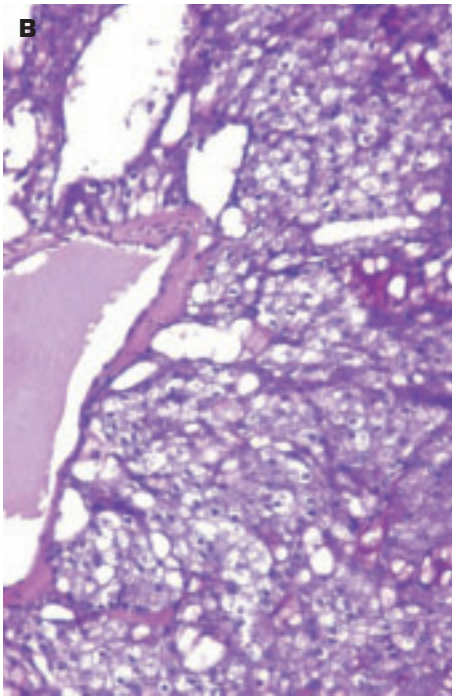

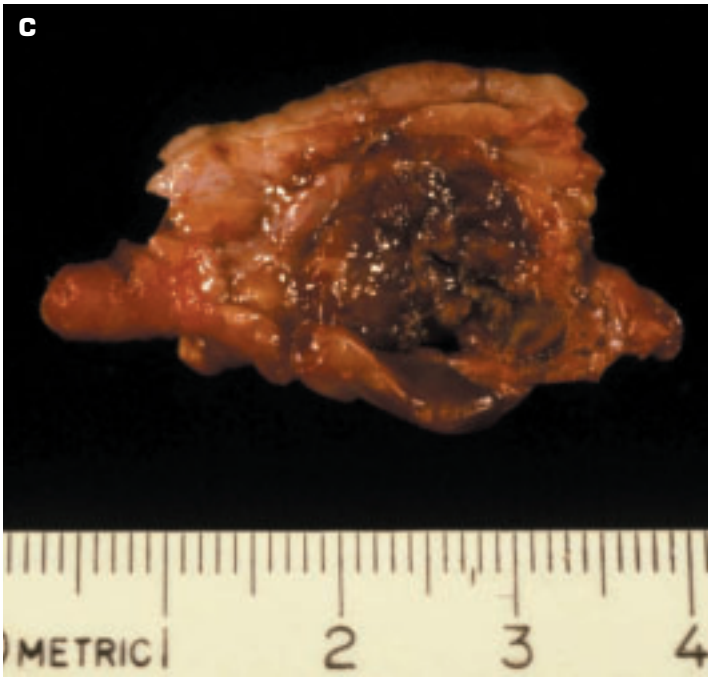

5-5. Malignant tumors of salivary glands include mucoepidermoid carcinoma, adenoid cystic carcinoma (cylindroma), and acinic cell carcinoma. **A.** Acinic cell carcinoma of the parotid gland shows areas of hemorrhage and necrosis on its cut surface. **B.** Histology of acinic cell carcinoma shows cells resembling the secretory (acinic) cells of normal salivary tissue. Although the 5-year survival of acinic cell carcinoma is very good, the 20-year survival is only about 50% due to a tendency for recurrences. **C.** Oncocytoma of the parotid gland.

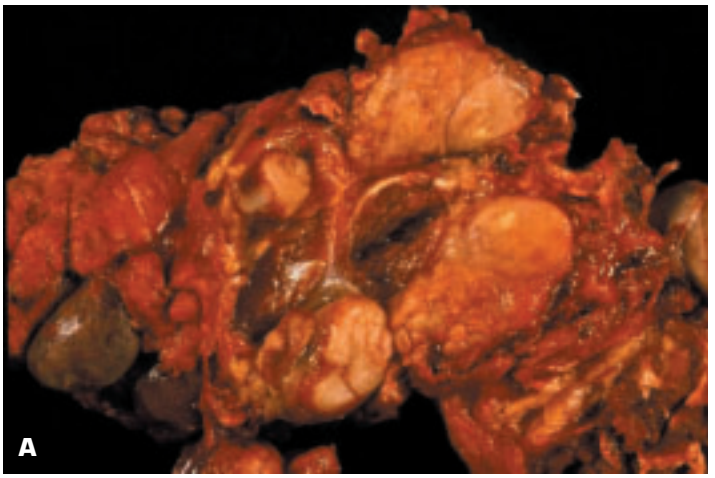

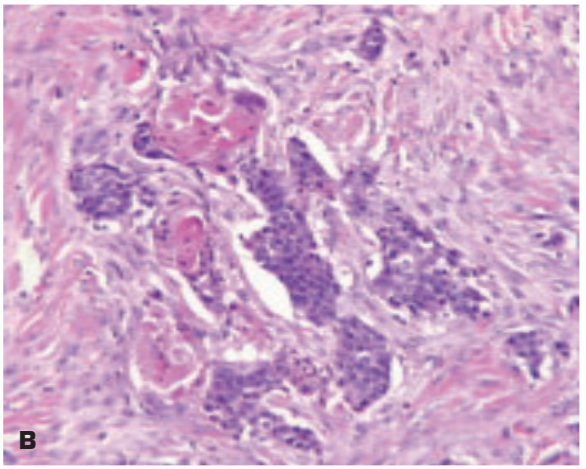

5-6. A. Basaloid squamous carcinoma of the parotid gland is invading the parenchyma and has spread into the intraparotid lymph nodes. **B.** Histology of basaloid squamous carcinoma shows focal squamous differentiation in the islands of basaloid-looking cells.

5-7. Follicular lymphoma has replaced an intraparotid lymph node (*arrows*).

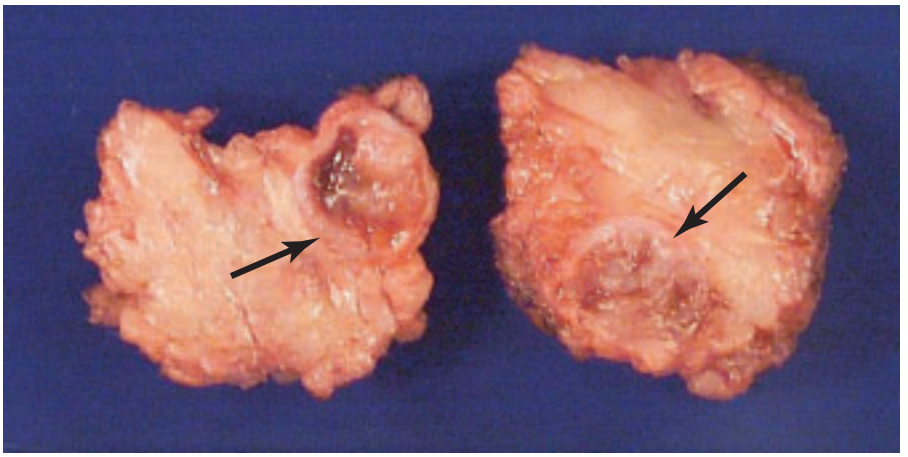

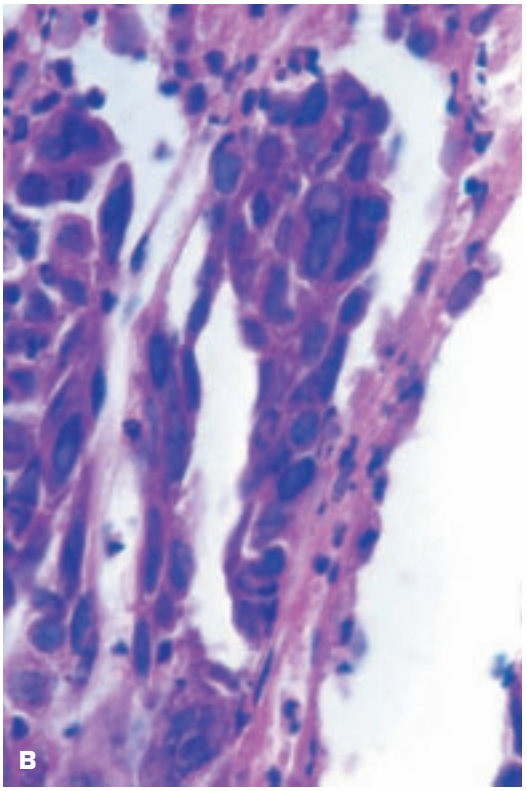

5-8. A. Herpetic ulceration of the tongue tip (*left*) and lateral border (*center*). **B.** Numerous herpesvirus hominis intranuclear viral inclusions within squamous epithelial cells at the edge of a herpetic ulcer.

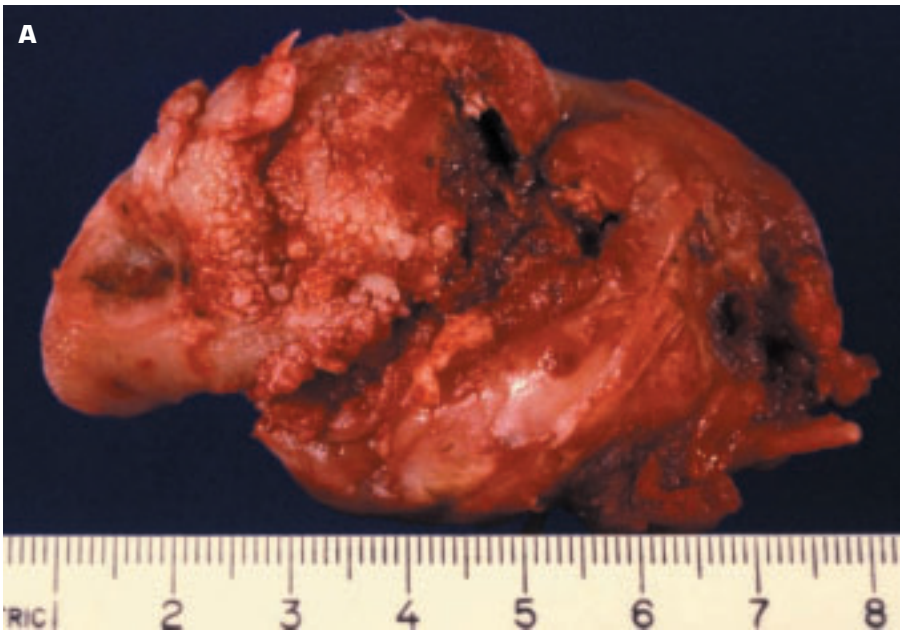

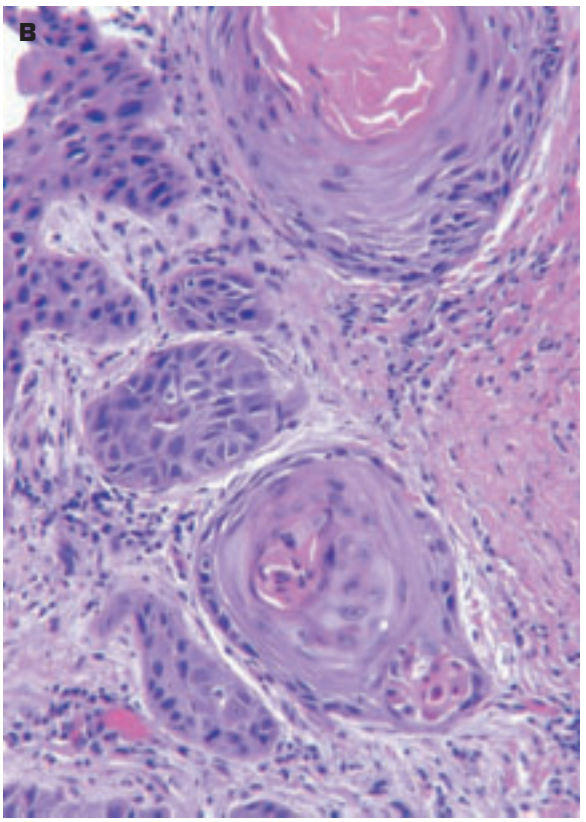

5-9. A. Squamous carcinoma of the lateral border of the tongue has destroyed the surface integrity of the tongue (*center*). **B.** Histology shows a well-differentiated (keratinizing) squamous carcinoma.

5-10. Polypoid juvenile angiofibroma of the nasopharynx in a teenage boy. Although a benign tumor, it may be locally aggressive (e.g., it may invade the skull bones). Biopsy is contraindicated due to the highly vascular nature of the tumor. Radiation treatment may be used in place of surgery.

5-11. Mucosal hemorrhage in the longitudinally divided upper esophagus due to trauma by a misdirected endotracheal tube that was intended for the trachea.

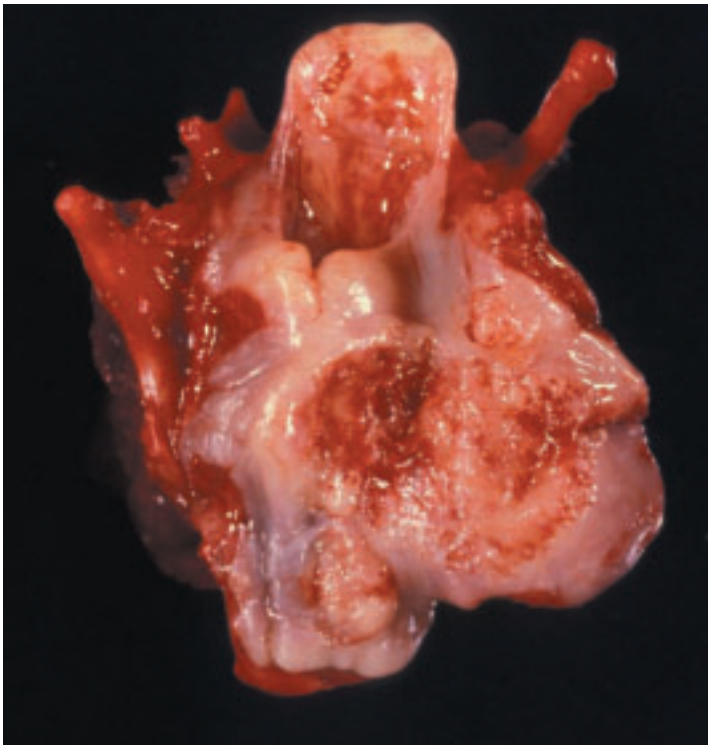

5-12. Squamous carcinoma of the proximal esophagus presenting as both ulceration and thickening of the inner lining of the esophagus.

5-13. Zenker (pulsion) diverticulum surgically excised from the proximal esophagus. The patient had suffered from regurgitation of food eaten days prior, plus episodes of aspiration pneumonia. (In contrast, a traction diverticulum occurs lower down in the esophagus due to adherent tuberculous lymph nodes. An epiphrenic diverticulum occurs near the diaphragm in patients with reflux, esophageal spasm, or achalasia.)

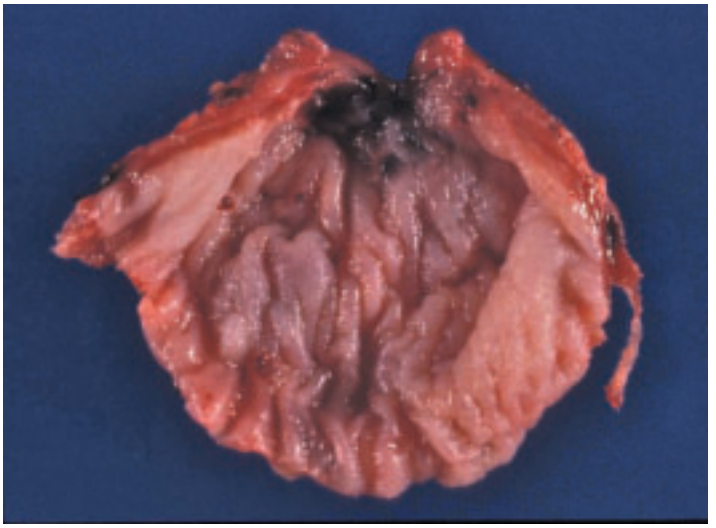

5-14. A. Focal, raised white plaques on the esophageal mucosal lining due to glycogenic acanthosis. **B.** The lesions comprise localized zones of squamous epithelial cells containing abundant glycogen (vacuolated cytoplasm).

5-15. Linear ulceration (*arrows*) of the esophageal mucosa secondary to pressure by a nasogastric tube.

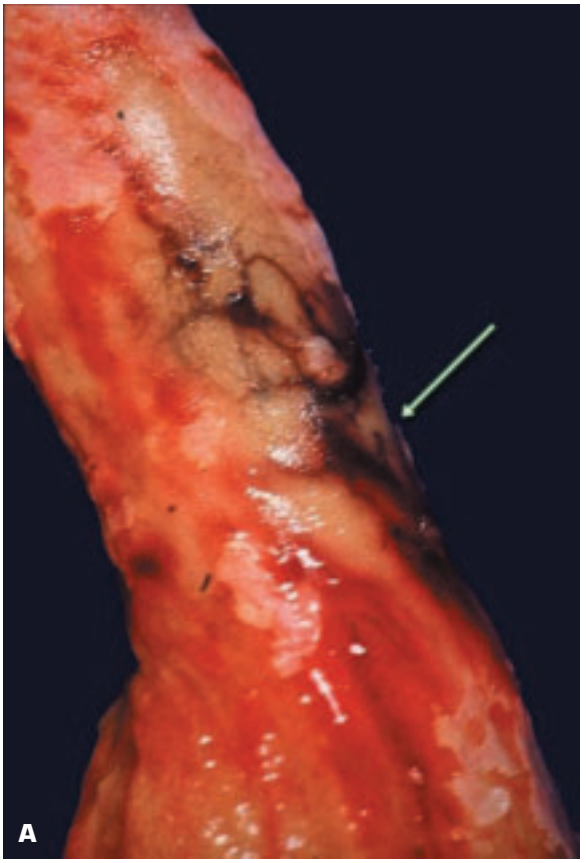

5-16. A. Esophageal varices (*arrow*) have been rendered prominent by turning the esophagus inside out and ligating both ends to prevent the blood draining out. **B.** Histologic appearance of a dilated esophageal vein (varix) within the lamina propria of the esophagus.

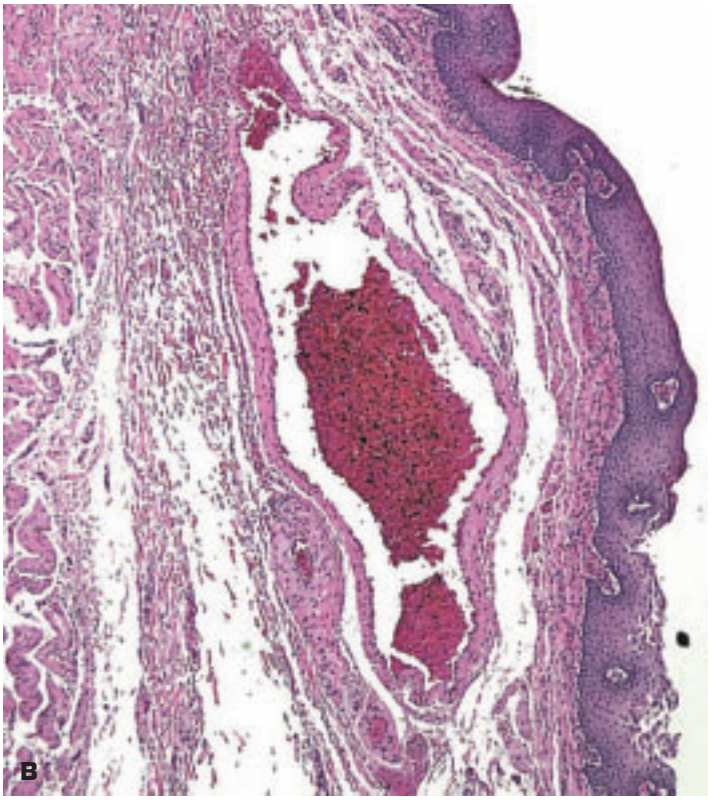

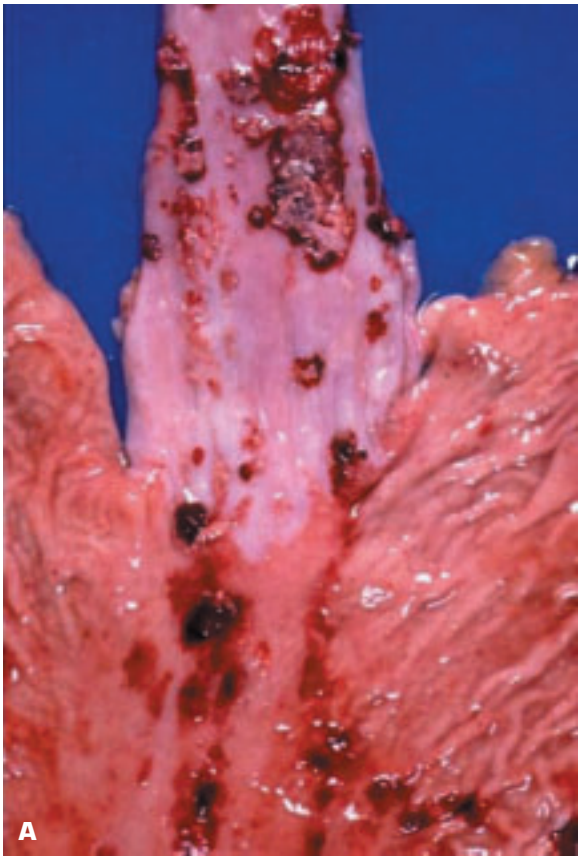

5-17. A. Herpetic ulceration of lower esophagus and stomach. The ulcers are covered by a mixture of necrotic epithelium, fibrin, and some blood. **B.** Herpetic (Cowdry type A) inclusions within squamous epithelial cells bordering an esophageal ulcer.

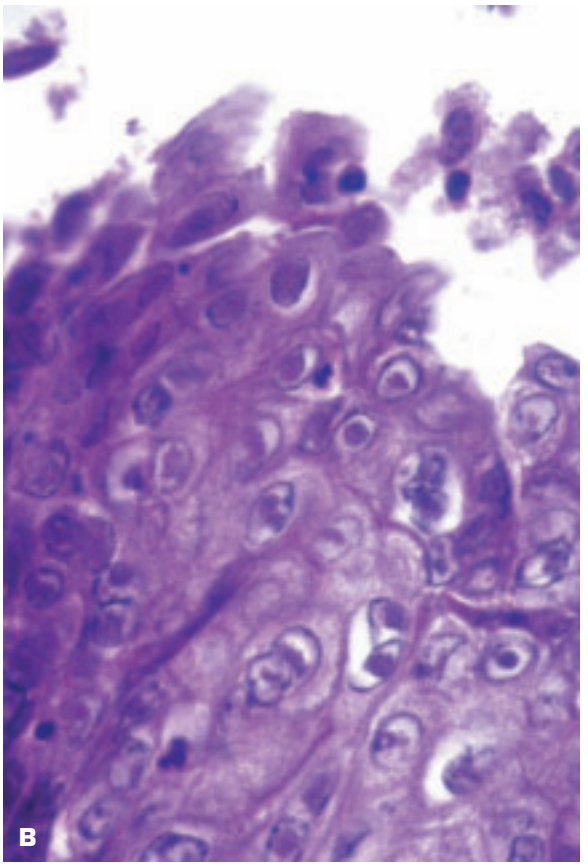

5-18. A. Severe *Candida* esophagitis showing white plaques and easily detachable pseudomembranes resembling oral thrush on the mucosal surface of the esophagus. **B.** Silver stain shows pseudohyphae of pathogenic *Candida*, plus budding yeast forms of the organism within the pseudomembrane.

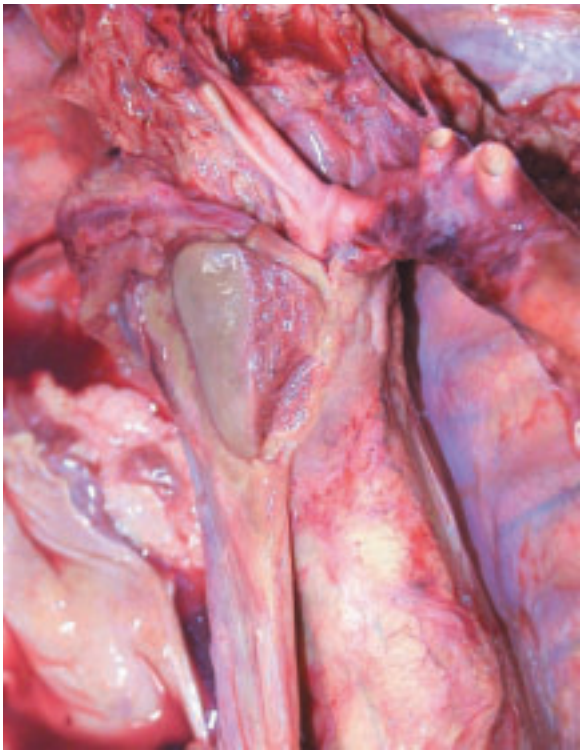

5-19. The proximal portion of the esophagus has been opened longitudinally to reveal a mucosal plaque of infection by *Aspergillus* fungus that has penetrated the esophagus and is invading the aorta from the outside.

5-20. A. Reflux esophagitis has led to ulceration of the lower end of the esophagus with some surviving pale islands of squamous epithelium. **B.** Histology of the epithelium at the edge of the ulcerated area shows eosinophils (*circled*) within the squamous epithelium. Basal cell hyperplasia is also noted.

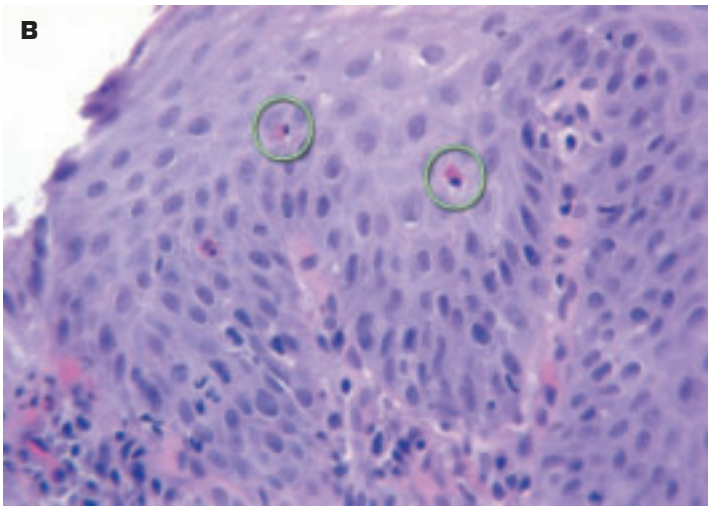

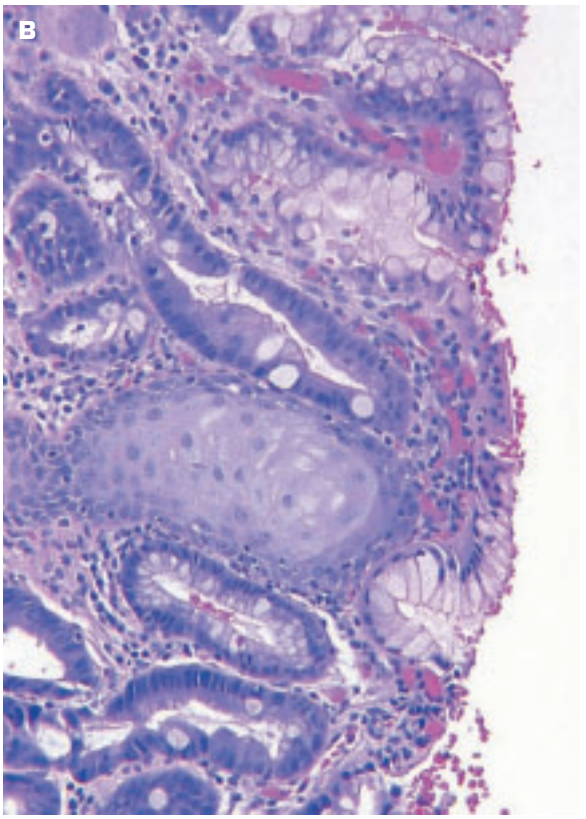

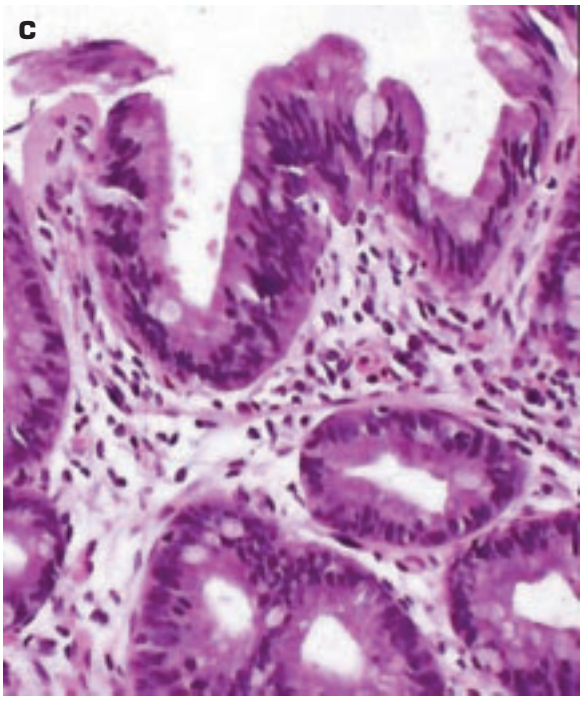

5-21. A. Esophageal surgical resection for Barrett esophagus (pale area of mucosa) (*arrows*). The external resection margins have been inked. **B.** Histology of Barrett esophagus shows the squamous epithelium becoming almost totally replaced by metaplastic, columnar epithelium. The diagnostic intestinal-type goblet cells are present in the surface epithelium. **C.** Low-grade dysplasia in another patient with Barrett esophagus.

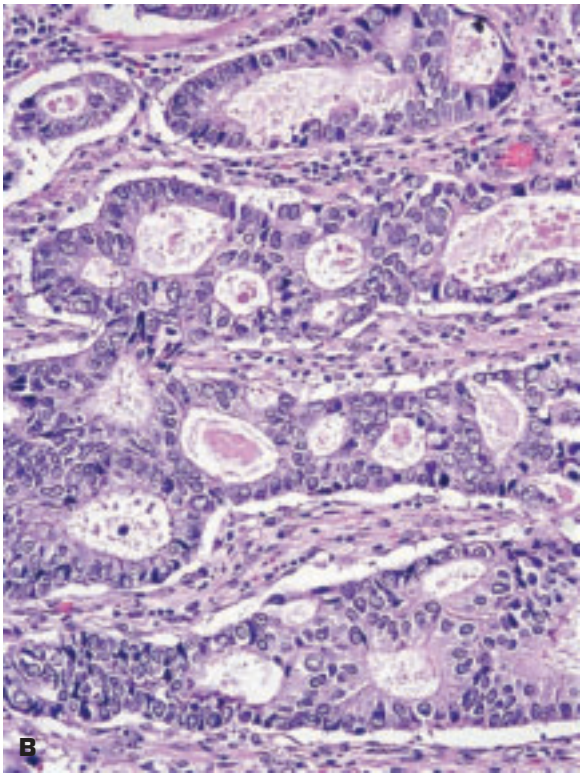

5-22. A. Adenocarcinoma that has arisen in an area of Barrett esophagus is infiltrating the gastroesophageal junction. **B.** Histology of the lesion shows an invasive adenocarcinoma of intestinal type.

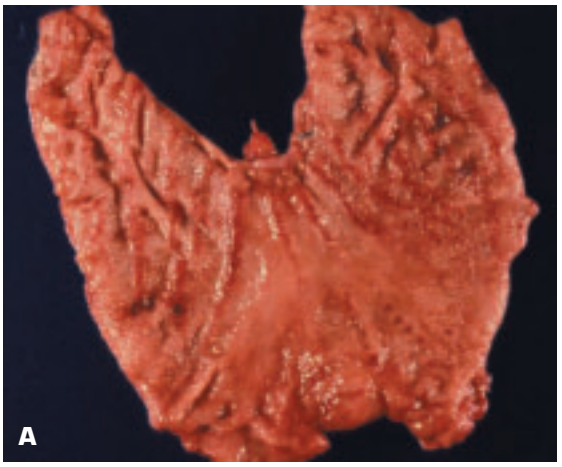

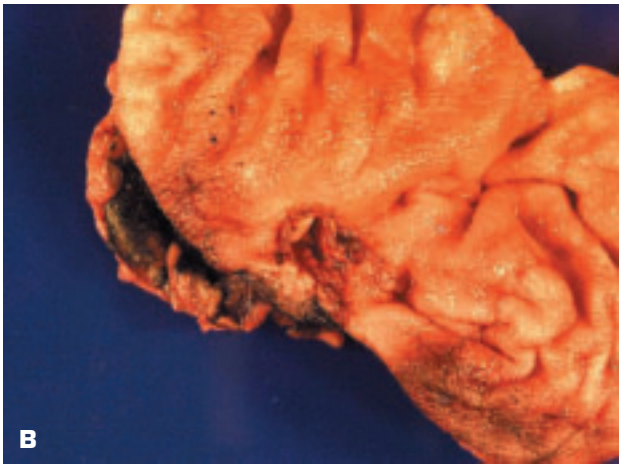

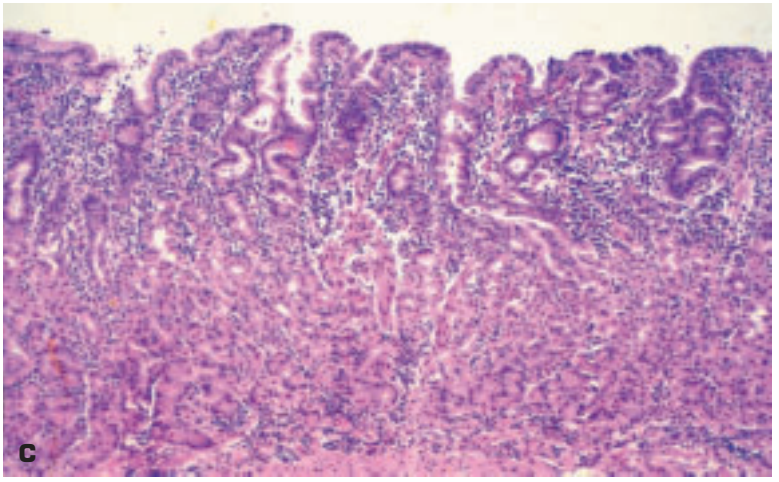

5-23. A. Acute on chronic gastritis. Note the reddened, granular appearance of the gastric mucosa that also appears smoother than normal in some areas. **B.** Chronic inactive gastritis. **C.** Histology of chronic gastritis showing numerous mononuclear cells (lymphocytes and plasma cells) within the gastric mucosa.

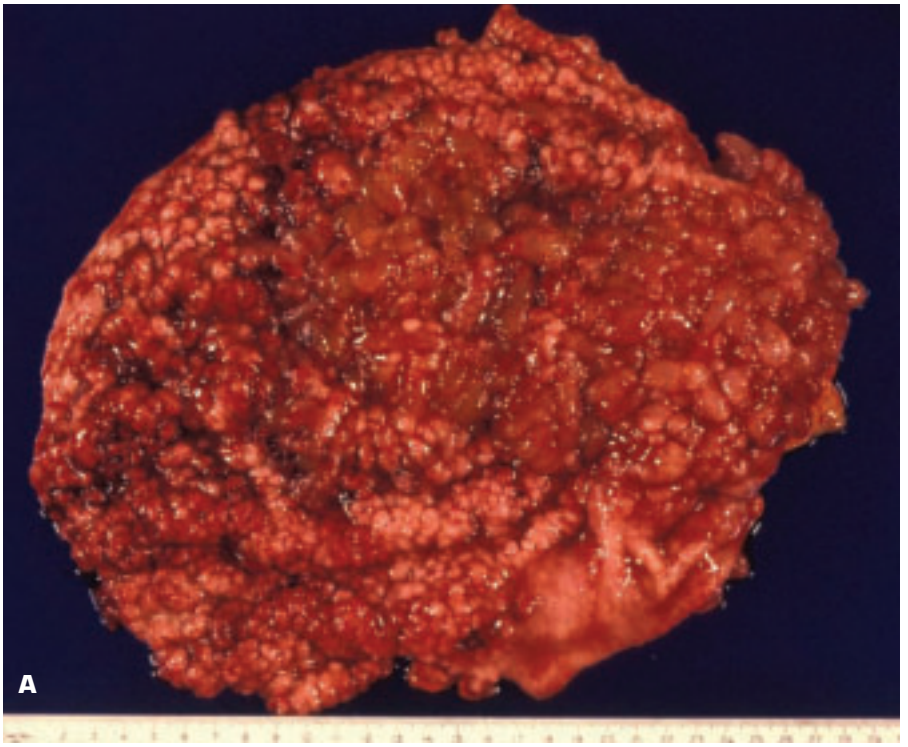

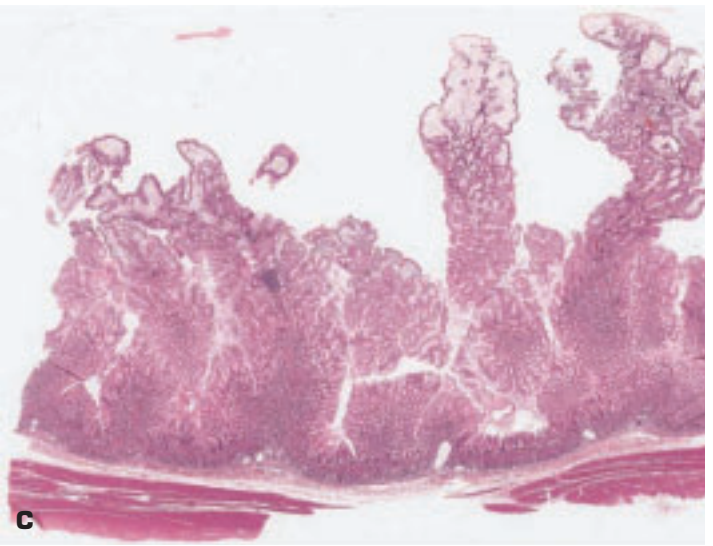

5-24. The feature of hypertrophic gastropathy (HG) is giant cerebriform rugal fold enlargement of the gastric mucosa. Three conditions may produce such an appearance: Ménétrièr disease (surface mucous cell hyperplasia with gland atrophy), hypertrophic-hypersecretory gastropathy (hyperplasia of parietal and chief cells), and gastric gland hyperplasia secondary to a gastrinoma/Zollinger–Ellison syndrome. **A.** Hypertrophic gastropathy shows an exuberant expansion of rugal folds that may be mistaken for a neoplasm on endoscopic or radiographic examinations. **B.** Slice of stomach showing the greatly thickened mucosal folds of HG. **C.** Histology shows a marked increase in the number of the surface mucous cells consistent with Ménétrièr disease.

5-25. A. Lymphoid hyperplasia of the stomach presenting as multiple small intramucosal nodules. **B.** Multiple reactive germinal follicles are situated in the deep aspect of the gastric mucosa adjacent to the muscularis mucosae.

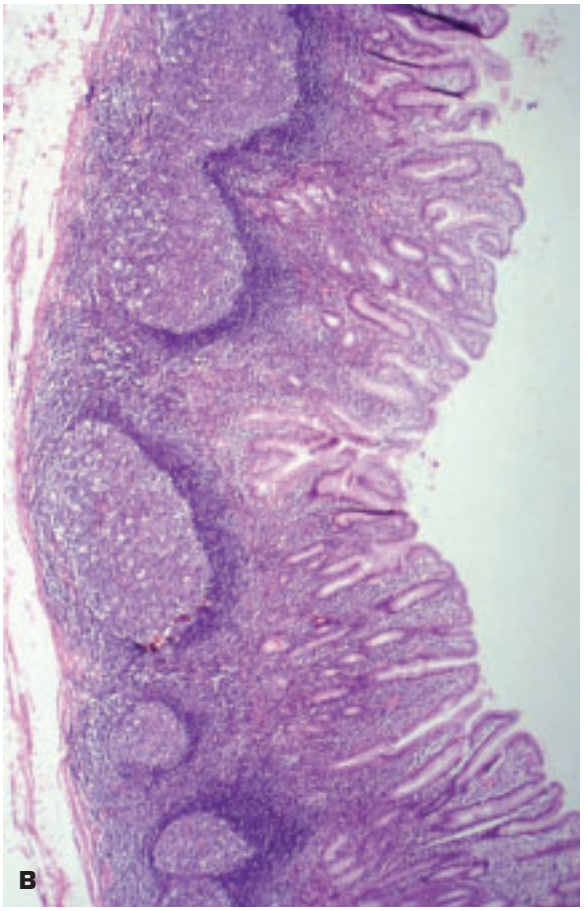

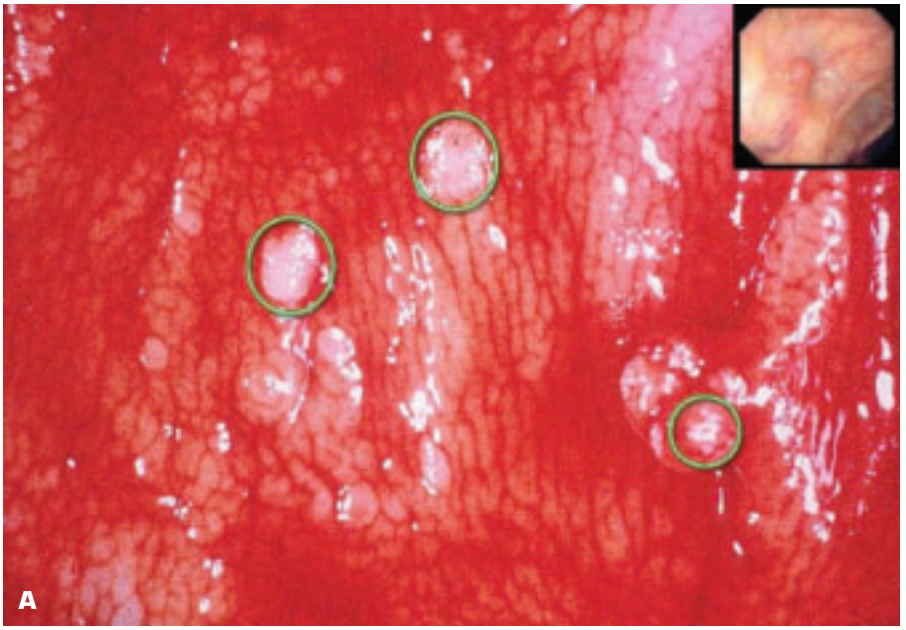

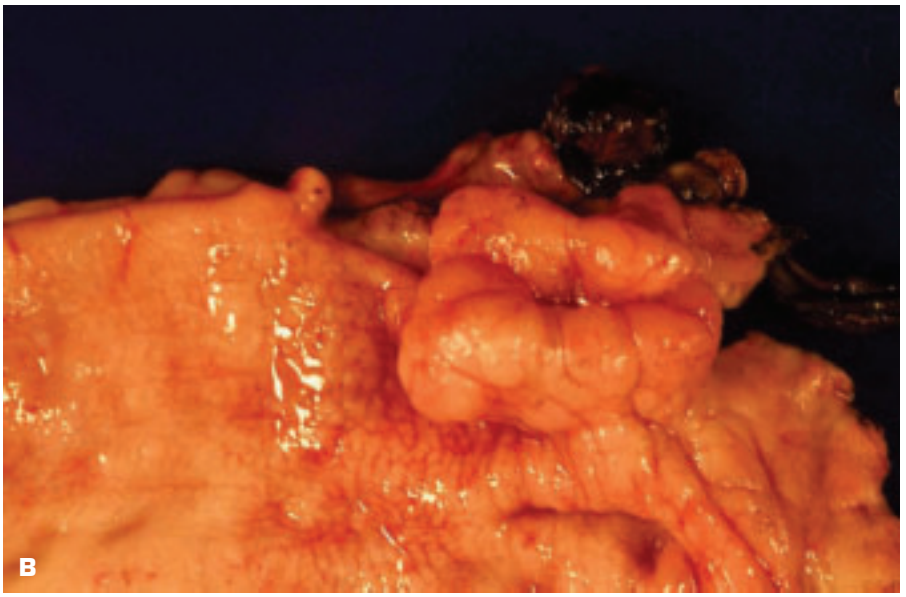

5-26. A. Multiple small hyperplastic polyps (*circled in close-up view*) of the stomach. These are the most common type of polyp found in the stomach. Hyperplastic polyps may occur in the atrophic body and fundal mucosa of patients with atrophic gastritis or in the antrum of patients with *Helicobacter pylori* infection. These polyps have no malignant potential (unlike adenomatous polyps). Proton pump inhibitor therapy may lead to the formation of benign fundic gland polyps. **B.** Single large hyperplastic polyp of the stomach. *(continued on next page)*

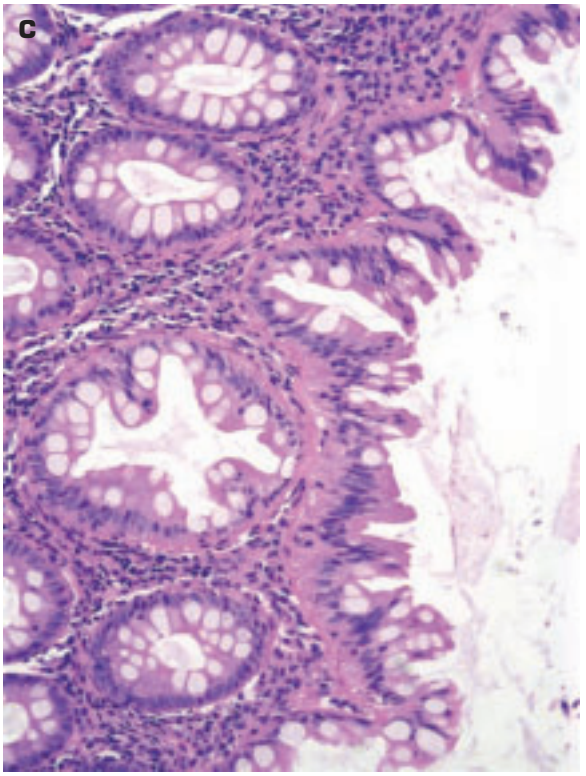

5-26. *(Continued)* **C.** Histology shows a serrated surface epithelium with foveolar epithelium lining the underlying crypts. **D.** Multiple tubular adenomas (adenomatous polypi) of the stomach with atypia. **E.** Histology of tubular adenoma showing mild atypia of the surface epithelium.

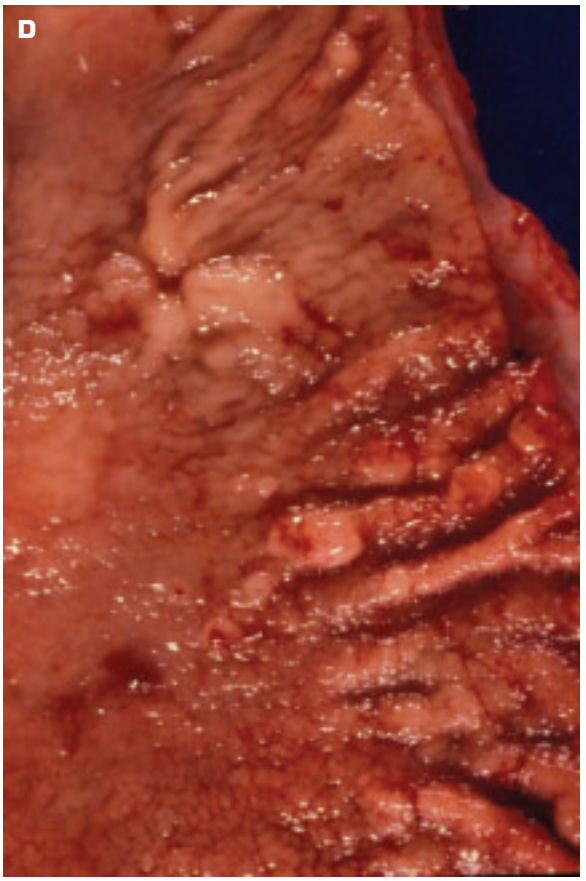

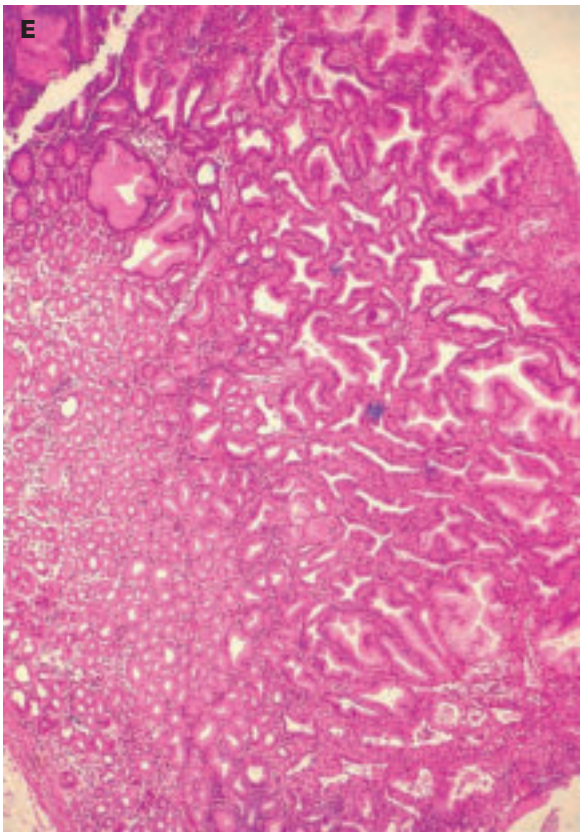

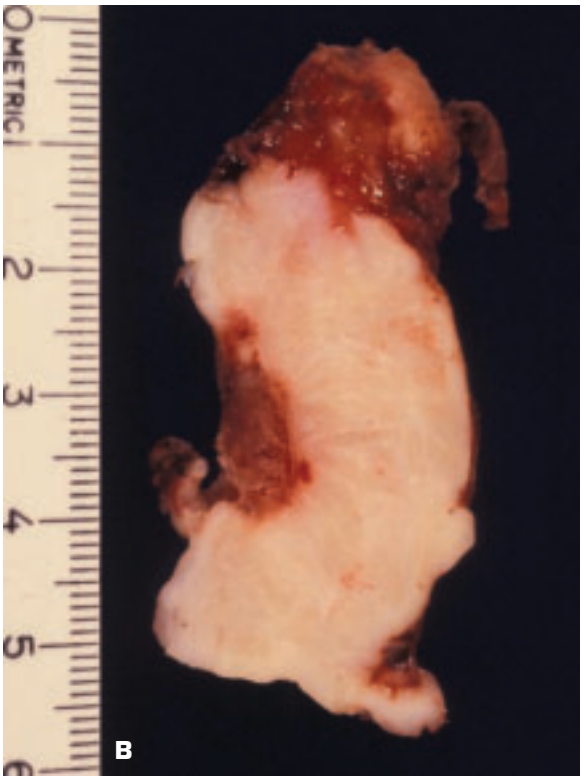

5-27. Gastrointestinal stromal tumor (GIST) of the stomach. **A.** Gastric mucosa with focal ulcerated, excavated area (*top left*) overlies a submucosal GIST. **B.** Transverse section of a GIST shows an area of necrosis (*left center*) with ulceration of overlying gastric mucosa.

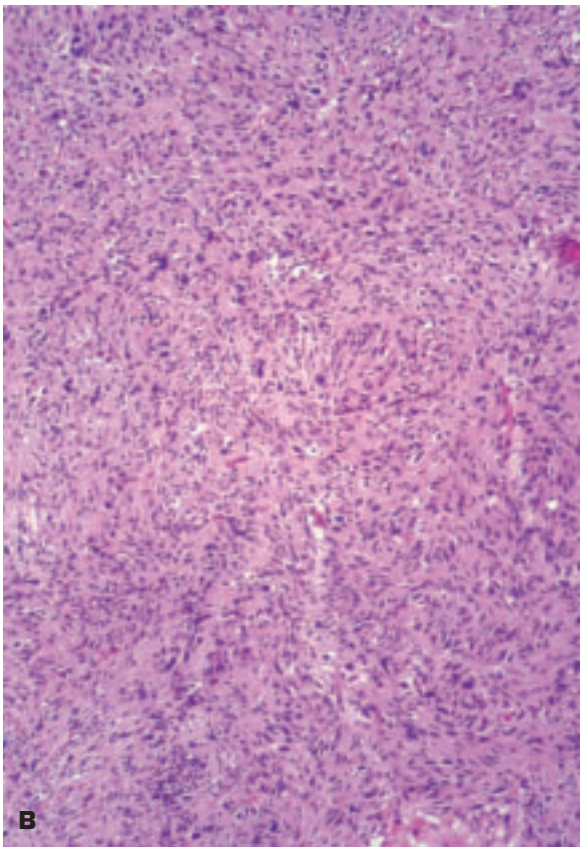

5-28. A. Desmoid tumor of mesentery in Gardner syndrome shows focal areas of necrosis and cystic degeneration. **B.** Histology of desmoid tumor showing interweaving fascicles of spindle-shaped cells in a fibrous stroma.

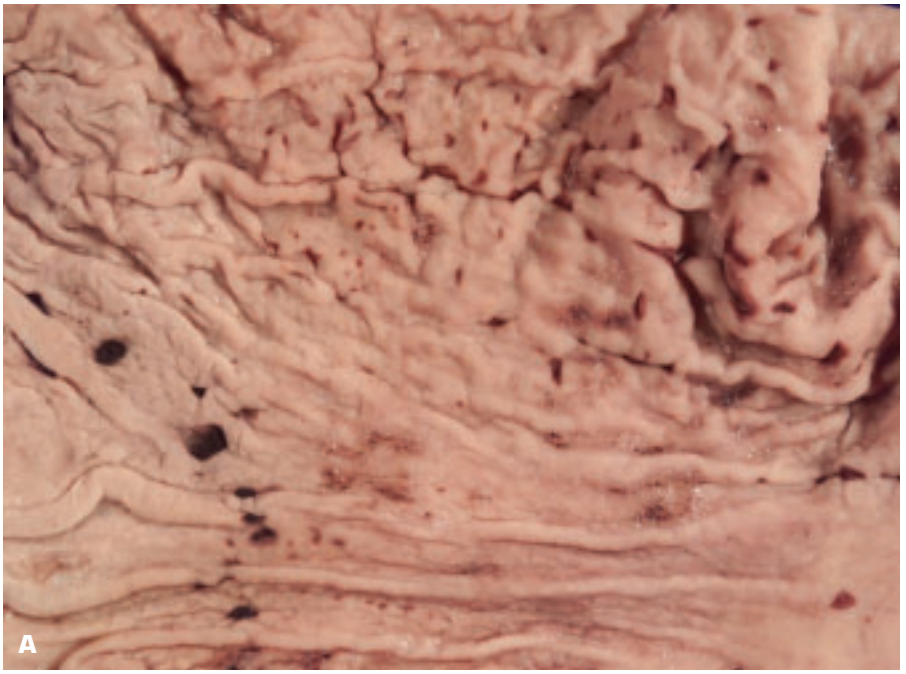

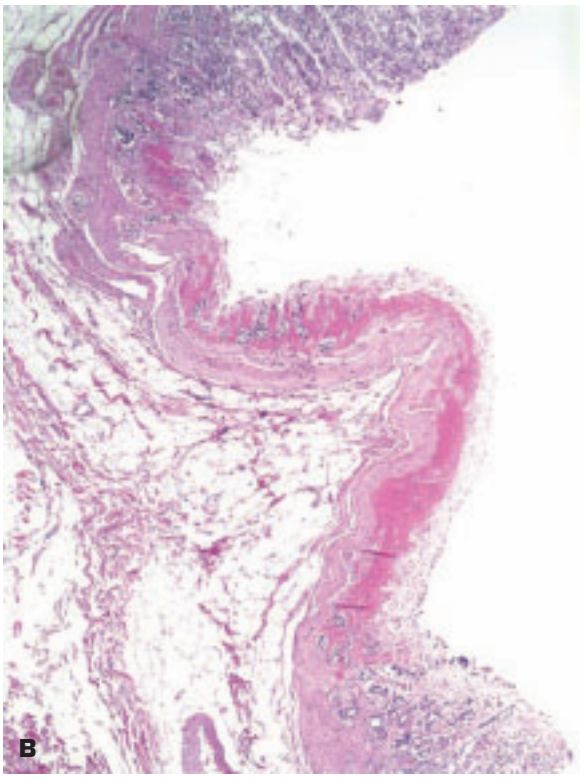

5-29. A. Acute gastric erosions (hemorrhagic gastropathy) are rendered more visible by associated superficial hemorrhage. **B.** Histology shows focal mucosal ulceration plus intramucosal hemorrhage.

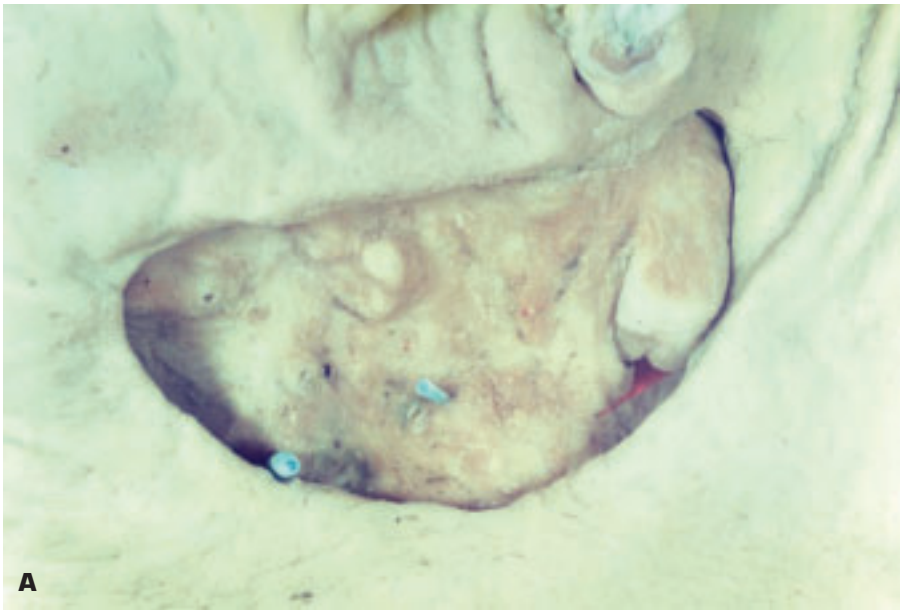

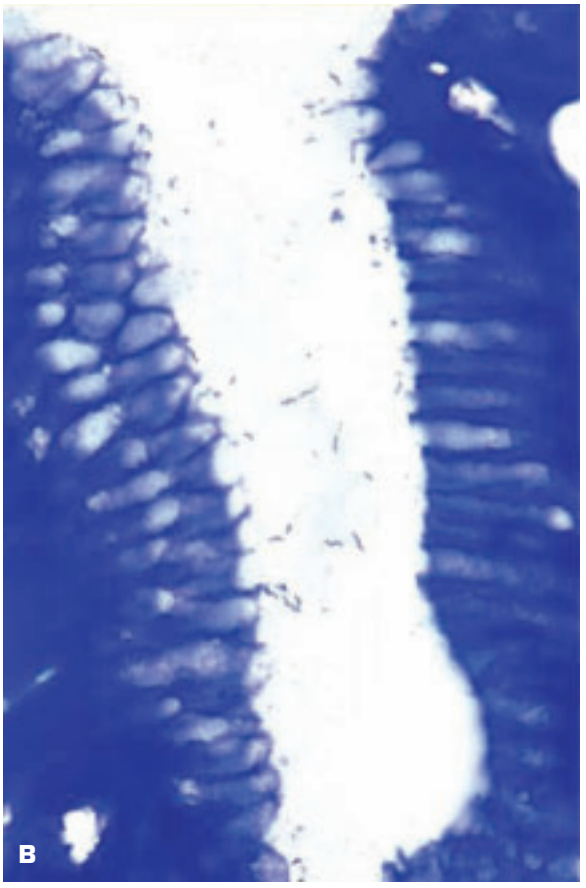

5-30. A. Chronic peptic ulcer of the stomach has a sharp, punched-out edge. Probes have been inserted into two small arteries in the ulcer base that caused significant bleeding. **B.** *Helicobacter pylori* organisms are seen on the surface epithelium. These organisms have been implicated in the etiology of peptic ulcers. *(continued on next page)*

5-30. *(Continued)* **C.** Healing gastric ulcer shows indrawing of the mucosal folds toward the ulcer margins due to contraction of fibrous tissue. **D.** Healed chronic gastric ulcer shows radiating folds pointing to the site of the healed ulcer.

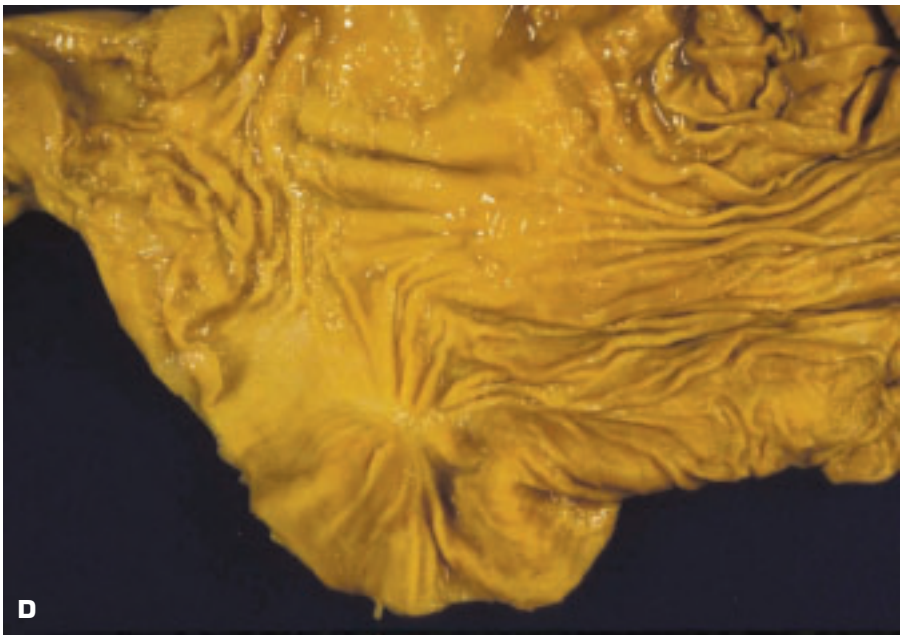

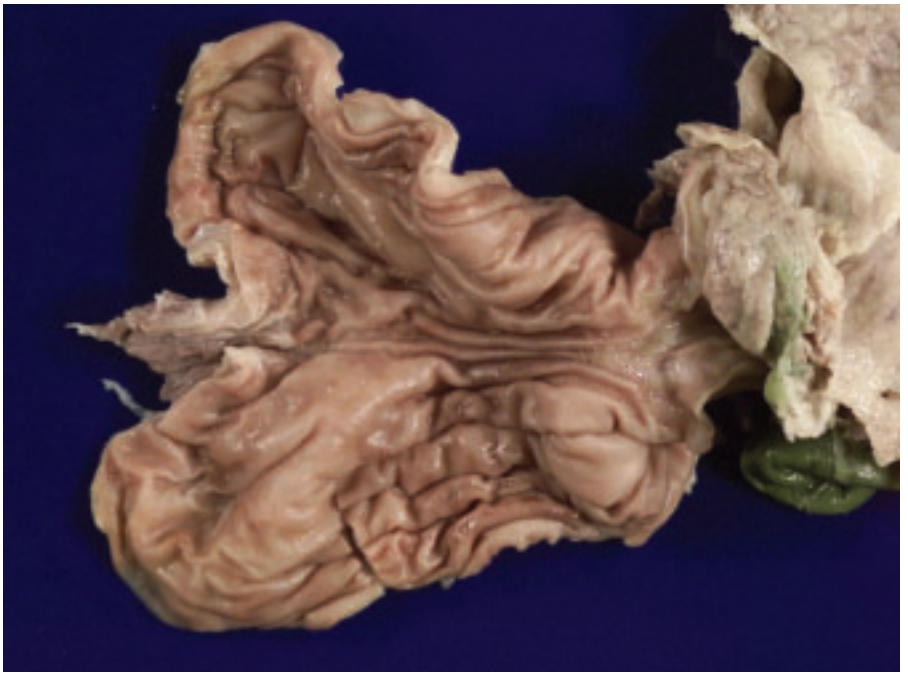

5-31. Massive edema of the stomach has caused ballooning of the mucosa, and the surface has a smoothed-out appearance. Patient had received an excessive amount of intravenous fluids in combination with cardiac failure.

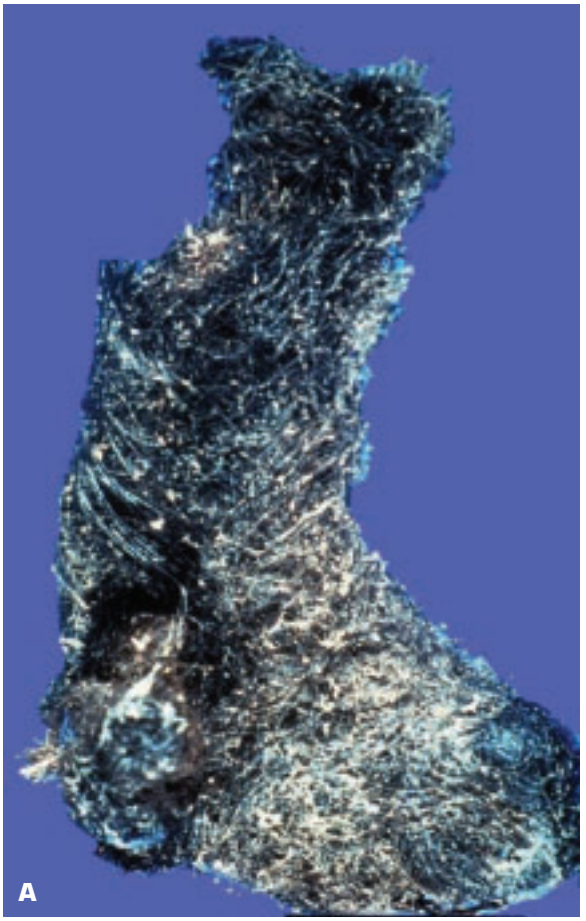

5-32. Foreign bodies within the stomach. **A.** Trichobezoar (hairball) of the stomach is composed of a mass of hairs swallowed by the patient that has become encased by food residues and mucus. Note that the hairball appears in the shape of a cast of the stomach. In the *Rapunzel syndrome*, long strands of hair may extend through the small gut into the colon. (In phytobezoars, vegetable matter takes the place of hair.) **B.** Left ventricular assist device (LVAD) pump casing that eroded into and came to occupy the lumen of the stomach. On gastroscopy, the endoscope viewed the serial number of the LVAD!

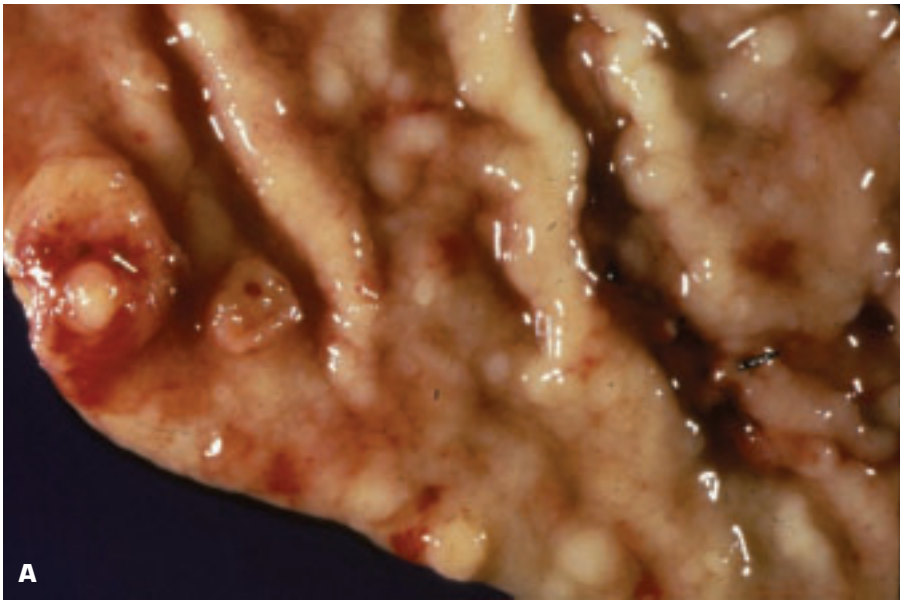

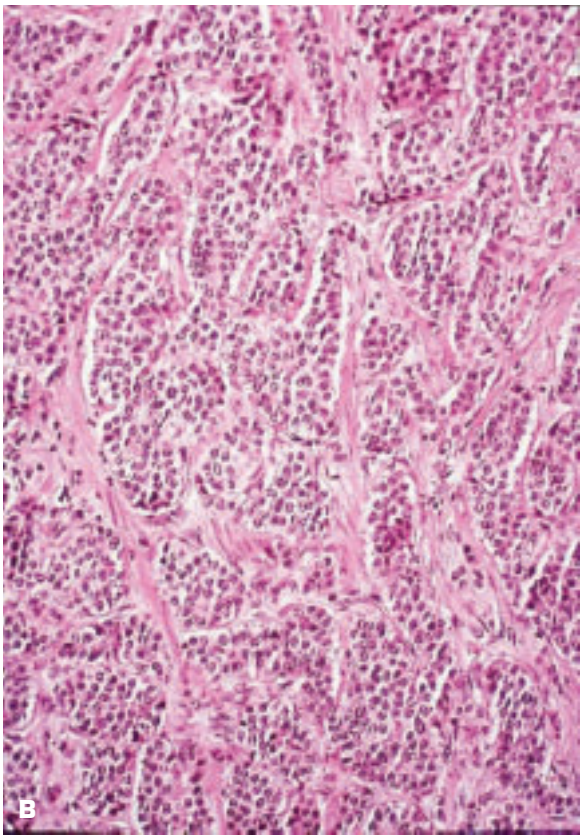

5-33. A. Multiple small carcinoid (neuroendocrine) tumors of the stomach. **B.** Histology of carcinoid tumor showing lack of anaplasia; the size of the tumor is more important than the histology in predicting the potential for metastasis.

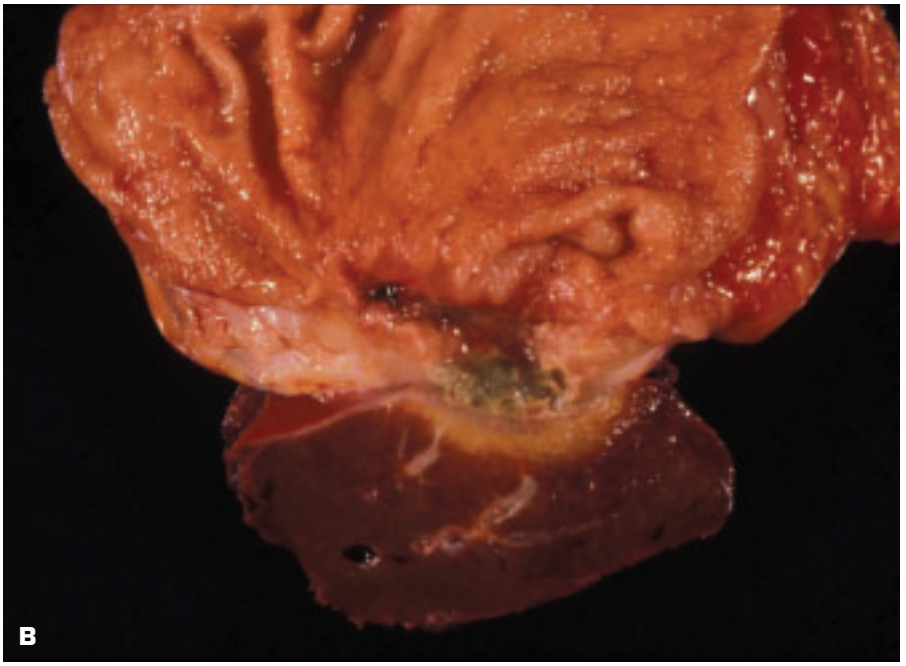

5-34. A. This ulcerated gastric cancer has a deceptively sharp border suggestive of a benign gastric ulcer. **B.** Section of the same lesion reveals that the cancer is directly invading the underlying liver. *(continued on next page)*

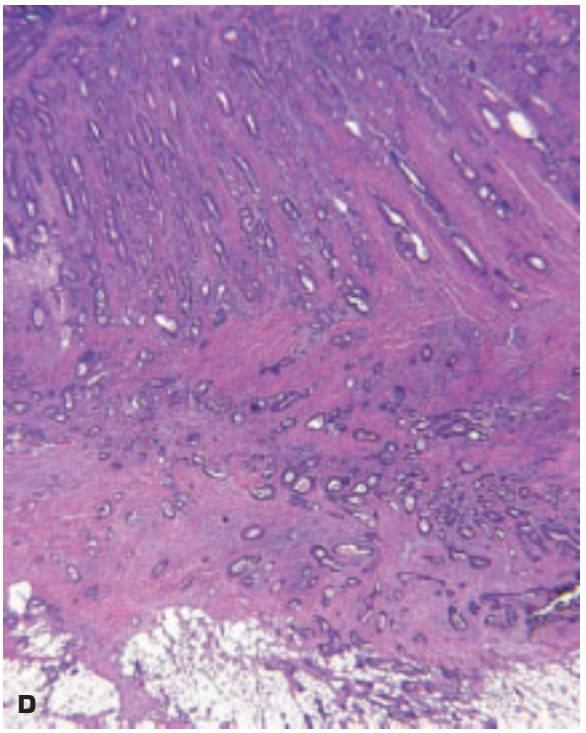

5-34. *(Continued)* **C.** Surgically resected gastric carcinoma. **D.** Histology of the gastric carcinoma shows an intestinal type of adenocarcinoma. *(continued on next page)*

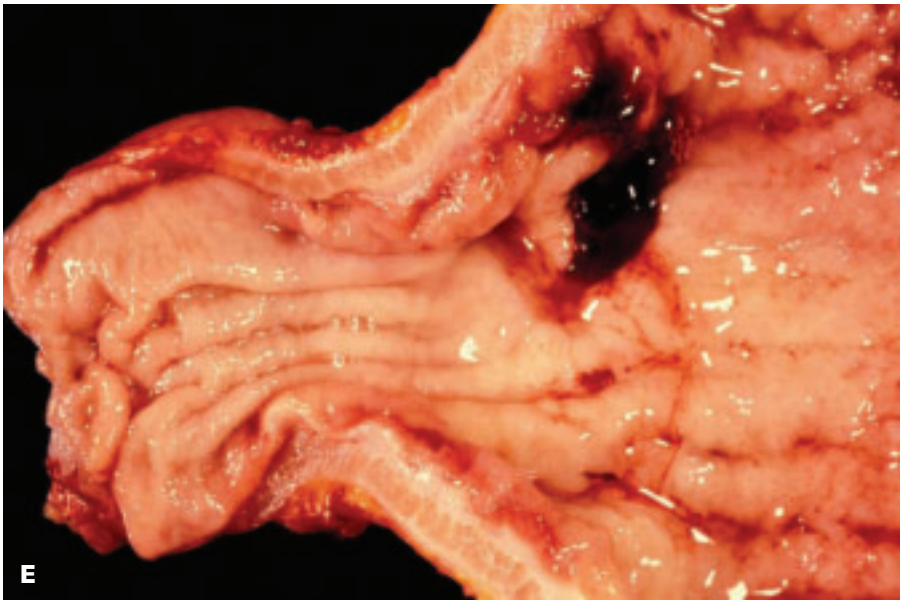

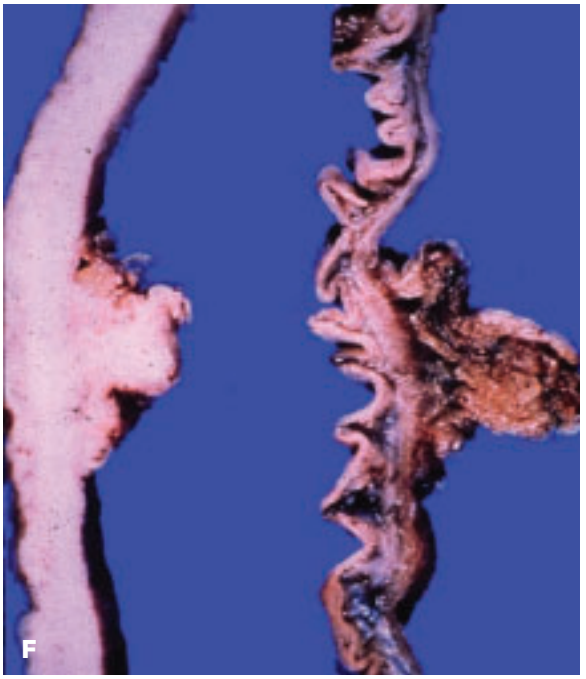

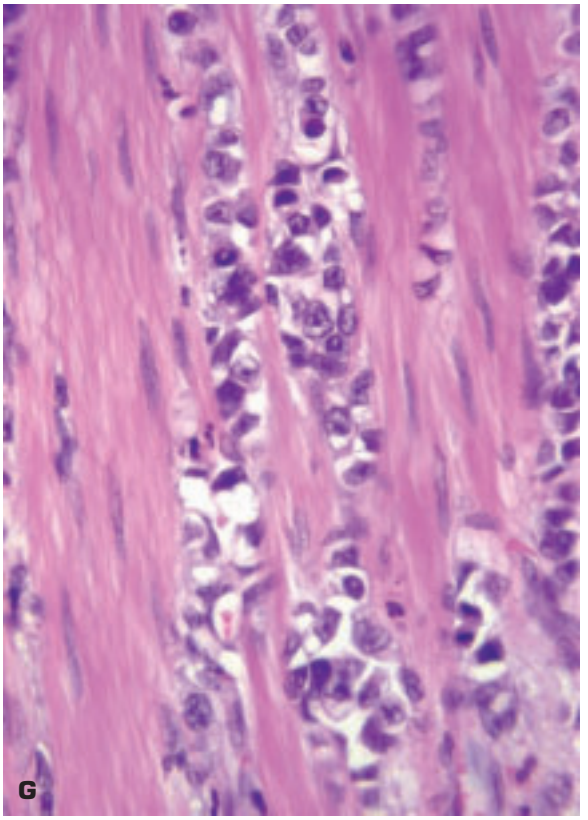

5-34. *(Continued)* **E.** Diffusely infiltrating gastric carcinoma (so-called leather bottle stomach). **F.** Sections of two stomachs comparing a diffusely infiltrating carcinoma (*left*) and a normal stomach (*right*). **G.** Histology shows diffusely infiltrating signet ring–shaped malignant cells between smooth muscle cells of stomach muscularis.

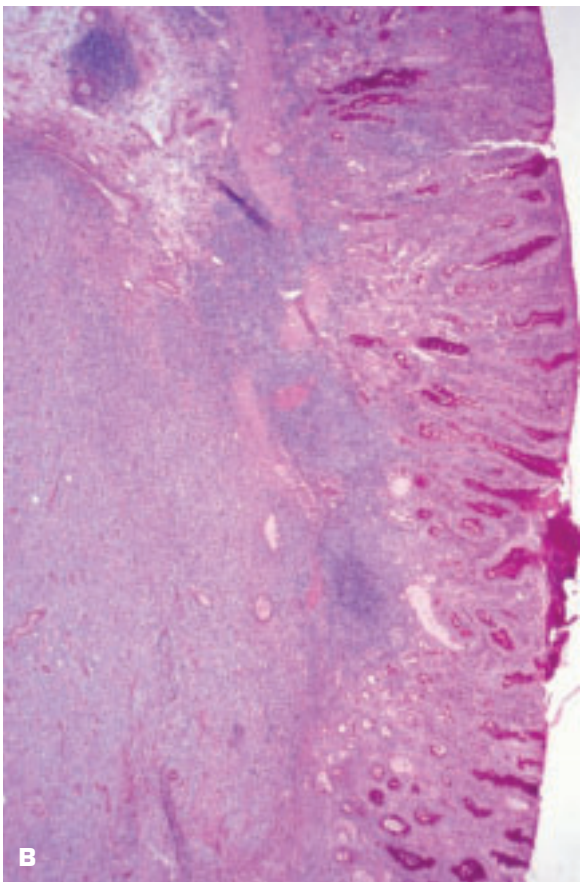

5-35. Lymphoma of the stomach. **A.** Mucosa shows multiple lymphomatous nodules, some of which have become ulcerated. (The esophagus shows glycogenic acanthosis.) **B.** Histology shows lymphoma infiltrating into the mucosa from the submucosa.

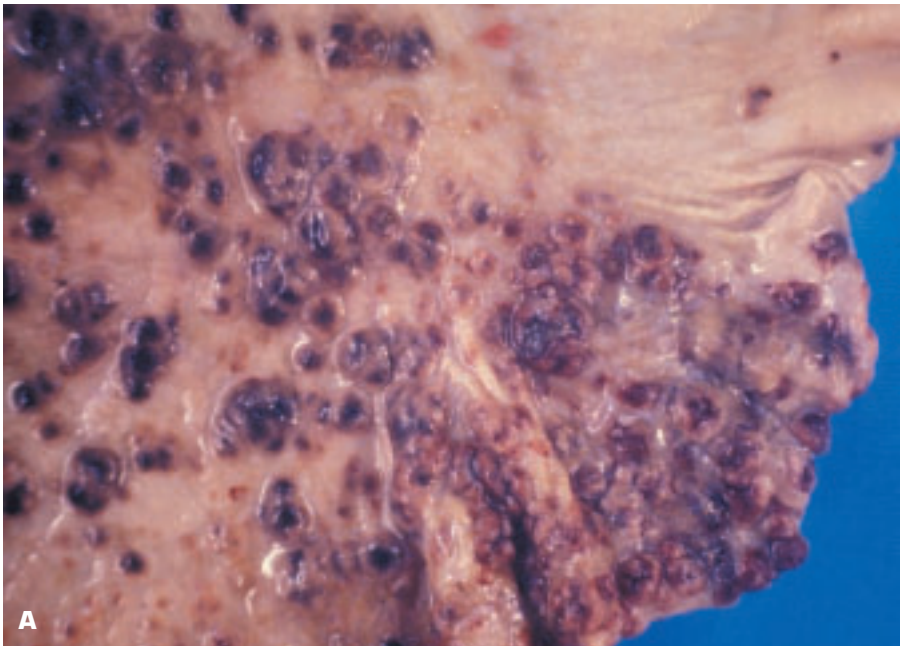

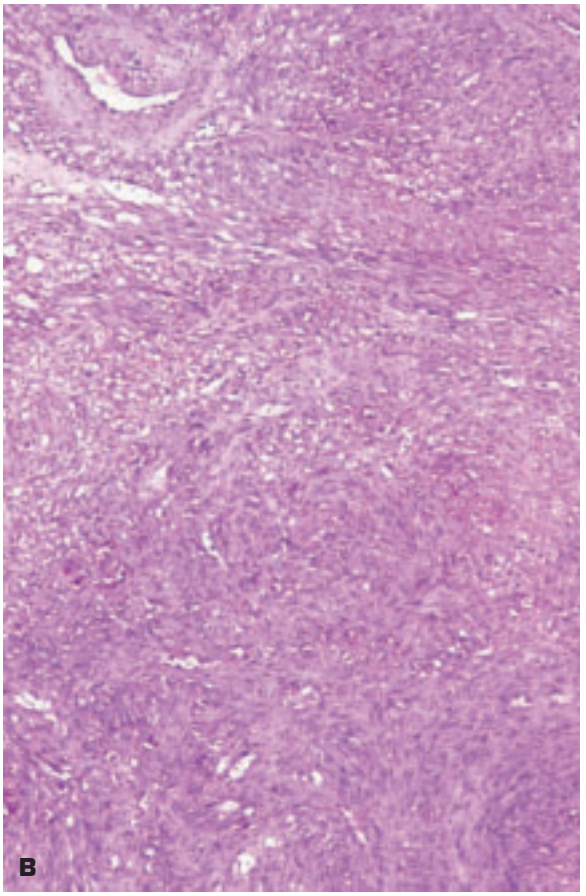

5-36. A. Kaposi sarcoma of the stomach. The multiple highly vascular-looking tumor nodules in the gastric mucosa should make one think of an angiosarcoma. **B.** Histology shows that interweaving fascicles of spindle-shaped cells surround many slit-like spaces.

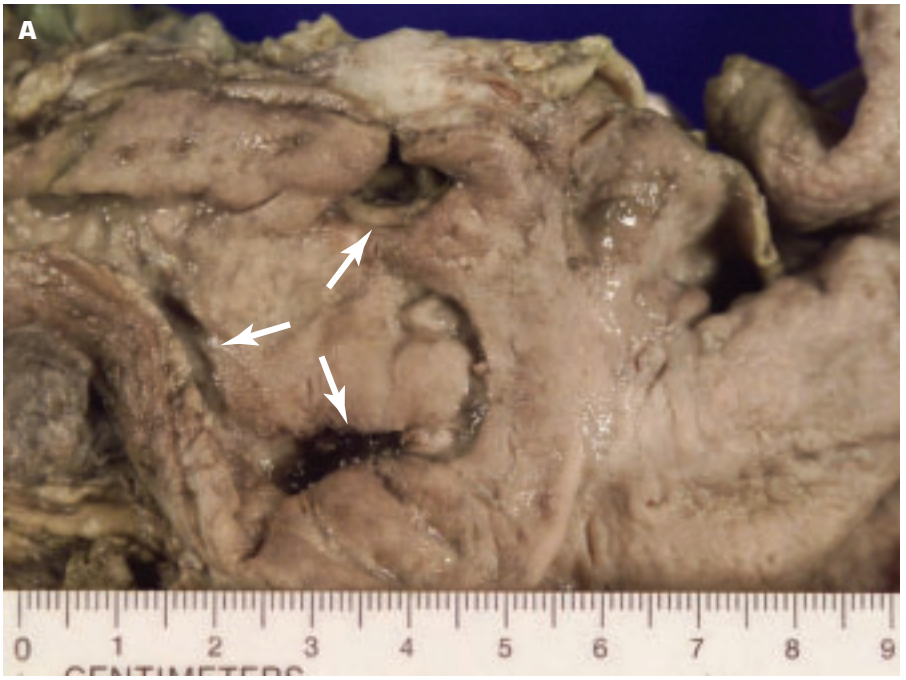

5-37. A. Duodenum contains multiple chronic peptic ulcers (*arrows*). **B.** Blood cast of the duodenum due to clotted blood from bleeding into the lumen.

5-38. Congenital atresia (*arrow*) of the duodenum: there is no continuity between the distal stomach (*left of center*) and the jejunum (*far left*).

5-39. Duodenal mucosa bears multiple tubular adenomas (adenomatous polypi), plus an adenocarcinoma (*arrow*).

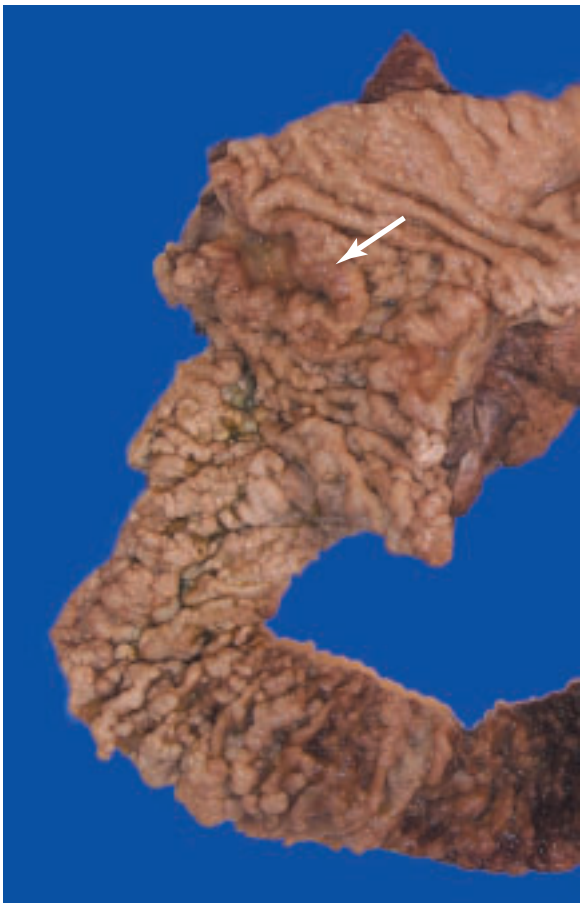

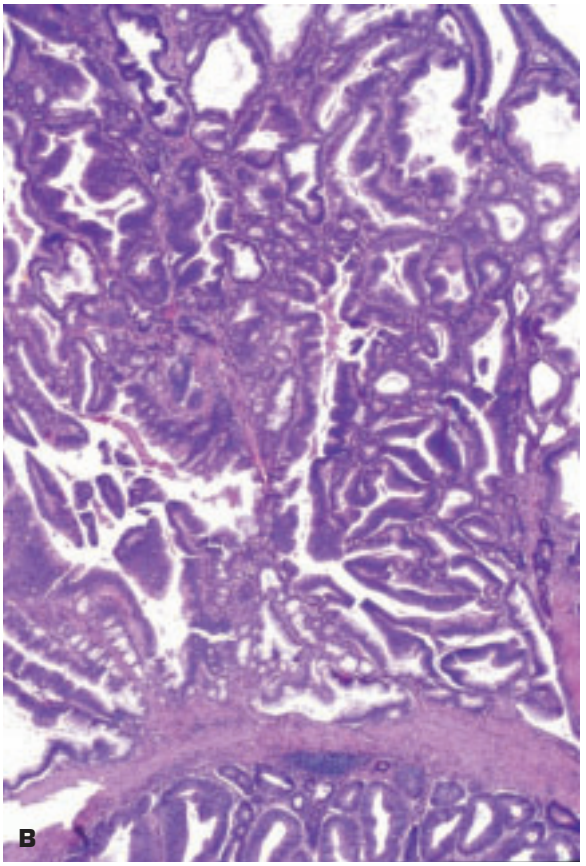

5-40. Adenocarcinoma of the ampulla of Vater in the second part of the duodenum. **A.** Tumor obstructs the lumen of the ampulla. **B.** Histology shows a well-differentiated papillary adenocarcinoma.

5-41. Volvulus has led to venous infarction of the small intestine. **A.** Note the purple, hemorrhagic appearance of the dilated, necrotic gut. **B.** Montage of pictures starting counterclockwise from lower left shows (i) infarcted small gut, (ii) and (iii) histologic hemorrhage filling the submucosa of colon, and (iv) extreme congestion and thrombosis of dilated veins in bowel wall. The arteries are patent.

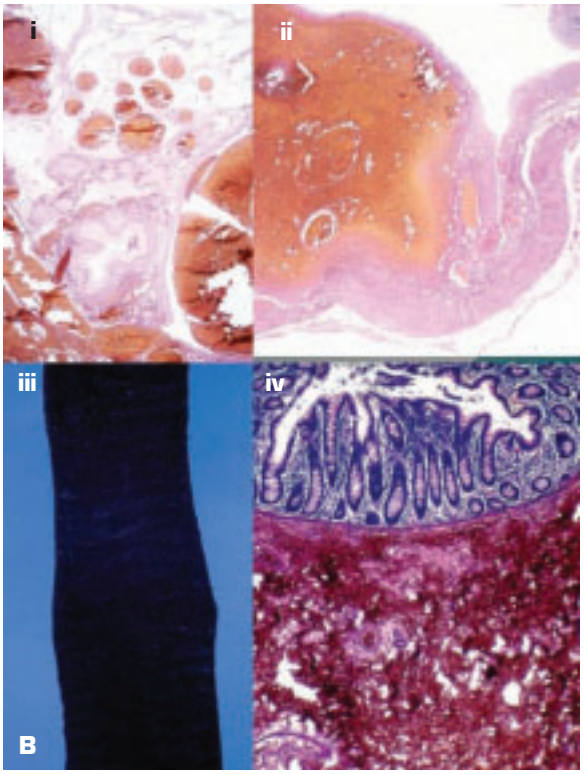

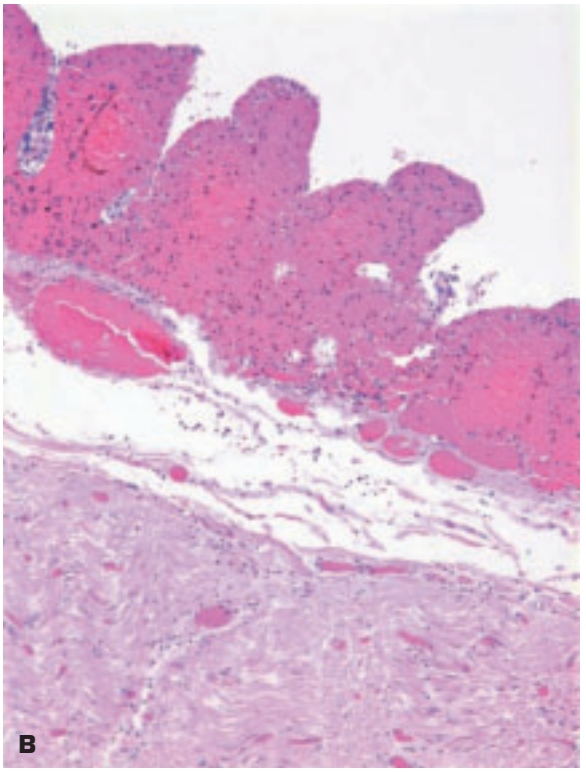

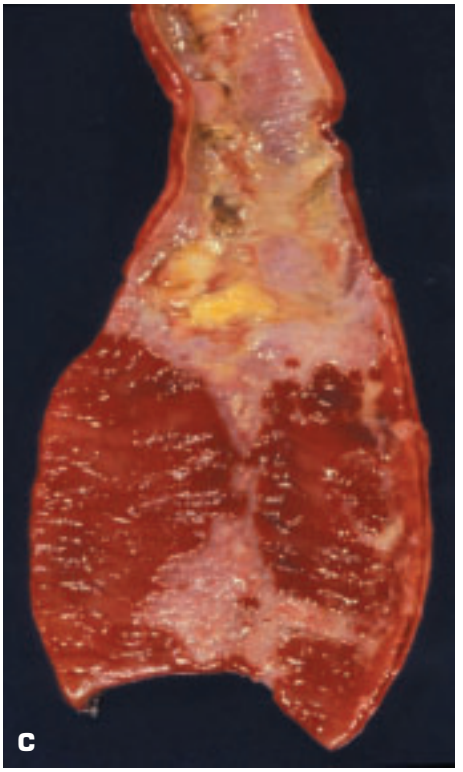

5-42. A. Arterial ischemia of the intestine. Skip areas of ischemic necrosis of small gut due to systemic hypotension and vasoconstriction of the splanchnic arterial bed. **B.** Acute necrosis of ileum showing hemorrhagic necrosis of the mucosa. **C.** Necrotizing enterocolitis due to an enterotoxin produced by *Clostridium perfringens* following ingestion of contaminated meat. This latter condition is rare in industrialized nations.

5-43. Diverticula of the jejunum. Diverticula may occur anywhere in the intestines but are most common in the sigmoid colon.

5-44. Multiple mucosal ulcers of jejunum due to graft-versus-host disease in a bone marrow transplant recipient.

5-45. Idiopathic perforation of the ileum of a few days' duration showing granulation tissue and early fibrosis at the edge of the defect.

5-46. Crohn disease (regional ileitis): segmental transmural inflammation of the gut. **A.** Transverse sections of ileum showing severe luminal narrowing. **B.** Early Crohn disease with prominent inflammation and mucosal ulceration. **C.** Chronic Crohn disease showing cobblestoning (due to edema and inflammation) between extensive areas of linear ulceration. *(continued on next page)*

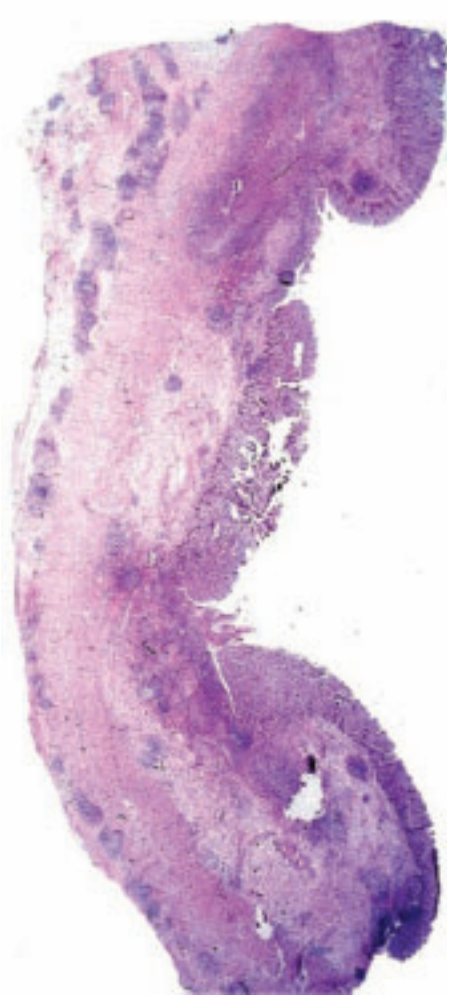

D

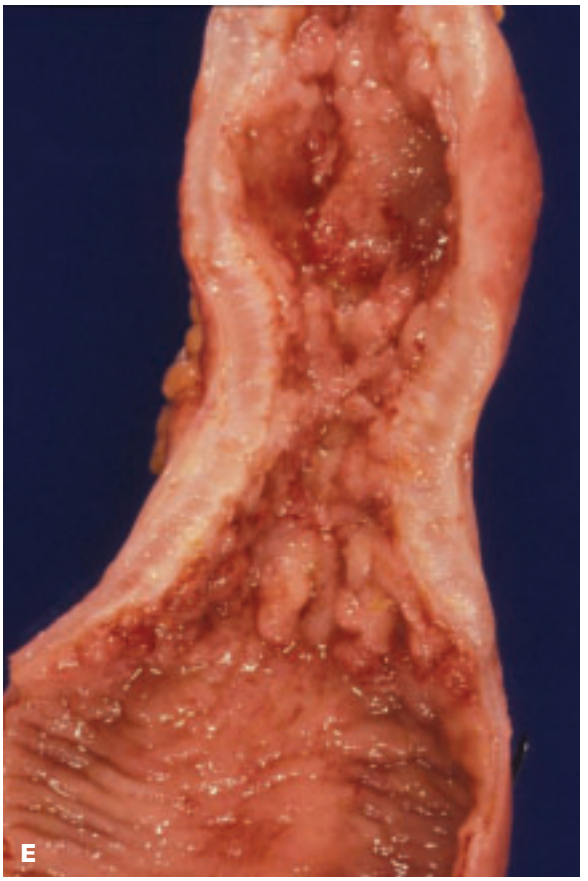

E

5-46. *(Continued)* **D.** Histology of Crohn disease showing transmural inflammation with lymphoid germinal centers and granulomas. **E.** Stenosis of the colon due to regional enteritis.

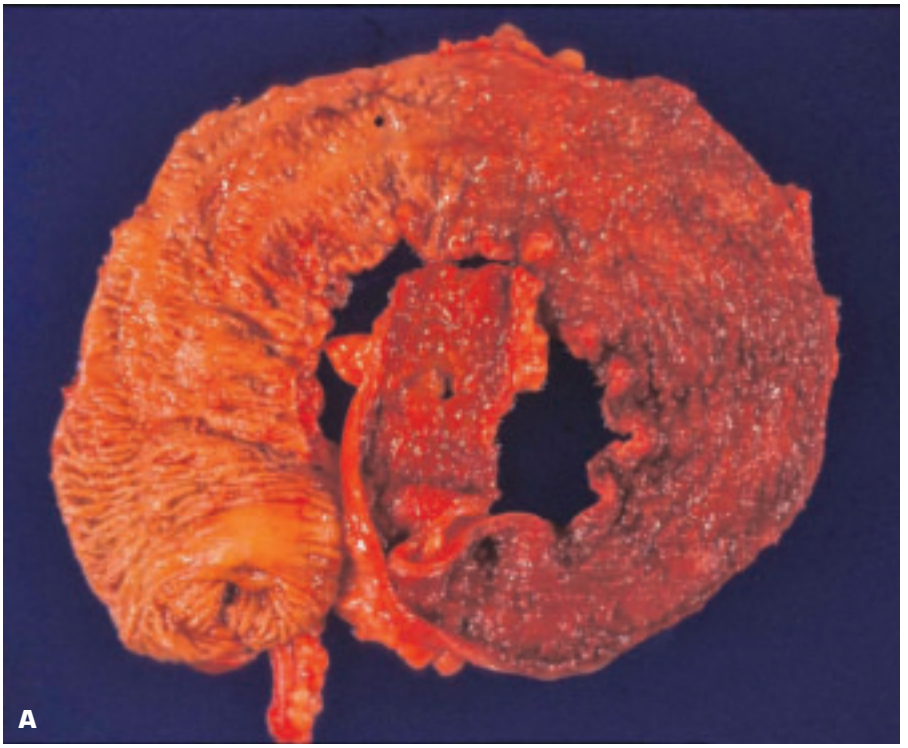

5-47. Ulcerative colitis (UC): chronic superficial ulceration of colon and rectum. **A.** Erythema and mucosal ulceration are more marked in the left colon and rectum (*right half of picture*) in this total colectomy specimen. Cecum and appendix are seen (*bottom left*). **B.** Close-up view shows granular-looking, acutely inflamed, ulcerated surface of colon. *(continued on next page)*

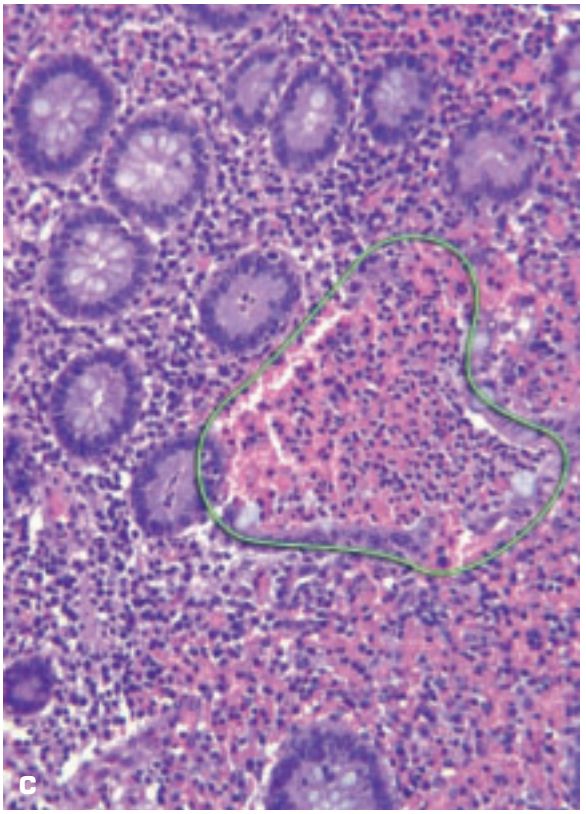

5-47. *(Continued)* **C.** Histology showing a crypt abscess (*outlined in green*) and basal lymphocytosis. **D.** Rectal involvement in UC. *(continued on next page)*

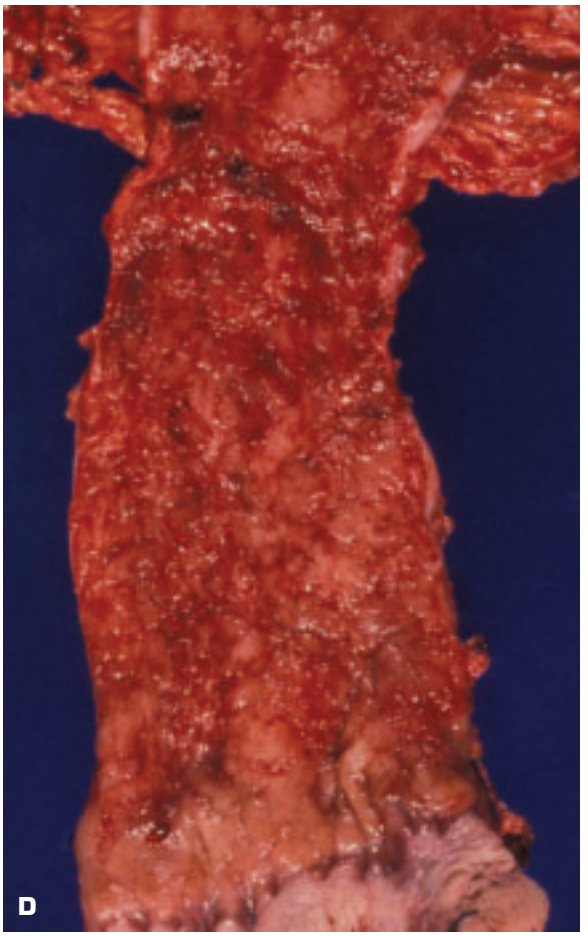

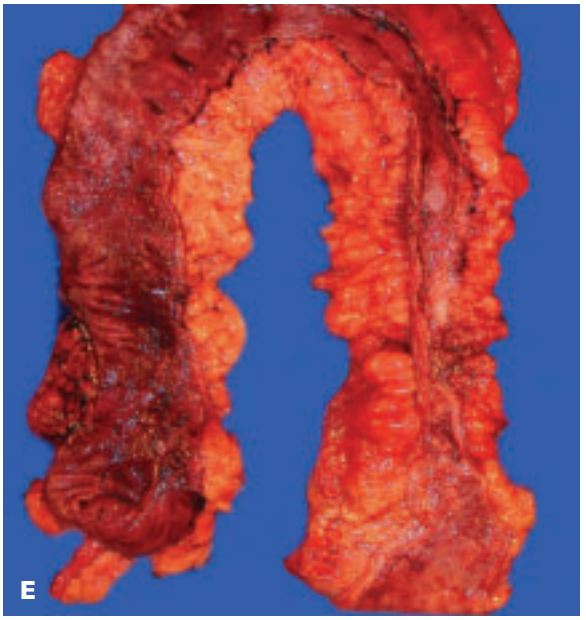

5-47. *(Continued)* **E.** Chronic UC that had biopsy-proven multiple areas of precancerous dysplasia. **F.** Pseudopolypi of the colon in UC due to nodular regeneration of the mucosa surrounded by ulceration. **G.** Histology of pseudopolypi showing focally exophytic, regenerative mucosa.

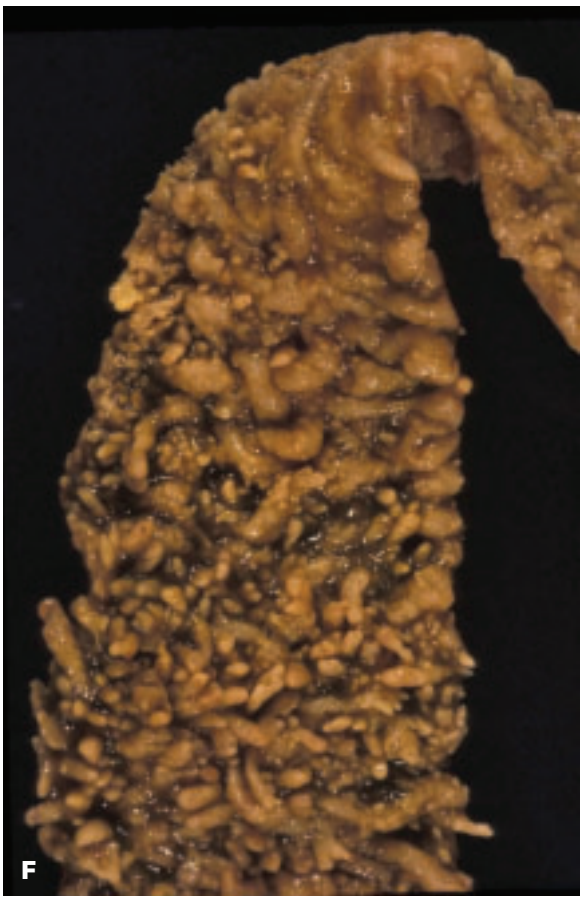

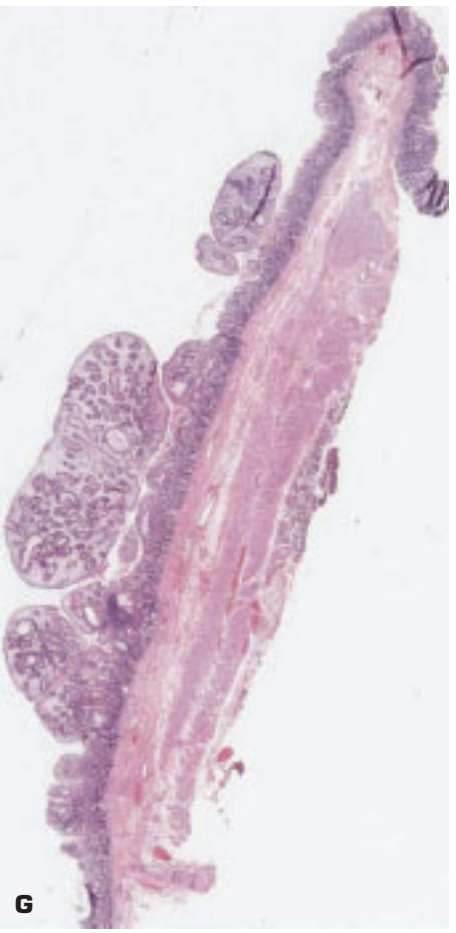

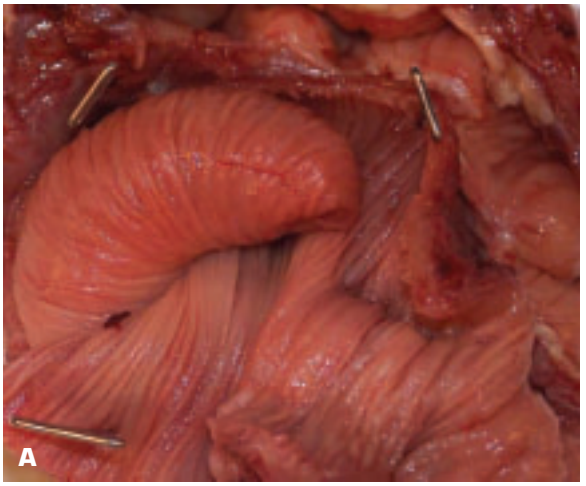

5-48. Intussusception of small intestine. In adults, the condition may be precipitated by a lesion in the bowel (e.g., Meckel diverticulum or tumor). **A.** Luminal obstruction has resulted from a portion of the gut (the intussusceptum) telescoping into the surrounding outer portion (the intussuscipiens). **B.** In this patient, the ileal intussusceptum has become infarcted due to compression of its blood supply by the cecal intussuscipiens. **C.** Intussusception of the vermiform appendix into the cecum.

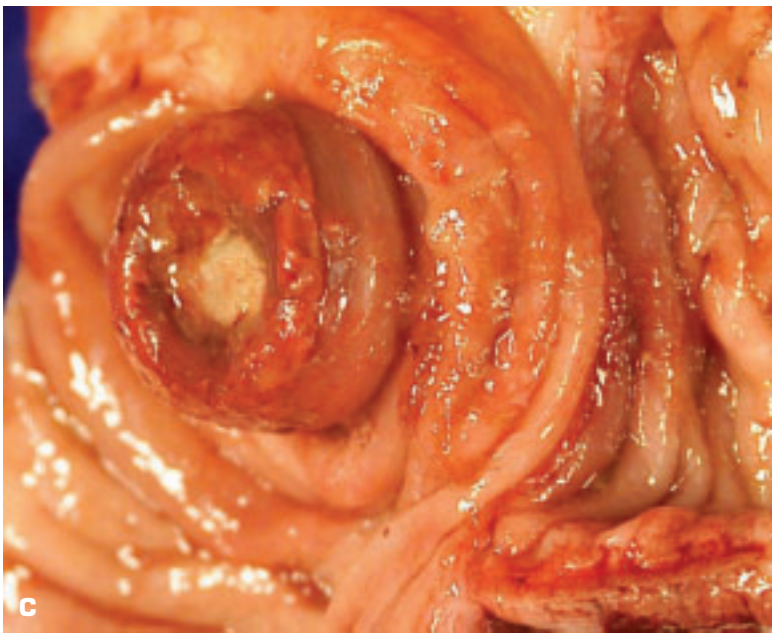

5-49. Meckel diverticulum (due to persistence of the vitelline duct) is an outpouching on the antimesenteric border of the ileum 60 to 100 cm from the ileocecal valve. It is a true diverticulum. Rare possible complications include intussusception, bleeding, inflammation (diverticulitis), perforation, and umbilical fistula.

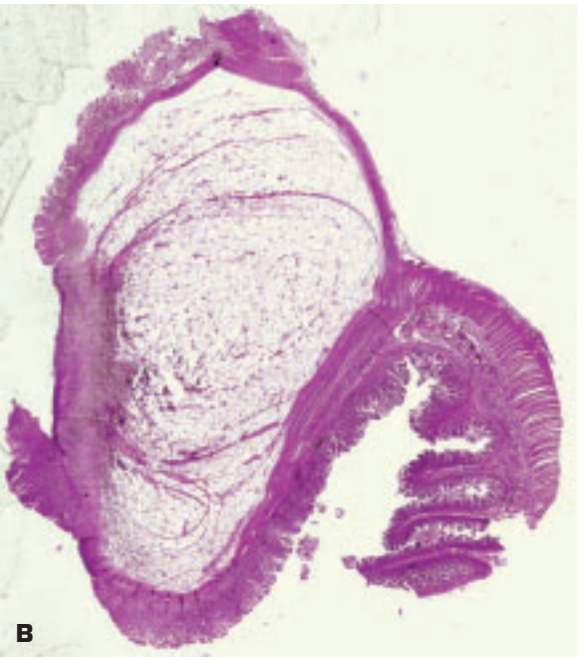

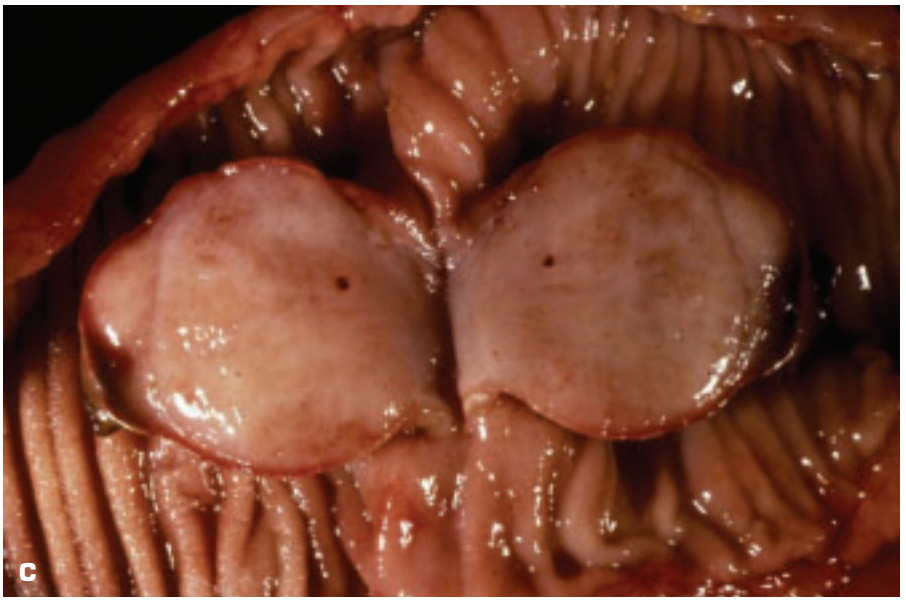

5-50. Masses that may protrude into the gut lumen and predispose to an intussusception. **A.** Lipoma of jejunum. Yellow, fatty-looking tumor has arisen in the submucosa and protrudes into the gut lumen. **B.** Histology of lipoma shows a well-circumscribed benign tumor composed of mature adipocytes. **C.** Bisected inflammatory fibrous tumor of small gut.

5-51. Dilated lacteals in ileum due to obstruction of the lymphatic drainage. **A.** Dilated lacteals in the mucosa appear as yellow nodules due to the normal absorption of lipids by the lacteals and the lymphatic system. If a lesion is transected, it collapses as the obstructed lymph fluid drains away. **B.** Histology confirms that the lesion comprises a lacteal distended by lymph fluid.

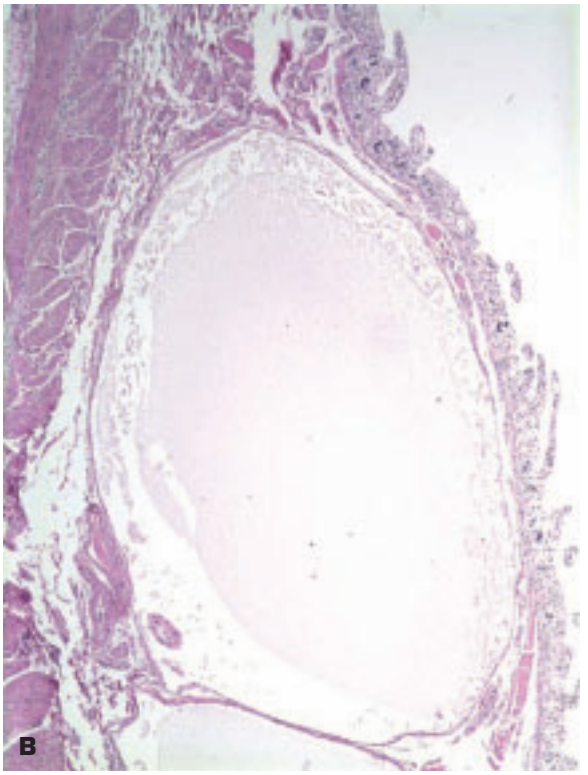

5-52. Linear distribution of ulceration of the ileum over Peyer's patches (mucosal lymphoid tissue) in typhoid fever.

5-53. Circumferential ulceration of the small gut due to tuberculous enteritis. The tuberculous infection spreads in the bowel wall via the lymphatic drainage that is circumferentially arranged. The probe indicates a perforation of the bowel that complicated the lesion.

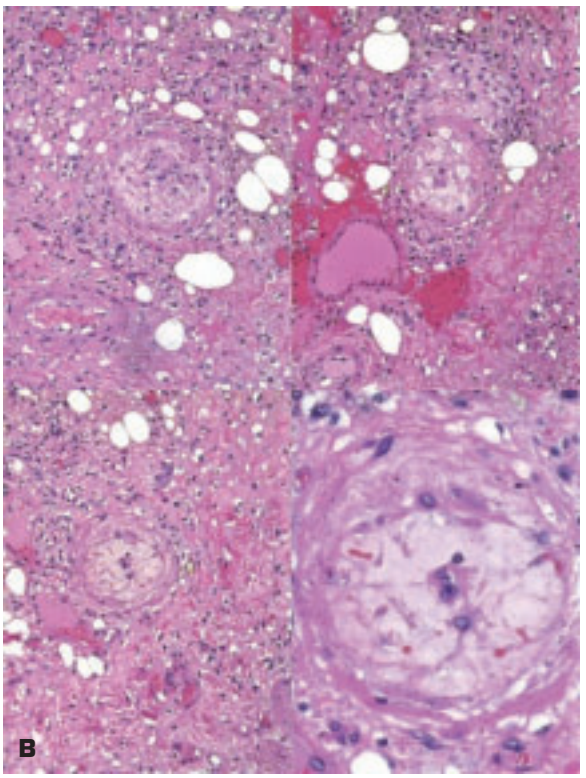

5-54. A. Radiation enteritis of the small gut. Note the luminal narrowing and intraluminal blood clot in the lower right picture. **B.** Histology of the gut shows radiation arteriopathy, including foam cells (ballooning degeneration of intimal cells).

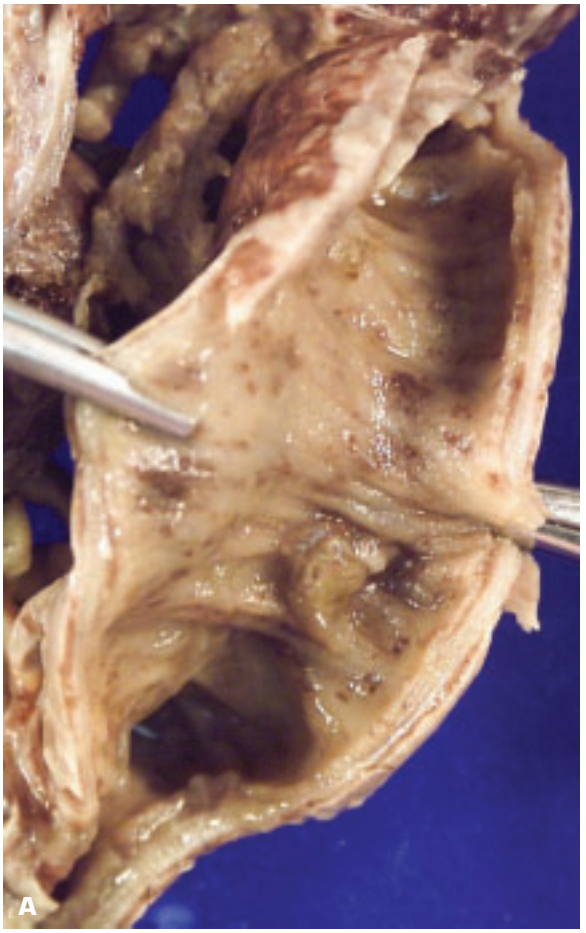

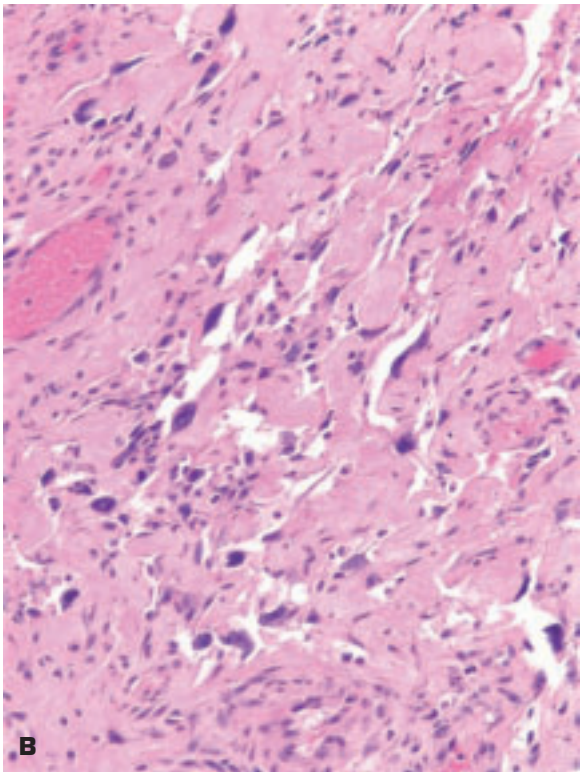

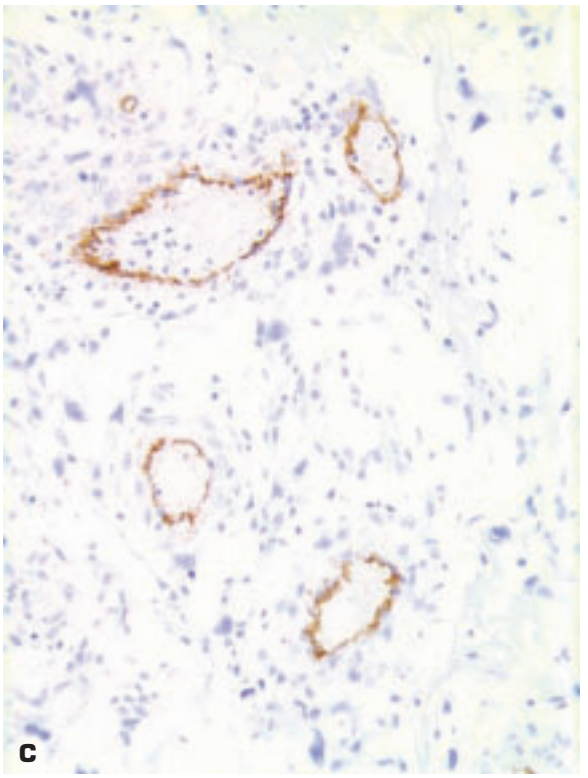

5-55. Angiosarcoma of small intestine. **A.** Multiple vascular-looking nodules are noted on the mucosal surface and on the cut surfaces of the small gut. **B.** Histology of angiosarcoma shows numerous small vascular spaces lined by atypical-looking endothelial cells. **C.** Positive CD34 staining confirms that the tumor cells are producing endothelial-lined vascular spaces.

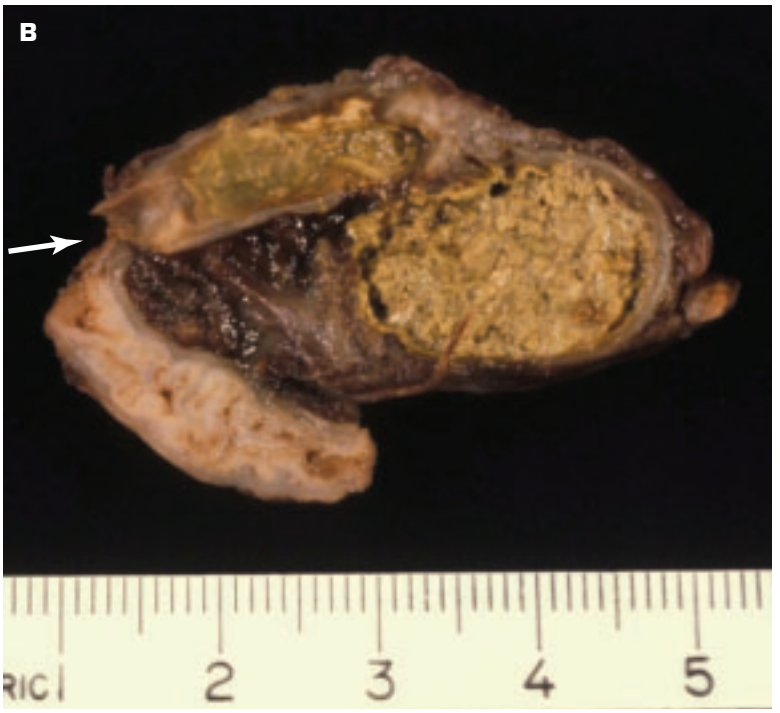

5-56. Intestinal atresia comes about due to vascular compromise of a portion of the gut in utero, leading to obliteration of the bowel lumen, as well as the gut becoming replaced by a fibrous cord that connects the normal proximal and distal segments. **A.** Long atretic segment of small bowel comprising a fibrous cord devoid of any lumen. **B.** Short atretic segment (*arrow*) separates dilated, feces-filled, proximal segment from the distal thinner segment that contains no fecal material.

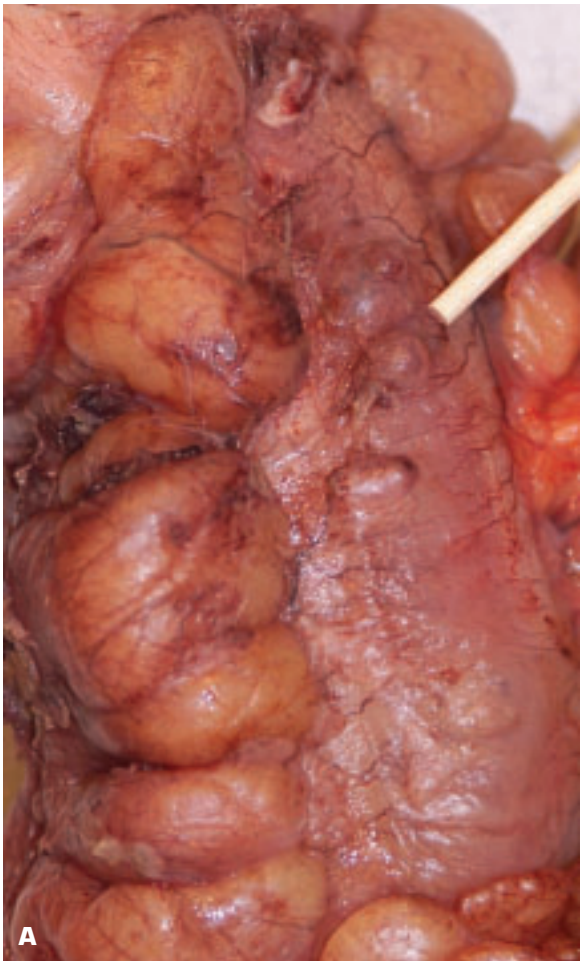

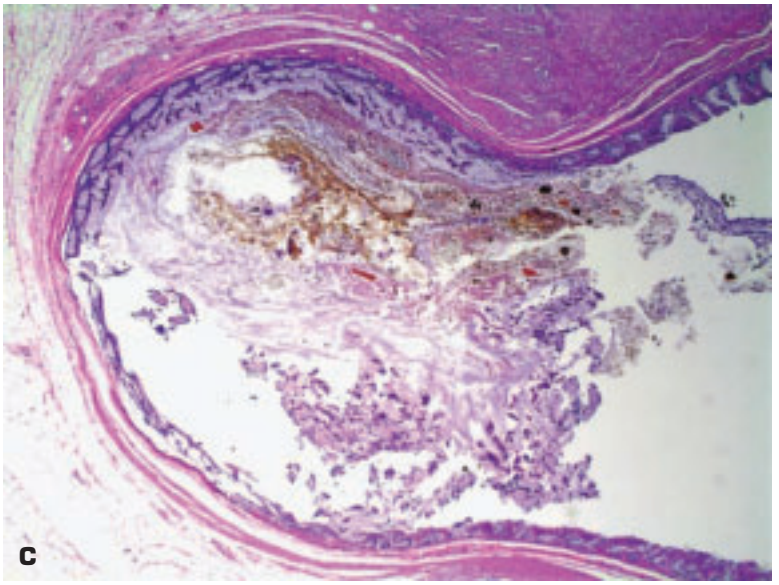

5-57. Diverticular disease (diverticulosis). **A.** External appearance of colonic diverticula. **B.** Transverse section showing diverticulosis. **C.** Histology of a diverticulum showing herniation of mucosa through the muscle coat. *(continued on next page)*

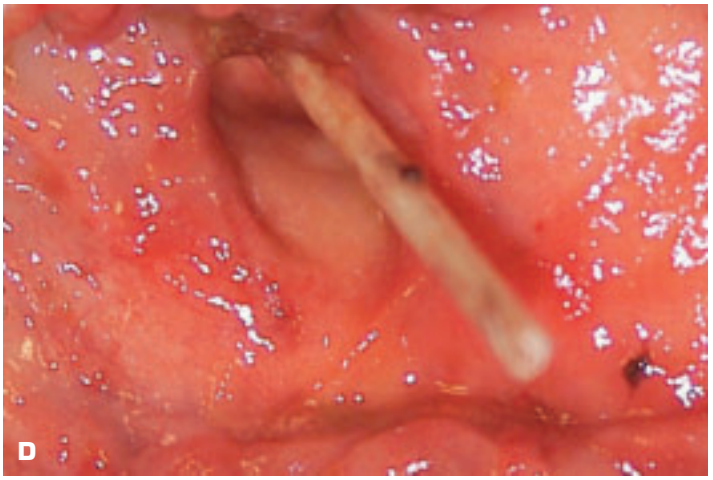

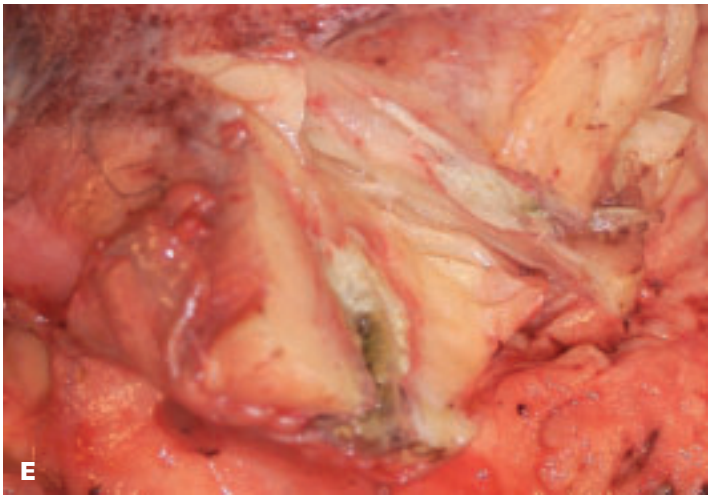

5-57. *(Continued)* **D.** Probe placed in a diverticulum that has led to abscess formation as shown in the next figure. **E.** Pericolic abscess derived from the inflamed diverticulum shown in D. **F.** Healed diverticulitis (*top*) has produced marked local fibrosis around the colon. The condition may mimic a malignant stricture clinically.

5-58. Pseudomembranous colitis (due to *Clostridium difficile*) following administration of antibiotics for renal tract infection. The mucosa shows focal superficial ulceration covered by a mixture of necrotic mucosal debris and acute inflammatory exudate.

5-59. Necrotizing enterocolitis in an adult with transmural infarction of a portion of cecum and ascending colon due to ischemia. The bowel mucosa is edematous and shows scattered small ulcers with scanty-covering exudate. The condition is more common in infants.

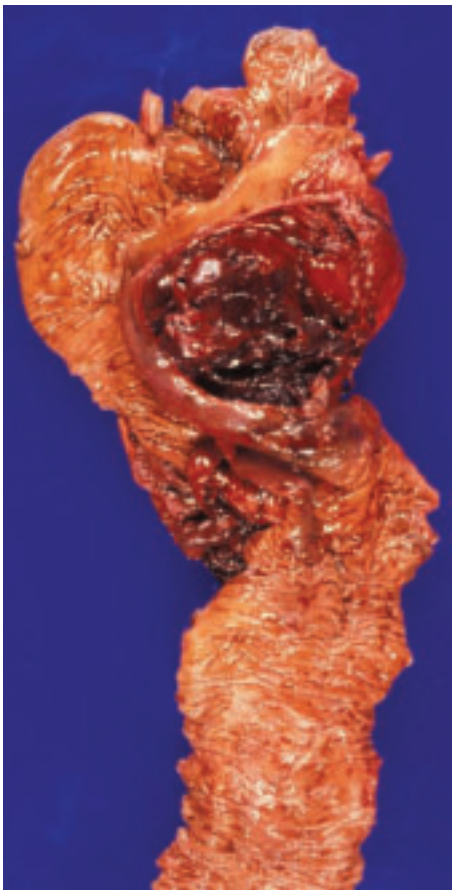

5-60. Two ischemic ulcers of the colon due to rheumatoid vasculopathy (severe intimal thickening of small arteries in the bowel submucosa).

5-61. Stercoral ulcers (*arrows*) of the colon due to constipation; hard, dehydrated fecal material has produced linear pressure necrosis of the colonic mucosa.

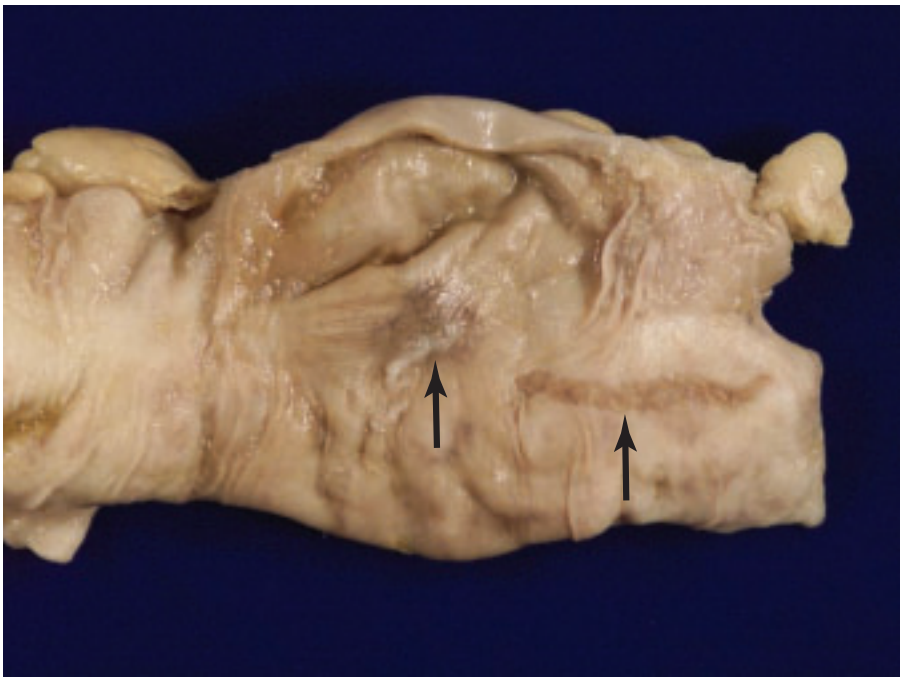

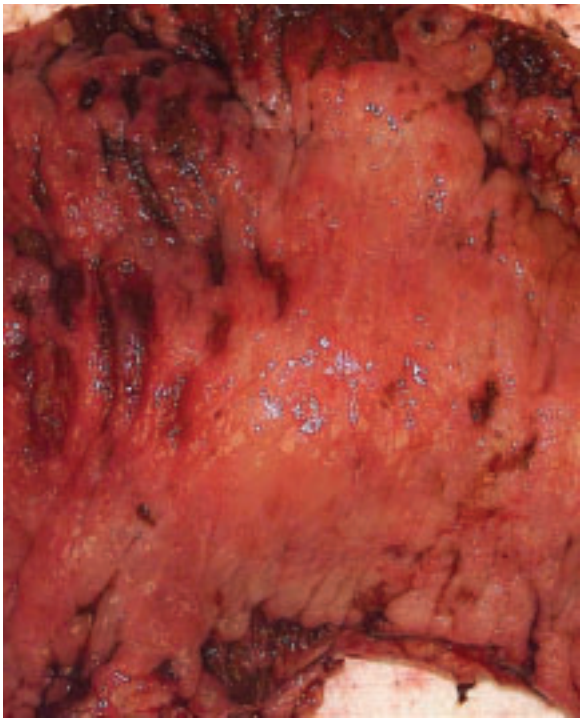

5-62. Drug-induced toxic megacolon with focal devitalization of the colonic wall. Toxic megacolon may also occur in ulcerative colitis. Congenital megacolon occurs in Hirschsprung disease. Acquired megacolon has been associated with laxative use, diabetic neuropathy, parkinsonism, systemic sclerosis, and amyloidosis.

5-63. Graft-versus-host disease of the colon. Multiple superficial mucosal ulcers are noted.

5-64. A. Amebic colitis has produced ulcers with a necrotic, slough-like base, and no surrounding inflammation is present. (Photo courtesy of Dr. R.M. Bowen.) **B.** Pathogenic amebae (*Entameba histolytica*) within colonic wall deep to ulcers. The organisms produce cytolysins that liquefy the tissue, and they also damp down the inflammatory response. The infected colon is very fragile and handles with the consistency of wet blotting paper.

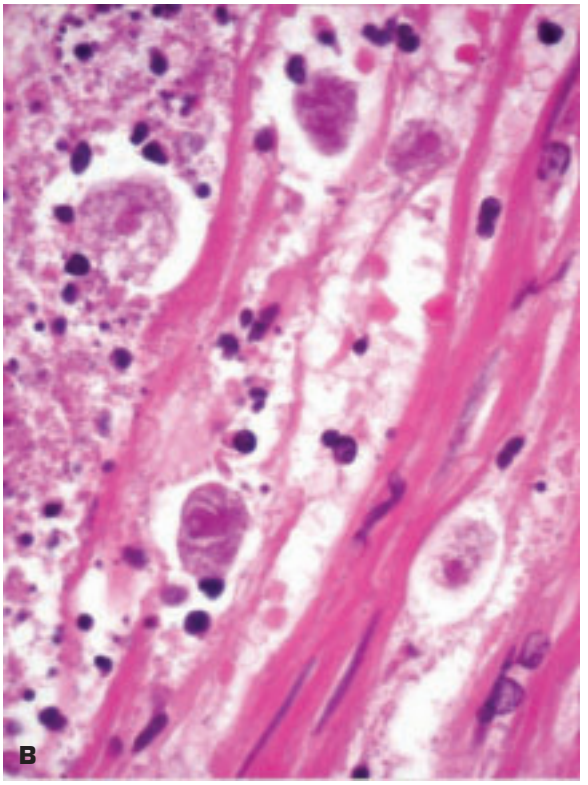

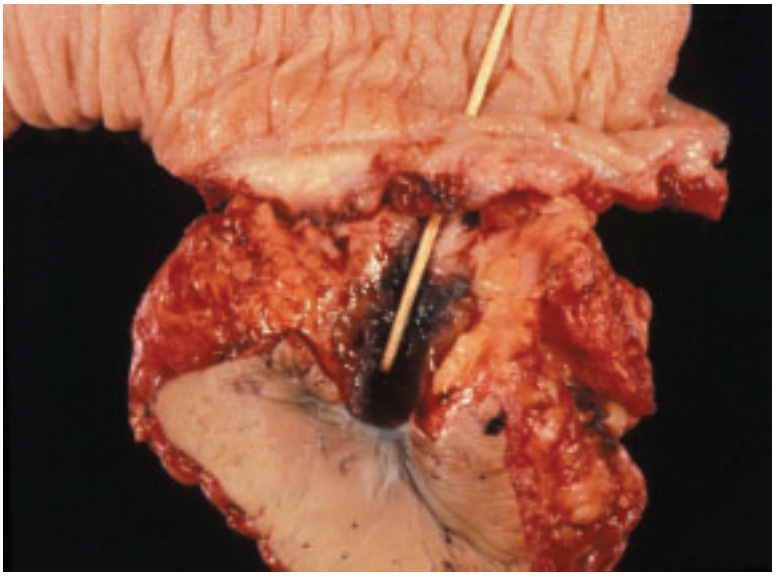

5-65. Colon-skin fistula (indicated by orange stick) following abdominal trauma.

5-66. A. *Candida* infection of a devitalized cecum. The ulcerated area is bile stained. **B.** Histology shows *Candida* organisms within the necrotic cecal wall.

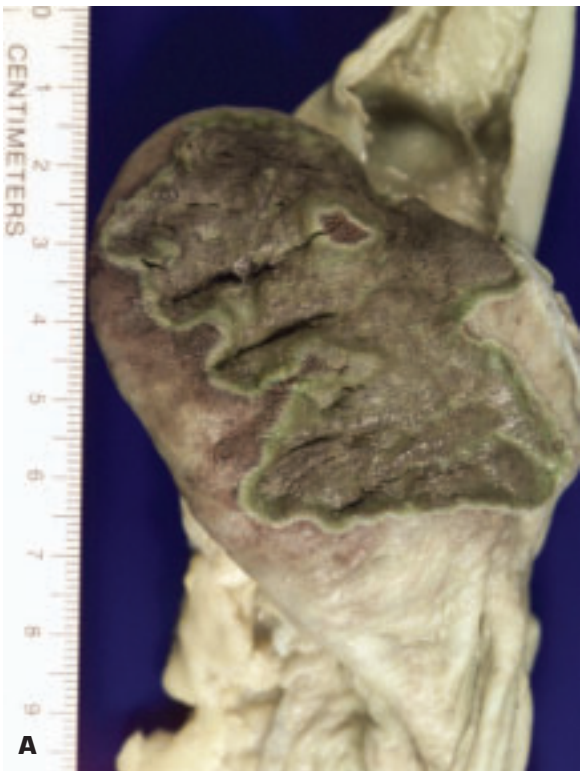

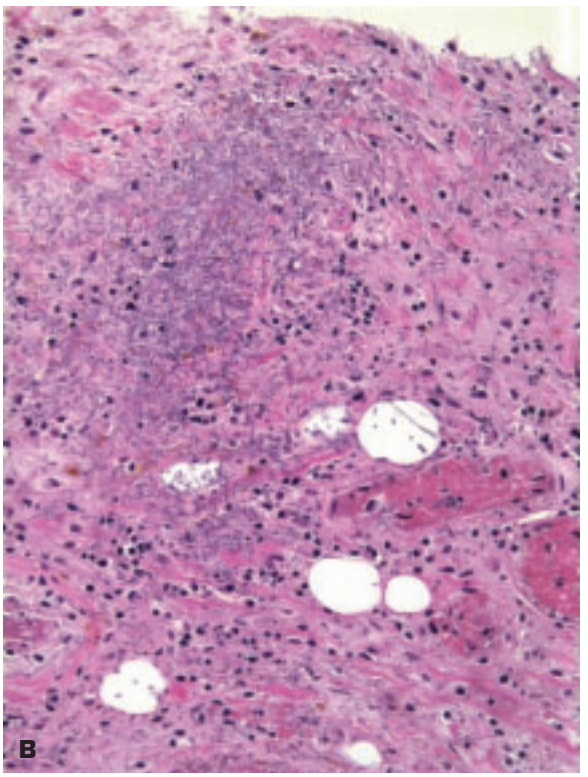

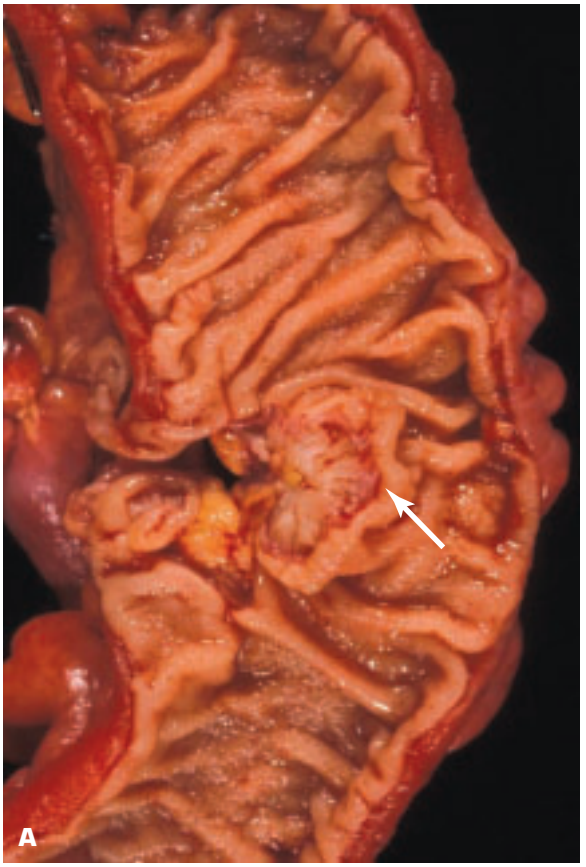

5-67. A. Stricture (*arrow*) of colon due to endometriosis. **B.** Histology shows endometrial-type glands and stroma within the fibrous reaction seen in A.

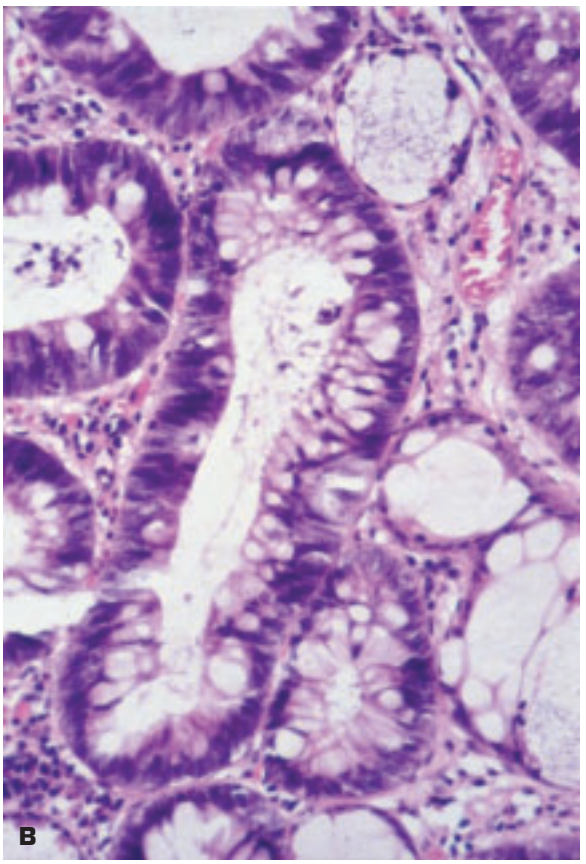

5-68. Pneumatosis cystoides intestinalis. The condition indicates the presence of gas in the bowel wall and may affect any part of the gastrointestinal tract. The gas may enter via a mucosal tear, be produced by microorganisms (e.g., in neonatal necrotizing enteritis), or be derived from an air leak in the lung (surgical emphysema). **A.** Cecal mucosa bears multiple nodules due to air trapping within the mucosa. **B.** Section of the cecum shows the intramucosal air bubbles. If chronic, a giant cell response may be elicited by the air within the tissues.

5-69. Polyps of the colon. **A.** Close-up view of multiple hyperplastic (metaplastic) polyps showing the characteristic small, sessile, and pale appearance. Such polyps may be found in up to 50% of colons in adults. **B.** Pedunculated adenomatous polyp (tubular adenoma). *(continued on next page)*

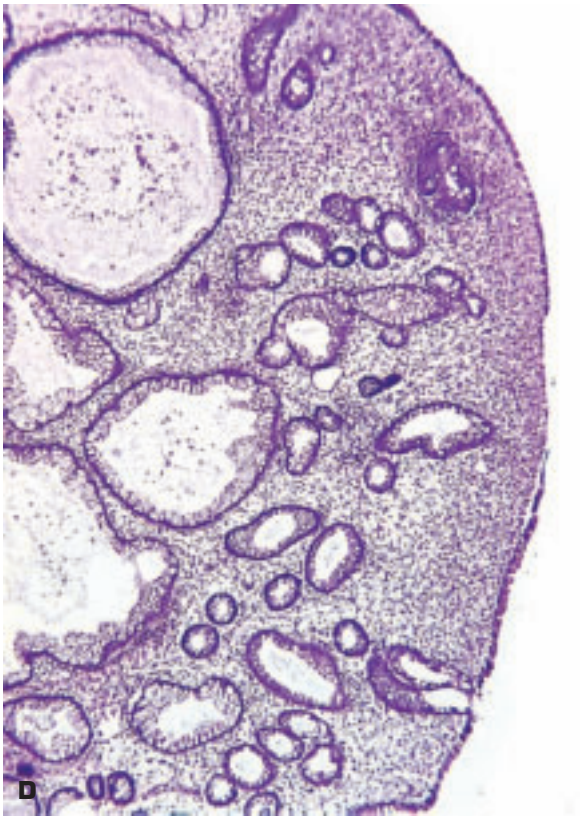

5-69. *(Continued)* **C.** Multiple juvenile (retention) polyps. The two upper polyps have the typical hyperemic, ulcerated surface of a juvenile polyp. This patient had *multiple juvenile polyposis* (with polyps distributed throughout the bowel). This condition may be associated with the development of adenomatous polypi and adenocarcinoma of the stomach, duodenum, gut, and pancreas. **D.** Histology of juvenile polyp showing cystically dilated glands that have no epithelial atypism.

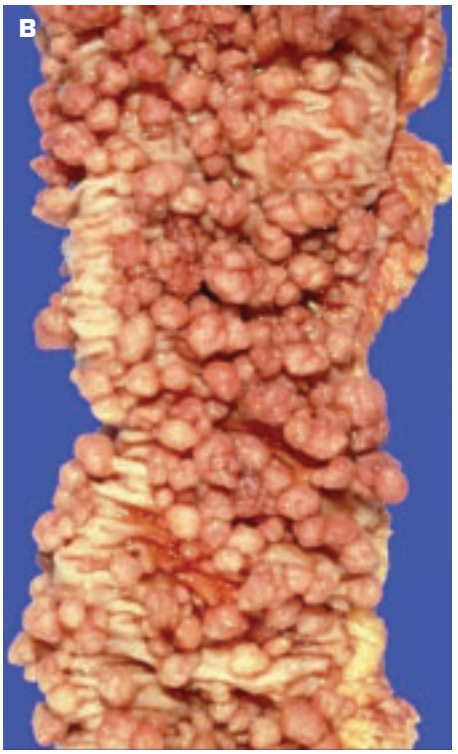

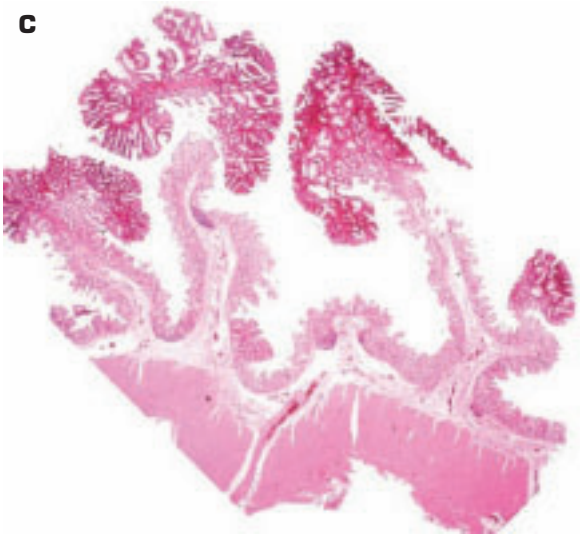

5-70. Familial polyposis of the colon. The diagnosis rests on the presence of at least 100 adenomatous polyps. **A.** Multiple small, widely scattered, sessile polypi are present. **B.** Another patient shows more numerous and larger adenomatous polypi. **C.** Histology of adenomatous polypi in familial polyposis. *(continued on next page)*

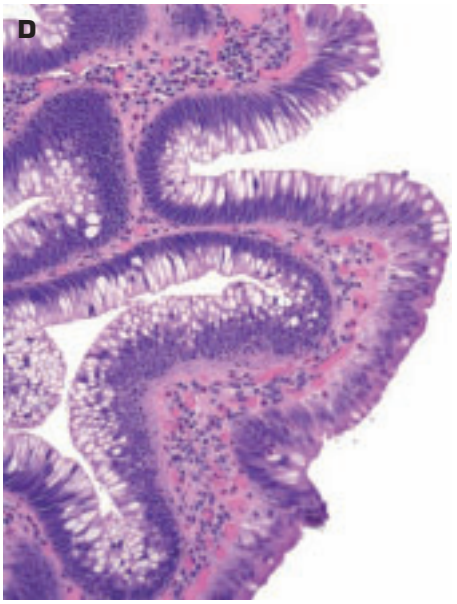

5-70. *(Continued)* **D.** Surface of adenomatous polyp showing some cellular atypism. **E.** Villoglandular polyp (mixed adenomatous and villous polyp). **F.** Bisected villoglandular polyp showing central adenomatous portion (*) ringed by branching villoglandular portion.

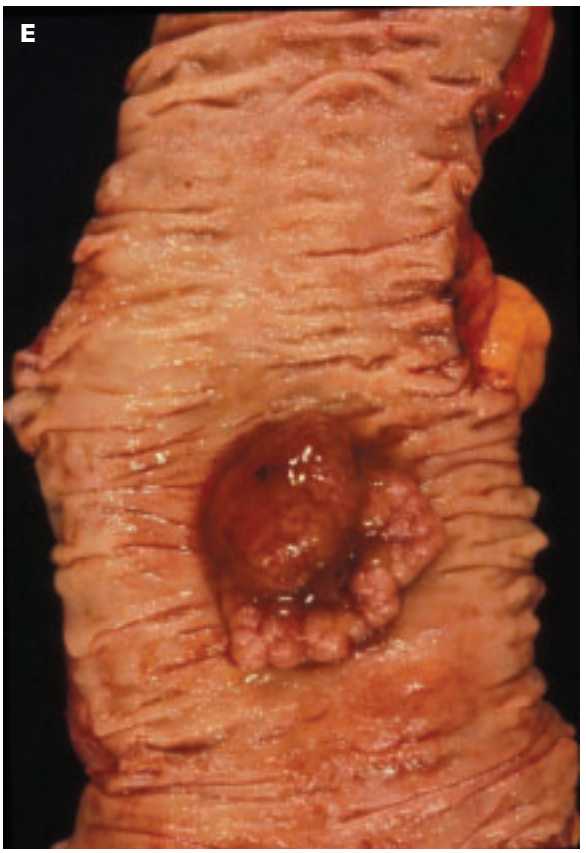

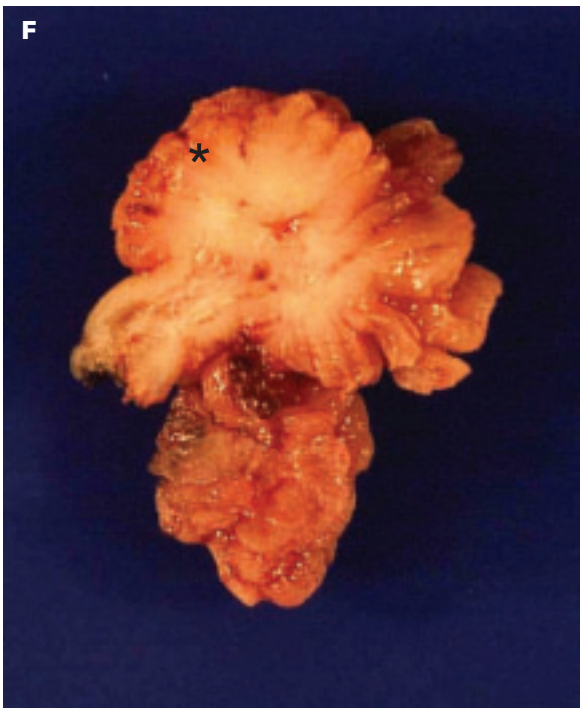

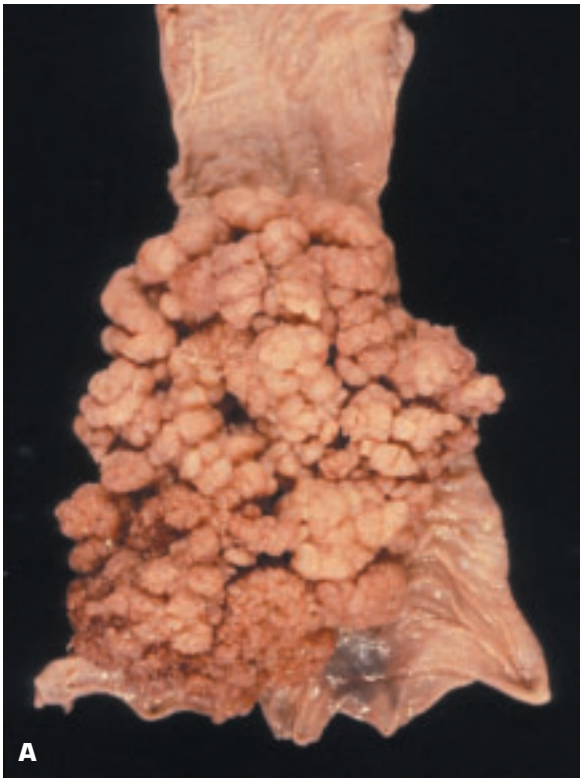

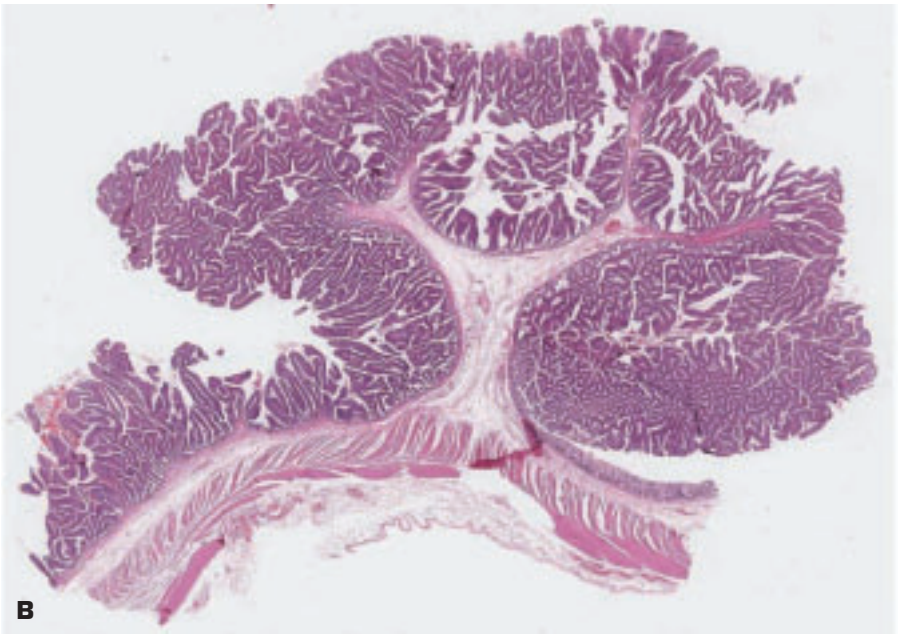

5-71. A. Villous adenoma of the colon exhibiting the usual large, sessile, and branching appearance of this lesion. **B.** Histology shows the typical branching pattern of a villous adenoma.

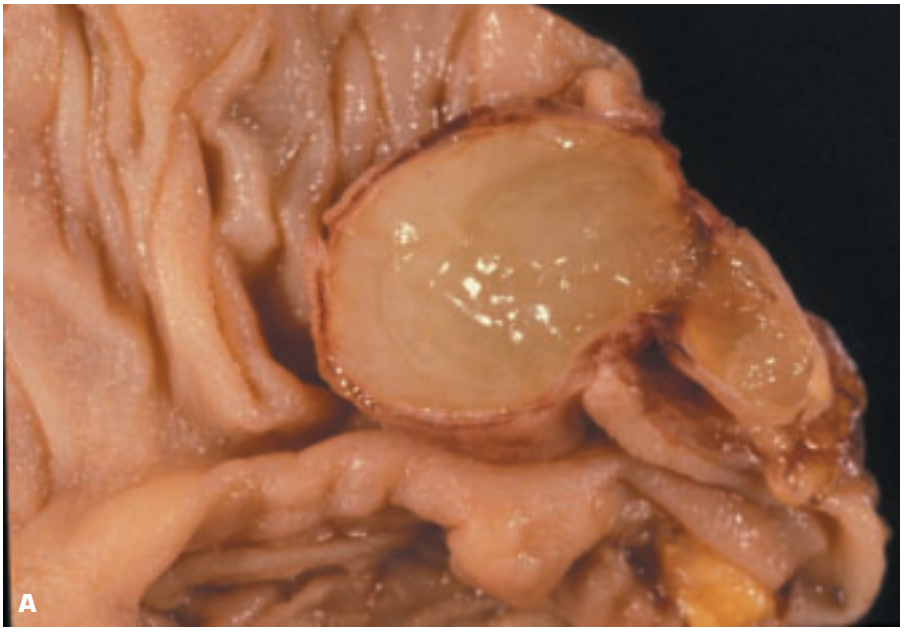

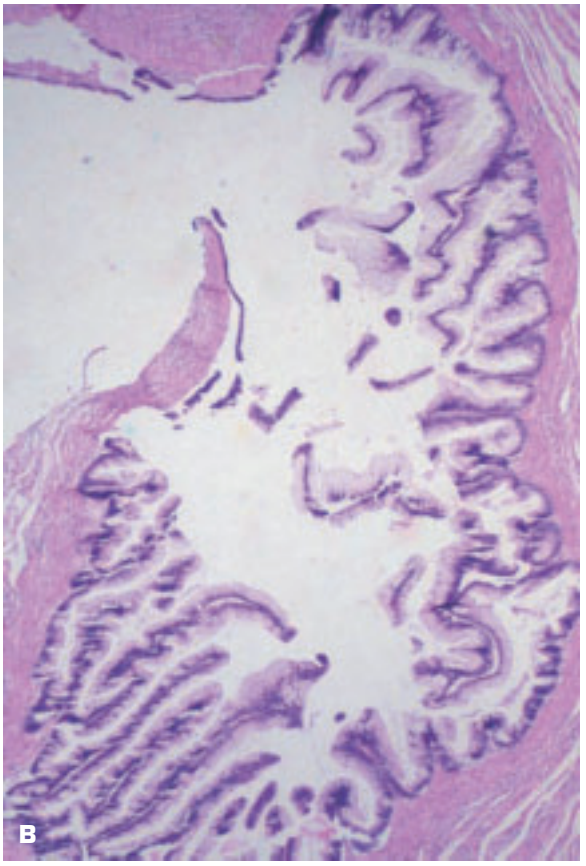

5-72. A. Mucinous cystadenoma of the cecum. A well-circumscribed unilocular cystic structure is filled with dense mucinous material. **B.** Histology shows a lining composed of benign-appearing, columnar-shaped, mucus-secreting cells.

5-73. Adenomatous polyp has evolved into an adenocarcinoma in the lower half of the polyp (*). This portion of the polyp has a denser, more solid appearance due to the increased cellular proliferation of the cancer.

5-74. A. The colon has become encircled by an adenocarcinoma that is obstructing the lumen and has invaded through the external muscle coat. **B.** Histology shows a well-differentiated adenocarcinoma.

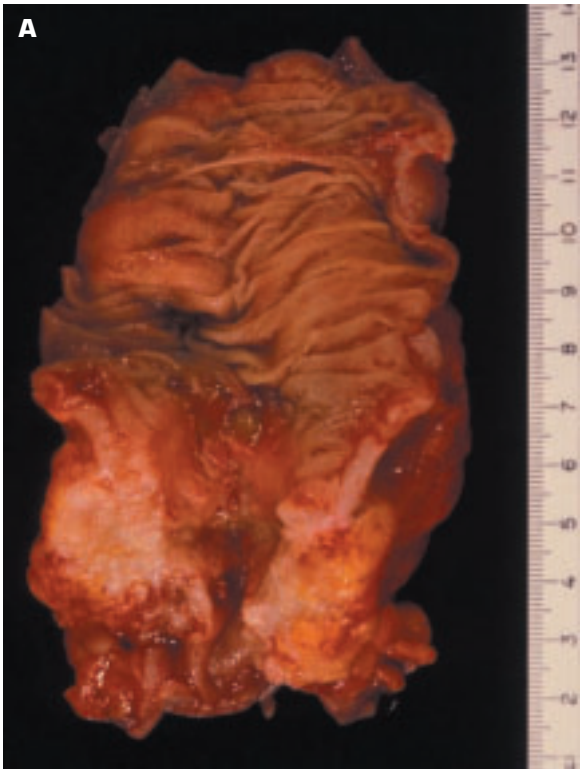

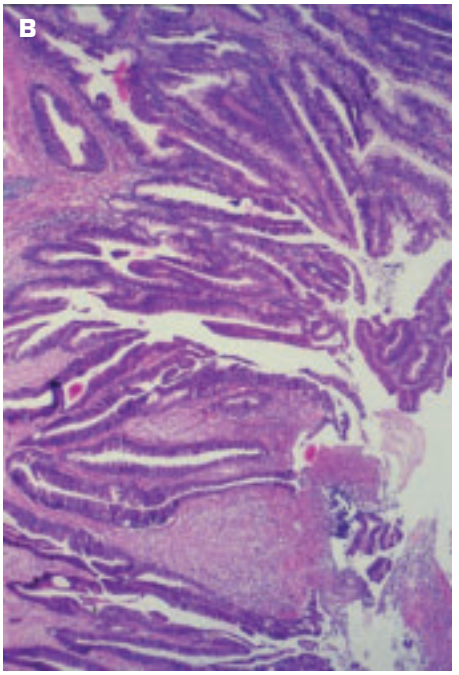

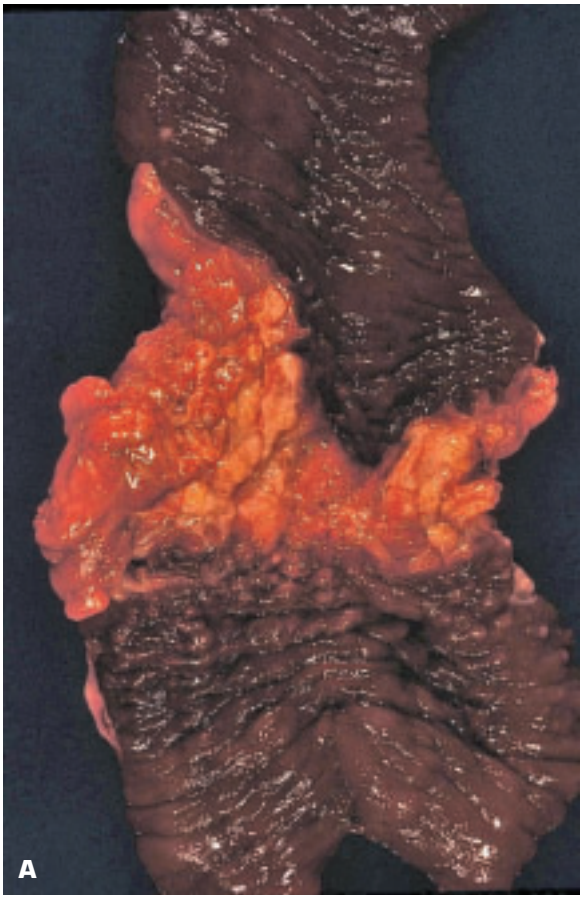

5-75. A. Adenocarcinoma of the colon in a patient with melanosis coli. The cancer contains no pigment. Melanosis coli is a misnomer because no melanin pigment is present – the pigment is related to lipofuscin and is derived from breakdown of cell membranes secondary to chronic use of anthracene laxatives. **B.** Histology of melanosis coli shows macrophages in the lamina propria are filled with brown-colored lipofuscin granules.

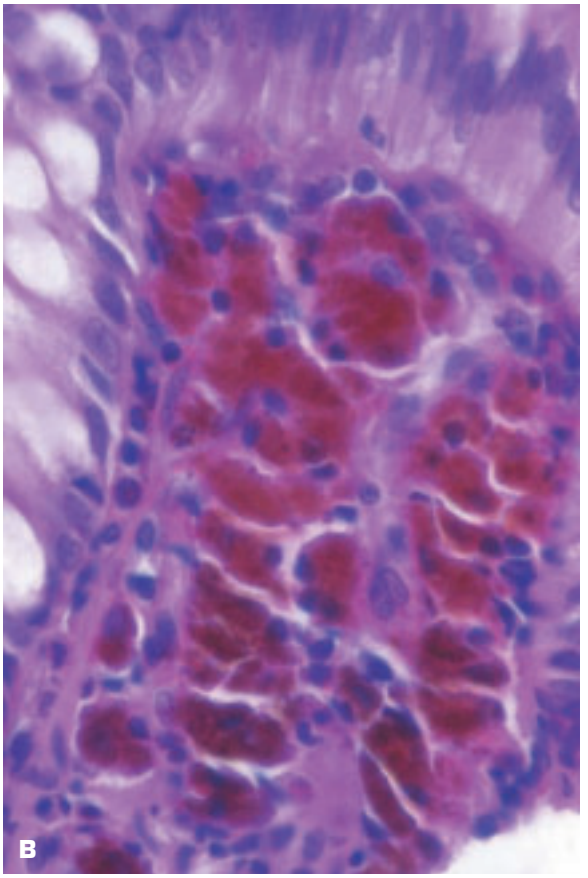

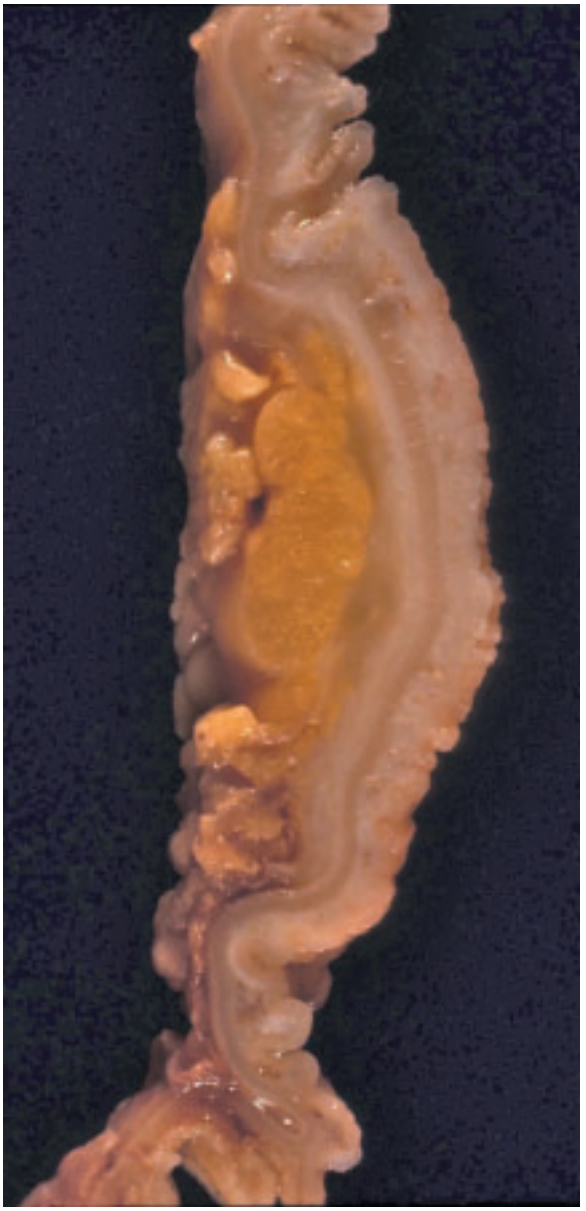

5-76. Diffuse infiltration of colon by undifferentiated signet ring cell carcinoma.

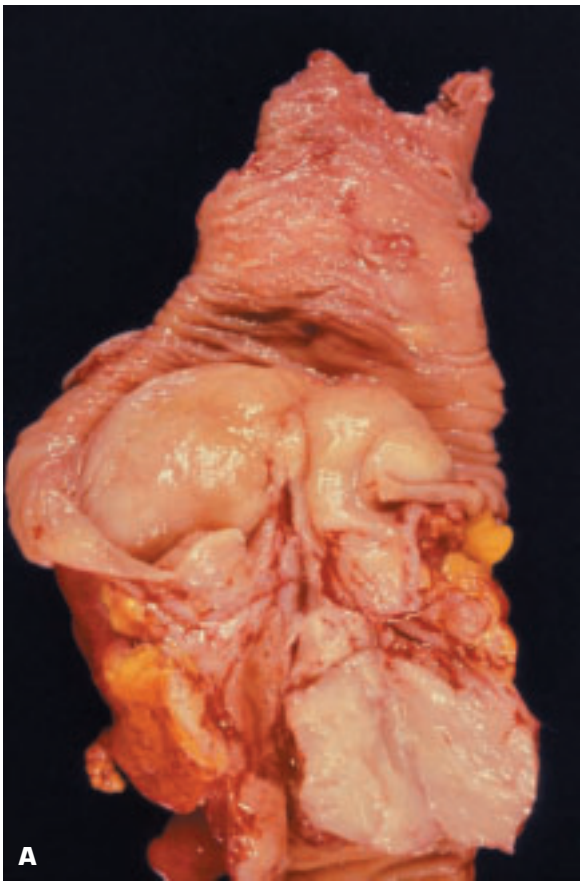

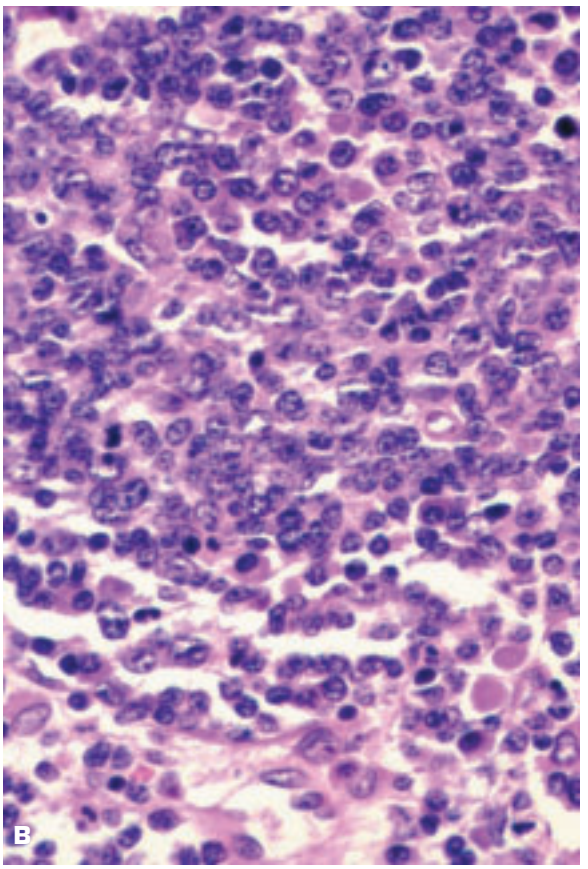

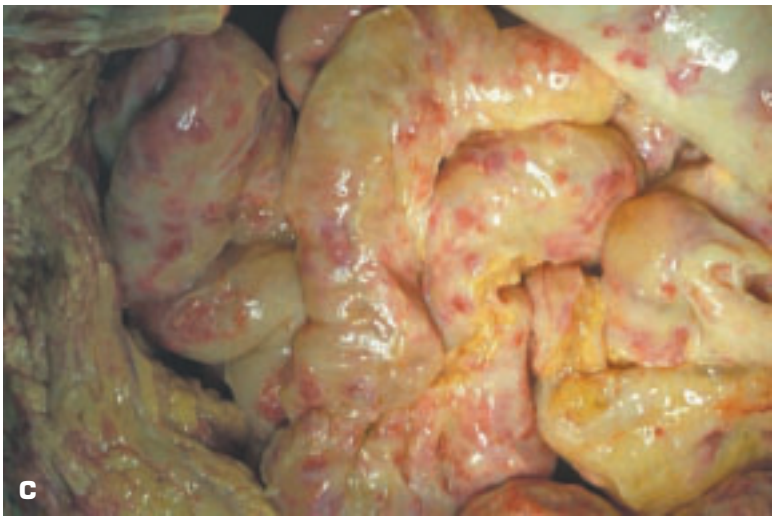

5-77. A. Bulky, fleshy-looking lymphoma of the colon (showing the so-called fish flesh appearance of the cut surface). **B.** Histology shows a diffuse large cell lymphoma. **C.** Matted loops of bowel due to peritoneal involvement by a posttransplant lymphoma in a lung transplant recipient. The lymphoma is related to a previous Epstein–Barr virus infection.

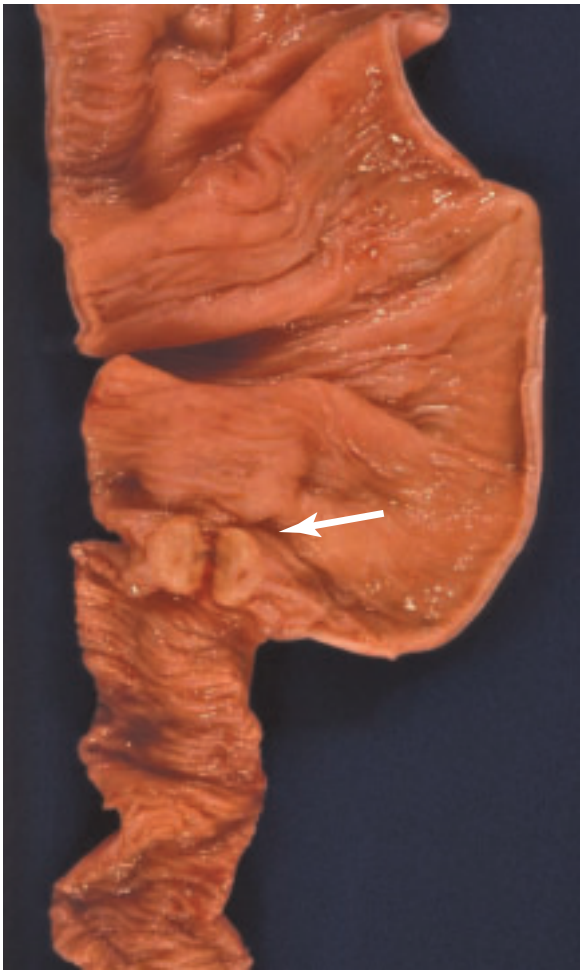

5-78. Carcinoid tumor (*arrow*) of the distal ileum.

5-79. Adenocarcinoma of the rectum.

5-80. A. Abdominoperineal resection and left hemicolectomy for a cloacogenic carcinoma of the rectum. This rare cancer arises from the transitional cloacogenic zone of the anorectal junction and behaves in an aggressive fashion. **B.** Histologically, the tumor has the appearance of a basaloid squamous carcinoma.

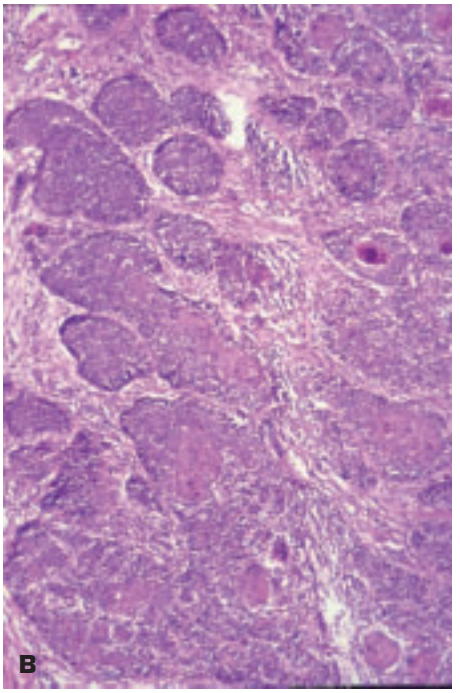

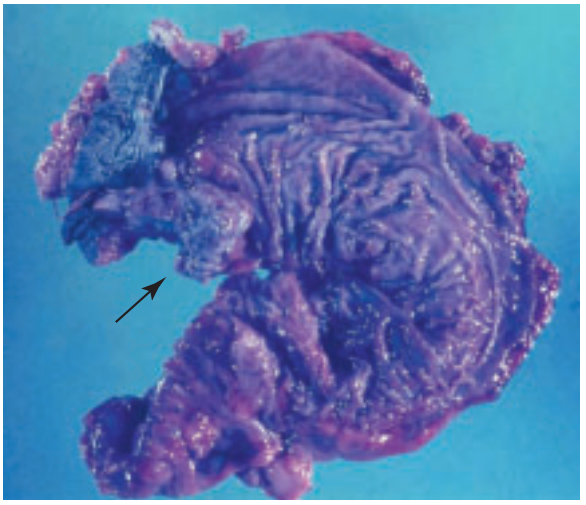

5-81. Malignant melanoma (*arrow*) of the anorectal junction is presenting as an exophytic mass protruding into the lumen.

5-82. Exomphalos (omphalocele) is a congenital abnormality in which the abdomen fails to close around the base of the umbilical cord producing an umbilical hernia in which abdominal organs may push into the umbilical cord. In this patient, small intestine is present in the hernial sac.

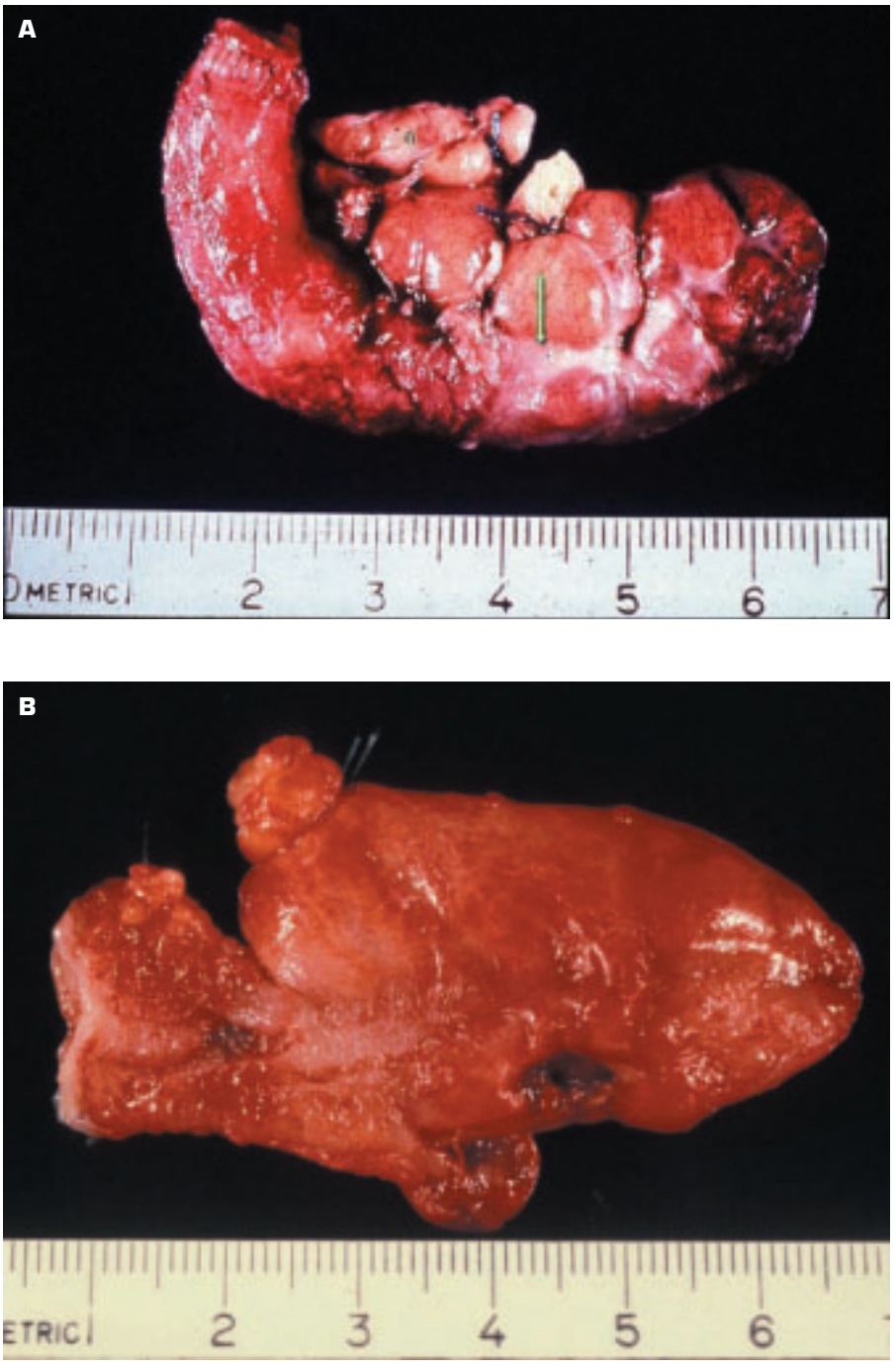

5-83. A. Acute appendicitis with acute inflammatory exudate (*arrow*) on the serosal surface. **B.** Acute appendicitis with rupture.

5-84. Large fecalith within a distended appendix in a patient with cystic fibrosis (mucoviscidosis).

5-85. Diverticulitis of the appendix with periappendicular fibrosis.

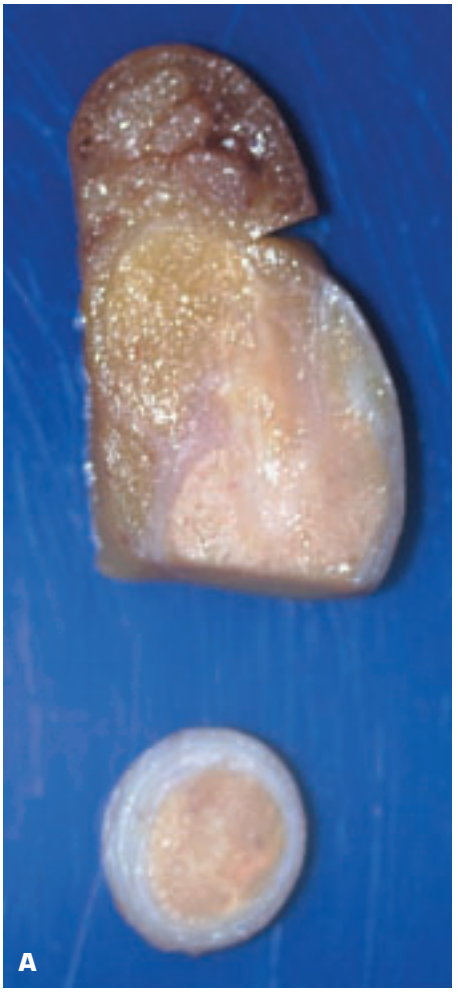

5-86. A. Carcinoid tumor of the distal appendix. **B.** Histology shows this carcinoid tumor to be confined to within the distal appendix.

5-87. Mucocele of the appendix indicates an appendix whose dilated lumen is filled with mucin. Causes include proximal obstruction by a fecalith to cystadenoma or cystadenocarcinoma. **A.** Inspissated mucus released from an obstructed appendix lies alongside the appendix. **B.** Mucinous cystadenoma of the appendix. **C.** Pseudomyxoma peritonei is compressing loops of small bowel. This condition may result from a mucinous cystadenocarcinoma of either the appendix or the ovary that has spread in the peritoneal cavity.

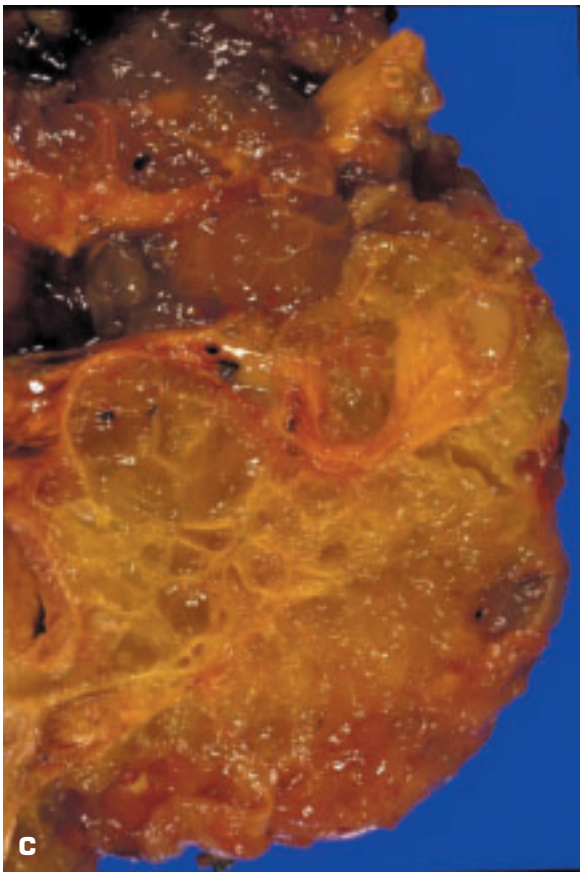

5-88. Ganglioneuroma has produced thickening of the distal portion of the appendix.

5-89. Benign cyst of the peritoneal lining of uncertain origin. Peritoneal cysts may be derived from lymphatic channels, enteric diverticula, urogenital ridge, or healed infection.

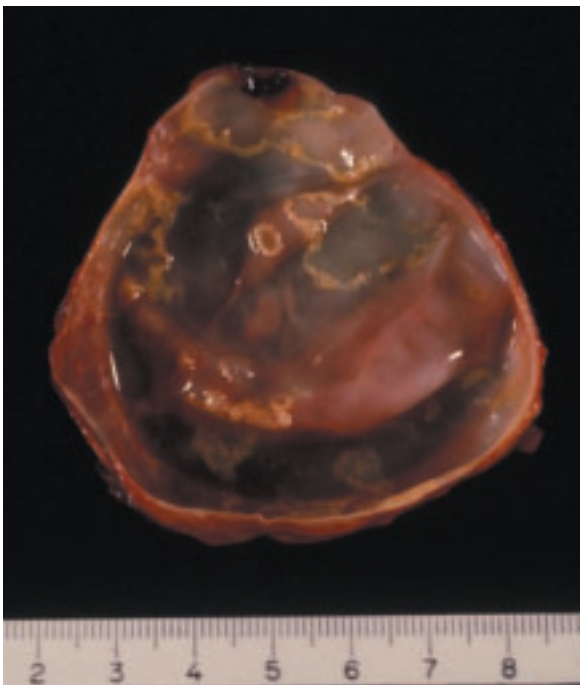

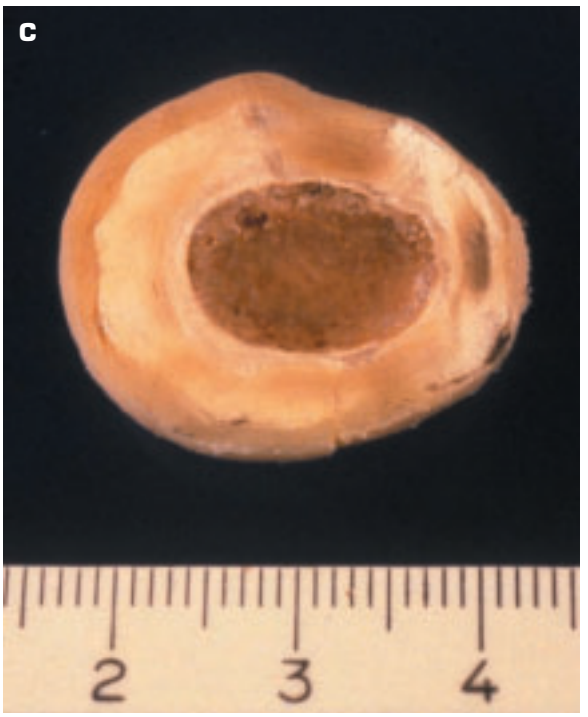

5-90. Infarcted appendix epiploica may present as a free-lying body in the peritoneal cavity. These pictures show the sequence of this process. **A.** Twisting of the base of the appendix epiploica is leading to its infarction. **B.** Free-lying, infarcted, and calcified appendix epiploica. **C.** Appearance of a transversely sectioned appendix epiploica showing a hollow center.

5-91. Foreign body in mesentery is an intrauterine contraceptive device (*arrow*) that had penetrated through the wall of the uterus to lie free in the peritoneal cavity.

5-92. Fibrinopurulent peritonitis in a paracolic gutter secondary to bowel perforation.

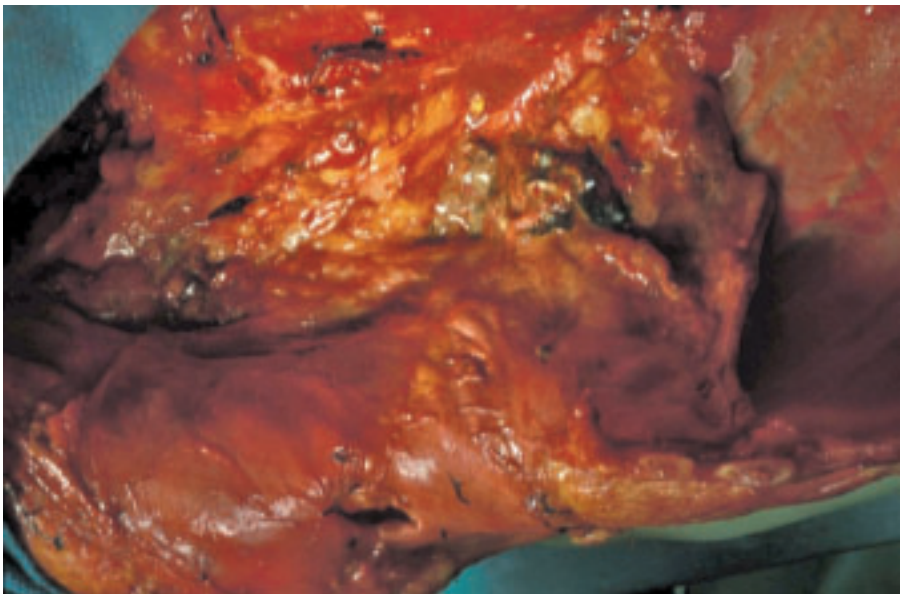

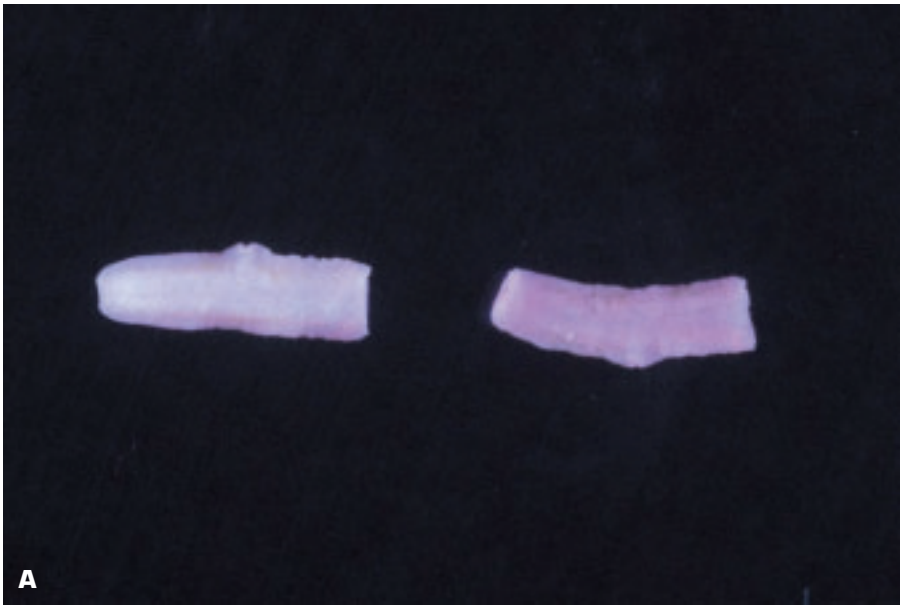

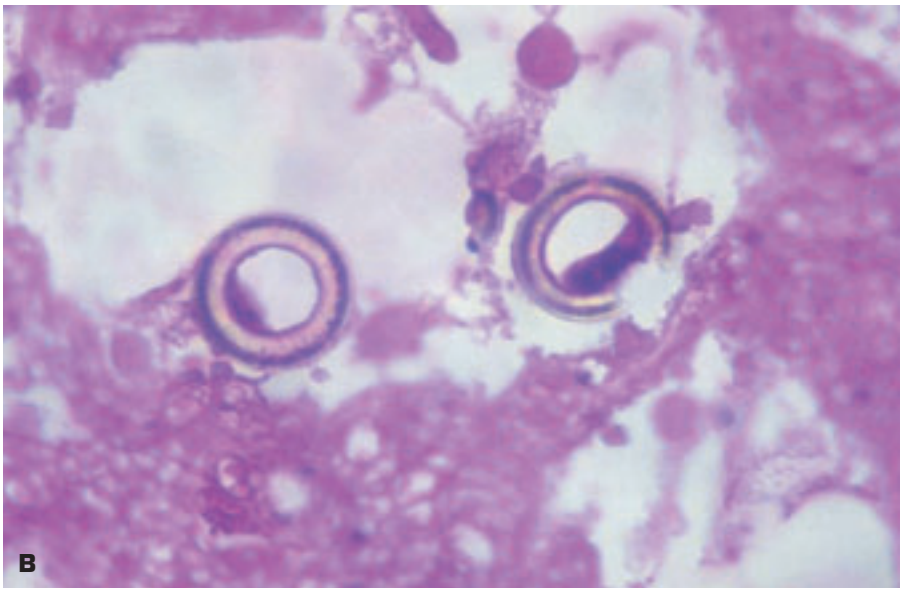

5-93. A. Tapeworm (*Taenia saginata*) segments from a stool. **B.** Histology shows typical ova of *T. saginata* within the segments.

6 Female Genital Tract and Breast

6-1. Hypertrophy of the clitoris (clitoromegaly or macroclitoris). The condition may be congenital (e.g., due to congenital adrenal hyperplasia or due to intersex development, graded according to Prader) or acquired (e.g., via the administration of androgenic anabolic steroids to females, such as the drug Danazol given to treat idiopathic thrombocytopenic purpura or female bodybuilders who take anabolic steroids). Idiopathic cases may also occur. The normal clitoris is 4 to 5 mm long and 3 to 4 mm wide, whereas the surgically excised clitoris shown is about 40 mm long.

6-2. A. A human papillomavirus–induced condyloma (*arrow*) is present in the short cuff of vagina attached to a uterus that is infiltrated by a malignant lymphoma. Note the rather flat, papillary-appearing lesion on the vaginal lining. **B.** Histology shows the typical appearance of a condyloma acuminatum with pointed, finger-like projections covered by squamous epithelium, many of whose cells show apoptotic changes (koilocytes).

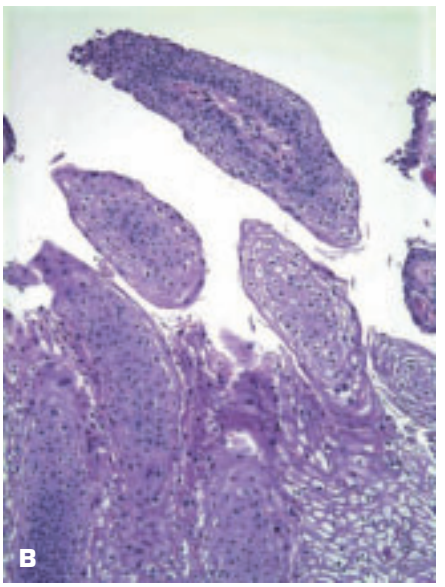

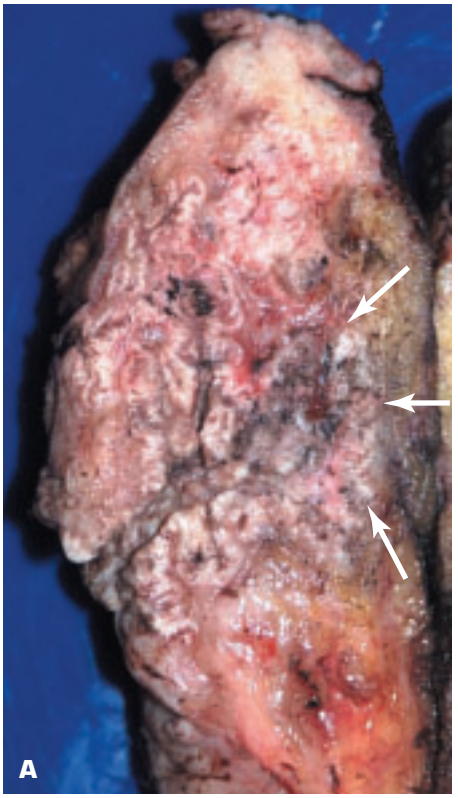

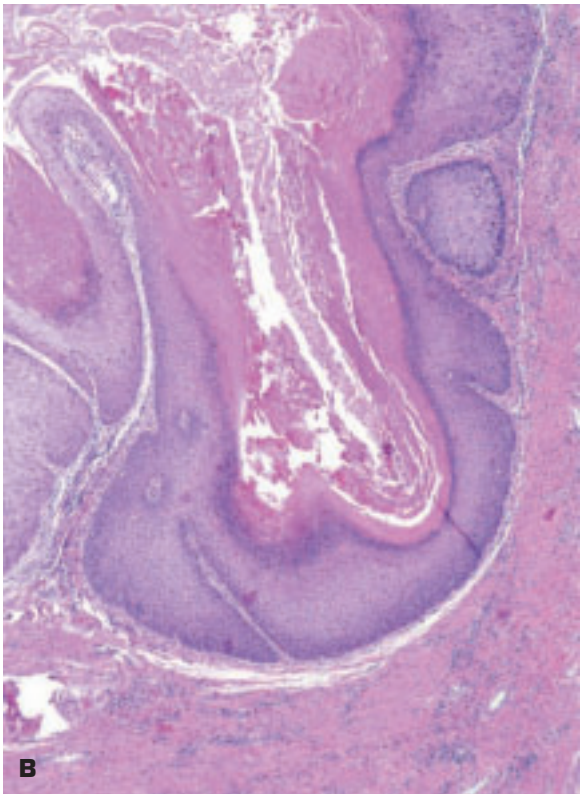

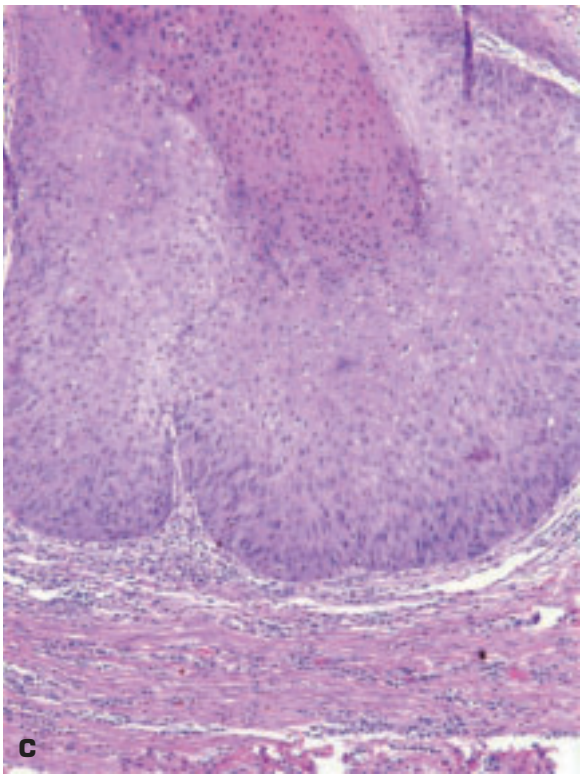

6-3. A. Bisected giant condyloma acuminatum of Buschke–Lowenstein of the vulva (skin surface is on the left of the specimen) due to human papillomavirus infection. These large condylomata form part of a spectrum of lesions that merge with the concept of a verrucous carcinoma. Note how the squamous epithelial proliferation (*arrows*) has penetrated into the underlying vulvar soft tissue. **B.** Histology shows the typical pushing margin of a verrucous carcinoma. **C.** Higher-power view of the same area shows the characteristic absence of signs of marked anaplasia that are characteristic of an ordinary squamous carcinoma.

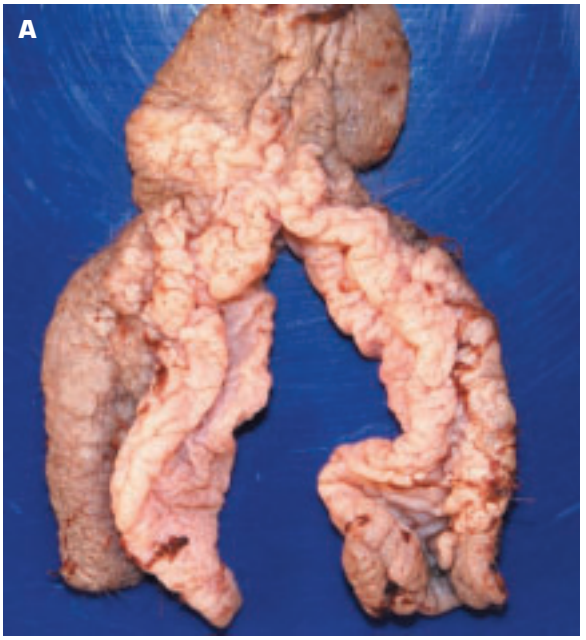

6-4. A. Widespread severe dysplasia and carcinoma in situ of the vulva. The labia minora and majora appear to be wrinkled and covered by a thicker epithelium than normal. **B.** Histology shows the junction (*arrow*) between normal excision margin (*left*) and the carcinoma in situ (*right*, more basophilic staining epithelium). Larger pink cells overlying the midportion of the sections are squamous epithelial cells probably derived from the staining solution. **C.** High-power view of severe dysplasia of the epidermis showing an abnormal mitosis (*center*) and some superficial keratinization.

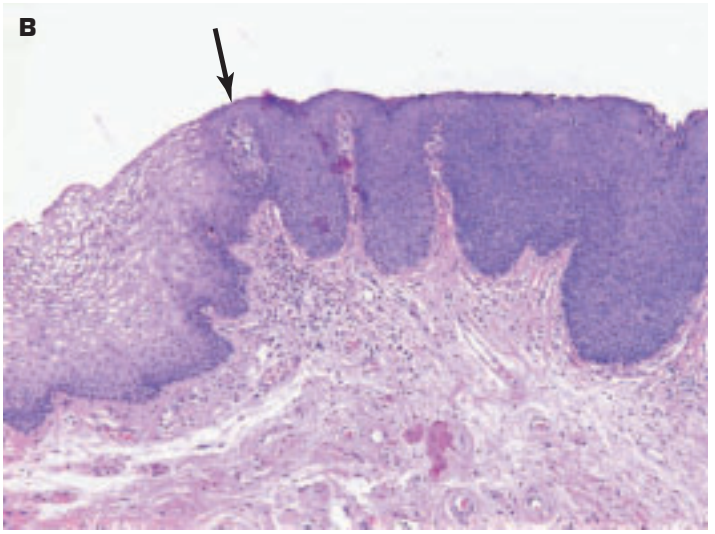

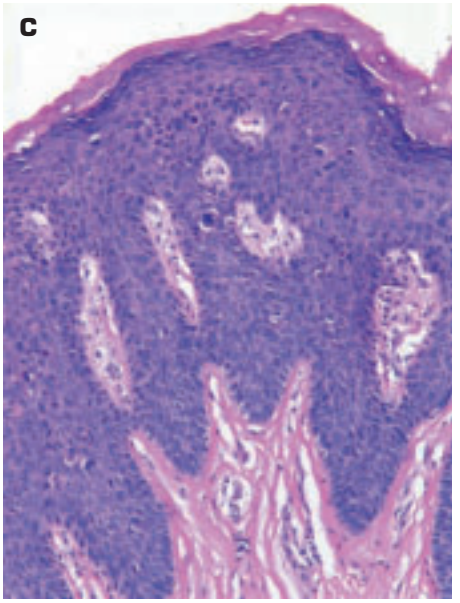

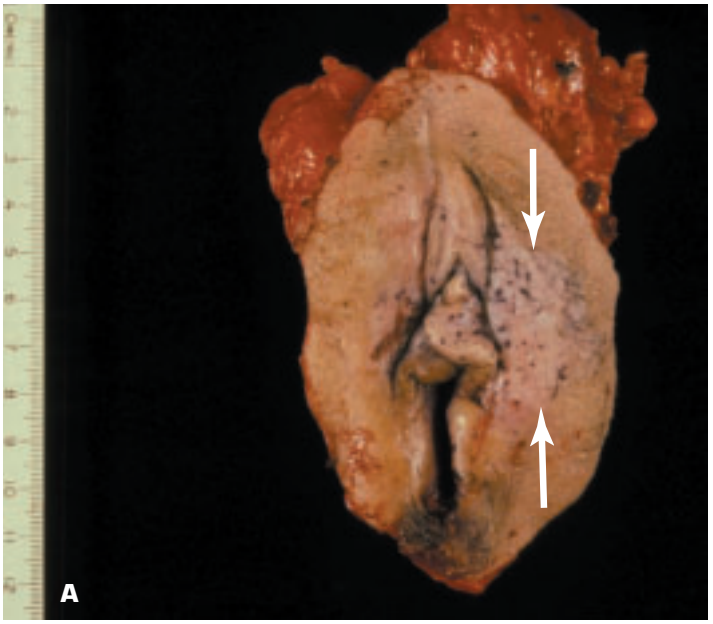

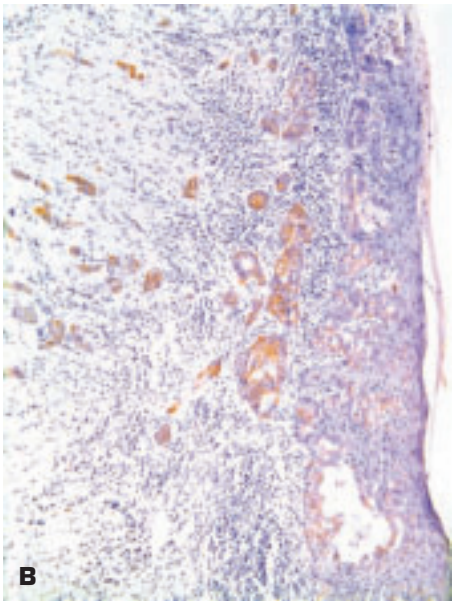

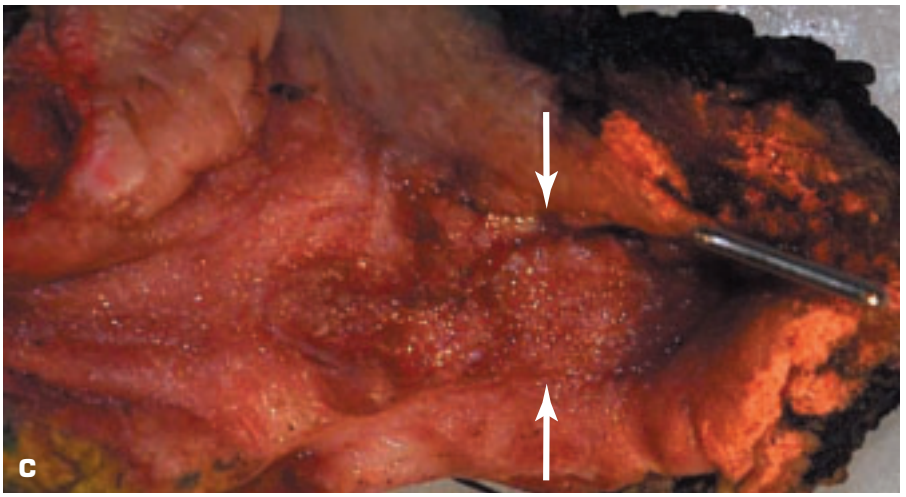

6-5. A. Paget disease (*arrows*) of the vulva – unlike the breast, there is often no underlying neoplasm. **B.** Cytokeratin-stained slide showing Paget disease of the vulva reveals malignant epithelial cells in both the dermis and epidermis. **C.** Vulval excision for microinvasive squamous cell carcinoma. The lesion is represented by the raised, velvety-looking area (*arrows*). **D.** Histology of the microinvasive squamous carcinoma that is in continuity with the atypical surface epithelium.

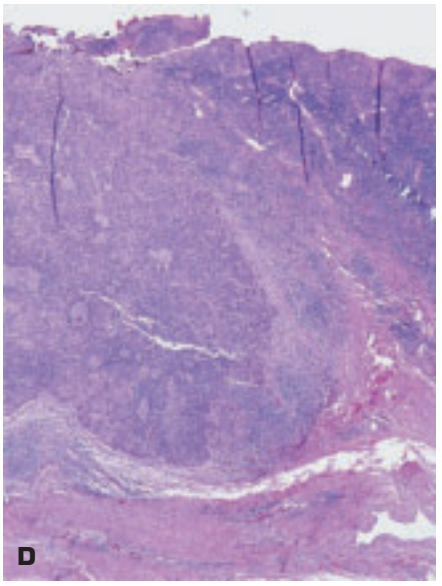

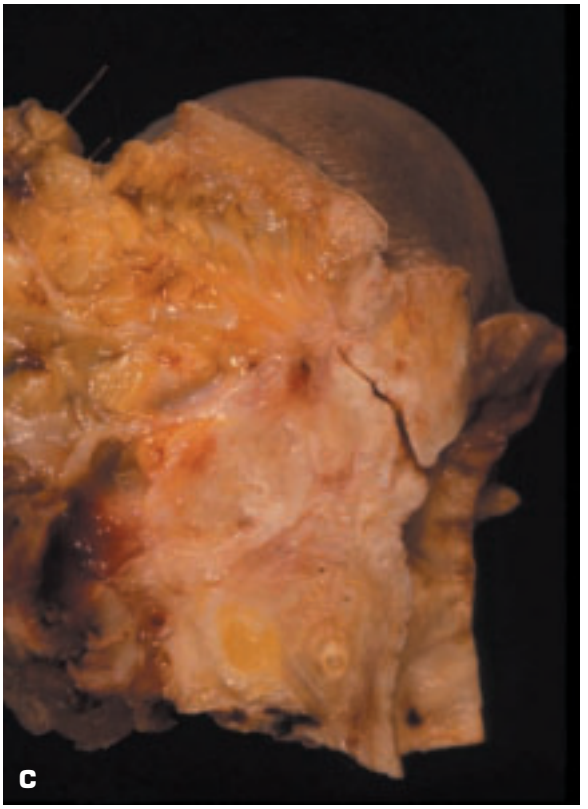

6-6. A. Early invasive squamous cell carcinoma (*arrow*) of the vulva. **B.** More advanced invasive squamous carcinoma of the vulva. **C.** Bisected vulvectomy specimen shows the pearly white-colored invasive squamous carcinoma invading the underlying soft tissue of the vulva.

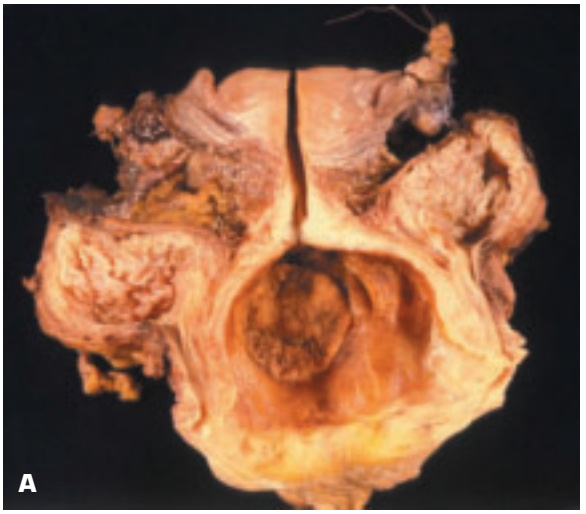

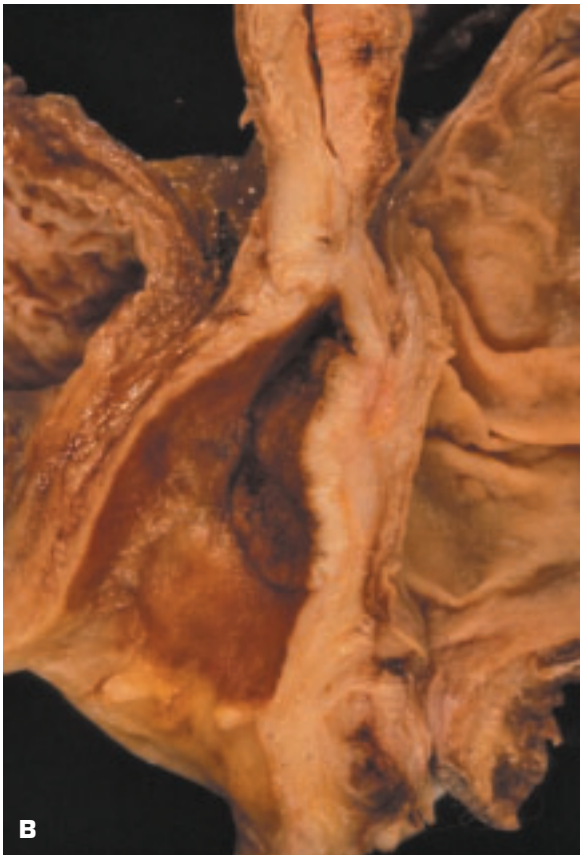

6-7. Squamous carcinoma of the vagina treated by pelvic exenteration (removal of bladder, vagina and uterus, and anorectum). **A.** Large tumor occupies upper, posterior wall of the vagina. Note the bisected urinary bladder on either side of the specimen. **B.** Bisection of the same specimen showing urinary bladder (*left*) and profile of vaginal squamous carcinoma (*center*) that has spread to involve portion of uterine cervix and is infiltrating into the rectum (*right*).

6-8. Chronic cervicitis with ectropion of the cervix (columnar epithelium has replaced squamous epithelium). The latter is shown as an extensive reddened zone. The cervix is also scarred and deformed from previous deliveries of infants.

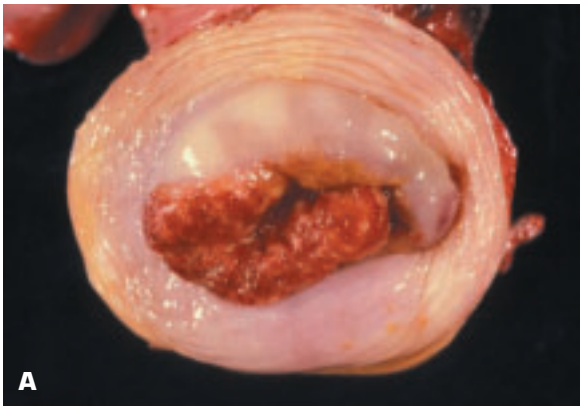

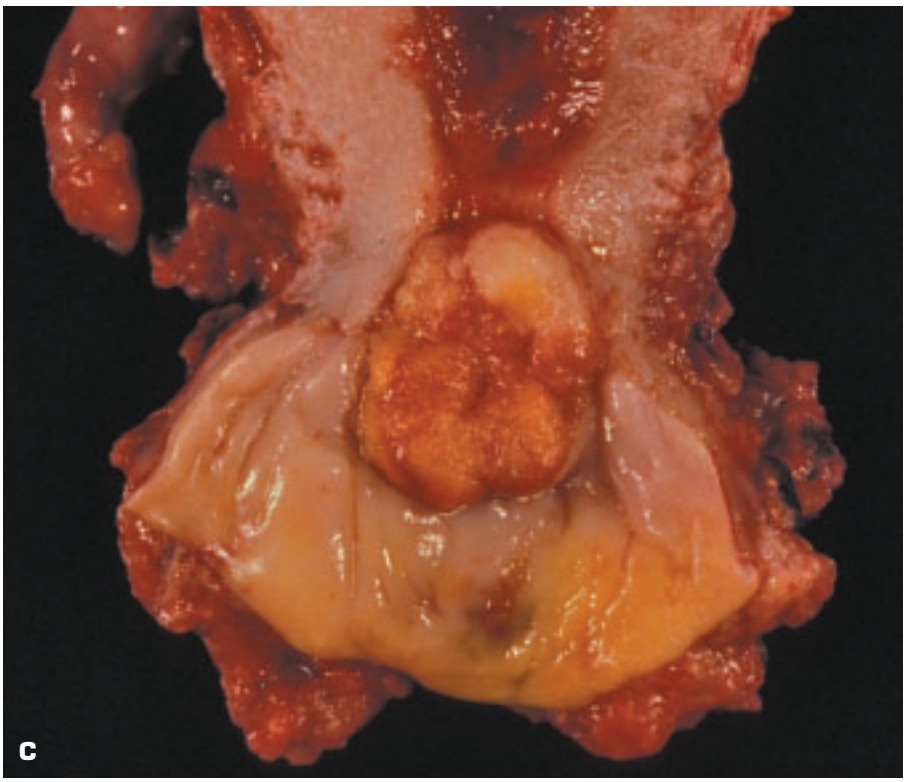

6-9. Less advanced squamous carcinoma of the cervix. **A.** Appearance of the exophytic, partly hemorrhagic-looking tumor protruding out of the external os of the cervix. **B.** The extent of the cervical cancer is better appreciated once the same specimen has been partially bisected. **C.** Adenosquamous carcinoma of the cervix has no macroscopic distinguishing features. *(continued on next page)*

6-9. *(Continued)* **D.** More advanced squamous cell carcinoma of the ectocervix. **E.** Appearance of the same cancer in the opened cervix.

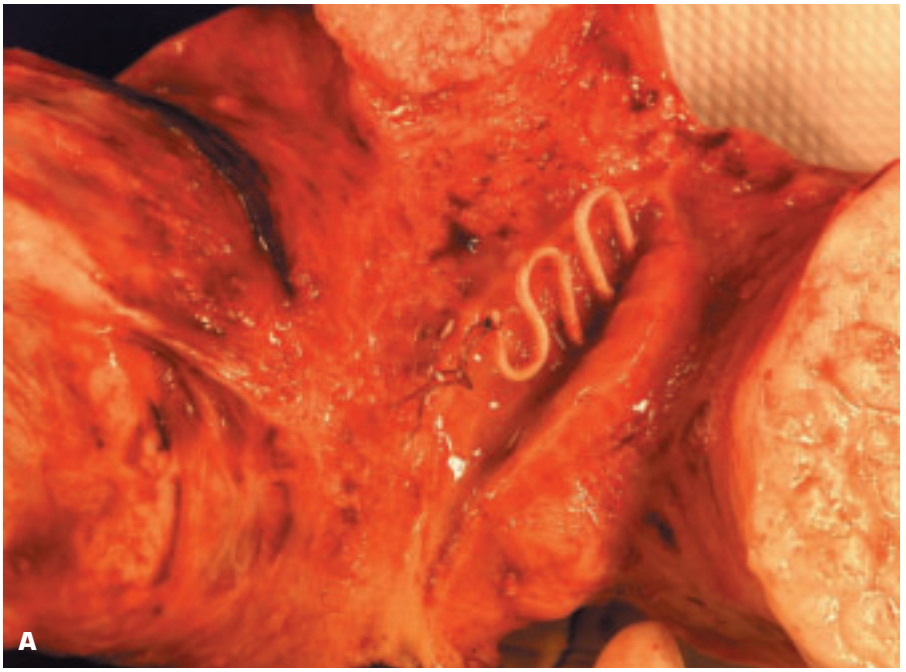

6-10. A. Uterine cavity of this bisected uterus contains an intrauterine contraceptive device (no longer used). Portions of a leiomyoma are also seen (*right*). **B.** Gross appearance of a recently postpartum uterus showing body (*top*), cervix (*middle*), and vagina (*bottom*).

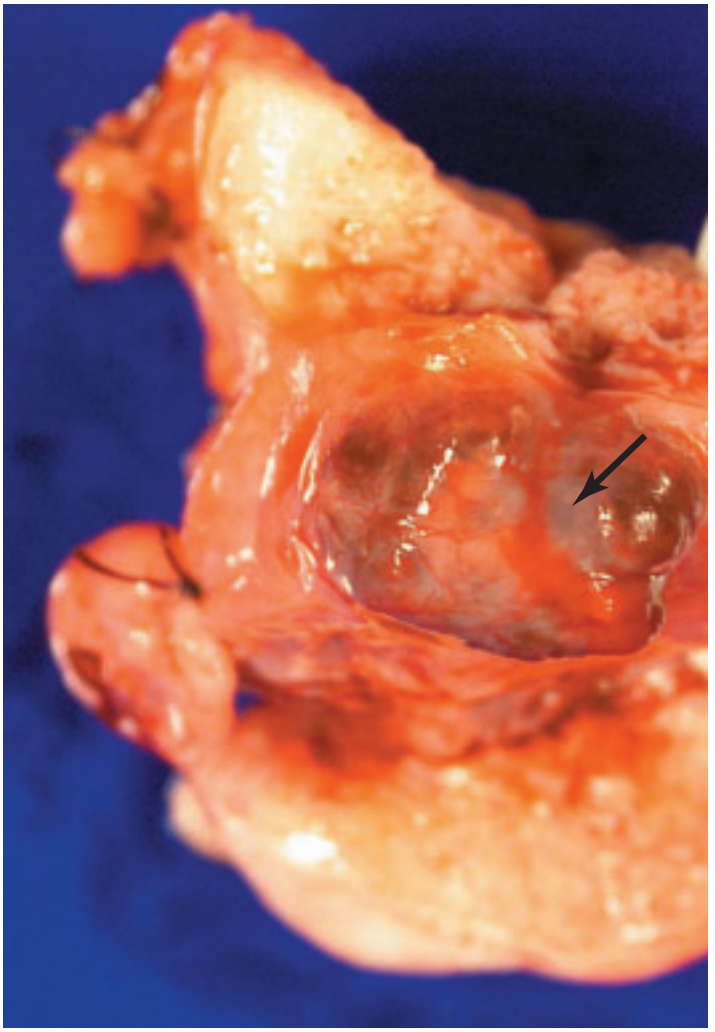

6-11. An interstitial pregnancy (IP) develops in the uterine (cornual) portion of the fallopian tube and comes into the differential diagnosis of other forms of tubal ectopic pregnancy and abdominal pregnancy. IP comprises only 2% to 4% of ectopic pregnancies and has a mortality rate double that of other ectopic pregnancies. In this picture, the decapitated cornus of the uterus shows an intact fetal sac (*arrow*).

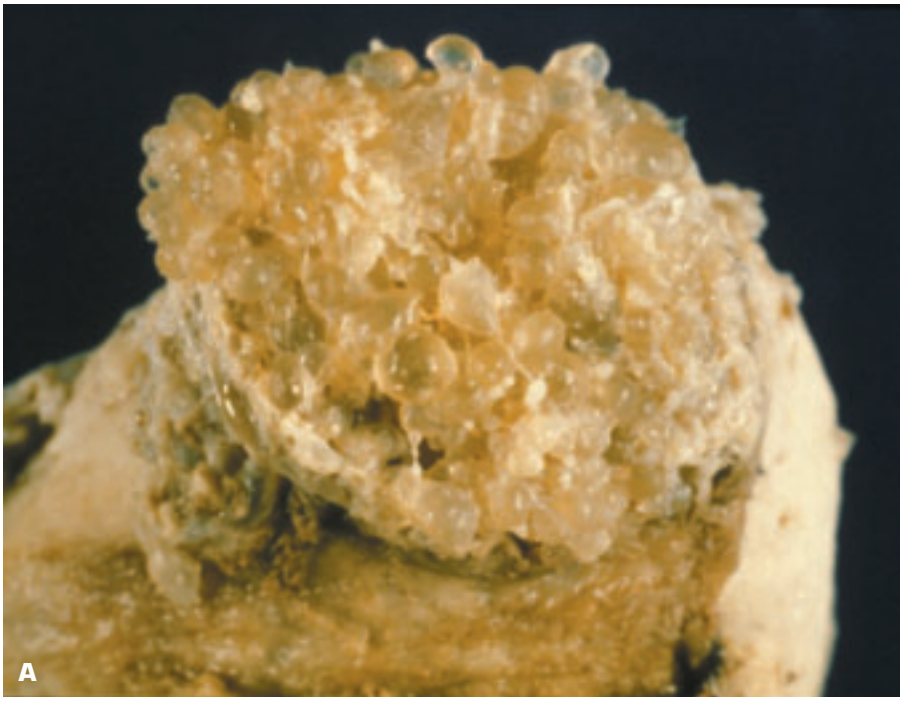

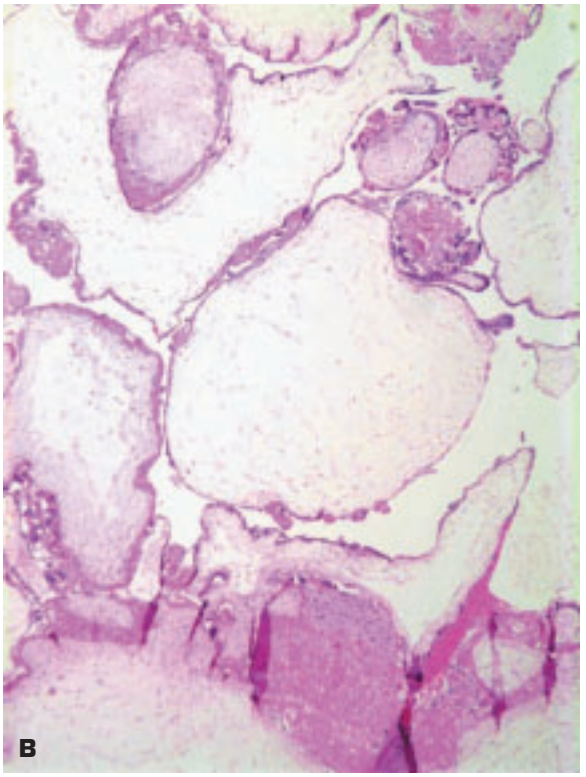

6-12. Complete hydatidiform mole. **A.** Uterine cavity is occupied by a mass of abnormal chorionic villi resembling a bunch of grapes. Each villus is distended by fluid to reach a diameter of about 1 to 3 mm. No fetus is present. **B.** Histology shows fluid-filled, avascular villi with overlying hyperplastic trophoblast that shows cellular atypia.

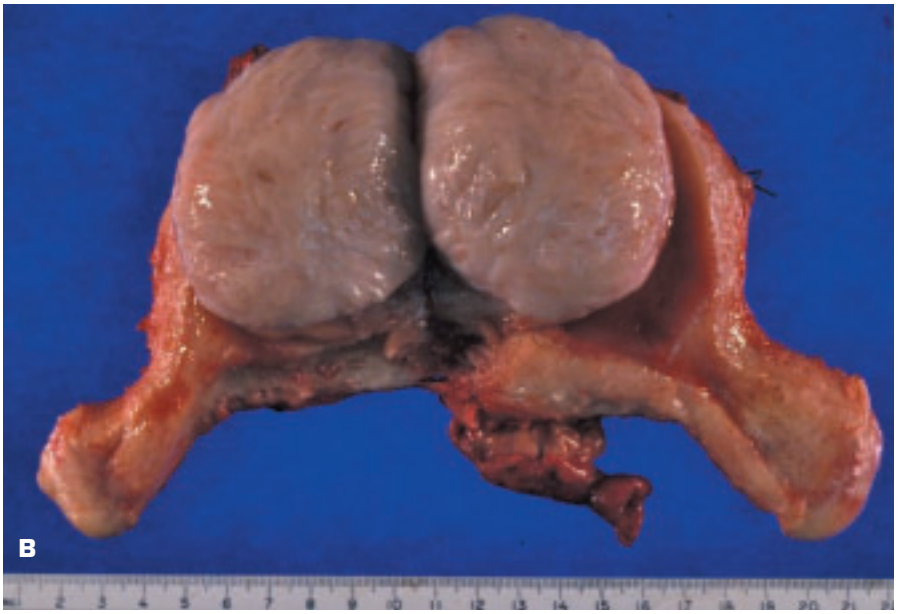

6-13. Leiomyoma of the uterus is the most frequent tumor of the female genital tract. **A.** Submucous leiomyoma fills most of the distended uterine cavity. **B.** Bisected leiomyoma shows the characteristic sharply circumscribed fleshy tumor with whorled cut surface commonly called a "fibroid." *(continued on next page)*

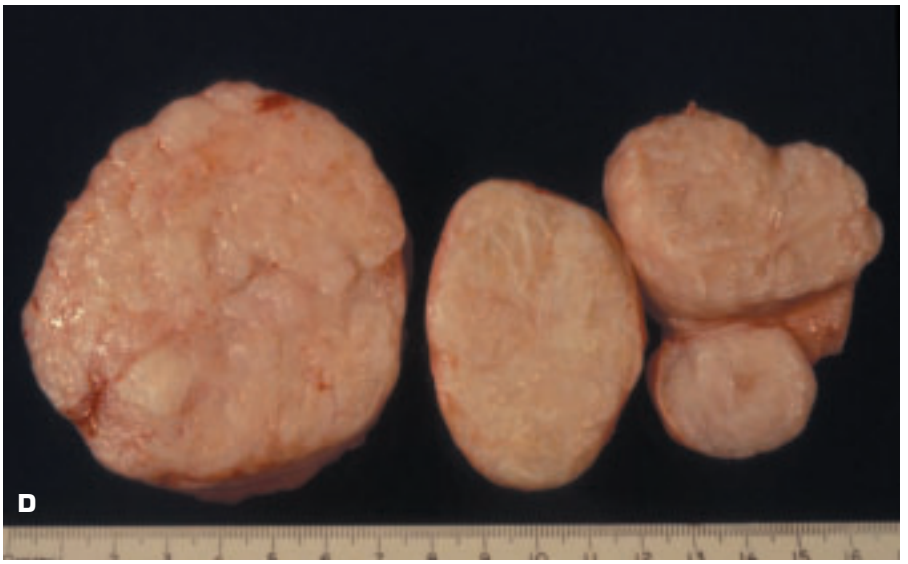

6-13. *(Continued)* **C.** Uterus bears multiple subserosal intramural and submucous leiomyomata. **D.** Cut surfaces of multiple leiomyomas of the uterus. *(continued on next page)*

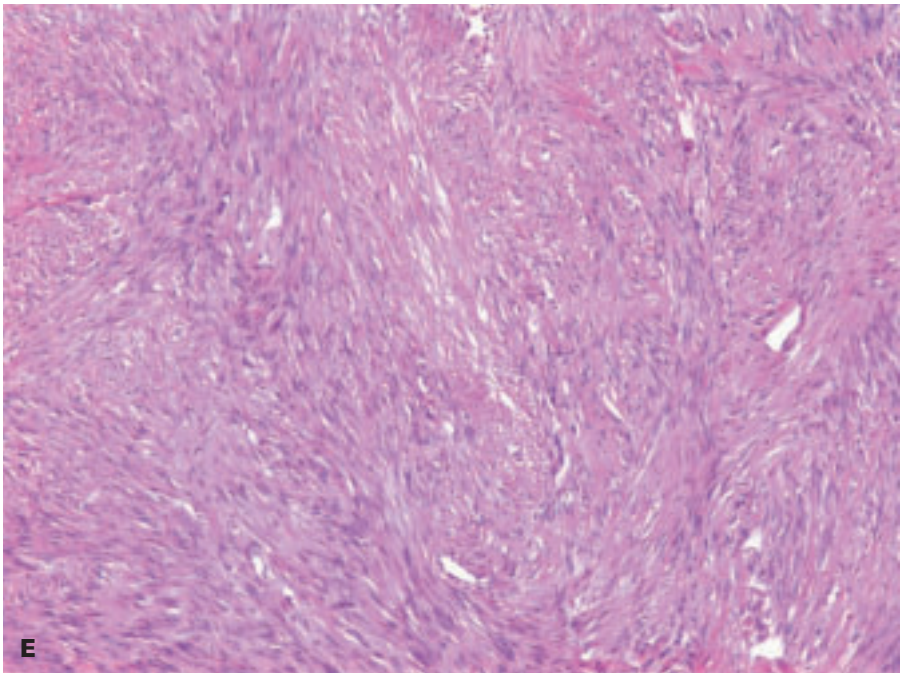

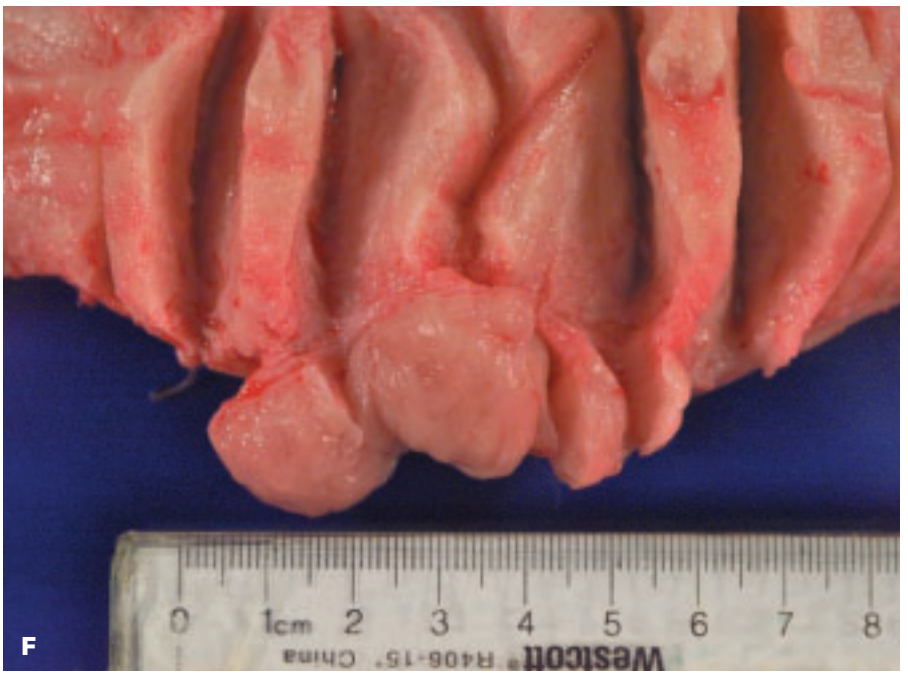

6-13. *(Continued)* **E.** Histology of a leiomyoma showing interlacing smooth muscle cells. **F.** Close-up view of a subserosal "cellular" leiomyoma.

6-14. Leiomyosarcoma of the uterus. The uterus is expanded by a massive, fleshy, partly necrotic and hemorrhagic-looking malignant tumor.

6-15. This bisected uterus shows hemorrhage occurring within proliferative phase endometrium and in a serosal focus of endometriosis (*arrow*).

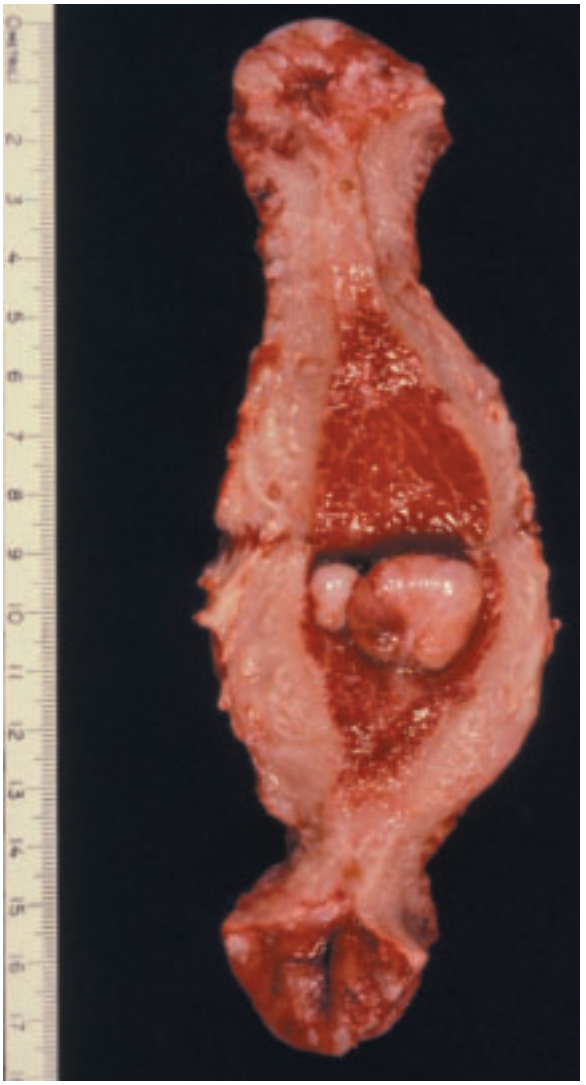

6-16. Two endometrial polyps protrude into the uterine cavity. The lesions are believed to arise from endometrial foci that are hypersensitive to estrogen stimulation and that fail to slough with menstruation.

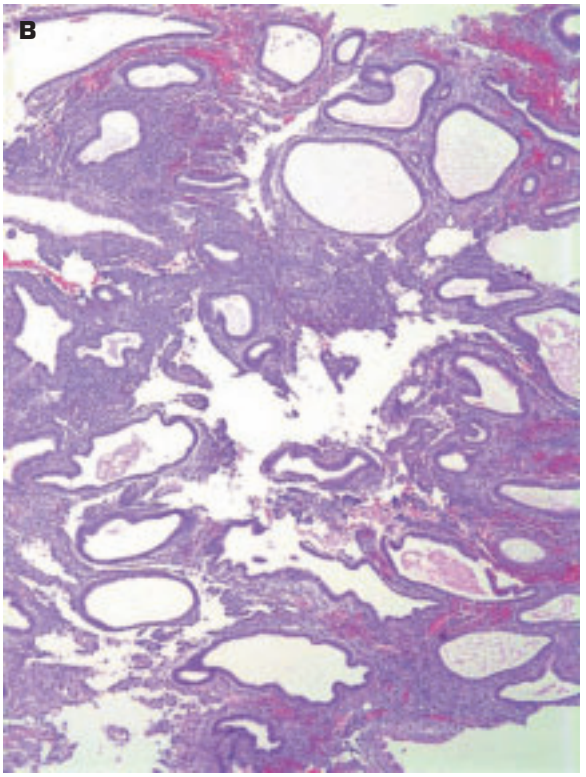

6-17. A. Endometrial hyperplasia (EH). The endometrial lining of the uterus is elevated in irregular heaped-up folds. The spectrum of EH merges with carcinoma. EH was originally classified into simple, complex, or atypical hyperplasia, but now it is termed *endometrial intraepithelial neoplasia*. Causes of EH include anovulatory cycles, polycystic ovary syndrome, estrogen-producing tumor, or obesity. **B.** Histology of simple EH shows prominent cystic dilatation of the glands, but no nuclear atypism is present (unlike atypical hyperplasia).

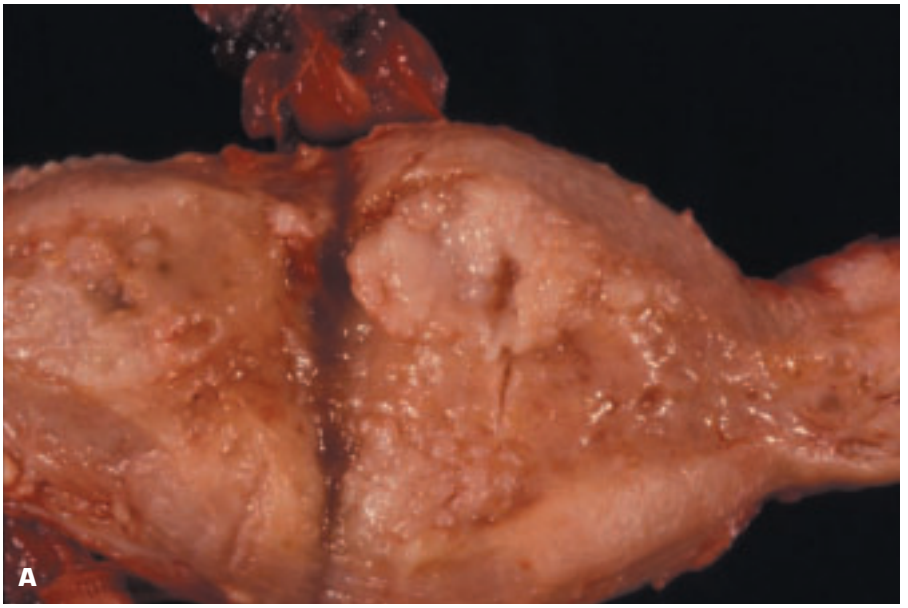

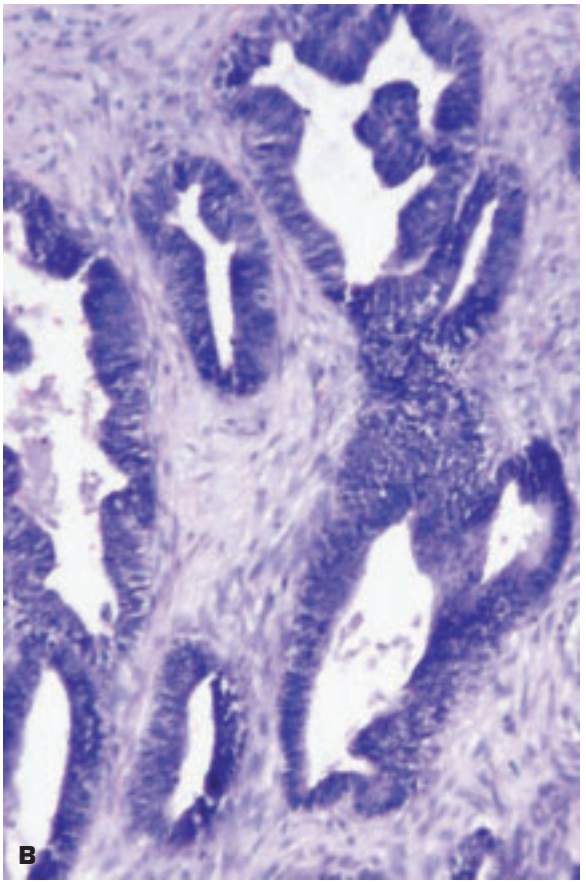

6-18. Endometrial adenocarcinoma (EA) may be due to extended estrogenic stimulation of the endometrium, and the median age at diagnosis is 63 years. **A.** Diffuse growth of an endometrioid type of EA with focal polypoid tumor growth pattern. **B.** Histology of the endometrioid carcinoma shows an adenocarcinoma resembling endometrium in appearance. *(continued on next page)*

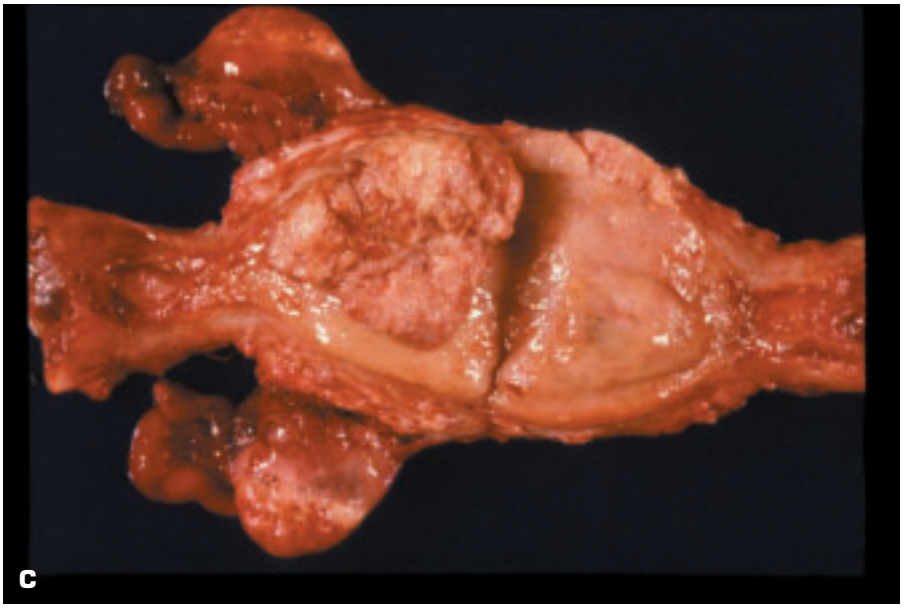

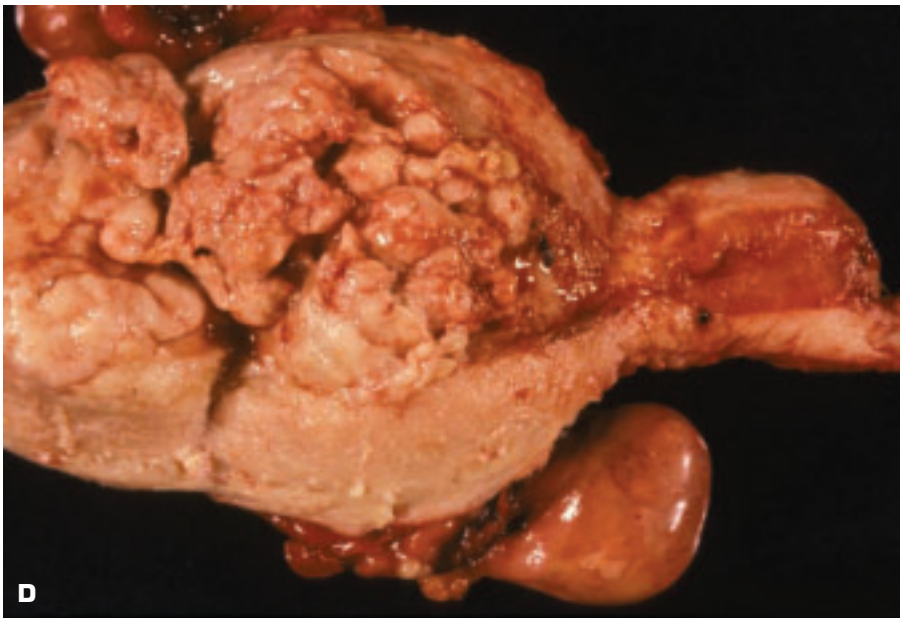

6-18. *(Continued)* **C.** This EA has formed a single large polypoid excrescence, in addition to its diffuse growth over the surface of the endometrial cavity. **D.** Advanced EA has invaded through the myometrium (*top*), and the bulky tumor has expanded the uterine cavity. *(continued on next page)*

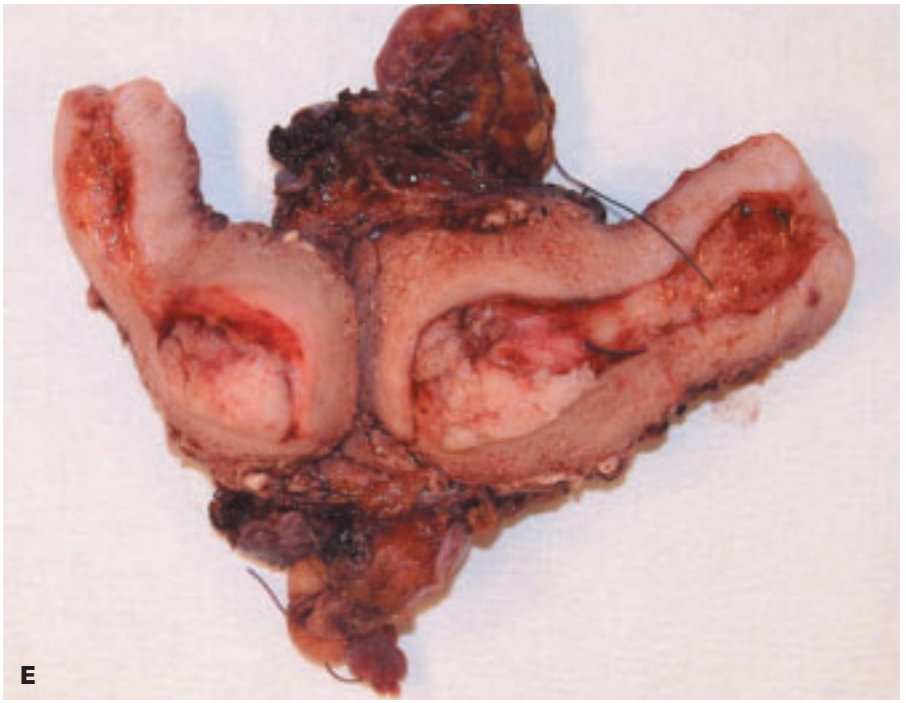

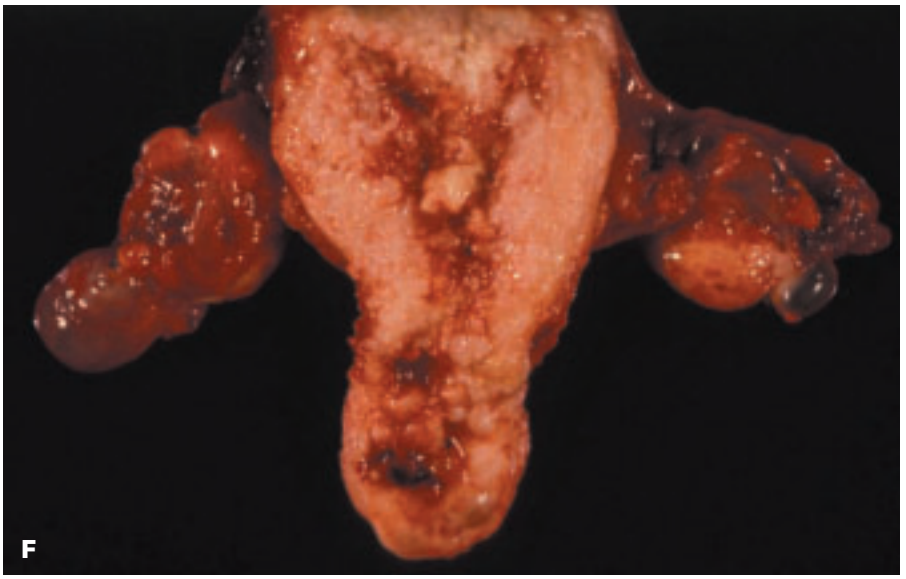

6-18. *(Continued)* **E.** Clear cell carcinoma of the endometrium. This tumor has a worse prognosis than endometrioid carcinoma. **F.** Advanced endometrial carcinoma has widely infiltrated the myometrium.

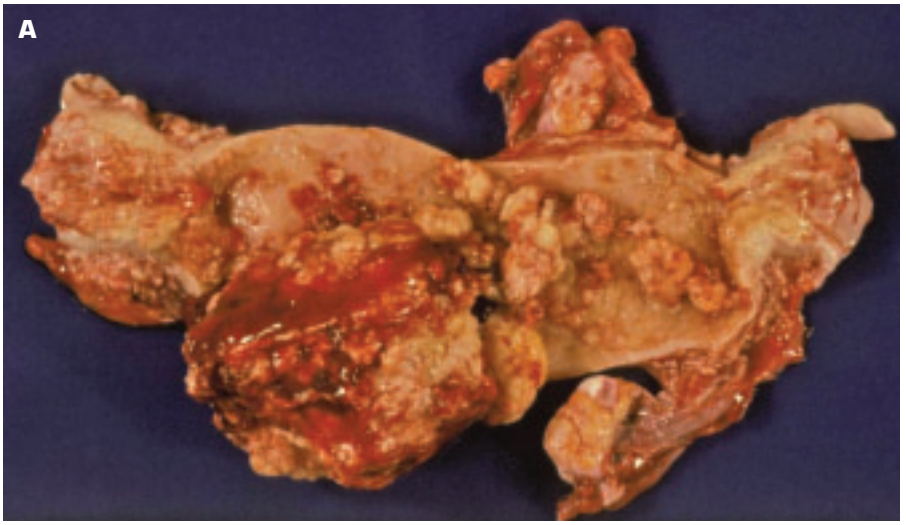

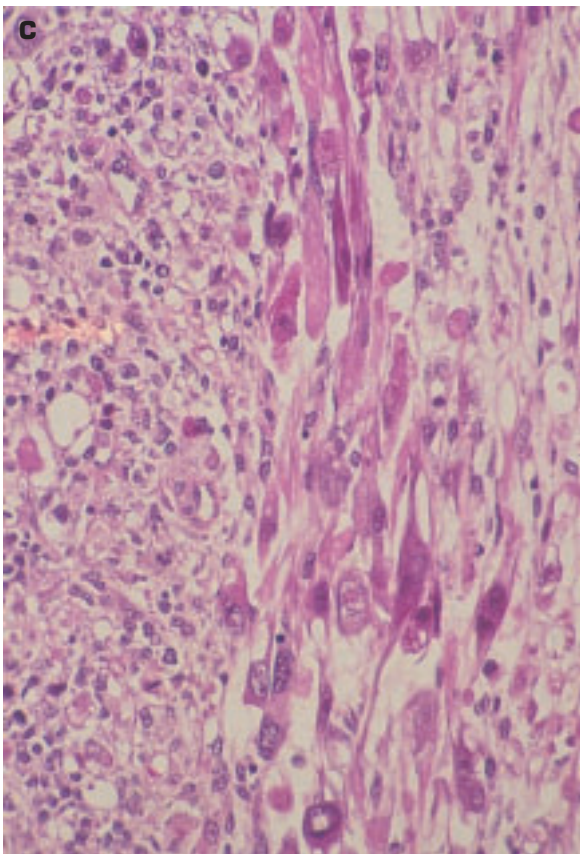

6-19. Carcinosarcoma (malignant mixed mesodermal tumor or MMMT) arises from multipotential stromal cells. Both the epithelial and the stromal components of the tumor are malignant. **A.** Bulky tumor massively expands the uterine cavity and shows implants elsewhere on the endometrial surface. **B.** This MMMT is pedunculated, having been attached to the uterus at its narrow end (*top*). **C.** Myogenic differentiation in a MMMT.

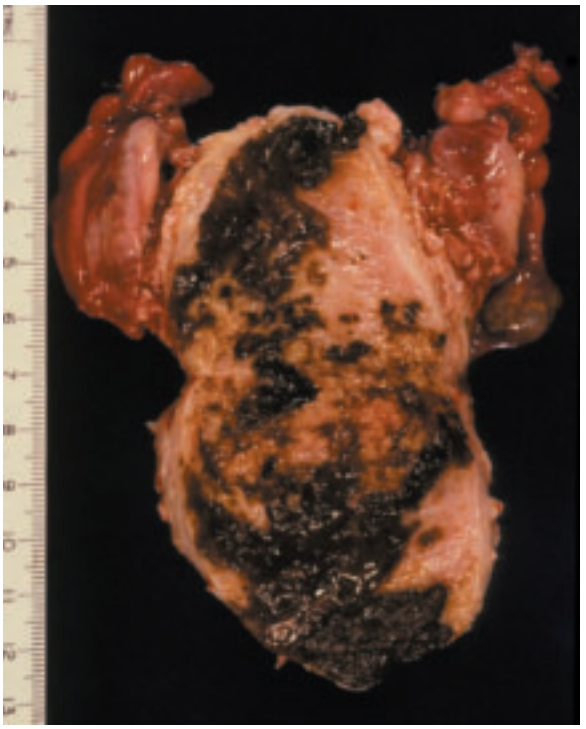

6-20. Hematometra. Previous cervical surgery led to uterine cavity outlet obstruction, and the cavity became distended with menstrual cyclical blood. Most of the old blood drained away after the uterus was bisected. No tumor is present, and the altered blood is black in appearance. The obstruction may have a congenital cause in some cases.

6-21. Malignant melanoma of the cervix uteri (*right*) is seen as irregular black nodules in the cervix. A metastatic, brown-colored deposit (*center*) is noted within the myometrium.

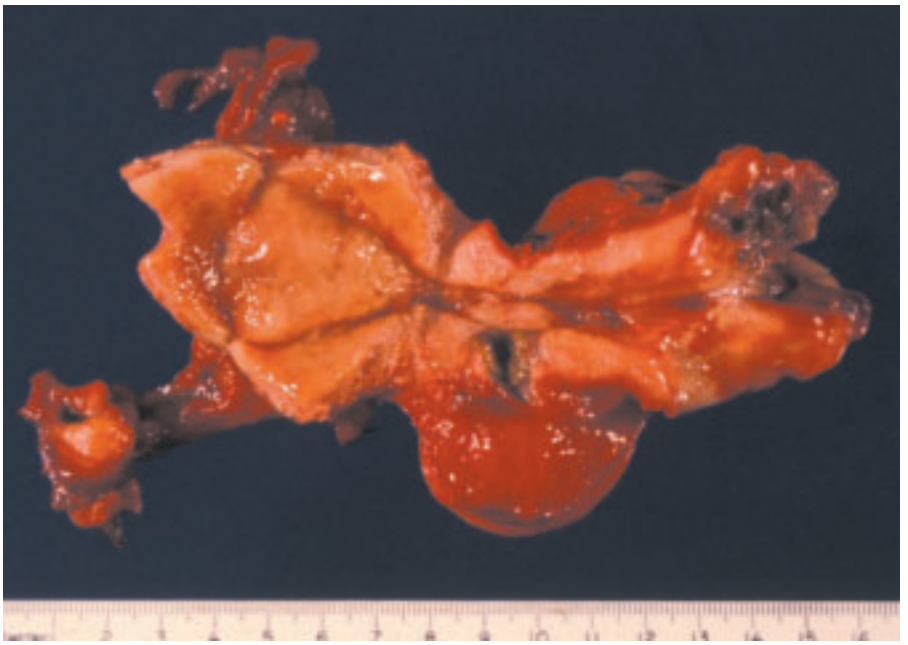

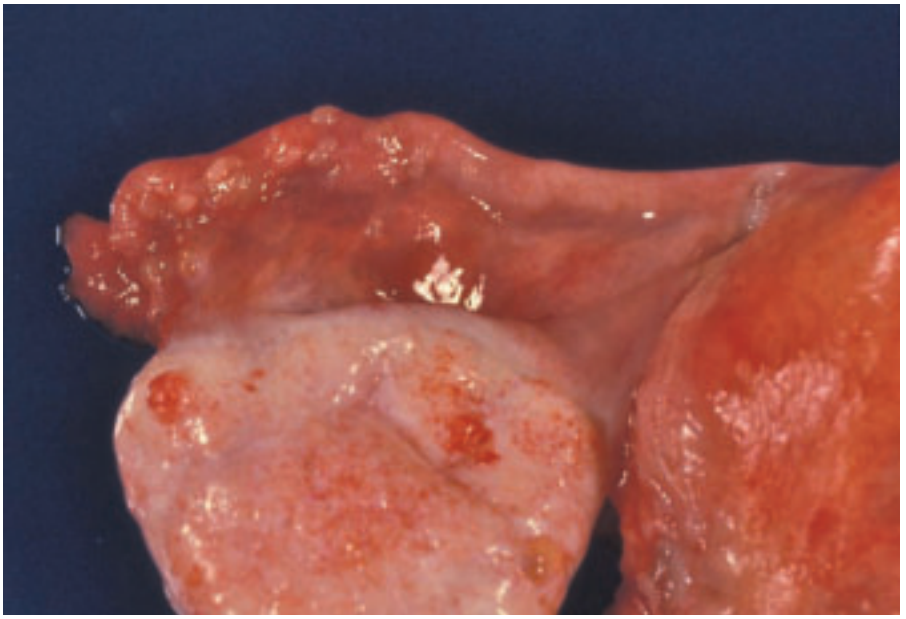

6-22. Walthard cell nests ("rests") of mesothelial origin are seen as multiple, small, partially cystic nodules on the serosal surface of the fallopian tube. In patients with intraabdominal malignancy, they may be mistaken for tumor deposits.

6-23. Paratubal cyst ("hydatid of Morgagnii") is attached to the fimbriated end of the fallopian tube by a short pedicle. The cyst is of müllerian origin.

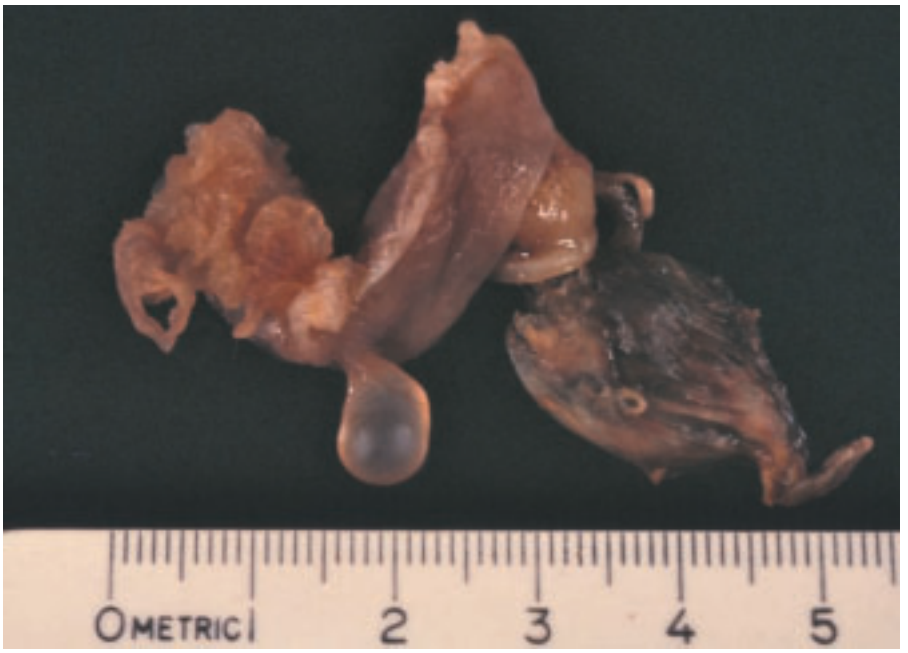

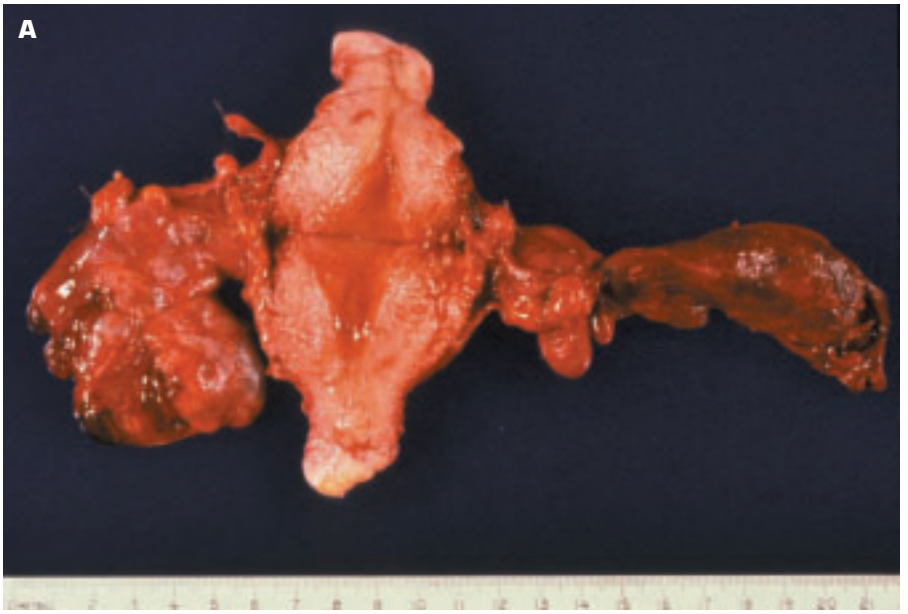

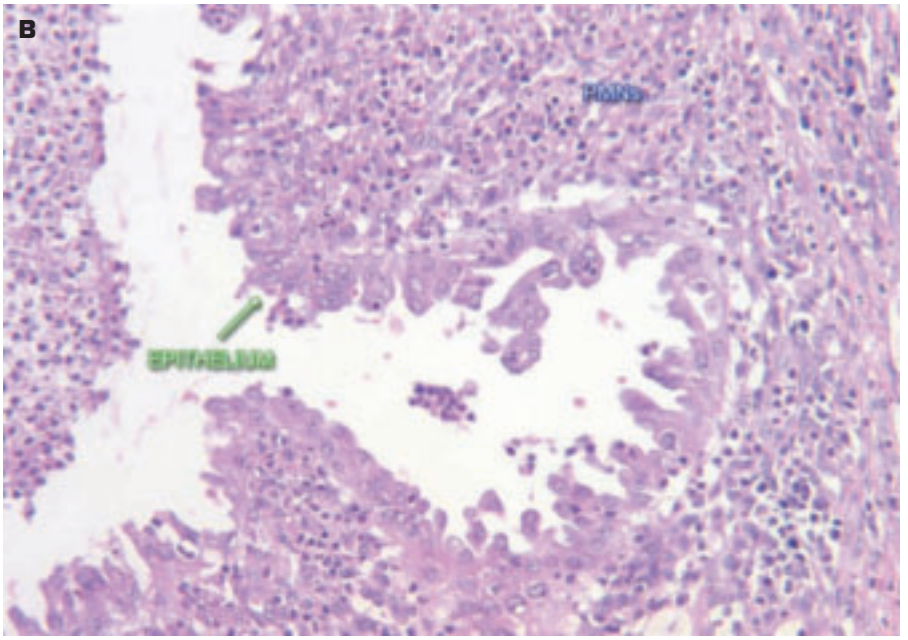

6-24. A. Bilateral subacute salpingitis evolving into early hydrosalpinx. The dilated fallopian tubes are still inflamed and congested. **B.** Polymorphonuclear leucocytes (PMNs) are seen both in the lumen and under the epithelium of the fallopian tube.

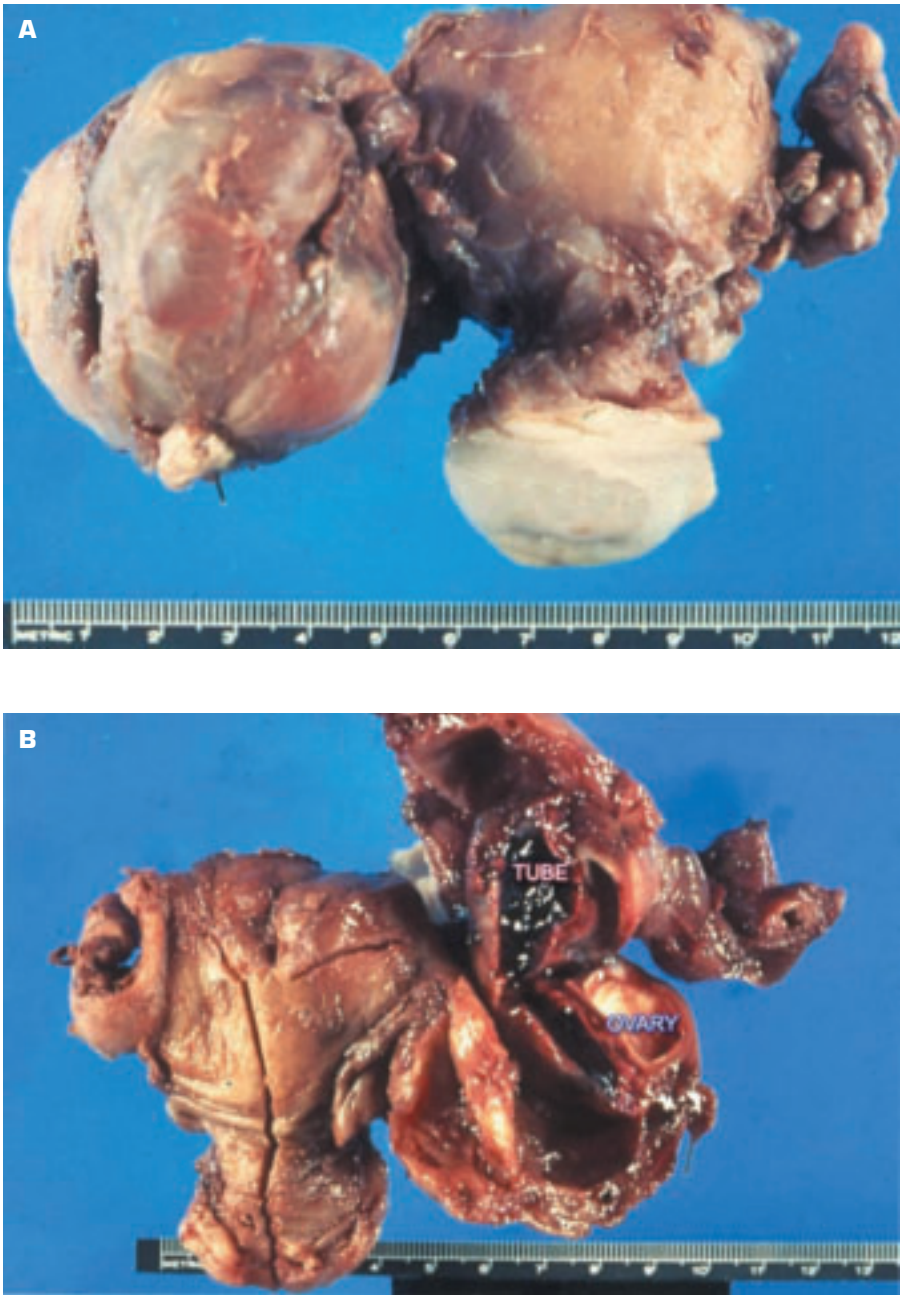

6-25. A. Fused tubo-ovarian mass composed of fallopian tube, ovary, and organized purulent exudate is present (*left*). **B.** Posterior view of same specimen transected shows dilated, thick-walled fallopian tube that has blood in its lumen and a cystic-appearing ovary.

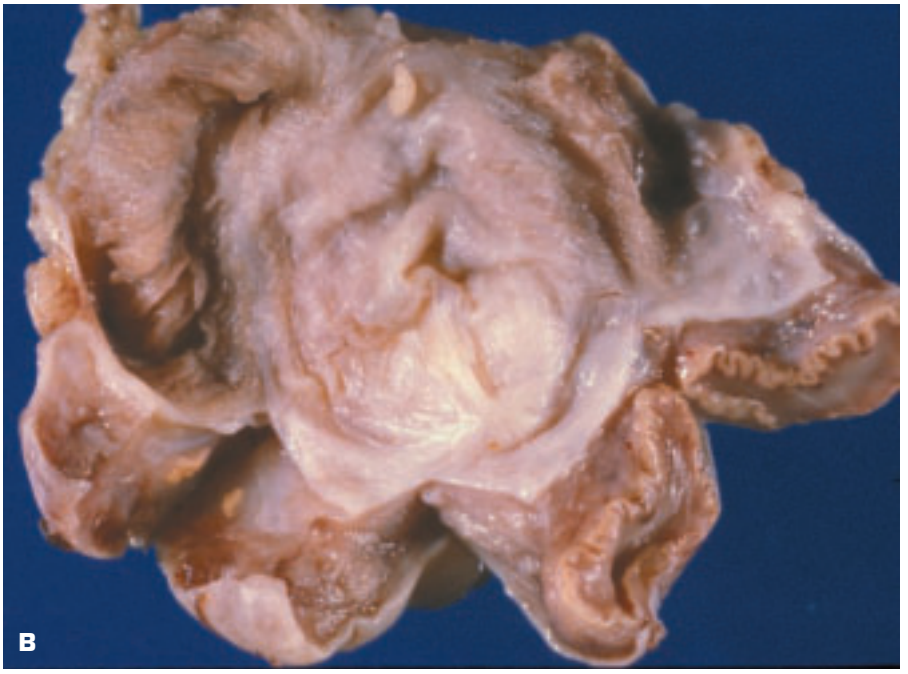

6-26. A. Hydrosalpinx has the appearance of an enlarged, sausage-shaped fallopian tube filled with fluid secondary to postinfective obstruction of the fimbrial end. The fluid is derived from tubal secretions. In a pyosalpinx, the tube is filled with pus. **B.** Interior view of an opened hydrosalpinx showing a smooth internal lining. Portion of an ovary containing a corpus luteum is attached to the tube (*right*).

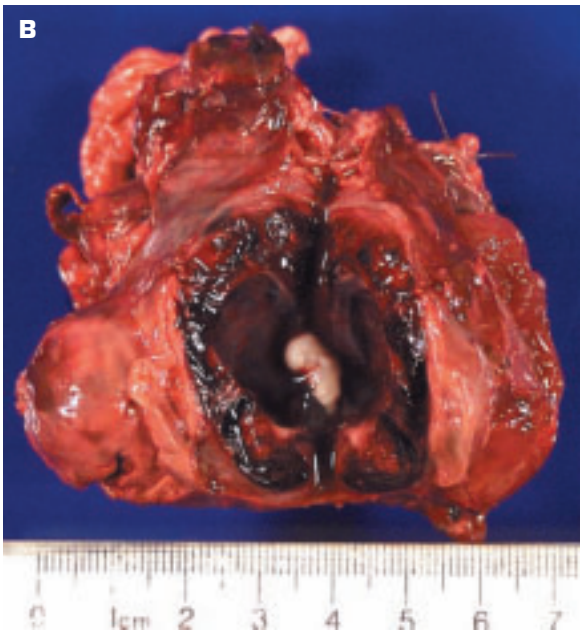

6-27. Ectopic pregnancy (EP) defines fetal implantation at a site other than the endometrium. About 95% of EPs occur in the fallopian tube, especially in its distal two-thirds. Interstitial EP is illustrated in Fig. 6-11. **A.** Ruptured EP shows a fetus within its membranes prolapsing through a defect in the distal portion of the tube. **B.** EP shows fetus lying within opened amniotic sac in this bisected, enlarged fallopian tube that had not yet ruptured.

6-28. Unilocular, simple follicular cyst of the ovary (*right*) is related to abnormalities in the release of pituitary gonadotrophins.

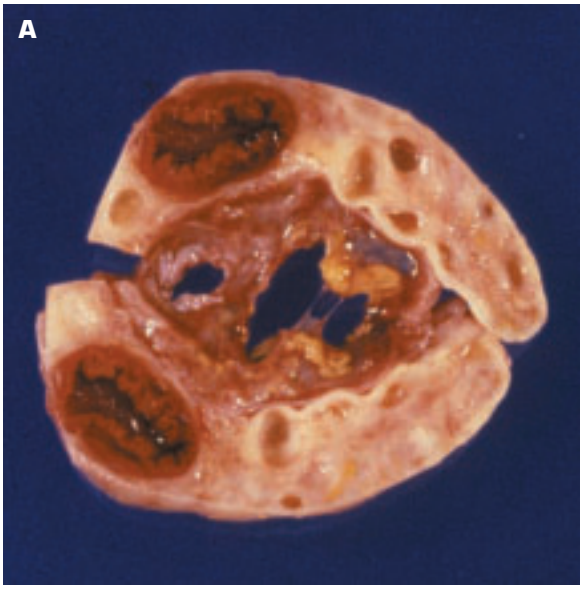

6-29. A corpus luteum in the ovary should not be mistaken for pathology (e.g., endometriosis). **A.** Hemorrhage into a corpus luteum. Multiple small follicular cysts are also present – the normal ovary is a cystic structure! **B.** Histology of a hemorrhagic corpus luteum. **C.** Corpus luteum cyst may follow previous hemorrhage and delayed resolution of the cavity associated with increased oncotic pressure may draw fluid into the cavity of the corpus luteum. A corpus luteum cyst is diagnosed once the diameter exceeds 2.5 cm.

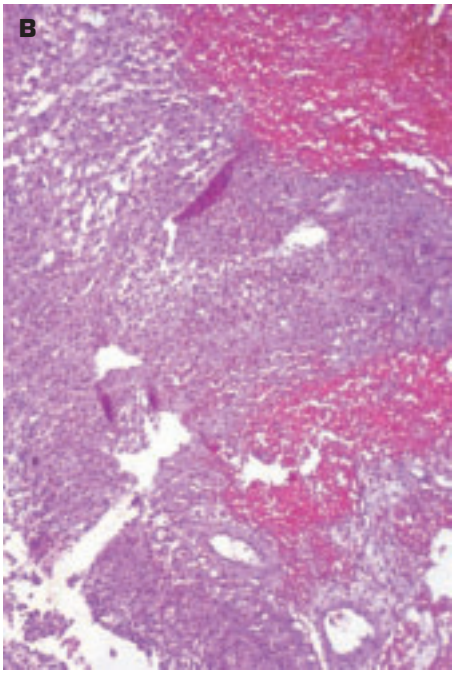

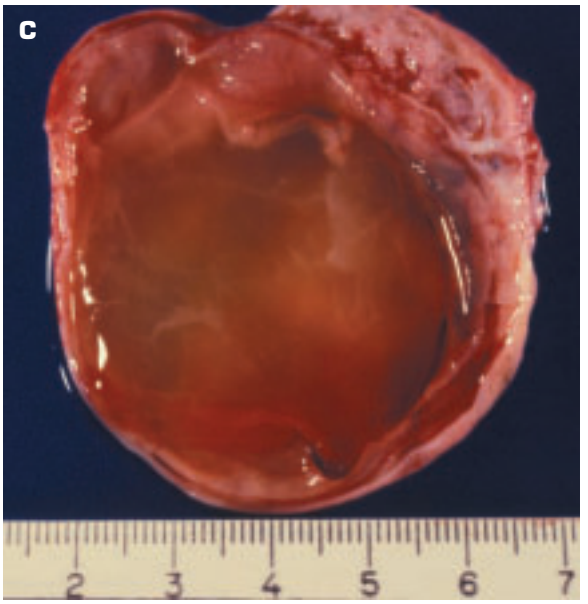

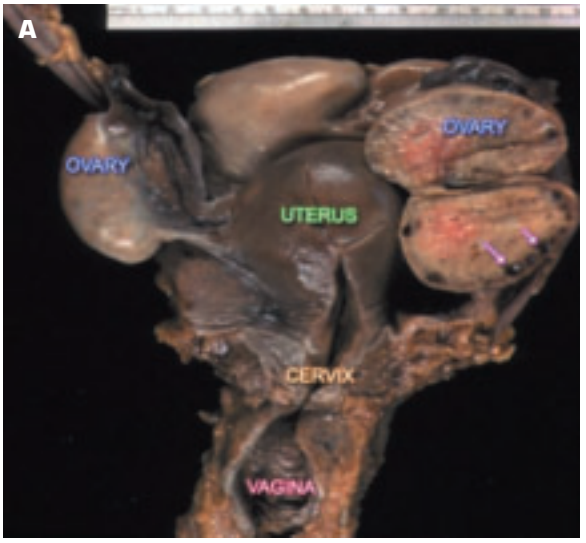

6-30. Polycystic ovaries contain multiple follicular cysts with variable luteinization of the theca interna, and there is overlying sclerosis of the stroma. Various syndromes may be associated, including Stein–Leventhal syndrome (metropathia hemorrhagica). **A.** Female organs are labeled in the picture. Both ovaries are enlarged. The bisected ovary contains multiple subcapsular cysts (*arrows*) deep to a thickened cortex. **B.** Close-up view of a polycystic ovary in a patient with Stein–Leventhal syndrome. No corpora lutea are seen. **C.** Histology of a portion of the polycystic ovary. The degree of luteinization of the cyst lining cannot be appreciated at this low power.

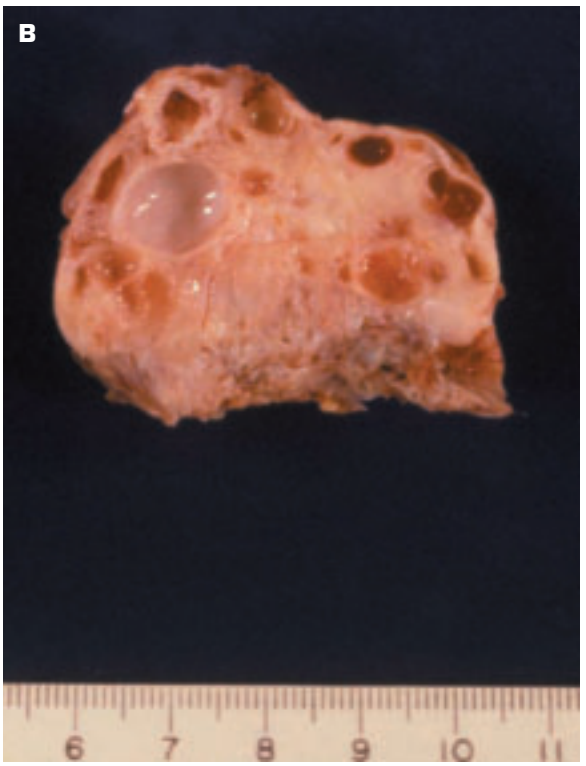

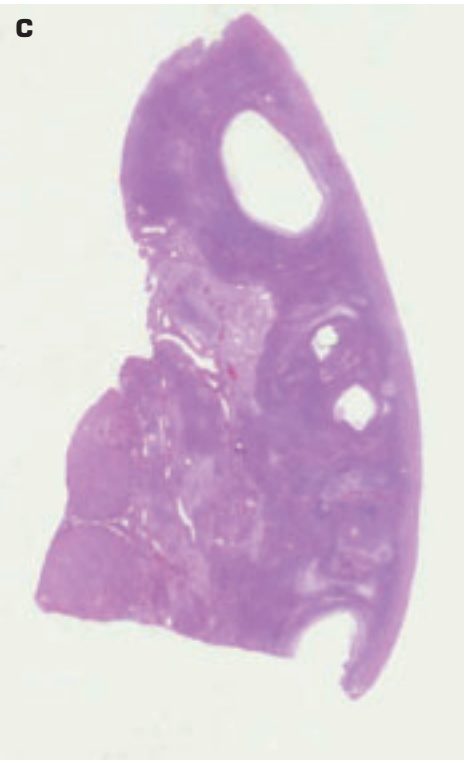

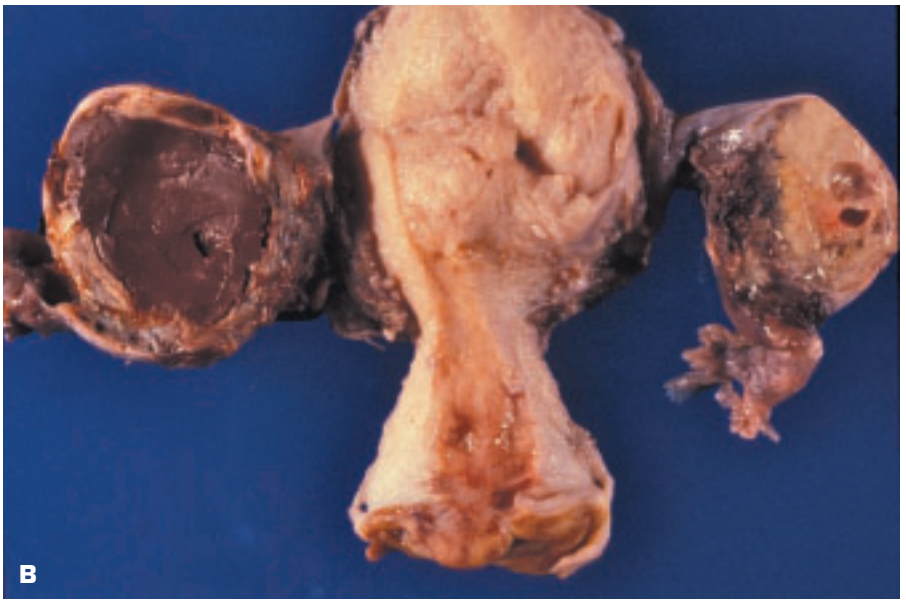

6-31. Endometriosis is the presence of endometrial glands and stroma in sites other than the body of the uterus. Common sites include the pouch of Douglas, the pelvic peritoneum, and the ovary. **A.** Both ovaries affected by endometriosis show recent hemorrhage. **B.** Repeated menstrual cycle-related hemorrhages lead to altered blood ("chocolate cyst"), as in the ovary on the left that also shows reactive fibrosis. *(continued on next page)*

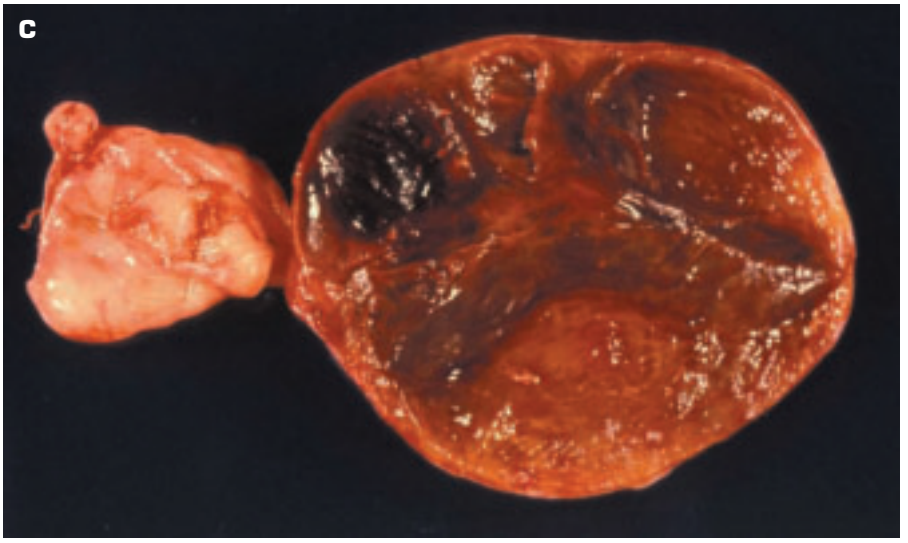

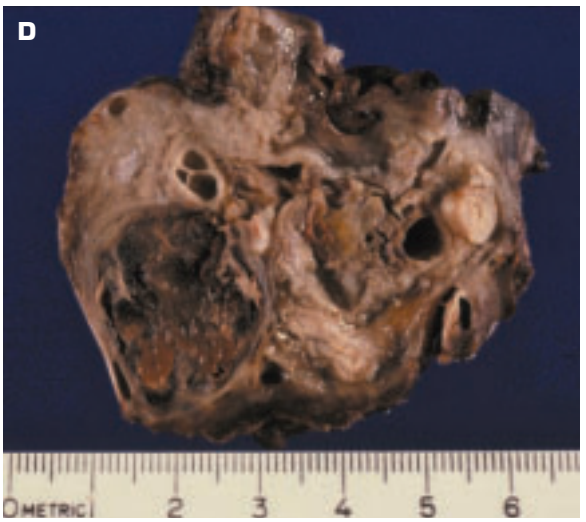

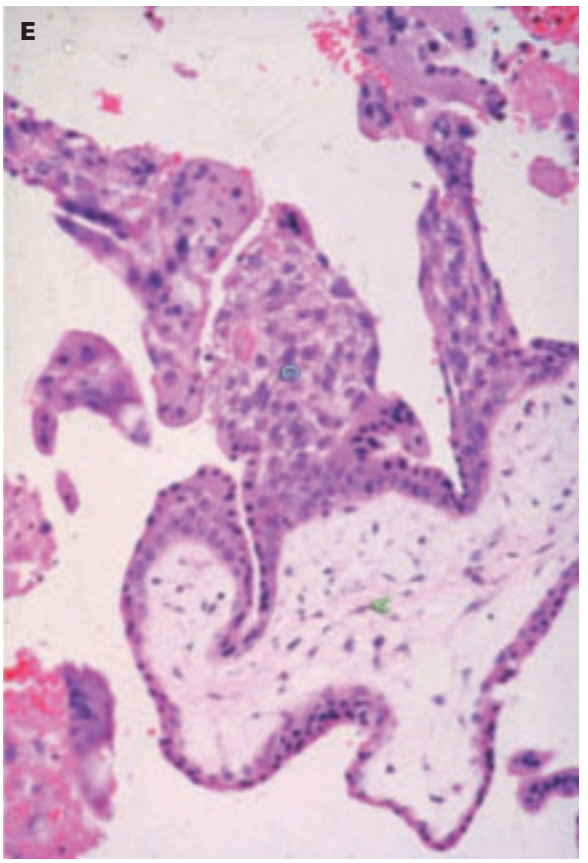

6-31. *(Continued)* **C.** Hemorrhage and necrosis of the ovary due to torsion may resemble endometriosis. **D.** Ectopic pregnancy in the ovary should not be mistaken for endometriosis. **E.** Histology of the ectopic pregnancy seen in D shows chorionic villi.

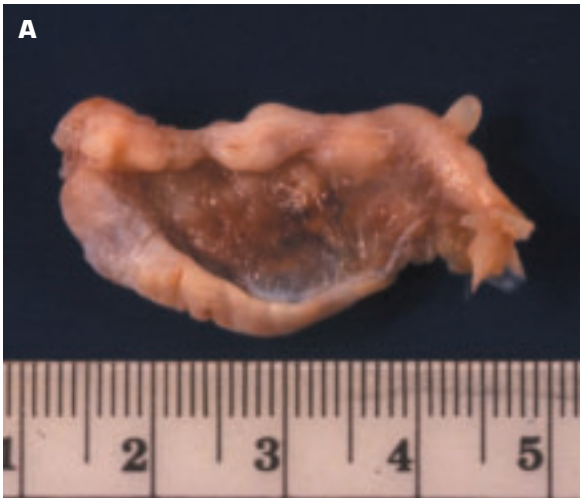

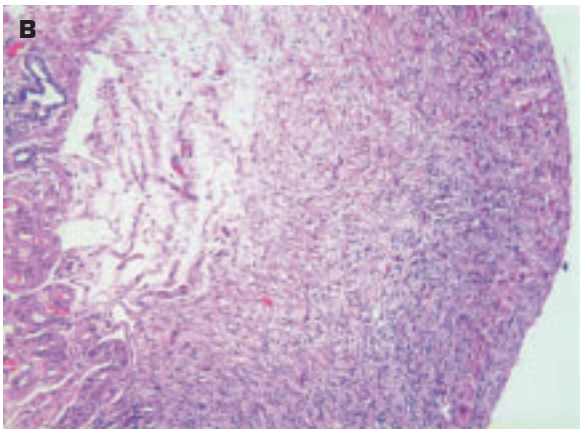

6-32. A. Streak gonad (*bottom*) in Turner syndrome runs parallel to the fallopian tube (*top*). Note the hydatid of Morgagnii attached to the tube. **B.** Histology of streak gonad shows fibrous tissue that has a pattern slightly reminiscent of ovarian stroma. **C.** Hypoplastic ovary is much smaller than a normal ovary and is out of proportion to its accompanying normal-size fallopian tube. Hypoplastic ovaries may lead to premature ovarian failure. Some patients have had mumps oophoritis.

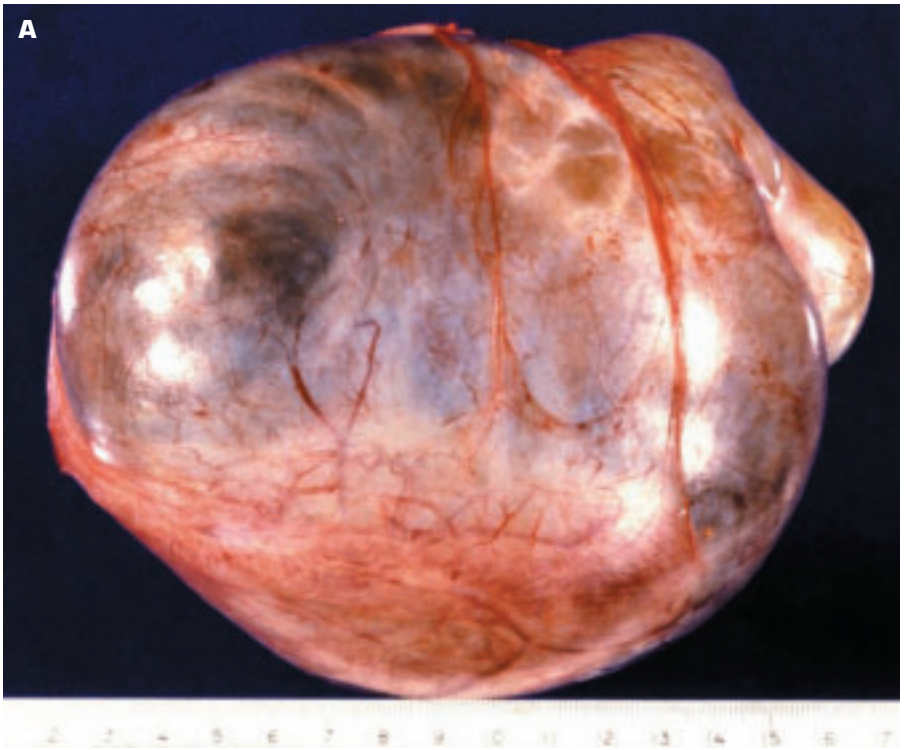

6-33. Tumors originating from germ cells form about 25% of all ovarian tumors. Germ cell tumors in adult women are mainly benign (e.g., dermoid cyst), while in younger patients most are malignant. A monodermal teratoma may show only thyroid tissue ("struma ovarii") or a carcinoid tumor. **A.** External appearance of a mature cystic teratoma (dermoid cyst). **B.** Contents of this dermoid cyst include hairs, inspissated keratin, and two teeth ("bucktooth," "smiling benign teratoma"). *(continued on next page)*

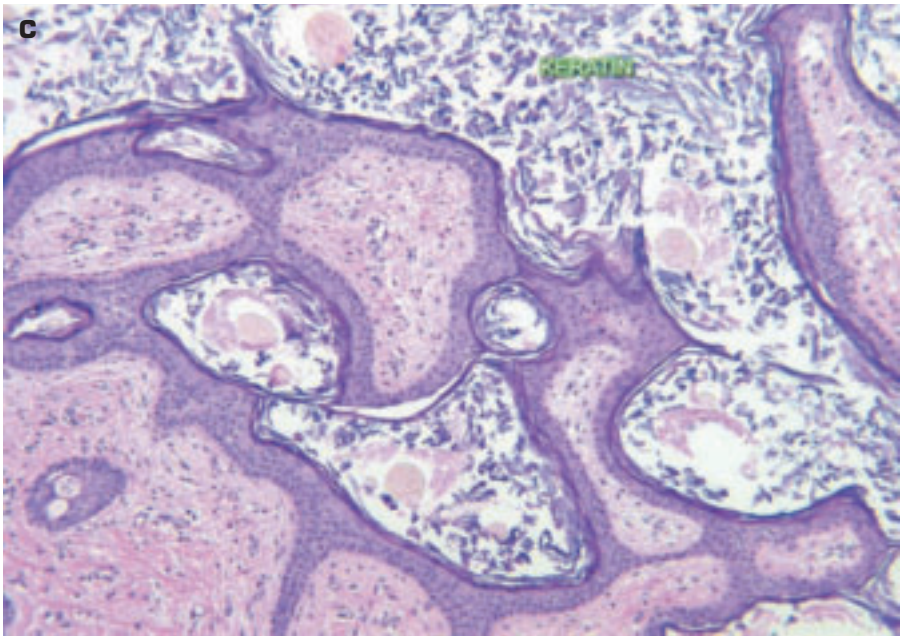

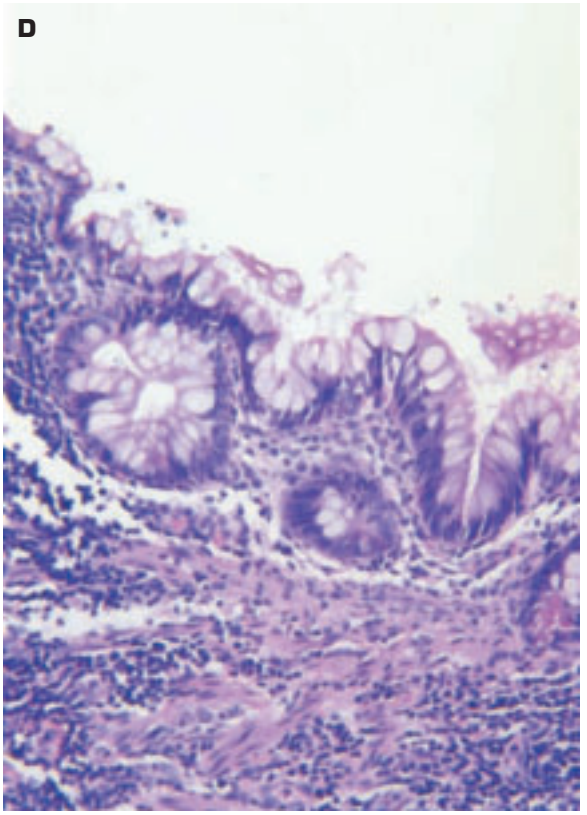

6-33. *(Continued)* **C.** Histology of the cyst lining shows skin with appendages covered by old keratin. **D.** Elsewhere, the dermoid cyst histology showed well-differentiated columnar cells suggestive of intestinal differentiation.

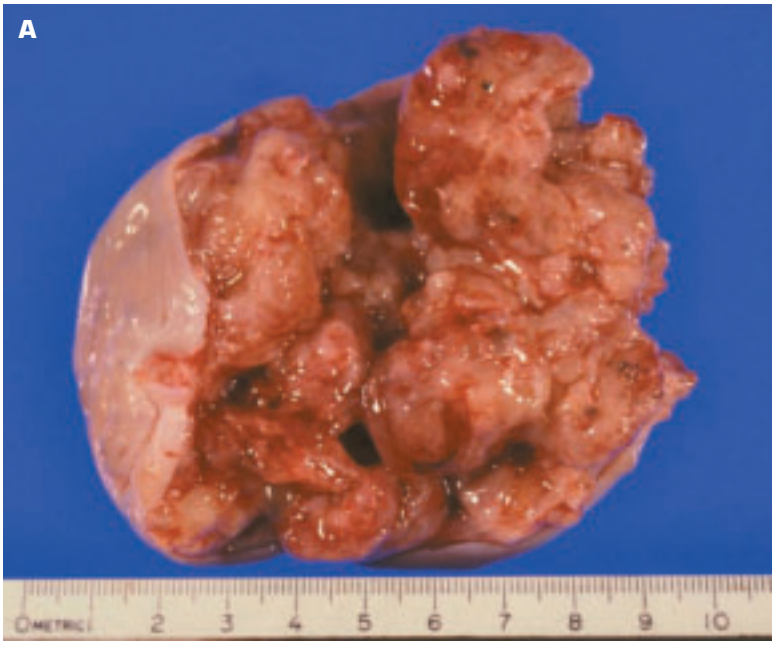

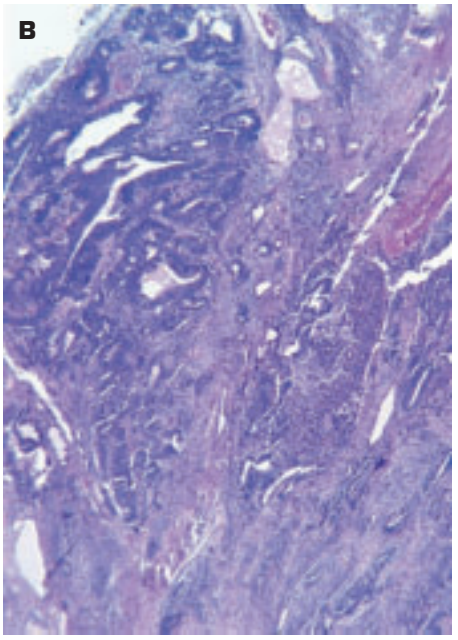

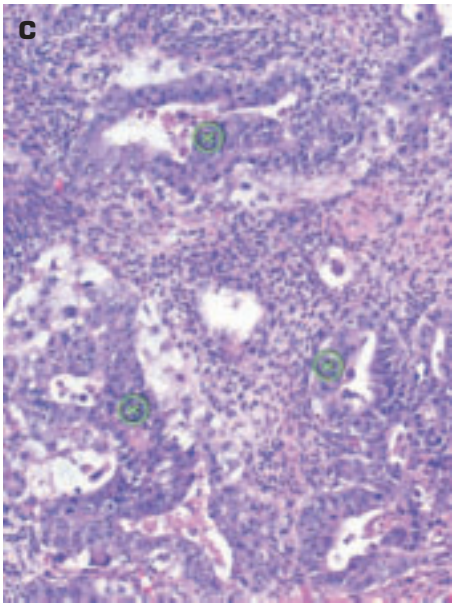

6-34. A. Immature (malignant) teratoma of the ovary in a child has a solid fleshy appearance with a few small cystic areas. **B.** Histology shows foci of immature neuroepithelium mixed with loose undifferentiated mesenchymal tissue. **C.** This immature teratoma also contained areas of embryonal carcinoma (X).

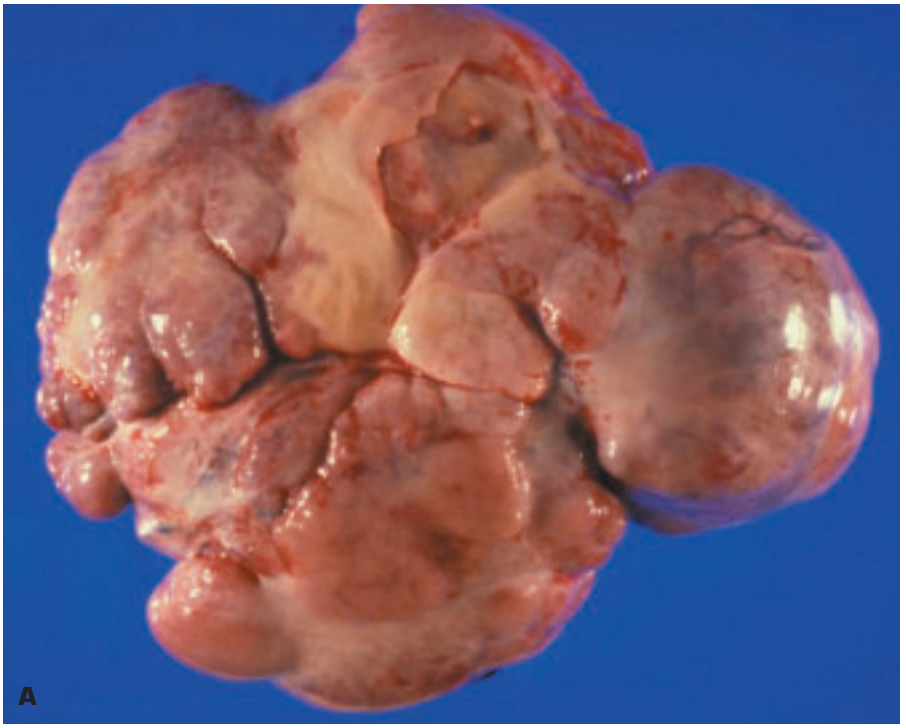

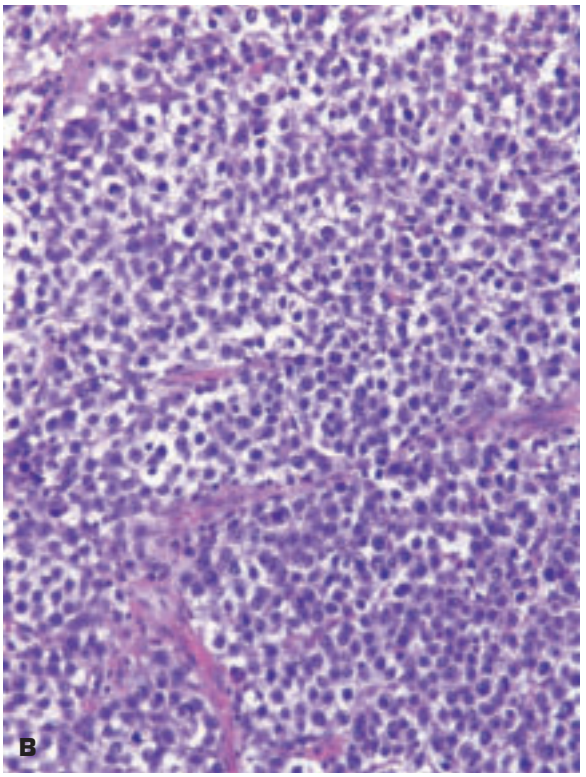

6-35. If the neoplastic germ cells in an ovary show no differentiation, then a dysgerminoma develops. This tumor is analogous to a testicular seminoma. **A.** External appearance of an ovarian dysgerminoma. **B.** Histology of dysgerminoma shows nests of uniform malignant cells resembling oogonia of the fetal ovary. Note the clear, glycogen-rich cytoplasm. The resemblance to a seminoma is striking.

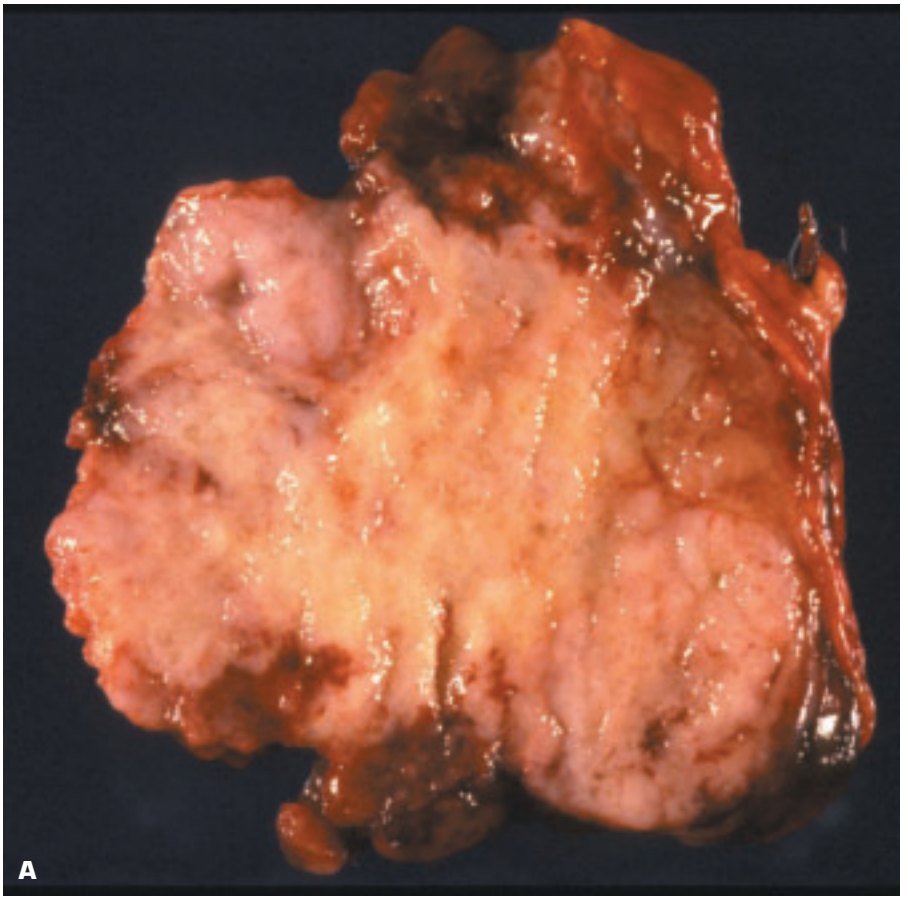

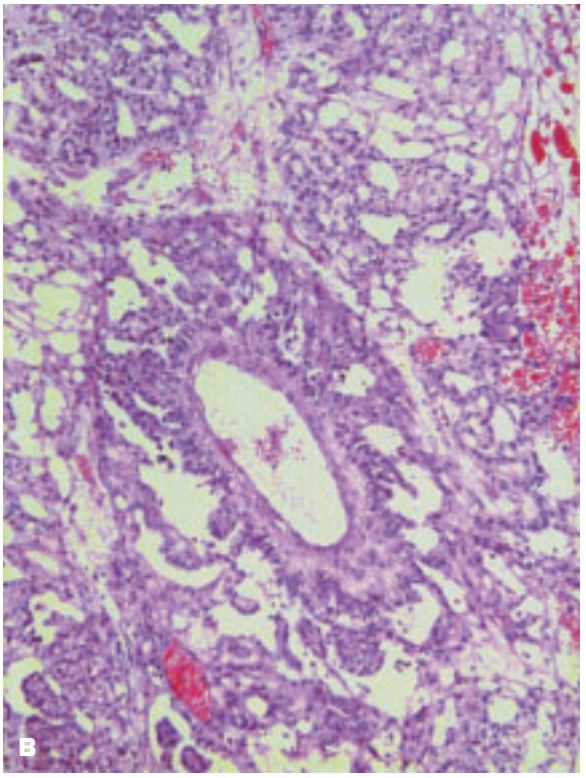

6-36. Yolk sac (endodermal sinus) carcinoma is highly malignant, occurs in young women, and is usually unilateral. **A.** Large, fleshy yolk sac tumor shows focal hemorrhage and necrosis at its periphery. The ovary is totally replaced by the tumor. **B.** Histology of yolk sac tumor shows epithelial cells forming microcysts. Immunohistochemistry will be positive for alpha-fetoprotein. Schiller–Duval body is the name given to the central structure that vaguely resembles a glomerulus in appearance and is said to be reminiscent of the endodermal sinuses of the rat placenta.

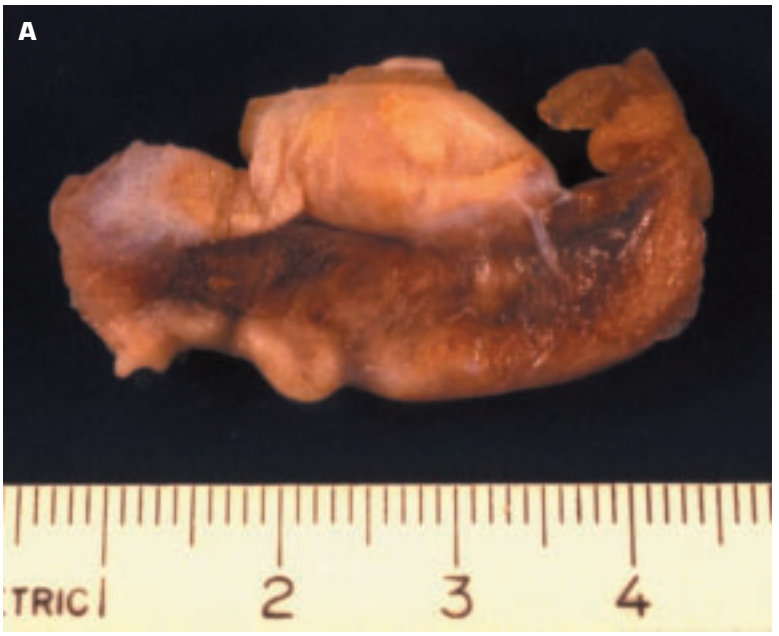

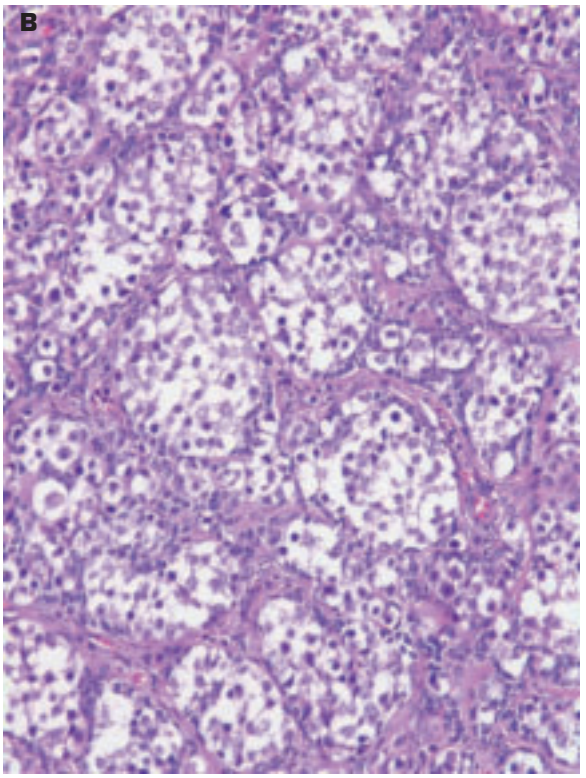

6-37. A. Gonadoblastoma is a rare tumor of the ovary that occurs in phenotypic women younger than 30 years who show virilization, primary amenorrhea, and abnormal genital development. These phenotypic women possess a "y" chromosome. The tumor may also be found in phenotypic men with cryptorchidism, hypospadias, and female internal organs. **B.** Histology of gonadoblastoma showing an appearance suggestive of a dysgerminoma in situ. These tumors show an organoid pattern of cell nests comprising germ cells that may be admixed with immature sex cord elements (Sertoli and granulosa cells).

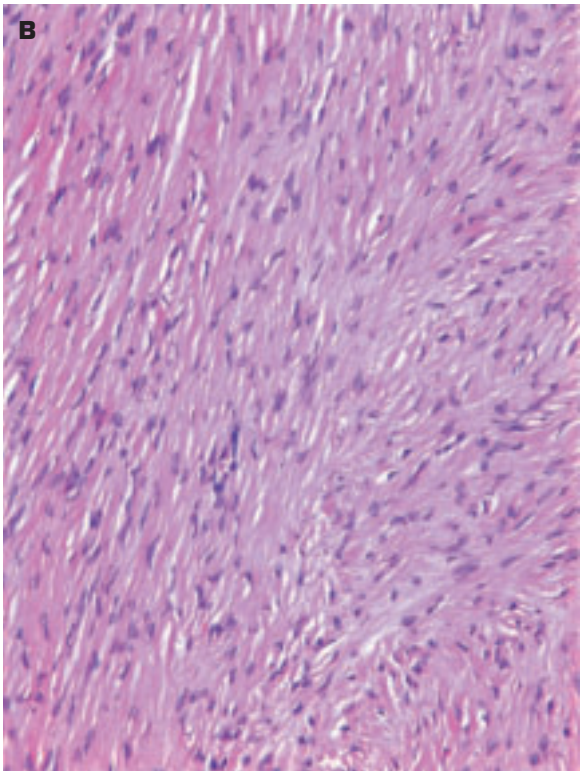

6-38. Tumors of sex cord and stroma may arise from the primitive sex cords or from the mesenchymal stroma of the developing gonad. **A.** Fibroma of the ovary comprises a well-circumscribed, yellow-white, firm solid tumor. **B.** Histology of fibroma shows mature-looking stromal spindle cells lying between mature collagenous tissue. *(continued on next page)*

6-38. *(Continued)* **C.** Fibroma-thecoma of the ovary. The fibroma component (white tissue, *left*) is well demarcated from the thecoma (yellow tissue, *right*). **D.** Thecoma of the ovary in a postmenopausal woman. Thecoma may produce estrogen or androgen. The yellow color is due to high lipid content of the tumor cells. *(continued on next page)*

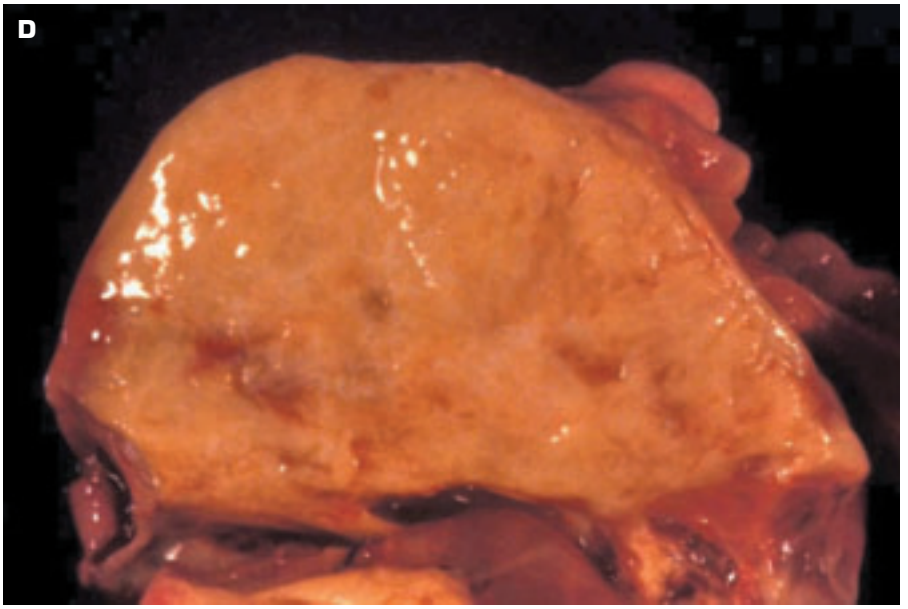

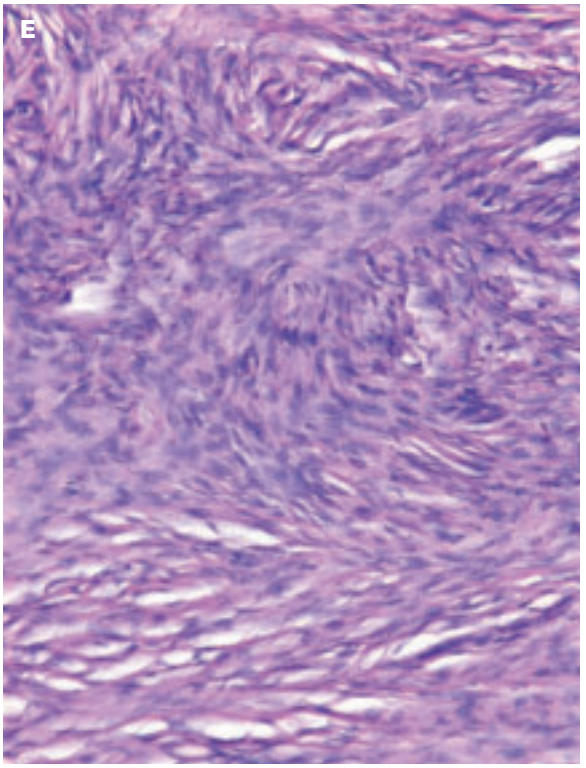

6-38. *(Continued)* **E.** Thecoma histologically shows elongated cells with central nuclei surrounded by collagen. Stains for lipid are positive in thecoma. **F.** Serous cystadenofibroma of the ovary. *(continued on next page)*

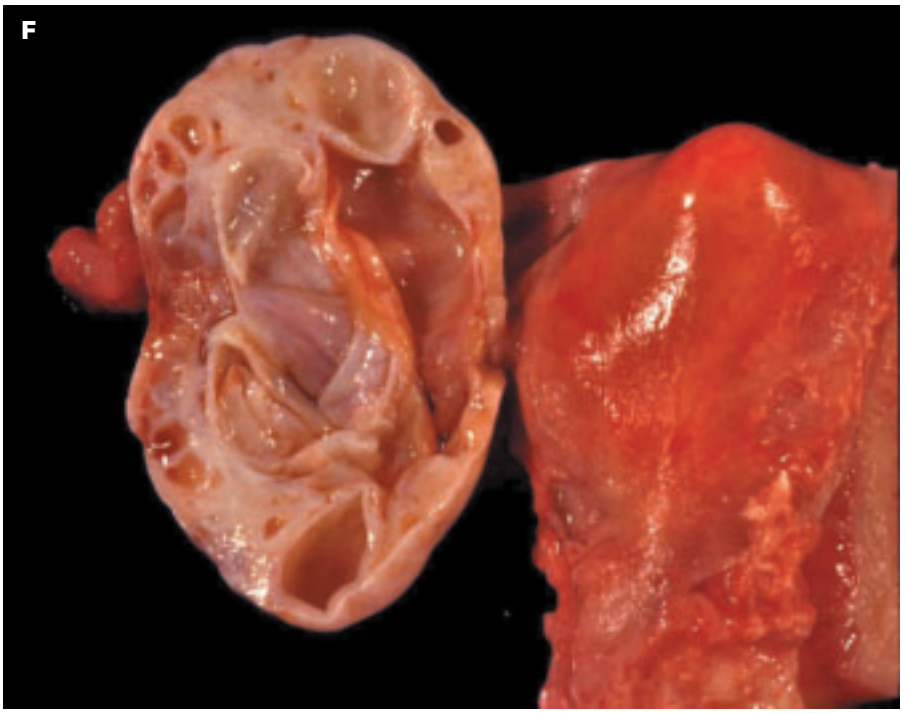

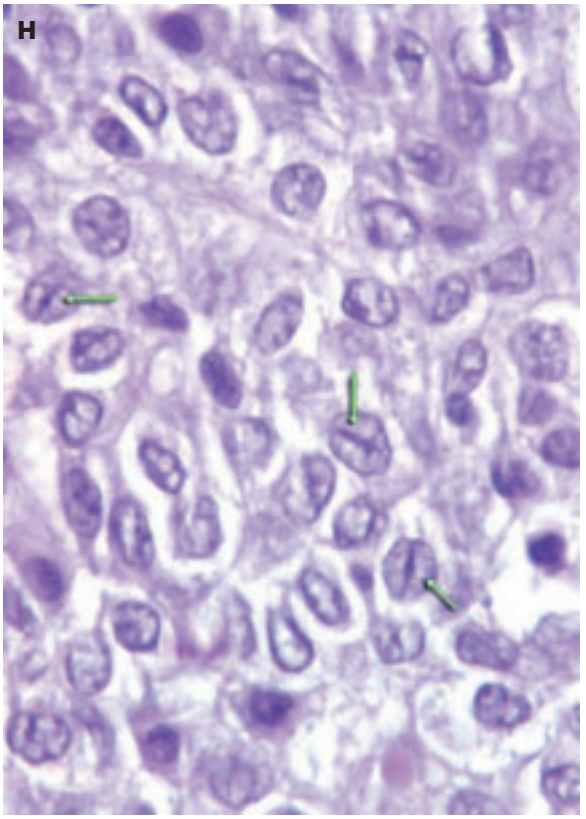

6-38. *(Continued)* **G.** Granulosa cell tumor in an adult woman shows areas of cystic change. Most granulosa cell tumors are malignant and secrete estrogen, which favors endometrial hyperplasia and cancer. **H.** Histology of granulosa cell tumor shows nuclear grooving (coffee bean appearance) (*arrows*).

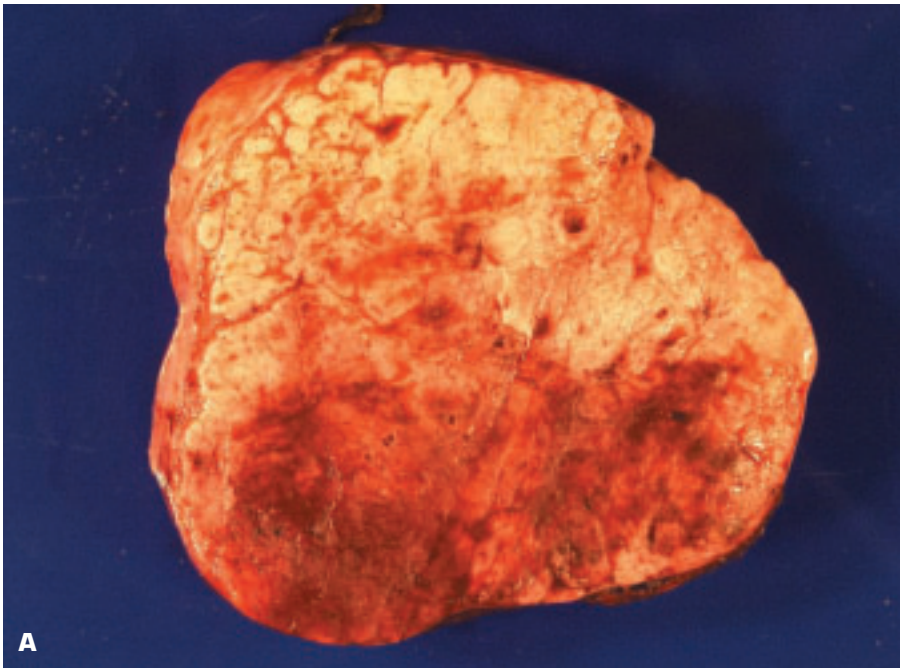

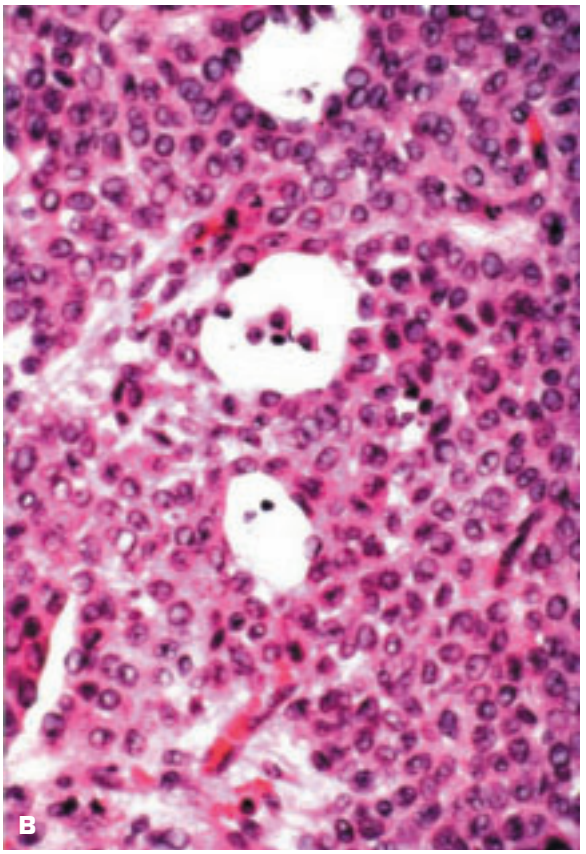

6-39. Rarely, an ovarian granulosa cell tumor may occur before puberty, and estrogen production by the tumor cells may lead to precocious puberty. **A.** Juvenile granulosa cell tumor has a bright yellow color due to the presence of lipid-laden luteinized granulosa cells. Areas of necrosis and hemorrhage are also present. **B.** Histology of juvenile granulosa cell tumor shows tumor cells surrounding spaces (secondary to degeneration) giving an appearance termed Call–Exner bodies.

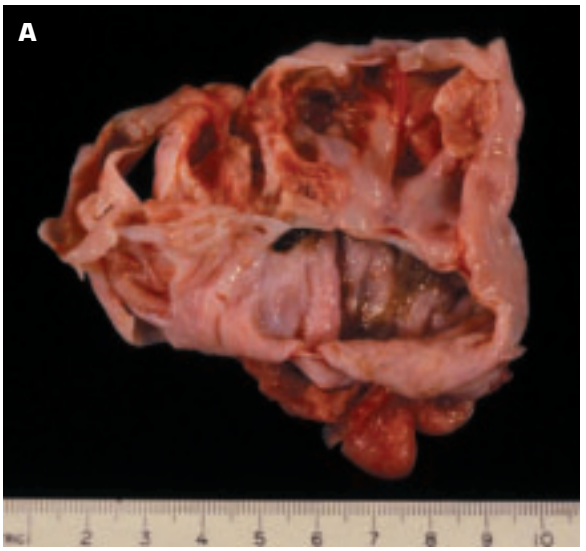

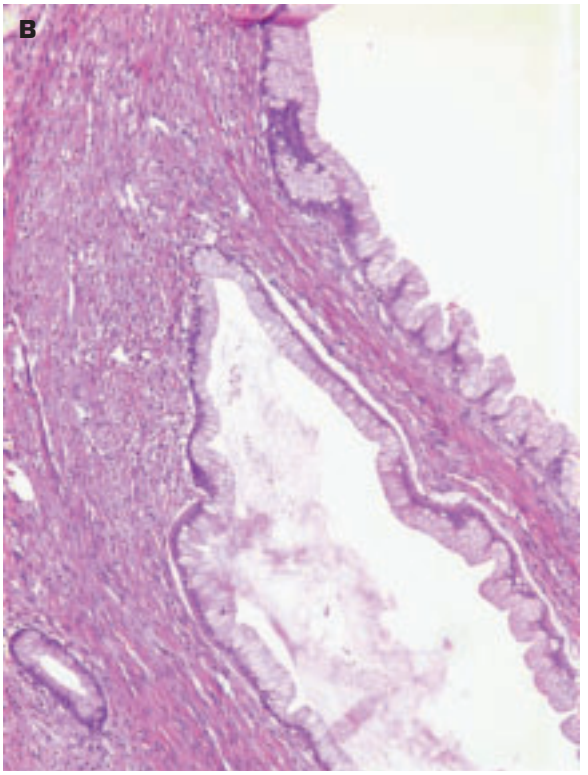

6-40. Epithelial tumors of the ovary comprise benign, borderline (low malignant potential), or malignant varieties. They are believed to arise from the mesothelial cell layer covering the ovarian surface that may undergo metaplasia to müllerian epithelium. Resultant tumors may differentiate to resemble tubal mucosa (serous tumors), endocervical mucosa (mucous tumors), or endometrium (endometrioid tumors). Transitional cell tumors (Brenner tumor) may also occur. **A.** Mucinous cystadenoma of the ovary consists of multiloculated mucin-filled cysts – most of the mucin has been washed away prior to photography. **B.** The mucinous cystadenoma is lined by a single layer of mature-looking mucinous epithelial cells. **C.** Brenner (transitional cell) tumor of ovary.

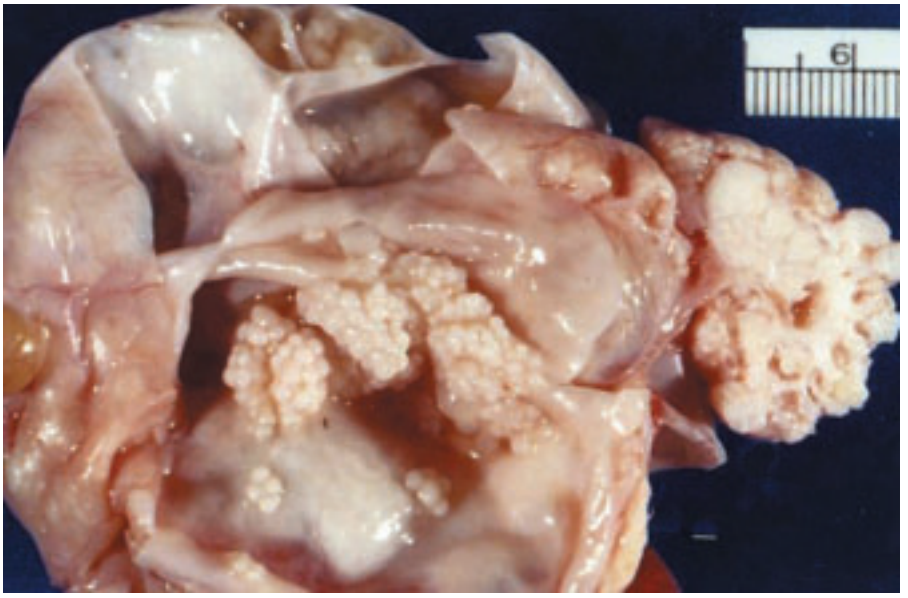

6-41. Serous ovarian tumor of borderline malignancy shows inwardly protruding papillary projections within the opened cyst.

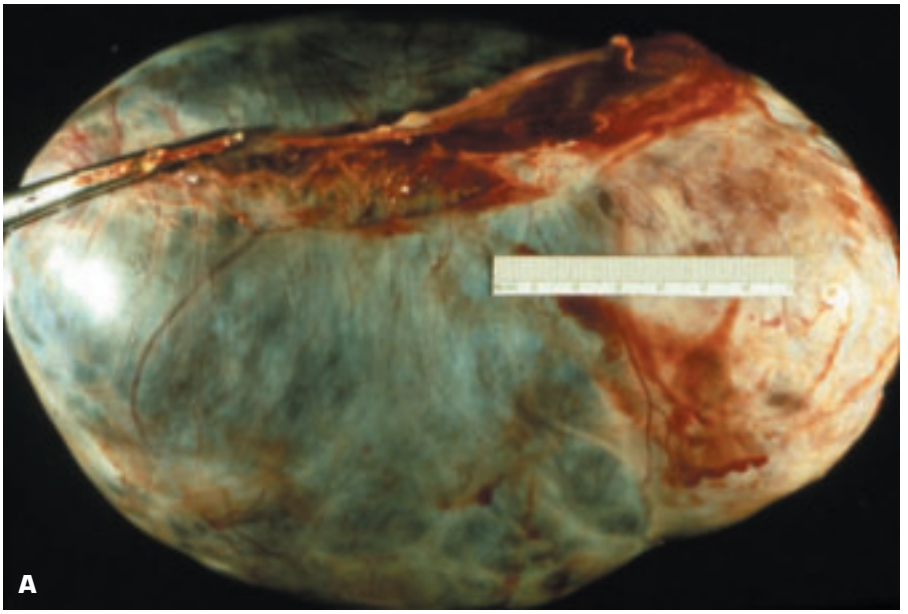

6-42. A. Massive mucinous cystadenocarcinoma is seen as a very large, tense, cystic structure. **B.** Bisected lesion shows scanty solid areas – the carcinoma is usually present in the solid areas. *(continued on next page)*

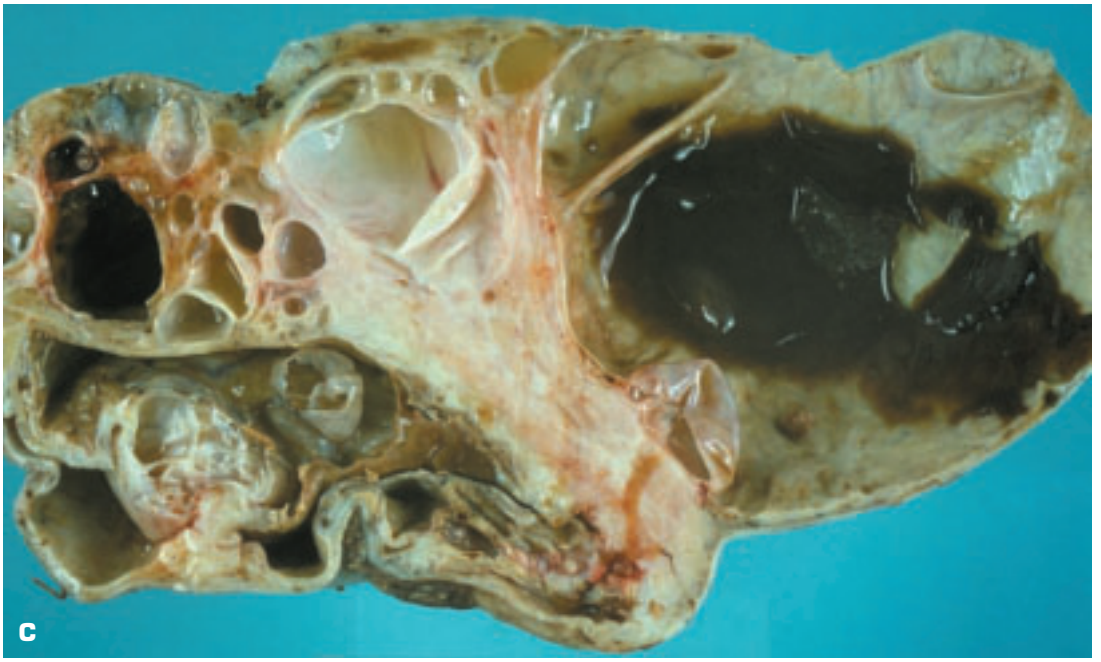

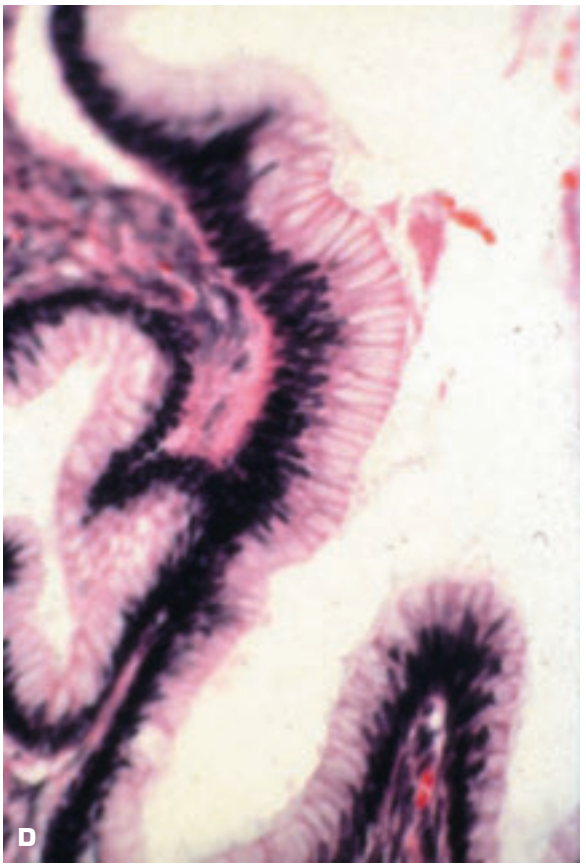

6-42. *(Continued)* **C.** Another mucinous cystadenocarcinoma shows more extensive solid areas (*center*). **D.** Multilayered mucinous cells comprise the lining of the glands of the invasive cystadenocarcinoma.

6-43. A. Serous papillary cystadenocarcinoma comprises about 30% of all ovarian primary malignancies. The external surface of this cystic tumor appears quite smooth. **B.** Serous papillary adenocarcinoma with a single, dominant, central cystic area containing tumor tissue. The tumor encompassing the cyst shows focal necrosis and cystic degeneration. *(continued on next page)*

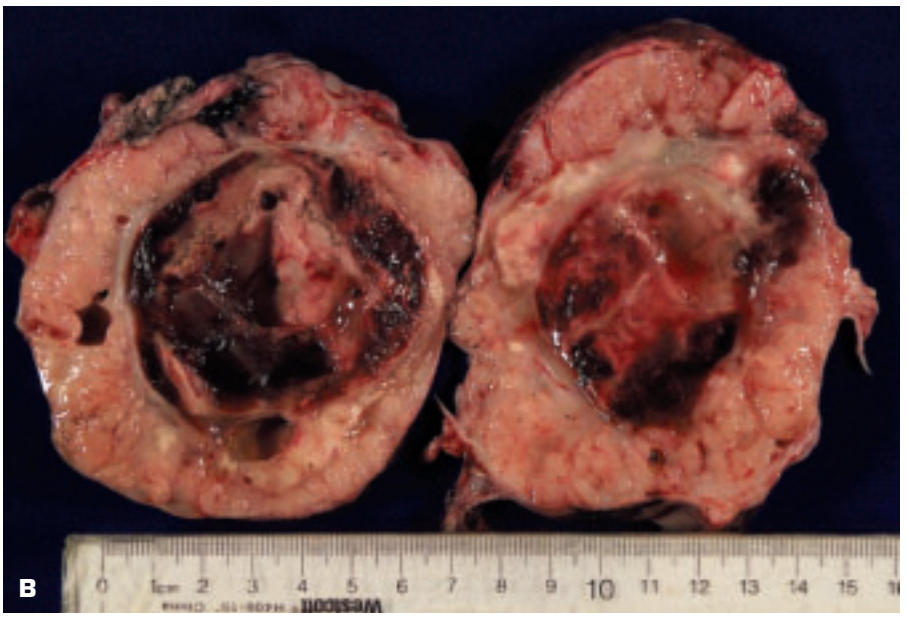

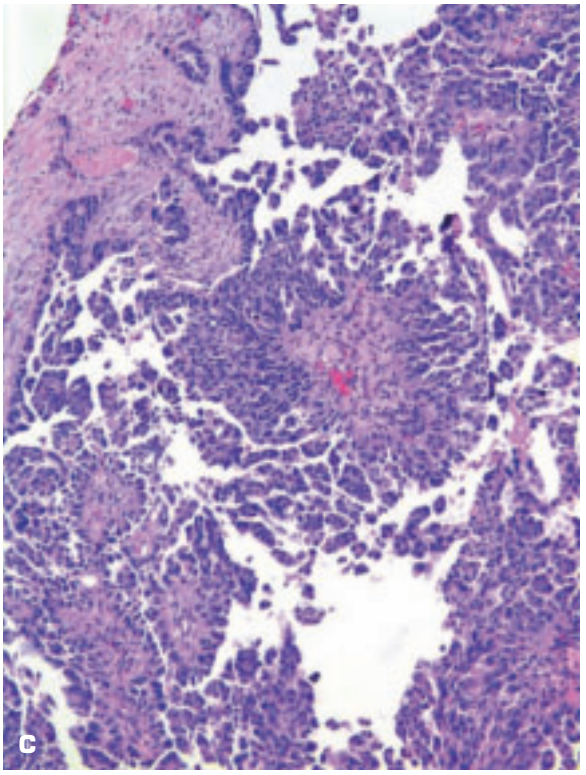

6-43. *(Continued)* **C.** Histology of serous cystadenocarcinoma showing papillary formations and stromal invasion. **D.** High-power view shows fibrovascular core supporting multilayered serous cells, which show pleomorphism and mitoses.

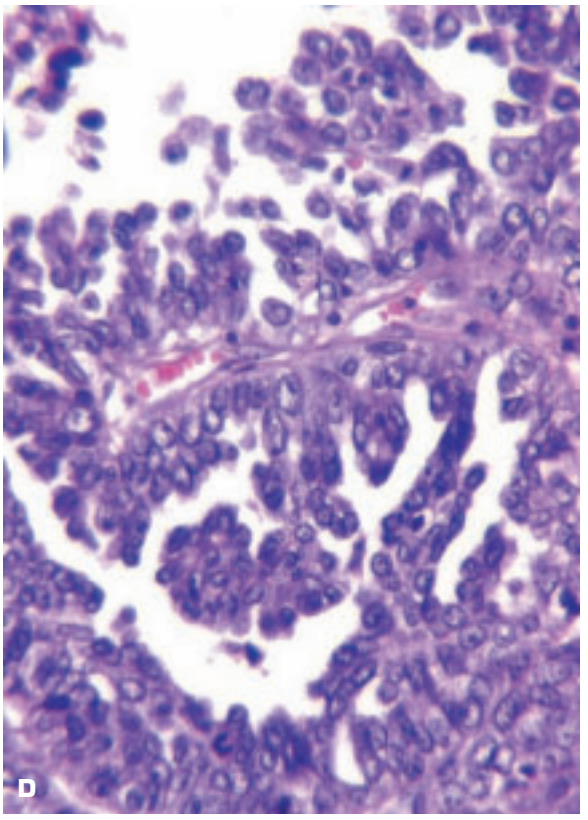

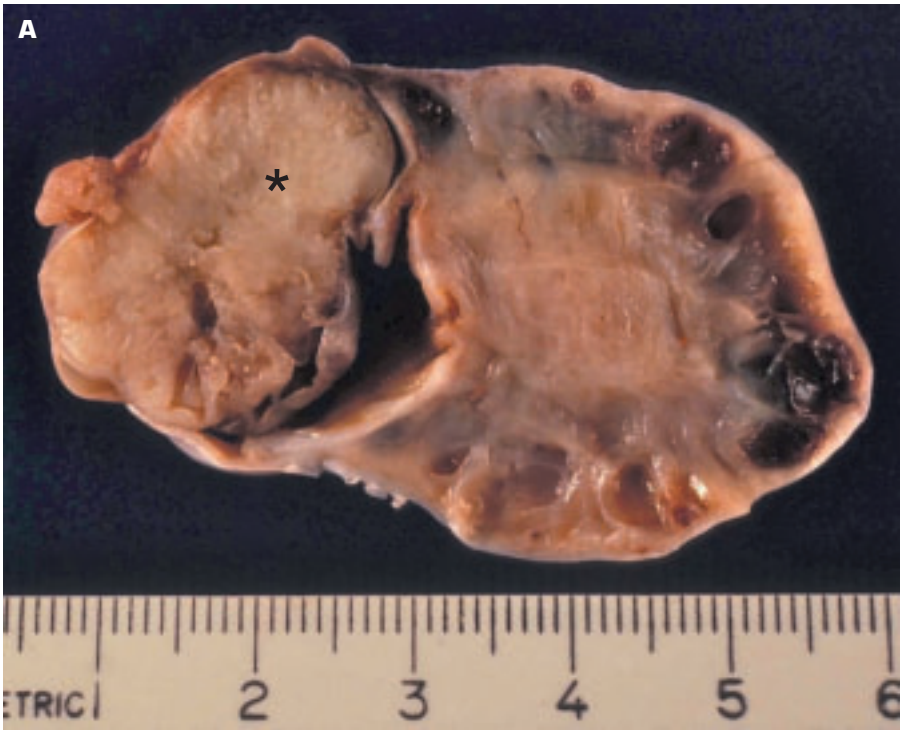

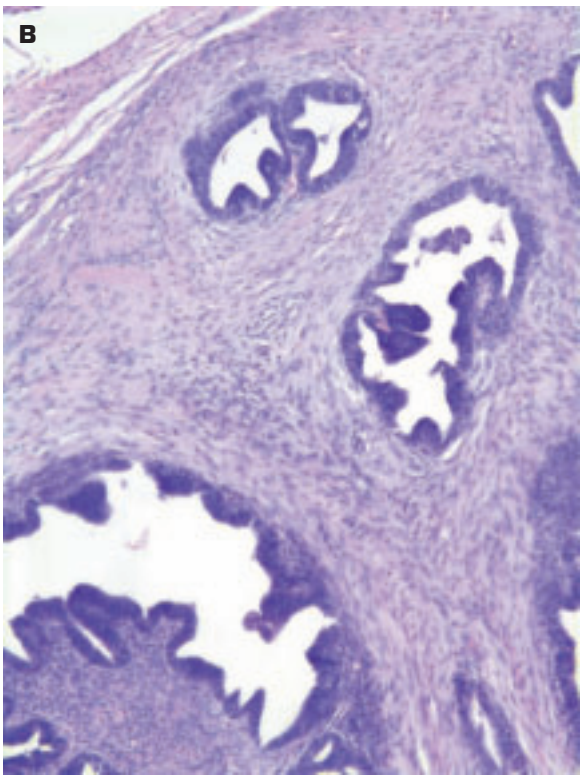

6-44. A. Well-differentiated endometrioid adenocarcinoma (*) of the ovary. **B.** Endometrioid carcinoma is seen in this histologic section of the ovary.

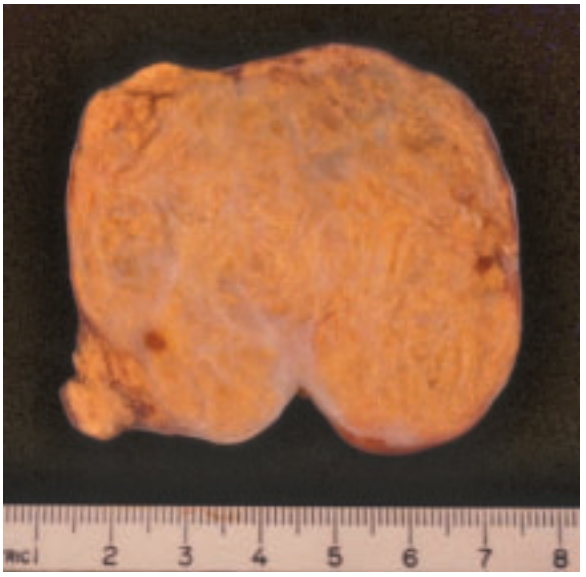

6-45. Fibrosarcoma that has arisen in the ovary.

6-46. Metastatic adenocarcinoma from the colon in the ovary. Bilateral ovarian involvement by secondary carcinoma (often from the stomach) is termed "Krukenberg tumors."

6-47. Involvement of the ovary by nodular-sclerosing Hodgkin disease.

6-48. Lactating breast plus enlarged pituitary gland (*right*) due to a prolactin-secreting pituitary adenoma.

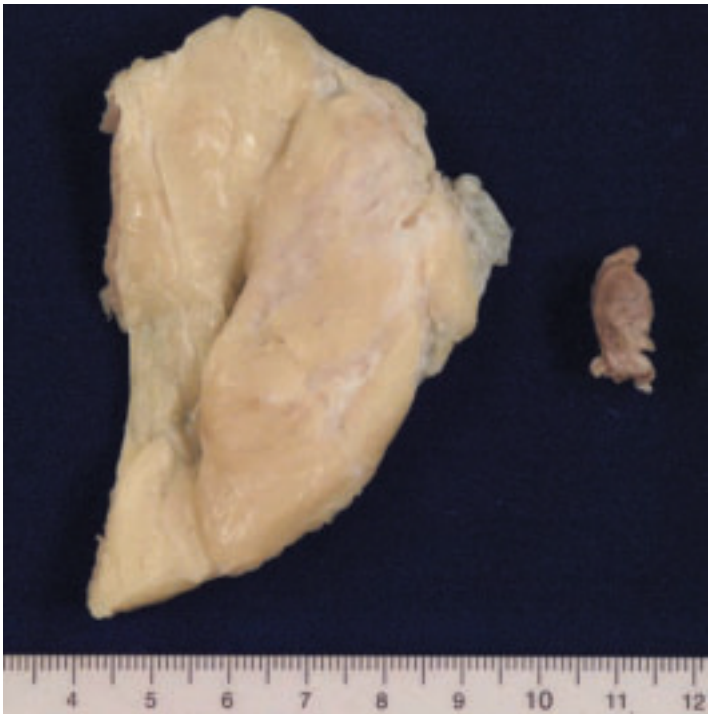

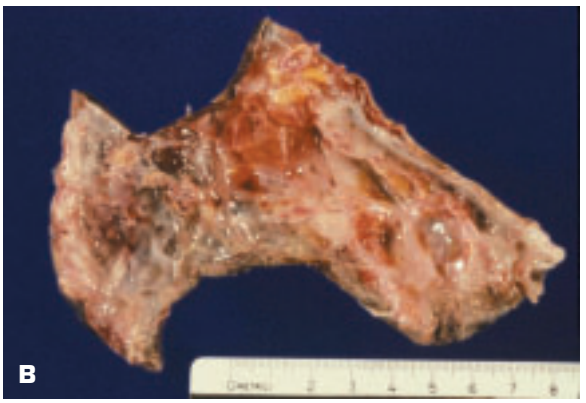

6-49. A. Breast shows mammary duct ectasia with prominent surrounding fibrosis. The bisected nipple is seen on the right. **B.** Duct ectasia of the breast with marked periductal inflammation and fibrosis.

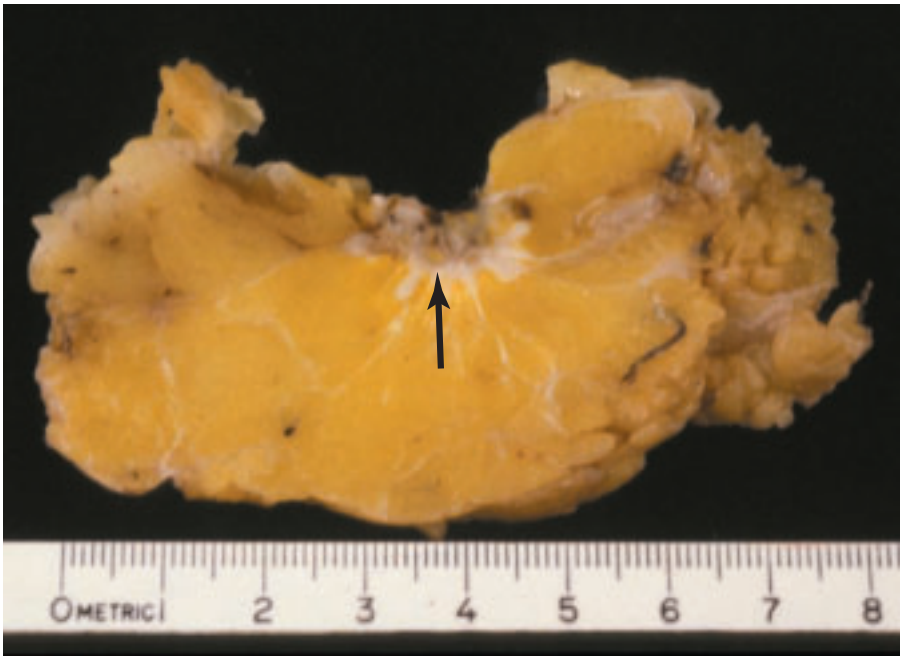

6-50. Fat necrosis (*arrow*) is present on the midportion of the upper end of the sample of breast tissue.

6-51. Plasma cell granuloma of the breast mimics the gross appearance of a neoplasm.

6-52. A. Fibroadenoma (FA) of the breast is sharply circumscribed and has a lobulated cut surface. **B.** Histology of FA in a low-power view shows epithelial-lined clefts in the fibrous tissue comprising most of the lesion. *(continued on next page)*

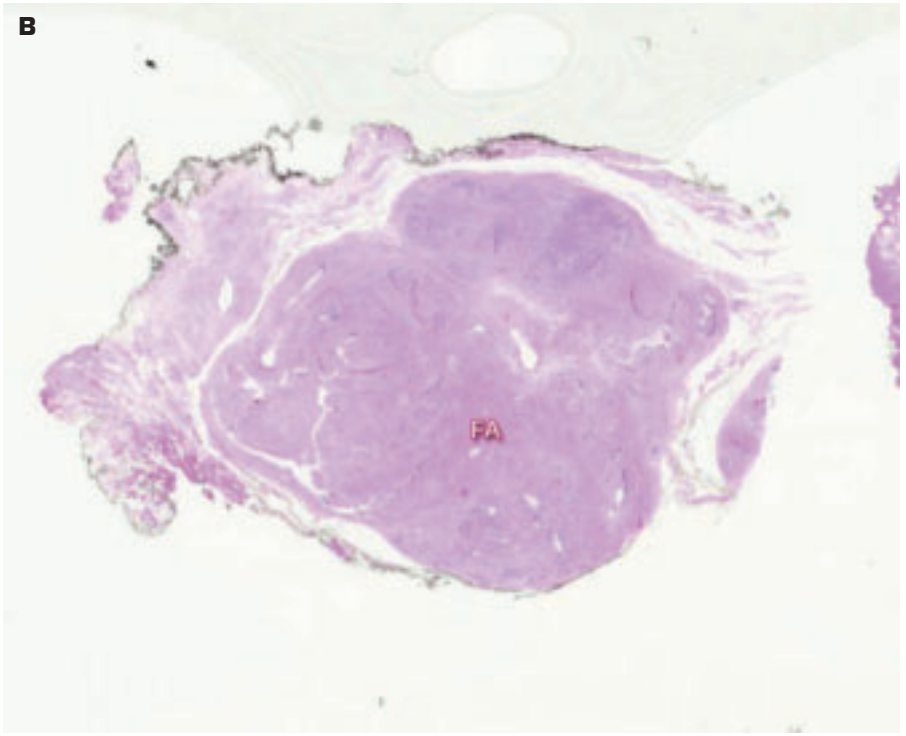

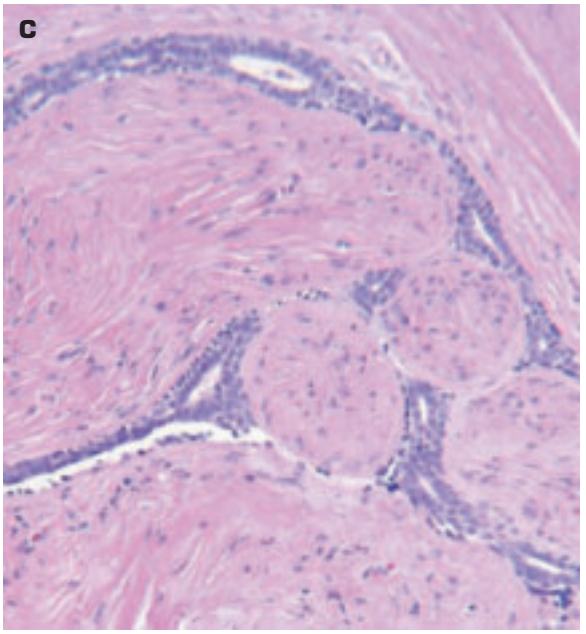

6-52. *(Continued)* **C.** Higher-power view of epithelial-lined clefts. **D.** Area of adenosis in a fibroadenoma. **E.** Old hyalinized fibroadenoma of the breast in an elderly woman.

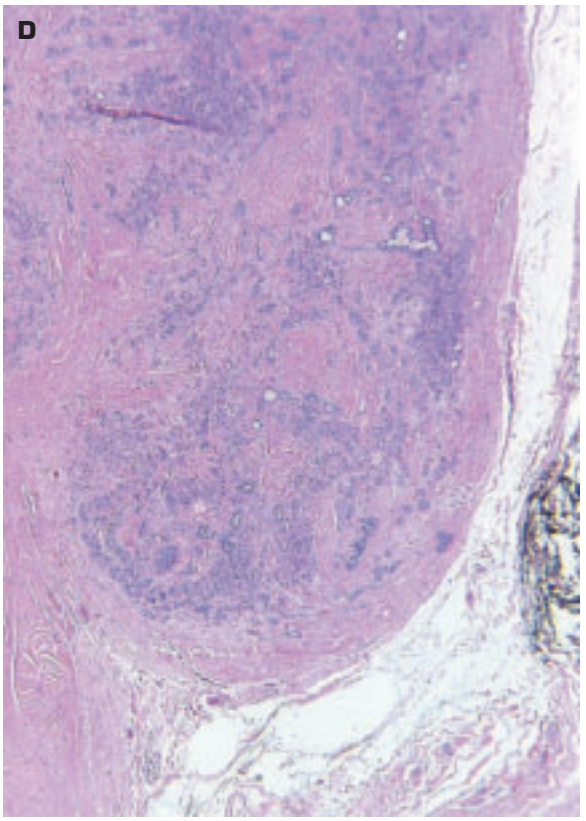

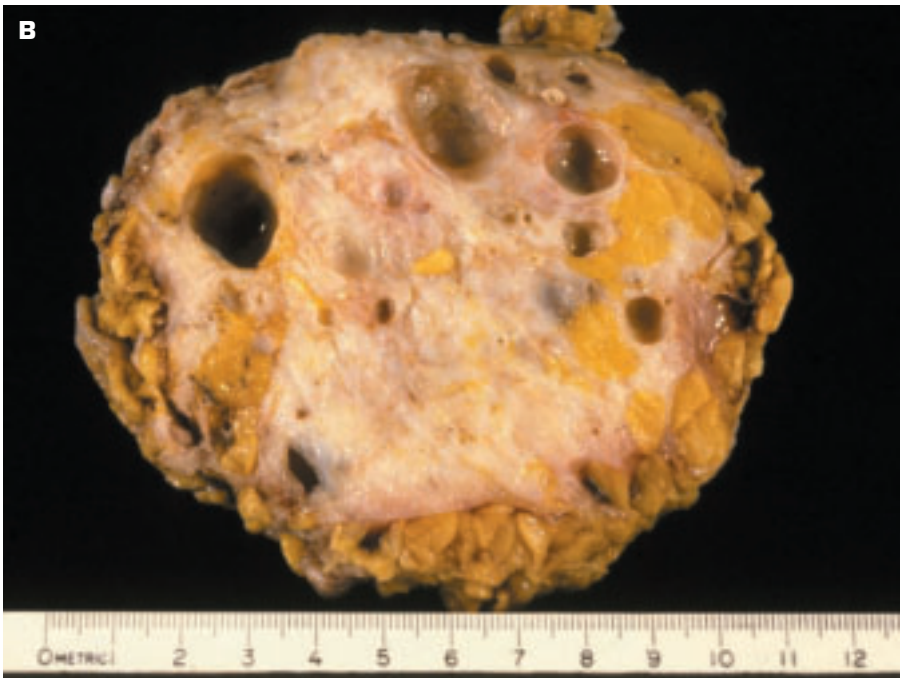

6-53. A. Nonproliferative fibrocystic disease of the breast is characterized by dense fibrous tissue encompassing a number of variable-size cysts. **B.** Another example of fibroadenosis showing more prominent cyst formation. *(continued on next page)*

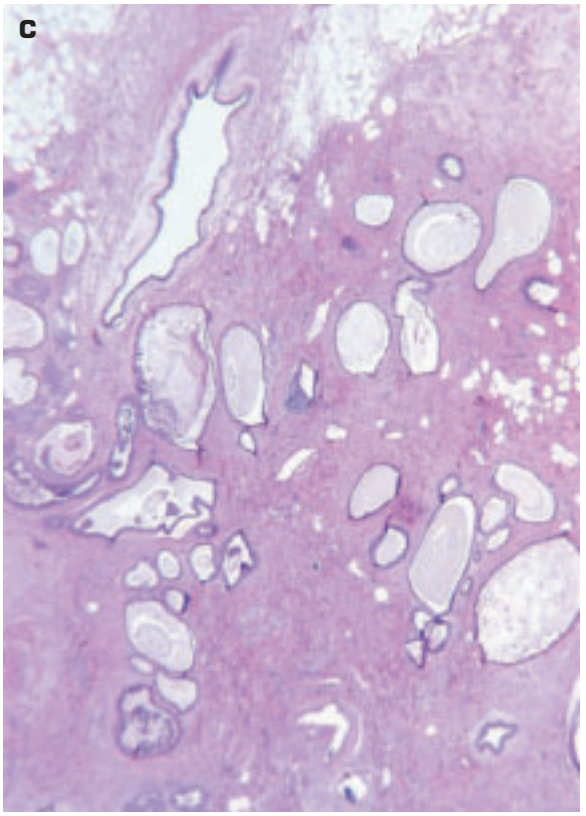

6-53. *(Continued)* **C.** Histology of fibrocystic disease shows cystic dilatation of the terminal ducts with increased surrounding collagen. **D.** Post fine-needle aspiration hemorrhage complicating fibrocystic disease of the breast.

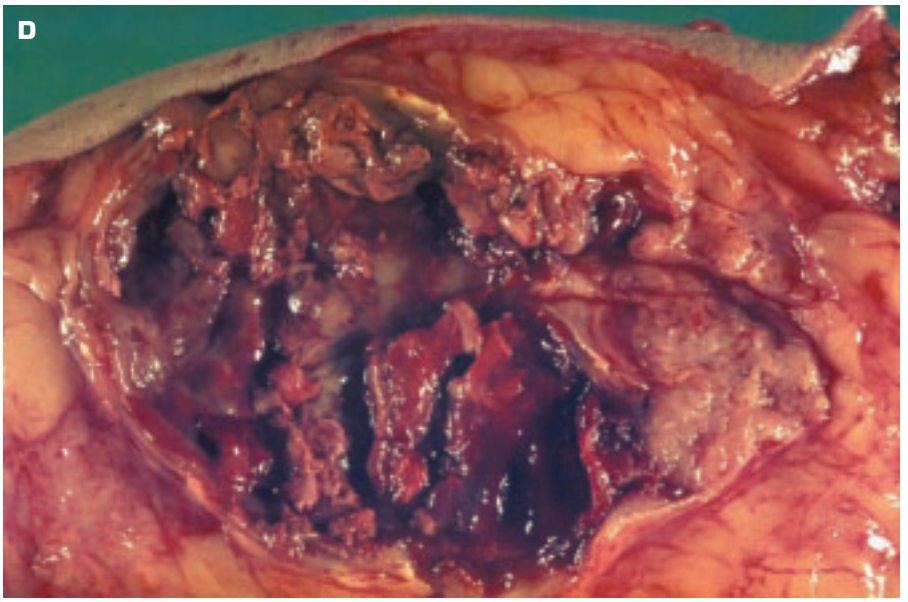

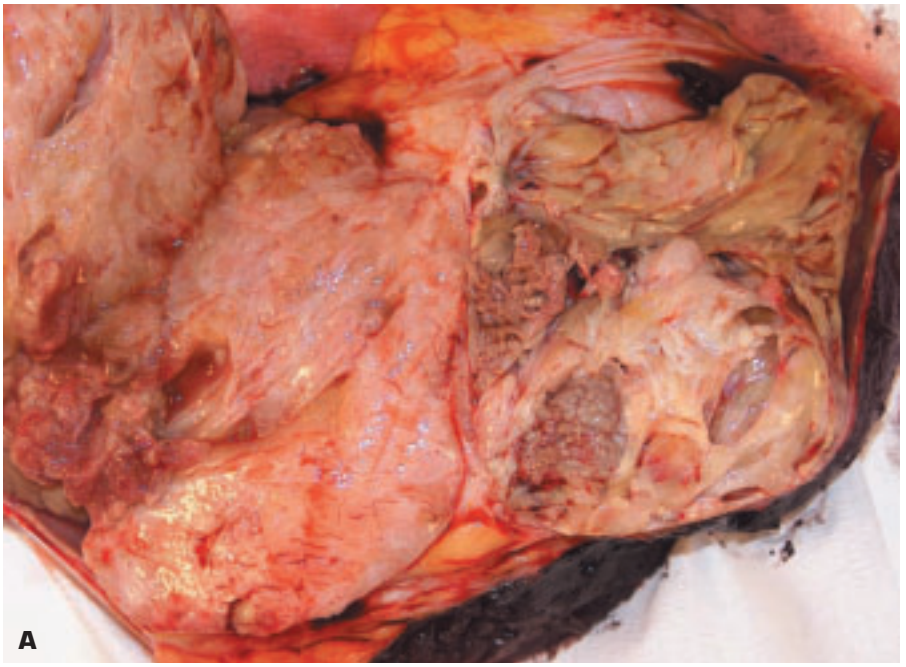

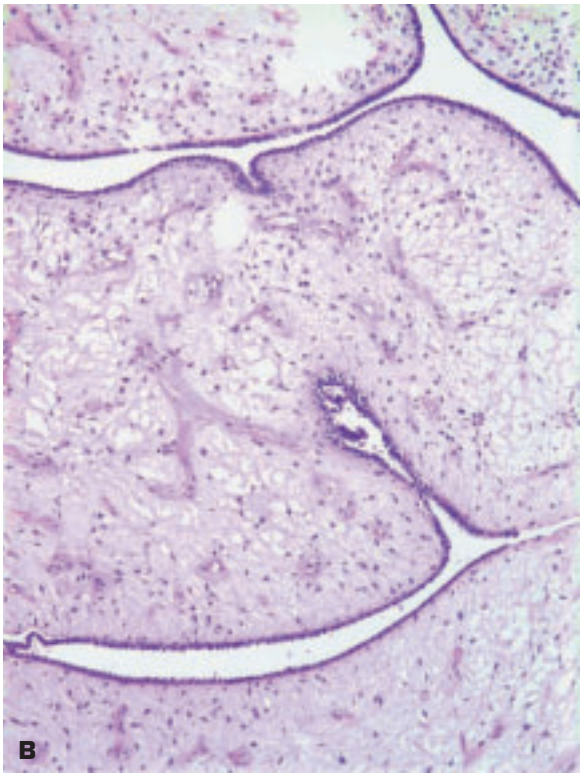

6-54. A. Bisected benign, well-circumscribed phyllodes tumor ("giant fibroadenoma") showing the characteristic macrolobulated (phyllodes = pages) appearance. **B.** Histology shows the characteristic leaf-like arrangement of a phyllodes tumor of the breast. The stroma is more cellular than a fibroadenoma. A malignant phyllodes tumor has a sarcomatous stroma that predominates over the ductal elements and invades the breast.

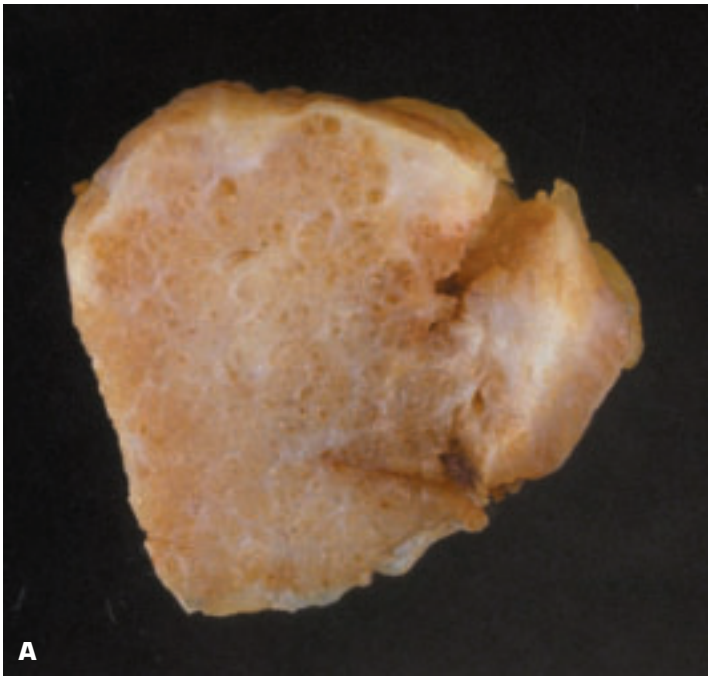

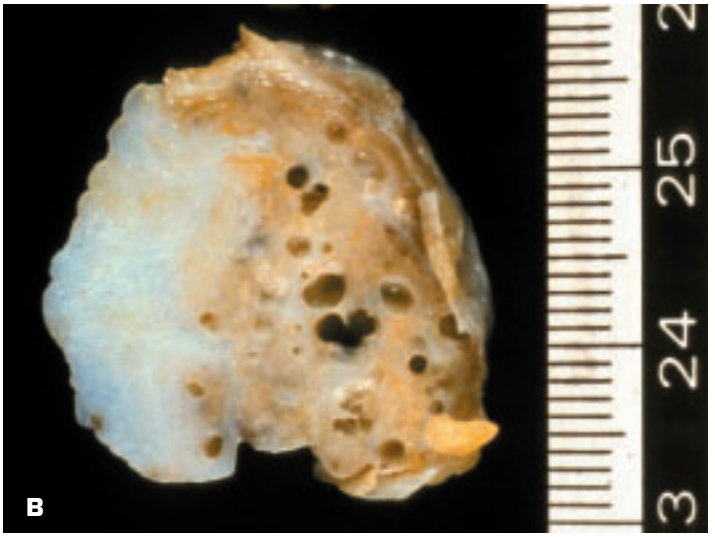

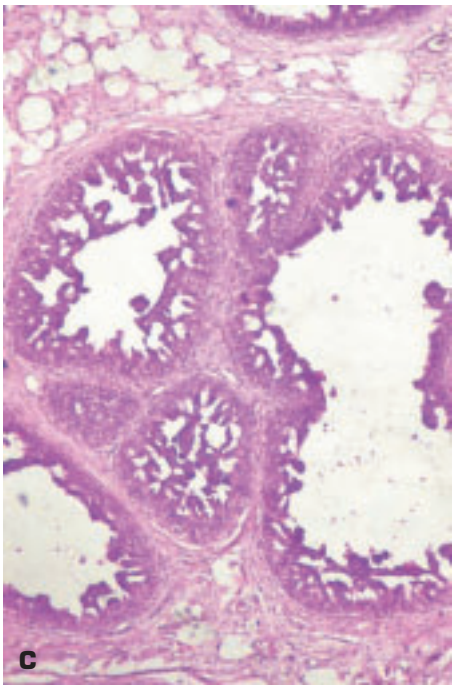

6-55. A. Juvenile papillomatosis (JP) ("Swiss cheese disease") presenting as a solitary, unilateral breast lump in a 9-year-old girl. The lesion is often mistaken for a phyllodes tumor clinically. Note the circumscribed, but not encapsulated, lesion containing multiple cysts. Differential diagnosis also includes fibrocystic disease, pubertal macromastia, and juvenile fibroadenoma. JP is a marker for families at risk for breast cancer coincidentally or later. **B.** JP with larger cysts and an appearance strongly resembling fibrocystic disease of the breast. **C.** Histology of JP shows dilated breast ducts lined by a proliferation of highly atypical-looking epithelium that would be regarded as precancerous in an older woman.

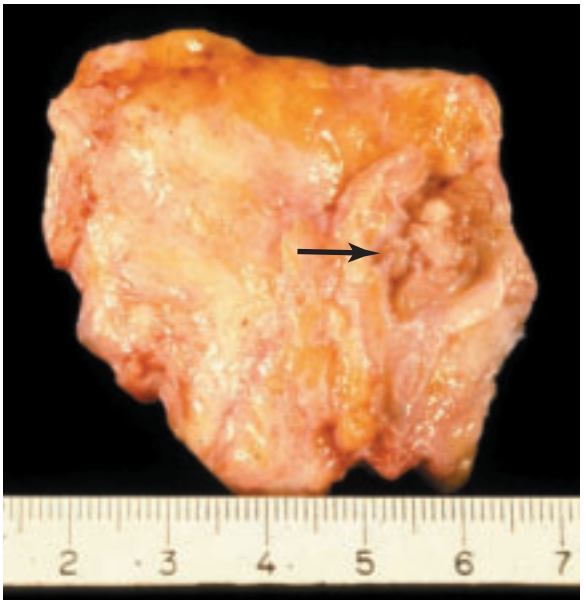

6-56. Intraduct papilloma (*arrow*) of the breast situated in a large subareolar duct. This middle-age woman presented with a bloody discharge from the nipple. The papilloma is not associated with an increased risk of developing breast cancer.

6-57. A. Focal area of intraductal carcinoma with a comedo appearance. **B.** Histology shows carcinoma confined within the duct.

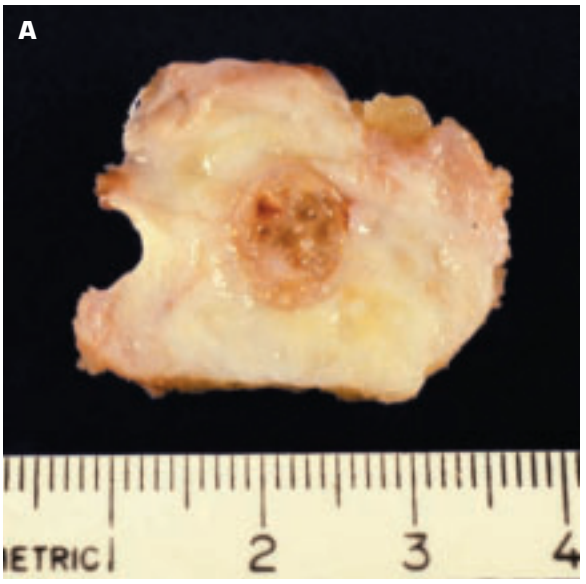

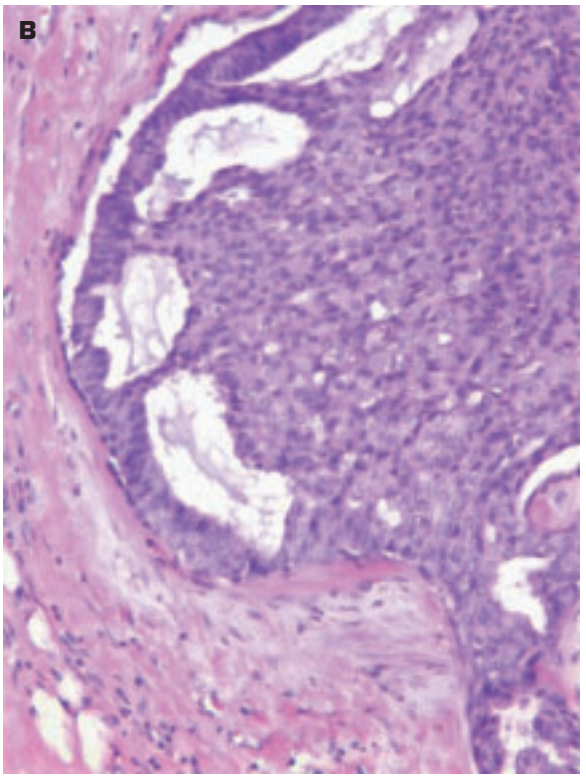

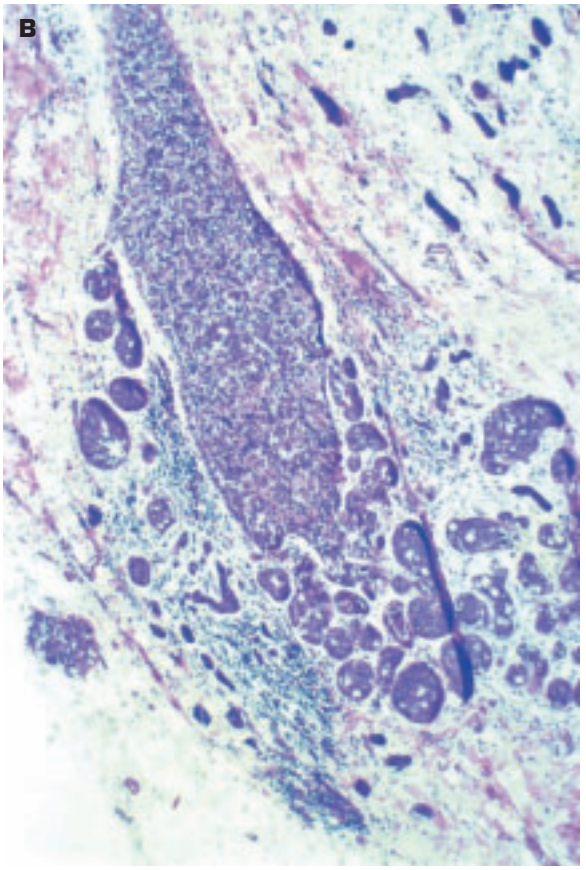

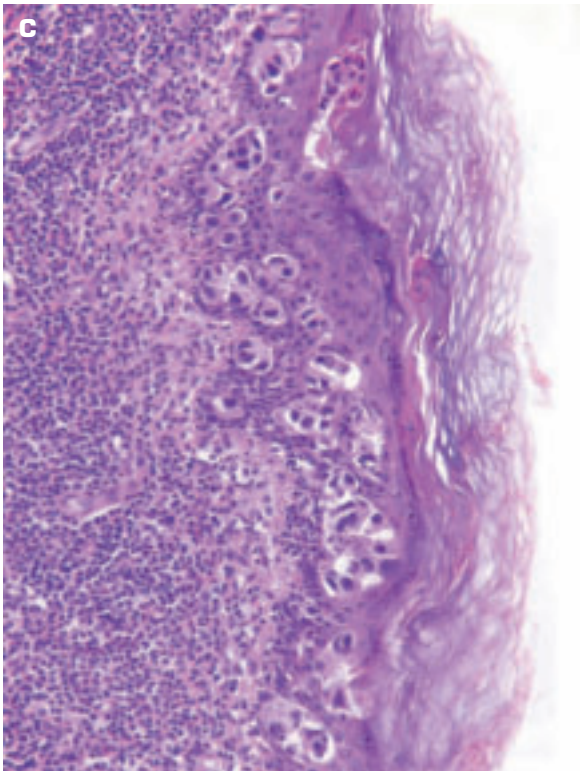

6-58. A. Paget disease of the breast. Eczematous-like changes in the skin of the nipple, areola, and adjacent areas of breast skin are due to infiltration by an intraduct carcinoma that has spread up the duct to the nipple. **B.** Histology also shows an intraduct cancer that has extended into the adjacent lobules. **C.** Histology of Paget disease shows intraepidermal cancer cells derived from an intraductal breast carcinoma.

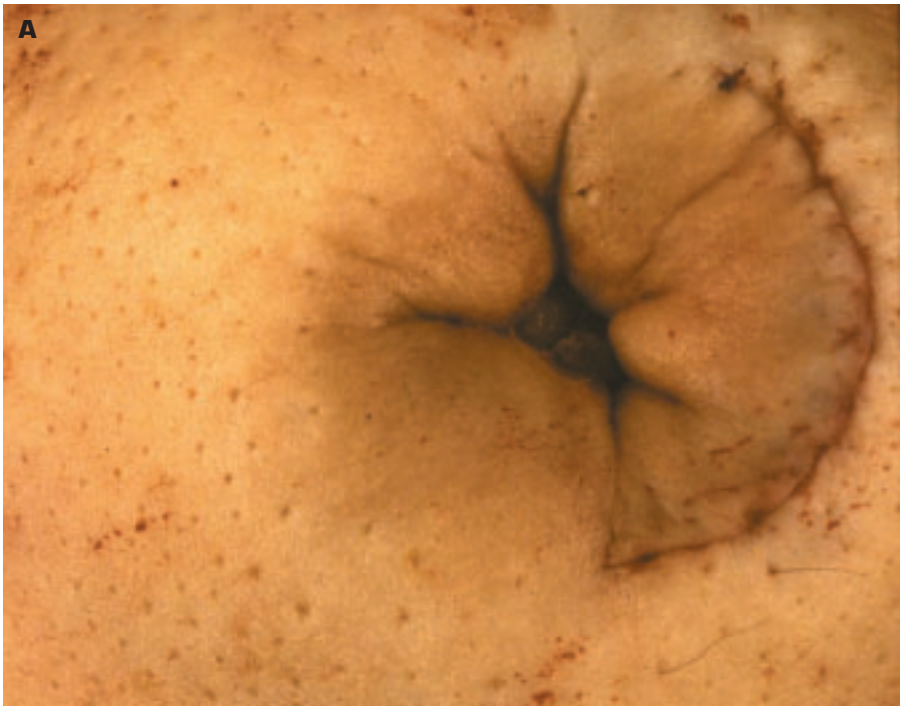

6-59. The most common form of breast cancer is invasive ductal carcinoma, which usually evokes a marked desmoplastic response (proliferation of fibroblasts producing collagen) that adds to the lesion's bulk. Prognosis is stage dependent. **A.** Indrawing of the nipple due to desmoplasia in an underlying advanced breast carcinoma is a late feature of breast cancer – the aim is to diagnose the cancer much earlier than this (see Fig. 6–60C). Note the "peau d'orange" (skin edema) appearance of the breast skin due to tumor obstruction of the dermal lymphatics. **B.** Bisected mastectomy specimen shows the crab-like outline of the invasive ductal carcinoma (cancer = a crab). *(continued on next page)*

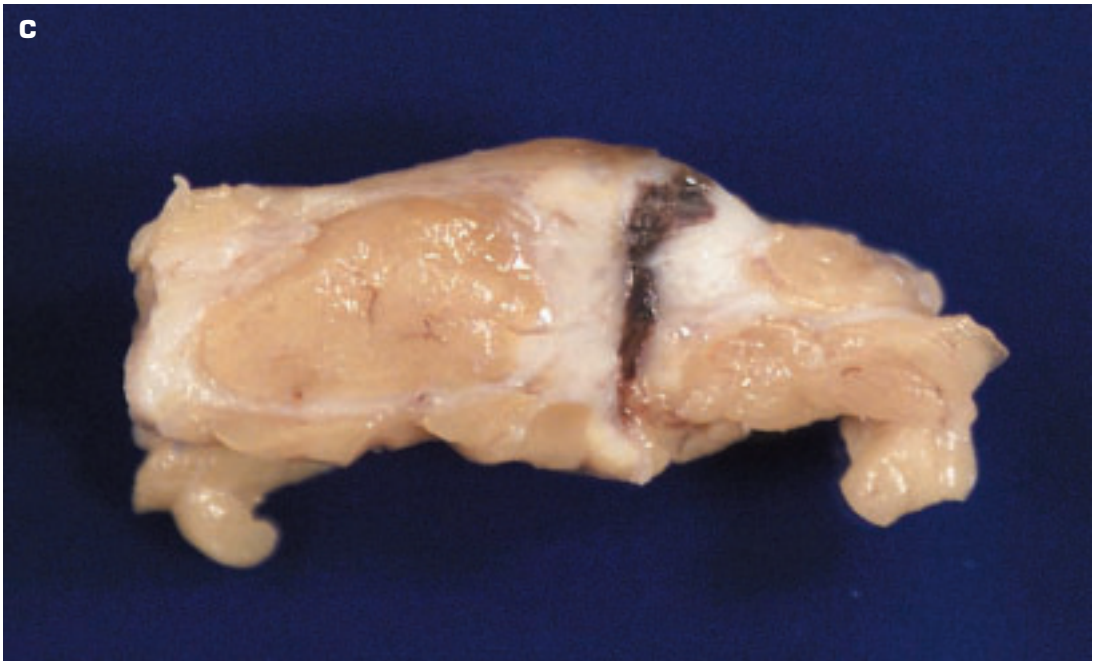

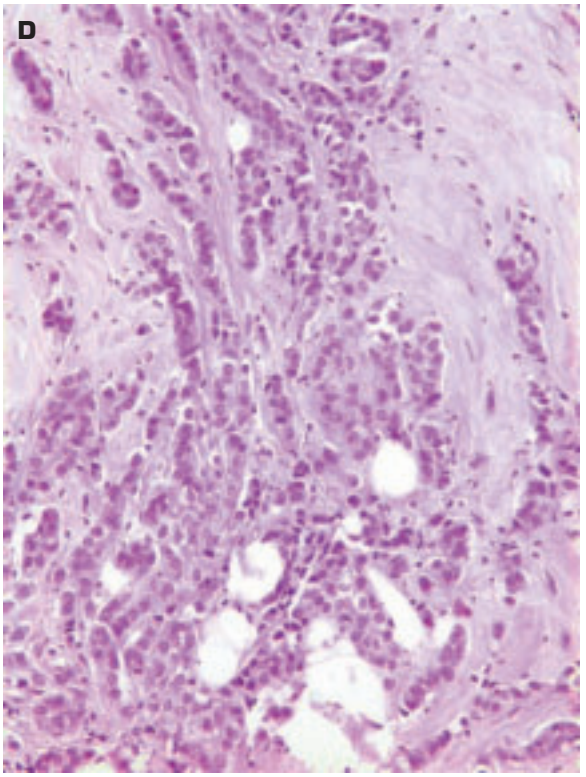

6-59. *(Continued)* **C.** Hemorrhagic needle biopsy tract within an occult, early breast cancer that was diagnosed by mammography. **D.** Histology of invasive ductal carcinoma of the breast shows cords of poorly differentiated adenocarcinomatous cells in a fibrous stroma. *(continued on next page)*

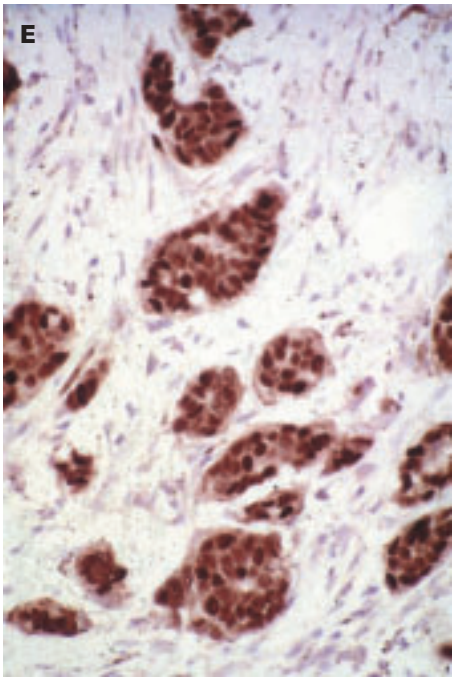

6-59. *(Continued)* **E.** Positive immunohistochemical staining for estrogen receptor protein in a breast cancer. **F.** Close-up view of an invasive ductal carcinoma. The tumor cuts with the consistency of an unripe pear. **G.** Composite picture of breast cancer from an autopsy shows clockwise from bottom right: mastectomy specimen with the cancer, adrenal gland with scattered small metastatic nodules, tumor-infiltrated axillary lymph node, and metastatic tumor in a vertebral body.

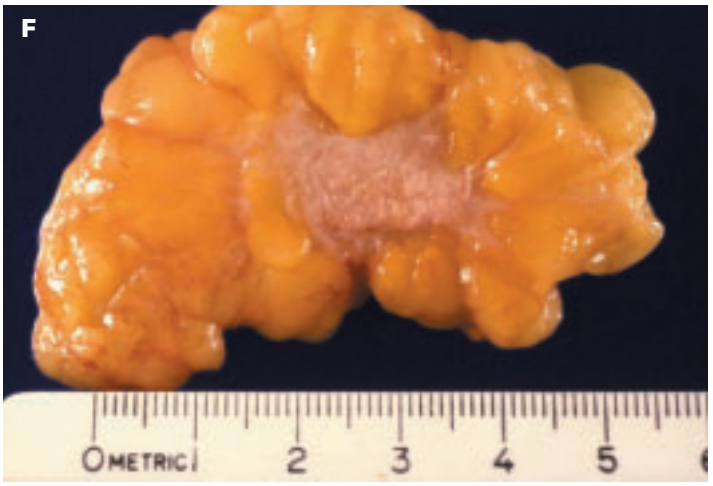

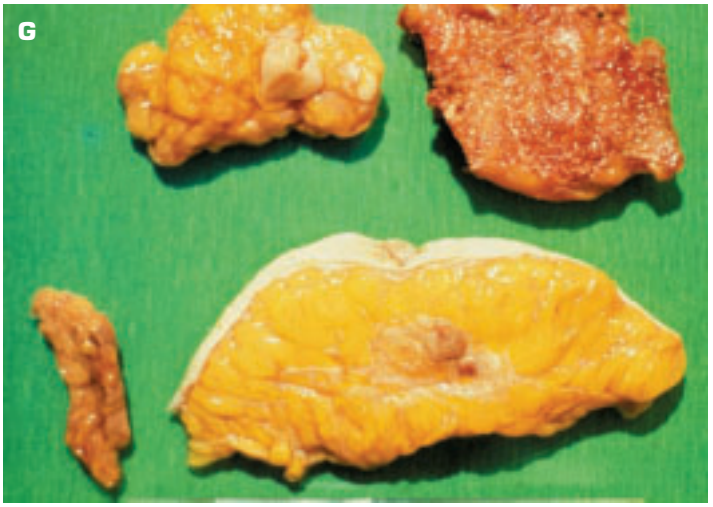

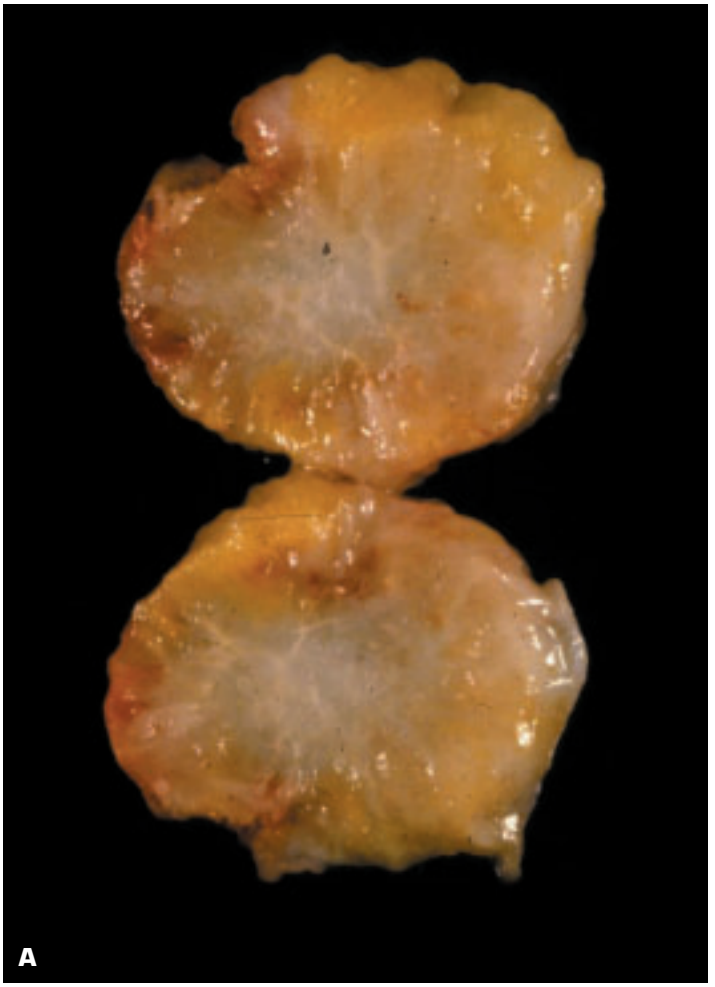

6-60. Invasive lobular carcinoma of the breast is second in frequency after invasive ductal cancer. It may produce a similar gross appearance to the latter, or, if less desmoplasia occurs, the tumor appears ill defined. **A.** Invasive lobular carcinoma with scanty desmoplasia forms an ill-defined mass in the breast tissue. **B.** Histology of lobular carcinoma showing tumor cells arranged in lines between the collagen bundles.

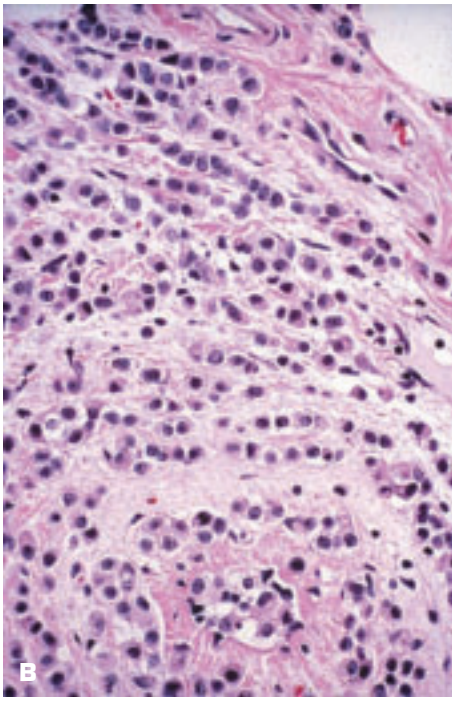

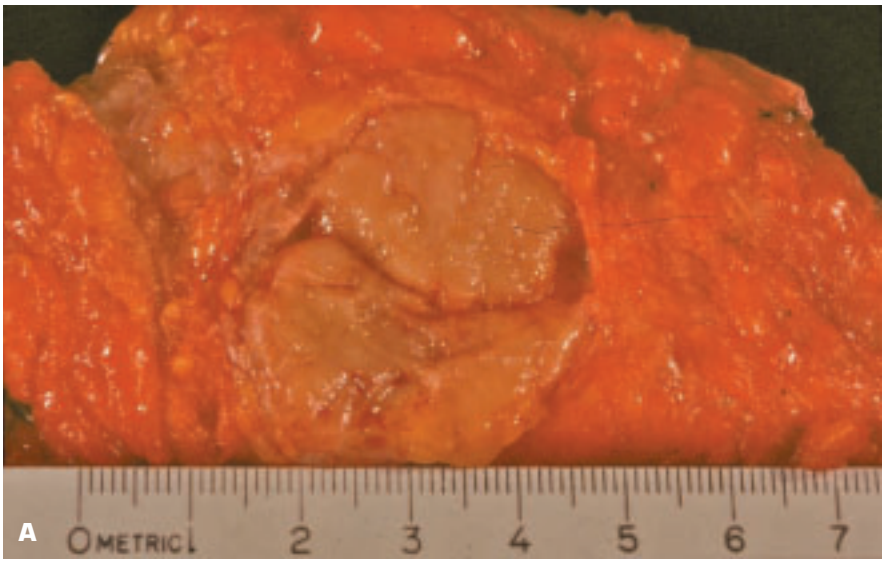

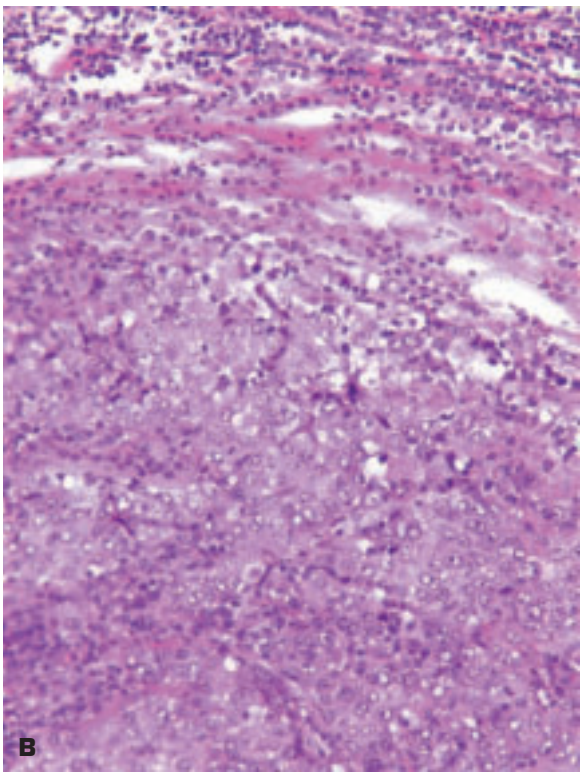

6-61. Medullary cancer of the breast has a better prognosis than invasive ductal carcinoma. **A.** Gross appearance of medullary cancer showing a well-circumscribed, fleshy, tan-colored tumor. **B.** Histologically, the margin of the tumor is encompassed by a lymphocytic infiltration (*top*).

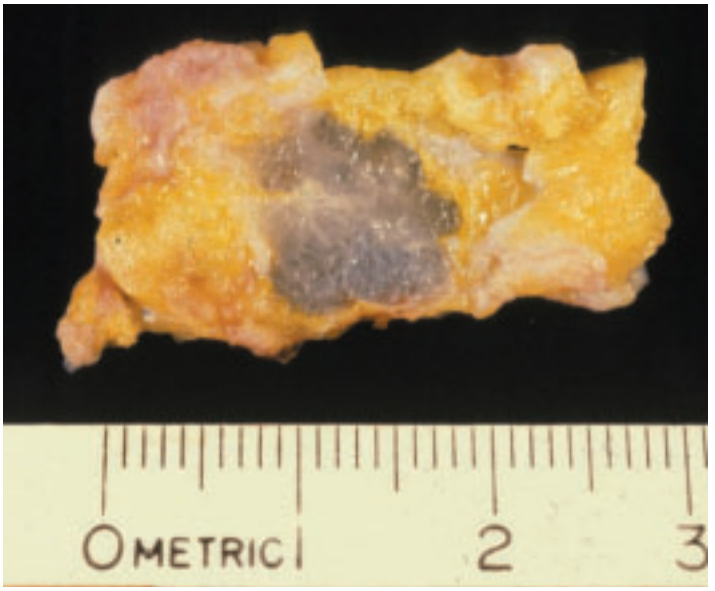

6-62. Typical glistening, mucoid cut surface of a colloid (mucinous) carcinoma of the breast. If not admixed with an ordinary ductal carcinoma, this tumor has a better prognosis than infiltrating ductal or lobular carcinoma.

6-63. A. Metaplastic carcinoma of the breast is a form of breast carcinoma that shows differentiation toward malignant squamous epithelium, cartilaginous, or bony tissue. **B.** Histology of this metaplastic breast carcinoma showed areas of malignant squamous epithelium.

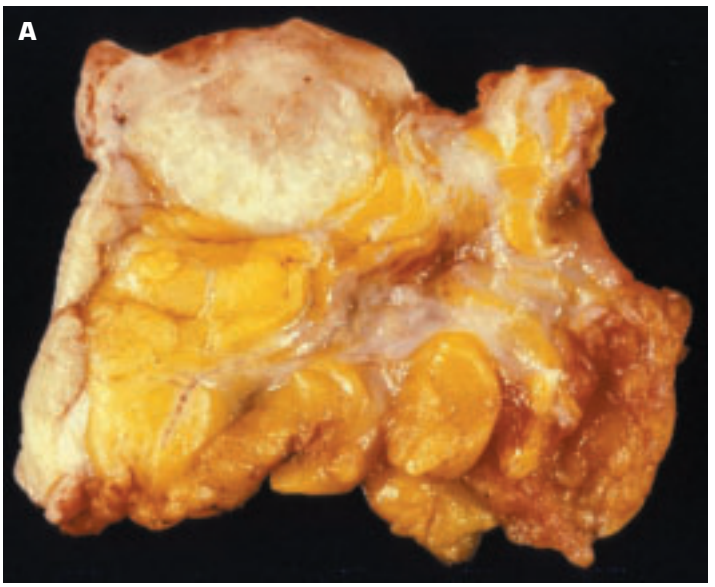

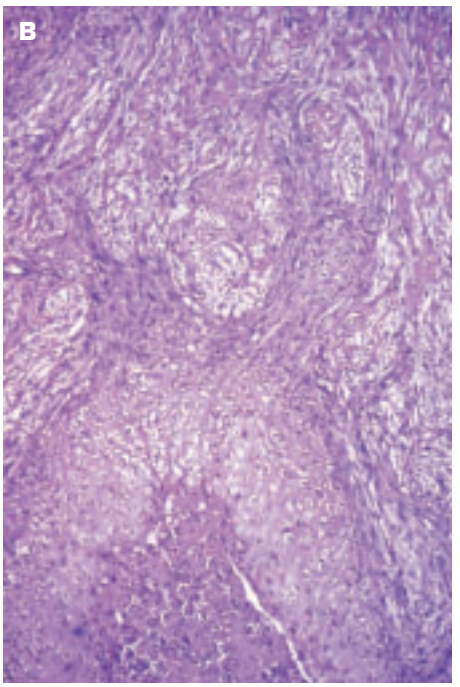

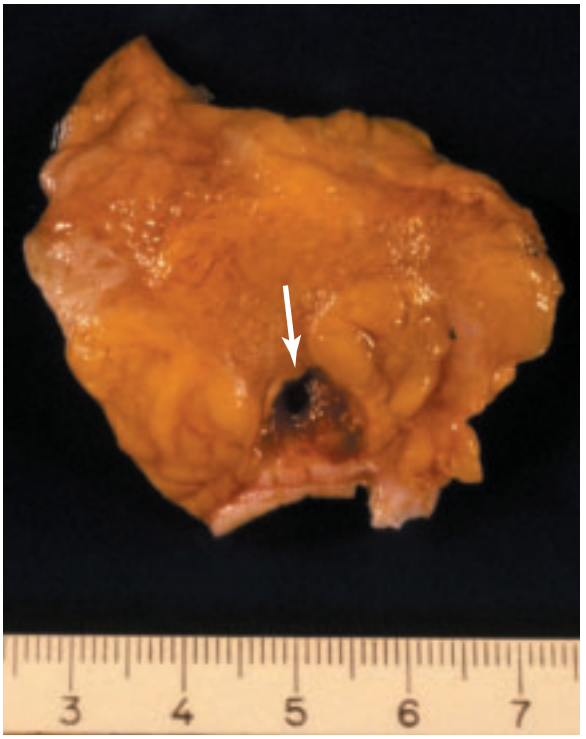

6-64. Angiosarcoma (*arrow*) of the breast is seen as a reddish, cavitated nodule within the mammary tissue.

6-65. Gynecomastia is enlargement of the male breast analogous to juvenile hypertrophy of the female breast. Histology shows active epithelium within a proliferation of mammary ducts with surrounding fibrosis.

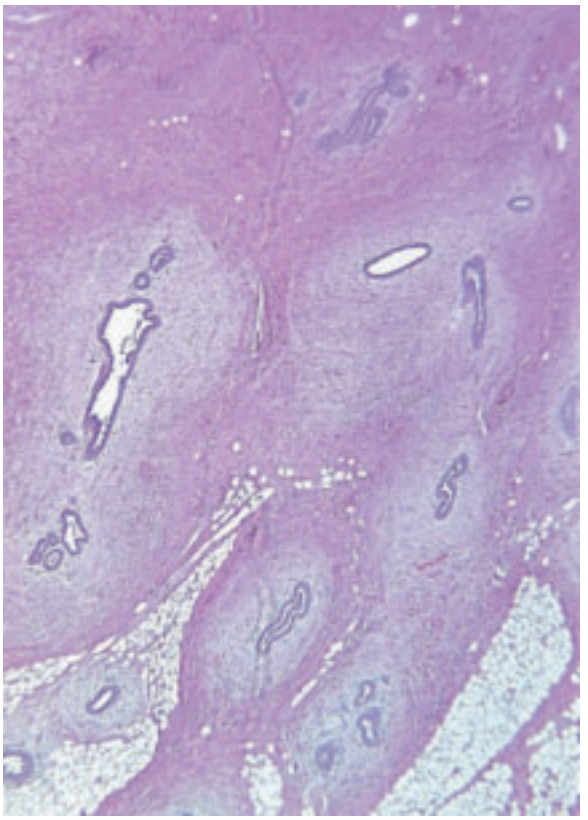

7 Diseases of the Male Genital System

7-1. Carcinoma in situ of the glans penis is seen as multiple focally depressed areas in which the epithelium appears both erythematous and more translucent. This form of carcinoma in situ of the penis has been called *erythroplasia of Queyrat* in contradistinction to *Bowen disease*, which produces a grayish-white plaque.

7-2. A. Microinvasive squamous cell carcinoma of the glans penis and the foreskin presenting as slightly depressed, vascularized areas with focal epithelial thickening. **B.** Histology shows microinvasion (i.e., the squamous carcinoma has penetrated the basement membrane and is starting to invade the underlying stroma).

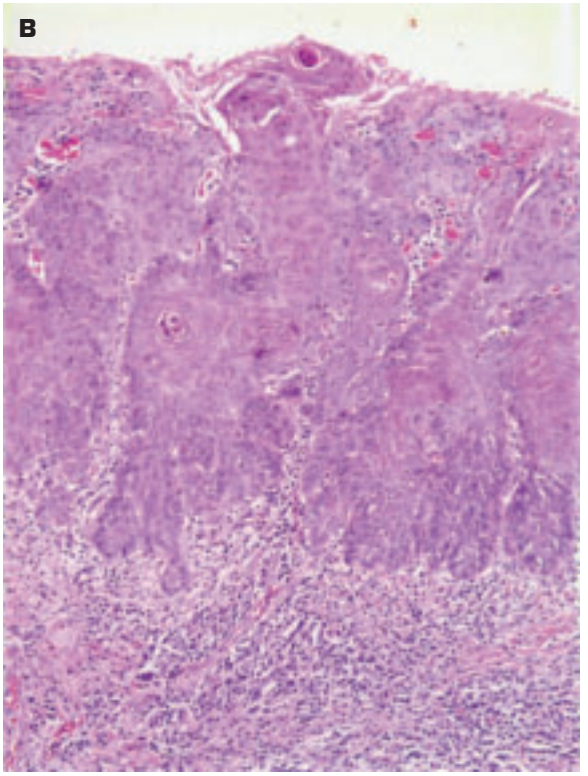

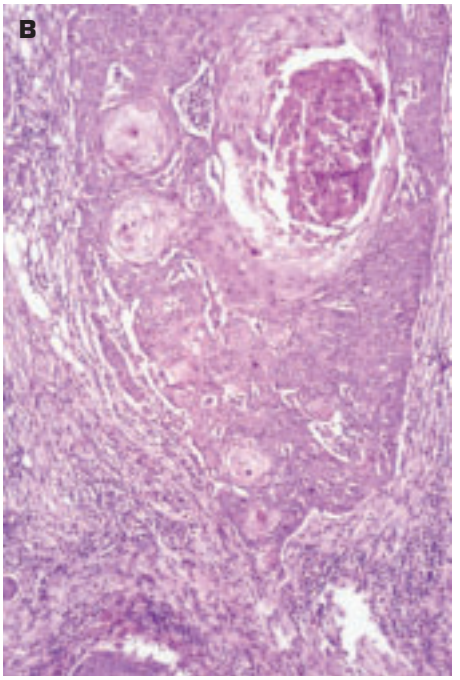

7-3. A. Invasive squamous cell carcinoma arising in the prepuce (foreskin) of the penis has formed an exophytic, papillary tumor. The disease is rare in the United States due to the popularity of circumcision. **B.** Histology of the lesion shows a keratinizing squamous carcinoma with surrounding nonspecific chronic inflammation.

7-4. Longitudinally sectioned penis that was surgically removed because of a squamous carcinoma (*) of the foreskin that is invading the distal end of the penis (*arrow*).

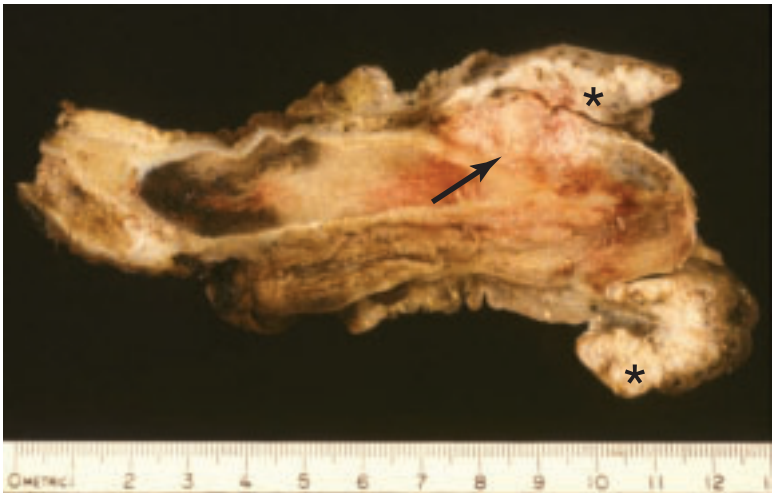

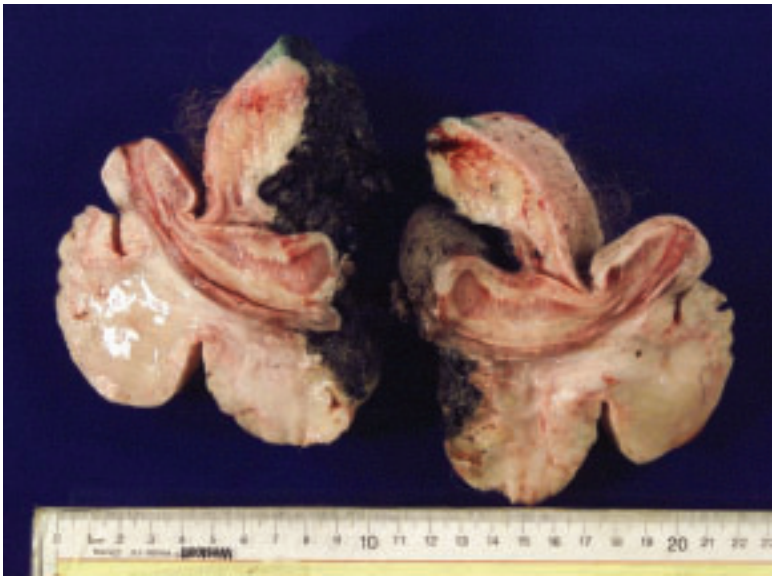

7-5. Bisected penile resection specimen shows a very advanced, large squamous carcinoma invading the inferior aspect of the penis, including the corpus cavernosum.

7-6. Paget disease of the skin of the penis and scrotum presenting as multifocal, thickened, scaling areas of skin.

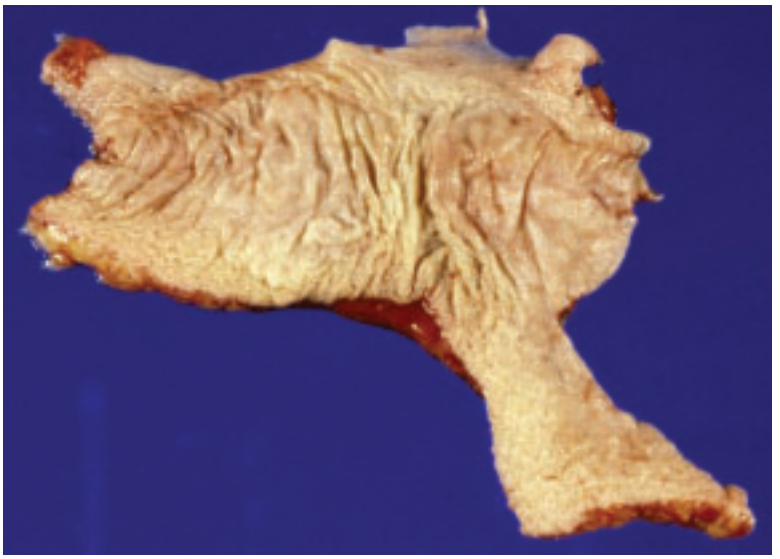

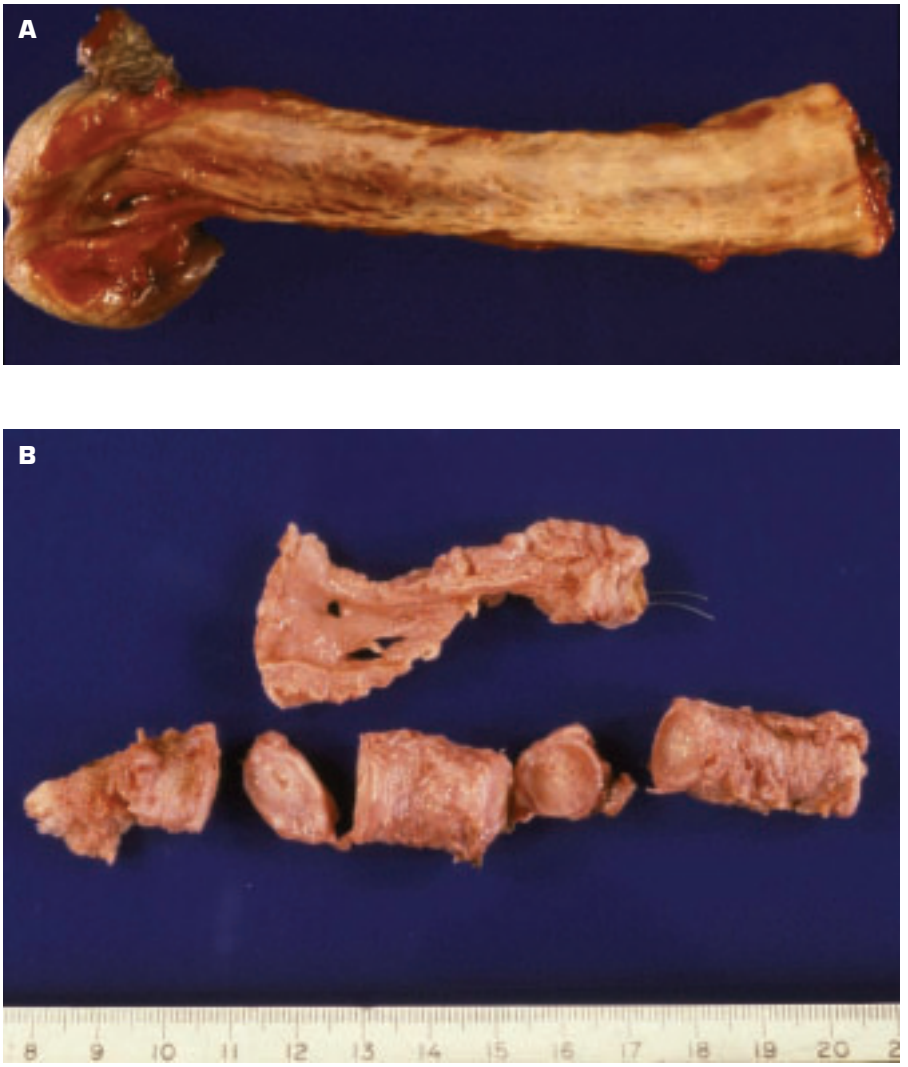

7-7. A. Penectomy specimen for multifocal carcinoma in situ of the distal urethra (*left*). **B.** Transitional cell carcinoma in situ of the penile urethra.

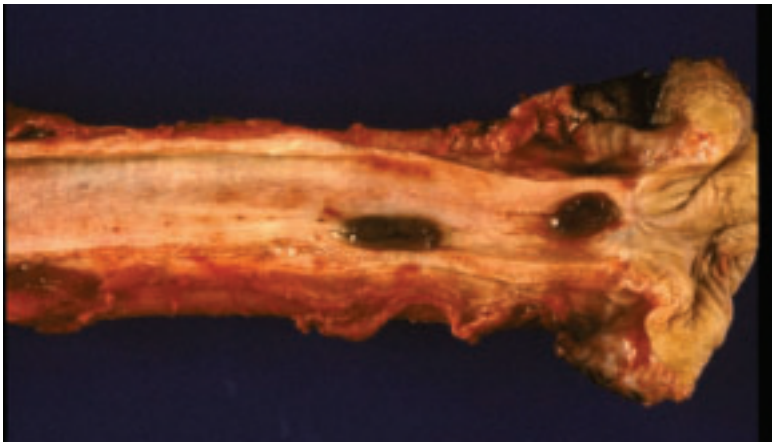

7-8. Metastatic malignant melanoma in the penile urethra.

7-9. Spermatocele surgically resected from a hilar, paratesticular situation is derived from cystic dilatation of a portion of the efferent ducts of the epididymis or the rete testis. Histology shows a cuboidal epithelial lining and degenerating spermatozoa.

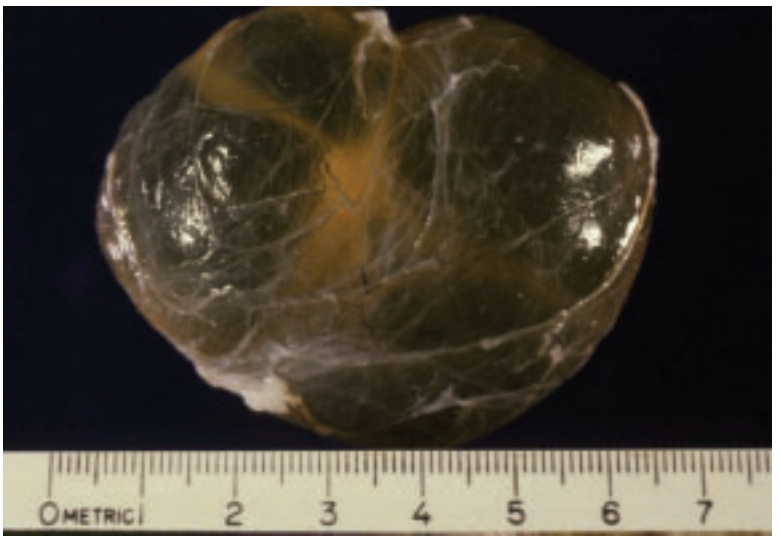

7-10. A. Epididymal cysts usually develop in men of about 40 years of age and may be multiple. They present as a cystic lump in the head of the epididymis (*top right*). The smooth, spherical cyst indents the upper pole of the testis and gives a spurious appearance of an intratesticular situation. **B.** The lining of the cyst (*left*) consists of low cuboidal epithelium, and a portion of the epididymis is present (*right*). *(continued on next page)*

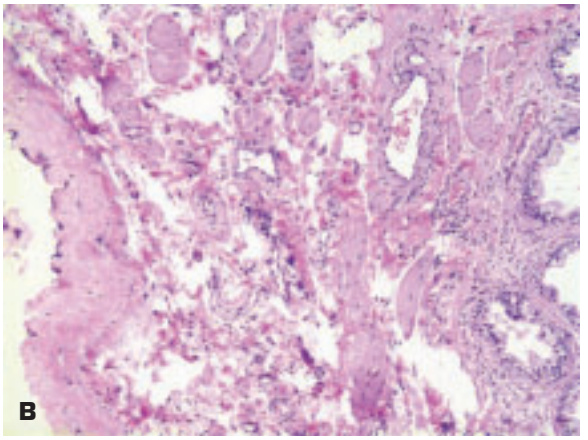

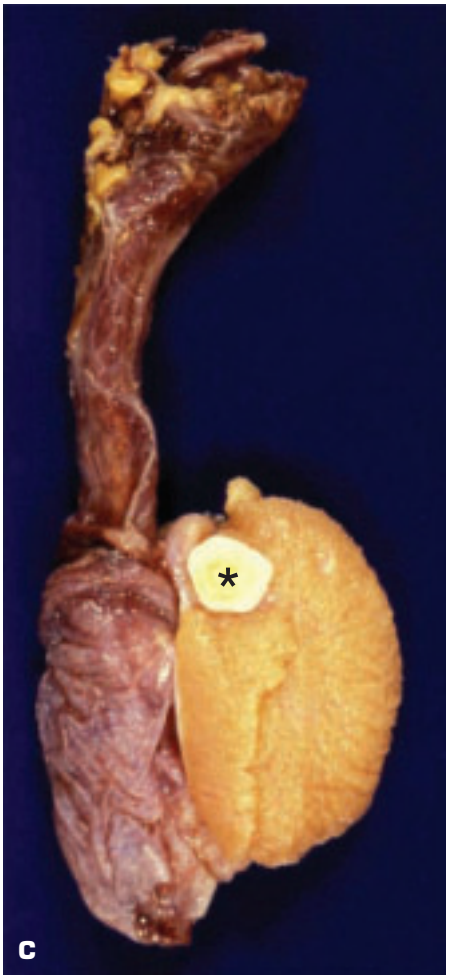

7-10. *(Continued)* **C.** Testis is indented by this white-colored, keratin-containing epididymal inclusion cyst (*). **D.** Histology shows a squamous epithelial lining to the cyst with inspissated keratin in its lumen.

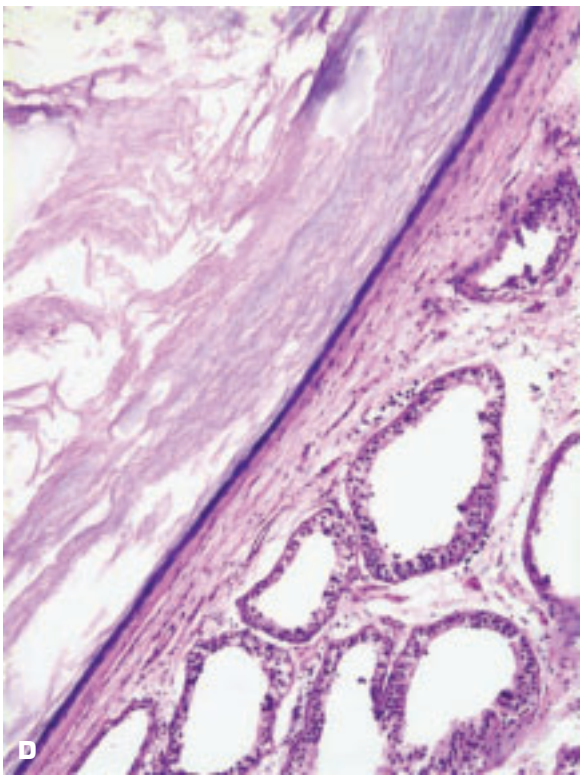

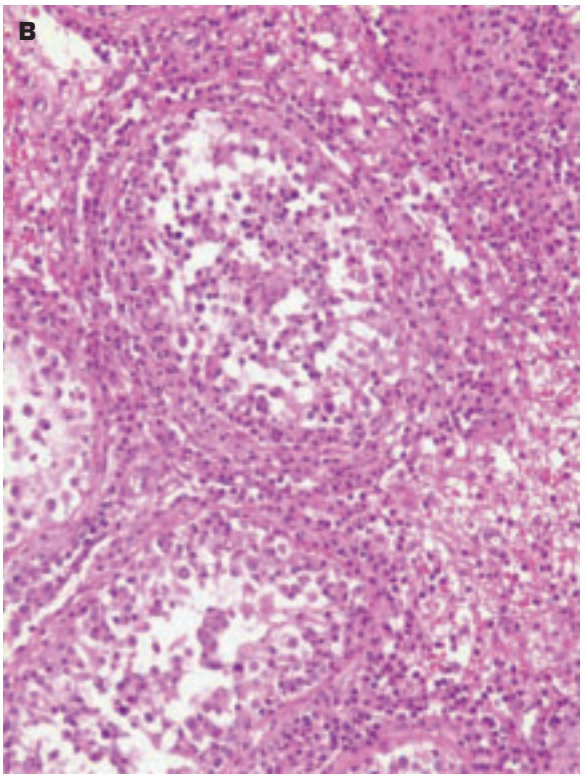

7-11. A. Acute orchitis may be part of epididymoorchitis following ascending infection (as in this patient), or it may occur as isolated orchitis secondary to bloodborne infection or autoimmune disease. Note the acutely inflamed testis showing focal hemorrhages and suppuration within the testis secondary to gram-negative bacterial infection of the genitourinary tract. **B.** Histology shows acute suppurative inflammation within and around seminiferous tubules in the testis.

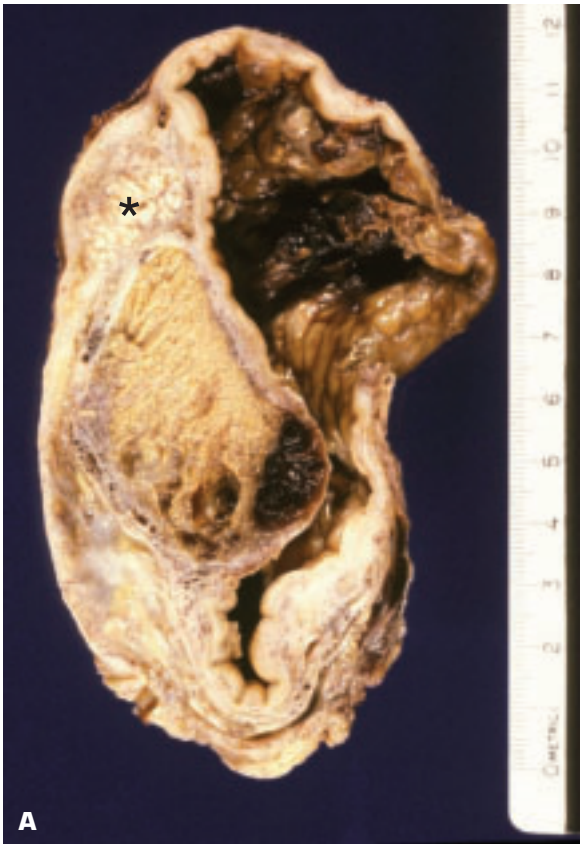

7-12. A. Subacute epididymoorchitis showing a large hydrocele (*right*) alongside distorted testis with partial cystic transformation. Note the lipid-rich postinflammatory deposits within the epididymis (*). **B.** Neutrophils, lymphocytes, and hemosiderin deposits in the fibrous tissue enclosing the hydrocele.

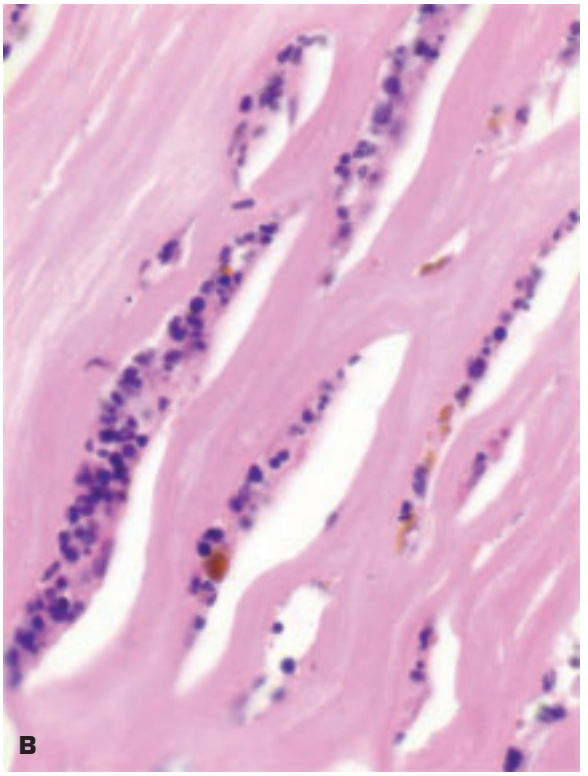

7-13. Suture granuloma (*) of the testis following orchiopexy (inguinal testis was surgically relocated into the scrotum). Histology is needed to make the diagnosis.

7-14. Granulomatous orchitis showing pale white solid tissue replacing most of the testis apart from the brownish remnant (*lower right*). The condition is a type IV (cell-mediated) noncaseating granulomatous response to the seminiferous tubules.

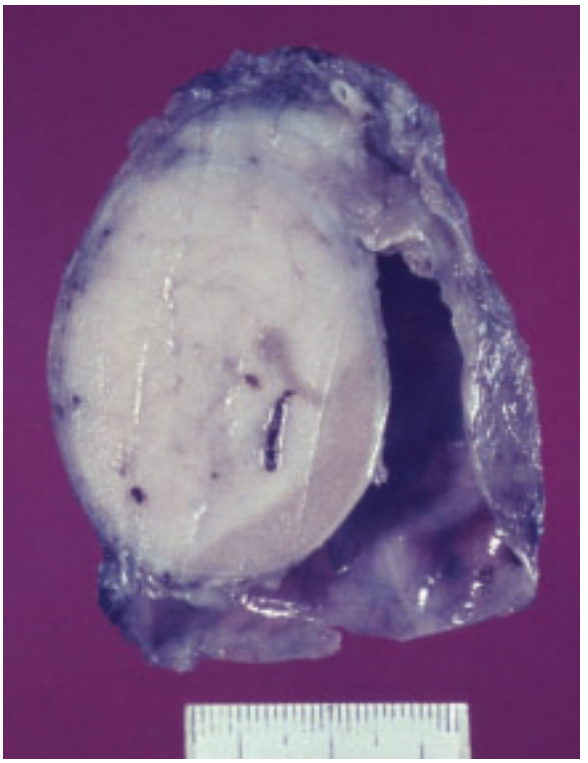

7-15. Infarction of the testis. **A.** Hemorrhagic infarction of the testis following arterial occlusion. Similar lesion may follow torsion of the testis. **B.** Focal infarction (*arrow*) of the upper pole of another testis.

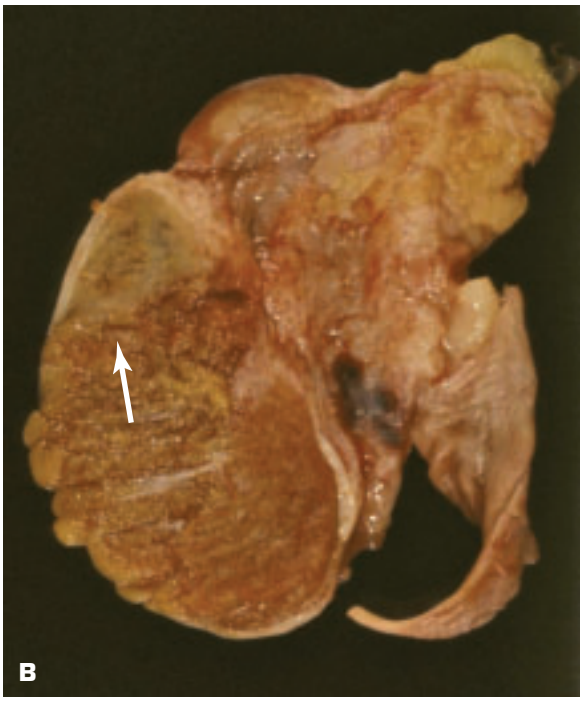

7-16. A. Organizing hematoma around the testis. **B.** Histology shows festoons of histiocytes growing into the hematoma.

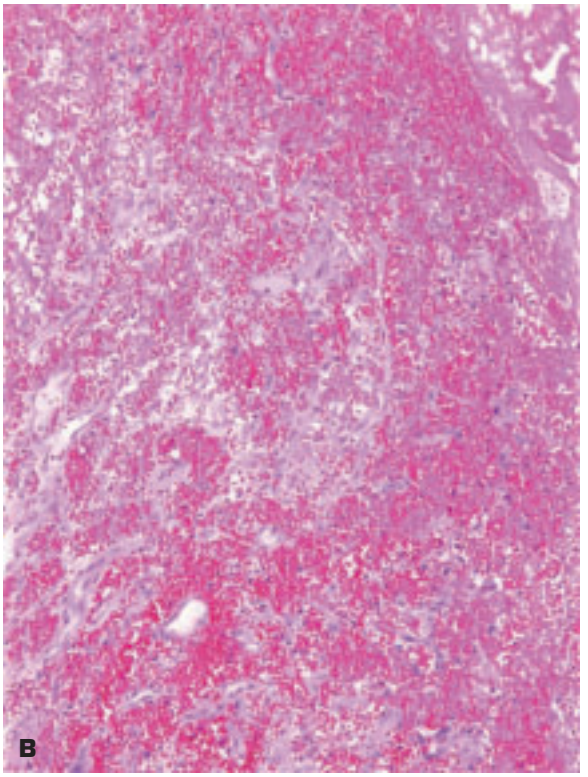

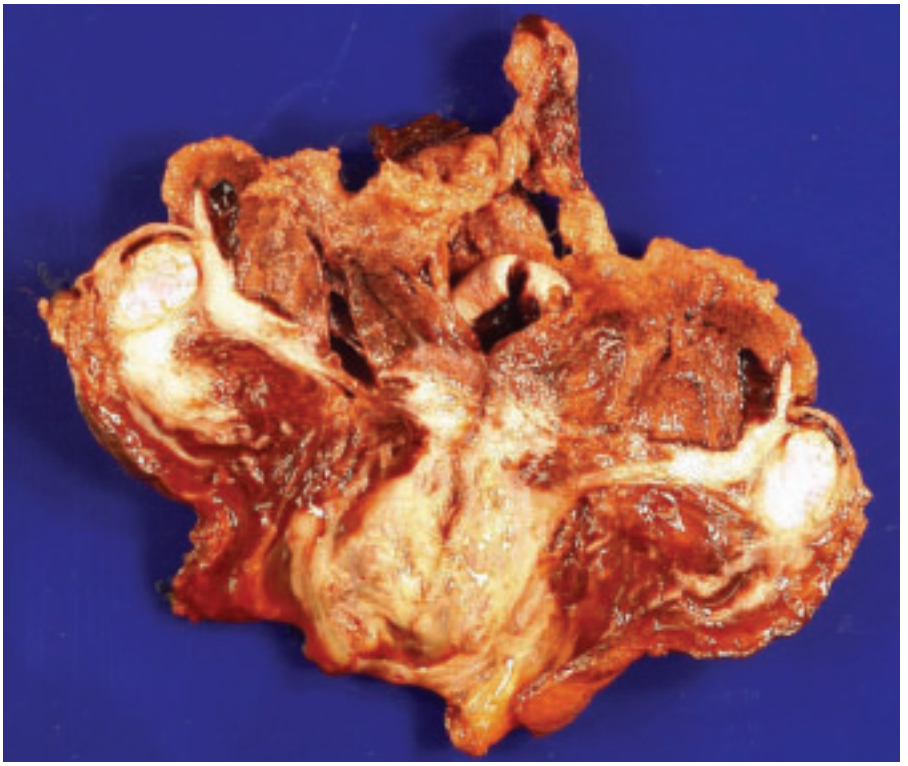

7-17. Traumatic injury to the testis (*bottom center*). The testis and scrotum have been bisected, and recent widespread hemorrhage is present within the scrotum.

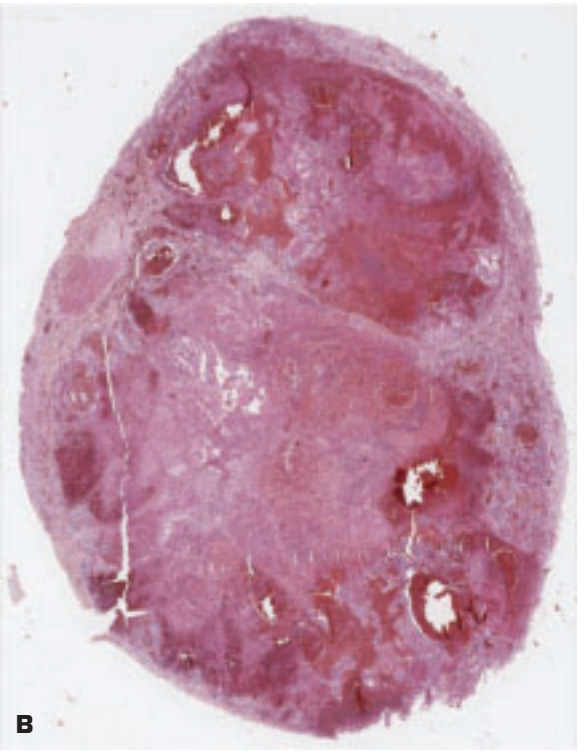

7-18. A. Hemorrhagic nodule within the testis due to polyarteritis nodosa. **B.** Whole mount section of a testis replaced by hemorrhagic choriocarcinoma. **C.** High-power view of the choriocarcinoma showing malignant cyto- and syncytiotrophoblast.

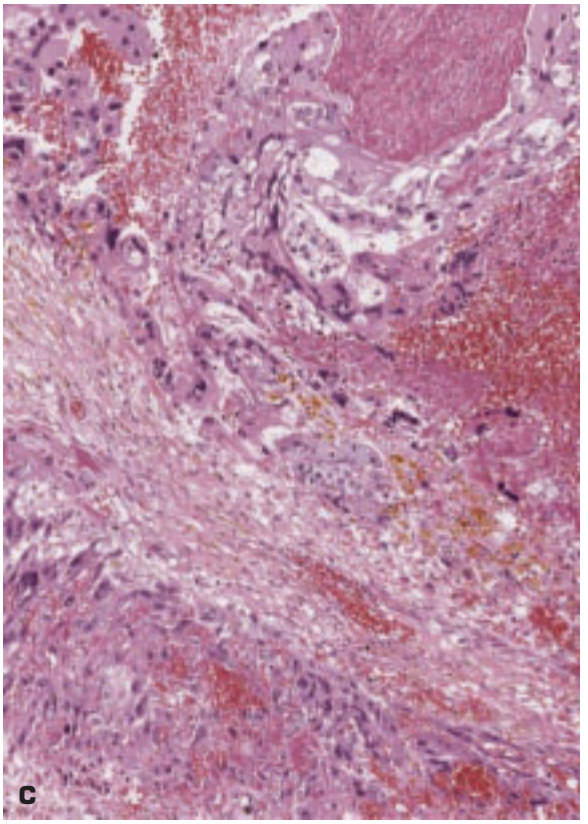

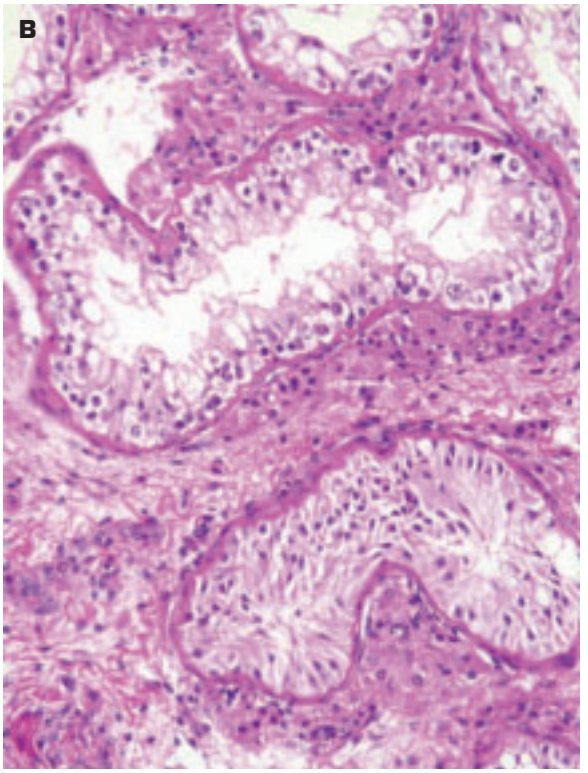

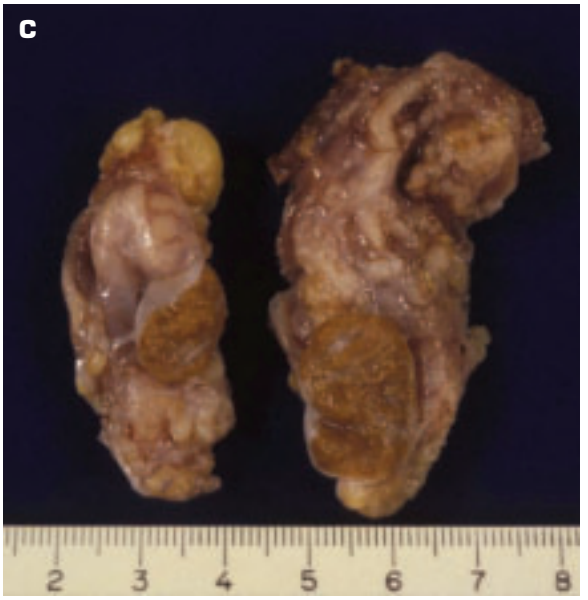

7-19. A. Bisected small, dysplastic testis of a patient with cryptorchidism that showed intratubular germ cell neoplasia (ITGCN). This change is a preinvasive form of germ cell tumor. **B.** Histology of ITGCN shows atypical germ cells lining seminiferous tubules having thickened basement membranes. No spermatogenesis is evident. **C.** Two intraabdominal testes removed after puberty from a phenotypically normal female with complete androgen insensitivity syndrome (previously termed "testicular feminization syndrome") and X and Y chromosomes. The gene mutation is on the X chromosome in band Xq11-q12. The subjects have no uterus, are infertile, and never menstruate.

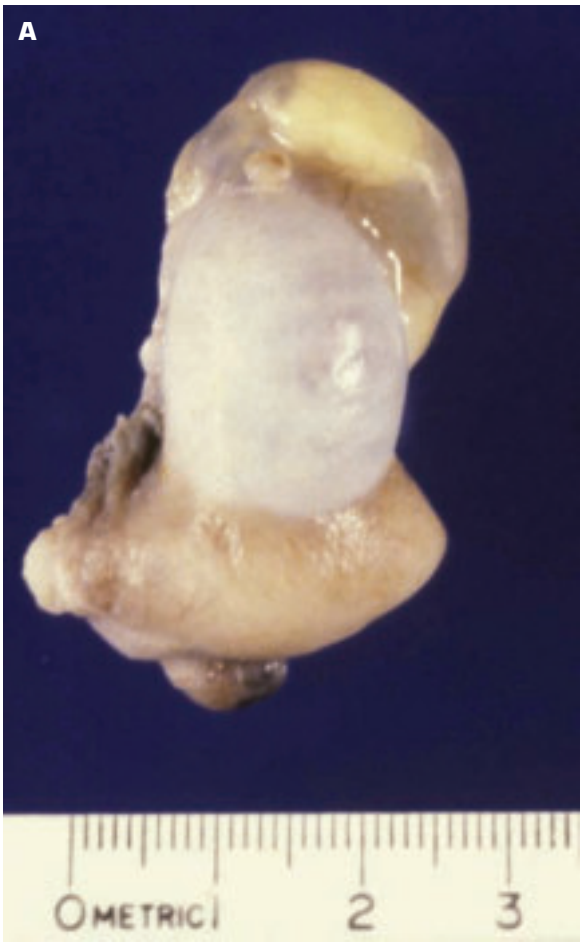

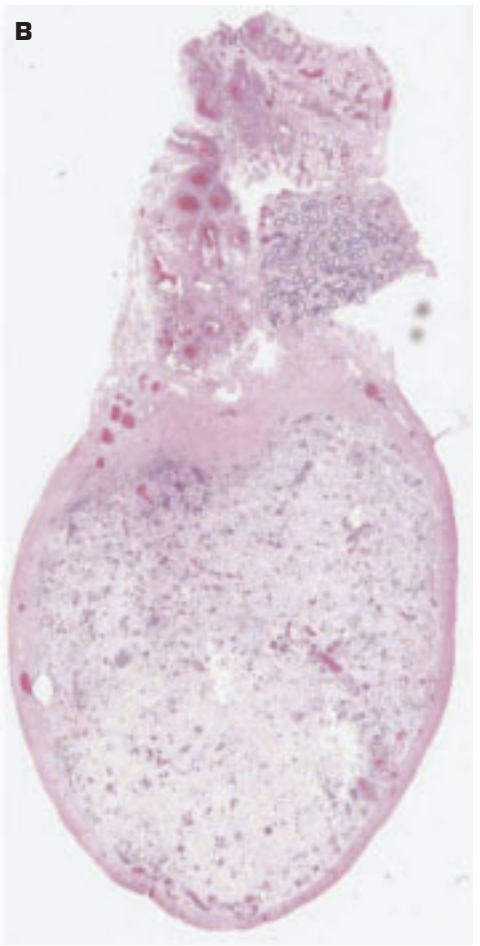

7-20. Atrophy of the testis may follow orchitis of any cause, cryptorchidism, ischemia, irradiation, and prolonged administration of female hormones, along with other causes. **A.** Atrophic testis following mumps orchitis. **B.** Whole mount section of testis and epididymis showing generalized atrophy of seminiferous tubules in testis. **C.** Hyalinized, atrophic seminiferous tubules are more easily appreciated at this higher power.

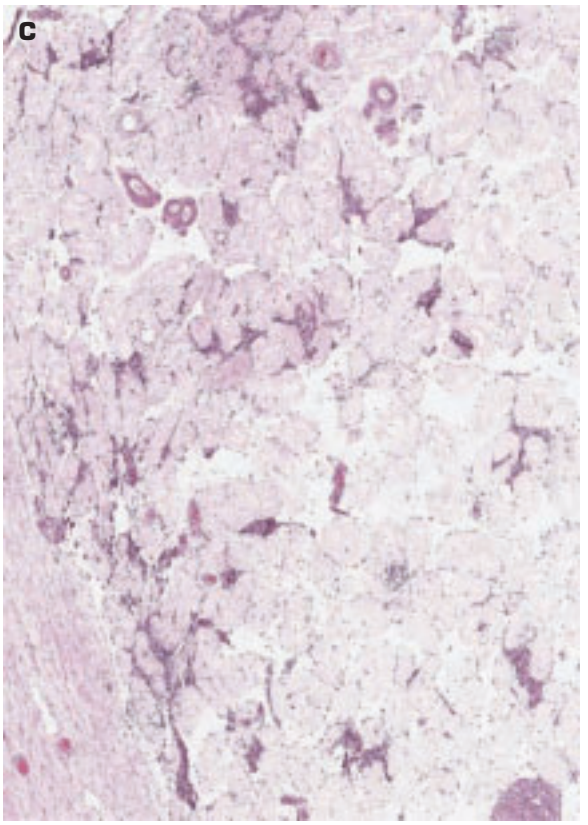

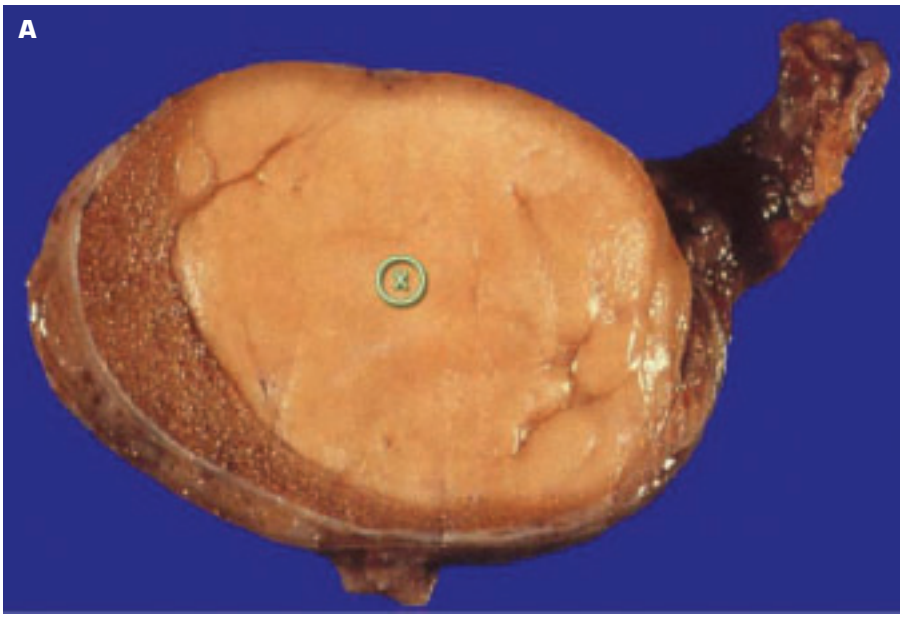

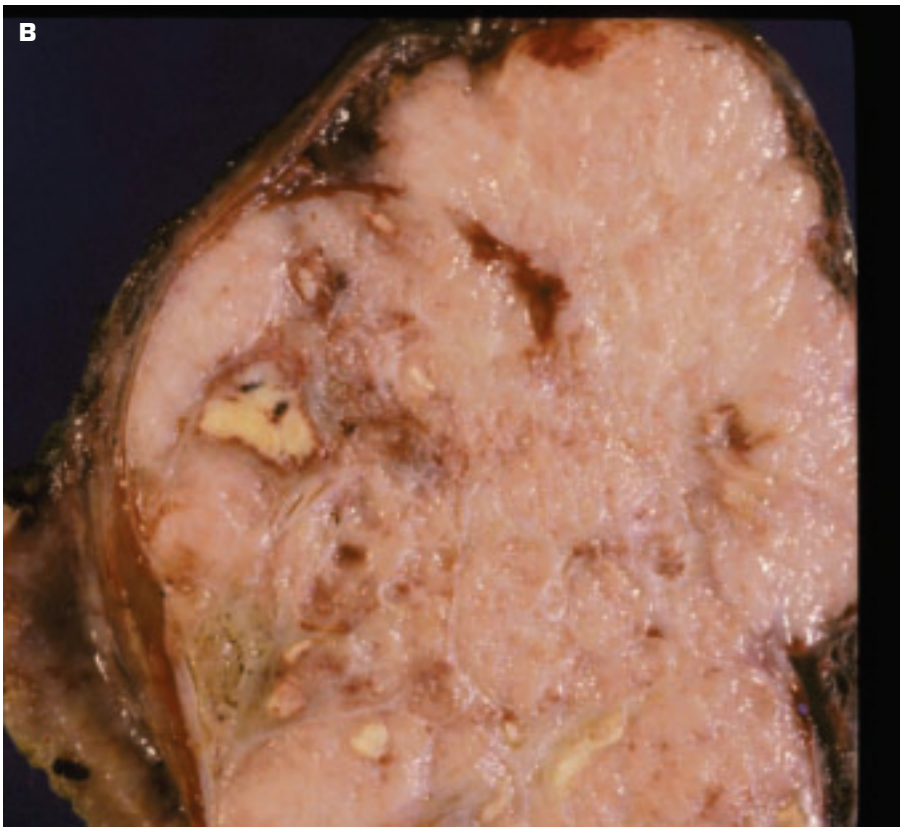

7-21. Seminoma of the testis. **A.** Large, homogeneous, light tan-colored tumor mass (X) has replaced much of the testicular tissue. Necrosis is uncommon in seminoma. **B.** Close-up view of another seminoma shows focal areas of necrosis (yellow) within the tumor. *(continued on next page)*

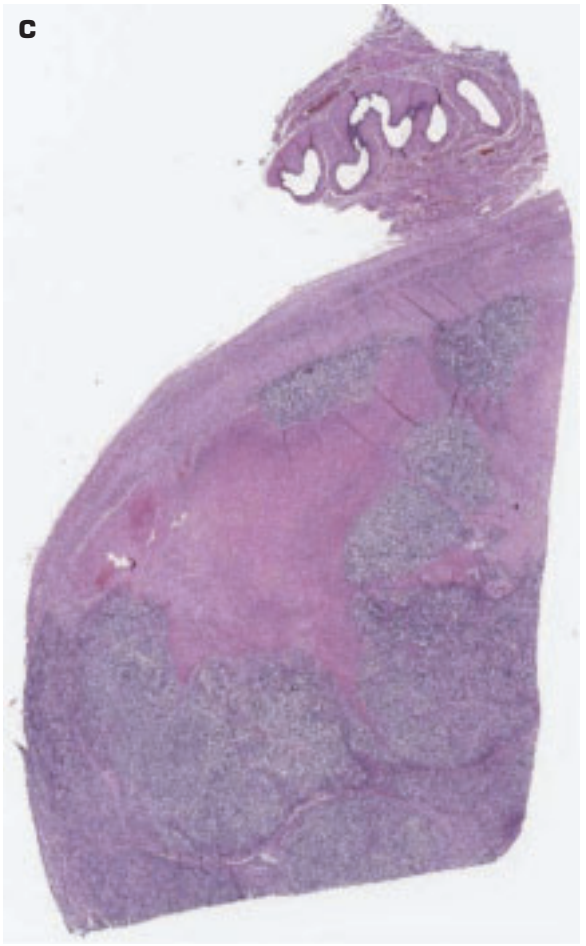

7-21. *(Continued)* **C.** Low-power histology of the seminoma shows a pink-colored area of necrosis within the cellular, blue-colored tumor. **D.** High-power view of seminoma shows the cells to have pale-staining nuclei with prominent nucleoli, well-defined cell borders, and scanty interstitial lymphocytes. *(continued on next page)*

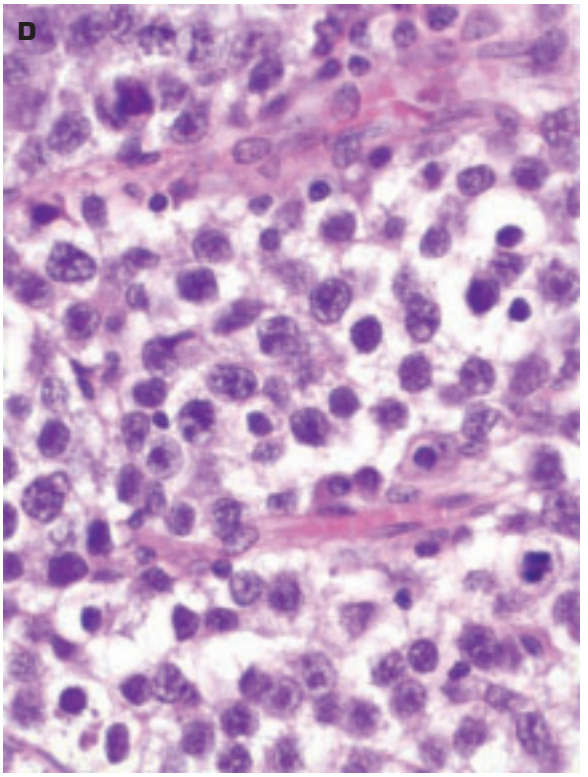

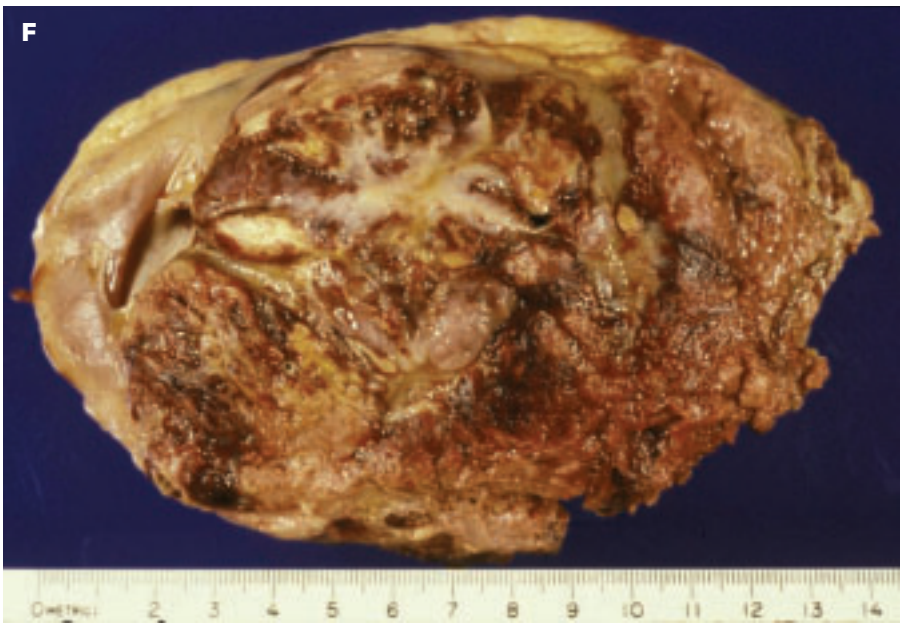

7-21. *(Continued)* **E.** Retroperitoneal lymph nodes post chemotherapy contain metastatic, partially necrotic, seminoma. **F.** Secondary spread of anaplastic seminoma to almost totally replace the kidney.

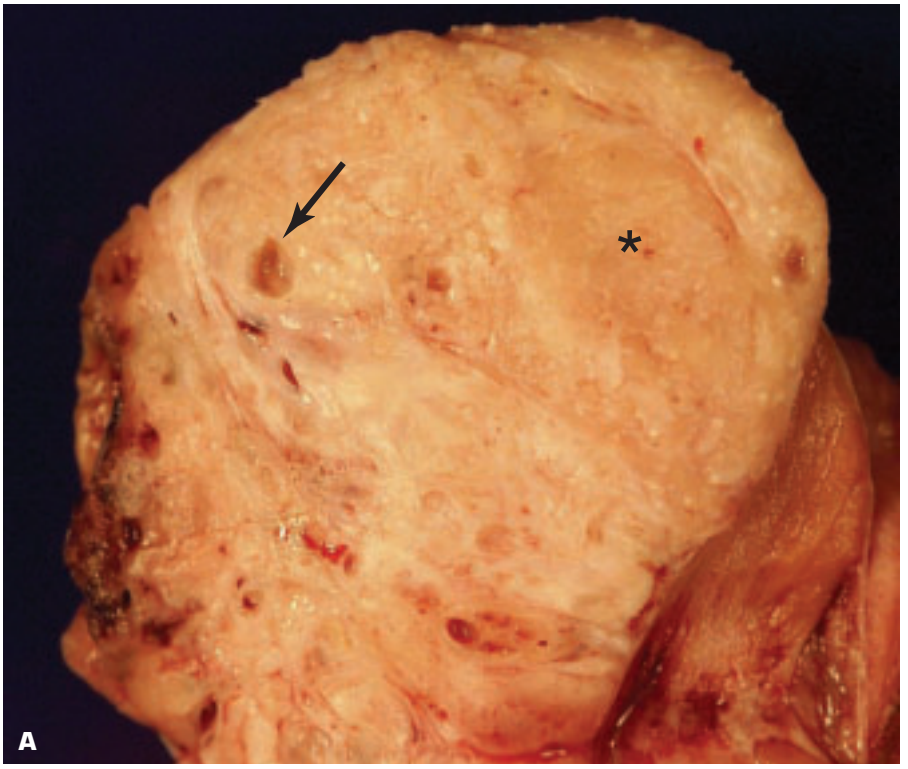

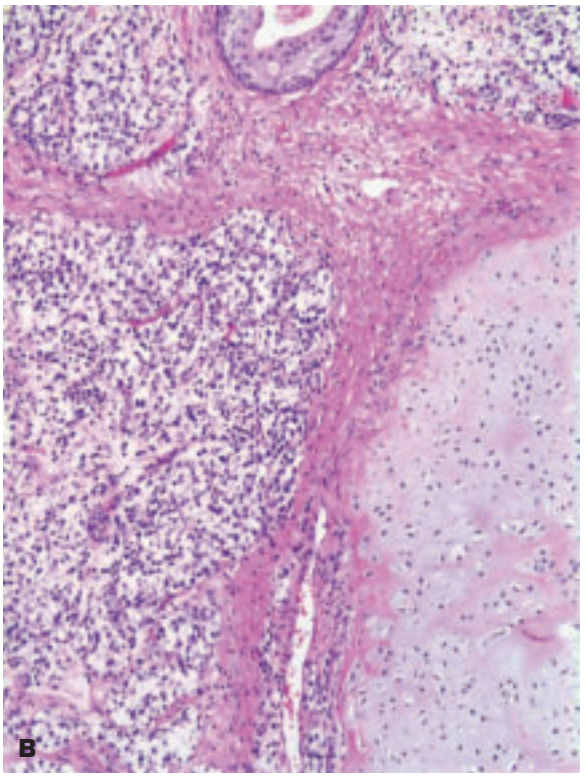

7-22. A. Combined seminoma (yellow, homogeneous areas) (*) and nonseminomatous (teratomatous) germ cell tumor (cystic areas with hemorrhage and necrosis) (*arrow*). **B.** Histology shows seminoma (*left*) and portion of teratoma (*top and right*).

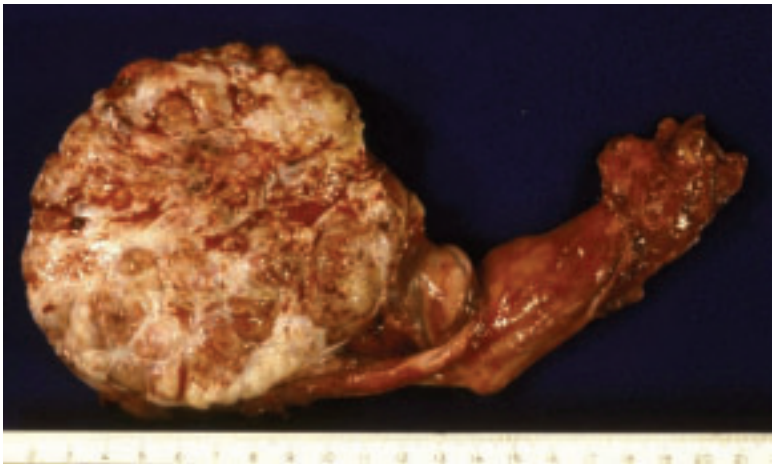

7-23. Teratocarcinoma (malignant transformation of a teratoma with the development of mucin-secreting adenocarcinoma in this case) has totally replaced the testis and extended beyond its original boundaries. The solid white tumor shows extensive necrosis and hemorrhage.

7-24. A. Embryonal carcinoma is poorly delineated and occupies the mid- and inferior portion of the testis. **B.** Histology of embryonal carcinoma shows sheets of primitive cells giving rise to glands.

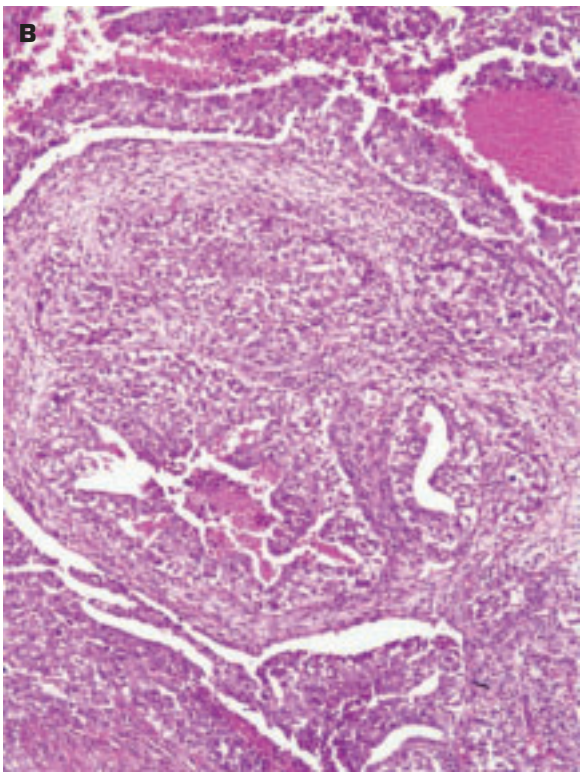

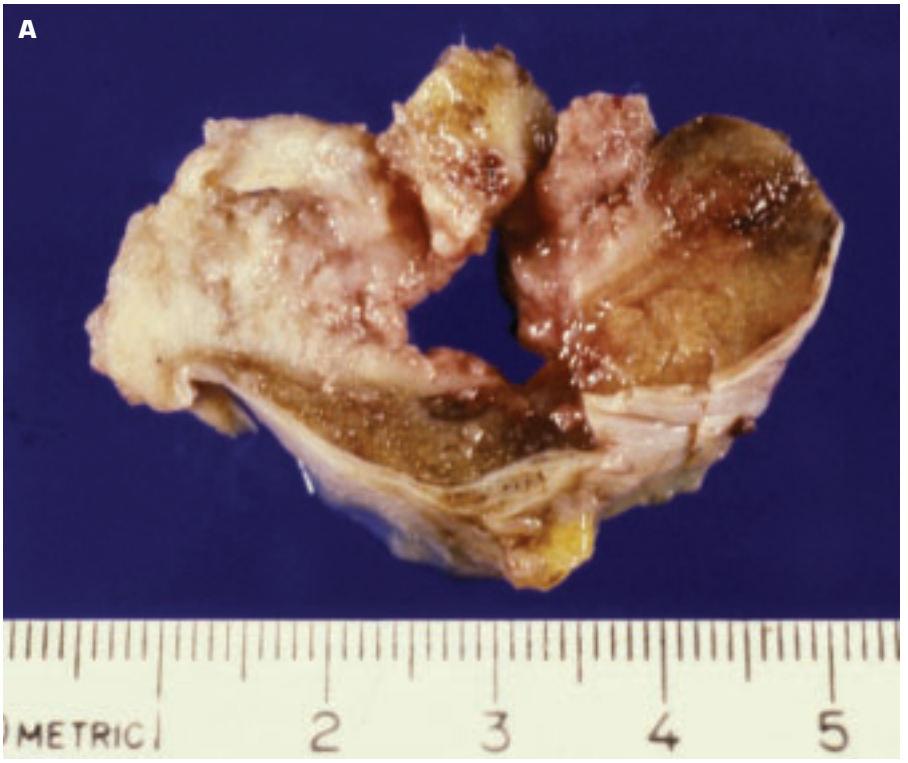

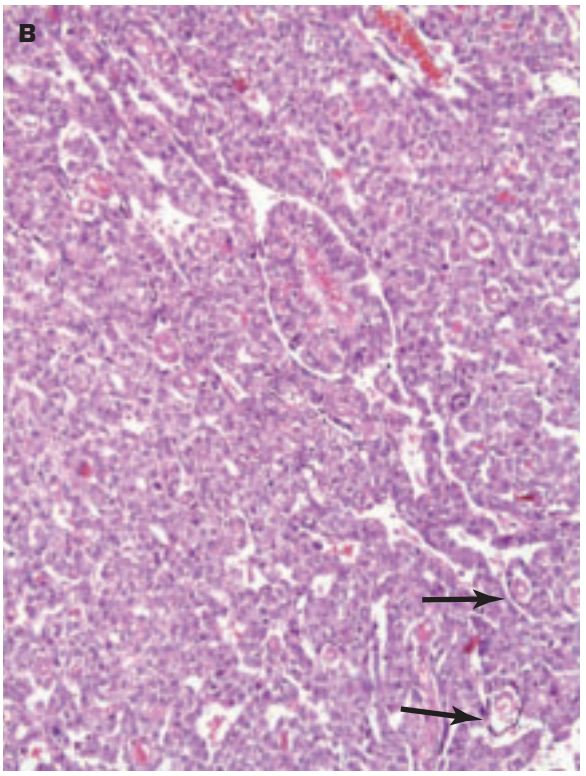

7-25. A. Solid white tumor in testis comprises embryonal carcinoma with yolk sac elements. Yolk sac tumor is the most common testicular tumor in infants (in whom it has a good prognosis). In adults, yolk sac tumor usually occurs in combination with embryonal carcinoma, as in this patient. **B.** Histology of embryonal carcinoma with yolk sac elements (*arrows*) comprising papillary projections covered by a double cell layer simulating a developing yolk sac.

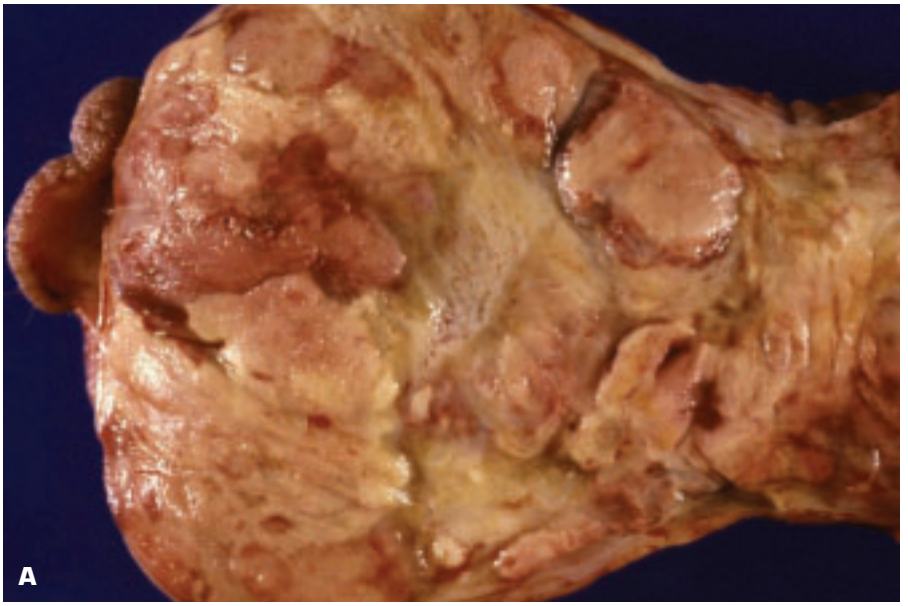

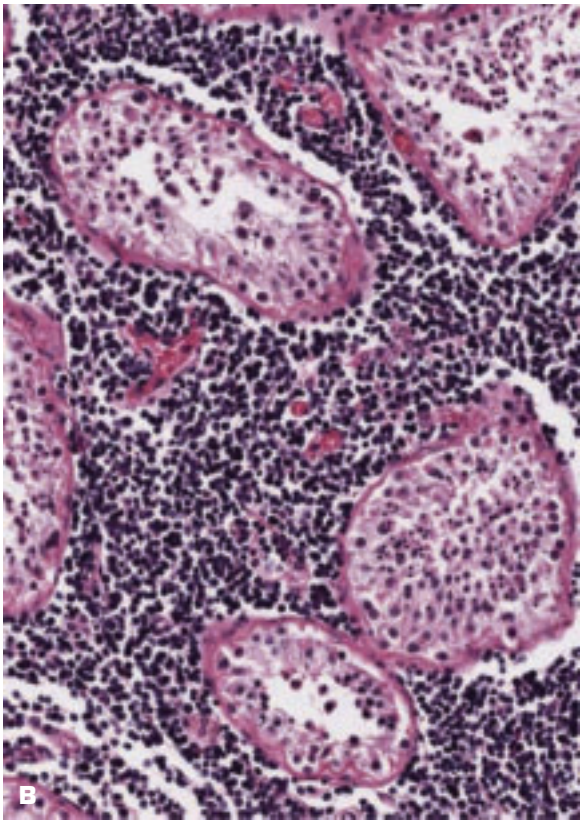

7-26. A. Malignant lymphoma of the testis showing an overgrowth by a solid, fleshy, yellow-white tumor tissue with extensive areas of necrosis. The lymphoma may arise in the testis (it is the most common testicular neoplasm in men older than 60 years), or it may spread there from elsewhere in the body. **B.** Infiltrating lymphomatous cells separate the seminiferous tubules.

7-27. A variety of malignant tumors may spread to the testis. A few examples are illustrated here. **A.** Diffuse myelomatous infiltration of the testis. **B.** Histology of the same testis shows sheets of neoplastic plasma cells surrounding a surviving seminiferous tubule. *(continued on next page)*

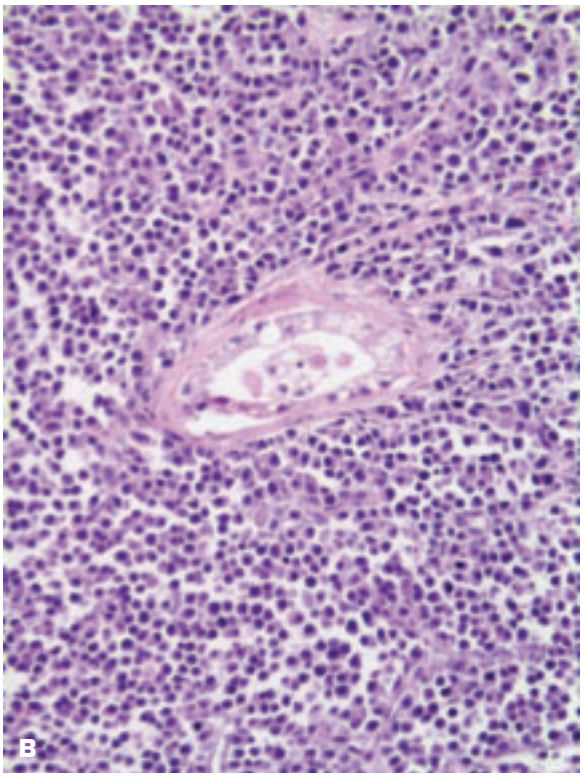

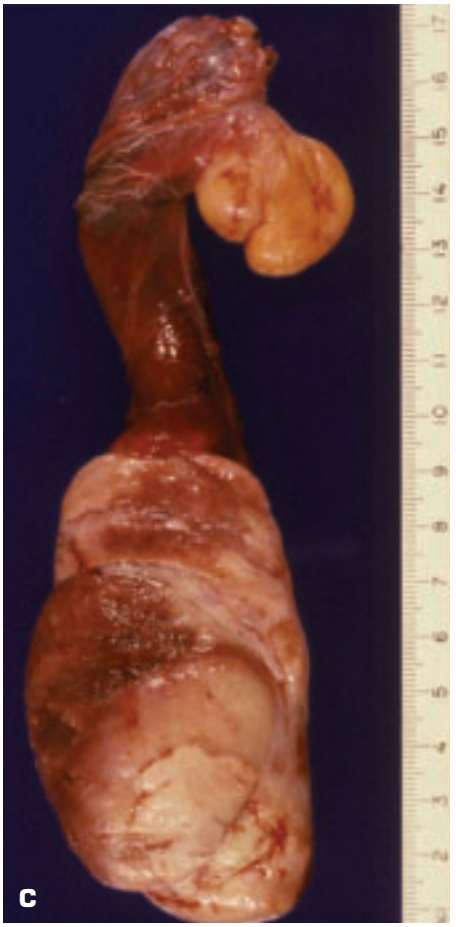

7-27. *(Continued)* **C.** Leukemic infiltration of the testis with partial necrosis of the malignant infiltrate. **D.** Metastatic neuroblastoma in the testis of an infant. Tumor nodules are also present on the spermatic cord. **E.** Histology of the same testis shows small, dark blue tumor cells of metastatic neuroblastoma.

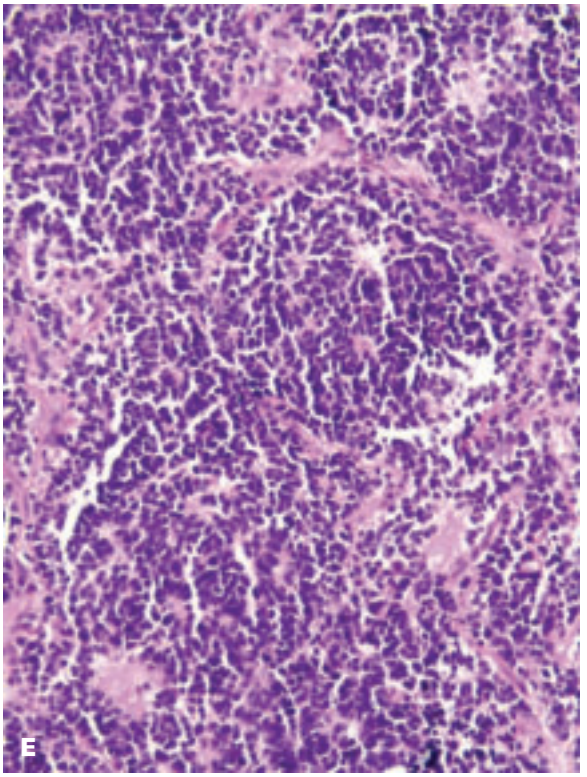

7-28. Partly macerated fetus showing the intraabdominal situation of both testes (*arrows*) approaching the inguinal canals.

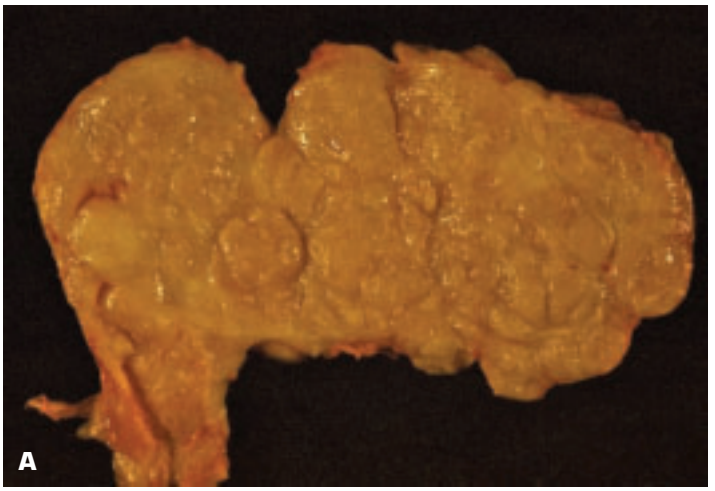

7-29. Benign prostatic hyperplasia (BPH). **A.** Macroscopic appearance of hyperplasia of the prostate gland showing the characteristic multinodular cut surface due to multifocal hyperplasia that led to overall glandular enlargement. **B.** Whole mount of BPH showing nodules composed of proliferating glands surrounded by stromal proliferation. Cystic dilatation of some glandular spaces is also evident. **C.** Higher-power view of BPH.

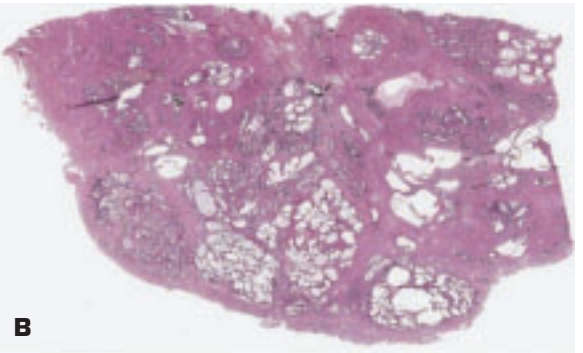

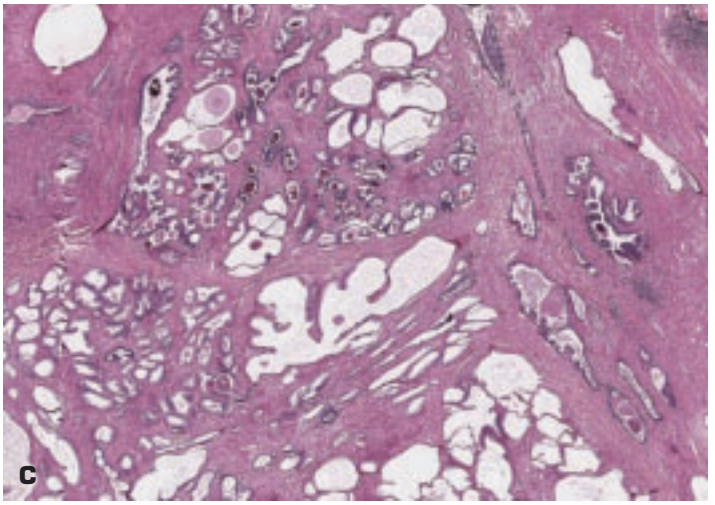

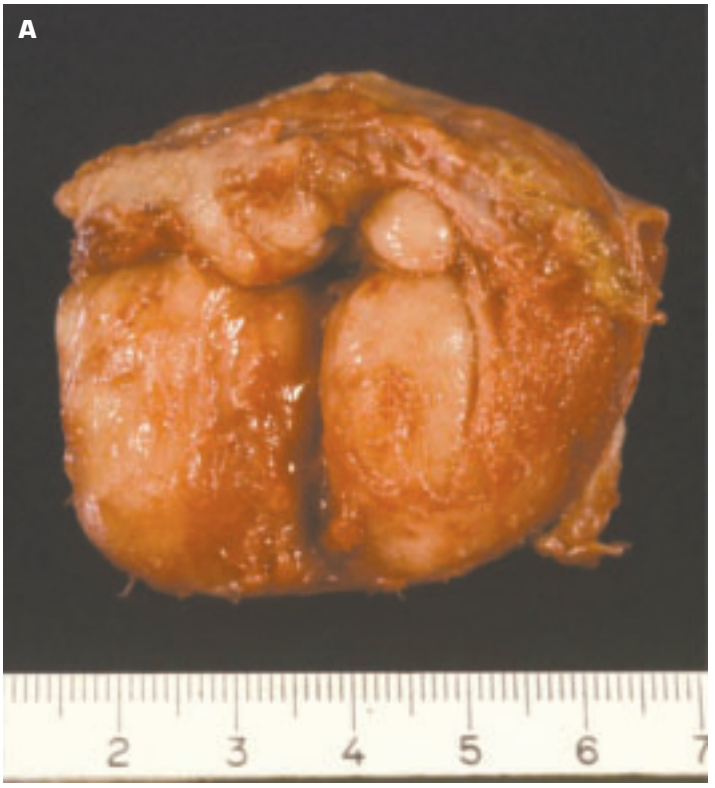

7-30. Adenocarcinoma of the prostate gland. **A.** Entire prostate gland that was excised by radical prostatectomy. **B.** Transverse section of prostate gland showing lipid-rich (yellow-colored) prostatic cancer that has arisen toward the periphery of the gland and has infiltrated inward. The resection line (prostate has no capsule) has been marked with black ink. *(continued on next page)*

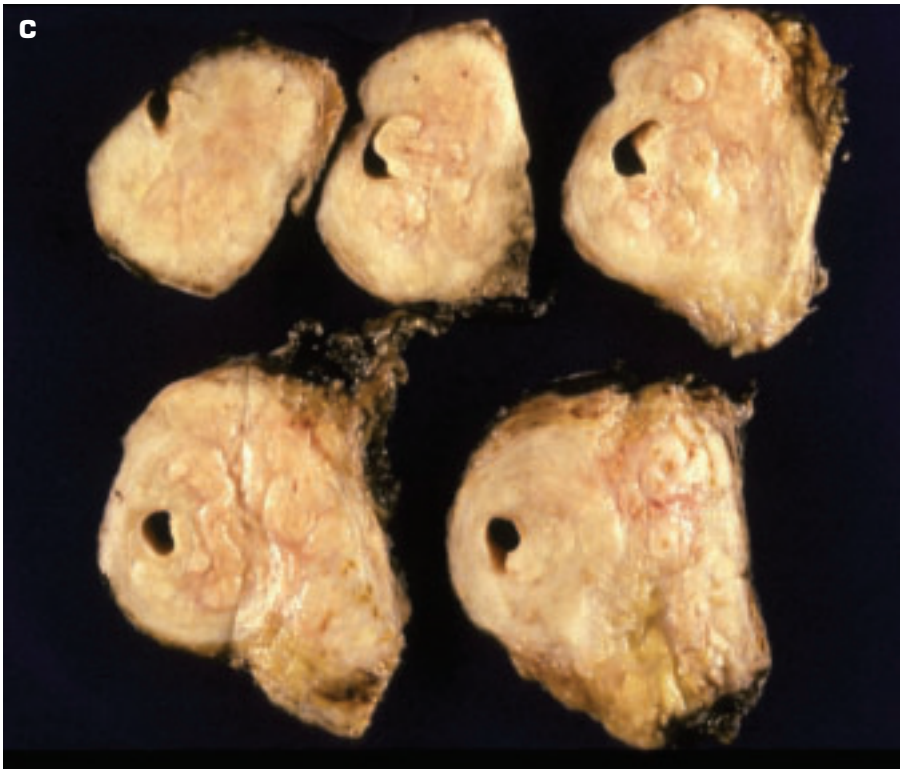

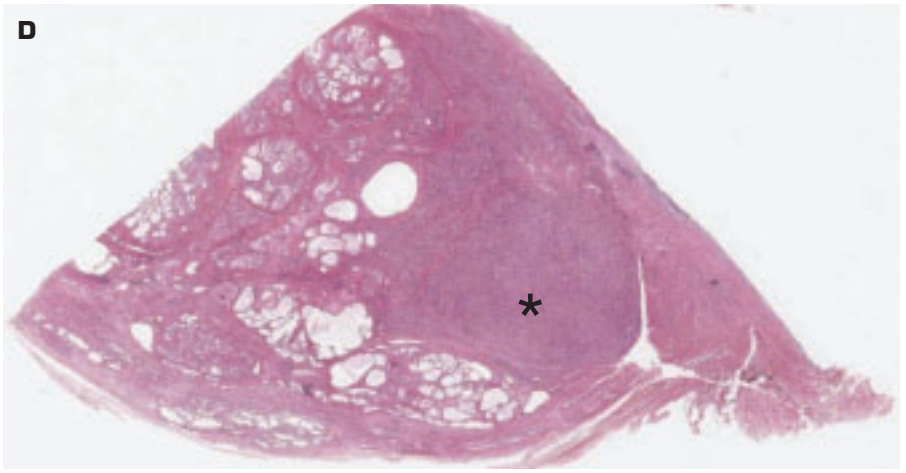

7-30. *(Continued)* **C.** Multiple slices of an advanced prostatic cancer that has replaced most of the gland. **D.** Whole mount section of prostate gland showing benign prostatic hyperplasia on the left and invasive cancer (solid tissue) on the right (*). *(continued on next page)*

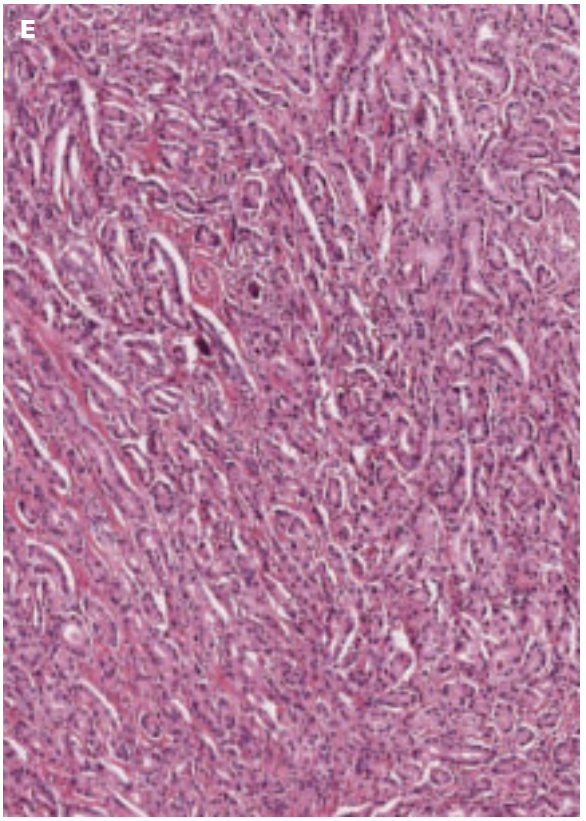

7-30. *(Continued)* **E.** Intermediate-power histology shows massive crowding of the malignant glandular acini. **F.** High-power view of prostatic cancer showing clear cells containing prominent nucleoli within large, clear nuclei. *(continued on next page)*

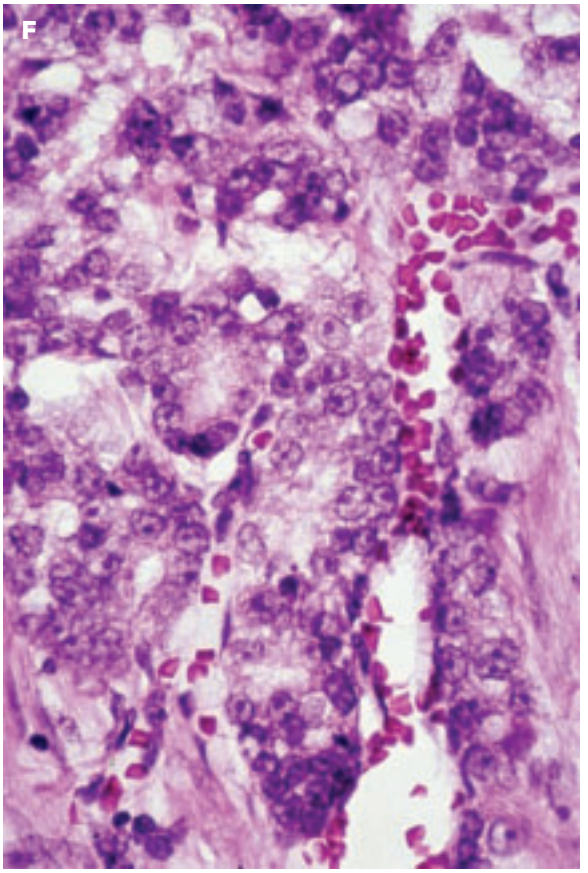

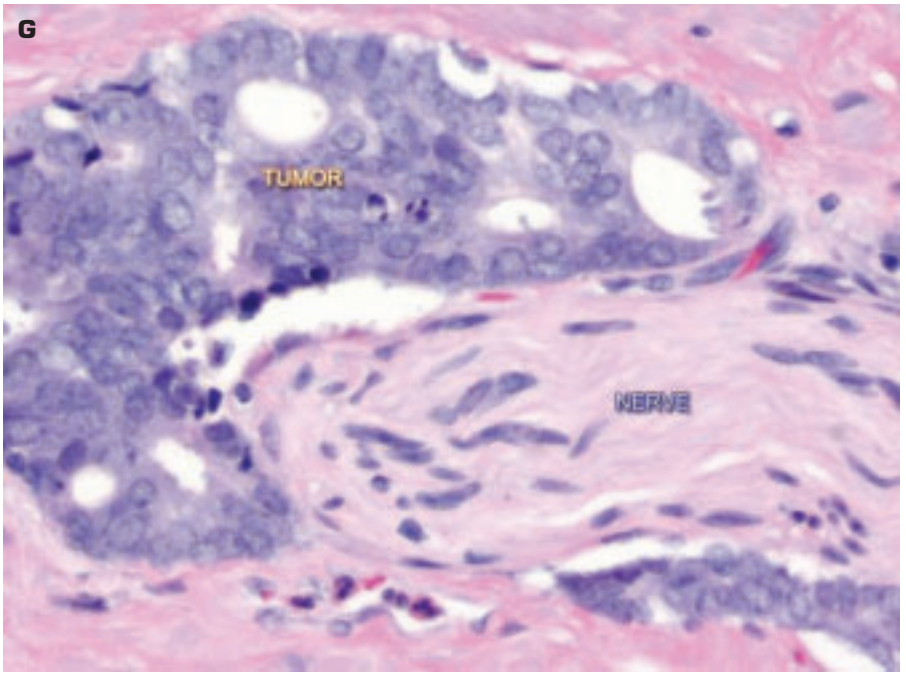

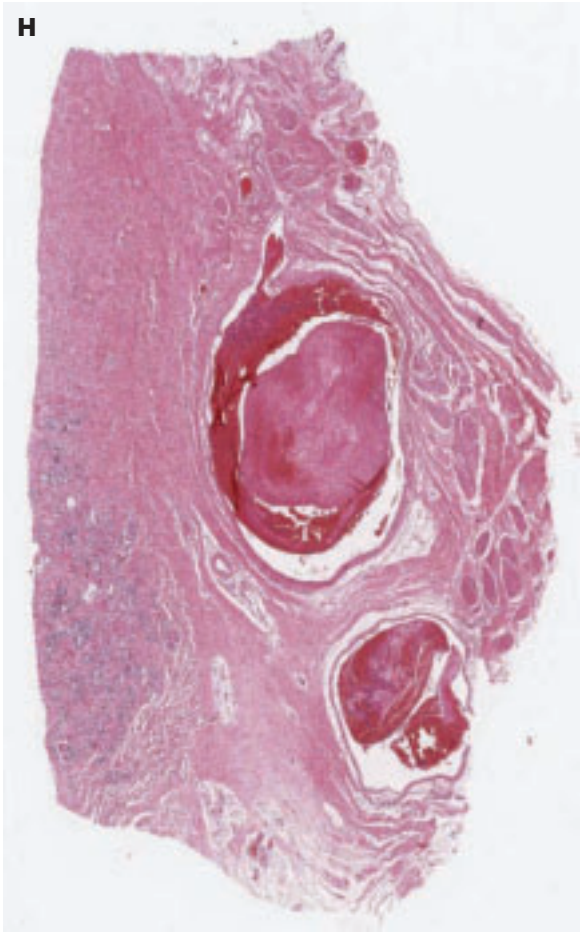

7-30. *(Continued)* **G.** Perineural invasion by cancer of the prostate gland. **H.** Thrombosed veins of the periprostatic venous plexus – this plexus bears prostatic cancer to the vertebral column.

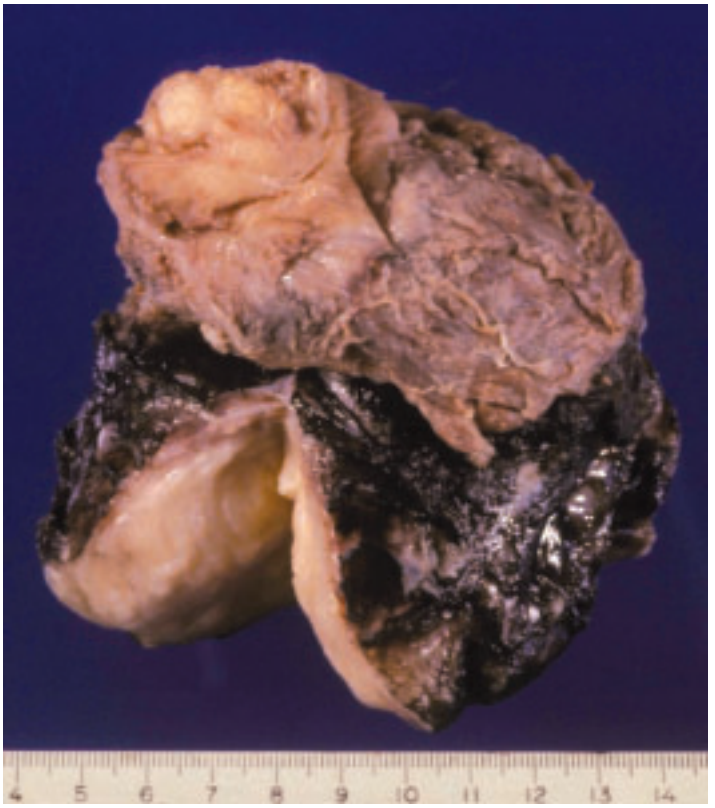

7-31. Malignant fibrous histiocytoma of the prostate gland grossly mimics cancer of the prostate gland.

7-32. Inflammatory fibrous pseudotumor of the scrotum. Without histology, the mass could be mistaken for a true tumor.

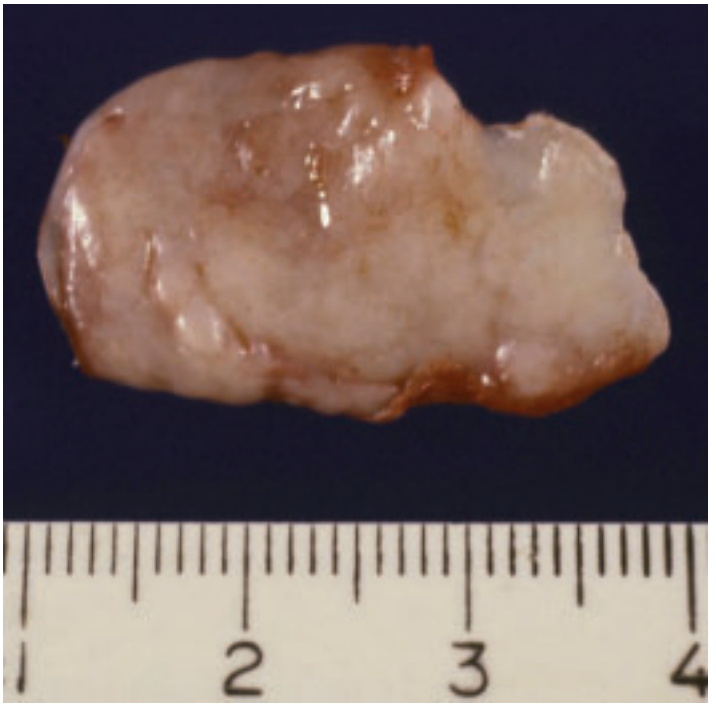

8 Bones and Joints

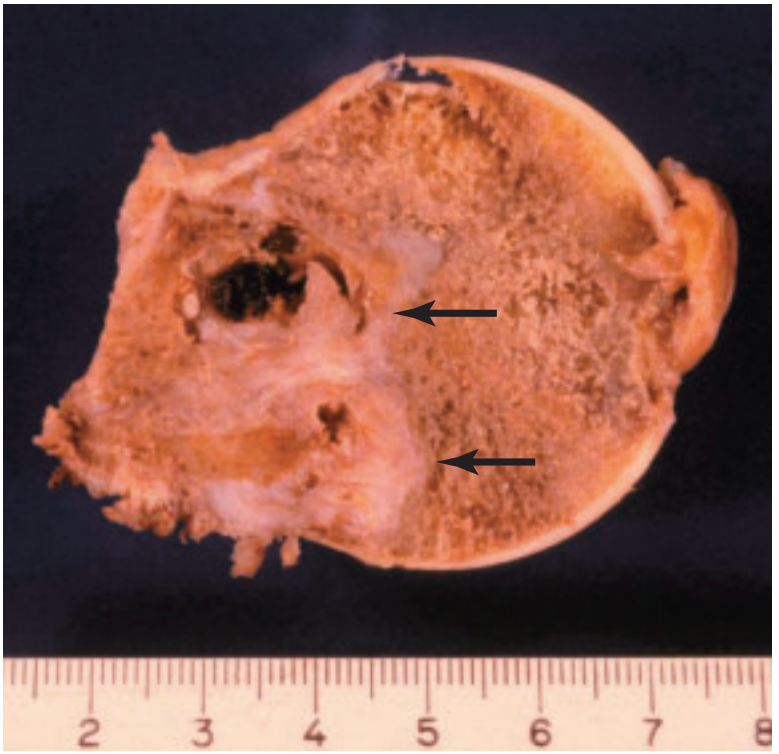

8-1. Head of femur shows a line of irregular fibrocartilaginous callus (*arrows*) consistent with a nonunited fracture of the head.

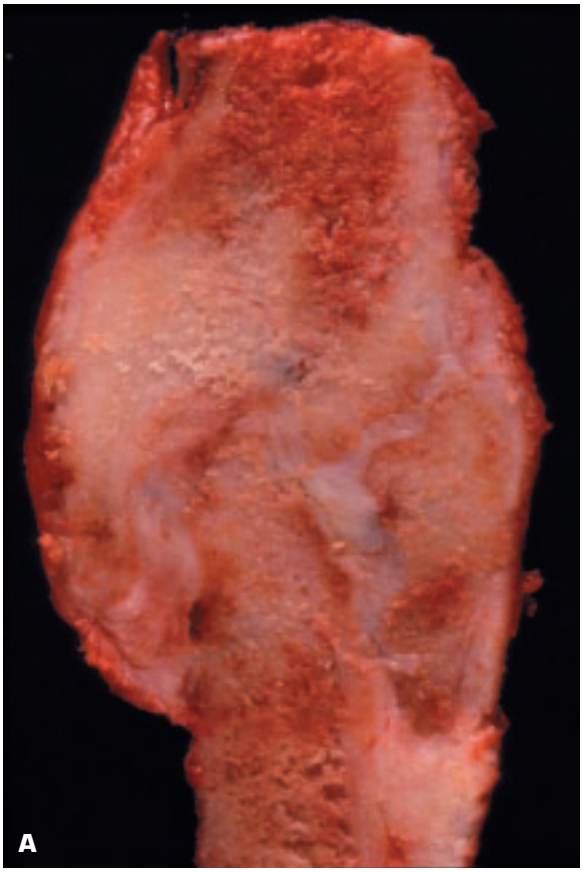

8-2. A. Nonunited fracture of the tibia that allowed movement at this site (i.e., a pseudoarthrosis is present). **B.** Appearance of fibrous tissue separating the fractured ends of the bone.

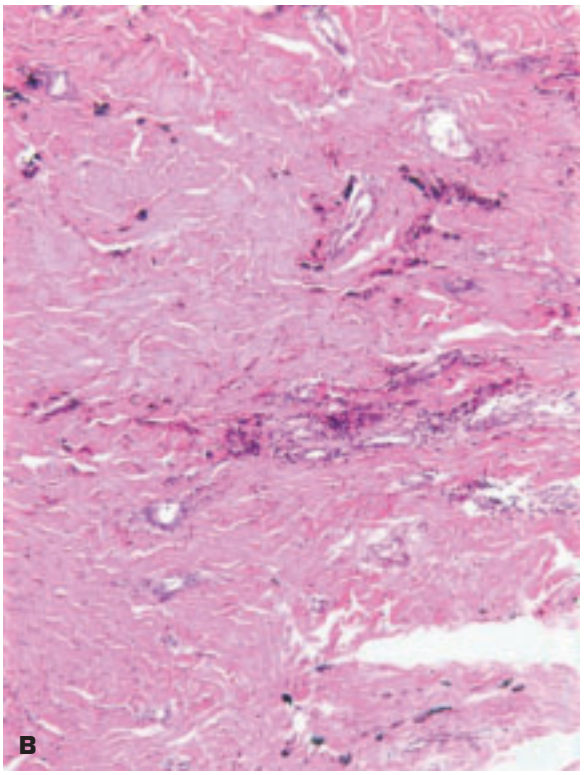

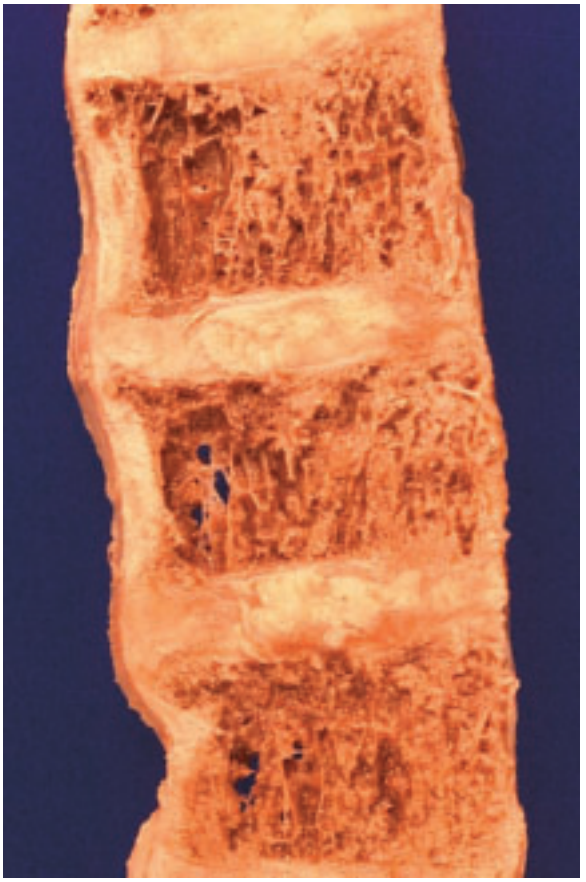

8-3. Osteoporosis of the vertebrae. A jet of water has been used to drive out most of the bone marrow, revealing a paucity of bony spicules.

8-4. Compression fractures of two vertebral bodies in a patient with osteoporosis.

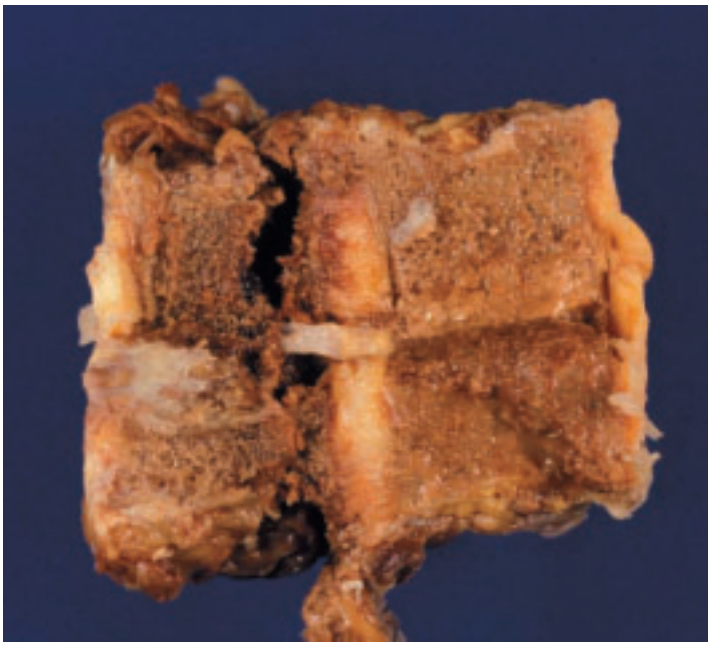

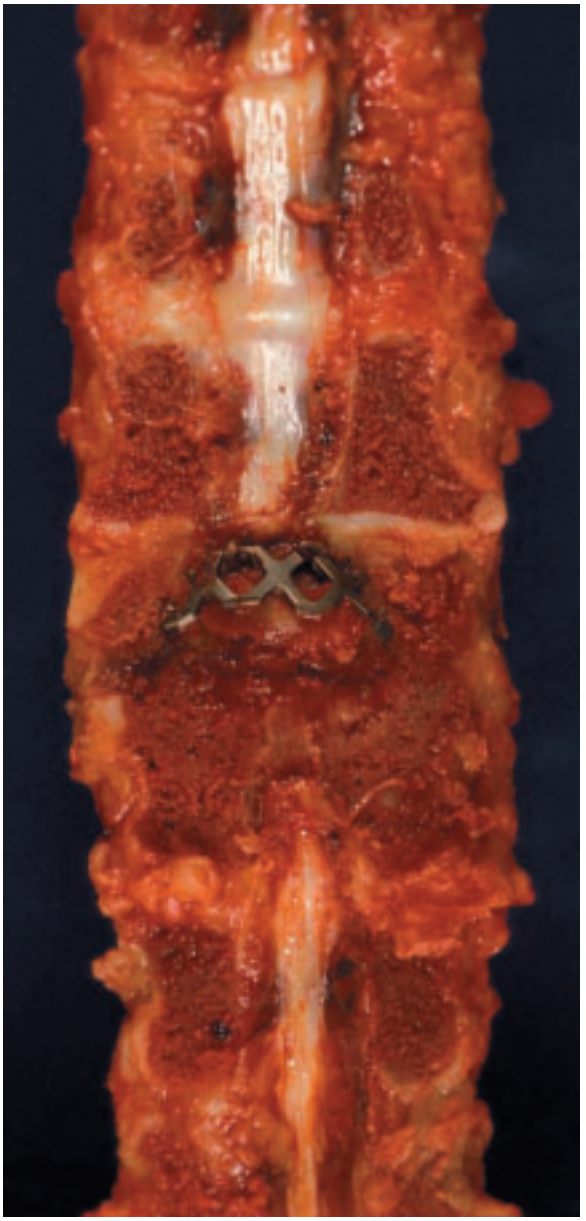

8-5. Orthopedic repair of vertebral fractures.

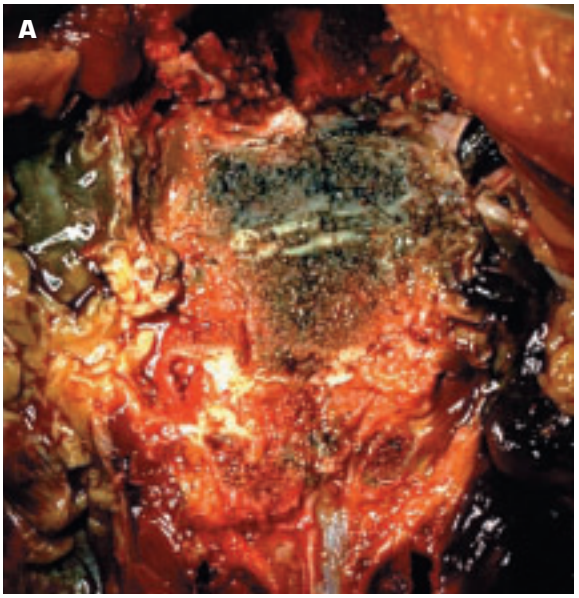

8-6. A. Osteitis of the lower lumbar vertebrae has produced a greenish discoloration of the affected bones, which have been transected obliquely. The greenish-colored material on the left of the picture is pus within a psoas abscess. **B.** Histology of osteitis shows necrotic bone (the sequestrum) lying within a sea of neutrophils. **C.** Dense new cortical bone has been laid down over the area of osteitis. *(continued on next page)*

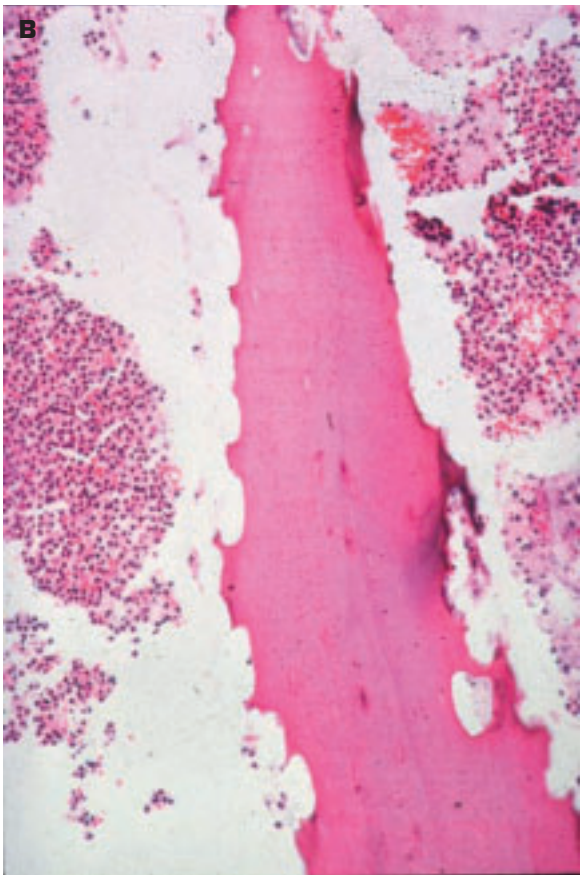

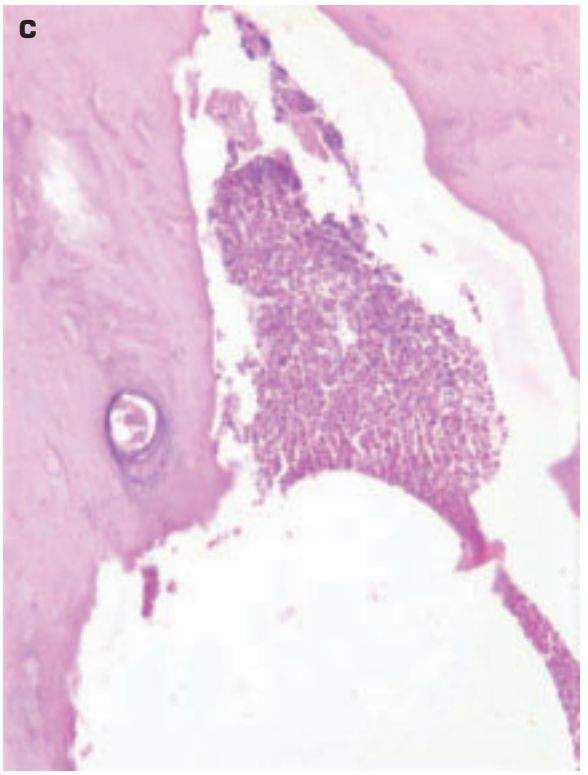

8-6. *(Continued)* **D.** Appearance of the psoas abscess prior to sectioning of the vertebral osteitis that gave rise to the abscess. **E.** Histology of the psoas abscess shows destruction of skeletal muscle with a cavity in the muscle that is filled with polymorphonuclear leukocytes (neutrophils).

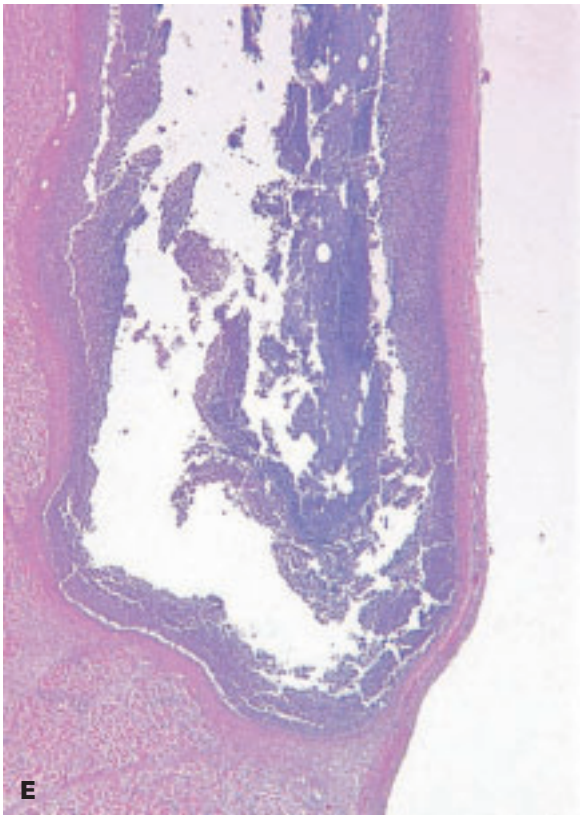

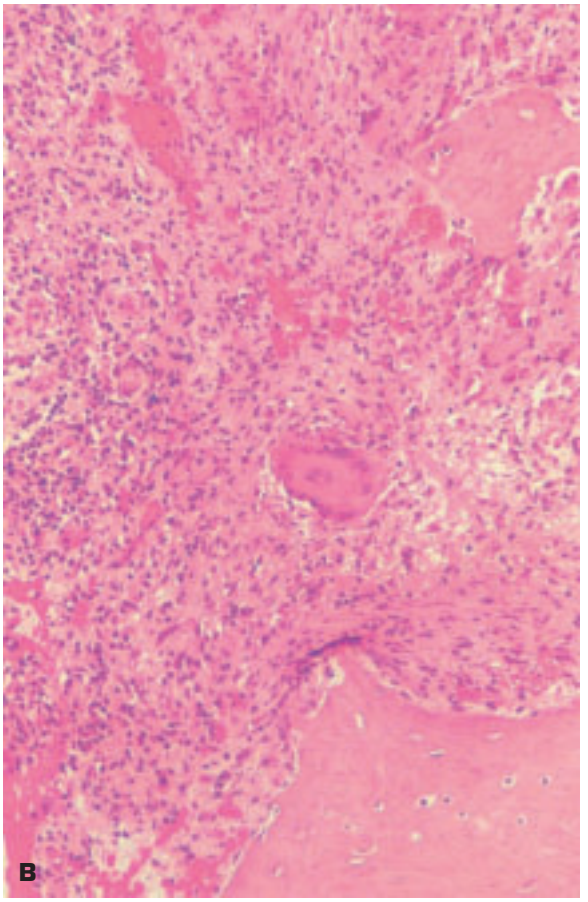

8-7. A. Tuberculous osteitis has produced a pathological fracture of a vertebra. The tuberculous infection is spreading as a "cold abscess" (due to absence of signs of acute inflammation) in the psoas muscle sheath to the left of the vertebrae in the picture. **B.** Histology shows active tuberculosis with bony fragments lying within the chronic inflammation. A single Langhans giant cell is present in the center of the field.

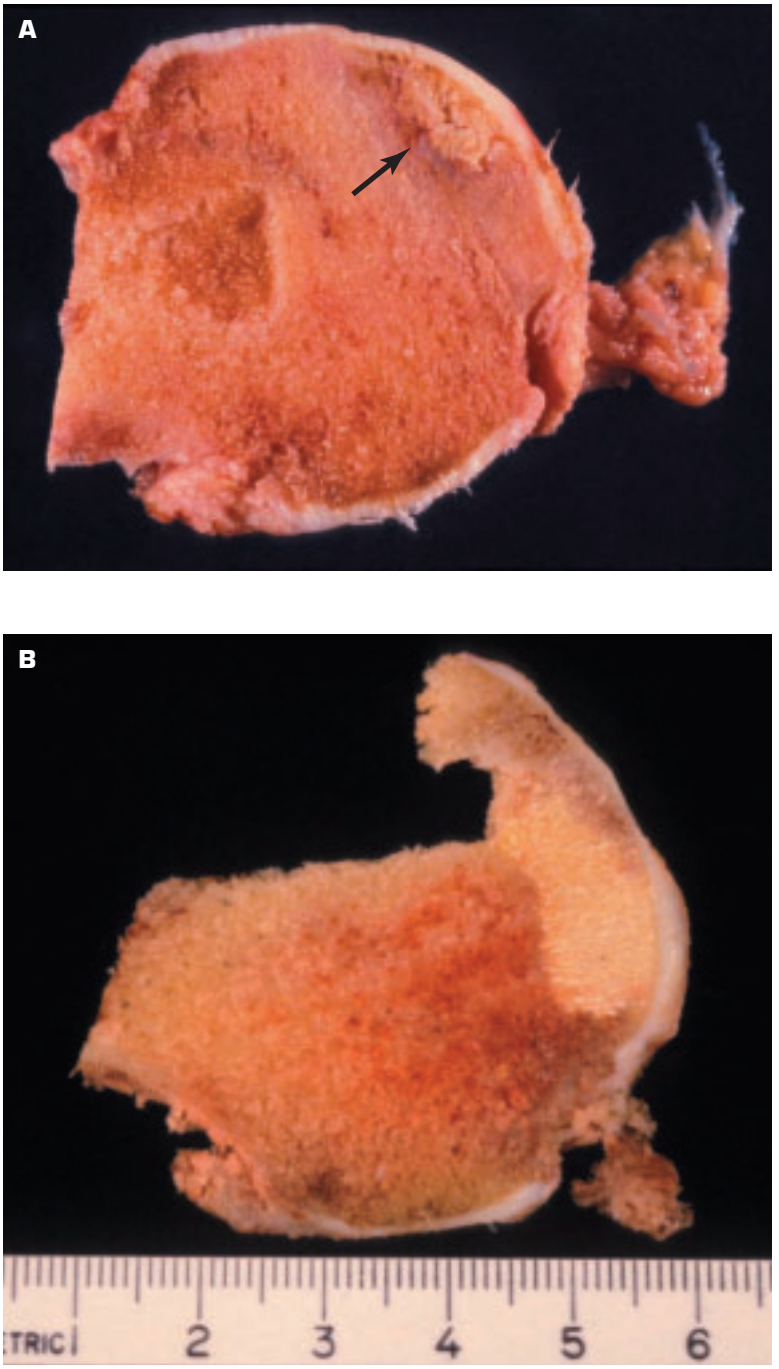

8-8. A. Aseptic necrosis of the femoral head. Most of the head is necrotic, but the necrosis is best appreciated in the local yellow area (*arrow*). **B.** Another level of the same head shows a wider area of recognizable necrosis just under the cartilage layer.

8-9. Infarction of the bone marrow in the lower end of the femur due to steroid therapy in an organ transplant recipient.

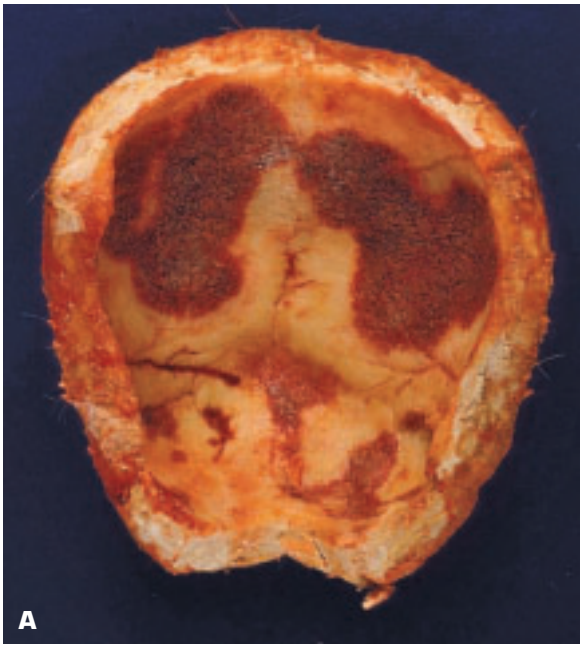

8-10. Osteopetrosis is an inherited defect in bone resorption due to inadequate osteoclastic function. This leads to abnormally dense but fragile bones that easily fracture. **A.** Osteopetrosis of the skull bone showing thickened, extremely dense bone devoid of any marrow cavity. Focal vascularization of the subperiosteal bone due to extramedullary hematopoiesis is noted. **B.** Close-up view of the hyperdense bone. *(continued on next page)*

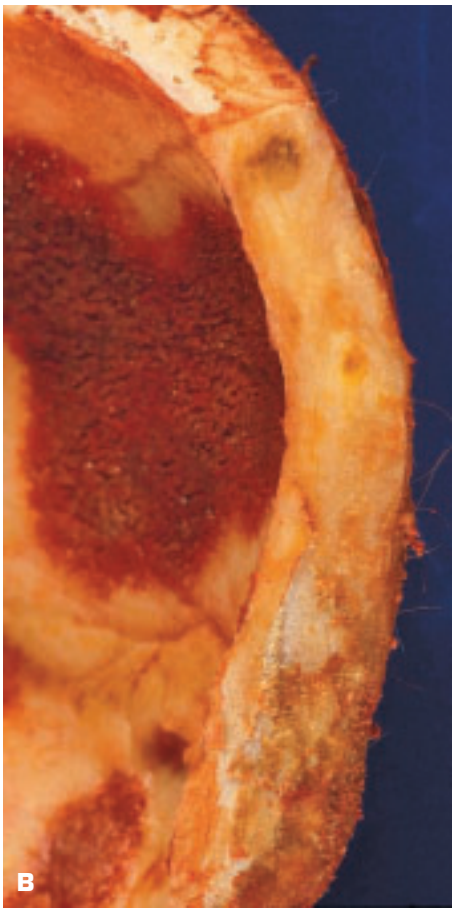

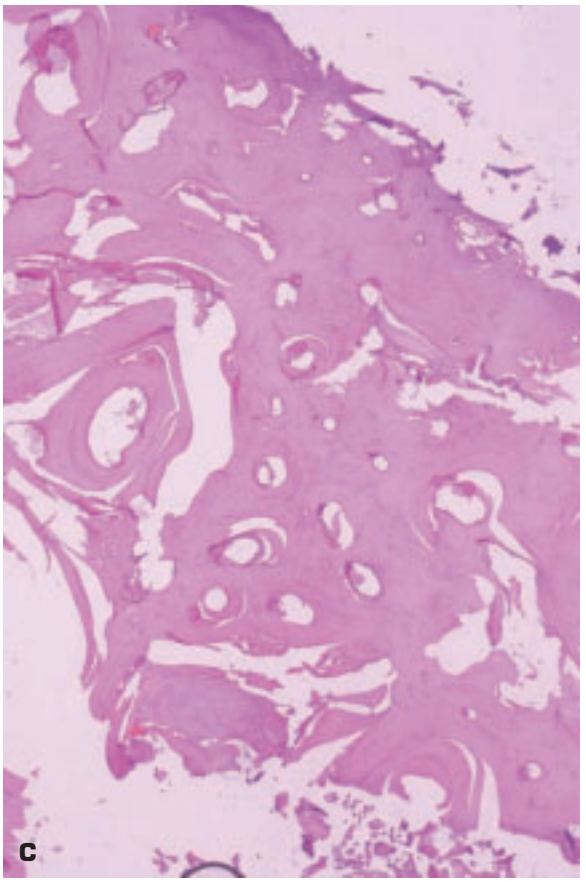

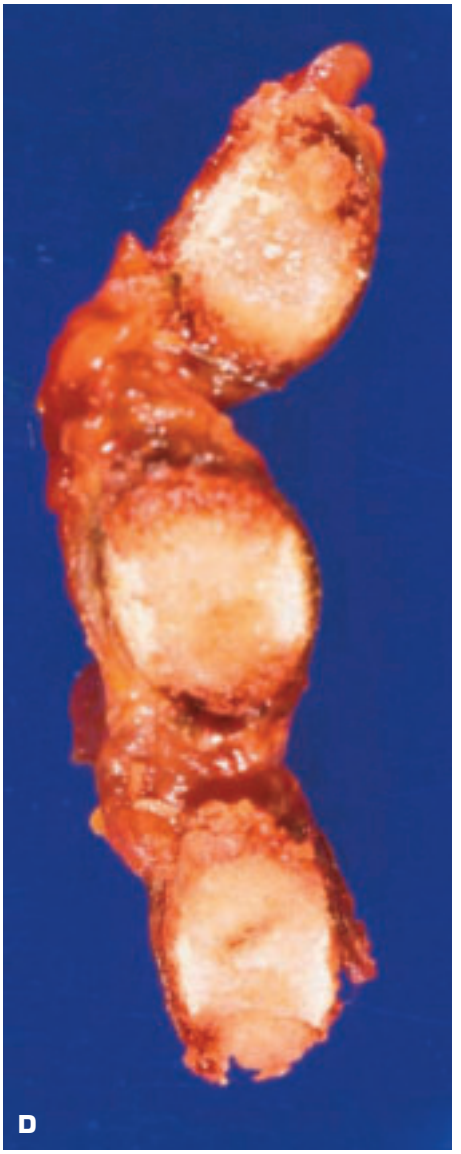

8-10. *(Continued)* **C.** Histology shows the full thickness of the bone to be comprised of dense, cancellous bone, only with no bone marrow. **D.** The ribs show similar features in cross-section.

8-11. Craniofacial dysostosis (Crouzon syndrome) leads to premature closure of sutures between the skull bones. Note the protruding eyes due to unusually shallow eye sockets. The ears are also low slung.

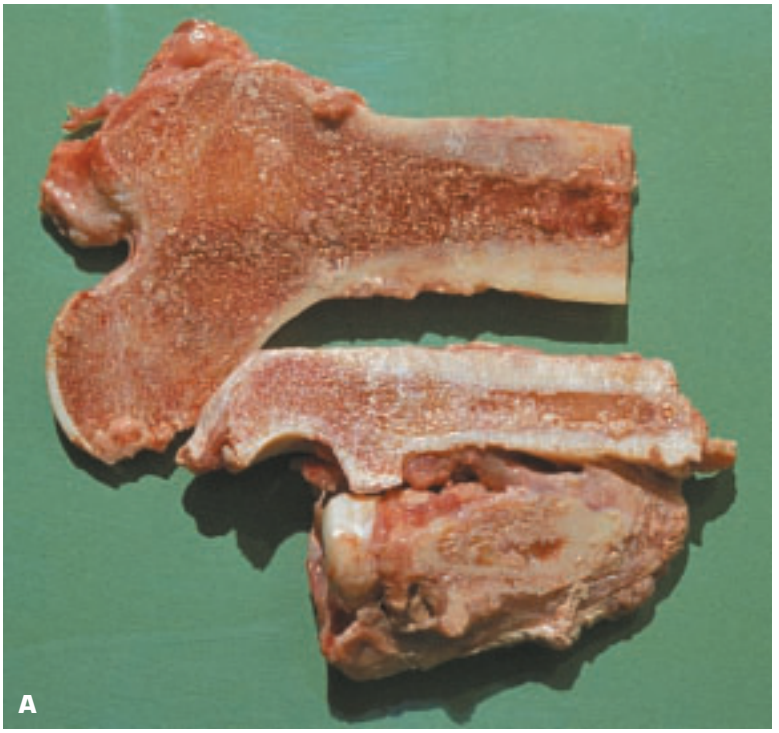

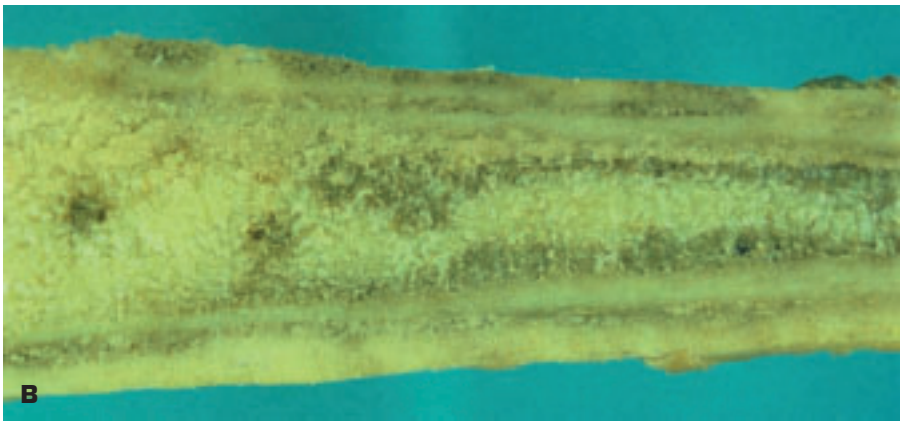

8-12. Hypertrophic osteoarthropathy associated with lung cancer. **A.** Proximal shaft of femur (*top*), proximal ulna bone (*middle*), and proximal radius bone all show additive subperiosteal ossification. **B.** The subperiosteal new bone is clearly evident as an additional layer of bone surrounding the original cortical bone of the shaft of this femur. *(continued on next page)*

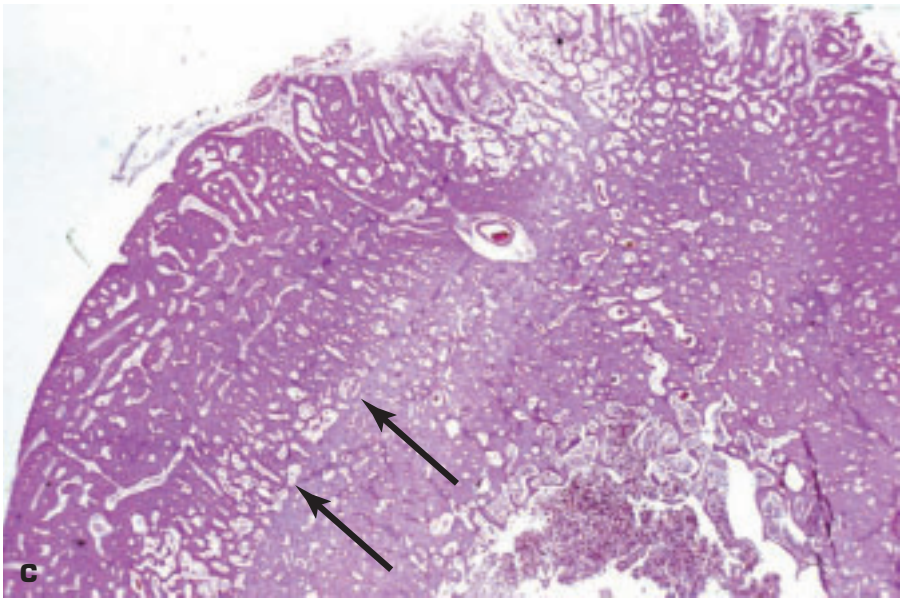

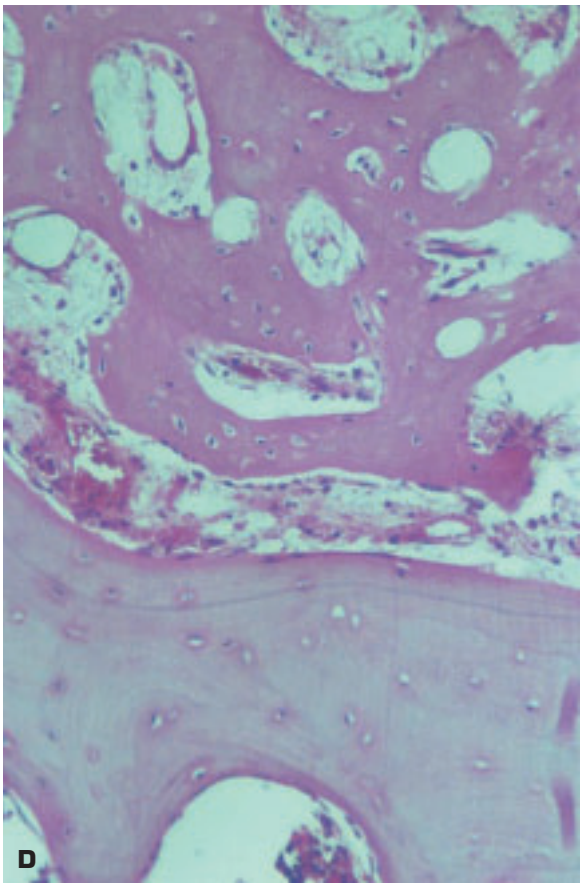

8-12. *(Continued)* **C.** Histology shows the outer new bone (*arrows*) to have a darker color than the underlying original cortical bone. This contrast is more evident in the left-hand side of the picture. **D.** Close-up histology shows the outer new bone (*top*) to be darker staining and to have thinner bony trabeculae.

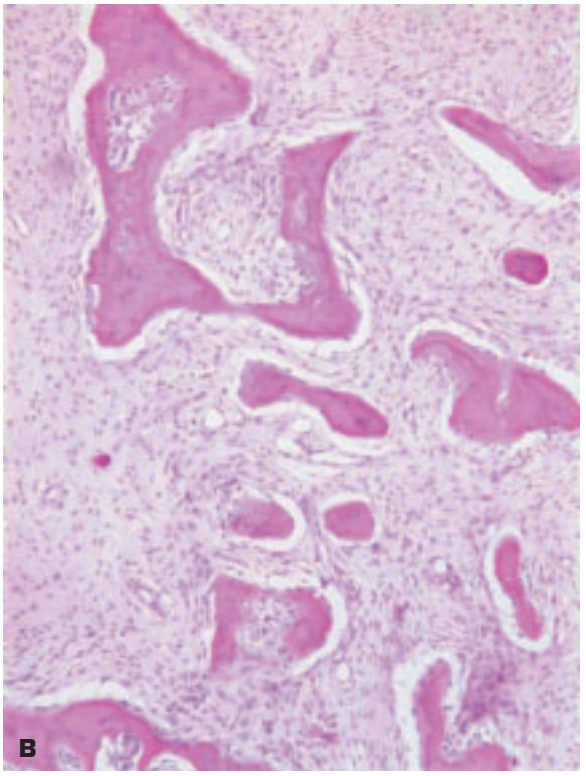

8-13. A. Expanded and distorted outline of a rib due to fibrous dysplasia. **B.** Histology of fibrous dysplasia shows irregularly shaped, acutely angled trabeculae (so-called Chinese letters) of woven bone lying in a fibrous stroma without any osteoblastic rimming.

8-14. Osteoma is a benign tumor of bone that occurs most often on the skull and facial bones. **A.** This osteoma is arising as a sessile, semicircular-shaped, bony mass on the surface of this skull bone. Multiple osteomas occur in Gardner syndrome. **B.** Osteoid osteoma is a small, often painful, osteoma that usually arises within one of the leg bones. X-ray of the tibia shows a central radiolucent zone surrounded by denser, less radiolucent bone. *(continued on next page)*

8-14. *(Continued)* **C.** Macroscopic appearance of an osteoid osteoma shows a central bony nidus within a small cavity. **D.** Histology shows the central osteoid osteoma (X) to be composed of more delicate, densely arranged bony lamellae than the surrounding bone, which shows reactive thickening around the lesion. The lesion is painful due to the constraint on its growth expansion.

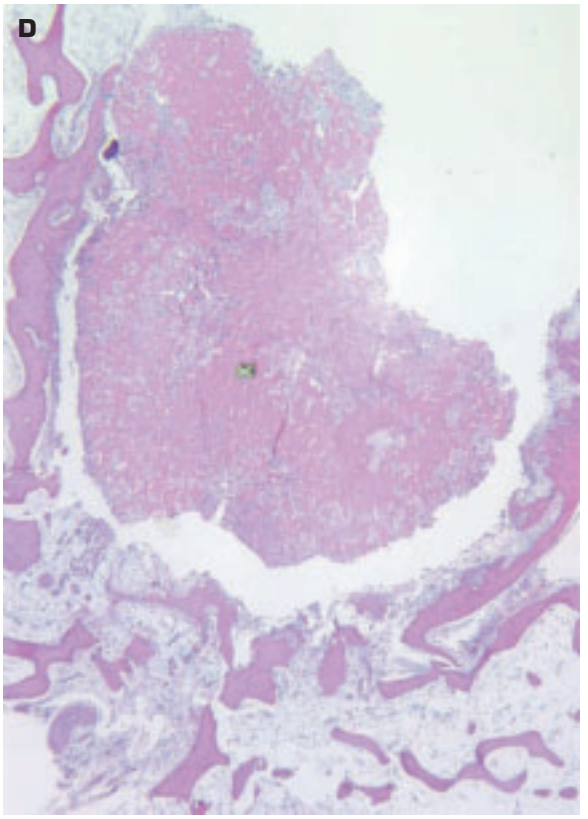

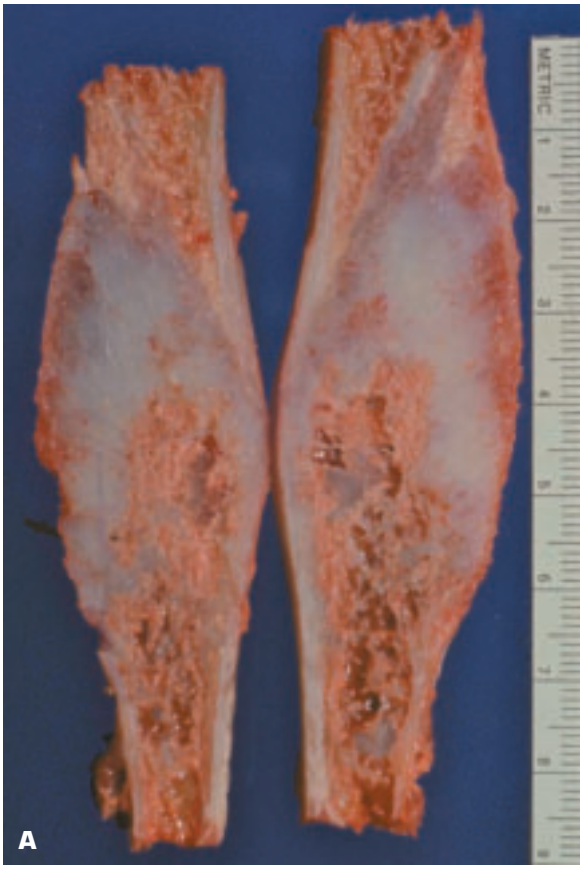

8-15. A. Enchondroma of the fibula is seen as contiguous islands of clearly recognizable cartilage within the substance of the bone. **B.** Histology shows the enchondroma to be composed of well-differentiated, mature-looking cartilage.

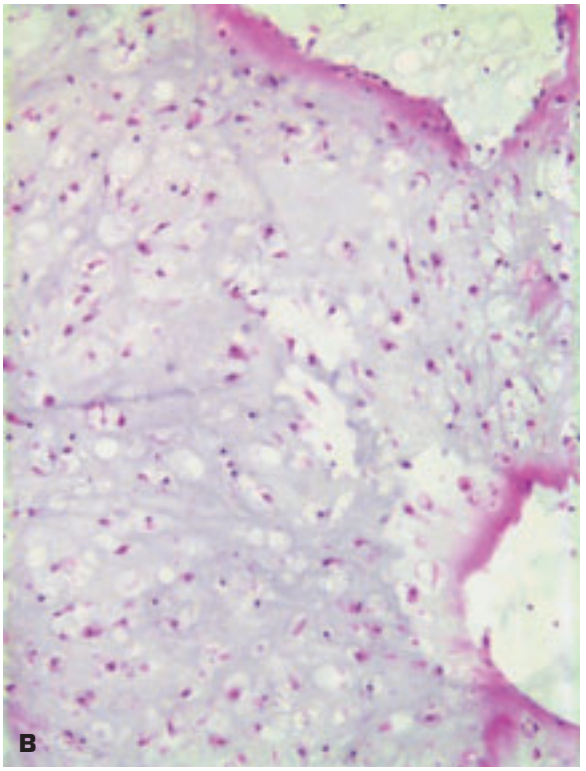

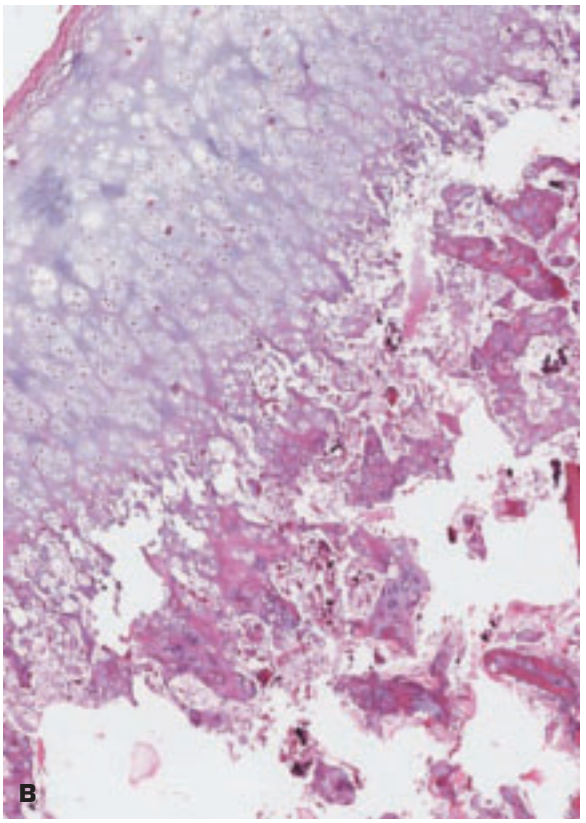

8-16. A. Osteochondroma (cartilage-capped exostosis) is a hamartoma that develops at the ring of Ranvier of the growth plate. The new bone growth occurs laterally instead of toward the metaphysis. **B.** Histology shows endochondral ossification is occurring under the cartilage cap.

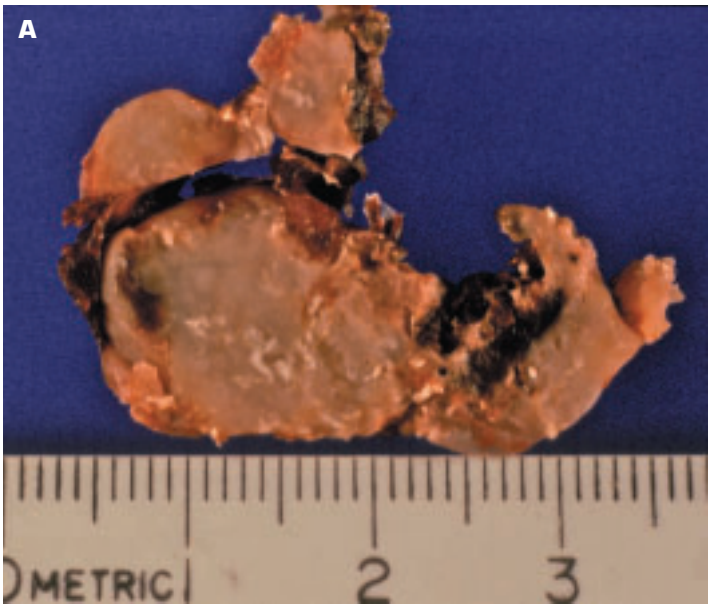

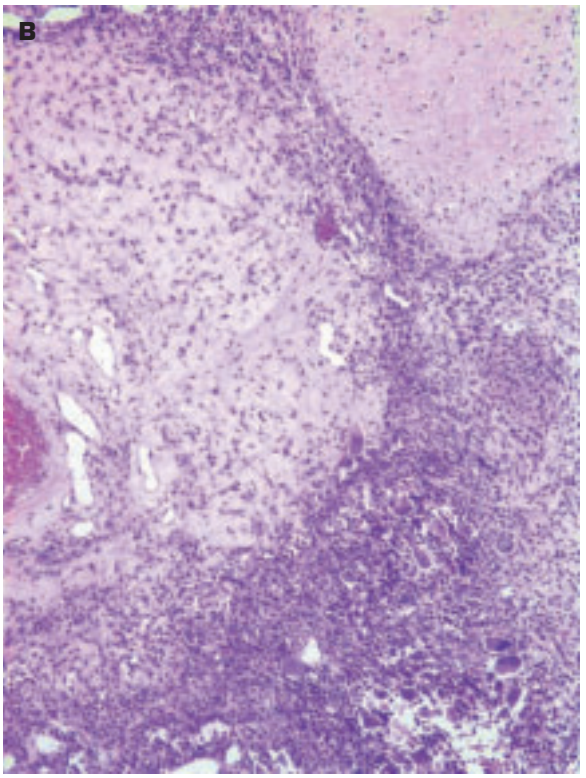

8-17. A. Surgically excised chondromyxoid fibroma comprises a firm, lobulated, yellow-gray tumor. **B.** Histology shows a cellular tumor composed of mononuclear and multinucleated giant cells in a myxoid and/or chondroid stroma.

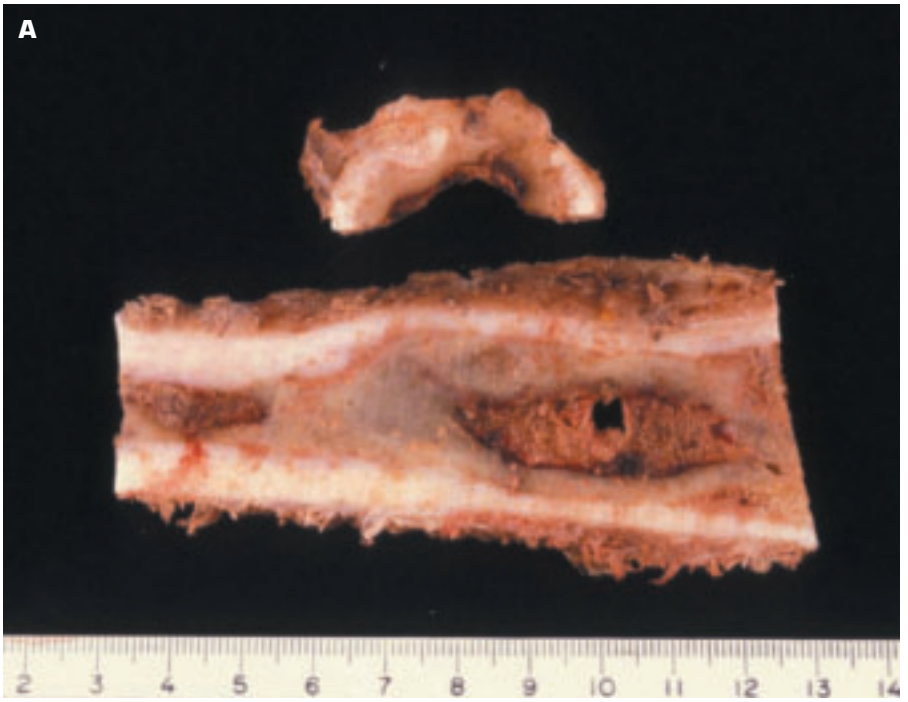

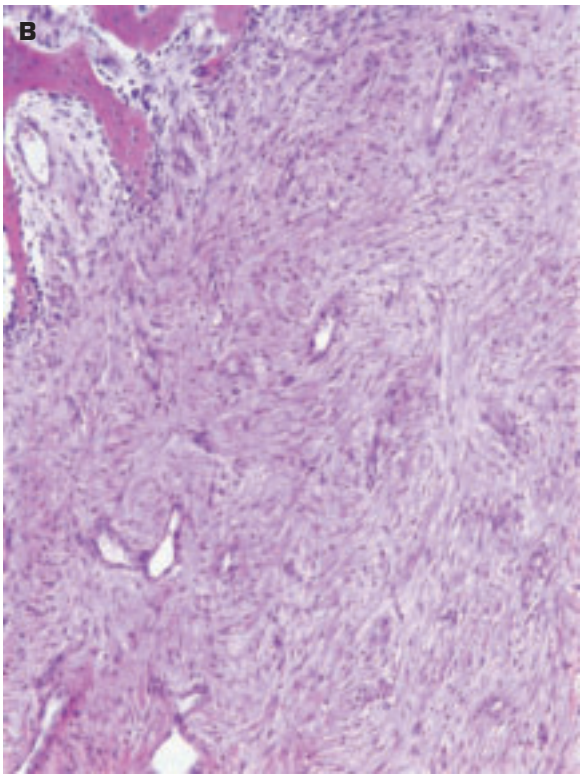

8-18. A. Nonossifying fibroma (metaphyseal fibrous defect) of bone is one of the more common benign tumors of children and adolescents. It comprises mainly fibrous tissue and occurs in the metaphysis of a long bone (e.g., the tibia), as in this patient. In the transverse section of bone (*top*), the lesion has penetrated the cortical bone. The usual treatment is curettage and bone grafting. The lesion may resolve spontaneously at skeletal maturity, but it may predispose to bone fracture. **B.** Histology shows that cortical bone has been replaced by mature fibrous tissue containing fibroblasts. Osteoclasts may also be present in some cases.

8-19. Aneurysmal bone cyst. **A.** Aneurysmal bone cyst has led to eccentric expansion of the fibula by a clotted, blood-filled cavity that also includes areas of solid tissue. The expanded bony cortex on the right has been reduced to a thin, brittle bony structure covering the lesion. The cause of the lesion is unknown but is believed to be related to a disturbance of the bony capillary network. In about 50% of cases, a preexisting tumor or other bone pathology may be present. **B.** Histology shows blood-filled spaces surrounded by fibroblasts and osteoclastic giant cells.

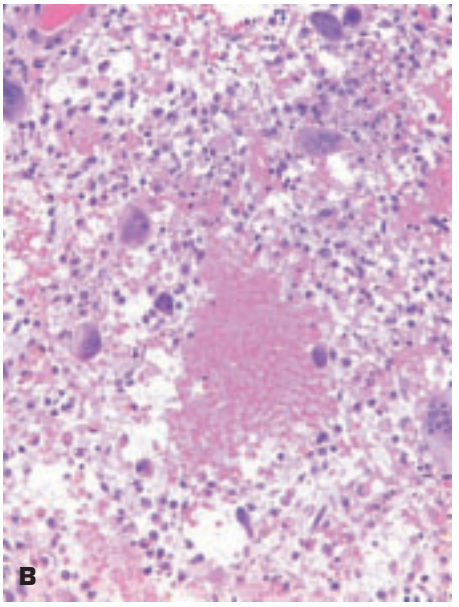

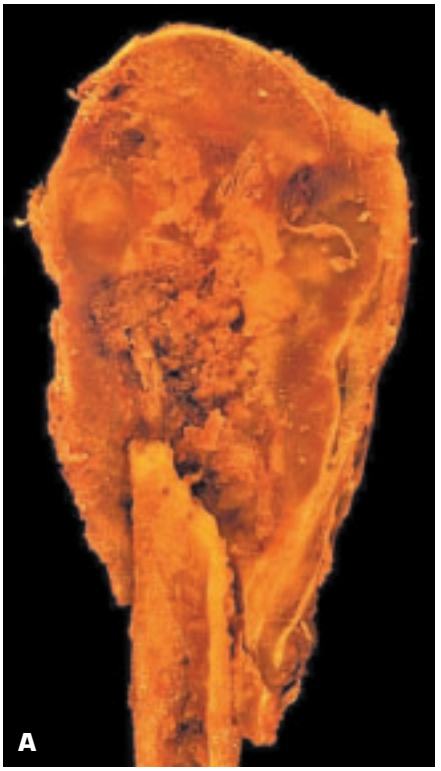

8-20. Giant cell tumor. **A.** Giant cell tumor (osteoclastoma) of the humerus has destroyed the epiphysis and the adjacent metaphysis, resulting in a pathological fracture. The tumor is invading the surrounding soft tissues. The tumor occurs after the age of 20 years and is more common in Asian women. **B.** Histology of giant cell tumor shows multinucleated giant cells of osteoclastic type, which are reactive in nature (i.e., not neoplastic), and the neoplastic stromal cells that have a plump, fibroblastic appearance.

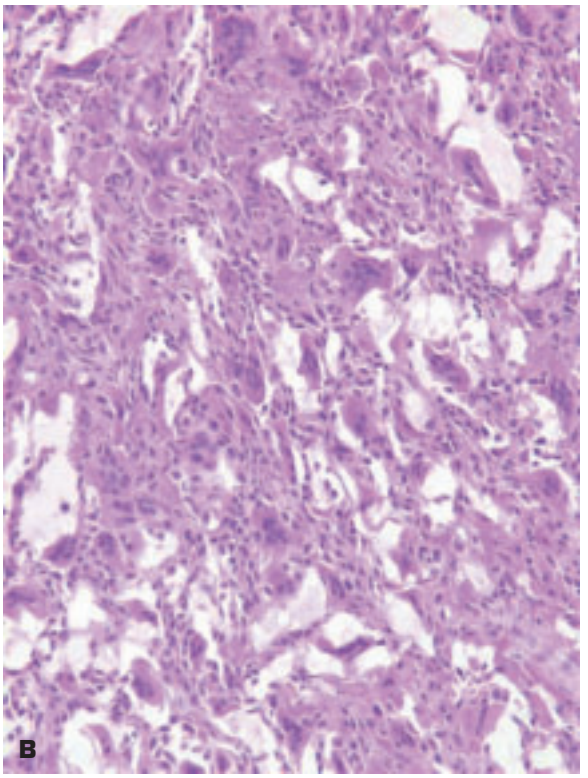

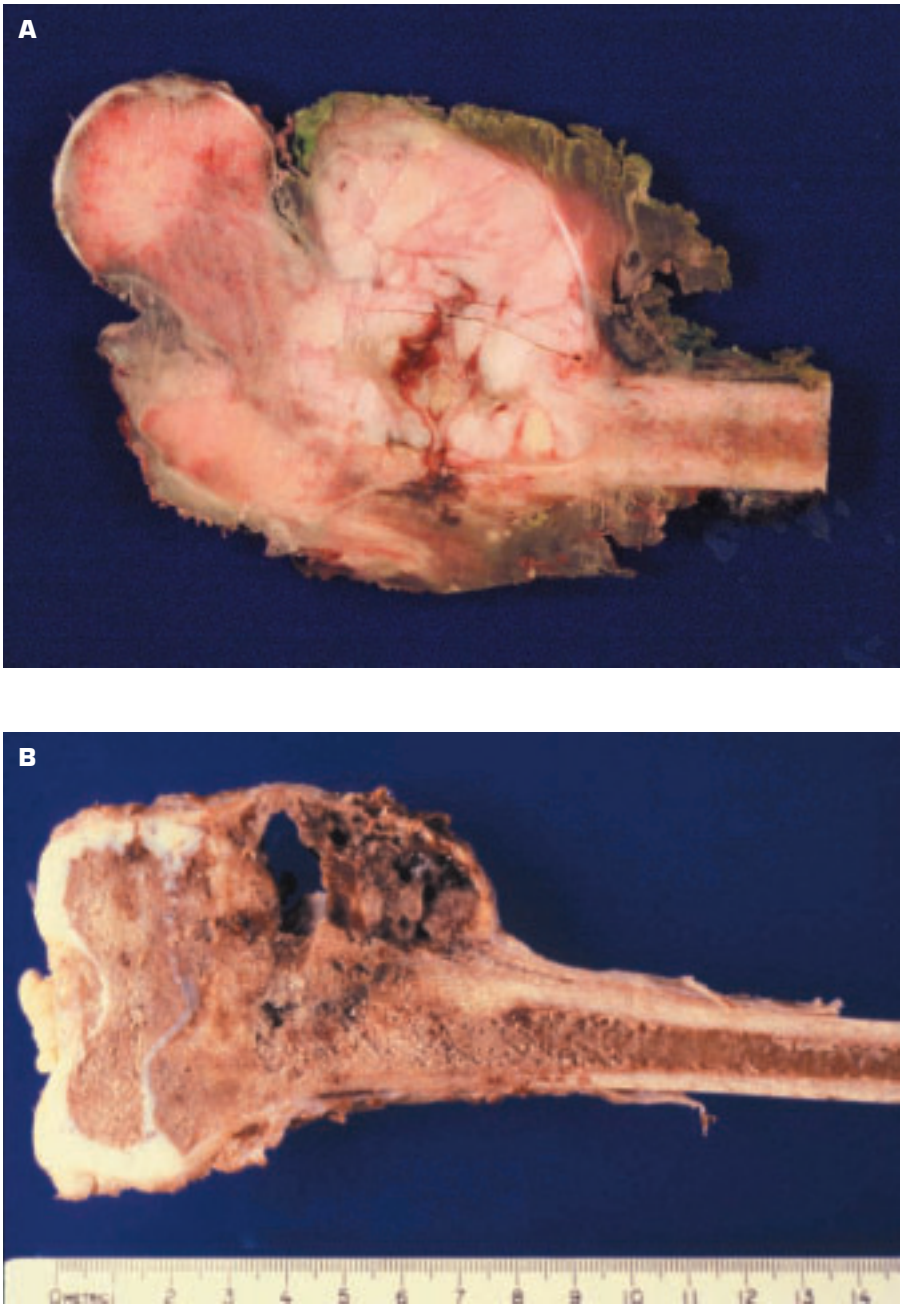

8-21. Conventional osteosarcoma. **A.** High-grade osteosarcoma of the upper femur has spread locally outside the bone. **B.** Osteosarcoma of the lower femur in a young child is invading through the epiphyseal plate (*left*). *(continued on next page)*

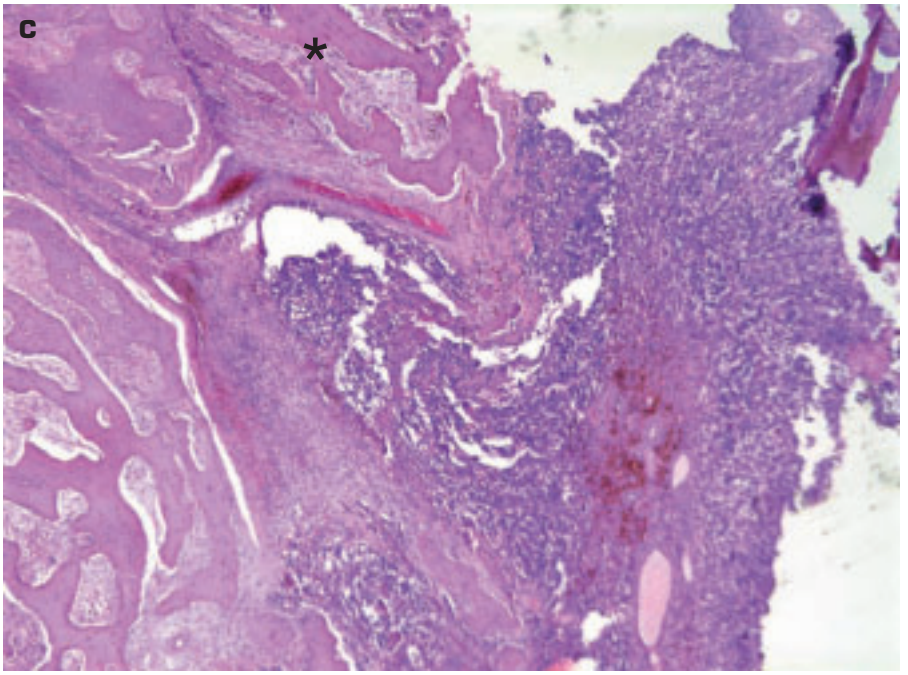

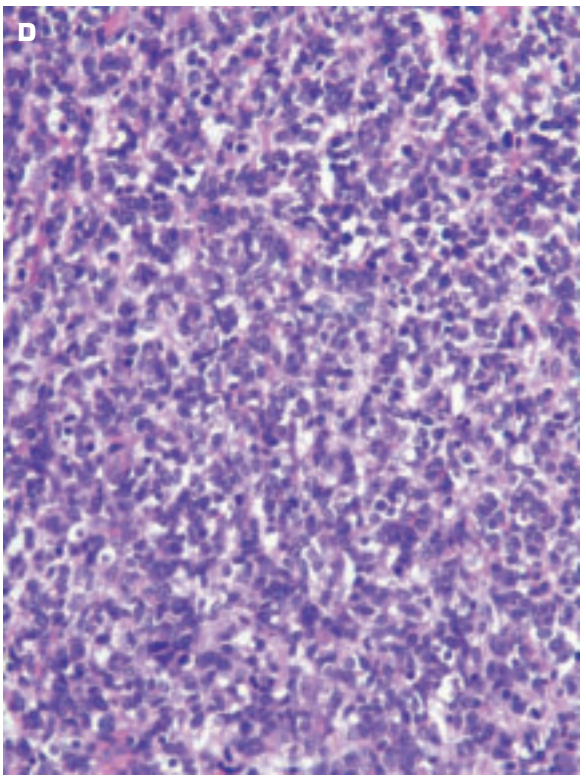

8-21. *(Continued)* **C.** A wedge-shaped tumor mass in Codman's triangle has elevated the periosteum, and new (nonneoplastic) bone is being laid down (*). **D.** Histology of the tumor shows a poorly differentiated osteosarcoma. *(continued on next page)*

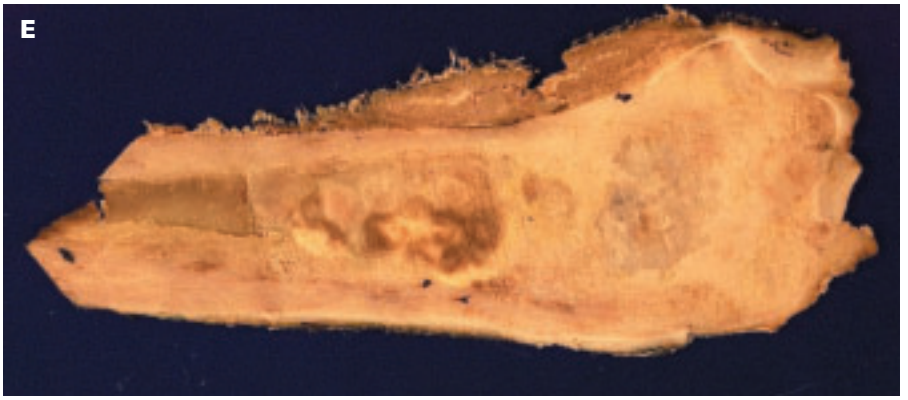

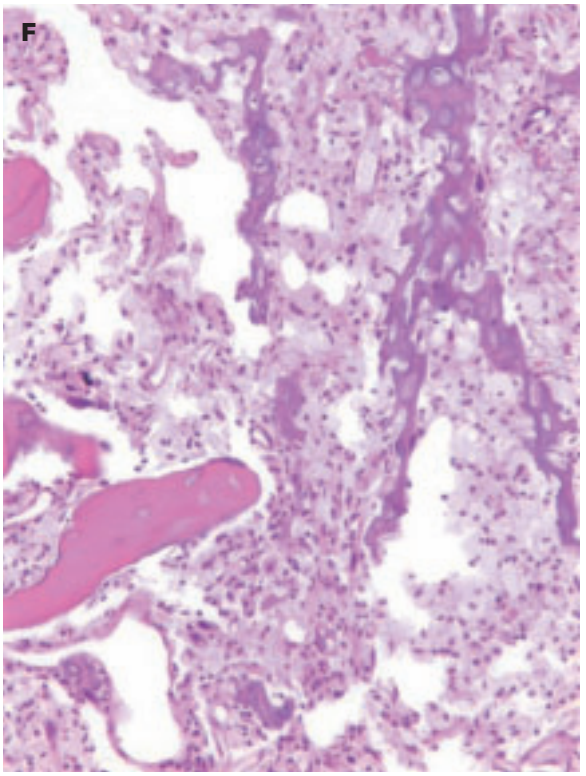

8-21. *(Continued)* **E.** Osteosarcoma of the tibia has undergone a therapy-induced regression, leaving only necrotic tumor. **F.** Histology of a postcytotoxic osteosarcoma shows no recognizable tumor tissue, only fibrosis and scanty residual tumor-derived osteoid (*right*).

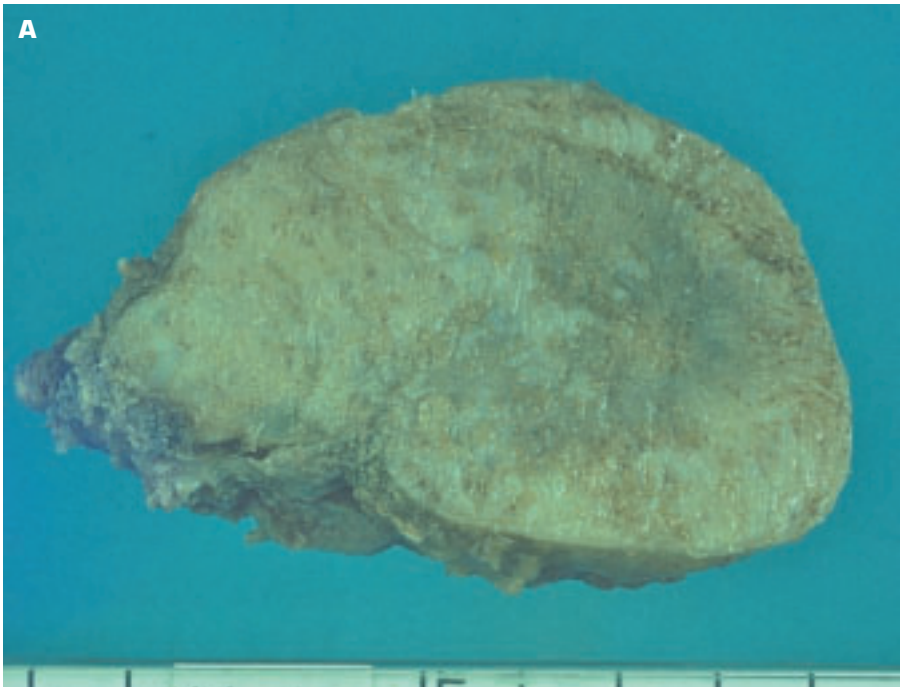

8-22. Juxtacortical (parosteal) osteosarcoma is a rare, slowly growing variant of osteosarcoma that often arises alongside the lower femur and may encircle the bone. **A.** Lobulated parosteal sarcoma that arose posterior to the lower femur in a young adult. **B.** Parosteal osteosarcoma is arising from the outer surface of the bone.

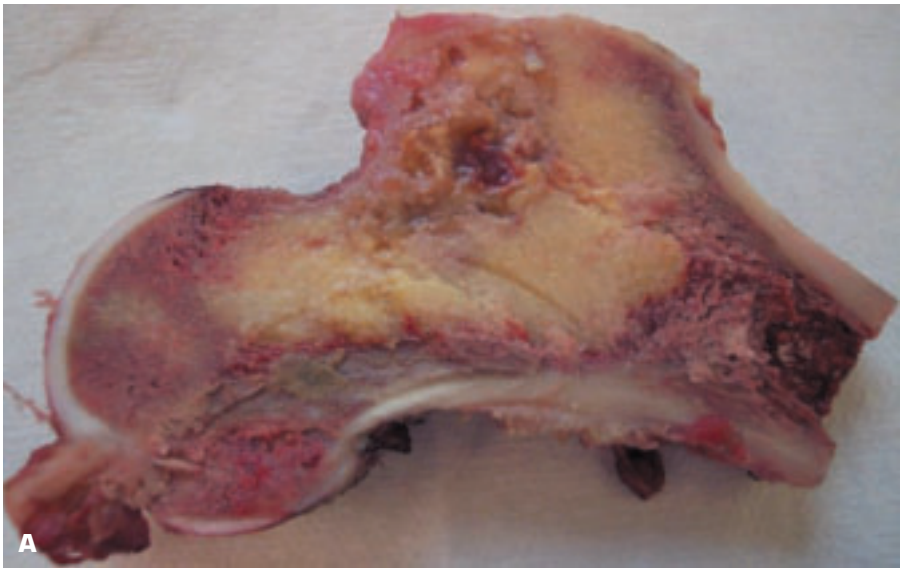

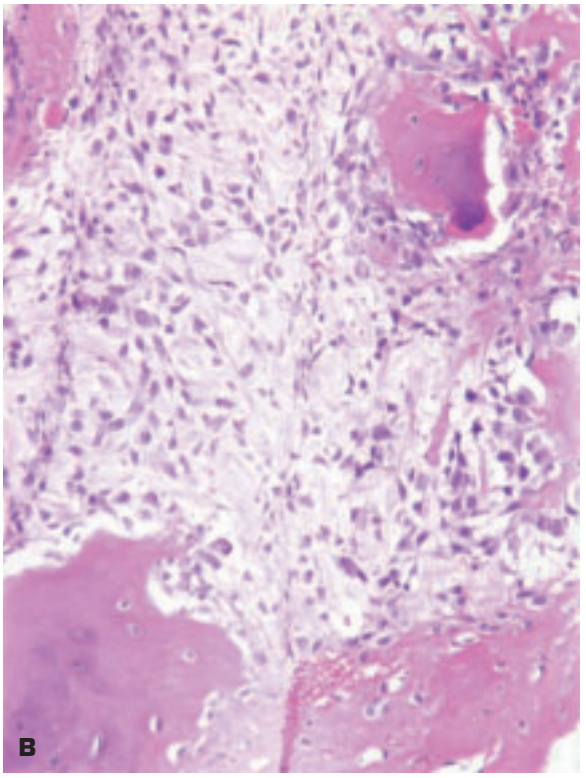

8-23. A. Well-differentiated, low-grade, intramedullary (intraosseous) osteosarcoma in head of femur. **B.** The lesion has a deceptively bland histologic appearance, but it does show both atypia and an infiltrative growth pattern with destruction of cortical bone.

8-24. A. Telangiectatic osteosarcoma is destroying the lower end of the femur and shows a prominent degree of vascularity and hemorrhage throughout much of the tumor. **B.** Unlike an aneurysmal bone cyst, this osteosarcoma shows malignant osteoblasts lining the blood-filled spaces.

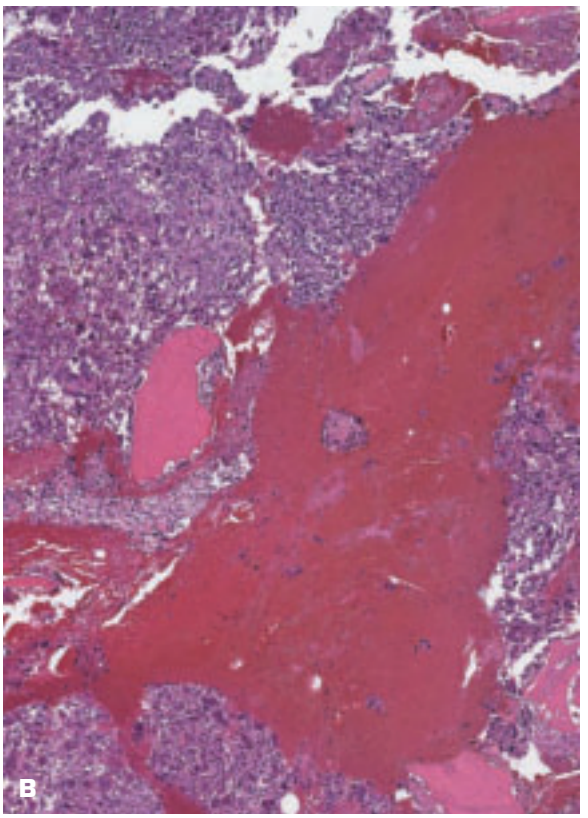

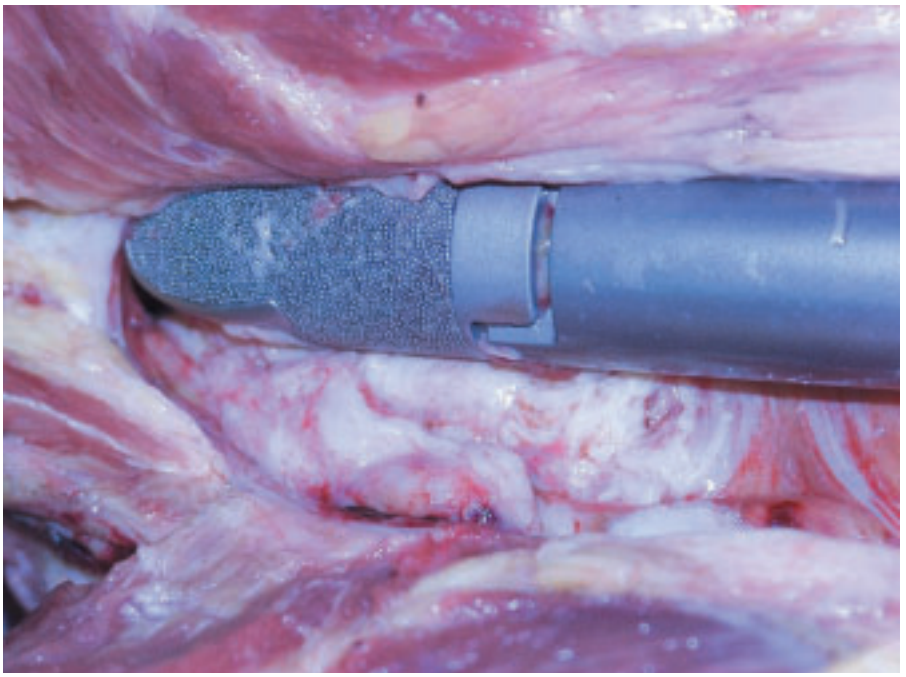

8-25. Recurrent osteosarcoma at the site of an implanted prosthesis that replaced the resected portion of the femur in a patient previously treated for an osteosarcoma.

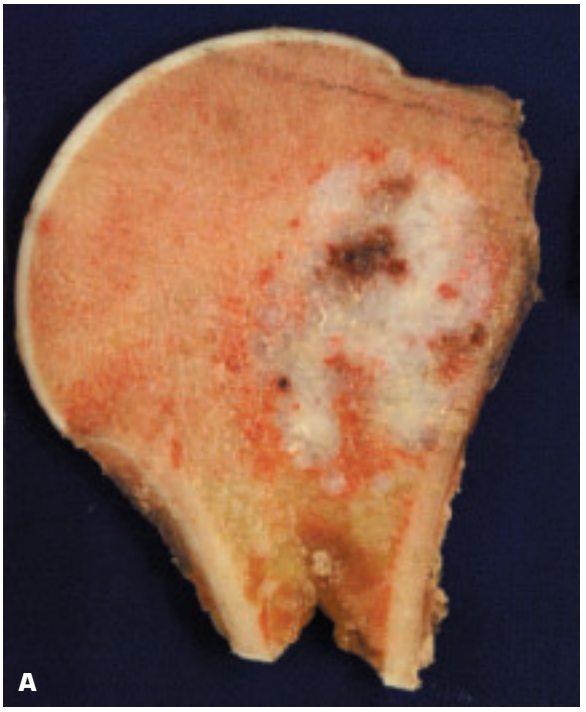

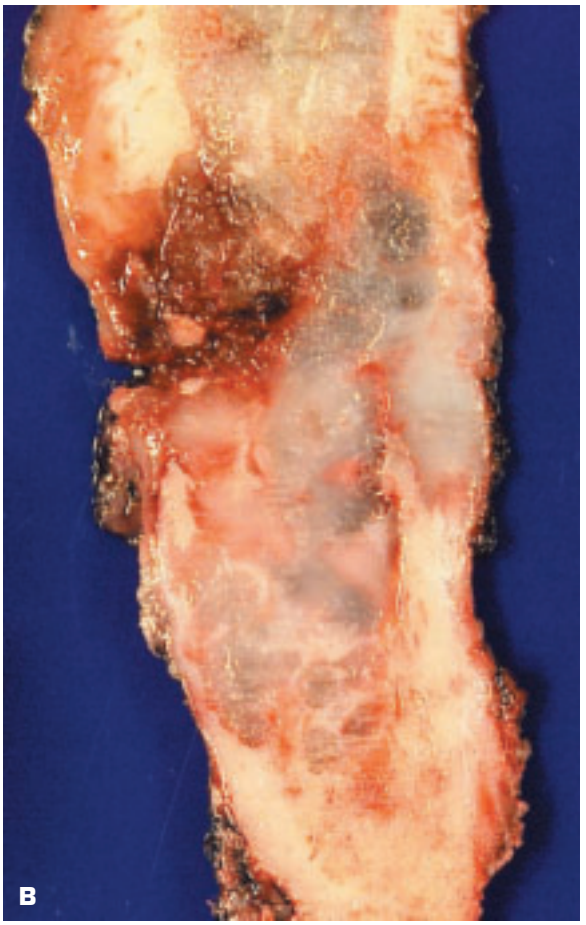

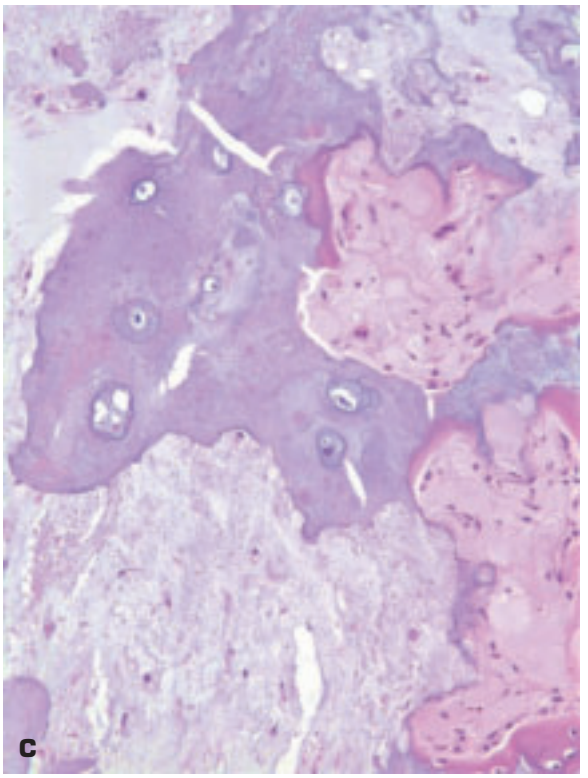

8-26. Chondrosarcoma. The cartilaginous nature of this malignant tumor of cartilage origin is clearly indicated in the macrophotographs. **A.** Low-grade chondrosarcoma within the head of humerus. **B.** This chondrosarcoma is extensively destroying the shaft of the humerus. **C.** Histologic appearance of a low-grade chondrosarcoma.

8-27. Fibrosarcoma of bone. **A.** This advanced fibrosarcoma of the humerus has extended into the soft tissues around the upper end of the bone. **B.** Typical histologic appearance of a fibrosarcoma.

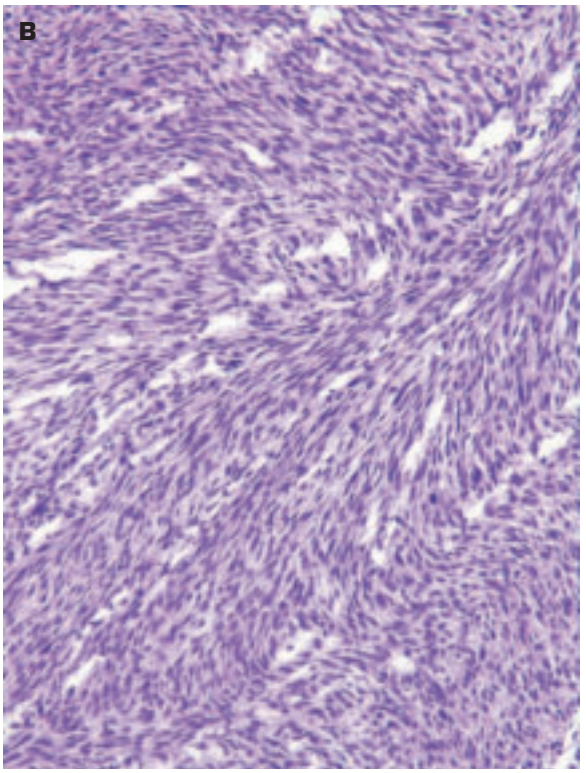

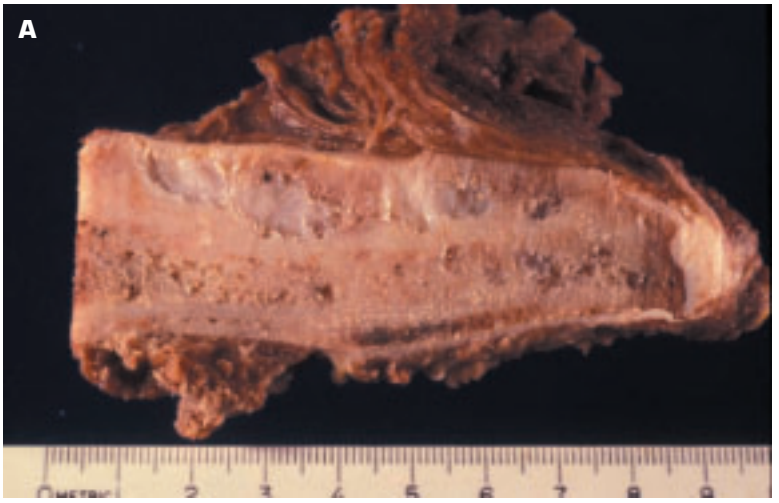

8-28. Ewing's sarcoma (primitive neuroectodermal tumor). **A.** This tumor has arisen within the marrow zone of the fibula and has spread through the cortex in areas. **B.** This tumor is arising in the lower femur, and the characteristic elevation of the periosteum is again evident (*arrow*). **C.** Histology of Ewing's sarcoma shows a neoplasm made up of small, dark-staining tumor cells having a very uniform appearance and filling the bone marrow space between bony trabeculae.

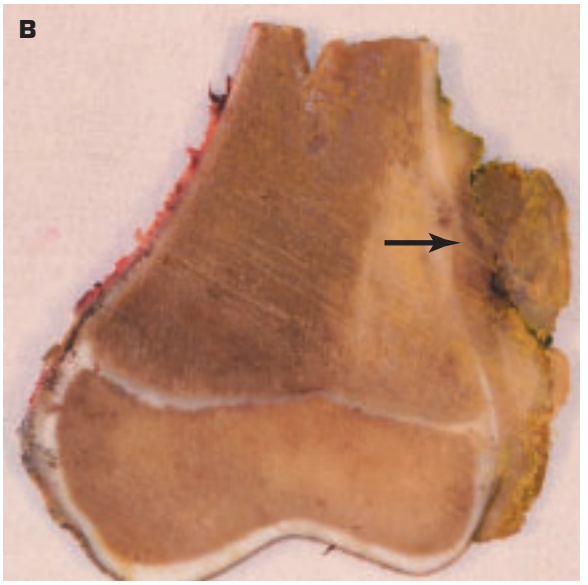

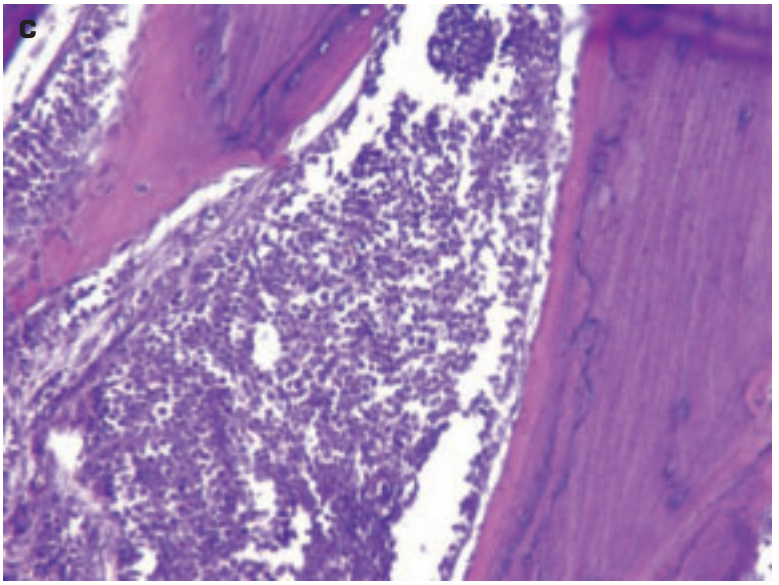

8-29. Malignant fibrous histiocytoma (MFH) has no distinguishing naked eye features but does not produce either bone or cartilage. This MFH is confined to within the femur but is eroding the cortical bone from within.

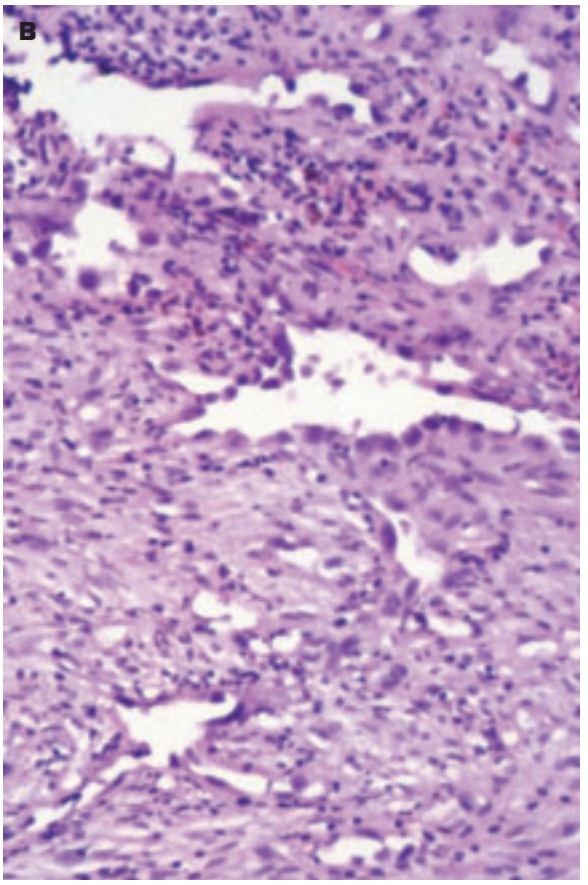

8-30. A. Angiosarcoma within bones of the ankle is seen as multiple highly vascularized, lytic lesions. **B.** Histology shows irregular vascular spaces lined by atypical-looking, hobnail-shaped endothelial cells. The lining cells will stain positively for CD31.

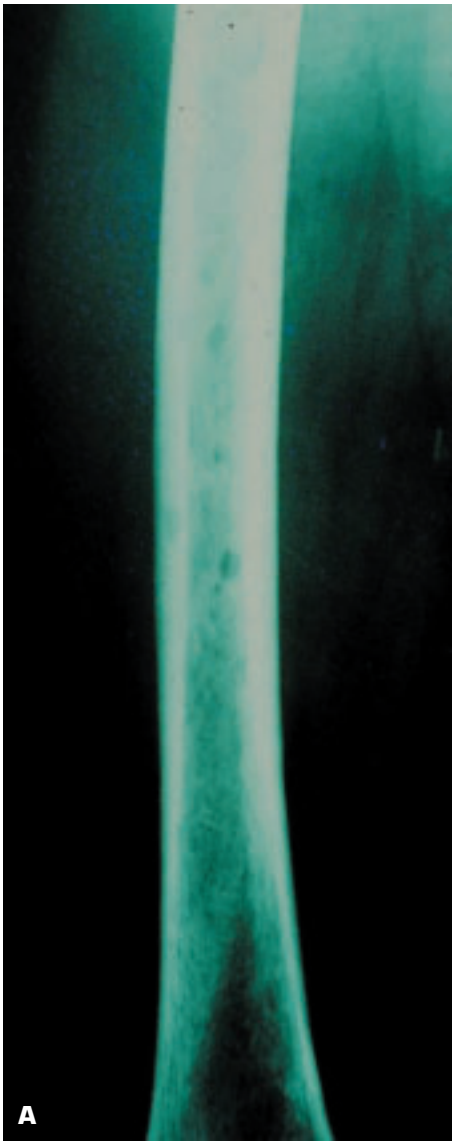

8-31. Multiple myeloma. **A.** X-ray shows multiple punched-out lytic lesions in the shaft of the femur. **B.** Plasmacytoma (*arrow*) in the head of the femur lies just under the articular cartilage, and adjacent hemorrhage is present. **C.** Multiple, rounded lytic lesions are discernible on the inner aspect of the skull bones. *(continued on next page)*

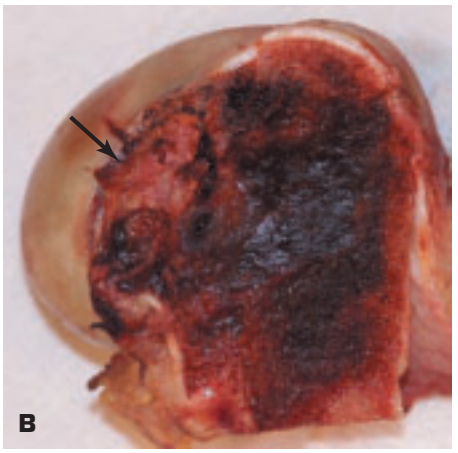

8-31. *(Continued)* **D.** Vertebral bodies contain metastatic myeloma. **E.** Histology of a well differentiated myeloma shows a proliferation of atypical-looking plasma cells, some of which are much larger than normal.

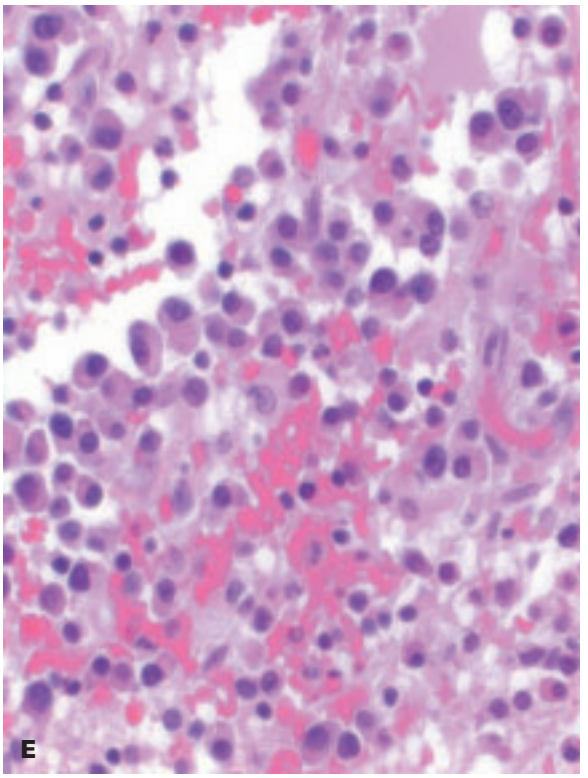

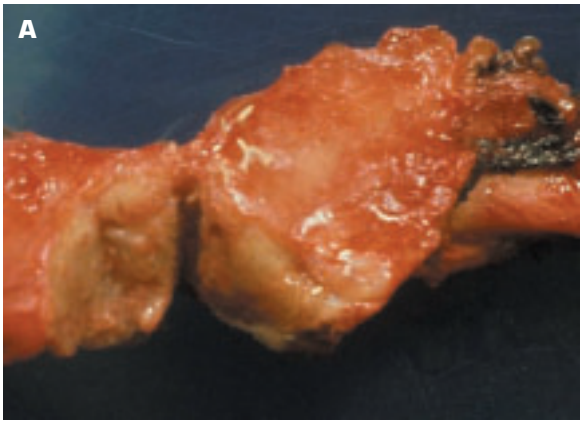

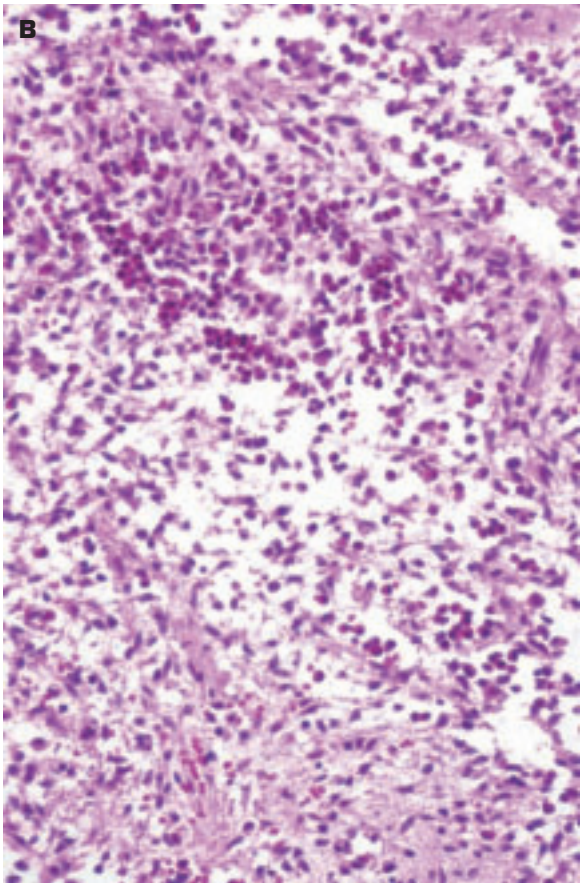

8-32. Langerhans cell histiocytosis (histiocytosis X). The lesion illustrated corresponds to so-called eosinophilic granuloma of bone. **A.** Transected rib shows an expansile, fleshy, yellow mass that has destroyed the bone at this site. **B.** Histology shows prominent eosinophils against a background of proliferating mononuclear cells (Langerhans cells). On electron microscopy, the latter cells contain the characteristic Birbeck granules.

8-33. Chordoma of the sacrum that is spreading into adjacent soft tissue shows the characteristic mucoid, gelatinous appearance of this tumor. Chordoma is believed to be derived from remnants of the primitive notochord.

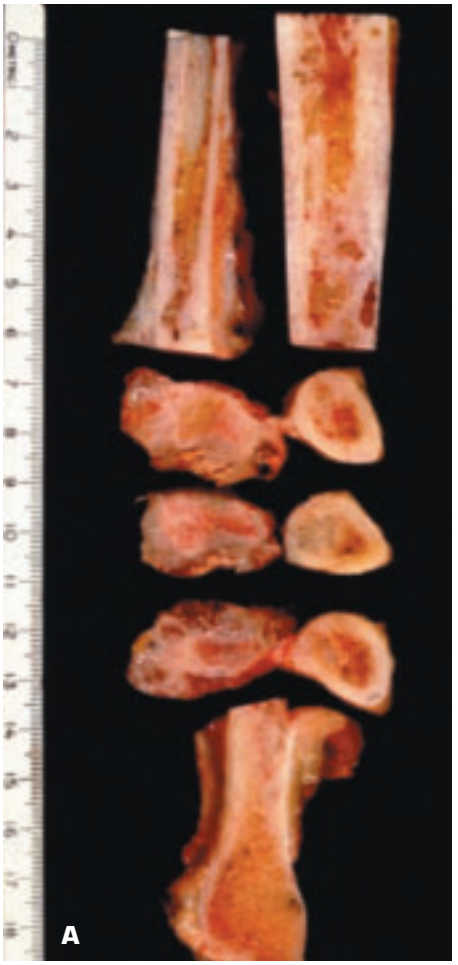

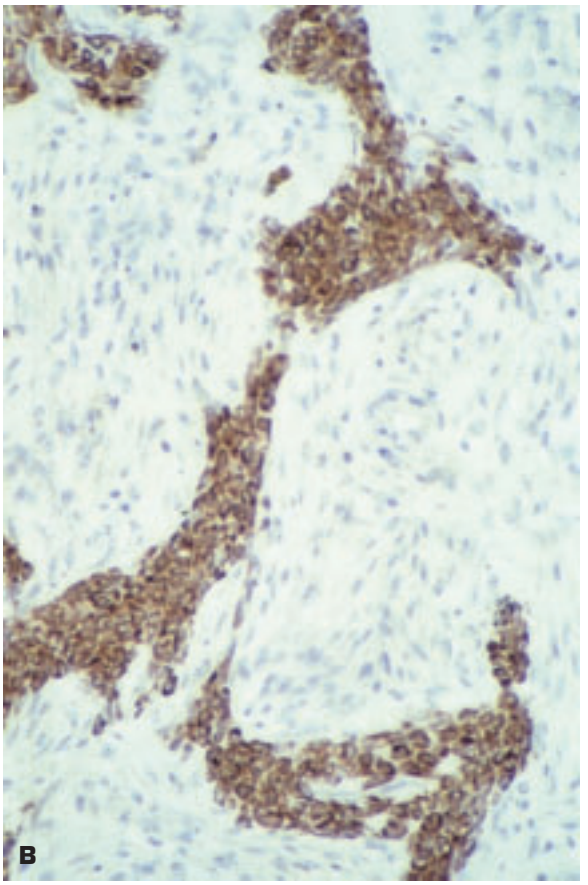

8-34. Extragnathic adamantinoma is a rare primary biphasic long bone tumor. Older patients (in the third decade) usually show the classic histology, whereas younger patients (younger than 15 years) usually show an osteofibrous dysplasia-like adamantinoma. **A.** Adamantinoma of the fibula and the tibia is seen in both longitudinal and transverse sections. The tumor has extended beyond the confines of the fibula. **B.** Histology shows a classical type of adamantinoma with positive staining for cytokeratin of the epithelial cellular component within the fibrous component.

8-35. Acute myeloid leukemic infiltration occupies the entire femoral bone marrow. No adipose tissue is noted in the marrow, and solid aggregates of tissue are focally present. In a normal middle-age adult, the hemopoietic tissue only occupies the proximal one-third of the femoral bone marrow, and the rest comprises fibroadipose tissue only.

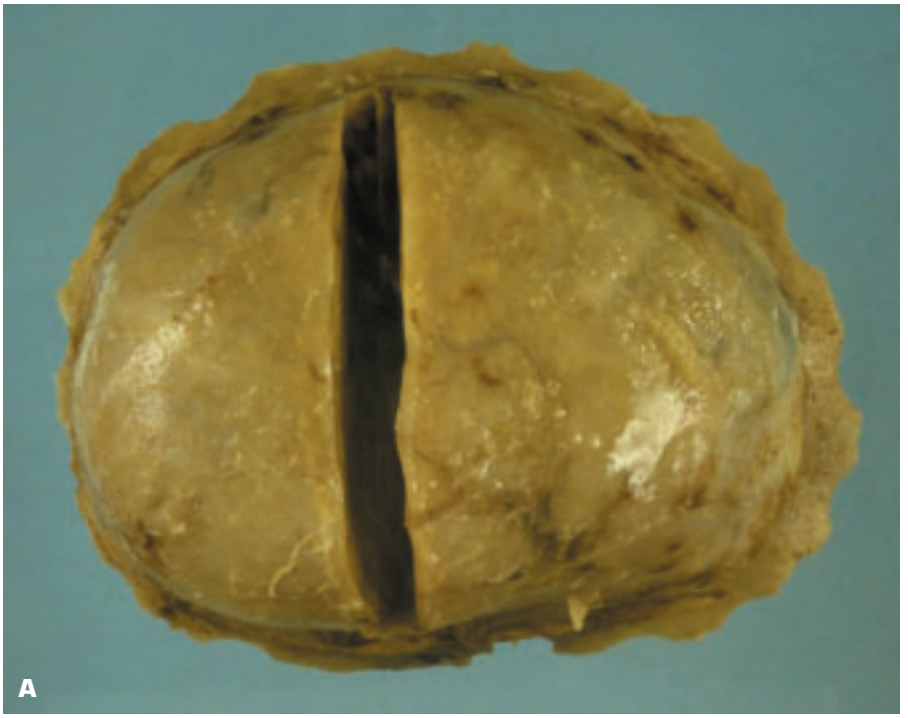

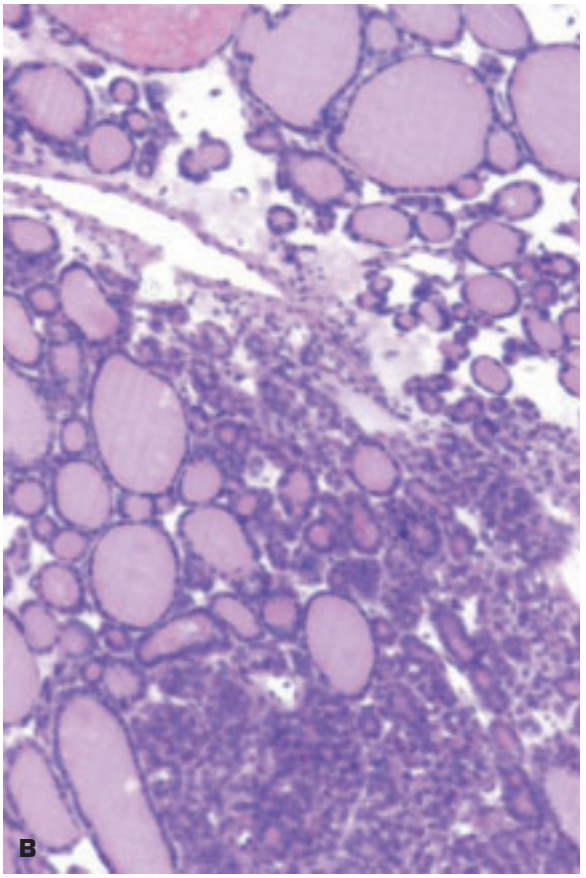

8-36. A. Metastatic thyroid carcinoma in the skull bone has been surgically resected. **B.** Histology shows a well-differentiated follicular carcinoma that closely mimics normal thyroid tissue in appearance.

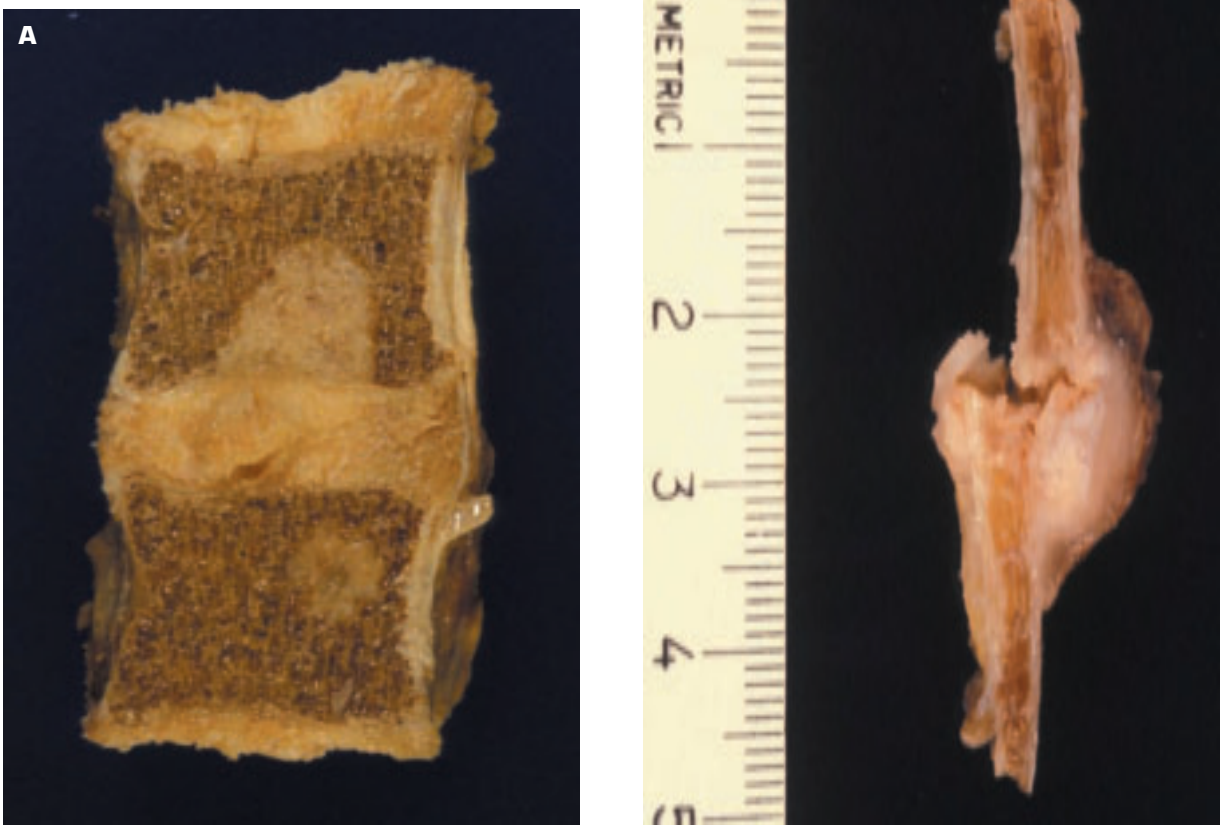

8-37. A. Metastatic osteolytic secondary deposits of breast carcinoma in two vertebral bodies. Prostatic carcinoma may produce osteosclerotic secondary deposits. **B.** Metastatic adenocarcinoma has produced a pathological fracture of the rib.

8-38. Metastatic chondrosarcoma affecting the toes of the foot.

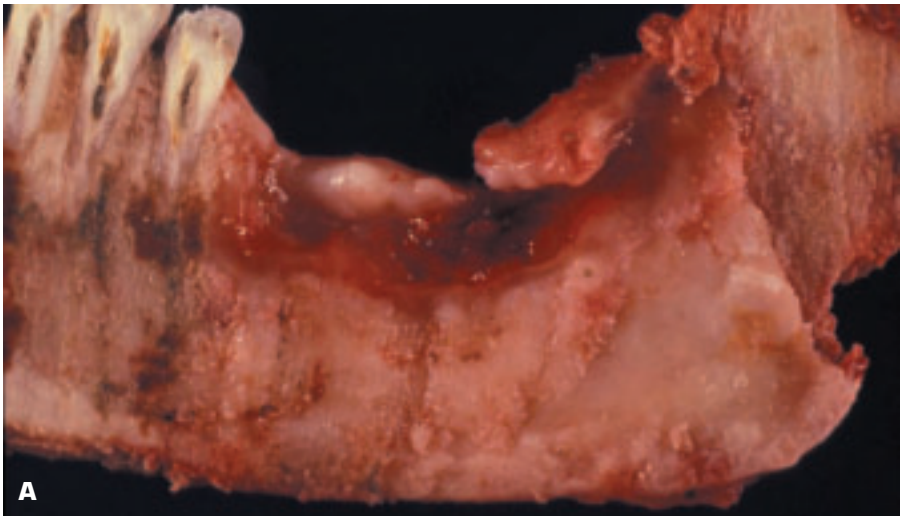

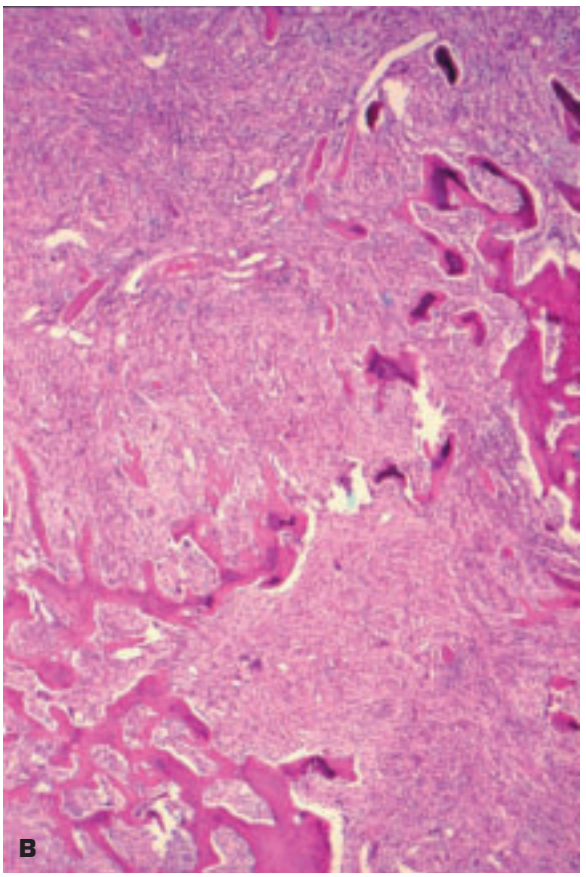

8-39. Osteosarcoma is the most common primary malignant tumor of the mandible and has a better prognosis than osteosarcoma of long bones. **A.** Odontogenic fibroblastic osteosarcoma of the mandible. Note the absent teeth overlying the tumor. **B.** Histology of odontogenic fibroblastic osteosarcoma showing new bone formation in an atypical fibroblastic stroma.

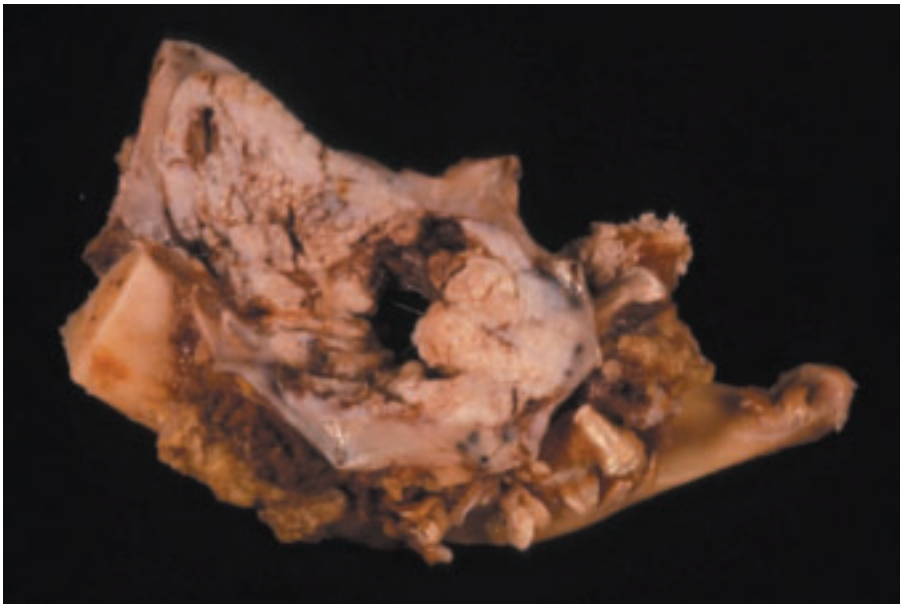

8-40. Squamous cancer of the buccal mucosa is invading the surgically resected mandible.

8.41. Camptomelic skeletal dysplasia in a 34-week-old fetus. **A.** Note the bowed upper and lower legs plus the talipes equinovarus of the feet. **B.** Postmortem x-ray of the fetus shows a highly radiolucent skull and bowed femurs and tibias. *(continued on next page)*

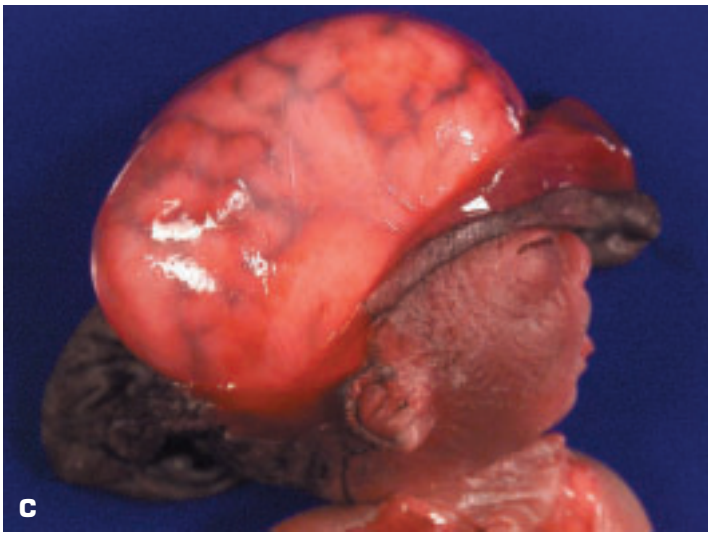

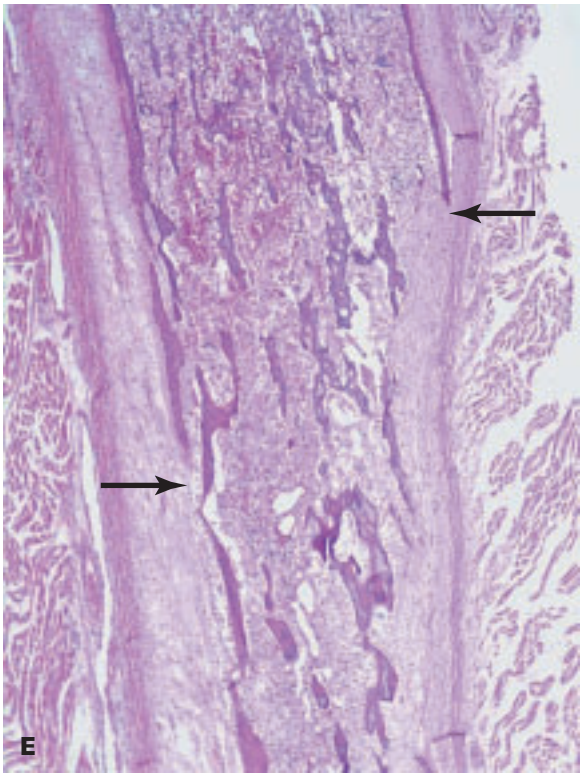

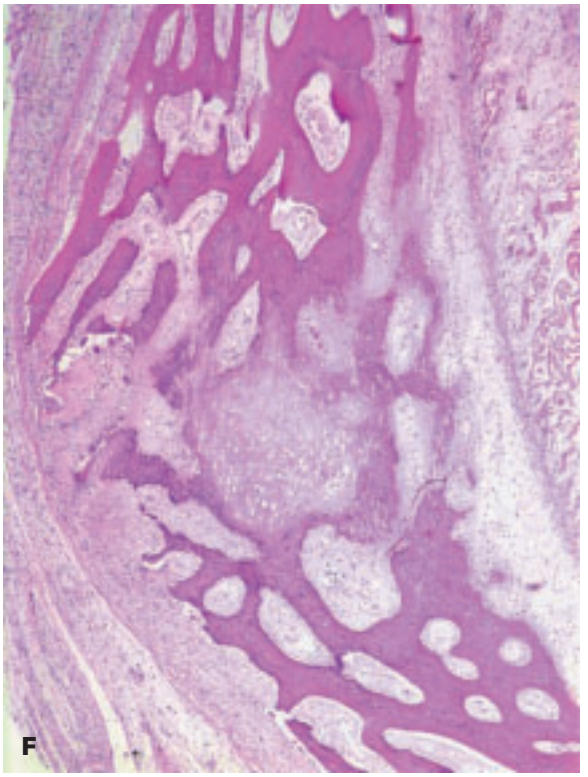

8.41. *(Continued)* **C.** The skull bones are so thin and attenuated that the brain is visible through them. **D.** Histology confirms severe thinning of this skull bone. **E.** Femur shows partial absence (*arrows*) of greatly thinned cancellous cortical bone plus compensatory thickening of bony lamellae in the marrow. **F.** Healed intrauterine fracture of a rib.

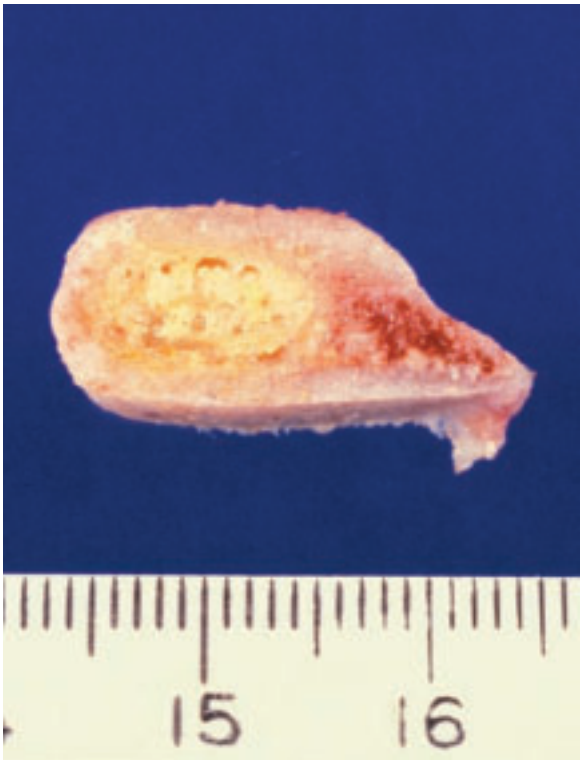

8-42. Chronically inflamed bursa of hip joint shows central yellowish discoloration due to old pus cells, and there is a surrounding paler zone of fibrosis with some calcification.

8-43. A. Pigmented villonodular synovitis of the knee joint. Note the characteristic nodular excrescences and infoldings of the synovium. **B.** Localized nodular tenosynovitis (giant cell tumor of tendon sheath).

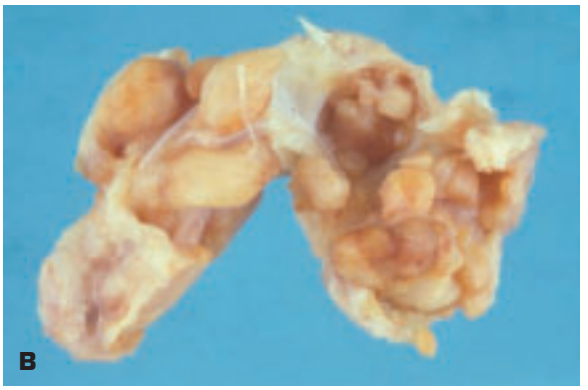

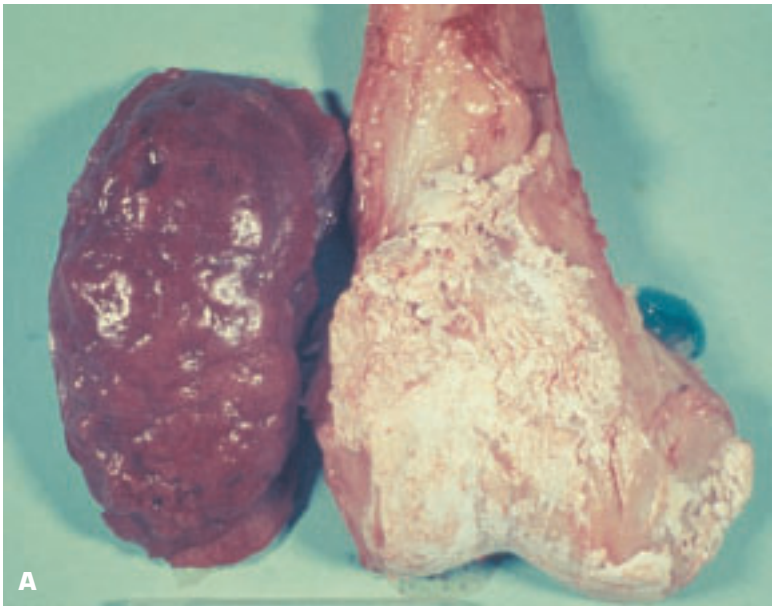

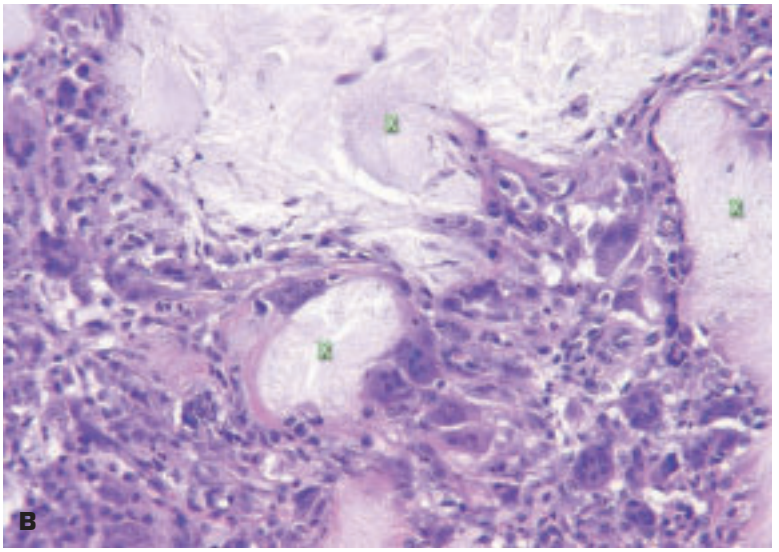

8-44. Gout. **A.** Lower femur in the knee joint is covered by chalky white deposits of uric acid. The kidney shows focal coarse scarring probably secondary to healed pyelonephritis. **B.** Gouty tophus in soft tissues contains crystals of uric acid (X).

8-45. A. Rheumatoid nodules over an interphalangeal joint of a patient with rheumatoid arthritis. **B.** Histology of a rheumatoid nodule shows central coagulative necrosis (necrobiosis) of soft tissues with surrounding palisaded histiocytes.

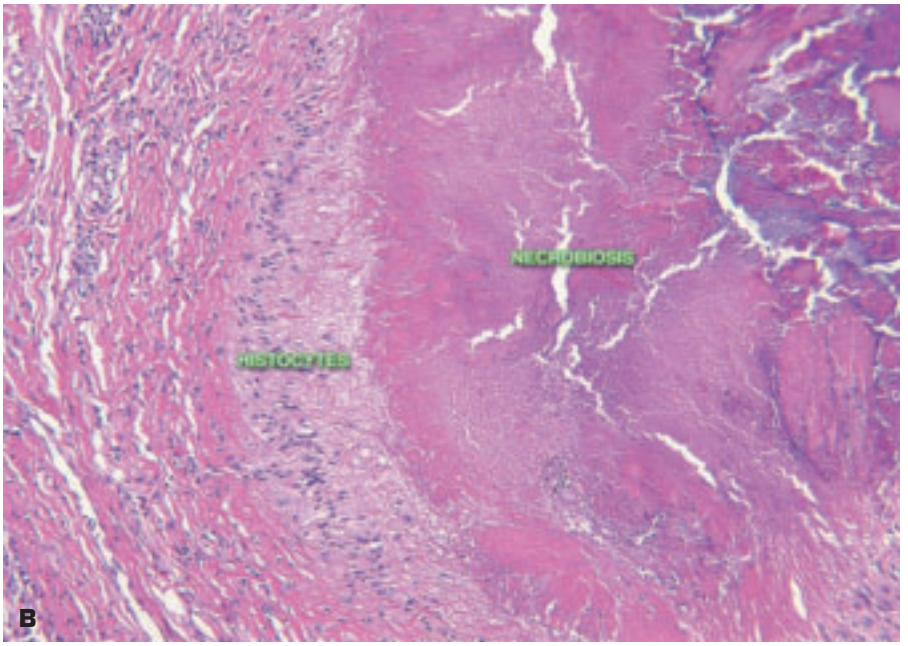

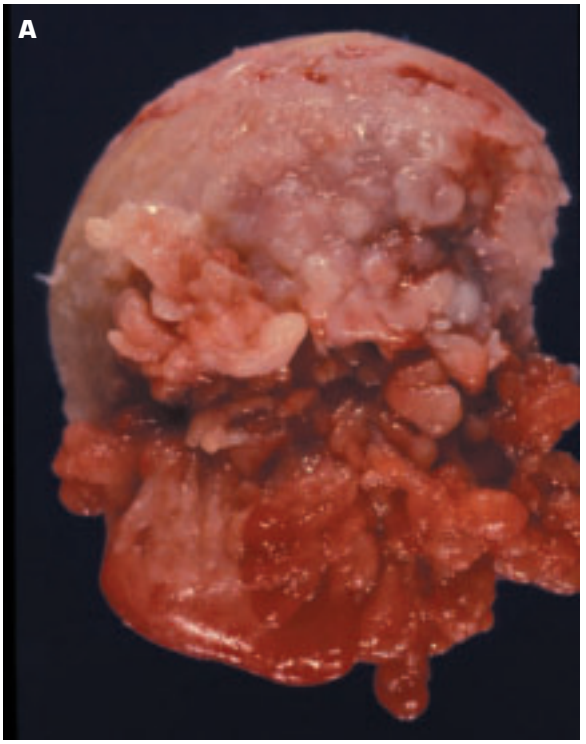

8-46. Rheumatoid arthritis (RA). **A.** Head of femur shows pannus overgrowth (whitish nodules, *top*), and the synovium (*bottom*) shows brownish nodules due to a combination of lymphoid hyperplasia and iron deposits secondary to hemorrhage. **B.** Synovitis in RA has produced a papillary appearance to the synovial lining. *(continued on next page)*

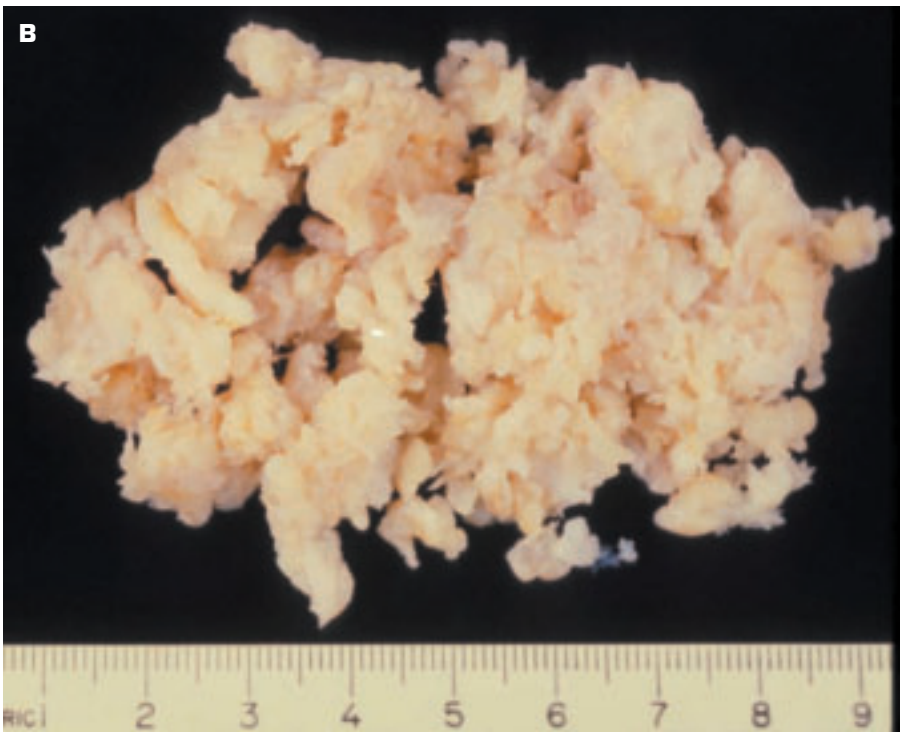

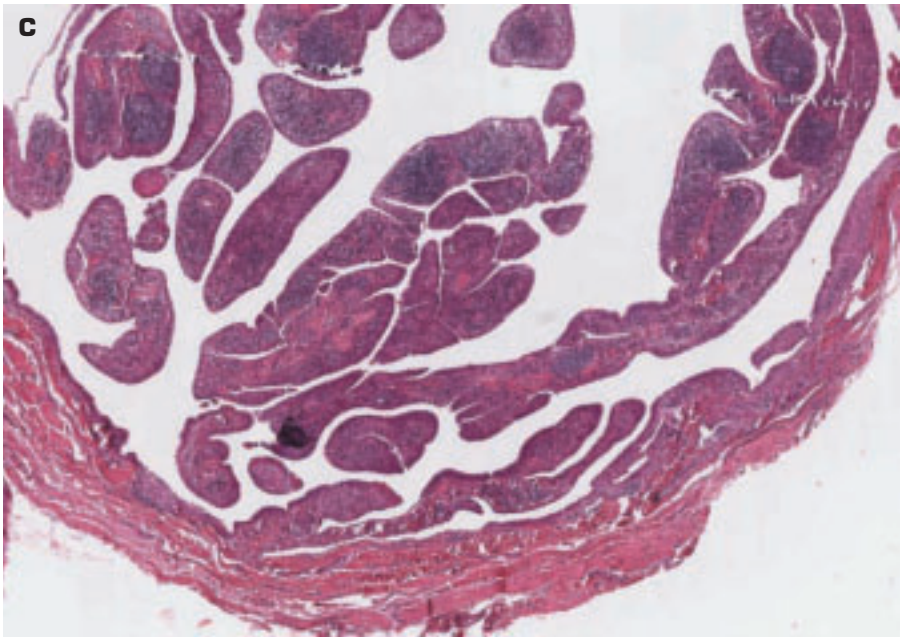

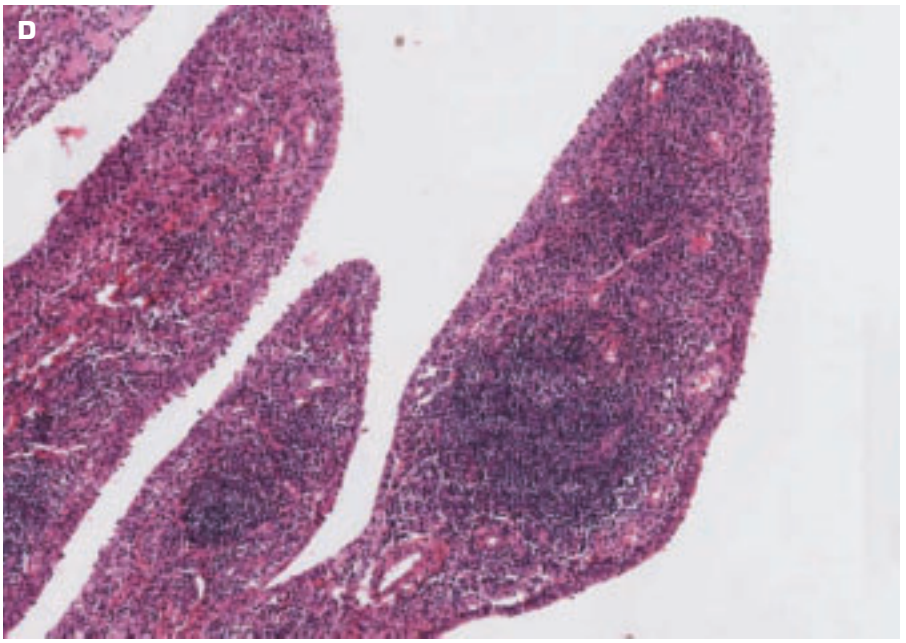

8-46. *(Continued)* **C.** Low-power histology of the hyperplastic synovium shows abundant lymphoid tissue occupying the papillary infoldings. **D.** High-power view of several lymphoid-filled papillary folds. *(continued on next page)*

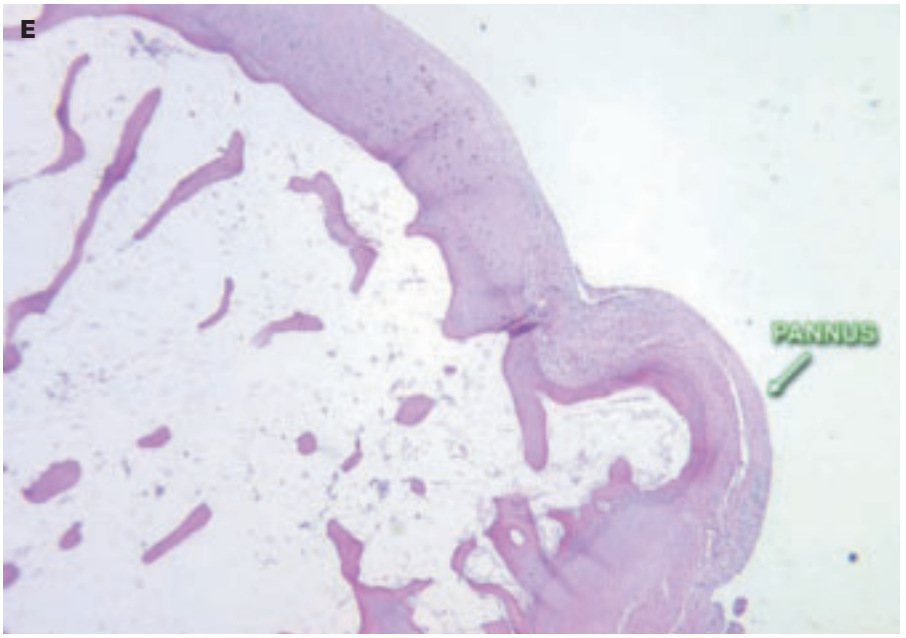

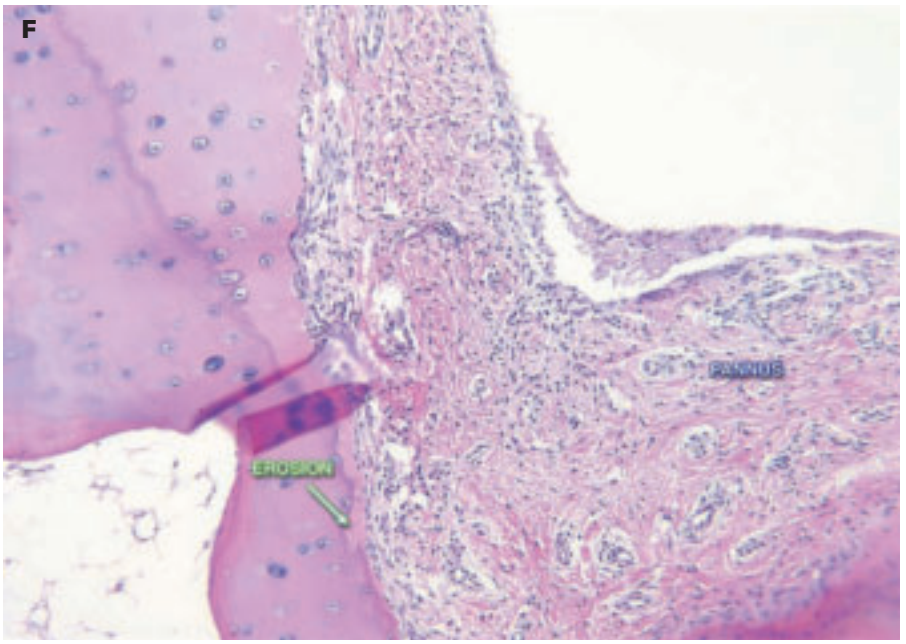

8-46. *(Continued)* **E.** Articular surface (*top*) shows loss of articular cartilage beneath pannus overgrowth. **F.** Pannus overgrowth on articular surface that has lost its cartilage layer, and the underlying bone is eroded.

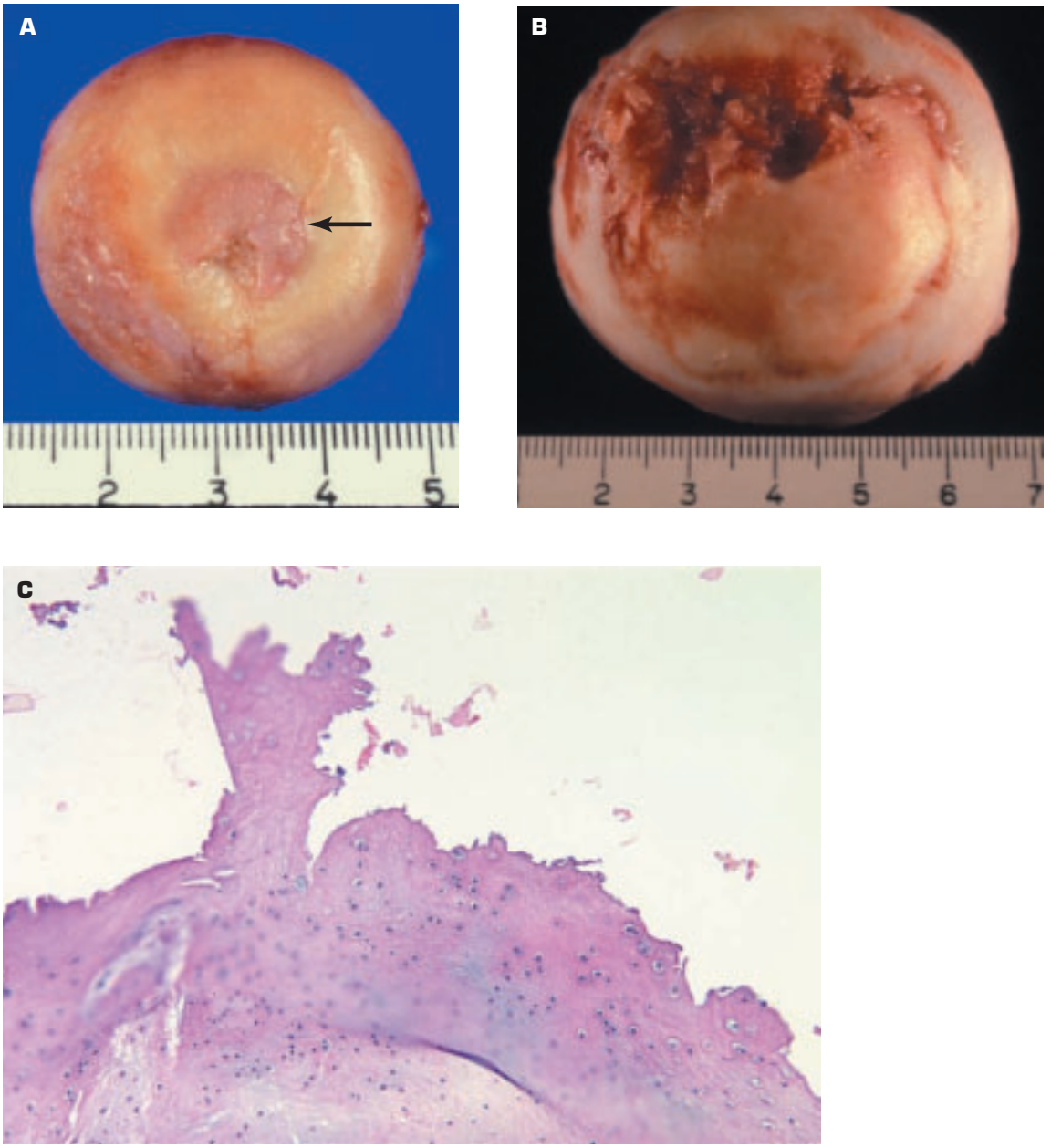

8-47. Osteoarthritis (OA) is characterized by wearing away of the articular cartilage of a joint. **A.** OA of the femoral head. Scanty residual cartilage (*arrow*) is seen as pinkish-colored areas elevated above the yellow-colored burnished bare bone. **B.** Fibrillated cartilage protrudes from the (*top*) edge of the central, eroded articular surface of the head of femur. **C.** Histology of a fibrillated cartilaginous excrescence. *(continued on next page)*

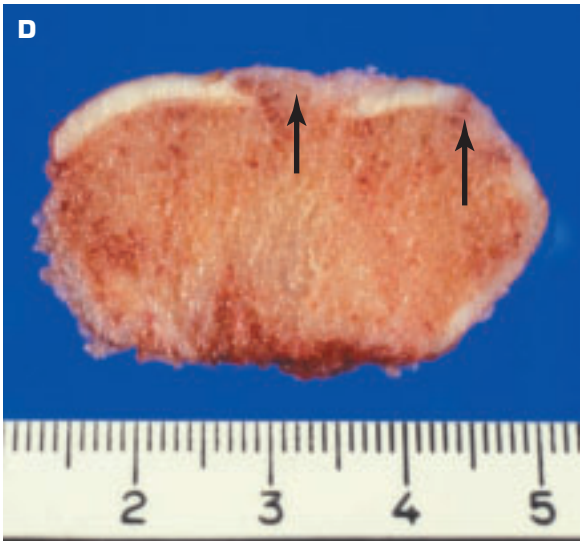

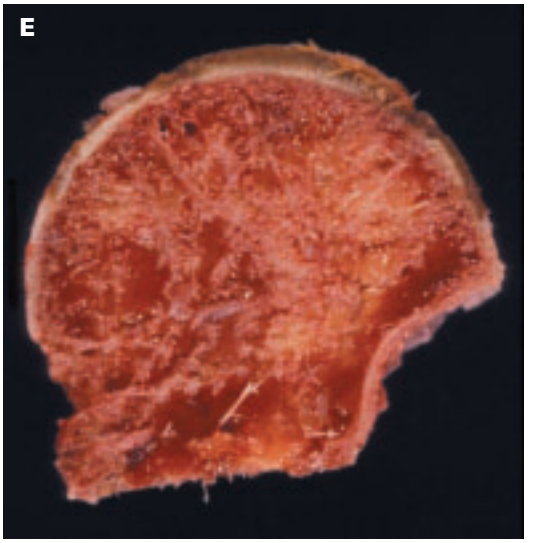

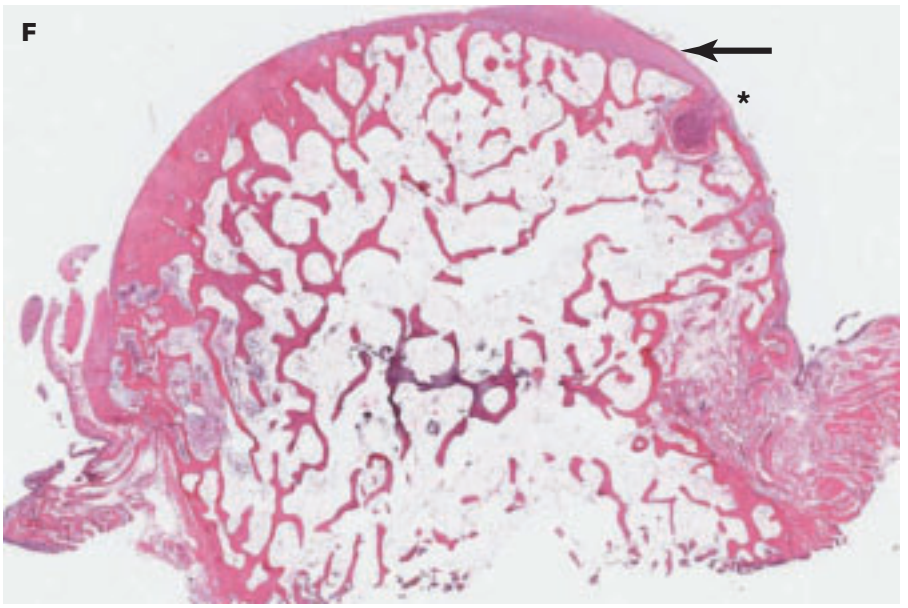

8-47. *(Continued)* **D.** Transected head of femur shows severe loss of cartilage (*arrows*). **E.** Bone is forming the articular surface of most of this femoral head. **F.** Histology of femoral head in OA shows subtotal loss of the articular cartilage apart from a small zone (*arrow*), which has a small subarticular cyst at its right margin (*). *(continued on next page)*

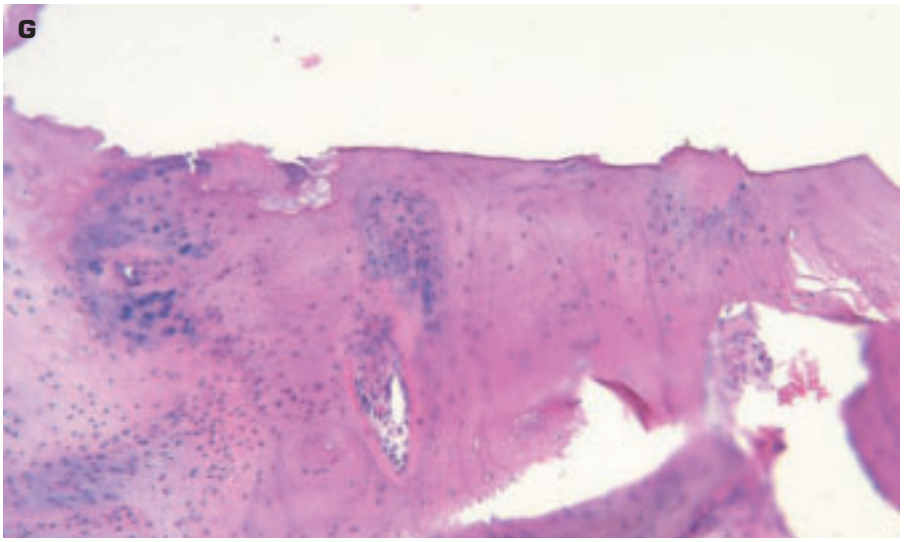

8-47. *(Continued)* **G.** Bare bone on the articular surface has become worn down and corresponds to eburnated bone seen grossly in A. **H.** Very advanced OA shows a large bone cyst due to a crack in the bone that allowed synovial fluid to enter the bone. Note the well-delineated, reactive bone surrounding the cyst.

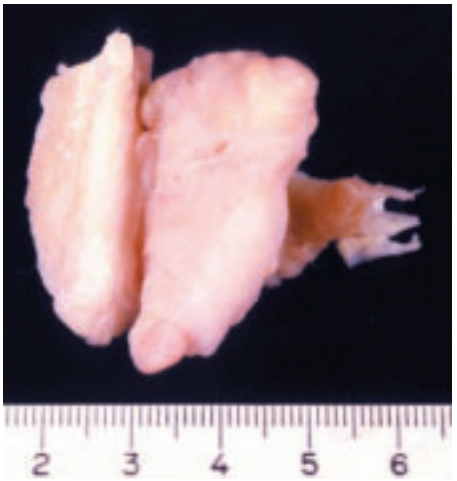

8-48. Fibrous histiocytoma of the synovium.

8-49. Fibroma of tendon sheath removed from the wrist.

8-50. Well differentiated synovial chondrosarcoma of the knee joint comprises numerous multinodular cartilaginous tumors.

9 Diseases of the Spleen, Lymph Nodes, and the Thymus Gland

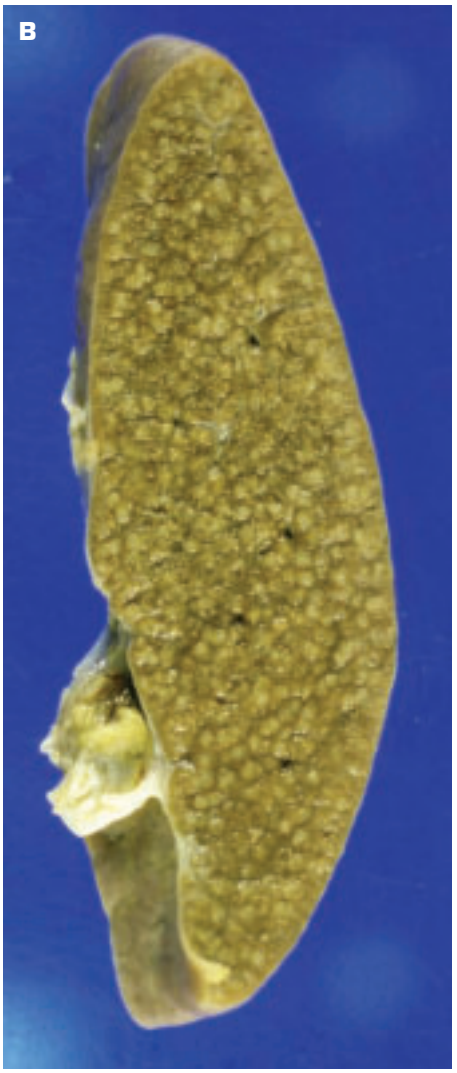

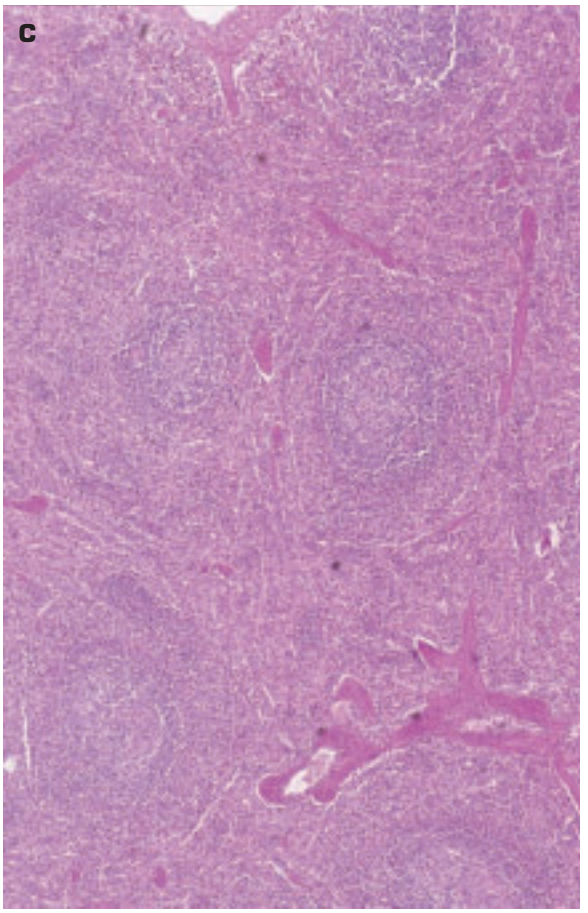

9-1. Mechanical disruption of the spleen. **A.** Rupture of the spleen and the splenic capsule in a patient with infectious mononucleosis due to weakening of the splenic trabecula and capsule by lymphocytic infiltration. **B.** Follicular hyperplasia of spleen in infectious mononucleosis. **C.** Histology shows follicular hyperplasia impinging on attenuated trabecula. *(continued on next page)*

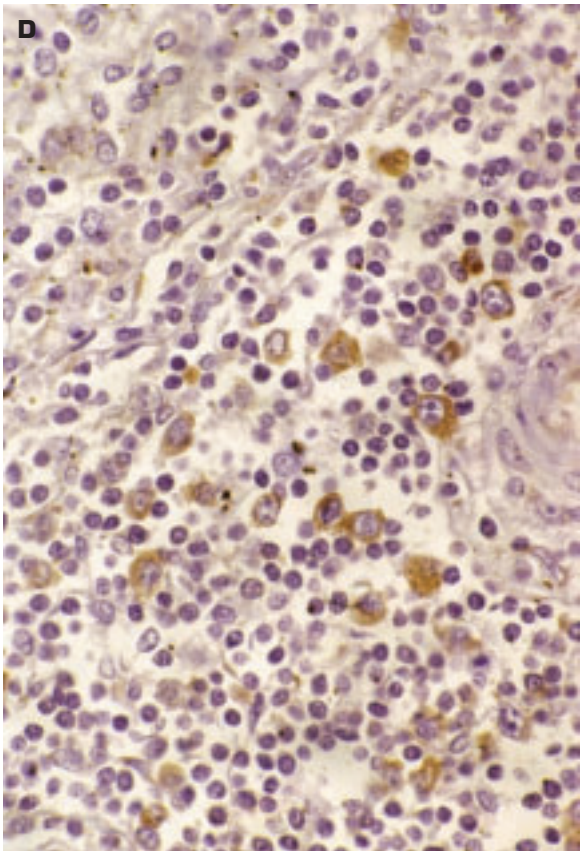

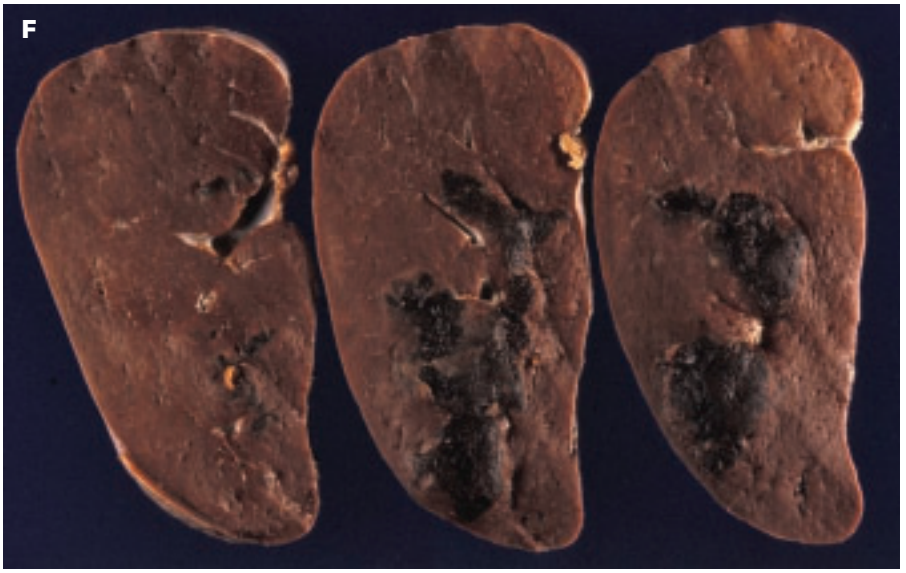

9-1. *(Continued)* **D.** The same spleen shows positive immunoperoxidase staining by labeled antibody against Epstein–Barr virus. **E.** Recent, circumscribed subcapsular hematoma (*bottom left*) after a blow to the abdomen. **F.** Sliced spleen is seen to contain an irregularly shaped, dark-colored hematoma within its substance.

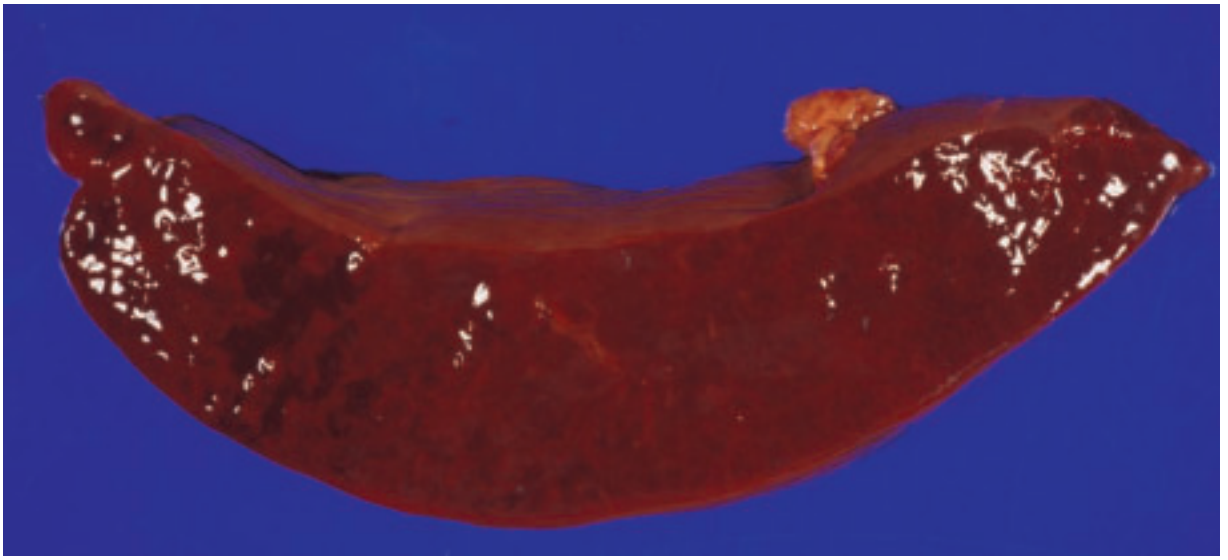

9-2. Reactive diffluent spleen due to infection. Note the rounded edge and the watery-looking splenic cut surface. (This is in contradistinction to chronic congestion of the spleen, which exhibits a sharp cut edge and a firm, nondiffluent cut surface.) On touching the cut surface of a reactive spleen, some of the splenic tissue becomes attached to the glove. Note that peritonitis does not cause a reactive spleen.

9-3. A. Gamna–Gandy body (localized area of calcium and iron encrustation due to a prior localized hemorrhage) within a reactive spleen is seen as a circumscribed brown area within the soft, diffluent splenic pulp. **B.** Healed "perisplenitis" (so-called sugar icing of the spleen) comprises thickening of the splenic capsule due to organization of previous fibrin deposits on the peritoneal surface of the spleen.

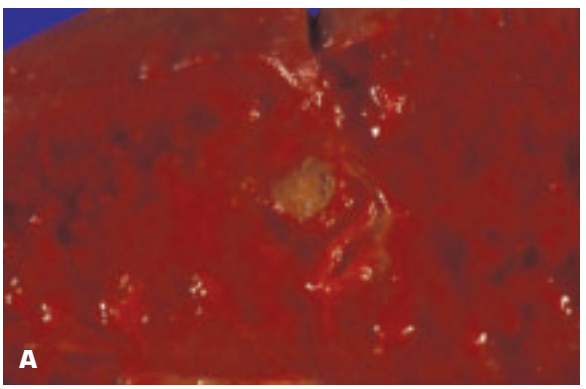

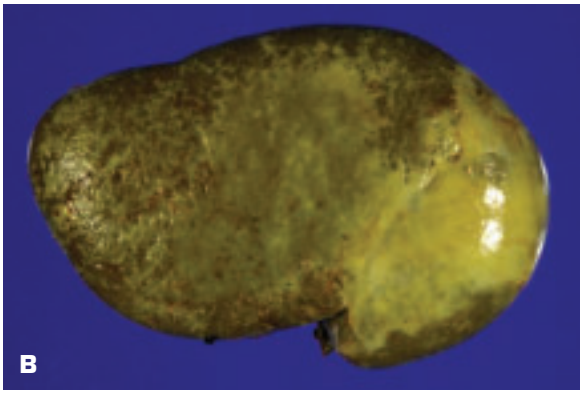

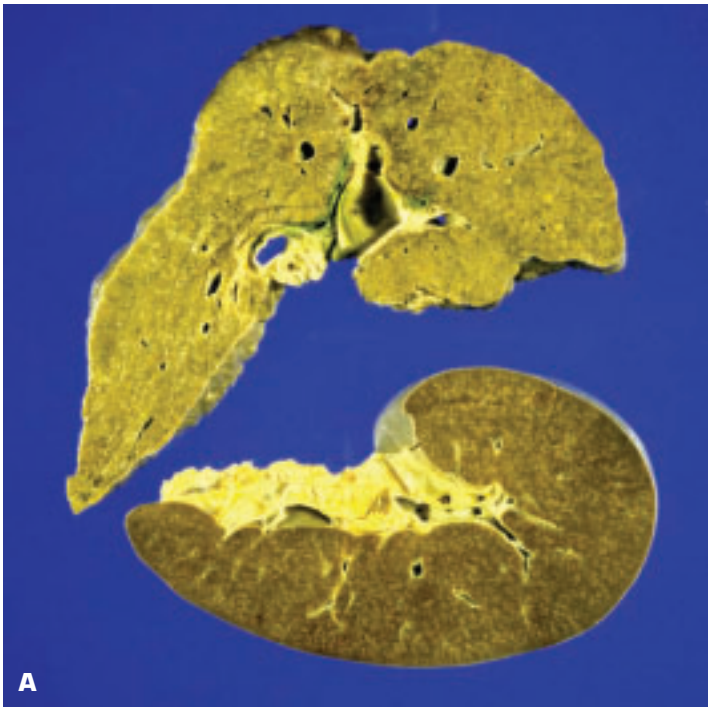

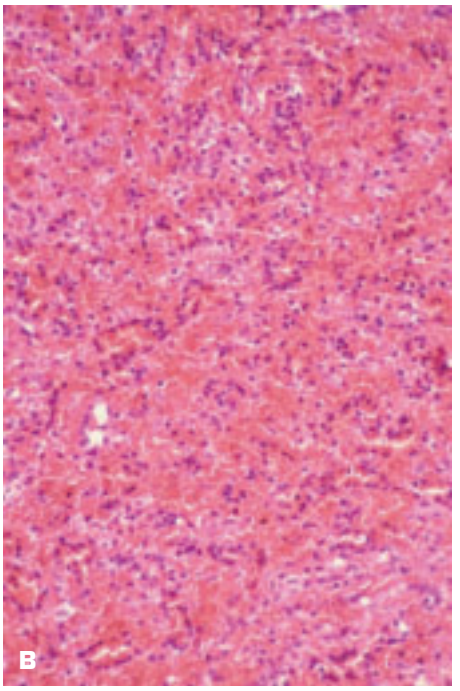

9-4. A. Chronic congestion of the spleen (*bottom*) secondary to portal hypertension in cirrhosis of the liver (*top*). Note the sharply defined cut edge of the spleen, the firm-appearing cut surface, and the prominent, thick-walled blood vessels. The congested spleen is enlarged to rival the liver in size. **B.** Histology of a congested spleen shows a very prominent red pulp with scanty lymphoid elements. **C.** Severe transfusional siderosis of a spleen that has a very brown cut surface. In siderosis, the iron deposits occur within the reticuloendothelial system, as opposed to hemochromatosis, in which the iron deposits occur within the parenchymal cells. Hence, the spleen is usually spared from siderosis in hemochromatosis.

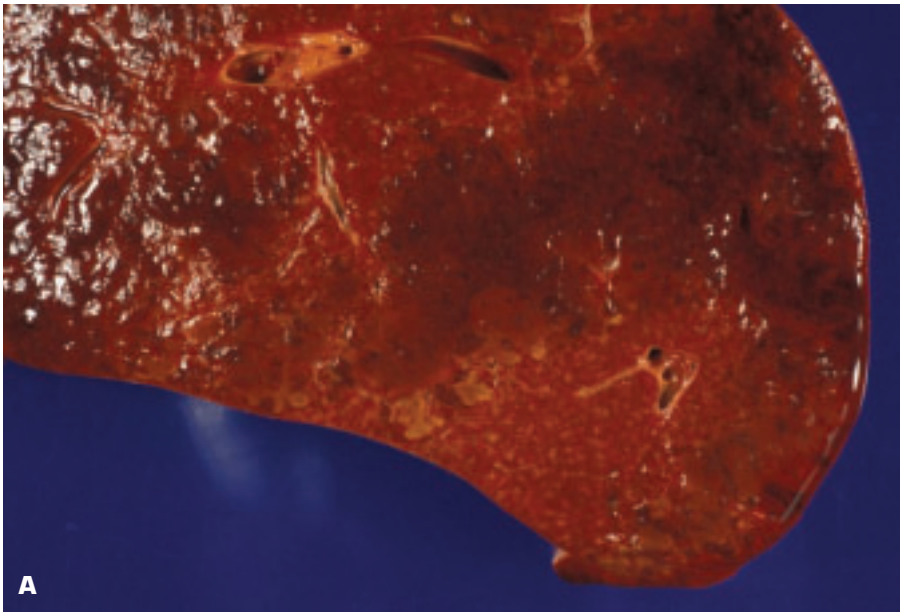

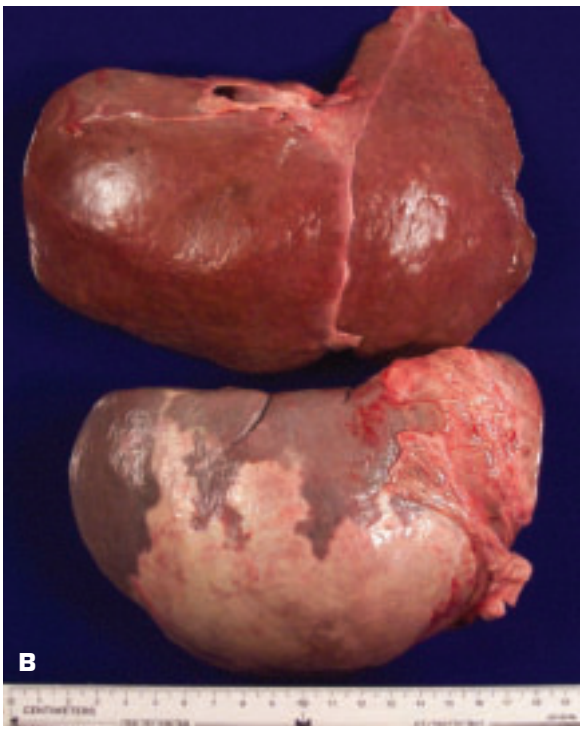

9-5. Infarction of the spleen. **A.** Venous infarcts, due to venular occlusion within the spleen, appear as mottled, darker red areas (*top right*). Scanty true infarcts due to arterial occlusion are noted as small pale yellow areas (*bottom center*). **B.** Pale infarct in a spleen (*bottom*) that is enlarged to the same size as the liver (*top*) due to immune deficiency. *(continued on next page)*

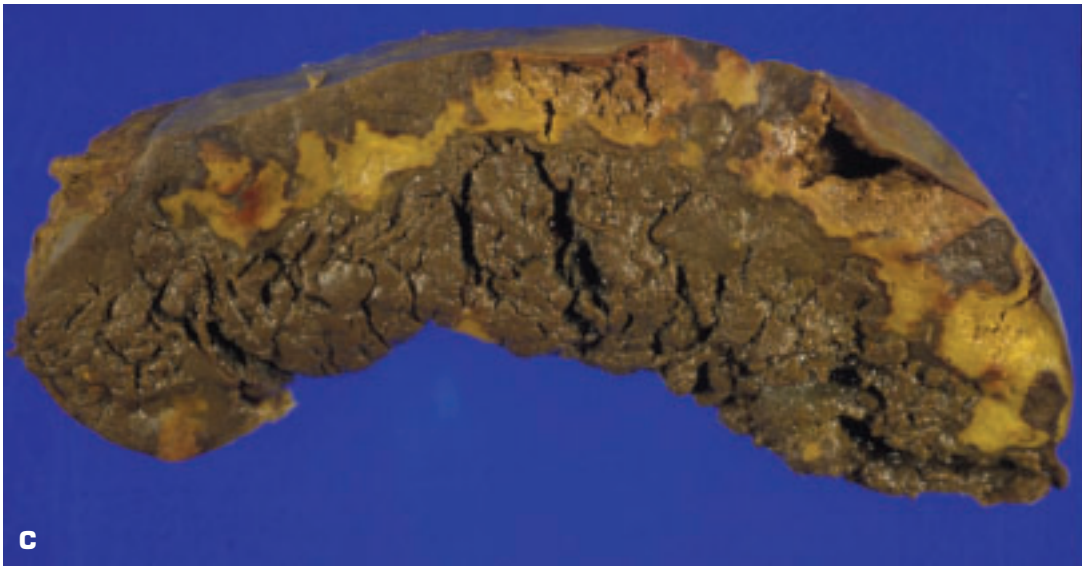

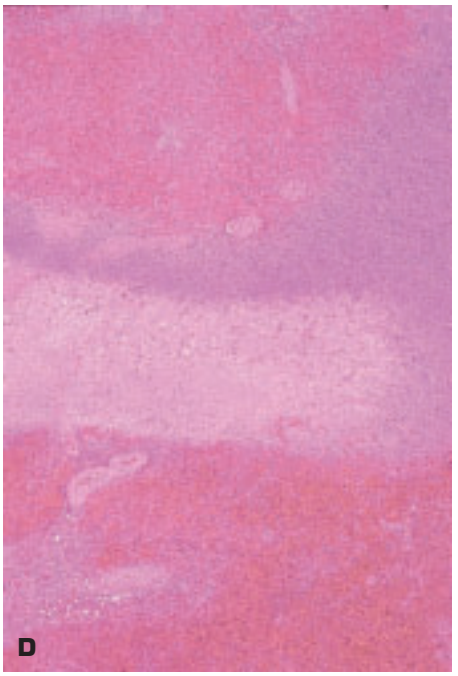

9-5. *(Continued)* **C.** Multiple, pale yellow, well-established infarcts of the spleen. **D.** Histology of a splenic infarct (horizontal pale band center) shows prominent neutrophilic infiltration at its top and right borders. *(continued on next page)*

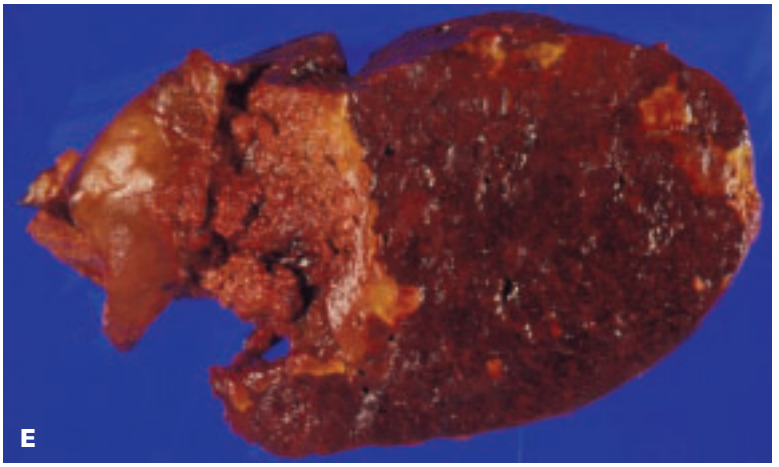

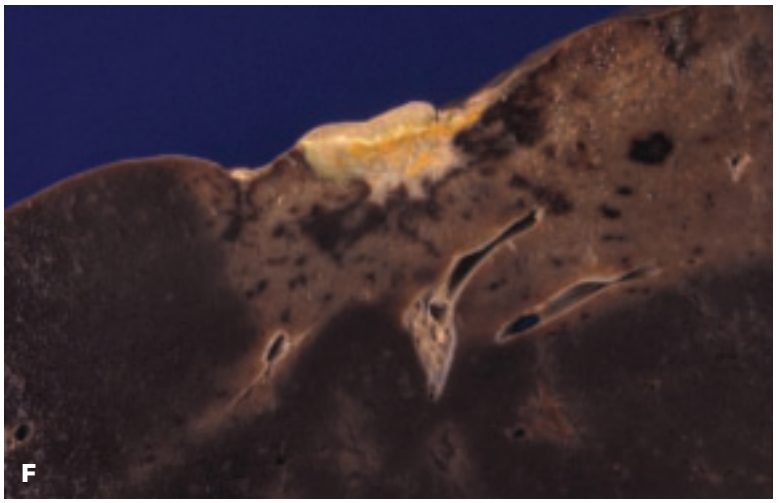

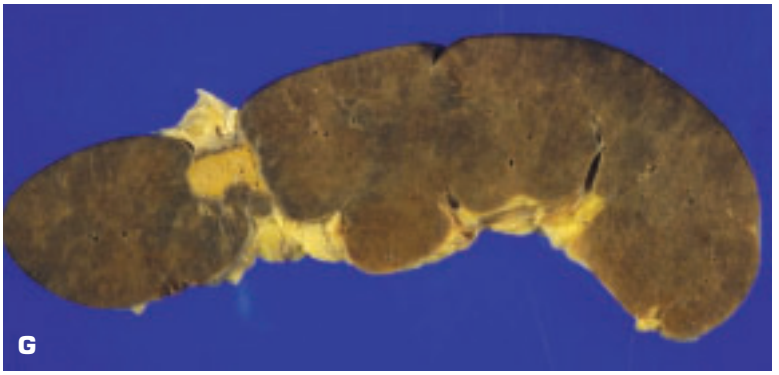

9-5. *(Continued)* **E.** Ruptured splenic infarct (*left*). **F.** Healed infarct (*top center*, yellow-gray area) is surrounded by a zone of pallor representing partially ischemic, nonnecrotic splenic parenchyma. **G.** Healed infarct (*top left*) has a peritoneal adhesion on its overlying depressed capsular surface.

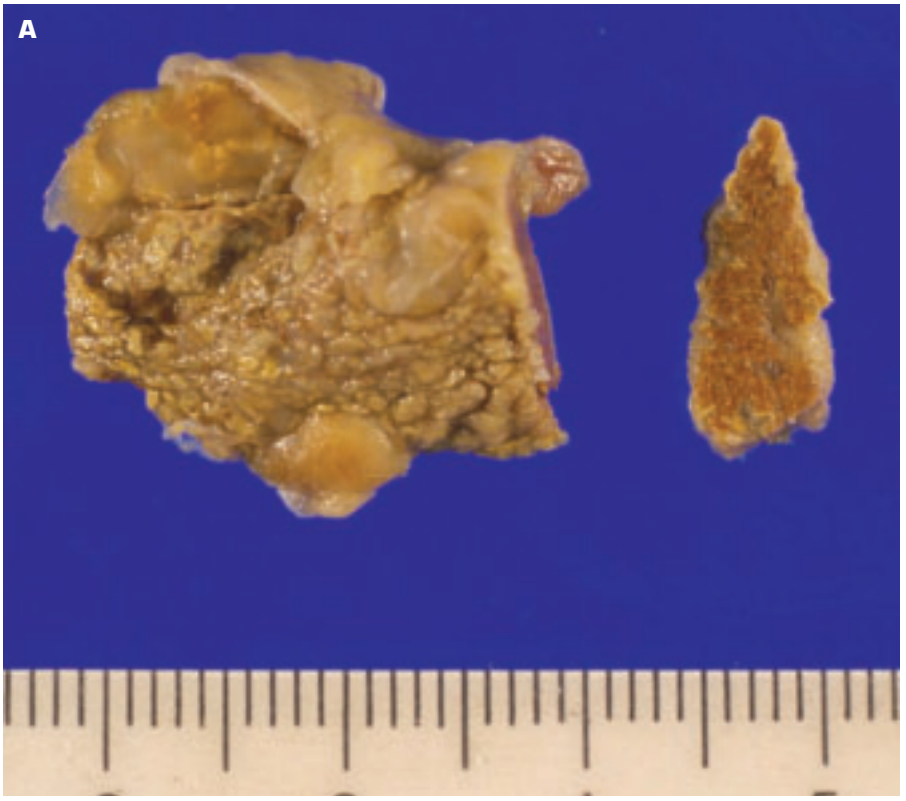

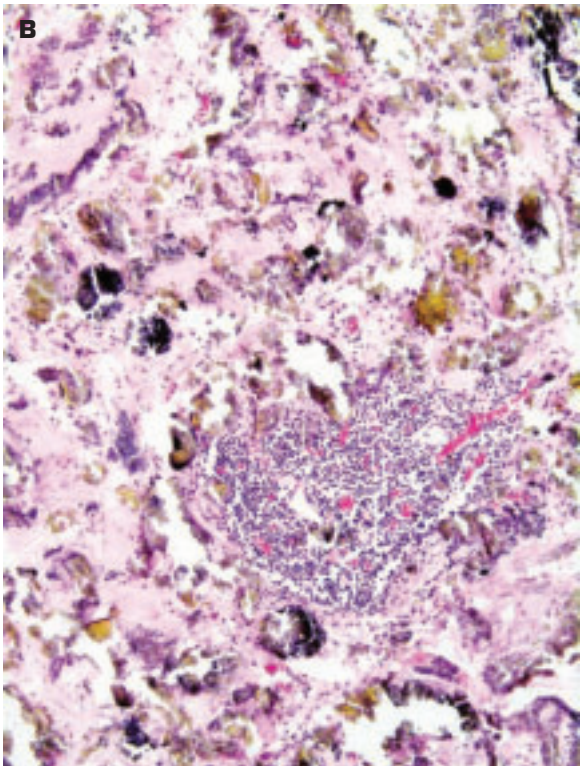

9-6. Sickle cell anemia. **A.** "Autosplenectomy" in a patient with sickle cell anemia. Repeated infarctions of the spleen have reduced it to a miniscule, shrunken, nonfunctioning organ. **B.** Histology shows abundant iron and calcium encrustations, with no normal splenic tissue visible apart from a small collection of lymphocytes (*center*).

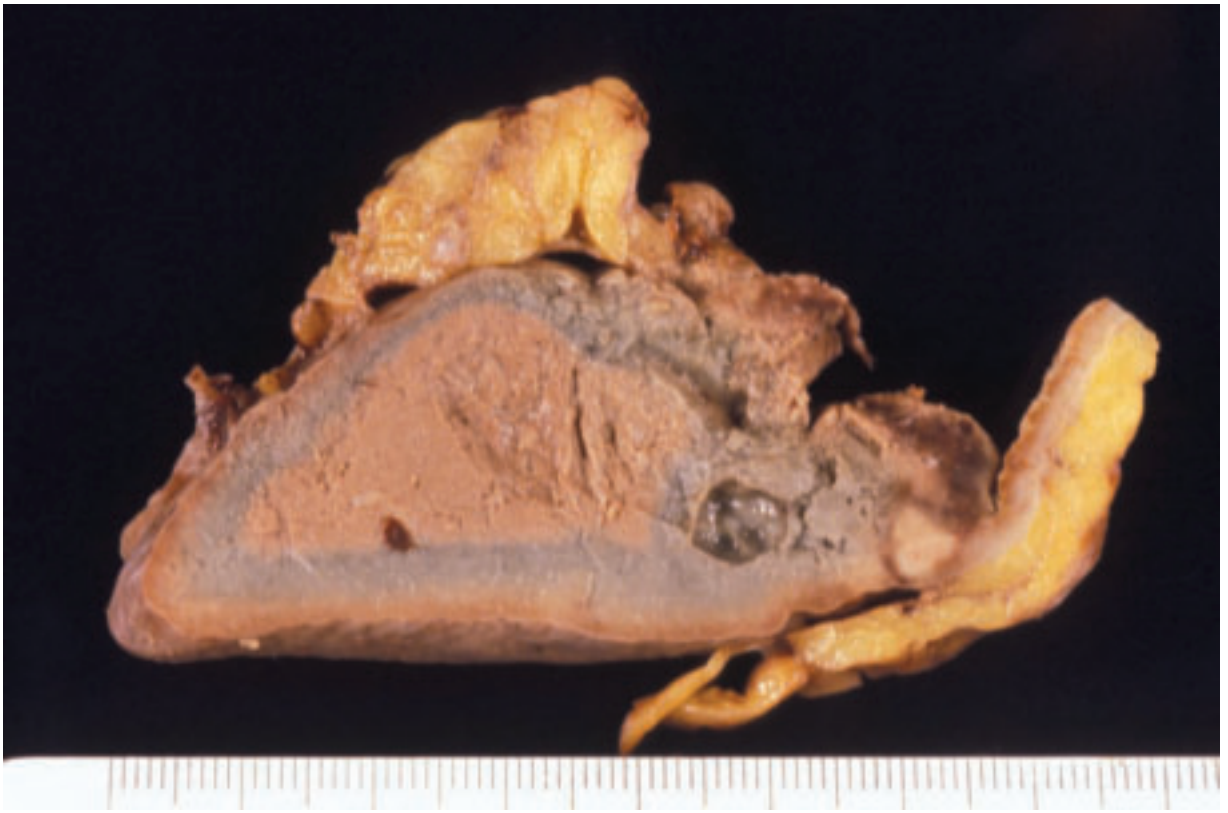

9-7. Splenic abscess (*bottom right*) is about to rupture. Only the outer portion of the spleen has been fixed, accounting for the lighter color of the core. Omental adhesions are also present.

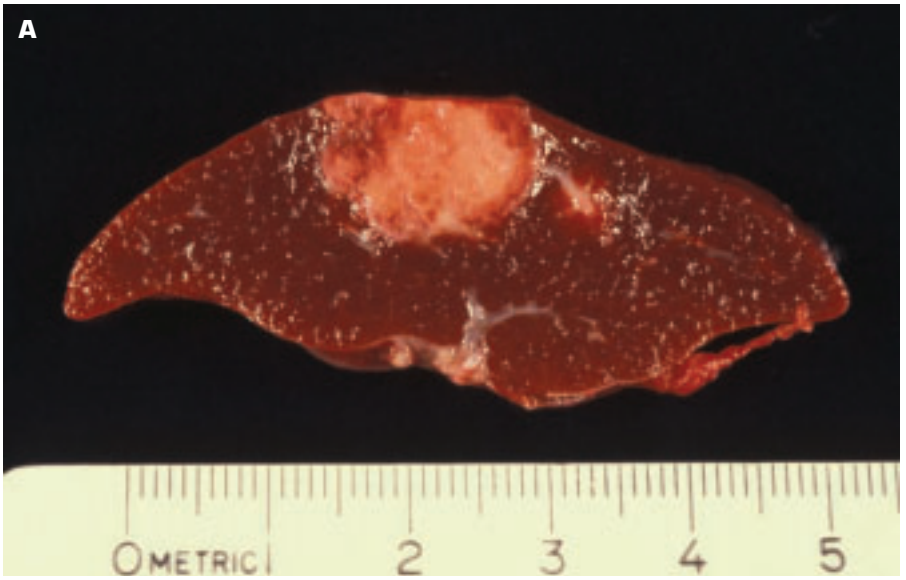

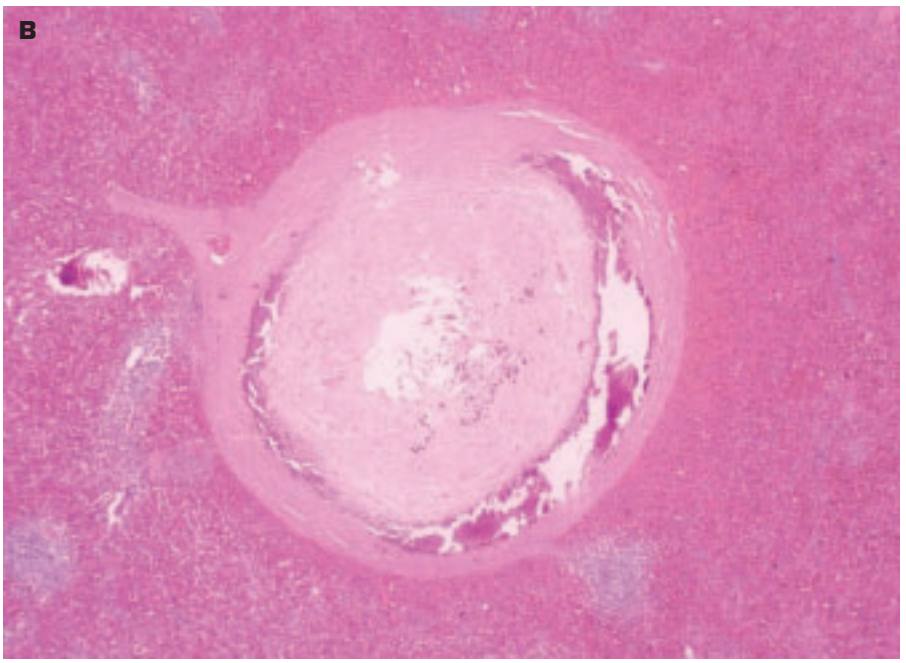

9-8. Granulomas in the spleen. **A.** Necrotizing granuloma in the spleen due to histoplasma infection. **B.** Histology of an encapsulated histoplasma granuloma in a spleen. *(continued on next page)*

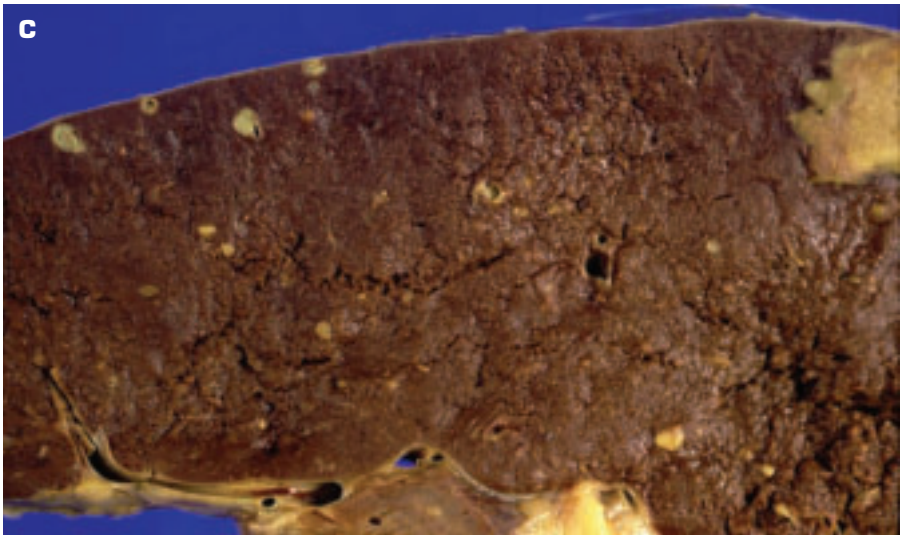

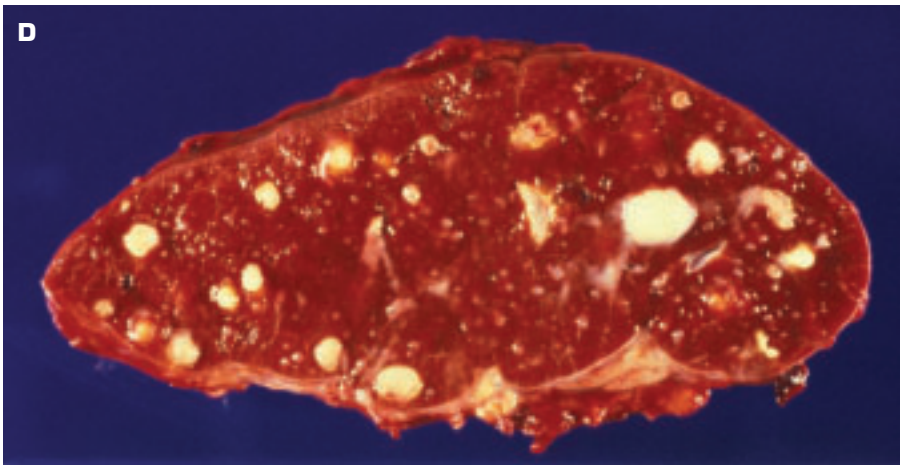

9-8. *(Continued)* **C.** Multiple small nodules in the spleen due to *Candida albicans* infection. Portion of an infarct is seen (*top right*). **D.** Multiple pyemic abscesses of the spleen in infective endocarditis.

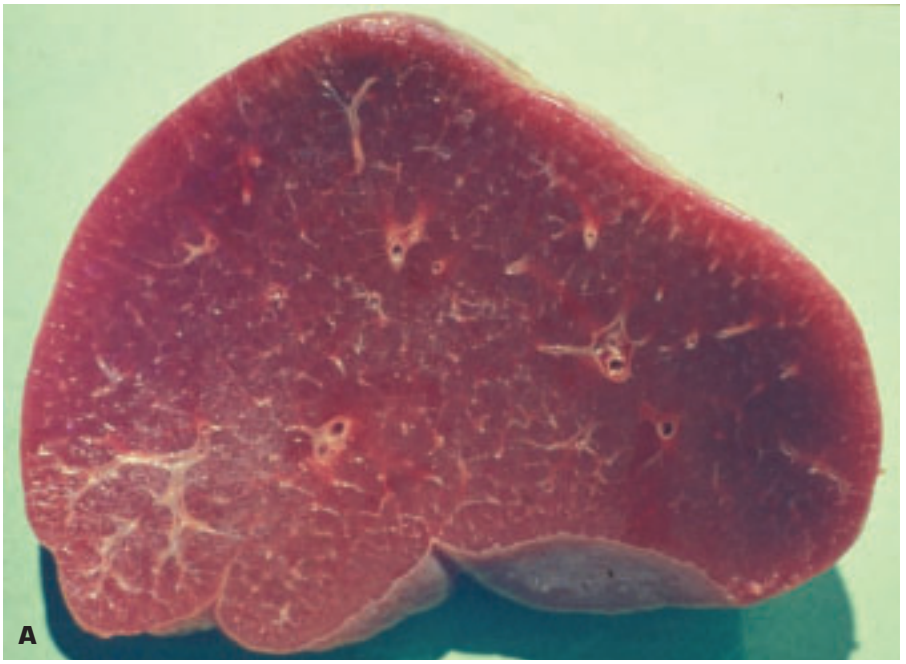

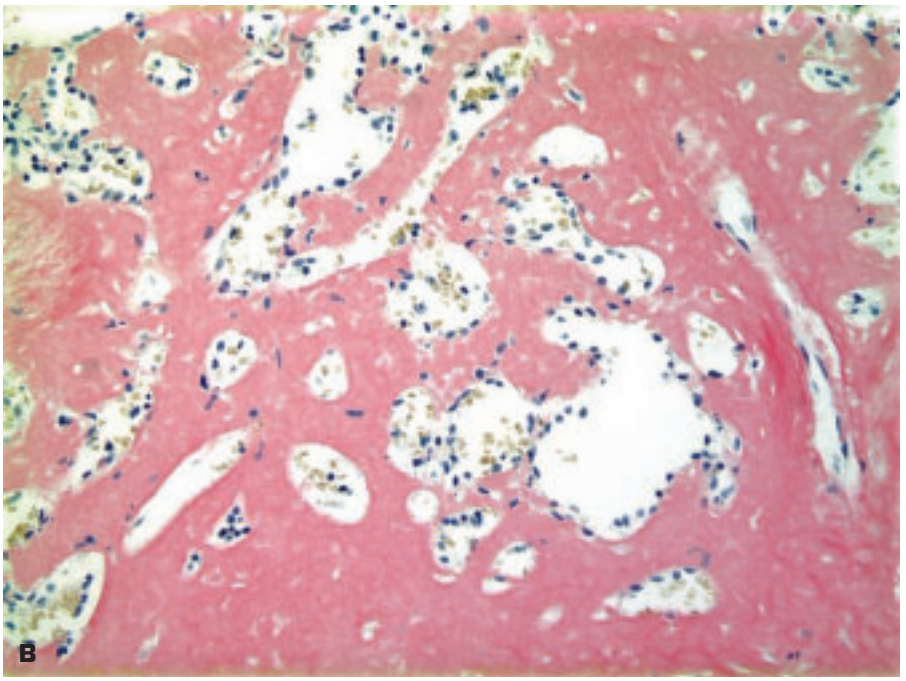

9-9. Amyloidosis of the spleen. **A.** Note the characteristic very sharp cut edge and the waxy-looking, translucent cut surface of amyloidosis. The spleen is hard at autopsy if the body has been refrigerated, but at normal body temperature during life amyloid has a soft consistency. **B.** Histology of the spleen shows massive deposits of amyloid staining positively with the Congo red stain.

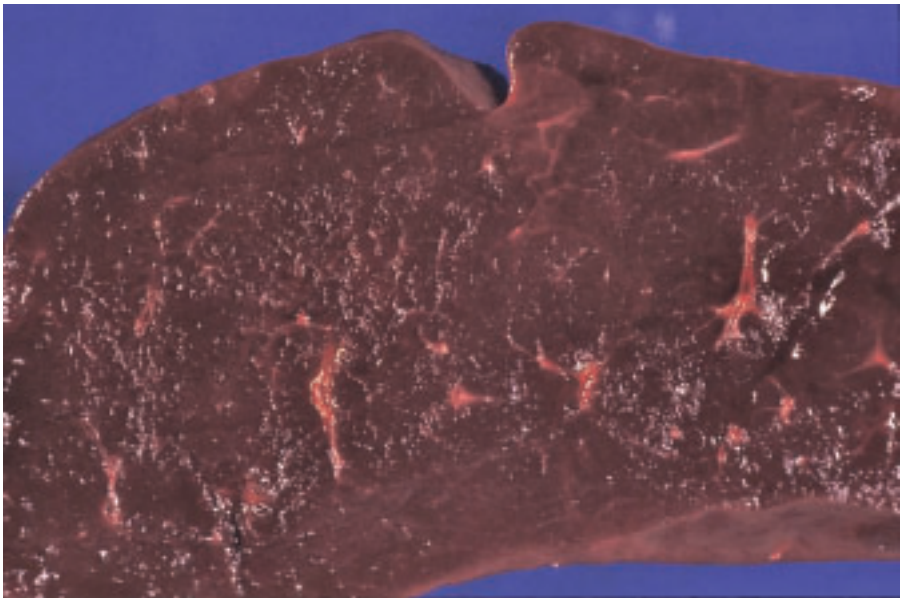

9-10. Myelofibrosis: the firm spleen has a diffuse dark plum-colored appearance due to extramedullary hematopoiesis.

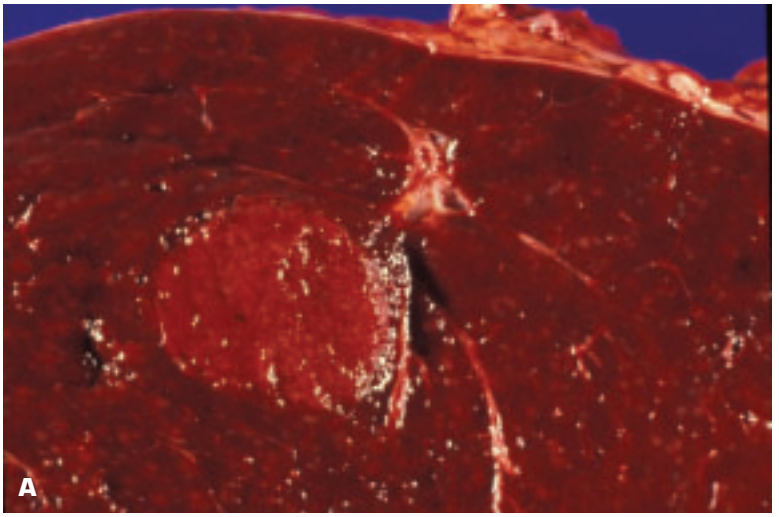

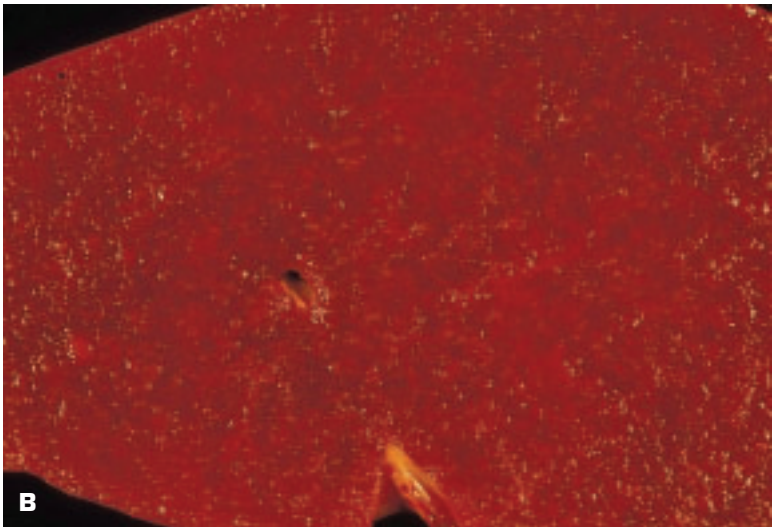

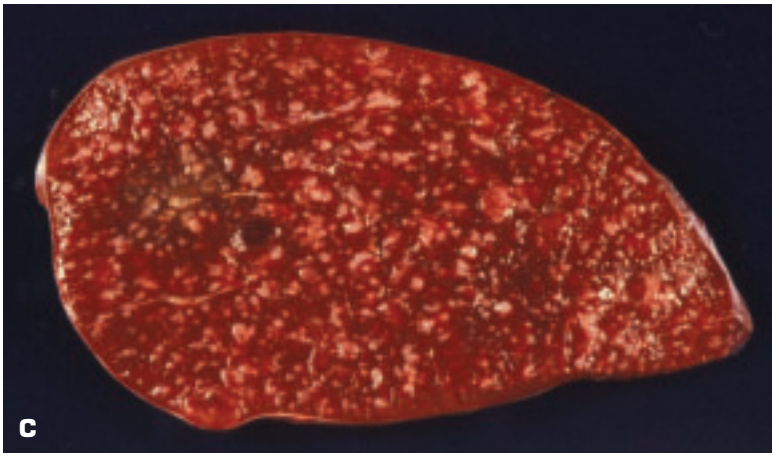

9-11. Spleen in leukemia. **A.** Solitary neoplastic nodule in a patient with chronic lymphocytic leukemia (CLL). **B.** CLL has produced numerous ill-defined tumor nodules on the splenic cut surface. **C.** Chronic lymphocytic leukemia has produced numerous, small well-defined neoplastic nodules.

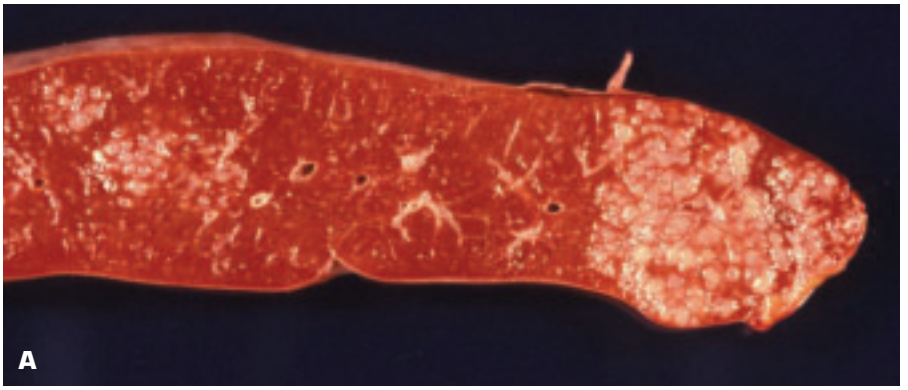

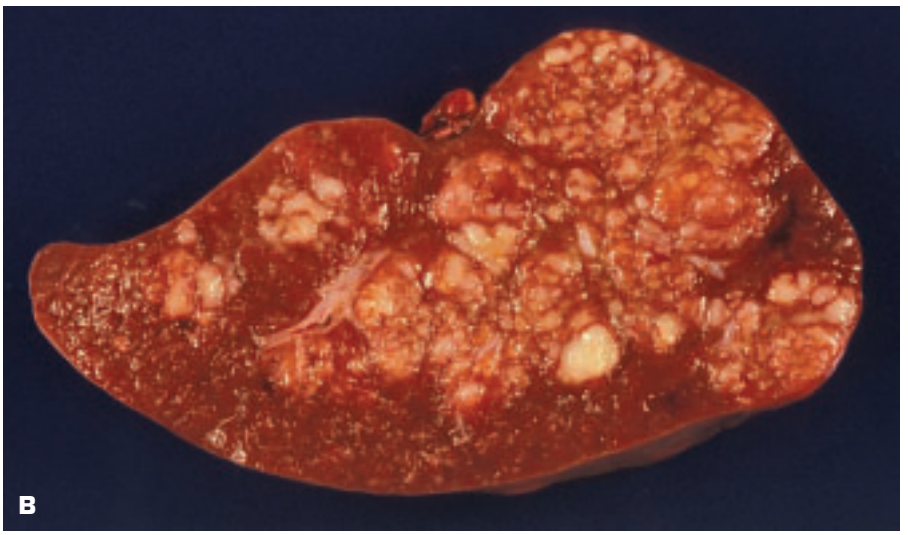

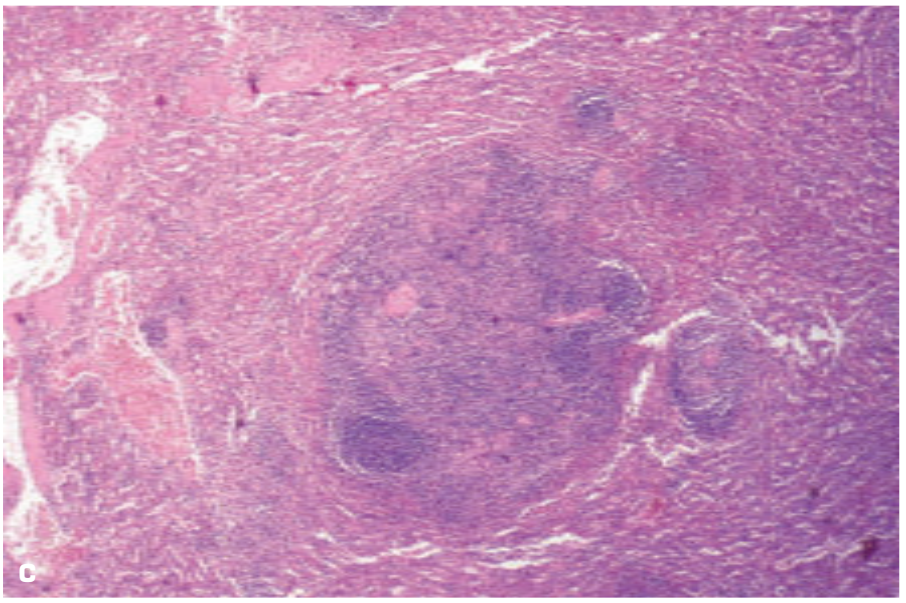

9-12. Lymphoma in the spleen. **A.** Nodular sclerosing Hodgkin disease in the spleen is seen as focally aggregated tumor nodules. **B.** More advanced Hodgkin disease of the spleen. **C.** Histologic appearance of a focal nodule of Hodgkin disease in the spleen. *(continued on next page)*

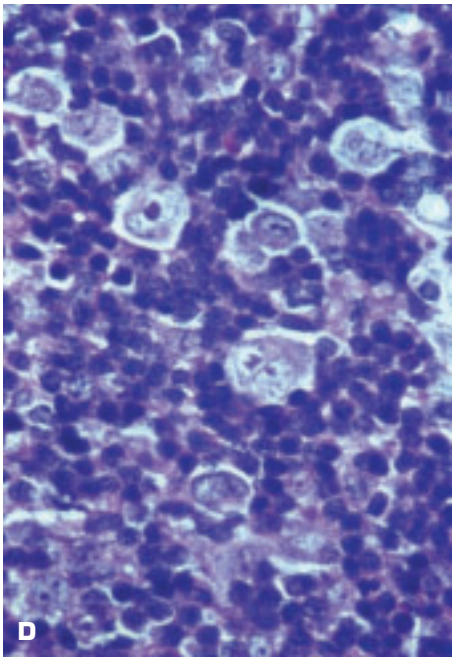

9-12. *(Continued)* **D.** Histology shows Hodgkin-type giant cells in the lesion. **E.** Extensive replacement of the spleen by a large cell, noncleaved follicular lymphoma. The tumor shows the characteristic "fish flesh" appearance strongly suggestive of a lymphoma. **F.** Small cell follicular lymphoma. The extreme multiplicity of tumor nodules is more in keeping with a lymphoma than with a secondary carcinoma. The background splenic tissue appears brown due to abundant iron deposits related to multiple blood transfusions.

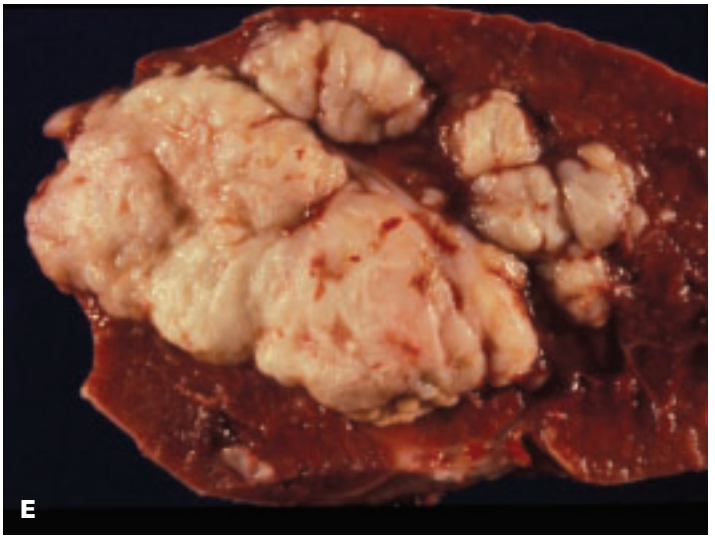

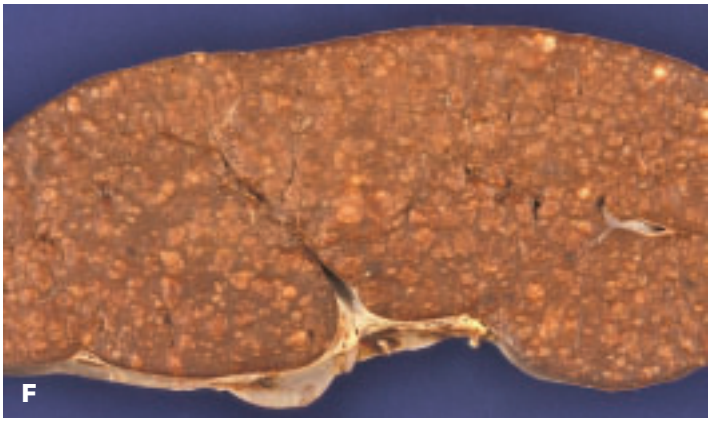

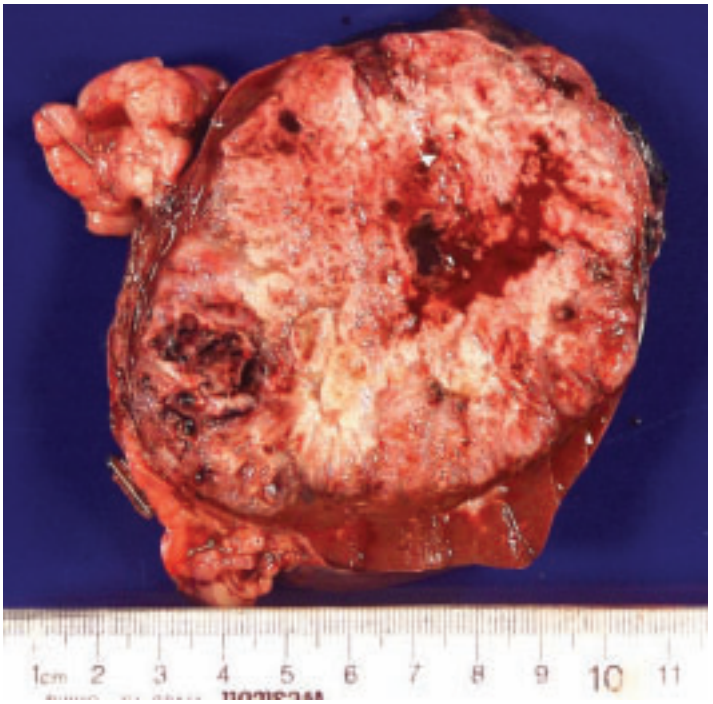

9-13. Metastatic renal cell adenocarcinoma in the spleen. The most common metastatic tumors in the spleen are due to cancers of the lung and breast, malignant melanoma, and leukemia.

9-14. Spleen in Langerhans cell histiocytosis (histiocytosis X) shows a diffuse nodular, reticular pattern.

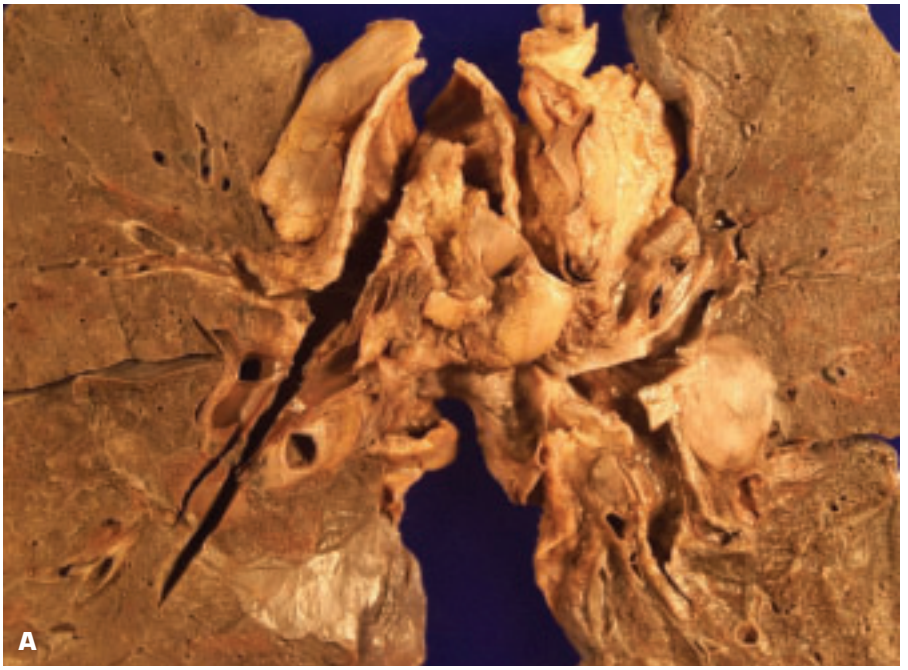

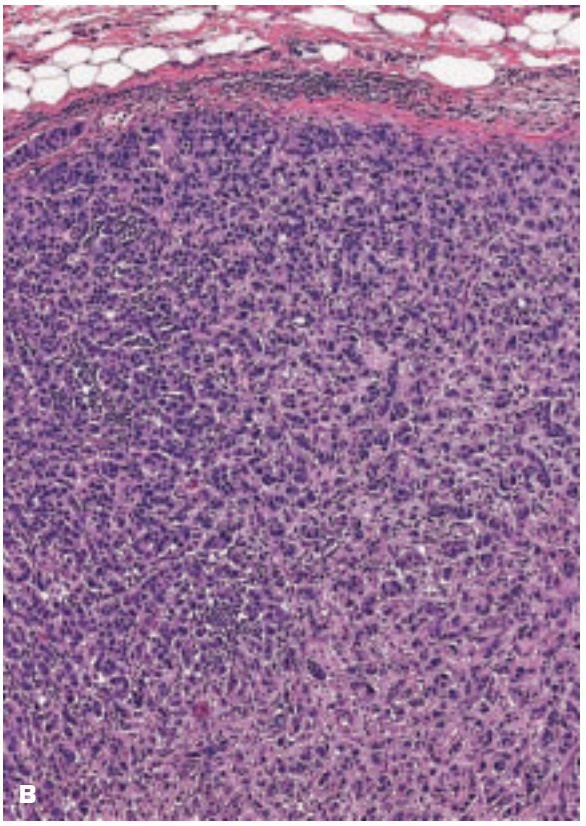

9-15. A. Pulmonary hilar and bronchopulmonary lymph nodes contain metastatic tumor. **B.** Histology of a lymph node infiltrated by metastatic undifferentiated ductal carcinoma of the breast. *(continued on next page)*

9-15. *(Continued)* **C.** Hilar nodes show residual carbon deposits within the metastatic lung cancer. **D.** Caseous tuberculous hilar lymph nodes in the lymph node component of a primary tuberculous complex of the lung. Note the prominent perinodal fibrosis.

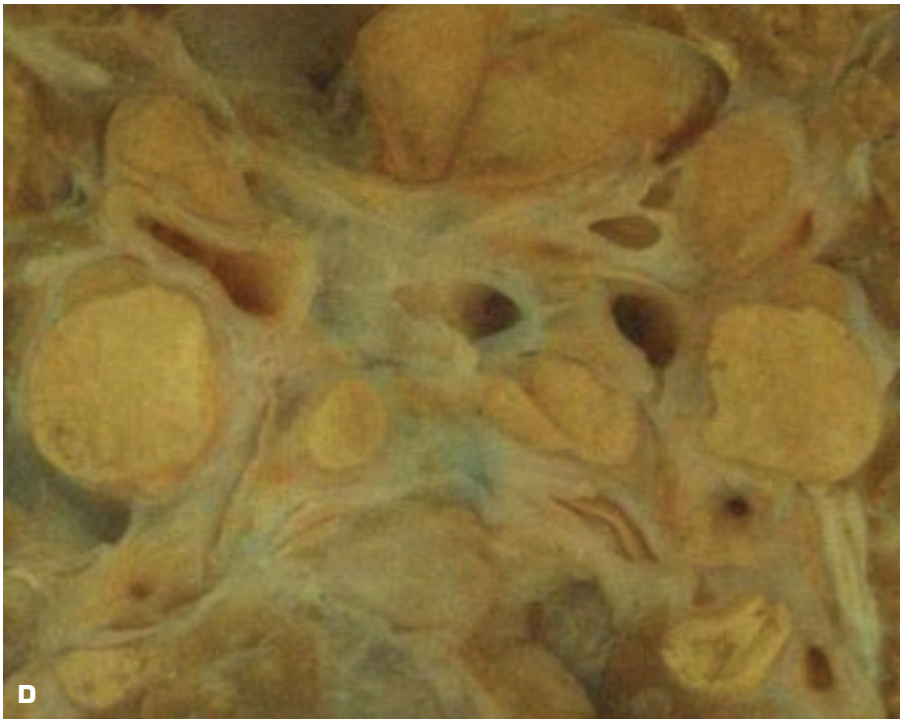

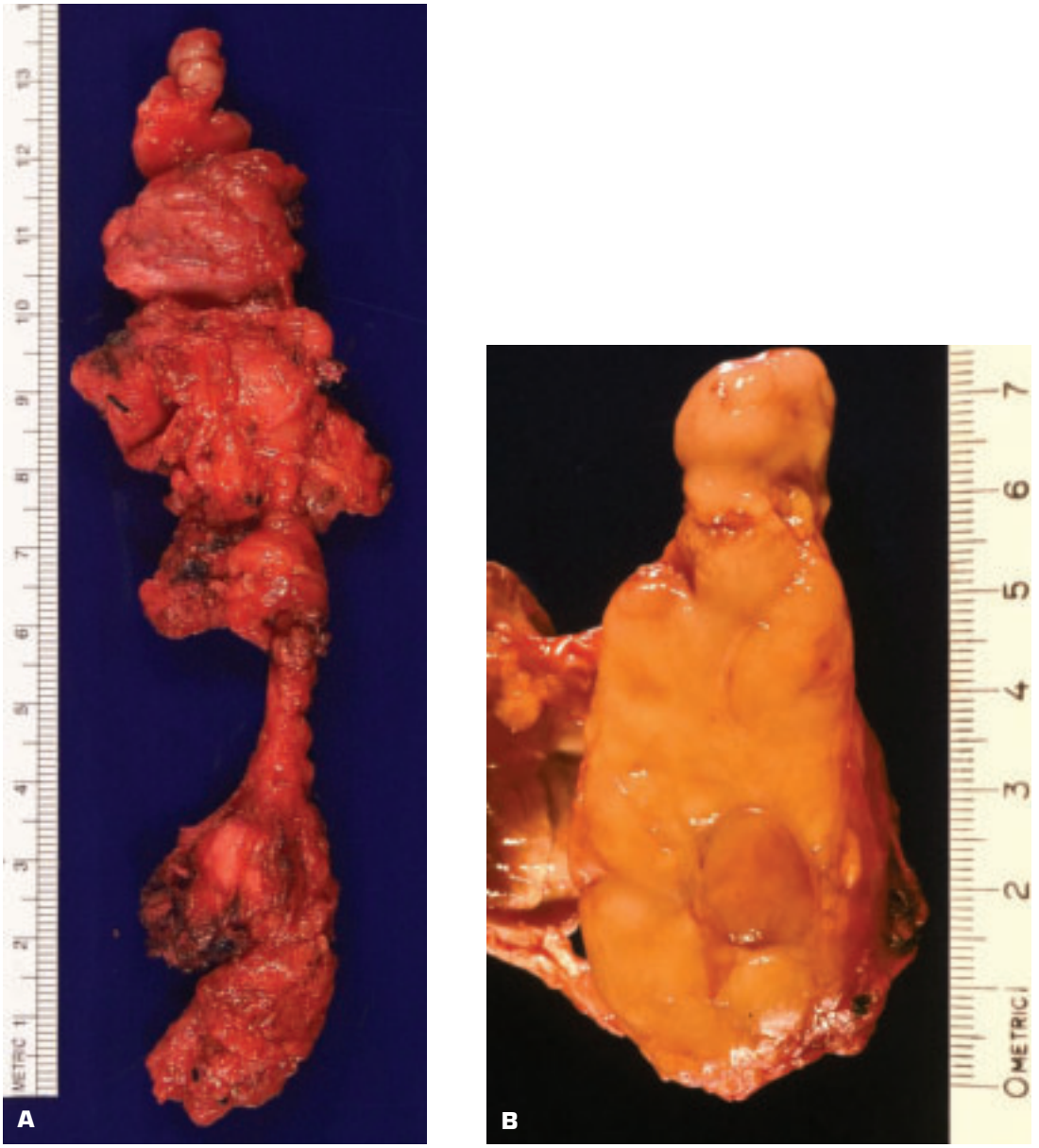

9-16. Radical dissection of deep cervical lymph nodes for metastatic carcinoma. **A.** Picture shows an undissected chain of tumor-infiltrated neck lymph nodes. **B.** Massive infiltration by metastatic carcinoma in cervical nodes has spread beyond the nodes to produce a fused tumor mass. *(continued on next page)*

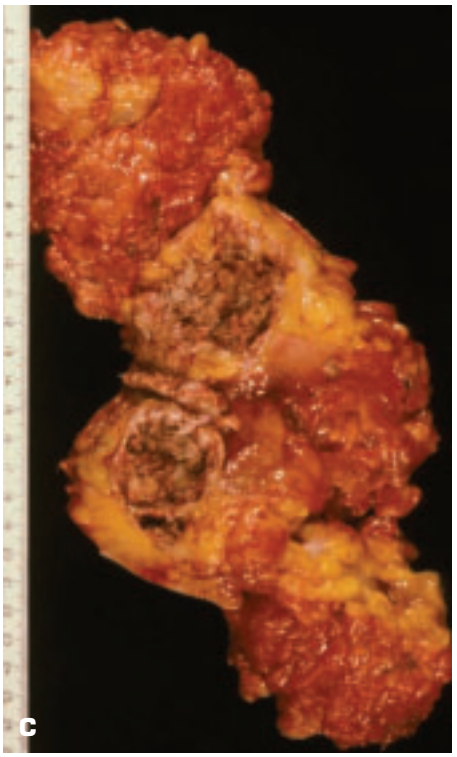

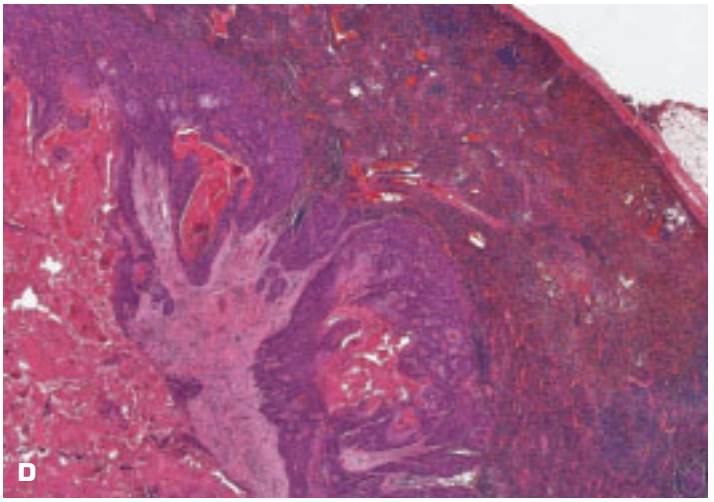

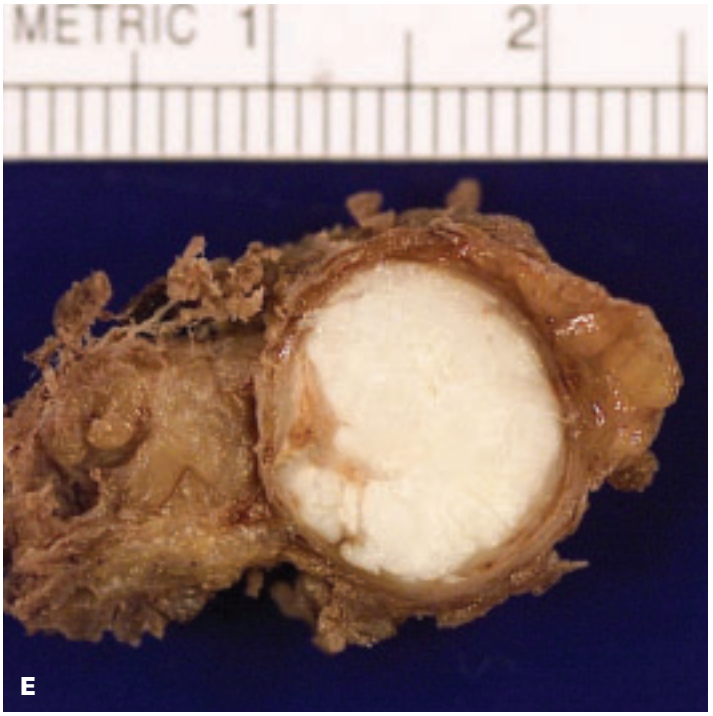

9-16. *(Continued)* **C.** Necrotic metastatic squamous carcinoma in nodes. **D.** Histology of the same node shows keratinizing squamous carcinoma with necrosis (*lower left*). **E.** Totally necrotic metastatic squamous carcinoma after irradiation appears white in color due to a granulomatous response to the keratin.

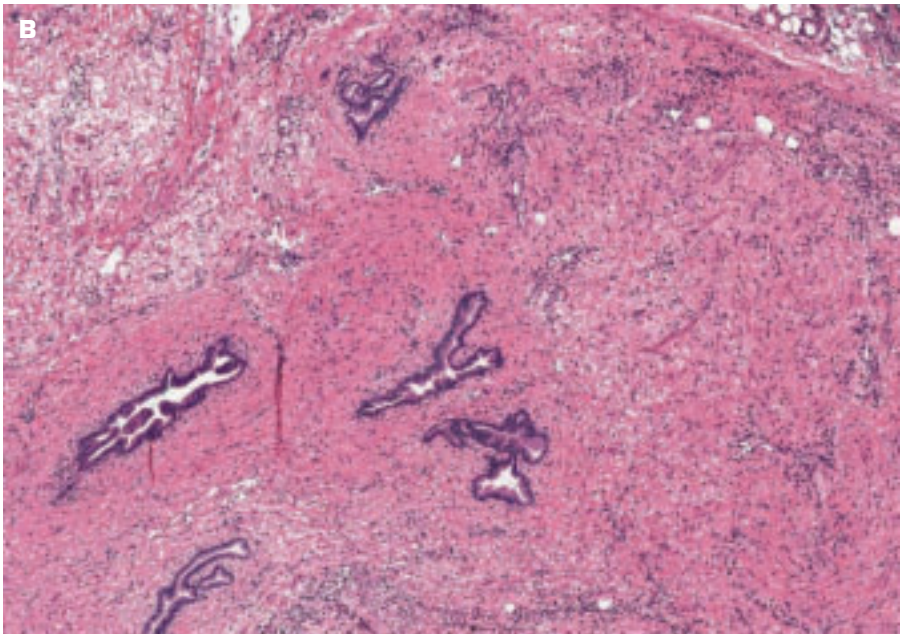

9-17. A. Metastatic colon cancer in peripancreatic lymph nodes *(arrow*). **B.** Nodal histology shows secondary adenocarcinoma in a desmoplastic stroma. *(continued on next page)*

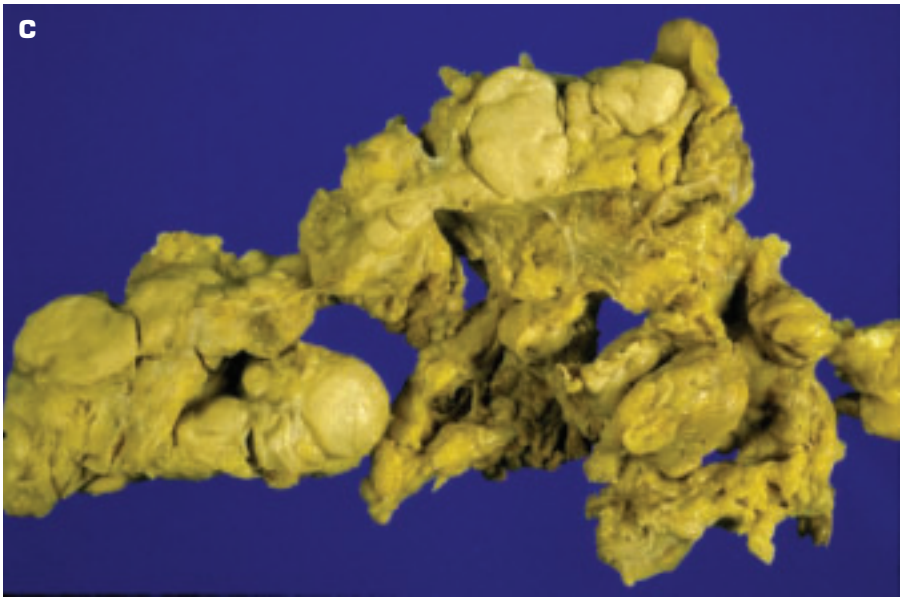

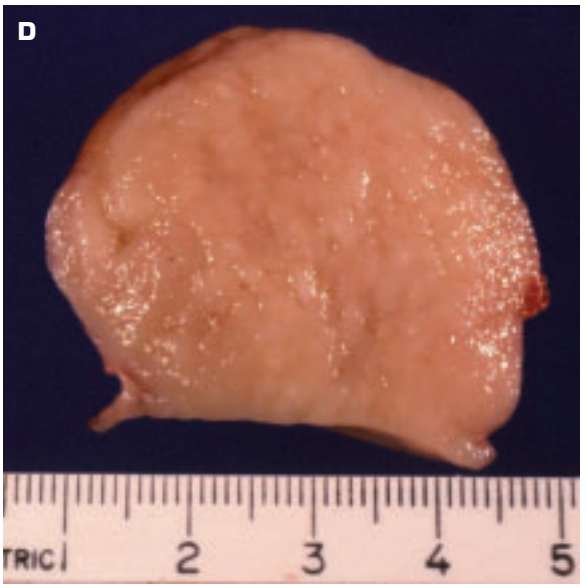

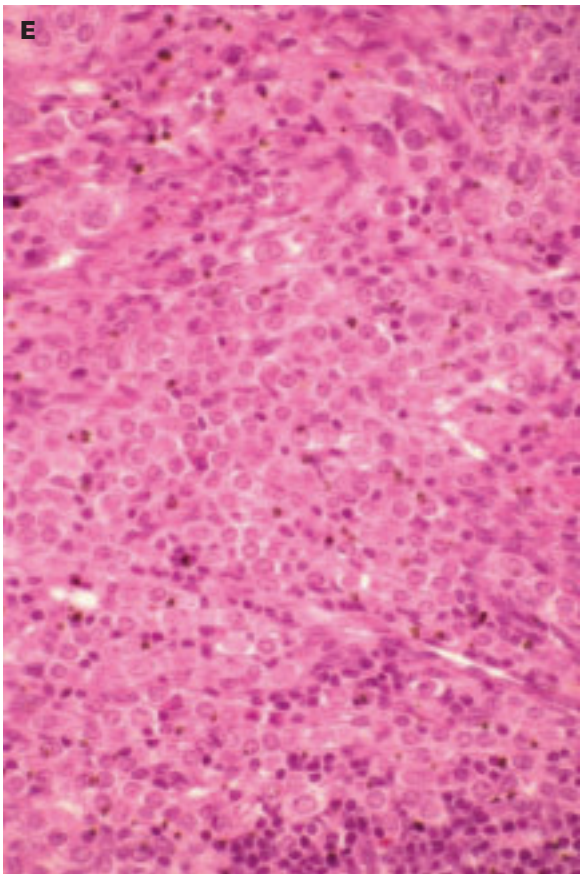

9-17. *(Continued)* **C.** Mesenteric nodes infiltrated by lymphoma show a fleshy, swollen appearance. **D.** Enlarged lymph node due to malignant follicular lymphoma. **E.** Histology shows a follicular lymphoma composed of a mixture of small and large cells.

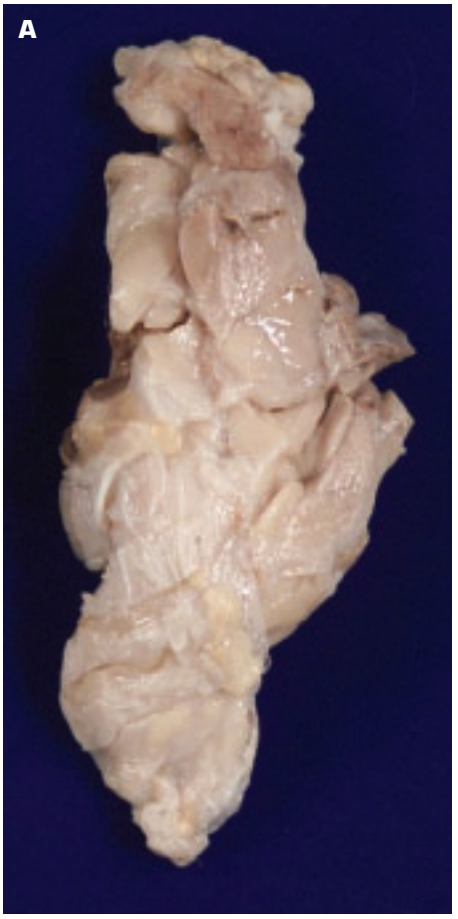

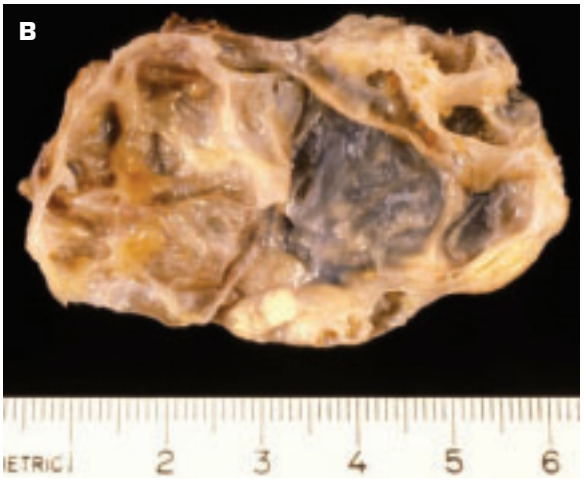

9-18. A. Hyperplastic thymus in an adult with myasthenia gravis that contained lymphoid follicles with germinal centers. **B.** Thymic cyst that had contained clear fluid. **C.** Thymoma that is still confined to the thymus gland. *(continued on next page)*

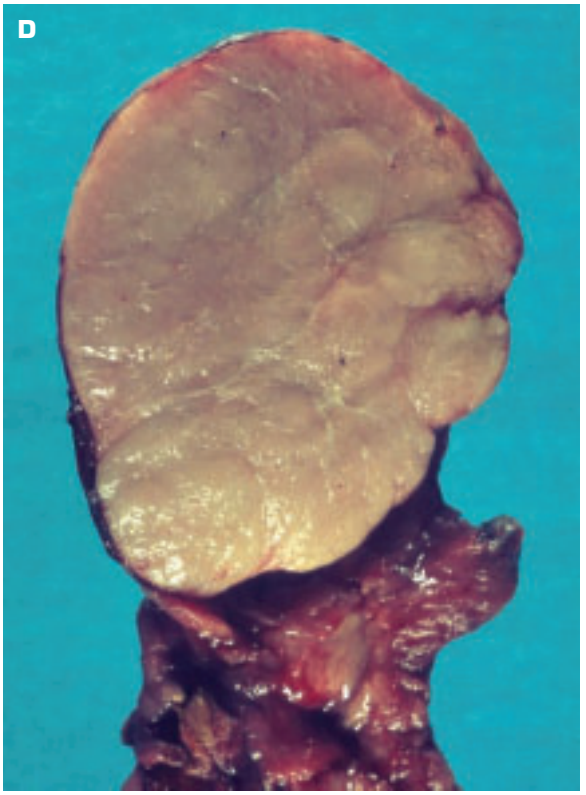

9-18. *(Continued)* **D.** Close-up view of the same tumor. Note the fleshy, lobulated appearance of the lesion. **E.** Histology of an epithelial thymoma shows a mixture of neoplastic epithelial cells and reactive lymphocytes. Prognosis of a thymoma depends more on the degree of infiltration found by the surgeon than on the histology.

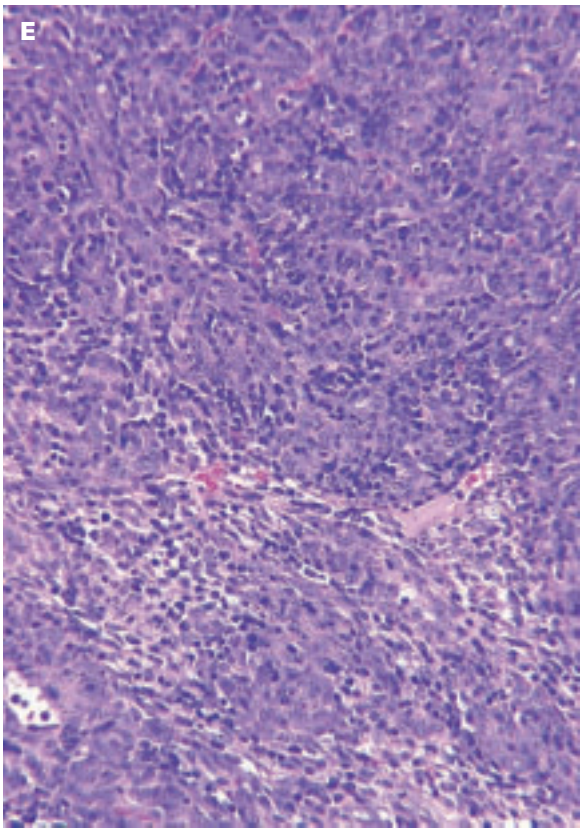

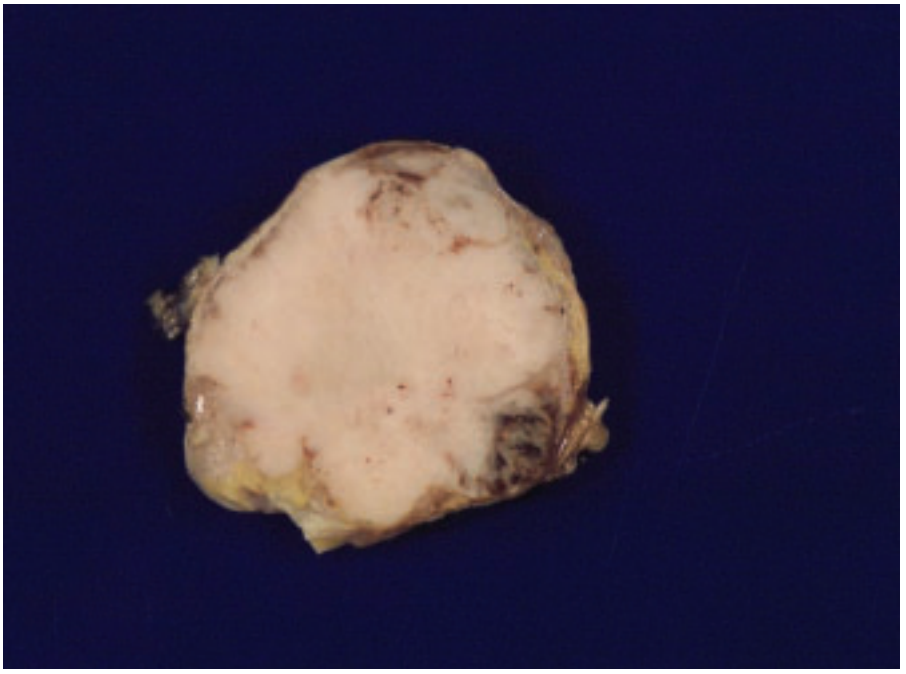

9-19. Malignant thymoma presenting as a solid white tumor that is infiltrating through the external margins of the thymus gland.

10 Pituitary, Carotid Body, Thyroid Gland, and Adrenals

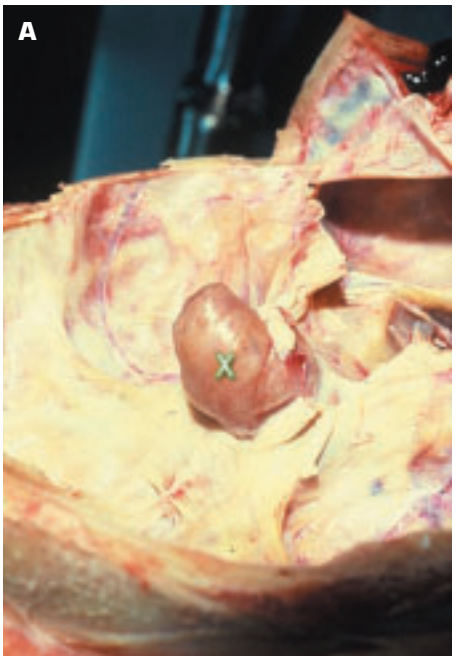

10-1. A. Suprasellar extension of a pituitary adenoma (X). **B.** Prolactin-secreting pituitary adenoma (*right*) has led to lactating breast tissue (*left*). **C.** Histology of a pituitary adenoma.

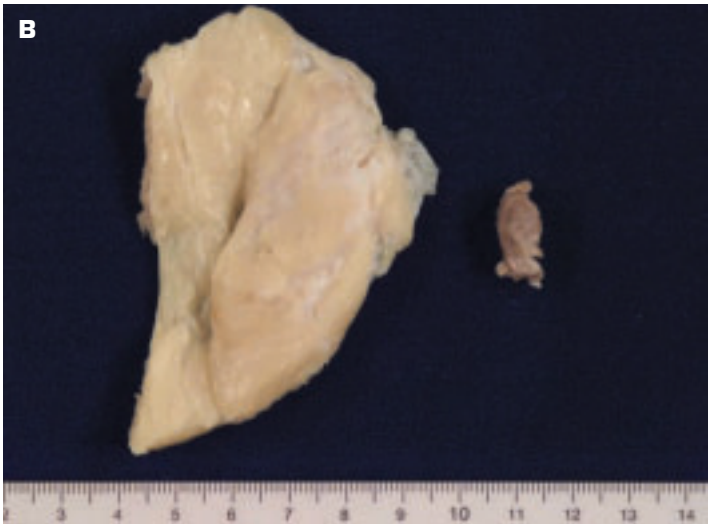

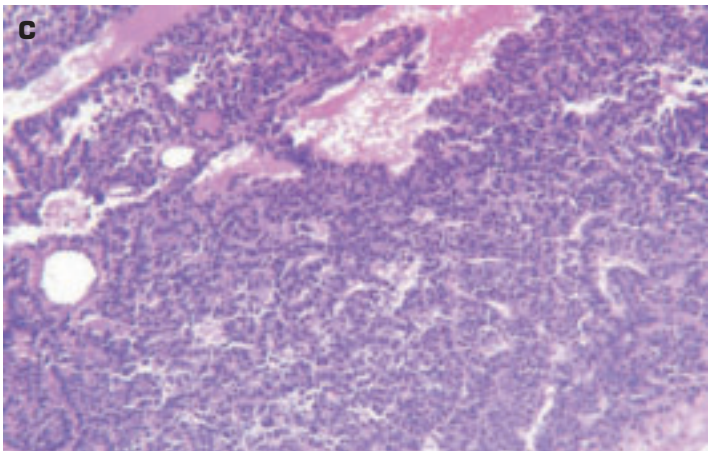

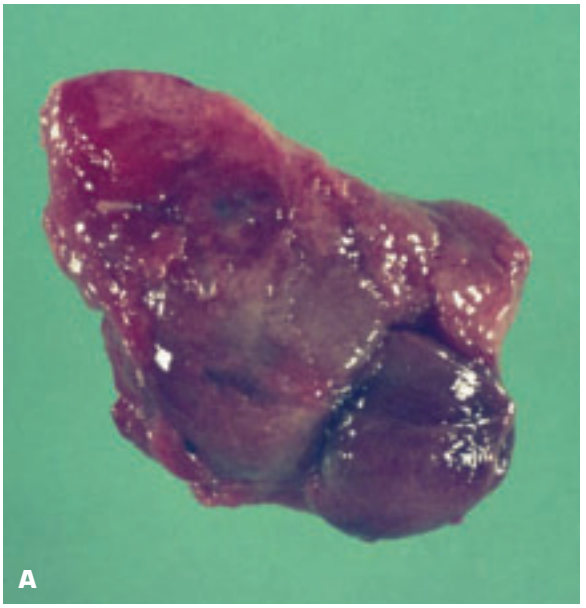

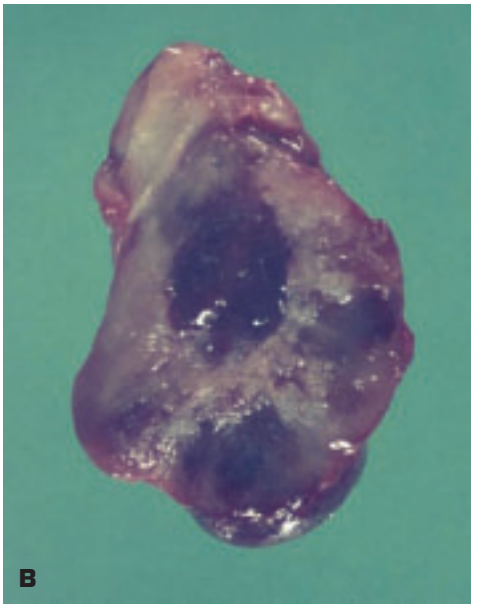

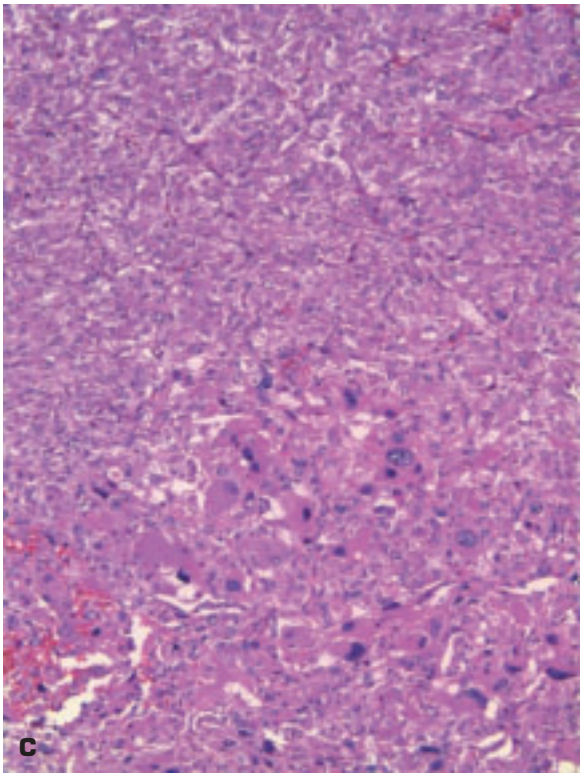

10-2. A. External appearance of a carotid body tumor that is a type of paraganglioma arising in the carotid artery body. **B.** Opposite side of the resected carotid body tumor includes a portion of the external carotid artery (*top*). **C.** Histology of the carotid body tumor exhibits the classical organoid pattern of a paraganglioma. Some cellular atypism is apparent in this benign tumor.

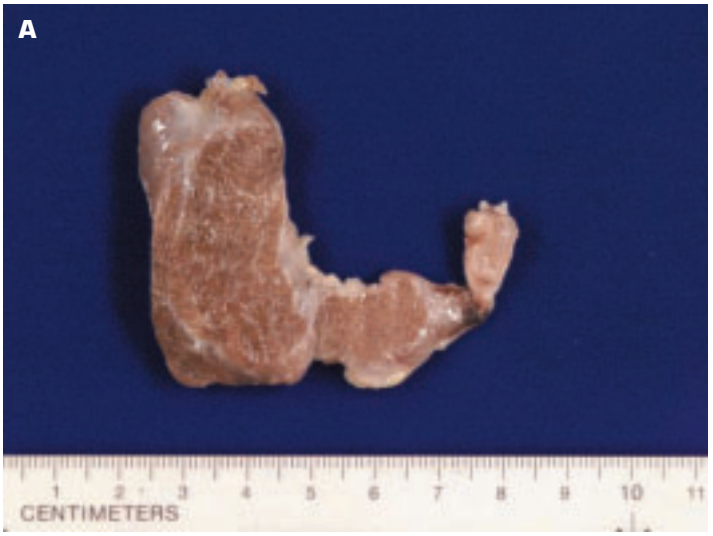

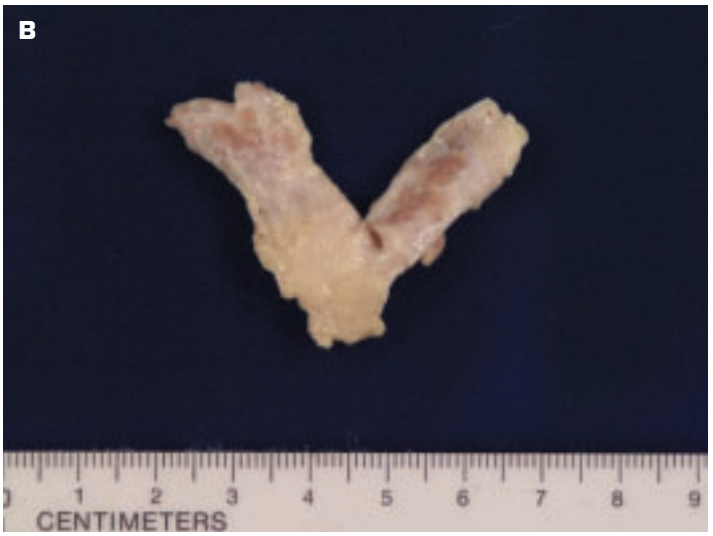

10-3. A. Hypoplastic left lobe (*right*) of the thyroid gland. **B.** This thyroid gland shows marked symmetric atrophy. **C.** Histology of the atrophic gland shows a healed thyroiditis.

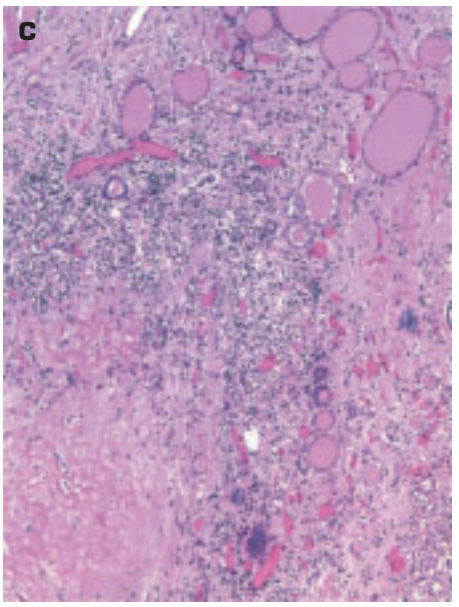

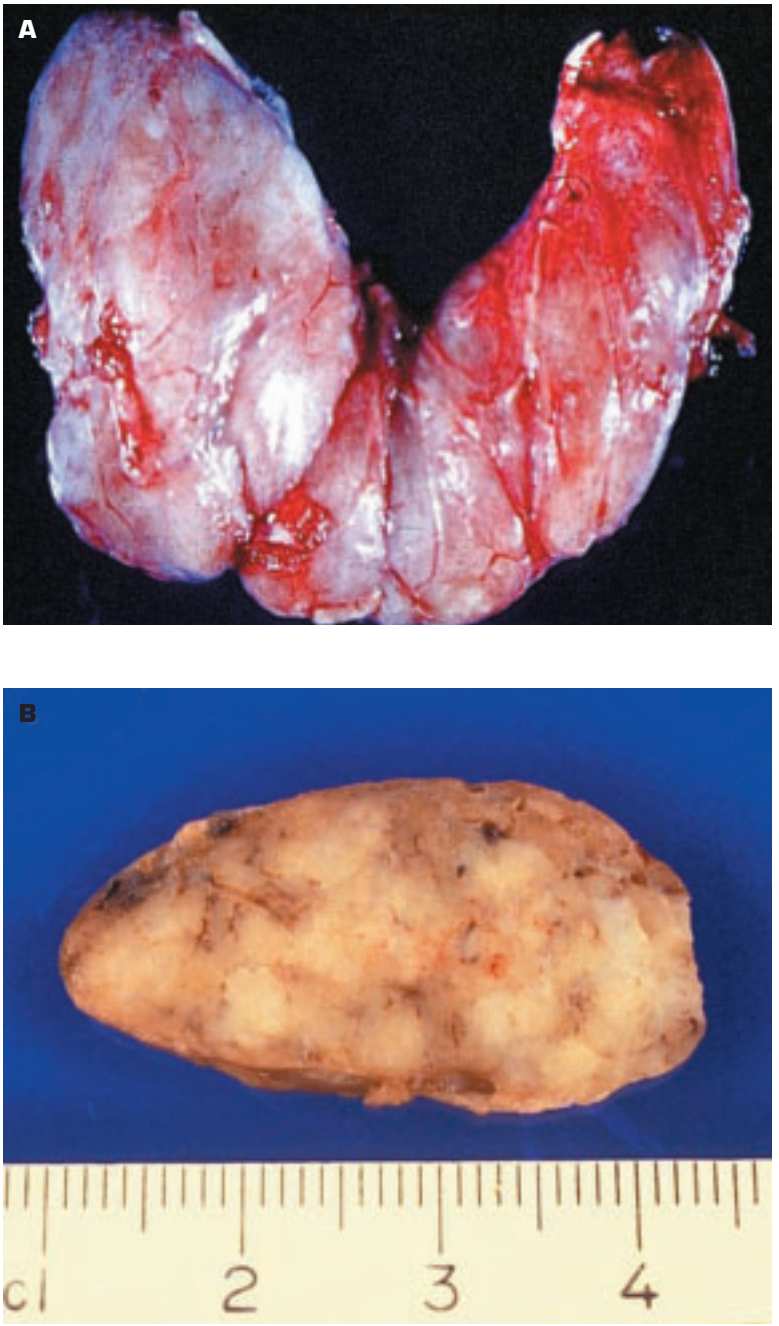

10-4. Chronic autoimmune (Hashimoto) thyroiditis. **A.** External surface of an enlarged, nodular-appearing thyroid gland. **B.** Cut surface of a lobe of thyroid gland in Hashimoto thyroiditis shows a lobulated arrangement. *(continued on next page)*

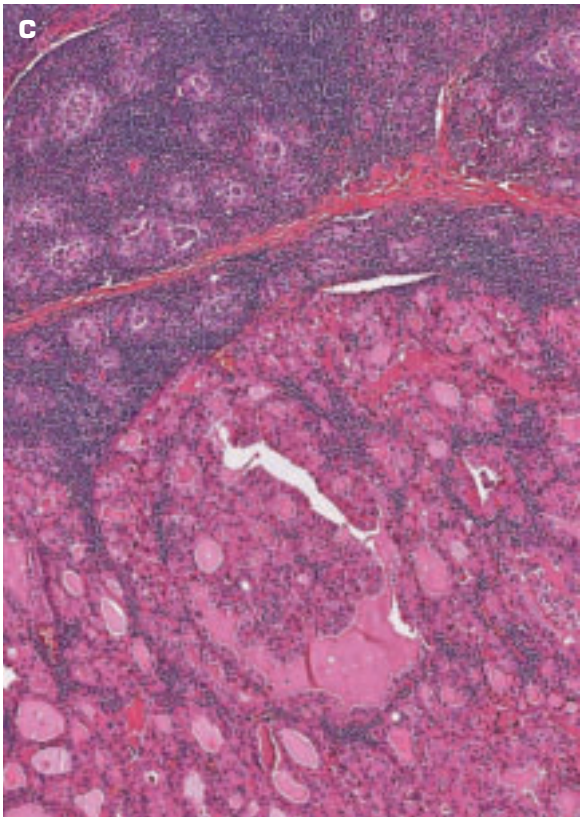

10-4. *(Continued)* **C.** Histology of Hashimoto disease shows massive lymphocytic infiltration between atrophic follicles. **D.** High-power view of Hashimoto disease showing a germinal center in the lymphoid infiltrate.

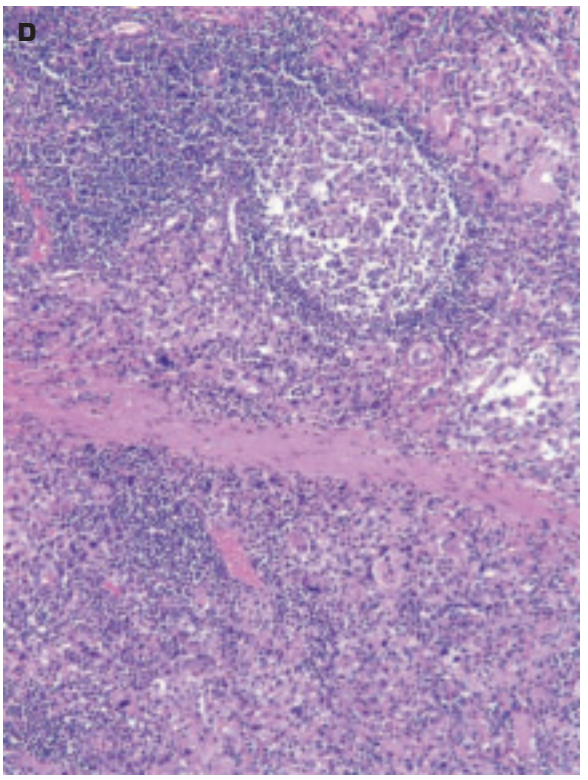

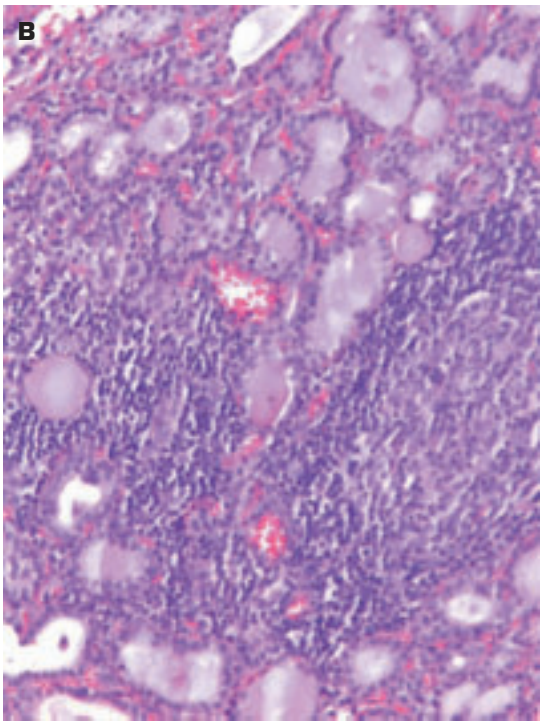

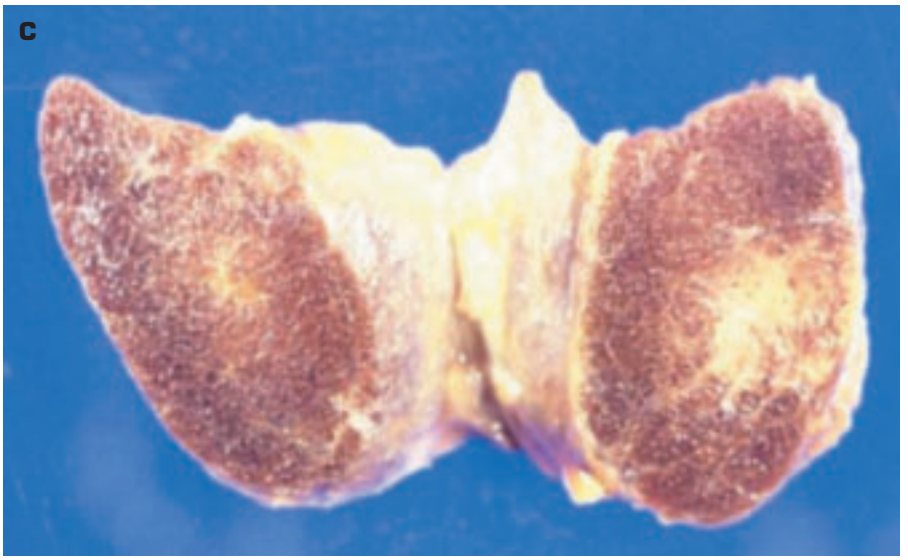

10-5. A. Thyroid gland in subacute lymphocytic thyroiditis shows muted zones of increased tissue density in an otherwise normal-appearing gland. **B.** Histology shows lymphocytic infiltration with follicular germinal center formation but no fibrosis or Hürthle cell metaplasia such as occurs in Hashimoto thyroiditis. **C.** *Aspergillus* abscess (*right*) of the left lobe of the thyroid gland. The thyroid gland is often affected in disseminated aspergillosis.

10-6. A. Colloid goiter (i.e., the phase of colloid involution of a diffuse nontoxic [simple] goiter in a geographic area of iodine deficiency). The colloid goiter shows early signs of transformation into a multinodular goiter. **B.** External aspect of a multinodular goiter. **C.** Cut surface of a multinodular goiter shows multiple nodules of varying sizes with cyst formation in areas. *(continued on next page)*

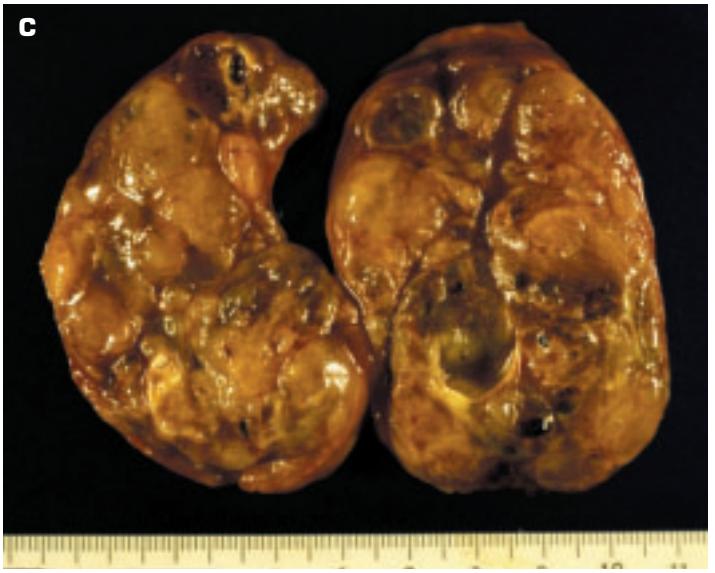

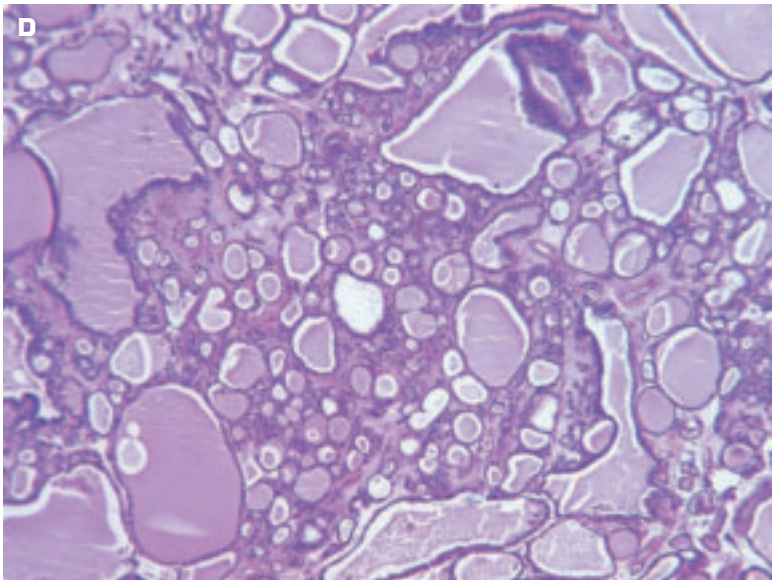

10-6. *(Continued)* **D.** Histology of multinodular goiter shows a portion of one of the hyperplastic nodules. **E.** Multinodular goiter with more abundant cysts and a calcified white nodule (*arrow*). *(continued on next page)*

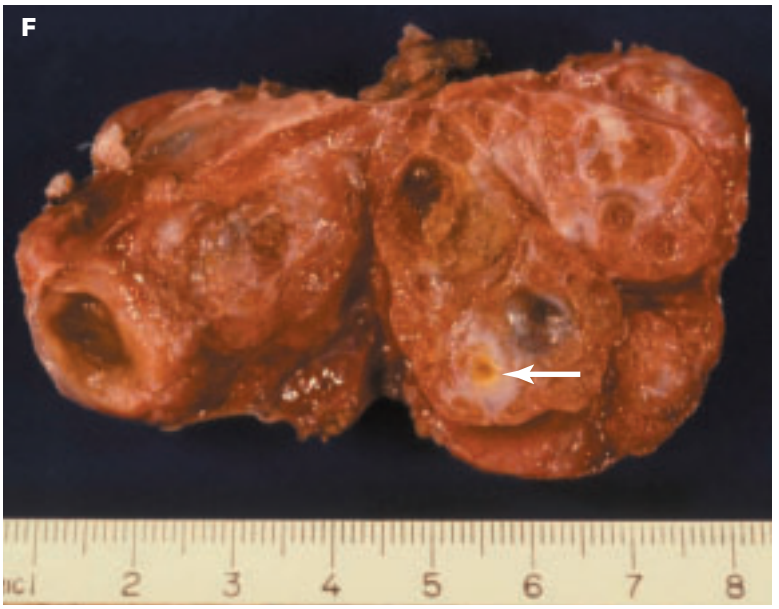

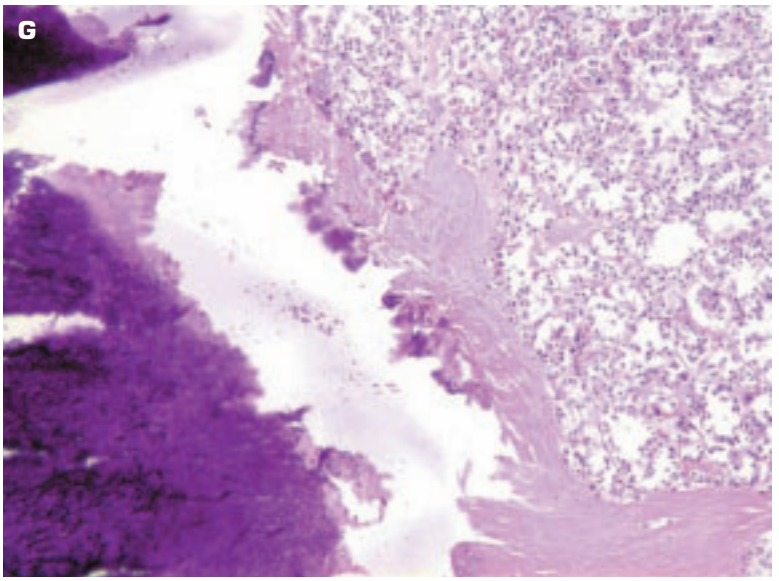

10-6. *(Continued)* **F.** Advanced multinodular goiter with abundant cysts and much fibrosis following involution of hyperplastic nodules. Focal calcification (*arrow*) appears yellow in color. **G.** Histology confirms the calcification (*bottom left*).

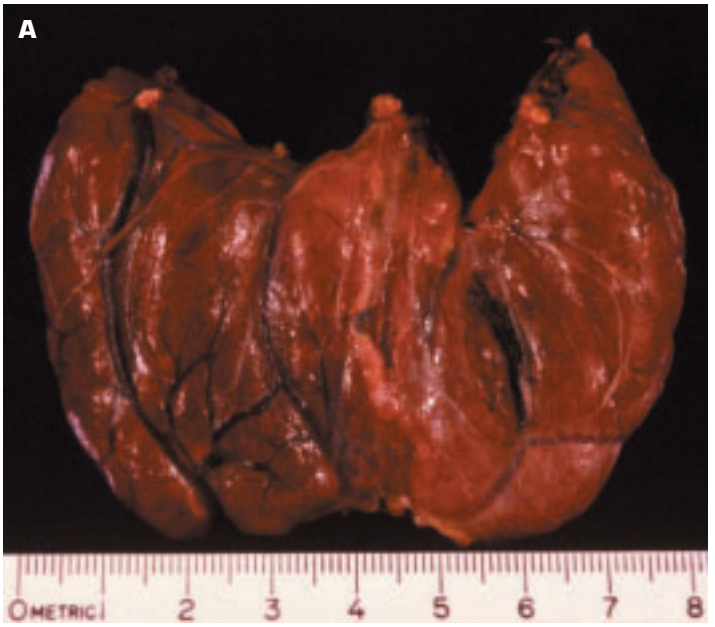

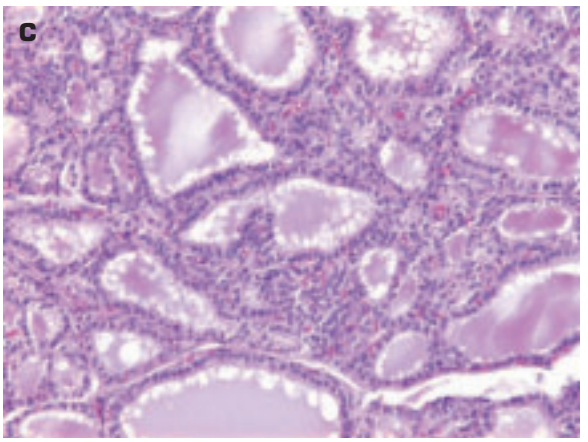

10-7. Thyrotoxicosis/diffuse hyperplasia of the thyroid gland (Graves' disease). **A.** The external surface of the diffusely enlarged thyroid gland shows a prominent vascularity and an erythematous parenchyma. **B.** The cut surface of the thyroid gland shows a hyperemic, meaty, shiny appearance. **C.** Histology of Graves' disease showing resorption-induced scalloping of the margins of the colloid. Hyperplastic papillary epithelial infolding results from the lining cells becoming columnar in shape and increased in number. Pretreatment of the gland may alter its morphology.

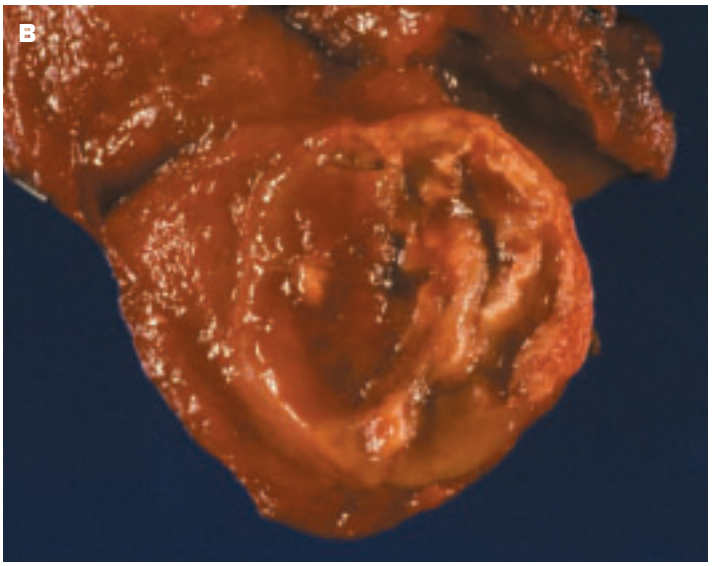

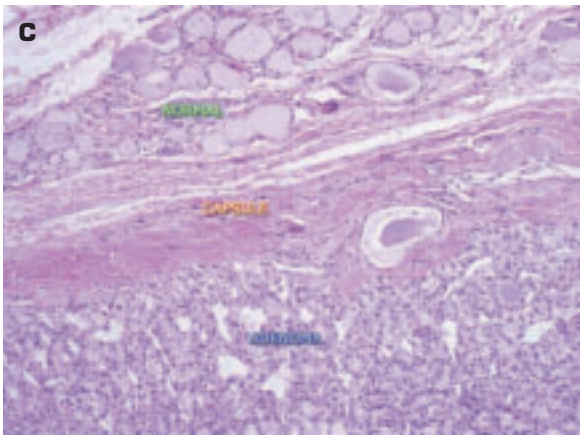

10-8. A. Follicular adenoma of the thyroid gland has a well-demarcated border surrounded by a thin fibrous capsule. **B.** This follicular adenoma shows some degeneration and focal calcification of the lesion. **C.** Histology of a well-differentiated follicular adenoma showing a capsule separating the adenoma (*bottom*) from the normal thyroid tissue (*top*).

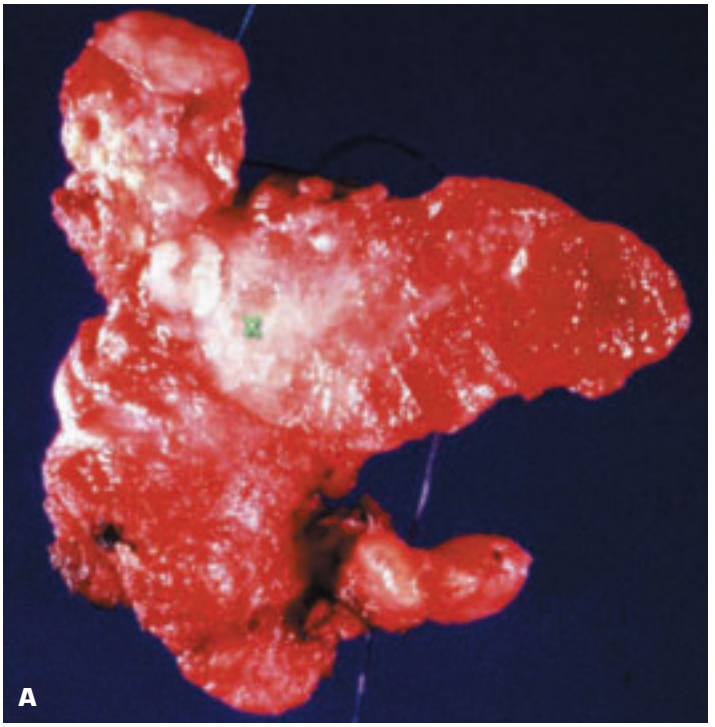

10-9. Papillary carcinoma of the thyroid gland. **A.** Macroscopic appearance of papillary cancer (X) of the thyroid gland comprises a fibrous-looking area within the gland. **B.** Fine-needle aspiration of the papillary cancer reveals epithelial cells with nuclear grooves (*arrows*). **C.** Typical vacuolated ("orphan Annie") nuclei of a papillary cancer of the thyroid.

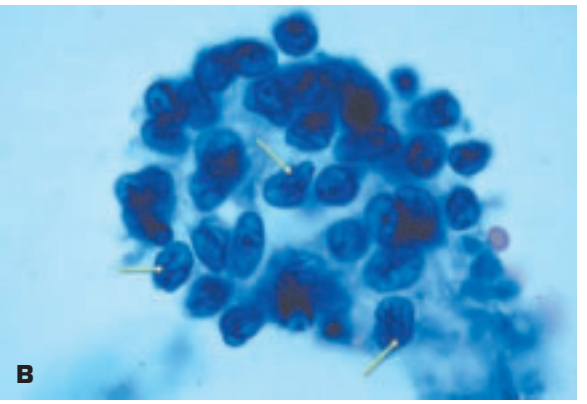

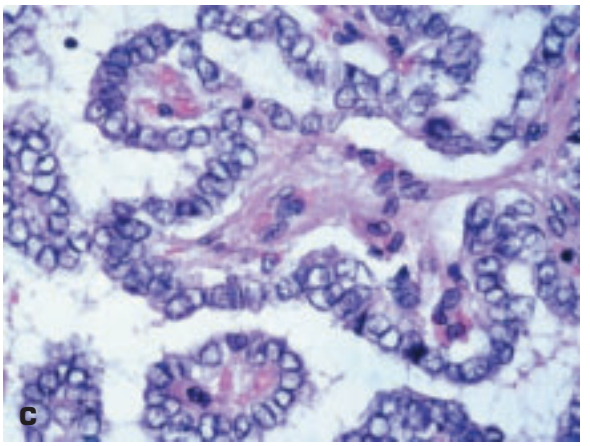

10-10. A. Follicular carcinoma of the thyroid gland appearing as a well-circumscribed nodule. **B.** Minimally invasive follicular carcinoma has been surgically resected. Note the inked resection margins. **C.** Histology of an invasive follicular carcinoma showing the neoplasm invading through the fibrous capsule (*arrow*).

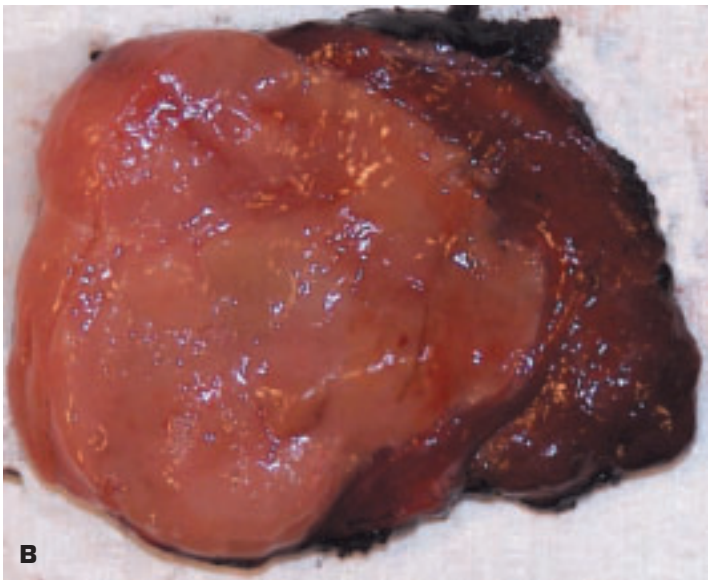

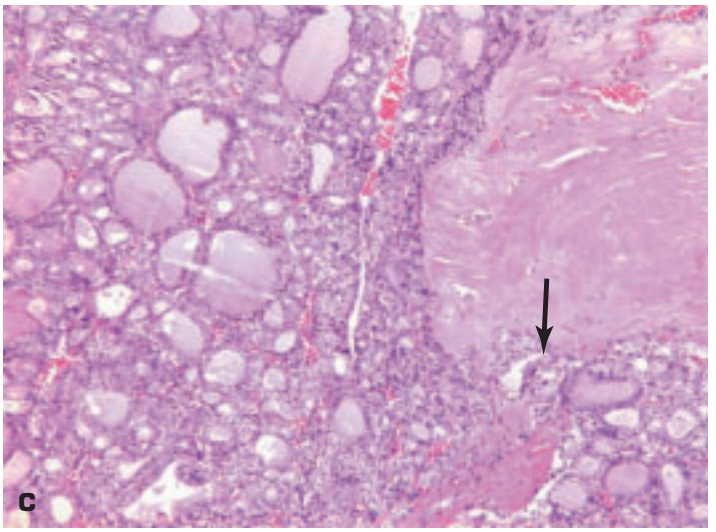

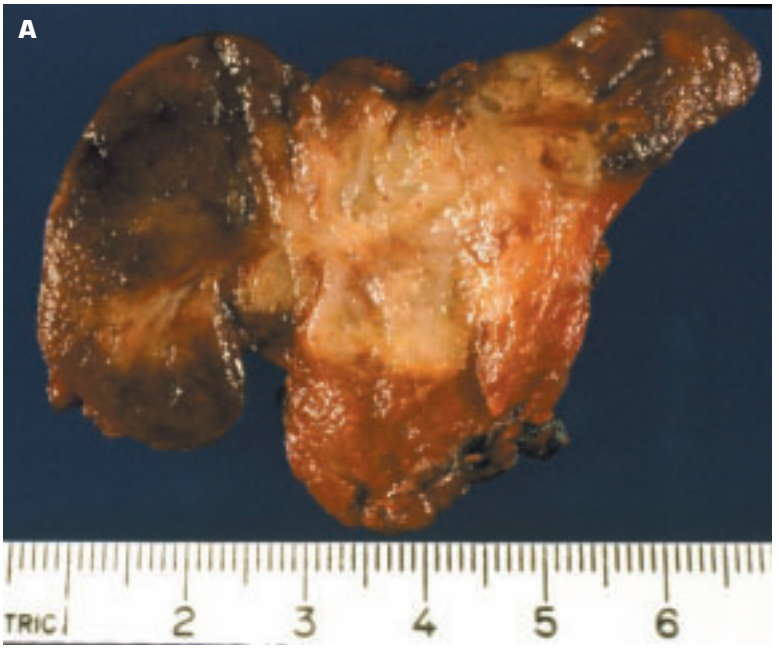

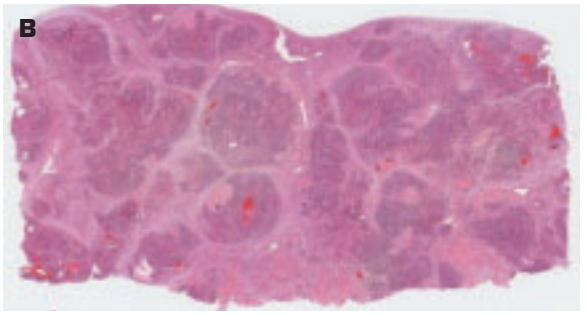

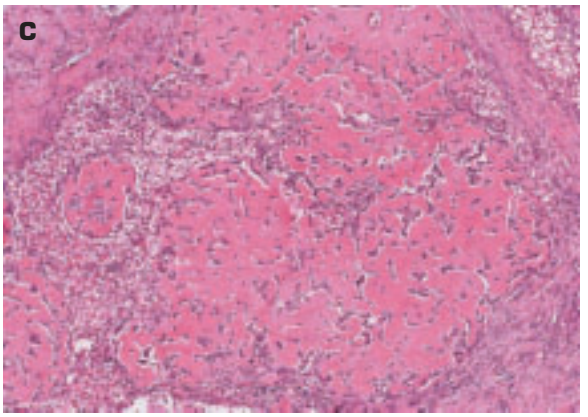

10-11. A. Medullary carcinoma of the thyroid gland shows its typical features of an unencapsulated, circumscribed, solid-looking, gray-white tumor mass. **B.** Whole mount section of a medullary carcinoma showing masses of tumor cells separated by a collagenous stroma. **C.** Higher power reveals amyloid production by the tumor cells.

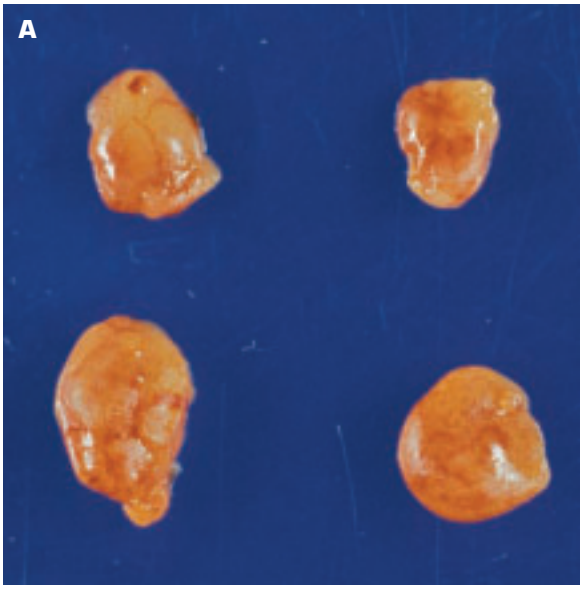

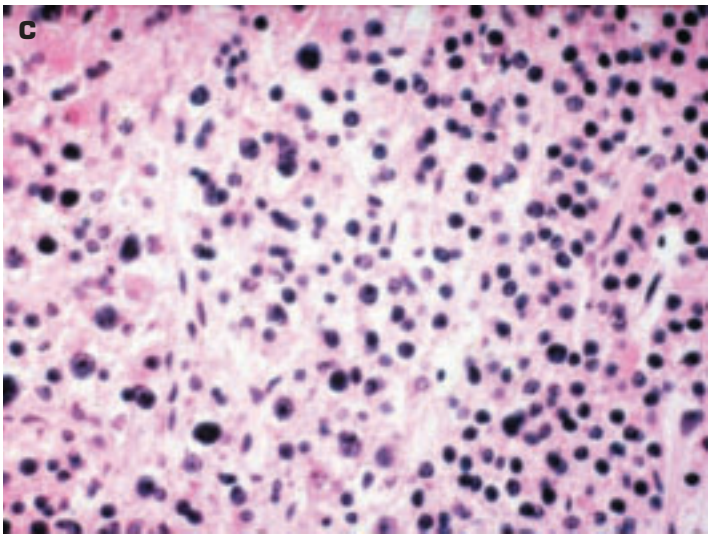

10-12. A. All four parathyroid glands are enlarged due to hyperplasia. This is in contradistinction to an adenoma of a single parathyroid gland, which would produce atrophy of the other three glands. **B.** Parathyroid adenoma has enlarged this parathyroid gland. **C.** Histology shows a proliferation of chief (clear) cells comprising the parathyroid adenoma.

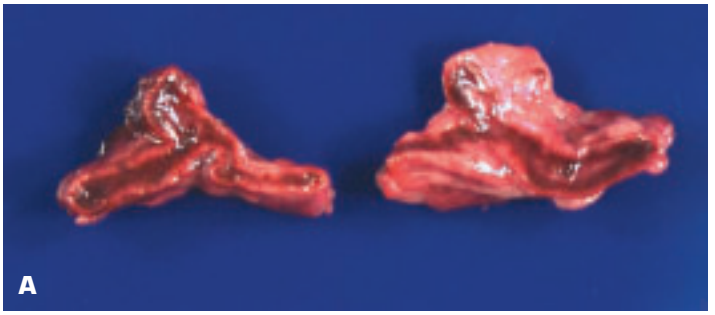

10-13. A. Mild hemorrhage into the adrenal glands. **B.** Massive, bilateral, intraadrenal hemorrhage. Portions of the adrenal cortices have been destroyed. The patient died of shock. In Waterhouse–Friderichsen syndrome, the entire adrenal gland may undergo hemorrhagic infarction (e.g., in association with meningococcal septicemia). **C.** Histology of hemorrhagic infarction of the adrenal gland in a neonate.

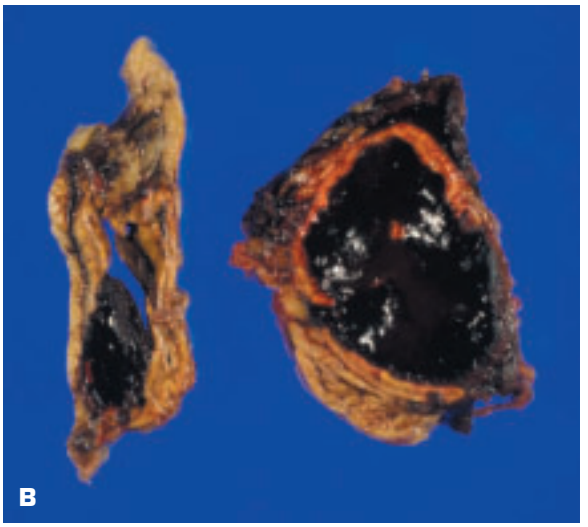

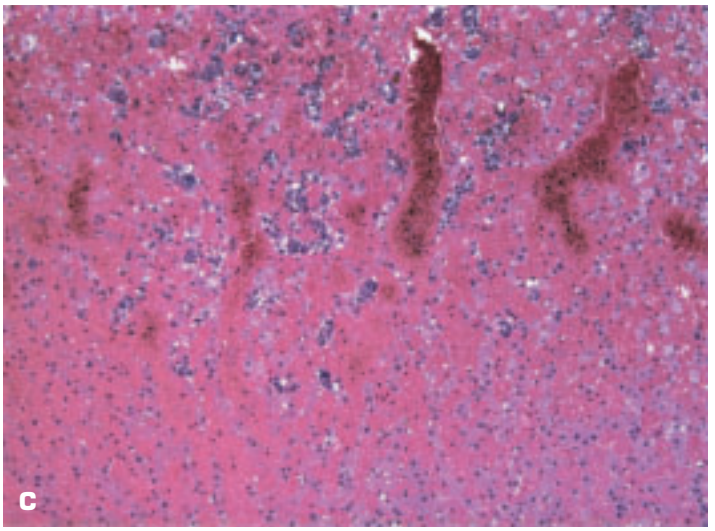

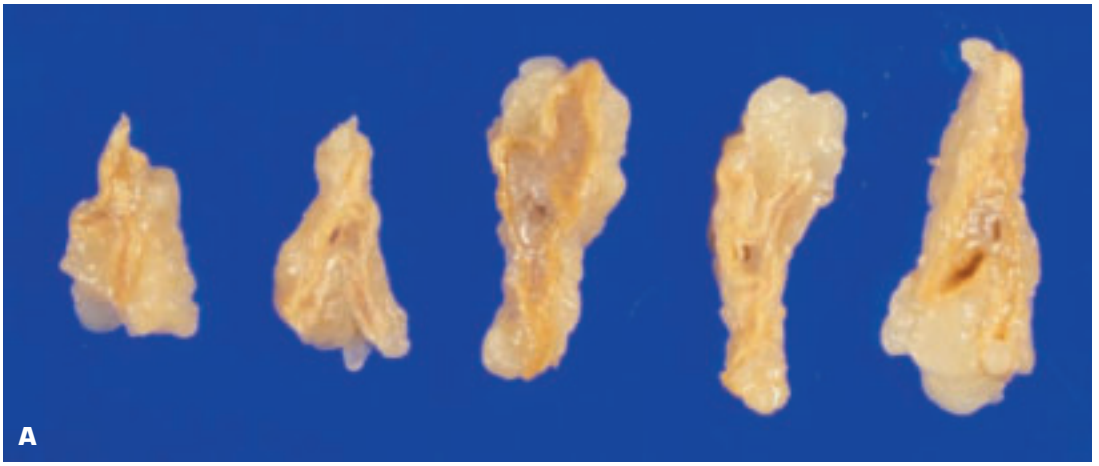

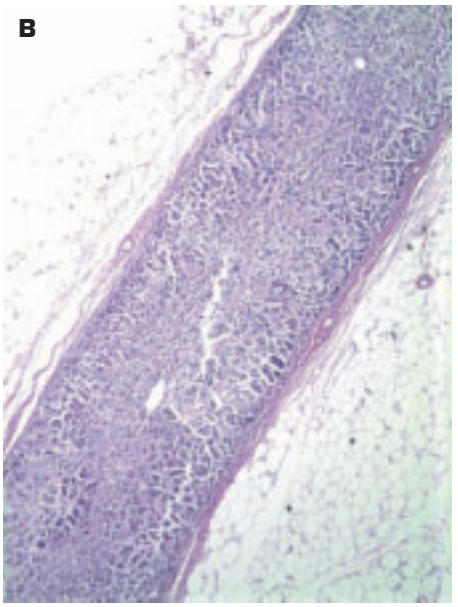

10-14. A. Atrophy of both adrenal glands due to corticosteroid therapy. **B.** Histology shows attenuation of all three zones of the adrenal cortex.

10-15. A. Extensive hyperplasia of the adrenal cortex. **B.** Adenomatous hyperplasia of the adrenal cortices: the cortices show diffuse widening with focal, nodular excrescences that are quite marked in areas. *(continued on next page)*

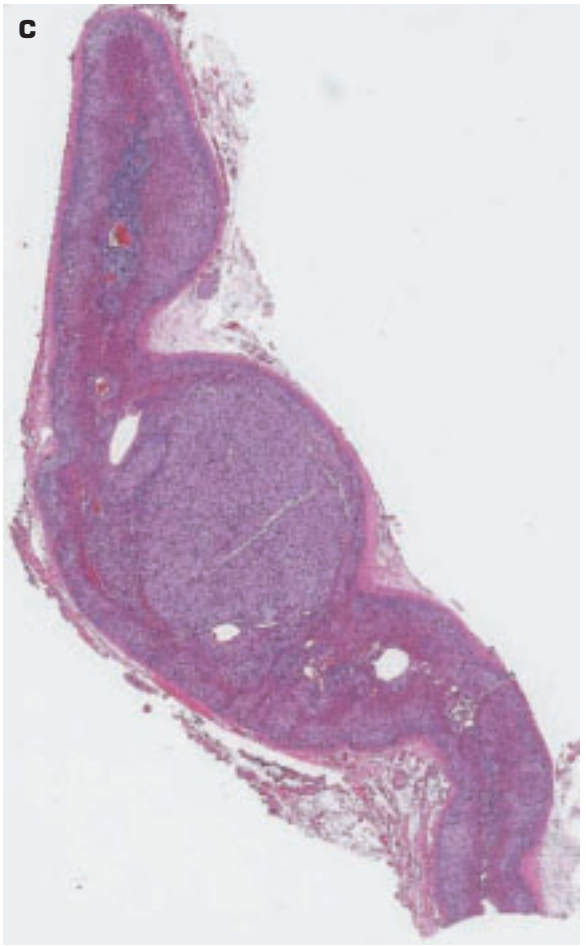

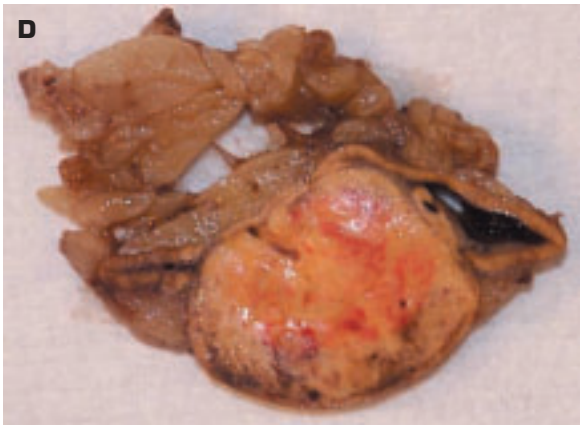

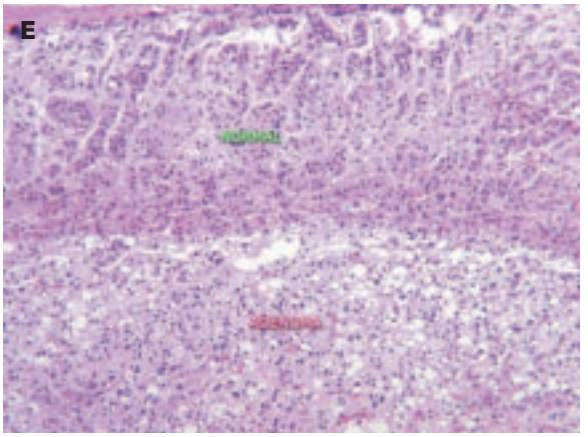

10-15. *(Continued)* **C.** Histology of focal nodular hyperplasia of the adrenal cortex. **D.** Adrenal cortical adenoma has a yellow color due to the high lipid content of its component cells. **E.** Histology of the junction between adenoma (*bottom*) and normal cortex (*top*). **F.** Multiloculated adrenal cyst of uncertain origin. The lesion may be a pseudocyst secondary to degeneration of a benign neoplasm or due to resolution of an intraadrenal hemorrhage.

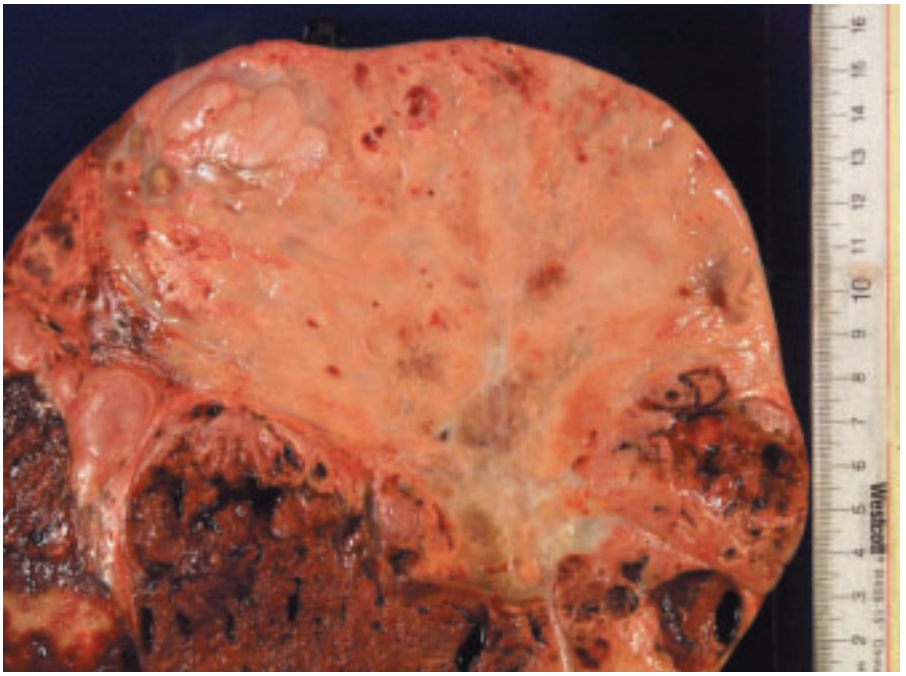

10-16. Carcinoma of the adrenal cortex presenting as a large, fleshy partially necrotic tumor that has completely effaced the adrenal gland.

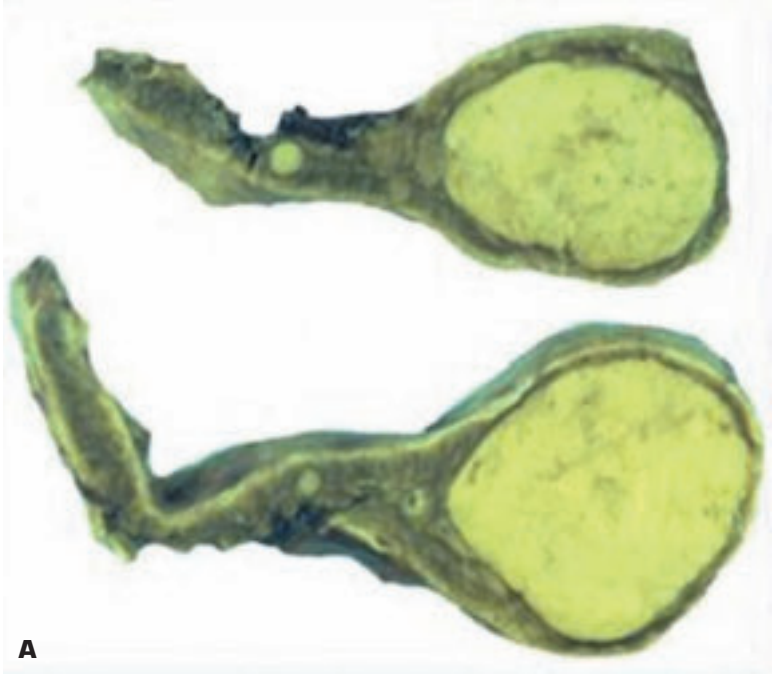

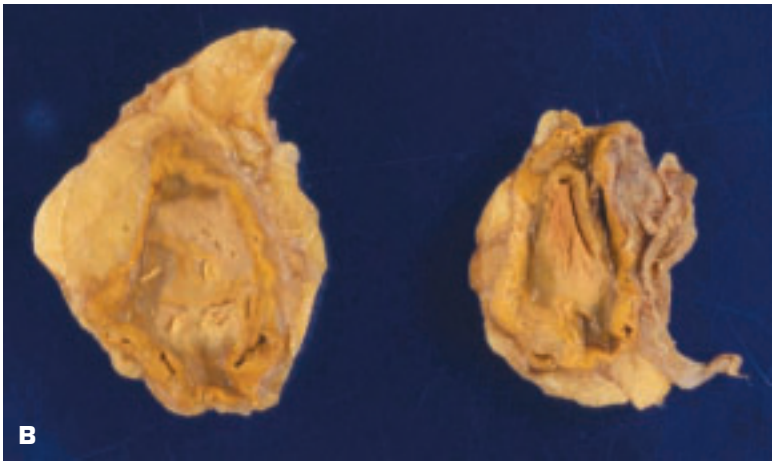

10-17. A. Bisected adrenal gland contains a pheochromocytoma in its central, medullary region. A second smaller adjacent tumor nodule is also noted. **B.** Bilateral pheochromocytomas of the adrenal glands. *(continued on next page)*

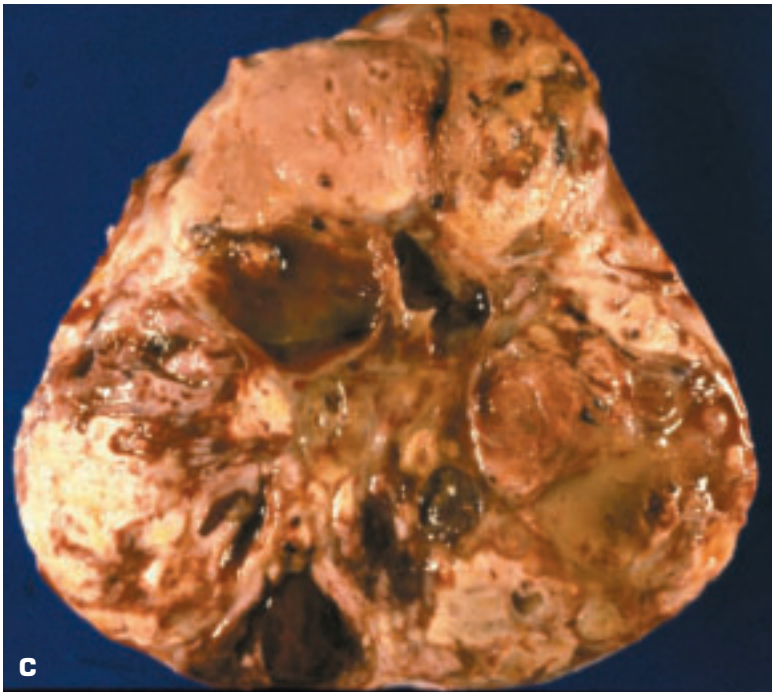

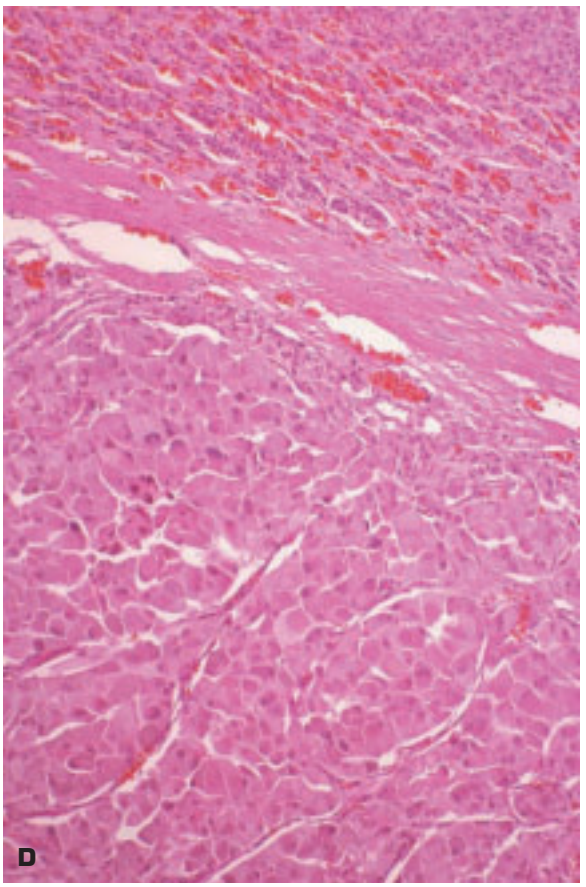

10-17. *(Continued)* **C.** This large pheochromocytoma shows extensive necrosis and cystic degeneration. **D.** Histology of a pheochromocytoma (*bottom*) showing an organoid growth pattern. The adrenal cortex (*top*) appears compressed.

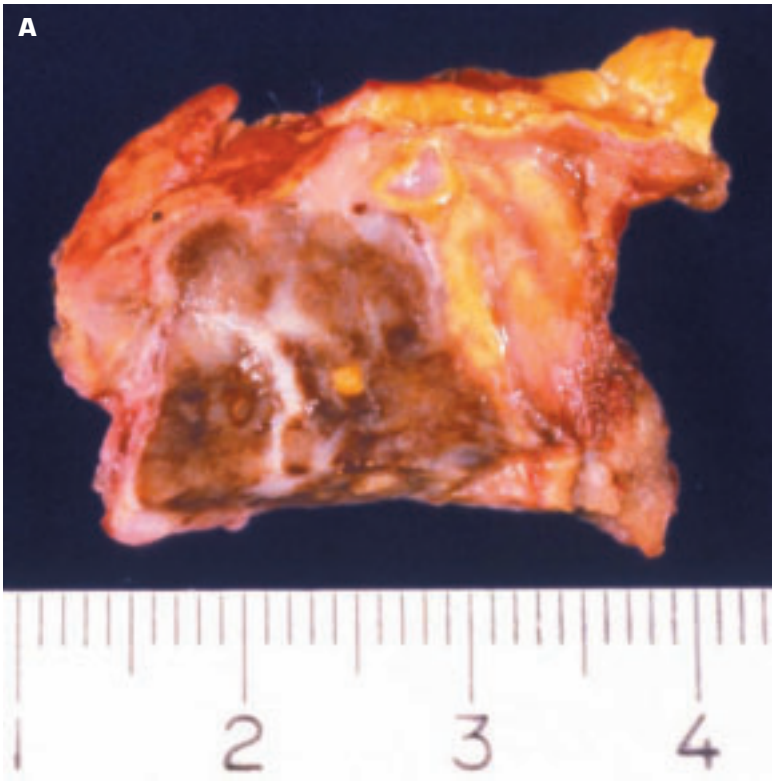

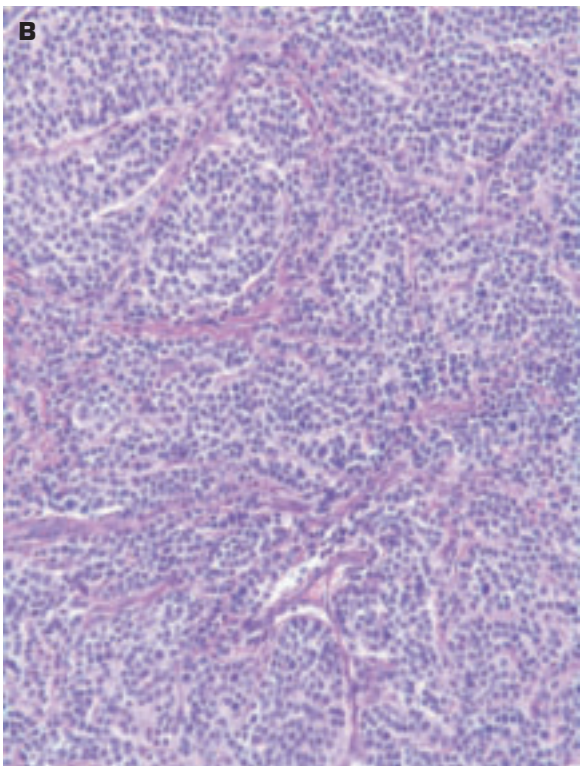

10-18. A. Neuroblastoma of the adrenal cortex of a young child. **B.** Histology of neuroblastoma showing nested groups of small, regular-size, dark tumor cells. *(continued on next page)*

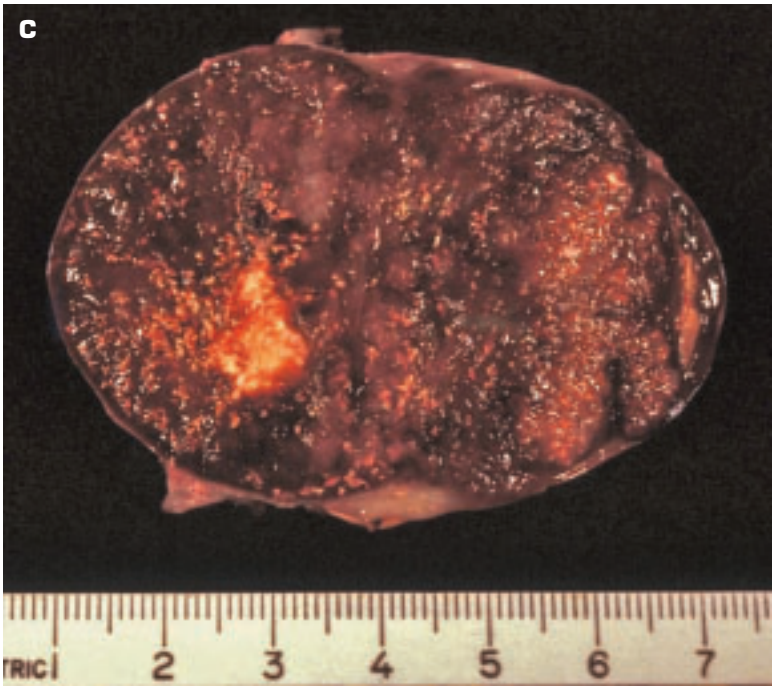

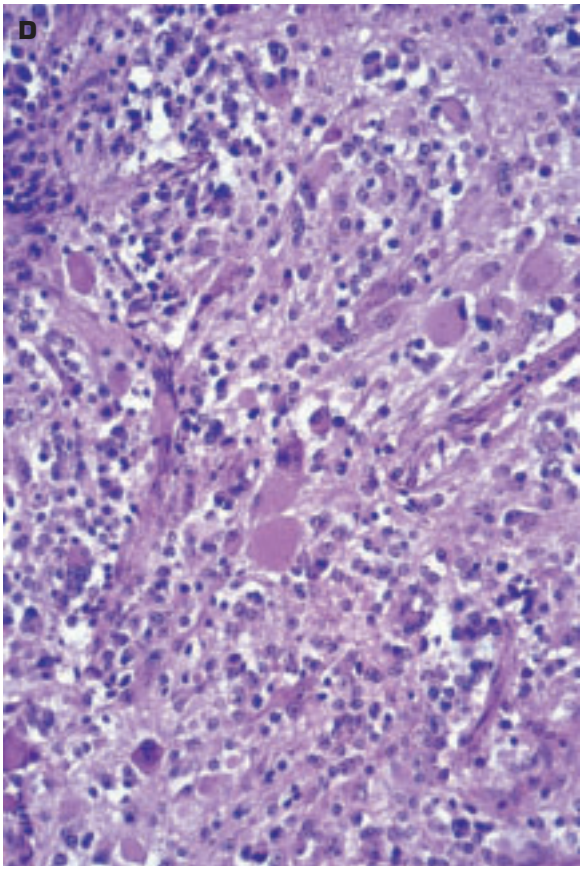

10-18. *(Continued)* **C.** Treated neuroblastoma has evolved into a ganglioneuroblastoma of the adrenal gland that shows focal necrosis (yellow area) and extensive hemorrhage (dark red areas). **D.** Histology of ganglioneuroblastoma shows ganglion-like cells emerging from a background of small neuroblasts.

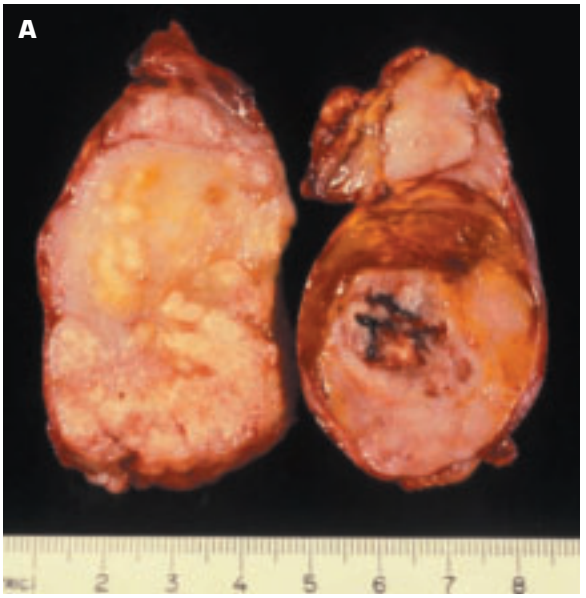

10-19. Metastatic tumors in the adrenal glands. **A.** Metastatic, partly necrotic, bronchial carcinoma in both adrenal glands. Lung cancer has a special affinity to spread to the adrenals. **B.** Metastatic malignant melanoma in a surgically resected (note the inked margins) adrenal gland.

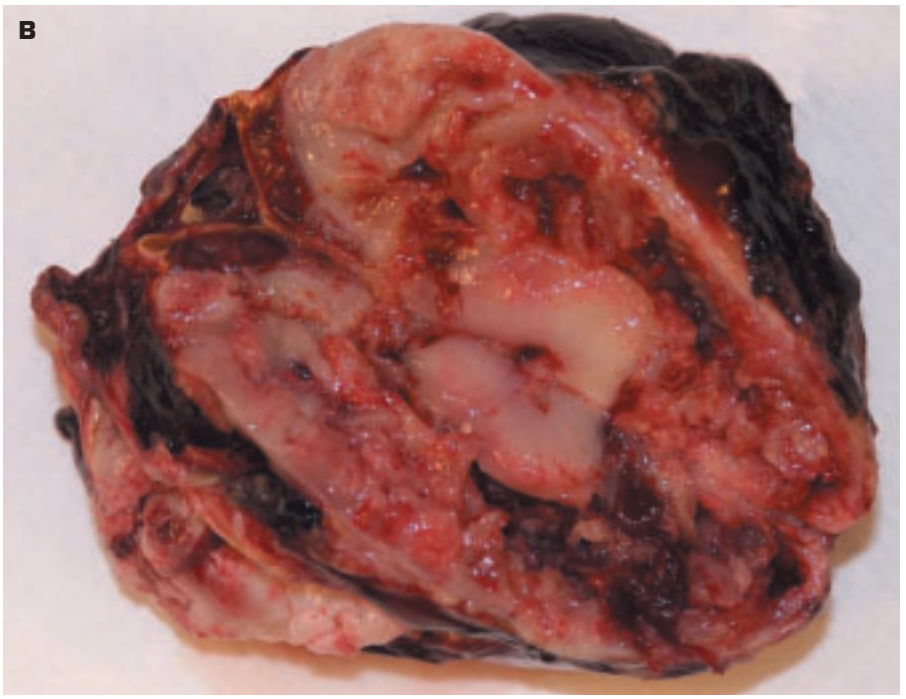

11 Skin and Soft Tissues

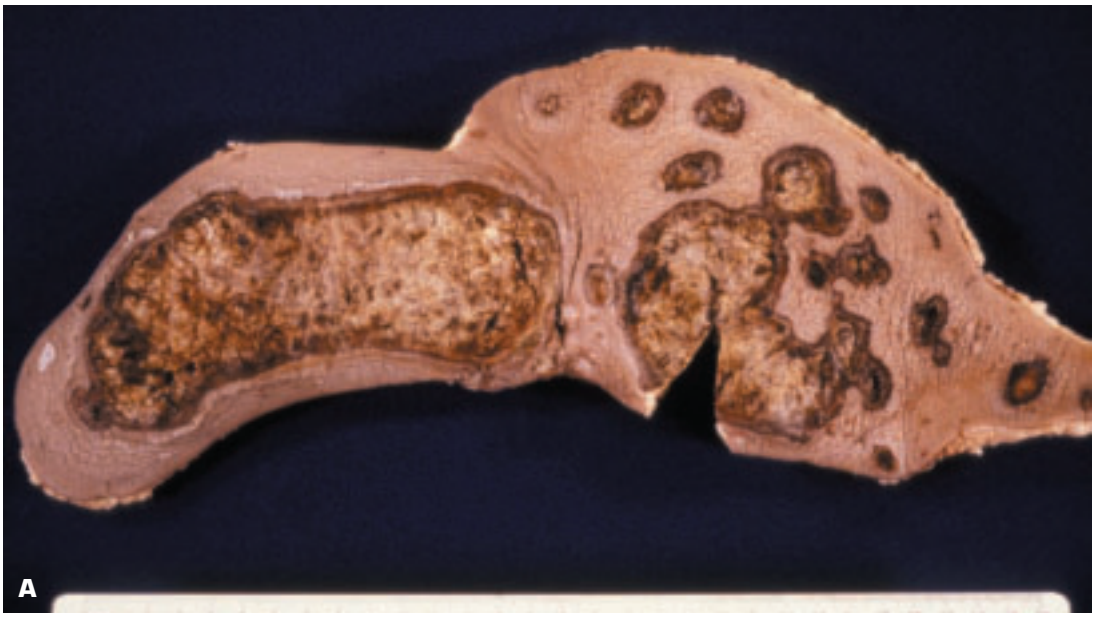

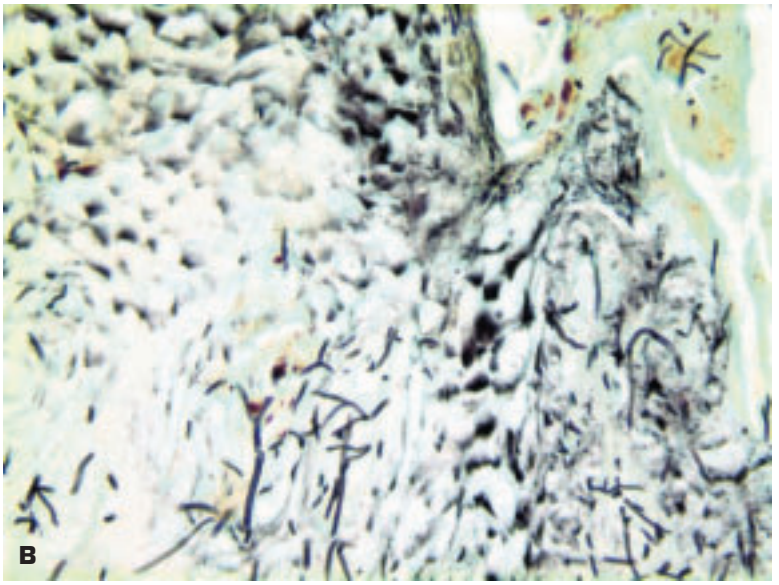

11-1. A. Multiple areas of ulceration of the skin due to an unidentified fungal infection that required surgical excision for a cure. **B.** Fungal methenamine silver stain shows branching fungal elements invading the epidermis from the dermis.

11-2. Chronic ischemic ulcer of the lower leg due to peripheral arterial narrowing by atherosclerosis. Note the sloping edge of the ulcer, and no sign of infection is evident. The red color of the ulcer base is due to the presence of granulation tissue.

11-3. Decubitus ulcer ("bed sore") due to pressure in a paralyzed patient. Such lesions are now regarded as indicative of inadequate nursing care and are notifiable in many states. The ulcer has penetrated as deep as the sacrum in its central portion. Treatment by surgical debridement will greatly increase the area of skin loss.

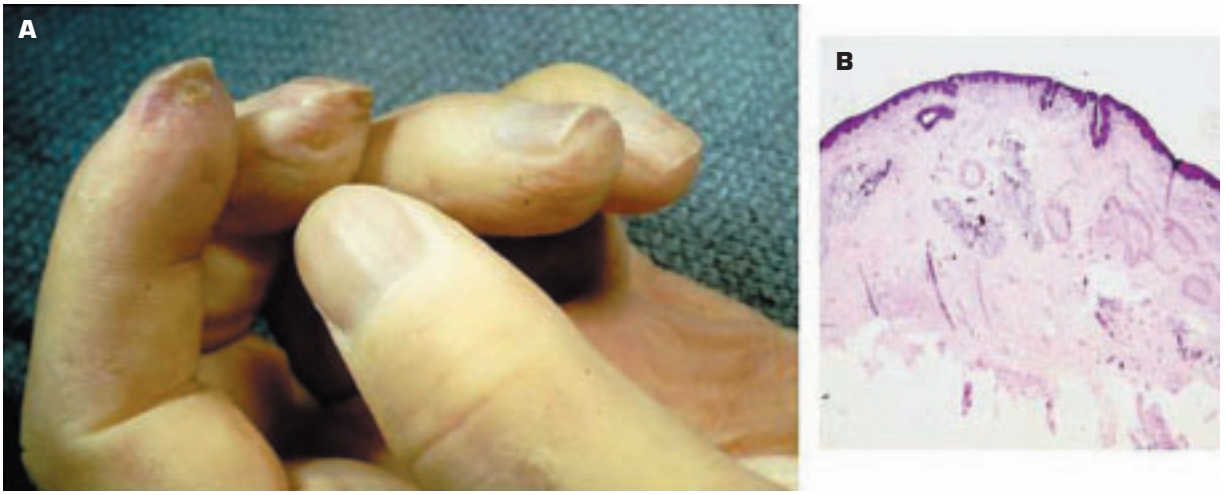

11-4. A. Atrophy of the pulp of the fingertips in a patient with systemic sclerosis (scleroderma). **B.** A section of skin (*right*) of the same patient shows severe luminal narrowing of the dermal blood vessels due to intimal fibrosis.

11-5. Dry gangrene of two toes in a diabetic patient with severe arterial atherosclerosis. Thickened basement membranes of small blood vessels plus a reduction in the number of small arteries contributes to the ischemia in diabetic individuals.

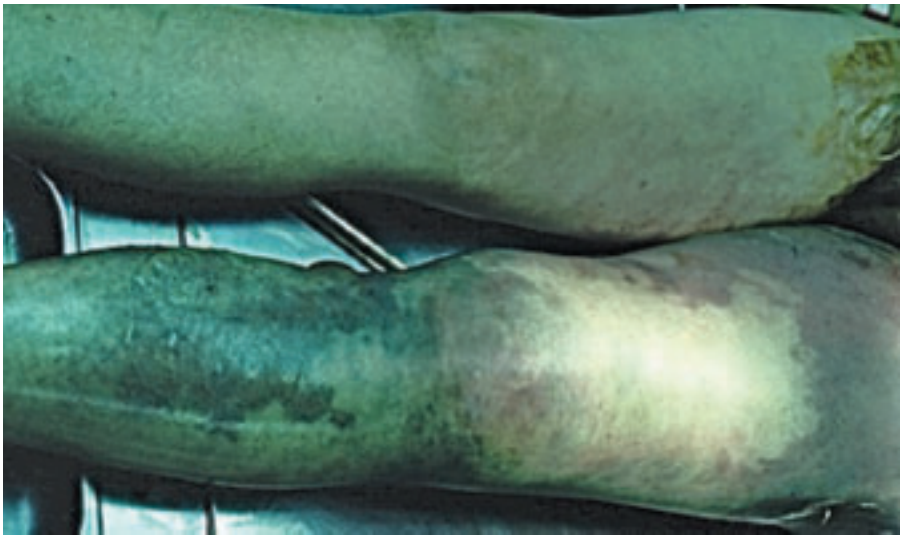

11-6. Necrotizing fasciitis of the left lower leg (*bottom*). Both the skin and the subcutaneous tissues and fascial sheets are rendered necrotic by a bacterial (commonly streptococcal) infection. The lesion carries a high mortality rate.

11-7. Supernumery (accessory) digit excised from ulnar side of little finger. A thin stalk linked the accessory digit to the finger. The extra digit may be excised or tied off at the base of the stalk soon after birth. The condition may be familial.

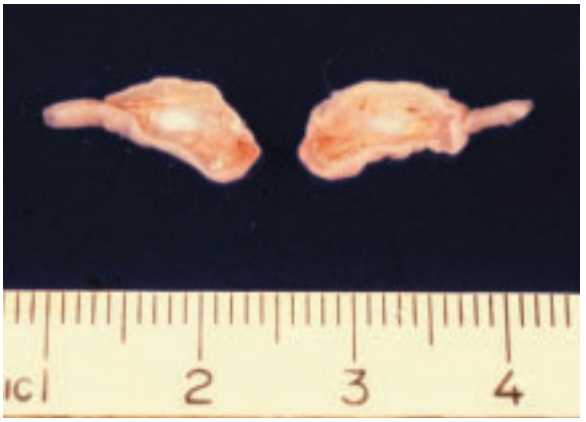

11-8. Skin tag (acrochordon) comprises a fibroepithelial polyp that forms in skin creases. It is more common in women and increases in incidence with age.

11-9. Two keloids removed from a person of African descent who developed this exaggerated scar formation at the site of piercing of the ear lobes. Histologically, the lesion shows dense, larger than normal collagen bundles. The keloid scar is larger in size than the original injury.

11-10. Epidermoid cyst removed from beneath the skin (*top*) comprises a smooth epithelial cystic cavity that contains inspissated keratinous material.

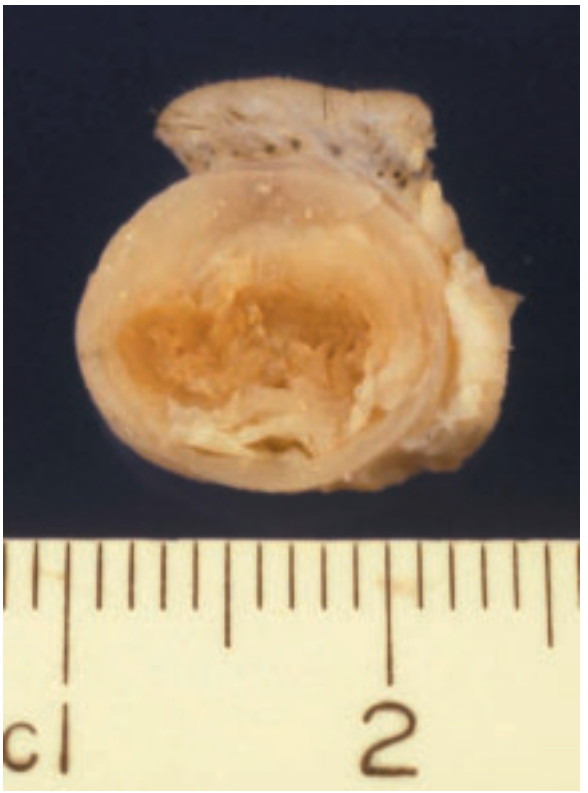

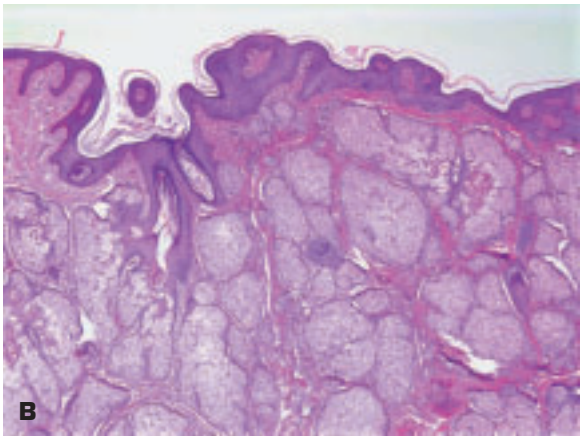

11-11. A. Nevus sebaceous is a localized lump made up of a hyperplasia of sebaceous glands with overlying epithelial hyperplasia. **B.** Histology of the lesion shows it to be composed of hyperplastic sebaceous glands underlying acanthotic epidermis.

11-12. Seborrheic keratosis is the most common benign tumor in elderly individuals and comprises an area of epithelial cellular proliferation. It is less common in darkly pigmented races. Lesser–Trélat's sign is the association of multiple eruptive seborrheic keratoses with an internal malignancy.

11-13. Congenital nevus. **A.** Congenital nevomelanocytic nevus (CNN), also termed "congenital giant hairy nevus," covers a large portion of this man's surface area. CNN has a serious risk for development of a malignant melanoma, which eventuated in this patient. **B.** Mixed CNN and neuroectodermal tumor that showed a mixed proliferation of melanocytes and neuroid (Schwannian) elements. The surface has a bosselated, nonpigmented appearance. *(continued on next page)*

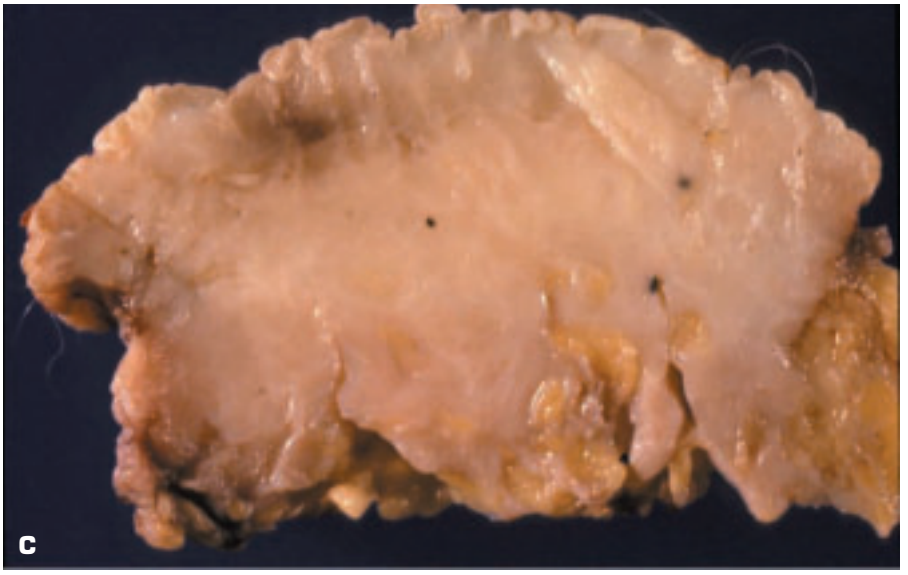

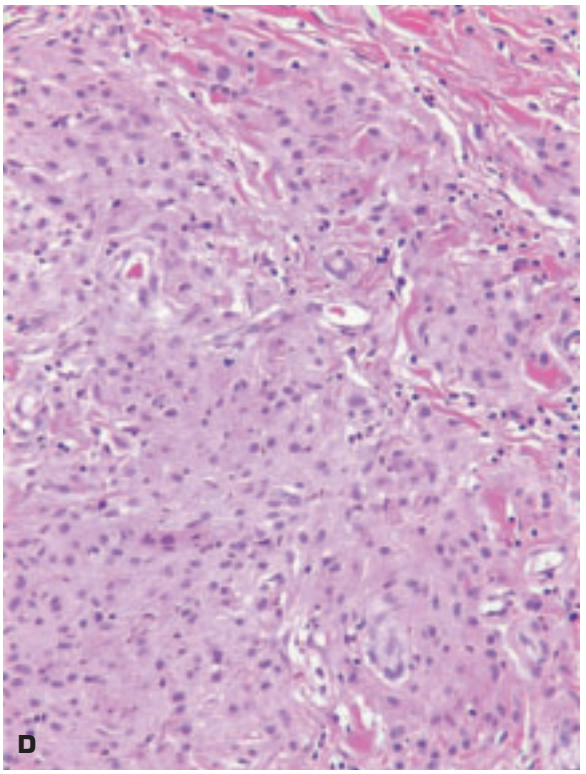

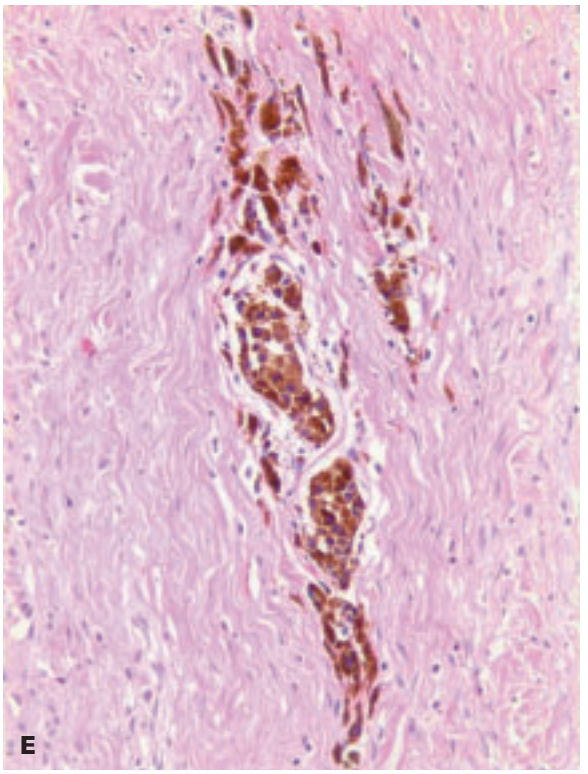

11-13. *(Continued)* **C.** Cut surface of the nevus shows a fibrous-looking lesion containing scanty areas of pigmentation. **D.** Histology of this same nevus shows neuroid elements. **E.** Focal area of the same nevus showing pigmented melanocytes.

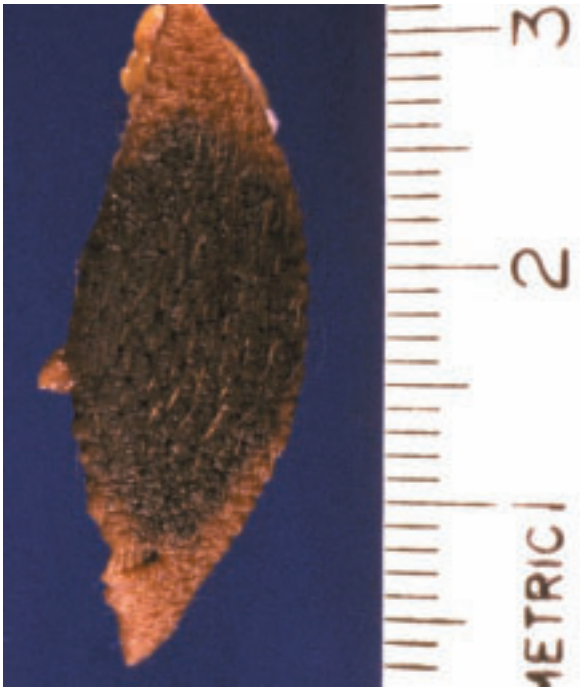

11-14. Intradermal nevus. In this lesion, the melanocytes lie within the dermis and have a lower potential for malignant change because no junctional activity is present.

11-15. Skin cancer. **A.** Basal cell carcinoma ("rodent ulcer") shows a central ulcerated area surrounded by nodular, heaped-up edges of tumor growth. **B.** Infiltrating squamous carcinoma of the skin shows elevation of the skin surface with minimal ulceration. Focal yellow areas of keratinization are noted. *(continued on next page)*

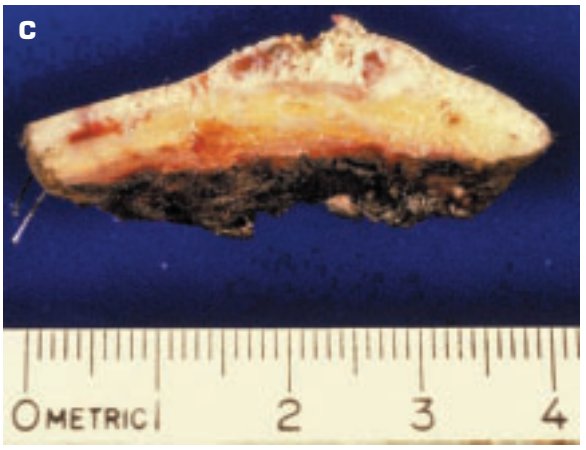

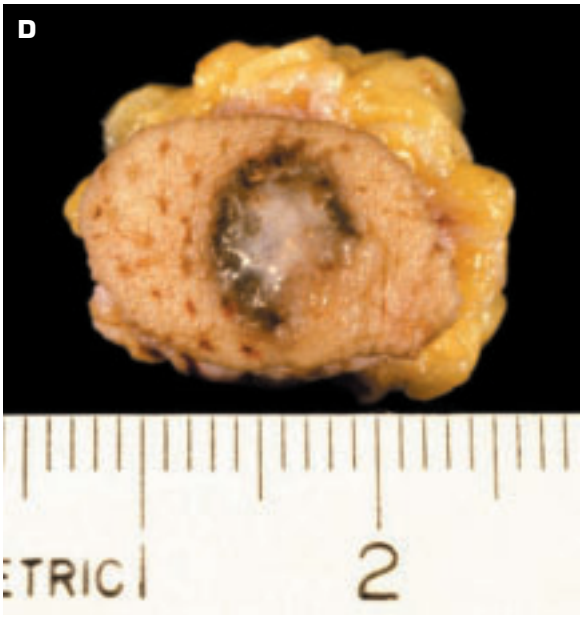

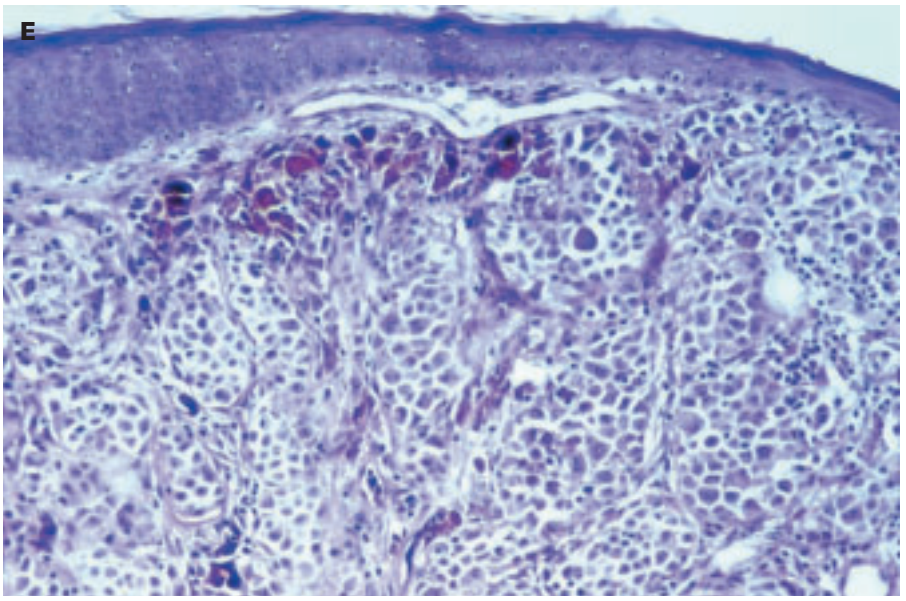

11-15. *(Continued)* **C.** Profile of a bisected squamous carcinoma of the skin showing the characteristic flaky appearance of a squamous carcinoma. Black ink marks the resection lines. **D.** Nodular malignant melanoma showing asymmetry of the lesion and irregular growth extensions on its border. The center of the lesion is hypopigmented compared to the edge. **E.** Histology of the nodular melanoma shows malignant melanocytes packing the dermis. The vertical depth of the lesion is important with regard to prognosis. *(continued on next page)*

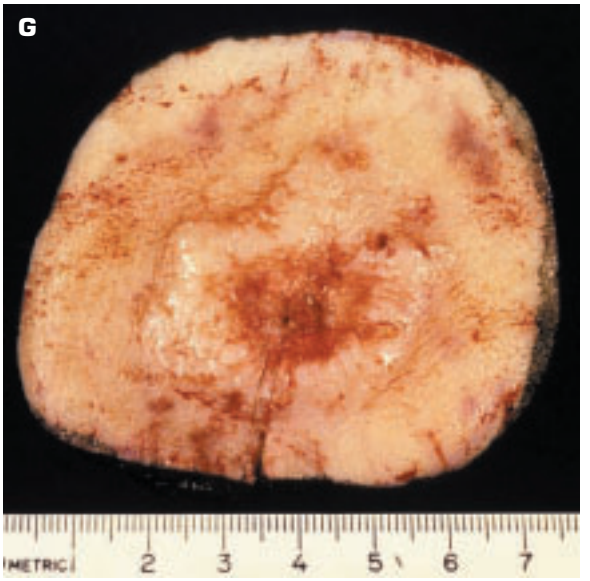

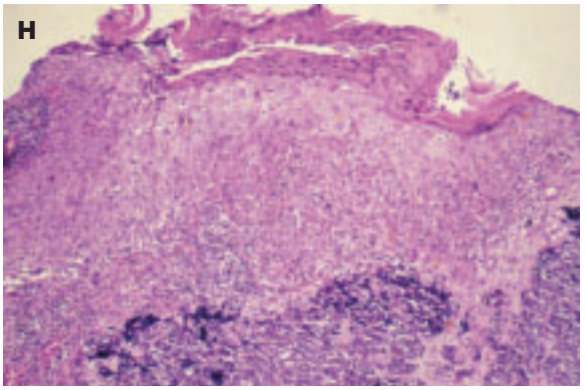

11-15. *(Continued)* **F.** Advanced malignant melanoma on the sole of the foot of an African man. Malignant melanomas are rarer in darkly pigmented individuals, and when they occur, they tend to occur on nonpigmented areas such as the sole of the foot or the palm of the hand. **G.** Merkel cell carcinoma resembles a basal cell carcinoma in appearance grossly. The Merkel cell in the epidermis is a neural crest-derived cell. The carcinoma behaves in an aggressive fashion. **H.** Histology of a Merkel cell tumor. The dermal infiltrate of small, dark blue, malignant Merkel cells (*bottom*) may be mistaken for lymphoma or secondary small cell cancer of the lung by the unwary. **I.** Sweat gland–derived adenocarcinoma of the skin – without histology, the specific type of carcinoma cannot be diagnosed. The cut surface shows a lobulated, slightly mucoid-looking tumor invading the subcutis.

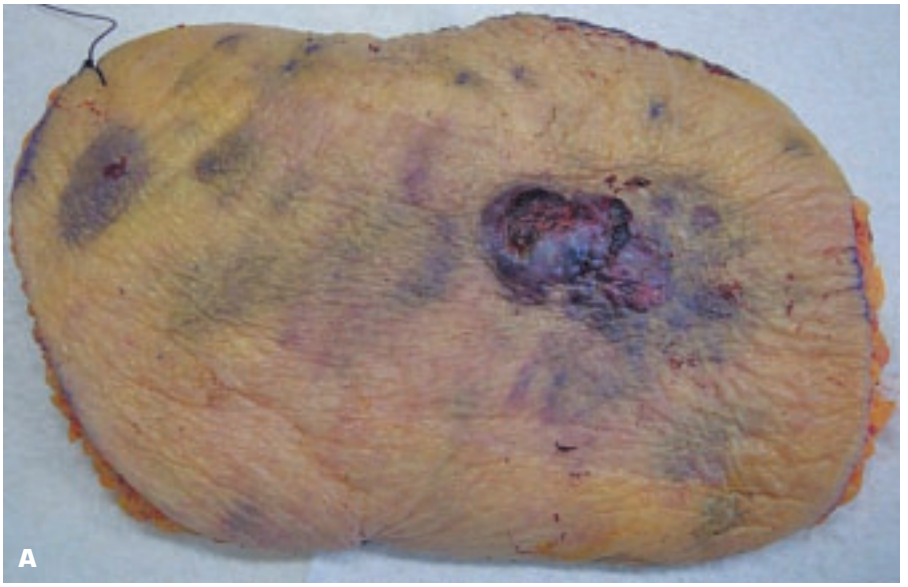

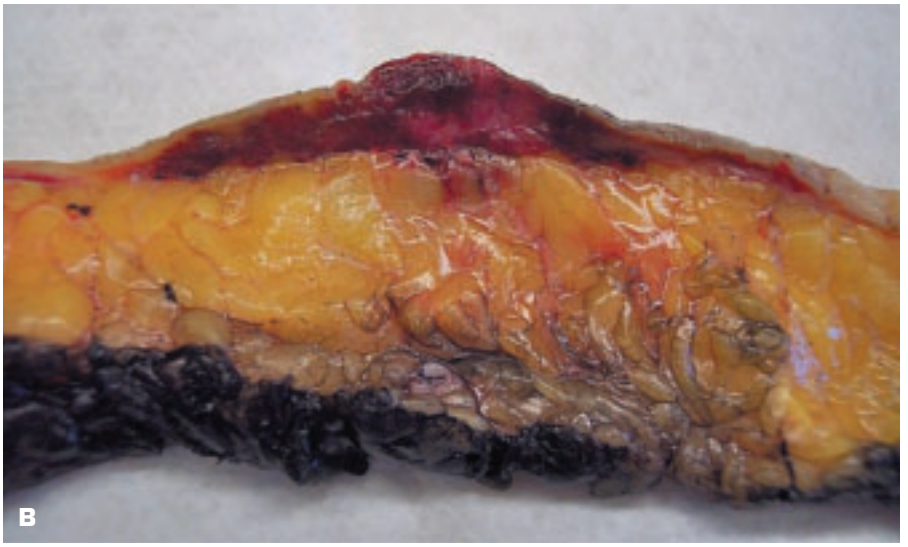

11-16. A. Angiosarcoma of the skin showing the characteristic reddish-violaceous hue of the main lesion (*center right*). Several smaller metastatic tumor nodules are also evident. **B.** This bisected angiosarcoma has such a marked degree of vascularity that it mimics an area of hemorrhage.

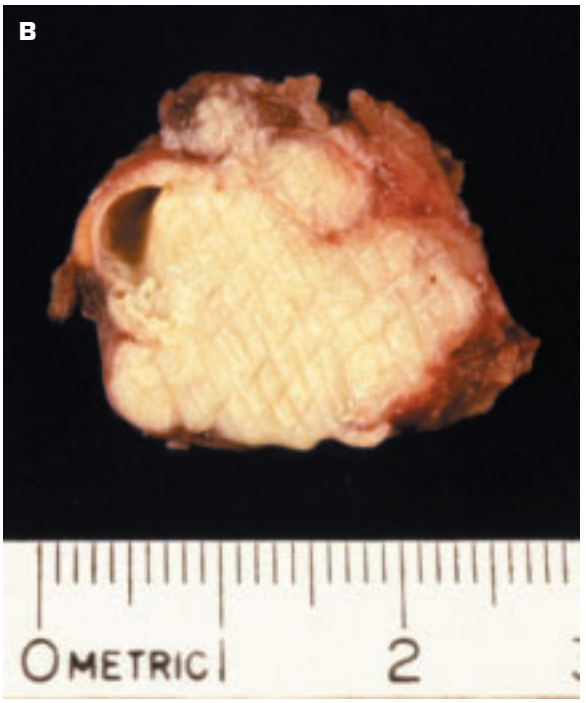

11-17. Cysts in the neck. **A.** Branchial cyst (lymphoepithelial cyst) occurs in the anterolateral part of the neck. This cyst is seen to have a smooth lining and a thick wall due in part to the presence of lymphoid tissue external to the epithelial lining. **B.** Thyroglossal tract cyst that was lined by squamous epithelium; abundant lymphoid tissue is present, accounting for the partly solid appearance.

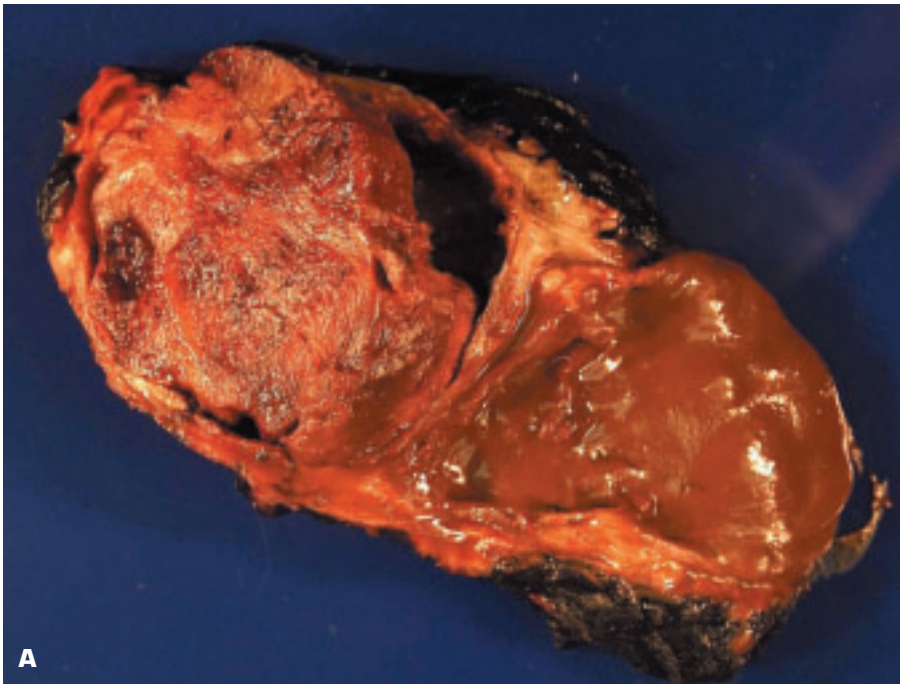

11-18. Soft tissue lesions related to "trauma." **A.** Organizing hematoma of soft tissues following blunt trauma. **B.** Piece of pine needle embedded in soft tissue of the hand. **C.** Transverse section of the same specimen confirms the plant-type arrangement of the internal structure of the foreign object. *(continued on next page)*

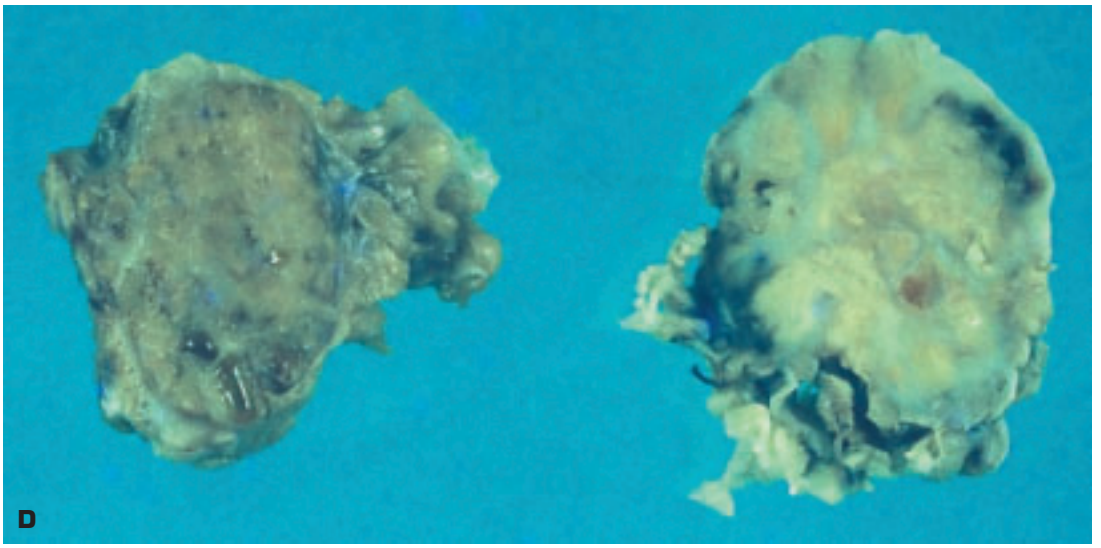

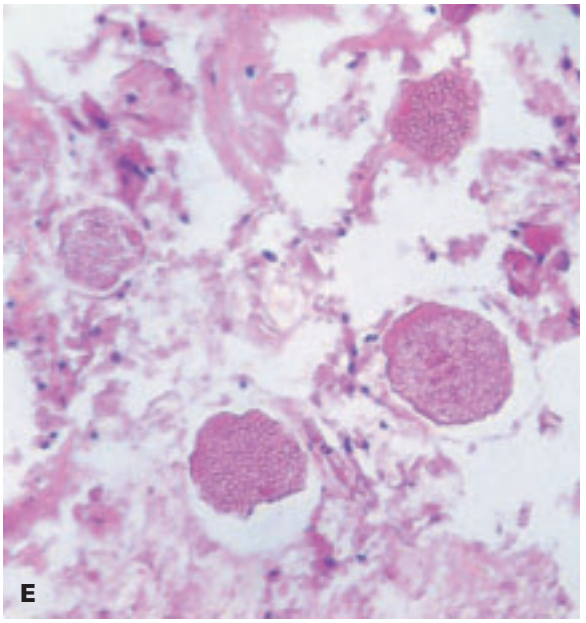

11-18. *(Continued)* **D.** Lipid-rich fibrous masses removed from the buttock: myospherulosis. **E.** Histology of myospherulosis shows clusters of erythrocytes surrounded by a membrane-like deposit of lipid-rich material following a prior injection. The condition may mimic a fungal infection.

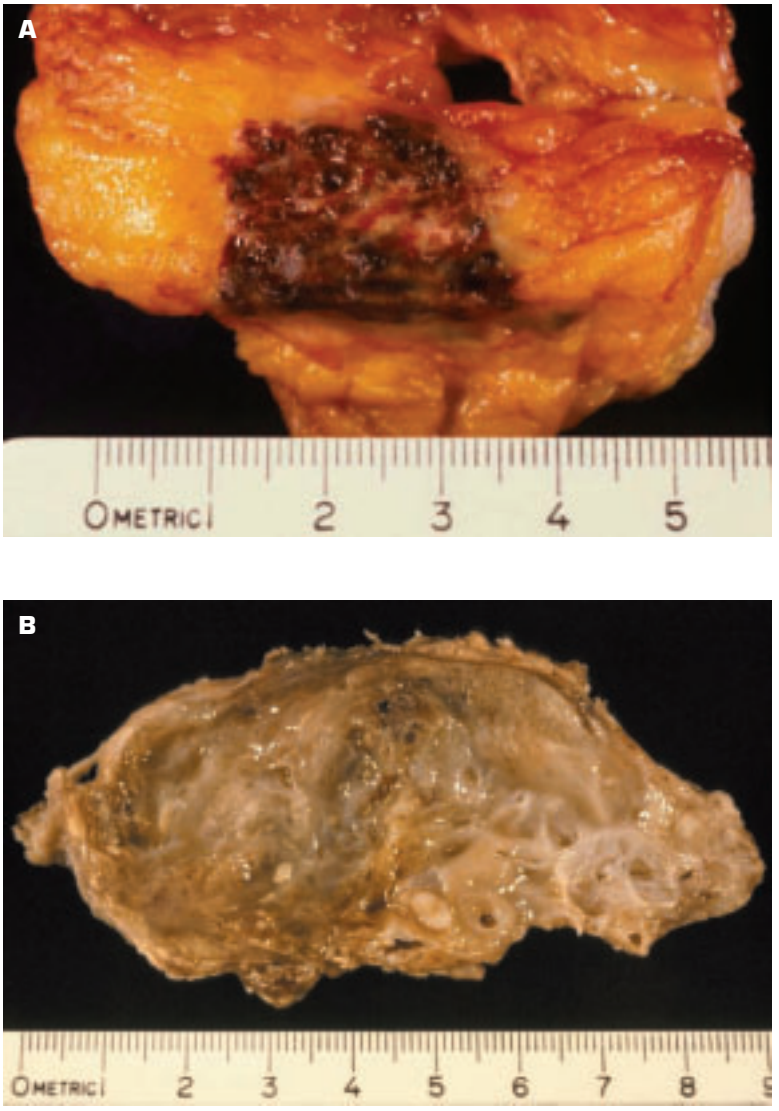

11-19. A. Cavernous hemangioma of soft tissues adjacent to a large vein. The hemangioma shows focal thrombosis (white areas) within which focal calcification is noted (yellow specks). **B.** Lymphangioma of soft tissues shows multiple interconnecting spaces containing no blood.

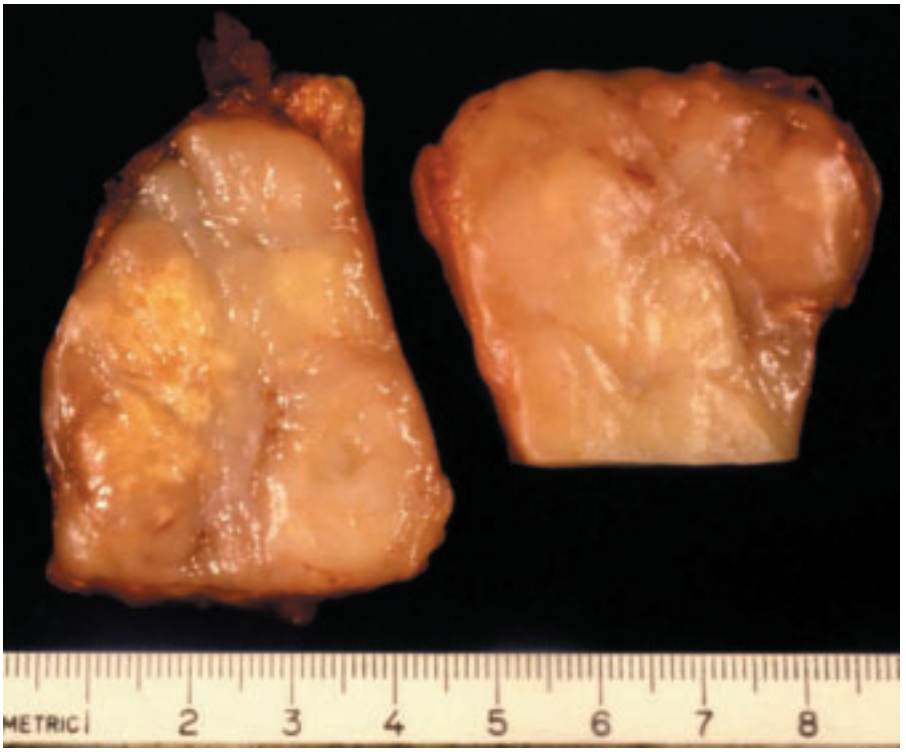

11-20. Fibrous histiocytoma is a benign tumor composed of lipid-filled histiocytes accounting for its yellow color naked eye.

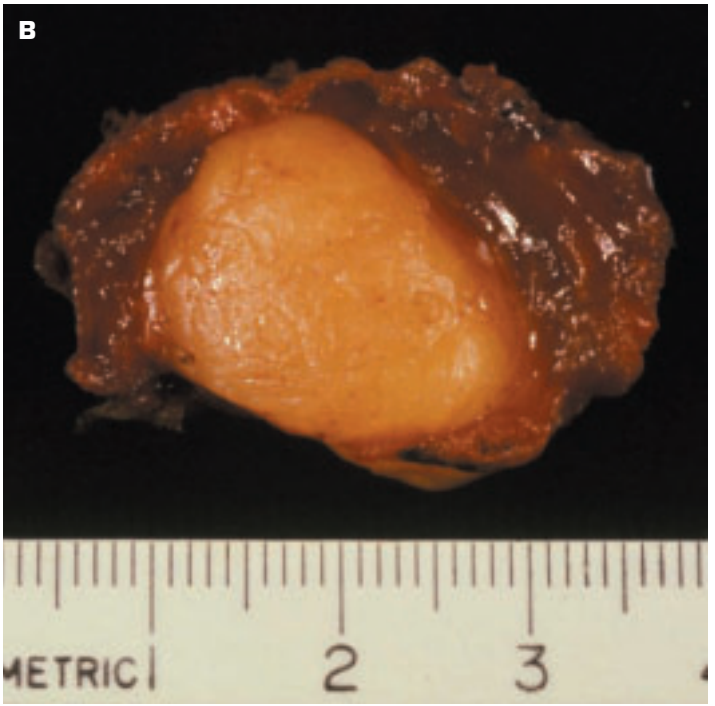

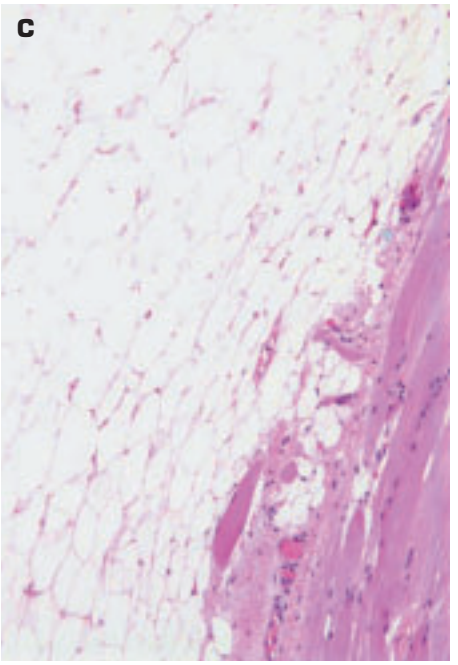

11-21. Benign tumors of adipose tissue. Cytogenetic alterations may assist in separating lipomatous soft tissue tumors. **A.** Encapsulation is the only feature that separates this lipoma from normal adipose tissue in appearance. Lipoma may show rearrangement of chromosome 12q in 75% of cases. **B.** Intramuscular lipoma is sited within a skeletal muscle. Such tumors tend to occur in the thigh or trunk of middle-age adults. **C.** Histology of this intramuscular lipoma shows well-differentiated fibroadipose tissue (*left*) abutting on skeletal muscle (*right*). *(continued on next page)*

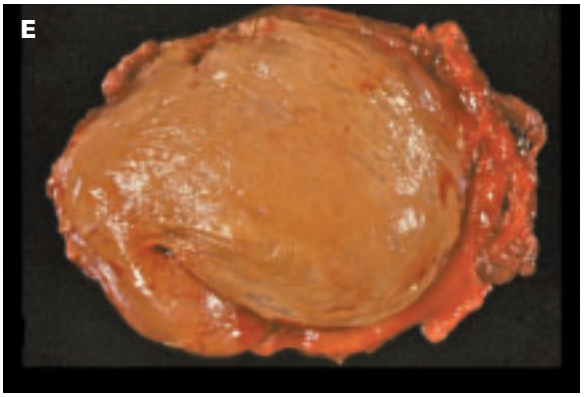

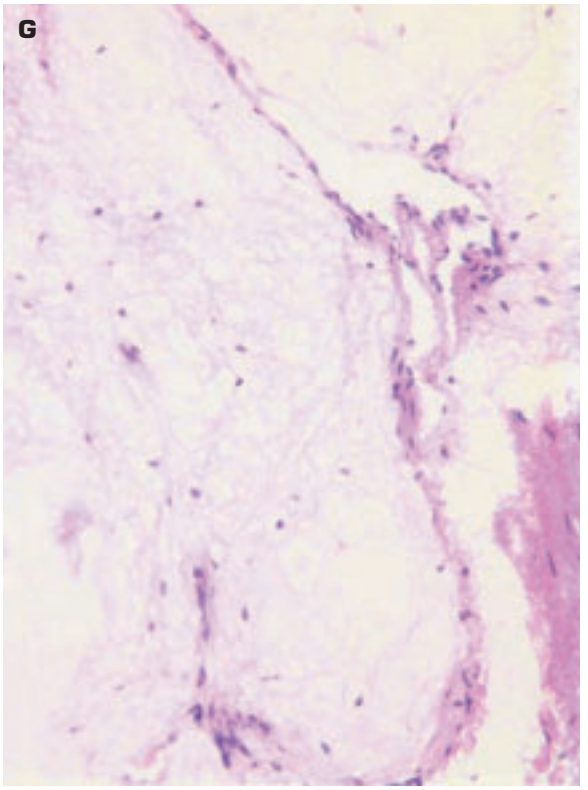

11-21. *(Continued)* **D.** Fibrolipoma is a lipoma that contains increased amounts of fibrous tissue permeating the adipose tissue. The white streaks of fibrous tissue are clearly evident on the cut surface of the tumor. **E.** Hibernoma is a rare tumor of young adults that occurs in the scapular region and shows differentiation toward brown fat. Rearrangement of chromosome 11q is observed. **F.** Lipoblastoma, a rare benign tumor affecting children younger than 7 years, usually occurs superficially in the limbs and shows rearrangements of chromosome 8. Grossly, lipoblastoma shows a prominent lobulated pattern. **G.** Typical histologic lobulation of a mature lipoblastoma. Patient showed cytogenetic rearrangement of chromosome 8q. Lipoblastoma is a benign lesion and matures into a lipoma if not removed.

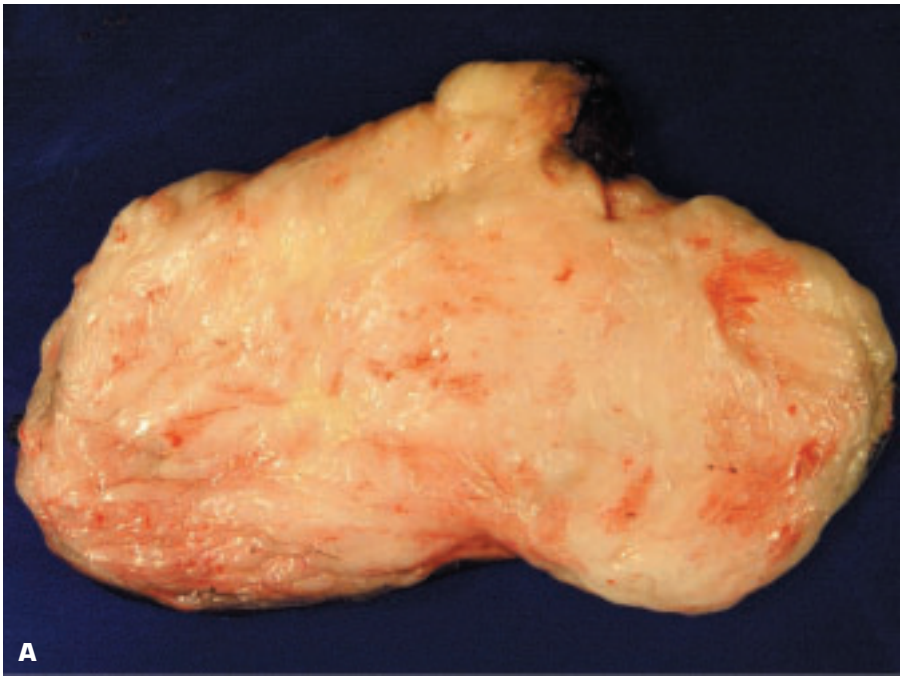

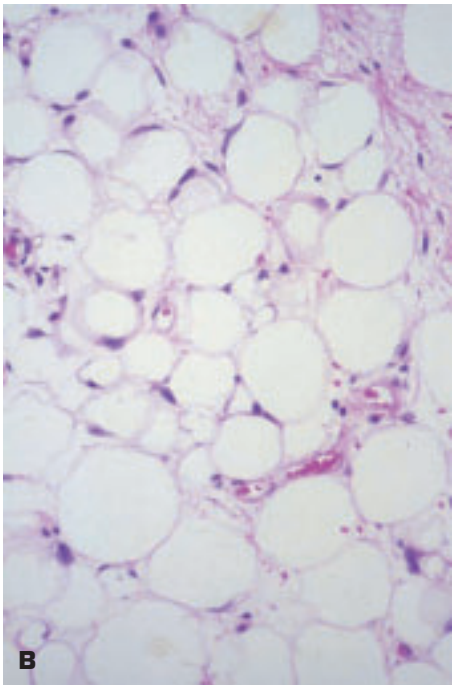

11-22. Well-differentiated liposarcomas commonly occur in the retroperitoneum or the limbs. Myxoid and round cell liposarcomas occur in the limbs of adults. **A.** Atypical lipomatous tumor (well-differentiated liposarcoma; sarcoma-like variant). About 45% of liposarcomas are well differentiated. Bizarre stromal cells may be found in the fibrous septa. Ring chromosome is derived from the q13–15 region of chromosome 12. **B.** Histology of a well-differentiated liposarcoma shows an appearance not all that dissimilar to normal fibroadipose tissue. Some variation in nuclear size and shape and staining qualities are noted. *(continued on next page)*

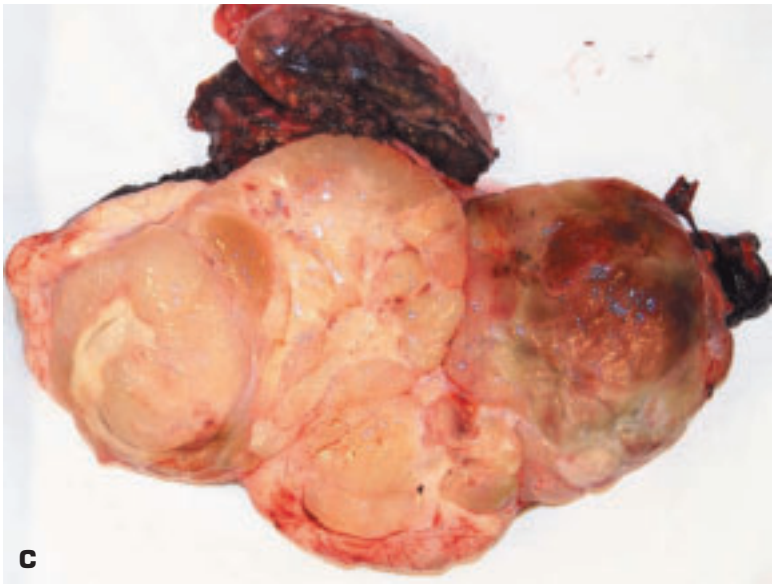

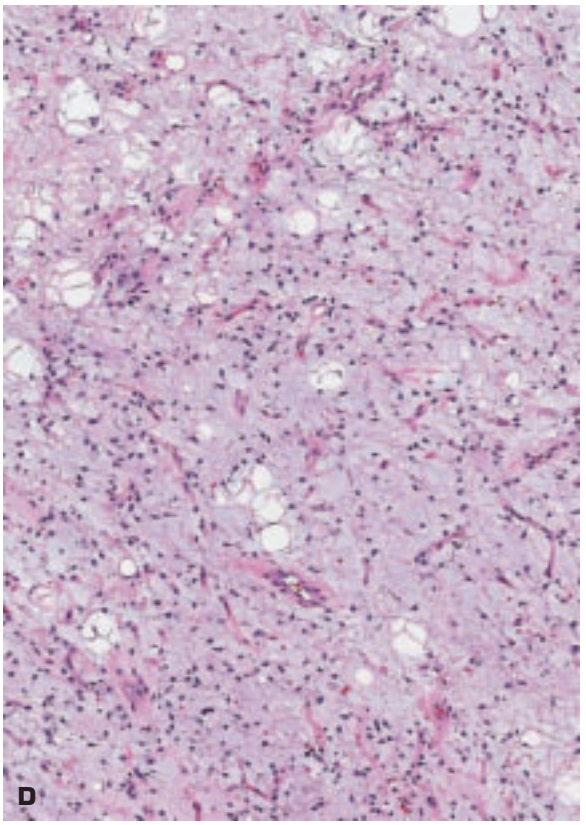

11-22. *(Continued)* **C.** Low-grade myxoid liposarcoma presents a more solid appearance than normal fibroadipose tissue, and it has a glistening, slimy appearance in areas reflecting its myxoid nature. A zone of necrosis and hemorrhage is evident on the right side of the specimen. **D.** Histology of a pure myxoid liposarcoma (a low-grade tumor) shows bland-looking spindle-shaped cells with a myxoid background and a "chicken wire fence" pattern to the blood vessels. *(continued on next page)*

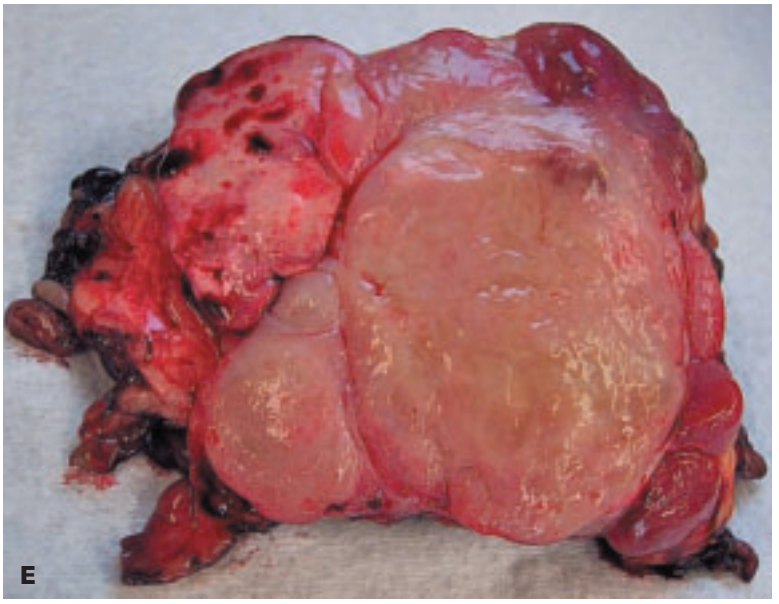

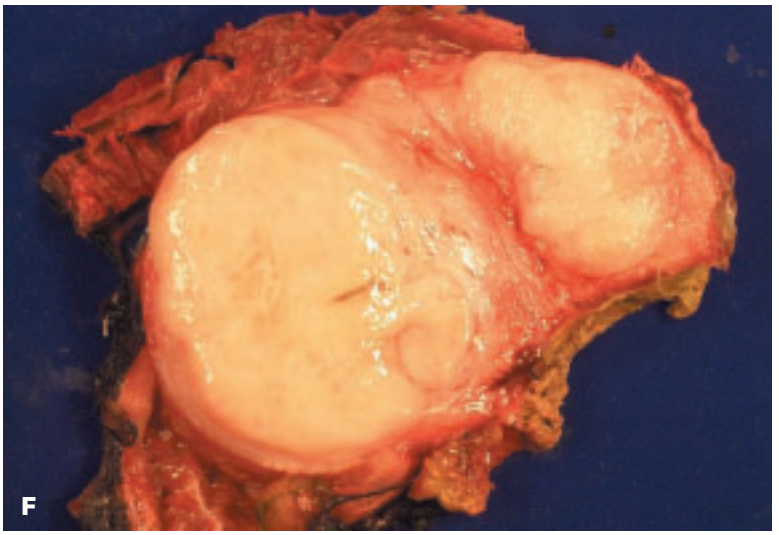

11-22. *(Continued)* **E.** Round cell liposarcoma is a poorly differentiated form of a myxoid liposarcoma; hence, the myxoid naked eye appearance of this tumor. **F.** This dedifferentiated liposarcoma has the gross appearance of a solid, fatty-looking tumor without distinguishing features. Dedifferentiated liposarcoma may evolve from recurrence of a previously excised liposarcoma, and in addition to lipoblasts, it may contain areas resembling a malignant fibrous histiocytoma histologically.

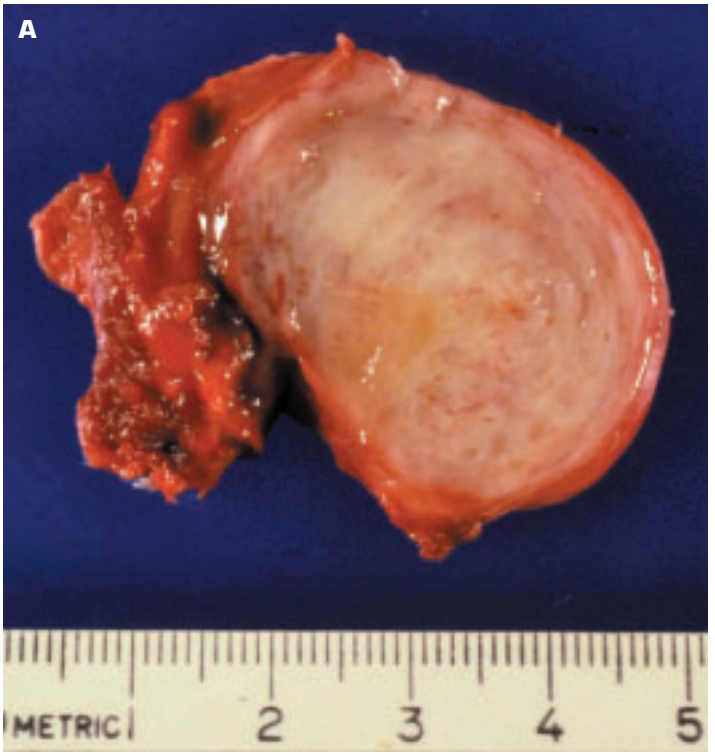

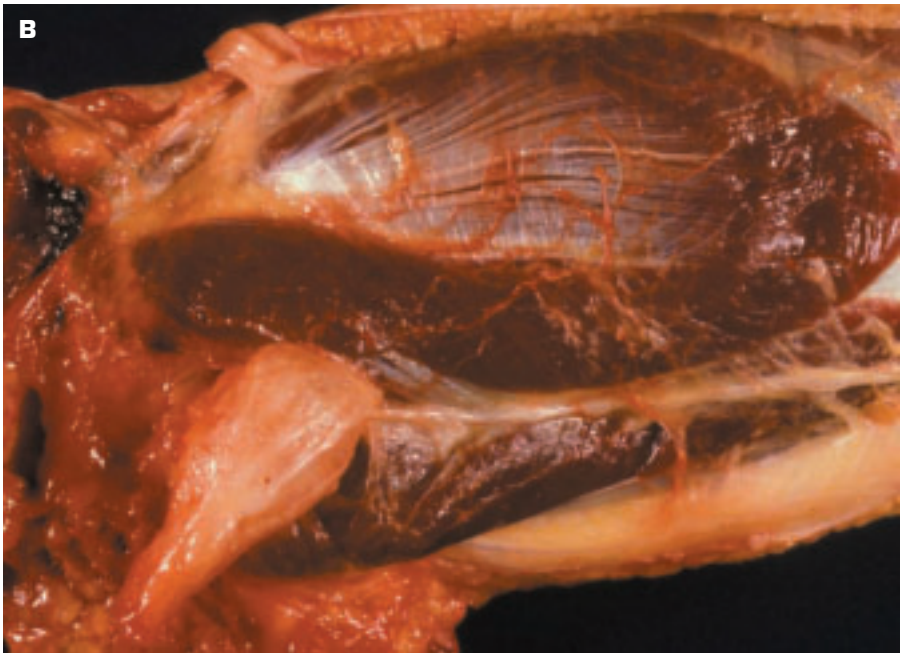

11-23. A. Neurofibroma of soft tissues has a myxoid, edematous-looking cut surface. The appearance can be variable, and the lesion is not encapsulated like a schwannoma. Unlike the latter lesion, a neurofibroma contains axons (revealed by silver stains) scattered throughout its substance. **B.** Plexiform neurofibroma of the popliteal nerve has expanded the nerve, making excision not feasible. This patient had type 1 neurofibromatosis. *(continued on next page)*

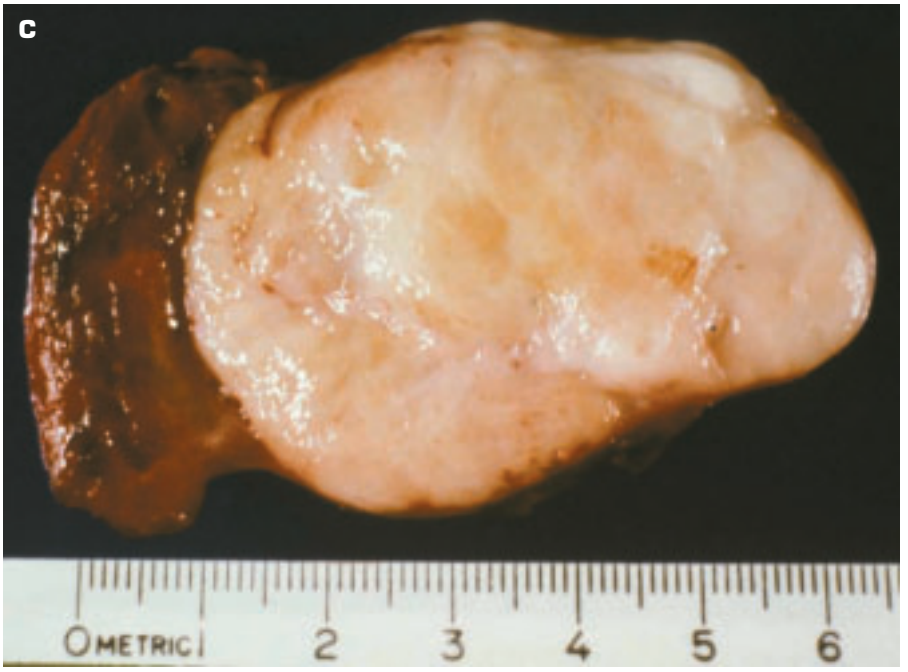

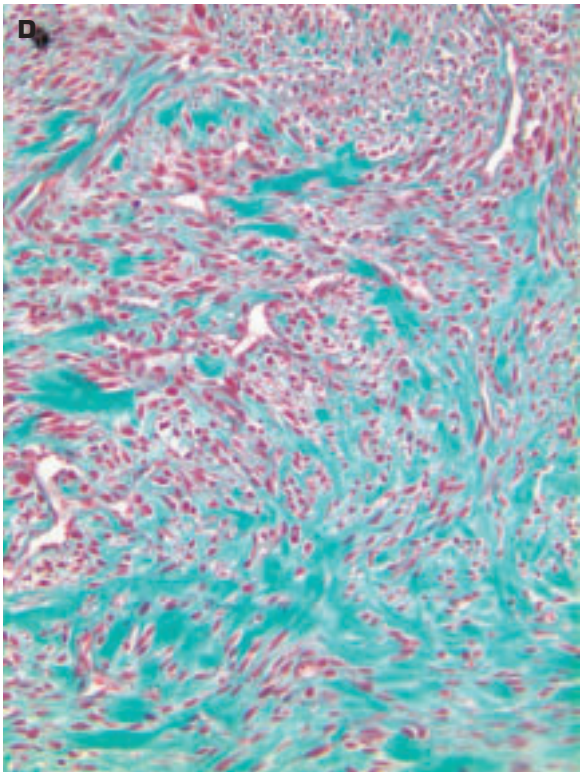

11-23. *(Continued)* **C.** Malignant peripheral nerve sheath tumor (MPNST, neurofibrosarcoma) presenting as a solid, white tumor with focal areas of degeneration and microcyst formation. Half of these tumors arise in von Recklinghausen syndrome (in association with chromosome 17 deletion and p53 mutations), and the other half arise de novo. **D.** Histology of a MPNST showing abundant collagen production by the malignant cells.

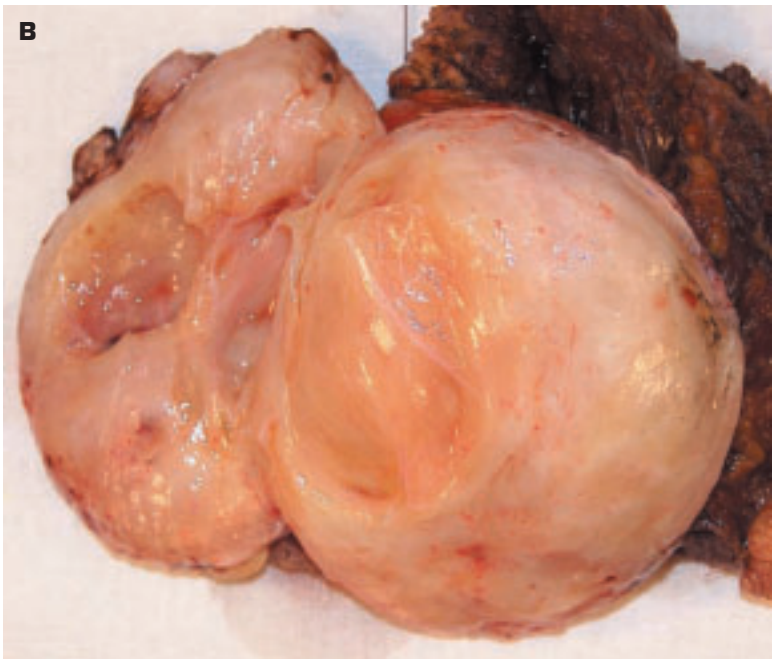

11-24. A. Small encapsulated schwannoma (neurilemoma) removed from the vocal cord shows no sign of degeneration. **B.** Larger schwannoma of soft tissues shows areas of cystic degeneration. *(continued on next page)*

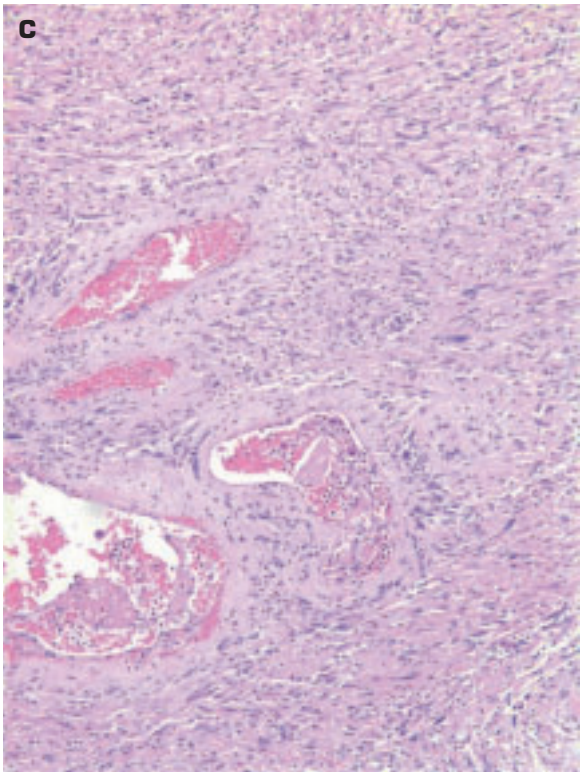

11-24. *(Continued)* **C.** Histology of a schwannoma shows faint nuclear palisading, plus prominent blood vessels in a collagen-rich stroma. **D.** Malignant schwannoma of a limb shows infiltration into adjacent skeletal muscle.

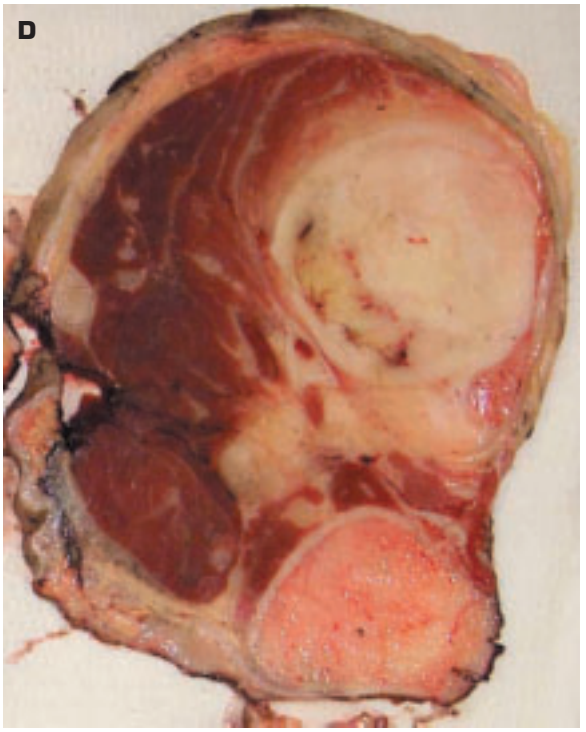

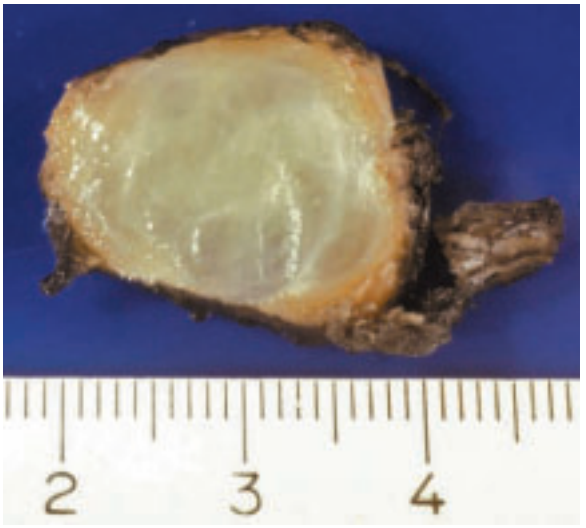

11-25. Myxoma of soft tissues shows a characteristic myxomatous, mucoid cut surface. Myxoma occurs most often in the thigh of adult females. Multiple myxomas may occur in Carney's syndrome.

11-26. A. Elastofibroma removed from posterior chest wall shows a yellow-white, imperfectly circumscribed mass within skeletal muscle. The lesion is believed to represent a reactive process involving abnormal elastogenesis. Local resection is curative, unlike fibromatosis, which requires wider excision. **B.** Histology shows multiple bands of elastin embedded in dense fibrous tissue.

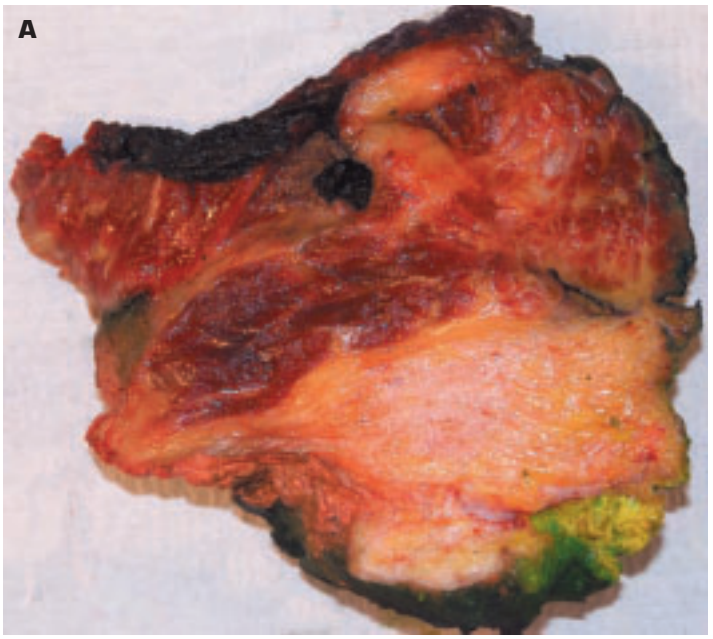

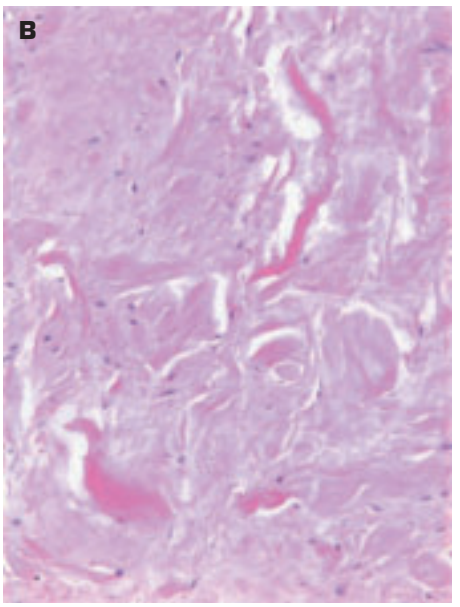

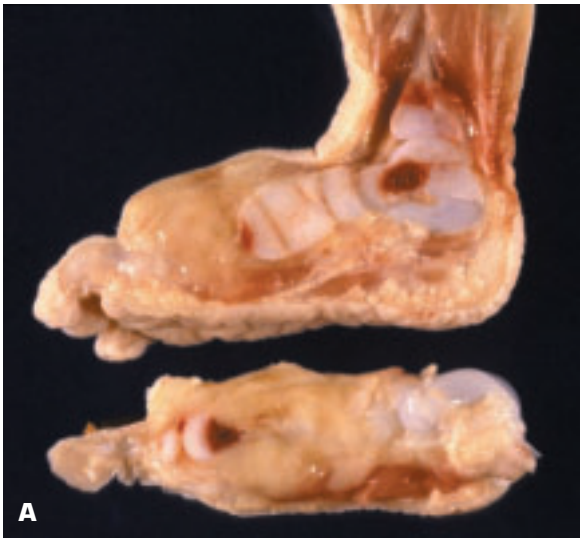

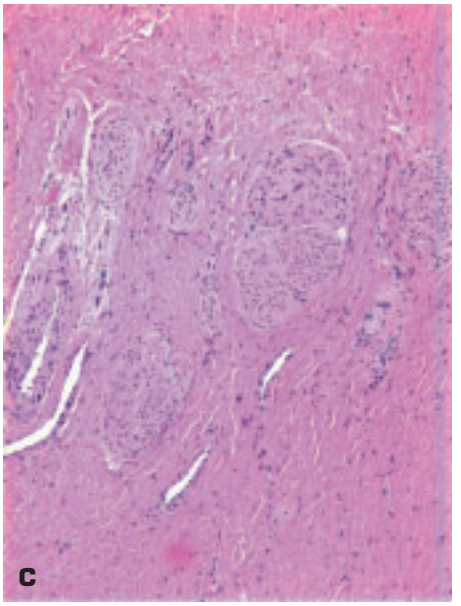

11-27. Fibromatosis. **A.** Fibromatosis of the foot that recurred after multiple excisions. Note the solid yellow-white tissue expanding the foot and infiltrating between the bones of the foot. **B.** Fibromatosis (desmoid tumor of anterior abdominal wall muscles) in a patient with Gardner syndrome. The lesion exhibits a characteristic whorled, fibrous-looking cut surface. **C.** Histology shows small peripheral nerves embedded in dense fibrous tissue.

11-28. Endometriosis of soft tissues. **A.** This gross lesion shows no evidence of iron deposits related to previous hemorrhage from the displaced endometrium. The lesion cannot be diagnosed without histology. **B.** Histology shows proliferative phase endometrial glands and stroma.

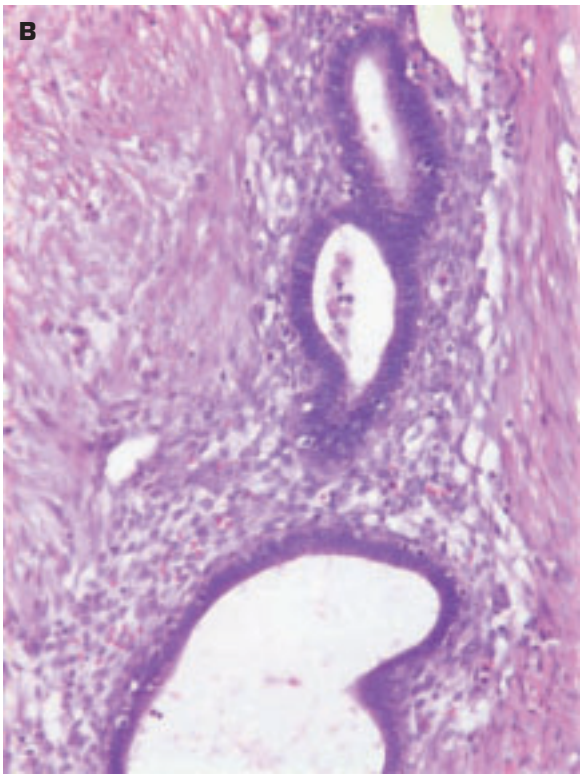

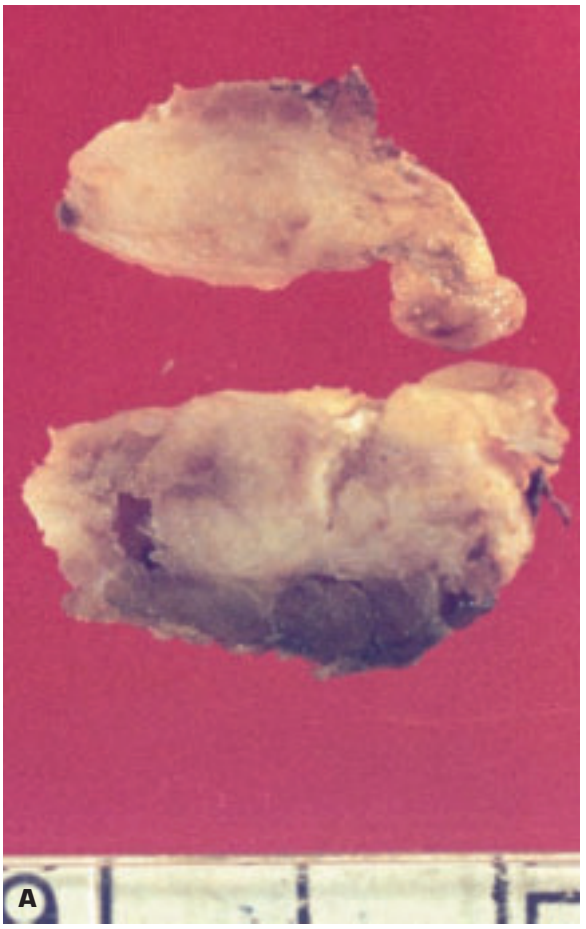

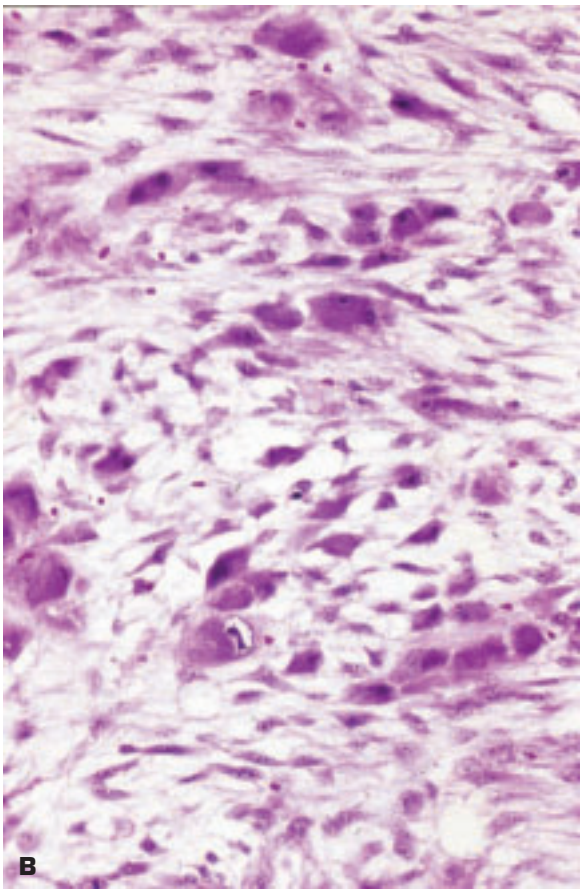

11-29. Proliferative myositis. **A.** A whitish-colored, tumor-like mass lies alongside darker-colored skeletal muscle at the site of a preexisting fascial plane. The surgeon is often concerned that the lesion may be a sarcoma. **B.** Histology shows plump, ganglion-like, spindle-shaped cells arising from a fibroblastic background. The histology is slightly reminiscent of proliferative fasciitis. The cells are myofibroblastic in nature, and simple excision is all that is needed to cure the lesion.

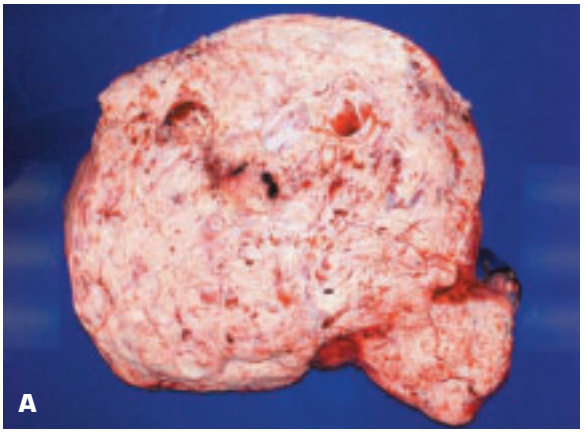

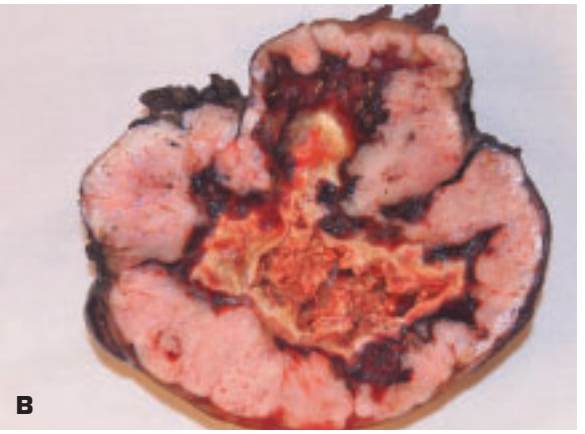

11-30. A. Massive soft tissue leiomyoma presenting as a pelvic mass in a male. **B.** Leiomyosarcoma of soft tissue showing central necrosis rimmed by recent hemorrhage. **C.** Histology of a well-differentiated leiomyosarcoma.

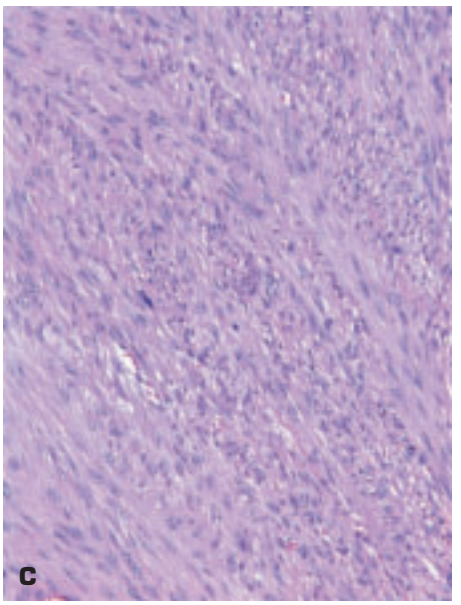

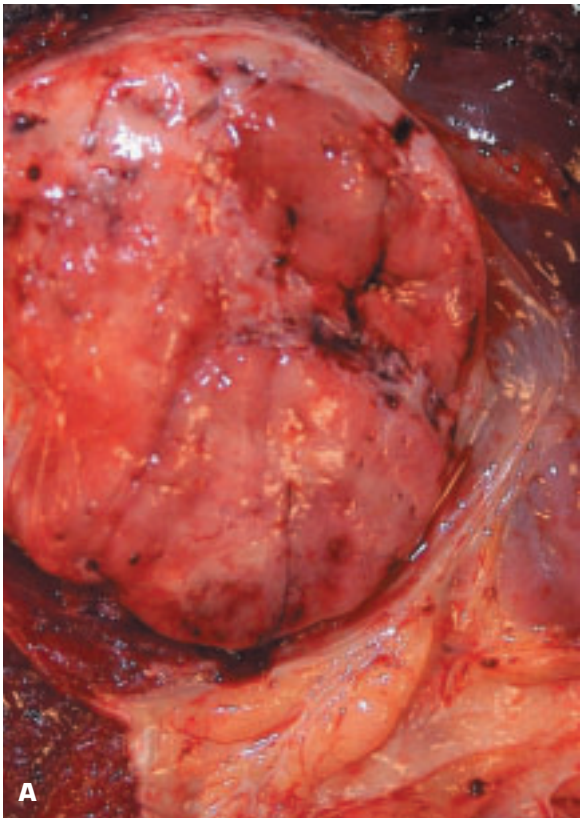

11-31. A. Solitary fibrous tumor (SFT) of soft tissues presenting as a lobulated, intermuscular solid mass. **B.** Histology of SFT shows a hemangiopericytomatous-like pattern with prominent small blood vessels between the tumor cells.

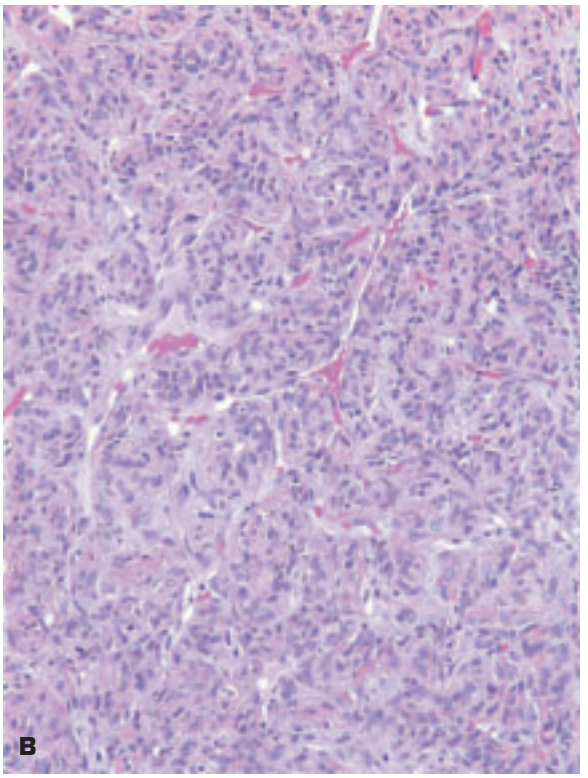

11-32. A. Benign chondroma of soft tissues. **B.** Soft tissue chondrosarcoma shows central necrosis and hemorrhage secondary to its rapid growth.

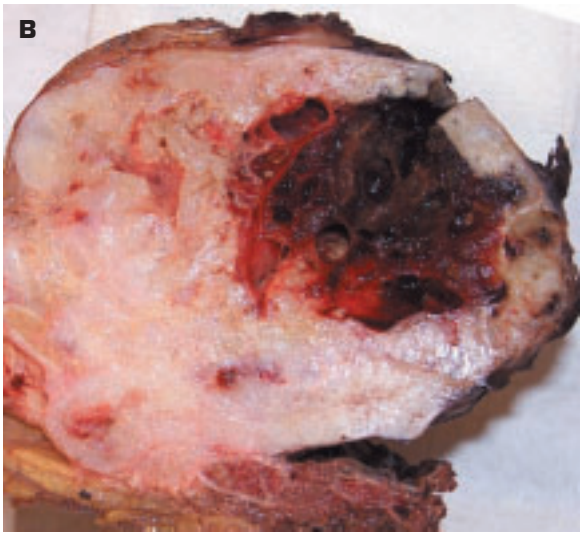

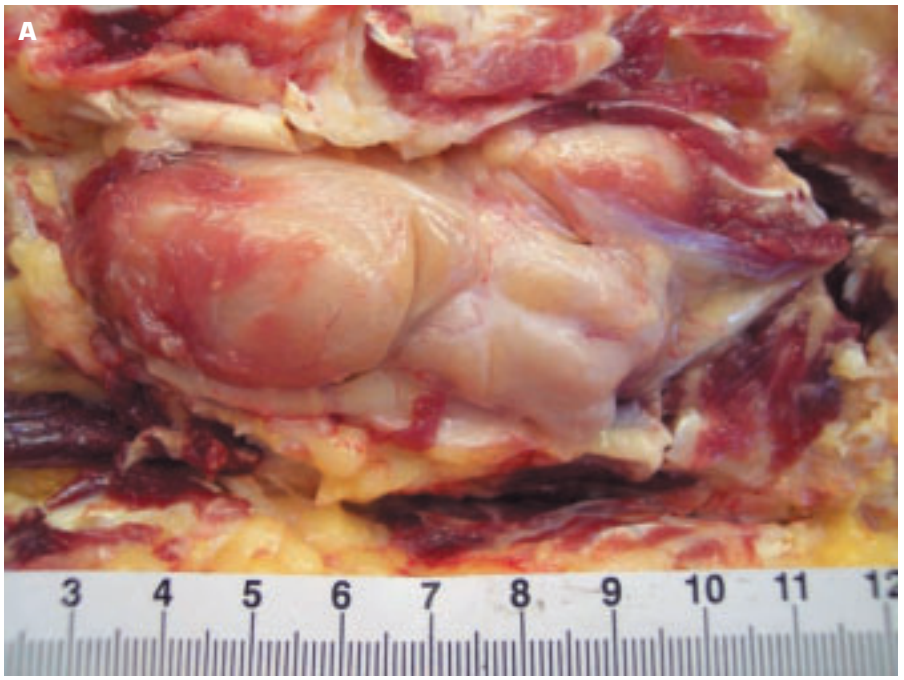

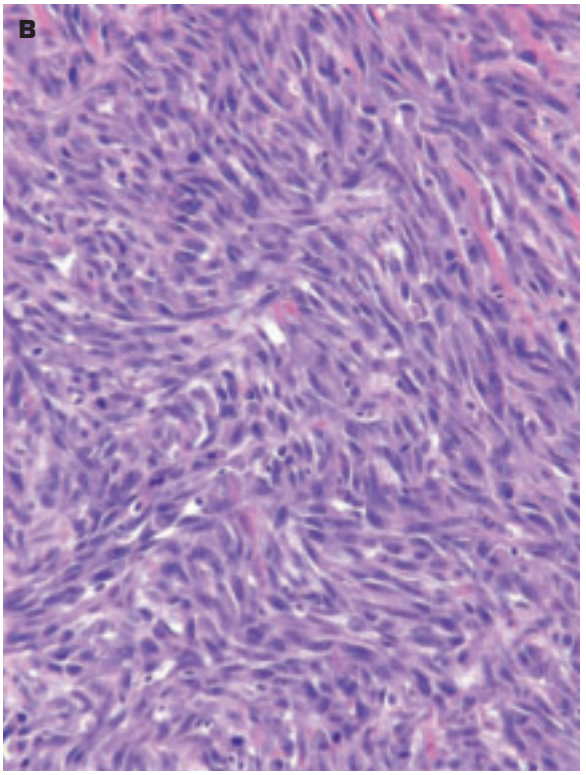

11-33. A. Synovial sarcoma of sole of the foot is presenting as a smoothly rounded mass. **B.** Histology shows a monophasic (spindle cell) synovial sarcoma. *(continued on next page)*

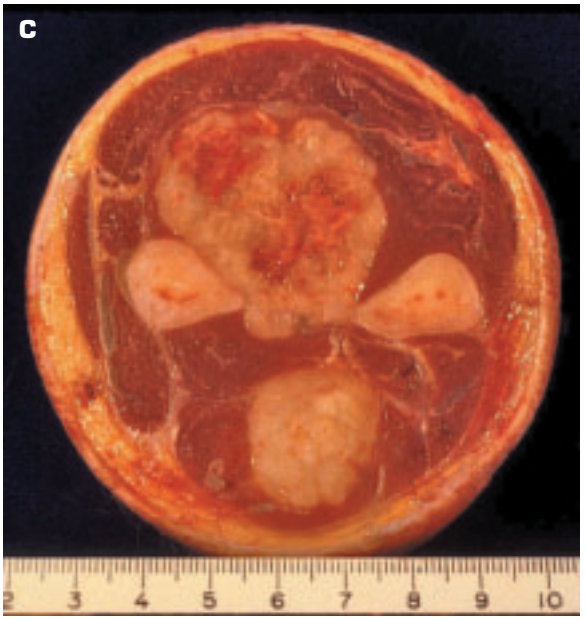

11-33. *(Continued)* **C.** Transverse section of resected lower leg shows synovial sarcoma on either side of the interosseous membrane. **D.** Malignant fibrous histiocytoma of soft tissues shows no gross distinguishing features. The entity is shrinking as more lesions are separated off from this diagnosis.

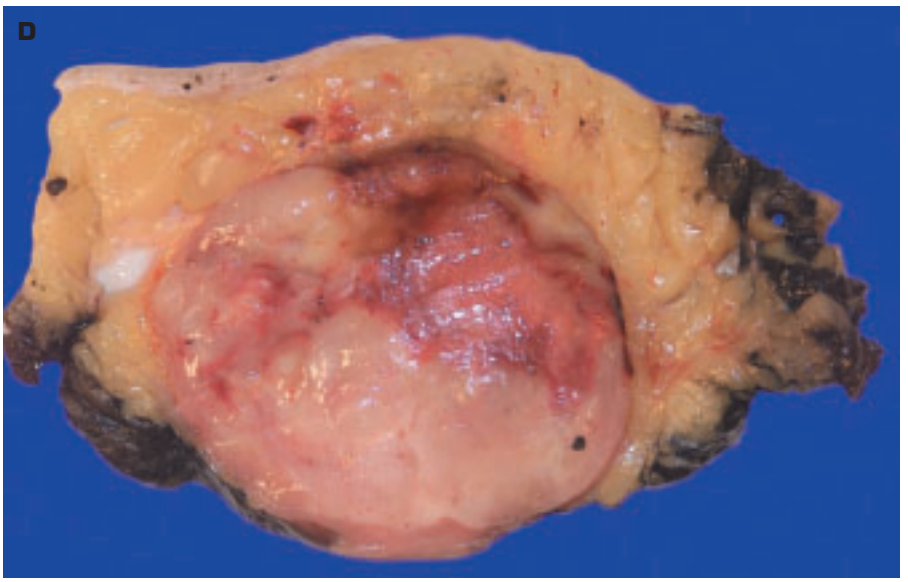

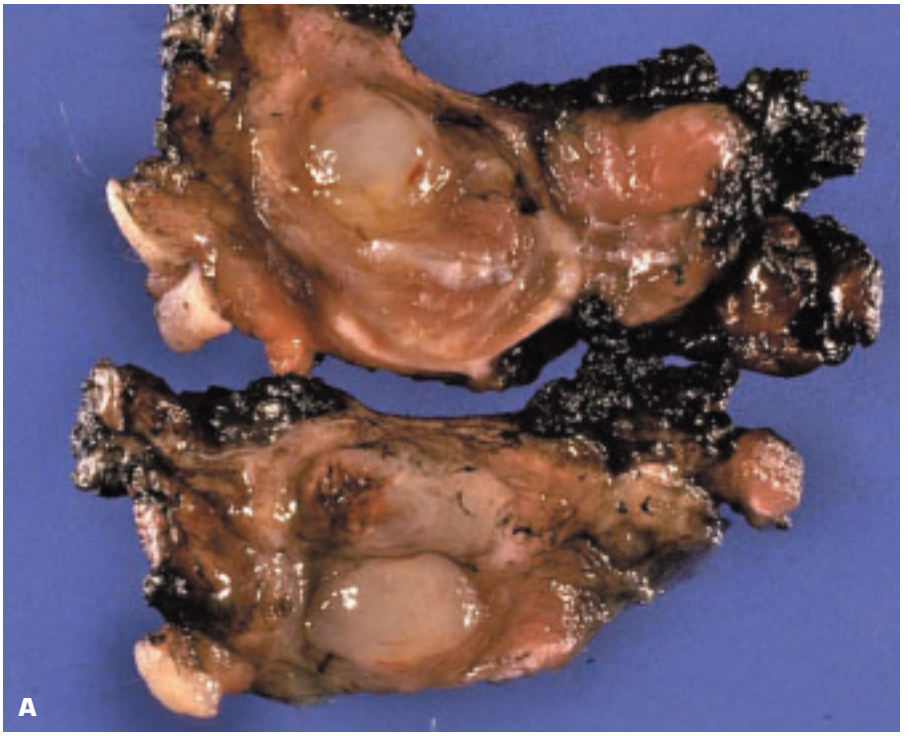

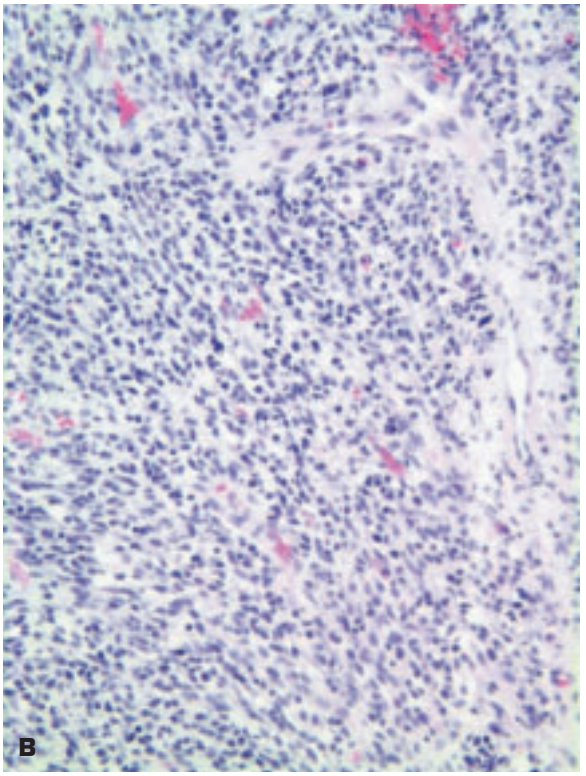

11-34. A. Embryonal rhabdomyosarcoma (ER) in a young child presenting as a misleadingly bland-looking lesion that is reminiscent of a nasal polyp or accumulation of mucus – referred to as the botryoid subtype of ER. **B.** Histologically, the ER is composed of small round malignant cells.

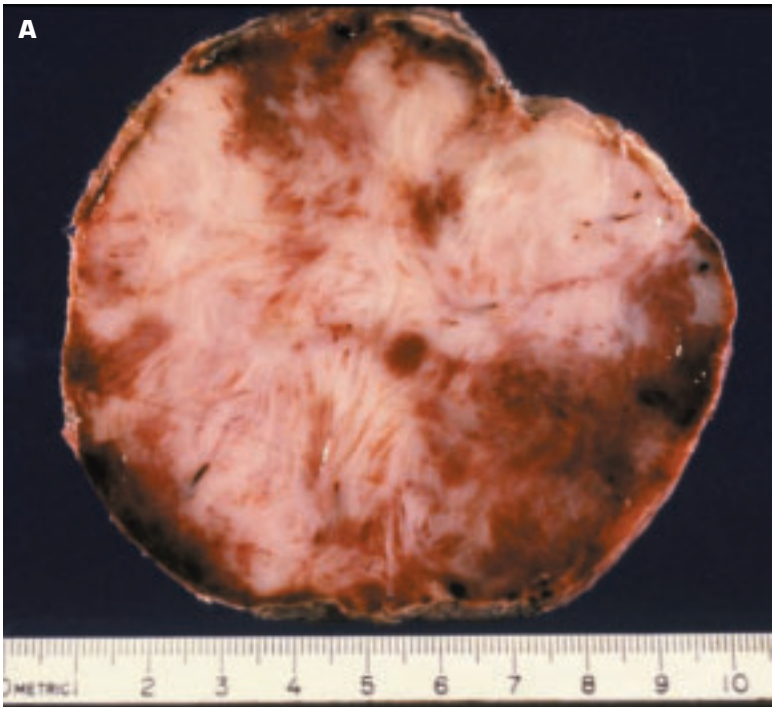

11-35. Miscellaneous tumors of soft tissues. **A.** Osteogenic sarcoma of soft tissues that showed histologic evidence of new bone formation. The tumor shows extensive areas of hemorrhage at its periphery. **B.** Fibrosarcoma of soft tissues presenting as a fleshy, circumscribed mass with an area of necrosis at its inferior margin (*arrow*). *(continued on next page)*

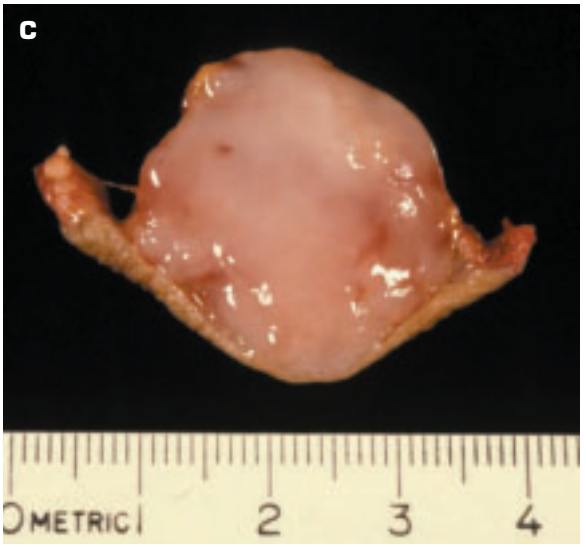

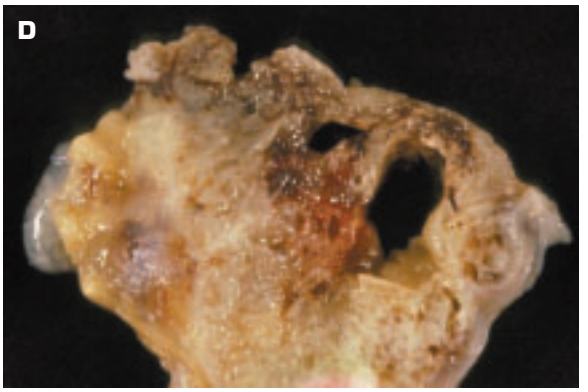

11-35. *(Continued)* **C.** Metastatic plasmacytoma under the skin. **D.** Yolk sac (endodermal sinus) tumor of the retroperitoneum is usually a malignant tumor. (Yolk sac tumors are the most common malignant testicular and ovarian tumors in children.) **E.** Histology of yolk sac tumor shows that the primitive germ cells have produced an ill-formed glomeruloid body (*arrow*). *(continued on next page)*

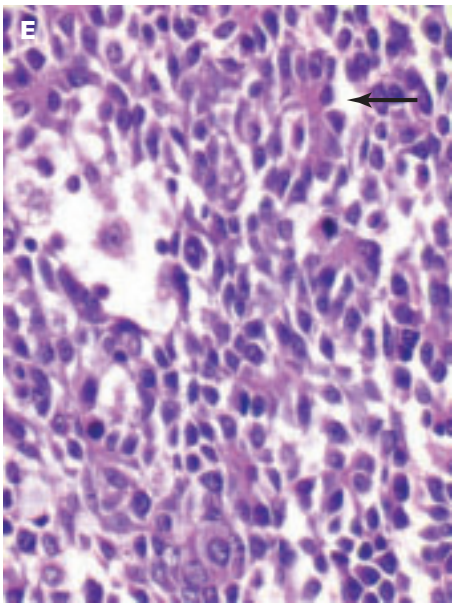

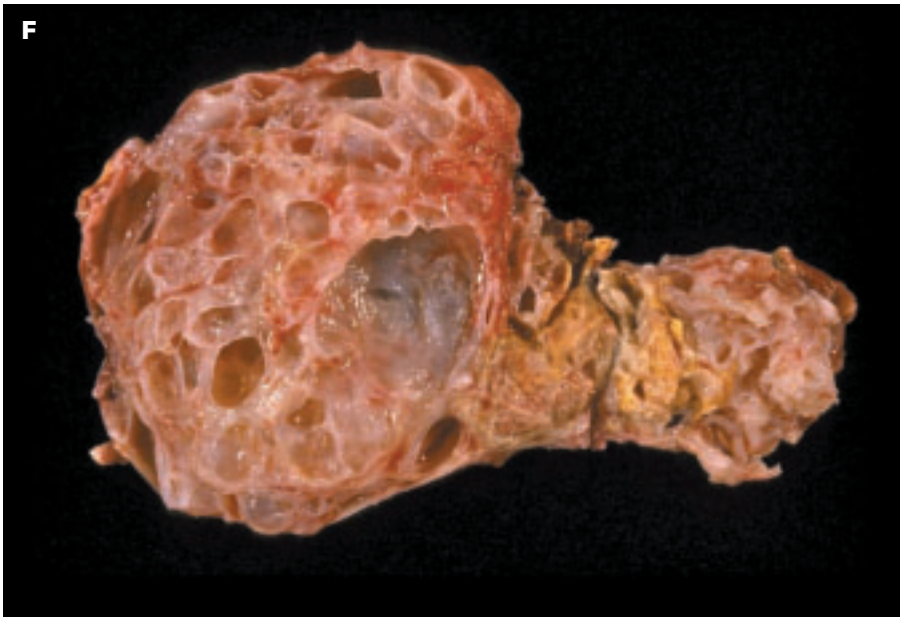

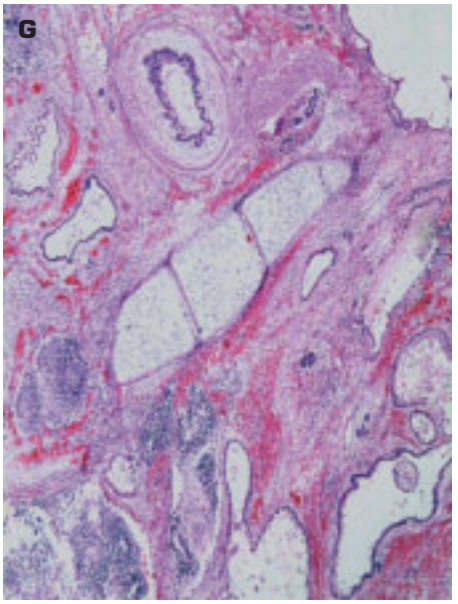

11-35. *(Continued)* **F.** Mature teratoma of the retroperitoneum has a multicystic internal structure with focal solid areas. **G.** Histology of this teratoma shows a variety of well-differentiated tissues resembling bronchial cartilage, spaces lined by bronchial epithelium, arteries, and lymphoid tissue.

11-36. Metastatic tumors in soft tissues. **A.** Metastatic renal cell carcinoma has a deep yellow color due to its abundant lipid content. **B.** Metastatic malignant melanoma (MM) in skeletal muscle. An MM should be considered in any metastatic tumor of uncertain origin.

11-37. Cystic hygroma (lymphatic dysplasia) at back of neck of a fetus. **A.** Front view of a generally hydropic fetus showing an halo-like cystic hygroma colli behind the head. **B.** Posterior view of a cystic hygroma after the fluid contents have been drained. Cystic hygroma may be associated with chromosomal abnormalities (including Turner syndrome, as in this patient) and/or congenital heart disease. Fetal Turner syndrome comprises cystic hygroma, generalized edema, and constrictions at the wrists and ankles.

12 Central Nervous System

12-1. A. Close-up view of a small berry aneurysm (*arrow*) on a cerebral artery. **B.** Precursor defect leading to a berry aneurysm is a localized gap in the medial muscle where only intima and adventitia comprise the vascular wall. The defect is beginning to bulge outward. Such defects may have a familial basis accounting for the familial occurrence of some berry aneurysms. **C.** Elastic-stained section of berry aneurysm at vascular branch point shows absence of muscle and internal elastic lamina in the wall of the aneurysm. *(continued on next page)*

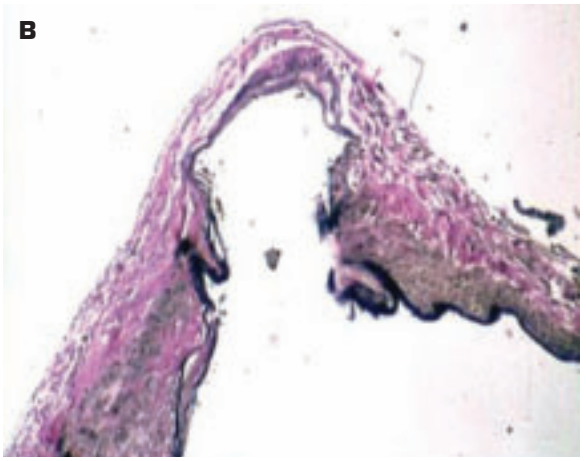

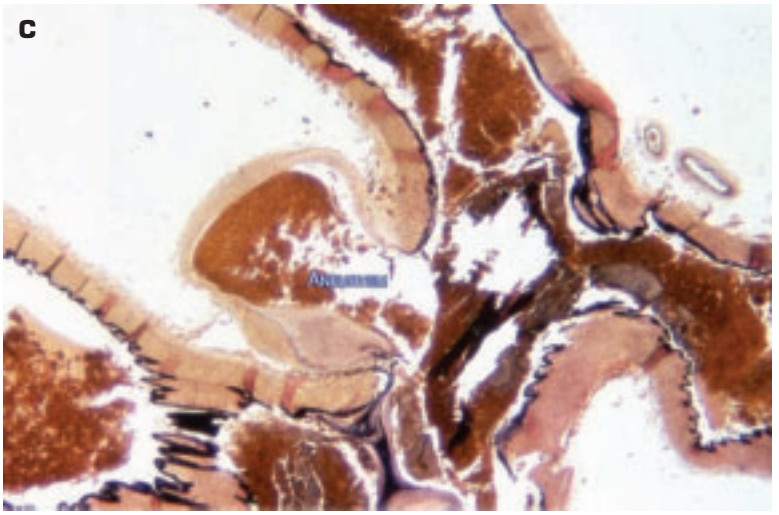

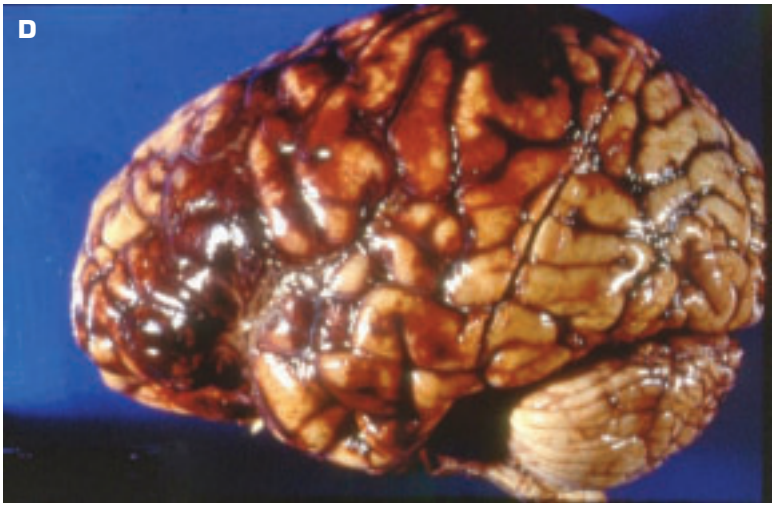
D

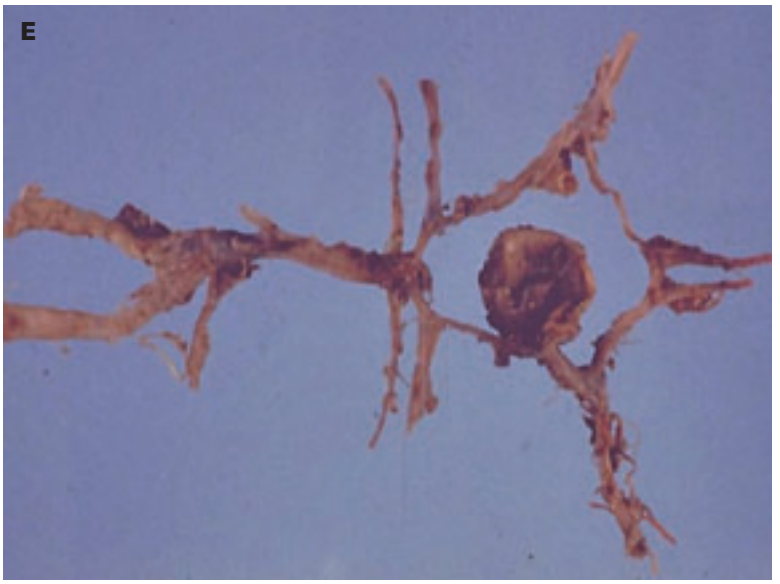
E


F

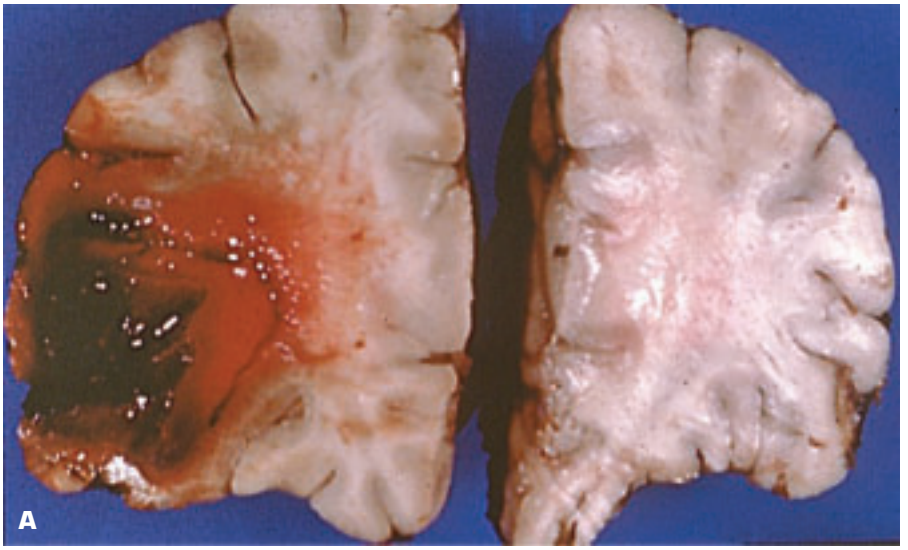

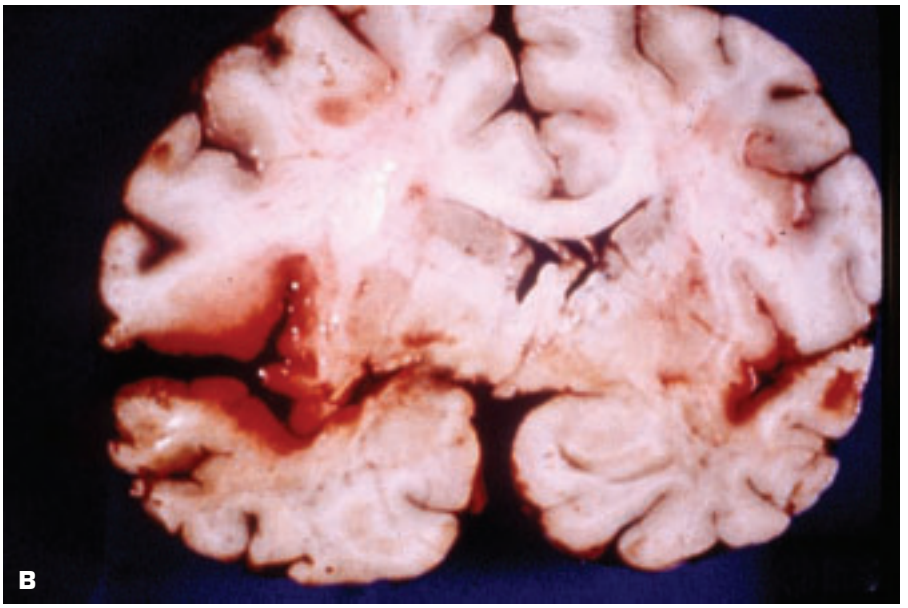

12-2. A. Coronal section of brain adjacent to site of rupture of a berry aneurysm shows that a jet of blood has entered the cerebral substance to produce an intracerebral hematoma. **B.** A more posterior coronal section of the same brain shows more blood in the Sylvian fissure plus significant brain swelling leading to a right-to-left shift.

Facing page:
12-1. *(Continued)* **D.** Subarachnoid hemorrhage. The blood lies deep to the arachnoid membrane and cannot be washed away by applying a gentle jet of water to the surface. **E.** Large ruptured berry aneurysm of circle of Willis. **F.** Large berry aneurysm (*top*) shows a coil protruding through its ruptured wall. The radiologically inserted coil had induced thrombosis but failed to prevent fatal bleeding.

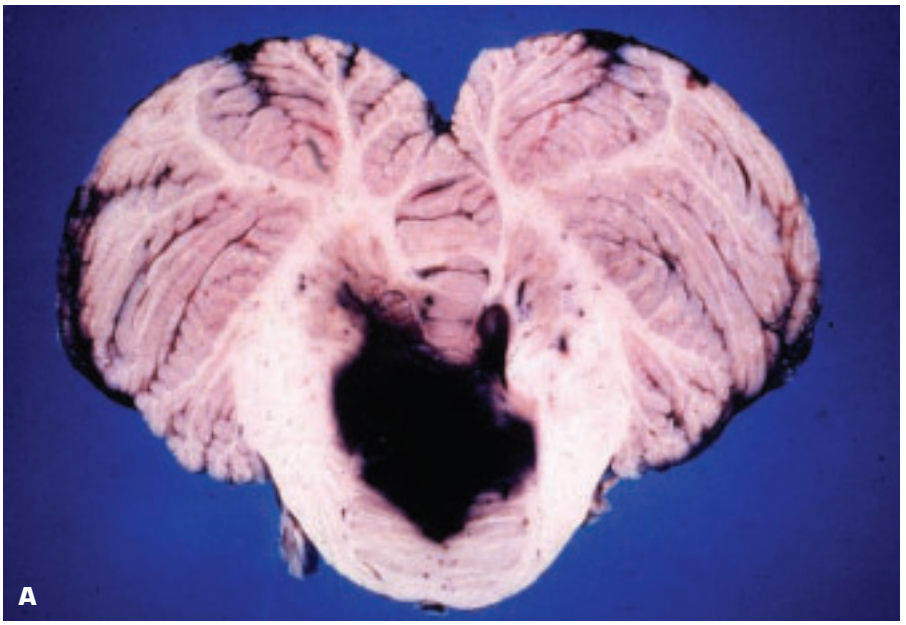

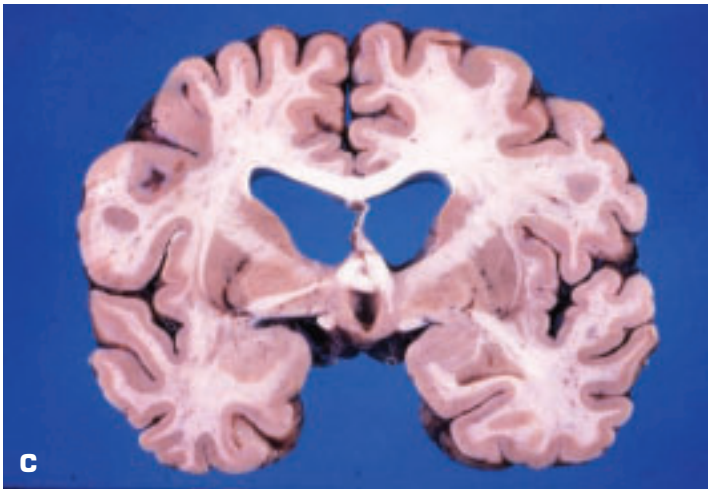

12-3. Hypertensive pontine hemorrhage. **A.** A transverse section of the cerebellum and brainstem shows a large hematoma in the dorsal aspect of the mid pons. **B.** Two more levels rostral to the prior section show extension of the pontine hemorrhage to involve the rostral portion of the fourth ventricle. **C.** Coronal section of the same brain at the level of the anterior commissure showing dilatation of the lateral ventricles secondary to compression of the fourth ventricle by the hematoma.

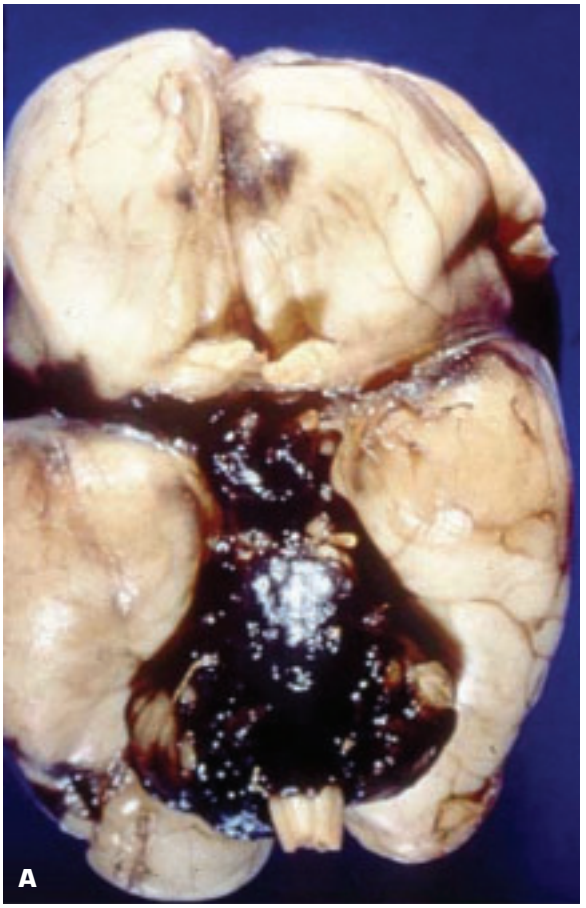

12-4. Intraventricular hemorrhage in a premature neonate. **A.** Photo of base of the brain shows subarachnoid hemorrhage in the area around the brainstem and the cerebellum. This pattern of hemorrhage suggests that the blood has tracked out from within the ventricular system. **B.** Coronal section of cerebral hemispheres shows extensive intraventricular blood in both lateral ventricles, the right temporal horn plus the third ventricle. This is the classical appearance of hemorrhage into the ventricles secondary to hemorrhage into the subependymal germinal matrix in premature infants. *(continued on next page)*

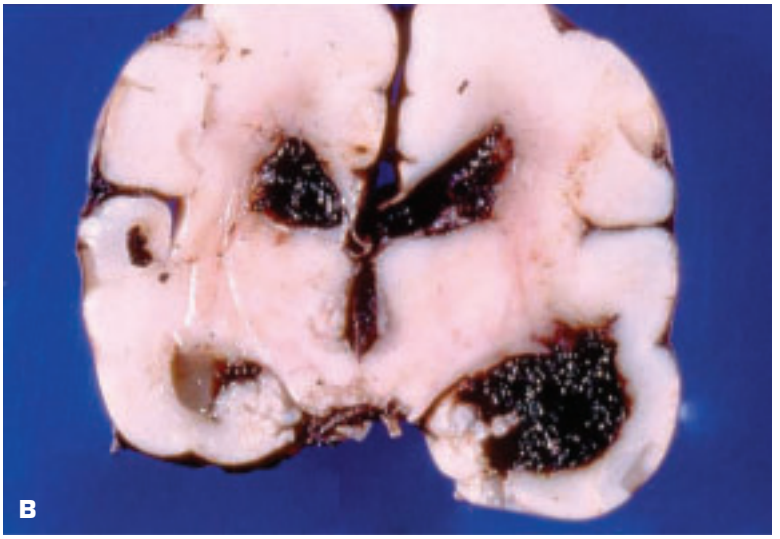

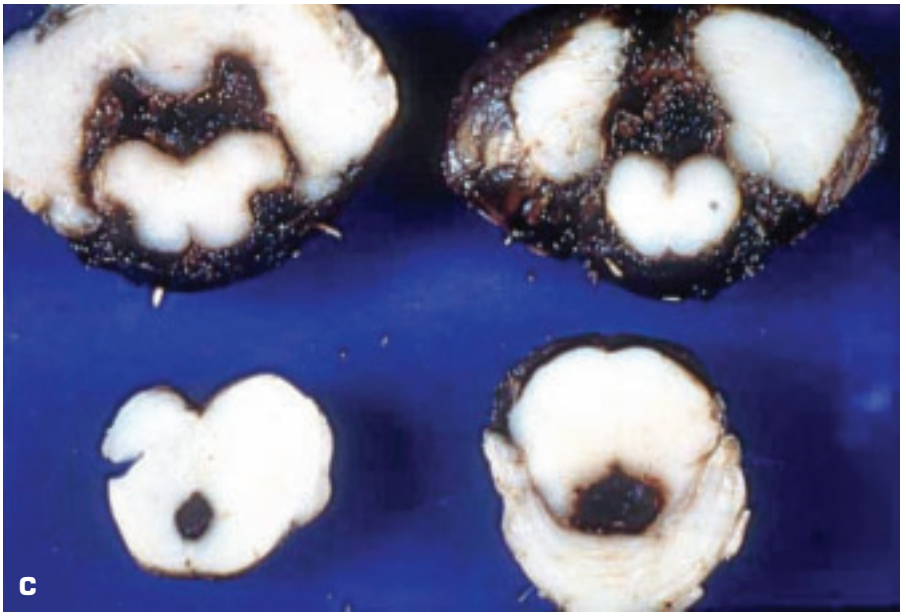

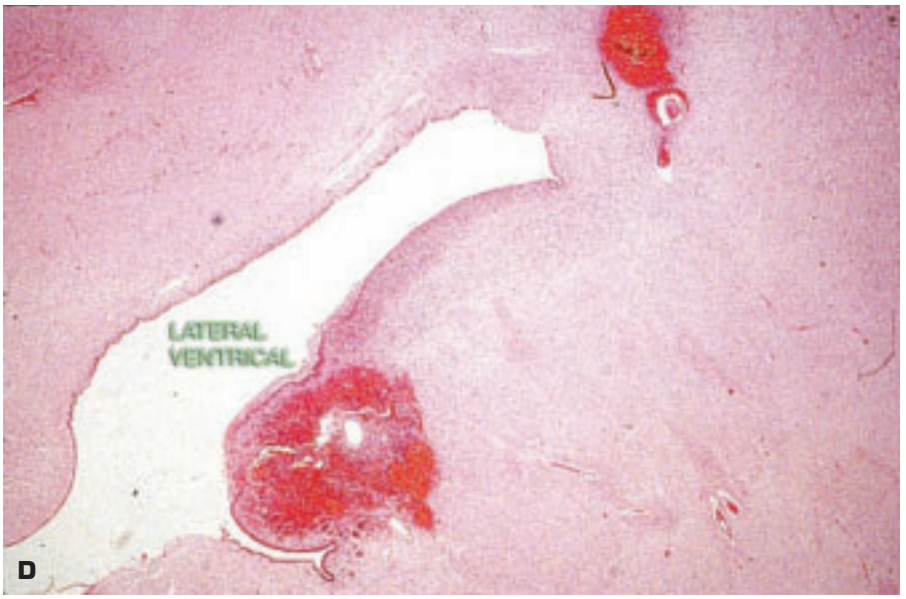

12-4. *(Continued)* **C.** Transverse sections through the brainstem and the cerebellum showing blood in the cerebral aqueduct and the fourth ventricle with extension into the subarachnoid space. **D.** Histology shows a small hemorrhage in the region of the subependymal germinal matrix. Such hemorrhages are the source of large intraventricular hemorrhages seen in premature infants.

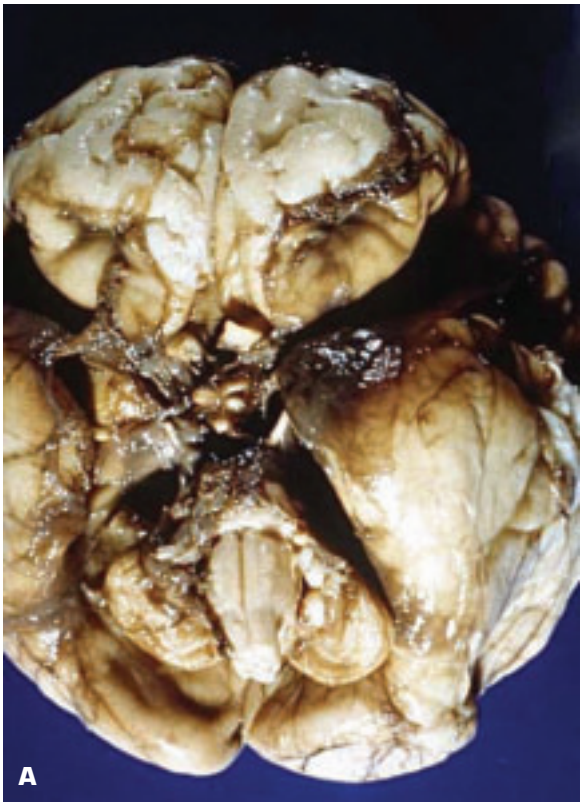

12-5. A. Brain of an infant who survived an intraventricular hemorrhage shows brownish discoloration and thickened leptomeninges at the base of the brain. **B.** Close-up view of the same region. **C.** Coronal section of this same brain shows hydrocephalus with dilatation of the lateral and third ventricles and accentuation of the temporal horns of the lateral ventricles. The old hemorrhage has given rise to brownish discoloration of the lining of the ventricles. *(continued on next page)*

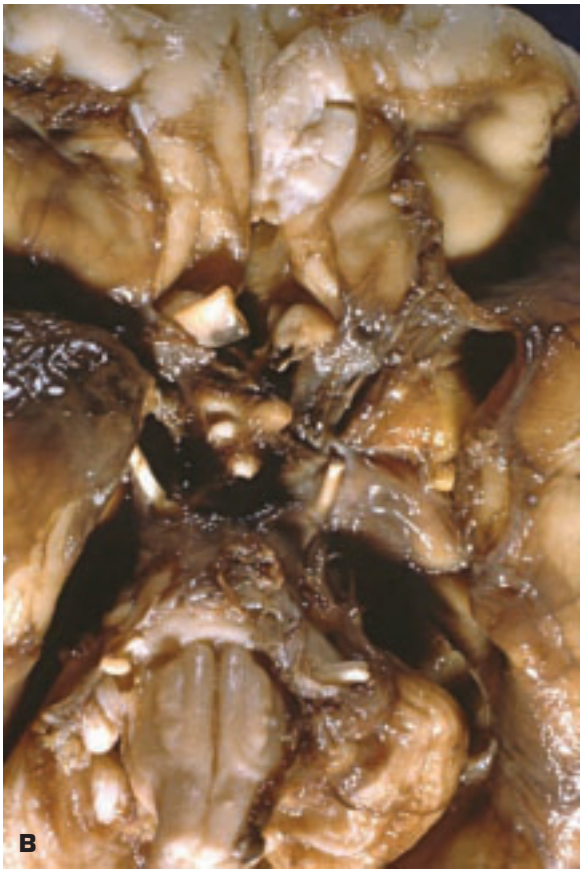

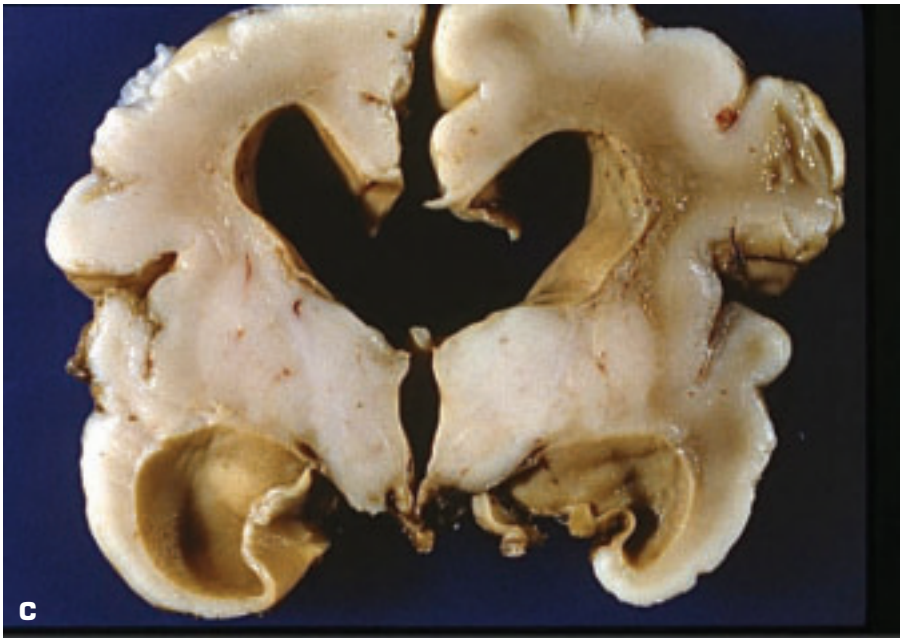

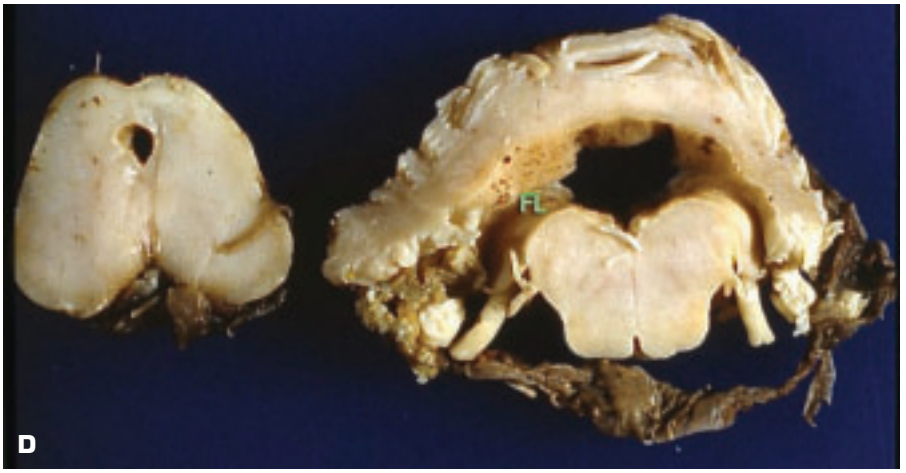

12-5. *(Continued)* **D.** Section of the midbrain, medulla, and cerebellum of the same patient shows a dilated cerebral aqueduct in the midbrain, as well as dilated foramina of Luschka in the lateral aspects of the medulla. This pattern is indicative of a communicating type of hydrocephalus, the obstruction being distal in the flow of cerebrospinal fluid (CSF). Note the thickened leptomeninges over the medulla (*bottom*). Such leptomeningeal scarring interferes with the flow of CSF to sites of resorption in the arachnoid granulations.

12-6. Cerebral infarction. **A.** Hemorrhagic infarct in the area of distribution of the right middle cerebral artery. The right hemisphere is swollen, and there is local disruption of the surface by hemorrhage. **B.** Lateral view of the same brain shows extensive cerebral softening with disruption of the surface and surrounding subarachnoid hemorrhage. **C.** Coronal section through frontal lobes shows hemorrhagic infarction in the right middle cerebral artery territory. Much of the hemorrhage is confined to the cortical regions. The right hemisphere is greatly swollen compared to the left. *(continued on next page)*

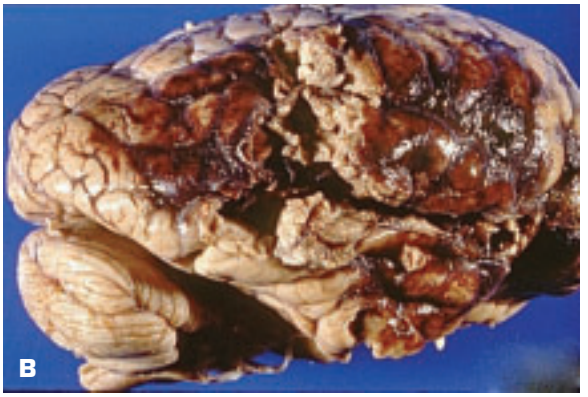

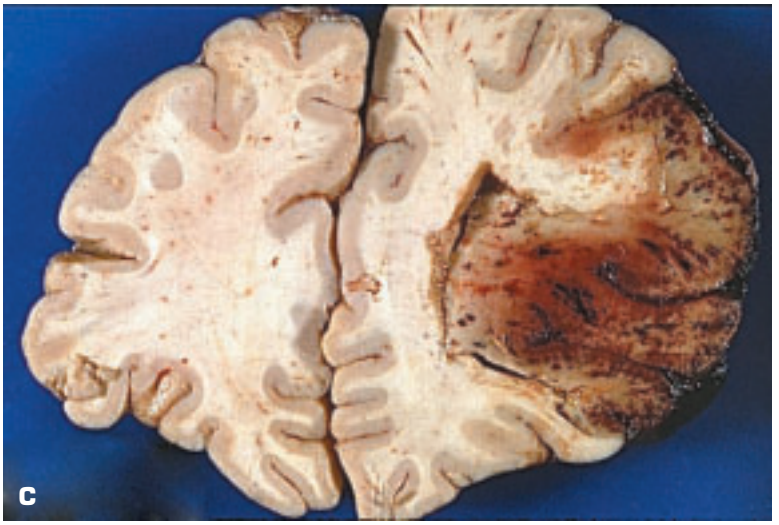

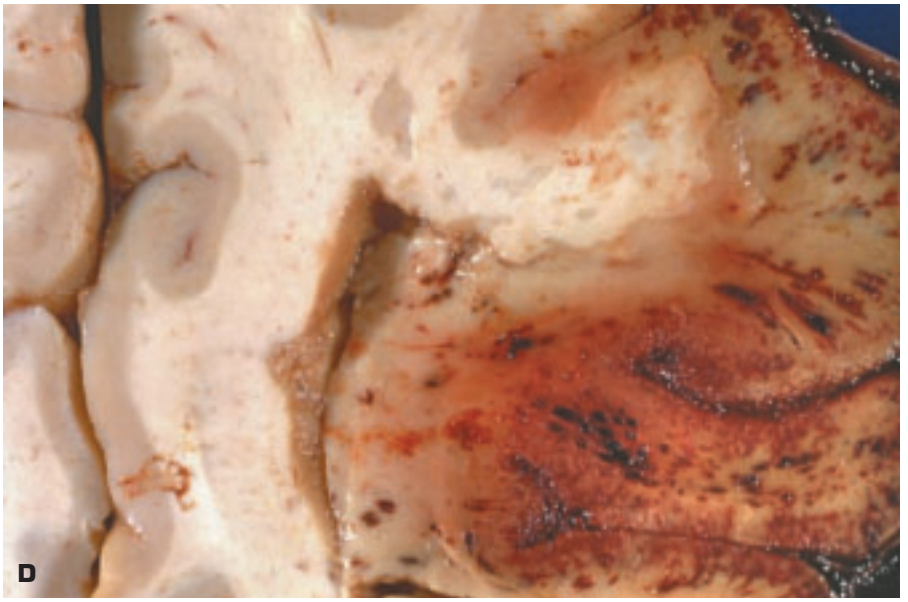

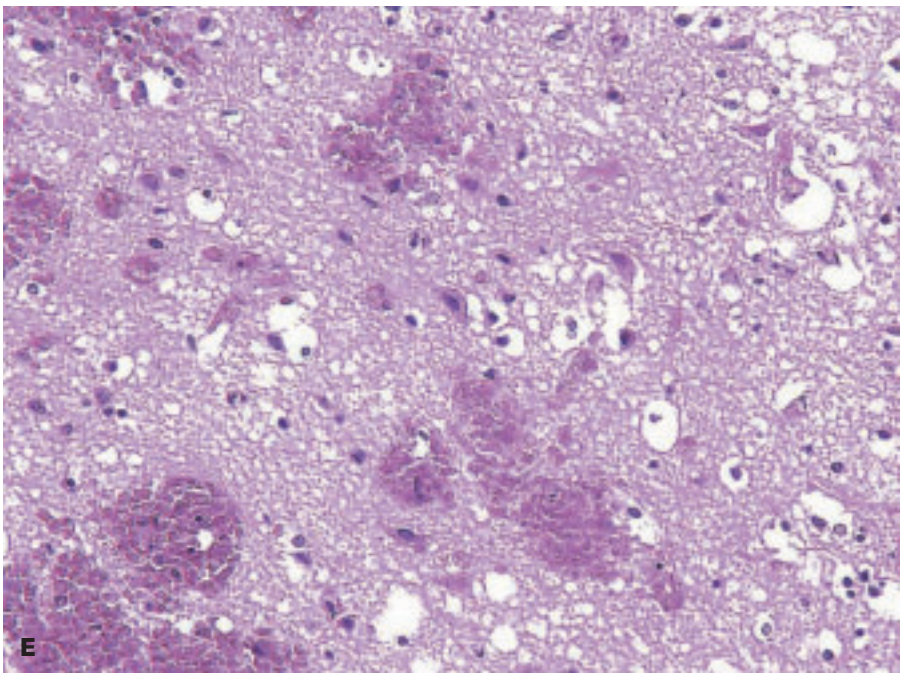

12-6. *(Continued)* **D.** Close-up view of the same infarct shows a sharp distinction between normal and abnormal white matter underlying the infarct. Note that the hemorrhage is largely within the gray matter with a perivascular or petechial appearance. This is due to gray matter having a five times greater vascularity than the white matter. **E.** Histology of this 4- to 5-day-old infarct shows eosinophilic degeneration of neurons, mild neutrophilic infiltration, perivascular cuffing by mononuclear cells, and several areas of hemorrhage.

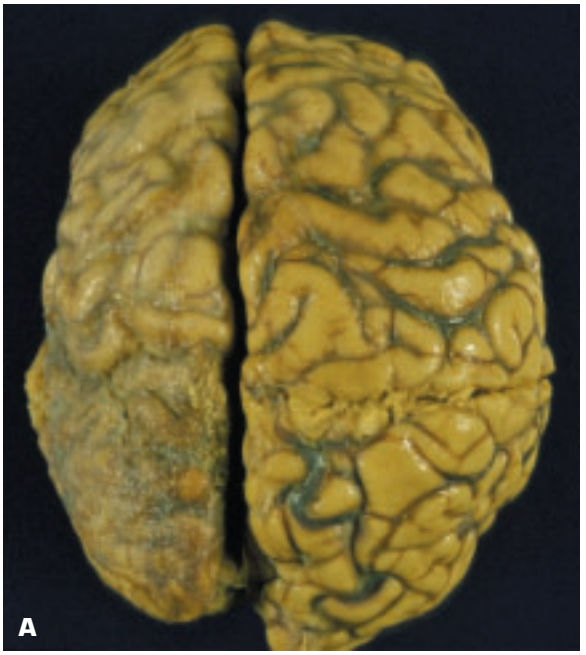

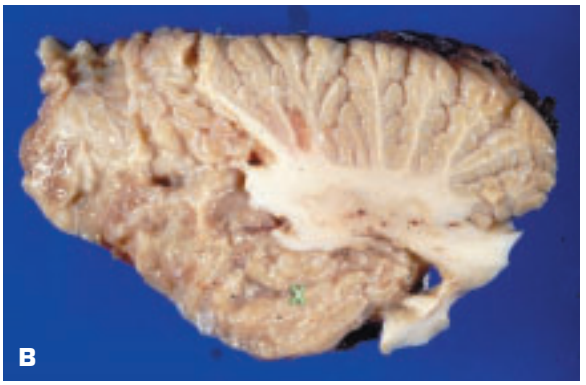

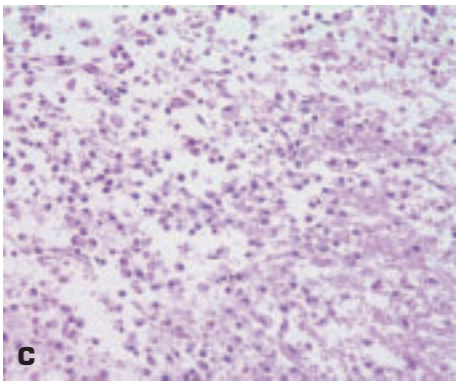

12-7. A. Well-established infarct of left occipital lobe shows shrinkage of the involved area. **B.** Liquefactive necrosis (X) of the cerebellum following infarction. **C.** Histology shows liquefactive necrosis of the cerebral tissue with large numbers of swollen microglial cells floating in a fluid-filled stroma.

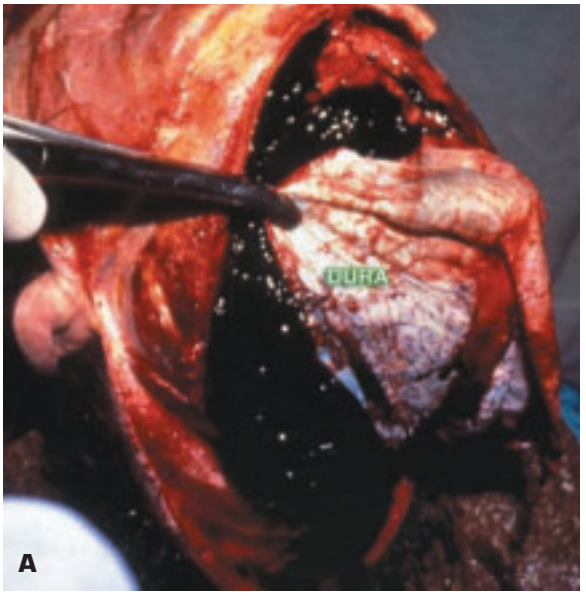

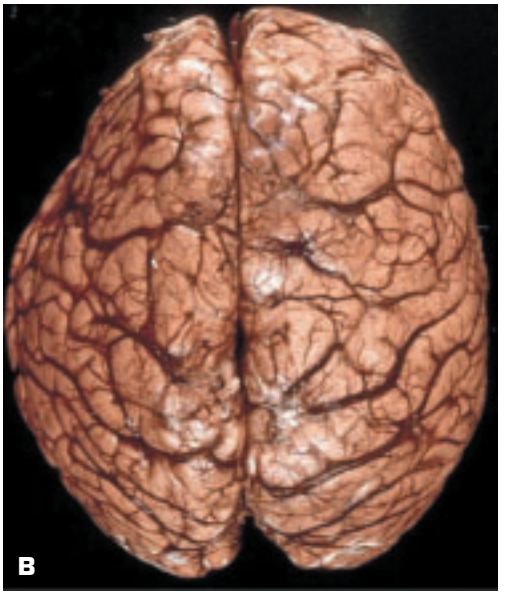

12-8. A. Massive subdural hematoma overlies left cerebral hemisphere. **B.** View of brain from the top shows indented left frontal lobe (*top left*) due to compression by the subdural hematoma. **C.** Coronal section through frontotemporal region shows indentation and left-to-right shift of brain with evidence of cingulated gyrus herniation. *(continued on next page)*

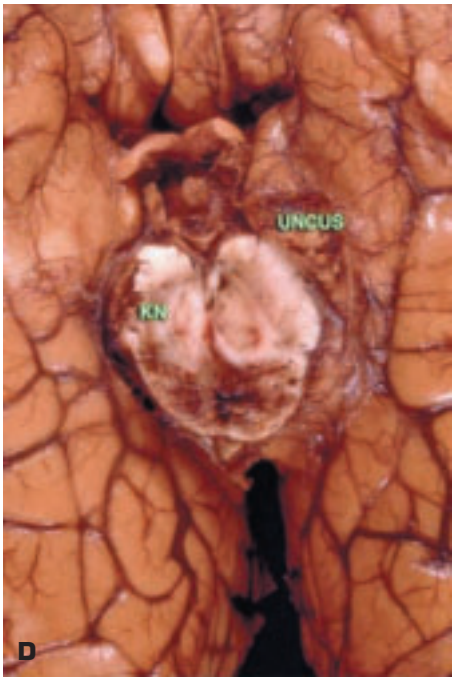

12-8. *(Continued)* **D.** Transected midbrain of the same brain shows herniation of the left uncus, which shows prominent notching and some hemorrhagic softening. The midbrain also shows secondary brainstem (Duret) hemorrhages. Also note the ragged destruction of the right cerebral peduncle (Kernohan's notch) (KN) due to compression of the opposite peduncle against the free edge of the tentorium. This lesion may lead to a paradoxical paresis ipsilateral to the side of the mass lesion. **E.** Sections through the rostral brain stem showing secondary Duret hemorrhages due to transtentorial herniation with rupture of penetrating vessels, which are anchored as the brainstem shifts downward.

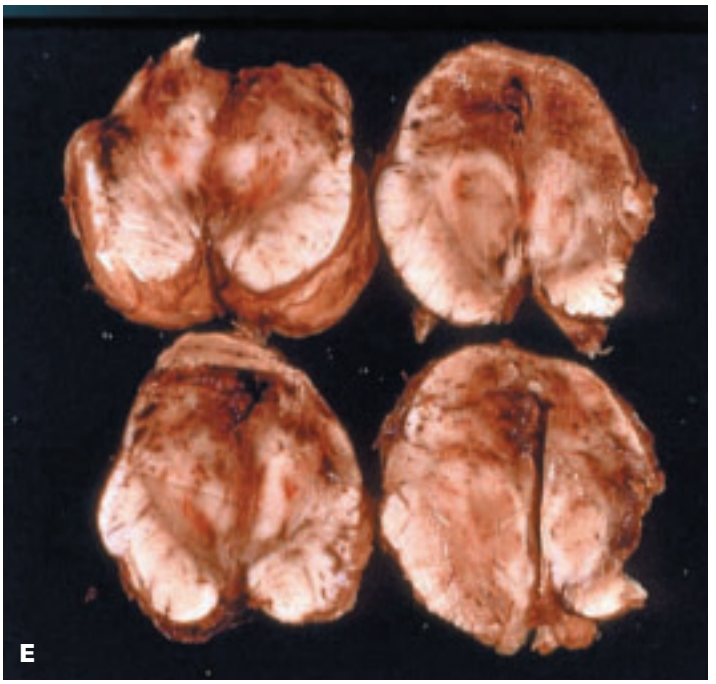

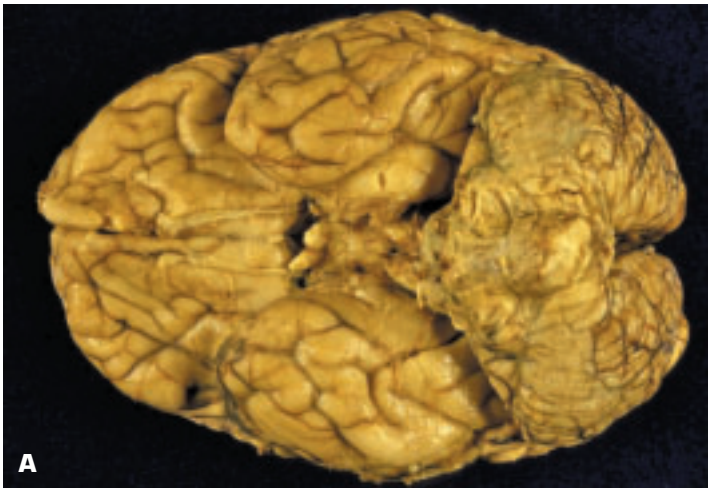

12-9. Leptomeningitis indicates inflammation localized to the pia mater/arachnoid mater that contain cerebrospinal fluid. **A.** Purulent basal meningitis over the pons and the cerebellum due to ascending spread of infection from the spinal cord region. **B.** Typical appearance of generalized purulent meningitis. The leptomeninges appear clouded, especially in the sulci, due to abundant purulent exudate in the subarachnoid space. **C.** The subarachnoid space is histologically seen to be filled by closely packed neutrophils. *(continued on next page)*

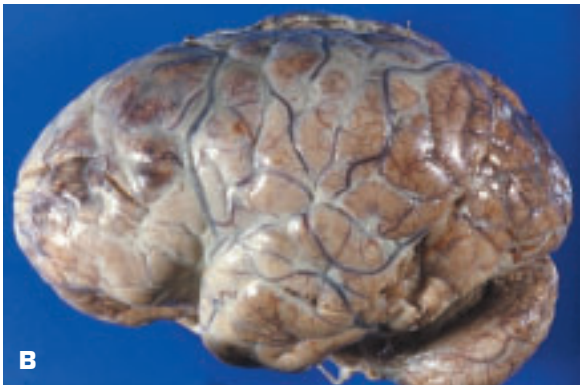

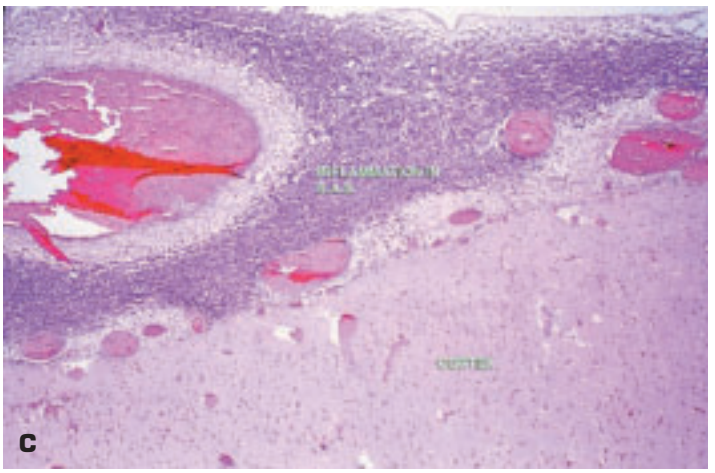

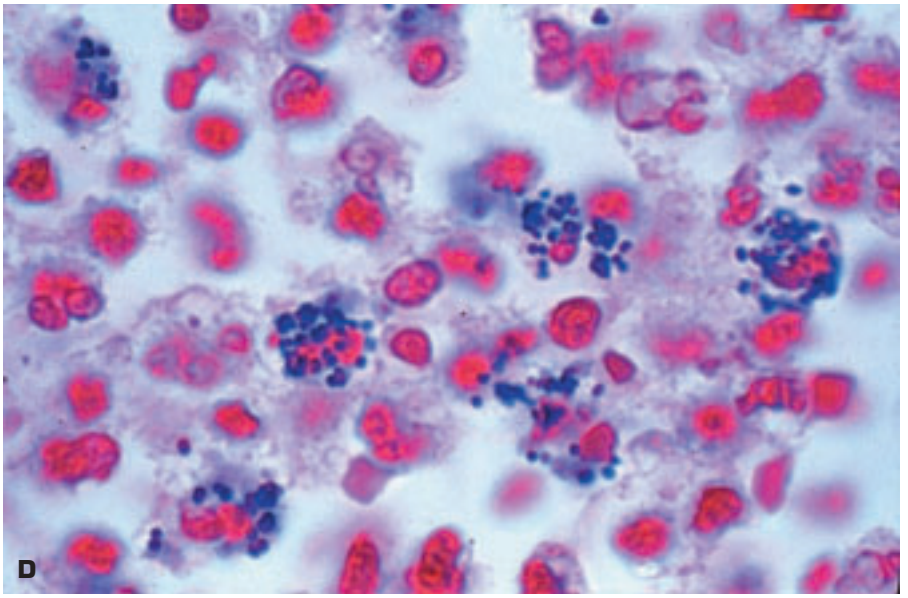

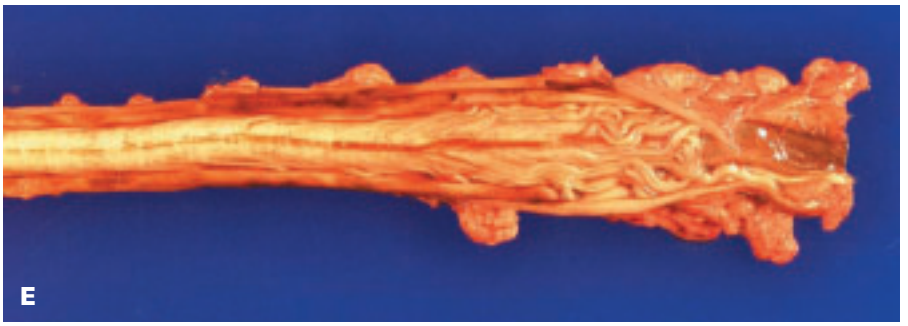

12-9. *(Continued)* **D.** Gram stain of inflammatory infiltrate shows gram-positive diplococci consistent with *Streptococcus pneumoniae*. This organism causes meningitis in older persons and often causes meningitis in persons with fractured base of skull. **E.** Cauda equina syndrome (compression of the nerves in the lower portion of the spinal canal below the termination of the cord) came about in this patient due to organized meningitis. The meninges appear thickened. The cauda equina histologically showed axonal degeneration and fibrosis of many spinal roots.

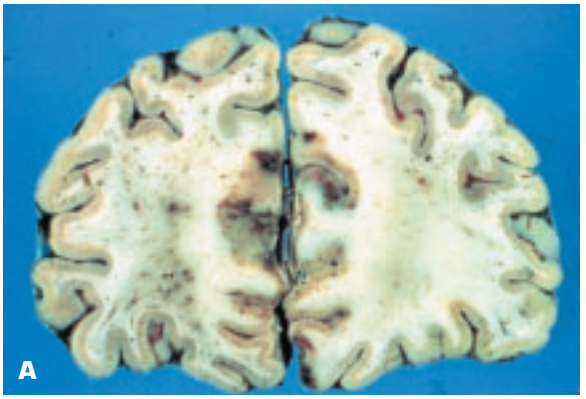

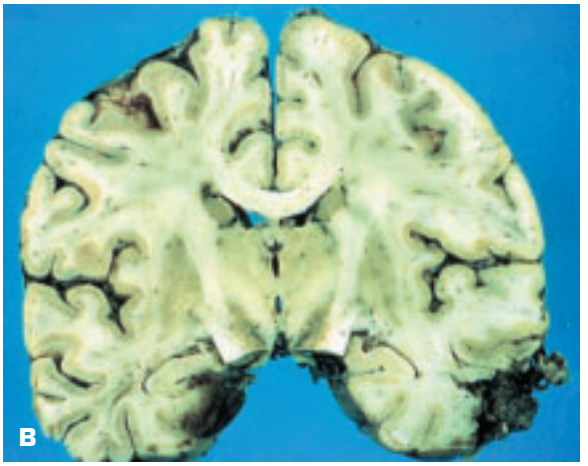

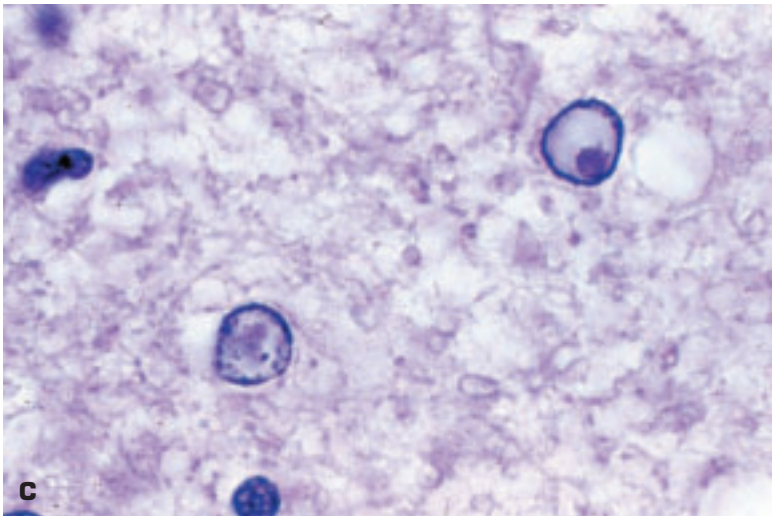

12-10. Herpes simplex virus type 1 (HSV-1) encephalitis presents as a fulminant infection and often affects the temporal lobes most severely. **A.** Softening, discoloration, and focal hemorrhages in the medial frontal lobes bilaterally. **B.** Coronal section at the level of the thalamus shows hemorrhagic softening (necrosis) in the left medial temporal lobe and the right lateral lobe. **C.** High-power histologic appearance of intranuclear inclusions due to HSV-1 infection. *(continued on next page)*

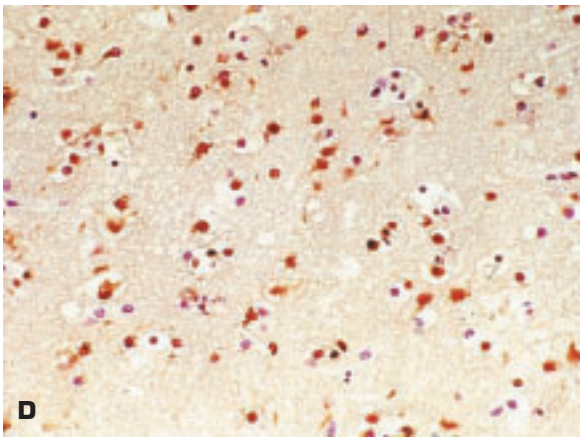

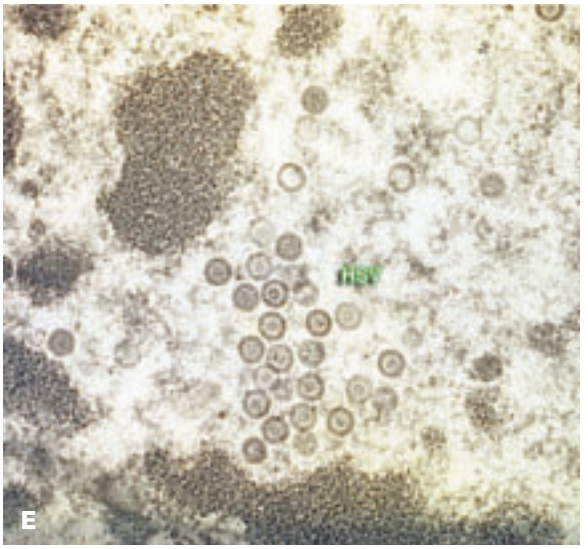

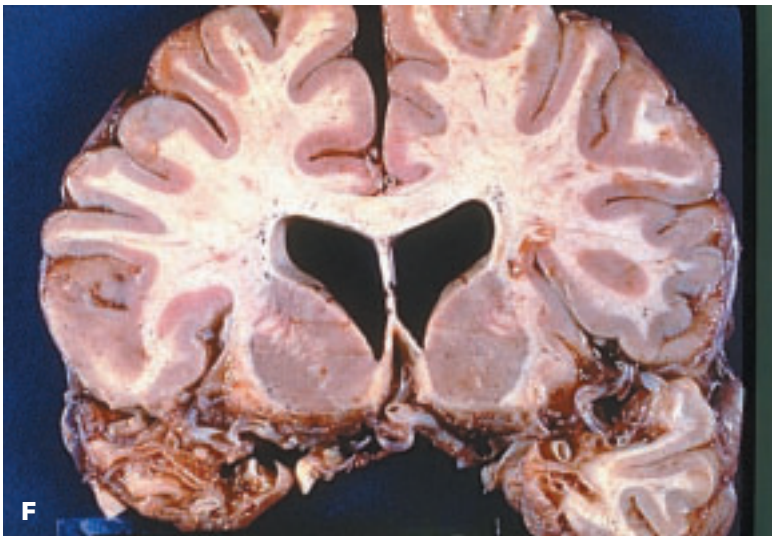

12-10. *(Continued)* **D.** Immunohistochemical stain (brown labeling) for HSV-1 antigens labels most cells in this brain section. **E.** Electron micrograph of brain tissue from the case illustrated previously shows typical herpesvirus particles within the nucleus of an infected cell. **F.** Coronal section of brain from a patient with resolved HSV-1 encephalitis shows bilateral extensive damage to the temporal lobes with much loss of brain substance. This distribution is typical for HSV-1 infection.

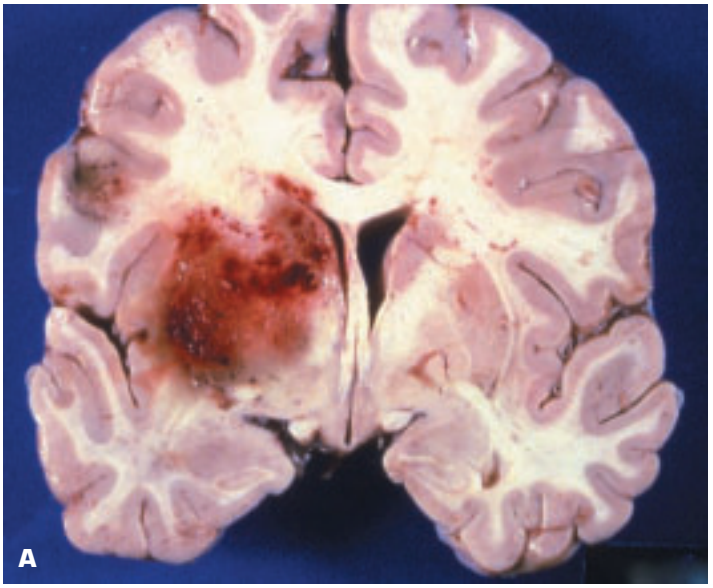

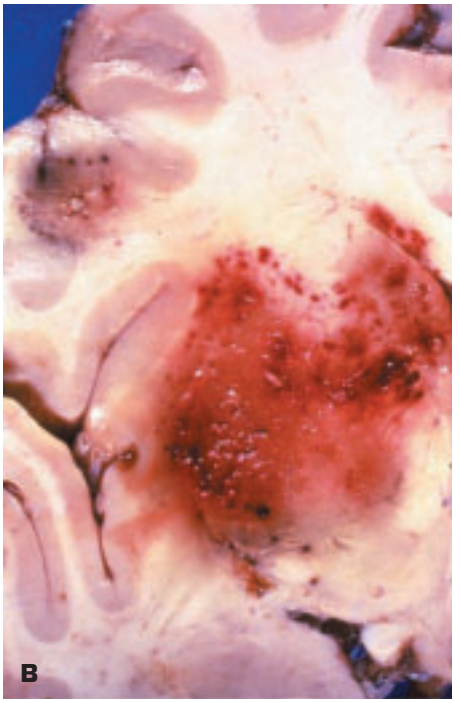

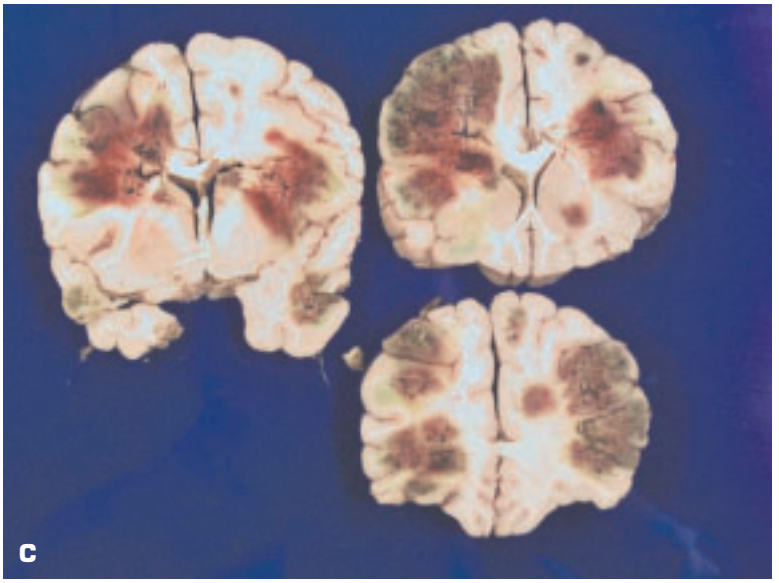

12-11. Cerebral aspergillosis is a complication of an initial pulmonary *Aspergillus* infection, which is more prone to become disseminated in immunocompromised individuals. **A.** Coronal section at level of hypothalamus shows a large area of hemorrhagic necrosis involving the left basal ganglia. A smaller lesion occupies the left inferior frontal gyrus. **B.** Close-up view of both lesions, which have a distribution unlike that of infarction based on a vascular distribution. **C.** Brain of another patient shows multiple infarct-like lesions due to aspergillosis. *(continued on next page)*

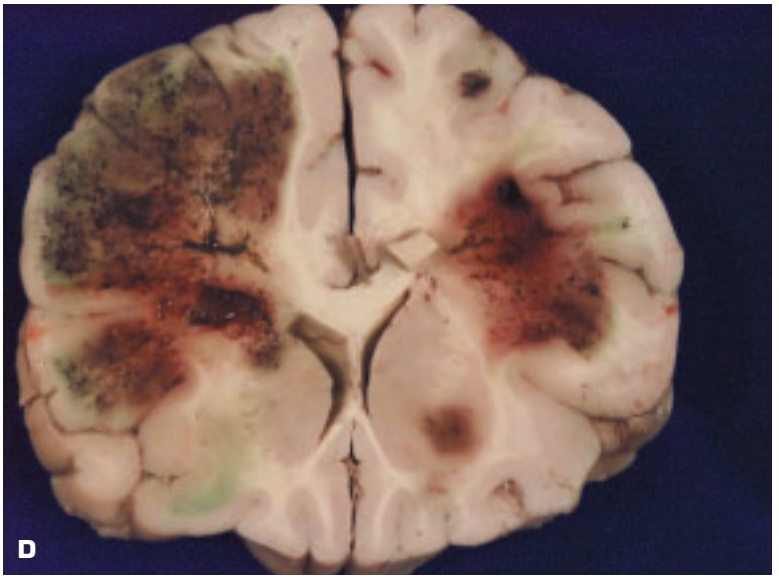

12-11. *(Continued)* **D.** Close-up view of one of the brain slices seen in C. **E.** Hyphae of *Aspergillus* within cerebral infarct show acute angle branching and surrounding necrotic tissue is infiltrated by disintegrating neutrophils. **F.** Grocott methenamine silver stain shows fungal hyphae infiltrating into the arterial media (*left*).

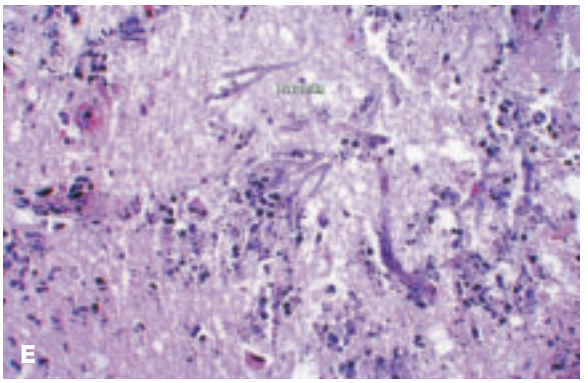

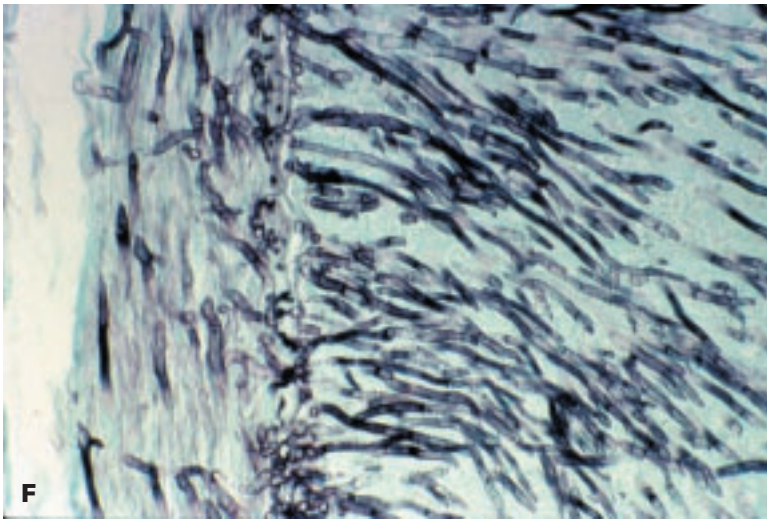

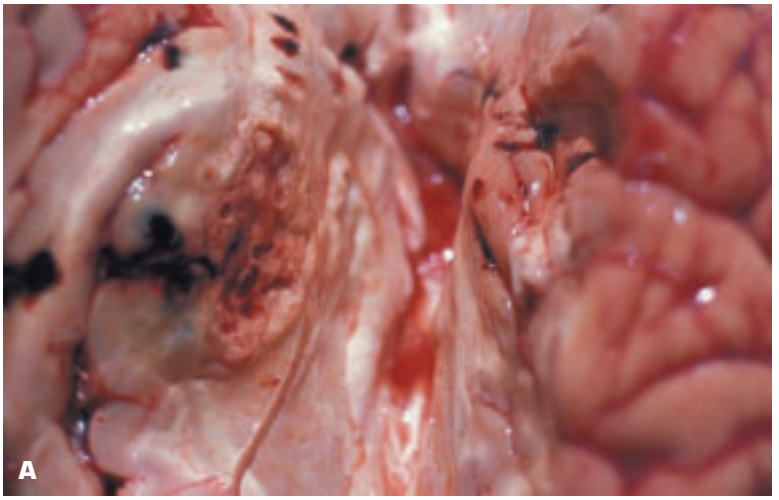

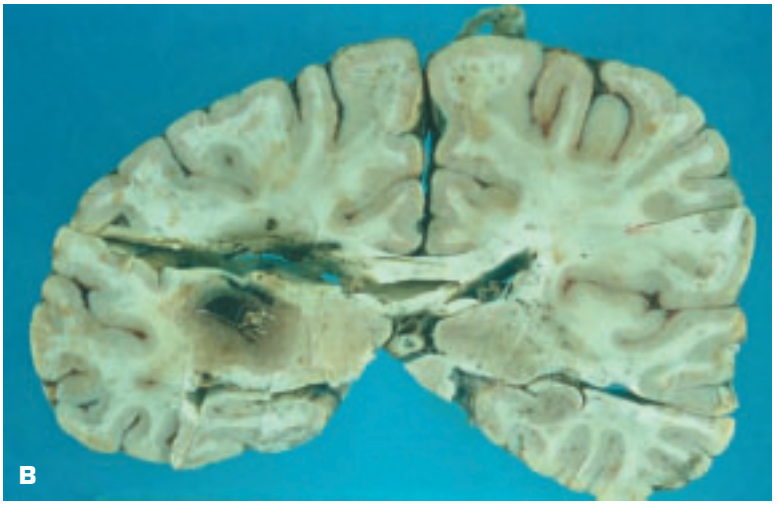

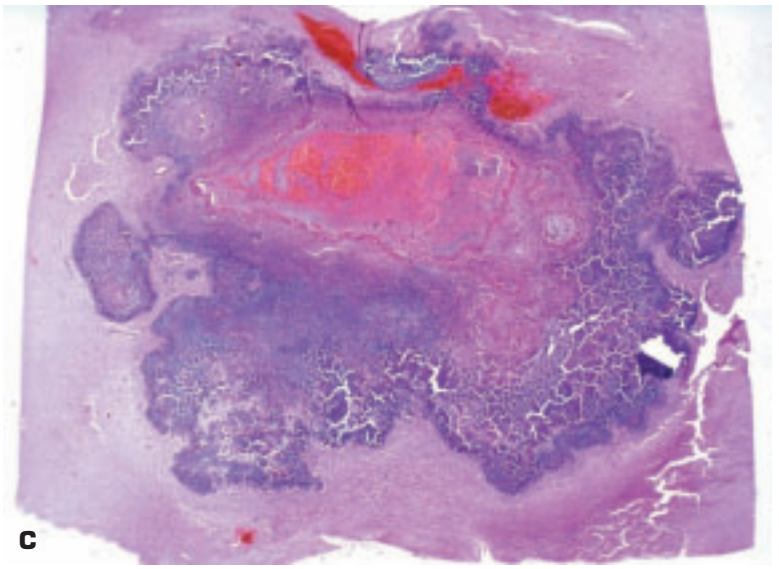

12-12. A. Brain abscess due to *Petriellidium boydii* infection in a heart transplant recipient. Hemorrhage is related to a recent neurosurgical procedure. **B.** Appearance of the same brain abscess in a coronal section. **C.** Whole mount histologic section of the brain abscess.

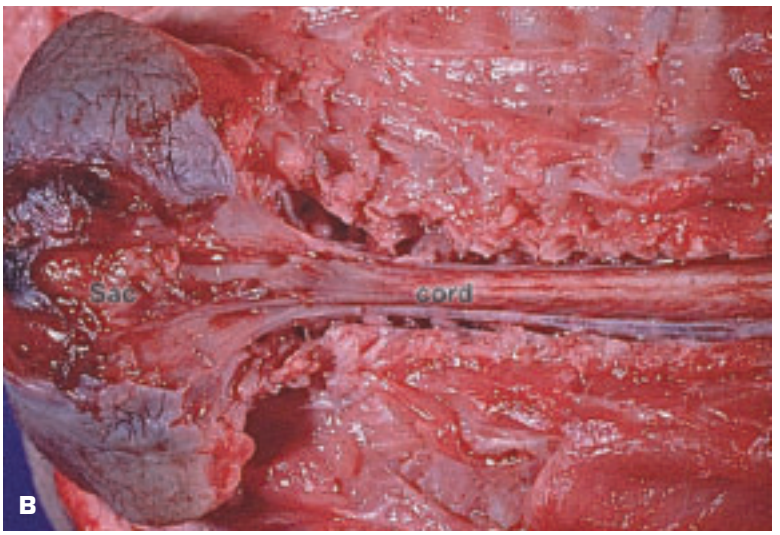

12-13. Arnold–Chiari malformation and associated lesions. **A.** Spina bifida with meningomyelocele at lumbar level of the spinal cord showing the ulcerated sac of the meningomyelocele communicating with the skin surface. **B.** Dissection of the meningomyelocele shows that the spinal cord terminates in the sac of the malformation. *(continued on next page)*

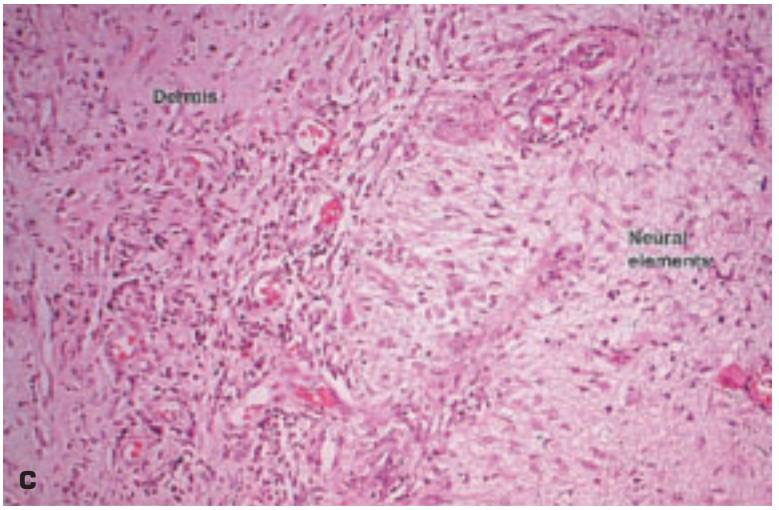

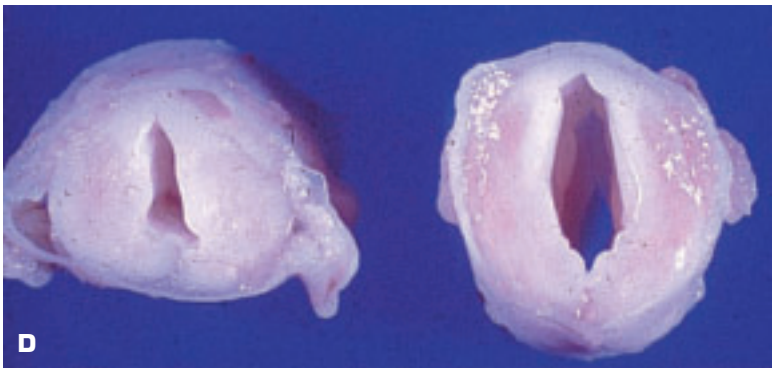

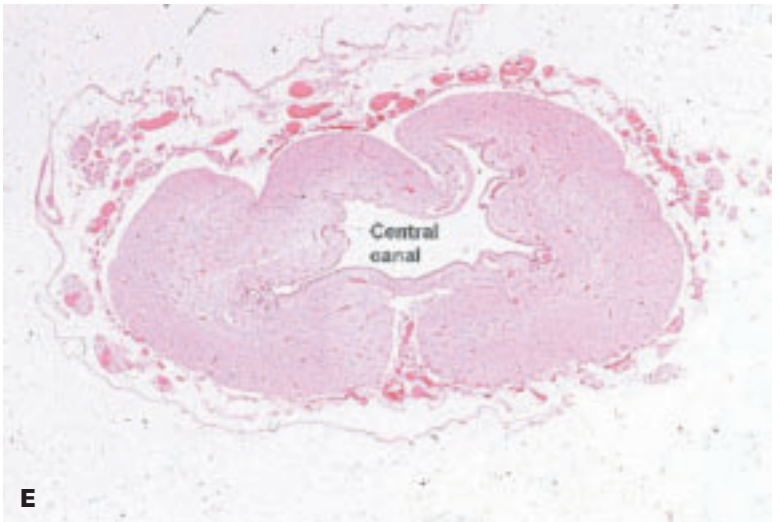

12-13. *(Continued)* **C.** Histology of the interface between the dermal and the neural elements of the meningomyelocele in spina bifida. Dermal elements lie on the left and dysplastic spinal cord elements with reactive gliosis lie on the right. **D.** Hydromelia of the spinal cord above the meningomyelocele. The central canal of the spinal cord is widely dilated. **E.** Dilated central canal of hydromelia has an intact ependymal lining. The condition is analogous to hydrocephalus. *(continued on next page)*

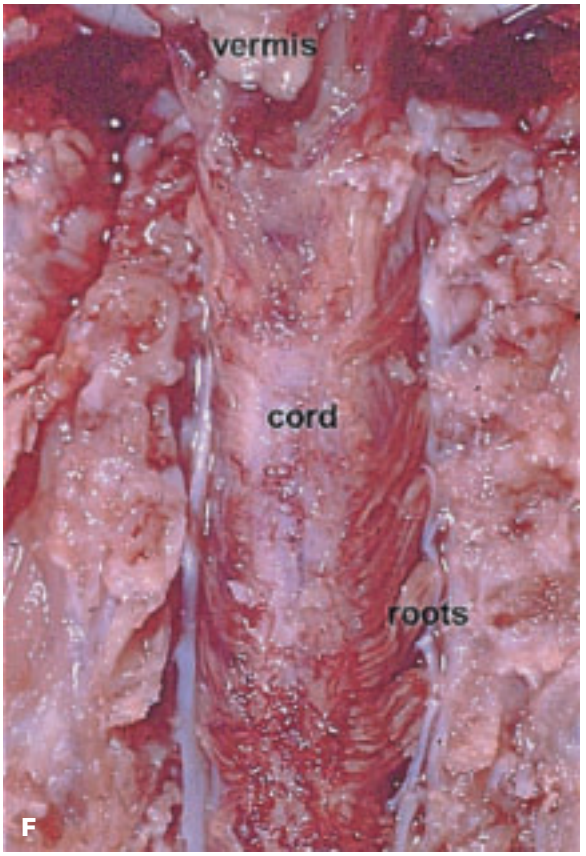

12-13. *(Continued)* **F.** Cervical spinal cord exposed from the posterior aspect in Arnold–Chiari malformation. Due to downward displacement of the spinal cord, the cervical roots must ascend to reach the spinal foramina. **G.** Posterior fossa abnormality in Arnold–Chiari syndrome. Upper specimen shows a sagittal section through the brainstem and the cerebellum of a normal child. Lower specimen shows a similar section in a patient with the Arnold–Chiari malformation. Note the elongated brainstem, fourth ventricle, and herniation of the posterior cerebellar vermis and caudal brainstem into the spinal canal. The level of the foramen magnum is labeled (FM). *(continued on next page)*

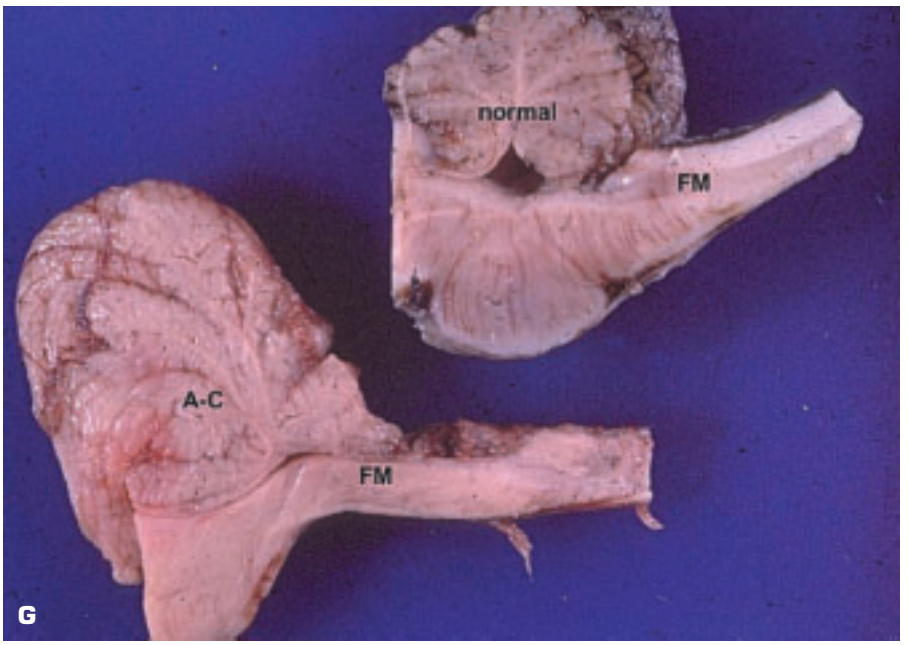

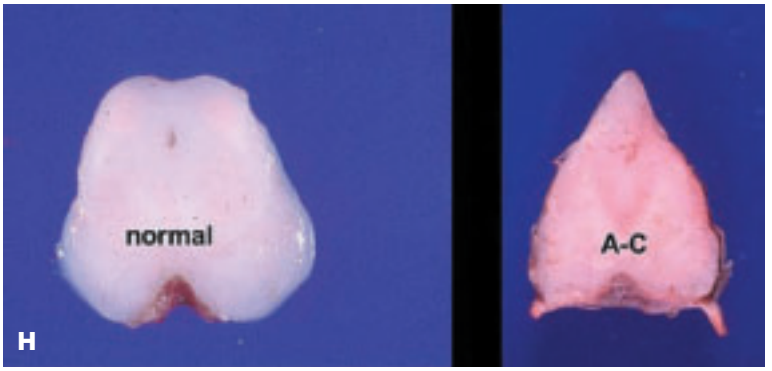

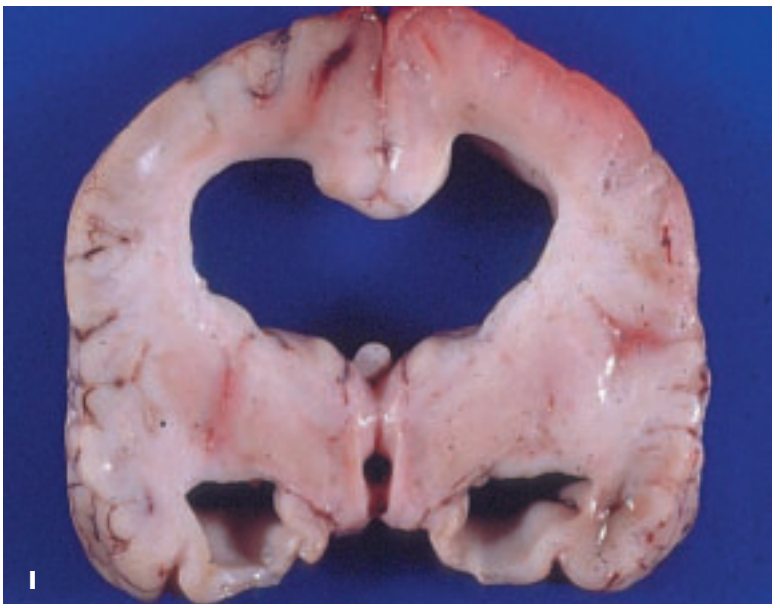

12-13. *(Continued)* **H.** Left specimen is a transverse section of midbrain from a normal infant. The sample on the right is a similar section from an infant with an Arnold–Chiari malformation showing the "beaked" appearance of the tectum with fusion of the colliculi and severe stenosis of the aqueduct. **I.** Hydrocephalus in a newborn with Arnold–Chiari malformation showing dilatation of the lateral ventricles and the temporal horns of the lateral ventricles. The septum pellucidum is absent, as it may be in severe, chronic hydrocephalus.

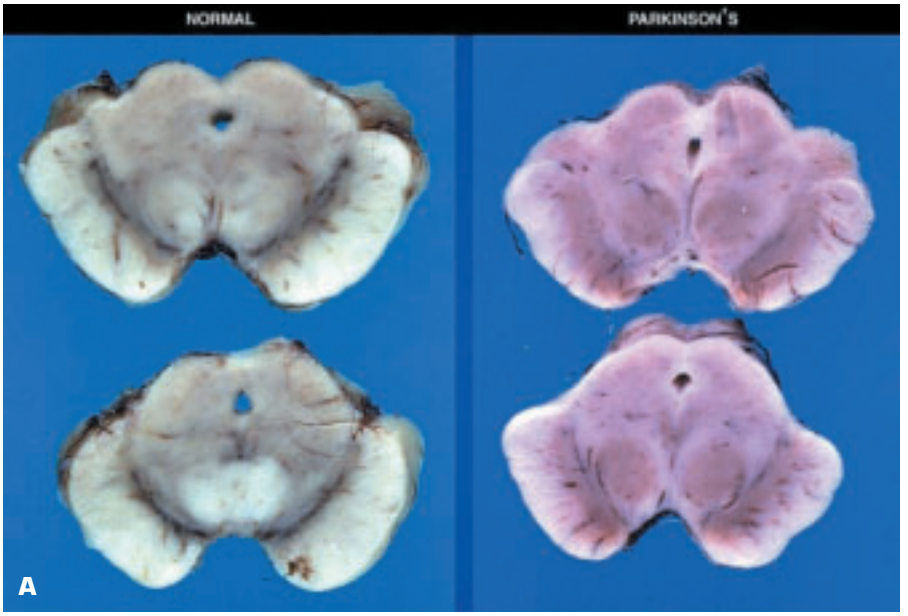

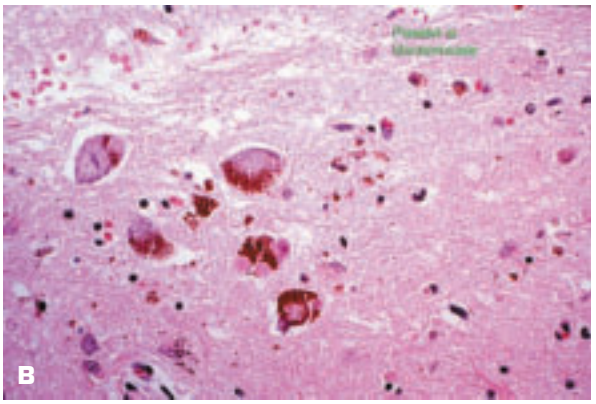

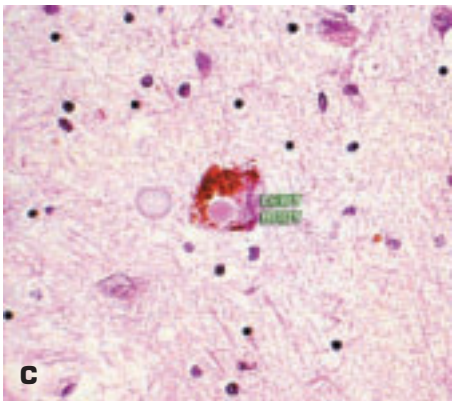

12-14. Parkinson disease (PD) is a common neurodegenerative disease, and Parkinsonism (syndrome) may have many causes, but most are associated with degeneration of the dopaminergic neurones of the substantia nigra. Dementia and dysautonomia are due to lesions elsewhere. **A.** Two sections of normal midbrain on the left showing normal substantia nigra (pigmented zones). Two sections on the right from a patient with PD show a loss of pigmentation in the areas corresponding to substantia nigra. **B.** Substantia nigra in PD showing loss of density of pigmented nuclei with scattered macrophages containing pigment. Occasional Lewy bodies are seen in surviving neurones. The characteristic pathological feature of PD is the presence of Lewy bodies (alpha-synuclein–containing inclusions) in the cytoplasm of surviving neurones in areas of neuronal loss. **C.** Prominent Lewy body in a neurone with reduced pigment content. The Lewy body comprises a brightly eosinophilic, amorphous structure surrounded by a clear halo.

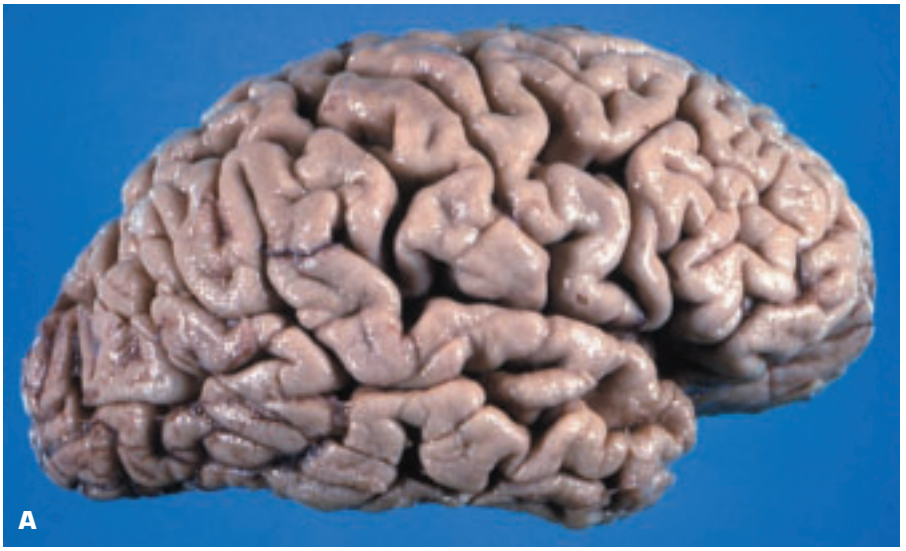

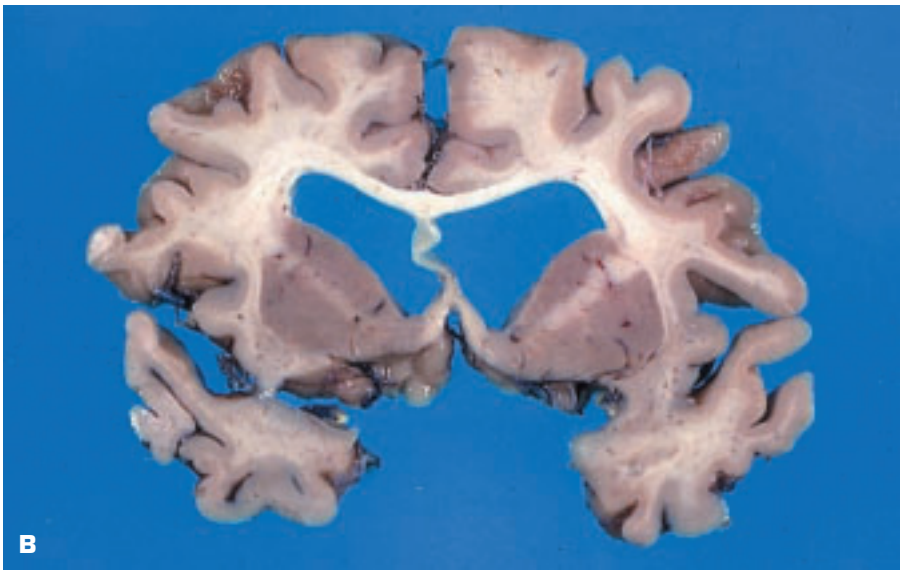

12-15. Alzheimer disease (AD) is the most common cause of neurodegenerative dementia. Morphologic changes usually begin in the mesial temporal lobe and then become more generalized. (Memory deficits precede global cognitive problems.) **A.** Lateral view of the brain in AD. Note that the accentuated sulci secondary to gyral atrophy is most apparent in the frontal and temporal lobes and is least apparent in the occipital lobe (*left*). **B.** Coronal section of the brain shows ventricular dilatation and pronounced cortical atrophy, especially in the region of the Sylvian fissure. *(continued on next page)*

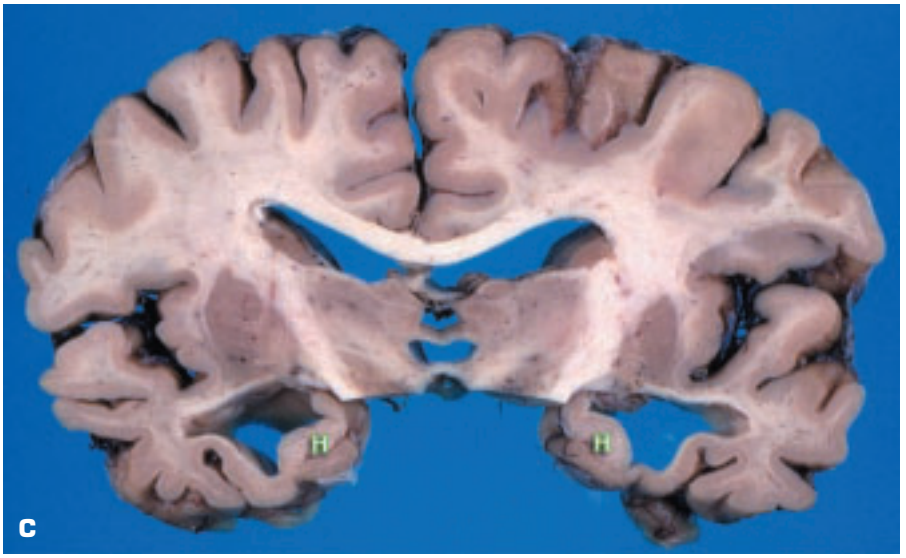

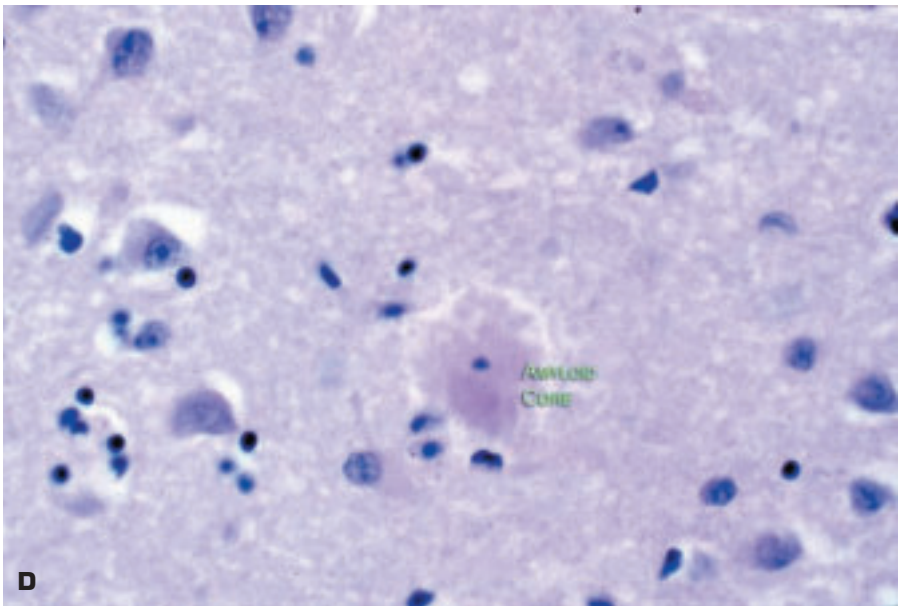

12-15. *(Continued)* **C.** Coronal section (slightly more posterior than the previous picture) shows marked atrophy of the temporal lobes. The temporal horns are dilated, and the anterior hippocampal formation (H) is greatly shrunken. **D.** Hematoxylin-eosin-stained section shows a plaque with an amyloid core (deeply eosinophilic central portion). Increased numbers of microglial cells are also evident. Amyloid angiopathy often accompanies AD. The amyloid in AD is composed of beta-amyloid, a form that is unique to AD. *(continued on next page)*

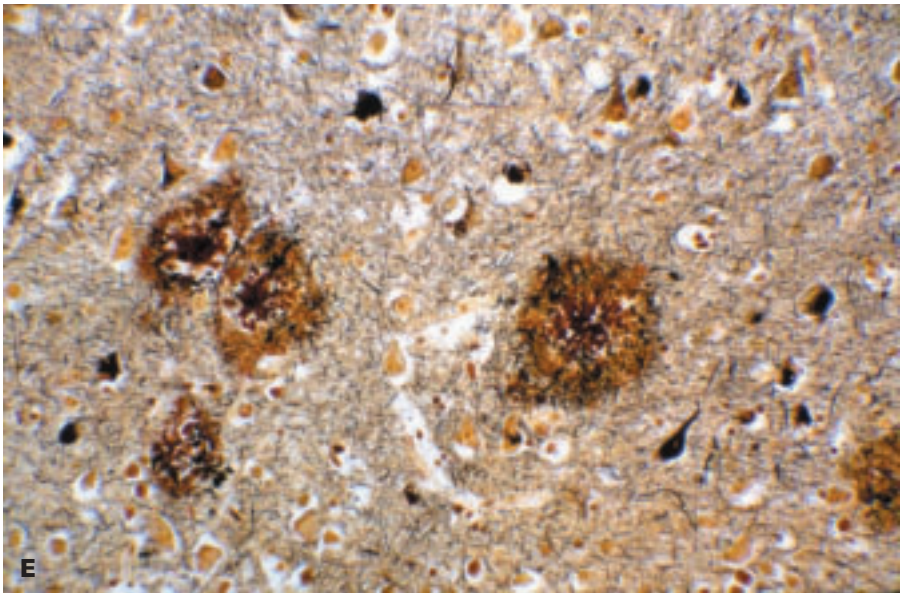

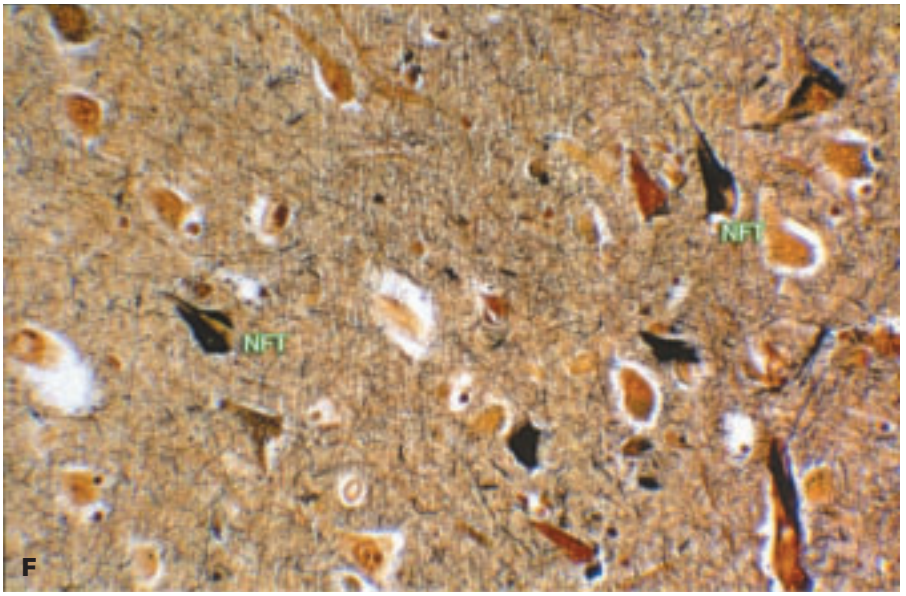

12-15. *(Continued)* **E.** Silver stain demonstrates several neuritic plaques (NPs) of AD that have a central dark brown core composed of amyloid. The periphery of each plaque bears silver positive neuritic processes. The diagnosis of AD is based on finding increased numbers of NPs for the patient's age. **F.** Multiple neurones are seen to contain neurofibrillary tangles in their cytoplasm. These tangles comprise accumulations of tau and MAP2 proteins and ubiquitin.

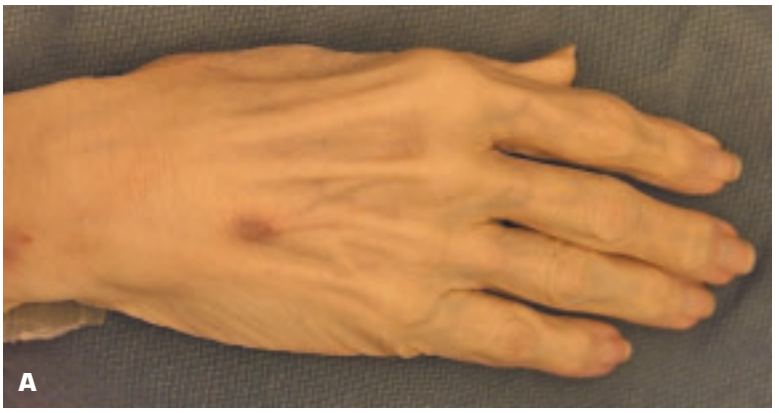

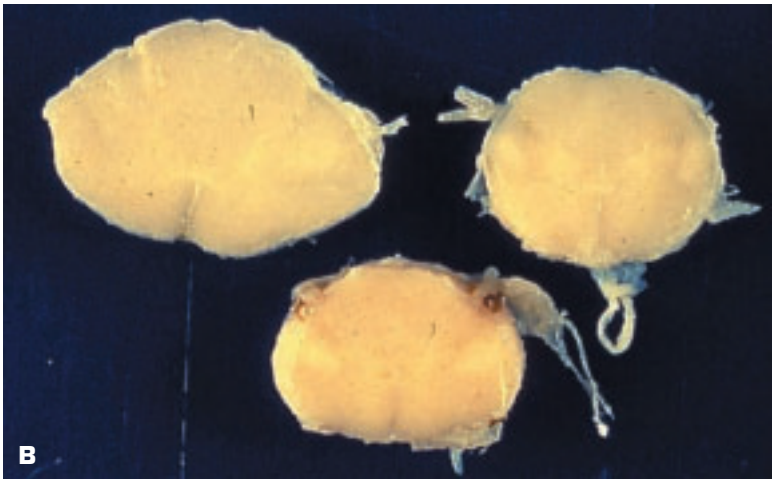

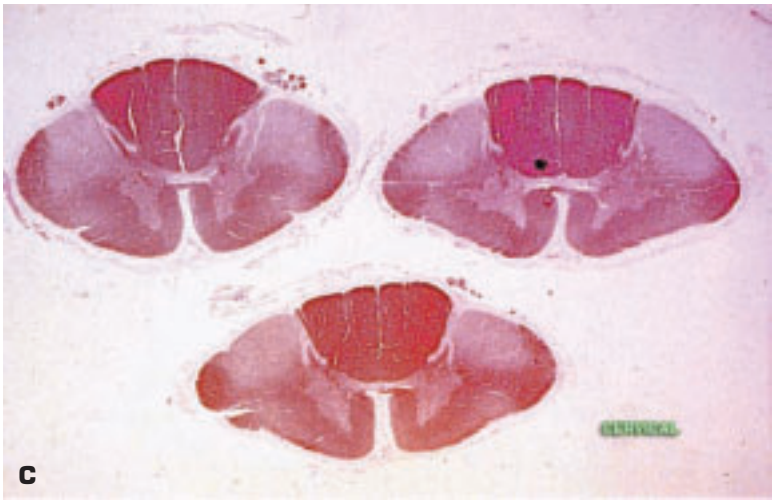

12-16. Amyotrophic lateral sclerosis (ALS) is the most common form of motor neurone disease, and it affects both upper and lower motor neurons. It is slightly more common in men, and up to 10% are familial, usually with an autosomal dominant inheritance. **A.** Atrophy of the interosseous muscles of the hand in ALS. **B.** Gross appearance of three levels of the spinal cord in ALS showing whitish discoloration of the lateral columns due to degeneration of the corticospinal tracts. **C.** Transverse sections of the cervical spinal cord stained with an immunostain against myelin basic protein shows loss of myelinated fibers in the lateral columns. *(continued on next page)*

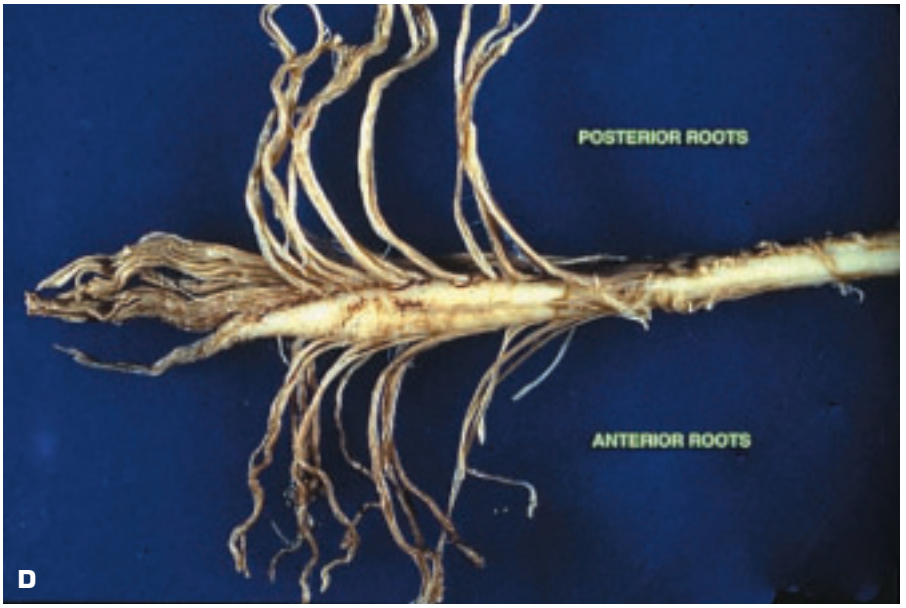

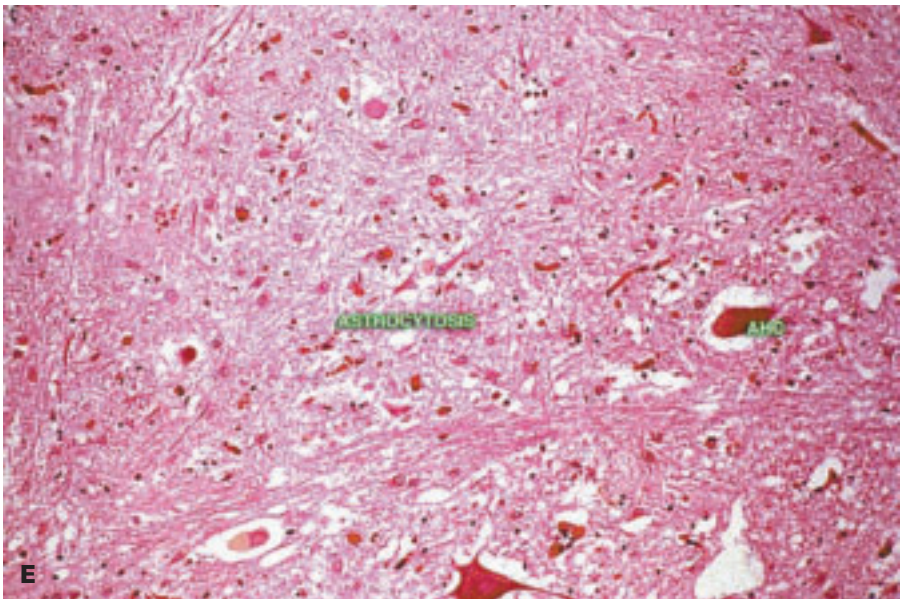

12-16. *(Continued)* **D.** Spinal cord shows marked atrophy of the anterior nerve roots (*below*) compared to the normal posterior (sensory) roots (*above*). **E.** Anterior horn of spinal cord shows significant loss of anterior horn cells with reactive gliosis.

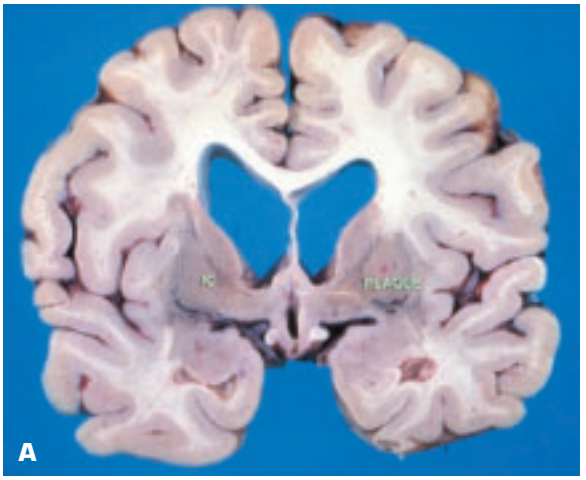

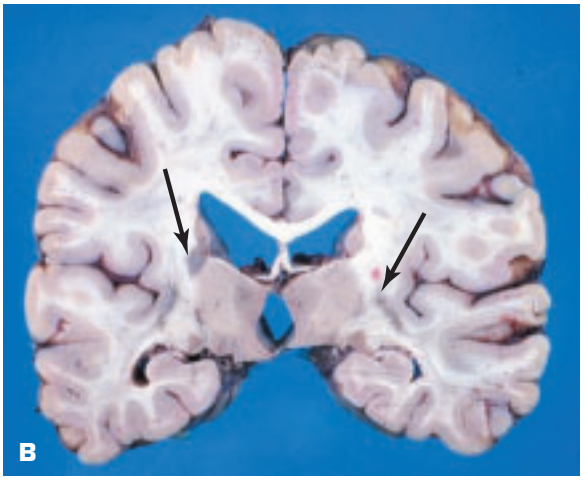

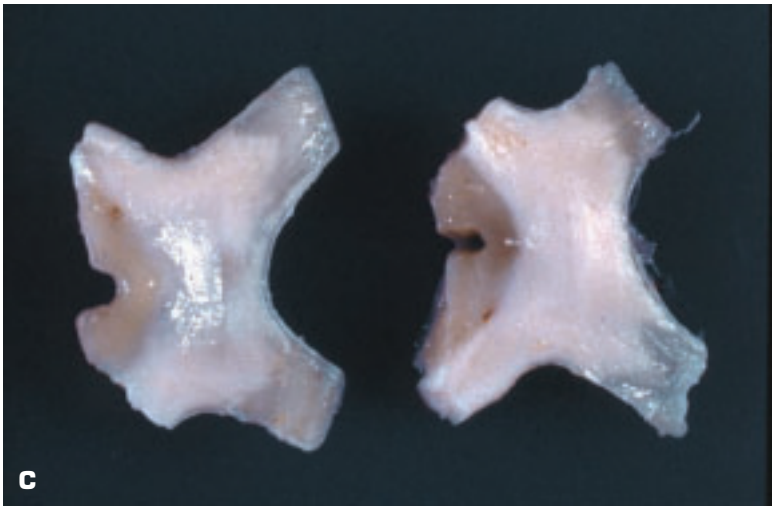

12-17. Multiple sclerosis (MS) shows variable clinical features according to the location of the pathological lesions. The acute lesions are due to an autoimmune inflammatory process with myelin loss. The Epstein–Barr virus may be implicated in its pathogenesis. Chronic pathology comprises sharply circumscribed areas of confluent loss of myelin with gliosis and partial loss of neurons. **A.** Coronal section at the level of the hypothalamus shows extensive plaque involvement of the basal ganglia bilaterally and also affecting both internal capsules. The white and gray matter is also extensively involved. Collapse of the internal capsules suggests neuronal loss in addition to demyelination. **B.** Coronal section at the level of the thalamus and the lateral geniculate bodies shows multifocal small plaques (*arrows*) in the white matter of the periventricular and perithalamic regions. **C.** Cross-sections through the optic chiasm showing extensive involvement by MS plaques. *(continued on next page)*

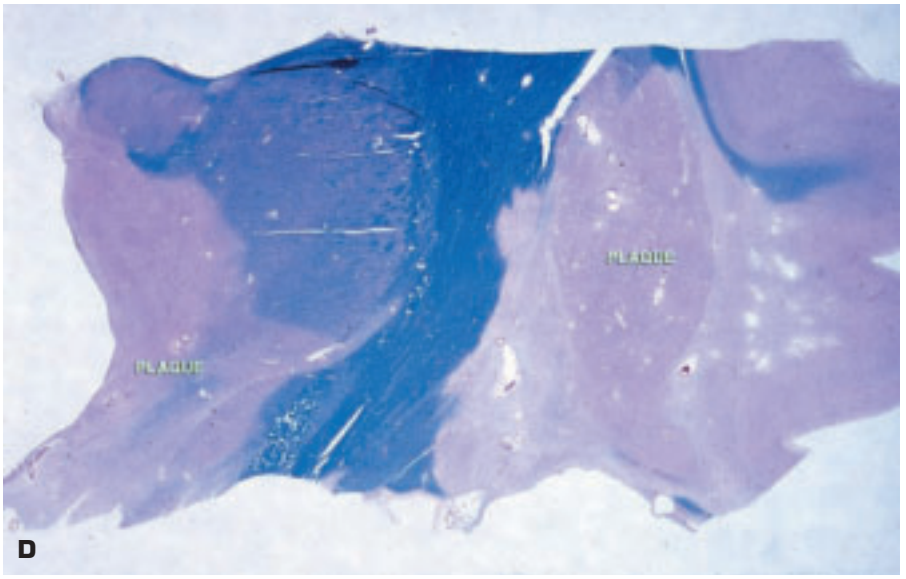

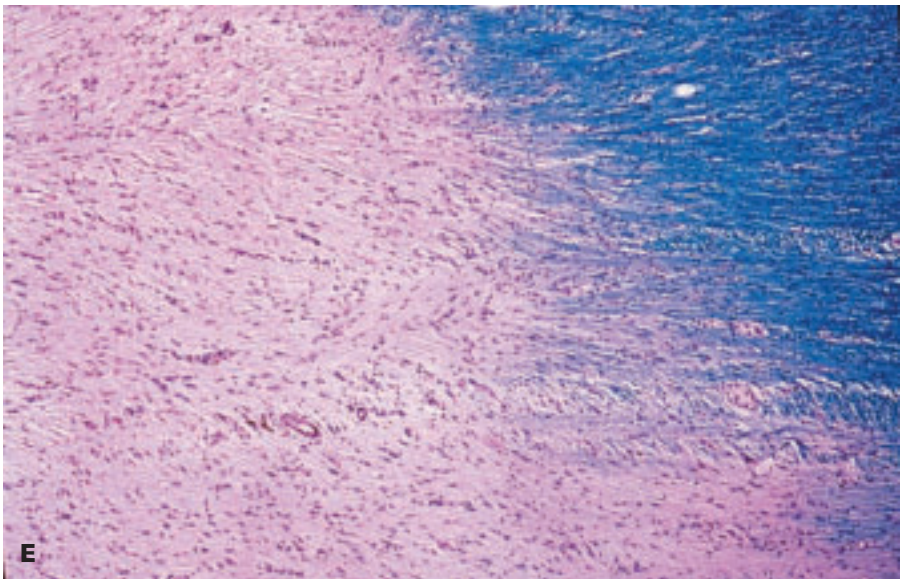

12-17. *(Continued)* **D.** Whole mount section of thalamus and hypothalamus stained by Luxol fast blue-periodic acid-Schiff stain for myelin shows MS demyelination plaques sparing the internal capsule. **E.** Higher-power view shows the edge of a plaque on the left, and myelinated fibers still stain blue on the right.

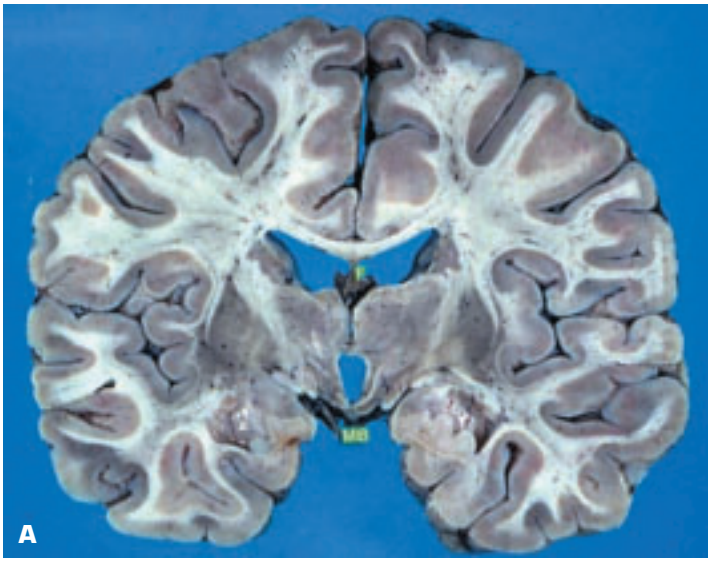

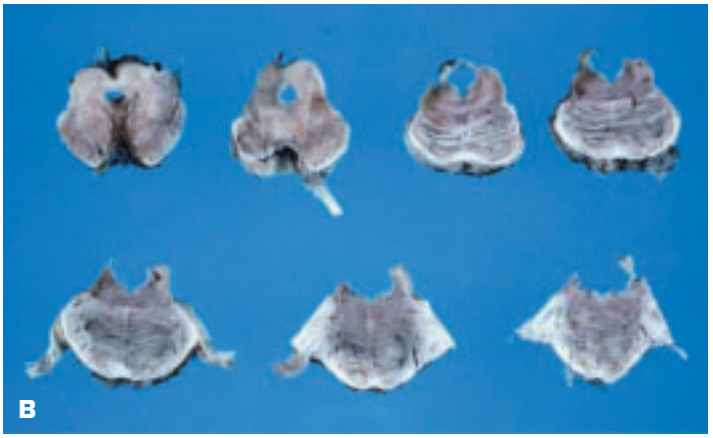

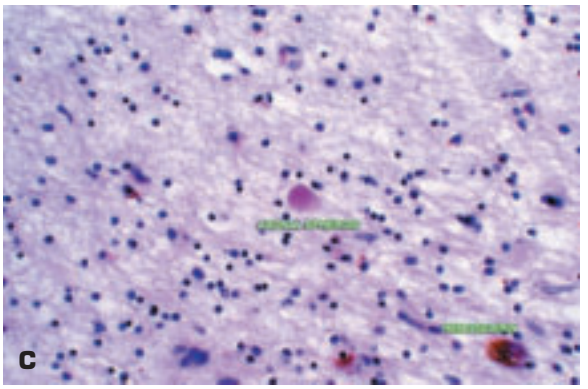

12-18. Diffuse axonal injury (DAI) is the most important mechanism producing long-term neurological deficits after closed head injury. DAI is secondary to axonal shearing that occurs from accelerative-decelerative forces on the brain during head trauma. **A.** Coronal section at the level of the hypothalamus shows shrinkage of the hypothalamus and enlargement of the third ventricle. There is discoloration of the fornices and the mamillary bodies (MB). The parasagittal white matter also appears discolored. **B.** Transverse sections through the rostral brainstem showing atrophy in the dorsolateral aspects of the midbrain and the pons. Note the enlarged cerebral aqueduct and rostral portion of the fourth ventricle. These areas are classical sites for involvement by shearing injury. **C.** This histological section of the pons shows the pathological hallmark of DAI, namely the presence of axonal spheroids that may persist for many years after the injury. Hemosiderin is present within an adjacent macrophage.

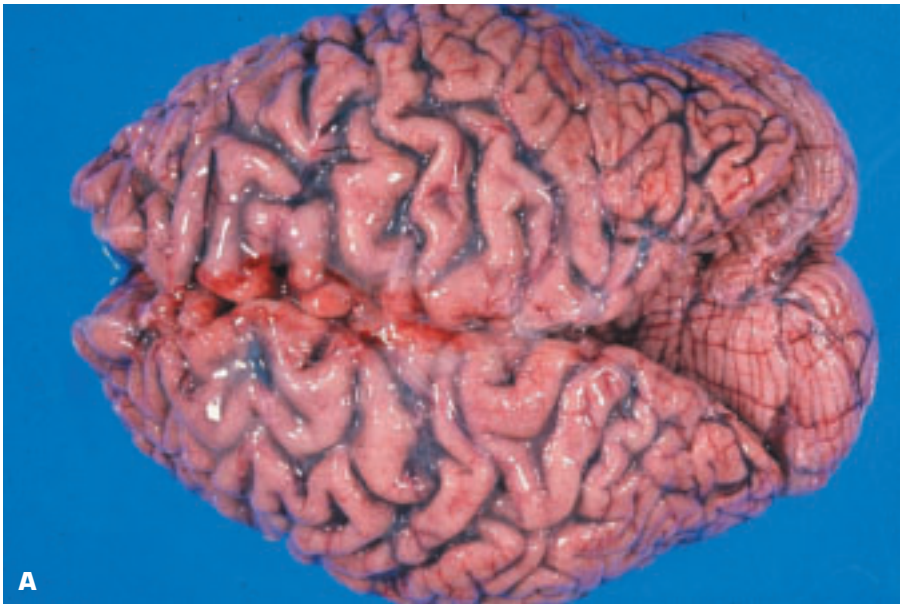

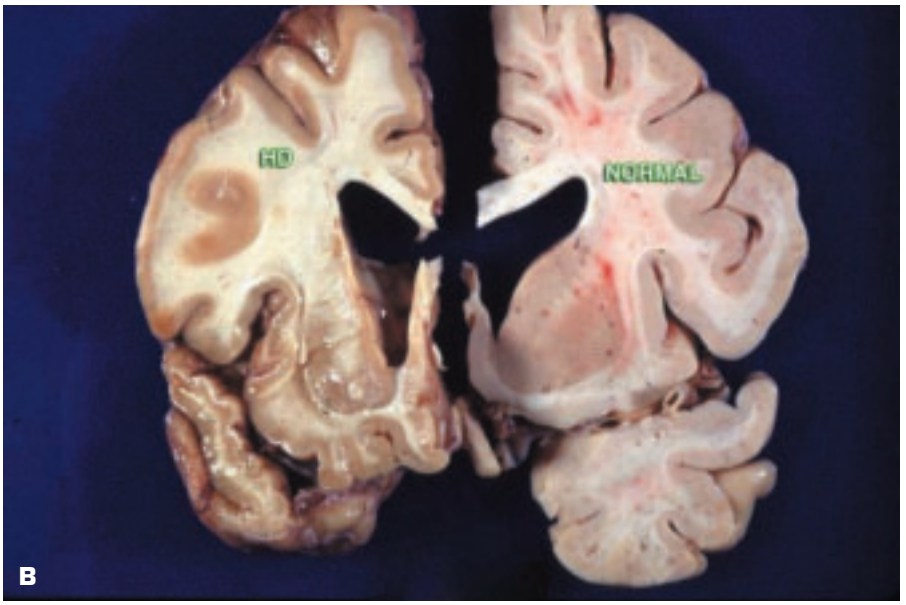

12-19. Huntington disease (HD) is an autosomal dominantly inherited neurologic disease characterized by chorea and cognitive decline. HD is the most common form of neurodegenerative disease due to an expansion of a CAG trinucleotide repeat in the affected gene (on chromosome 4p16.3) that codes for a novel protein (*huntingtin*). **A.** Unfixed brain from a patient with HD showing cortical atrophy with accentuation of the cortical sulci. **B.** Comparison of coronal brain sections of a patient with HD (*left*) and a normal patient (*right*). Note the swollen basal ganglia and dilated lateral ventricle in the HD slice. The HD slice also shows a reduction in cortical thickness plus a brownish discoloration of the gray matter. *(continued on next page)*

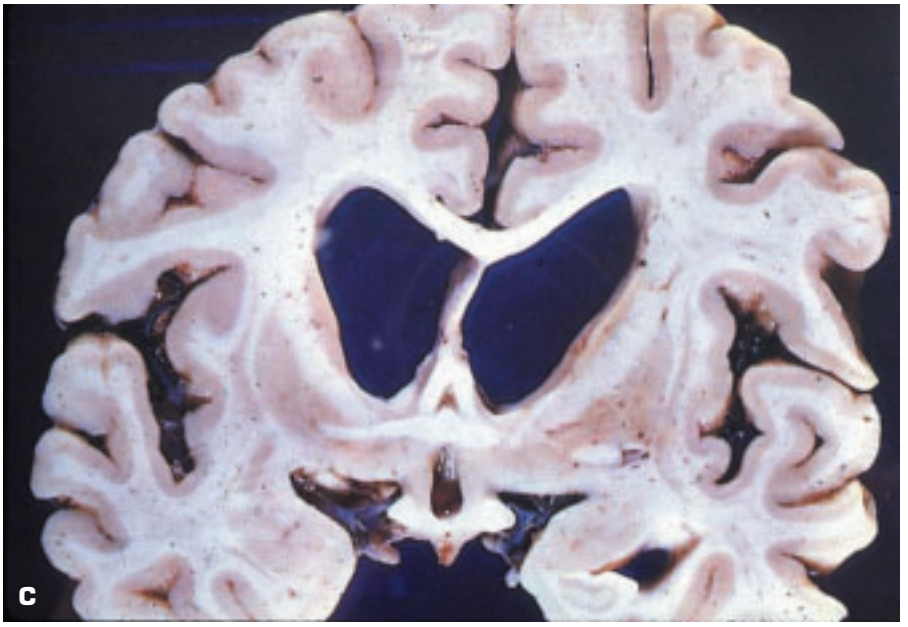

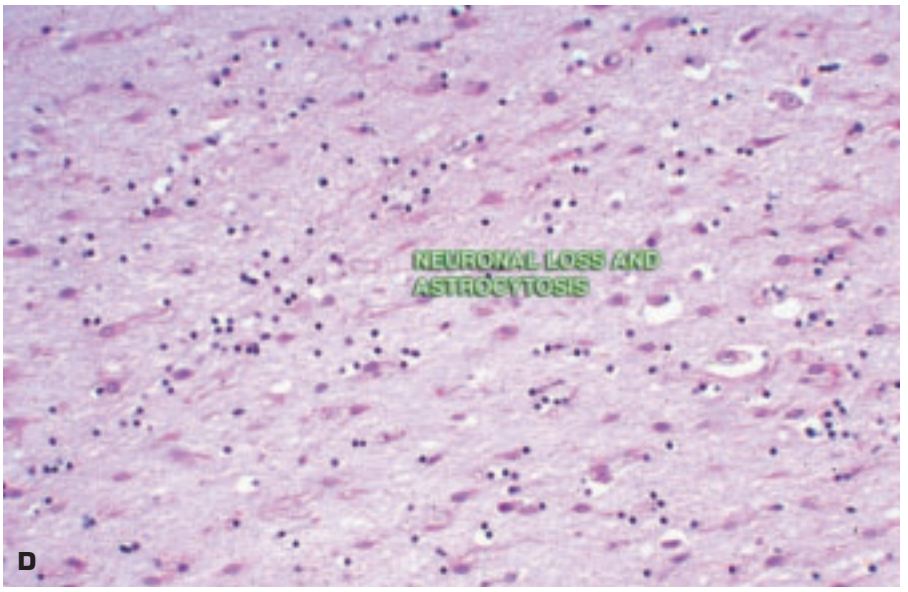

12-19. *(Continued)* **C.** Coronal section of HD brain showing enlarged lateral ventricles due to shrinkage of the caudate nucleus and the putamen. Cortical atrophy plus enlargement of the Sylvian fissures are also noted. The globus pallidus is also atrophic. **D.** Histology of the caudate nucleus in HD shows increased cellularity due to proliferation of astrocytes concomitant with the loss of most neurons. A characteristic feature of HD is intranuclear inclusions that stain positively with labeled antibody against *huntingtin*.

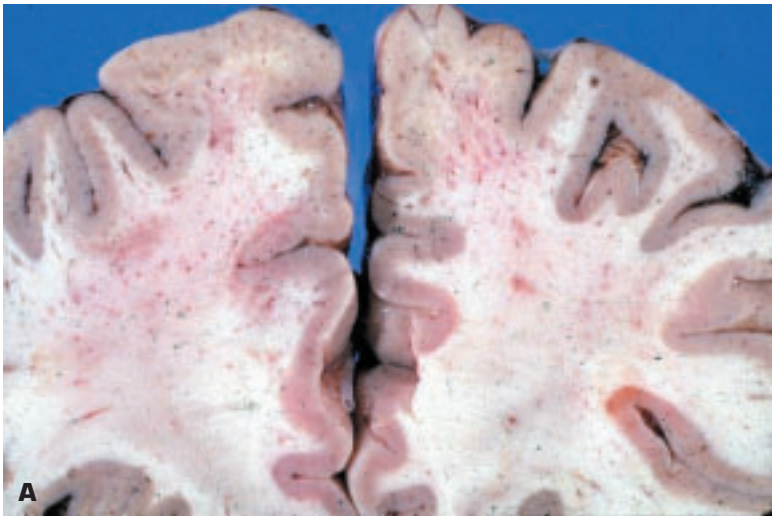

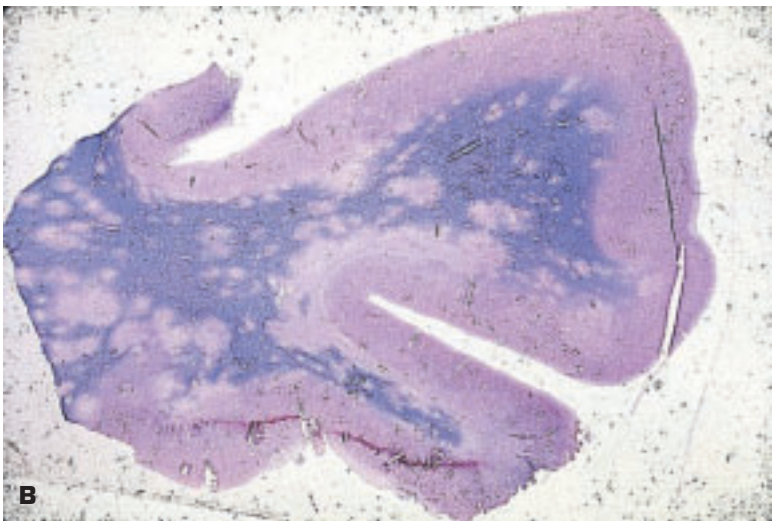

12-20. Progressive multifocal leukoencephalopathy (PML) is a fatal opportunistic viral infection caused by the JC virus in oligodendrocytes that presents as a subacute demyelinating disease. It may also occur in patients with HIV disease. **A.** Gross appearance of the brain in PML showing numerous areas of tan discoloration in the subcortical white matter. These plaques are not as discrete as those of multiple sclerosis. **B.** Whole mount section of the brain in PML showing multifocal, coalescing demyelinated lesions. *(continued on next page)*

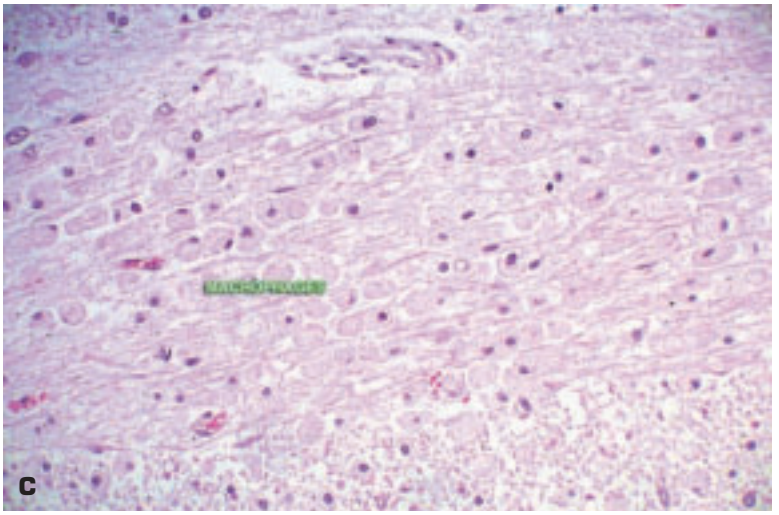

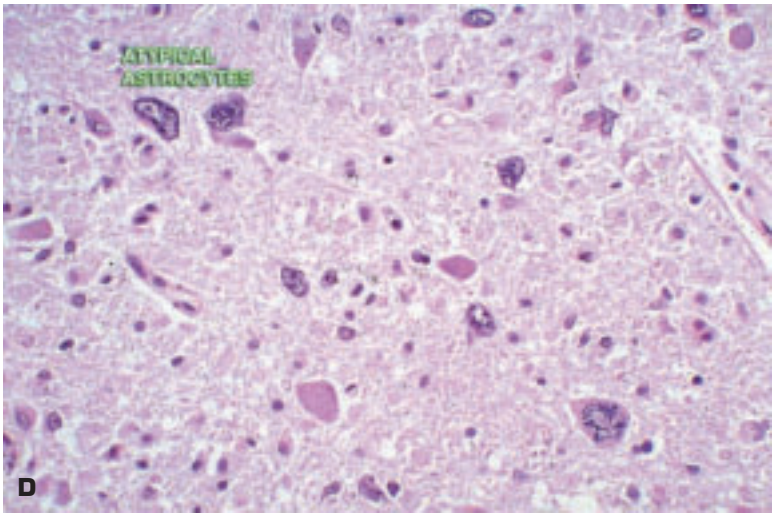

12-20. *(Continued)* **C.** Demyelinated lesion in PML shows abundant macrophages but no other inflammatory cells. **D.** Chronic PML has led to cytologically atypical astrocytes similar to those seen in glioblastoma multiforme due to incorporation of the viral genome into the host cells' genome.

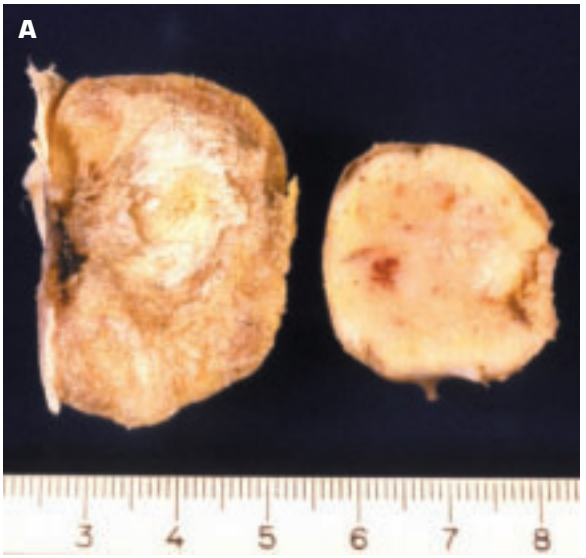

12-21. Meningioma is a tumor that arises from the arachnoid external to the brain, most commonly in a parasagittal situation. **A.** Meningioma is attached to the dura (*left*) and shows a central area of degeneration. **B.** This meningioma has spread to involve both sides of the dura (*center*).

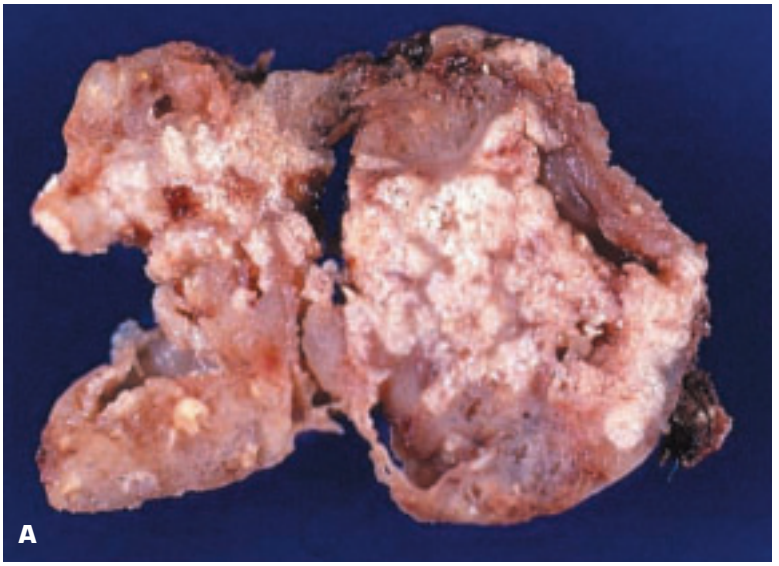

12-22. Craniopharyngioma (CP) is a benign neoplasm that arises above the sella turcica from the epithelium of Rathke's pouch. **A.** Multiloculated CP contains cheesy degenerated keratinous material, some of which is calcified. **B.** Lining of the CP comprises squamous epithelium with alternating areas of fibrovascular stroma. **C.** Section of brain showing a CP invading the hypothalamic region (*bottom center*).

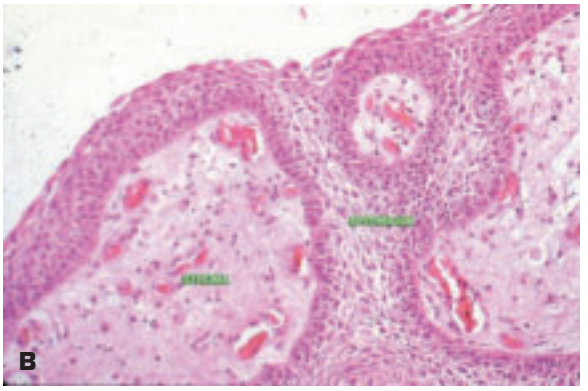

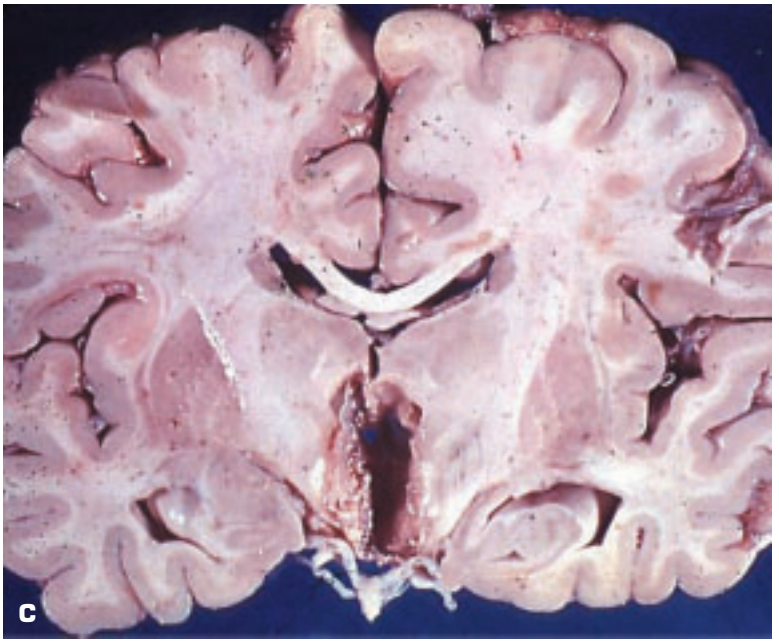

12-23. Astrocytic tumors vary from benign astrocytoma to anaplastic astrocytoma and glioblastoma multiforme. **A.** Mixed glioma of brain presenting as a small, circumscribed-appearing tumor. **B.** Glioblastoma multiforme (GM) is present (*arrow*) in this coronal section of brain at the level of the hypothalamus. An area of necrosis is present within the GM. **C.** Similar involvement (*arrow*) of the temporal and frontal lobes is seen in this coronal section slightly more posterior to the previous slice. Note the shift to the right. *(continued on next page)*

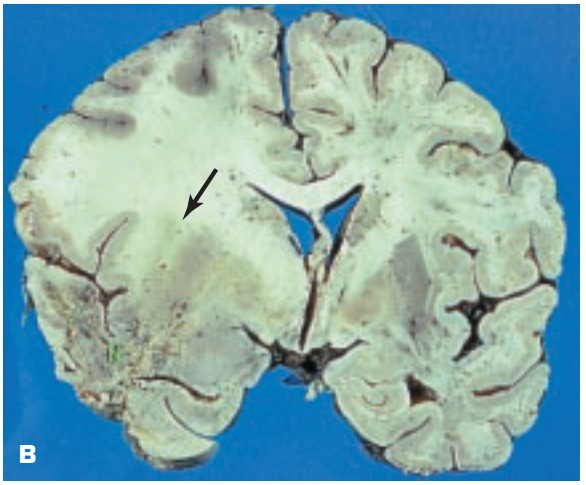

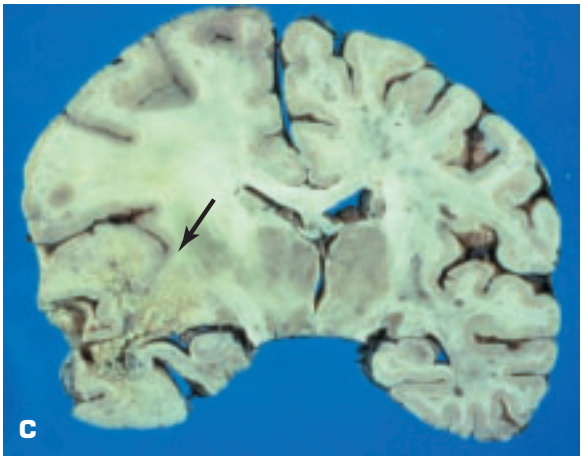

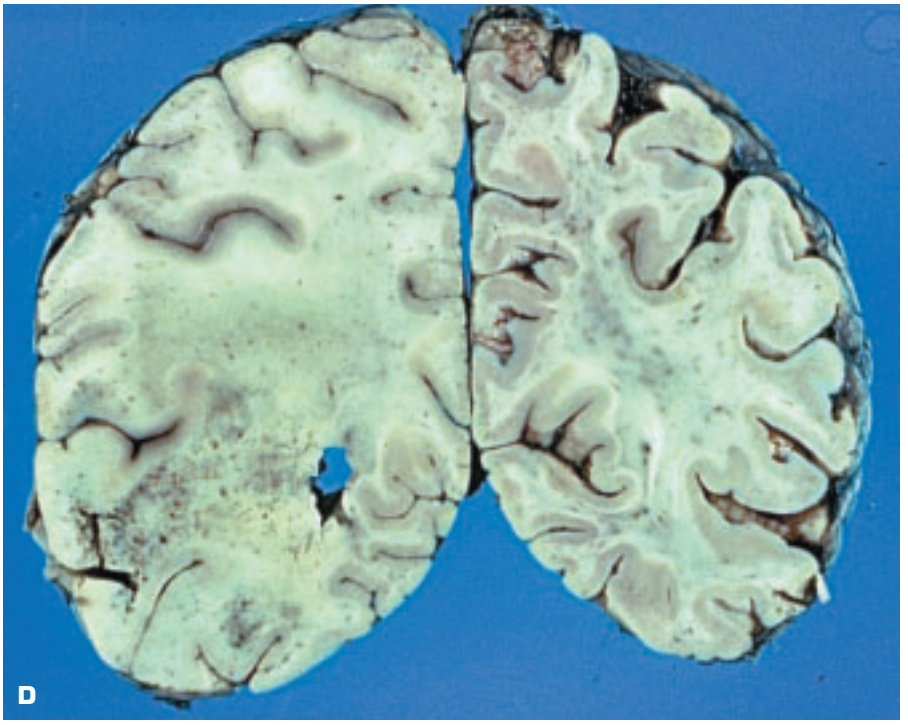

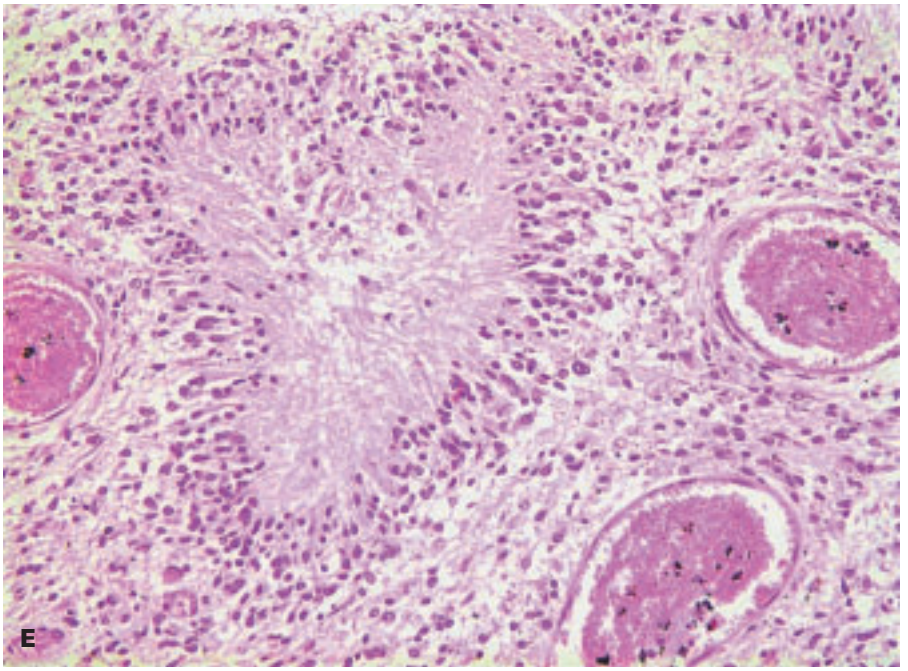

12-23. *(Continued)* **D.** Coronal section in the parietal and occipital regions shows typical features of an infiltrative glial tumor, namely distention of normal structures and blurring of anatomical margins plus focal necroses. **E.** Characteristic histologic pseudopalisading by tumor cells around an area of necrosis in a glioblastoma multiforme.

12-24. Medulloblastoma is the most common intracranial neuroblastic-derived lesion and always arises in the cerebellum in children. **A.** Cerebellum of a child shows overgrowth by medulloblastoma in the inferior midline (*top*) and over the leptomeninges. **B.** Whole mount section of cerebellum showing extensive infiltration of the leptomeninges by a medulloblastoma. **C.** Histology shows the medulloblastoma to be composed of small, dark blue tumor cells. A small area of necrosis is present (*arrow*).

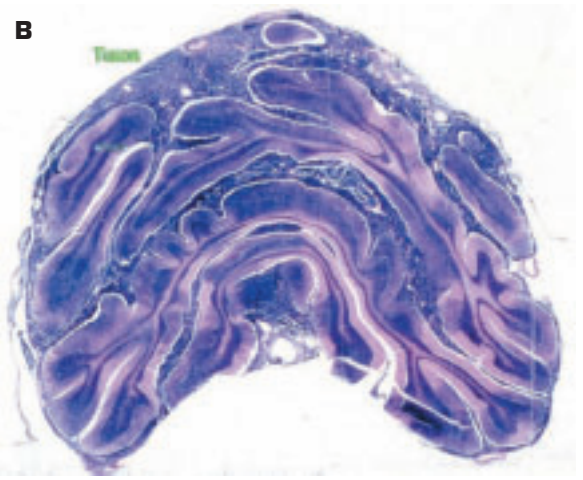

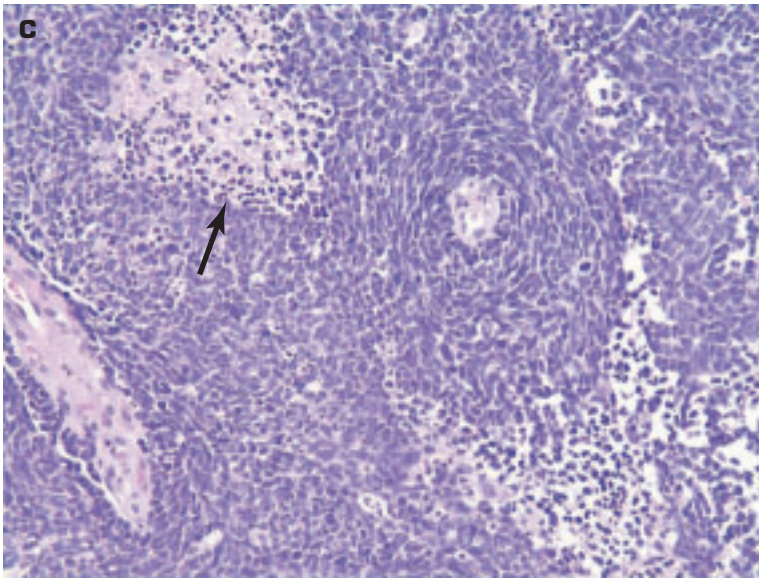

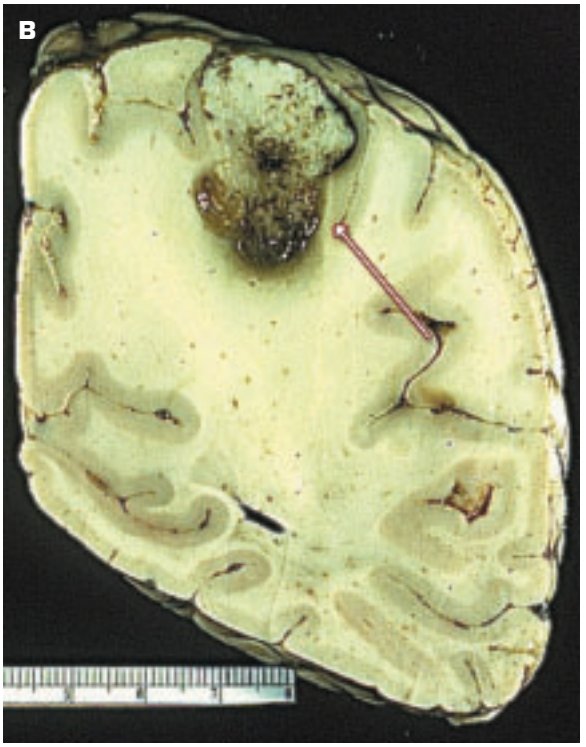

12-25. A. Metastatic cancer involving the cerebral cortex from below. **B.** Secondary lung adenocarcinoma (*arrow*) in the brain.

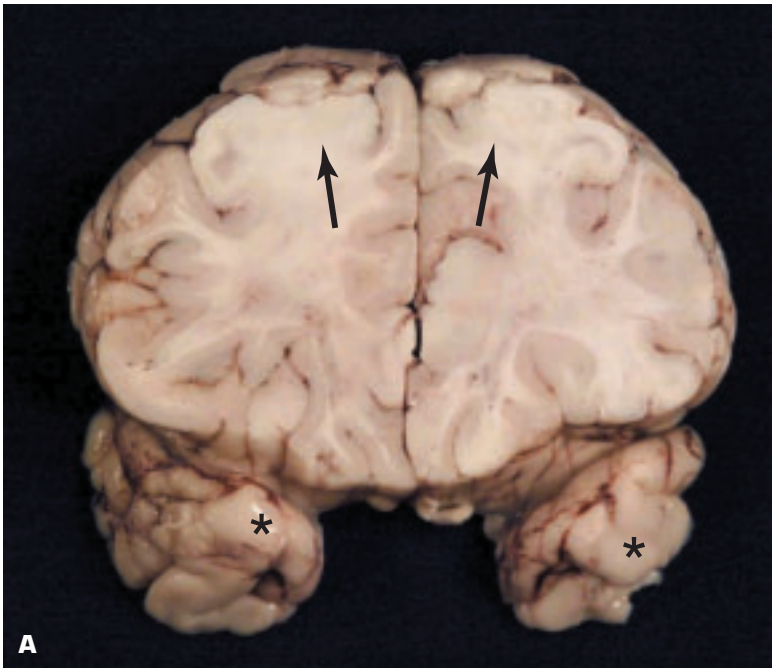

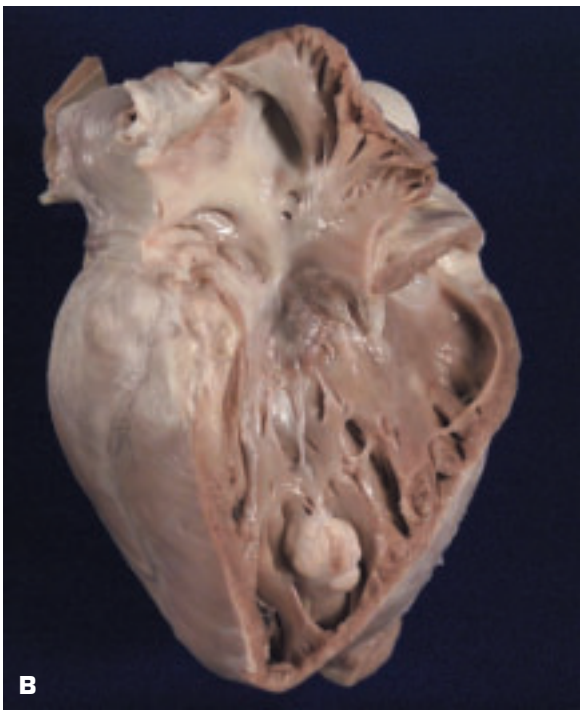

12-26. Tuberous sclerosis is an autosomal dominantly inherited disease that leads to hamartomas ("tubers") of the brain, retina, and viscera. **A.** Tubers are present parasagittally (*arrows*) and on both temporal lobes (*). **B.** Cardiac rhabdomyoma in the same patient with tuberous sclerosis.

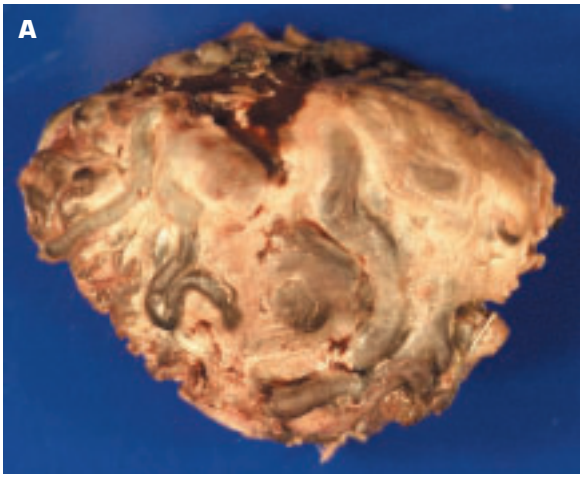

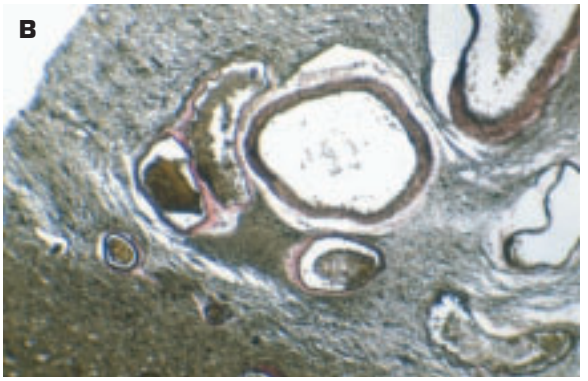

12-27. Arteriovenous malformation (AVM) of the brain is a congenital abnormality comprising multiple direct connections between arteries and veins with no intervening capillary circulation. Symptoms may develop later in life due to rupture or pressure on brain tissue, seizures may occur, or even heart failure may occur, mimicking dilated cardiomyopathy if the shunt is large. **A.** Surgically removed AVM shows brain tissue containing blood vessels having a "bag of worms" appearance due to dilatation and elongation secondary to the greatly increased flow resulting from high arterial pressure leading directly into low venous pressure vessels. Endovascular treatment or radiosurgery may be used to treat AVM. **B.** Histology of the lesion shows a mixture of dilated arteries and veins coursing through the cerebral tissue. **C.** AVM surgically removed from the spinal cord.

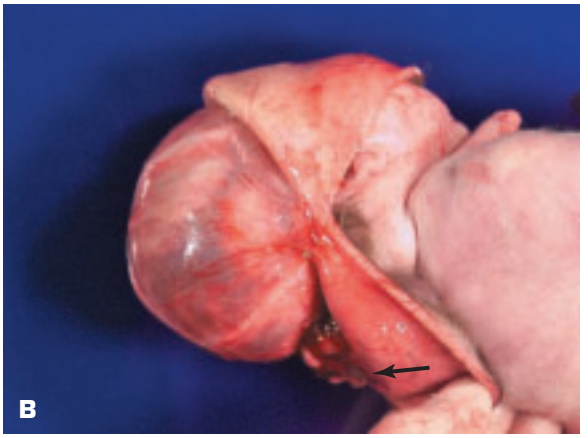

12-28. An encephalocele occurs when the neural tube fails to close completely, resulting in portions of the brain and its membranes protruding from the skull in a sac-like formation. Like spina bifida, this "cranium bifida" may be linked to maternal folic acid deficiency during pregnancy (among other causes). **A.** Posterior encephalomeningocele is elevating the skin over the lower back of the head. **B.** Sac comprising brain and membranes is present (*arrow*), just deep to the reflected scalp. **C.** Following removal of the brain, the circular defect in the lower posterior skull through which the encephalomeningocele protruded is clearly seen (bottom hole near lowest forceps).

12-29. Anencephaly is another neural tube anomaly. It is characterized by the absence of scalp, calvarium, and normal brain, which is substituted by an angiomatous mass. This figure shows a bisected newborn with anencephaly. The upper spinal cord ends at the site of maldevelopment of the anterior end of the neural tube.

12-30. Holoprosencephaly, a developmental field defect of impaired midline cleavage of the embryonic forebrain in which the facial appearance predicts the brain anatomy in about 80% of cases, may show a range of appearances. The most extreme form is cyclopia in which there is a single midline eye. The illustrated fetus shows two closely set eyes, arhinia, and a proboscis formation on the forehead. The brain had failed to cleave into two cerebral hemispheres, and no olfactory tracts or bulbs were present.

INDEX

M

N

O

W

Y

Z